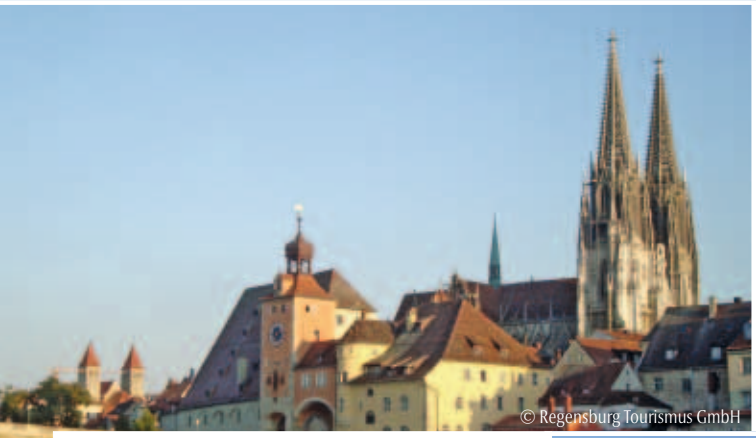

MC 2013 Regensburg

August 25–30, 2013
University of Regensburg
Regensburg/Germany

Universität Regensburg

Organizers

DGE – German Society for Electron Microscopy e. V.

ASEM – Austrian Society for Electron Microscopy

SSOM – Swiss Society for Optics and Microscopy

CMS – Croatian Microscopy Society

CSMS – Czechoslovak Microscopy Society

HSM – Hungarian Society for Microscopy

SDM – Slovene Society for Microscopy

SISM – Italian Society of Microscopical Sciences

SSM – Serbian Society for Microscopy

TEMD – Turkish Society for Electron Microscopy

EMS – European Microscopy Society

Plenary Lectures • Poster Sessions • Workshops • Industrial Exhibition

PROCEEDINGS
LIFE SCIENCES (LS)
MULTIMODAL AND INTERDISCIPLINARY MICROSCOPIES (MIM)

MC 2013 PROCEEDINGS

Core/shell Nanostructures Embedded in Solid

V. R. Radmilović[1,2]

[1]University of Belgrade, Faculty of Technology and Metallurgy, Nanotechnology and Functional Materials Laboratory, 11120 Belgrade, Serbia.
[2]National Center for Electron Microscopy, Lawrence Berkeley National Laboratory, Berkeley, CA 94720, USA.

VRRadmilovic@tmf.bg.ac.rs; VRRadmilovic@lbl.gov

Keywords: aberration-corrected HRTEM, core/shell nanostructures, light element imaging.

This study illustrates the importance of understanding the fundamental features that underlie the behavior of nanoscale phases with coherent interfaces embedded in a solid and their role in the evolution of microstructure in materials. The fundamental principles established using model systems are employed in the design and testing of new materials such as systems for energy-related applications. Key requirements for advanced alloys are high strength, light weight, coarsening resistance, corrosion resistance, high temperature stability, etc. Unfortunately, these requirements are mutually exclusive in many Al-based alloys. The extraordinary effects on mechanical properties arising from the formation of second-phase particles are well known, and exploited in applications ranging from energy generation to aerospace structures [1].

Al-Li and Al-Sc alloys are of great interest for aerospace and cryogenic applications due to their low density and high strength-to-weight ratio. The excellent mechanical properties of these alloys are based on a fine dispersion of coherent Al_3Li metastable and Al_3Sc stable precipitates. The aim of this report is to show the effect of Li addition on core/shell precipitate formation in the ternary Al-Li-Sc alloys. The atomic structure of these precipitates has been studied by a range of advanced microscopy techniques, such as high resolution TEM with exit wave reconstruction, atomic resolution HAADF imaging, and energy filtered electron energy loss spectroscopy (EELS), combined with the first principle calculation and continuum thermodynamic modeling to uncover the role of Li. We demonstrated that monodisperse Al_3LiSc core/shell ordered precipitates with a Sc and Li-rich core surrounded by a Li-rich shell can be created via a two-stage heat treatment. During the first aging stage at 450°C, Li incorporation into the cores leads to a burst of nucleation followed by rapid depletion of Sc solute. In the second stage, at 190°C, $Al_3(LiSc)$ cores become spherical substrates for solid-state epitaxial growth of Al_3Li, which leads to shell formation through a barrier-less process of solid state wetting [2]. The thickness of the core and shell are anti-correlated, such that the size distribution of the total core-shell particle is narrower than that of either the core or the shell. Li-rich shell shows almost no compositional differences between adjacent columns. By contrast, the core superlattice columns are highly disordered, evidence for random mixing of Li and Sc on these sites. The columns surrounding the superlattice columns are very uniform, showing the amount of solute atoms occupying these sites to be negligible. In fact, no anti phase boundary (APB) defects were observed in any of the investigated $Al_3(LiSc)$ core/shell precipitates. These defects are known to be very energy-costly at room temperature, i.e. 290 mJ/m^2 in Al_3Sc [3] and 118 mJ/m^2 in Al_3Li [4]. The first principle calculation predicts that the core-shell precipitates in the investigated AlLiSc alloy to be thermodynamically stable phases, with no driving force for the diffusion of Li out of the core into the shell. High-resolution phase contrast imaging and geometric phase analysis shown in Figure 1a and b, respectively, reveal that both, the core and the shell are fully ordered in the $L1_2$ structure and fully coherent with the surrounding fcc matrix. With prolonged aging time, for more than 1000h at 190°C, these particles exhibit coarsening, and create an interfacial dislocation at the Al_3Li shell/Al matrix interface, in order to accommodate coherent strain increase due to misfit in their lattice parameters, as shown in Figure 2a and b. Aberration corrected transmission electron microscopy was employed to image Li using exit wave reconstruction [5]. The phase of the exit wave shown in Figure 3 distinguished clearly Al columns from Li columns in the Li rich $L1_2$ shell [6]. Li concentration in the core could be calculated from scanning transmission electron microscopy of $Al_3(LiSc)$ nanoparticles. This procedure uses an analysis technique that normalizes the signal from the $L1_2$ superlattice columns to the immediately adjacent pure Al columns. By knowing that the total amount of Sc and Li is 25 at.%, the composition of each column can be determined individually. This calculation shows appreciable and uniform incorporation of 9.7 ± 2.4 at.% Li in the core of the precipitates. For this ternary AlLiSc alloy we show a way of producing an uniform distribution of coarsening resistant monodispersed $Al_3(LiSc)$ core/shell particles in an Al matrix with unusually narrow size distribution. A detailed analysis of these precipitates has provided important insights into their atomic structure and composition [7].

1. K. Lu, Science 328 (2010) 319.
2. V. Radmilović et al., Nature Materials 10 (2011) 710.
3. K. Fukunaga et al., Materials Science and Engineering A239–240 (1997) 202.
4. S.M. Jeon and J.K. Park, Acta Materialia 44 (1996)1449.
5. Y. Shao-Horn et al., Nature Materials 2 (2003) 464.
6. M. Rossell et al., Physical Review B 80 (2009) 024110.
7. I would like to thank to my former graduate students, post-docs and colleagues at The National Center for Electron Microscopy at Berkeley and at The University of Belgrade, Serbia, for their contributions to this project. This research is supported by the Department of Energy under contract no. DE-AC02-05CH11231. Supports of Nanotechnology and Functional Materials Center, funded by the European FP7 project No. 245916, and from the Ministry of Education and Science of the Republic of Serbia (project No. 172054), are also acknowledged.

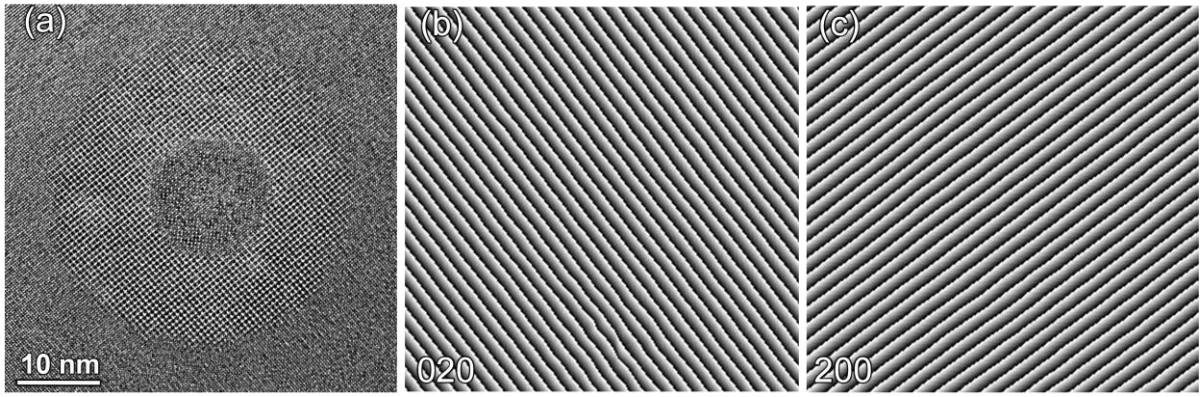

Figure 1. (a) HRTEM micrograph of a single $Al_3(LiSc)$ core-shell precipitate obtained at peak aging, after 4h at 190°C; (b) and c) Moire images created using 020 and 200 reflections in digital diffractogram, respectively, showing perfect alignment of {200} planes in both, Al matrix and core/shell precipitate; no dislocations at Al_3Li shell/Al matrix interface are present.

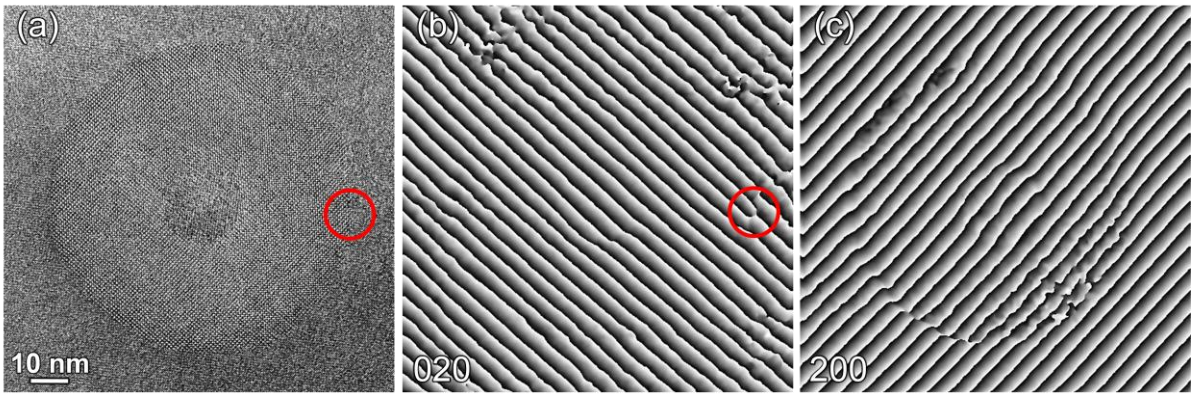

Figure 2. (a) HRTEM micrograph of a single $Al_3(LiSc)$ core-shell precipitate obtained from overaged sample, after 1000h at 190°C; (b) and (c) Moire images created using 020 and 200 reflections in digital diffractogram, respectively, showing significant distortion of {200} planes and the presence of dislocation at the Al_3Li shell/Al matrix interface (in the red circle).

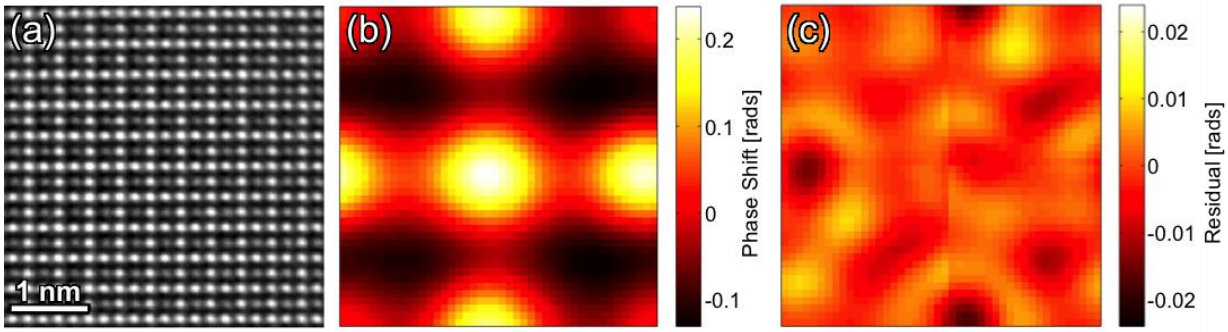

Figure 3. (a) Experimental high resolution exit wave phase image of Al_3Li ordered structure taken close to [001] zone axis; white dots are from Al columns and gray dots are from Li columns; (b) and (c) are 2D representation of the statistics of the experimental data, shown as the average experimental unit cell and the standard deviation image.

Scanning transmission electron microscopy (STEM) and analytical electron microscopy of biological and nano materials

R. D. Leapman[1], J. Zhang [2], J. S. Diamond[2], X. Chen[3], T. S. Reese[3], A. A. Sousa[1]

1. Laboratory of Cellular Imaging & Macromolecular Biophysics, NIBIB, National Institutes of Health, Bethesda, MD 20892, USA
2. Synaptic Physiology Section, NINDS, National Institutes of Health, Bethesda, MD 20892, USA
3. Laboratory of Neurobiology, NINDS, National Institutes of Health, Bethesda, MD 20892, USA

leapmanr@mail.nih.gov
Keywords: STEM, analytical EM, electron tomography

The scanning transmission electron microscope (STEM) offers high collection efficiency for signals generated by interaction of a finely focused, nanometer-sized, electron probe, which makes STEM well suited for analyzing beam-sensitive biological specimens [1]. In particular, elastically scattered electrons collected by the STEM's annular dark-field detector (ADF) yield a signal that is proportional to the mass of a biological structure contained within the volume illuminated by the probe. This mass mapping technique enables molecular weights of large protein assemblies to be determined [2,3]. For example, it is possible to characterize the organization of subunits in filamentous proteins that have indefinite total mass but well defined mass-per-length, such as disease-associated amyloid fibrils [4,5]. The strong ADF elastic scattering signal from heavy atoms can also be applied to visualize heavy atom clusters, which are used to label specific protein assemblies in their cellular context [6].

By collecting the inelastic scattering signal using an electron energy loss spectrometer (EELS), it is possible to quantify the distributions of metal ions and low atomic number atoms contained within macromolecular complexes or subcellular compartments [7,8]. The STEM-EELS spectrum-imaging technique enables weak spectral features to be extracted, e.g., to measure minute concentrations of calcium, an important regulatory element, in specific subcellular compartments of freeze-dried preparations of cells and tissues [9]. It has also been possible to detect the iron cores of individual ferritin molecules distributed in regions of unstained brain, where iron regulates important cellular processes and, when stored as ferritin, gives rise to magnetic resonance imaging contrast [10].

A combination of STEM and EELS has been used in a number of laboratories to analyze the structure and composition of hybrid organic-inorganic bio-nanoparticles developed as diagnostic and therapeutic reagents in applications to nanomedicine [11-13].

Important advantages can be realized when the STEM is employed to perform electron tomography [14-20]. We have demonstrated that STEM tomography enables determination of the three-dimensional ultrastructure of embedded cells sectioned to a thickness of 1 to 2 μm [17-19]. Such specimens are considerably thicker than can be analyzed by conventional TEM tomography, for which resolution is limited by chromatic aberration of the objective lens due to multiply inelastic scattering. We have utilized a probe of small angular convergence (approximately 1 mrad) to give a diffraction-limited probe size of about 1 nm. The small angular convergence also results in a large depth-of-field throughout the specimen thickness since geometrical spreading of the probe is only a few nanometers. Moreover, the use of an on-axis bright-field detector reduces effects of beam broadening, since most electrons that undergo multiple elastic scattering in the lower part of thick specimens do not reach the detector (Fig. 1). Therefore, spatial resolution in bright-field STEM tomograms is improved relative to STEM tomograms acquired with an annular dark-field detector [17].

We have recorded dual-axis bright-field STEM tomograms in an FEI Tecnai TF30 transmission electron microscope equipped with a Shottky field emission gun operating at an acceleration voltage of 300 kV. Specimens were prepared by fixation, dehydration, embedding, ultramicrotomy and post-staining, with or without rapid freezing and freeze-substitution. Gold nanoparticles were deposited on the top and bottom surfaces of the sections to aid in alignment of the tilt series. Images were acquired over an angular range of ±54° after pre-irradiation with a broad beam in TEM mode to stabilize ultrastructure. Tomograms were reconstructed by means of the IMOD program (University of Colorado) [21], and were visualized with the Amira software package.

The STEM tomography approach is ideally suited to visualizing whole neuronal synapses, which have dimensions of order 0.5 to 1 μm, and for making quantitative measurements on the numbers, sizes and shapes of synaptic components. For example, we have applied the technique to study the architecture of two types of retinal ribbon synapses, which are specialized structures at presynaptic active zones encoding a wide dynamic range of sensory signals through continuous vesicle release. We have applied the technique to determine the full 3D architecture of ribbon synapses in mammalian (rat) cone photoreceptor cells and rod bipolar cells as shown in Fig. 2 [22,23].

In another application of STEM tomography, we have reconstructed entire spine postsynaptic densities (PSDs) in cortical regions of mouse brain. It was possible to determine the thickness, shape and area of PSDs for every synapse within defined 60 μm^3 volumes of neuropil [24]. STEM tomography of thick sections provides a useful approach for determining the nanoscale structure of entire synapses in different types of neuronal tissues, which can help to gain insight into specialized synaptic function.

In summary, the STEM offers a variety of quantitative imaging modes for identifying heavy-atom labels, determining molecular mass, measuring elemental content, and elucidating the 3D structure of biological and bio-nanomaterials [25].

1. A.V. Crewe and J.S. Wall, *J. Mol. Biol.* 48 (1970) 375.
2. A. Engel, *Ultramicroscopy* 3 (1978) 273.
3. J.S. Wall and J.F. Hainfeld, *Ann. Rev. Biophys. Biophys. Chem.* 15 (1986) 355.
4. A.T. Petkova, et al., *Proc. Natl. Acad. Sci. USA* 99 (2002) 16742.
5. N. Norlin et al., *J. Struct. Biol.* 180 (2012) 174.
6. J.F. Hainfeld, *Science* 236 (1987) 450.
7. R.D. Leapman et al., *Ultramicroscopy* 49 (1993) 225.
8. R.D. Leapman, *J. Microsc.* 210 (2003) 5.
9. J. Feng, A.V. Somlyo and A.P. Somlyo, *J. Microsc.* 215 (2004) 92.
10. M. Fukunaga et al. *Proc. Natl. Acad. Sci. USA* 107 (2010) 3834.
11. M.M. van Schooneveld et al., *Nature Nanotech.* 5 (2010) 538.
12. R.D. Leapman, *Nature Nanotech.* 5 (2010) 480.
13. A.E. Porter et al., *Nature Nanotech.* 2 (2007) 713.
14. P.A. Midgley et al., *Ultramicroscopy* 96 (2003) 413.
15. I. Arslan, J.R. Tong and P.A. Midgley, *Ultramicroscopy* 106 (2006) 994.
16. A.E. Yakushevska et al., *J. Struct. Biol.* 159 (2007) 381.
17. M.F. Hohmann-Marriott et al., *Nature Methods* 6 (2009) 729.
18. A.A. Sousa et al., *Ultramicroscopy* 109 (2009) 213.
19. A.A. Sousa et al., *J. Struct. Biol.* 174 (2011) 107.
20. N. de Jonge and F.M. Ross, *Nature Nanotech* 6 (2011) 695.
21. J.R. Kremer, D.N. Mastronarde and J.R. McIntosh, *J. Struct. Biol.* 116 (1996) 71.
22. J.S. Diamond, *Nature Neuroscience* 14 (2011) 1097.
23. J. Zhang et al., *Proc. ARVO* (2012) 4318.
24. X. Chen et al., *J Neurosci.* 31 (2011) 6329.
25. This research was supported by the intramural programs of NIBIB and NINDS, NIH.

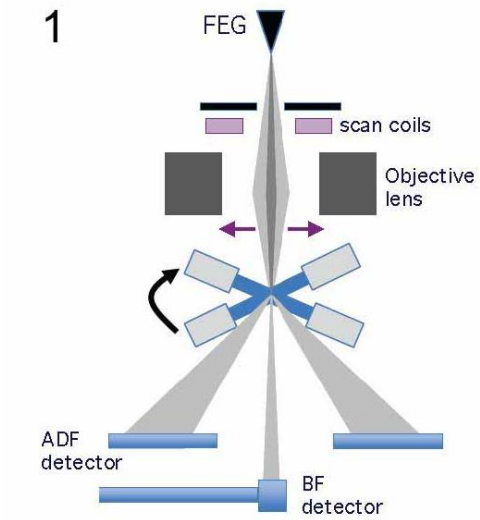

Figure 1. Schematic diagram of STEM tomography acquisition showing field-emission gun (FEG), scan coils, objective lens, and high-angle annular dark-field (ADF) and axial bright-field (BF) detectors.

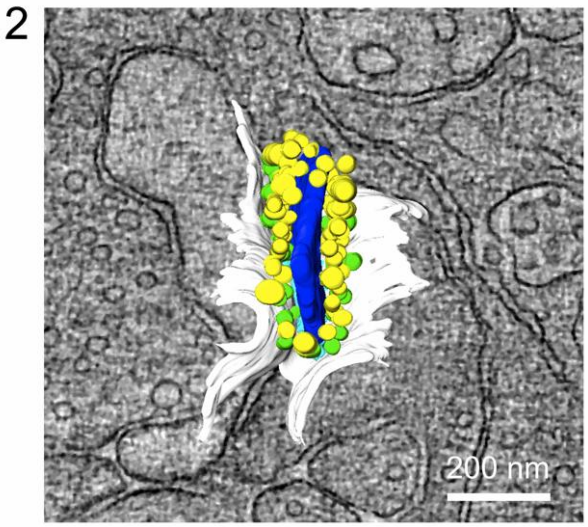

Figure 2. Ortho-slice through portion of dual-axis STEM bright-field tomogram of 1.2-µm thick section of stained rat retina, with superimposed visualization of entire ribbon synapse in cone photoreceptor cell. A central ribbon is evident with a series of docked vesicles (yellow); vesicles that are adjacent to the membrane are shown in green.

Three-dimensional imaging and analysis at the nanoscale by optical sectioning and confocal methods in the transmission electron microscope

P. D. Nellist[1]

[1]Department of Materials, University of Oxford, Parks Road, Oxford, OX1 3PH, UK.

peter.nellist@materials.ox.ac.uk
Keywords: optical sectioning, confocal, 3D

The development of hardware correctors for the spherical aberration of electron lenses has resulted in dramatic improvements in the resolution of electron microscopes (for example [1]). The resolution improvement arises from the increase in numerical aperture allowed by the aberration correction. Increase in numerical aperture results in a reduction in the depth of focus of the microscope, with the depth of focus depending on the inverse square of the numerical aperture. In a state-of-the-art transmission electron microscope (TEM), the depth of focus may be just a few nanometres, which can often be smaller than the thickness of the TEM sample. Although this situation may be regarded as a problem, one could say that the aberration corrector has *improved* the depth resolution to the point where features can be resolved in samples in three-dimensions (3D).

Early work by Van Benthem et al. [2] showed that the height of single impurity atoms in a sample could be determined from their visibility in a focal series of images using annular dark-field imaging in the scanning TEM (ADF-STEM). Each image in such a series can be regarded as representing a lateral section of the sample at the depth set by the focus, hence the term “optical sectioning”. To explore the 3D resolution limits of such an approach, the 3D transfer function can be examined. Figure 1 shows the 3D transfer functions for three different imaging geometries. It can be seen that the incoherent nature of ADF-STEM imaging much improves the 3D transfer compared to conventional high-resolution TEM, but that a large missing cone of transfer persists, which will rapidly worsen the depth resolution for laterally extended objects [3]. Nonetheless, at atomic lateral resolution, ADF-STEM can achieve nanoscale depth resolution. Figure 2 shows how the core of dislocation in GaN, inclined relative to the beam direction, can be seen to translate laterally between frames in a focal series. Optical sectioning in ADF-STEM has also been used to observe the depth dependent displacements that arise from the so-called Eshelby twist effect for dislocations containing a screw component [4]. This approach allows the existence and sign of a screw component to be determined for dislocations viewed end-on, and allows observed dislocation core structures to be associated with specific dislocation types [5].

In light microscopy, optical sectioning is commonly performed in a confocal mode. We have developed the technique of scanning confocal electron microscopy (SCEM), making use of an instrument fitted with both probe and imaging correctors. A theoretical and computational analysis of contrast and resolution limits in SCEM [3] shows that no contrast will be observed for weak-phase objects using elastic scattering, but that the incoherent nature of inelastic scattering will lead to a transfer function that fills the missing cone of information seen in the transfer function of ADF-STEM and provides the most complete transfer of 3D information. Experimental implementation of an energy-filtered SCEM (EF-SCEM) technique confirms that nanoscale depth resolution is maintained for laterally extended objects [6]. It is also found that the effect of the focus spread caused by chromatic aberration does not degrade the depth resolution, but does result in a loss of signal strength. Figure 3 shows the application of the EF-SCEM technique to 3D elemental mapping of a core-shell structure, where the observation of Si in the core material helps elucidate the mechanism of formation of the overall structure [7]. Finally, the development of hardware correctors for chromatic aberration provides a mechanism by which signal strength for EF-SCEM can be improved.

1. P.D. Nellist, M.F. Chisholm, N. Dellby et al., Science 305 (2004) 1741.
2. K. Van Benthem, A.R. Lupini, M. Kim et al., Appl. Phys. Lett. 87 (2005), 034104.
3. E.C. Cosgriff, P.D. Nellist, A.J. D'Alfonso et al. Adv. Imaging and Electron Phys. 162 (2010) 45.
4. J. Lozano, M.P. Guerrero-Lebrero, A. Yasuhara et al., submitted (2013).
5. P.B. Hirsch, J.G. Lozano, S. Rhode et al., Phi. Mag. In press (2013) available online.
6. P. Wang, G. Behan, M. Takeguchi et al., Phys. Rev. Lett. 104 (2010) 200801.
7. P. Wang, A. Hashimoto, M. Takeguchi, Appl. Phys. Lett. 100 (2012) 213117.

8. I am indebted to the former and current members of my research group, and colleagues elsewhere, who have collaborated on this work, including Peng Wang, Gavin Behan, Eireann Cosgriff, Juan Lozano, Prof Sir Peter Hirsch FRS, Angus Kirkland, Les Allen, Adrian D'Alfonso, Scott Findlay, Ayako Hashimoto, Masaki Takeguchi, Kazutaka Mitsuishi, Masayuki Shimojo, Prof Sir Colin Humphreys FRS, Michelle Moram, Sneha Rhode, S. Zhang, Matthew Horton, A. Yasuhara and E. Okunishi.

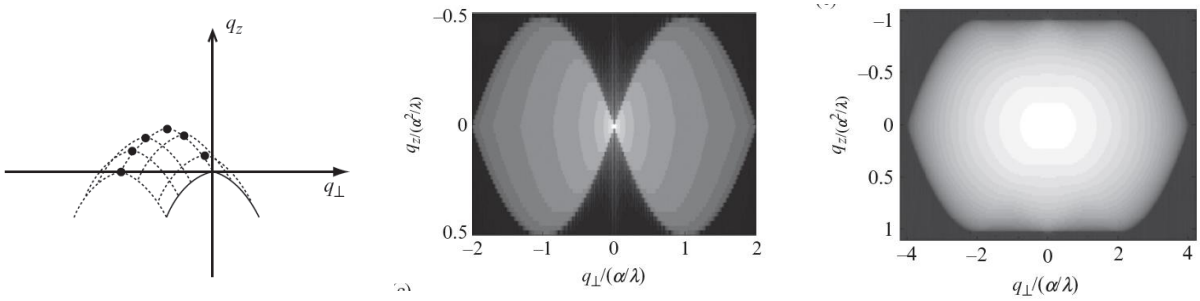

Figure 1. (left) The solid line shows the region of reciprocal space transferred by conventional HRTEM; (middle) incoherent imaging by ADF-STEM gives a larger volume of transfer but with a significant missing cone; (right) EF-SCEM gives the largest volume of transfer with no missing cone ensuring maximum depth resolution over a range of lateral spatial frequencies. For further details on this figure see Ref. [3].

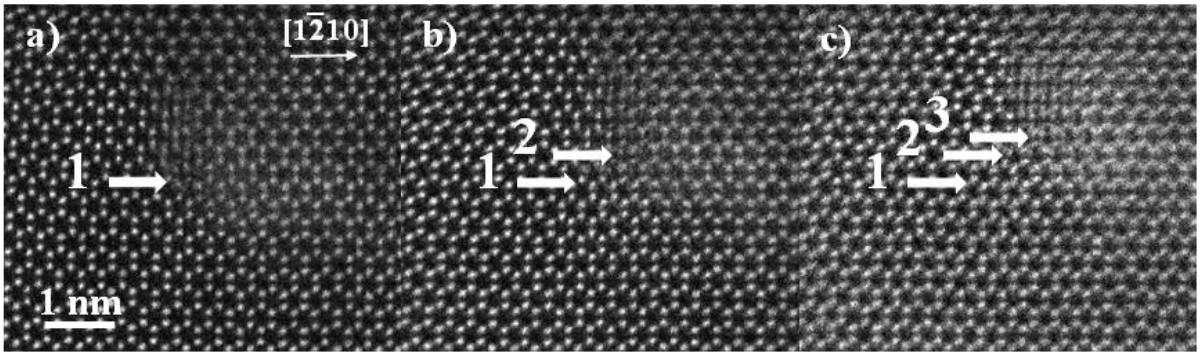

Figure 2. Part of a high resolution STEM-HAADF focal series of micrographs of a mixed dislocation in GaN imaged end-on recorded at three different focus values, showing the shift of the core structure seen below the arrows arising from the inclination of the dislocation. For further details on this figure see Ref. [5]

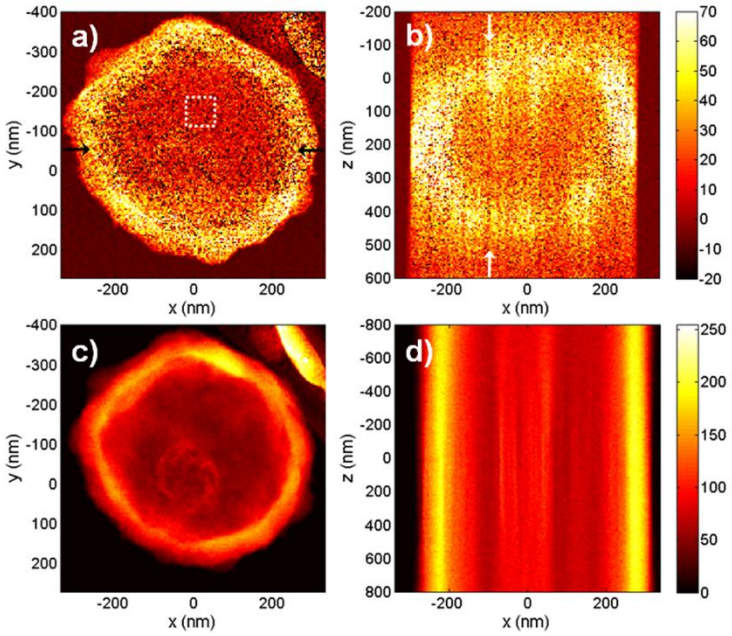

Figure 3 EF-SCEM on a hollow Fe_2O_3@SiO_2 mesoporous sphere. (a) and (b) Si core-loss signals from x-y and x-z scans, respectively, using the "three-window" technique; (c) and (d) HAADF x-y and x-z scans, respectively of the same region. The core can be seen to contain Si. Note the reduction in depth elongation in EF-SCEM compared to ADF-STEM.

High-resolution 3D Structure Determination of Dynamic Macromolecular Complexes by Single Particle cryo-EM

N. Fischer[1], E. Paleskava[1], A. Konevega[1], M. Rodnina[1], H. Stark[1]

[1]Max-Planck-Institute for biophysical Chemistry, 37077 Goettingen, Germany

Using the latest developments in electron microscopic hardware combined with advanced computational image processing it is now possible to determine structures of large and dynamic macromolecular complexes at near atomic resolution. We have determined the structure of a 70S ribosome-SelB complex at 3.8 Å resolution which is sufficient to determine a de novo structure of SelB bound to the ribosome. SelB is the elongation factor specific for the delivery of the selenocysteine-tRNA to the ribosome. This also requires a stop codon in the mRNA being recoded into a signal for selenocysteine incorporation by a SECIS element in the pre-mRNA. Selenocystein incorporation is already a rather inefficient process in vivo making the structure determination of SelB bound to the ribosome an evasive target in structural biology for a long time. Successful structure determination in fact requires extensive optimization of the ribosome-SelB complex preparation and image sorting of a rather heterogeneous population of ribosome complexes. This strategy allows not only the structure determination at very high resolution but also the simultaneous structure determination of numerous functionally distinct states of the ribosome-SelB complex.
As a control we also have determined the structure of the ribosome-EFTu complex at 3.2 Å resolution. EF-Tu is the elongation factor responsible for transport of all canonical aminoacyl-tRNAs to the ribosome. Having both structures available at high resolution we obtained a detailed view of how the ribosome can be hijacked by SelB to allow the recoding of a stop signal into a signal for selenocysteine incorporation.

From form factors to vortex electrons: Following Ariadne's thread

P. Schattschneider

Since the days when spectrometers for the TEM became commercially available, EELS has seen enormous theoretical and experimental progress. Fundamental problems concerning the inelastic interaction of fast probe electrons with matter have occupied the community for decades. It turns out that inelastic scattering can be understood on the basis of the dynamic form factor and its generalisation, the mixed dynamic form factor (MDFF), introduced by Harald Rose more than three decades ago. Amazingly, the experimental verifications of this concept rely on two other well-known contributions of the same researcher: energy filters and correctors.

Like Ariadne’s thread in the Greek myth, the MDFF is a guide throught the maze of so disparate aspects of inelastic interactions as coherence, delocalisation, mapping of orbitals, circular dichroism, and vortex electrons.

Shifting the paradigm in modern light microscopy: Light Sheet-based Fluorescence Microscopy (LSFM, SPIM, DSLM)

E. H. K. Stelzer[1]

[1]Physical Biology (FB 15, CEF-MC, BMLS), Goethe Universität, Frankfurt am Main, Germany

ernst.stelzer@physikalischebiologie.de

Specimens scatter and absorb light. Thus on one hand, the delivery of the probing light and the collection of the signal light (e.g. fluorescence) become inefficient, when relevant almost mm-thick specimens are investigated. On the other hand, not only fluorophores, but many endogenous biochemical compounds absorb light and suffer degradation of some sort (photo-toxicity), which can induce a malfunction of a specimen. In conventional and confocal fluorescence microscopy, whenever a single plane is observed, the entire specimen is illuminated (Verveer 2007). Recording stacks of images along the optical z-axis thus illuminates the entire specimen once for each plane. Hence, cells are illuminated 10-20 and fish embryos 100-300 times more often than they are observed (Keller 2008). This can be avoided by using light sheets, which are fed into the specimen from the side and overlap with the focal plane of a wide-field fluorescence microscope. In contrast to an epi-fluorescence arrangement, an azimuthal arrangement uses at least two independently operated lenses for illumination and detection (Stelzer 1994; Huisken 2004). A SPIM employs a cylindrical lens to generate a light sheet. A collimated laser beam is focused into the plane of the detection lens along one direction while the other direction remains collimated (Engelbrecht & Stelzer, 2006; Greger et al., 2007). Although this approach is relatively simple and straightforward it suffers from the low quality of the cylindrical lens and the inefficiency of the illumination system (Breuninger et al., 2007). The major advantage of a digital scanned laser light sheet-based fluorescence microscope (DSLM; Keller et al., 2008) is that it relies entirely on cylindrically symmetric optics and hence provides a very good optical quality. In addition, a DSLM employs a minimal number of optical components and does not suffer from excessive wavefront aberrations. In general, optical sectioning and no photo-toxic damage or photo-bleaching outside a small volume close to the focal plane are intrinsic properties of light sheet-based fluorescence microscopy (LSFM). It takes advantage of modern camera technologies and can be operated with laser cutters (e.g. Colombelli 2009) as well as in fluorescence correlation spectroscopy (FCS, e.g. Wohland 2010). We have also successfully evaluated the application of structured illumination in a LSFM (SPIM, Breuninger et al., 2007; DSLM, Keller 2010). We also designed and implemented a wide-field frequency domain fluorescence lifetime imaging (FLIM/FRET, Greger 2011) setup. More recently, we applied LSFM for investigations in plant biology (Maizel 2011), three-dimensional cell biology as well as emerging model organisms and developed new scanning schemes based on novel optical arrangements that allow us to take full advantage of very high resolution light microscopy. The development of LSFM draws on many previous developments. In particular, confocal theta fluorescence microscopy played a very important role. About a dozen papers on theta microscopy describe its properties, its relationship to 4Pi microscopy and that of LSFM (single & two-photon, annular/Bessel beams, (a)symmetric arrangements) theoretically as well as practically.

1. http://www.researcherid.com/rid/A-7648-2011

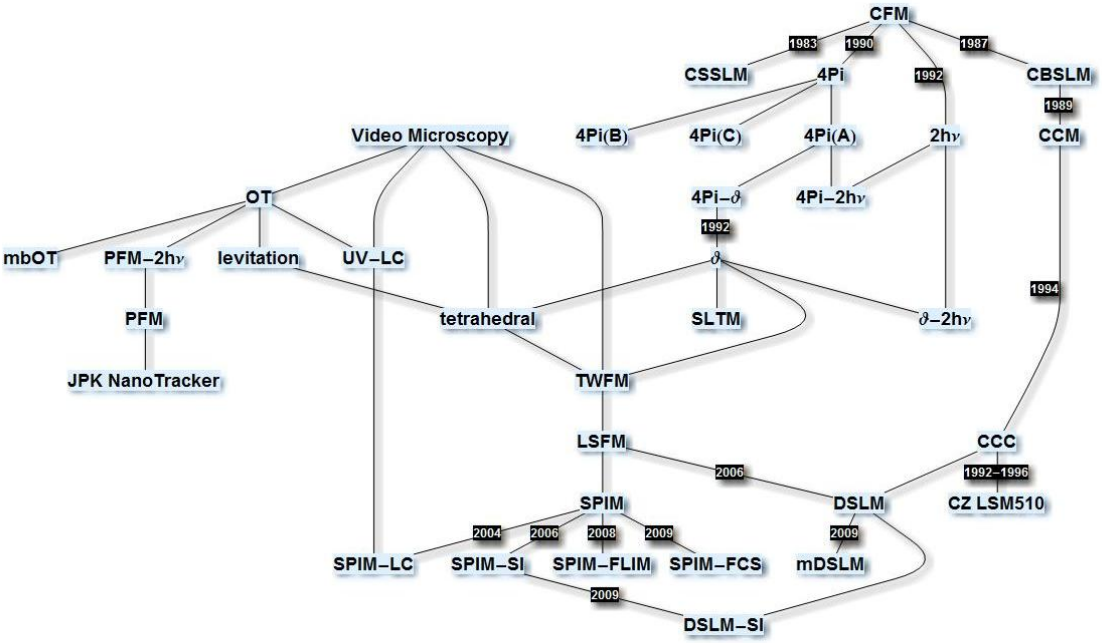
CFM
1983
1990
1987
CSSLM
4Pi
1992
CBSLM
1989
Video Microscopy
4Pi(B)
4Pi(C)
4Pi(A)
2hν
CCM
OT
4Pi–ϑ
4Pi–2hν
1992
mbOT
PFM–2hν
levitation
UV–LC
ϑ
1994
PFM
tetrahedral
SLTM
ϑ–2hν
JPK NanoTracker
TWFM
LSFM
CCC
2006
1992–1996
SPIM
DSLM
CZ LSM510
2004
2006
2008
2009
2009
SPIM–LC
SPIM–SI
SPIM–FLIM
SPIM–FCS
mDSLM
2009
DSLM–SI

Figure 1.

Cryofixation of biological specimens – electron spectroscopic imaging of calcium and phosphorus of osteoblastic cell cultures and an elegant way to produce section ribbons with the help of a newly developed micromanipulator.

D. Studer[1], J. P. Gorski[2], T. Hillmann-Marti[1], A. Klein[1], M.-I. Iacovache[1], H. Gnaegi[3]
B. Zuber[1]

[1]Institute of Anatomy, University of Bern, Bern, Switzerland
[2]Center of Excellence in Mineralized Tissues and Department of Oral Biology, School of Dentistry, University of Missouri Kansas City, Kansas City, USA
[3]Diatome SA, Helmstrasse 1, 2560 Nidau, Switzerland

studer@ana.unibe.ch
Keywords: dry- and cryo-sectioning, oscillating knife, high pressure freezing, electron spectroscopic imaging, bone mineralisation foci, micromanipulation

Transmission electron microscopy has provided most of what is known about the ultrastructural organization of tissues, cells and organelles. Most samples were prepared according to the classical protocol of so called chemical fixation. During fixation with aldehydes, postfixation with heavy metals, dehydration in a solvent and subsequent embedding into a resin samples are preserved in such a way that they are easy processed for electron microscopic evaluation. However chemical fixation cannot preserve the native ultrastructural details in a satisfactory way. Quite some artefacts are introduced by this procedure (precipitations, loss of molecule, swelling, 1,2,3). Furthermore due to the recording of heavy metal staining patterns only an indirect visualization is possible. Subcellular structures of biological samples are preserved close to native state by cryofixation. Bulk specimens (thicker than some micrometre) are only well frozen or vitrified when high pressure freezing is applied. Subsequent cryosectioning and investigation in the cryo-electron microscope (CEMOVIS) leads to a structural preservation which is close to the native state of the sample (4).

A compromise is freezing followed by freeze-substitution. The samples show better structural preservation in comparison to samples chemically fixed (1,2,3). However freezing leading to vitrification is only possible in small samples: experience shows that sample thickness of a biological sample should not exceed a thickness of 200μm. Exceptions are based on the fact that some biological samples contain much more (or less) intrinsic cryoprotectants (eg solutes, sugars etc).

As a recent improvement in elemental analysis of temporally synchronized UMR106-01 osteoblastic cell cultures we discuss calcium and phosphorus distributions which were optimal only when cultures were processed using high pressure freezing (HPF), freeze-substitution and dry ultrathin sectioning with an oscillating knife (5). Three types of culture conditions were analyzed: mineralized, non-mineralized (limiting exogenous phosphate), and inhibited mineralization (treated with protease inhibitor AEBSF). UMR 106-01 cells were grown on fibronectin-coated sapphire discs and processed conventionally or for high pressure freezing (6; EMPact, Leica-microsystems, Vienna). HPF specimen holders containing sapphire discs with frozen cells were transferred to the freeze-substitution apparatus. Specimens were washed in anhydrous acetone and embedded in Epon Araldite resin. Dry 50 nm sections were produced with an oscillating diamond knife (Ultra sonic, Diatome, Nidau, Switzerland). With the help of electron spectroscopic imaging (ESI; Leo 912 with omega filter, Zeiss, Oberkochen, Germany) we could localize calcium and phosphorus in micrographs.

To facilitate the application of cryomethods the improvement and development of tools is necessary. Due to tremendous advances in crystallography and magnetic resonance imaging, almost any protein can now be modeled at atomic resolution. To fully understand the workings of biological “nanomachines” it is necessary to obtain images of intact macromolecular assemblies in situ. Cryofixation by high pressure freezing followed by cryosectioning circumvents many of the artefacts related to staining, dehydration and embedding. The approach immobilizes complex macromolecular assemblies in their native state in situ and the images in some cases reach such a good resolution that macromolecule structure can be fitted into them (7). Sophisticated instruments and software packages are needed, e.g. high voltage electron microscopes equipped with precise goniometers (for high resolution tomograms) that work at low temperature and digital cameras of high sensitivity and pixel number to get this structural information. However first of all good cryosections have to be produced. To get them is quite a challenge. Very steady hands are a prerequisite. To facilitate cryo-sectioning we developed a tool with two micromanipulators. One to guide the ribbon of cryo-sections produced during the sectioning process and the other one to put in place the grid for adsorbing the

ribbon with the help of an ionisation unit developed by Pierson et al. (8, Crion, Leica- microsystems, Vienna, Austria)

1. Hunziker EB, Michel M, Studer D. Microscopy Research and Technique (1997), 37, p.271-284.
2. Vanhecke D, Bellmann R, Baum O, Graber W, Eggli P, Keller H, Studer D. J Microsc. (2008), 230, p. 253-62.
3. Studer D, Hennecke H, Müller M. Planta (1992) 188, p.155-163.
4. Al-Amoudi et al. EMBO J. (2004) 23(18), p. 3583-3588.
5. Studer D, Hillmann-Marti T, Huffman NT, Gorski JP Cells Tissues Organs. (2011) 194(2-4) p. 138-145.
6. Studer, D., W. Graber, A. Al-Amoudi, P. Eggli. J Microsc (2001) 203 p. 285–294.
7. Studer D, Humbel BM, Chiquet M Histochem Cell Biol. (2008) 130(5) p. 877-889
8. Pierson J J Struct Biol. (2010) 169(2) p. 219-25.
9. This study was supported by NIH NIAMS grant AR-052775 (J.P.G.) and a Swiss National Foundation grant (No. 3100AO-118394) (D.S.). The authors wish to thank Barbara Krieger for her excellent photographic services.

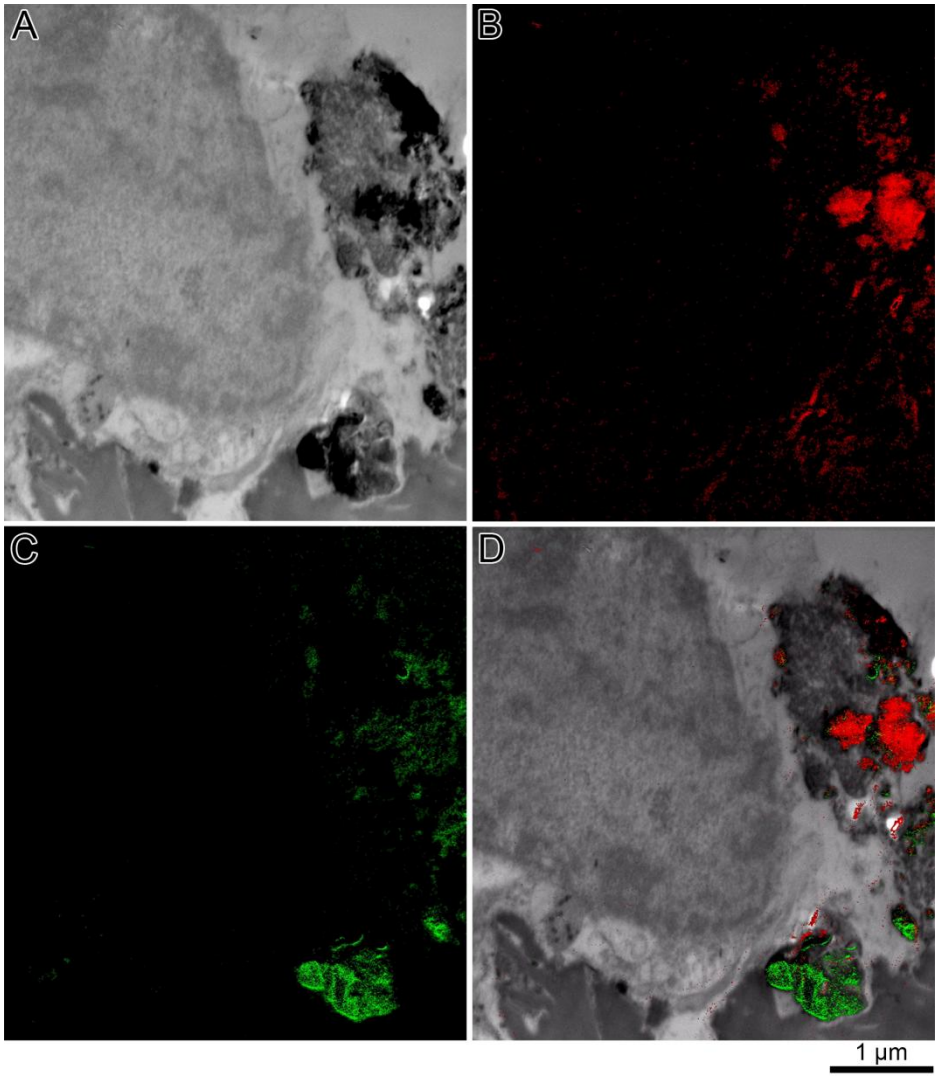

Figure 1. Part of a high pressure frozen osteoblastic cell is shown with portions of closely associated extracellular biomineralization foci containing separated calcium and phosphorus (explanation see above). The sample was freeze-substituted in acetone containing 2% of osmium tetroxide, embedded in Epon and dry ultrathin sectioned with an oscillating knife. In the electron spectroscopic imaging mode we recorded in Fig. 1A the zero loss image (nicely focused sample because no inelastically scattered electrons are present). Fib 1B shows the very same location recorded with inelastic electrons having suffered an energy loss of 346 eV corresponding to calcium (red) and in Fig. 1C inelastic electrons have lost 132 eV corresponding to phosphorus (green). Finally in Fig. 1D all three images are superimposed.

Nanoscale X-ray Tomography of Cells

G. Schneider[1], P. Guttmann[1], S. Werner[1], S. Rehbein[1]

[1]Helmholtz-Zentrum Berlin für Materialien und Energie GmbH, Albert-Einstein-Str. 15, 12489 Berlin

gerd.schneider@helmholtz-berlin.de
Keywords: X-ray microscopy, tomography, cell nucleus, correlative microscopy

X-ray imaging offers a new 3-D view into cells. With its ability to penetrate whole hydrated cells it is ideally suited for pairing fluorescence light microscopy and nanoscale X-ray tomography. Driven by scientific applications in life science, we developed a full-field transmission X-ray microscope (TXM) for automated cryo-tomography and spectroscopy. The system operates at the undulator beamline U41 at the BESSY II electron storage ring which provides a spectral resolution of 104. The spatial resolution of the X-ray microscope is 11 nm (half-pitch).

For high resolution tomography, we adopted a tilt stage originally developed by FEI for electron tomography which supports automated data collection of cryogenic or heated samples. The stage is able to tilt samples in the X-ray microscope up to ± 80°. Such a large tilt of flat sample holders is impossible with soft X-ray microscopes at bending magnet sources because they require a monochromator pinhole to be positioned close to the specimen. Therefore, the HZB full-field TXM overcomes two main limitations of previous concepts. Firstly, it permits spectromicroscopy with high spectral resolution and short exposure times in the range of one second. Secondly, its sample holder geometry is not restricted to glass tubes for 3-D investigations.

Conventional fluorescence images are diffraction-limited to ~200 nm, whereas current X-ray imaging can achieve a ten-fold improvement in resolution. Since fluorescence and X-ray microscopy permit analysis of whole cells, it is possible to investigate the same cell in both microscopes by correlative microscopy. These
correlative studies are ideally suited to X-ray microscopy because of its ability to image cells in 3-D. In the talk, we present the cryo TXM and selected applications. In particular, we will show studies of the internal structure of frozen-hydrated cryogenic mammalian cells and present ways towards 10 nm 3D imaging of cells.

1. G. Schneider, et al., Nature Methods 7 (2010), 985-987

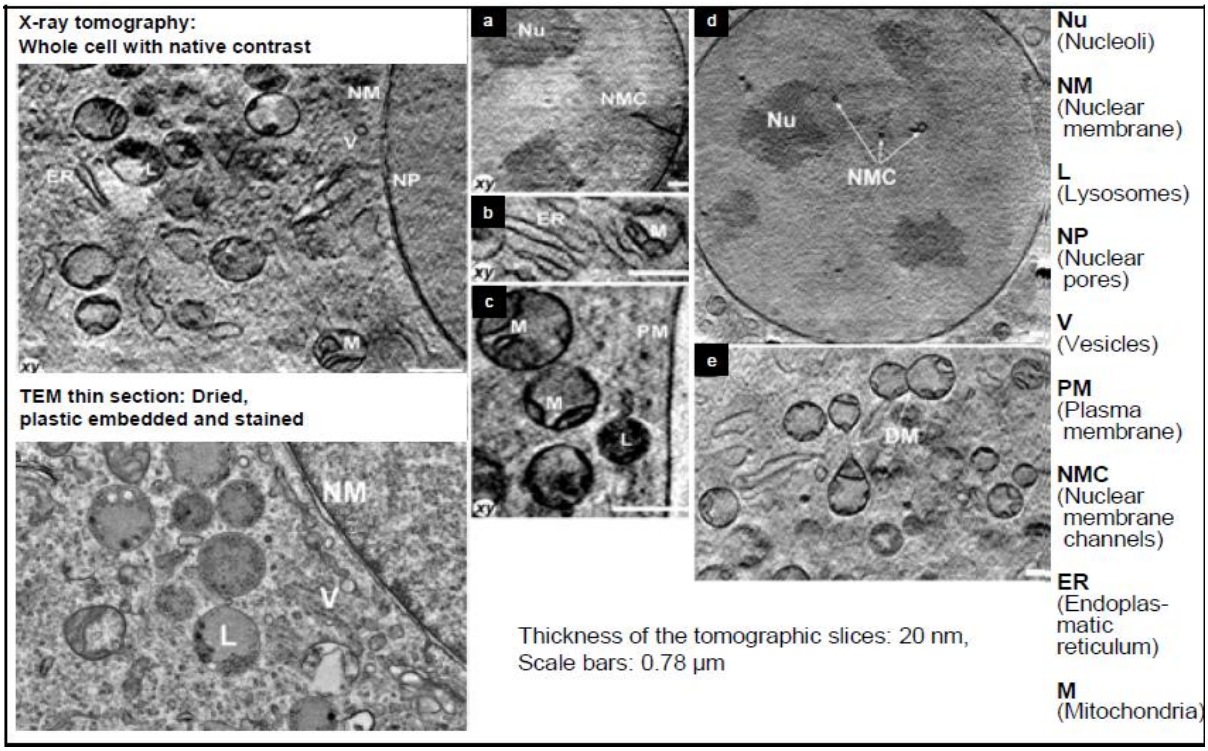

Figure 1. The cyro TXM at HZB allows routinely to visualize the plasma membrane, nuclear membrane, nuclear pores, nucleoli, endoplasmic reticulum, vesicles, lysosomes and mitochondria. It is now also possible to resolve internal organellar structures, such as mitochondrial cristae, the double nuclear membrane and lysosomal inclusions.

Microorganisms and Biofilms

LS.1.001
Raman microspectroscopy for the functional characterization of microbes

M. Schmid[1], C. Böhm[1], M. Palatinszky[1], D. Berry[1], M. Wagner[1]

[1]University of Vienna, Department of Microbial Ecology, Vienna, Austria

schmid@microbial-ecology.net

Raman spectroscopy is a vibrational spectroscopy based on Raman scattering of monochromatic light (we use a confocal LabRAM HR800 system from Horiba, Germany, equipped with a 532.17 nm laser as light source, Figure 1). The photons interact with the different molecules in the sample and while most photons are scattered without changing their energy, about one out of 108 photons experiences an energy shift after collision with the molecules if these start to vibrate. These Raman scattered photons have a modified wavelength and are indicative for chemical structures in the sample. As whole microbial cells contain many compounds, their Raman spectra are rather complex, but nevertheless allow the accurate identification of compound classes and of some specific molecules with strong Raman peaks like phenylalanine (Figure 2). Raman spectroscopy is a quick method, which works on single cell level, and is generally non-destructive (spectra of microbial cells can be acquired in vivo). Furthermore, samples can be solids, liquids or gases and they can be measured in aqueous solutions, because water does not generate Raman peaks in the biochemically or biologically relevant regions of Raman spectra. In our laboratory Raman spectroscopy is applied to different aspects of microbial ecology:

Raman spectroscopy allows us to detect storage compounds like sulphur, phosphate, glycogen or polyhydroxyalcanoates in single cells of cultures or of larger microbial consortia. Especially, the allocation of sulphur and phosphate in a marine anaerobic methane oxidizing sulphate reducing consortium consisting of archaea (ANME) and bacteria (sulphate reducers) contributed to astonishing new insights into the role of the two partners in the process (Milucka et al. 2012).

Raman spectroscopy is also a very reliable method for the detection of uptake of non-radioactive isotope labelled substrates in single microbial cells of cultures or environmental samples. With this we could show that commonly believed obligate intracellular Chlamydia are metabolically active outside of their host cells (Haider et al., 2010).

The capability for single cell isotope probing renders Raman microspectroscopy (Figure 2), if combined with fluorescence in situ hybridization (FISH) (our LabRAM HR 800 is also equipped with the optics and a camera to acquire fluorescence images) an alternative method to FISH-microautoradiography or stable isotope probing with many advantages for functional analysis of microbes (Huang et al. 2007; Wagner, 2009).

Recently, a 1064 nm laser, which functions as an optical tweezer (Huang et al. 2009), was added to our Raman setup. We started to capture living or fixed cells of an environmental sample in the tweezer laser beam, and to measure their Raman spectrum. By applying the above mentioned Raman spectroscopic approaches the identity or physiological traits of microorganisms in environmental samples could be determined. After separating the desired microorganisms with the optical tweezer, downstream applications like single cell genomics or cultivation experiments will follow.

1. J. Milucka, T.G. Ferdelman, L. Polerecky, D. Franzke, G. Wegener, M. Schmid, I. Lieberwirth, M. Wagner, F. Widdel and M.M.M. Kuypers, Nature 491 (2012), p. 541-546.
2. S. Haider, M. Wagner, M.C. Schmid, B.S. Sixt, J.G. Christian, G. Häcker, P. Pichler, K. Mechtler, A. Müller, C. Baranyi, E.R. Toenshoff, J. Montanaro and M. Horn, Molecular Microbiology 77 (2010), p. 687-700.
3. W.E. Huang, K. Stoecker, R. Griffiths, L. Newbold, H. Daims, A.S. Whiteley and M. Wagner, Environmental Microbiology 9 (2007), p. 1878-1889.
4. M. Wagner, Annual Reviews in Microbiology 63 (2009), p. 411-429.
5. W.E. Huang, A.D. Ward and A.S. Whiteley Environmental Microbiology Reports 1 (2009), p. 44–49

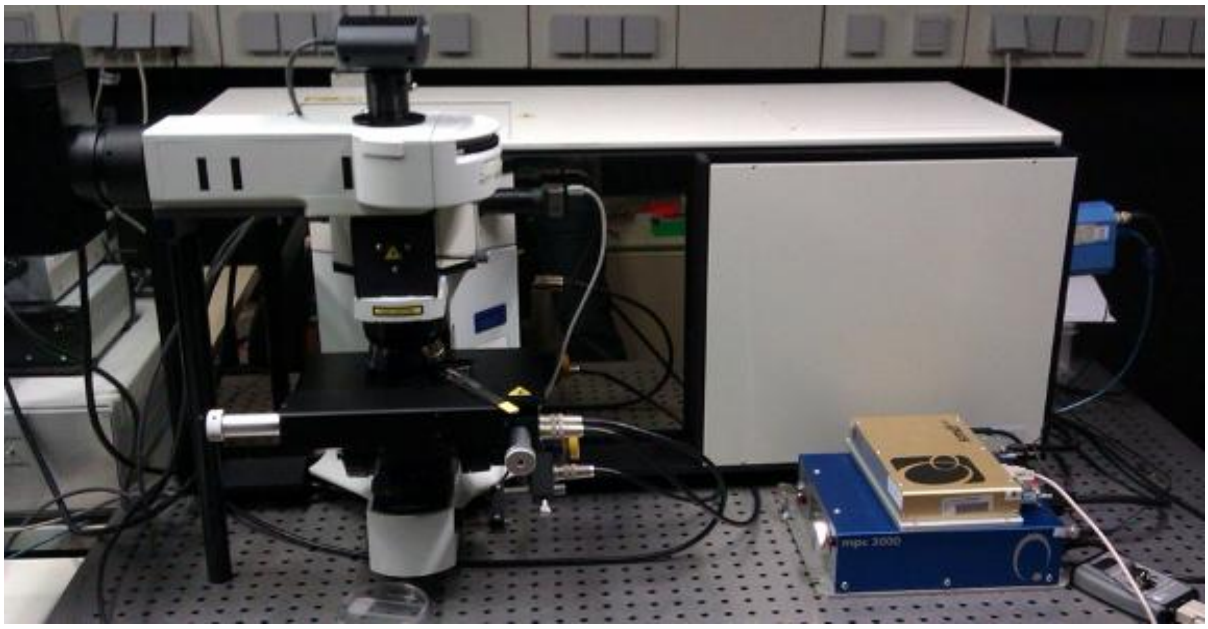

Figure 1. Horiba LabRam HR 800 equipped with a 532.17nm measuring laser, a 1064nm tweezer laser, a fluorescence unit and a back illuminated EMCCD detector.

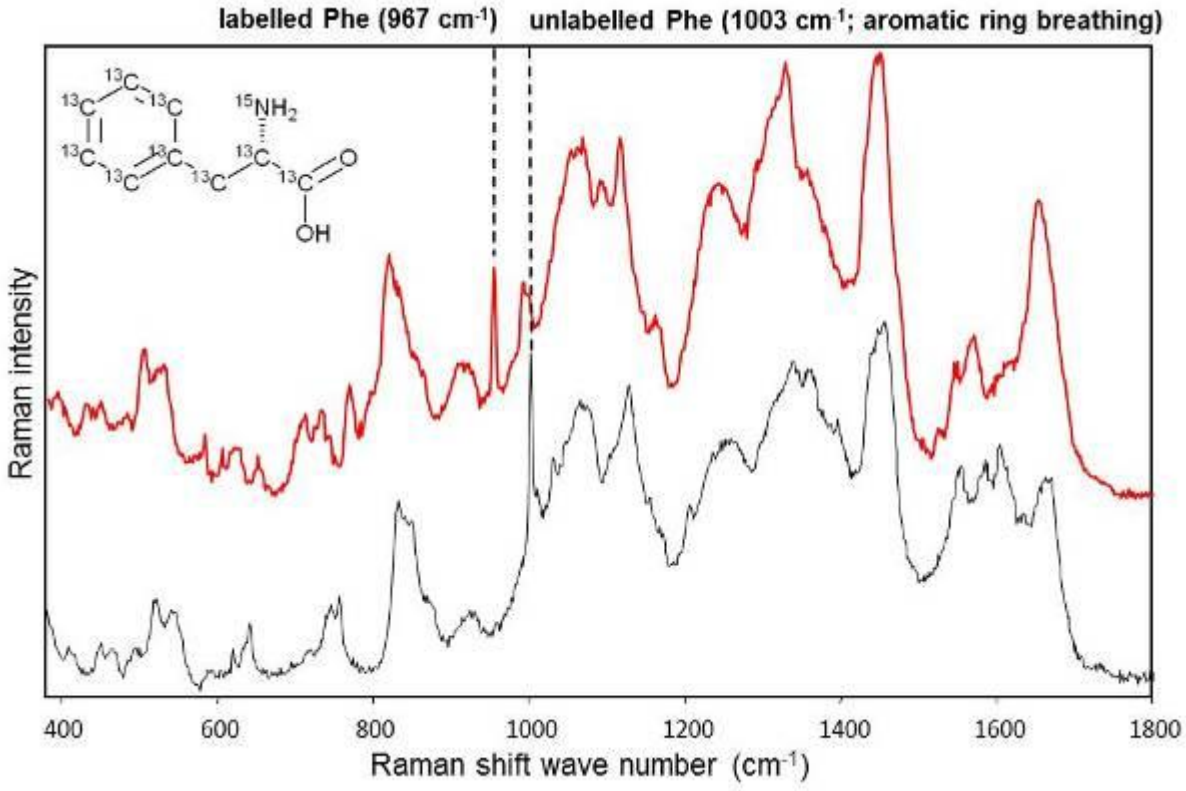

Figure 2. Raman spectra of microbial cells grown with ^{13}C labelled (red) and with unlabelled (black) phenylalanine (taken from Haider et al., 2010).

Microorganisms and Biofilms

LS.1.002
Electron and light microscopy of yeast biofilm

K. Dobranska[1], F. Ruzicka[2], J. Nebesarova[3], Z. Burdikova[4], J. Dluhos[5], J. Collakova[6], R. Chmelik[6]
O. Samek[1], V. Krzyzanek[1]

[1]ISI ASCR, Brno, Czech Republic
[2]St. Anne´s hospital, Brno, Czech Republic
[3]Biology center of the ASCR, Ceske Budejovice, Czech Republic
[4]Institute of physiology of the ASCR, Praha, Czech Republic
[5]Tescan, Brno, Czech Republic
[6]UT Brno, Brno, Czech Republic

dobranska@isibrno.cz
Keywords: biofilm, cryo-SEM, light microscopy

Microbes like bacteria or yeast have different ways of living; they are able to live like planktonic cells or in more dangerous form in adherence to surfaces or interfaces, where are embedded in a matrix of extracellular polymeric substances that they can produce. Biofilm allows protection for the microbial cells from attacks by the immunity system as well as from the effect of antibiotics [1]. Therefore, study of biofilms is important for clinical research. It may help to develop more efficient treatment strategies for biofilm infections. Here we investigate the extracellular matrix of yeast *Candida parapsilosis* and *Candida albicans*.

Yeast and its biofilm have been investigated by scanning electron microscopy (SEM) as well as light microscopy. For surface imaging of the samples both classical and cryo-SEM techniques were employed and compared. For structural characterization also focused ion beam SEM (FIB-SEM) and the cryo-SEM freeze-fracturing technique were applied. FIB-SEM was used for both precise cross section preparations as well as for tomographical acquisition of 3D dataset using the signal of backscattered electrons (BSE) [2]. Freeze fracture provides planar views of the internal organization of membranes or biofilms and thus gives unique structural information.

For in vitro imaging coherence-controlled holographic microscopy (CCHM) [3] is employed; the main advantage remains the quantitative phase contrast imaging for non-invasive label-free live cell. Another light microscopy technique is the two-photon fluorescent confocal microscopy that gives much higher resolution than classical confocal light microscopes. Various labelling are used and compared.

A comprehensive view of the structure of fully hydrated system of yeast cultures living in the polymer matrix is obtained due to using a number of different imaging techniques. The sample preparation is the most critical point and therefore it is important and valuable to compare different microscopic approaches with different sample handling.

1. R.M. Donlan, and J.W. Costerton, Clin. Microbiol. Rev., 15, 167-193 (2002).
2. M. Zadražil in “The Step Towards an Ultimate Multifunctional Tool for Nanotechnology” et al., (3M Nano 2012 Proceedings, X'ien) (2012) 175
3. P. Kolman, and R. Chmelik, Optics Express, 18 (2010), p. 21990
4. The authors acknowledge the support by the grants CZ.1.07/2.3.00/20.0103 and CZ.1.05/1.1.00/02.0068 (EC and MEYS CR), P205/11/1687 (GACR), TE01020118 (TACR), FR-TI4/660 (MIT CR) and Z60220518 (ASCR).

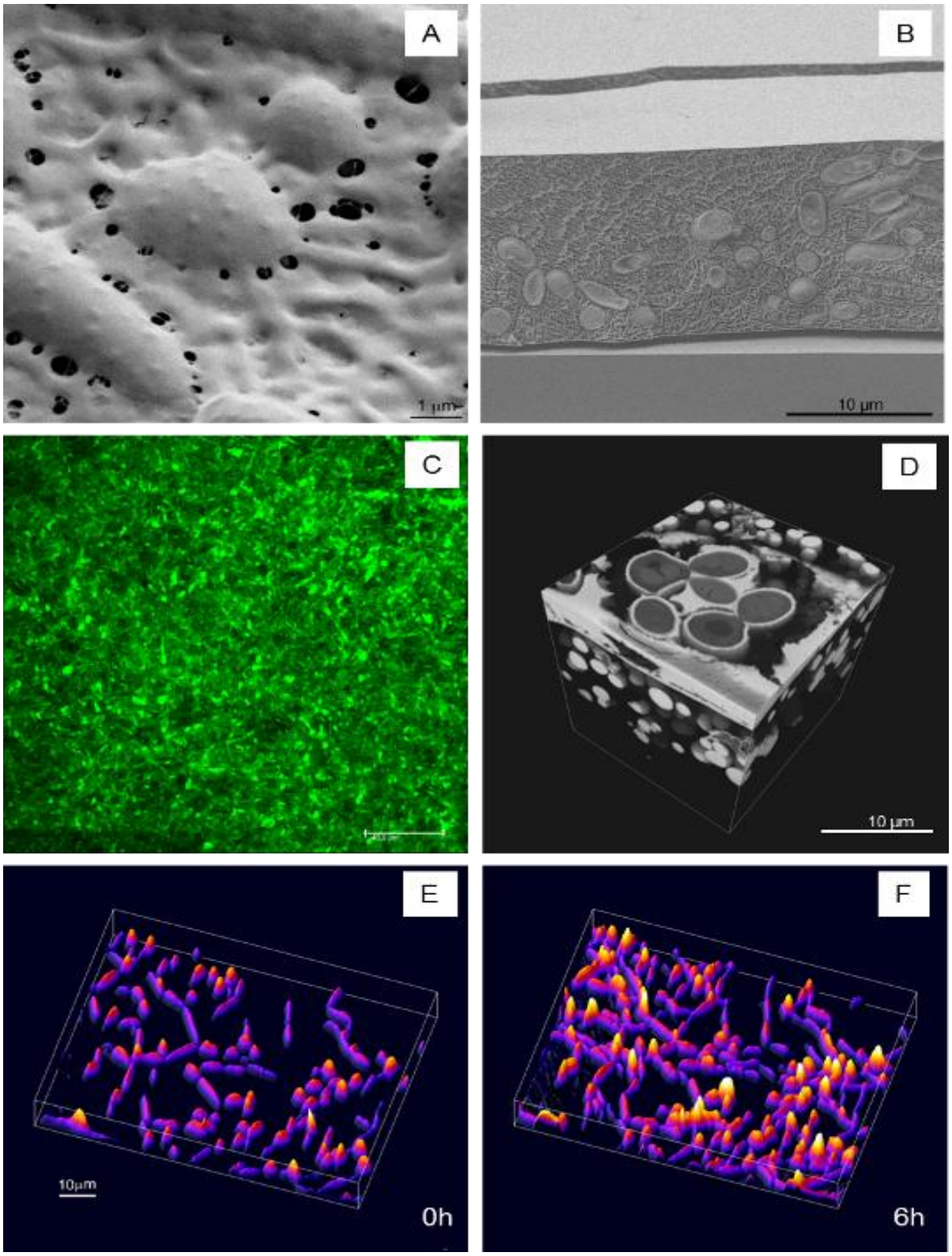

Figure 1. (A) Surface of yeast *C. parapsilosis* grown on the agar (cryo-SEM); (B) Freeze-fracturing and cryo-SEM of grown yeast culture of *C. parapsilosis* on cover glass; (C) Maximal projection of *C. parapsilosis* grown on cover glass with Calcofluor labelling; (D) FIB-SEM tomograph of *C. albicans* after freeze-substitution; (E,F) Series of quantitative phase contrast (CCHM) of growing yeast C. parapsilosis culture at times 0h and 6h.

Microorganisms and Biofilms

LS.1.003
FIB/SEM tomography analysis of the structure of bacteriogenic cell-mineral aggregates

F. Zeitvogel[1], M. Obst[1], G. Schmid[1], P. Ingino[1], L. Hao[1], Y.-D. Stierhof[1], C. Burkhardt[1], B. Schroeppel[1]

[1]University of Tuebingen, Center for Applied Geoscience, Tuebingen, Germany

fabian.zeitvogel@uni-tuebingen.de
Keywords: FIB/SEM tomography, cell-mineral aggregates

Bacterial Fe(II) oxidation and subsequent Fe(III) mineral formation are important environmental processes as Fe(III) minerals can act as sorbents for pollutants and nutrients [1]. Previous studies observed the formation of specific aggregates of bacterial cells, extracellular polymers and bacteriogenic Fe(III) minerals [2]. Understanding the physical structure of such aggregates is a fundamental basis for research on bacterial biomineralization and sorption processes. Density and porosity of these aggregates influence intra-particle diffusion and the concentration of sorption sites available e.g. for other metal ions.

In this study, FIB/SEM tomography was applied to investigate the internal structure of cell-mineral aggregates formed by the bacterial *Acidovorax sp*. strain BoFeN1 [3], a well-studied neutrophilic nitrate-reducer that is known to cause precipitation of Fe(III) minerals when grown in circumneutral, anoxic, Fe(II)-enriched medium.

Bacterial cells were high-pressure frozen, freeze-substituted and embedded in Epon. FIB/SEM data were acquired using a Zeiss Auriga CrossBeam® system. Using the combined FIB serial sectioning / SEM imaging routine, 10 nm thick slices were milled off with a FIB current of 2 nA and images were acquired with an energy-selective backscattered electron (EsB) detector. Thus, contrast was dominated by the Fe-content of the sample. The lateral pixel size was 9.9 nm, accounting for approximately isotropic voxels; the final dataset corresponded to a volume of 20 x 15 x 6 µm³. Data was processed using ImageJ [4] and displayed using UCSF Chimera [5].

In this study it became obvious that most cells and particles formed an interconnected structure (Figure 1). On cellular level, a great variety of different mineralization patterns were observed, such as different forms of extracellular precipitates as well as dense, intracellular precipitates (Figure 2).

Compared to other tomography methods, FIB/SEM tomography proved ideal for the analysis of this type of sample, combining a high spatial resolution with the possibility of analyzing comparably large volumes. In addition, the results are highly reliable as the grey value of a voxel is directly detected by SEM imaging of the FIB-prepared surfaces instead of resulting from calculations, as is the case for angle-scan approaches.

1. T. Borch et al., Environ Sci Tech 44 (2010), pp. 15-23.
2. J. Miot et al., Geochim Cosmochim Acta 73 (2009), pp. 696-711.
3. A. Kappler et al., Geobiology 3 (2005), pp. 235-245.
4. M.D. Abràmoff et al., Biophotonics International 11 (2004), pp. 36-41.
5. E.F. Pettersen et al., J Comput Chem. 25 (2004), pp. 1605-1612.
6 We appreciate the help of N. Klueglein (cell culture), M. Floetenmeyer (access to HPF), the EAM group as well as Andreas Kappler and the Geomicrobiology groups at the U. of Tuebingen for help and discussion. This project was supported by the DFG, Emmy-Noether grant (OB 362/1-1) to MO.

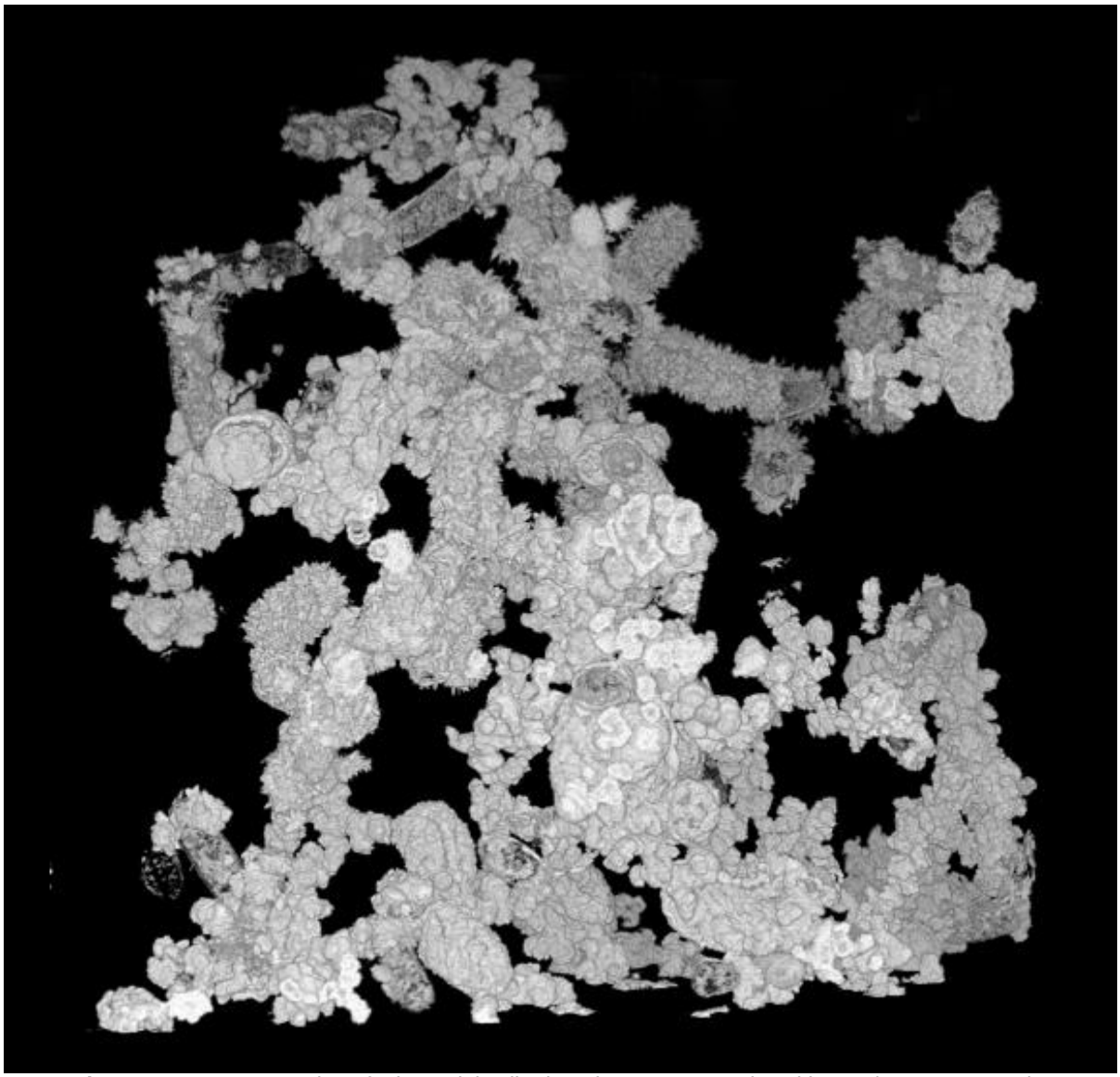

Figure 1. 3D reconstruction of a bacterial cell-mineral aggregate analyzed by FIB/SEM tomography

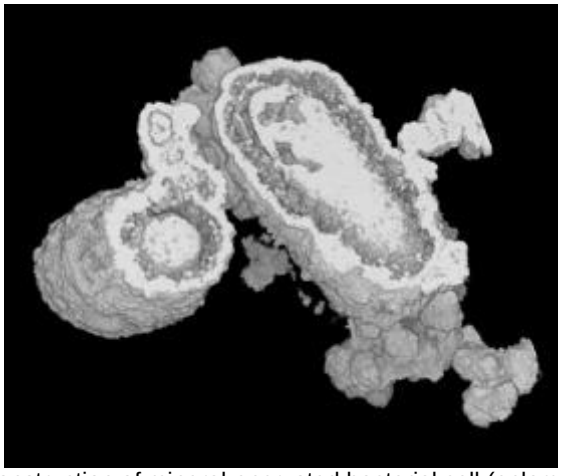

Figure 2. 3D reconstruction of mineral-encrusted bacterial cell (enlarged subvolume)

Microorganisms and Biofilms

LS.1.004
Anammox bacteria: microbes with identity issues

S. Neumann[1], M. van Teeseling[1], R. Mesman[1], L. van Niftrik[1]

[1]Radboud University Nijmegen, Microbiology, Nijmegen, Netherlands

l.vanniftrik@science.ru.nl
Keywords: anammox bacteria, cell compartmentalization, (cryo)electron microscopy

Anammox bacteria convert ammonium and nitrite to nitrogen gas to obtain energy for growth. The anammox reaction was deemed impossible until its discovery in the early 1990s. Now, anammox is recognized to contribute significantly to oceanic nitrogen loss and is estimated to be a major source of gaseous nitrogen on Earth. In addition, anammox bacteria are extremely valuable for wastewater treatment where they are applied for the removal of ammonium. Besides their importance in industry and the environment, anammox bacteria defy some basic biological concepts. Whereas most other bacteria have only one cell compartment, the cytoplasm, anammox bacteria have three independent cell compartments, from out- to inside; the paryphoplasm, riboplasm and anammoxosome. The anammoxosome is the largest cell compartment and is proposed to be dedicated to energy transduction. As such it would be analogous to the mitochondria of eukaryotes. The riboplasm contains the nucleoid and ribosomes and the paryphoplasm has a yet unknown function. Having three cellular compartments poses challenges to protein sorting, substrate transport and cell division and it is largely unknown how anammox bacteria achieve these functions. In addition, anammox bacteria are proposed to have an atypical cell wall devoid of both peptidoglycan and a typical outer membrane. We use cell fractionation, proteomics and immunolocalization studies combined with advanced (cryo)electron microscopy techniques (such as (cryo)electron tomography) to study the ultrastructure and function in anammox bacteria.

Microorganisms and Biofilms

LS.1.005
Microscopic techniques to investigate malaria pathogenesis

K. Quadt[1], M. Streichfuss[1], M. Cyrklaff[1], J. Spatz[2,3], F. Frischknecht[1]

[1]Parasitology - Department of Infectious Diseases University of Heidelberg Medical School, Im Neuenheimer Feld 324, 69120 Heidelberg Germany
[2]Biophysical Chemistry, Institute for Physical Chemistry, Heidelberg University, 69117 Heidelberg, Germany
[3]Max Planck Institute for Intelligent Systems, Department of New Materials and Biosystems, 70569 Stuttgart, Germany

katharina.quadt@gmx.de
keywords: malaria, gliding motility, cell adhesion, optical tweezers, AFM

Malaria is transmitted to vertebrate hosts by the bite of female Anopheles mosquitoes that are infected with the sporozoite form of protozoan parasites of the genus Plasmodium [1]. Sporozoites are deposited in the skin upon transmission into vertebrate hosts and move at high speed (1-2 µm/s) to find and enter into blood vessels [Fig 1]. Once in the blood they are transported to the liver, where they enter hepatocytes to differentiate into blood cell invading forms. These so-called pre-erythrocytic stages of the malaria parasite are clinically silent yet critical for establishing infection in the mammalian host [2].

Sporozoites migrate using a unique locomotion called gliding motility [2], which enables them to penetrate host tissues (skin and liver), entering the blood vessel and to invade hepatocytes. The clinical symptoms of malaria manifest during the erythrocytic cycle of the parasite [3]. A characteristic feature of infection is the accumulation or sequestration of parasite-infected red blood cells (RBCs) in various organs avoiding the spleen-dependent killing mechanism [4]. Sequestration results from adhesive interactions between parasite-derived proteins expressed on the surface of infected RBCs and a number of host molecules on the surface of endothelial cells [Fig 2] [5].

In order to investigate the interaction between the parasite and the host at the different stages of the complex life cycle, we employ in vitro and in vivo imaging approaches, high-resolution microscopy (AFM) and other biophysical instruments (optical tweezers) to study the pathogenesis of the parasite. These will be presented in the talk.

1. L. Schofield and G.E. Grau, Nat Rev Immunol 5 (2005), 722.
2. P. Sinnis, Coppi A. Parasitol Int (2007);56:171-8.
3. Taylor-Robinson AW. Front Biosci (2000);5:E16-E29.
4. Rowe JA, Claessens A, Corrigan RA, Arman M. Expert Rev Mol Med (2009);11:e16.
5. Beeson JG, Brown GV. Cell Mol Life Sci (2002);59:258-71.

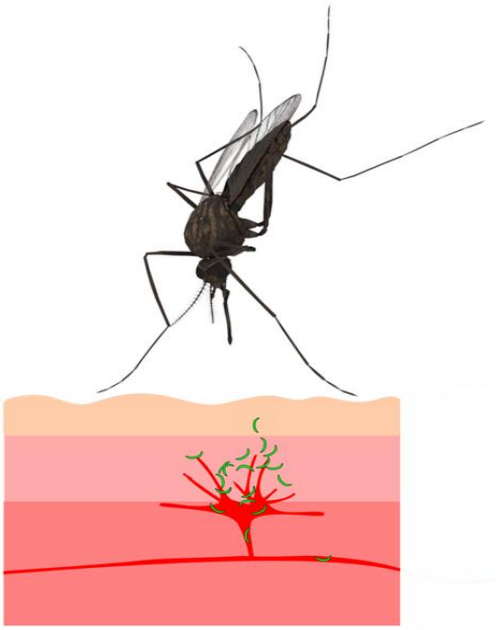

Fig 1. : Female *Anopheles* mosquitoes inject the sporozoite form of the parasite into a human host. To successfully continue the infection, sporozoites must invade blood vessels in the dermis using their gliding motility system.

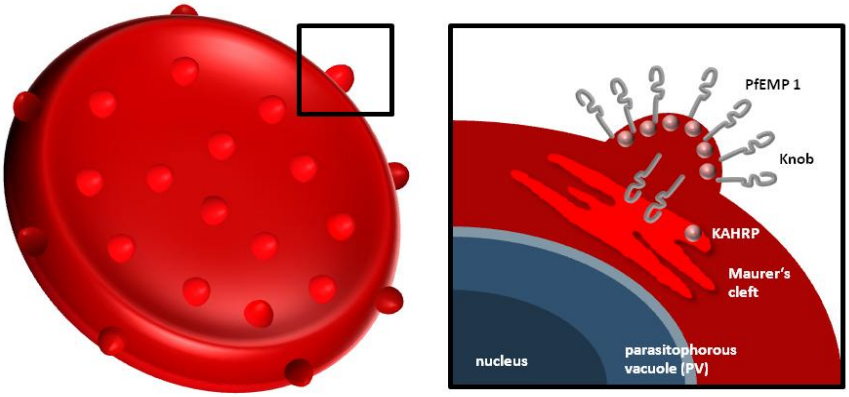

Fig 2. : The virulence of *Plasmodium falciparum* malaria is related to the parasite's ability to evade host immunity through tissue-specific adhesion of infected erythrocytes (IEs). The *P. falciparum* erythrocyte membrane protein 1 (PfEMP1) family expressed on dome-shaped protrusions called knobs on the IE surface is central to both.

Microorganisms and Biofilms

LS.1.006
Cell-to-cell transfer of *Leishmania* amastigotes observed by multidimensional live imaging: participation of extrusomes in host cell egress and reinfection

F. Real[1], P. Florentino[1], P. Veras[2], R. Mortara[1]

[1]Escola Paulista de Medicina - UNIFESP, Parasitology, São Paulo, Brazil
[2]Fiocruz, Parasitology, Salvador, Brazil

The last step of Leishmania intracellular life cycle is the egress of amastigotes from the host cell and their uptake by adjacent cells. Taking advantage of multidimensional live imaging of macrophage cultures infected with L. amazonensis, we describe some previously unseen features of this process [1,2].

Amastigotes were transferred from cell to cell when the donor host macrophage collapses; transfer between live cells was not detected. We found that amastigotes were extruded from the collapsed host macrophage within zeiotic structures (blebs) rich in late endosome/lysosome components such as LAMP1 and Rab7. These structures were classified in this study as parasitophorous extrusomes. The extrusome was selectively internalized by vicinal macrophages and the rescued amastigotes, carrying host lysosomal components attached to their surfaces (but dissociated from host cytoskeleton components such as actin) were able to survive in recipient macrophages (Figure 1). To induce cell-to-cell amastigote transfer, the nuclei of infected GFP-expressing macrophages were microirradiated by 405 nm laser, what induced apoptosis in these cells but not in vicinal macrophages [3] (Figure 2). Non-irradiated macrophages were able to rescue amastigotes from apoptotic, irradiated cells, suggesting that amastigotes benefit from host cell apoptosis to spread among other cells. Amastigote transfer occurred concomitantly to macrophage GFP leakage, what is suggestive of pore formation on host cell membrane during the process. Transfer was also stimulated when macrophages are treated with streptolysin O, a pore-forming protein innocuous to amastigotes.

The participation of host lysosomal components associated with amastigote surfaces in transfer of parasites was investigated; amastigotes isolated from LAMP1/LAMP2 knockout cells were less phagocytosed by macrophage cultures when compared to amastigotes isolated from wild-type cells. Amastigotes covered with LAMP proteins also increased the production of TGF-β by macrophages in comparison with amastigotes displaying host membrane caps devoid of these lysosomal components.

We provide evidence that amastigotes, enclosed within host cell membranes, can be transferred from cell to cell without full exposure to the extracellular milieu. The presence of lysosomal components on egressing amastigotes increase their uptake by vicinal cells and modulate cytokine production, what represents an important strategy developed by parasite to evade host immune system[1].

1. N. Friedrich, M. Hagedorn, D. Soldati-Favre and T. Soldati, Microbiol Mol Biol Rev 76 (2012), p. 707-720.
2. M. G. Rittig and C. Bogdan, Parasitol Today 16 (2000), p. 292-297.
3. L. Soustelle, B. Aigouy, M. L. Asensio and A. Giangrande, Neural Dev 3 (2008), p. 11.

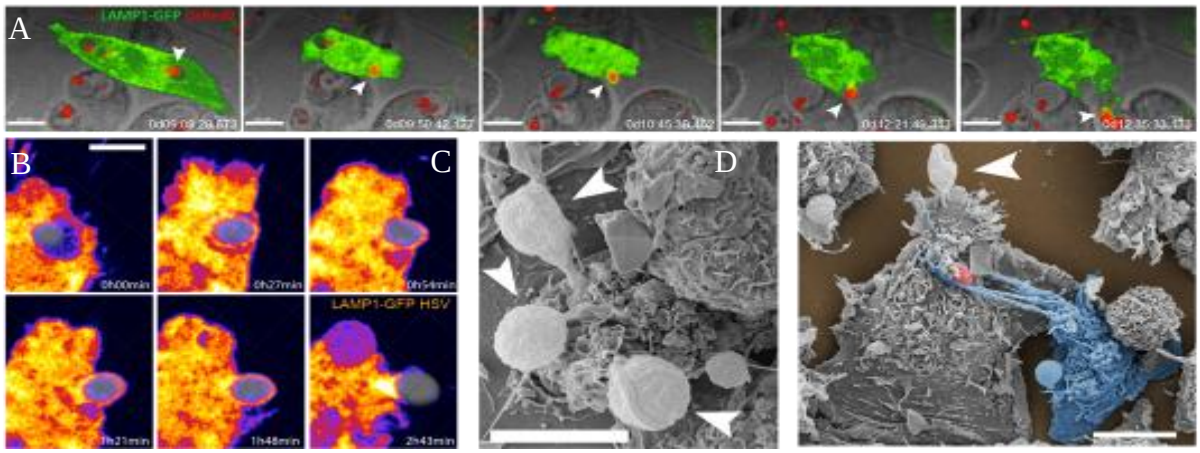

Figure 1. Amastigotes are transferred from cell to cell associated to phagolysosomal components. (A) Multidimensional imaging of RAW 264.7 cells expressing GFP-tagged Lysosome-associated membrane protein 1 (LAMP1, in green) and infected with L. amazonensis-DsRed2 (red) for 24 hours. RAW cells were microirradiated (405 nm near UV laser, 400 Hz, 120 seconds) to induce extrusion and transference of amastigotes. Arrowheads indicate an extruded amastigote rescued from vicinal macrophage. The amastigote carries a polarized cap of LAMP1 protein. Time of image acquisition is represented by days:hours:minutes:seconds:miliseconds (d:hh:mm:ss:sss). Image acquisition started after 24 hours of infection plus 2 minutes of microirradiation. Bars=10 µm. (B) LAMP1 is expressed on amastigote extrusion. The temporal sequence of the extrusion event presented in A shows that amastigote is surrounded by phagolysosomal components during the host cell egress. Relative time of extrusion is represented by hours:minutes (h:mm). (C-D) Field-emission scanning electron microscopies of BMDMØ infected with L. amazonensis-DsRed2 for 20 days. The left image (C) shows a shrunk macrophage presenting extrusions with dimensions compatible to amastigotes (arrowheads). Bar=5 µm. On the right image (D), one macrophage (colored in blue) interacts with an oval-shaped structure (red) from another macrophage. This structure has similar dimensions to an amastigote. Bar=10 µm.

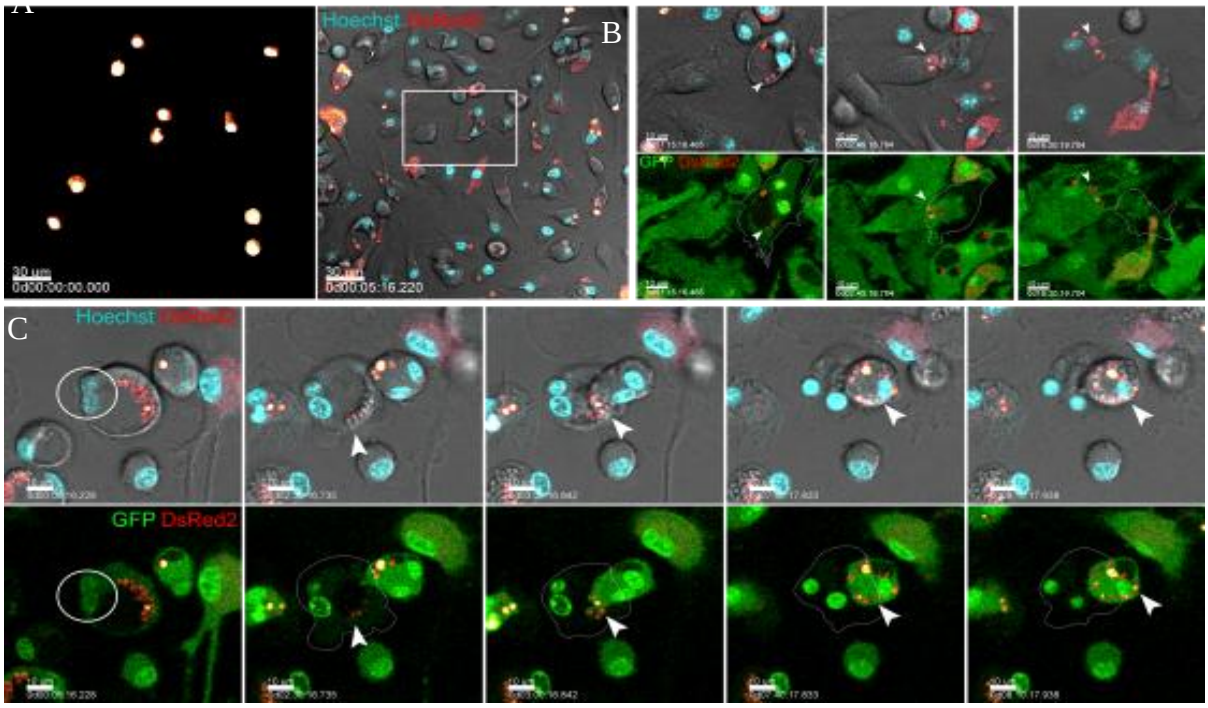

Figure 2. Microirradiation of host cell nuclei induces cell death and amastigote transfer. (A) On the left panel, microscopic field (63x objective) in which 10 nuclei were microirradiated with near UV (405 nm) laser at 400Hz for 300 seconds. On the right panel, the corresponding field showing microirradiated BMDMØ-GFP infected for 72-120 hours (*L. amazonensis*-DsRed2 in red and Hoechst 33342 in cyan, over DIC image). Square indicates an example of an amastigote transfer induced by microirradiation shown in B. Bar=30 µm. (B-C) Live cell imaging of amastigote transfer induced by microirradiation. The upper panel shows *L. amazonensis*-DsRed2 in red and Hoechst 33342 in cyan merged with DIC image at defined time intervals. The lower panel shows the corresponding green channel (GFP fluorescence) and *L. amazonensis*-DsRed2 (in red). Amastigotes are transferred with concomitant GFP leak out of the host cell (arrowhead). Time of image acquisition is represented by days:hours:minutes:seconds:miliseconds (d:hh:mm:ss:sss). Image acquisition started after 72 hours (B) or 120 hours (C) of infection plus 5 minutes of microirradiation. Bar=10 µm.

Microorganisms and Biofilms

LS.1.P007
Adhesive properties of Aspergillus Fumigatus biofilms probed by atomic force microscopy and effects of Alginate Lyase enzyme.

A. Maiorana[1], M. Papi[1], F. Bugli[2], R. Torelli[2], B. Posteraro[2], V. Palmieri[1], G. Ciasca[1], M. Chiarpotto[1] G. Maulucci[1], M. De Spirito[1], M. Sanguinetti[2]

[1]Cattolica University, Physics Institute, Rome, Italy
[2]Cattolica University, Microbiology Institute, Rome, Italy

alessandro.maiorana@rm.unicatt.it
Keywords: Atomic Force Microscopy, *Aspergillus Fumigatus*, Biofilms

Aspergillus fumigatus (A. fumigatus) has become a leading cause of fungal morbidity and mortality, especially in immunocompromised patients [1]. This fungus is able to grow as a multicellular community and produce a hydrophobic extracellular matrix (ECM), mainly composed of galactomannan and α1,3 glucans, to protect itself from host defenses and antimicrobial drugs [2]. This matrix envelops the fungus hyphae, binding them into a contiguous sheath on the colony surface, forming the biofilm and increasing the fungal resistance to adverse environmental factors [3]. Adhere to host cells and resist physical removal play a key role in fungal colonization and invasion of the host and in a wide range of infections. In cases of pharmacological investigations, the efficiency of an antifungal agent can only be assessed by clinical symptoms since repeated biopsy and fungal cultures hinder continuous observation of treatment response [4].

Combining high resolution atomic force microscopy (AFM) and adhesion force spectroscopy we were able to detect simultaneously the pathophysiological conditions of ECM, hyphae and spores. We show that, by using AFM, is possible to exploit the peculiar hydrophobicity of the biofilm components (i.e. cell walls, ECM) to detect the biofilms spread, its growth and lysis on rough surfaces.

We tested our approach by means of several pharmacological strategies commonly used in clinic-treatment, moreover we tested a new approach based on Alginate Lyase (AlgL), an enzyme known to reduce negatively charged alginate levels in microbial biofilms [5]. We also mixed these with amphotericin B (AMB) deoxycholate and its lipid formulations (e.g., liposomal AMB [LAMB]). AFM analysis showed that when A. fumigatus biofilms were treated with AlgL or polyene alone, as well as with their combination, both a reduction of hyphal thicknesses and an increase of adhesive forces were observed compared to the findings for untreated controls, probably owing to the different action by the enzyme or the antifungal compounds. Our results suggest that a combination of AlgL and a polyene antifungal may prove to be a new therapeutic strategy for invasive aspergillosis, while reinforcing the EPS as a valuable antibiofilm drug target. Finally, an important fall out of our results is that AFM and adhesion force spectroscopy, it's possible to develop an effective diagnostic tool able to detect the pharmacological effects on biofilms fungus and thus to transfer advanced microscopy techniques to a clinical purpose.

1. G. R. Thompson and T. F. Patterson, Semin. Respir. Crit. Care Med. 29, 103 (2008).
2. C. Loussert, C. Schmitt, M. C. Prevost, V. Balloy, E. Fadel, B. Philippe, C. Kauffmann-Lacroix, J. P. Latgé and A. Beauvais, Cellular Microbiol. 12, 405 (2010).
3. E. Mowat, J. Butcher, S. Lang, C. Williams and G. Ramage, J. Med. Microbiol. 56, 1205 (2007).
4. J. Weber and E. Balish. Mycopathologia 90, 47 (1985).
4. M. A. Alkawash, J. S. Soothill and N. L. Schiller, APMIS 114, 131 (2006).

Microorganisms and Biofilms

LS.1.P008
The S-Layer of *Nitrosopumilus maritimus*

V. Heinz[1,2], E. Gagen[2], M. Könneke[3], K.-U. Hinrichs[3], C. Palmer[4], J. Löwe[4], M. Thomm[2], R. Rachel[1,2]

[1]University of Regensburg, Centre for Electron Microscopy, Regensburg, Germany
[2]University of Regensburg, Institute for Microbiology, Regensburg, Germany
[3]University of Bremen, Department of Geosciences & MARUM Centre, Bremen, Germany
[4]University of Cambridge, MRC Laboratory of Molecular Biology, Cambridge, United Kingdom

veronika.heinz@ur.de
Keywords: S-Layer , cell wall ultrastructure, *Nitrosopumilus maritimus*

In 2005, the first ever isolated and cultivated **A**mmonia **O**xidizing **A**rchaeum (AOA), the mesophilic, marine and extremely small Archaeon *Nitrosopumilus maritimus* [1] was successfully enriched from a tropical marine tank. Only three years later, the use of ribosomal proteins as phylogenetic markers led to the proposal of a new archeal phylum, the Thaumarchaeota [2], with *N. maritimus* as one of the first members (see fig. 1 [3]). Due to its extraordinary metabolic [4] and phylogenetic features, *N. maritimus* rapidly gained the interest of researchers around the world. Since then, it has been recognized that AOA make a significant contribution to the first and rate limiting step in nitrification [5] and are highly abundant in their habitats. The discovery of a novel type of ammonia monooxygenases and putative new metabolic pathways [4] further emphasize their role in the global nitrogen circle.

Nevertheless, ultrastructural information on *N. maritimus* is still scarce; the S-Layer as its most obvious surface structure has not yet been investigated (see fig. 2). The quasi-periplasmic space between the cellular membrane and the S-Layer lattice comprises about one third of the total volume of a single cell. This astonishing figure points to the importance of the S-Layer for *N. maritimus* cells and indicates that is has to fulfill a certain, yet unknown, function. The question whether it is also providing a functional compartmentalization to the cell remains to be answered. To address these topics, our current experiments focus on the structural and biochemical investigation of the S-Layer and its composing protein(s). This work gives a first insight into compositional, organizational and molecular details of the *N. maritimus* S-Layer. The investigative methods that were used for this study include TEM preparations [6] like freeze etching, (ultra-)thin sectioning, tomography and cryo tomography as well as biochemical approaches. The center to center-distance was determined to be ~20 nm. A two-dimensional reconstruction of the S-Layer lattice was done to identify its symmetry (p6 or p3), while a three-dimensional reconstruction provides information about putative pores and links between the protein subcomplexes. By this multi-technical approach we examined our target structure from different points of view, in 2D and 3D, regarding compositional and biochemical aspects. The resulting, overall image shows that the S-Layer has not only structural, but also a putative functional importance for *N. maritimus* cells. A comparison with other archaeal relatives will be given as a conclusion.

1. Könneke, M. et al., 2005; Nature 437: 543-546
2. Brochier-Armanet, C., et al., 2008; Nat Rev Microb 6: 245-252
3. Stahl & de la Torre, 2012; Annu Rev Microbiol 66: 83-101
4. Walker, C. B. et al., 2010; PNAS 107: 8818-8823
5. Pester, M. et al., 2011; Curr Opin Microbiol 14: 300-306
6. Rachel, R. et al., 2010; Meth Cell Biol 96: 47-69
7. This project was financially supported by the DARCLIFE project.

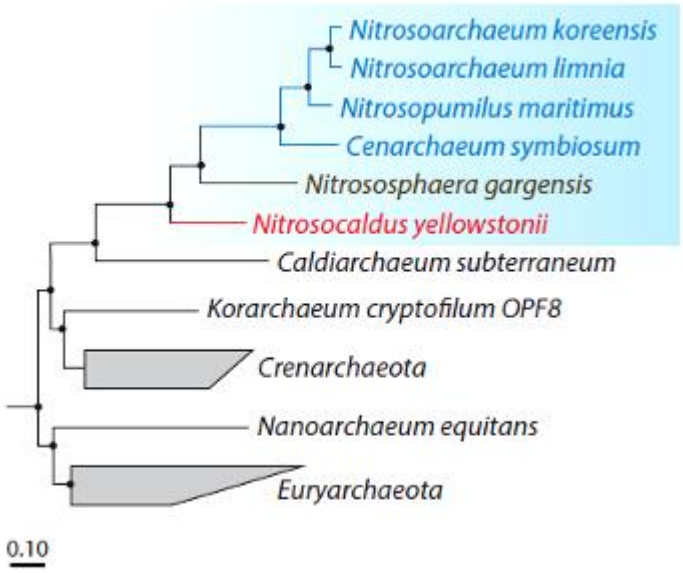

Figure 1:
Phylogenetic tree of the Archaea

Figure 1. Recently published phylogenetic tree of AOA, based on ribosomal proteins [3]; Thaumarchaeota are marked blue.

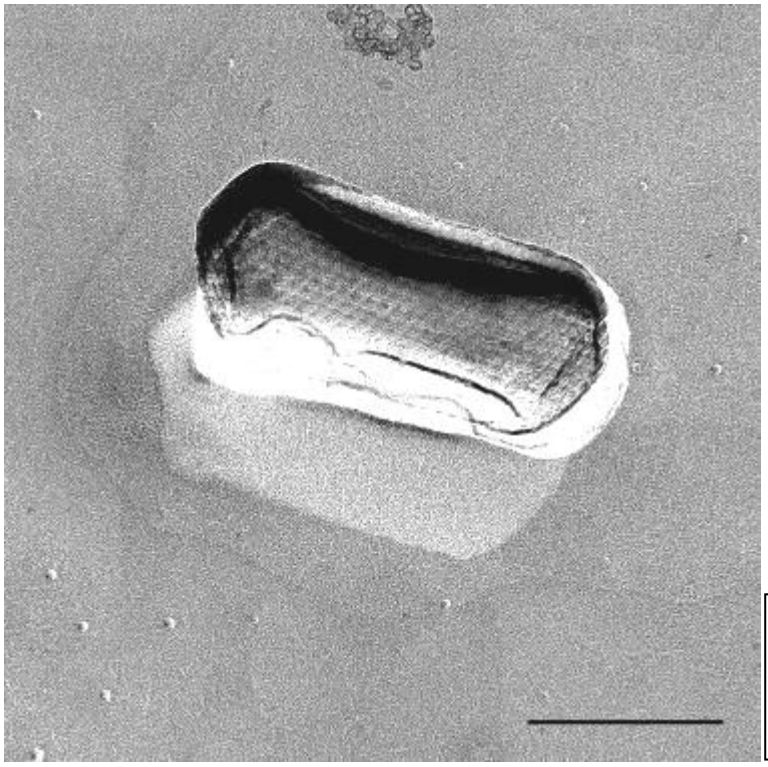

Figure 2:
Freeze etching preparation of *N. maritimus*;
bar = 200 nm

Figure 2. Freeze etched *N. maritimus* cell, revealing the S-Layer (unpublished data). The regularly arranged protein oligomers are clearly visualized; center to center distance ~ 20 nm, symmetry p6 or p3.

Microorganisms and Biofilms

LS.1.P009
3D STXM chemical tomography of cell-mineral aggregates formed by Fe(II)-oxidizing bacteria

G. Schmid[1], L. Hao[1], F. Zeitvogel[1], M. Obst[1]

[1]University of Tuebingen, Center for Applied Geoscience, Tuebingen, Germany

gregor.schmid@uni-tuebingen.de
Keywords: STXM tomography, 3D spectromicroscopy, chemical tomography, soft X-rays

Ferrous iron can be oxidized under anoxic or microoxic conditions at neutral pH by Fe(II)-oxidizing bacteria, forming cell-mineral aggregates. The resulting biogenic cell-mineral aggregates efficiently retain toxic heavy metals as well as other pollutants by sorption processes [1].

To further our understanding of the underlying mechanisms, the mixotrophic, nitrate-reducing Fe(II)-oxidizing *Acidovorax sp.* strain BoFeN1 was selected as a model strain to study the Fe(III)-biomineral formation at high spatial resolution and subsequently its influence on the sorption of heavy metals on the submicron scale. BoFeN1 shows initial iron biomineralization in the periplasm followed by cell encrustation in iron minerals that are associated with extracellular polymeric substances (EPS) [2].

Synchrotron-based scanning transmission (soft) X-ray microscopy (STXM) in combination with angle-scan tomography were performed, which enables mapping the distribution of iron and organic macromolecules (e.g. proteins, polysaccharides) in 3D [3]. A substantial advantage of STXM over other tomography approaches such as FIB-SEM or TEM tomography is the combination of microscopy at high spatial resolution (~10-50 nm) with X-ray absorption spectroscopy that provides quantitative chemical speciation information. Strain BoFeN1 was cultured in anoxic mineral medium supplemented with 10 mM Fe(II). Bacterial samples were prepared either by air-drying or in wet cells for STXM tomography of hydrated samples [4]. Organic carbon, protein and iron 3D composition maps were obtained from image sequences acquired across the C1s, O1s and Fe2p X-ray absorption edges. Tomography reconstructions of air-dried BoFeN1 cells revealed 3D biomineralization patterns in form of total encrustation in Fe(III) oxyhydroxides (Figure 1). A BoFeN1 cell in its natural, hydrated state indicated partial iron encrustation with hydrated extracellular “protein” in proximity to the cell (Figure 2).

In contrast to other tomography techniques, STXM in combination with angle-scan tomography allows 3D chemical tomography. Our results also indicated that STXM tomography measurements of pristine bacterial samples in their natural, hydrated state prevent typical preparation artifacts such as dehydration and shrinking [5].

1. J. Dynes et al., Environmental Science & Technology 40 (2006), pp. 1556-1565
2. J. Miot et al., Geochimica Et Cosmochimica Acta 73 (2009), pp. 696-711
3. M. Obst et al., Geobiology 7 (2009), pp. 577-591
4. M. Obst et al. in “Canadian Light Source Activity Report 2008”, ed. M. Dalzell (Canadian Light Source, Saskatoon) (2009), pp. 142-143
5. Dohnalkova et al., Applied and Environmental Microbiology 77 (2011), pp. 1254-1262
6. We thank the spectromicroscopy beamline team at the Canadian Light Source for help during the STXM measurements. We appreciate also the help of A. Picard, E. Struve, M. Abbas, W. Kuerner and the Geomicrobiology Group of A. Kappler Tuebingen for providing knowledge and samples. This project was supported by the DFG, Emmy-Noether grant (OB 362/1-1) to MO.

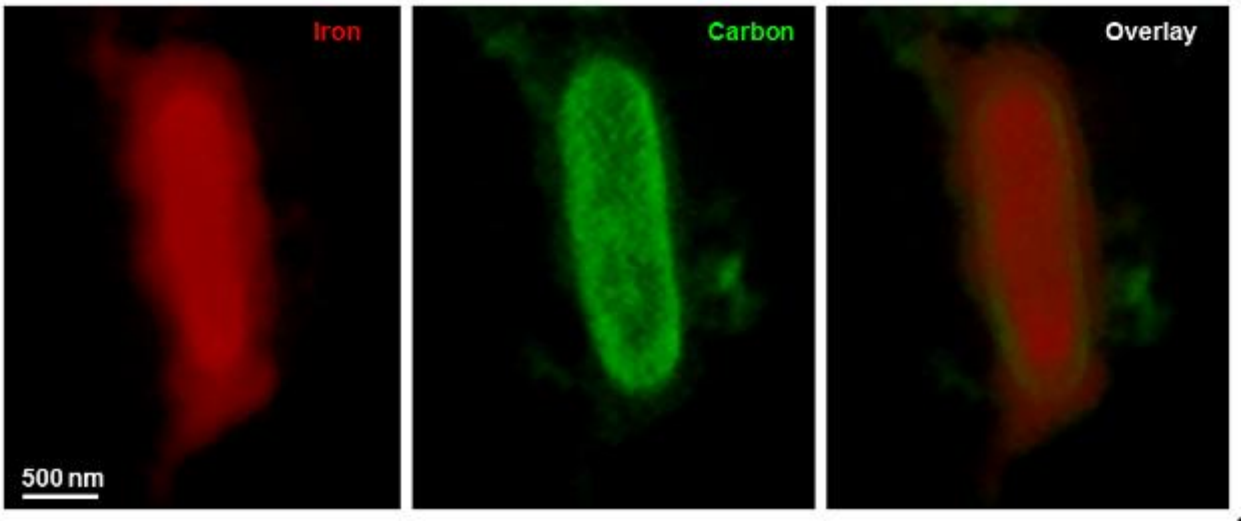

Figure 1. STXM 3D maps of iron and organic carbon for an encrusted BoFeN1 cell.

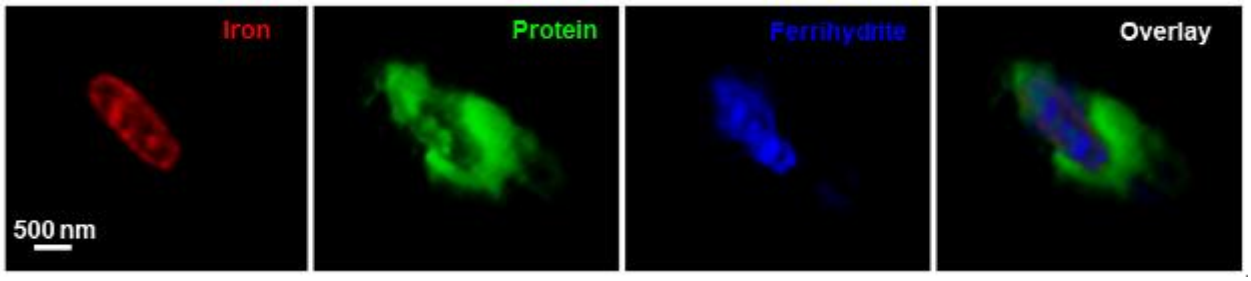

Figure 2. STXM 3D maps of iron and spectral fits for protein and ferrihydrite of a hydrated, partially iron encrusted cell.

Microorganisms and Biofilms

LS.1.P010
The Lyme disease spirochete *Borrelia burgdorferi* is able to disseminate directly to the tick salivary glands after a bloodmeal.

M. Strnad[1,2], M. Vancova[1], L. Grubhoffer[1,2], R. Rego[1], N. Rudenko[1], M. Golovchenko[1], J. Nebesarova[1,3]

[1]Biology Centre of the Academy of Sciences of the Czech Republic, České Budějovice, Czech Republic
[2]Faculty of Science, University of South Bohemia, České Budějovice, Czech Republic
[3]Faculty of Science, Charles University , Prague, Czech Republic

martin.strnad.cze@gmail.com
Keywords: B. burgdorferi, tick transmission, confocal microscopy

The Lyme disease is the most common vector-borne infection in the Western world with an annual incidence usually in excess of 100 cases per 100 000 people in temperate areas of the United States and Europe [1]. If not diagnosed early and treated appropriately, the disease may lead to severe arthritic, cardiovascular and neurological complications.

B. burgdorferi, the causative agent of this disease, circulates among wildlife vertebrate hosts and *Ixodes* tick vectors but may sometimes infect humans. Its natural enzootic cycle usually occurs as follows: The larval/nymphal stage tick feeds on an infected host. During this engorgement, the spirochetes reach the tick gut and stay confined to it [2]. After the tick molts into the next developmental stage, it finds a second host. The new bloodmeal triggers the spirochetes to multiply within the midgut and traverse the gut endothelium in a highly organized manner. They finally disseminate through the hemocoel up to the tick salivary glands and into the new host [3]. We studied whether *B. burgdorferi* is capable of reaching the tick salivary glands during the first feeding period in uninfected ticks.

By employing an *in-vitro* feeding assay designed for hard ticks [4], we fed uninfected adult *Ixodes ricinus* ticks on blood containing >1 x 10^7 spirochetes/mL. In our study, we examined the ability of low- (<7) and high-passage (>15) *B. burgdorferi* to invade the salivary glands and correlate its dissemination potential to the presence of particular plasmids within the genome.

B. burgdorferi isolate B31, the first sequenced *B. burgdorferi* strain, contains at least 12 linear plasmids (lp) and 9 circular plasmids (cp) [5]. Some of the plasmids which are undisputedly connected with pathogenesis and infectivity in the mammalian host and, to a lesser extent, in the tick vector have been already identified. Lp25, lp28-1 and lp36 were proven to exhibit a direct correlation with the persistent infection within mice when present in the spirochete *[6]-[8]*. The plasmids being reported to take part in the establishment of infection and dissemination within the tick vector include lp25, lp54, and cp26 [9]-[11].

The low-passage borrelia, used for this study, possessed all of the aforementioned essential plasmids. The plasmid content of the high-passage spirochetes, however, was incomplete. Using confocal laser scanning microscopy and correlative light electron microscopy to image the spirochetes, we observed that the high-passage bacteria were unable to disseminate to the tick salivary glands. On the other hand, we were able to localize the low-passage spirochetes on the surface of the salivary gland acini (Figure 1).

Our data suggest that *B. burgdorferi* sensu stricto has the ability to traverse the tick gut and migrate straight to the salivary glands during a single tick feeding. The plasmid composition does appear to play an important role in this process. These findings help to possibly shed new light on the survival and adaptation of the Lyme disease spirochete within the tick vector and its transmission to a new mammalian host.

1. R.M. Bacon, K.J. Kugeler and P.S. Mead, MMWR Surveill. Summ. 57 (2008), p. 1.
2. T.G. Schwan and J. Piesman, Emerg. Infect. Dis. 8 (2002), p. 115.
3. S.M. Dunham-Ems, M.J. Caimano, U. Pal, et al., J. Clin. Invest. 119 (2009), p. 3652.
4. T. Kröber and P.M. Guerin, Trends. Parasitol. 23 (2007), p. 445.
5. C.M. Fraser, S. Casjens, W.M. Huang, et al., Nature. 390 (1997), p. 580.
6. J.E. Purser and S.J. Norris, Proc. Natl. Acad. Sci. U S A. 97 (2000), p. 13865.
7. M. Labandeira-Rey and J.T. Skare, Infect Immun. 69 (2001), p. 446.
8. M.W. Jewett, K. Lawrence, A.C. Bestor, et al., Mol. Microbiol. 64 (2007), p. 1358.
9. D. Grimm, K. Tilly, D. M. Bueschel, et al., J. Med. Entomol. 42 (2005), p. 676.
10. X.F. Yang, U. Pal, S.M. Alani, et al., J. Exp. Med. 199 (2004), p. 641.
11. U. Pal, X.F. Yang, M. Chen, et al., J. Clin. Invest. 113 (2004), p. 220.
12. The study was supported by Academy of Sciences of the Czech Republic (Z60220518) and by the Technology Agency of the Czech Republic (TE01020118)

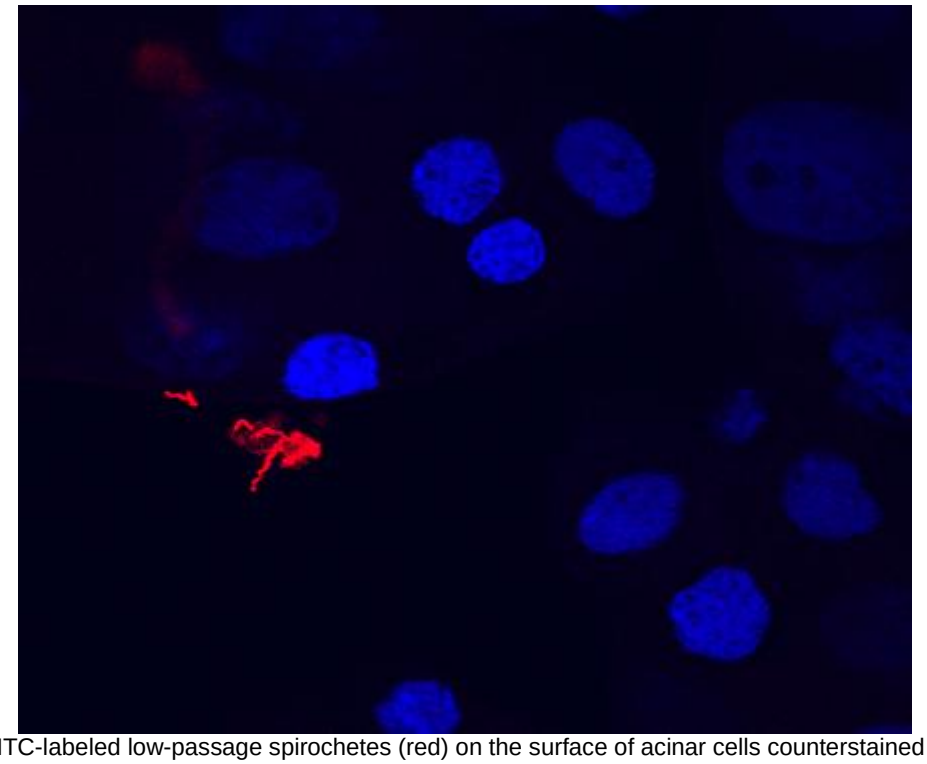

Figure 1. TRITC-labeled low-passage spirochetes (red) on the surface of acinar cells counterstained with DAPI.

Microorganisms and Biofilms

LS.1.P011
The adhesion of bacteria to austenitic stainless steel with different surface roughness

M. Hočevar[1], M. Godec[1], M. Jenko[1], D. Drobne[2], N. Gunde Cimerman[2], S. Novak [2]

[1]Institute of Metals and Technology, Ljubljana, Slovenia
[2]University of Ljubljana, Biotechnical Faculty, Department of Biology, Ljubljana, Slovenia

matej.hocevar@imt.si
Keywords: stainless steel, microbial adhesion, SEM, AES, AFM

The adhesion of bacteria to surfaces is an important biological process governed by the material surface properties (chemical composition, roughness, topography and surface energy), bacterial properties (surface charge, hydrophobicity, cell size, possession of flagella and pili) and the properties of the environment (temperature, flow, composition and ionic strength of the aqueous medium) [1-3]. The presence of bacteria on the surface enhances corrosion of material and presents chronic source of microbial contamination in medical and food industries [3-7].

The aim of our research was to examine the effect of different surfaces of austenitic stainless steel AISI 316 L on the adhesion of bacteria (*Escherichia coli* DH5 alpha) using field emission scanning electron microscopy (FE-SEM) and atomic force microscopy (AFM). The surface topography and roughness have been widely discussed as parameters influencing bacterial adhesion. We assumed that surface roughness correlates with the density of adhered bacteria. By using different surface treatments (grinding, polishing) on austenitic stainless steel different surface roughness (R_a) values and topographies (Aizv, A100, A320, A800, A1200, Apol) were achieved.

Surface characterization was made by Auger Electron spectroscopy (AES), x-ray photoelectron spectroscopy (XPS), AFM and contact angle goniometer. Samples were exposed to suspension of bacteria and the non-adhering bacteria were removed by rinsing the substrate with sterile phosphate buffered saline (PBS). Samples were then prepared for SEM observations regarding the distribution and the number of adhered cells.

As expected, the number and distribution of the attached bacteria varied among different samples. However, we did not entirely confirm our assumption. First results show that the least bacteria was on A800 sample (R_a=0.08 µm), attachment to both smoother and rougher surfaces was higher. The bacteria usually attach to the vicinity of the previously attached bacteria, so that they form clusters (Figure 1). The bacteria prefer scratches, cracks and surface irregularities over the smoother surface as they can provide shelter from unfavourable environmental factors (Figure 2, 3).

1. M. Katsikogianni and Y.F. Missirlis, European Cells and Materials 8 (2004), p.:37-57.
2. N. Kouider, F. Hamadi, B. Mallouki, J. Bengourram, M. Mabrouki, M. Zekraoui, M. Ellouali and H. Latrache, International Journal of Pure and Applied Science 4 (2010), p.(1):1-7.
3. E. Medilanski, K. Kaufmann, L. Y. Wick, O. Wanner and H. Harms, Biofouling: The Journal of Bioadhesion and Biofilm Research 18 (2002), p.(3):193–203.
4. J. W. Arnold and G. W. Bailey, Poultry Science 79 (2000), p.:1839–1845.
5. H. A. Videla and L. K. Herrera, International Microbiology 8 (2005), p.:169-180.
6. Q. Zhao, Surface and Coatings Technology 185 (2004), p.(2-3):199-204.
7. J. P. Maréchal and C. Hellio, International Journal of Molecular Science 10 (2009), p.(11):4623-4637.

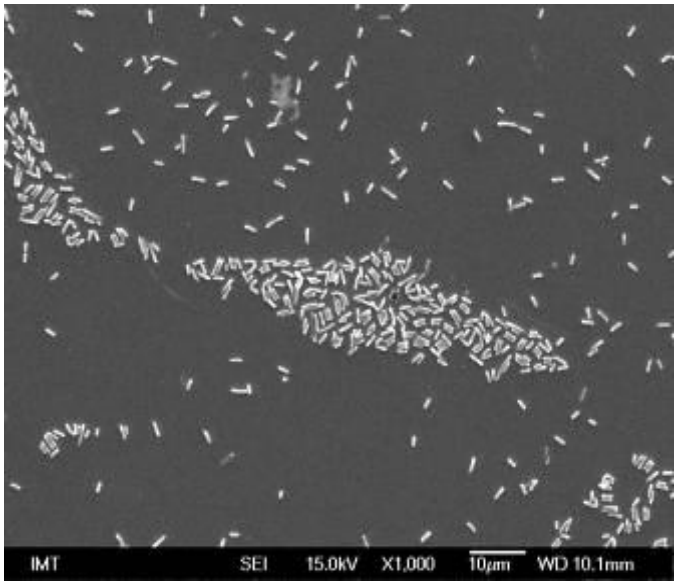

Figure 1. SEM image of attached *E. coli* to stainless steel sample Apol (polished surface).

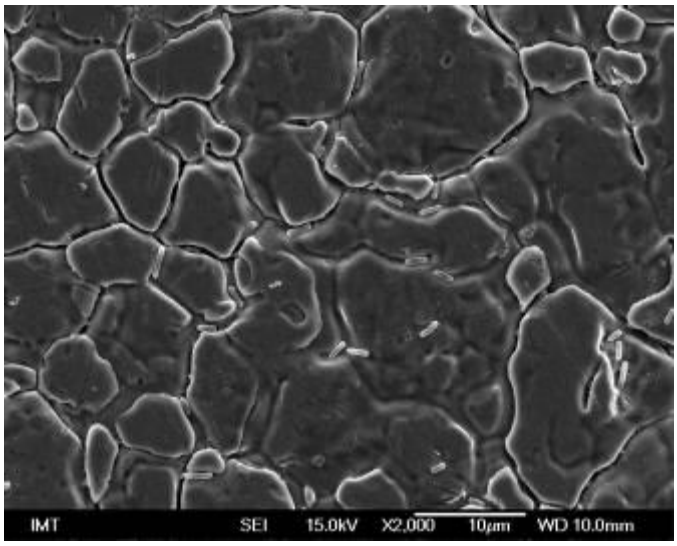

Figure 2. SEM image of attached *E. coli* to stainless steel sample Aizv (as received).

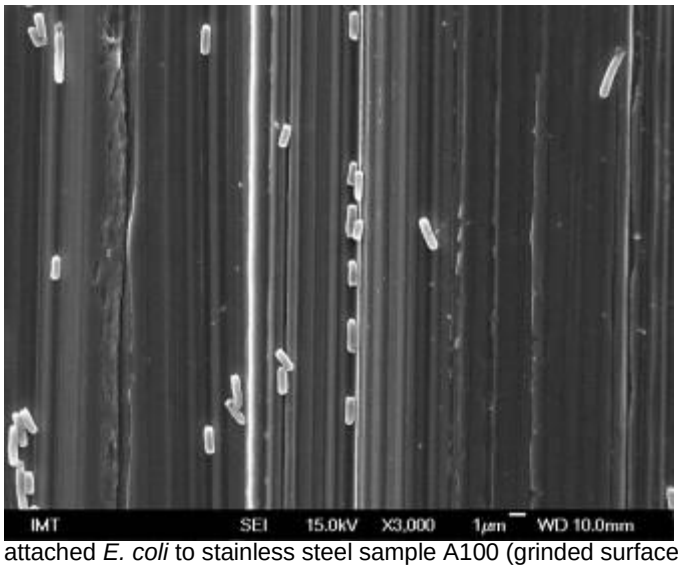

Figure 3. SEM image of attached *E. coli* to stainless steel sample A100 (grinded surface with grit P100)

Microorganisms and Biofilms

LS.1.P012
Studies on novel mechanisms of NK cell activation and their role in anti-mycobacterial immunity

A. Stringaro[1], M. Colone[1], A. Aulicino[2], S. Esin[2], G. Batoni[2], M. Campa[2]

[1]Italian National Institute of Health , Technologies and Health, Rome, Italy
[2]University of Pisa, Dept of Translational Research and New Technologies in Medicine and Surgery, Pisa, Italy

annarita.stringaro@iss.it
Keywords: Mycobacterium tuberculosis, HIV infection, NK cells, electron microscopy

Tuberculosis (TB) represents the most frequent opportunistic infection in AIDS patients. TB is the leading cause of death among HIV-infected persons and may accelerate the course of HIV infection [1]. HIV and *Mycobacterium tuberculosis* (MTB) (Figure 1a) annually cause 3 million and 2 million deaths, respectively. 600,000 of these deaths are among individuals doubly infected with HIV and MTB and each year there are around 2 million new double infections [2]. Control of the infection is dependent on innate immune cells such as macrophages and DCs that play a key role in engulfing and eliminating the intracellular pathogen, while NK cells and granulocytes also play a protective role [3].

The possibility that NK cells, similarly to other cells of innate immunity, can directly recognize pathogens via their surface receptors is a hypothesis that is being increasingly taken into consideration. However, to date there are only a few reports that have studied the effects of the direct interaction of human NK cells with microorganisms or with their products. This might be due, at least partially, to the inherent difficulty of obtaining a highly purified NK cell population and to the known ability of even a few contaminating monocytes/macrophages to activate NK cells, making it difficult to fully discriminate between direct and indirect NK cell activation signals.

Previous studies have demonstrated that *Mycobacterium bovis* bacillus Calmette-Guerin (BCG) can directly interact with human NK cells in the absence of monocytes/macrophages or interleukin 12 (IL-12) and can induce the proliferation, IFN production, and cytotoxic activity of such cells [4]. In order to investigate novel effector functions of NK cells upon direct interaction with mycobacteria, in this study we provide an insight into the mechanism of microorganism interaction with human resting NK or interleukin-2-activated NK (LAK) cells by scanning electron microscopy (SEM) analysis. When resting NK cells were incubated with mycobacteria (at effector/target ratio 1:10 for 2 h) a very low percentage of the lymphocytic effectors bound to the bacteria target. In contrast to the above results, LAK cells had more frequent contacts with microorganisms. Upon contact the surface morphology of the LAK cell was extensively modified, with villous protrusions which tended to envelope the target (Figure 1b). Since these results seem to be very promising, in order to clarify the mechanisms of this interaction, observations by transmission electron microscopy (TEM) of the same samples are in progress.

1. J. H. Day et al., J. Infect. Dis. 190 (2004), p. 1677.
2. S. Kaufmann and A.J. McMichael, Nat. Med. 11 (2005), p. S33.
3. P. L. Lin, J. L. Flynn, J. Immunol. 185 (2010), p. 15.
4. S. Esin, G. Batoni, M. Pardini, et. al., Immunology 112 (2004), p. 143.

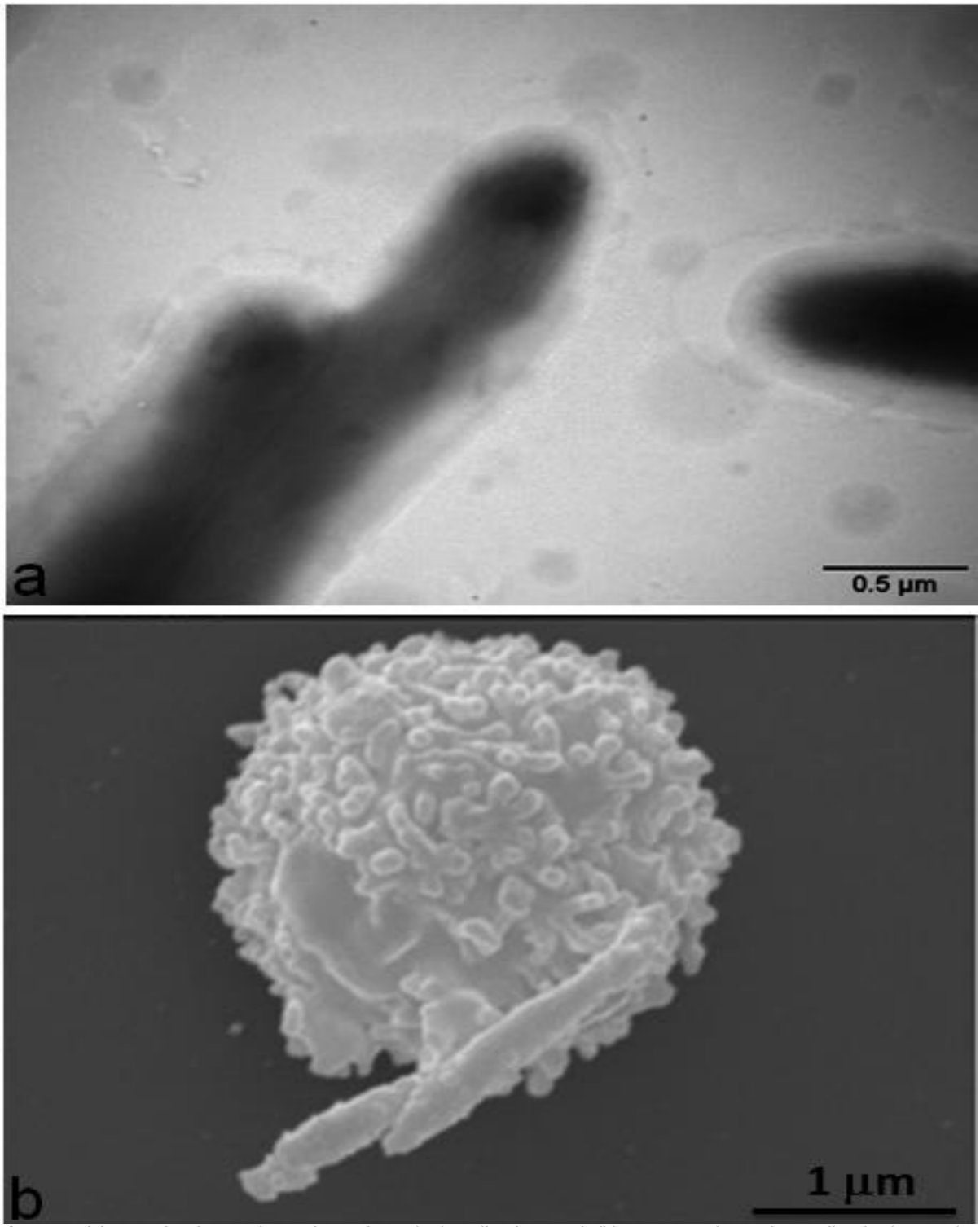

Figure 1. (a) Unstained Mycobacterium tuberculosis cells observed. (b) LAK-Mycobacterium cell pair observed by SEM.

Microorganisms and Biofilms

LS.1.P013
'Candidatus Troglogloea absoloni' - novel lineage of *Nitrospirae*, forming sprout-like bacterial aggregates in Dinaric Karst subterranean stream

R. Kostanjsek[1], L. Pasic[1], H. Daims[1], B. Sket[1]

[1]University of Ljubljana, Biotechnical Faculty, Department of Biology, Ljubljana, Slovenia

rok.kostanjsek@bf.uni-lj.si
Keywords: TEM, FESEM, FISH, '*Candidatus* Troglogloea absoloni', cave microorganisms

Subterranean habitats, including karst caves, are unique environments characterized by constant climatic parameters, absence of light and a limited availability of nutrients. Although cave microorganisms were often neglected, several microorganisms capable of formation of macroscopic formations were described and characterized in cave environments in past few decades [1].

One of the earliest mentions of macroscopic microbial structures in cave environments dates almost a century ago, when gross morphology of whitish, sprout-like aggregates attached to rocky streambed of subterranean stream of cave Vjetrenica in Herzegovina were described [2]. A single sprout-like aggregate measured 1–2 cm in length, several millimeters in diameter at the base and narrows progressively towards the tip. The aggregates occurred in groups, ranging from few to thousands, covering considerable parts of the stream bed in meadow-like formations.

Since these aggregates were not further characterized after initial description, we applied the combination of transmission electron microscopy (TEM), field emission scanning electron microscopy (FE-SEM), cloning, sequencing and fluorescent *in situ* hybridization (FISH) to describe the architecture, ultrastructure and microbial composition of these formations.

For scanning electron microscopy the samples were fixed in 1% glutaraldehyde and 0,4% paraformaldehyde in 0.1 M sodium cacodylate buffer (pH 7,2) at the sampling spot. Samples were postfixed OsO_4, dehydrated in a graded series of ethanol, critical point dried mounted on aluminum holders, sputter coated with platinum and examined by Jeol JSM-7500F FESEM. The samples for transmission electron microscopy were fixed in 3,5% glutaraldehyde in 0,1 M sodium cacodylate buffer (pH 7,2). Prior to embedding in Agar 1000 medium the samples were washed, postfixed and dehydrated as described above. After staining with uranyl acetate and lead citrate, the ultrathin sections were examined with Philips CM100 microscope. For fluorescence *in situ* hybridization (FISH) the samples were fixed in 4% paraformaldehyde in 0,1 M sodium phosphate buffer (pH 7,2), dehydrated and embedded in paraffin. Histological sections were rehydrated in ethanol series and hybridized to oligonucleotide probes that target the largest phylogenetic groups detected by sequence analysis [3] and observed on AxioImager Z.1 microscope (Zeiss) upgraded by Apotome system, for optical sectioning by structured illumination [3].

Ultrastructural analysis revealed complex structure of sprout-like aggregates. Their core consists of rod-shaped bacteria embedded in a thick extracellular matrix (Figure 1A). A closer examination of these bacteria revealed small protuberances on the cell surface, expansions of periplasmic space, as well as electron-dense spherical inclusions and translucent vesicles in the cytoplasm (Figure 1B). The core of the aggregates is covered by an electron denser crust, consisting of mineral inclusions and complex community of predominantly of filamentous bacteria (Figure 2A). The crust is thicker at the base and gets gradually thinner towards the tip of the aggregate, where it is completely missing, exposing the rod-shaped bacteria in the core (Figure 2B). FISH experiments and phylogenetic analysis based on 16S rRNA affiliated the rod-like bacteria in the core to novel lineage of the bacterial phylum *Nitrospirae* provisionally named "*Candidatus* Troglogloea absoloni", while most of bacteria in the crust was successfully hybridized by probe specific to *Betaproteobactera*. (Figure 3)

Although a possible ecological role of *Ca. Troglogloea absoloni* remains unknown, the surprising discovery of this novel *Nitrospirae* lineage in the sprout-like formations demonstrates our limited knowledge of the microbial biodiversity in subterranean habitats and contributes to biodiversity of subterranean ecosystems in Dinaric Karst, which is already recognized as one of the reaches in the world.

1. Summers Engel A. In »Encyclopedia of Caves«, ed. W.B. White, D.C. Culver (Academic Press, Chennai) (2012), pp. 490–499.
2. Smolikova O. (1919), Časopis Moravskeho Musea Zemskeho 17–19:177–188
3. Kostanjšek R., Pašić L., Daims H., Sket B. (2013), Microbial Ecology, in press

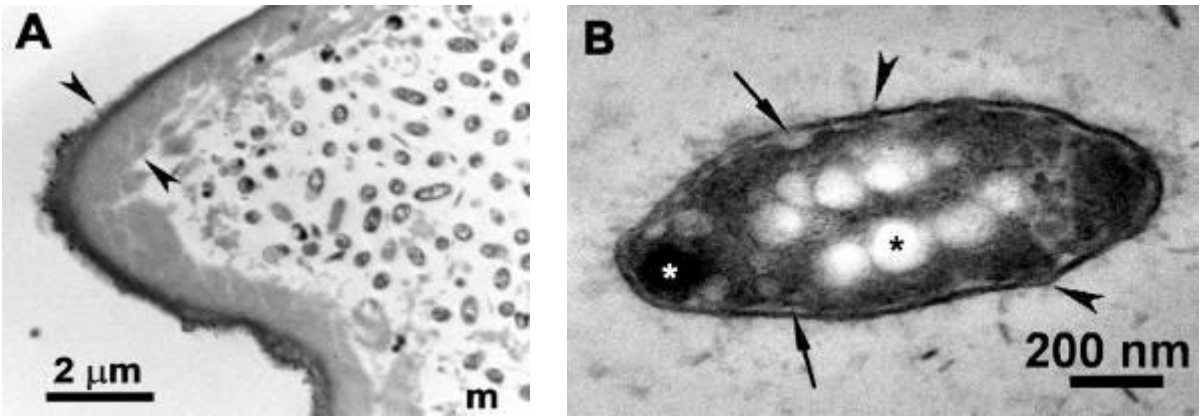

Figure 1. A. Cross-section of single sprout-like aggregate, showing rod -like bacteria embedded in extracellular matrix (m) and covered by crust (between arrowheads). B. Ultrastructure of single rod-like bacterium, showing protuberances on its surface (black arrowheads), expansions of periplasmic space (black arrows), cytoplasmic vacuoles (black asterisk) and dense inclusions (white asterisk).

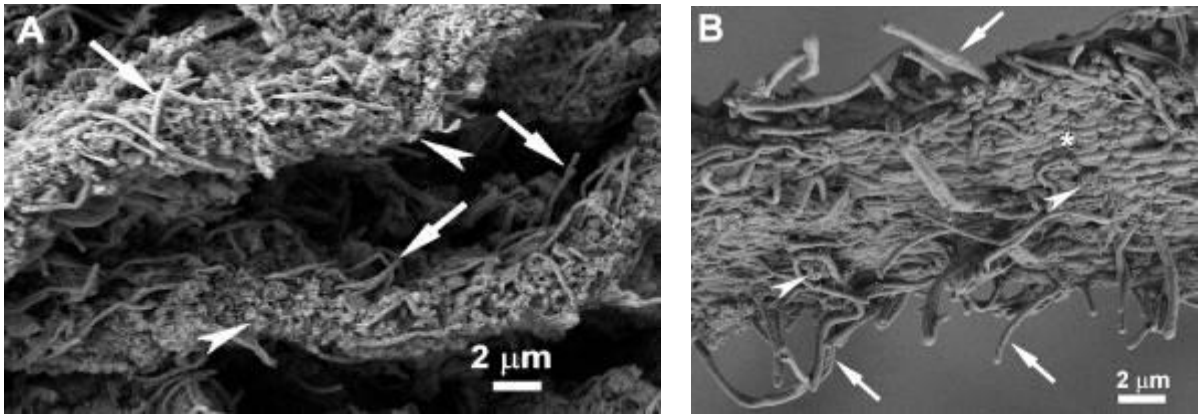

Figure 2. A. Basal part of sprout-like aggregate covered by crust consisting filamentous bacteria (arrows) and mineral inclusions (arrowheads). B. Apical part of the aggregate with exposed rod-like bacteria in the core (asterisk), filamentous bacteria (arrows) and mineral inclusions (arrowheads) on the surface.

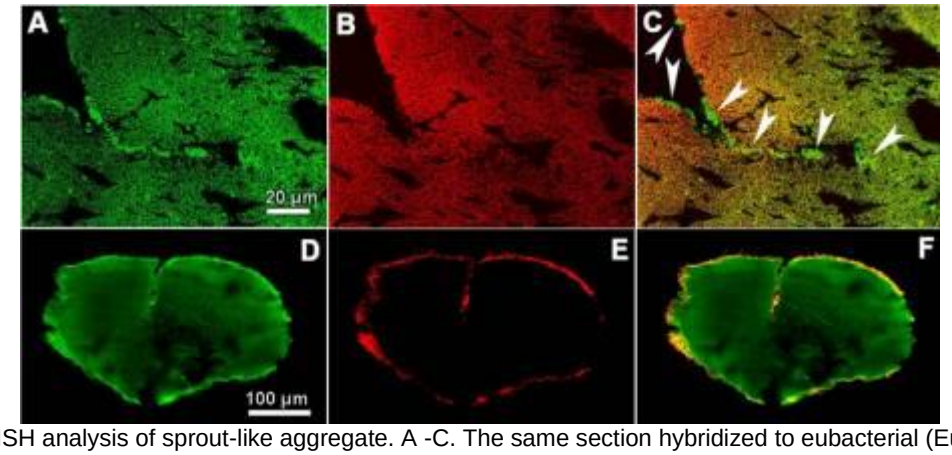

Figure 3. FISH analysis of sprout-like aggregate. A -C. The same section hybridized to eubacterial (Eub338) probe (A) or to probe specific to Ca. *T. absoloni* (B). A combination of both images (C) shows the bacteria not hybridized by probe specific to Ca. *T. absoloni* on the surface of aggregate (arrows). Panels D to F show the same section hybridized to eubacterial probe (D) or to probe specific for *Betaproteobacteria* (E). A combination of both images (F) shows the absence of *Betaproteobacteria* in the core and their location on the surface of the sprout-like structure.

Microorganisms and Biofilms

LS.1.P014
Tracking mineral particles and metal(oid)s from armor stones in freshwater biofilms

J. Meier[1], A. Grün[1], W. Manz[1], B. Hauröder[2]

[1]University of Koblenz-Landau, Institute for Integrated Natural Sciences, Koblenz, Germany
[2]Central Institute of the Federal Armed Forces Medical Service, Electron Microscopy, Koblenz, Germany

Keywords: armor stones, biofilm, minerals, metal(oid)s, SEM, TEM, EDX

Industrially produced copper slag is widely used as armor stone in inland waterways. Copper slag still contains significant amounts of sulfidic minerals and leaching of metal(oid)s poses a potential risk for the aquatic environment [1]. Biofilms may function as a sink due to metal(oid)s binding to functional groups of extracellular polymeric substances and cell surfaces or through intracellular storage. Additionally, the biofilm matrix may trap small, abrasive particles. These bound metal(oid)s or mineral particles may be transferred to organisms of higher trophic levels, particularly to biofilm grazing organisms. Furthermore, biofilms may harbor microorganisms, which enhance the dissolution of the trapped mineral particles, e.g. the oxidative dissolution of sulfidic minerals. The fate of metal(oid)s and small mineral particles released from armor stones remains so far unclear. Little is known about how these particles integrate into a biofilm matrix and how they interact with the biota.

In cooperation with the German Federal Institute of Hydrology, an environmental impact assessment of copper slag (CUS) was performed with basanite (BAS) as reference material of natural origin. Six indoor stream mesocosms were set up containing water and sediment from the river Rhine. CUS and BAS were applied as crushed sand (grain size < 2 mm). The experiments were run for 6 months, after which biofilm was sampled from acrylic glass walls. In order to unveil the pathways of dissolved metal(oid)s or released mineral particles within biofilms, ultrathin sectioned embedded biofilm samples were investigated by transmission electron microscopy. EDX was used to determine particle elemental composition in order to discriminate prime armor stone minerals from secondary minerals formed by microbial activity. Scanning electron microscopy was employed to demonstrate the diverse nature and complex structure of investigated biofilms.

SEM of biofilms showed a dominance of a variety of diatom species accompanied by a sheathed, filamentous cyanobacterium affiliated to the genus *Leptolyngbya* (Fig. 1a). In addition, various smaller, morphologically diverse bacterial cells were observed, either attached on diatom shells, cyanobacterium sheaths or mineral surfaces (Fig. 1b). TEM of ultrathin sections showed both the cells of the different biofilm microorganisms as well as many mineral particles, which were very small in size (<500 nm in diameter). These particles were apparently loosely attached to cell surfaces or extracellular structures such as sheaths or capsules and did not reveal specific adhesion or incorporation. Their elemental composition reflected the main elements present also in the original armor stone minerals (spectra in Fig. 1c, 1d). However, a high spatial heterogeneity on a very small scale was detected revealing iron rich spots in BAS biofilms and iron and sulfur rich spots in CUS biofilms.

The incorporation of small mineral particles from copper slag can initiate enhanced interaction with biota due to their high surface to volume ratio. Oxidative dissolution of sulfidic minerals by microorganisms present in the biofilm may result in a stronger release of dissolved metal(oid)s and decrease in pH. The small particle size and the heterogeneous mineral composition may contribute to the overall heterogeneity of the biofilm and hence its metabolic and physiological diversity. A direct evidence for the removal of dissolved metal(oid)s from the water phase by precipitation (secondary mineral formation), i.e. the selective enrichment of specific elements on cell surfaces or extracellular structures, could not be found.

1. A. Schmukat, L. Duester, D. Ecker, H. Schmid, C. Heil, P. Heininger, T.A. Ternes, J. Hazard. Mat., 227-228 (2012) 257-264.

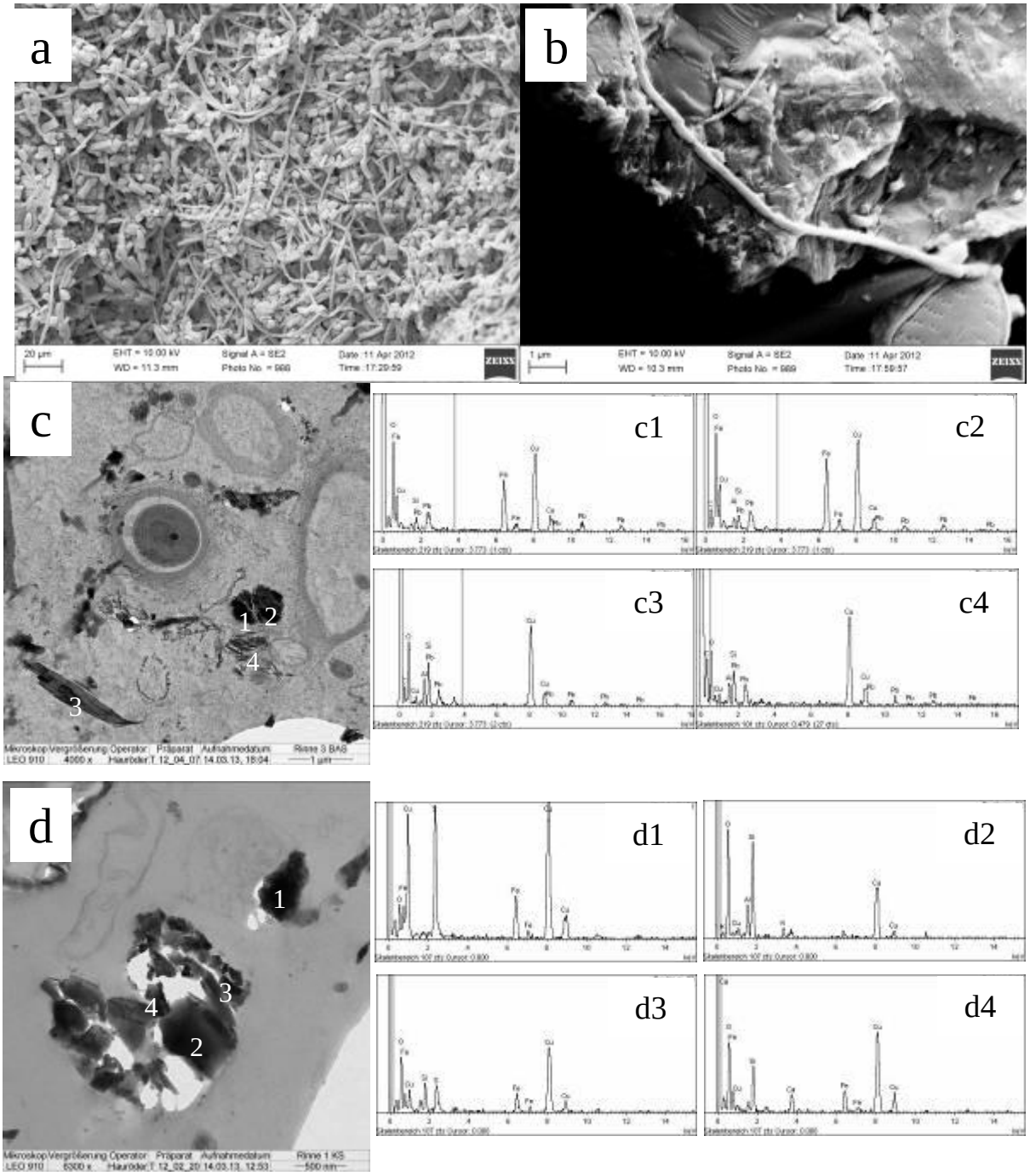

Figure 1. SEM images of biofilm from mesocosm 1 (CUS) (a,b), TEM images and EDX spectra of biofilm from mesocosm 3 (BAS) (c) and from mesocosm 1 (CUS).

Microorganisms and Biofilms

LS.1.P015
Application of an image analysis system for quantification and classification of environmental microbes from agricultural biogas plants

Y.-S. Kim[1], P. Scherer[1]

[1]HAW-Hamburg, Biotechnology, Hamburg, Germany

paul.scherer@haw-hamburg.de
Keywords: quantification, methanogen, biogas

The goal of this study was to find a new tool to evaluate the biological vitality of a biogas plant. Therefore, a simple microscopic method for quantification and morphological classification of microorganisms was developed. Cell counts and its morphology are supposed to be a direct indicator for the performance of a methanogenic habitate [1]. Since environmental samples contain interfering fibrous material, an appropriate sample preparation is required such as an optimal visualizing stain, homogenous distribution of sample on the slide as well as ~~a~~ proper image analysis algorithms. SYBR Green I was found to be the most sensitive dye for total cell counts in environmental samples with minimal background fluorescence [2]. For detection of methanogens, auto-fluorescence based on the typical methanogenic fluorescent coenzyme F_{420} was used. A low viscosity methylcellulose was successfully applied as a fixing agent for microscopic slide. It showed better adhering character and supplied more regular surface related to agar or gelatin. With the help of accompanying molecular analysis [3], morphological classification algorithms for methanogens could be established by the image analysis software Image Pro 7. During analyzing one biogas plant for more than 26 weeks and several different anaerobic digesters for a shorter time, its reliability as a counting method was verified.

The correctness of the counting by image analysis system was proven by Neubauer counting chamber with microbial cells like *Staphylococcus* and *Escherichia coli.* Furthermore, interfering particles were tested by inorganic nano particles, maize fibres and artificial fluorescent beads. The results showed a good congruence between quantitative image analysis and Neubauer counting chamber representing a deviation of 0.2 – 2.6 %.

1. Dolfing J., Mulder J. Comparison of methane production rate and coenzyme F_{420} content of methanogenic consortia in granular sludge. Applied and Environmental Microbiology (1985), 49(5), 1142-1145.
2. Singer V.L., T.E. Lawlor, and S. Yue. Comparison of SYBR Green I nucleic acid gel stain mutagenicity and ethidium bromide mutagenicity in the Salmonella / mammalian microsome reverse mutation assay (Ames test). Mutation Research.(1999), 439:37-47.
3. Krakat N., Westphal A., Schmidt S. and Scherer P. Anaerobic digestion of renewable biomass: Thermophilic temperature governs methanogen population dynamics. Applied and Environmental Microbiology (2010), 76(6), 1842–1850.

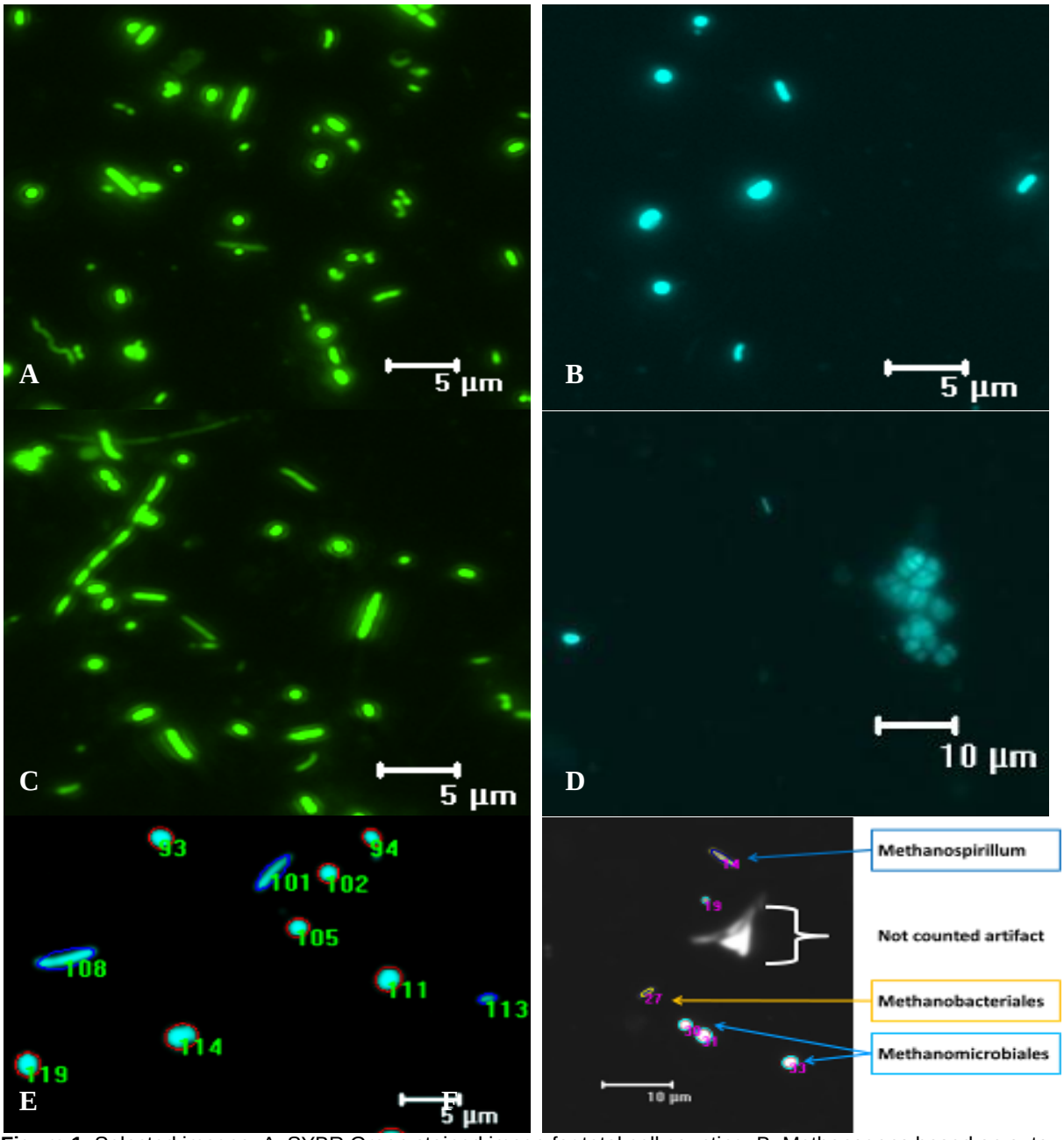

Figure 1. Selected images: A: SYBR Green stained image for total cell counting; B: Methanogens based on auto-fluorescence; C: Long and sheated filament of *Methanosaeta (left) being surrounded by different morphotypes*; D: Cellular packets of *Methanosarcina*; E, F: Automatically counted methanogens with different coloured circles around them. They were classified and quantified by developed algorithms of the image analysis software Image Pro 7 according to the morphology.

Microorganisms and Biofilms

LS.1.P016
Characterization of the S-layer of the anammox bacterium Kuenenia stuttgartiensis

M. van Teeseling[1], N. de Almeida[1], A. Klingl[2,3], R. Rachel[2], M. Jetten[1], L. van Niftrik[1]

[1]Radboud University Nijmegen, Microbiology, Nijmegen, Netherlands
[2]Universitaet Regensburg, Center for Electron Microscopy, Regensburg, Germany
[3]Philipps Universitaet Marburg, LOEWE Center for Synmikro, Marburg, Germany

m.vanteeseling@science.ru.nl
Keywords: anammox, *Kuenenia stuttgartiensis*, S-layer, cell wall, electron microscopy

"Candidatus Kuenenia stuttgartiensis" is an anaerobic ammonium oxidizing (anammox) bacterium belonging to the order of Brocadiales in the phylum of the *Planctomycetes*. Anammox bacteria are important in nature where they contribute significantly to oceanic nitrogen loss and are applied in wastewater treatment for the removal of ammonium. The cell biology of anammox bacteria is extraordinary; the cells are divided into three membrane-bounded compartments (Figure 1). The inner compartment, the anammoxosome, is the location of the anammox reaction, where energy is generated via a proton motive force and an ATP synthase in the anammoxosome membrane [1]. The surrounding riboplasm is the location of the nucleoid and ribosomes [2]. The function of the outermost compartment, the paryphoplasm, is unknown. The cell wall of anammox bacteria deviates from the typical bacterial cell wall, since it is hypothesized to lack peptidoglycan. In addition, the identity of the outermost membrane, which has originally been defined as a cytoplasmic membrane, is still under debate. The detection of putative outer membrane (OM) proteins and other OM biosynthesis markers in the genome and proteome of the anammox bacteria *Kuenenia stuttgartiensis* and *Scalindua profunda* might suggest the outermost membrane to have characteristics typically associated with an outer membrane of Gram-negative bacteria [3]. This study focuses on the cell wall of the anammox bacterium *K. stuttgartiensis* using electron microscopy. Transmission electron micrographs of freeze etched *K. stuttgartiensis* cells showed the presence of a hexagonal surface layer (S-layer) in the majority of *K. stuttgartiensis* cells. S-layers are crystalline two-dimensional arrays of proteinaceous subunits that make up the outermost layer of many bacterial and archaeal cell envelopes. Enrichment of the S-layer of *K. stuttgartiensis* cells has indicated a putative S-layer protein. This putative S-layer protein was identified via mass spectroscopy and used to immunize rabbits in order to obtain polyclonal antibodies. The antibody was used for immunogold localization on thin sections of cells that were high pressure frozen and then treated with the rehydration method [4]. The putative S-layer protein was localized to the outside, the S-layer, of the *K. stuttgartiensis* cell which verifies that it indeed forms the S-layer. This study showed the presence of an S-layer as the outermost layer of the anammox bacterium *K. stuttgartiensis* and identified the S-layer protein. Additional research should lead to understanding of the function of this S-layer in anammox bacteria. In addition, further studies should address the cell wall of anammox bacteria, to elucidate the complete composition of the cell wall of these bacteria.

1. L. van Niftrik et al., Mol. Microbiol. 77 (2010) p. 701.
2. MR. Lindsay et al., Arch. Microbiol. 175 (2001) p. 413.
3. DR. Speth, MCF. van Teeseling, MSM. Jetten, Front. Microbio. 3 (2012) p.304.
4. E. van Donselaar et al., Traffic 8 (2007) p.471.
5. MCF. van Teeseling, S. Neumann, L. Van Niftrik. J Mol Microbiol Biotechnol 23 (in press).

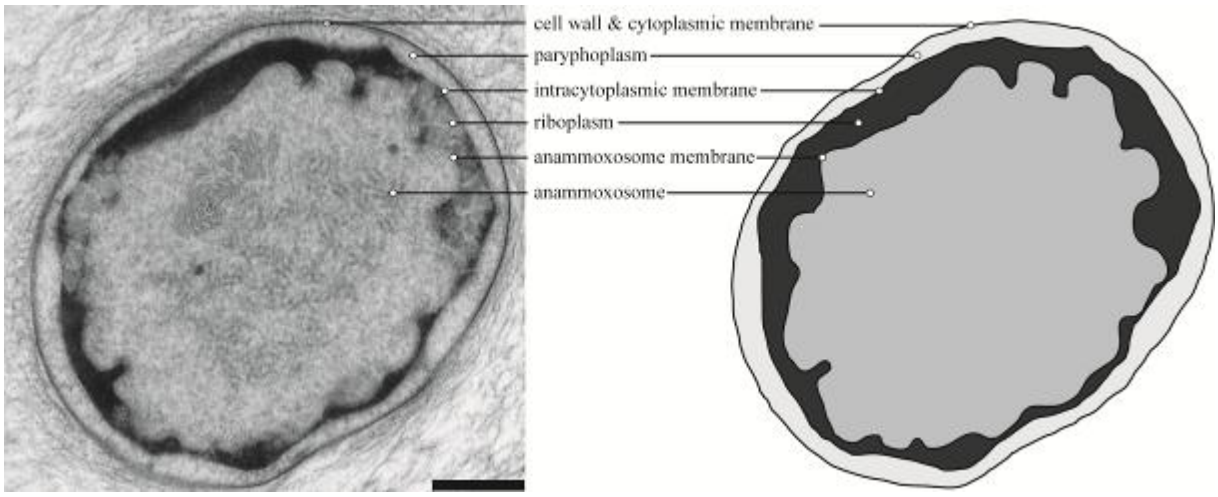

Figure 1. Transmission electron micrograph and schematic drawing of the cell plan of anammox bacteria. Scale bar; 200 nm. Adapted from [5].

Microorganisms and Biofilms

LS.1.P017
Linking ultrastructure and function in the uniquely compartmentalized anammox bacteria

S. Neumann[1], M.S.M. Jetten[1], L. van Niftrik[1]

[1]IWWR, Radboud University Nijmegen, Microbiology, Nijmegen, Netherlands

s.neumann@science.ru.nl
Keywords: anaerobic ammonium oxidation; bacteria; cell compartmentalization

Prokaryotic cells belonging to the domain *Bacteria* are commonly subdivided into a Gram-positive and a Gram-negative type based on the organization of their cell wall. However, some bacteria defy this traditional classification. One of the most notable phyla in this respect is the *Planctomycetes*. These bacteria are thought to be devoid of several characteristics associated with Gram-positive or Gram-negative bacteria: a periplasmic space, a peptidoglycan-containing cell wall and an outer membrane [1]. In addition, the planctomycete cell is subdivided into two compartments: the outermost compartment – the paryphoplasm – is thought to be surrounded by the cytoplasmic membrane, but its function is so far unknown. An internal lipid bilayer membrane separates the paryphoplasm from the riboplasm, which contains the DNA, RNA and ribosomes of the cell [2].

The anammox (**an**aerobic **amm**onium **ox**idizing) bacteria belong to the phylum *Planctomycetes*. Prokaryotic organisms conserve the energy required for growth and maintenance of the cell by oxidation of organic or inorganic compounds. Although thermodynamically favorable, the oxidation of ammonium with nitrite as electron acceptor was not known to be facilitated by any organism until the anammox bacteria were discovered [3]. Anammox bacteria have been found in many different habitats around the world. Their importance for the biogeochemical cycling of nitrogen on a global scale is now recognized and they are currently applied for the cost-efficient and eco-friendly removal of nitrogen compounds from wastewater [4, 5, 6]. Aside from their metabolism, anammox bacteria presented another novelty in the bacterial world: the majority of the volume of the anammox cell is taken up by a central cell compartment, which has not been observed in other planctomycetes and has been named the anammoxosome [7]. Anammox bacteria are therefore subdivided into three compartments: the cell is rimmed by the paryphoplasm that surrounds the riboplasm, and innermost lies the anammoxosome (Figure 1). This cell plan is present in all anammox bacteria discovered so far. Based on previous studies that used transmission electron microscopy (TEM) combined with immunogold labeling to localize key metabolic proteins [2, 8], and peroxidase staining for localization of cytochrome c proteins [9], it is hypothesized that the anammoxosome is a “prokaryotic cell organelle” harboring the energy metabolism of the cell. Our understanding of the cell ultrastructure is, however, still incomplete. In particular the function of the paryphoplasm remains elusive, except for being the location of the cell division ring [10], and the central role of the anammoxosome in the catabolism of the anammox cell has not yet been directly demonstrated. The latter is due to the fact that the anammoxosome has not been isolated from the rest of the cell in sufficient quantities and purity for conclusive experiments.

Our aim was to gain further insight into the function of the anammoxosome and the cell compartmentalization in anammox bacteria by isolating the anammoxosome. The isolation by itself provided strong evidence that anammoxosomes are truly independent “cell organelles”. They were then used in biochemical assays in order to show the conversion of anammox substrates by isolated anammoxosomes outside of their regular cellular context, since this would corroborate that they harbor the energy metabolism of the anammox cell. Furthermore, proteome analysis of isolated anammoxosomes substantiated their hypothesized role in energy conservation and might also lead to new insights about the anammoxosome. Finally, we located several enzymes of interest, i.e. proteins with possible structural functions as well as enzymes involved in the energy metabolism, inside the anammox cell by immunogold localization.

1. J.A. Fuerst and E. Sagulenko, Nature Reviews Microbiology 9 (2011) p. 403.
2. M.R. Lindsay *et al*, Archives of Microbiology 175 (2001) p. 413.
3. M. Strous *et al*, Nature 400 (1999) p. 446.
4. K.R. Arrigo, Nature 437 (2005) p. 349.
5. M.S.M. Jetten *et al*, Critical Reviews in Biochemistry and Molecular Biology 44 (2009) p. 65.
6. M.M.M. Kuypers *et al*, Proceedings of the National Academy of Sciences of the United States of America 102 (2005) p. 6478.
7. L. van Niftrik *et al*, Fems Microbiology Letters 233 (2004) p. 7.
8. L. van Niftrik *et al*, Molecular Microbiology 77 (2010) p. 701.
9. L. van Niftrik *et al*, Journal of Bacteriology 190 (2008) p. 708.
10. L. van Niftrik *et al*, Molecular Microbiology 73 (2009) p. 1009.
11. S. Neumann, M.S.M. Jetten and L. van Niftrik, Biochemical Society Transactions 39 (2011) p. 1805.

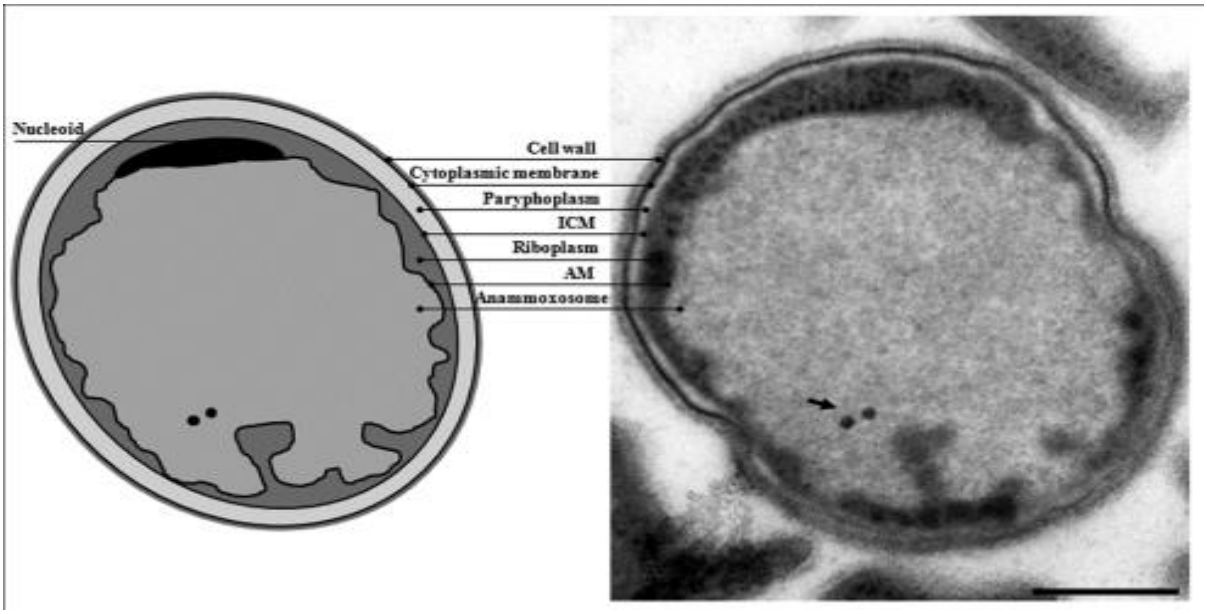

Figure 1. The ultrastructural organization of the anammox bacterium "*Candidatus* Kuenenia stuttgartiensis"; ICM: intracytoplasmic membrane; AM: anammoxosome membrane; scale bar: 200 nm [11].

Microorganisms and Biofilms

LS.1.P018
Microbial assemblages within crustacean calcium bodies

M. Vittori[1], R. Kostanjšek[1], A. Rozman[1], J. Štrus[1]

[1]University of Ljubljana, Biotechnical Faculty, Department of Biology, Ljubljana, Slovenia

milos.vittori@gmail.com
Keywords: biomineralization, bacterial community, symbiosis

Different crustacean groups have evolved various forms of transient calcium deposits, enabling them to minimize calcium loss during molt [1]. Trichoniscids, a group of terrestrial isopod crustaceans, store calcium in special organs, the calcium bodies (Figure 1). These organs are epithelial sacs containing mineral concretions and are located in the hemolymph space alongside the digestive system [2,3,4]. In our recent work on the subterranean trichoniscid *Titanethes albus,* we established that calcium bodies contain high densities of bacteria [4]. Unlike most animal tissues, which provide a constant environment for symbiotic microorganisms, periodical deposition and resorption of minerals in calcium bodies subjects the microorganisms within them to high solvent concentrations and strong fluctuations of their chemical environment.

Since the observation of bacteria within calcium bodies evoked further questions, we aimed to establish which microorganisms inhabit the calcium bodies, whether they are present in different crustacean species and whether or not calcium bodies are colonized by a single microbial species or by a complex microbial community.

To confirm the presence of microorganisms within calcium bodies and classify them to the level of domain, we used fluorescence *in situ* hybridization on paraffin sections of fresh *T. albus* specimens fixed overnight in formaldehyde. We used Cy3-labeled fluorescent probes complementary to archeal or eubacterial 16S rRNA sequences.

The morphological characteristics of microorganisms within *T. albus* calcium bodies were studied with scanning electron microscopy (SEM). For this, calcium bodies were isolated from narcotized specimens of *T. albus* and immediately fixed in a mixture of glutaraldehyde and formaldehyde in cacodylate buffer. The organs were then postfixed with OsO_4, dried in HMDS, sputter coated with platinum and observed with a JSM-7500F field emission scanning electron microscope (JEOL). For ultrastructural observations of the bacteria with transmission electron microscopy (TEM), *T. albus* specimens were dissected, fixed as described above, embedded in Spurr's resin and sectioned. Ultrathin sections were contrasted with uranyl acetate and lead citrate and observed with a CM 100 transmission electron microscope (FEI).

To investigate the possible presence of bacteria in calcium bodies of trichoniscids other than *T. albus*, specimens of *Hyloniscus riparius*, *Haplophthalmus mengii*, *Trichoniscus noricus* and *Androniscus roseus* were prepared as described above, sectioned and observed with TEM. For SEM observation of small species in which manipulation of calcium bodies is difficult, whole animals were fixed, embedded in paraffin and sectioned. Sections and cut paraffin blocks were then deparaffinized and prepared for SEM observation as described for *T. albus*.

As demonstrated with *in situ* hybridization, calcium bodies of *T. albus* are inhabited by eubacteria. TEM and SEM analyses showed that the calcium bodies of this species contain predominantly rod-shaped Gram-negative bacteria. The morphological examination demonstrated the presence of several bacterial morphotypes within an individual calcium body (Figure 2), indicating the presence of a diverse bacterial community rather than a single species. This observation was further supported by preliminary analyses of 16S rDNA clone libraries constructed from DNA isolated from *T. albus* calcium bodies. Further analyses of bacterial communities within calcium bodies and additional work on how bacteria colonize these organs during ontogenetic development are needed; however, the consistent presence of large bacterial populations in calcium bodies of all examined trichoniscids strongly indicates that bacteria are involved in calcification processes in this group of crustaceans.

1. G. Luquet, ZooKeys 176 (2012), pp. 103-121.
2. L. V. Méhely, Studia Zoologica 2 (1932), pp. 103-120.
3. A. Ziegler in “The Biology of Terrestrial Isopods V”, eds. S. Sfenthourakis, P. B. de Araujo, E. Hornung, H. Schmalfuss, S. Taiti and K. Szlavecz, (Leiden, Koninklijke Brill NV) (2003), pp. 299-309.
4. M. Vittori, R. Kostanjšek, N. Žnidaršič, K. Žagar, M. Čeh and J. Štrus, Journal of Structural Biology (2012), 180, pp. 216-225.
5. The authors would like to thank the research group for speleobiology (Department of Biology) for contributing *T. albus* specimens and J. Murko Bulić for her laboratory assistance.

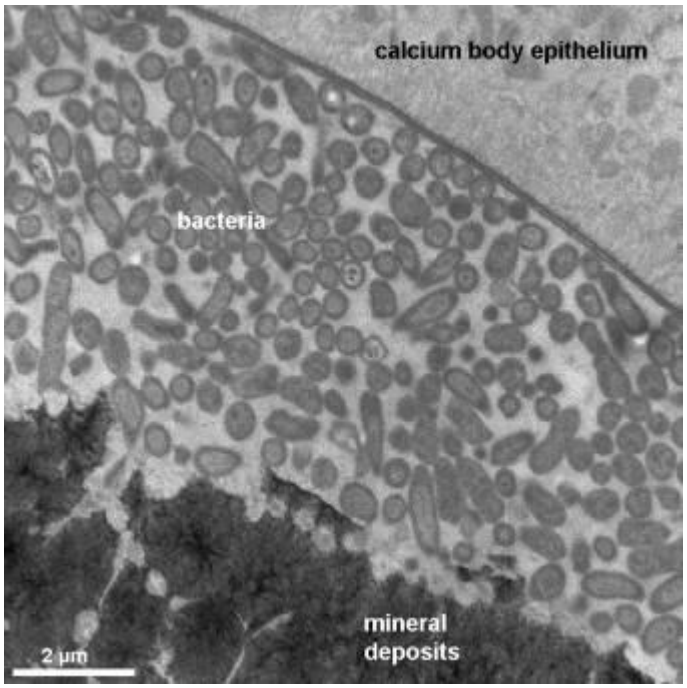

Figure 1. Section through a posterior calcium body of *Hyloniscus riparius*. Bacteria fill the lumen of the organ and surround the mineral deposits at its center.

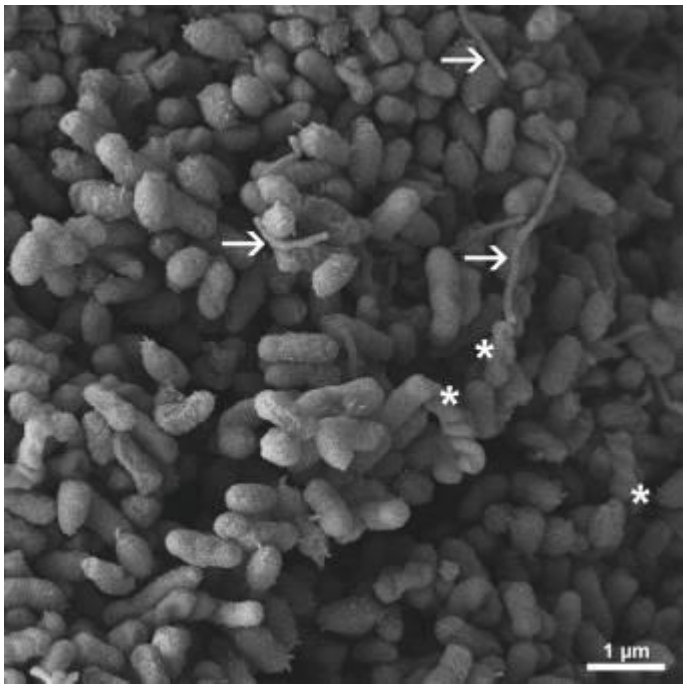

Figure 2. SEM image of the bacterial community within a calcium body of *Titatnethes albus*. In addition to numerous rod-shaped bacteria, filamentous (arrows) and helical (asterisks) forms are visible.

Microorganisms and Biofilms

LS.1.P019
Quantification of *Rhodococcus* actinobacteria adhesive properties using atomic force microscopy

E. Rubtsova[1,2], Y. Chen[3], H.C. van der Mei[3], A. Krivoruchko[1,2], M. Kuyukina[1,2], I. Ivshina[1,2]

[1]Institute of Ecology and Genetics of Microorganisms, Russian Academy of Sciences, Perm, Russian Federation
[2]Perm State National Research University, Perm, Russian Federation
[3]W.J. Kolff Institute, University Medical Center and University of Groningen, Department of Biomedical Engineering, Groningen, Netherlands

rev85@rambler.ru

Actinobacteria of the genus *Rhodococcus* are promising for biotechnology group of microorganisms that possesses a wide variety of catabolic pathways for transformation and degradation of various organic substrates, such as aliphatic and aromatic hydrocarbons, chlorinated phenols, heterocyclic compounds, nitriles, sterols, pesticides, lignin, coal and crude oil. Implementation of *Rhodococcus* biotechnological capabilities requires the study of bacterial adhesion to substrates and to each other. In the present study, adhesion forces of *Rhodococcus* cells were studied using atomic force microscopy (AFM) and combined with other physical methods.

Bacterial strains used were *Rhodococcus corynebacteroides* IEGM 929^T, *R. qingshengii* IEGM 1016^T and *R. ruber* IEGM 1122, IEGM 1126 from the Regional Specialized Collection of Alkanotrophic Microorganisms (IEGM; WFCC # 768, www.iegm.ru/iegmcol/index.html). Rhodococcal cells were grown in nutrient broth (Oxoid, UK) at 28°C for 48 h in an orbital shaker (160 rpm). Force spectroscopy measurements and imaging of *Rhodococcus* cells were performed using the BioScope Catalyst (Bruker) and MFP-3D-Bio (Asylum Research) AFMs. Bacteria were attached to both glass microscope slide and tip-less cantilever (Bruker, Camarillo, CA) positively charged through adsorption of poly-L-lysine solution (Sigma-Aldrich, St. Louis, MO). Force spectroscopy measurements were performed in 10 mM potassium phosphate buffer at room temperature immediately after the probe preparation [1]. Results were presented as an average of 30 force curves, taken on 3 randomly selected glass sides and analyzed using NanoScope Analysis Software (Bruker Corporation). Scanning Electron Microscopy (SEM) images of *Rhodococcus* cells were taken using a SEM model JSM-50A (Jeol, Japan). Cell surface hydrophobicity was estimated using MATH-test towards n-hexadecane [2]. Zeta potentials of *Rhodococcus* cells were registered on a ZetaSizer Nano ZS analyzer (Malvern Instruments, UK). The data obtained were automatically processed using the Malvern Zetasizer software (Malvern Instruments, UK).

Interaction forces between *R. ruber* IEGM 1122 cells and a glass surface were high (9.4-11.2 nN), whereas adhesion forces of *R. corynebacteroides* IEGM 929^T, *R. qingshengii* IEGM 1016^T and *R. ruber* IEGM 1126 did not exceed 0.6-2.1 nN (Table). Also, the strength of adhesion with glass depended on the contact time; the initial adhesion force of *R. ruber* IEGM 1126 to glass was 0.5-1.2 nN, and increased to 0.6-2.6 nN after 10 s of interaction. Figure 1A shows the force curve of the interaction between *R. ruber* cells immobilized on glass, and these cells immobilized on the cantilever. Interestingly, the interaction force between *R. ruber* cells was lower (0.8 nN) than adhesion of these cells to the glass surface (1.4 nN). Revealed differences in adhesion forces can be explained by rhodococcal cell surface properties, such as hydrophobicity and zeta potential. In particular, *R. ruber* IEGM 1122 demonstrated the highest (100%) cell surface hydrophobicity and high (-25.9 mV) zeta potential among strains studied (Figure 1B). However, our results suggested that rhodococcal adhesion to solid surfaces is determined rather by the cell surface hydrophobicity than zeta potential. The SEM image showed, that *Rhodococcus* cell wall contain appendages (Figure 2B), which may play an important role in bacterial attachment to surfaces and to each other. Dynamic AFM experiments are currently initiated to study the adhesion of growing *Rhodococcus* cells to solid surfaces and to examine the effect of physicochemical factors on rhodococcal growth and adhesive properties.

Research was funded by the Russian Academy of Sciences Program “Molecular and Cell Biology”, the Russian President Program for Leading Scientific School Support (grant 5589.2012.4) and the Perm Region Ministry of Education grant for international research group support (C-26-206).

1. Y. Chen, W. Norde, H.C. van der Mei, H.J. Busscher, mBio 3 (2012), p. e00378-12.
2. M.S. Kuyukina, E.V. Rubtsova, I.B. Ivshina, R.V. Ivanov, V.I. Lozinsky, Journal of Microbiological Methods 79 (2009), p. 76-81.

2. Bacterial strain	Curve characteristics			
	F_0 (nN)	λ (nm)	Adhesion (%)	F_{adh} (nN)
R. corynebacteroides IEGM 929^T	1.2 ± 0.4	16.2 ± 44.0	82	-0.8 ± 0.6
R. qingshengii IEGM 1016 ^{T}	1.6 ± 0.6	7.0 ± 24.6	100	-1.3 ± 0.3
R. ruber IEGM 1122	1.3 ± 0.3	16.1 ± 10.0	100	-8.7 ± 0.8
R. ruber IEGM 1126	1.6 ± 0.6	4.3 ± 3.2	100	-1.1 ± 0.4

F_0 is the repulsive force at zero separation distance, λ is the decay length of this repulsive force upon approach, % adhesion is the percentage of the force-distance curves showing adhesion, F_{adh} is the average adhesion force recorded upon retraction. Results were presented as an average of 30 force curves, taken on 3 randomly selected glass sides.

Table 1. Characteristics of force-distance curves measured by AFM between *Rhodococcus* strains and glass

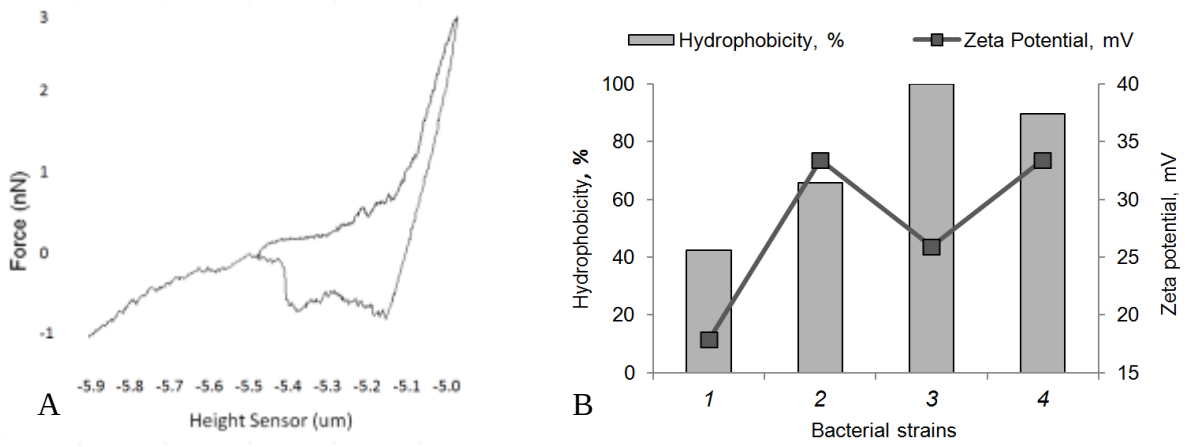

Figure 1. Force curve of the interaction between *R. ruber* IEGM 1126 cells (A); results of MATH-test (hydrophobicity) and zeta potential of *Rhodococcus* cells (B). Bacterial strains: 1 – *R. corynebacteroides* IEGM 929^T, 2 – *R. qingshengii* IEGM 1016^T, 3 – *R. ruber* IEGM 1122, 4 – *R. ruber* IEGM 1126.

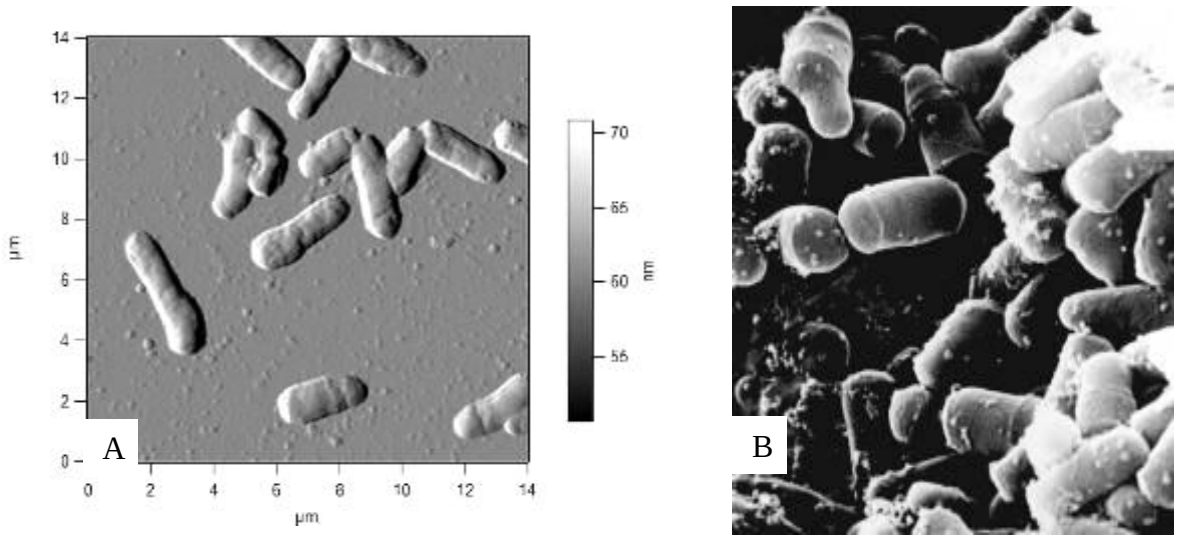

Figure 2. Micrographs of *Rhodococcus* cells. A – AFM image of R. *ruber* IEGM 1122 attached to the glass slide, scan size 14×14 μm; B – SEM image of *R. ruber* IEGM 333 (×20 000).

Microorganisms and Biofilms

LS.1.P020
Ultrastructural analyses of dormant and germinating bacterial endospores

C. Dittmann[1], M. Grabenbauer[2], H. Han[2], M. Laue[1]

[1]Robert Koch Institute, Advanced Light and Electron Microscopy (ZBS 4), Berlin, Germany
[2]Max-Planck-Institute for Molecular Physiology, Department of Systems Cell Biology, Dortmund, Germany

dittmannc@rki.de
Keywords: *Bacillus subtilis*, spore, germination, ultrastructure

The soil bacterium *Bacillus subtilis*, like other *Bacillus* and *Clostridium* species, forms spores to survive unfavorable environmental conditions. Spores are robust and can resist heat, radiation, desiccation, pH extremes and toxic chemicals [1]. The presence of nutrients or other chemicals, so called germinants, lead to the activation of a spore and to the transformation into a metabolically active bacterium, which is called germination. During the germination process significant structural and molecular changes occur, like release of molecules from the spore core, rehydration of the core and degradation of the cortex and coats [1]. Although basic ultrastructural data about the germination are available from Santo *et al*. [2], analysis by modern microscopy techniques and correlation with molecular events are still lacking. Thus, we have started a project to get more detailed information about the structural and topochemical aspects of the dormant spore and their germination by using current methods for ultrastructural research.

To study the germination of *Bacillus subtilis* spores we firstly established a germination assay that uses the activation of spores by tryptone soy broth which leads to a rapid and homogenous activation of the entire spore population. Activation of spores was measured over time by phase-contrast light microscopy as a change of the spore´s refraction revealing the time course of activation and germination. To analyze the morphological changes by transmission electron microscopy (TEM) activated spores were fixed at different time points during germination using high pressure freezing. The fixed spores were freeze-substituted, embedded in epon and cut into ultrathin sections. In parallel, samples were chemically fixed and analyzed by light microscopy and by conventional scanning electron microscopy (SEM).

The analysis by TEM revealed six different morphological stages (Fig. 1 A-F) during the germination process. The increase in volume of the spore core (Fig. 1 B) and the distinct rupture within the coats (Fig. 1 D) are obvious hallmarks of the germinating spore. The change of the spore´s refraction in phase-contrast light microscopy correlates with the change from stage one (Fig. 1 A) to stage three (Fig. 1 C), with stage two as an intermediate stage (Fig. 1 B). Furthermore we found particular morphological structures in some stages, for example vesicle-like formations of the inner spore membrane at the poles of the spores. With SEM we could determine five different morphological stages which we correlated with results from TEM and light microscopy. The dormant *Bacillus subtilis* spore possesses a complex structure with a core, a cortex and a multilayered coat. In addition to these well-known structures, we could find features, like crystalline regions within the core and membrane-like loops localized underneath the inner spore membrane. Analysis by cryo-electron microscopy of vitreous sections (CEMOVIS, [3]) proved the presence of these structures in samples that were structurally preserved close to native state. Ongoing investigations are focused on the analysis of the particular structures by using methods like electron tomography and immunocytochemistry. We have also started to analyze the germination process of other species like *Bacillus thuringiensis*, *B. anthracis*, *B. cereus* and *Clostridium difficile* to find out about the similarities and differences in the transformation process from a spore to a vivid bacterium.

1. P. Seltow, Curr. Opin. Microbiol. 6 (2003), p. 550
2. L. Y. Santo and R. H. Doi, J. Bacteriol. 120 (1974), p. 475
3. H. Han, J. Huebinger, M. Grabenbauer, J. Struct. Biol. 178 (2012), p. 84

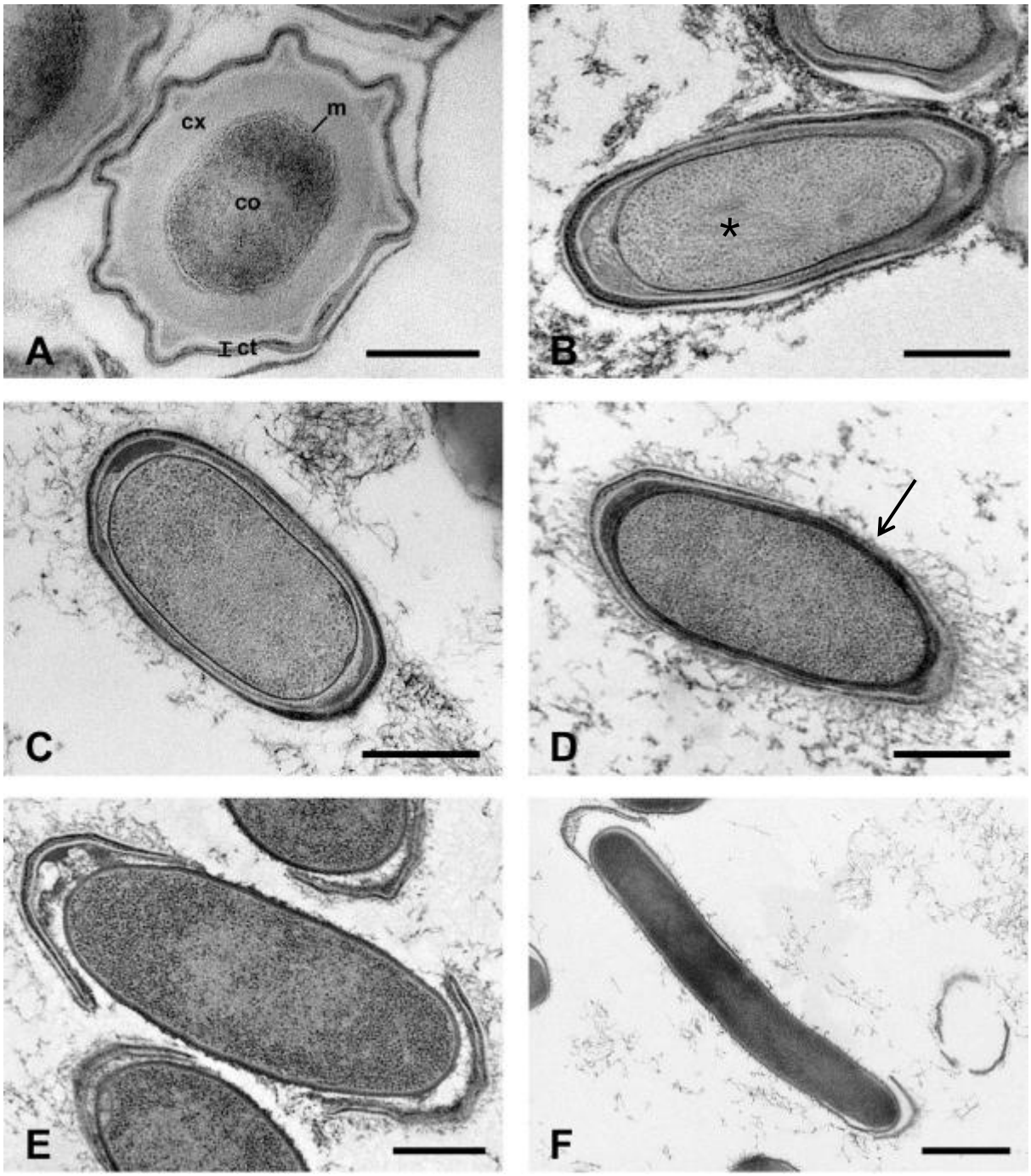

Figure 1. Transmission electron microscopy of ultrathin sections of germinating *Bacillus subtilis* ATCC 6633 spores after high pressure freezing. Six morphological stages could be distinguished. **A** Stage one reveals the typical spore structure with core (co), inner spore membrane (m), cortex (cx) and coats (ct). **B** The spores from stage two show an increased core and beginning cortex degradation. The core exhibit filament-like structures (*). **C** In stage three the cortex is almost degraded and the core has further expanded. **D** The rupture in the coats (arrow) is visible in stage four. **E** The outgrowing spore that has stripped the coat characterizes stage five. **F** Stage six represents the vegetative bacteria, which immediately starts cell division. (Bars: A = 200 nm; B - E = 500 nm; F = 1 µm)

Microorganisms and Biofilms

LS.1.P021
3D ultrastructure of the archaeon *Ignicoccus hospitalis*, analysed by different tomography techniques

T. Heimerl[1], J. Flechsler[1], H. Huber[2], G. Wanner[3], R. Rachel[1]

[1]Universität Regensburg, Centre for EM, Regensburg, Germany
[2]University of Regensburg, Microbiology, Regensburg, Germany
[3]University of Munich, Biocentre, Planegg, Germany

reinhard.rachel@biologie.uni-regensburg.de

Cells of the hyperthermophilic, anaerobic archaeon *Ignicoccus hospitalis* thrive optimally at T=90°C, by chemolithoautotrophy; they gain energy by reducing elemental sulfur with molecular hydrogen. They also exhibit exclusive structural features, with their unique cell envelope lacking an S-layer but consisting of two membranes: they encase two cell compartments, a tightly packed cytoplasm, and a weakly stained intermembrane compartment (IMC) with a variable width of 20 to 1000 nm, containing round or elongated vesicles [1]. In addition, *I. hospitals* cells can serve as host in a unique biocoenosis, when cultivated together with *Nanoarchaeum equitans*: cells of *N. equitans* cannot be grown alone, but require cell-cell contact to host cells for being able to thrive, and they obtain at least their lipids and (some) amino acids from the host [2].

We are interested in analysing the ultrastructure of the membrane system and cell-cell interaction of these prokaryotes at high resolution. In particular, we want to identify the path and the interconnectivity of the membranes; for this, structural investigations with an isotropic resolution of about or better than 5 nm are a prerequisite.

The width of *I. hospitalis* cells of up to 3 µm makes them unsuitable for direct observation using cryo-TEM. In addition, we aimed for localizing proteins using immunolabeling on ultrathin sections. Therefore, we favour embedding the samples into resins, for detailed (S)TEM/SEM observation. The labile cell structure of *I. hospitalis* (due to the lack of a solid cell wall) and the fragile cell-cell interaction between *I. hospitalis* and *N. equitans* requires great care when preparing samples for electron microscopy. It turned out the cryo-processing is absolutely necessary. Our routing protocol includes the following steps: cultivation in capillary tubes, or enrichment of cells using ultrafiltration membranes; high-pressure freezing; freeze-substitution fixation in acetone/ glutaraldehyde/ Uranyl acetate/ water [3]; and embedding in a resin, usually Epon, and recently also Lowicryl. So far, the 3D analysis is done using different routes: serial ultrathin sections [6], also including serial section labelling; serial 200 nm sections and analysing each by TEM tomography at 200 kV; and FIB-SEM tomography [4]. In addition, we aim to analyse thicker sections (>500 nm) using either BF or HAADF STEM tomography [5].

Datasets obtained so far confirm earlier results [6], and highlight some exclusive structural features, in particular the polar, highly asymmetric organization of the cells; and the energized outer cellular membrane [1], which hosts the primary and secondary proton pumps / energy converting enzymes: the sulfur hydrogen oxidoreductase, and the A_OA_1 ATP synthase (Fig 1). The data also show that the vesicles in the IMC are not only round but can frequently be found elongated like a tubular system. They are likely to shed off from the cytoplasmic membrane, and can contain low amounts of the ATP synthase, probably in the course of transport from the cytoplasm to the outer cellular membrane.

1. H. Huber, U. Küper, S. Daxer, R. Rachel, Antonie van Leeuwenhoek 102 (2012) 203–219.
2. U. Jahn, et al. J. Bacteriol. 190 (2008) 1743-1750.
3. C. Buser, P. Walther, J. Microscopy 230 (2008) 268-277.
4. C. Villinger et al., Histochem Cell Biol 138 (2012) 549-556.
5. J. Biskupek, J. Leschner, P. Walther, U. Kaiser, Ultramicroscopy 110 (2010) 1231-1237.
6. B. Junglas et al., Arch Microbiol 190 (2008) 379-388.
6. We kindly acknowledge the support of the DFG by a grant to HH and RR.

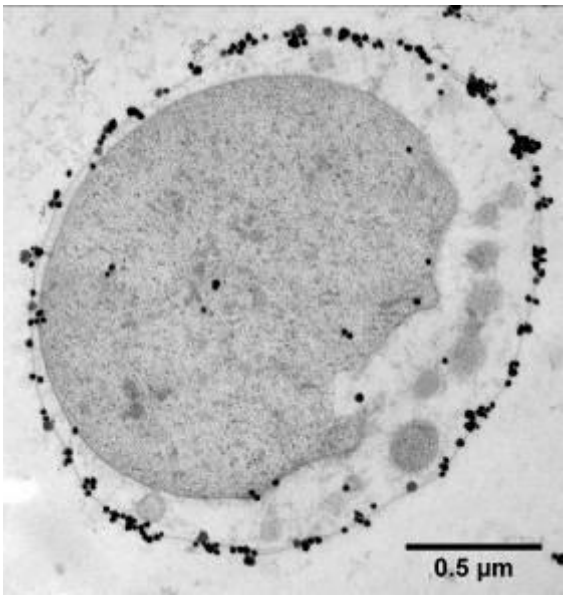

Figure 1. Ultrathin section of *I. hospitalis*; immuno-localization of the A_OA_1 ATP synthase (secondary antibody with US gold, plus silver enhancement).

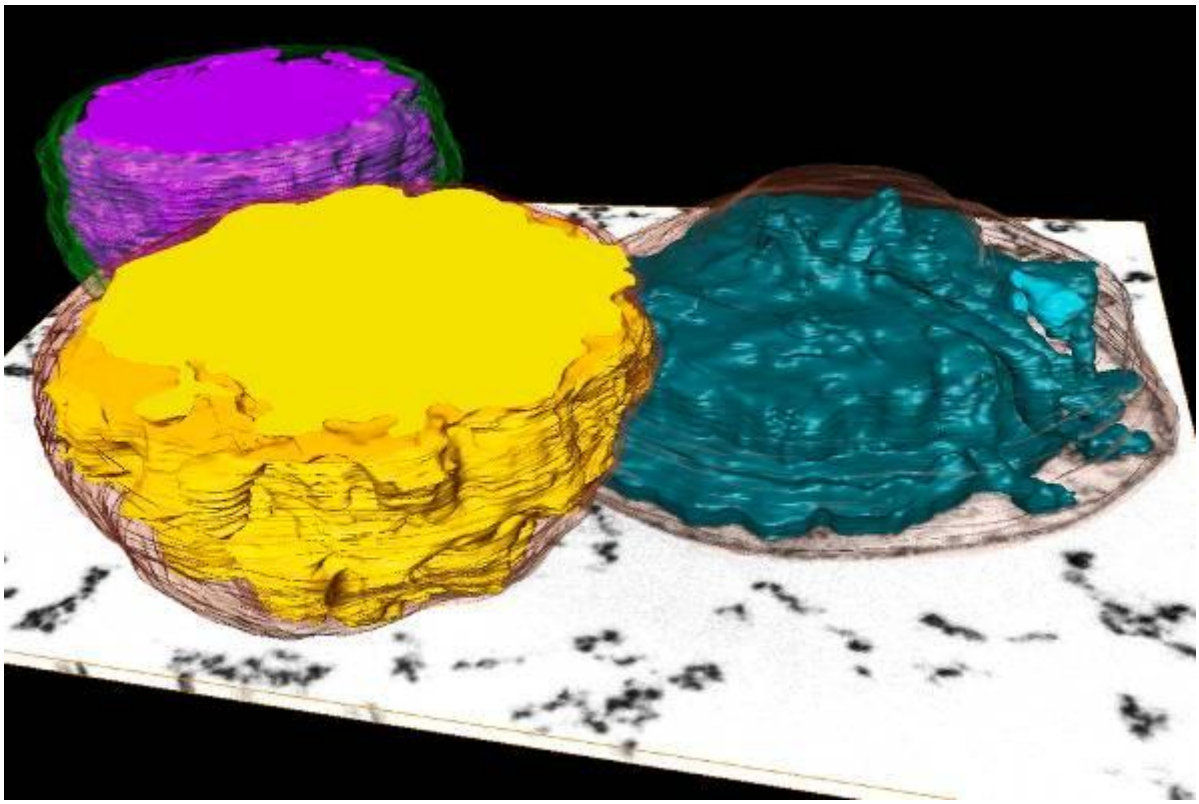

Figure 2. 3D visualization of three cells of *I. hospitalis* after HPF, FSF, Epon embedding, and FIB-SEM data recording (1024 x 768 x 299 voxel; each about 5 nm). Data were aligned and visualized using AMIRA. Scale: one single cell is about 2.0 µm in diameter.

Microorganisms and Biofilms

LS.1.P022
High resolution surface imaging of uncoated bacteria with Helium Ion Microscopy

C. Burkhardt[1], F. Zeitvogel[2], B. Schroeppel[1], M. Obst[2]

[1]NMI, Reutlingen, Germany
[2]University of Tuebingen, Center for Applied Geoscience, Tuebingen, Germany

Claus.Burkhardt@nmi.de

Helium Ion Microscopy (HIM) [1] offers increased lateral resolution, increased depth of field and new contrast mechanism compared to state of the art low voltage field emission scanning electron microscopy (LV-FESEM). In addition imaging of non-conductive samples using charge compensation with an electron flood gun is possible. This enables high resolution true surface imaging of uncoated samples. The He+ ion source consists of a tungsten needle with 3 atoms (trimer) at the very end and an electrode to extract ions. This gas field ion source delivers a bright He+ ion beam (>5 109 A/cm2sr), which can be focused with the final electrostatic objective lens in a sub 0.5nm probe.

Probe current can be defined with selectable apertures of 5, 10 and 20µm diameter. For high resolution imaging we use probe currents below 1pA. For lower magnification imaging, currents of several 10pA may be used. A range of ion energies can be selected between 15 and 35keV; in this work we used 30keV.

Due to the small surface interaction volume [2] and enhanced secondary electron signal (SE1) generation, the surface sensitivity and topographical contrast are well increased. For charge compensation a low energy electron flood gun is implemented (energy ranges from 100eV to 5000eV, typically 900eV in this work). The current density can be optimized for charge compensation by adjusting focus, x and y position as well as the flood time of the e-beam.

Possible drawbacks of HIM include sputter erosion of the sample (at high current densities on materials with high sputter rate, e.g. Au) and deposition of hydrocarbon contamination layers during imaging. Contamination can be reduced through sample cleaning with an integrated plasma cleaner.

In this work we present application of HIM for imaging of cell-mineral aggregates (CMAs) that contain both sensitive soft matter such as bacterial cells and bacteriogenic extracellular polymers and insensitive, inorganic Fe(III)-oxides. These heterogeneous CMAs were formed by nitrate-reducing bacteria under anoxic, circumneutral pH conditions as described elsewhere [3]. Samples were freeze-dried after plunge freezing in liquid propane. Samples for HIM were analyzed without surface coating whereas samples for FESEM were sputter-coated with a 4nm Pt layer.

HIM-SE images showed increased surface-sensitive material contrast (i.e. Fe(III)-oxides on the cell surface) (Figure 1) compared to FESEM that shows a rather homogeneous, topography-dominated contrast (Figure 2). Since no Pt-coating was applied, true fine surface structures without distortions became more clearly visible and can be analysed with more precision in the HIM as compared to FE-SEM.

1 B.W. Ward, J.A. Notte, N.P. Economou J. Vac. Sci. Technol. B 24 (2006), pp. 2871- 2874.
2. D. Cohen-Tanugi & N. Yao J. Appl. Phys. 104 (2008)
3. N. Klueglein & A. Kappler, Geobiology 11 (2013), pp. 180–190.
4. We thank the EAM and Geomicrobiology groups at the U. of Tuebingen. Project supported by DFG (OB 362/1-1).
5. We thank Carl Zeiss and NIH for possibility to use the HIM.

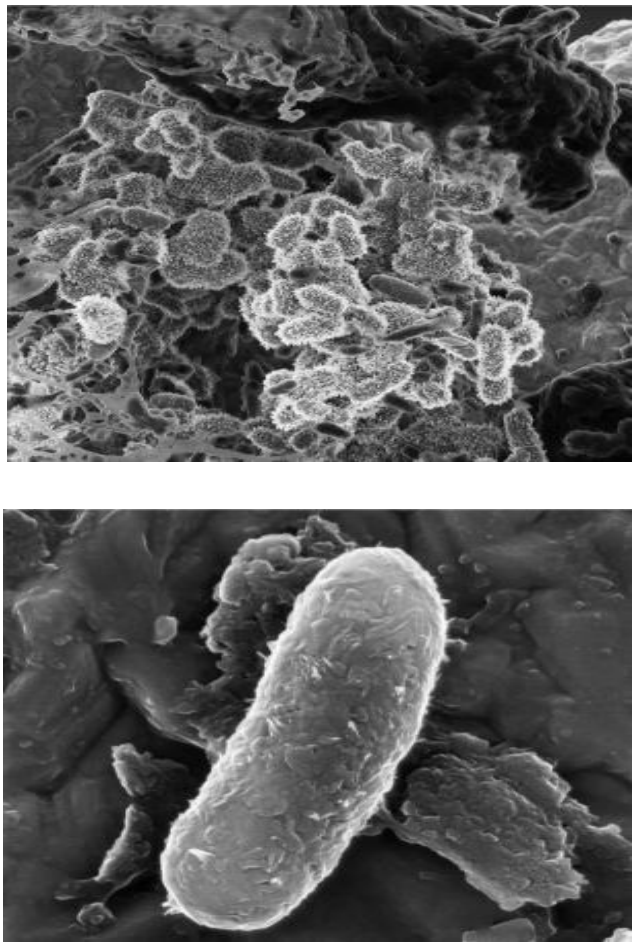

Figure 1. HIM secondary electron images of a CMA (left) and surface image of a bacteria with different level of mineral encrustation (right); uncoated samples.

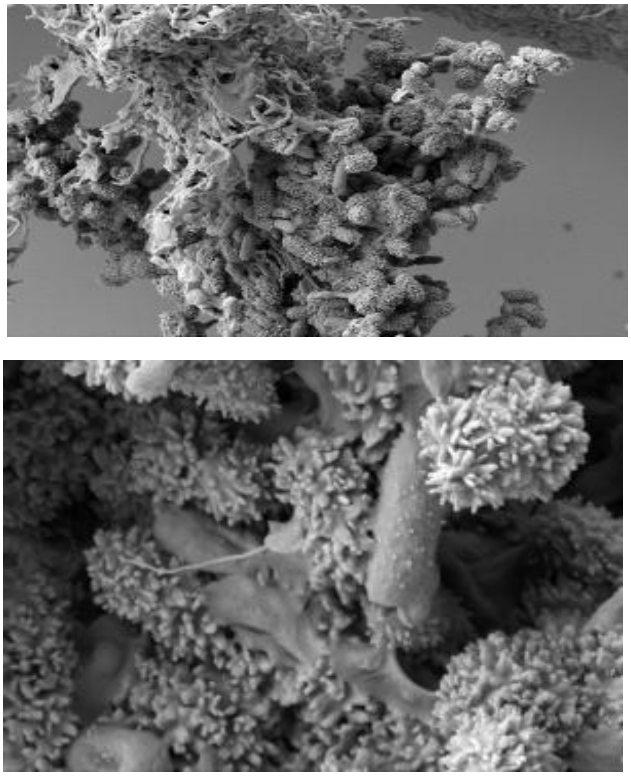

Microorganisms and Biofilms

LS.1.P023
Nanoparticles production and inclusion in Staphyloccus Aureus incubated with Polyurethane: an electron microscopy analysis

D. Lyubov[1], A. George[2], S. Natalya[1], S.C. Claudio[3], T. Francesco[4], P. Mauro[5]
M. Marziale[6]

[1]Gamaleya Research Institute for Epidemiology &Microbiology, Moscow, Russian Federation
[2]Moscow State Medical and Stomatological University, Moscow, Russian Federation
[3]ST Microelectronics, Milano, Italy
[4]FEI, Italy, Italy
[5]FEI, Eindhoven, Netherlands
[6]Universita degli Studi di Milano-Bicocca, Dipartimento di Scienza dei Materiali, Milano, Italy

lyubov_didenko@mail.ru
Keywords: Polyurethane; Staphylococcus aureus; Biodestruction; Endocytosis; FIB/SEM (Focused Ion Beam/Scanning Electron Microscope); TEM (Transmission Electron Microscope); STEM (Scanning Transmission Electron Microscope)

The interaction of S. aureus with polyurethane is studied with electron and ion microscopy instrumentation (SEM, FIB and TEM). Biodestruction is a corrosion process of natural and artificial materials operated by microorganisms; it is remarkable for the polymeric materials commonly used in medicine, especially in prosthetic stomatology where polyurethane occupies a special position. Prostheses in the oral cavity are constantly attacked by microorganisms and their colonization often concurs in the destruction of the artificial materials. Moreover biodegradation is associated to the release of allergenic substances, toxic to the human body. Scanning Electron Microscope (SEM) and Focused Ion Beam (FIB) are used to evaluate the damage of artificial materials in the different stages of chemical and physical factors in the external interaction with microorganisms (adherence, environment, bacteria can form a biofilm formation of microcolonies and biofilm). Transmission Electron Microscope (TEM) is a is directly related to the increase of the complementary technique to identify and trace biodegradation capacity. This study shows that submicron/nano particles found in bacterial cells (Staphylococcus aureus) incubated with polyurethane (a material commonly used for prosthesis in odontostomatology) are a consequence of biodestruction. Formation of small particles of polyurethane occurs under the influence of bacterial enzymes (esters). The presence of polyurethane nanoparticles into bacterial vesicles suggests that the internalization process occurs through endocytosis... TEM and FIB/SEM are a suitable set of correlated instruments and techniques for this multi facet investigation: polyurethane particles influence the properties of Staphylococcus. aureus from the morpho-functional standpoint that may have undesirable effects on the human body. S. aureus and Candida. albicans are symbiotic microorganisms; it was observed that C. albicans has a similar interaction with polyurethane and an increment of the biodestruction capacity is expected by its mutual work with S. aureus.

Microorganisms and Biofilms

LS.1.P024
Ultrastructural characterization of the hyperthermophilic Archaeon *Methanocaldococcus villosus*

A. Bellack[1], G. Wanner[2], M. Ugele[1], T. Heimerl[3], R. Rachel[3], R. Wirth[1]

[1]University of Regensburg, Institute of Microbiology and Archaea Centre, Regensburg, Germany
[2]LMU Munich, Department Biology I - Botany, Planegg-Martinsried, Germany
[3]University of Regensburg, Centre for Electron Microscopy, Regensburg, Germany

annett.bellack@ur.de
Keywords: Archaea, flagella, FIB-SEM, tomography, 3D reconstruction

The hyperthermophilic Archaeon *Methanocaldococcus villosus* was isolated from a shallow submarine hydrothermal system at Kolbeinsey Ridge, north of Iceland. Cells are regular to irregular cocci with a diameter of 1 µm and possess an S-layer with (pseudo-) sixfold symmetry and up to 50 polar flagella. These cell appendages were shown to be multifunctional organelles which mediate swimming, adhesion to abiotic surfaces, and formation of cell-cell contacts [1]. Using *M. villosus* as a suitable novel model organism, the aim of this study was to gain detailed insights into the whole-cell architecture of Archaea with aid of various microscopic techniques.

To determine the cellular ultrastructure of *M. villosus*, cells were prepared for electron microscopy by high-pressure freezing/freeze substitution or conventional chemical fixation [2]. Specimens were embedded, ultrathin sectioned and analysed by focused ion beam scanning electron microscopy (FIB-SEM) with regard to substructures in the cell and anchoring of flagella in the membrane. In addition, ultrastructural transmission electron microscopy (TEM) investigations were performed using electron tomography of (serial) semi-thin sections. Digital images were then aligned and read into Amira™. For reconstruction of 3D-models, contours of the cells and flagella were colour-coded and movies of rotating cells were recorded with aid of a movie maker.

Electron microscopic analyses of the *M. villosus* cells revealed a densely packed cytoplasm containing distinct globules with a diameter of 80-120 nm (Figure 1). The well-preserved cell envelope consisted of the cytoplasmic membrane, a thin periplasm and the S-layer from which glycoproteins protruded. Some of the cells additionally possessed a submembraneous layer which could be connected with a complex cytoplasmic assembly that closely resembled bacterial chemoreceptor arrays. FIB-SEM allows nearly isotropic imaging of the cells and their 11-nm flagella (Figure 2).

Combining FIB-SEM and electron tomography, three-dimensional analyses of cells and subcellular structures were obtained. The different microscopic techniques used herein confirmed previous ultrastructural findings on flagella and cell envelope construction of the *Methanococcales* and gave new insights into the anchoring of flagella.

Altogether, these findings enhance our general understanding of archaeal cell structures.

1. A. Bellack, H. Huber, R. Rachel, G. Wanner, and R. Wirth, IJSEM 61 (2011), 1239-1245.
2. R. Rachel et al. in “Methods in Cell Biology: Electron microscopy of model systems”, ed. T. Möller-Reichert (Academic Press, New York) (2010), 47-69

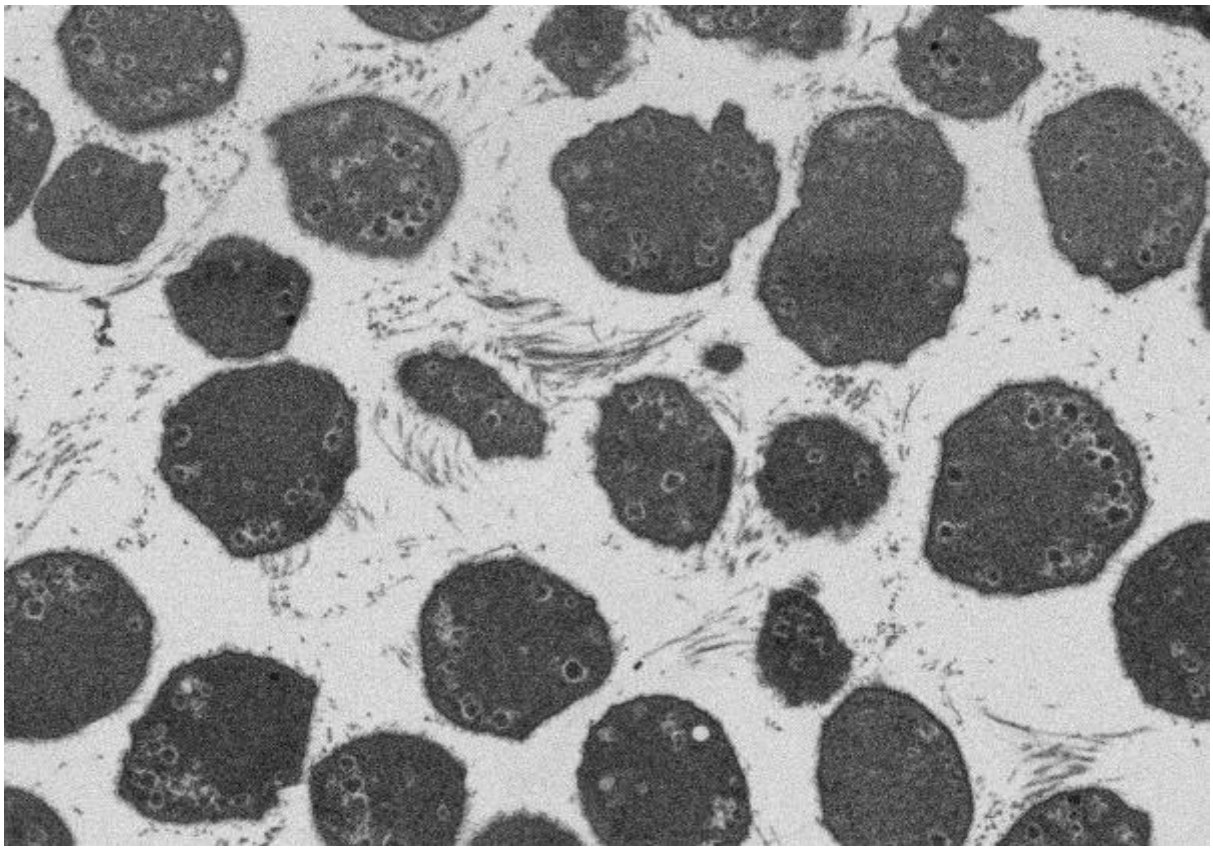

Figure 1. Overview of *M. villosus* cells recorded with FIB-SEM.

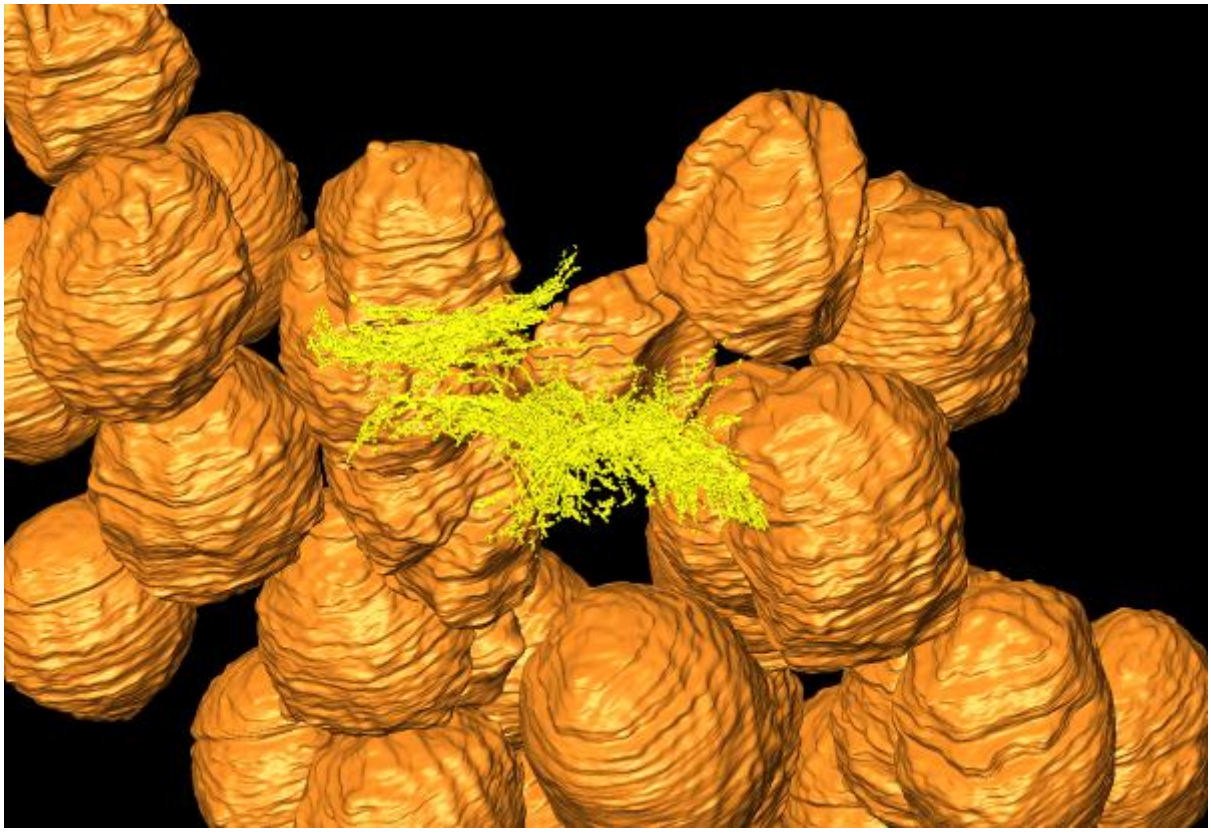

Figure 2. 3D-reconstruction of *M. villosus* cells from a FIB-SEM dataset of around 1100 8-nm slices; S-Layer orange, flagella yellow.

Microorganisms and Biofilms

LS.1.P025
The Morphology and Ultrastructure of a new 2 - Methoxyethanol utilizing Pseudomonas *SP.*

F.O. Ekhaise[1]

[1]University of Benin, Department of Microbiology, Faculty of Life Sciences, Benin City, Nigeria

aiyevbosa.ekhaise@gmail.com
Keywords: Pseudomonas sp. Strain VB, electron microscope, morpholo534gy and cell structure

A new strain of *Pseudomonas* designated as *Pseudomonas* sp., strain VB, degrading 2-methoxyethanol was isolated from anaerobic sewage sludge. The cells are rod-shaped, motile with polar lophotrichous flagella numbering between 7 and 9. Electron microscopy revealed cells aggregating to form a network connected by interconnecting filaments. A thin section of the filaments showed an outer sheath surrounding a core area and an inner electron dense area. A thin section of the cell showed the typical Gram-negative cell

Microorganisms and Biofilms

LS.1.P026
Quantification of Indigenous Bacterial Phylogenetic and Functional Groups at Terrebonne Bay along the coastline of the Gulf of Mexico using combinations of Fluorescence *in situ* Hybridization and Epifluoresence Microcopy.

O. Olapade[1]

[1]Albion College, Biology, Albion, United States

oolapade@albion.edu
Keywords: Fluorescence *in situ* hybridization, epifluorescence microscopy, pollution, coastal marine

The detection and quantification of bacterial phylogenetic and functional groups at the site of the Deepwater Horizon oil spill in Terrebonne Bay along the Gulf of Mexico {GOM} were carried out using combinations of nucleic acid staining, and fluorescence *in situ* hybridization {FISH} and epifluoresence microcopy approaches. Overall, simultaneous analyses of both planktonic and benthic bacterial communities at the bay along GOM by FISH revealed the numerical dominance of members of the type I methanotrophic bacteria (MB) over the type II populations. The study clearly reflects the change in the bacterial community structure and composition in response to the tragic methane and crude oil discharges from the Deepwater Horizon rig along the Gulf of Mexico.

Tissues, Pathology, and Diagnostic Microscopy

LS.2.027
Quantitative micro-structural assessment of animal models of human lung disease

M. Ochs[1,2,3]

[1]Institute of Functional and Applied Anatomy, Hannover Medical School, Hannover, Germany
[2]Biomedical Research in Endstage and Obstructive Lung Disease Hannover (BREATH), Member of the German Center for Lung Research (DZL), Hannover, Germany
[3]Cluster of Excellence REBIRTH (From Regenerative Biology to Reconstructive Therapy), Hannover, German

ochs.matthias@mh-hannover.de
Keywords: lung, morphometry, stereology

Each day a human being inhales and exhales more than 10,000 litres of air into and out of the lung. The parenchyma of the lung consists of a very large number of terminal air bubbles (alveoli) separated by tissue septae which contain a dense network of blood capillaries. At the end of a deep breath, more than 80% of total lung volume is air, about 10% is blood, and only the remaining about 5-10% is tissue. The main function of the lung is gas exchange, in particular the uptake of oxygen from the ambient air into the pulmonary capillaries. The lung´s functional capacity is determined by its structure. Efficient oxygen uptake requires a large alveolar surface and a thin air-blood barrier for diffusion. Within the human lung, the exchange surface for the diffusion of gases is distributed over about 300 to 500 million alveoli and is as large as 120 - 140 m² (nearly the size of a tennis court). At the same time, the thickness of the exchange barrier is only about 2 µm (50 times thinner than a sheet of air-mail stationary).

Several lung diseases are characterized either by a loss of surface area (e.g. emphysema) or by a thickening of the barrier (e.g. intraalveolar edema or fibrosis). These alterations can be induced in animal models of human lung disease which can then be studied under defined experimental conditions. In order to make statistically valid comparisons between experimental groups, lung structure has to be measured to provide quantitative (morphometric) data. The methods of choice to obtain such data in microscopy are those of stereology, a set of unbiased sampling and measurement tools derived from stochastic geometry. The principles of design-based lung stereology have been summarized and adopted as an official research policy statement of the American Thoracic Society (ATS) and the European Respiratory Society (ERS) [1].

Different animal models require the use of different stereological designs, which have to be integrated in the planning phase of the study. Specific steps include the mode of lung fixation, tissue sampling and processing, preparation of sections, microscopic technique, and analysis parameters. Specific recommendations for various animal models of human lung disease have been given recently [2,3].

Microscopic techniques (including light and electron microscopy, immuno-EM, electron tomography) in combination with stereology are essential to characterize lung structure in health and disease. A particular strength of stereological methods is the fact that they can be applied to any imaging dataset, including non-destructive imaging techniques which can visualize whole fixed small animal lungs with alveolar resolution ex vivo (e.g. micro-CT [4,5] and scanning laser optical tomography (SLOT) [6]). This combination allows for a comprehensive quantitative lung phenotype analysis. Here, we give an overview on our recent work on the microscopy-based stereological analysis of the normal and disordered lung.

1. C.C.W. Hsia, D.M. Hyde, M. Ochs and E.R. Weibel: Am J Respir Crit Care Med 181 (2010), p. 394-418
2. M. Ochs and C. Mühlfeld: Am J Physiol (2013) (in press)
3. C. Mühlfeld and M. Ochs: Am J Physiol (2013) (in press)
4. D. Vasilescu, Z. Gao, P.K. Saha, L. Yin, G. Wang, B. Haefeli-Bleuer, M. Ochs, E.R. Weibel and E.A. 5. Hoffman: Proc Natl Acad Sci USA 109 (2012), p. 17105-17110
6. D. Vasilescu, C. Klinge, L. Knudsen, L. Yin, G. Wang, E.R. Weibel, M. Ochs and E.A. Hoffman: J Appl Physiol 114 (2013), p. 716-724
7. M. Kellner, M. Heidrich, R. Beigel, R.A. Lorbeer, L. Knudsen, T. Ripken, A. Heisterkamp, H. Meyer, M.P. Kühnel and M. Ochs: J Appl Physiol 113 (2012), p. 975-983

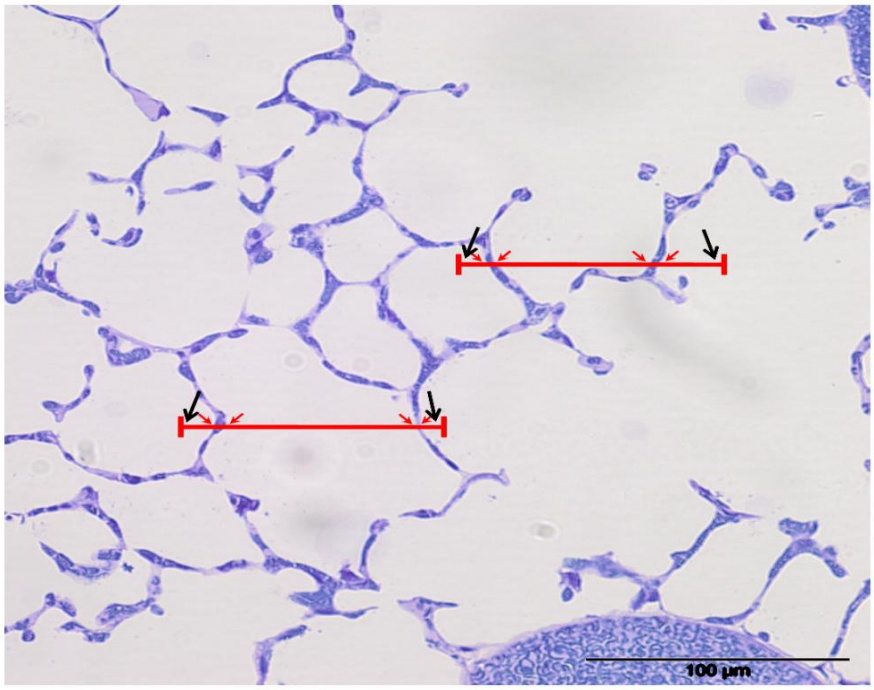

Figure 1. Estimation of alveolar surface area by counting of intersections (red arrows) between test lines and alveolar septae.

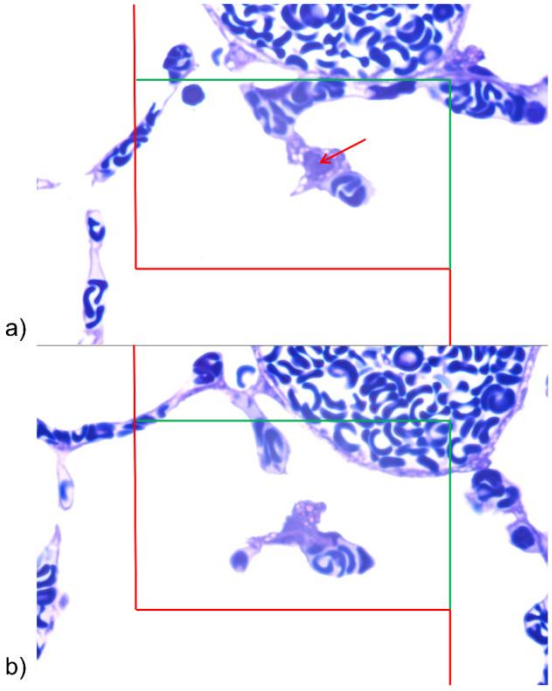

Figure 2. Estimation of alveolar epithelial type II cell number by counting of nucleoli (red arrow) in a disector.

Tissues, Pathology, and Diagnostic Microscopy

LS.2.028
Tissue elasticity: from tissues to single molecules back to tissues

D. Quaglino[1]

[1]University of Modena and Reggio Emilia, Department of Life Sciences, Modena, Italy

quaglino.daniela@unimore.it
Keywords: connective-tissue, elastin, peptides, disease, biomaterials

Soft connective tissues are comprised of a three-dimensional network made of a variety of proteins, glycoproteins and glycosaminoglycans that take part and contribute to strength as well as to plasticity and deformability of the tissue. Amount and ratio of different constituents, protein and cell interactions and supramolecular organization of matrix components are strictly dependent on the capacity of tissues to retain their original shape when relaxed after stretching. Within this context, elastin, the major component of elastic fibers, is secreted as a soluble monomer, undergoes few post-translational modifications and is organized into a polymer that forms lamellae, fibers or hive-like structures according to organ's requirements in order to better provide the recoil properties and the resilience essential to accomplish repetitive distension and physical stress typical for instance of arteries, lung, bladder and skin. Changes of these characteristics, as in aging and in the course of several genetic and acquired disorders, may have therefore dramatic consequences on the structural and functional performance of tissues/organs.

Since the largest amount of elastin is produced during the fetal and neonatal period with a negligible turnover in the following years, the elastin produced during body growth and development has to be maintained for lifespan and any proteolytic damage is essentially irreparable. Moreover, the age-dependent increased stiffness of tissues results from an increase in elastin fragmentation as well as from abnormal deposition of collagens, calcium and lipids, in addition to non-enzymatic post-translational modifications of matrix proteins such as carbamylation and glycoxydation.

During atherosclerosis and vascular aging, the extracellular environment and elastin in particular are importantly modified due to the local inflammatory context. Interestingly, proteolytic enzimes, as elastases and endopeptidases, are responsible for elastic fragmentations thus affecting the structural properties of tissue, but also generating an incredible amount of the so-called elastin-derived peptides (EDP) that can modulate the physiology of cells such as fibroblasts, smooth muscle cells, endothelial cells, monocytes/macrophages and lymphocytes. These active peptides are also known as elastokines since they belong to the matrikine family and trigger a plethora of biological activities: some beneficial to heart as protection against ischemia/reperfusion injury or to tissue repair, whereas others are deleterious as in aortic abdominal aneurysms, calcification of vessel walls, formation of hyperplasic neointima and in the progression of cancer growth and invasion.

The organization of the elastin molecule into alternate hydrophobic and hydrophilic domains stimulated studies tending to elucidate the specific role of domains implicated in the assembly of molecules into fibers or in the interactions with cells or with other extracellular constituents. Attention has been also paid to the conformation characteristics of domains in order to explain the elastic behaviour in water of the whole molecule. It is worth mentioning in fact that peptides with amino acid sequences corresponding to the various tropoelastin domains exhibit peculiar chemical physical characteristics and form, depending on environmental conditions, aggregates with distinctive supramolecular organization and biological properties. Exploring these characteristics has a fundamental impact for a better understanding of a disease-related pathomechanisms but also for an improved formulation of nano-biocomposites to be used as implants into living beings. One of the main concerns as far as the use of biomaterials should be to check for the activation of the inflammatory process and of the immune response. These processes may in fact alter the implant and would favour its retention or its rejection.

The inflammatory process is in fact characterised by recruitment and activation of macrophages, production of molecules with proteolytic activities and of cytokines with stimulatory effects on macrophages themselves, lymphocytes and fibroblasts. Moreover, proteolysis may favour elastin breakdown leading to the formation of elastin fragments, which, in turn, may have immuno-modulatory effects.

In vitro studies have demonstrated that even very simple elastin-derived peptides exhibit rather specific biological activities. Consistently, investigations on the chemotactic activity of peptides derived

from the coding sequence of exon 26A of the elastin gene (i.e. an exon that is not expressed in humans in normal conditions, whereas it is expressed in some pathological processes, such as in hypertension) revealed that these peptides exhibit a conformation-dependent chemotactic activity for monocytes/macrophages, indicating that the biological activity of elastin-derived peptides mostly depends on their structural organization.

As a whole, elastin-derived peptides have been shown to elicit a series of cellular responses, from elastase release, to free radical production and LDL oxidation. However, not all elastin peptides would seem to stimulate inflammatory cells in the same way, being some peptides more active than others in the production of free radicals, or in the elastase release or in the intracellular free calcium metabolism.

Furthermore, recent studies have also disclosed the amyloidogenic properties of several elastin-derived peptides, further highlighting the role of the extracellular matrix in many pathologic conditions and the importance to investigate each matrix constituents at molecular and supramolecular levels to get further insights into tissue structural and functional properties.

Within this context elastin and elastin peptides can be regarded as a paradigm to explore the complexity of the mechanisms responsible and/or contributing to tissue elasticity.

.

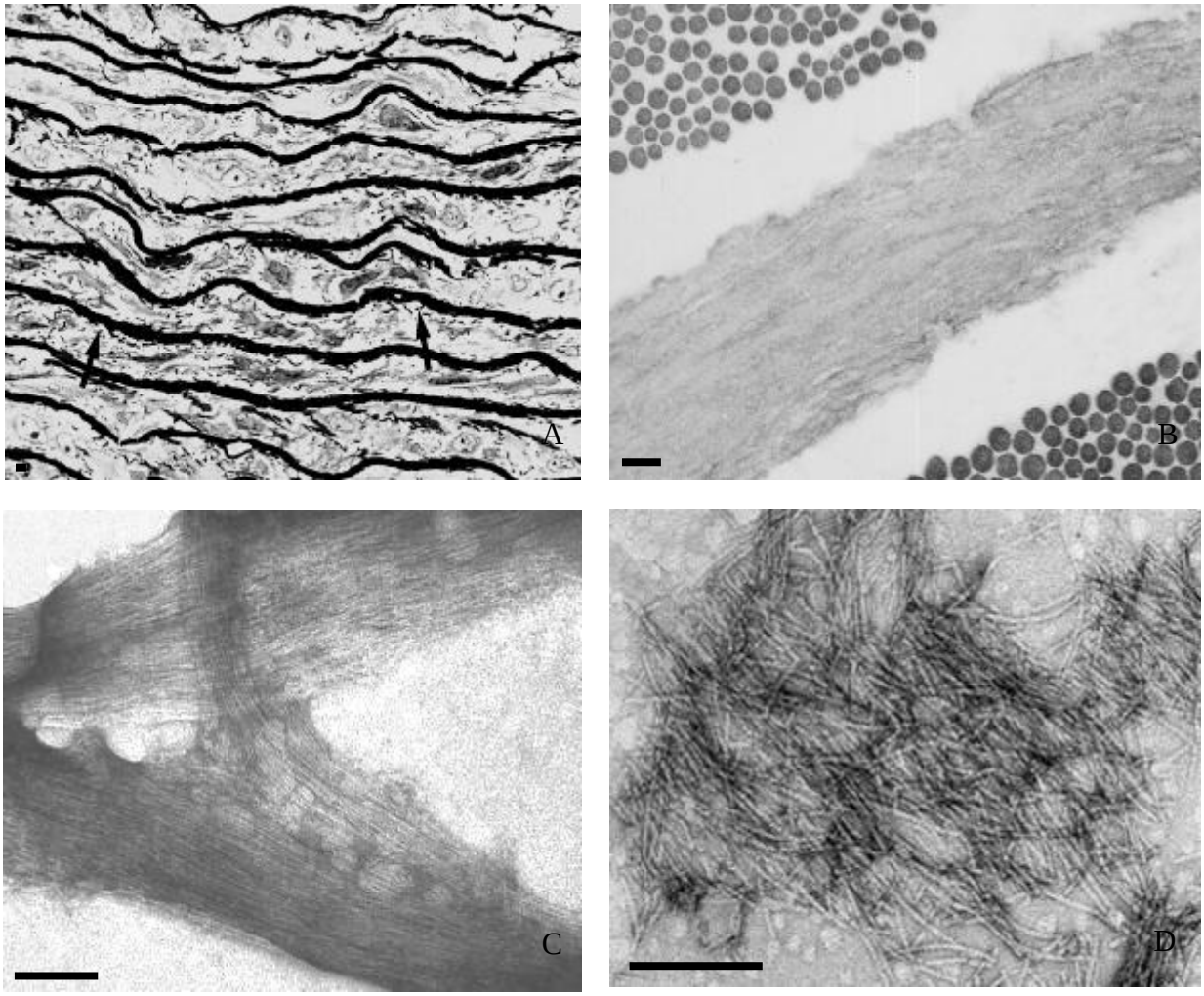

Figure 1. Light microscopy showing the elastic component organized as lamellae (arrows) between layers of vascular smooth muscle cells (A). Transmission electron microscopy of a typical dermal elastic fiber in a skin biopsy (B), of in vitro coacervated tropoelastin (C) and of isolated and purified elastin peptides (D). Bar 1 □m.

Tissues, Pathology, and Diagnostic Microscopy

LS.2.029
Diagnostic electron microscopy of pathogens in emergency situations

M. Laue[1]

[1]Robert Koch Institute, ZBS 4, Berlin, Germany

lauem@rki.de
Keywords: diagnostic electron microscopy, pathogen, negative staining, rapid thin sectioning

Electron microscopy serves as an important method for the diagnosis of pathogens in emergency situations that pose a considerable risk to the public health, like outbreaks of dangerous infectious diseases or cases of bioterrorism [1]. The role of electron microscopy in those situations is to provide rapid information about the pathogens involved, especially in cases where no indication about the pathogen exists. Diagnostic electron microscopy is a generic „catch all“ method which visualizes all objects of a diagnostic sample and guides a further, more specific diagnosis by other methods. In addition, it serves as a valuable independent control to minimize the risk of false diagnoses.

Negative staining electron microscopy is the method of choice for a rapid diagnosis in emergency situations, because preparation is simple and quick and allows the assessment of a few samples within a short time, usually well below one hour [2]. If compact or dense samples must be analysed, rapid thin section techniques can be employed. Efficient protocols provide a diagnosis within a few hours (e.g. 2 h [3]).

Diagnostic features of many pathogens are well documented and serve as a reference which allows to assign pathogens to a certain systematic group [4]. This usually works even if the pathogen has been modified by mutation because structural features are usually rather conservative. However, specificity of the diagnosis is comparatively low and depends on the group investigated. While viruses can be identified down to the family or rarely genus level, discrimination of bacteria is only possible at more general levels. In some groups of parasites (e.g. Microsporidia) the number of possible infectious species in humans is rather low and structural features allow a diagnosis down to the species level. At any case, electron microscopy provides valuable information about the presence of microbiological objects and their morphological features which supports obtaining a final diagnosis.

The contribution will give an overview about methods (including data on detection limit and inactivation procedures), applications (bioterrorism, outbreaks, zoonosis; compare Figure 1) and new developments (combination with spectroscopy; compare Fig. 2) in diagnostic electron microscopy of pathogens.

1. P. R. Hazelton and H.R. Gelderblom, Emerging Infectious Diseases 9 (2003), p.294.
2. M. Laue, Methods in Cell Biology 96 (2010), p.1.
3. M. Laue, B. Niederwöhrmeier, N. Bannert, Journal of Microbiological Methods 70 (2007), p.45.
4. A. Curry, in „Diagnostic electron microscopy: A practical guide to interpretation and technique“, eds. J.W. Stirling, A. Curry and B. Eyden, (Wiley, Chichester) (2013), p.181.
5. M. Laue and G. Fulda, Journal of Microbiological Methods *(in press)*

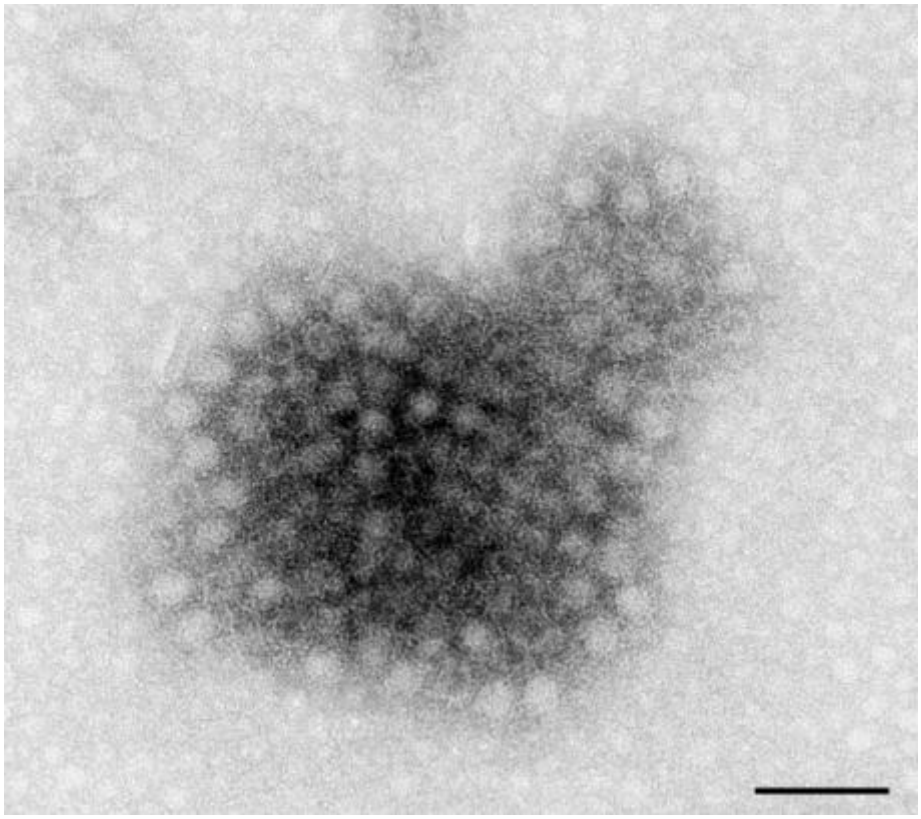

Figure 1. A cluster of Norovirus particles from a stool sample that was analysed during the large outbreak (over 11.000 cases) of gastroenteritis in Germany, 2012. Diagnostic electron microscopy was used to check samples for other viruses, because only a fraction of samples were PCR-positive for Norovirus. Bar = 100 nm.

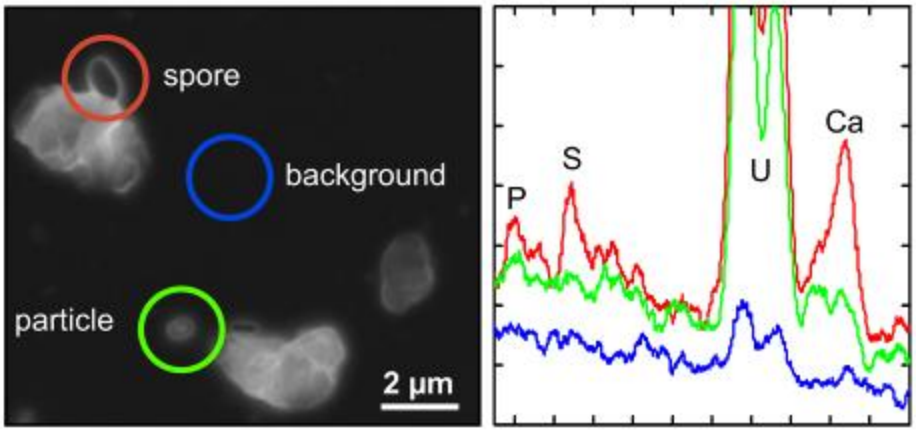

Figure 2. Diagnosis of putative bioterrorist samples for bacterial spores by scanning electron microscopy combined with X-ray microanalysis. Analysis of a control sample, which has been spiked with spores of *Bacillus subtilis* as a positive control, is shown. Left Suspicious particles are identified based on morphological criteria. Right Spectra from X-ray microanalysis (counts versus energy are plotted) allow to decide clearly between spores (red circle/graph) and other constituents, like the particle highlighted with the green circle, because spores reveal a typical element signature comprising of phosphorus (P), sulphur (S) and a prominent amount of calcium (Ca) [5]. The uranium (U) peak derives from the contrasting of the sample with uranyl acetate. Measurement of the background (blue circle/graph) gives information on dissolved material that has spread over the entire sample.

Tissues, Pathology, and Diagnostic Microscopy

LS.2.030
Ultrastructural view on cellular uptake of metal oxide nanoparticles

M. Condello[1], B. De Berardis[1], M.G. Ammendolia[1], S. Meschini[1]

[1]Istituto Superiore di Sanità, Rome, Italy

stefania.meschini@iss.it

Nanoparticles (NPs) can efficiently enter in living cells with different mechanisms because they have a similar size to the main cellular components. A detailed understanding of the molecular processes involved in the cellular uptake is very important to develop efficient NPs in drug delivery for conveying chemotherapeutic only in specific cells. However, is not to be underestimated the importance of knowing the potential harmful effects due to an incorrect penetration into live normal cells. However the uptake of NPs is not still clear and sufficiently characterized. Besides few data are available on the relationship between NPs internalisation and their physico-chemical properties. Recent works have shown that depending on the cell histotype, the uptake occurs either by passive diffusion or energy-dependent endocytosis mediated through clathrin pits, caveolae or macropinocytosis.

In our work we have studied the uptake of two different types of metal nanoparticles of zinc oxide, ZnO and titanium dioxide, TiO_2 on colon cancer cell lines (LoVo WT and HT29). ZnO and TiO_2 nanoparticles are widely applied in personal care products, paints, textiles foods and food packaging. Recent studies showed that these NPs are versatile plataforms for biomedical applications in cancer diagnosis and therapy. NPs were characterized by analytical electron microscopy and primary size, size distribution and chemical composition were determined. The primary size ranged between 45-170 nm and 20-60 nm for ZnO and TiO_2 respectively. The size distributions of NPs showed an average diameter equal to 196 nm for ZnO and 289 nm for TiO_2. 34% of ZnO NPs possessed dimensions below 100 nm, whereas for TiO_2 NPs large agglomerates were observed and only 11% of particles possessed sizes below 100 nm.

LoVo WT cells treated with ZnO NP (5 $\mu g/cm^2$ for 48h) and observed by SEM showed huge ultrastructural alterations at the plasma membrane level (Figure 1e) compared to the treated cells for 24h (Figure 1c) and control untreated cells (Figure 1a). These morphological alterations (holes in the cell membrane indicated by the arrows) should correspond to the presence of ZnO NPs inside the cell cytoplasm, instead no NPs were found by TEM inside the cell cytoplasm (Figure1b, control cell, Figure 1d, ZnO NP 5$\mu g/cm^2$ for 24h, Figure 1f, ZnO NP 5$\mu g/cm^2$ for 48h). TEM observation showed evident alterations at mitochondrial level suggesting an NP-cell interaction mediated by ion release. This evidence has led to hypothesize that only the zinc ions release may determine the observed cytotoxic effect.

The other colon carcinoma cell line, HT29, treated with TiO_2 (2.5 $\mu g/cm^2$ for 24h), showed the presence of metallic nanoparticles leaning to the cell membrane, wrapped by cell protrusion (Figure 2b, arrow). In the cytoplasm of HT29 cells, TiO_2 NPs were free in the cytoplasm, not surrounded by vacuoles. TiO_2 NPs were well visible in some altered mitochondria demonstrating a direct cytotoxic organelle damage (Figure 2a). These results suggest that nanoparticles may widely permeate or to only release the ionic component through the cell in a variety of biological mechanisms.

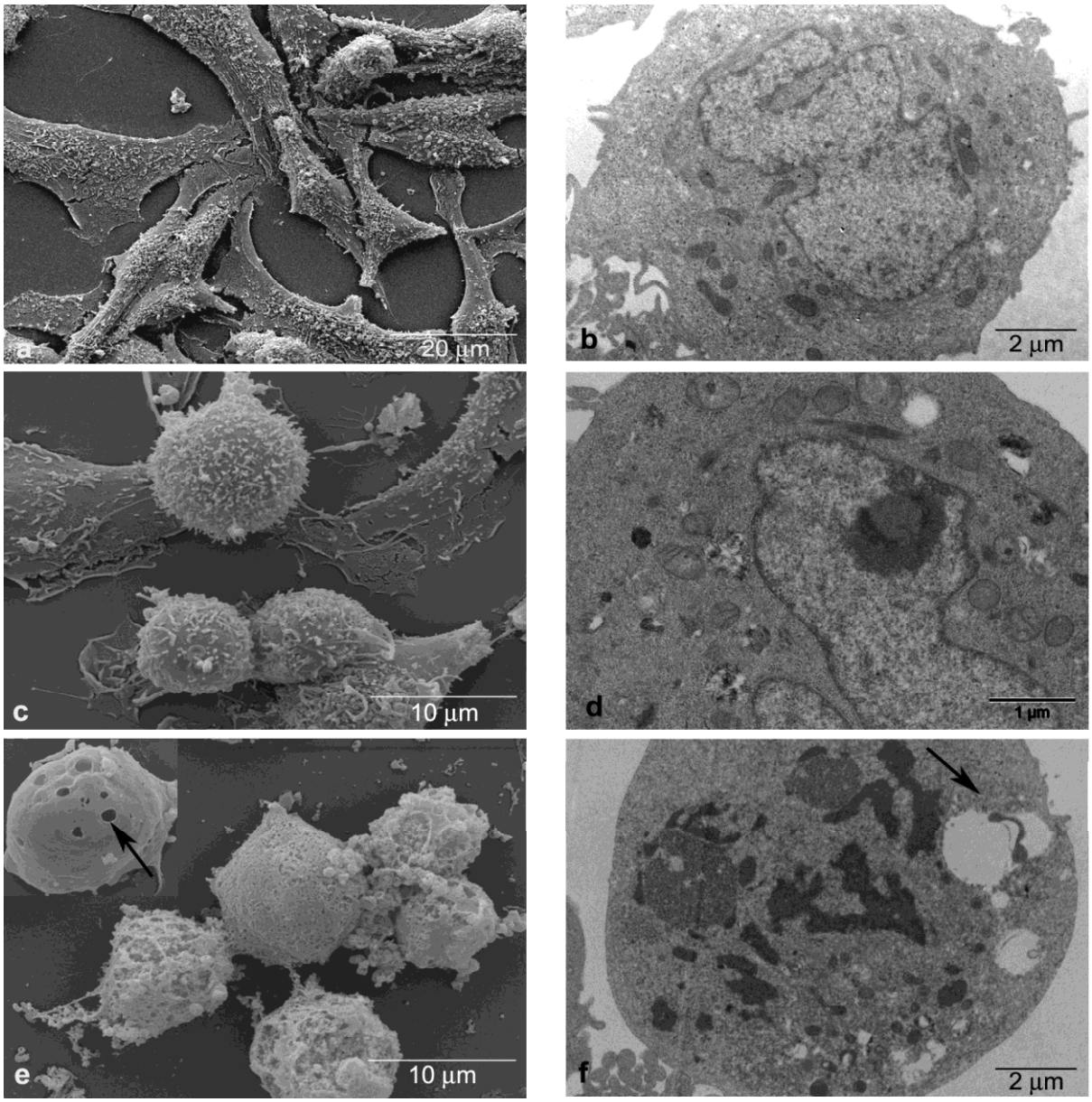

Figure 1. Morphological and ultrastructural modifications induced by ZnO on LoVo WT cells.

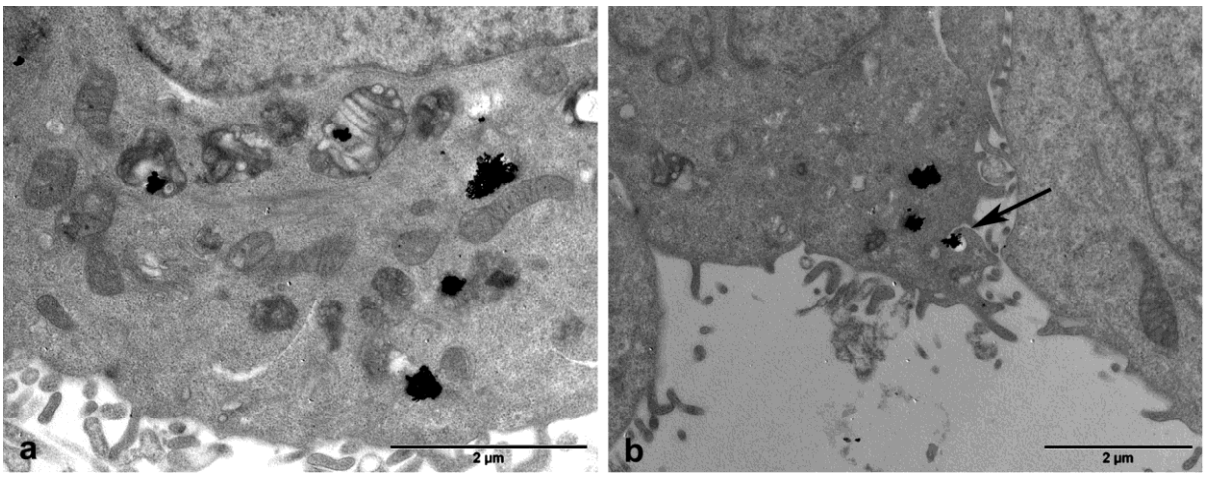

Figure 2. Ultrastructural modifications induced by TiO_2 on HT29 cells.

Tissues, Pathology, and Diagnostic Microscopy

LS.2.031
Impact of electron microscopy in clinical context.

J. Schröder[1], H. Siegmund[1], F. Hofstädter[1]

[1]Central EM-Lab, University Hospital, Pathology, Regensburg, Germany

josef.schroeder@klinik.uni-regensburg.de

Transmission electron microscopy (TEM), with the potential of 1000x higher resolving power compared with light microscopy (LM), is still used as an ancillary tool, quality control method or gold standard to complement, support or confirm the result of specific histopathological diagnoses. TEM was a very efficient approach in pathological diagnosis in the 1960s till early 1990s, it importance declined with the emerging use of immunohistochemistry (IHC) and molecular methods as well as due to some intrinsic EM limitations like scanty sample processing automation and long turnaround time. Today a resurgence of TEM as a complementary diagnostic modality can be observed [1].

Due to the relative small size (approx. 1-2mm³) of the examined tissue samples, the right sample collection and processing is a crucial step to avoid sampling errors and to secure adequate quality of tissue preservation for the TEM examination. The optimal standard approach is to immerse the biopsy specimen immediately in a buffered fixative (Karnovsky formulation), subsequent osmium tetroxide postfixation for lipid stabilization and structure contrast enhancement, dehydration in graded ethanol, and embedding in epoxy resin for heat polymerisation into hard blocks. In a number of cases formalin-fixed and wax-embedded tissue for light pathology can be reprocessed for EM as well as frozen samples to obtain useful diagnostic information by TEM examination.

Routine sample processing is performed in our lab by a computer-controlled tissue processor (LYNX) saving reagents, time, and labour (standardized batch processing overnight); the total sample turnaround time (TAT) is 3-5 workdays. For urgent clinical cases, the use of microwave-assisted tissue processing (AMW, Leica/Austria; REM, Milestone/Italy) reduce the TAT to less than 6 hours, facilitating the “same-day diagnosis” [2]. After ultramicrotomy the resin sections are examined in a TEM (LEO912AB, ZEISS) equipped with a customized side-entry digital camera image acquisition system (iTEM, OSIS/Münster). Interactive remote TEM operation via Internet allows instant and live “second opinion” consultation of difficult cases worldwide (“ultrastructural telepathology”) [3].

Based on the experience of our centralized EM unit, which is integrated in the diagnostic service of the pathology department of the medical centre, we confirm the continuing value of TEM diagnosis in a broad spectrum of diseases.

This includes the classical rapid virus detection in herpetiform skin lesions by the negative-staining procedure of particle suspensions which is a very efficient and low-cost method (e.g. herpesvirus: yes/no in 30 minutes TAT). The intrinsic “open view” of the method can be of great help in identification and morphological classification of infectious agents also in emerging situations (e.g. SARS, bird flu, Schmalenberg virus, parapox and many others). Another example of routine virus diagnosis, polyoma viruses detected in urine of a patient suffering complications after kidney transplantation, is shown in Figure 1.

Ultrastructural study of tissue sections improves significantly diagnostic interpretation in a number of neoplastic and especially non-neoplastic conditions of the kidney, muscle, nervous system, skin, cilia defects, storage diseases, liver biopsies, respiratory diseases, toxic lesions, male infertility (centriolopathy), microsporidia and opportunistic infections, as referred in detail elsewhere [4]. Distinct diagnostic immunophenotype is lacking in many tumours, aberrant immunostaining or small amounts of antigens are not detectable by LM, these and other pitfalls of affinity labelling systems makes TEM findings indispensable for exact diagnosis of poorly differentiated e.g. carcinomas, sarcomas, melanomas, mesotheliomas, and neuroendocrine neoplasms.

We display a number of examples of non-neoplastic disorders, in which a diagnosis cannot be rendered without TEM studies like numerous renal glomerular lesions, mitochondriopathy or sarcomere structure lesions in skeletal muscle and in ptosis condition (Figure 2), amyloid deposition in hearth and skin, structural abnormalities in immotile cilia of the respiratory tract causing insufficient airways clearing; skin biopsies from patients suffering of granulomatous, CADASIL (=inherited vascular disorder), and NSF (=Nephrogenic Systemic Fibrosis) condition with spectroscopic imaging (EELS=Electron Energy Loss Spectroscopy) of the causative Gadolinium deposits, and more.

In conclusion, we demonstrate the impact of TEM studies as a complementary tool in modern pathological diagnostic approach with obvious implications for prognosis and selection of therapy. This becomes very important with the paradigm shift in pathology and future aspects of personalized patient pathological predictive diagnosis and medical care management [5].

1. R. Erlandson in “Modern Surgical Pathology”, ed. W. Cote, (Saunders, Philadelphia) (2003), p. 81.
2. J. Schroeder et al., Micron 37,6 (2006), p. 577.
3. J. Schroeder in “Telepathology”, ed. S. Kumar, (Springer, Berlin) (2009), p. 179.
4. J. Stirling, A. Curry and B. Eyden, ed. “Diagnostic Electron Microscopy”, (Wiley, Chichester) (2013), p. 1.
5. M. Dietel and R. Schafer, Virchows Archiv 453,4 (2008), p. 309.

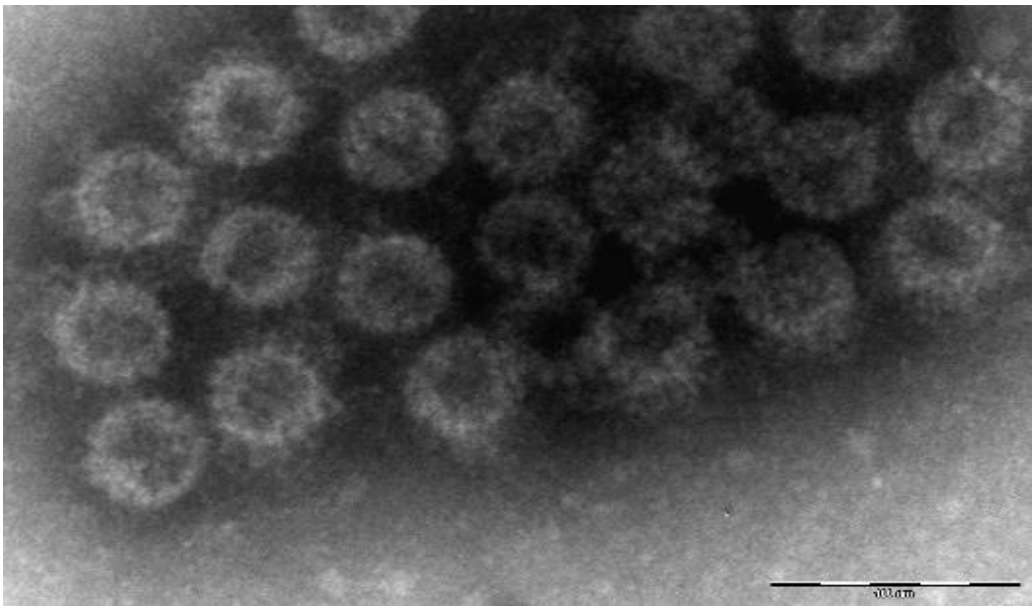

Figure 1. Polyoma viruses from urine of a nephritis patient after kidney transplantation (DD: acute rejection). Rapid negative-staining method (including ultracentrifugation of urine sample), diagnosis rendered in 60 minutes!

Figure 2. Mitochondriopathy in skeletal muscle biopsy of a patient suffering of myopathy of unknown ethiology. Note numerous paracrystalline and dark inclusions in abnormal sized and shaped mitochondria.

Tissues, Pathology, and Diagnostic Microscopy

LS.2.032
Scanning electron microscopy of vascular corrosion casts is still an excellent technique to study microvascular anatomy and vascular pattern formation of tissues and organs in health, disease and experimental conditions.

A. Lametschwandtner[1], H. Bartel[1], C. Radner[1], B. Minnich[1]

[1]University of Salzburg, Cell Biology, Salzburg, Austria

Alois.Lametschwandtner@sbg.ac.at
Keywords: Scanning electron microscopy, vascular casting, microvascularization

In 1971 Murakami [1] for the first time used the scanning electron microscope to study vascular corrosion casts (VCCs) gained by filling the vascular bed of tissues and organs with a polymerizing resin. Because the hardened resin resists tissue maceration by strong alkali as well as removal of bones by hydrochloric acid remaining plastic casts are termed “vascular corrosion casts”.

Since Murakami`s pioneering study the technique was refined in several aspects. These refinements are: (1) Micromanipulator guided fine-tipped glass electrodes allow to cannulate and inject the cardiovascular system of embryos, fetuses, larvae and of animal and human tissue and organ fragments gained during routine surgery or postmortem [2-5]; (2) Resins used – for details see [6-8] – nowadays consist of two components only – a prepolymerized base resin and a catalyst – which easily can be mixed to gain the ready-to-inject-resin; (3) VCCs can be frozen in distilled water and be sectioned in any desired level by a mini-wheel-saw placed in the chamber of a cryo-microtome [9] or can be cut simply by razer blades if casts are made from PU4ii [10]; (4) cut VCCs can be re-frozen in distilled water and subequently freeze-dried to preserve the spatial integrity of even the most delicate vascular territories; (5) VCCs can be quantitatively studied by 3D-morphometry using stereopaired SEM images [11-12] enabling new insights into the construction (optimality) principles underlying the design of cardiovascular systems [13]; and lastly (6) VCCs can be used for microcomputertomography (μ-CT) to study cardiovascular systems without the need to further section or dissect the specimen as virtual images can be reconstructed from data gained from micro- computer tomograms.

At present SEM of VCCs in combination with 3D-morphometry enables to qualitatively and quantitatively study the 3D arrangement of normal and diseased cardiovascular systems from early fetal/larval development to senescence (Figures 1 and 2). In detail, the technique allows (i) to study endothelial surface morphology of vessels by their imprints preserved on cast surfaces (Figure 3), (ii) to analyze branching patters of arterial and capillary vessels in terms of diameters of and branching angles between parent and daughter vessels, (iii) to define interbranching and intervascular distances, (iv) to localize flow regulating structures like flow dividers (Figure 4), intimal cushions, (Figure 5), microvenous valves [14] (Figure 6), and sites of vascular sphincters (Figure 7), and (v) allows to visualize signs of ongoing sprouting (Figure 8) and non-sprouting angiogenesis and its facets invoved in maturation, adaptation and reshaping of vascular territories [2] (Figure 8).

1. T. Murakami, Arch histol Jpn 32 (1971), 445.
2. A. Lametschwandtner, M. Höll, H. Bartel, V. Anupunpisit, B. Minnich, Anat Sci Intern 87 (2012), 88.
3. B. Minnich, A. Lametschwandtner in “Microscopy: Science, Technology, Applications and Education” Vol 1. ed. A. Méndes-Vilas, J. Diaz Alvarez (Formatex Research Center, Badajoz) (2011), 29.
4. D. Kachlik, V. Baca, H. Stingl, B. Sosna, A. Lametschwandtner, B. Minnich, M. Setina. J Vasc Res 44 (2007), 157.
5. F. Aigner, H. Gruber, F. Conrad, J. Eder, T. Wedel, B. Zelger, V. Engelhardt, A. Lametschwandtner, V. Wienert, U. Böhler, R. Margreiter, H. Fritsch, Intern J Colorectal Dis 24 (2009),105.
6. KC. Hodde, JA. Nowell. Scanning Electron Microsc 1980, 88.
7. A. Lametschwandtner, U. Lametschwandtner, T. Weiger. Scann Microsc 4 (1990), 889.
8. SH. Aharinejad, A. Lametschwandtner. Scanning Electron Microscopy of vascular corrosion casts. Springer Verlag, Berlin-Wien, 1992.
9. A. Lametschwandtner, U. Lametschwandtner in “ Scanning electron microscopy of vascular casts: methods and applications” ed. PM. Motta, T. Murakami, H. Fujita (Kluwer Academic Publishers, Boston, Dordrecht, London) (1992), p 1.
10. EP Krucker, A. Lang, EP Meyer, Microvasc Res Tech 69 (2006), 138.
11. W. Malkusch, MA. Konderding, B. Klapthor, J. Bruch, Anal Cell Pathol 9 (1995), 69
12. B. Minnich, H. Leeb, EWN Bernroider, A. Lametschwandtner, J Microsc 195 (1999), 23.
13. B. Stöttinger, M. Klein, B. Minnich, A. Lametschwandtner, Microsc Microanal 12 (2006), 376.
14. A. Caggiati, M. Phillips, A. Lametschwandtner. Eur J Vasc Endovasc Surg 32 (2006), 444.
15. This work was supported in part by the Fonds zur Förderung der Wissenschaftlichen Forschung (FWF; Project 19050-B17) and by the Stiftungs- und Förderungsgesellschaft der Paris-Lodron–Universität Salzburg. We thank OR Dr. WD Krautgartner for providing excellent working conditions in the SEM facility, S. Tholo for technical assistance and D. Schuster for animal care.

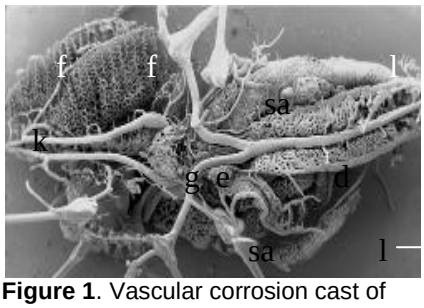

Figure 1. Vascular corrosion cast of a tadpole of the African Clawed Toad, *Xenopus laevis*. Dorsal view. SEM micrograph. Dorsal view. d dorsal aorta, e esophagus, f filterplate, g glottis, k kidney, l lung, sa systemic arch.

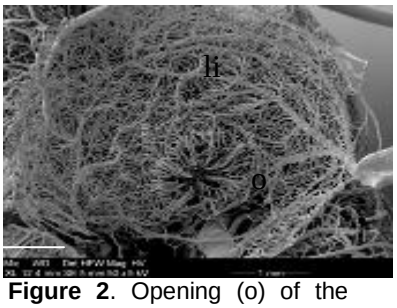

Figure 2. Opening (o) of the small intestine into the large intestine (li) as seen from the large intestine. Adult *Xenopus laevis*.

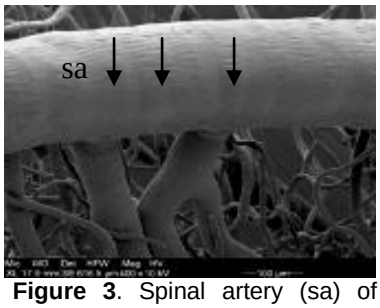

Figure 3. Spinal artery (sa) of adult *Xenopus laevis*. Note the slender longish endothelial cell nuclei imprints orientated parallel to the vessel long axis characteristic for arterial vessels. Arrows indicate circular imprints from vascular smooth muscle cells.

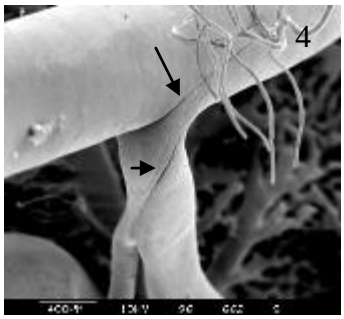

Figure 4. Flow dividers (arrows).

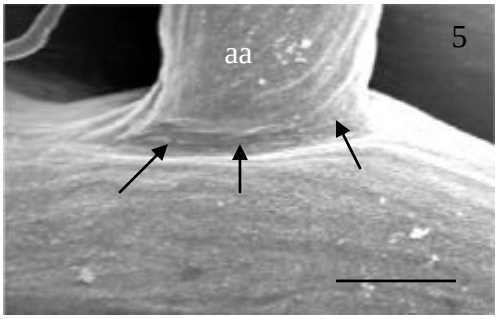

Figure 5. Intimal cushion (arrows) at the origin of an arteriole (aa).

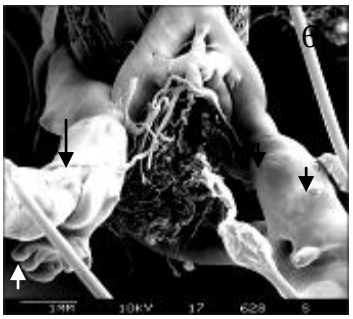

Figure 6. Venous valves of the renal portal vein cast orthogradely (large arrow) and retrogradely (small arrows). Adult *Xenopus laevis*.

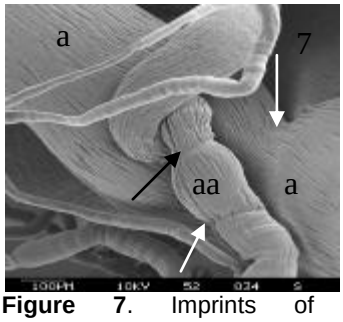

Figure 7. Imprints of muscular sphincters (arrows) on a small artery (a) and an arteriole (aa). Note the characteristic endothelial cell nuclei imprints on artery and arteriole.

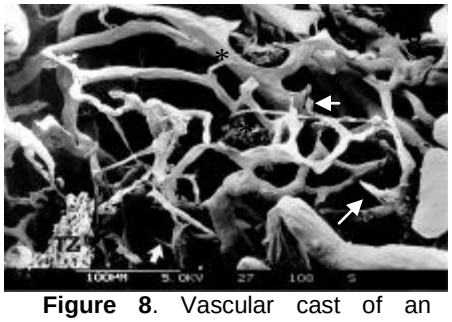

Figure 8. Vascular cast of an experimental glioma in the rat cerebral cortex. Note compressed flattened tumor vessels (asterisks) and vascular sprouts (arrows). a artery, TZ tumor center.

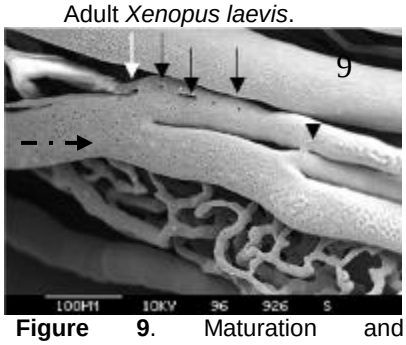

Figure 9. Maturation and remodelling of vascular branching patterns by intussusceptive microvascular growth (IMG). Note first signs of formation and ingrowth of tissue pillars (arrows) which will lead to a new side branch whose origin will be shifted distally. A small anastomosis (arrowhead) is still present between two closely neighbouring distal branches of the same vessel. If this anastomosis is preserved and enlarges or if it regresses cannot be defined yet. Dashed arrow indicates proposed direction of blood flow.

Tissues, Pathology, and Diagnostic Microscopy

LS.2.033
Effects of growth hormone and/or resistance exercise on the myotendinous junction of the plantaris muscle in hind-limb unloaded rats.

D. Curzi[1], D. Lattanzi[1], S. Burattini[1], R.E. Grindeland[2], V.R. Edgerton[3,4], R.R. Roy[3], J.G. Tidball[5] E. Falcieri[1,6]

[1]University of Urbino, Department of Earth, Life and Environmental Sciences, Urbino; Italy, Italy
[2]NASA - Ames Research Center, Life Sciences Division, Moffett Field, CA; USA, United States
[3]University of California, Department of Integrative Biology and Physiology and the Brain Research Institute, Los Angeles, CA; USA, United States
[4]University of California, Department of Neurology and Neurosurgery, Los Angeles, CA; USA, United States
[5]University of California, Molecular, Cellular & Integrative Physiology Program, Los Angeles, CA; USA, United States
[6]IGM-CNR, Rizzoli Orthopaedic Institute, Bologna; Italy, Italy

davide.curzi@uniurb.it
Keywords: Myotendinous junction, exercise, growth hormone, atrophy

The myotendinous junction (MTJ) is the site where muscle contractile force is transmitted from the myofibrils across the plasma membrane to the extracellular matrix (ECM), therefore it is a key structure for the locomotor system [1]. At ultrastructural level, the interface between muscle cell membrane and ECM is highly folded and interdigitated [2]. We recently demonstrated that changes at MTJ level occur as an adaptation to exercise-induced tension increase. In particular, branching of finger-like processes increases, so enlarging the whole tendon-muscle surface area and, consequently, allowing a better tension resistance [3].
In this ultrastructural study, we analyze MTJ behavior in the atrophic condition and during particular prevention protocols. Twenty, hypophysectimized, Sprague-Dawley rats were assigned to one of five groups: control (CTRL), hind-limb suspended (HS), hind-limb suspended and exercised (EX), hind-limb suspended and growth hormone injected (GH) and hind-limb suspended, GH injected and exercised (GH+EX). After sacrifice, MTJs of plantaris muscles were processed for electron microscopy [4]. The contact between muscle and tendon was evaluated with IL/B ratio, where “B” is the base and “IL” is the interface length of tendon finger-like processes at MTJ level (Figure 1a) [5]. After 10 days of suspension the IL/B ratio decreases from 6.39 in CTRL to 3.92 in HS. After unloading, the prevention treatments increase IL/B ratio to 4.18 in GH, 5.25 in EX and 7.3 in GH+EX, respectively. For investigating the causes of the decrease in IL/B ratio in HS and the effects of prevention protocols, we measured the finger-like process extension (Figure 1b), the percentage of branched primary processes and their bifurcation means. In the HS group, there was a lower number of muscle-tendon interdigitations compared to the CTRL group. Finger-like processes were frequently absent and, where present, appeared small and irregular (Figure1c-d). Growth hormone treatment appears not to stimulate the healing of MTJ but it has a partially effect on the muscle, that seem to slightly recover some CTRL features (Figure 1e). The resistance exercise protocol, as well as GH treatment, was not capable of maintaining the contact surface between tissues, but an interesting observation in both exercised groups was the higher number of bifurcated interdigitations than in the CTRL group (Figure 1f). The combination of GH treatment and exercise protocol prevent any significant adverse effects of chronic unloading on the MTJ interface (Figure 1g).
In conclusion, ultrastructural changes occur at MTJ organization level in HS, as an adaptation to muscle unloading. Differently, MTJ structure is partially maintained by resistance exercise protocol or GH treatment, while the exercise with simultaneous somatropin administration showed a greater effect.

1. A. P. Ciena et al., Micron 41(2010):1011-4.
2. H. Kojima et al., J Orthop Sci 13(2008):233-9.
3. D. Curzi et al., Eur J Histochem 56(2012):117-22.
4. D. J. Law et al., Muscle Nerve 18(1995):216-23.
5. L. De Palma et al., Rom J Morphol Embryol 52(2011):105–9.

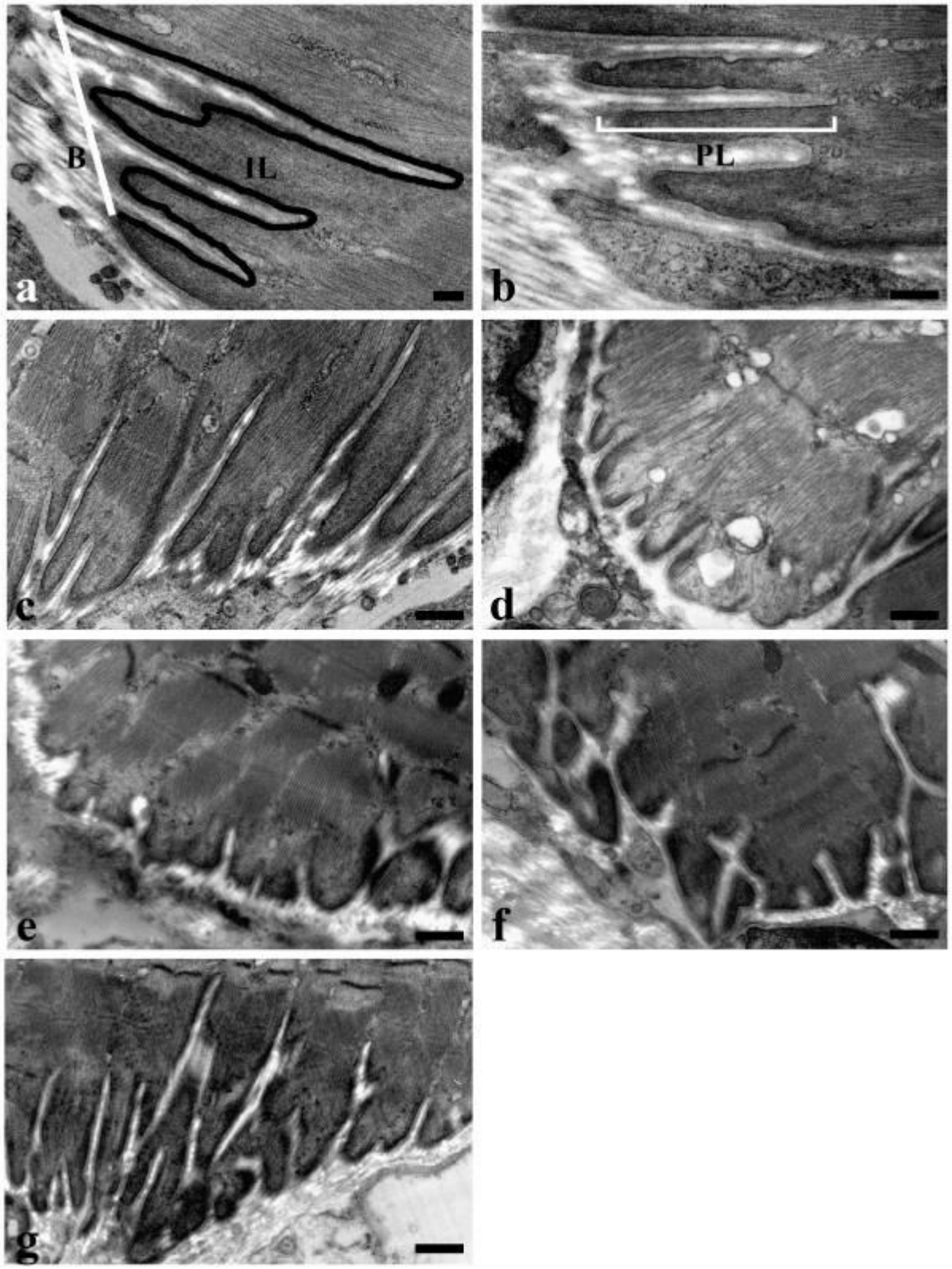

Figure 1. Plantaris muscle MTJs. a) MTJ from CTRL group, the base (B) and the interface length (IL) of junction are highlighted. b) Measure of the primary finger-like process extension (PL). c) Long and numerous tendon interdigitations in the CTRL group. d) Short and rare finger-like processes in the HS group. e) In the GH group, changes appear similar to HS group, but occurring to a lesser extent. f) In the EX group, the length of the finger-like processes was similar to control and a large number of branched interdigitations were observed. g) In the GH+EX group, the tendon interdigitations increase their length and start to branch. A, B Bar 0.25 µm; C, D, E,F,G Bar 0.5 µm.

Tissues, Pathology, and Diagnostic Microscopy

LS.2.034
Three-dimensional reconstruction of regular and damaged podocytes by FIB-SEM

T. Burghardt[1], B. Salecker[1], G. Wanner[2], R. Rachel[3], R. Witzgall[1]

[1]Universitaet Regensburg, Mol Cell Anatomy, Regensburg, Germany
[2]University of München, Biocentre, Planegg, Germany
[3]Universität Regensburg, Centre for EM, Regensburg, Germany

tillmann.burghardt@vkl.uni-regensburg.de
Keywords: Podocytes, LMX1B, FIB-SEM, 3D reconstruction

Nail-patella syndrome (NPS) is a rare autosomal-dominant hereditary disorder with an incidence of ~1:50,000. The prognosis of NPS patients is determined by chronic kidney failure. In 1998 the first mutations in *LMX1B*, a gene encoding the LIM-homeodomain transcription factor 1 beta, were reported to be responsible for NPS [1-3]. Ultrastructural analyses of affected kidneys revealed pronounced alterations of the glomerular filtration barrier. This barrier consists of endothelial cells, the glomerular basement membrane and podocytes. Podocytes form a tight meshwork of primary and secondary processes on the urinary side of the glomerular filtration barrier. Beside a thickened glomerular basement membrane NPS patients regularly show an effacement of foot processes accompanied by the loss of slit diaphragm [4,5]. This prompted us to develop and characterize inducible podocyte-specific *Lmx1b* knock-out mice in order to analyze the role of LMX1B in maintaining the structural differentiation status of podocytes.

3D reconstructions of the glomerular filtration barrier were performed on induced and noninduced 3 month old *Lmx1b* knock-out mice. Mice were fixed by perfusion through the distal abdominal aorta with 4% formaldehyde, 1x PBS. Subsequently, kidney slices were fixed overnight in 2% glutaraldehyde, 1x PBS. The specimens were incubated with cacodylate-buffered 1% OsO_4 for 2 hours at room temperature and then embedded in Epon. The specimens were initially screened by conventional TEM (Zeiss 902), before they were analyzed by focused ion beam scanning electron microscopy (FIB-SEM). Data were collected using a Zeiss Auriga FIB-SEM. Subsequent digital analysis, 3D reconstruction and manual segmentation was performed with the software package Amira ®.

Our data allow a comprehensive view onto ultrastructural changes at the glomerular filtration barrier in kidneys of *Lmx1b* knock-out mice. The 3D reconstruction emphasizes the essential role of Lmx1b for the maintenance of appropriately structured podocytes. Already one week after the inactivation of *Lmx1b* in adult mice, the highly ordered structure of podocytes is markedly disturbed. The foot processes disappear thus leading to increased leakage of the glomerular filter and the loss of protein into the urine. Further 3D analyses will resolve more details of the podocyte processes at higher resolution using TEM tomography.

1. S.D. Dreyer, G. Zhou, A. Baldini, A. Winterpacht, B. Zabel, W. Cole, R.L. Johnson and B. Lee, Nat Genet 19 (1998) p. 47.
2. I. McIntosh, S.D. Dreyer, M.V. Clough, J.A. Dunston, W. Eyaid, C.M. Roig, T. Montgomery, S. Ala-Mello, I. Kaitila, A. Winterpacht, B. Zabel, M. Frydman, W.G. Cole, C.A. Francomano and B. Lee, Am J Hum Genet 63 (1998) p. 1651.
3. D. Vollrath, V.L. Jaramillo-Babb, M.V. Clough, I. McIntosh, K.M. Scott, P.R. Lichter and J.E. Richards, Hum Mol Genet 7 (1998) p. 1091.
4. H. Chen, D. Ovchinnikov, C.L. Pressman, A. Aulehla, Y. Lun and R.L. Johnson, Dev Genet 22 (1998) p. 314.
5. R. Morello, G. Zhou, S.D. Dreyer, S.J. Harvey, Y. Ninomiya, P.S. Thorner, J.H. Miner, W. Cole, A. Winterpacht, B. Zabel, K.C. Oberg and B. Lee, Nat Genet 27 (2001) p. 205.
6. C. Villinger et al., Histochem Cell Biol 138 (2012) 549-556
7. This study was supported by the DFG, SFB 699.

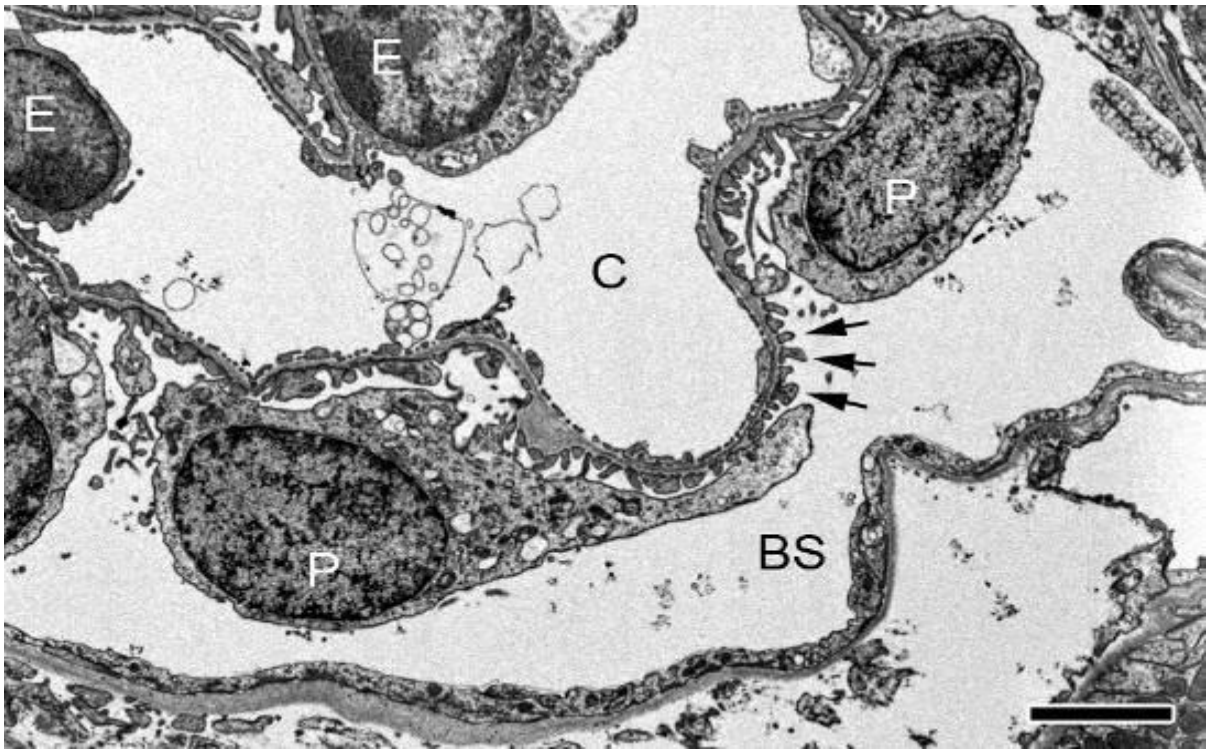

Figure 1. Kidney section from a noninduced *Lmx1b* knock-out mouse analyzed by FIB-SEM. The glomerular filtration barrier is properly formed between the capillary space (C) and the Bowman space (BS). The filter is composed of endothelial cells (E), the glomerular basement membrane, and podocytes (P) branching into characteristic foot processes (arrows). Bar, 2 µm

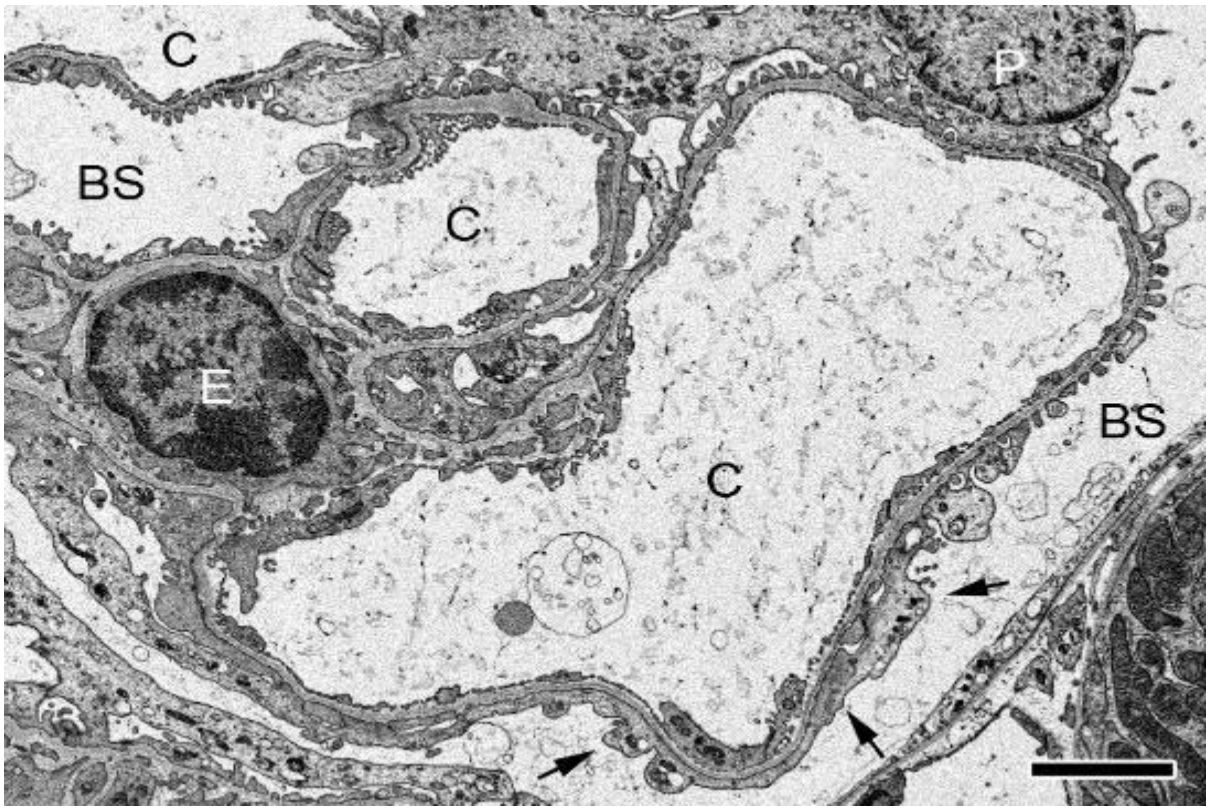

Figure 2. Kidney section from an induced *Lmx1b* knock-out mouse analyzed by FIB-SEM. The organization of the glomerular filter is disturbed; effacement of podocyte foot processes is evident (arrows). Bar, 2 µm

Tissues, Pathology, and Diagnostic Microscopy

LS.2.P035
The Myometrium Ultrastrecture Study by Transmission Electron Microscope

A. Chesca[1]

[1]Faculty of Medicine, Transilvania University of Brasov, Fundamental, Prophilactic and Clinic Disciplines, Romania

anto_chesca@yahoo.com
Keywords: myometrium, ultrastructure, non-pregnancy, pregnancy

The study aims at presenting certain ultrastructural aspects concerning the compounds of the human myometrium, during non-pregnancy and pregnancy at term, as a physiological stage [1].
The transmission electron microscopy technique has been used for observing the ultrastructural aspects of the myometrium compounds, in non-pregnancy and in the pregnancy. In this context, the ultrastructural changes in the physiological pregnancy are considered to be according with the particularities of the hormonal status, comparing with the non-pregnancy stage [3].

According to the reserachers studies referring to the uterus, as a hormone-responsive reproductive organ, influenced by the ovaries hormones, different types of muscle jonctions can be observed in the myometrium, as characteristics for the effect of the estrogens and/or of the progesterone, as most important hormones, implied in pregnancy stage ultrastructural changes. In this context, we monitored the ultrastructural particularities appearing at the myometrium compounds, as smooth muscle, connective tissue and blood vessels, in pregnancy by comparison with non-pregnancy [2].
This study has been done between collaboration of obstetrics-gynecology physicians, pathology specialists and researchers from medical faculty.

The study was achieved by comparison, using two lots constituted of non-pregnant womens and pregnant womens at term. The samples of myometrium taken from both lots of patients implied in the study were taken under the strict observation of the specialists, physicians in obstetrics - gynecology, according to the medical ethics principles.

In the study there was used an electronic transmission microscope Philips 300 with magnifications between x1000-x5000.

The fragments taken for examination with the electronic microscope were processed by the technique that includes following stages such as the fixation with glutaraldehyde in cacodyl pad for 90 minutes at 4˚C, washing with cacodyl pad pH 7.4, three times for 5 minutes at 4˚C; incubation in GÖMÖRI environment; postfixation in OsO4 of 1%, for 90 minutes at 4˚C; rinsing in bidistilled water three time for 5 minutes each, at room temperature, block coloring in uranyl acetate for 30 minutes, at 4˚C in the dark, washing with 10% alcohol, twice, 3 minutes each, at room temperature; dehydration with propilenoxide, twice for 5 minutes each at room temperature; dehydration with absolute ethylic alcohol, 3 times, 5 minutes each at room temperature; dehydration with propilenoxide twice, 5 minutes each at room temperature; penetration in Epon with inclusion in propilenoxide (1:1), for minimum one hour, followed by the evaporation of propilenoxide, up to 8 hours, penetration with Epon inclusion for 2 hours, inclusion, ultra sectioning at microtoms, grids contrasting and grids examination at the electronic microscope.

The myometrium infracentrimetric samples from the non-pregnant womens, were taken during the hysterectomies and the myometrium samples from the pregnant womens at term, were taken according with accept of the pregnant womens, during the Caesarian, by respecting the ethical principles and without affected the health of the future mother or the health of the future newborn baby.

The observations at the transmission electron microscope aimed appreciations concerning the compounds particularities of the myometrium in non-pregnancy and pregnancy at term. In this context, there were noticed changes concerning the muscle fibres, surrounding connective tissue and concerning the blood vessels of the myometrium. The ultrastructural aspects of these compounds, was observing comparatively during physiological pregnancy at term stage and non-pregnancy stage.
In the present ultrastructural study we may distinguish the sarcoplasma of the muscle fibres and also we may distinguish the adherens jonctions and the gap jonctions, between and among the uterine muscle fibres.

Also in the present study the pregnancy is considered as being myometrium active stage, fact that brings informations referring at the ultrastructure of the myometrium muscle fibres and them

functionality, taking into consideration them particularities related to the vicinity with the surrunding connective compounds and blood vessels. In this context, the study allowed electron microscopy appreciations, concerning the characteristics of the myometrium ultrastructural compounds, according to each of both physiological states, taking into consideration the aspects referring to the hypertrophy and hyperplasia of the uterine muscular compound in pregnancy at term.
Using the electron microscopy technique, the orientation to the study of these aspects is compliant with the remarks confirming that in the uterus, besides the smooth muscle tissue, we may at the same time notice the presence of the connective tissue and of the blood vessels.

In this context, by observing the varied forms of myocytes, has been concluded the specific functions of the smooth muscle, such as tension, contraction and relaxation, which are considered to be the result of the coordinated activity of the muscle cells. Also, the study help for answering if the myometrial contraction is isotonic or isometric. From this point of view, we consider that the function of the myometrium, is known as an isometric contraction with changes in pregnancy at term compared with non-pregnancy stage and, as a conclusion, referring to the myometrium, are appreciations, as being a functional syncytium.

1. A. Cheşcă, The ultrastructure of the connective cells from the myometrium, Sibiul Medical, no. 1/ 2002, p.111-112.
2. I. Crişan, Obstetrics, Metropol Publishing House Bucharest,1995.
3 I. Diculescu, D. Onicescu, Medical Histology, vol. I, Medical Publishing House Bucharest, 1987.

Tissues, Pathology, and Diagnostic Microscopy

LS.2.P036
Environmentally realistic doses of cadmium affects the vascular tonus in Wistar testis: An experimental study paralleling human environmental exposure to cadmium.

R. Leite[1], F.R. Gadelha[2], L.H. Ribeiro[2], M.A. Diamante[1], H. Dolder[1]

[1]State University of Campinas, Cell Biololgy, Campinas, Brazil
[2]State University of Campinas, Biochemistry, Campinas, Brazil

rpleite@gmail.com

Cadmium is a widespread toxic metal that has increasingly been introduced into the environment due to anthropogenic activities. Although industrial processes are among the major contributors to increase cadmium concentration in the environment, phosphate fertilizers have significantly increased the percentage of cadmium in soil, making food and tobacco the main source of cadmium exposure to humans [1]. Worldwide population surveys have shown a consistent link between environmental exposure to cadmium and several idiopathic pathologies among non-occupationally exposed subjects. Although the main route of exposure to cadmium among the general population refers to low chronic doses, current understanding of cadmium toxicity is usually based on experimental models employing highly concentrated injected doses. Epidemiological investigations and animal experiments paralleling human chronic exposure to environmental cadmium are, therefore of major importance for establishing a relationship between cadmium and several pathologies of unspecific etiology. In the present study, Wistar rats were randomly divided into different groups and subjected to increasing cadmium doses ranging between low to moderate environmentally realistic doses [2].

Twenty male adult Wistar rats (70 days old) were divided into four different groups containing 5 animals each: control group (Cadmium 0 mg/L), Cd25 group (Cadmium 25 mg/L), Cd50 group (Cadmium 50 mg/L) and Cd75 group (Cadmium Cd 75 mg/L). Except for control, each group was orally exposed to different concentrations of cadmium. Metal salts were diluted in drinking water and given to the animals *ad libitum* over thirty consecutive days. In order to make the water more attractive and assure that different groups would consume the same amount of water on a time range, sucrose 10% was added to the water [2]. At the end of the treatment, the testis was dissected free and subjected to stereological and biochemical analysis.

Our results show that oral exposure to environmental doses of cadmium clearly affects the vascular tonus in the testis, either by increasing the lumen proportion or by decreasing it (Table I)(Figure I). Previous literature shows that both vasocontractile and vasorelaxation responses could be enhanced in cadmium-exposed subjects, although either condition might take place depending on the dose [3,4]. The mechanistic pathways through which cadmium exerts its toxicity are not totally understood, although a review of the literature have shown that Reactive Oxygen Species (ROS) may play an important role in this process. Such reactive species are known to oxidize a wide range of biological molecules and therefore might be on the basis of cadmium-related cellular damages. Our biochemical assays have assessed a significant increase in lipid peroxidation in the Cd75 group, whereas the remaining groups (Cd25 and Cd50), did not show any significant change in such a parameter (Chart I). However, all cadmium-treated groups have shown a sharp increase in catalase activity (Chart II), indicating therefore that the cellular oxidative status has been somehow affected, probably due to a systemic increase in reactive oxygen species. It is therefore hypothetically viable that a consistent link between cadmium and several idiopathic pathologies could be established, although further studies should be carried out in order to confirm such a relationship.

1. Järup, L., and Akesson, A., 2009. Current Status of Cadmium as an environmental health problem. Toxicology and applied pharmacology 238, 201-208.
2. Benoff, S., Auborn, K., Marmar, J.L., Hurley, I.R., 2008. Link between low-dose environmentally relevant cadmium exposures and asthenozoospermia in a rat model. Fertil. Steril. 89, 73-79.
3. Suto, D., Akiyama, K. 2000. Effect of cadmium or magnesium on calcium-dependent central function that reduces blood pressure. Arch Toxicol. 74, 1-4.
4. Skoczynska, A., Martynowicz, H., 2005. The impact of subchronic cadmium poisoning on the vascular effect of nitric oxide in rats. Human and Experimental Toxicology. 24, 353-361.
5. Research Funding: São Paulo Research Foundation (FAPESP), *Coordination for the Improvement of Higher* Education Personnel (CAPES), National Counsel of Technological and Scientific Development (CNPQ).

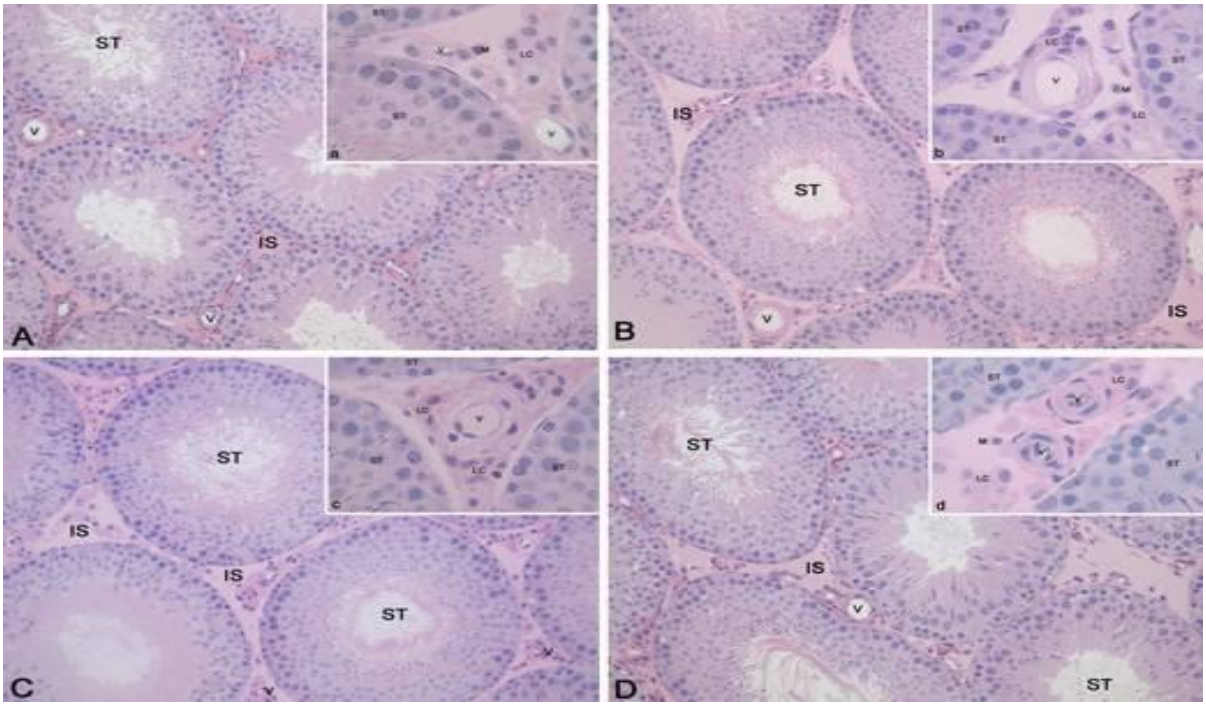

Figure 1.

Parameters		Control group	Cd25 Group	Cd50 Group	Cd75 Group
Blood Vessel Lumen	(ml)	0.007 ± 0.004^{a}	0.025 ± 0.004^{b}	0.024 ± 0.06^{b}	0.006 ± 0.002^{a}
	(%)	0.46 ± 0.37^{a}	1.45 ± 0.3^{b}	1.39 ± 0.44^{b}	0.36 ± 0.14^{a}

Figure 2.

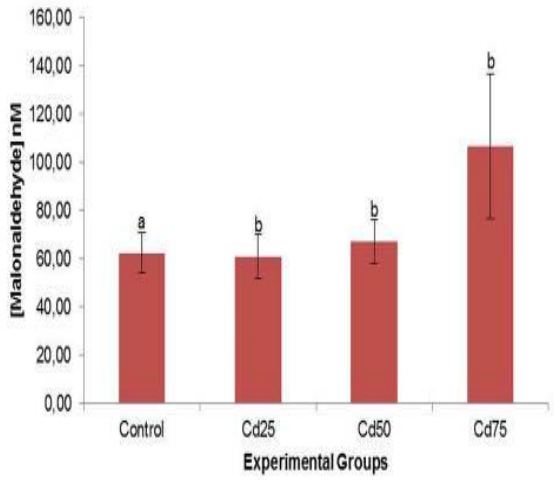

Figure 3.

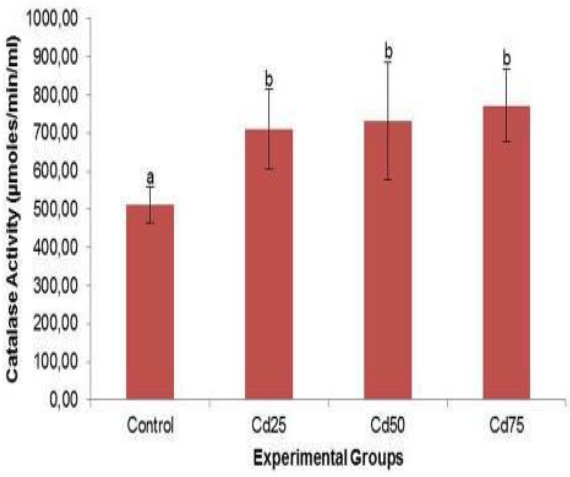

Figure 4.

Tissues, Pathology, and Diagnostic Microscopy

LS.2.P037
Parameters of microcirculatory blood flow in human skin under long-term thermal stress (model experiment)

A. Fedorovich[1]

[1]Russian Cardiolody Research and Production Complex, Moscow, Russian Federation

faa-micro@yandex.ru

To study peculiarities of skin microcirculatory blood flow of the upper limbs according to computer capillaroscopy during the model experiment, restoring the conditions of the hot summer of 2010 in Russia.

The study included 6 healthy men aged 24 to 44 years (34.3±9.6), who stayed in the airproof accommodation module for 30 days, with constant day temperature +30+38ºC (33.9±2.3), relative humidity 30-50% (38.3±6.9) and night temperature values +26+31ºC (28.1±1.5), relative humidity 50-75% (68.5±7.1). Investigation of microvasculature was performed twice a day (in the morning and evening) every other day in the sitting airproof accommodation module with air temperature +29+30ºC and humidity 30%.

According to the computer capillaroscopy, there were marked a dramatic increase in the capillary blood flow speed >3500 µm/s and significant elevation in the size of pericapillary zone (PZ), reflecting the hydration degree of the interstitial space (figure 1). Pericapillary zone had a distinct daily fluctuations - in the morning it was higher ($p<0.000001$) than in the evening, and was significantly correlated (figure 2) with systolic blood pressure (SBP) - $r = -0.59$ ($p = 0.000000002$) and diastolic blood pressure (DBP) - $r = -0.46$ ($p = 0.000007$).

In the long-term heat stress efficiency thermoregulatory processes in the skin depends on the filtration process at the level of capillaries. Formation and evaporation of sweat and have a significant effect on the parameters of blood pressure.

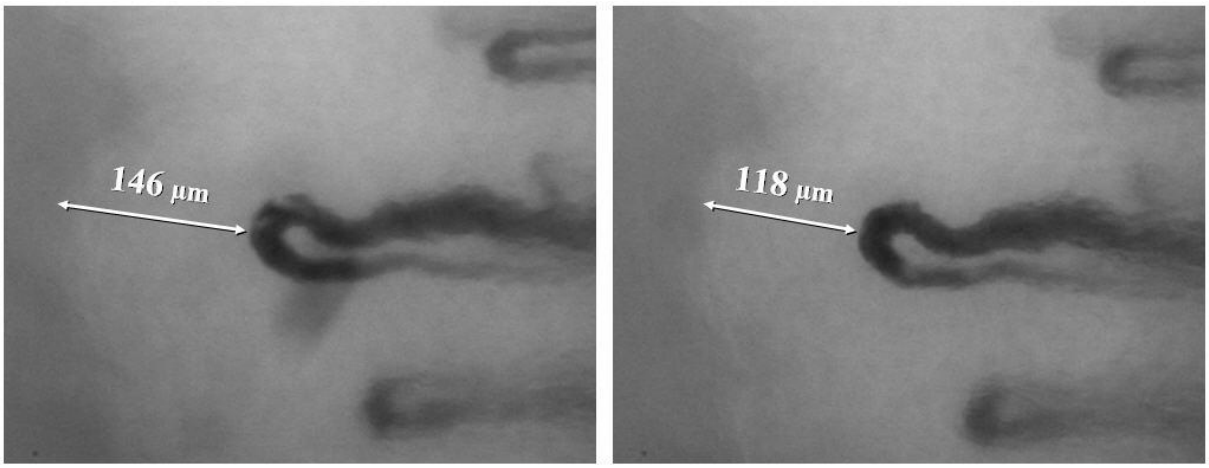

A B

Figure 1. Dimensions of the pericapillary zone: **A** – morning; **B** – evening.

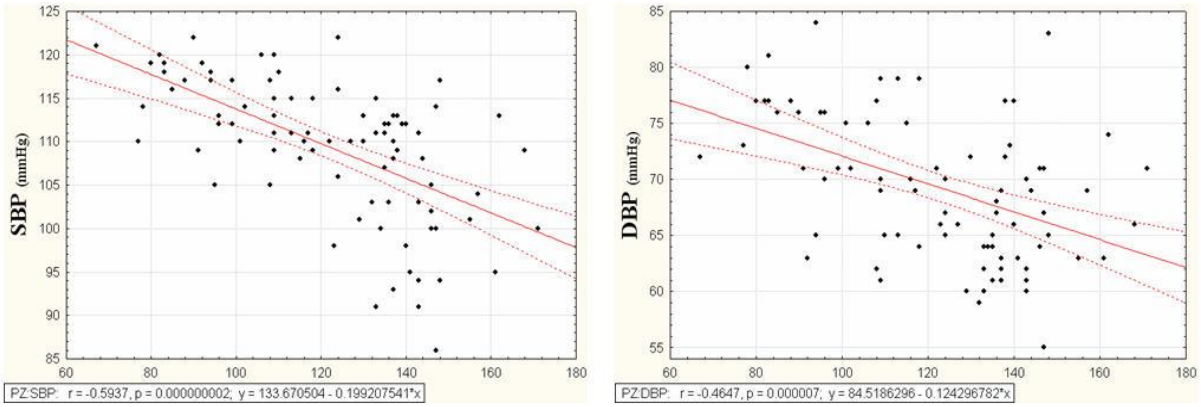

A B

Figure 2. Relationship size pericapillary zone with blood pressure: **A** – systolic; **B –** diastolic.

Tissues, Pathology, and Diagnostic Microscopy

LS.2.P038
Nanodiagnostics of pelvic organ prolapse based on the atomic force microscopy analysis of extracellular matrix

S. Kotova[1], P. Timashev[2], A. Guller[3], V. Timofeeva[1], A. Shekhter[3], A. Solovieva[1]

[1]N.N.Semenov Institute of Chemical Physics, Dept. of Polymers and Composites, Moscow, Russian Federation
[2]Institute of Laser and Information Technologies , Troitsk, Russian Federation
[3]I.M. Sechenov First Moscow State Medical University, Moscow, Russian Federation

slkotova@mail.ru
Keywords: atomic force microscopy, extracellular matrix, pelvic organ prolapse

Extracellular matrix, consisting mainly of collagen, forms a basis of human connective tissue, providing its specific mechanical properties. The supramolecular packing of collagen macromolecules results in a characteristic nano- and microtexture for each type of connective tissue (skin, ligament, intervertebral disc etc.). Pathological processes may lead to significant changes in the structure of extracellular matrix of connective tissue, and, in particular, in the collagen packing.

Here we have applied atomic force microscopy (AFM) to diagnose pathological changes in the extracellular matrix of connective tissue caused by pelvic organ prolapse (POP). POP is a common condition affecting women which considerably decreases the patients' quality of life [1].

We have studied clinical specimens from skin biopsy of patients with POP and those without connective tissue disorders (control group). AFM imaging was performed on air on deparaffinized tissue sections.

AFM images of normal human skin demonstrated a characteristic "basket-weave" pattern of collagen fibers (Figure 1, *a*) [2], consisting mostly of tightly packed quasi-parallel collagen fibrils (Figure 1, *b* and *c*), with occasionally found disordered regions. The specific banding of collagen fibrils (D-period) was clearly resolved, especially in the phase images. The details of collagen molecular packing could be visualized at a high resolution, with the "gap" (corresponding to 4 parallel collagen molecules in the collagen microfibril) and the "overlap" (5 collagen molecules in the microfibril) regions forming together the D-period of collagen [3], and their finer structure. Besides the collagen bundles, fibers without banding (presumably, elastic fibers) and regions with high deformability and adhesion (apparently, non-fibrous components of the extracellular matrix) were found.

For the specimens taken from the POP patients, we detected significant deviations from the normal skin structure. The "basket-weave" pattern of collagen bundles became coarser, with the holes visibly expanded (Figure 2, *a*). The increased deformability and probe adhesion to the surface testified increase in the fraction of non-collagenous components of the extracellular matrix. In contrast to the normal skin morphology, we only rarely observed the tight quasi-parallel packing of collagen fibrils, while the disordered weaving of separate fibrils prevailed (Figure 2, *b* and *c*). Within the tightly packed regions, we often found deformation, rupture and shortening of collagen fibrils, as well as decrease in the average fibril thickness comparing to the normal skin from the control group.

The hardness and Young's modulus of the bundles of collagen fibrils measured by nanoindentation appeared to be considerably lower for the POP tissue samples as compared to those for the control group. Thus, both the morphological and mechanical data have been found to be meaningful in the potential POP diagnostics.

The AFM data were compared to the data of standard clinical morphological studies (including histological and electron microscopy studies) of the same specimens. According to the traditional methods, similar signs of deterioration of the normal extracellular matrix structure were found for the POP patients' tissue, including visible separation of collagen fibers, thinning and fragmentation of collagen fibers, disintegration and disordering of collagen structures up to the complete destruction of the specific dermis architecture. The consistency of the AFM findings and the results of the standard morphological methods points out to the validity of the AFM analysis as a diagnostic tool for the POP-related structural changes of extracellular matrix.

1. M. H. Kerkhof, L. Hendriks, H. A. M. Brölmann, Int. Urogynecol. J. 20 (2009), p. 461.
2. Graham H.K., Hodson N. W. , Hoyland J. A. et al., Matrix Biol. 29 (2010), p. 254.
3. J.P.R.O. Orgel, T.C. Irving, A. Miller, T.J. Wess, PNAS 103 (2006), p. 9001.
4. We kindly acknowledge the financial support from the Russian Foundation for Basic Research (Grant #12-02-00633-a).

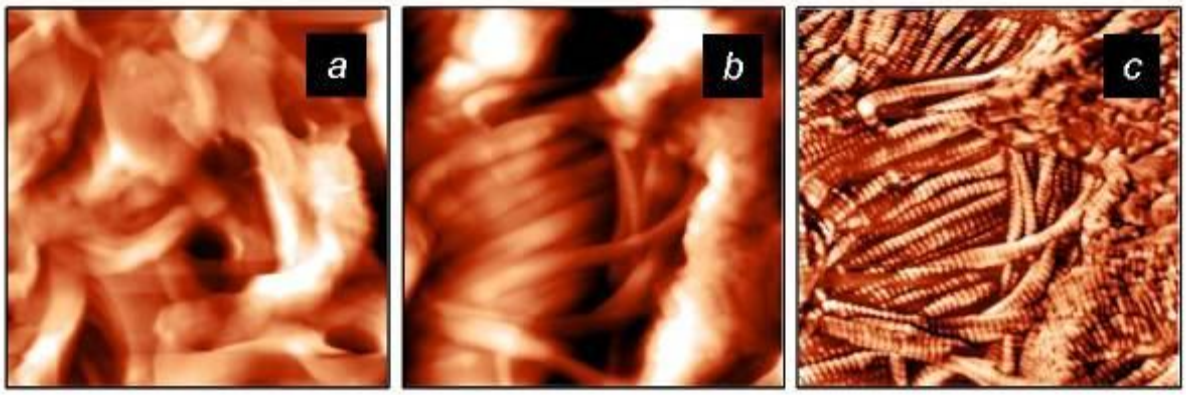

Figure 1. Micro- (*a*) and nanotexture (*b, c*) of extracellular matrix of normal human skin.
a – topography, scan size is 14×14 μm, height scale is 0 - 4.0 μm.
b – topography, *c* – phase, scan size is 3×3 μm, height scale is 0 – 500 nm.

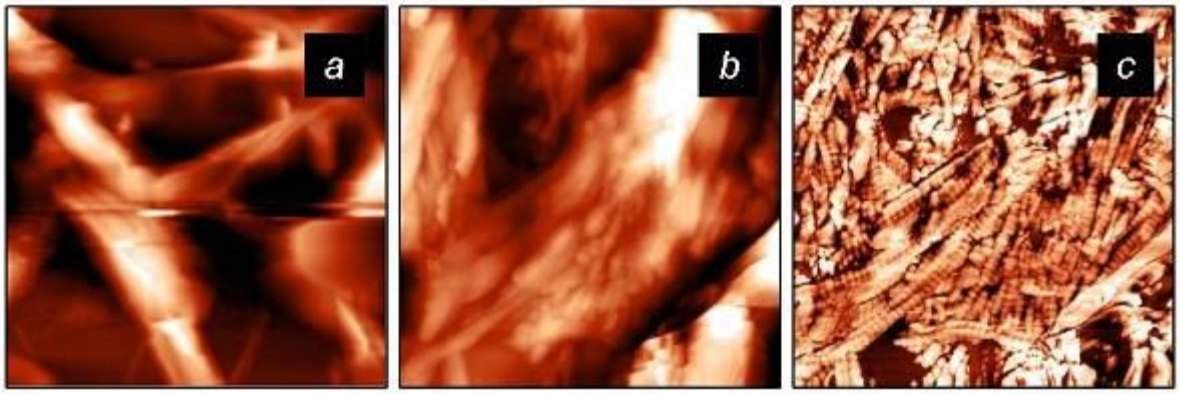

Figure 2. Micro- (*a*) and nanotexture (*b, c*) of extracellular matrix of the skin of a patient with POP.
a – topography, scan size is 14×14 μm, height scale is 0 - 4.0 μm.;
b – topography, *c* – phase, scan size is 3×3 μm, height scale is 0 – 500 nm.
Note the inferior quality of Image *a* resulting from the deep holes, material softness and high adhesion to the probe.

Tissues, Pathology, and Diagnostic Microscopy

LS.2.P039
Ultrastructural localization of laminin 5 at dentogingival border

T. Sawada[1]

[1]Tokyo Dental College, Ultrastructural Science, Chiba, Japan

sawada@tdc.ac.jp
Keywords: junctional epithelium, basal lamina, laminin 5

The junctional epithelium of the gingiva is firmly attached to the tooth enamel by the internal basal lamina and hemidesmosomes at the dentogingival border of the tooth. In an earlier ultrastructural study [1], we found that the internal basal lamina was made up of lamina densa and lamina lucida, and that the former was much thicker than other types of basement membrane. Dental cuticles are often observed at the dentogingival border in healthy teeth, but their origin is unknown. Recent immunohistochemical studies have demonstrated that laminin 5 was localized at the dentogingival border in rodent or human tooth [2, 3]. However, the ultrastructural distribution of laminin 5 at the border remains to be elucidated. The aim of the present study was to demonstrate the immunolocalization of laminin 5 at the interface between the junctional epithelium and tooth enamel in detail.

Japanese monkeys (*Macaca fuscata*) were perfused with paraformaldehyde solution under anesthesia and jaw segments including the deciduous molars and associated gingiva isolated and demineralized with EDTA. After demineralization, the samples were quickly frozen and stored in a freezer at -80°C before immunohistochemistry. Three protocols were used for immunoelectron microscopic observation: 1) pre-embedding immunoperoxidase staining; 2) pre-embedding colloidal-gold immunolabeling; and 3) modified post-embedding colloidal-gold immunolabeling. Cryosections 10-□m in thickness were incubated with rabbit polyclonal anti-human laminin 5 antibody (ab 14509) at 4°C overnight. They were then incubated again with a horseradish peroxidase-labeled secondary antibody or a 5- or 10-nm colloidal-gold labeled secondary antibody overnight. The sections were then further incubated in osmium tetroxide, followed by dehydration with ethanol and embedding in epoxy resin. For post-embedding, the cryosections were dehydrated with ethanol and flat-embedded in LR White resin using the inverted gelatin capsule method. Ultrathin sections mounted on nickel grids were incubated with laminin 5 antibody followed by colloidal-gold labeled secondary antibodies and observed under a transmission electron microscope with uranyl acetate and lead citrate staining.

Intense immunostaining for laminin 5 was observed at the dentogingival border under a light microscope. At high magnification, immunoperoxidase reaction products were detected at the ultrastructural level in the lamina densa and lamina lucida of the internal basal lamina (Figure 1). Junctional epithelial cells located near the sulcus contained immunolabeled rough endoplasmic reticuli, indicating the production of laminin 5 protein. With pre-embedding colloidal-gold immunolabeling, amorphous material in the intercellular spaces was also intensely labeled (Figure 2). With post-embedding, the detailed immunolocalization of laminin 5 could be observed by electron microscopy. Gold particles were localized in the lamina densa, particularly under the hemidesmosomes of the junctional epithelium cells facing the tooth enamel. Gold particles gradually increased in number in the coronal direction, resulting in a large accumulation of gold particles in the internal basal lamina near the sulcus. A few gold particles were also observed dispersed on the dental cuticles (Figure 3), which had shown less labeling with the other pre-embedding methods employed in this study.

These results suggest that laminin 5 was actively synthesized by junctional epithelium cells and the secretory product incorporated into the internal basal lamina, resulting in a thick basal lamina capable of tightly sealing the periodontal tissue from the oral environment. The localization of gold particles on the dental cuticles suggests a cellular origin, as indicated in an earlier study by this group [4].

1. T. Sawada and S. Inoue, Anat Rec 246 (1996), p. 317.
2. J. Oksanen, L.M.Sorokin, I. Virtanen, and M. Hormia, J Dent Res 80 (2001), p. 2093.
3. M. Hormia, K. Owaribe, and I. Virtanen, J Periodontol 72 (2001), p. 788.
4. T. Sawada and S. Inoue, J Periodontal Res 36 (2001), p. 101.
5. This work was supported in part by a Grant-in-Aid for Scientific Research (24592779) from the Ministry of Education, Culture, Sports, Science and Technology of Japan.

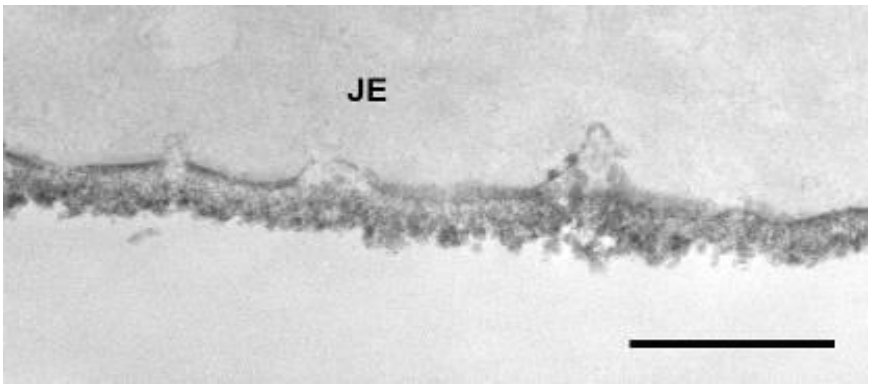

Figure 1. Pre-embedding immunoperoxidase. Laminin 5 was localized both in lamina densa and lamina lucida. JE: junctional epithelium. Bar = 0.5 □m

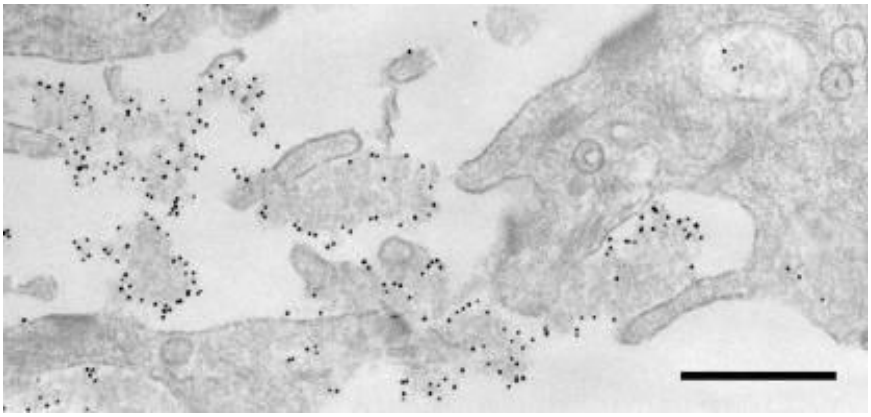

Figure 2. Pre-embedding colloidal-gold labeling . Amorphous material was labeled by gold particles. Bar = 0.5 □m

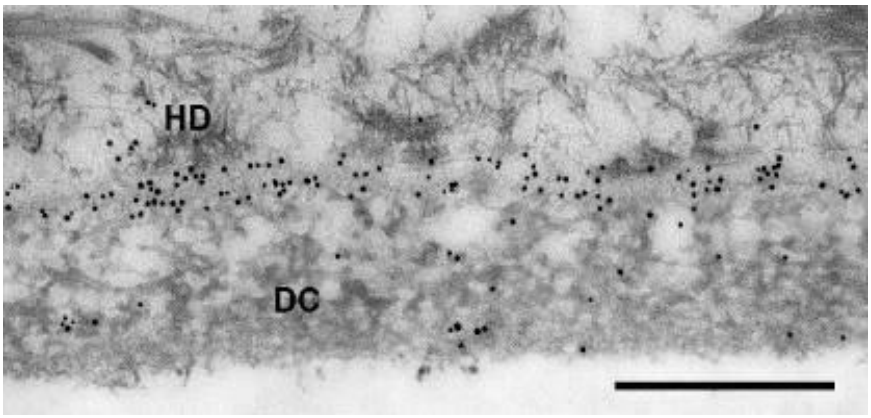

Figure 3. Post-embedding colloidal-gold labeling. Large number of gold particles was observed in internal basal lamina under hemidesmosomes (HD). A few gold particles were distributed on dental cuticles (DC). Bar = 0.5 □m

Tissues, Pathology, and Diagnostic Microscopy

LS.2.P040
3D imaging of the lacunar-canalicular network of compact bone

T. Congiu[1], U.E. Pazzaglia[2], P. Basso[1], M. Raspanti[1]

[1]Insubria University, Dept. Surgical & Morphological Sciences, Varese, Italy
[2]Brescia University, Dept. Surgical Specialties, Brescia, Italy

mario.raspanti@uninsubria.it
Keywords: bone, corrosion cast, SEM

The canalicular network which interconnects osteocytic lacunae in compact bone and which maintains the osteocytes in reciprocal contact is a critical pathway for the supply of fluid and nutrients that keep the bone cells alive and functional. In addition it has been hypothesized that the flow of fluids and substances through the lacunar-canalicular network may be a necessary element for the regulation of the bony cells activity and the balance between bone resorption and deposition.

The intricate meshwork of tiny passages has been the subject of a few studies, always carried out by sectional techniques – either by serial sections of embedded specimens, or by confocal laser scanning microscopy, or by FIB/SEM imaging. All these techniques can only visualize a limited volume of the bone matrix, and in all cases the persistence of the dense bone matrix represents a major obstacle to the visualization of the finer details.

In the present research the lacunar-canalicular meshwork of the compact bone has been studied by a variation of the corrosion casting technique, an approach which so far was rarely used [1,2]. Small fragments of bone compact from the diaphysis of human tibiae were thoroughly cleaned in hydrogen peroxide in order to get rid of the cells, the blood vessels and the non-mineralized tissues in general. Two different acrylic resin were then used to obtain a detailed cast of the bone cavities, that has been subsequently visualized by scanning electron microscopy (SEM).

In a first case the clean bone block was infiltrated with a biocompatible polymethylmetacrylate (PMMA) resin, usually used as an orthopaedic cement (DePuy International, Blackpool, UK). The infiltration of the monomer in the Havers canals and hence in the lacunar-canalicular network was simply driven by capillarity, helped by the evaporation. In a successive variant a different PMMA formulation (Heraeus Kulzer, Hanau, Germany) was used. In this case, being the monomer preparation more viscous, the infiltration was helped by high pressure (approx. 700 kPa).

The specimen was then etched in HCl and then in KOH solution to completely dissolve the bone matrix, freeing the cast of the canalicular mesh and allowing its observation by SEM (Figure 1). The cast duplicated faithfully the shape, position and connection of the osteocytic lacunae and afforded an unrestricted exploration of their spatial relations without any other manipulation.

Our observation revealed the existence of two distinct systems of canalicula: in addition to a radial canalicular system which interconnects the osteocytes of successive lamellae there is indeed an equatorial system of canalicula which interconnect the osteocytes of the same plane (Figure 2). Together, these two groups form a really three-dimensional network.

A morphometric study of the length and width of the osteocytic interconnection is still under way. Our results, however, already suggest that a fluids flow trough the canalicular network is not necessary, and that the supply of oxygen and metabolites from the vascular canals to the most peripheral osteocytes could be assured simply by cell-to-cell diffusion through the canalicular network.

1. Gorustovich A.A. Microsc.Microanal. 16 (2010), 132-136
2. Kubek D.J., Gattone V.H., Allen M.R. Microsc.Res.Techniq. 73 (2010), 182-186

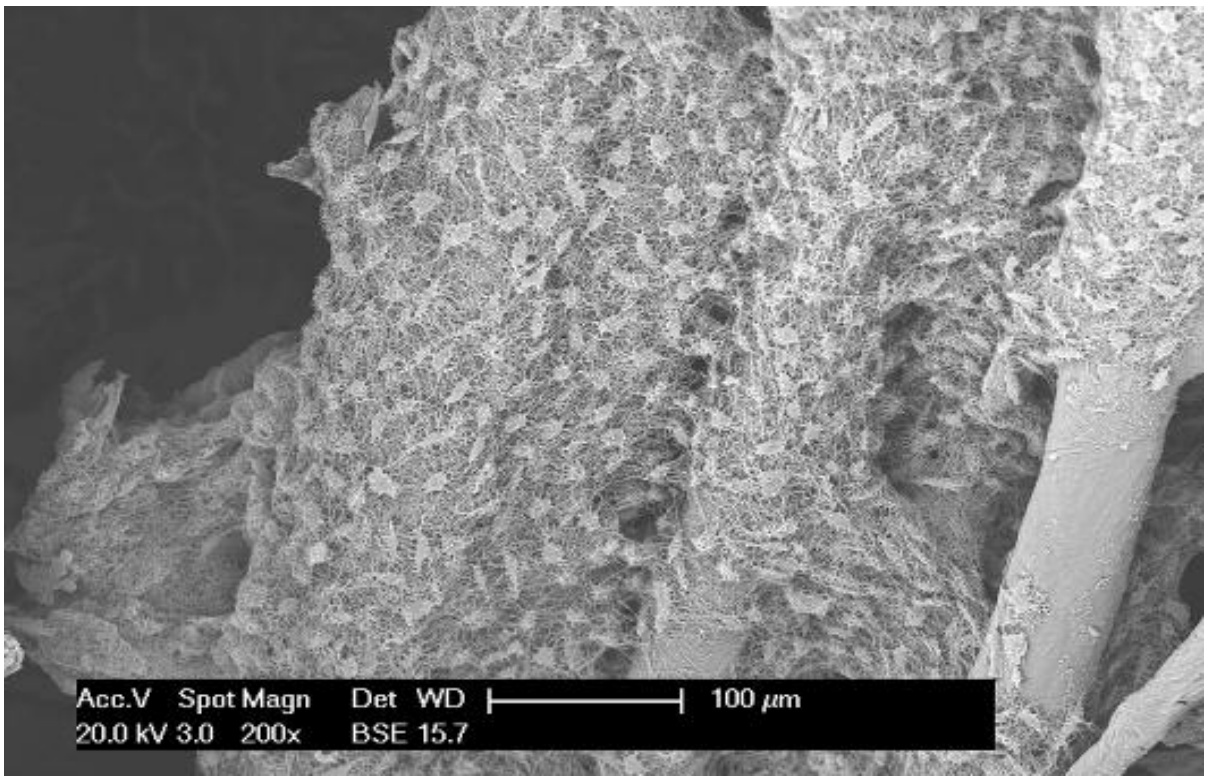

Figure 1. Low-magnification of the lacunar-canalicular network around the Haversian canals.

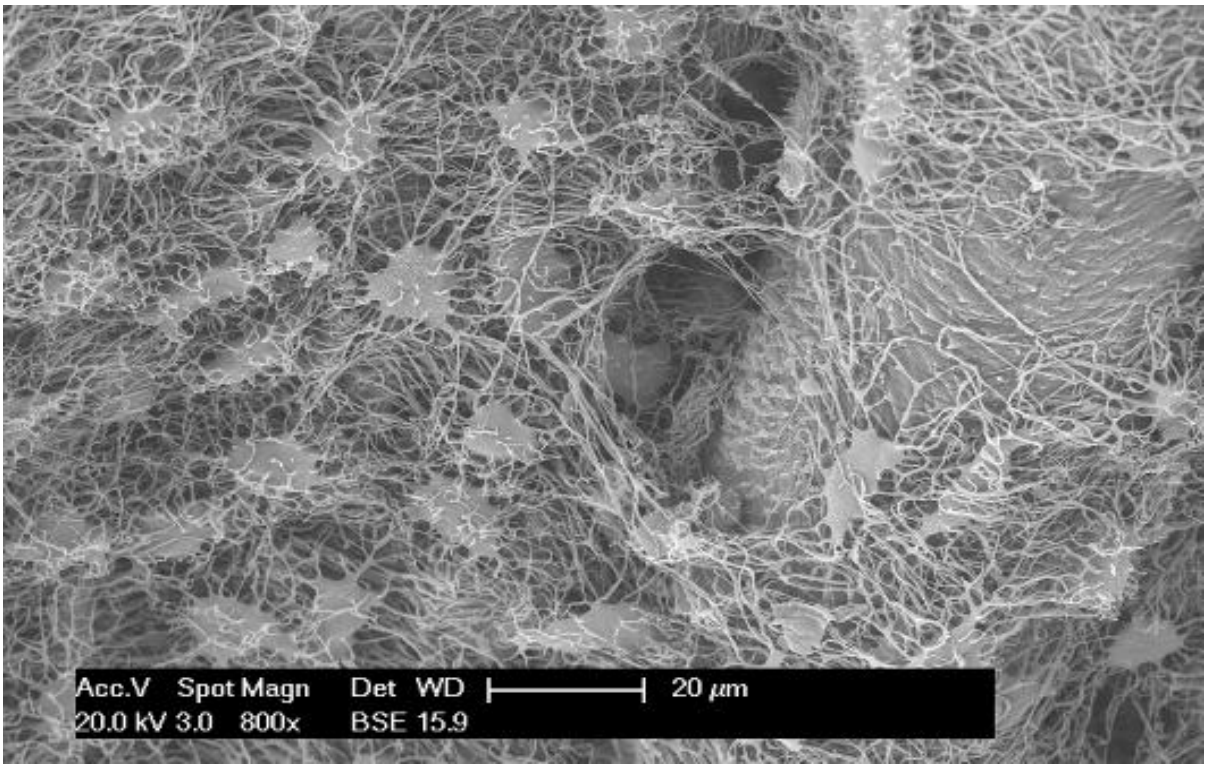

Figure 2. A higher magnification reveals the emergence of the canalicula not only from the osteocytes radial surfaces but from their edge as well.

Tissues, Pathology, and Diagnostic Microscopy

LS.2.P041
Melatonin impact on cyclosporine-induced liver damage: an update

A. Stacchiotti[1], G. Favero[1], A. Lavazza[2], L.F. Rodella[1], R. Rezzani[1]

[1]Brescia University, Clinical and Experimental Sciences, Brescia, Italy
[2]Istituto Zooprofilattico Sperimentale della Lombardia e Emilia Romagna, Brescia, Italy

stacchio@med.unibs.it
Keywords: melatonin, liver, autophagy

Cyclosporine A (CsA) is the elective immunosuppressive drug in transplantation and autoimmune disorders, even if among its multiple side effects, liver damage limits clinical application. Chronic CsA delivery induces in the liver a hypermetabolic state and oxidative damage, ROS production, associated with a stress response [1]. Melatonin, the indolamine produced by the pineal gland, has been proven to be particularly effective in the amelioration of respiratory balance in health and diseases [2].

Nevertheless the contribution of autophagy (or macroautophagy), the pivotal process that removes abnormal proteins or organelles, like mitochondria and peroxisomes, to preserve homeostasis during CsA therapy is still emerging.

This microscopic study aimed to further demonstrate the beneficial melatonin role in the liver treated with CsA focusing on autophagosomes, mitochondria, ER morphology and chaperones expression in the rat.

Sprague-Dawley rats were s.c. injected with CsA (15 mg/Kg/day), melatonin alone (1 mg/Kg/day), or with melatonin and CsA, at the above dosage, for 30 days. The liver was extracted and processed for histopathological, enzymatic, immunohistochemical and ultrastructural analysis.

Mitochondria damage was evaluated by citochrome c-oxidase histochemistry, ER stress by immunostaining of resident chaperones (GRP78, GRP94), autophagic flux by the presence of autophagosomes and autophagolysosomes by TEM analysis and by immunostaining of ubiquitin and p62/sequestome-1 protein, a marker of autophagic flux. To best characterize an efficient autophagic flux in the liver and mitochondria ultrastructure we inserted, as positive control, 24h fasted rats [3].

Melatonin supplementation restored cytochrome c oxidase-positive brown signal in the cytoplasm of hepatocytes whereas it almost disappeared in CsA-treated group.

Moreover during immunosuppressive regimen, RER fragmentation (Figure 1) and chaperones overexpression, late autophagosomes, often mitophagosomes, together with intense ubiquitin and p62-positive aggregates were seen in hepatocytes.

By contrast, in rats given CsA plus melatonin, RER morphology was restored and autophagosomes almost absent (Figure 2), p62 and ubiquitin immunostainings became weak. In 24h-fasted rats ER dilatation, perinuclear elongated mitochondria and autophagic vacuoles were detected in hepatocytes (Figure 3).

These novel observations suggest that melatonin alleviates CsA-induced hepatotoxicity by restoring proper mitochondria, ER organization and stimulating autophagic flux, so keeping an adequate cellular detoxification ability.

In conclusion, in this chronic in vivo model melatonin, acting in the recovery of adaptive autophagy and hampering ER stress-driven apoptosis, further confirms its efficacy to contrast hepatic damage.

1. R.Rezzani et al., Int Immunopharmacol 5 (2005), p.1397-1405.
2. D.Acuna-Castroviejo et al., Curr Topics Med Chem 11 (2011), p. 221-240.
3. L.Gomes, G.Di Benedetto, L.Scorrano, Nature Cell Biol 13 (2011), p.598-598.
4. Authors would like to thank S.Castrezzati and G.Bozzoni for expert assistance in TEM samples preparation

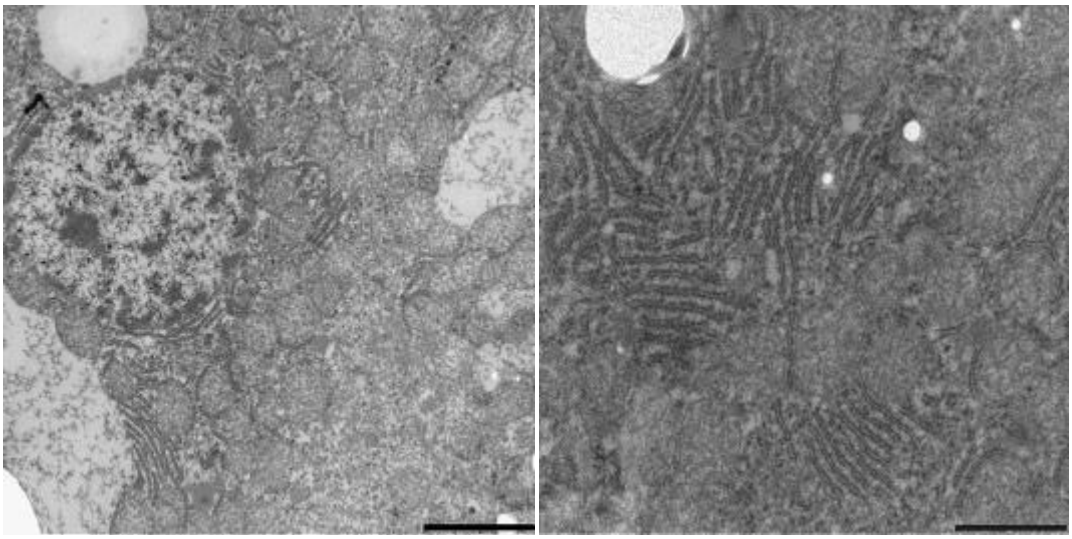

Figure 1. Electron micrographs of CsA-treated liver: scattered RER stacks and amorphous mitochondria. TEM FEI Tecnai G2Spirit; bar = 2µm and 1µm respectively

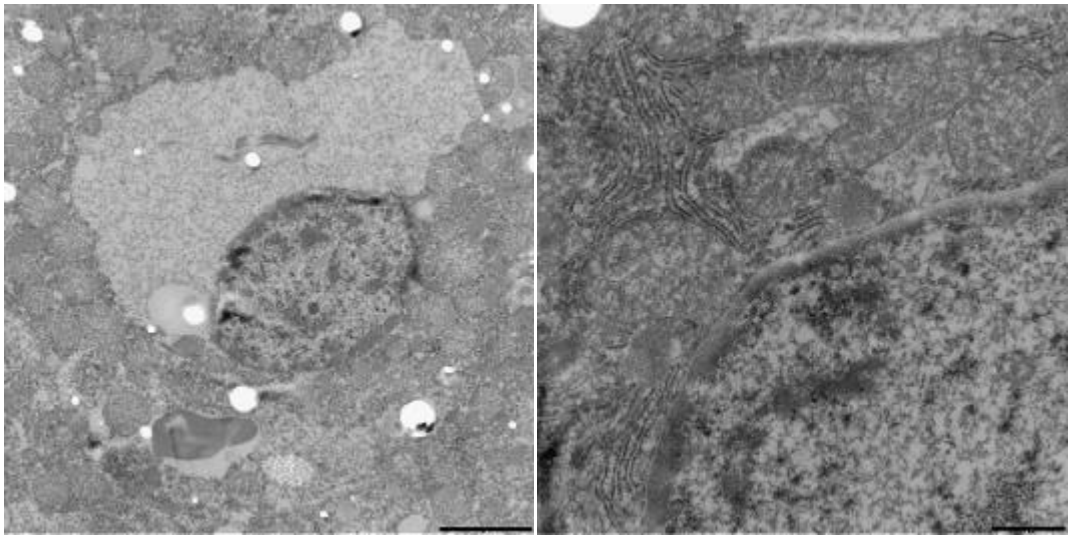

Figure 2. Electron micrographs of CsA plus melatonin-treated liver: regular RER, round and elongated mitochondria. TEM FEI Tecnai G2Spirit; bar = 2µm and 500nm respectively

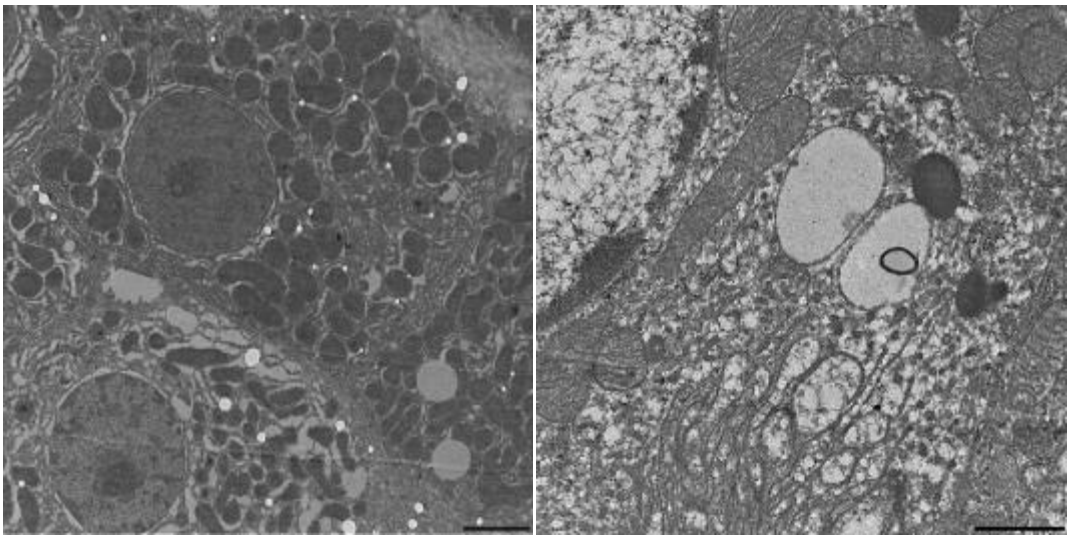

Figure 3. Electron micrographs of 24h fasted rat liver: dense elongated mitochondria and RER dilation, autophagic vacuoles. TEM FEI Tecnai G2Spirit; bar = 2µm and 1µm respectively

Tissues, Pathology, and Diagnostic Microscopy

LS.2.P042
The effect of exogenous oxytocin on streptozotocin (STZ) -induced diabetic adult rat testes

P. Köroğlu[1], G. Erkanlı Şentürk[2], D. Yücel[2], S. Arbak[2]

[1]Istanbul University, Faculty of Science, Department of Biology, Istanbul, Turkey
[2]Acibadem University, Medicine Faculty,Department of Histology and Embryology, Istanbul, Turkey

pnnar88@hotmail.com
Keywords: Oxytocin, STZ, Testes.

Oxytocin (OXY) is known as an antioxidant in several organs. The aim of this study is to investigate the therapeutic and protective effects of oxytocin treatment on streptozotocin (STZ) induced diabetes in testicular tissue (1, 2).

Wistar Albino rats were divided into four groups: 1) Control group (n:6): 0.3 ml saline solution was injected intraperitoneally (i.p.), 2) STZ group (n:6): a daily single dose of STZ (65 mg/kg) was injected i.p. for 4 consecutive weeks, 3) Pre-Oxytocin group (n:6): 5 µg/kg of oxytocin was injected i.p. for 5 days before administration of a daily single dose of STZ injection for 4 consectutive weeks, 4) Post-Oxytocin group (n:6): a daily single dose of 5 µg/kg oxytocin was injected i.p. for 5 days following STZ injection for 4 weeks. The rats whose blood glucose levels were more than 200 mg/dL were included to the experiment. Following sacrification at the end of the 4th week, testes tissue samples were taken to be processed for light and transmission electron microscopy.

Testicular tissues were stained with Haematoxylin and Eosin (H&E) and Periodic acid-Schiff (PAS) reaction and evaluated under light microscope to determine the degree of histopathological damage. Light microscopy, as well as transmission electron microscopy revealed that oxytocin treatment decreased the testicular tissue damage in pre- and post-oxytıocin groups, as being significantly increased in STZ group.

In conclusion oxytocin is suggested as an potential agent to protect STZ- induced diabetic rat testes.

1. G. Ricci, A. Catizone, R. Esposito, F.A. Pisanti, M. T. Vietri, M Galdieri, Andrologia 41, (2009), p.361.
2. M. Mohasseb, S. Ebied, M. Yehia, N.T. Hussein, J. Physiol Biochem. 67 (2), (2011), p.185.

Tissues, Pathology, and Diagnostic Microscopy

LS.2.P043
Prevention of UVB radiation-induced skin damage: “in vitro” studies.

M. Battistelli[1], S. Salucci[1], V. Baldassarri[1], D. Curzi[1], E. Falcieri[1,2,]

[1]Urbino University, DiSTeVA, Urbino, Italy
2Rizzoli Orthopaedic Institute, IGM,CNR, Urbino, Italy

michela.battistelli@uniurb.it
Keywords: Keratinocyte, UV-B, Hydroxytyrosol, Melatonin, Apoptosis

The ultraviolet component of sun light consists of UVA, UVB and UVC rays. They differentially penetrate the skin barrier, thus prevalently affecting epidermal (UVB) or dermal (UVA) cells and causing various pathologies.

UVB represent an environmental hazard because of their role in skin aging, cancer and infection exacerbation.

UVA and UVB rays stimulate indeed the production of reactive oxygen species (ROS) in epidermal cells, resulting in skin lesions, accelerating aging and eliciting malignancies.

At least 50% of UVB-induced damage is attributable to the formation of reactive ROS [1]. Although ROS also appear in normal physiologic processes, including aerobic metabolism, they may cause cellular damage if antioxidant defense mechanisms are down-regulated [2]. Skin cells are also equipped with an elaborate system of antioxidant substances and enzymes, which maintains the balance between oxidative stress and anti-oxidant defense and keeps the cells away from oxidative stress damage. Thus, exogenous supplementation of antioxidants may be an effective strategy to reduce or prevent skin damage.

In the last years, we demonstrated the antioxidant effects of melatonin (Mel) in hemopoietic human cells [3]. On the other hand, data concerning its antioxidant effect on keratinocytes have been also reported [4]. Recently, our research group demonstrated an anti-oxidant and anti-apoptotic action of hydroxytyrosol (HyT), and its derivatives in muscle and hemopoietic cells exposed to H2O2. These data suggest interesting properties of HyT, and its potential application in biology and clinic [5].

Therefore, in this project we propose to evaluate the antioxidant and anti-apoptotic effect of Mel and HyT in HaCaT human keratinocytes exposed to UVB rays, well known cell death inducers.

Keratinocytes in the non-irradiated condition are morphologically similar in Mel and HyT-treated and untreated group. Cells appear flattened and closely confluent, with fusiform or, sometimes, polygonal shape (Fig. 1 A, B, C). In HyT-treated ones a significant confluence increase can be revealed (Fig. 1 D, E, F), cells appear polygonal, slightly swollen and closely in contact each other. TUNEL reaction appears negative in both conditions (Fig 1 C,F).

UV-B radiations induce a significant decrease in cell confluence with the occurrence of cell detachment and the appearance of consequent empty spaces (Fig 1I). Detached cells appear rounding with surface blebbing (Fig. G, H, I) .

TUNEL reaction, observed at confocal microscopy, evidences several nuclei with DNA fragmentation in UV-B treated keratinocytes. In addition, cell viability evaluated by means of propidio iodide (PI) supravital staining [6] evidences a diffuse positivity.

Pre-treatment with HyT or Mel reduce cell death. Cells maintain unchanged the shape, appear fusiform or polygonal and monolayer confluence can be again revealed.

We can conclude that HyT and Mel evidentiate an intringuing capability to prevent cell death in keratinocytes too. They could so represent a potential tool in skin protection from UVB radiations.

1. Wölfle et al., Free Radic. Biol. Med., 2011
2. Sander et al., Int. J. Dermatol., 2004
3. Luchetti et al., Toxicol. In vitro, 2007
4. Fischer et al., J. Pineal Res., 2008
5. Burattini et al., Food Chem Toxicol., 2013
6. Zamai et al., Cytometry, 2001

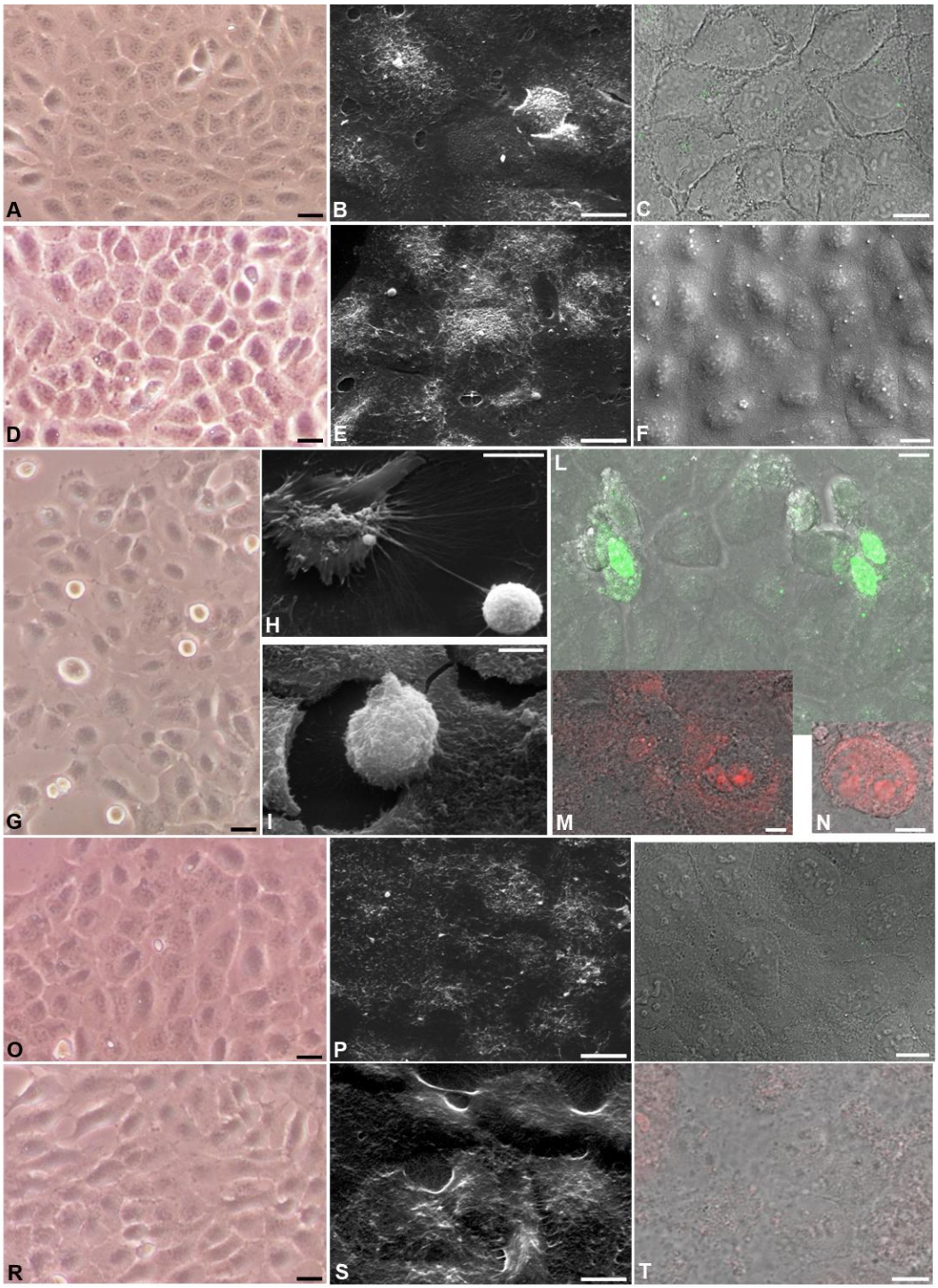

Figure 1. Inverted Microscope: A,D,H,N,Q; Scanning Electron Microscopy: B,E,H,I,P,S; TUNEL: C,F,L,T, PI staining: M,N,Q. Keratinocytes in different conditions: A,B,C control cells; D,E,F, HyT treated cells; G,H,I,L,M,N UVB-treated cells; O,P,Q; HyT pre-treated cells; R,S,T Mel pre-treated cells.
A,D Bar = 25µm; C,F,G,H,L,Q,P,S, , Bar = 12µm; B,E,O,R Bar = 9µm; I,M,N Bar = 6µm.

Tissues, Pathology, and Diagnostic Microscopy

LS.2.P044
Z-disc formation along myogenic differentiation: the role of α-actinin

S. Burattini[1], V. Baldassarri[1], S. Salucci[1], D. Curzi[1], E. Falcieri[1,2]

[1]Urbino University "Carlo Bo", DiSTeVA, Urbino, Italy
[2]Rizzoli Orthopaedic Institute, IGM,CNR, Urbino, Italy

sabrina.burattini@uniurb.it
Keywords: α-actinin, Z-disc, myogenic differentiation

α-Actinin belongs to the spectrin superfamily of proteins and exists in, at least, six different isoforms [1]. The cytoskeletal isoforms (α-actinin-1 and -4) can be observed along microfilament bundles and in adherent junctions, where they are involved in binding actin to the plasma membrane. The muscle-specific isoforms (α-actinin-2 and -3) are necessary for actin filament attachment to the Z-discs in skeletal muscle fibers and to the analogous dense bodies in smooth muscle cells [2]. In the Z-discs, actin filaments from adjacent sarcomeres overlap and are held together to form an highly stable structure, composed by a variable number of α-actinin cross-links [3]. Furthermore sarcomeric α-actinin links several other proteins, providing membrane integrity during muscle contractions, and it is also able to modulate membrane receptors and channels and to interact with metabolic proteins [4]; not least, it serves as a scaffold to connect the sarcomere to several signaling pathways [5]. Thus, α-actinin is a multitasking protein that contributes to proper muscle physiology. Moreover, it has been shown to be dysregulated in several myopathies involving aberrant accumulation of myofilaments, called Z-discopathies [6].

The aim of this work was to investigate *in vitro* the Z-disc formation, which is closely related to α-actinin behavior. For this purpose, murine C2C12 skeletal muscle cells were analyzed at three time points of differentiation: at undifferentiated stage (T_0), after 4 days of differentiation (T_1) and after 7 days of differentiation (T_2) [7]. Finally, murine skeletal muscle tissue was used for the comparison between the last stage of cell differentiation and the adult skeletal muscle. Confocal laser scanner microscopy (CLSM) and transmission electron microscopy (TEM), with the immunogold technique, were utilized to carry out the immunolocalization of the protein [8].

Our results reveal that in T_0 myoblasts α-actinin is uniformly distributed throughout the cytoplasm: spot-like α-actinin Z-bodies can be observed, but Z-discs are not yet visible. T_1 myoblasts become spindle-shaped and fuse together to form early myotubes with few nuclei. They show filamentous α-actinin molecules, probably as a result of the lateral fusion of Z-bodies, and the labeling is evident especially beneath the plasma membrane and at the cell ends. T_2 myotubes appear intensely labeled: α-actinin is arranged into longitudinal arrays across the cytoplasm and almost all myotubes show evident Z-discs (Figure 1). Immunogold labeling, observed at TEM, confirmed α-actinin localization in all differentiation steps. The initial diffuse cytoplasmic labeling of α-actinin is followed by its progressive association with actin bundles, and gradual appearance of Z-discs (Figure 2).

So, when differentiation is induced, α-actinin links at first membrane-associated proteins, such as vinculin and integrins [9], then it aligns longitudinally throughout the cytoplasm and finally binds actin, giving rise to the Z-discs.

1. B. Sjöblom *et al*., Cell Mol Life Sci 65 (2008), p. 2688-2701.
2. N. Ichinoseki-Sekine *et al*., Biochem Biophys Res Commun 419 (2012), p. 401-404.
3. D.S. Courson and R.S. Rock, J Biol Chem 285 (2010), p. 26350-26357.
4. M. Lek, K.G. Quinlan and K.N. North, Bioessays 32 (2009), p. 17-25.
5. C.A. Otey and O. Carpen, Cell Motil Cytoskeleton 58 (2004), p. 104-111.
6. R. Knöll, B. Buyandelger and M. Lab, J Biomed Biotechnol (2011), ID 569628.
7. L. Casadei *et al*., Eur J Histochem 53 (2009), p. 261-268.
8. F. Luchetti *et al*., Apoptosis 2 (2002), 143-152.
9. J.M. Lewis and M.A. Schwartz, Mol Biol Cell 6 (1995), p.151-160.

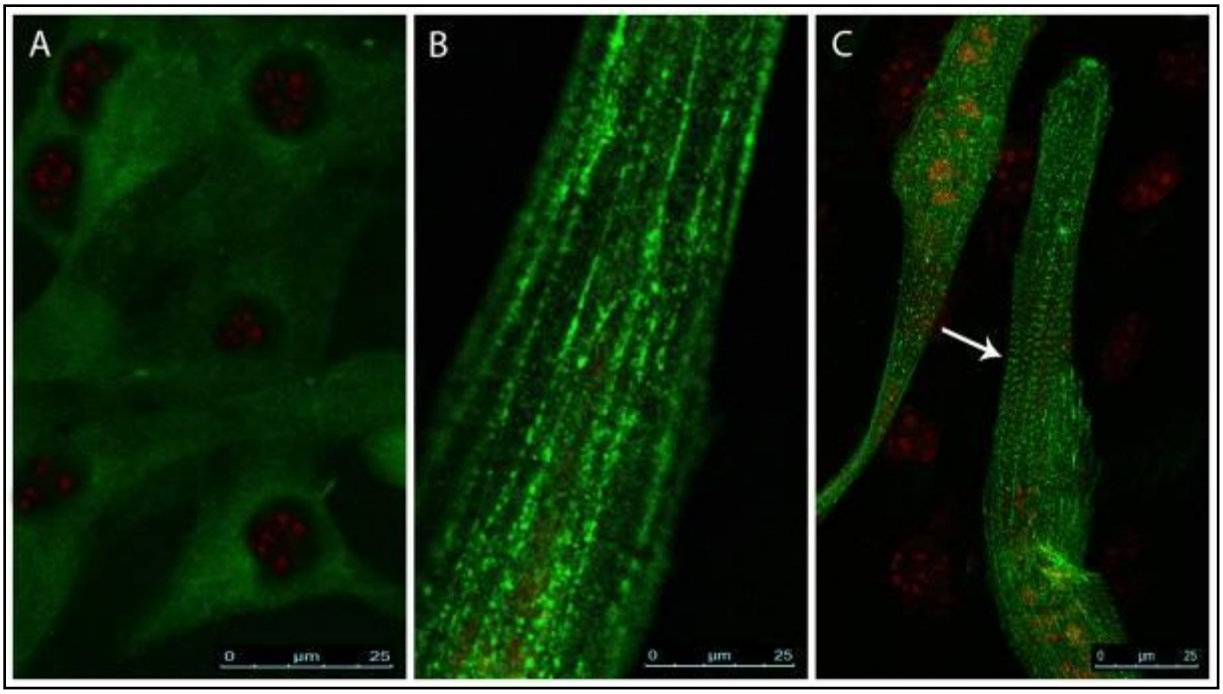

Figure 1. C2C12 cells, at three time points of differentiation, have been labeled for α-actinin; nuclei have been evidenced using propidium iodide. Myoblasts at T_0 (A); cells at T_1 (B); myotubes at T_2: Z-discs are clearly visible (arrow) (C). Bar scale = 25 µM.

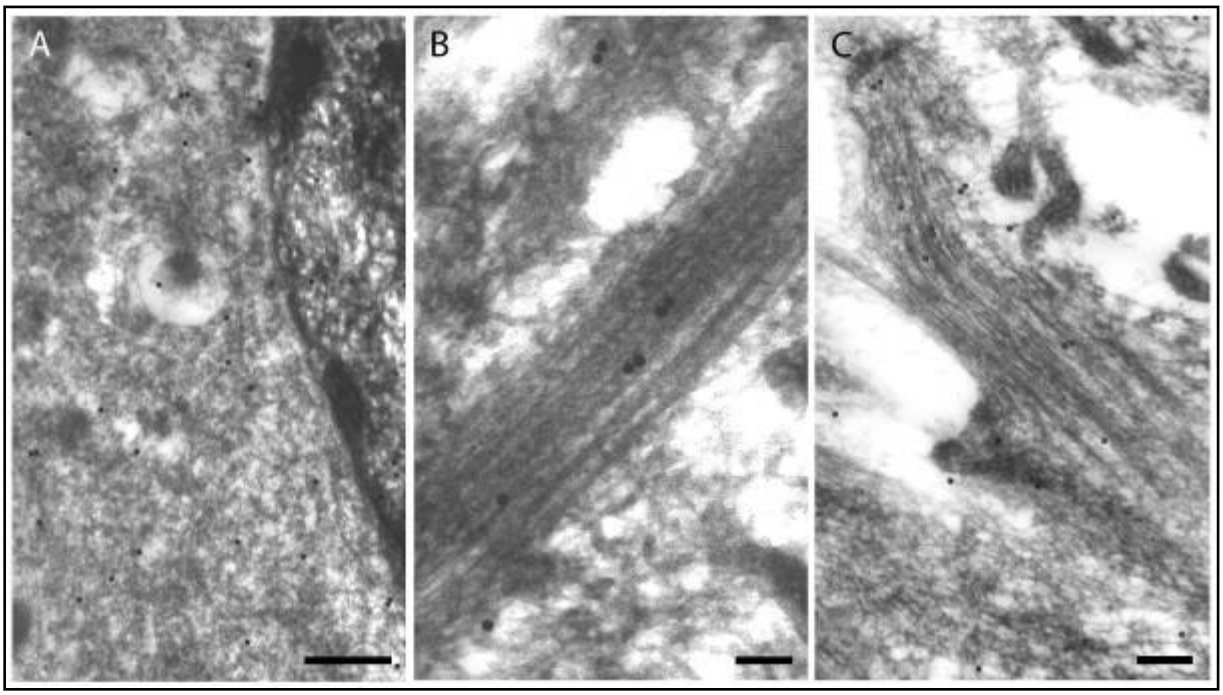

Figure 2. Immonogold labelling of C2C12 cells, at three time points of differentiation, observed at TEM. Myoblasts at T_0 (A); cells at T_1 (B); myotubes at T_2 (C). Bar scale: A = 0.5 µM; B = 0.1 µM; C = 0.25 µM.

Tissues, Pathology, and Diagnostic Microscopy

LS.2.P045
Chemical-induced hemopoietic cell death: the protective action of melatonin

S. Salucci[1], S. Burattini[1], V. Baldassarri[1], M. Battistelli[1], E. Falcieri[1,2]

[1]University of Urbino , Department of Earth, Life and Environmental Sciences, Urbino University "Carlo Bo", Urbino, Italy, Italy
[2]IGM-CNR, Rizzoli Orthopaedic Institute, Bologna, Italy, Italy

sara.salucci@uniurb.it
Keywords: melatonin, chemical triggers, cell death

Melatonin is a methoxyindole synthesized by the pineal gland. The hormone is secreted during the night and appears to play multiple roles in the human organism.

Melatonin is a powerful anti-oxidant in tissues [1] as well as within cells [2], with a fundamental role in ameliorating homeostasis in a number of specific pathologies. It acts both as a direct radical scavenger and by stimulating production/activity of intracellular anti-oxidant enzymes, i.e. superoxide dismutase and glutathione peroxidase as well as up-regulating their expression. Its function consists in the reduction of oxidative stress, i.e. molecular damage produced by reactive oxygen and nitrogen species [3].

A survey of literature shows that in leukocytes melatonin mainly exerts an anti-apoptotic role, as also demonstrated in an our previous work exposing hemopoietic cells to UVB rays [4].

In this work, some chemical triggers (hydrogen peroxide, etoposide and staurosporine), with different mechanism of action and able to increase radical oxygen species levels [5], have been chosen to induce cell death in U937 hemopoietic cell line. Cells were pre-treated with different melatonin concentrations (1 or 0.1 mM) and then exposed to chemical agents.

Potential melatonin anti-oxidant and anti-apoptotic effects were evaluated through morphological and statistical analyses, the latter by means of Tali Image-Based Cytometer, able to monitor cell viability as well as apoptosis presence. Samples, observed at scanning (SEM) and transmission electron microscopy (TEM), revealed a preserved morphology in control (Figure 1A-B) and melatonin alone (Figure 1C-D) conditions. After all chemical treatments typical apoptotic features appeared. Cells showed membrane blebs, nuclear cup-shaped masses, micronuclei, altered and swollen mitochondria, cytoplasmic vacuolisation and secondary necrosis (Figure 1E, F, I, L, O, P). A cell death decrease was observed in all experimental conditions pre-treated with melatonin (Figure 1G, H, M, N, Q).

In addition, in cells pre-incubated with melatonin (in both concentrations) and then exposed to chemicals, autophagic vacuoles appeared at TEM (Figure 1R).

Melatonin anti-apoptotic activity was also demonstrated by quantitative analyses. Supravital propidium iodide [6], used to evaluate cell viability, evidenced that melatonin administration significantly prevents cell death (Table 1). In particular, melatonin 100 µM showed an elevated protection against apoptosis induced by hydrogen peroxide (H_2O_2), staurosporine and etoposide. Melatonin 1mM has moderate anti-oxidant and anti-apoptotic effects *vs* chemical treatments.

In conclusion, we found that in U937 cell line melatonin can be considered a powerful molecule in preventing chemical apoptotic cell death.

1. G. Baydas, S.T. Koz, M. Tuzcu, E. Etem and V.S. Nedzvetsky. J Pineal Res. 43 (2007), p.225.
2. F. Luchetti,B. Canonico, F. Mannello, C. Masoni, A. D'Emilio, M. Battistelli, S. Papa and E. Falcieri. Toxicol In Vitro. 21 (2007), p. 293..
3. R.J. Reiter, D.X. Tan, L.C. Manchester and W. Qi. Cell Biochem Physiol 34 (2001), p, 237.
4. F. Luchetti, B. Canonico, R. Curci, M. Battistelli, F. Mannello, S. Papa, G. Tarzia and E. Falcieri. J Pineal Res. 40 (2006), p.158.
5. S. Salucci, M. Battistelli, S. Burattini, C. Squillace, B. Canonico, P. Gobbi, S. Papa and E. Falcieri. Micron. 41(2010), p.966.
6. L. Zamai, B. Canonico, F.Luchetti, P. Ferri, E. Melloni, L. Guidotti, A. Cappellini, G.Cutroneo, M.Vitale, S. Papa. Cytometry. 44 (2001), p.57.

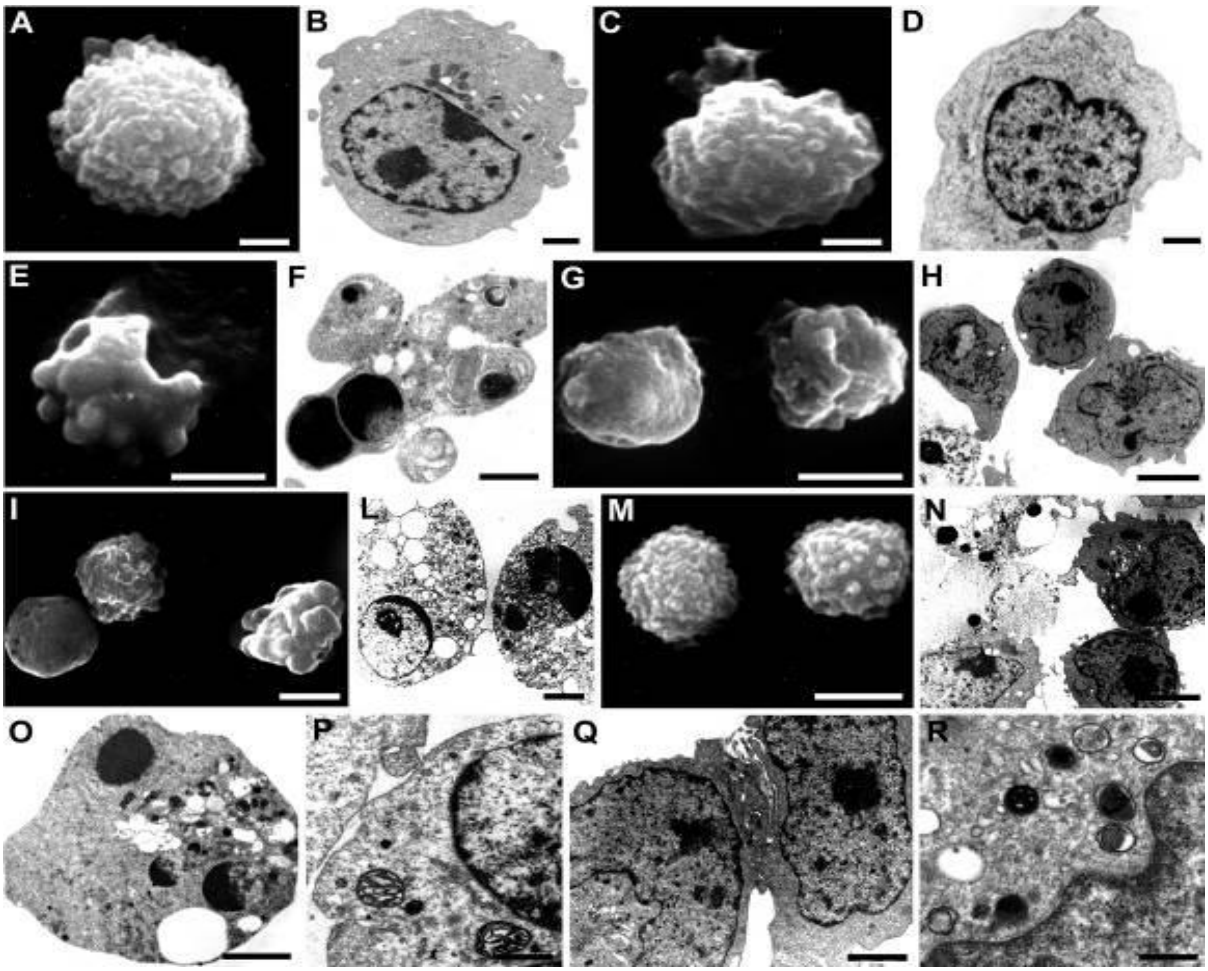

Figure 1. U937 cells at SEM (A, C, E, G, I, M) and TEM (B, D, F, H, L, N,O,P,Q,R). A preserved morphology is evident in control (A,B) and melatonin (0.1mM) alone conditions (C,D). Cells treated with H_2O_2 (E,F) etoposide (I,L) and staurosporine (O,P) reveal typical apoptotic patterns. Melatonin added to H_2O_2 (G,H) etoposide (M,N) and staurosporine (Q) treated cells prevents cell death. In R, autophagic vacuoles appeared in melatonin added to etoposide. Bars: 2µm in A-D, O,Q; 5 µm in E-N; 1 µm in P; 0.5 µm in R.

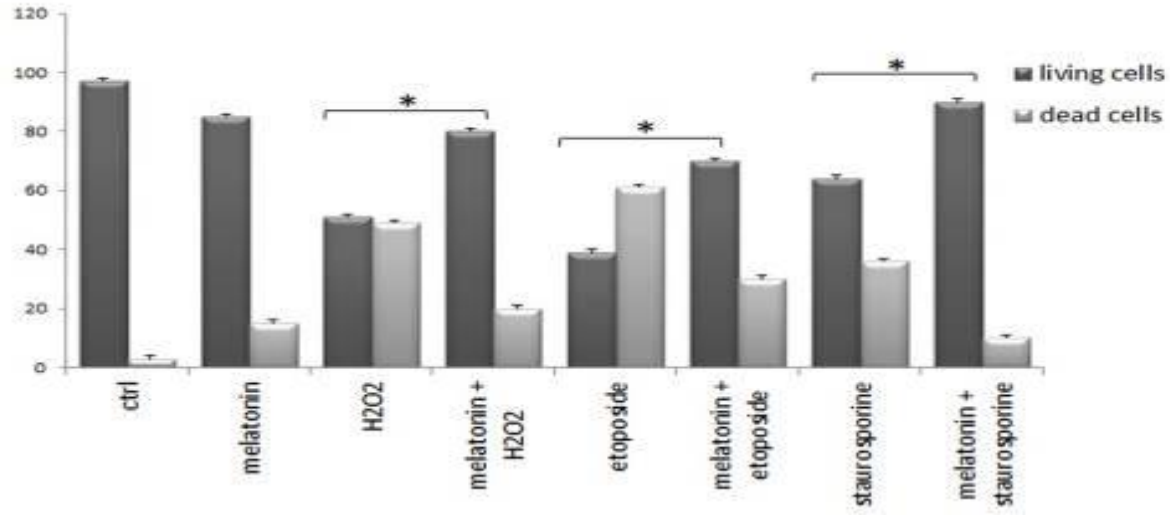

Table 1. Cell viability percentage. Data have been are verified by t-test and appeared statistically significant ($p < 0.05$).

Tissues, Pathology, and Diagnostic Microscopy

LS.2.P046
Melatonin role in the prevention of myoblasts apoptosis induced by chemical triggers

V. Baldassarri[1], S. Salucci[1], S. Burattini[1], M. Guescini[2], E. Falcieri[1,3]

[1]Urbino University, DiSTeVA, urbino, Italy
[2]Urbino University , Biomolecular Sciences Department, Urbino, Italy
[3]CNR Bologna, IGM,Rizzoli Orthopaedic Institute, Bologna, Italy

elisabetta.falcieri@uniurb.it
Keywords: melatonin, apoptosis, muscle

Melatonin, or N-acetyl-5-methoxytryptamine, is a hormone principally secreted by the pineal gland that regulates the sleep-wake cycle maintaining the circadian rhythm. Due to its ability to induce sleep, melatonin is used in pharmacological doses to resynchronize the internal biological clock [1]. Furthermore, melatonin regulates gonadal function, stimulates the immune response, has anti-inflammatory actions and exhibits strong antioxidant effects [2]. In fact, it is able to act directly as a radical scavenger and it also has an indirect activity, stimulating the production of antioxidant enzymes (i.e. glutathione peroxidase and glutathione reductase) and increasing electron transport chain efficiency at mitochondrial cristae level. Due to this property, it is present in moderate amounts in the cell nucleus, where it protects DNA from oxidative damage, potentially acting as a key factor in cancer prevention [3].

Our experiments relied on the antioxidant properties of melatonin and the aim of our work was to test melatonin effects on the cytotoxicity induced by various chemical triggers, in murine C2C12 skeletal muscle cells. Muscle apoptosis is attracting growing interest, due to its demonstrated involvement in several pathological conditions, such as sarcopenia and disuse muscle atrophy [4], myotonic dystrophy, Duchenne muscular dystrophy [5], collagen myopathies [6] and others. It has also been demonstrated that oxidative stress is involved, at least in part, in most of these conditions involving muscle apoptosis [7]. In literature we can find numerous evidences which indicate that melatonin treatment is able to normalize or prevent oxidative stress, leading to an improvement of certain pathological conditions [8]. Furthermore, in previous works carried out by our research group, it was shown that melatonin prevents apoptosis induced by UVB [9] and H_2O_2 [10], in human U937 hematopoietic cells.

For our purpose, C2C12 myoblasts were pre-treated with 100 µM melatonin for 24 hours and then treated for further 24 hours with various chemical triggers: 0.5 mM H_2O_2, 30 µM cisplatin, 0.25 µM staurosporine, 25 µM etoposide. These chemicals were chosen on the basis of their know pro-apoptotic effect and of their different mechanisms of action. Cellular growth and viability were monitored using inverted microscopy (IM), while the cellular response to treatments was investigated by means of transmission electron microscopy (TEM), TUNEL technique and supravital propidium iodide staining [11], analyzed by means of confocal laser scanning microscopy (CLSM), and DNA gel electrophoresis.

All treatments resulted in the alteration of cellular morphology with typical apoptotic features, such as detachment from the substrate, membrane blebbing, chromatin condensation and micronuclei formation, production of apoptotic bodies. Autophagic features were also observed. Our results indicate that melatonin pre-treatment prevents apoptosis induced by H_2O_2 and, to a lesser extent, by cisplatin and etoposide (Figure 1); conversely, no protective effect was observed in samples treated with staurosporine, and this may be due to its mechanism of action (Figure 2). Agarose gel electrophoresis revealed that DNA oligonucleosomal cleavage is absent in all experimental conditions. Intriguingly, melatonin increases the autophagic rate, probably as a further protective mechanism.

1. I. Haimov *et al*., BMJ 309 (1994), p. 167.
2. R.J. Reiter *et al*., J Biomed Sci 7 (2000), p. 444–458.
3. G. Di Bella *et al*., Int J Mol Sci 14 (2013), p. 2410-2430.
4. Vde O. Teixeira, L.I. Filippin and R.M. Xavier, Rev Bras Reumatol 52 (2012), p. 252-259.
5. E. Abdel-Salam *et al*., Acta Myol 28 (2009), p. 94-100.
6. L. Merlini *et al*., Proc Natl Acad Sci USA 105 (2008), p. 5225-5229.
7. M. Braga *et al*., Apoptosis 13 (2008), p. 822-832.
8. Y. Hibaoui, E. Roulet, U.T. Ruegg, J Pineal Res 47 (2009), p. 238-252.
9. F. Luchetti *et al*., J Pineal Res 40 (2006), p. 158-167.
10. S. Salucci *et al*., Microscopie 13 (2010), p. 51-57.
11. L. Zamai *et al*., Cytometry 23 (1996), p. 303-311.

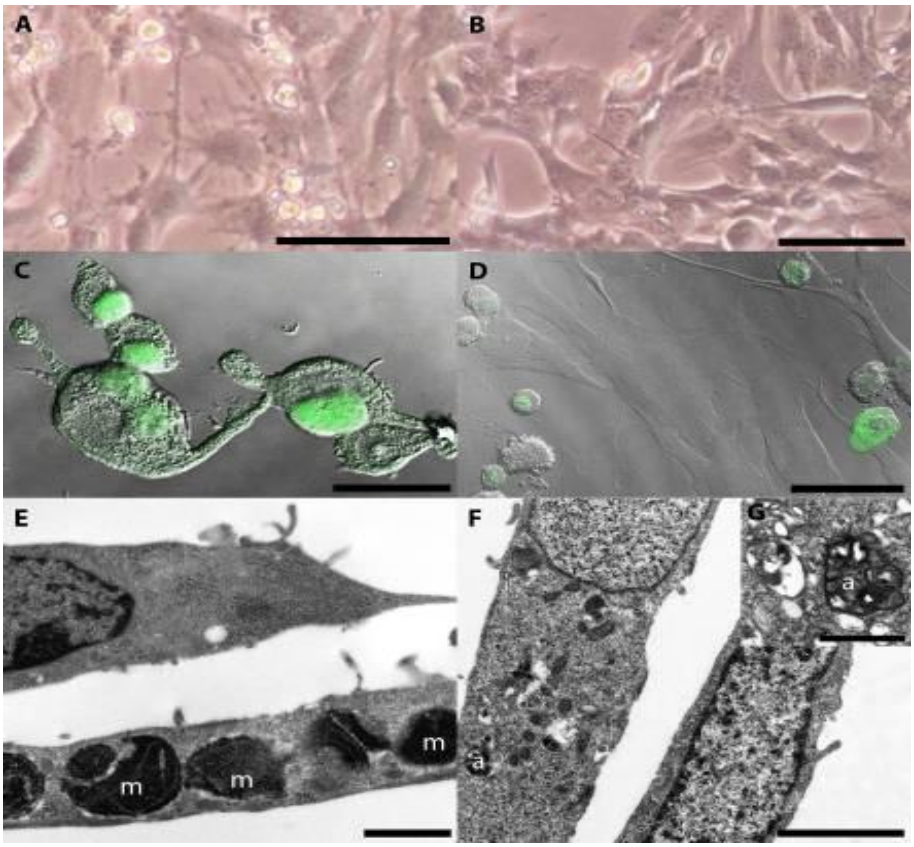

Figure 1. IM of cisplatin-treated (A) and melatonin pre-incubated cisplatin-treated (B) myoblasts; CLSM of TUNEL reaction after H_2O_2 exposure (C) and melatonin pre-treatment H_2O_2-exposure (D); TEM of etoposide-treated myoblasts (E) and melatonin pre-treated etoposide-exposed ones (F); detail of autophagic vacuoles (G). m = micronuclei, a = autophagic vacuole. Scale bar: A, B = 15 µm; C = 20 µm; D = 25 µm; E = 2 µm; F = 5 µm; G = 1 µm.

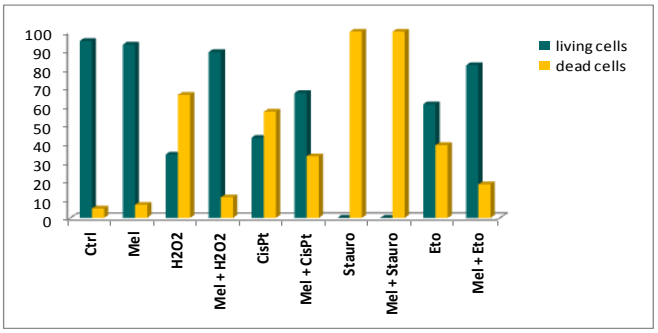

Figure 2. Histogram showing the cell viability, using the trypan blue exclusion assay, after all treatments. * = p<0,05

Tissues, Pathology, and Diagnostic Microscopy

LS.2.P047
Analysis of epidermal growth factor receptor (EGFR) expression in hepatocellular carcinoma; a comprasion of fluorescence in situ hybridization (FISH) and immunohistochemisrty (IHC)

S. Uslu[1], H. Kirimlioglu[2], U. Ince[2]

[1]Acibadem University, Vocational school of health services pathology laboratory technician program, Istanbul, Turkey
[2]Acıbadem university, pathology, ıstanbul, Turkey

musiuslu@gmail.com
Keywords: Hepatocellular carcinoma, epidermal growth factor receptor, fluorescence in situ hybridization, immunohistochemistry

Hepatocellular carcinoma (HCC) is a poor prognostical tumor. Though it is a leading cause of death, the conventional systemic therapy strategies are not effective. In recent studies the expression of EGFR in the majority of HCCs makes it a promising target of anti-EGFR therapies. In our study, we aimed to demonstrate and compare the EGFR gene aberration by fluorescence in situ hybridization (FISH) and immunohistochemical (IHC) method, to determine if it can be used practically. Several studies have demonstrated positive immunoexpression of cytokeratin (CK) 19 in HCC, and CK19-positive HCC has a high metastatic potential, which is also associated with a poor prognosis. Recent studies indicate that, the activation of the EGF–EGFR signaling pathway is associated with the development of CK19-positive HCC, and the EGF-induced increase in growth abilities of HCC, may account for the poor prognosis of the patients (1). We also aimed to demonstrate the relation between established prognostic features, like tumor differentiation, vascular invasion with the CK-19 immuohistochemical positivity. Twenty-six patients with hepatocellular carcinoma (HCC) without having any metastasis and recurrences clinically at the time of tumor resection were recruited in our study. The age, gender, chronic liver disease and the size of the tumor were extracted from clinical and pathologic in records. Five-micrometer thick sections were cut from paraffin blocks and were stained with hematoxyline and eosin (H&E) The pattern of the tumor, presence of clear cell change, steatosis, giant cell formation, tumor necrosis and tumor grade were noted. Immunohistochemistry for EGFR and CK19 was performed on three–micrometer thick serial sections by streptoavidin-biotin method utulizing Ventana Benchmark Ultra automated stainer (Arizona, USA).To the five-micrometer thick sections were used for FISH analyses by The SPEC EGFR/CEN 7 dual color probe and the SPEC EGFR/CEN 7 dual color probe kit (ZytoLight, ZytoVision GmbH, Germany). After the FISH procedure, the slides were examined on an Olympus Bx50 microscope and photographed with an Olympus Dp20 camera. One hundred non-overlapping nuclei were counted by a histologist in a double-blind manner. No amplification: 1-5 copies of the gene present per nucleus in >50% cancer cells, low amplification: 6-10 copies of the gene, or a small gene cluster, present per nucleus >50% cancer cells, amplification >10 copies, or large clusters, of the gene present per nucleus in >50% cancer cells (2,3).

In our study although there was correlation with vascular invasion ($p<0.01$) we could not find any association between gene expression of EGFR and IHC expression of CK19 positivity, however tumor size, chronic hepatitis etiology, tumor pattern presence of clear cell change, steatosis, giant cell formation, tumor necrosis and tumor grade ($p>0.05$). We have shown that the IHC expression of EGFR in HCC is not related to EGFR gene copy number. Contrary to other studies, we could not identify EGFR gene amplification in our cases by FISH. IHC expression of EGFR gene, made up 42% of our HCC cases, which coincides with the results of the study of Buckley et al. and our study, the IHC expression of EGFR supported that, the EGFR is certainly associated with the development of HCC (4). In our study none of our cases had either metastasis or recurrence which was found to be different from the previous studies (4). In contrary to the previous studies, we could neither find any statistically significant amplification by FISH method, nor any strong EGFR expression by IHC analysis, which may be attributable to the early stage of the HCC cases. However, the nuances, compared with the other studies suggested that, the EGFR may also pose a role of the HCC progression. As there is considerable disparity in the literature about the relationship of EGFR expression and prognostic features in HCC further studies of larger series are needed.

1. Yoneda N, Sato Y, Kitao A, Ikeda H, Sawada-Kitamura S, Miyakoshi M, Harada K, Sasaki M, Matsui O, Nakanuma Y. Epidermal growth factor induces cytokeratin 19 expression accompanied by increased growth abilities in human hepatocellular carcinoma. Laboratory Investigation 2011; 91, 262–272.
2. Bernardes VF, Gleber-Netto FO, Sousa SF, Rocha RM, Aguiar MCF. EGFR status in oral squamous cell carcinoma: comparing immunohistochemistry, FISH and CISH detection in a case series study. BMJ open accessible medical research 2013;3:e002077. Doi:10.1136/bmjopen-2012-002077.
3. Shia J, Klimstra DS, Li AR, Qin J, Saltz L, Teruya-Feldstein J, Akram M, Chung KY, Yao D, Paty PB, Gerald W, Chen B. Epidermal growth factor receptor expression and gene amplification in colorectal carcinoma: an immunohistochemical and chromogenic in situ hybridization study. Modern Pathology 2005:18;1350-1356.
4. Anne F. Buckley, MD PhD,1 Lawrence J. Burgart, MD,2 Vaibhav Sahai,3 and Sanjay Kakar, MD3. Epidermal Growth Factor Receptor Expression and Gene Copy Number in Conventional Hepatocellular Carcinoma. Am J Clin Pathol 2008;129:245-251.

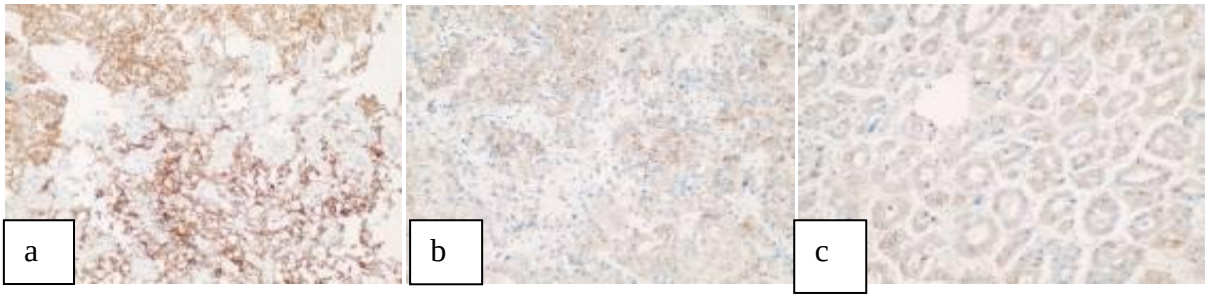

Figure 1. Immunohistochemical analysis for epidermal growth factor receptor showing strong membrane expression (a), moderate membrane expression (b), mild expression (c) in hepatocellular carcinoma (x40).

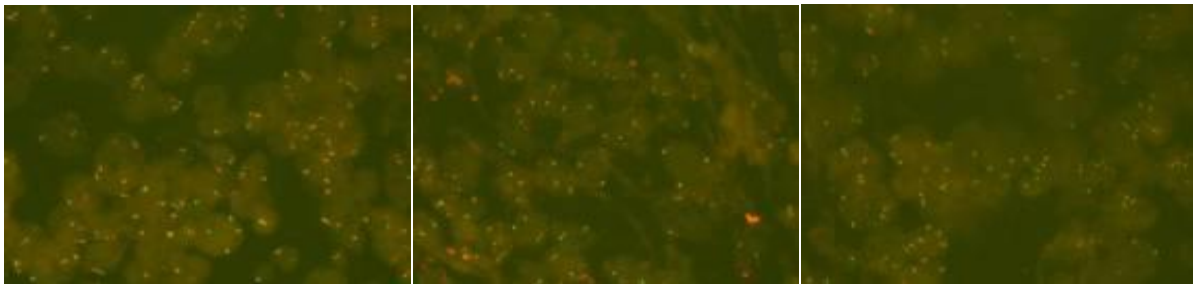

Figure 2. Fluorescence in situ hybridization using probes directed against the epidermal growth factor receptor (EGFR) gene (green) and centromere of chromosome 7 (red) (x1000).

Tissues, Pathology, and Diagnostic Microscopy

LS.2.P048
NF-κB involvement in hyperoxia-induced myocardial damage in newborn rat hearts

S. Zara[1], M. De Colli[1], M. Rapino[1,2], V. Di Valerio[3], A. Cataldi[1], V. Macchi[4], R. De Caro[4], A. Porzionato[4]

[1]University "G.d'Annunzio" Chieti-Pescara, Department of Pharmacy, chieti, Italy
[2]Institute of Molecular Genetics CNR, Unit of Chieti, Chieti, Italy
[3]Department of Medicine and Ageing Sciences, Chieti, Italy
[4]Department of Molecular Medicine, University of Padova, Padova, Italy

s.zara@unich.it
Keywords**:** hyperoxia, heart, NF-κB, Akt, Bcl2, p-IκBα

Premature newborns are frequently exposed to hyperoxia ventilation and some literature data indicate the possibility of hyperoxia-induced myocardial damage [1,2]. Since Nuclear Factor κB (NF-κB) is a crucial signaling molecule involved in physiological response to hyperoxia in different cell types as well as in various tissues [3], our attention has been focused on the role played by NF-κB pathway in response to moderate and severe hyperoxia exposure in rat neonatal heart tissue. Akt and IkBα levels, involved in NF-κB activation [4], along with the balance between apoptotic and survival pathways have also been investigated.Experimental design of the study has involved exposure of newborn rats to room air (controls), 60% O2 (moderate hyperoxia), or 95% O2 (severe hyperoxia) for the first two postnatal weeks. Morphological analysis shows a less compact tissue in rat heart exposed to moderate hyperoxia and a decreased number of nuclei in samples exposed to severe hyperoxia (Figure 1). A significant increase of NF-κB positive nuclei percentage (Figure 2A,B) and p-IκBα expression (Figure 2C) in samples exposed to 95% hyperoxia compared to control and to 60% hyperoxia is evidenced; in parallel, an increase of p-Akt/Akt ratio in both samples exposed to 95% and 60% hyperoxia is shown (Figure 3). Furthermore, a more evident cytochrome c/Apaf-1 immunocomplex (Figure 4) and a decreased Bcl2 expression in 95% hyperoxia exposed sample respect to 60% exposed one is evidenced (Figure 5A,B,C).

Our findings show the involvement of the Akt-mediated NF-κB intracellular signaling in the occurrence of oxidative stress related apoptosis upon hyperoxia exposure, as shown by cytochrome c/Apaf-1 immunocomplex formation and Bcl-2 expression downregulation. In conclusion, our study has confirmed the occurrence of signs of heart damage in newborn rats exposed to hyperoxia and has allowed the identification of NF-kB as molecular target for preventive and/or therapeutic approaches.

1. R.B. Hirschl, K.F. Heiss and R.H. Bartlett, J Pediatr Surg 27 (1992), p. 48-53.
2. B.S. Allen, M.J. Barth and M.N. Ilbawi, Semin Thorac Cardiovasc Surg 13 (2001), p.56-72.
3. L.A. Madden, R.V. Vince and G. Laden, Cell Biochem Funct 29 (2011), p 71-3.
4. A. Hoffman and D. Baltimore, Immunol Rev 210 (2006), p.171-86.

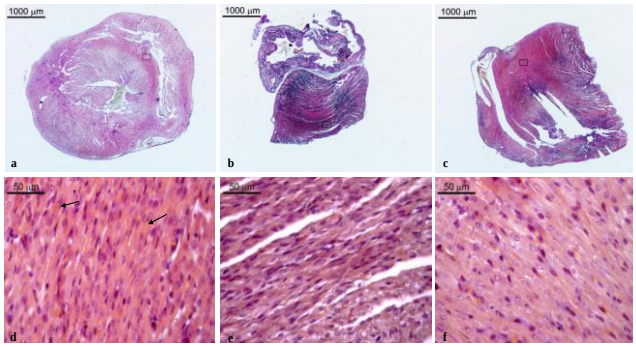

Figure 1. Trichrome Mallory staining of neonatal rat heart. Overviews and correspondent higher magnifications of hearts of rats exposed to ambient air (a, d), 60% hyperoxia (b, e) and 95%

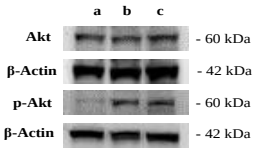

	Akt	p-Akt	p-Akt/Akt
a	0.74 ± 0.06	0.15 ± 0.01*	0.20 ± 0.01°
b	0.71 ± 0.06	0.45 ± 0.04*	0.63 ± 0.05°
c	0.73 ± 0.06	0.45 ± 0.03*	0.61 ± 0.05°

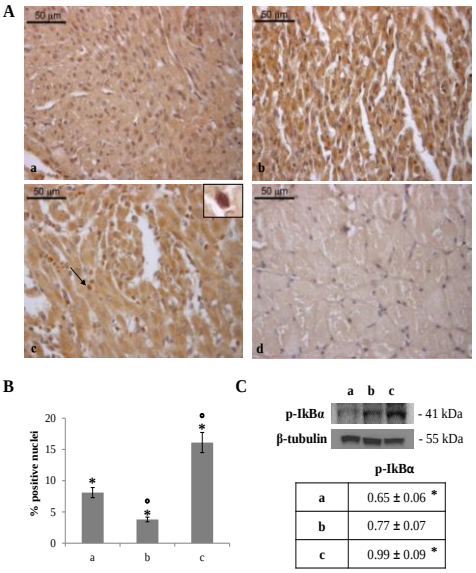

	p-IkBα
a	0.65 ± 0.06 *
b	0.77 ± 0.07
c	0.99 ± 0.09 *

Figure 2. A Immunohistochemical detection of NF-kB expression in neonatal rat heart; arrow indicates NF-kB positive nuclei; inset shows NF-kB nuclear staining; a) ambient air; b) 60% hyperoxia; c) 95% hyperoxia; d) negative control. **B** Graphic representation of NF-kB positive nuclei % (±SD);

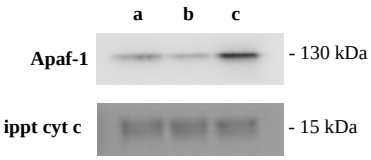

Figure 4. Co-immunoprecipitation of cytochrome c and Apaf-1 in neonatal rat heart. Immunoprecipitated (ippt) cytochrome c has been probed against

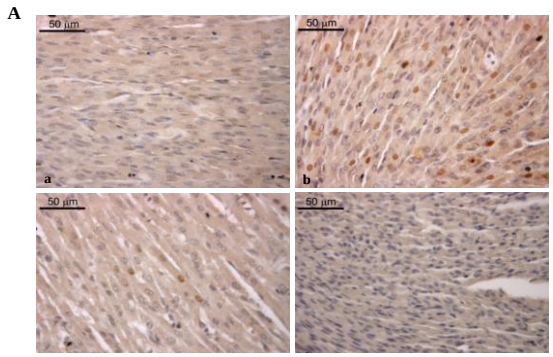

Figure 5. A Immunohistochemical detection of Bcl-2 expression in neonatal rat heart; a) ambient air; b) 60% hyperoxia; c) 95% hyperoxia; d) negative control;. **B** Graphic representation of Bcl-2 % positive area (±SD) *60% hyperoxia *vs* ambient air; °95% hyperoxia *vs* 60% hyperoxia $p<0.05$;
C Western blotting analysis of Bcl-2 expression; each membrane has been probed with β-tubulin antibody to verify loading evenness. Data are the

Tissues, Pathology, and Diagnostic Microscopy

LS.2.P049
Effects of retinoic acid on Leydig cell morphology

L. Tapul[1]

[1]İstanbul Faculty of Medicine, Histology and Embryology, İstanbul, Turkey

leylakuntsal@yahoo.com

Retinoic acid (RA) shows its effect on male reproductive system by organizing the production of testosterone and ensuring the continuity of blood-testis barrier. The aim of this study was to investigate the effects of RA on Leydig cell morphology.

In this study 3 groups were formed including 6-8 week old Spraque Dawley male rats. 40mg/kg RA and 80mg/kg RA were administered by gavage for 3 weeks to two experimental groups respectively. No drug administration was used for control group. The testis tissues were investigated with the microscope.

In control group, polygonaly shaped Leydig cells had spherical or ovale nuclei. Their cytoplasm included numerous mitochondria with tubular cristae and smooth endoplasmic reticulum (SEM) cisternae. Macrophages ,which were identified by their irregular shapes and intense bulges, had lots of secondary lysosomes, endocytotic vesicles, mitochondria with flat cristae, smooth (SER) and rough endoplasmic reticulum (GER) cisternae in their cytoplasm. Fibrocytes and endotelial cells showed normal and intact morphology “Figure 1”.

In 40mg/kg RA administered experimental group no difference was detected on morphology of Leydig cells, macrophages and fibrocytes in comparison to control group. Intercellular adhesion regions were seen clearly between Leydig cells and macrophages. Although the endothelial cells had intact plasma membranes and organelles we detected degenerative areas indicating karyolysis in nuclei of few endothelial cells “Figure 2”.

Disturbed Leydig cell integrity with ruptured plasma membrane and dissolved cytoplasm were detected in 80mg/kg RA administered experimental group. Dilated SER and GER cisternaes were seen in their cytoplasm. Although the chromatin material resembled the control group degenerations indicating karyolysis were detected in the nuclei of a few Leydig cells. Because of the disruption of plasma membranes, borders between Leydig cells were not visible. Cytoplasms of macrophages included phagocytic vacuoles with degenerated organelles and numerous phagolysosomes. Cytoplasmic extensions of macrophages were detected as targeted to damaged Leydig cells. Although fibrocytes in interstitium, pericytes around vessels and endothelial cells were intact regarding cytoplasm, some of these cells showed karyolysis “Figure 3”.

The effects of RA on cell viability are dose and time dependent. Tucci et al. [2008] reported that, physiological doses of RA did not initiate cell death but high doses stimulated apoptosis, caused lipid peroxidation and decreased cell viability of cultured Leydig cells. Distinct from apoptosis, necrotic cell death is defined with cellular swelling, ruptured plasma membrane and loss of cellular components. Destabilization of intracellular membranes like plasma membrane or ER by lipid peroxidation causes leakage of proteases and Ca to the cytosole. These processes are parts of necrotic cell death [2]. Undetermined and ruptured plasma membranes of Leydig cells in 80mg RA treated group may be an indicator of necrosis. This may be related to RA induced lipid peroxidation. Null areas as a result of dissolution of cytoplasm and dilated DER and GER cisternae showed that the triggered cell death is not apoptotic but necrotic. Necrotic cell death induced by high doses of RA were also reported. Examined ceramid levels formed by hydrolysis of cell membrane sphingomyelin showed that high RA doses increased ceramid formation which trigger necrotic cell death [1]. Recent reports showed that necrotic cells have transparent cytoplasm and undetermined, damaged plasma membrane [3]. In our study, plasma membranes of cells from high dose RA treated group were discontinuous and because of dilated cisternaes, cytoplasmic content seemed pale in comparison to control group. Our findings were compatible with this study. Necrotic cell death features such as spotted nuclear content and karyolysis were also seen in Leydig cells, endothelial and connective tissue cells. Phagocytic vacuoles and phagolysosomes seen in macrophages and macrophage extensions targeted to necrotic cell content in 80mg RA treated group may indicate a process that triggers inflammation and macrophage activity in interstitial area of this group.

All these findings that we detected suggest that RA triggers necrotic cell death in interstitial cells, especially Leydig cells, in a dose dependent manner.

1. P. Tucci, E. Cione, G. Genchi, Bioenerg Biomembr 40 2008, p.111–115.
2 N. Vanlangenakker, T.V. Berghe, D.V. Krysko, N. Festjens, P. Vandenabeele, Current Molecular Medicine 8 2008, p. 207-220
3. G. Brouckaert, M Kalai, D.V. Krysko, X. Saelens,D. Vercammen, M. Ndlovu, G. Haegeman, K. D.Herde, P. Vandenabeele, Molecular Biology of the Cell 15, 2004, p.1089–1100

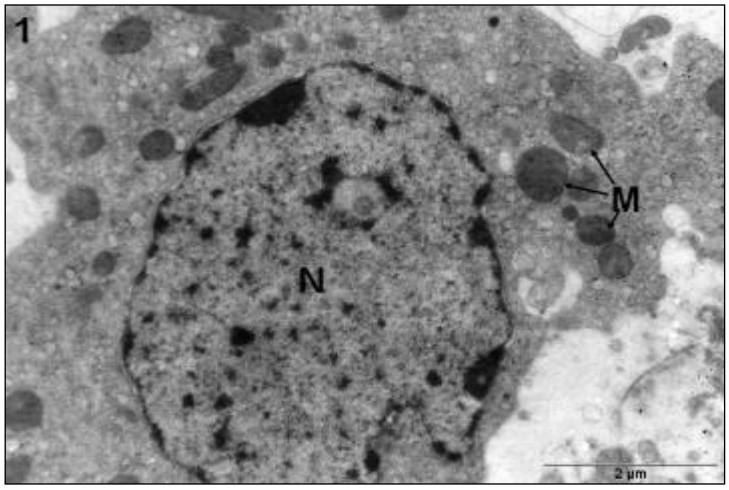

Figure 1. Kontrol group: Intact Leydig cell. M: Mitochondria, N: Nucleus.

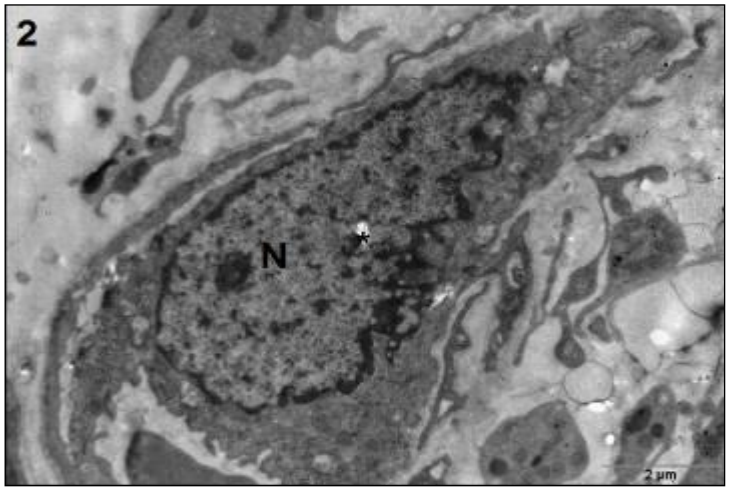

Figure 2. Experimental group (40mg RA): N: Nucleus, Asterix: Karyolysis

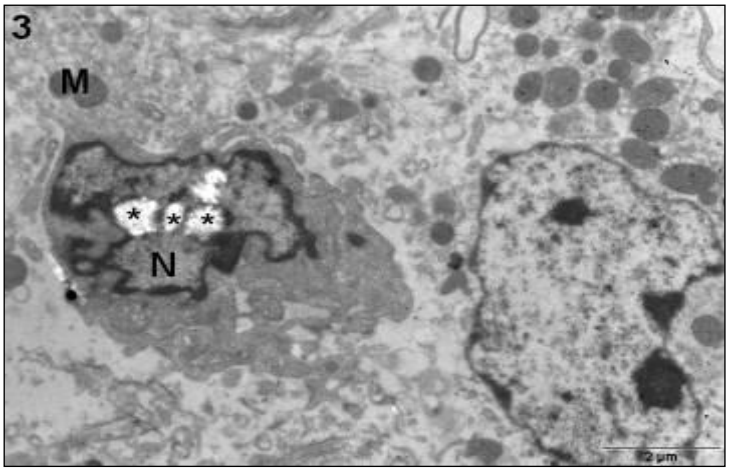

Figure 3. Experimental group (80mg RA): N: Nucleus, M: Mitochondria, Asterix: Karyolysis.

Tissues, Pathology, and Diagnostic Microscopy

LS.2.P050
Expression of nestin in foetal human testis

V. Kozina[1], T. Goluža[2], D. Ježek[1], M. Kordic[3]

[1]University of Zagreb, School of Medicine, Department of histology and Embryology, Zagreb, Croatia
[2]University of Zagreb, School of Medicine, Department of Gynaecology and Obstetrics, Zagreb, Croatia
[3]University of Mostar, Clinic for Urology, Mostar, Bosnia And Herzegovina

vkozina@mef.hr

Nestin is an intermediate filament expressed mostly in nerve cells. It seems that this filament plays certain role in the radial growth of the axon. During the early stages of development, nestin is expressed in dividing cells in the central nervous system, peripheral nervous system and in muscular and other tissues [1]. Upon differentiation, nestin becomes downregulated and is replaced by tissue-specific intermediate filament proteins. In the adult normal human testis, nestin is expressed in some vascular endothelial cells, in a subset of peritubular spindle-shaped cells and some Leydig cells. In normal Leydig cells, nestin has been distributed in the perinuclear cytoplasm. Interestingly, this filament was also found accumulated in the crystalloids of Reinke [2].

In the developing testis of rat and mouse, the reaction for nestin is weak in the gonadal ridge, whereas the cells of the mesonephric mesenchyme show a prominent reaction for this filament. Later on, nestin has been found in the Sertoli cells. In the interstitial cells, nestin is expressed together with vimentin and desmin, and is most prominent in the differentiating myoid cells. After birth, nestin gradually disappears from the testicular cells and in the rat at puberty has been found only in the endothelial cells of some blood vessels [3]. Since there is a lack of data on the presence of nestin during the human foetal development, the aim of the current study was to investigate the expression of this intermediate filament in human foetal testis.

A total of 39 human foetal testicles form 15^{th} to 36^{th} week of gestation were used in the study. The tissue samples were obtained during the routine paedopathological section of miscarried children during year 1994 (approved by the ethical committee).The samples were fixed in Bouin's fluid, dehydrated and embedded in paraffin. Paraffin blocks were cut extensively in order to provide sections for hematoxylin & eosin (H.E.) and nestin immunohistochemical staining (IHC).

H.E. stained sections demonstrated the existence of sex cords that had 40-50 μm in diameter and were composed of pre-spermatogonia and foetal Sertoli cells. The future lamina propria consisted of several gentle layers of peritubular cells. In general, sex cords and associated blood vessels in the interstitium grew progressively from 15^{th} to 36^{th} week of gestation achieving rather tortuous structures. Strong expression of nestin was noted in the cytoplasm of foetal Sertoli cells and some peritubular cells. Pre-spermatogonia seemed to be negative. No positive reaction could be noted in foetal Leydig cells. However, some fibroblast-like cells were positive, especially within the future tunica albuginea. The strong expression has been also found in interstitial blood vessels. The results obtained suggest the role of nestin in the development of human foetal Sertoli cells, some peritubular cells, blood vessels and fibroblast-like interstitial cells. Cells of blood vessels could generate future nestin-positive Leydig cells, as noted in the rat and mouse models.

1. M.F. Gjerstorff, L. Harkness, M. Kassem et al. Hum Reprod 23 (2008), pp. 2194-201.
2. M.V. Lobo, M.I. Arenas, F.J. Alonso et al. Cell Tissue Res 316 (2004), pp.369-76.
3. G.R. Hutchison, H.M. Scott, M. Walker et al. Biol Reprod 78 (2008), pp. 352-60.

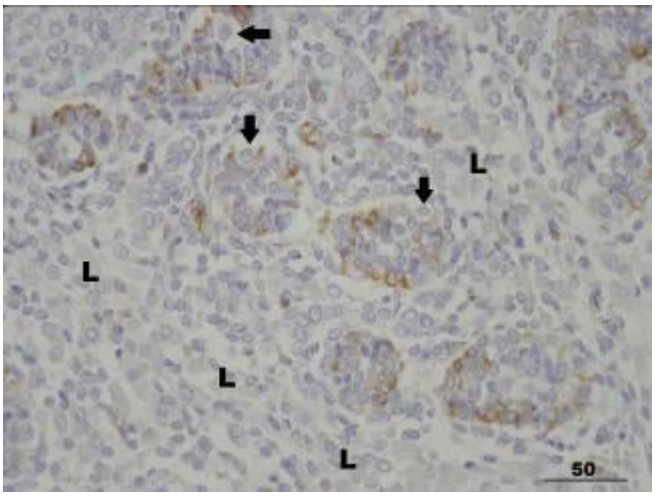

Figure 1. Foetal human testis in the 23rd week of devepment. Within sex cords, some Sertoli and peritubular cells were positive. No signal was recorded in pre-spermatogonia (➔) and Leydig cells (**L**). Nestin expression was also seen in some fibroblast-like interstitial cells. 3,3´Di-aminobenzidine (DAB), H. counterstain; x400, bar = 50 µm

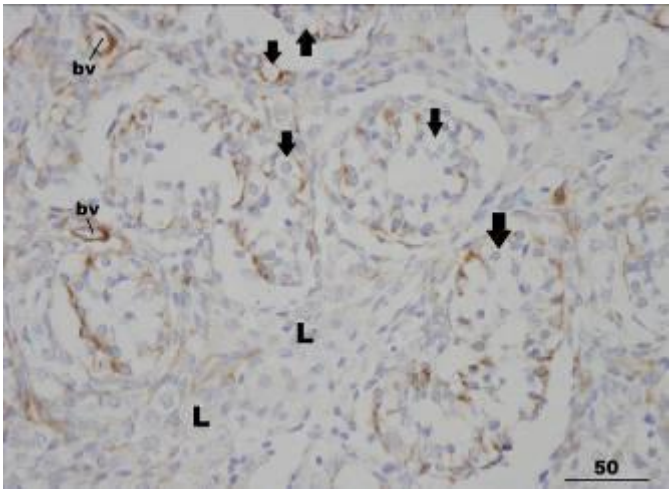

Figure 2. Foetal human testis in the 31st week of development. Apart from Sertoli cells, strong nestin expression was seen in the wall of blood vessels (bv) (pre-spermatogonia /➔/; Leydig cells /L/). 3,3´Di-aminobenzidine (DAB), H. counterstain; x400, bar = 50 µm

Tissues, Pathology, and Diagnostic Microscopy

LS.2.P051
Hyperinsulinaemia-induced structural remodeling of visceral and subcutaneous white adipose depots in rats

M. Markelic[1], K. Velickovic[1], I. Golic[1], A. Jankovic[2], M. Vucetic[2], A. Stancic[2], V. Otasevic[2], B. Korac[2] B. Buzadzic[2], A. Korac[1]

[1]University of Belgrade, Faculty of Biology, Chair of Cell and Tissue Biology, Belgrade, Serbia
[2]University of Belgrade, Institute for Biological Researches "Sinisa Stankovic", Belgrade, Serbia

milica.markelic@bio.bg.ac.rs

Insulin has a central role in the regulation of anabolic responses in fat through the stimulation of glucose and free fatty acids uptake, inhibition of lipolysis and stimulation of *de novo* fatty acids synthesis in adipocytes. In addition, insulin regulates adipose tissue growth and differentiation. Recent studies demonstrated morphological and functional differences among visceral and subcutaneous fat, including differences in the responsiveness to insulin [1]. To investigate effects of hyperinsulinaemia on different white adipose tissue (WAT) depots, male Wistar rats were treated acutely (1 day) or chronically (3 days) with low (0.4 IU/kg bm) or high (4 IU/kg bm) dose of insulin. Saline-treated animals served as controls. The portions of retroperitoneal, epididymal and subcutaneous WAT (rWAT, eWAT, sWAT, respectively) were removed and prepared for the microscopic examinations. In order to determine the ratio of WAT components (adipocytes, blood vessels, stroma) in the overall tissue volume, stereological analyses of their volume densities were performed (Vv_{AC}, Vv_{BV}, Vv_{ST}, respectively). Also, the number of adipocytes per 10^6 μm^3 of WAT was counted and their mean volume was estimated. To reveal differences among WAT depots in the insulin-induced activation of its receptor, immunofluorescence detection of phosphorylated insulin receptor (IR-p) was performed. Morphometric and stereological analyzes revealed differences among sWAT and visceral WAT depots in their response to hyperinsulinaemia since the most pronounced structural changes were demonstrated in rWAT, especially after acute insulin treatments which lead to the increase of Vv_{BV} followed by the increase of adipocyte number per the volume unit of WAT and the decrease of their mean size. The microscopic analysis confirmed this finding, demonstrating higher abundance of preadipocytes in these groups. Chronic insulin treatments return adipocyte number and size to the control level probably through the lipogenic mechanisms and the maturation of preadipocytes. The most prominent effect in rWAT of the animals which were treated chronically with insulin (especially in the group treated with the lower dose) was the increase of Vv_{BV}. In eWAT significant increase of Vv_{BV} occurs only in the group treated acutely with the lower dose of insulin and is followed by the decrease of Vv_{AC}, since no signs of hypertrophy and hyperplasia of adipocytes are visible (no changes in their number and size, no microscopic evidence of higher abundance of preadipocytes). On contrary, in sWAT no significant changes in Vv_{BV} were demonstrated in the hyperinsulinaemic groups. Acute insulin treatments lead to the increase of Vv_{AC}, but since no changes in their number and size are visible, this could be a consequence of Vv_{ST} decrease in these groups. Immunofluorescence detection of IR-p revealed its weakest immunoexpression in sWAT in comparison with the visceral depots. This is in line with the absence of the hyperinsulinaemia-induced structural alterations in this depot.

Hyperinsulinaemia-induced structural remodeling and higher responsiveness to insulin in visceral WAT depots, especially in rWAT, may contribute to the visceral obesity associated with metabolic and cardiovascular risks.

1. This study was supported by Serbian Ministry of Education, Science and Technological Development, Grant # 173055.
2. Laviola, L., et al., *Insulin signaling in human visceral and subcutaneous adipose tissue in vivo.* Diabetes, 2006. 55(4): p. 952-61.

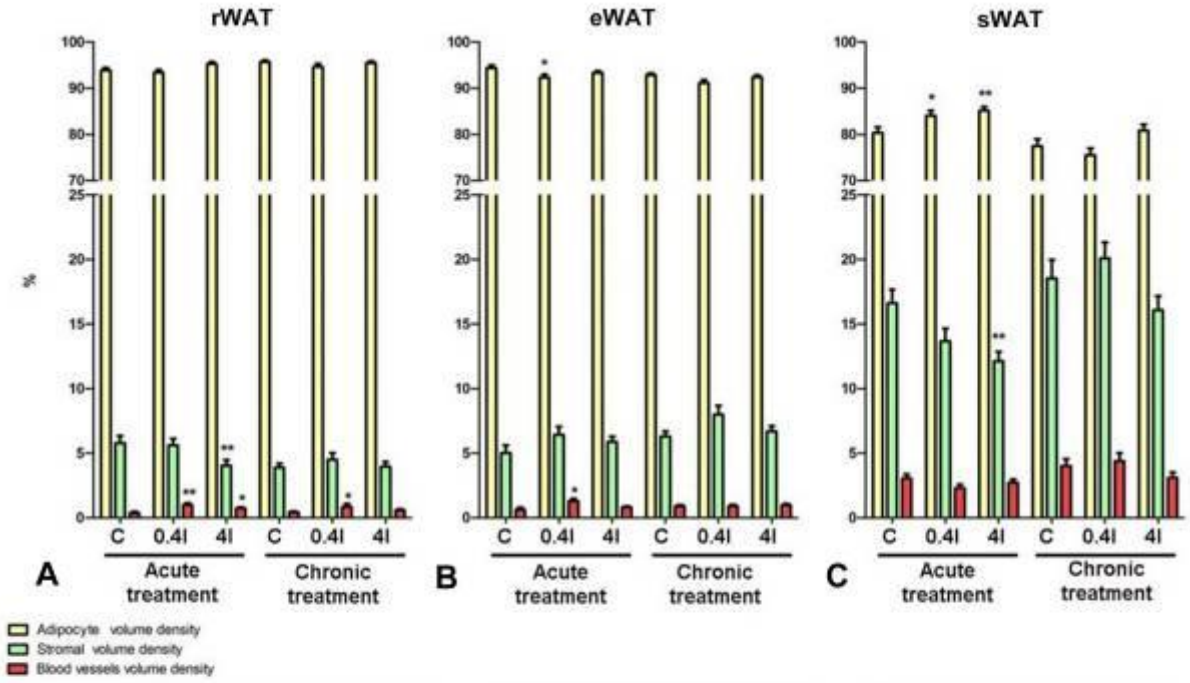

D

	rWAT						eWAT						sWAT					
	Acute treatment			Chronic treatment			Acute treatment			Chronic treatment			Acute treatment			Chronic treatment		
	C	0.4l	4l	C	0.4l	4l	C	0.4l	4l	C	0.4l	4l	C	0.4l	4l	C	0.4l	4l
Adipocytes number per 10^6 µm^3	4.08	5.98**	5.87**	4.31	4.55	4.47	9.34	10.62	8.76	6.65	7.18	8.31*	14.05	13.16	14.44	19.25	20.32	15.7
±SEM	0.19	0.28	0.37	0.14	0.29	0.40	0.44	0.58	0.35	0.21	0.45	0.53	0.98	0.53	0.75	1.40	1.64	1.13
Mean adipocyte volume (µm^3)	266165	184897***	213351**	259232	270786	282362	115563	116133	129063	165679	183806	160747	89818	84375	80572	80405	67323	84313*
±SEM	13160	8003	11997	9036	15988	15312	4578	5249	3417	6455	9870	7032	4839	3342	3970	4587	6453	6868

Figure 1. Volume density of adipocytes, stroma and blood vessels in (A) retroperitoneal (rWAT), (B) epididymal (eWAT) and (C) subcutaneous white adipose tissue depots. (D) Adipocytes number per unit volume (10^6 µm^3) of three WAT depots and mean volume of adipocytes (µm^3).

Tissues, Pathology, and Diagnostic Microscopy

LS.2.P052
Analysis of human myocardial tissue by means of atomic force microscopy

S. Mayr[1], S. Hutterer[2], R. Silye[3], G. Zauner[2], K. Schilcher[1]

[1]University of Applied Sciences, School of Applied Health and Social Sciences, Linz, Austria
[2]University of Applied Sciences, School of Engineering and Environmental Sciences, Wels, Austria
[3]Neuropathic hospital Wagner-Jauregg, Pathology, Linz, Austria

sandra.mayr@fh-linz.at
Keywords: cardiac tissue, atomic force microscopy, cardiovascular disease

According to a study by the European Heart Network and the European Society of Cardiology [1], cardiovascular disease (CVD) causes over 4 million deaths in Europe and is therefore the main cause of death in Europe. Getting new insights into the physiology and pathology of cardiomuscular tissue may be a promising way to reduce cardiovascular-based mortality, so histological tissue sections of human hearts without and with known cardiac disease were analyzed by means of atomic force microscopy (AFM) to find characteristic differences in known morphological structures.

Up to now, we have focused our studies on sarcomeres, which are the smallest morphological subunits of the striated muscle, and it seems that variations in its length distributions may serve as a potential marker for discrimination between healthy and hypertrophic hearts (Figure 1). The sarcomere lengths (SL) were determined from 20 x 20 µm images recorded using an Agilent 5400 AFM in contact mode (Figure 1B).To ensure the heart tissue samples to be in a defined state of contraction and relaxation, they were treated with solutions that mimic the physiological states of contraction and relaxation, respectively [2].

First results reveal differences in sarcomere lengths reflecting the physiological state of relaxation and contraction (Figure 2): In the untreated heart, the values typically vary between 1.27 µm (first quartile, Q1) and 2.05 µm (third quartile, Q3) with a median value (Q2) at 1.60 µm. Between rigor and relaxed state it was found out that the values slightly differ. The preliminary results also show that hearts without cardiac disease seem to have greater variety in sarcomere lengths. This difference may be interpreted as the inability to react in a physiological adequate manner on various demands.

To examine whether sarcomeres may serve as potential marker, we applied special data mining techniques using the three different classification algorithms Support Vector Machines, Random Forest classification, and Genetic Programming. Feature vectors were defined describing available length specifications (mean, median, absolute range and variance-to-mean ratio of the sarcomere length values) and combined with the physiological states. In the course of this, Random Forests performed best as classification algorithm achieving 87.87 % [3].

The study is still under work, but first results are highly encouraging to get mathematically based insights in the physiology and pathology of the heart muscle.

1. European Cardiovascular Disease Statistics, 2012 edition, © European Heart Network and European Society of Cardiology, September 2012, ISBN 978-2-9537898-1-2
2. J. Zhu, T. Sabharwal, A. Kalyanasundaram, L. Guo, G. Wang, 2013 ,J Biomech. 42(13) p. 2143 – 50
3. Hutterer et al, 2013: Data Mining Supported Analysis of Medical Atomic Force Microscopy Images, IEEE Symposium Series on Computational Intelligence (SSCI), Singapore
4. This work was supported by means of the EU programme Regionale Wettbewerbsfähigkeit OÖ 2007-2013, Regio 13 (CARDIO-AFM).

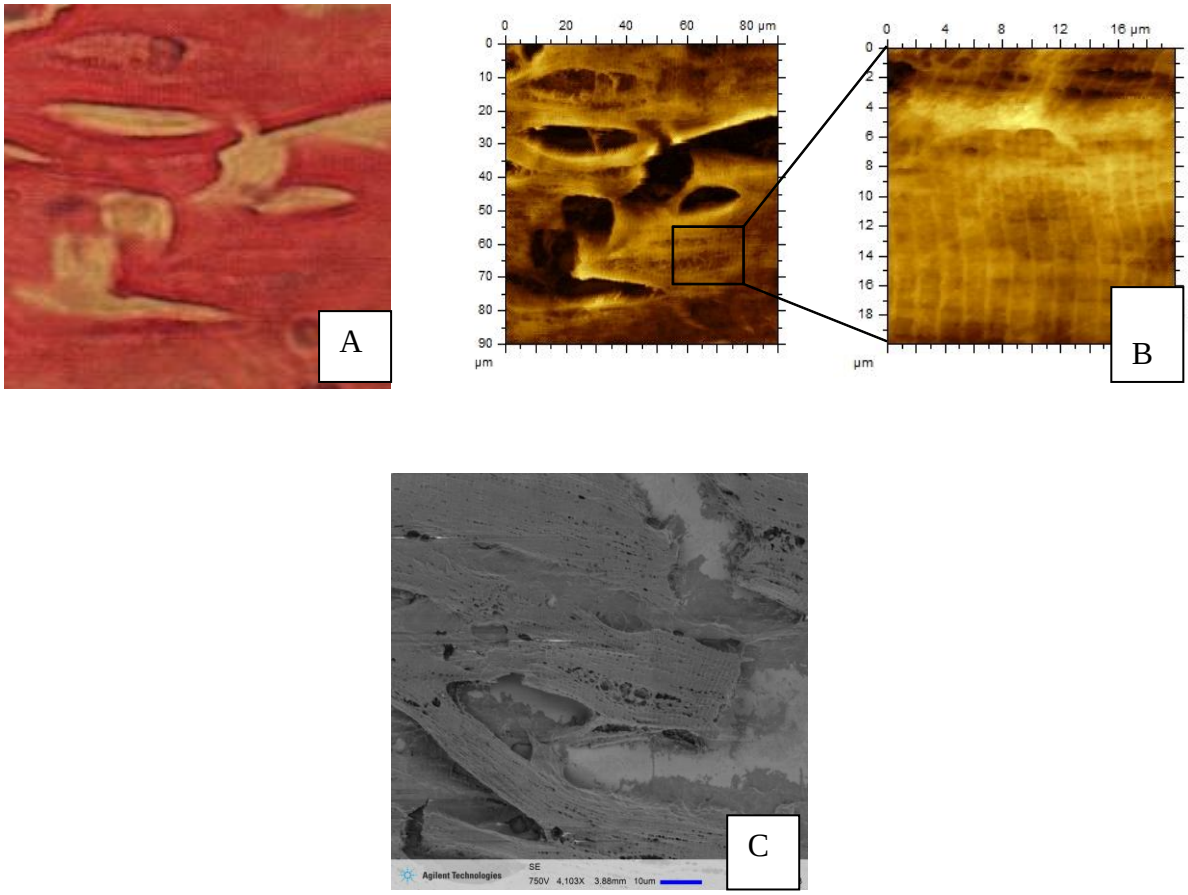

Figure 1. Characteristic images of cardiomyocytes of an untreated, healthy heart A. Light microscopic image B. corresponding AFM topographic images (survey of 100 x 100 µm and close-up of 20 x 20 µm) C. SEM image

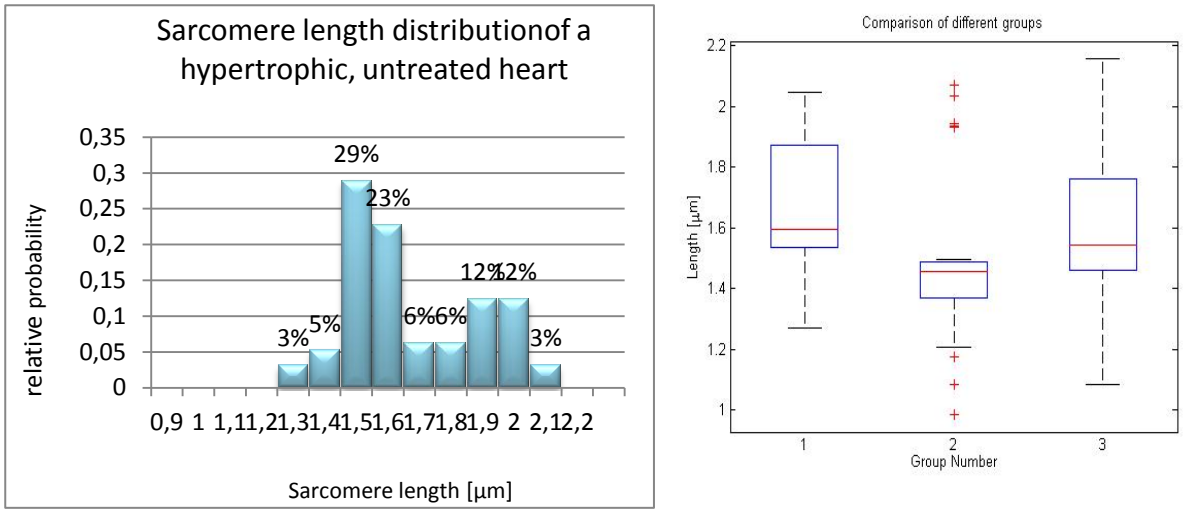

Figure 2. Evaluation of sarcomere lengths of a hypertrophic heart.
Left: Histogram; **right**: boxplot

Tissues, Pathology, and Diagnostic Microscopy

LS.2.P053
Trefoil factor family proteins 1, 2 and 3 in the developing kidney of mouse embryo

N. Bijelić[1], T. Belovari[1], M. Baus-Lončar[2,3]

[1]Faculty of Medicine Osijek, Department of Histology and Embryology, Osijek, Croatia
[2]Institute Ruđer Bošković, Department of Molecular Medicine, Zagreb, Croatia
[3]Faculty of Medicine Osijek, Department of Clinical Chemistry and Biochemistry, Osijek, Croatia

nbijelic@mefos.hr
Keywords: trefoil factor, mouse, embryonic development, kidney, immunohistochemistry

Trefoil factor family (TFF) comprises three small peptides, TFF 1, 2 and 3, which have an important role in protection of various epithelial tissues by promoting restitution through various mechanisms [1,2]. All three members of this peptide family were found in the urinary system, and in the urine. Various roles in the urinary system are proposed for them, from epithelial protection to correlation with pathological conditions [3-5]. The aim of this research was to determine if TFF proteins are present in the developing embryonic kidney.

Mouse embryos, at developmental stages E15 to E17 were isolated, fixed in 4% paraformaldehyde, embedded in paraffin blocks, cut into 6 µm sections, and processed for immunohistochemical staining. Primary polyclonal rabbit anti-TFF1, anti TFF2, and anti TFF3 antibodies were used, and PBS as a negative control. Secondary biotinylated antibody, streptavidin-HRP and DAB were used to create and visualize immunocomplexes.

All three TFF proteins were found in the embryonic kidney at all monitored stages of embryonic development. TFF1 and 3 were predominantly found in ducts morphologically and topographically corresponding to collecting ducts [Figure 1 and 2]. TFF2 was found in the glomerular podocytes, with some mild signal in the ducts as well [Figure 3].

Various effects exerted by TFF proteins in different epithelia might reflect their role in embryonic development of the urogenital system. This preliminary data show that there are some similarities between adult and embryonic kidney. Further research may elucidate the relationship between TFFs and urinary system of developing embryo.

1. G. Regalo, N.A. Wright, J.C. Machado, Cell. Mol. Life Sci. 62 (2005) p.2910-2915.
2. M. Baus-Loncar, A.S. Giraud, Cell. Mol. Life Sci. 62 (2005) p.2921-2931.
3. S. Chutipongtanate, Y. Nakagawa, S. Sritippayawan, J. Pittayamateekul, P. Parichatikanond, B.R. Westley, F.E. May, P. Malasit, V. Thongboonkerd, J Clin Invest. 115 (2005), 3613-3622.
4. M. Rinnert, M. Hinz, P. Buhtz, F. Reiher, W. Lessel, W. Hoffman, Cell. Tissue Res. 339 (2010), p.639-647.
5. Y. Yu, H. Jin, D. Holder, J.S. Ozer, S. Villarreal, P. Shughrue, S. Shi, D.J. Figueroa, H. Clouse, M. Su, N. Muniappa, S.P. Troth, W. Bailey, J. Seng, A.G. Aslamkhan, D. Thudium, F.D. Sistare, D.L. Gerhold, Nat Biotechnol. 28 (2010), p.470-477.

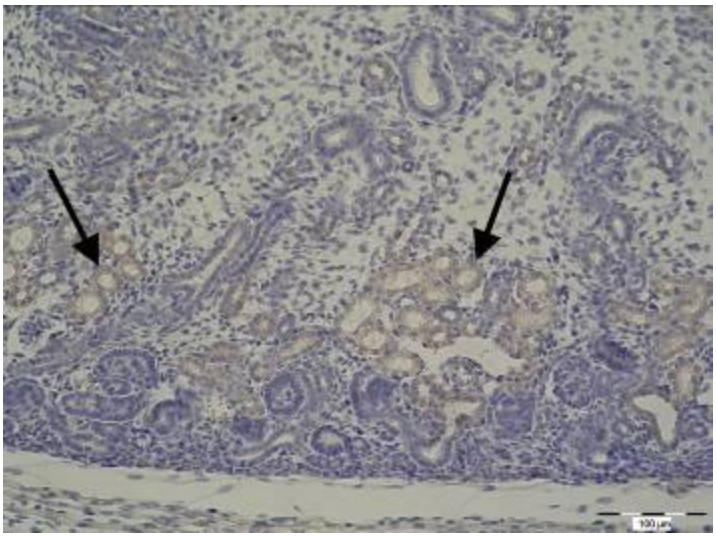

Figure 1. Presence of TFF1 in the collecting ducts, 16-day old embryo.

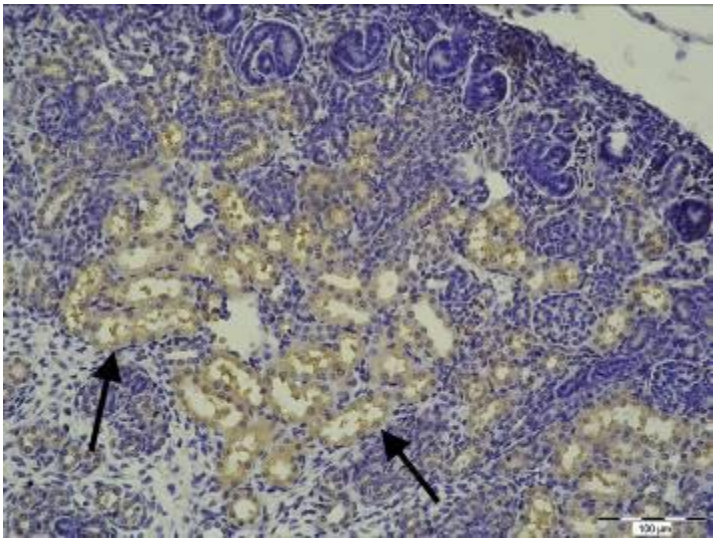

Figure 2. Collecting ducts positive for TFF3, 17-day old embryo.

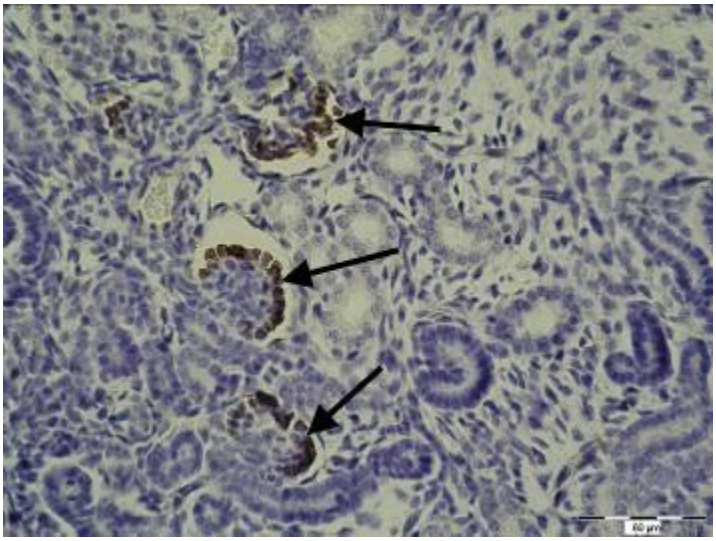

Figure 3. Pronounced TFF2 signal in the glomerular podocytes of 15-day old mouse embryo.

Tissues, Pathology, and Diagnostic Microscopy

LS.2.P054
Cold-induced brown adipose tissue hyperplasia: role of bone morphogenic proteins

K. Velickovic[1], A. Korac[1], M. Markelic[1], I. Golic[1], B. Korac[2], V. Otasevic[2], M. Vucetic[2], A. Stancic[2] A. Jankovic[2], B. Buzadzic[2]

[1]Faculty of Biology, Chair of Cell and Tissue Biology, Belgrade, Serbia
[2]Institute for Biological Research,"Sinisa Stankovic" , Belgrade, Serbia

ksenija@bio.bg.ac.rs.
Keywords: bone morphogenic proteins, brown adipose tissue

Brown adipose tissue (BAT) is specialized for energy expenditure through expression of uncoupling protein 1 (UCP1) and thus provides a natural defence against cold and obesity. Cold exposure activates BAT thermogenic program, a complex process comprising proliferation and differentiation of precursor cells [1]. Among numerous hormones and environmental signals, it was recently shown that bone morphogenic proteins (BMPs), members of the transforming growth factor-β superfamily, provide inductive signals for adipose cell fate determination. Namely, the results from *in vitro* studies showed that BMP4 induces a mature white fat cell phenotype, while BMP7 triggers progenitor cell commitment to brown adipocytes lineage [2]. Given these considerations, Mill Hill rats were exposed to cold (4±1 °C) 3, 6, 12, 24, 48 or 72 hours in order to investigate the expression pattern of BMP7 and BMP4 during of BAT *in vivo* hyperplasia followed by proliferation and differentiation. Interscapular portion of BAT was isolated and prepared for Western blot analysis and light microscopy.

The changes in UCP1, BMP7 and BMP4 in BAT are depicted in Fig. 1. As seen, UCP1 and BMP7 contents were significantly higher in all groups acclimated to low temperature in comparison with the corresponding controls kept at room temperature ($P<0.005$). Compared with untreated group, BMP4 protein content was higher between hour 6 and hour 12 ($P<0.005$), but lower ($P<0.025$) on hour 72.
Light microscopic examination (Fig. 2) of BAT showed that majority of adipocytes was multilocular, but unilocular cells were also observed. Strong immunopositive reaction for BMP7 was found in multilocular adipocytes, preadipocytes as well as in surrounding connective tissue of cold-expossed animals. In contrast, BMP4 immunoexpression revealed moderate cytoplasmic reaction in multilocular and strong reaction in unilocular brown adipocytes. Interestingly, strong BMP4 immunoreaction was seen around lipid droplets in multilocular cells of cold-exposed groups.

The fact that cold exposure already after 3 hours significantly increases UCP1 expression points to its fast thermogenic response, indicating enormous plasticity of BAT. Western blot and immunohistochemical results clearly showed that BAT of control as well as cold exposed groups expresses both BMP7 and BMP4, indicating their important role in BAT physiology and cold-induced hyperplasia. Bearing in mind important role of BMPs in lipid accumulation [3], as well as increased number of precursor cells during BAT hyperplasia, it is possible that BMP7 and BMP4 lead to lipid accumulation in preadipocytes cooperatively. Also, strong BMP4 immunopositivity around lipid droplets noticed in this study suggests that BMP4 could participate in lipid synthesis and/or transport in brown adipocytes. The similar pattern of BMP7 and UCP1 protein expression in cold exposed groups supports the notion that BMP7 plays an important role in BAT thermogenic response, suggesting multiple roles of BMPs during BAT hyperplasia.

1. V. Petrovic, A. Korac, B. Buzadzic and B. Korac, J Exp Biol, 208 (2005), p. 4263-71.
2. TJ. Schulz and YH. Tseng, Cytokine Growth Factor Rev, 20 (2009), p. 523-31.
3. YH. Tseng et al, Nature, 454 (2008), p. 1000-4
4. This research was supported by grant from Serbian Ministry of Education, Science and Technological Development, #173055

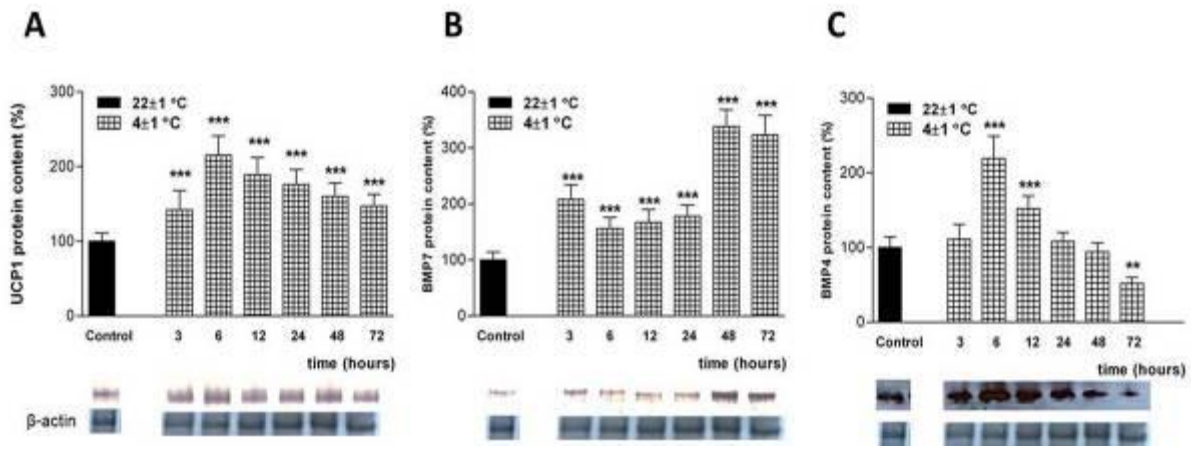

Figure 1. Time-dependent protein expressions of UCP1 a), BMP7 b) and BMP4 c) in rats´ BAT during cold acclimation. Protein content is expressed relative to a control acclimated to room temperature, which was standardized as 100 % as mean ± SEM. *Compared to control, **p<0.025,***p<0.005.

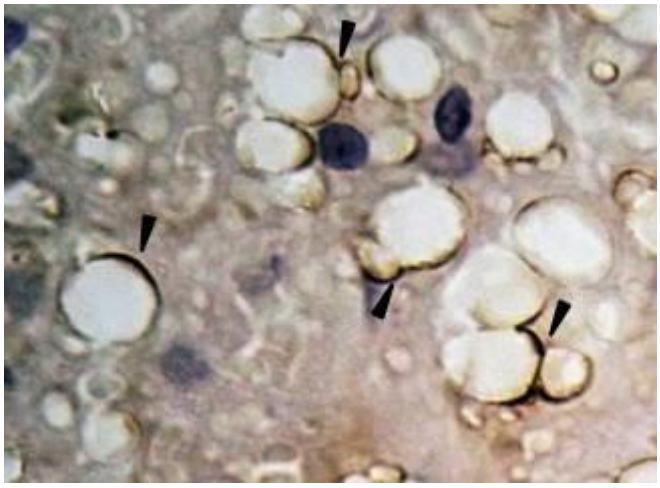

Figure 2. Immunohistochemical detection of BMP4 in BAT of group exposed to cold 12 hours. Note the strong reaction around lipid droplets (arrows). Magnification: x40.

Tissues, Pathology, and Diagnostic Microscopy

LS.2.P055
Distribution of TNF-α, TGF-β2 and FURİN in endometrium of Missed Abortion and Voluntary First Trimester Termination Cases

K. Özbilgin[1]

[1]Celal Bayar Üniversitesi, Histoloji ve Embriyoloji AD, Manisa, Turkey

kemalozbilgin@yahoo.com

In this study, we have compared distribution of TNF-α, TGF-β2, and a member of proprotein convertase family; FURIN molecules that have lots of cellular functions, in desidua and placenta samples of missed abortion and voluntary termination cases to investigate the effects in the etiology of missed abortion.

Desidual materials were collected from patients that are diagnosed missed abortion (n=10) and legal voluntary termination cases (n=10) under 10 gestastational week. Tissue samples were collected from each group by dilatation curettage (D&C) under mask anesthesia. Materials were divided into two groups for examination. For all samples, TNF-α (Tumour Necrosis Factor-alfa), TGF-β2 (Tumour Growth Factor-beta 2), and FURIN primary antibodies were performed by immunohistochemical staining. The number of stained cells was calculated using H-Score technique.

Missed abortion group (n=10) mean age was 28.7 (18- 41) and control group (n=10) mean age was 27.5 (21-37). There is no significant difference between the two groups in terms of obstetric history. In histochemical examination, at missed abortion group a lower vessel formation, structuring of trophoblast and larger decidua cells with lots of vacuoles viewed. In immunohistochemical examination at decidual cells of missed abortion group; FURIN immunoreactivities was detected higher then control group (Figure 1). Between the two groups significantly ($p < 0.005$) difference was found in terms of FURİN. Detection of placental cells, the immunoreactivities of TNF-α (Figure 2). and TGF-β2 (Figure 3) were found higher both syncytiotrophoblast and cytotrophoblast cells of missed abortus group and significantly difference ($p<0,005$) were determined between two groups. Also high immunoreactivitiy of FURİN molecule was established only in cytotrophoblastic cells of missed abortus group and significantly difference ($p<0,005$) were determined between two groups.

It is considered that high levels of factors which play important roles in proliferation, invasion, migrasion, differentiation and survival of cells may be reason of proceeding decidualization, placentation and preventing from abortion in spite of concluding the fetal life.

Missed abortion, proprotein convertase, POMC, FOXO3A

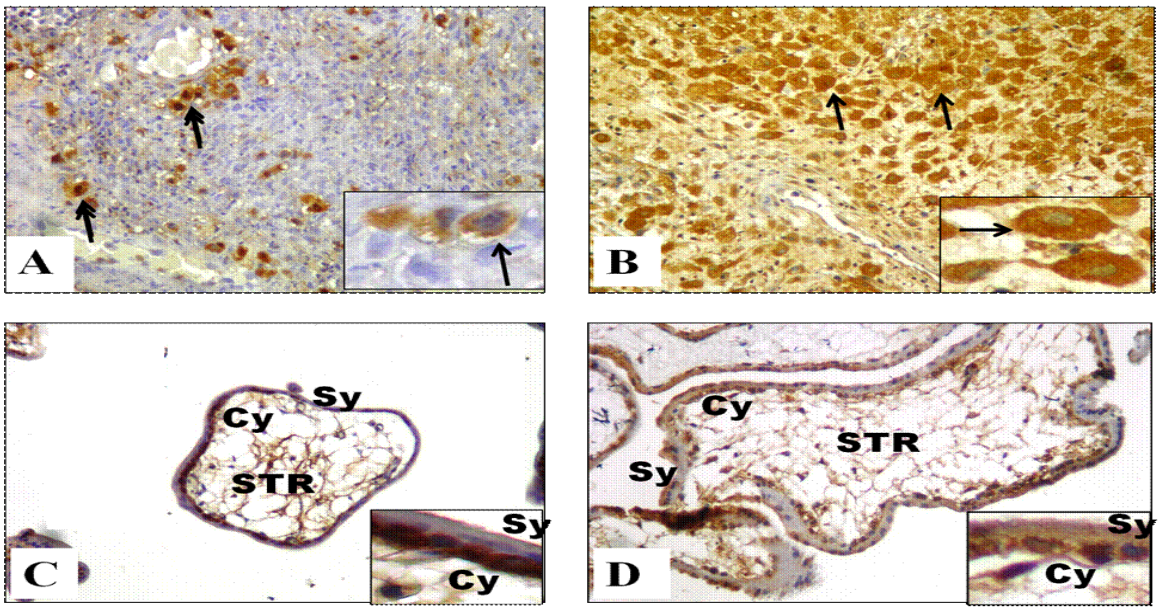

Figure1 . Immunohistochemical analysis of Furin expression were seen in the decidual (A, B) and plasental chorionic villi (C, D) of normal pregnancy (A, C) and missed abortion (B, D) groups. The arrows indicate decidual cells stained with Furin which were high in number on missed abortion group (B) than normal pregnacy (A). The high Furin expresion were seen in syncytiotrophoblast (Sy) and cytotrophoblast (Cy) on missed abortion group (d) than normal pregnancy group (c). STR: Stroma (Original Magnification: 200×.)

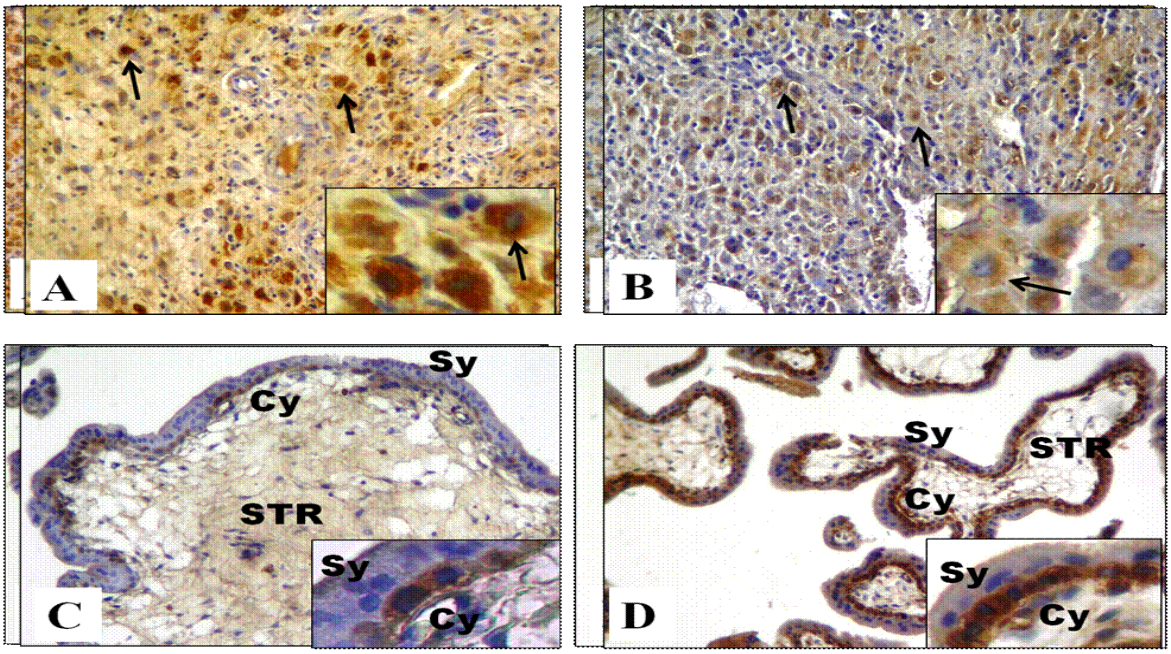

Figure 2. Immunohistochemical analysis of TNF-α expression were seen in the decidual (a, b) and plasental chorionic villi (c, d) of normal pregnancy (a, c) and missed abortion (b, d) groups. The arrows indicate decidual cells stained with TNF-α which were high in number on normal pregnacy (a) than missed abortion group (b). The high TNF-α expresion were seen in syncytiotrophoblast (Sy) and cytotrophoblast (Cy) on missed aboriton group (d) than normal pregnancy group (c). STR: Stroma (Original Magnification: 200×.)

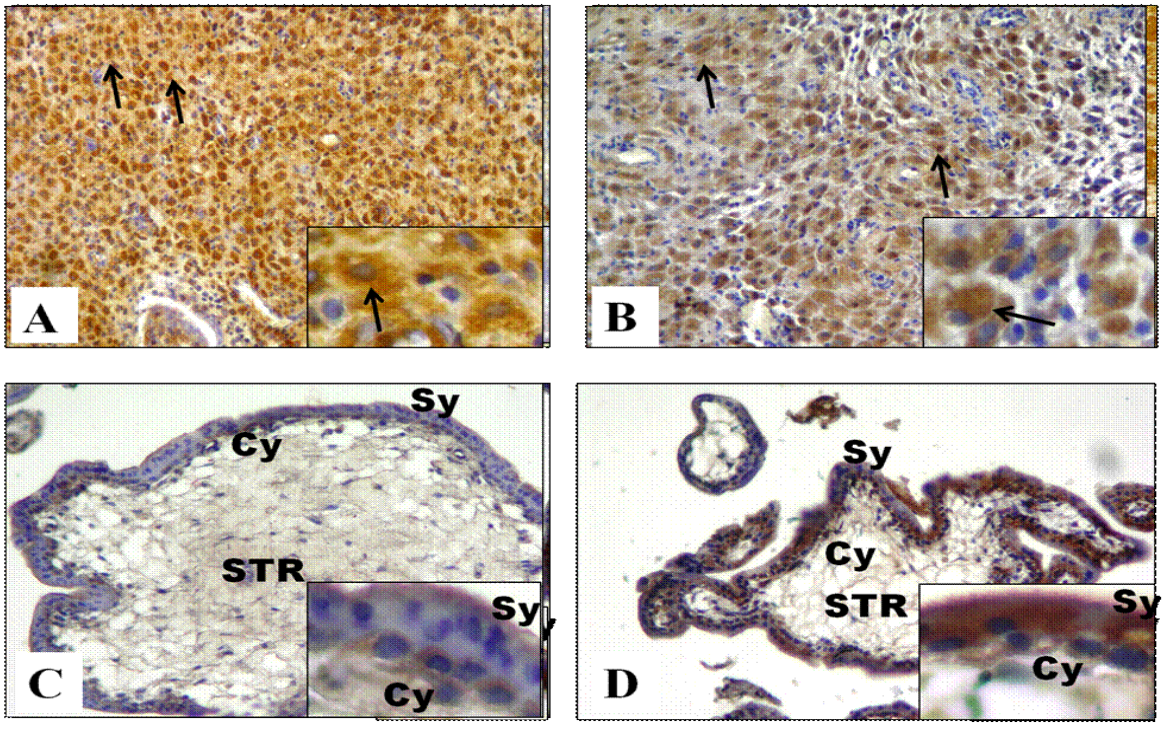

Figure 3 . Immunohistochemical analysis of TGF-β2 expression were seen in the decidual (a, b) and plasental chorionic villi (c, d) of normal pregnancy (a, c) and missed abortion (b, d) groups. The arrows indicate decidual cells stained with TGF-β2 which were high in number on normal pregnacy (a) than missed abortion group (b). The high TGF-β2 expresion were seen in syncytiotrophoblast (Sy) and cytotrophoblast (Cy) on missed aboriton group (d) than normal pregnancy group (c). STR: Stroma (Original Magnification: 200×.)

Tissues, Pathology, and Diagnostic Microscopy

LS.2.P056
Airway wall remodeling in young and adult rats with experimentally provoked bronchial asthma

J. Uhlik[1], P. Simunkova[2], K. Berankova[2], L. Vajner[1]

[1]Charles University, 2nd Faculty of Medicine, Department of Histology and Embryology, Prague, Czech Republic
[2]Charles University, 2nd Faculty of Medicine, Department of Paediatrics, Prague, Czech Republic

jiri.uhlik@lfmotol.cuni.cz
Keywords: bronchial asthma, Brown Norway rat, ovalbumin, morphometry, airway remodeling

Obstructive airway disorders represent one of the major health issues in industrialized countries. It is reported that approximately 40 % of the population is at increased risk of the allergy that can melt into bronchial asthma [1]. Morphological and immunological studies having documented the presence of an active inflammation in the airway mucosa have been gradually changing the opinion on this disease and its treatment. Together with the inflammation, various structural changes known as remodeling constantly appear in the bronchial walls of patients suffering from the bronchial asthma [2]. The principle of the remodeling mainly consists in changes of properties of the bronchial epithelium including hyperplasia of its goblet cells, thickening of the basement membrane predominantly in the area of its reticular lamina, differentiation and activation of myofibroblasts and proliferation of smooth muscle in the airway walls, growth of submucosal glands, deposition of extracellular proteins to the lamina propria mucosae and changes of vascularization [3]. While these morphological changes in bronchial walls of patients with asthma have been thoroughly described, predominantly in the adults, fewer papers exist about the bronchial remodeling in small children and even lesser about the changes in laboratory animals. The reason of this state is probably the fact that the spontaneous asthma practically does not occur in animals [4].

There is only one isolated paper describing differences in the remodeling changes in two age groups of animals that simulates the developing asthma in children [5]. This study showed the more pronounced airway remodeling at a young age. Thus, we decided to analyze structural changes of intrapulmonary airways in rats of Brown Norway (BN) strain, which are especially responsive to sensitization by various allergens and tend to develop the state that clinically and morphologically highly resembles the human bronchial asthma when stimulated with appropriate allergen challenges.

Young (4 weeks) and adult BN rats were sensitized by repeated intraperitoneal injections of ovalbumin (OA). During following 2 weeks, the rats regularly inhaled the aerosolized OA of low concentration. Two control groups of each age were housed simultaneously. The first of them was injected and inhaled by saline (S), the second group was untreated (C). At the end of the experiment, the animals were sacrificed, their lungs were processed for the light microscopy and the intrapulmonary airways were examined. In this study, we concentrated to the airway morphometric parameters, occurrence of eosinophilic granulocytes in the airway walls and number of epithelial secretory cells together with a glycoconjugate quality of their secretion.

The airway walls of the OA group were showing marks of remodeling in both young and adult animals. The total wall areas of all intrapulmonary airways were significantly increased compared to groups S and C (Figure 1). The thickening of inner wall areas (mucosal and muscular layer) was more pronounced in adult rats; outer wall areas (adventitia) were more increased in the young group. There were some significant signs of the muscular hypertrophy or hyperplasia only in young challenged animals (Figure 2). The number of eosinophilic granulocytes was predominantly increased in airway walls of OA young rats (Figure 3). The cells were found mainly in the tunica adventitia (Figure 5). Secretory cells were more multiplicated in airway epithelium of OA adult animals (Figure 4). Proportions of neutral and acidic glycoconjugates in their secretion were shifted towards the acidic ones in adult rats (Figure 6).

The study confirmed the bronchial sensitivity of BN rats and different reactivity of adult and young individuals. The remodeling changes were ascertained in all layers of the airway wall; more in the epithelium and connective tissue than in the muscle. A morphological base for further experiments was constituted. We expect significant changes in the extracellular matrix composition.

1. S. Siddiqui and J.G. Martin, Curr. Allergy Asthma Rep. 8 (2008), p. 540-547.
2. W.R. Roche, R. Beasley, J.H. Wiliams and S.T. Holgate, Lancet 1 [8637] (1989), p. 520-524.
3. L.P. Boulet and P.J. Sterk, Eur. Repir. J. 30 (2007), p. 831-834.
4. G.R. Zosky and P.D. Sly, Clin. Exp. Allergy 37 (2007), p. 973-988.
5. E. Palmans, N.J. Vanacker, R.A. Pauwels and J.C. Kips, Am. J. Respir. Crit. Care. Med. 165 (2002), p. 1280-1284.
6. The study was supported by the grant IGA MH CR NT 11459.

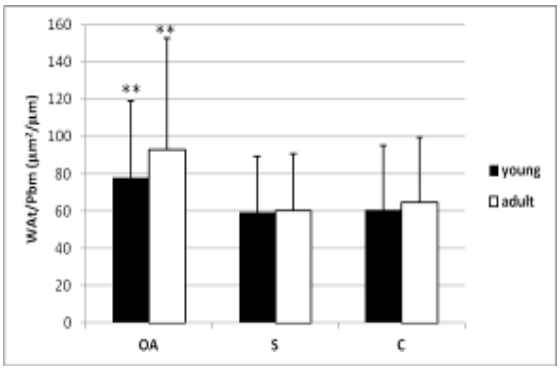

Figure 1. Total wall area (WAt) normalized to perimeter of basement membrane (Pbm) in all measured intrapulmonary airways.
** p < 0.01 versus S and C

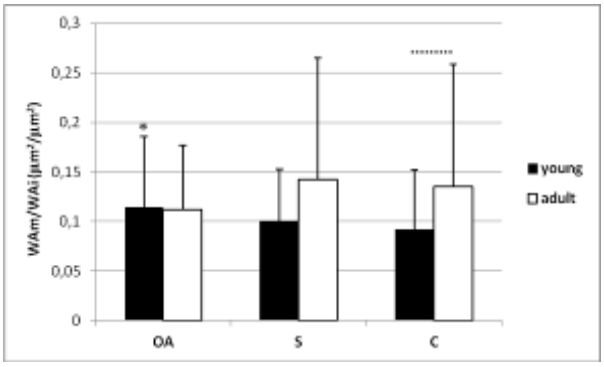

Figure 2. Area of smooth muscle (WAm) / inner wall area (WAi, mucosa and muscular layer) in all measured intrapulmonary airways.
* p < 0.05 versus C, dashed line p < 0.05

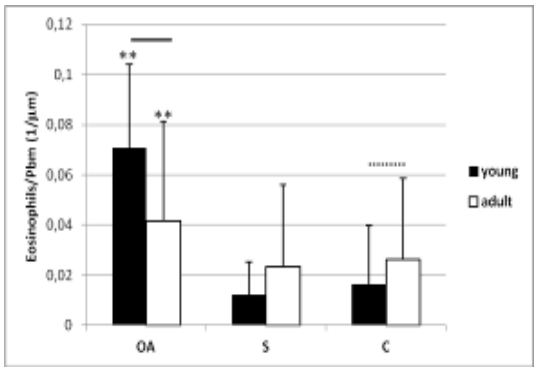

Figure 3. Number of eosinophilic granulocytes normalized to perimeter of basement membrane (Pbm) in all measured intrapulmonary airways.
** p < 0.01 versus S and C, solid line p < 0.01, dashed line p < 0.05

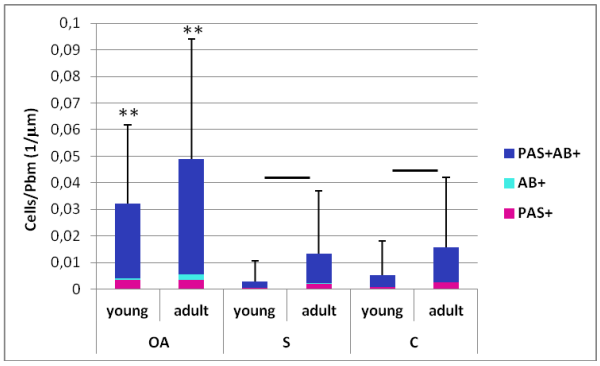

Figure 4. Number of epithelial secretory cells normalized to perimeter of basement membrane (Pbm) in all measured intrapulmonary airways. Proportions of PAS and/or alcian blue (AB) positive cells are showed.
** p < 0.01 versus S and C, solid line p < 0.01

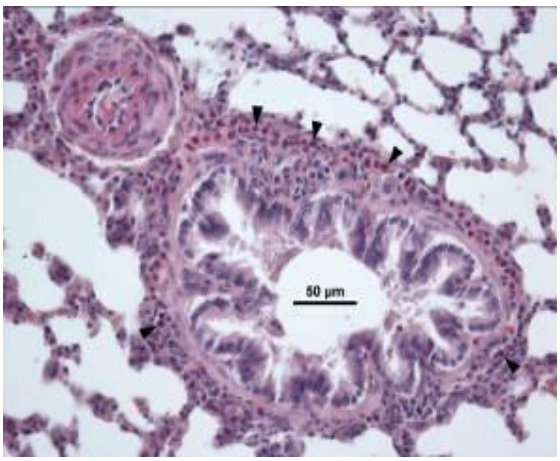

Figure 5. Small bronchiole of OA young rat. Many eosinophilic granulocytes (arrowheads) are present mainly in tunica adventitia. Hematoxylin and eosin staining, objective magnification 40x.

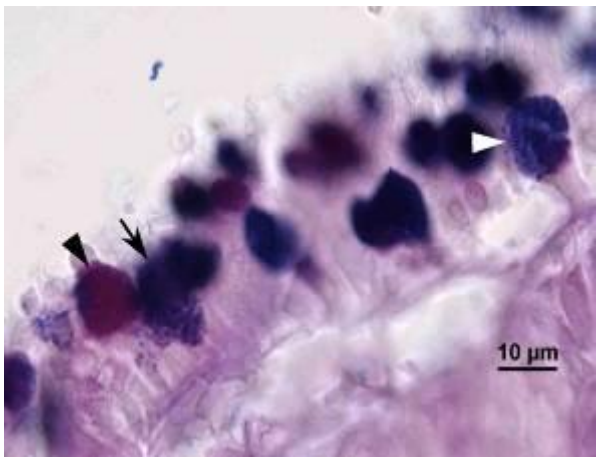

Figure 6. Secretory cells in bronchial epithelium of an OA adult rat. Glycoconjugates are visualized by PAS and alcian blue (AB), pH 2.5. All three histochemical reactions of secretory granules are visible: neutral PAS+ (black arrowhead), acidic AB+ (white arrowhead), combined PAS+AB+ (black arrow). Objective magnification 100x.

Tissues, Pathology, and Diagnostic Microscopy

LS.2.P057
Influence of the morphology of lysozyme-shelled microparticles on the cellular association, uptake and degradation in SKBR3 cells

M. Colone[1], A. Calcabrini[1], F. Cavalieri[2,3], M. Tortora[2], M. Zhou[3], M. Ashokkumar[3], A. Stringaro[1]

[1]Istituto Superiore di Sanità, Technology and Health, Rome, Italy
[2]University of Tor Vergata, Department Chemical Science and Technology, Rome, Italy
[3]University of Melbourne, School of Chemistry, Melbourne, Australia

marisa.colone@iss.it
Keywords: microparticles, breast cancer, electron microscopy

The application of nanomedicine for cancer therapy has received considerable attention in recent years. The key issue is to achieve the desired concentration of therapeutic agents in tumor sites, thereby destroying cancerous cells while minimizing damage to normal cells. To pursue this approach, biomaterial science has stepped into the formulation of smart materials and miniaturized drug delivery devices [1].

The ultrasound assisted self-assembly and crosslinking of lysozyme at the water-air and water-perfluorohexane interface is shown to produce lysozyme-shelled hollow microbubbles (LSMBs) and microcapsules (LSMCs) [2, 3].

Herein, we report on the interaction of LSMBs and LSMCs with human breast adenocarcinoma cells (SKBR3). Biocompatibility of microcapsules and microbubbles has been evaluated by MTT test. The cellular internalization kinetics of LSMBs and LSMCs and the effects on cell cycle were evaluated using flow cytometry. LSMBs and LSMCs were phagocyted by cells within 2 hours without exerting a cytotoxic activity. Internalization of microparticles and degradation within the cell were also monitored by confocal analysis (Figure 1). Cell membrane integrity and cell cycle progression were not affected by LSMBs and LSMCs uptake. These studies have shown that the positively charged LSMBs and LSMCs were not cytotoxic and can be readily internalized and degraded by SKBR3 cells. LSMBs and LSMCs showed a different uptake kinetics and intracellular degradation pattern due to differences in the arrangement of protein at the air-liquid or oil-liquid interfaces. Furthermore, scanning electron microscopy (SEM) analysis was used to gain understanding on the mechanism of cell-microparticle interaction. A strong adhesion of microparticles on cell surface was observed confirming the absence of cytotoxic effects along with the maintenance of cell integrity, even when numerous particles were laying on the cell surface (Figure 2).

These results highlight the potential uses of LSMBs and LSMCs as ultrasound responsive platforms suited for biomedical and pharmaceutical applications.

1. F. Cavalieri, M. Colone et al., Part. Part. Syst. Charact. 30 (2013), p 1–9.
2. F. Cavalieri, M. Zhou et al., Curr. Top. Med. Chem. 10 (2010), p 1198.
3.. F. Cavalieri, M. Ashokkumar et al., Langmuir 24 (2008), p 10078.

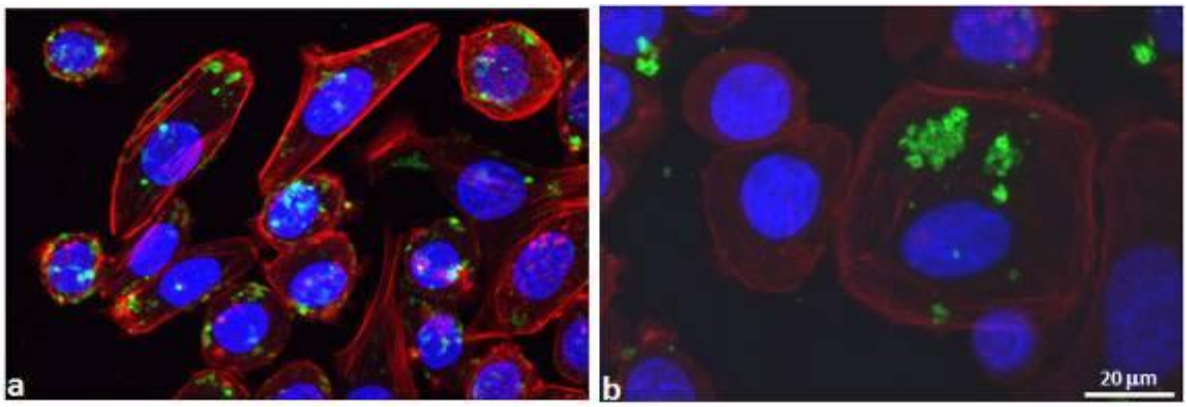

Figure 1. Confocal microscopy images of internalized microparticles. SKBR3 cells were incubated for 2 hours with LSMB-FITC (a) and LSMC-FITC (b). Green, red and blue indicate FITC-conjugated microparticles, actin filaments and nuclei stained with Hoechst 33342, respectively. LSMBs and LSMCs appear to be efficiently internalized by the cells.

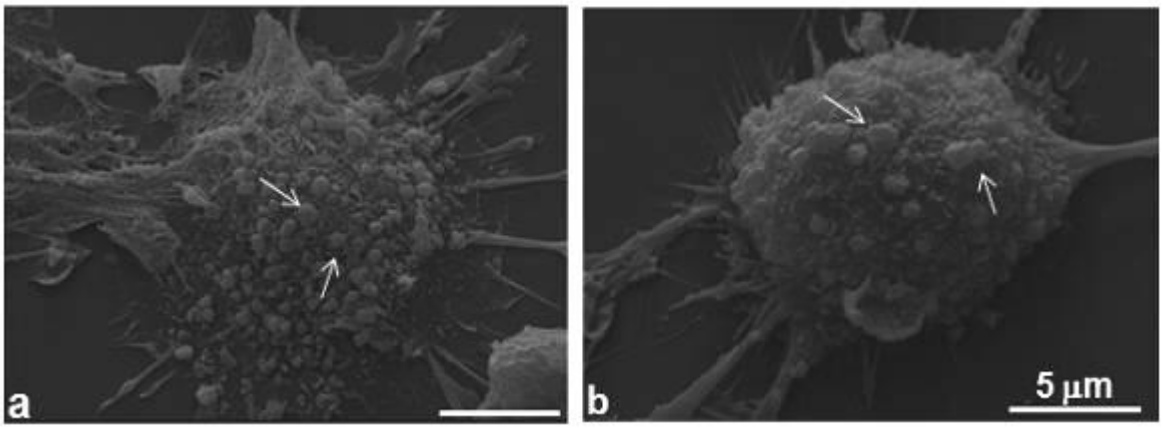

Figure 2. Scanning electron microscopy images of SKBR3 cells after incubation with LSMBs (a, arrows) and LSMCs (b, arrows) after 2 hours of incubation.

Tissues, Pathology, and Diagnostic Microscopy

LS.2.P058
Characterisation of the intracellular surfactant-pool in a mouse-model of pulmonary fibrosis

J. Hegermann[1], B. Birkelbach[1], D. Lutz[1], P. Mahavadi[2], L. Knudsen[1], M. Ochs[1]

[1]MHH, Funktionelle u Angewandte Anatomie, Hannover, Germany
[2]University Gießen Marburg, Internal Medicine II, Gießen, Germany

hegermann.jan@mh-hannover.de

Alveolar epithelial type II (AEII) cells are crucial for surfactant metabolism, keeping alveoli open, dry and clean. In recent years, increasing evidence has been found that dysfunctions of AEII cells play a central role in the development of pulmonary fibrosis. This has been attributed to an increased endoplasmatic reticulum stress and alterations in autophagy of AEII cells. Autophagy is a conserved mechanism known to degrade cellular components (e.g. organelles, misfolded proteins) by formation of autophagosomes. Amiodarone is a drug which can induce a fibrotic remodeling in the lung. In the present study, we characterized the intracellular surfactant pool (defined by the total amount of lamellar bodies (LB)) and autophagy within AEII cells in the amiodarone mouse model of pulmonary fibrosis. Using design-based stereology we observed a marked increase in the intracellular surfactant pool after amiodarone treatment within two weeks which was associated with hyperplasia and hypertrophy of AEII cells.

Immuno-gold labeling showed a preferable binding of LC3b at the limiting membrane as well as in the interior of the LB in both control and amiodarone treated mice. Autophagosomes as defined by pure morphological criteria were found preferably after amiodarone exposure. TEM tomography was used to characterize the 3-dimensional morphology of autophagosomes within AEII cells after amiodarone exposure. A contact between the LB and the autophagosome could be observed in the TEM tomogram, meaning that these structures share the source of lipid.

Tissues, Pathology, and Diagnostic Microscopy

LS.2.P059
Histopathology as a biomarker of effect in ecotoxicological studies on natural populations of small mammals

A. Sánchez-Chardi[1], A. Dols-Pérez[1], J. Repullés[1], C. Rodríguez-Cariño[2], M. Vendrell[1], M.A. Sans-Fuentes[3,4]

[1]Universitat Autònoma de Barcelona, Microscopy Facility, Cerdanyola del Vallès, Spain
[2]Universidad de Venezuela, Pathology, Maracay, Spain
[3]Universitat de Barcelona, Biologia animal, Barcelona, Spain
[4]University of Arizona, School of Geography and Development, Tucson, Spain

Alejandro.Sanchez.Chardi@uab.cat
Keywords: Ecotoxicology, small mammals, Mediterranean protected sites, light microscopy, biomarker of effect

The search of suitable biomarkers is a crucial aspect in ecotoxicological studies, especially in natural populations inhabiting protected areas. Whereas histopathological evaluations are common tools in toxicological studies, there is scarce information of both structural and ultrastructural alterations induced by environmental pollution. Here, we compared different approaches of quantitative and qualitative pathological assessments on two species of small mammals exposed to metals and other common environmental pollutants: the greater white toothed shrew (C*rocidura russula)* and the wood mouse (*Apodemus sylvaticus*).

Specimens used in this study include 91 *C. russula* from polluted and reference sites of Doñana (National Park of Doñana, Spain), Garraf (Garraf Park, Spain), and Alentejo (Portugal), and 49 *A. sylvaticus* from Garraf. Both hepatic and renal tissues were analysed, focusing on a qualitative and semiquantitative assessment of pathologies based on the extension and severity of alterations (Alentejo [1], Garraf [2]) or quantitative analyses based on morphological differences of cells (Doñana [3]).

The results revealed liver as the main organ affected by the pollution in all disturbed sites. The damage observed that may be attributed to chronic exposure to pollutants includes cell cycle arrest (necrosis and apoptosis), inflammation, cytoplasmic vacuolation, microsteatosis and preneoplasic nodules. In Garraf, kidneys of the specimens exposed to environmental pollution showed a significant increase of medullar and cortical alterations, namely tubular dilatation and necrosis, and hyaline cylinders in the lumen of tubules from renal medulla, together with multifocal inflammation in cortical and medullar areas. In Garraf, the comparison of sympatric populations of mice and shrews showed that the latter species was more tolerant to pollution than *A. sylvaticus*. In Doñana, the specimens from the polluted site showed an increase of apoptosis and a tendency to increase cellular perimeter in the hepatic tissue. In Alentejo, increases of frequency and severity of necrosis, apoptosis, and vacuolation were observed in livers of animals from the polluted area. These results pointed out the necessity of pathological studies as a crucial management tool in protected sites.

1. Sánchez-Chardi A, Marques CC, Gabriel SI, Capela-Silva F, Cabrita AS, López-Fuster MJ, Nadal J, Mathias ML. Haematology, genotoxicity, enzymatic activity and histopathology as biomarkers of metal pollution in the *shrew Crocidura russula*. Environmental Pollution 156(3) (2008), 1332-1339.
2. Sánchez-Chardi A, Peñarroja-Matutano C, Borrás M, Nadal J. Bioaccumulation of metals and effects of a landfill in small mammals. Part III. Structural alterations. Environmental Research 109(8) (2009), 960-967.
3. Sánchez-Chardi A, Oliveira Ribeiro CA, Nadal J. Metals in liver and kidneys and the effects of chronic exposure to pyrite mine pollution in the shrew *Crocidura russula* inhabiting the protected wetland of Doñana. Chemosphere 76(3) (2009), 387-394.

Tissues, Pathology, and Diagnostic Microscopy

LS.2.P060
Scanning Electron Microscopy (SEM) as a supportive technique in paleoparasitological investigation

H. Hajjaran[1], G.R. Mowlavi[1]

[1]School of Public Health,Tehran Univ.Med.Sciences., Medical parasitology, Tehran, Iran, Islamic Republic of

hajaranh@tums.ac.ir
Keywords: SEM, Helminth, eggs, Paleoparasitology

Searching for helminthic parasites in archeological materials is mainly dependent on distinguishing of the eggs morphologic and morphometric features. Different types of eggs have been identified in human and animal organic remains including, paleofeces, sediments and latrines obtained from archeological sites in the world so far. Apart from exclusive occasions such as finding parasite eggs in mummified bodies and/or in unique natural situation like trapped eggs in amber, coming to a firm diagnosis seems to be complicated. Factors including, geographical condition, climate, soil texture, duration of time and the egg structure itself are fundamentally affecting reliable paleoparasitological identification. Taphonomical changes that might be happened due to these basic items can make the classical procedure of identification more difficult. A definitive diagnosis can be supported by carful collection of sample, appropriate rehydration procedure and increased number of slide examination. Egg shell pattern which is characteristic for some parasite eggs may underwent ultra structural changes over the years .Performing a practical method to observe the hidden morphological details of helminthes eggs recovered from archeological remains can be led to a reliable taxonomic identification. In this study Scanning Electron Microscopy which has been used in paleoparasitology is definitely a reliable technique to study the details of egg shell structures and taphonomic changes resulted over a long period of time.

Tissues, Pathology, and Diagnostic Microscopy

LS.2.P061
An ultrastructural study of conventional 'cell to cell contact' *in vitro* swine influenza virus infection

C. Rodríguez-Cariño[1], T. Mussá[2], M. Pujol[2], A. Sánchez-Chardi[3], L. Córdoba[2], N. Busquets[2]
E. Crisci[4]J. Domínguez[5], L. Fraile[6], M. Montoya[2]

[1]Universidad Central de Venezuela, Veterinary Pathology, Maracay, Venezuela
[2]Universitat Autònoma de Barcelona, Centre de Recerca en Sanitat Animal (CReSA), Cerdanyola del Vallès, Spain
[3]Universitat Autònoma de Barcelona, Biologia cel·lular, fisiologia i immunologia, Cerdanyola del Vallès, Spain
[4]Linkoping University, Institutionen for klinisk och experimentell medicin, Linkoping, Sweden
[5]INIA, Biotechnology, Madrid, Spain
[6]Universitat de Lleida, Lleida, Spain

Alejandro.Sanchez.Chardi@uab.cat
Keywords: ultrastructural, virus, influenza, dendritic cells.

Influenza viruses are enveloped, single stranded RNA viruses in the family *Orthomyxoviridae*, and causes sub-acute or acute respiratory infection in swine farms. Pigs play a crucial role in the interspecies transmission of influenza viruses, they can act as "mixing vessels" for new influenza strains. In fact, swine population are susceptible to avian and human influenza strains, and have been recently demonstrated that these virus can easily cross the species barrier, as it has happened with the new A (H1N1) 2009 pandemic virus. In the other hand, the dendritic cells (DCs) mediate the induction of immunity to pathogens, but their interaction with SwIV is not fully characterized. The main aim of the present study was to evaluate the interaction between porcine DCs and SwIV and the possible role by the former in being carriers of porcine influenza virus using ultrastructural and immunolocalization evaluations by transmission electron microscopy (TEM).

Bone marrow hematopoietic cells were obtained from femurs of healthy Large white X Landrace pigs of eight weeks of age, free from porcine reproductive and respiratory syndrome virus (PRRSV) and negative to type-2 porcine circovirus (PCV2) and influenza virus. Bone marrow dendritic cells (poBMDCs) where generated in an eight days protocol as previously described by (Kekarainen et al., 2008), and previously to be infected, morphologically evaluated. Influenza virus infection has been thoroughly investigated on permissive epithelial cells as MDCK, in this sense SwIV poBMDCs infected and the interaction MDCK cells was analyzed. The poBMDCs cells were exposed *in vitro* to a conventional circulating strain of SwIV, H3N2. The DMEM infected was taken to incubate MDCK. Infected and control poBMDCs and MDCK cells were fixed and processed for conventional and immunogold labelling EM studies. The inmunomarker was made with the monoclonal antibody to influenza A virus.

The ultrastructural evaluation revealed abundant 80-100 nm virus like-particles resembling influenza virus inside vesicles but also freely in cytoplasm in infected poBMDCs. Remarkably, several SwIV like-particles freely in the cytoplasm were observed in close contact with Golgi complex, budding from internal cistern of the Golgi complex membrane to the trans-Golgi network. By contrast with SwIV-infected poBMDCs, in MDCK mature SwIV like-particles were observed in the extracellular space next and attached to cellular membrane. In the cytoplasm of MDCK, small and large vesicles were observed containing mostly immature SwIV like-particles (± 80 nm). Viral particles from infected-poBMDCs were able to induce cytopathic effect in susceptible cells only when cell-to-cell interaction was favored. Considering that this is the first report about the fine interaction of porcine influenza viruses with poBMDCs, these data may help understanding the role of DCs as important antigen presenting cells in the pathogenesis and epidemiology of influenza virus and the role of pigs as virus reservoirs with medical interest.

1. Heinen, 2002.
2. Horimoto and Kawaoka, 2001.
3. Lipatov et al., 2004.
4. Garten et al., 2009

Tissues, Pathology, and Diagnostic Microscopy

LS.2.P062
The Morphological Evaluation in Azoospermia Cases of Testicular Tubular Tight Junctions

C. Hurdag[1], A. Altun[1], Y. E.Canıllıoglu[2], A. Kandil[3], E. Unsal[1], V. Karpuz[4], S. Solakoglu[5]

[1]Istanbul Bilim University, Histology-Embryology, İstanbul, Turkey
[2]Bahçeşehir University, Histology and Embryology, İstanbul, Turkey
[3] Istanbul University, Biology, İstanbul, Turkey
[4] Istanbul Bilim University, Pathology, İstanbul, Turkey
[5] Istanbul University, Histology and Embryology, İstanbul, Turkey

canan.hurdag@istanbulbilim.edu.tr
Keywords: azoospermia, TESE, ZO-1, immunohistochemical, ultrastructural

Testis possesses intrinsic mechanisms to modulate and regulate different stages of germ cell development under the intimate and indirect cooperation with Sertoli and Leydig cells [1]. In the seminiferous tubules the epithelium is physically divided into the adluminal compartment by the blood-testis barrier (BTB) which is constituted by adjacent Sertoli cells near the basement membrane. BTB is the crucial role to spermatogenesis. Spermatogenesis is a highly complicated process in which functional spermatozoa are generated from primitive mitotic spermatogonia. A compromise in this process can lead to infertility [2]. Tight junctions (TJs) at the site of the BTB function in the testis are maintained by intricate regulatory mechanisms. Several TJ-related proteins, such as claudins, occludin, junctional adhesion molecules and zonula occludens-1 (ZO-1), -2 and -3 have been identified [3]. Of these, ZO-1 is the main constituents. In this study we aim to compare the ZO-1 in human testicular tissue with azoospermia, either with spermatozoa or without by using immunohistochemistry and electron microscopy.

For this study, we obtained samples from ages between 22-55 year old man presented infertile laboratory. Tissue samples were obtained from azoospermic patients whose semen fluids did not contain spermatozoa. These azoospermic patients were divided into two groups which do have spermatozoa in testicular sperm extraction (TESE) samples (n=20) and which don't have spermatozoa in their TESE samples. The localization of ZO-1 protein was analyzed by immunohistochemistry and these groups were also examined by transmission electron microscopy.

It was observed that ZO-1 expression in blood testis barrier. BTB was normal in localization in spermatozoa-detected group "Figure 1". Sertoli cell-only syndrome we refer to as the spermatozoa-absent group was examined and ZO-1 in the structure of TJs was not only in the basal compartment of the seminiferous epithelium but also observed on the lateral surface covering the adluminal compartment "Figure 1". The ultrastructural results were also supported with light microscopy findings "Figure 3-4".

These findings suggested that disturbance of ZO-1 reaction in Sertoli cells might be one of the factors involved in the impairment of spermatogenesis. Especially spermatozoa absent group we assumed that maturation of Sertoli cells is not completed. Therefore, TJs among Sertoli cells are regarded as having crucial roles in spermatogenesis.

1. Nikki P. Y. Lee and C. Yan Cheng, Nitric Oxide and Cyclic Nucleotides: Their Roles in Junction Dynamics and Spermatogenesis. Oxidative Medicine and Cellular Longevity 1:1, (2008), 25-32.
2. Nikki P. Y. Lee and C. Yan Cheng, Nitric oxide/Nitric oxide Synthase, Spermatogenesis and Tight Junction Dynamics. Biology of Reproduction 70, (2004), 267-276.
3. Chiba K, Yamaguchi K, Ando M, Miyake H, Fujisawa M. Expression pattern of testicular claudin-11 in infertile men Urology. Nov;80(5):1161, (2012), e13-17.

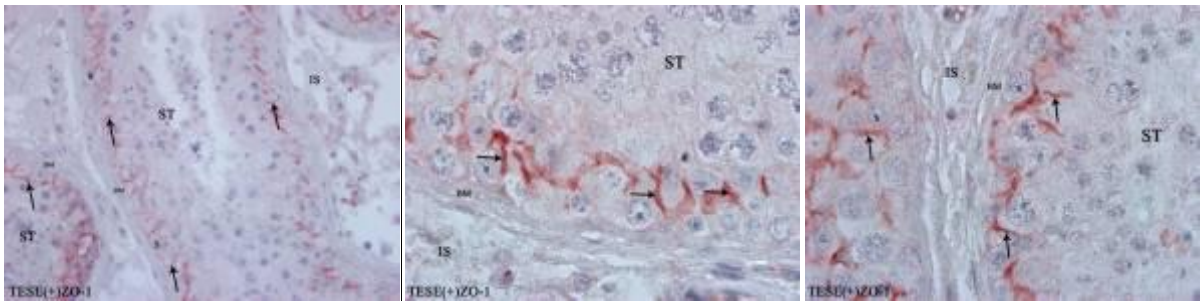

Figure 1. Photomicrographs of azoospermic cases' testicular tissue with spermatozoa detected group [TESE(+)] after testicular sperm extraction. ZO-1 immunostaining (arrows) is present between Sertoli cells (S) in normal localization. The diameter of the seminiferous tubules (ST) were normal and were lined by Sertoli cells and spermatogenic cells. Semineferous tubules were outlined by basement membrane (BM). In the interstitium (IS) where the Leydig cells appear normal. Magnifications: x40 and x100.

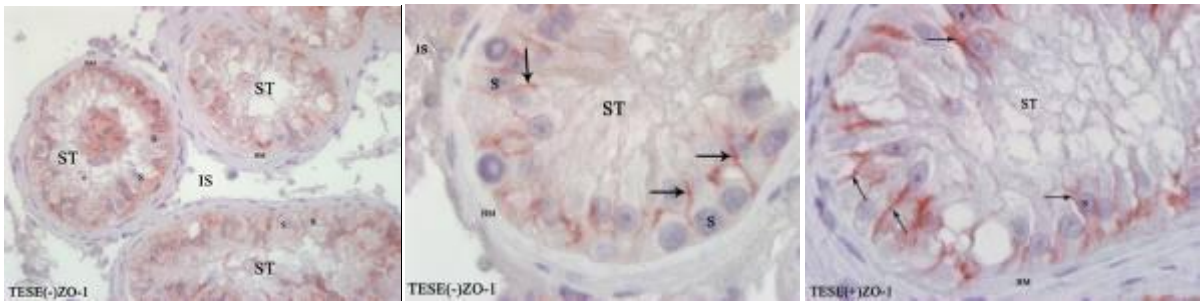

Figure 2. Photomicrographs of azoospermic cases' testicular tissue with spermatozoa absent group [TESE(-)] after testicular sperm extraction. Sertoli cell sendrome was determined in the tubules. ZO-1 immunostaining (arrows) was examined not only in the basal compartment of the seminiferous epithelium (ST) but also observed on the lateral surface covering the adluminal compartment. In the interstitium area (IS) Leydig cells were not seen. Sertoli cells (S) and basement membrane (BM). Magnifications: x40 and x100.

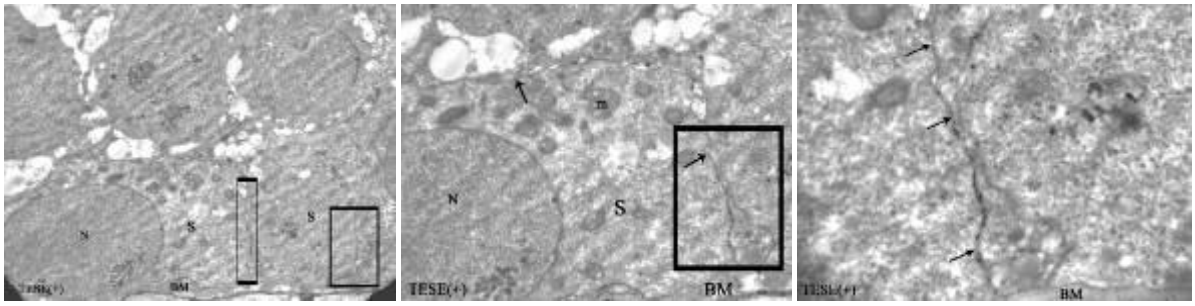

Figure 3. Electron micrographs showing the cross section of a seminiferous tubule from the spermatozoa detected group [TESE(+)]. Tight junctions (arrows,) were seen between Sertoli cells. Sertoli cells (S), Sertoli cells' nucleus (N), basement membrane (BM) and mitochondria (m). Magnifications: x5000, x7500, x20000.

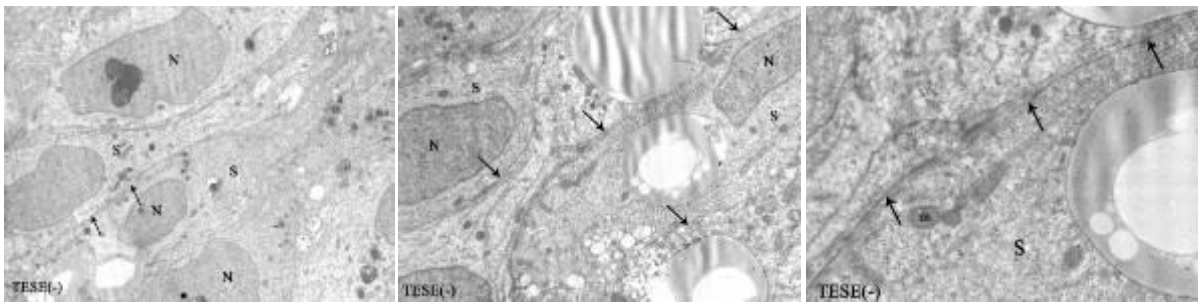

Figure 4. Electron micrographs showing the cross section of a seminiferous tubule from the spermatozoa absent group [TESE(-)]. Tight junctions (arrows) were seen adluminal compartment. Sertoli cells (S), Sertoli cells' nucleus (N) and mitochondria (m). Magnifications: x5000, x7500, x 20000.

Tissues, Pathology, and Diagnostic Microscopy

LS.2.P063
Spatial distribution of heterochromatin bodies in vectors of Chagas' disease as studied by confocal microscopy

M.L. Mello[1]

[1]University of Campinas, Dept of Structural and Functional Biology, Campinas, Brazil

mlsmello@unicamp.br
Keywords: heterochromatin, spatial distribution, confocal microscopy

Most interphase cells of the insects *Triatoma infestans* and *Panstrongylus megistus*, vectors of the Chagas' disease, are characterized by high levels of polyploidy and the presence of constitutive heterochromatin bodies assembled in chromocenters, which are maintained during all the insect life [1, 2]. In *T. infestans* the chromocenters are contributed by three pairs of autosomes and the sex chromosomes whereas in *P. megistus* the chromocenter is contributed by the Y chromosome [2, 3]. These chromocenters contain AT-rich/GC-poor DNA and H3K9 trimethylation; in addition, they display histone hypoacetylation and non-methylated DNA [4, 5] and reveal transcription inertness [1]. In higher vertebrates it is generally accepted that most heterochromatin concentrates close to the nuclear periphery, although gene transcription may also occur at this region [6-8]. However, it was suspected that in the case of *T. infestans* and *P. megistus* the localization of the chromocenters could not always be restricted to the nuclear periphery. In the present work confocal microscopy was found to be necessary for studies concerned with the spatial distribution of these heterochromatic bodies.

Whole-mounted Malpighian tubules of *T. infestans* and *P. megistus* 5th instar male nymphs were subjected to fluorescent Feulgen reaction and examined under a Carl Zeiss LSM510 META confocal scanning laser microscope using λ = 543 nm (81%) and C-Apochromatic 63x water immersion objective and pixel depth of 8 bits. The images were captured and processed using the software Carl Zeiss LSM Image Examiner – Advanced Imaging Microscopy release 4.0.

Conspicuous chromocenters were highlighted in the fluorescent images of the Feulgen-stained nuclei of *T. infestans* and *P. megistus* (Figures 1 and 2). The analysis of the orthogonal optical sections of the nuclei revealed that in 91% of the cases analyzed in *T. infestans* the chromocenters appeared positioned near one side of the nuclear periphery. In 85.7% of the cell nuclei of *P. megistus,* the chromocenter appeared at the inner part of the nuclei.

It is concluded that the spatial distribution of the chromocenter bodies in the cell nuclei of *T. infestans* and *P. megistus* can differ when comparing the two species from each other and vary inside the nuclei of the same species. This situation was probably related to cell physiological events other than those related to cell cycle, or the topology was maintained from previous cell cycles [9], as Malpighian tubule cells in late 5th instar nymphs no longer undergo DNA replication [1, 2].

1. M.L.S. Mello, Cytologia 36 (1971), 42-49.
2. M.L.S. Mello et al., Ann. Trop. Med. Parasitol. 80 (1986), 641-648.
3. G. Schreiber et al., Braz. J. Biol. 32 (1972), 255-263.
4. E.M. Alvarenga et al., Micron 42 (2011), 568-578.
5. E.M. Alvarenga et al., Acta Histochem. 114 (2012), 665-672.
6. L. E. Finlan et al., PLoS Genetics 4 (2008), e1000039.
7. M. Dieudonné et al., EMBO J. 28 (2009), 2231-2243.
8. E. Deniaud and W.A. Bickmore, Curr. Op. Genet. Dev. (2009), 187-191.
9. T. Cremer and C. Cremer, Nature Rev. Genet. 2 (2001), 292-301.
10. We are indebted to Dr. Toshie Kawano ("in memoriam") for facilities at her confocal microscopy laboratory, to Mr. Alexsander S. Souza for microscopy technical support and to FAPESP (2010/50015-6) and CNPq (301943/2009-5, 475261/2012-2) for financial support.

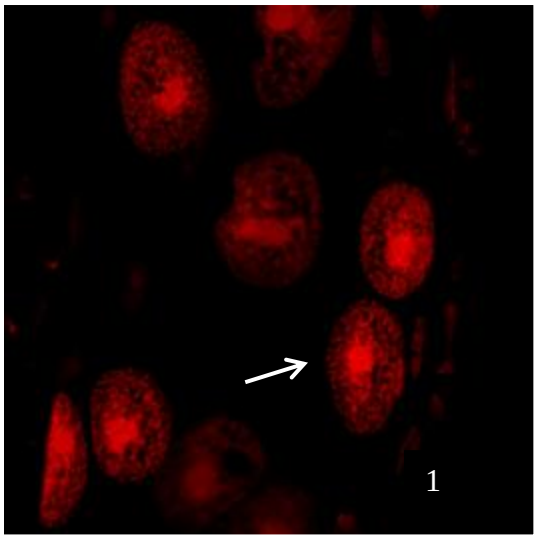

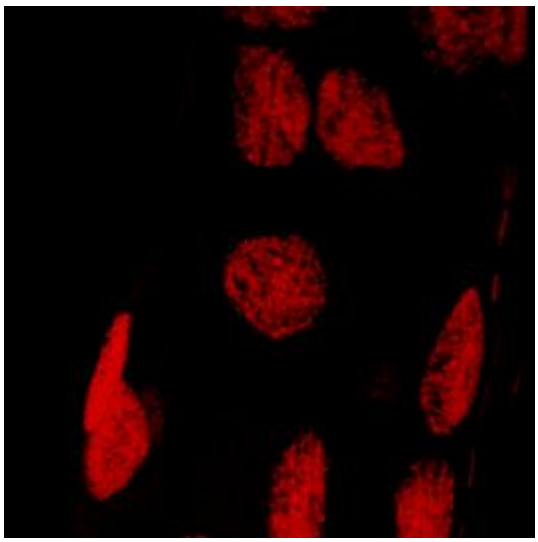

Figures 1 and **2**.Feulgen-stained fluorescent images of *T. infestans* (1) and *P. megistus* nuclei (2). Arrows indicate chromocenters. Bars, 10 µm

Tissues, Pathology, and Diagnostic Microscopy

LS.2.P064
The effect of ozone therapy at the early period of bone healing in an experimental non-fixed fracture model

A. Irban[1,2,3], S. Uslu[1,4], A. Gereli[1,2,3,5], E. Ilgaz Aydinlar[1,2,3,5,6], N. Lulecil[1,2,3,5,6,7], G. Suyen[1,2,3,5,6,7,8]

[1]Acibadem University, Vocational school of health services pathology laboratory technician program, Istanbul, Turkey
[2]Acibadem University, Vocational schoo of health services pathology laboratory program, Istanbul, Turkey
[3]Medipol University, Anesthesiology and Reanimation, Istanbul, Turkey
[4]Acibadem University, Vocational School of Health Services, Istanbul, Turkey
[5] Acibadem University, Orthopedic and Traumatology, Istanbul, Turkey
[6] Acibadem University, Neurology, Istanbul, Turkey
[7]Emsey Hospital, Pain Clinic, Istanbul, Turkey
[8] Acibadem University, Physiology, Istanbul, Turkey

musiuslu@gmail.com
Key words: bone fracture healing, ozone, histomorphometry, immunohistochemistry

Ozone is a chemical compound, consisting of 3 oxygen atoms. Systemic application of ozone leads to delivery of super enriched oxygen at a cellular level and optimizes cell function. This is achieved by activating the red blood cell, immune-competent cells and the enzymatic antioxidants and radical scavengers at a cellular level (1, 2). Aim of this study was to evaluate the effect of ozone therapy at the early period of bone healing in an experimental non-fixed fracture model.

After ethic committee approval, 48 Spraque-Dawley rats were included in the study. After the standard anesthesia induction technique with intraperitoneal (i.p.) ketamine and xylazine (50 mg/kg from each) rats were randomly divided into 2 groups (n:24 for each groups). In both groups, after anesthesia induction open-femoral fracture (ffx) was performed according to the classical technique. After ffx was performed; in Group Ozone, 4 mL of ozone (10 mcg/mL) and in Group Control, 4 mL of medical air were insufflated rectally during 1 min. via an 18 G cannula once a day for 5 consecutive days.

Open femoral fracture (ffx) technique: After shaving right legs, surgical fields were draped under sterile conditions. Vertical lateral incision at femur was followed by muscular blunt dissection. Femur bone was fractured transversally with bone cutter manually at the level of diaphysis. Bone was not fixated. At Day 4, 7 and 13, eight rats from each group were euthanized with decapitation. Femurs were removed. Samples were evaluated immunohistochemically (via expressions of Vascular endothelial growth factor (VEGF), Transforming growth factor (TGF) and Beta catenin (β-catenin)) and histomorphometrically (thickness of periosteum, trabecule's number and thickness, and trabecular, cartilogenous and new bone areas). One-way analysis of ANOVA was used statistical analysis ($p<0.05$).

In histomorphometric analysis, cartilaginous, new bone and trabecular areas were found smaller in ozone ($p<0.001$ for each). Immunohistochemical analysis revealed that ozone resulted in significant increase in VEGF expressions in Day 7 and 13 ($p<0.01$ and $p<0.05$ respectively). Also, TGF expressions are more intense at all time in ozone group ($p<0.01$ for each) β-catenin expression studied as an indicator of regulation of osteoblast were found higher in ozone group at Day 7 and 13. Although control group had better results at histomorphometric analysis at the early period of non-fixated bone fracture; ozone group, showed more intense expressions of TGF and β-catenin. In the light of this data, we can speculate that however at the early period of non-fixated bone fracture, the results for the cartilaginous, new bone and trabecular areas are worse in ozone group, higher levels of VEGF, TGF and β-catenin could have positive impact on the later period of bone healing process.

1. Viebahn R. The Use of Ozone in Medicine, 5th Edition. Germany:Druckerei Naber 2007;
Bocci V. Autohaemotherapy after treatment of blood with ozone: a reappraisal. J Int Res 1994;22:131-144
2. Almeida M., Han L., Bellido T., Manolagas SC.,Kousteni S. Wnt proteins prevent apoptosis of both uncommitted osteoblast progenitors and differentiated osteoblasts by beta-catenin dependent and -independent signaling cascades involving Src/ERK and phosphatidylinositol 3-kinase/AKT. J Biol Chem 2005;280:41342-51.

Tissues, Pathology, and Diagnostic Microscopy

LS.2.P065
Notch 1 and Notch 3 expressions can modulate the liver fibrosis and Resveratrol can prevent liver injury by inhibiting Notch signaling.

G. Tanriverdi[1], F. Kaya-Dagistanli[2], S. Ayla[3], M. Eser[1], S. Demirci[1], M. Cengiz[2], H. Oktar[1]

[1]Istanbul University, Cerrahpasa Medical Faculty, Histology and Embryology Dept., Istanbul, Turkey
[2]Istanbul University, Cerrahpasa Medical Faculty, Medical Biology Dept., Istanbul, Turkey
[3]Zeynep Kamil Gynecology and Maternity Training and Research Hospital, IVF Unit, Istanbul, Turkey

gamzetanriverdi@gmail.com
Key words: Liver injury, Notch signaling and resveratrol

Notch signaling pathway is an evolutionary conserved signalling mechanism that regulates cell fate specification, stem cell maintenance, and initiation of differentiation in embryonic and postnatal tissues. There are four Notch receptors (Notch1, 2, 3 and 4) in mammals. Some researches reported that Notch signaling was implicated in human fibrosis diseases, such as pulmonary, renal and peritoneal fibrosis. And also, Lots of studyings about the Notch effects on development and embryogenesis has been well studied, too. But only several studies emphasized the involvement of the Notch signalling pathway in liver fibrosis recently. In our study we investigated whether Notch signaling can increase in an experimental liver fibrosis model or not and we also wanted to see the effects of an antioxidant therapy on Notch expressions. CCl_4 is a hepatotoxic agent which widely used to form an experimental liver damage. It causes liver cirrhosis, fibrosis, and necrosis by producing free radicals, initiating lipid peroxidation and causing centrilobular necrosis by activating especially hepatic stellate cells (HSC). Resveratrol is a naturally occurring polyphenol, mainly present in skin of grapes, red wine, mal berries, and peanuts. It has several pharmacological activities including anticancer, antioxidant, anti-inflammatory, antidiabetic activity.

In this study, 40 wistar-albino rats were used and devided to four groups. It was given SF to 1st group (control), CCl_4 to 2nd group, CCl_4+resveratrol to 3rd group and only resveratrol to 4th group.
At the and of the experiment (6 week), the tissue samples were collected and applied an immunostaining for Notch 1 and Notch 3 proteins. Sirius red and laminin stainings were applied for detecting fibrosis. And also samples were evaluated for GSH, CAT and protein oxidation biochemically.
As a result, Notch 1 and 3 protein expressions were stronger on fibrotic areas in CCl_4 group. Protein oxidation levels were higher in CCl_4 group than resveratrol applied 3rd group. In contrast, GSH and CAT levels were higher in 3rd group than the 2nd one.

In conclusion, Increasing of the Notch 1 and Notch 3 proteins in fibrotic areas can be indicating the importance of Notch mediating signaling on liver fibrosis by HSC activations. Although, resveratrol prevents liver fibrosis by decreasing lipid peroxidation and can be effective for inhibiting the Notch proteins.

Tissues, Pathology, and Diagnostic Microscopy

LS.2.P066
PDX1 expression in rat pancreas induced by sucrose-rich diet

M. Ukropina[1], V. Petković[1], M. Čakić-Milošević[1]

[1]University of Belgrade, Faculty of Biology, Belgrade, Serbia

mirela@bio.bg.ac.rs
Keywords: pancreas, PDX-1, acinar cells, cell reprogramming

Pancreas is an organ with endocrine and exocrine function. Endocrine cells clustered in islets of Langerhans secrete depending on type, various hormones involved mainly in maintaining glucose homeostasis. Prevailing type are glucose sensitive β-cells, whose product insulin lowers blood sugar level. The dominant, exocrine part of an organ comprises of ductal cells, and relatively homogenous population of acinar cells which are dedicated to digestive enzyme production.

Both endocrine and exocrine cells originate from the same progenitor cell. During the organ development many transcription factors are necessary for determining the cells fate and lineage differentiation: pancreatic and duodenal homeobox 1 (PDX1) homeodomain protein is essential for initiation of all pancreatic lineages. In mature pancreas PDX1 is highly expressed in insulin-producing β-cells, while its downregulation in the exocrine pancreas is required for normal acinar cell function [1].

In the β-cell nucleus, PDX1 is an activator of insulin gene transcription, thus PDX1 localization correlates with β-cell function and survival [2]. It has been reported that acute hyperglycemia induces β-cell proliferation and insulin production, while chronically elevated glucose concentrations deteriorate β-cell function, inducing apoptosis [3], and thus create a perfect milieu for onset of diabetes. In present study we wanted to investigate how both endocrine and exocrine component of the pancreas respond to sucrose-rich diet, in terms of PDX1 expression.

Young adult male Wistar rats fed with commercial rat food, were divided into two groups: control animals (C, n=6) had access to tap water, and sucrose group (S, n=8) to 10% sucrose solution in tap water, both *ad lib*. Animals were raised and kept under 12:12 light:dark cycle, at 21±1 °C. Experimental treatment lasted for three weeks and was approved by the local ethic committee. Pancreas tissue samples were routinely processed for light microscopy, and 5 μm thick sections were obtained. Presence of PDX1 protein was detected by LSAB immunohistochemistry method, using rabbit polyclonal anti-PDX1 antibody acording to manufacturers recommendations (Abcam). Photographs of approximately 30 islets per group, orig. magn. 40x were analyzed using Image J 1.45 software: data on islets profile area, and number of both PDX1-positive and -negative nuclei were collected.

In endocrine pancreas of control animals moderately strong reaction for PDX1 protein was detected, while in sucrose group PDX1 positivity was more intense and abundant (Figure 1, a and b). In both groups PDX1-positive nuclei were predominantly positioned in the central part of the islet, corresponding to location of insulin-secreting cells. Moreover, in S group in distinct portions of exocrine lobes, clusters of PDX1-positive nuclei were observed; PDX1 expression was mostly evident in peculiar binucleate population of acinar cells, with usually one nucleus remaining negative (Figure 1c). Results of morphometric analyzes revealed (Table 1) statistically significant increase of PDX1-positive nuclei number relative to number of all nuclei in S group. In addition, total number of nuclei per unit area of islet of Langerhans showed statistically greater value for S group also.

Glucose is one of the determinants of β-cell growth, thus principally this population of all endocrine cells within the islets undergoes accelerated growth in response to elevated glucose level [4]. This corresponds to our findings documenting the rise of PDX1-positive nuclei in S group, per unit area, most probably at the expense of proliferation of PDX1-positive, functional β-cells, since the number of negative nuclei in both groups remained unchanged. In exocrine portion of pancreas distinct population of PDX1 +/- binucleate acinar cells suggests the involvement of these cells in both insulin and digestive hormone production. In S group these specific acinar cells underwent fate switching, shifting towards PDX1 expression, and possibly insulin producing surogate β-cells. Similar cell reprogramming was achieved in different, non diet induced experimental setting [5]. We suggest that this gene reprogramming represents a good layout for insulin secretion in the case of more serious β-cell functional overload. In conclusion, moderately applied sugar-rich diet makes the pancreatic acinar cells alert to possible environmental challenges.

1. J. Jonsson, L. Carlsson, T. Edlund, and H. Edlund, Nature 371(1994), pp. 606-609.
2. A . Ardestani, N. S. Sauter, F. Paroni, G. Dharmadhikari, J. H. Cho, R. Lupi, P. Marchetti, J. Oberholzer, J. Kerr, Conte, and K. Maedler, J Biol Chem. 286 (2011), pp. 17144–17155.
3. K. Maedler, G. A. Spinas, R. Lehmann, P. Sergeev, M. Weber, A. Fontana, N. Kaiser, and M. Y. Donath, Diabetes 50 (2001), pp.1683-1690.
4. K. Fujimoto, and K. S. Polonsky, *Diabetes Obes*. *Metab*. 11 (*2009*), pp. 30-37.
5. Q. Zhou, J. Brown, A. Kanarek, J. Rajagopal, and D. A. Melton, Nature 455 (2008), pp. 627-632.

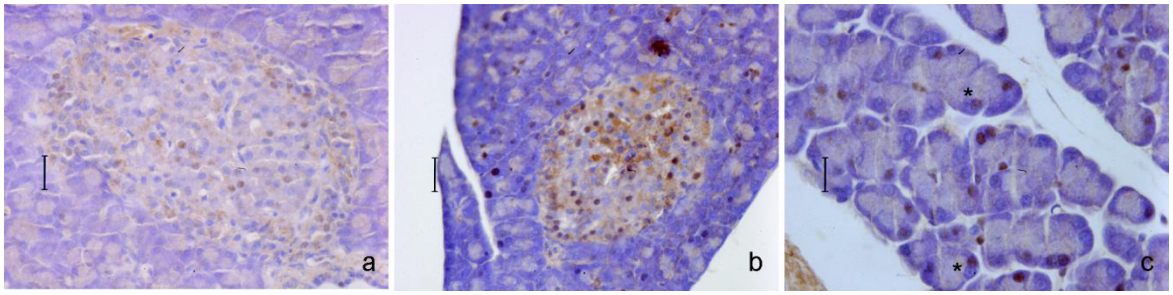

Figure 1. PDX1 localization is present in nuclei of islets of Langerhans in both control (a) and sucrose-fed rats with more prominent reaction in later (b). In sucrose group PDX1 +/- binucleate acinar cells was also detected (c, asterisk) (orig. magn. a and b – 40x, c – 63x).

	% of nuclei		Number of nuclei/μm^2		
	PDX1-	PDX1+	PDX1-	PDX1+	Total
Control group	55.08±3.44	44.92±3.44	0.0035±0.0003	0.0030±0.0003	0.0065±0.0003
Sucrose-fed group	45.70±2.96*	54.30±2.96*	0.0035±0.0004	0.0043±0.0004*	0.0078±0.0006*

Table 1. Results of morphometric analyzes of some parameters in islets of Langerhans in control and animals on sucrose-rich diet. Values are expressed as mean±standard error, statistical significance was determined with Student's t-test, * $p<0.05$.

Tissues, Pathology, and Diagnostic Microscopy

LS.2.P067
Could Vaccination be Reduced Adipogenic Effects of Human Adenovirus Serotype 36 in Rats?

T. Sanlidag[1], H.S. Vatansever[2], S. Akcali[1], T. Onal[2], C. Cicek[3], E. Cakmaklioglu-Kal[1], S. Gokalp[2]

[1]Celal Bayar University, Microbiology, Manisa, Turkey
[2]Celal Bayar University, Histology and Embryology, Manisa, Turkey
[3]Ege University, Microbiology, Izmir, Turkey

sedavatansever@yahoo.com
Keywords: Ad-36, obesity, vaccination

Obesity is a serious chronic disease that has numerous etiologies in human and childhood. The prevalence of obesity has increased dramatically since about 1980 in the United States and worldwide in both developed and developing countries. This rapid spread is compatible with an infectious origin. Four animal and 3 human viruses have been shown to cause obesity in animals and some evidence as well support virus-induced obesity. Adenovirus serotypes 36 (Ad-36) was the first human adenovirus serotype to be tested for adipogenic effect. We aimed to investigate the adipogenic effect of Ad-36 at liver and adipose tissue in rats using histochemical and immunohistochemical methods.

Wistar albino rats (n=30) were separated randomly into three groups, first group was control group and only culture medium was injected in same time with other groups. Second group was injected with inactivated Ad-36 with UV radiation, after 5 days, they were infected with Ad-36 for 12 weeks. Third group was inoculated with Ad-36 for 12 weeks. After 12 weeks, liver and adipose tissue from intraperitoneal region were collected and fixed with %10 formaldehyde. They were then embedded in paraffin after routine procedure. Morphological analyses were detected after hematoxylene-eosine and oil red staining. The lipid accumulation was also analyzed leptin distribution using imnohistoperoxidase technique.

After histochemical analysis, hepatocytes were hypertrophic and lipid vacuoles were detected in its cytoplasm of group 3 liver. Hepatocytes in liver from group 1 and 2 were detected normally.

After immunohistochemical analysis, in group 3 liver tissue, leptin immunoreactivity was detected moderate or strongly in zone-1, zone-2 and zone-3, respectively. The leptin immunoreactivity was detected in liver from both group 1 and 2, but, it was less than group 3 intensity. Leptin immunoreactivity was also increased in group 3 adipose tissue when compared with group 1 and 2 adipose tissue.

Our result support that, after inoculation with Ad-36 was observed lipid accumulation in liver, these effects was decreased giving inactivated Ad-36. In conclusion, vaccination with human or animal models may be decrease adipogenic effect of Ad-36 and other serotypes of adenovirues. Therefore, the obesity caused from after adenoviral infection may be controlled.

1. Atkinson RL. Viruses as an Etiology of Obesity. Mayo Clin. Proc. 82, 1192-1198, 2007.
2. Dhurandhar NV. A framework for identification of infections that contribute to human obesity. Lancet Infect. Dis. 11,963-989, 2011.
3. Na HN, Kim J, Lee HS, et al. Association of human adenovirus-36 in overweight Korean adults. Int. J. Obes. 36, 281–285,2012.

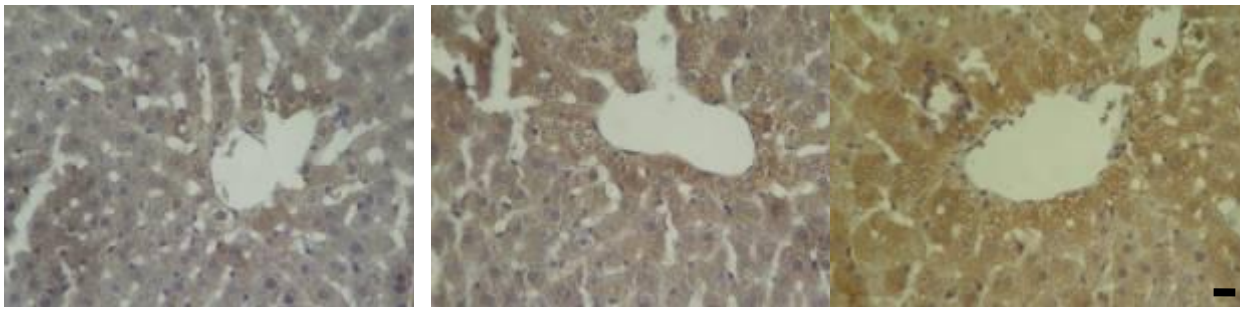

Group 1 Group 2 Group 3

Figure 1. Leptin immunoreactivity I group 1, group 2 and group 3 liver. (Scale bar = 25 μm).

Tissues, Pathology, and Diagnostic Microscopy

LS.2.P068
The Role of Wnt/Beta-Catenin Pathways in Postnatal Mouse Female and Male Gonadal Development

M. Kivanc[1], H.S. Vatansever[1], B. Lopez-Escobar[2], P. Ybot Gonzalez[2]

[1]Celal Bayar University, Histology and Embryology, Manisa, Turkey
[2]Virgen del Rocio Universitary Hospital , İnstituto de Biomedicina de Sevilla (IBIS)/, Sevilla, Spain

sedavatansever@yahoo.com
Keywords: wnt, beta-catenin, gonadal, female, male, development

Differentiation of gonad from both female and male is start during early stage of development. Ovary or testis inducers factors are allow to emergence differentiation of gonad. Although similar to the initial development of the reproductive organs of the two different course of developments in different control mechanisms and / or can be connected to the same control mechanisms are activated at different times. Different members of the Wnt family is a large family as a result of the different receptors and β-catenin activation or inhibition of control of transcription is controlled by the cell such as proliferation, differentiation, survival, apoptosis, cell polarization and migration. In our study, we investigated the role of Wnt/β-catenin pathways in postnatal developmental period of ovary and testis.

Four weeks old, six weeks old and adult both female and male mouse were sacrificed. Testis and ovary were collected from each group. They were preceding routine paraffin embedding procedure. The sections were stained with hematoxylene-eosine for morphological analyses. Distributions of GSK3β, Dickkopf-1 (Dkk-1), Frizzled-6 (Fzd-6) and Wnt5a were analyzed using indirect immunoperoxidase technique.

While GSK3β immunoreactivity was negative in both ovary and testis from different postnatal age, Wnt5a immunoreactivity was weakly detected in 4 and 6 weeks old testis. This immunoreactivity was increased in adult testis. However, Wnt5a immunoreactivity was negative in ovary from all groups. Dkk-1 immunoreactivity was also negative in all testis, positive immunoreactivity of Dkk-1 was detected in 4 and 6 weeks old ovary. Fzd-6 immunoreactivity was also negative both ovary and testis in all groups, β-catenin immunoreactivity was observed weak and moderate in 6 weeks old and adult testis, respectively.

Problems in the development of the testes or ovarium embriyonic life, as well as abnormalities in male and female reproductive organ may be result because of molecular pathways signaling problems. A disorder in the development of the testis and ovaries is important to know in order to understand the mechanisms that control the developmental process. In our study supported that postnatal developmental stage of testis and ovary was control different Wnt/ β-catenin pathway molecules, in addition, GSK3β may not play a role during postnatal stage of both testis and ovaries. In ovary, Dkk-1 and Wnt5a were expressed, therefore, they may main molecules in ovary rather than testis. In testis, especially β-catenin expression was started early pubertal stage and continues in adult with Wnt5a expressions.

1. Liu C-F, Bingham L, Parker L, Yao HH.-C Sex-specific roles of β-catenin in mouse gonadal development. Human Molecular Genetics, 18(3); 405–417, 2009.
2. Naillat F, Prunskaite-Hyyryla, R, Pietila I, Sormunen, R, Jokela, T, Shan, J, Vainio, SJ. Wnt4/5a signalling coordinates cell adhesion and entry into meiosis during presumptive ovarian follicle development. Human Molecular Genetics, 19 (8), 1539–1550, 2010,
3. Kobayashi, A, Stewart, CA, Wang, Y, Fujioka, K, Thomas, NC, Jamin, SP, Behringer, RR. β-Catenin is essential for Müllerian duct regression during male sexual differentiation, Development, 138, 1967-1975, 2011.

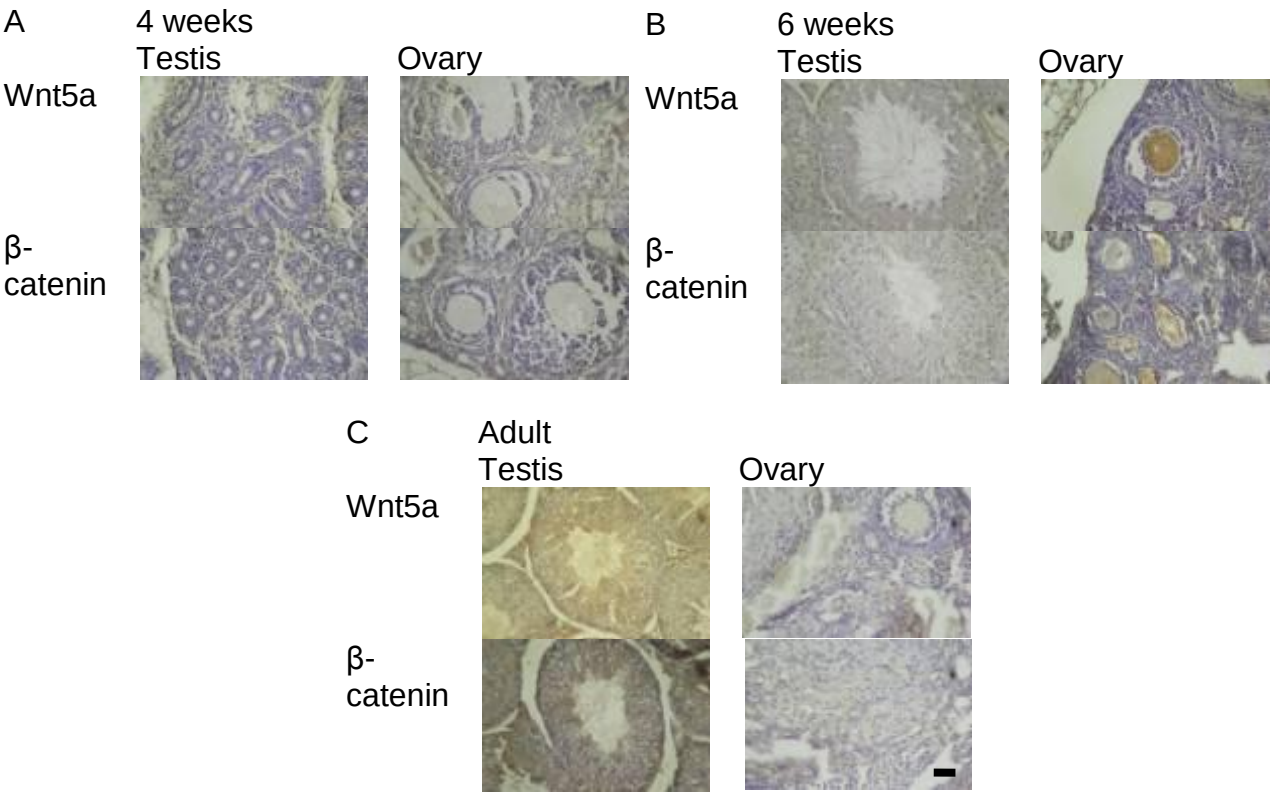

Figure 1. Expression of Wnt5a and β-catenin in ovary and testis in different stage of postnatal period. A: 4 weeks, B: 6 weeks, C: Adult. (Scale bar = 15 μm).

Tissues, Pathology, and Diagnostic Microscopy

LS.2.P069
Immunohistochemical detection of leptin in interscapular brown adipose tissue of hypothyroid rats

M. Čakić-Milošević[1], N. Milad Ali Rajab[1], M. Ukropina[1]

[1]Faculty of Biology University of Belgrade, Institute of Zoology, Belgrade, Serbia

maja@bio.bg.ac.rs
Keywords: brown adipocytes, leptin, hypothyroidism

Leptin is protein hormone involved in regulation of many physiological processes including energy expenditure [1]. In mammals, adipose organ is the most important source of leptin. White adipose tissue (WAT) synthesizes and secretes leptin in proportion to body fat, while contribution of brown adipose tissue (BAT) is somewhat controversial and generally considered as less important. In rodents, acting via hypothalamic receptors, leptin enhances sympathetic input in BAT, stimulates uncoupling protein-1 synthesis and energy dissipation [2,3].

Thyroid hormones (THs) regulate numerous cellular processes in all tissue types. BAT thermogenic function is closely related to optimal THs supply. In systemic hypothyroidism, in the presence of even minimal circulating THs, BAT-deiodinase 2 provides sufficient triiodothyronine locally and protects BAT from hormone deficiency [4]. Given that leptin and THs are engaged in regulation of BAT thermogenesis and bearing in mind that role of brown adipocytes in leptin production is not clearly defined, the aim of this study was to investigate the pattern of leptin immunoexpression in BAT of systemic hypothyroid rats.

Male Wistar rats (130-150 g) maintained under standard laboratory conditions were used. The animals from the experimental group (n=8) were made hypothyroid by drinking methimazole solution (Sigma, St. Louis, MO, USA) (0.02% in tap water), for three weeks. The other animals (n=6) were untreated controls. At the end of the experiment interscapular BAT was isolated and routinely prepared for light microscopy. Leptin-immunoreactivity was assessed on 5 μm thick paraffin sections by avidin-biotin peroxidase method, using rabbit primary polyclonal anti-leptin and secondary goat anti-rabbit antibodies (both at 1:200) (SantaCruz Biotechnology, Santa Cruz, CA, USA).

Leptin-positive cells were observed in BAT of both control and hypothyroid rats. They could be classified into three morphological categories: (a) multilocular adipocytes containing few large lipid droplets, (b) unilocular adipocytes commonly present in BAT and (c) classic multilocular brown adipocytes (Figure 1A, B and C). Immunopositive adipocytes (a) and (b) were seen in both control and experimental group, while positive adipocytes (c) were noticed almost exclusively in hypothyroid rats. Leptin-positive cells were noticeably more abundant in BAT of hypothyroid rats.

It has been reported previously that in rodents serum levels of THs and leptin are inversely regulated [5]. Increase in circulating leptin in hypothyroid rats was explained by increased leptin synthesis in WAT depots [6]. Relatively frequent occurrence of leptin-positive brown adipocytes in interscapular BAT of hypothyroid rats observed in this study suggests the possibility that aforementioned leptin increment may at least in part be the result of enhanced synthesis in BAT. Modulation of leptin synthesis in brown adipocytes is probably caused by intensified lipogenesis characteristic for BAT in hypothyroidism [7]. Considering that, leptin is also able to exert direct effects on brown adipocytes [8] and that such effects are in general sense positively correlated with their function, observed local increase in leptin expression may support thermogenic activity of BAT in systemic hypothyroidism.

1. M. Wauters, R.V. Considine and L.F. van Gaal, Eur. J. Endocrinol 143 (2000), p. 293.
   P.J. Scarpace, M. Matheny, B.H. Polock and N. Tumer, Am. J. Physiol. 273(1997), p. E226.
2. A.L. Mark, K. Rahmouni, M. Correia and W.G. Haynes, Acta Physiol. Scand. 177 (2003), p. 345.
   J.E. Silva, Physiol. Rev. 86 (2006), p. 435.
3. H.F. Escobar-Morreale, F. Escobar del Rey and G. Morreale de Escobar, Endocrinol.138 (1997), p. 4485.
4. U. Leonhardt, E. Gerdes, U. Ritzel, G. Schäfer, W. Becker and G. Ramadori, J. Endocrinol. 163 (1999), p. 115.
5. W.J. Yeh, P. Leahy and H.C. Freake, Am. J. Physiol. 265 (1993), p. E252.
   C.A Siegrist-Kaiser, V. Pauli, C.E. Juge-Aubry, O. Boss, A. Pernin, W.W. Chin, I. Cusin, F. Rohner-Jeanrenaud, A.G. Burger, J. Zapf, and C.A. Meier, J. Clin. Invest. 100 (1997), p. 2858.

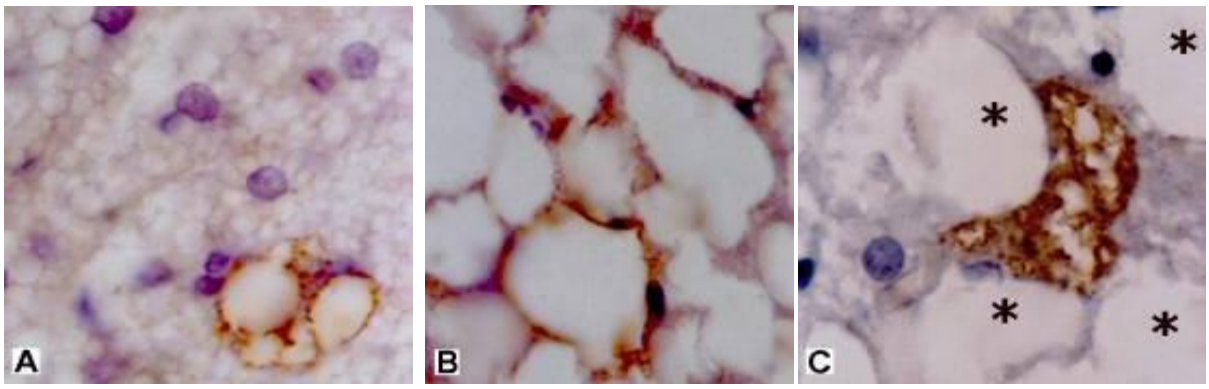

Figure 1. Types of adipocytes showing leptin-immunopositivity: multilocular adipocytes containing few large lipid droplets, observed in BAT of both control and hypothyroid rats (A), unilocular adipocytes observed in BAT of both control and hypothyroid rats (B) and classic brown adipocyte observed almost exclusively in hypothyroid rats. Note leptin-negative unilocular adipocytes closely apposed to leptin-positive brown adipocyte (✱). Magnification 100 x orig.

Tissues, Pathology, and Diagnostic Microscopy

LS.2.P070
N-acetylcysteine counteracts oxidative stress and protects alveolar epithelial cells from lung contusion-induced apoptosis in rats with blunt chest trauma

Y. Topcu Tarladacalisir[1], T. Tarladacalisir[2], M. Sapmaz Metin[1], A. Karamustafaoglu[1], Y.H. Uz[1]
M. Akpolat[3], A. Cerkezkayabekir[1], F.N. Turan[1]

[1]Trakya University, Edirne, Turkey
[2]Edirne State Hospital, Edirne, Turkey
[3]Bulent Ecevit University, Zonguldak, Turkey

yeter_topcu@yahoo.com
Keywords: Lung contusion, apoptosis, oxidative stress, N-acetylcysteine, rat

Blunt chest trauma is a common clinical problem in emergency medicine and trauma care [1]. Lung contusion affecting 17-25% of adult patients with trauma, is the most frequently diagnosed intrathoracic injury caused by blunt chest trauma [2]. Recent studies emphasized the role of inflammatory process and oxidative mechanisms have demonstrated the protective effects of anti-inflammatory and anti-oxidant agents in lung contusion after blunt trauma [3]. Despite these studies, the relationship between antioxidants and alveolar cell apoptosis in blunt trauma-related lung contusion remains to be elucidated. The aim of the present study was to investigate the frequency of apoptosis in the pulmonary epithelial cells of rats following lung contusion caused by blunt chest trauma and to determine the protective effect of N-acetylcysteine (NAC) on the peroxidative and apoptotic changes as well as alterations of surfactant protein D (SP-D) expression, mainly synthesized by alveolar type II cells in the contused lungs.

Rats were randomly divided into three groups: control, contusion and contusion + NAC groups. All groups was performed a moderate lung contusion except the control. Daily intramuscular NAC treatment (150 mg/kg) was administered immediately after blunt chest trauma and was continued for two additional days. Lung tissue samples were obtained to evaluate tissue malondialdehyde (MDA) level, histopathology and epithelial cell apoptosis by terminal deoxynucleotidyl transferase dUTP nick-end labelling (TUNEL) assay and active caspase-3 immunostaining. Furthermore, we evaluated expression of surfactant protein D (SP-D) in lung tissue, immunohistochemically.

Blunt chest trauma-induced lung contusion caused severe histopathological injury, increase in the MDA level, the numbers of TUNEL and active caspase-3 positive epithelial cells, whereas decrease in the numbers of SP-D positive alveolar type II cells. NAC treatment effectivelly attenuated histopathologic, peroxidative and apoptotic changes as well as alterations of SP-D expression in lung tissue (Figures 1,2 and Table 1).

The above findings indicate that the beneficial effects of NAC administrated following blunt chest trauma is mediated through regulation of oxidative stress and apoptosis.

1. Shorr RM, Crittenden M, Indeck M, Hartunian SL, Rodriguez A. Blunt thoracic trauma. Analysis of 515 patients. Ann Surg. 206 (1987), 200-5.
2. Miller PR, Croce MA, Bee TK, Qaisi WG, Smith CP, Collins GL, et al. ARDS after pulmonary contusion: accurate measurement of contusion volume identifies high-risk patients. J Trauma. 518 (2001), 223-8.
3. Türüt H, Ciralik H, Kilinc M, Ozbag D, Imrek SS. Effects of early administration of dexametahasone, N acetylcysteine and aprotinin on inflammatory and oxidant- antioxidant status after lung contusion in rats. Injury 40 (2009), 521–7.
4. The authors are grateful to Trakya University Research Center for the financial support of this study (Project no: 2012/90).

	Control	Contusion	Contusion + NAC	p value
Alveolar disruption/oedema/haemorrhage score	0.50 (0-1)	2.50 (2-3)[a]	1.25 (1-1.25)[b]	0.0001
Leukocyte infiltration score	1.00 (0-1)	2.25 (2-2.75)[a]	1.50 (1.25-1.50)[b]	0.0001
MDA level (µmol/L)	1.35±0.16	2.78±0.41[c]	1.38±0.12[d]	0.0001

[a]p<0.05 vs control, [b]p<0.05 vs contusion group, [c]p<0.001 vs control, [d]p<0.001 vs contusion group

Table 1. The effects of the blunt chest trauma and NAC treatment on lung histology, MDA levels and the alveolar epithelial cells apoptosis. Values are expressed as mean±S.D and median (min-max), n=6.

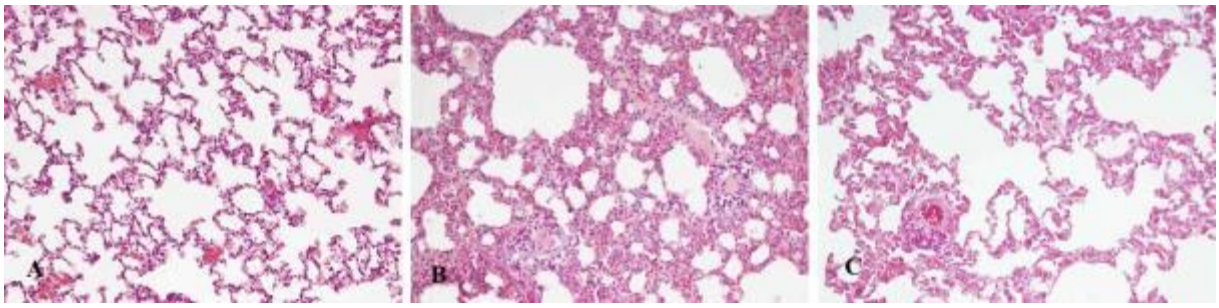

Figure 1. Photomicrographs of the histological examinations of the rat lung tissues. (A) Control, (B) Contusion, (C) Contusion+NAC. Hematoxylin-eosin; X40.

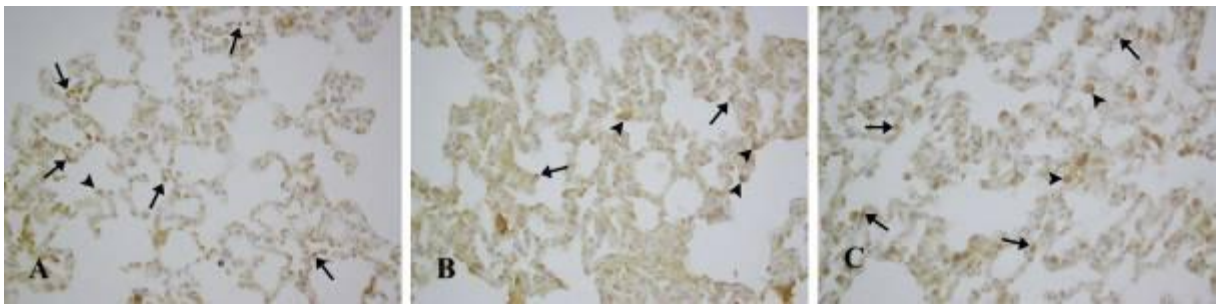

Figure 2. Photomicrographs of the immunohistochemical staining for SP-D (X40) in the lung tissues. (A) Control, (B) Contusion, (C) Contusion+NAC. Arrows; alveolar type II cells, arrow heads; alveolar macrophages.

Tissues, Pathology, and Diagnostic Microscopy

LS.2.P071
Porcine adenovirus detected in urothelial cell culture isolated from porcine urinary bladder

M. Kolenc[1], U. Dragin Jerman[2], P. Veranič[2], A. Steyer[1], M. Poljšak Prijatelj[1], M. Erdani Kreft[2]

[1]Institute of Microbiology and Immunology, Faculty of Medicine, University of Ljubljana, Ljubljana, Slovenia
[2]Institute of Cell Biology, Faculty of Medicine University of Ljubljana, Ljubljana, Slovenia

marko.kolenc@mf.uni-lj.si
Keywords: urinary bladder, cell culture, adenovirus

Cell cultures are an important research tool frequently used in life science today. Advances in cell cultivation and development of various *in vitro* models have found a number of applications in studying tissue development and function in health and disease. However, to provide reliable results, cell cultures must be free of pathogens. Contamination with bacteria and fungi usually causes visible effects on cell cultures, in contrast, mycoplasmas and viruses are difficult to detect visually and usually require special detection methods. Therefore, when establishing cell cultures from animal tissue, special caution should be taken as the animal tissue could be a potential source of contamination with pathogens.

For harvesting primary and subsequent urothelial cell (UC) cultures porcine urinary bladders were cut in large segments and UCs were gently scraped from urothelium, seeded onto plastic tissue flasks and grown in UroM medium [1]. After 3 weeks in culture, UC cultures were prepared for transmission electron microscopy [2]. Unexpectedly, in ultrathin sections of embedded cells, large paracrystalline structures in nuclei were found. Virus particles were also seen in the cytoplasm of infected cells ″Figure 1.".

For negative staining UC cultures were frozen, thawed three times and clarified by centrifugation at 1000 x *g*. Clarified supernatant was ultracentrifuged at 100 000 x *g* for 1h. Resulting pellet was resuspended in saline solution, placed onto formvar coated grids and negatively stained using phosphotungstic acid. The grids were examined with transmission electron microscope at 80 kV. From characteristic icosahedral shape morphology and size measurements between 70-90 nm, adenoviruses were identified ″Figure 2.".

Molecular diagnostic tests to detect human adenovirus as possible agent of UC contamination were performed and were negative. In addition, broader reaction primers were used to confirm adenovirus infection of UC cultures. Adenovirus was detected using PCR amplification of adenovirus hexon gene as previously described [3]. The presence of *Mastadenovirus* was confirmed by sequence analysis of hexon gene showing the highest similarity to recently described novel porcine adenovirus genotype (strain PAdV-W1) [3].

Since human tissue is usually difficult to obtain, majority of research is still done using cell cultures of animal origin. However, when establishing primary and subsequent UC cultures from animal tissue, the microbiological screening of urinary bladder tissues and UC cultures for potential pathogens is highly recommended.

1. M.E. Kreft, et al., Biol Cell 102 77 (2010), p. 593-607.
2. T. Višnjar, et al., Histochem Cell Biol 137 (2012), p. 177-186.
3. S.D. Sibley, et. Al., Appl. Environ. Microbiol 77 14 (2011), p. 5001-5008
4. We kindly acknowledge the technical assistance of Sanja Čabraja in Nada Pavlica.

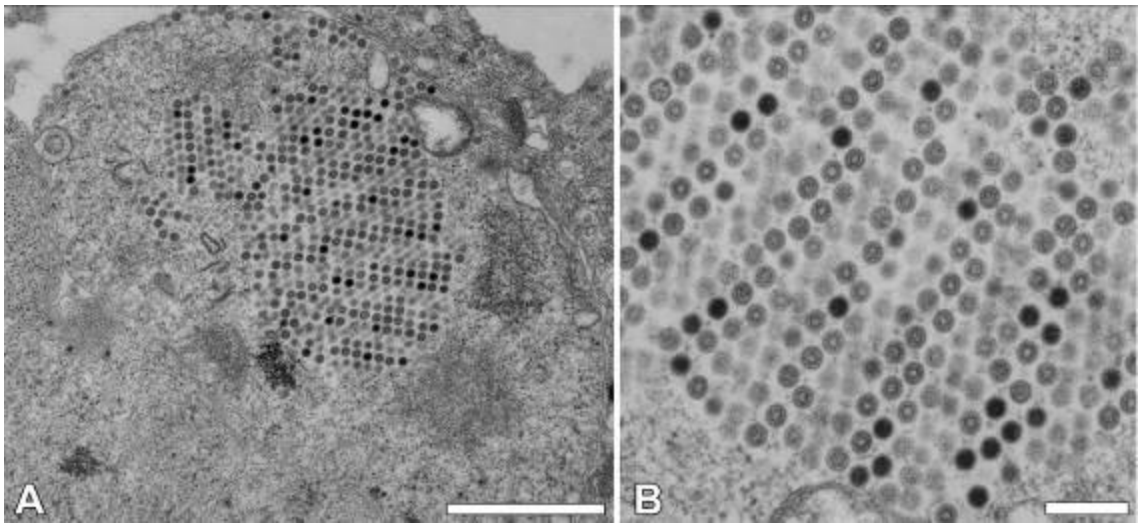

Figure 1. Transmission electron micrographs of porcine adenovirus in urothelial cell culture isolated from porcine urinary bladder. Epon resins. Scale bars, 1 µm (A) in 200 nm (B).

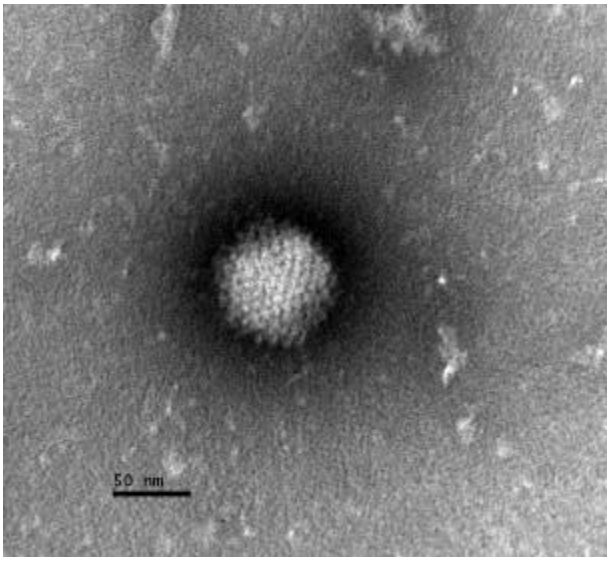

Figure 2. Transmission electron micrograph of negative stained adenovirus from porcine urothelial cell culture suspension. Scale bar 50 nm.

Tissues, Pathology, and Diagnostic Microscopy

LS.2.P072
Allopurinol ameloriates ischemia-reperfusion injury in ovarian torsion-detorsion subjected rats.

M. Sapmaz-Metin[1], Y. Topcu Tarladacalisir[1], Y.H. Uz[1], M. Inan[2], I. Kurt Omurlu[3], A. Cerkezkayabekir[4] G. Kizilay[1], M. Akpolat[5], T. Karaca[1]

[1]Trakya University, Medicine Faculty, Histology&Embryology Dept., Edirne, Turkey
[2]Trakya University, Medicine Faculty, Pediatric Surgery Dept., Edirne, Turkey
[3]Adnan Menderes University, Medicine Faculty, Biostatistics Dept., Aydin, Turkey
[4] Trakya University, Faculty of Science, Biology Dept, Edirne, Turkey
[5]Bulent Ecevit University, Medicine Faculty, Histology&Embryology Dept., zonguldak, Turkey

melikesapmaz@yahoo.com
Keywords: allopurinol, iNOS, ovary, torsion-detorsion, rat.

Adnexal torsion is the twisting of the ovary and /or tube around its vascular axis [1]. It is a gynecologic syndrome occurs mostly in adolescent girls and in women of child-bearing age [2]. Traditional treatment has been oophorectomy for these cases while the conservative approach is detorsion of the twisted segment. Thus, circulation of the ovary can be maintained after the ischemic condition, but detorsion causes primary pathophysiologic event called “reperfusion injury” [3]. The mechanisms underlying ischemia-reperfusion injury are related with oxidative stres and neutrophil activation. The inducible form of NOS (iNOS) is expressed in pathological processes and in response to pro-inflammatory agents, which produces large amounts of NO and contributes to the pathophysiology of I/R injury [4]. Reactive oxygen and nitrogen species are produced in ischemia-reperfusion conditions, at least in part, to the activation of xanthine oxidase. Allopurinol competitively inhibits the action of xanthine oxidase and effectively counteracts oxidative stress. However, its unknown whether allopurinol can ameloriate ovarian ischemia-reperfusion injury in the adnexal torsion cases. Therefore, the aim of the present study was to investigate the protective effect of allopurinol on the ovarian histopathology, inflammation and the alterations of iNOS immunoreactivity after 24 hour reperfusion period in rat ovary.

The rats were randomly divided into 3 groups; sham, 24 h detorsion plus saline, allopurinol group. Thirty minutes before detorsion, a single dose of 200 mg/kg allopurinol was administred by intraperitoneally. Ovarian tissue samples were obtained to evaluate the histopathology and to determine iNOS immunoreactivity. Furthermore, serum myeloperoxidase activity was measured as a marker of inflammation. Histopathological alterations were shown in detorsion subjected torsioned ovary. Severe to moderate hemorrhage, edema and congestion were detected in the detorsion group and increased tissue damage score also reflected this condition. Also, detorsion caused an increase in the MPO activity. Allopurinol pretreatment effectively attenuate histopathologic alterations, reduced MPO levels, without affecting iNOS immunoreactivity. (Figures 1,2).

The results indicate that allopurinol may exert its antioxidant effect via inhibition of inflammation as well as direct radical scavenging role in this model. However, detailed experimental studies are needed to elucidate the inhibitor effects on iNOS activity.

1. Oral A, Odabasoglu F, Halici Z, Keles ON, Unal B, Coskun AK, et al. Protective effects of montelukast on ischemia-reperfusion injury in rat ovaries subjected to torsion and detorsion: biochemical and histopathologic evaluation. Fertil Steril. 95 (2011), 1360-6. doi: 10.1016/j.fertnstert.2010.08.017. Epub 2010 Sep 20.
2. Descargues G, Tinlot-Mauger F, Gravier A, Lemoine JP, Marpeau L. Adnexal torsion: a report on forty five cases. Eur J Obstet Gynecol Reprod Biol. (2001), 91–6.
3. Yazici G, Erdem O, Cimen B, Arslan M, Tasdelen B, Cinel I. Genistein attenuates postischemic ovarian injury in a rat adnexal torsion-detorsion model. Fertil Steril. 87, (2007), 391-6.
4. Wu B, Iwakiri R, Tsunada S, Utsumi H, Kojima M, Fujise T, et al. iNOS enhances rat intestinal apoptosis after ischemia–reperfusion. Free Rad Biol Med. 33 (2002), 649–58.
5. The authors are grateful to Trakya University Research Center for the financial support of this study (Project no: 2011/121).

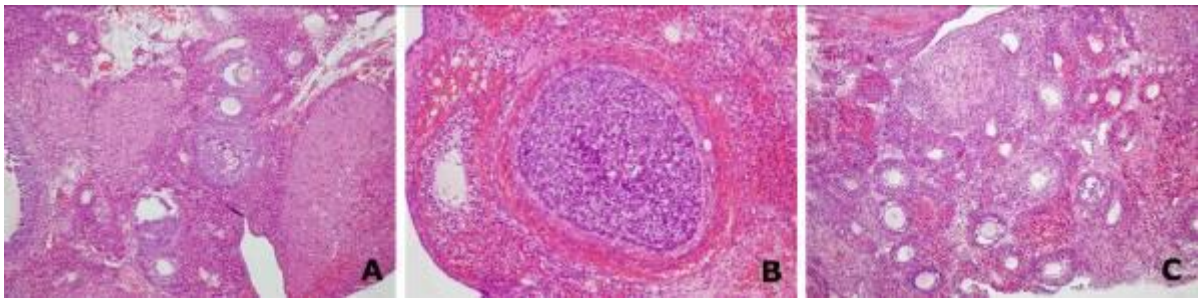

Figure 1. Photomicrographs of the histological examinations of the rat ovarian tissues. (A) Control, (B) Detorsion, (C) Detorsion+Allopurinol. Hematoxylin-eosin; X10.

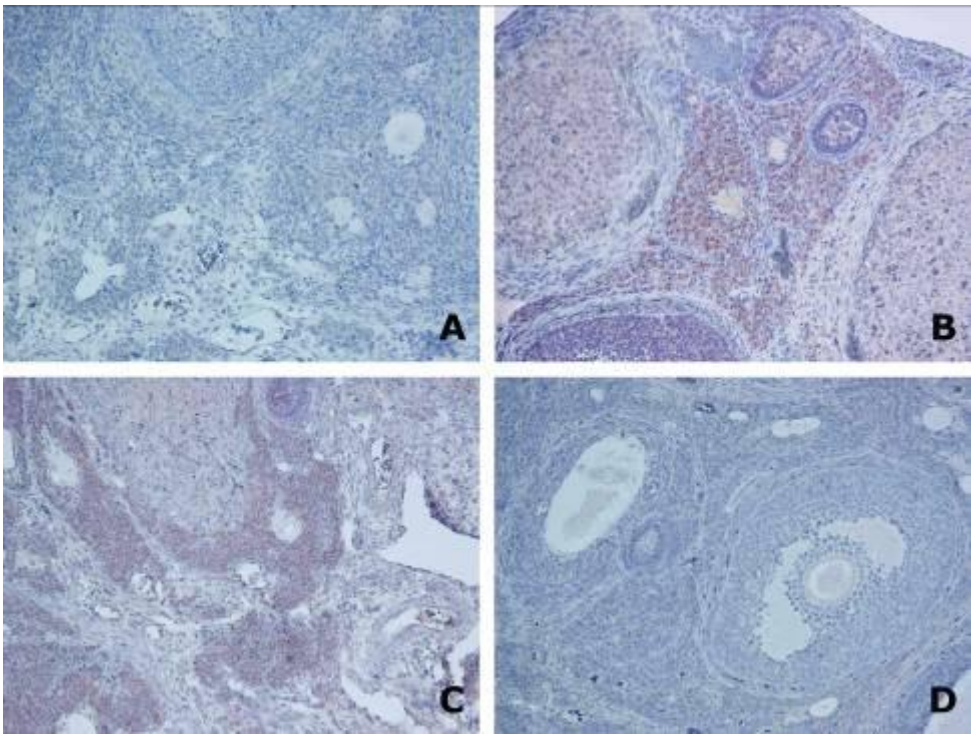

Figure 2. Photomicrographs of the immunohistochemical staining for iNOS (X20) in the ovarian tissues. (A) Sham group, (B) Detorsion group, (C) Detorsion+Allopurinol group, (D) Negative control.

Tissues, Pathology, and Diagnostic Microscopy

LS.2.P073
Does Notch1 effect on beta-cell regeneration or apoptosis in nicotinamide treated neonatal diabetic rats?

F. Kaya Dagistanli[1], M. Ozturk[1]

[1]Istanbul University Cerrahpasa Medical Faculty, Medical Biology, Istanbul, Turkey

fkaya@istanbul.edu.tr

The Notch genes are expressed in a differently of tissues in both the embryonic and adult organism. Notch signaling activated by its ligands also plays key roles in regulating proliferation, differentiation, and apoptosis [1,2]. But the molecular details are unclear and controversial. Streptozotocin (STZ), typical diabetogenic agents, induces pancreatic beta-cell DNA strand breaks through the formation of free radicals. The breaks induce DNA repair involving the activation of poly (ADP-ribose) polymerase. Nicotinamide (NA), a PARP inhibitor, is a biochemical precursor of nicotinamide adenine dinucleotide that protects beta cells from several toxic agents [3,4]. In this study we investigated the relationship between expression of notch1 with pancreas regeneration and apoptosis in NA treated neonatal diabetic rats.

Three groups were performed. The first group was the control group. The second and third groups were injected i.p with 100 mg/kg streptozotocin on the second day after birth. Second group was not given any treatment (n2-STZ). The third group received, 500mg/kg/day NA for 5 days (n2-STZ+NA) by starting from third day. The pancreatic tissue sections were immunostained with insulin, pdx-1, active caspase-3 and Notch1 antibodies and also double immunostained with insulin and PCNA antibodies. In situ hybridization carried out with insulin probe. TUNEL assay was used for detection of DNA degradation in apoptotic cells. Body weight and blood glucose levels of the animals in all groups were measured. All values were analyzed with statistical methods.

The increase of the blood glucose levels in n2-STZ+NA group were significantly decreased by NA treatment (p<0.05). The number of insulin/PCNA double-positive cells significantly increased in the n2-STZ+NA group compared with the n2-STZ *and control groups* (p<0.001). n2-STZ group had lower number of insulin and pdx-1 positive cells whereas higher number of active caspase-3 and apoptotic cells compared to control and n2-STZ+NA groups (Figure 1). We found immunopositive insulin and pdx-1 cells located in small cell clusters or scattered in exocrine tissue and close to ducts in n2-STZ+NA. There was significant difference between the numbers of Notch1 immunopositive cells when the n2-STZ+NA group pancreas tissue sections were compared with n2-STZ and control groups (Figure 2).

In conclusion, this study showed that NA treatment stimulates the duct epithelium or acinar cell differentiation into the beta cell and inhibits apoptosis. The increase of the Notch expression is inversely correlated with apoptosis while it is parallel with the beta-cell regeneration. The increased Notch1 expression in the NA treated STZ diabetic group might be protective effect on beta cells.

1. Artavanis-Tsakonas S, Rand MD, Lake RJ. Science.1999; 284:770–776
2. Dror V, Nguyen V, Walia P, Kalynyak TB, Hill JA, Johnson JD. Diabetologia. 2007;50(12):2504-15.
3. Yamamoto H, Uchigata Y, Okamoto H. Biochem Biophys Res Commun.1981,103(3):1014-20.
4. Alenzi FQ.Iran J Allergy Asthma Immunol March 2009; 8(1): 11-18.

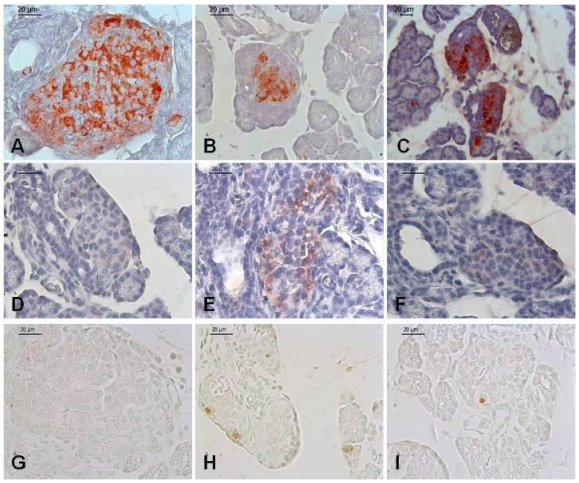

Figure 1. Immunostaining for (A-C) insulin and (D-F) caspase-3 and (G-I) labelled nuclei (brown) of apoptotic cells with TUNEL Method in the pancreatic islets of Control, n2-STZ diabetic and n-STZ+NA groups. (A,D,G) Control; (B,E,H) n2-STZ; (C,F,I) n2-STZ+NA groups. Bar: 20 µm

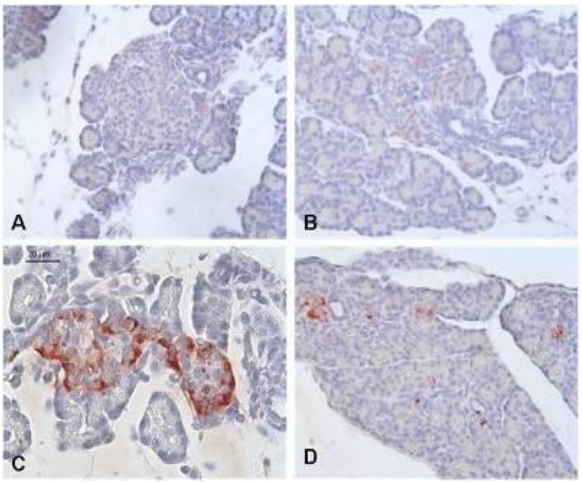

Figure 2. Immunolocalisation for notch1 in the pancreas of all groups. A, Control; B, n2-STZ; C-F, n2-STZ+NA groups (A,B,D: X20; C: X40).

Tissues, Pathology, and Diagnostic Microscopy

LS.2.P074
Protective effects of Caffeic Acid Phenethyl Ester through PI3K/AKT/mTOR pathway on ischemia-reperfusion damage in rat testicular tissue

S. Inan[1], Y. Sarica[1], G. Alper Ercan[2], A. Sencan[3]

[1]Celal Bayar University, Histology and Embryology, Manisa, Turkey
[2]Ege Universtity, Biochemistry, Izmir, Turkey
[3]Celal Bayar University, Pediatric Surgery, Manisa, Turkey

sevincinan@yahoo.com
Keywords: testicular torsion, PI3K/AKT/mTOR, CAPE, immunohistochemistry

Testicular torsion is the most common genital trauma of the adolescent boy and has been implicated in testicular injury, altered hormone production, subfertility and infertility [1]. Testicular artery occlusion causes an enhanced formation of reactive oxygen species, which contributes to the pathophysiology of testis damage [2]. In this study, we aimed to investigate the effects of caffeic acid phenethyl ester (CAPE), an antioxidant and anti-inflammatory agent [1], in rats subjected to testicular torsion ischemia/reperfusion (I/R) damage and the effects on PI3K/AKT/mTOR pathway, which involved in cell survival [3].

Twentyone male rats (2 months, 200 gr weights) were divided into three groups: control group (n=7), testis torsion Ischemia/Reperfusion (I/R) group (n=7), I/R+CAPE group (n=7). Rats, except the control group, were subjected to left unilateral torsion (720º rotation in the clockwise direction) without including the epididymis (Fig.1A). After torsion (2 h) (Fig.1B) and detorsion (4 h) periods (Fig.1C), CAPE (10 µmol/kg, i.p.) was applied after 60 min after torsion I/R. Rats were sacrificed and orchidectomy was performed after application. Testicular tissue were fixed in Bouine's solution and they were then dehydrated and embedded in paraffin. Serial sections (thickness, 5 mm) were obtained, deparaffinized, and stained with hematoxylin-eosin (H&E). Light microscopy was performed without knowledge of the groups. Histological lesions were evaluated in both the tubular and extratubular compartments. Tissue samples were then analyzed via an avidin biotin peroxidase immunohistochemistry method. Anti-PI3K, anti-AKT and anti-mTORC-1 primary antibodies were used. Staining intensities were evaluated as mild, moderate and strong using semi-quantitative method. ANOVA statistical test was used to compare the results.

Testes of control group showed no changes in histological appearance either in the tubular and the extratubular compartments (Fig. 2A). On the other hand, histological observation following ischemia-reperfusion displayed interstitial effusion together with blood vessel dilation, loosening of Leydig cells, detachment of spermatogenic cells from the basement membrane and separation between the cells and disorganisation of seminiferous tubule cells were seen in the I/R testes (Fig. 2B). Administration of CAPE reduced the histological changes in testicular tissue (Fig. 2C).

Normal seminiferous tubule cells had moderate/moderate/strong PI3K, AKT and mTORC1 immunoreactivities in control group; mild/mild/moderate immunoreactivities were seen in I/R group and strong/moderate/strong immunoreactivities in I/R+CAPE treated groups, respectively (Fig. 2).

Our results demonstrate that CAPE treatment exerts a reperative and protective effects on testicular torsion I/R damage and part of this effect may be due to activating the PI3K/AKT/mTOR signal pathway. It was thought that these pathway may play an important role in testicular ischemia/reperfusion damage pathogenesis and CAPE might be preventive role in approach to the treatment of unilateral testicular torsion.

1. E.Uz, S.Sogut, S.Sahin, et al., World J Urol (2002) 20: 264–270
2. R.J.Aitken, S.D.Roman, Oxid Med Cell Longev (2008) 1(1): 15-24
3. L.Minutoli, P.Antonuccio, C.Romeo et al., Biology of Reproduction (2005) 73, 730–736
4. Acknowledment: This project is supported by Celal Bayar University Research Foundation Project No : SAGBE 2012/055

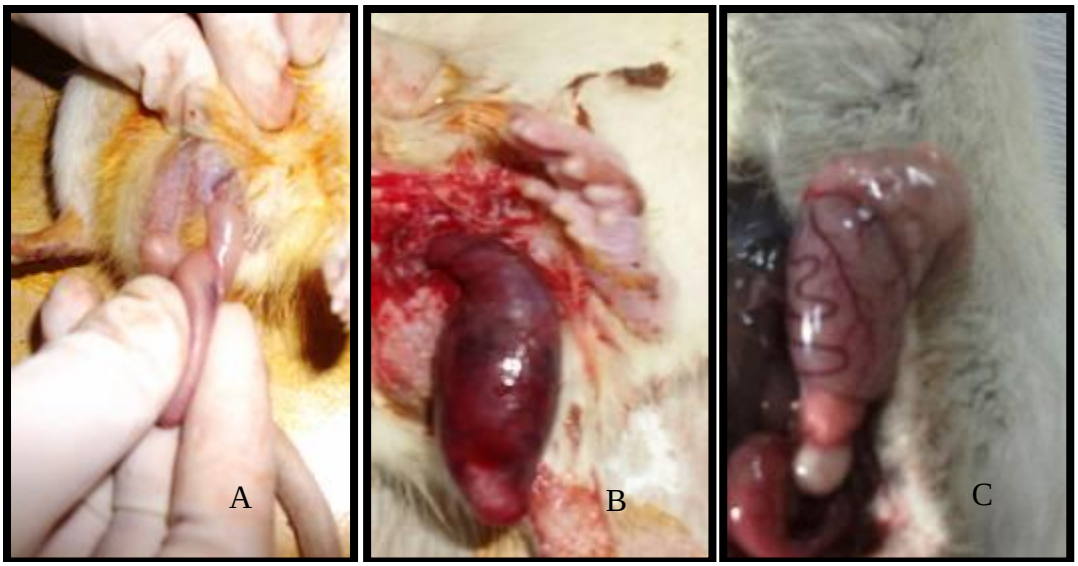

Figure 1. Photomicrographs of rat testis from Ischemia/Reperfusion Group (A), 2 Hour Torsion group (B), 4 Hour Detorsion group (C).

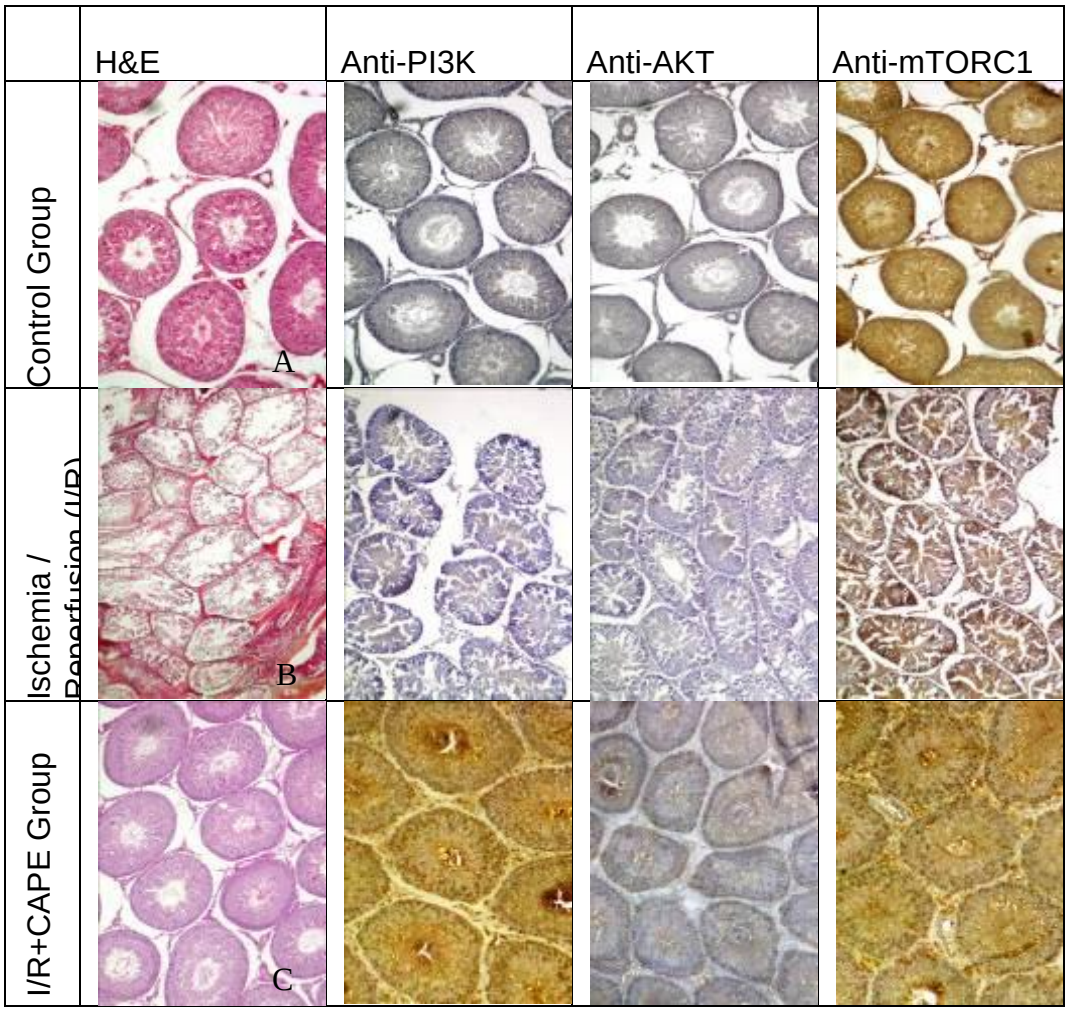

Figure 2. Immunohistochemical appearance of rat testis from control, I/R and I/R+CAPE Groups. Testicular damage in seminiferous tubules were seen in the I/R group. Immunoreactivities were seen as mild/mild/moderate in I/R group, while strong/moderate/strong in I/R+CAPE group respectively (X200).

Tissues, Pathology, and Diagnostic Microscopy

LS.2.P075
Evalution of Rapamycin Effects on MDA-MB 231 Breast Cancer Cell Line Using Immunohistochemistry and TUNEL Methods

E. Turkoz Uluer[1], M. Kıvanc[1], Y. Sarıca[1], G. Evirgen[1], S. Inan[1]

[1]Celal Bayar University, Histology and Embryology, Manisa, Turkey

drelginturkoz@gmail.com
Key words: MDA-MB 231 breast cancer cell line, Rapamycin, PI3K, Apoptosis, Immunohistochemistry

Breast cancer is the most common cancer type in the women [1]. PI3K/AKT/mTOR and Ras/Raf/MEK/ERK pathways are frequently dysregulated in cancer [2]. In this study, we aimed to evaluate the effects of Rapamycin, which is an inhibitor of mTORC1, on the MDA-MB 231 breast cancer cell line with primary antibodies involved in PI3K, ERK and apoptotic signal pathways using indirect immunohistochemistry and TUNEL methods.

MDA-MB 231 breast cancer cells were cultured in RPMI-1640 medium containing 10% fetal bovine serum, 1% L-glutamine and 1% Penicillin/Streptomycin. After growing cells on 24 well-plate, the IC_{50} dose of Rapamycin was applied to the cells and the effect of 24^{th} hour was evaluated. For the indirect immunohistochemistry and TUNEL methods, cells were fixed in 4% paraformaldehyde. Cells were incubated with anti-mTORC1, anti-mTORC2, anti-pAKT, anti-PI3K, anti-ERK, anti-IGF, anti-caspase3, anti-caspase8, anti-caspase9, anti-APAF primary antibodies with the 1:100 dilution for immunohistochemistry and TdT for TUNEL method. Diaminobenzidine was applied to the cells as chromogen and for the background staining, Mayer's hematoxylin was used. Cells were covered with mounting medium, then viewed under light microscope (Olympus BX40). The distribution of immunohistochemical intensities of primary antibodies were scored as mild (+), moderate (++), strong (+++) and very strong (++++). After counting the percent of positive staining cells, statistical significance was determined by assessment of differences using the ANOVA test. Significance was defined as $p<0.05$.

According to the immunohistochemical evaluation, mTORC1 and IGF immunoreactivities were observed to be very strong, pAKT, PI3K and ERK immunoreactivities were strong in the MDA-MB 231 breast cancer cell line (control group); while mTORC1, PI3K and IGF immunoreactivites were observed to decrease, on the other hand pAKT and ERK immunoreactivities were observed to increase in Rapamycin treated group (Rapamycin group). mTORC2 immunoreactivity was observed to be very strong in both control and Rapamycin groups (Table 1, Figure 1).

While caspase3, 8, 9 and APAF immunoreactivities were observed as moderate in control group, caspase3 and APAF immunoreactivities were observed as strong and caspase8, 9 immunoreactivities were very strong in Rapamycin group. In concordance with the immunohistochemistry results there were much more TUNEL positive cells in Rapamycin group when compared with the control group ($p<0.05$) (Figure 1, Table 1).

In this study, we showed the activation of PI3K/AKT/mTOR and ERK-related molecular signal pathways in MDA-MB 231 human breast cancer cell line using indirect immunohistochemistry and TUNEL methods. The increased immunoreactivities of pAKT and ERK might be related with negative feedback of mTORC1 inhibition by Rapamycin [3]. The intensity of immunoreactivities of caspase3, 8, 9 and APAF were higher in Rapamycin treated group compare to control group ($p<0.05$). Both intrinsic and extrinsic pathways of caspase activation might be involved in Rapamycin caused apoptosis. In conclusion, these pathways may play an important role in cancer pathogenesis and new drug development for PI3K and mTORC2 inhibition is required.

1 D.R. Youlden, S.M. Cramb, N.A.M. Dunn et al., Cancer Epidemiology 36 (2012), p. 237-248.
2. S. Grant, JCI 118 (2008), p. 3003-3006.
3. L.F. Hernandez-Aya, A.M. Gonzalez-Angulo, The Oncologist 16 (2011), p. 404-414.

ANTIBODY NAME	Control Group	Rapamycin Group	ANTIBODY NAME	Control Group	Rapamycin Group
mTORC1	++++	++	IGF	++++	+++
mTORC2	++++	++++	Caspase3	++	+++
pAKT	+++	++++	Caspase8	++	++++
PI3K	+++	++	Caspase9	++	++++
ERK	+++	++++	APAF	++	+++

Table 1. Intensity of the immunoreactivities of mTORC1, mTORC2, pAKT, PI3K, ERK, IGF, Caspase3, Caspase8, Caspase9 and APAF on Control and Rapamycin Groups

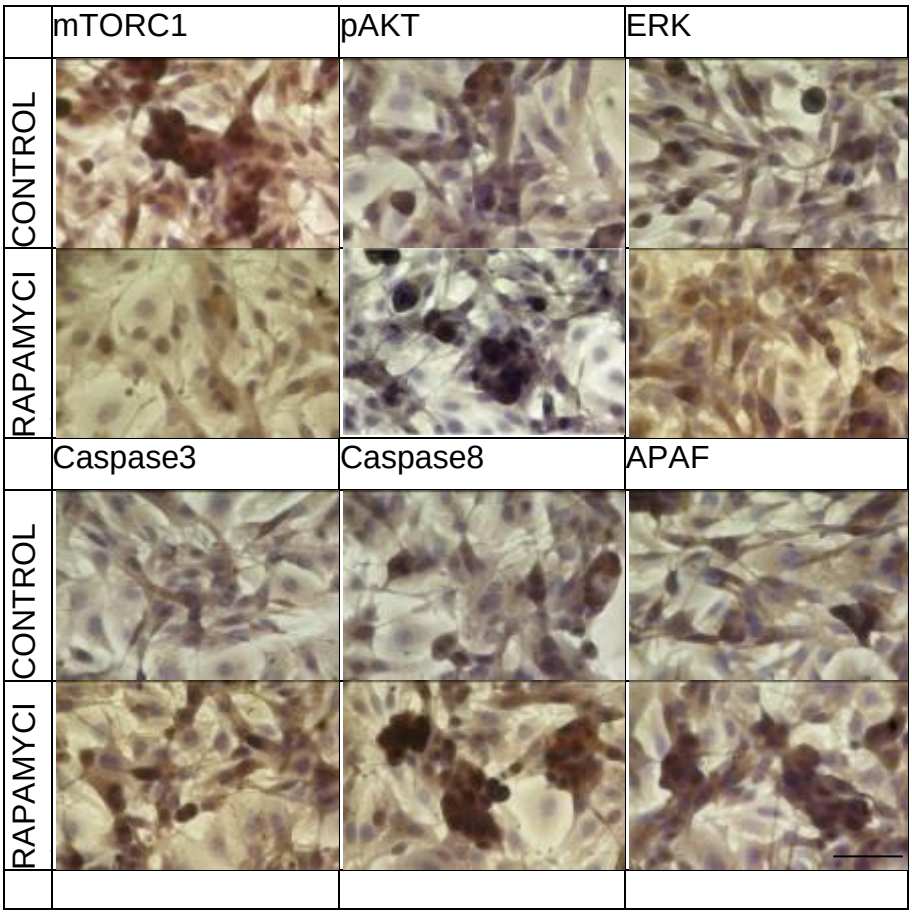

Figure 1. Distribution of mTORC1, AKT, ERK, Caspase3, Caspase8, APAF immunoreactivities of samples from Control and Rapamycin Group. Scale bar: 25µm

Tissues, Pathology, and Diagnostic Microscopy

LS.2.P076
Ultrastructural aspects of Bbil-TX (Asp49 PLA_2) from *Bothriopsis bilineata smargadina* snake venom (forest viper) in the skeletal muscle

R.S. Floriano[1], V.C. Carregari[1], R. Oun[1], S. Marangoni[1], M.A. da Cruz Höfling[1], T. Rocha[1]
L. Rodrigues Simioni[1]

[1]State University of Campinas, Department Pharmacology - FCM, Campinas, Brazil

rafast@fcm.unicamp.br
Keywords: ultrastructural analysis, Bbil-TX PLA_2, myotoxicity.

Snakebite envenoming is considered a neglected tropical disease and an important public health problem in many tropical and subtropical countries. In Brazil, there are 26 species of *Bothrops* which are responsible for ~70% of snakebites per year [1]. The venoms of these species consist of a complex mixture of toxins with various properties including proteolytic, coagulant, hemorrhagic and myotoxic activities [2,3,4]. In addition, these venoms have shown to induce *in vitro* postsynaptic and/or presynaptic neuromuscular blockade which can potentially cause tissue damage [5,6,7]. In this study, we analyzed the myotoxic effect of Bbil-TX toxin, an Asp49 PLA_2 isolated from *Bothriopsis bilineata smargadina* snake venom [8], on mammalian and avian isolated neuromuscular preparations at concentrations of 10 µg/ml and 30 µg/ml, respectively, under transmission electron microscopy (TEM). Results show that the muscle fibers affected were presented with necrotic aspects such as structural disorganization of myofibrils with severe mitochondrial damage and empty-looking sarcoplasmic reticulum which indicates loss of regular actin-myosin myofilaments pattern. The sarcoplasmic reticulum showed dilated cisterns and swollen mitochondria devoid of cristae. Schwann cells exhibited mitochondrial damage and infiltrated processes between pre- and postsynaptic compartments. Previously, we have shown that Bbil-TX has an unusual neurotoxic effect in which it produced marked neuromuscular facilitation followed by complete blockade in mammalian preparations and potent blockade at a very low concentration in avian preparations [9,10]. Experimental evidence suggests that this venom causes neuromuscular blockade by a presynaptic mechanism involving phospholipase A_2 (PLA_2). Together, these results indicate that Bbil-TX exerts a variety of *in vitro* neuromuscular effects causing muscle damage.

1. R.S. Bérnils. Brazilian Society of Herpetology. http://www.sbherpetologia.org.br/. 2010.
2. U. Kuch, D. Mebs, J.M. Gutiérrez, A. Freire. Toxicon (1996), p. 714–717.
3. B.N. Porto, C.A. Telli, T.P. Dutra, L.S. Alves, M.T. Bozza, C.A. Fin, F.V. Thiesen, M.F. Renner. Toxicon (2007), p. 270–277.
4. M.F.D. Furtado, S.T. Cardoso, O.E. Soares, A.P. Pereira, D.S. Fernandes, D.V. Tambourgi, O.A. Sant'Ana. Toxicon (2010), p. 881–887.
5. J.C. Cogo, J. Prado-Franceschi, J.R. Giglio, A.P. Corrado, M.A. da Cruz-Höfling, J.L. Donato, G.B. Leite, L. Rodrigues-Simioni. Toxicon (1998), p. 1323–1332.
6. C. R. Borja-Oliveira, A. M. Durigon, A.C.C. Vallin, M.H. Toyama, C. Souccar, S. Marangoni, L. Rodrigues-Simioni. Braz. J. Med. Biol. Res. (2003), p. 617–624.
7. L. Rodrigues-Simioni, S.R. Zamunér, J.C. Cogo, C.R. Borja-Oliveira, J. Prado-Franceschi, M.A. da Cruz-Höfling, A.P. Corrado. Toxicon (2004), p. 633–638.
8. C.V. Carregari, R.S. Floriano, L. Rodrigues-Simioni, F.V. Winck, P.A. Baldasso, L.A. Ponce-Soto, S. Marangoni. BioMed. Res. Int. (2013), article ID 612649, *in press*.
9. L. Rodrigues-Simioni, R.S. Floriano, S. Rostelato-Ferreira, N.C. Sousa, S. Marangoni, L.A. Ponce-Soto, C.V. Carregari, S. Hyslop. Toxicon (2011), p. 140–145.
10. R.S. Floriano, V.C. Carregari, V.A. de Abreu, B. Kenzo-Kagawa, L.A. Ponce-Soto, M.A. da Cruz-Höfling, S. Hyslop, S. Marangoni, L. Rodrigues-Simioni. Toxicon (2013), *in press*.

Tissues, Pathology, and Diagnostic Microscopy

LS.2.P077
The effects of Subepineurial Hyaluronic Acid injection on Nerve Regeneration.

A. Altinkaya[1], G. Cebi[2], G. Tanriverdi[3], O. Cetinkale[2], F. Alkan[3]

[1]Kahramanmaras Necip Fazil City Hospital., Plastic and Recontructive and Aesthetic Surgery Clinic, Kahramanmaras, Turkey
[2]Istanbul University, Cerrahpasa Medical Faculty, Plastic and Recontructive and Aesthetic Surgery Dept., Istanbul, Turkey
[3]Istanbul University, Cerrahpasa Medical Faculty, Histology and Embryology Dept., Istanbul, Turkey

altualtinkaya@yahoo.com
Key words: hyaluronic acid, nerve regeneration, nerve healing.

Establishing epineural integrity is very important for nerve healing. Reporting usage of substances considered that had positive effect on the nerve healing in experimentally induced nerve defect models is increasing. In this study, effects of subepineural injection of hyaluronic acid in sciatic nerve defect model that was created while maintinig the integrity of epineurium, was investigated.

Thirty - two Sprague -Dawley type female rats weighing between 200 – 250 gram were randomly divided into four groups of eigth rats each. Control Group :The right sciatic nerve was dissected from the sciatic notch to the distally and no additional surgery was performed. Experimental Group 1: The right sciatic nevre was transected in the middle part then repaired end to end with epineural sutures. Experimental Group 2: One centimeter defect was created while preserving epinerium then defect was repaired by end to end suturation of preserved epineurium. Experimental Group 3: In addition to surgical procedure was carried out in experimental group 2, subepineural injection of hyaluronic acid was performed.

In 0, 2, 4, 8 and 12th weeks walking track analysis were performed and sciatic functional index was calculated according to Bain - Mackinnon – Hunter formula. Sciatic nerve samples taken from animals were examined histologically in 12th week and average number of myelinated nerve fibers were calculated for each group.

In the end of the functional and histological examinations, healing in hyaluronic acid applied group (Experimental Group 3) is much better than no application + nerve defect only group (Experimental Group 2) and were found almost the same level with epineural repair group (Experimental Group 1) (Figure 1). As a result hyaluronic acid application enhances nerve regeneration.

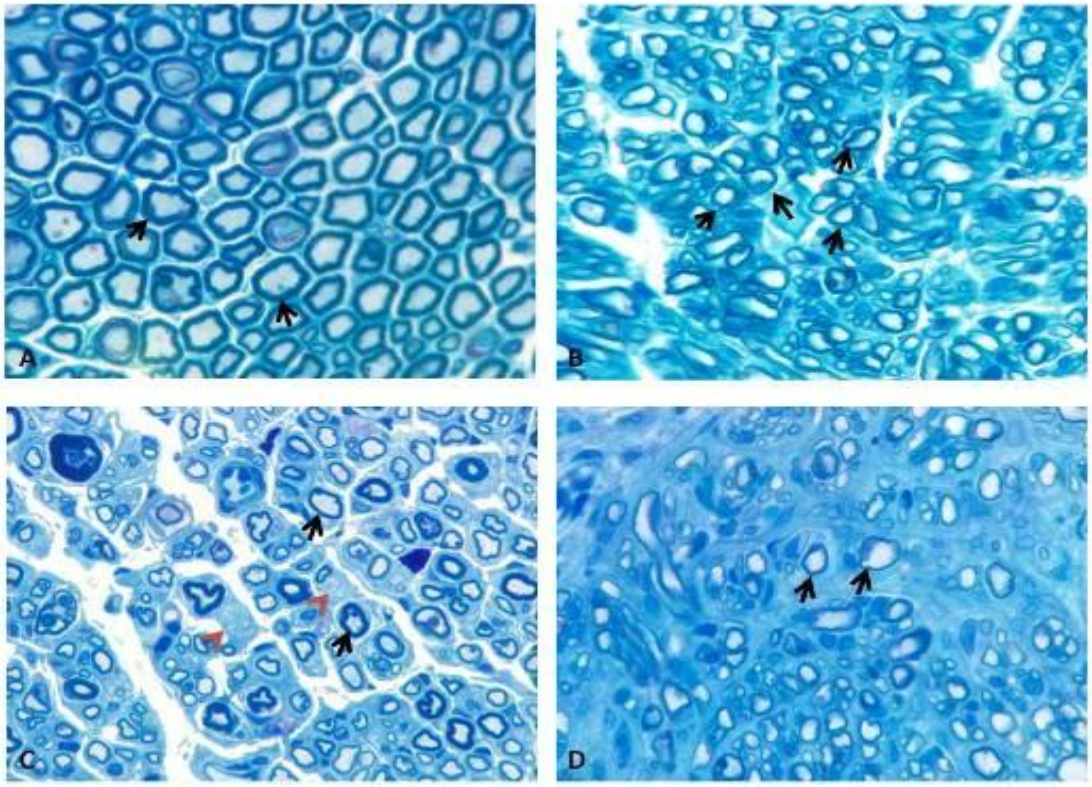

Figure 1
a.) Control Group: Myelinated nerve fibers (black arrow) Toluidin Blue x100.
b.) Experimental Group 1: Lots of Myelinated nerve fibers with different diamater (black arrow) Toluidin Blue x100.
c.) Experimental Group 2 : Lots of Myelinated nerve fibers with different diamater and also degeneratif and fibrotic areas can be seen (red arrows) Toluidin Blue x100.
d.) Experimental Group 3: Myelinated nerve fibers with different diamater were seen. Toluidin Blue x100.

Tissues, Pathology, and Diagnostic Microscopy

LS.2.P078
Confocal microscopy of expression of gingival epithelial tight junction components

P. Ye[1], H. Yu[2], M. Simmonian[1], N. Hunter[1,3]

[1]Westmead Hospital, Institute of Dental Research, Westmead Millennium Institute and Westmead Centre for Oral Health, Westmead Hospital, Australia
[2]Westmead Hospital, Microscopy laboratory, Westmead Millennium Institute, Westmead, Australia
[3]University of Sydney, Faculty of Dentistry, Sydney, Australia

Confocal microscopy was used to analyse patterns of expression of tight junction components in gingival epithelium. The gingival attachment of healthy tissues was characterized by uniform strong staining at cell contacts for tight junction components ZO-1, ZO-2, occluding, JAM-A and claudins-4 and -15. In contrast, the pocket epithelium of the periodontal lesion showed scatted, uneven staining for oral epithelial cells in culture. Following ligation of CD24 expressed by these cells the pattern of tight junction component expression of the healthy gingival attachment developed rapidly.

There was evidence for non-uniform and focal expression only of tight junction components in the pocket epithelium. In the cell culture model ligation of CD 24 induced a tight junction expression profile equivalent to that observed for the healthy gingival attachment. Ligation of CD24 expressed by gingival epithelial cells by lectin-like receptors of commensal oral streptococci could meditate the phenotype of health, whereas pathogenic organisms associated with periodontal disease might not effectively signal through CD24.

Tissues, Pathology, and Diagnostic Microscopy

LS.2.P079
Age-related changes in structural complexity of liver tissue architecture: light microscopy fractal analysis

I. Pantic[1], M. Basailovic[2], J. Paunovic[2], S. Pantic[3], M. Perovic[4], M. Trajkovic[5], D. Djuricic[6], M. Pesut[5]

[1]University of Belgrade, Faculty of Medicine, Institute of Medical Physiology, Belgrade, Yugoslavia
[2]University of Belgrade, Faculty of Medicine, Belgrade, Serbia
[3]University of Belgrade, Faculty of Medicine, Institute of Histology, Belgrade, Serbia
[4]Hospital Center "Narodni Front", Belgrade, Serbia
[5]Clinical Hospital Center "Dr. Dragisa Misović", Belgrade, Serbia
[6]Health Center Savski Venac, Belgrade, Serbia

milos.basailovic@live.mfub.rs
Keywords: Structure, Hepatic, Aging

Recent studies have determined that structural complexity of various tissues and organs may change during postnatal development and aging [1, 2]. In this study, on a mouse experimental model, we demonstrate the age-related reduction of liver tissue architecture complexity evaluated by fractal dimension.

The study was performed on the total of 64 male albino mice divided into 8 different age groups (n=8): newborns (0 days old), 10 days, 20 days, 30 days, 120 days, 210 days, 300 and 390 days old. Liver tissue was stained with conventional hematoxylin/eosin, and DNA-binding toluidine blue dyes (Figure 1). Liver lobuli were visualized with Olympus BX41 light microscope, and digital micrographs were created with Olympus C-5060 Wide Zoom digital camera instrument. After micrograph binarization, for each animal, average values of tissue fractal dimension and lacunarity were calculated using the National Institutes of Health (NIH) ImageJ software package, as previously described [1]. Parameters of tissue texture were also measured by applying Grey level co-occurrence matrix (GLCM) method on 8-bit micrographs [3].

Results indicate that during postnatal development liver tissue fractal dimension decreases while lacunarity increases. Statistically highly significant trends ($p<0.01$) were detected for both parameters. GLCM textural parameters on the other hand remained unchanged ($p>0.05$). These findings are in accordance with previous studies that suggested complexity reduction in biological structures during aging. This is also one of the first studies to apply methods of fractal and textural analysis in evaluation of liver cytoarchitecture.

1. I. Pantic, G. Basta-Jovanovic, V. Starcevic, J. Paunovic , S. Suzic, Z. Kojic and S. Pantic. Nephrology. 18 (2013), p. 117-124.
2. A. Warren, S. Chaberek, K. Ostrowski, V. C. Cogger, S. N. Hilmer, R. S. McCuskey, R. Fraser and D. G. Le Couteur. Microcirculation 15 (2008), p. 191-202.
3. I. Pantic, S. Pantic and G. Basta-Jovanovic. Microsc Microanal. 18 (2012), p. 470-5.

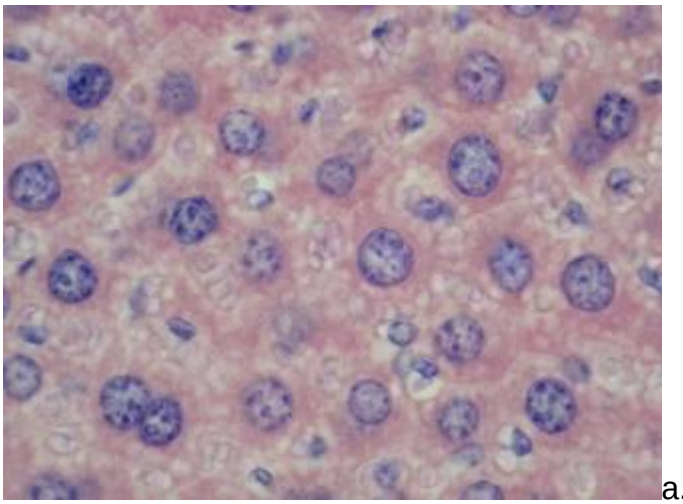
a.)

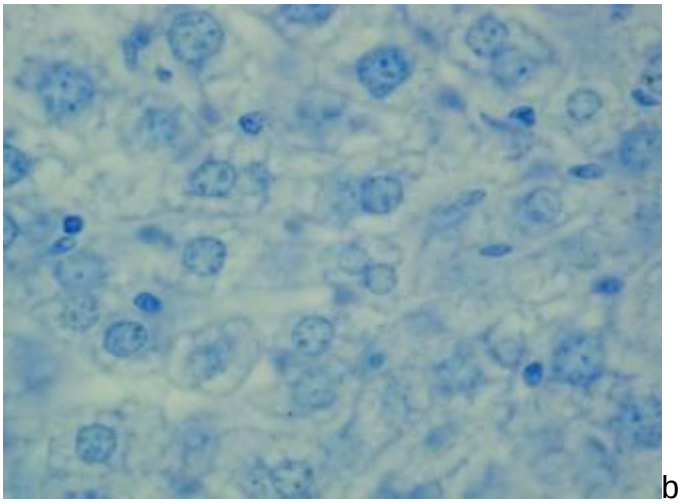
b.)

Figure 1. Digital micrographs (magnification 1000x) of the liver tissue stained with conventional hematoxylin/eosin (A), and DNA-binding toluidine blue (B) dyes

Tissues, Pathology, and Diagnostic Microscopy

LS.2.P080
Toluidine blue-stained chromatin exhibits different textural properties in thymus cortical and medullar lymphocytes

I. Pantic[1], M. Basailovic[2], J. Paunovic[2], M. Pesut[3], S. Pantic[4], M. Trajkovic[3], M. Perovic[5]

[1]University of Belgrade, Faculty of Medicine, Institute of Medical Physiology, Belgrade, Yugoslavia
[2]University of Belgrade, Faculty of Medicine, Belgrade, Serbia
[3]Clinical Hospital Center "Dr. Dragisa Misović", Belgrade, Serbia
[4]University of Belgrade, Faculty of Medicine, Institute of Histology, Belgrade, Serbia
[5]Hospital Center "Narodni Front", Belgrade, Serbia

milos.basailovic@live.mfub.rs
Keywords: Thymocyte, Texture, DNA

Texture analysis is a novel, exact and affordable computational biology technique, today commonly used for evaluation of digital micrographs in light and electron microscopy. In this study, on a mouse experimental model, we demonstrate that there is a significant difference between lymphocytes in thymus cortex and medulla regarding textural features of their toluidine blue-stained chromatin.

The study was performed on 56 male albino mice. Thymus tissue was stained with DNA-binding toluidine blue dye (Figure 1). A total of 1120 nuclear structures (560 cortical and 560 medullar lymphocytes; 20 nuclei per animal) were analyzed using Grey level co-occurrence matrix (GLCM) method as previously described [1, 2]. The algorithm based on MATLAB code (MathWorks, Natick, Massachusetts, USA) was performed on 8-bit segmented nuclei micrographs using ImageJ software (National Institutes of Health, USA). For each animal, the average values of chromatin angular second moment, GLCM contrast, entropy, and inverse difference moment, were determined.

The results indicate that the cortical lymphocytes have significantly higher values of inverse difference moment ($p<0.001$), and significantly lower values of entropy ($p<0.001$) and GLCM contrast ($p<0.001$), when compared to medullar lymphocytes. There was no significant difference in chromatin angular second moment between the two cell populations ($p>0.05$). These findings further suggest that textural analysis may become a valuable addition to conventional morphometric methods in evaluation of structural changes that take place in cell genetic material during lymphocyte migration and maturation in thymus.

1. I. Pantic, G. Basta-Jovanovic, V. Starcevic, J. Paunovic , S. Suzic, Z. Kojic and S. Pantic. Nephrology. 18 (2013), p. 117-124.
2 I. Pantic, S. Pantic and G. Basta-Jovanovic. Microsc Microanal. 18 (2012), p. 470-5.

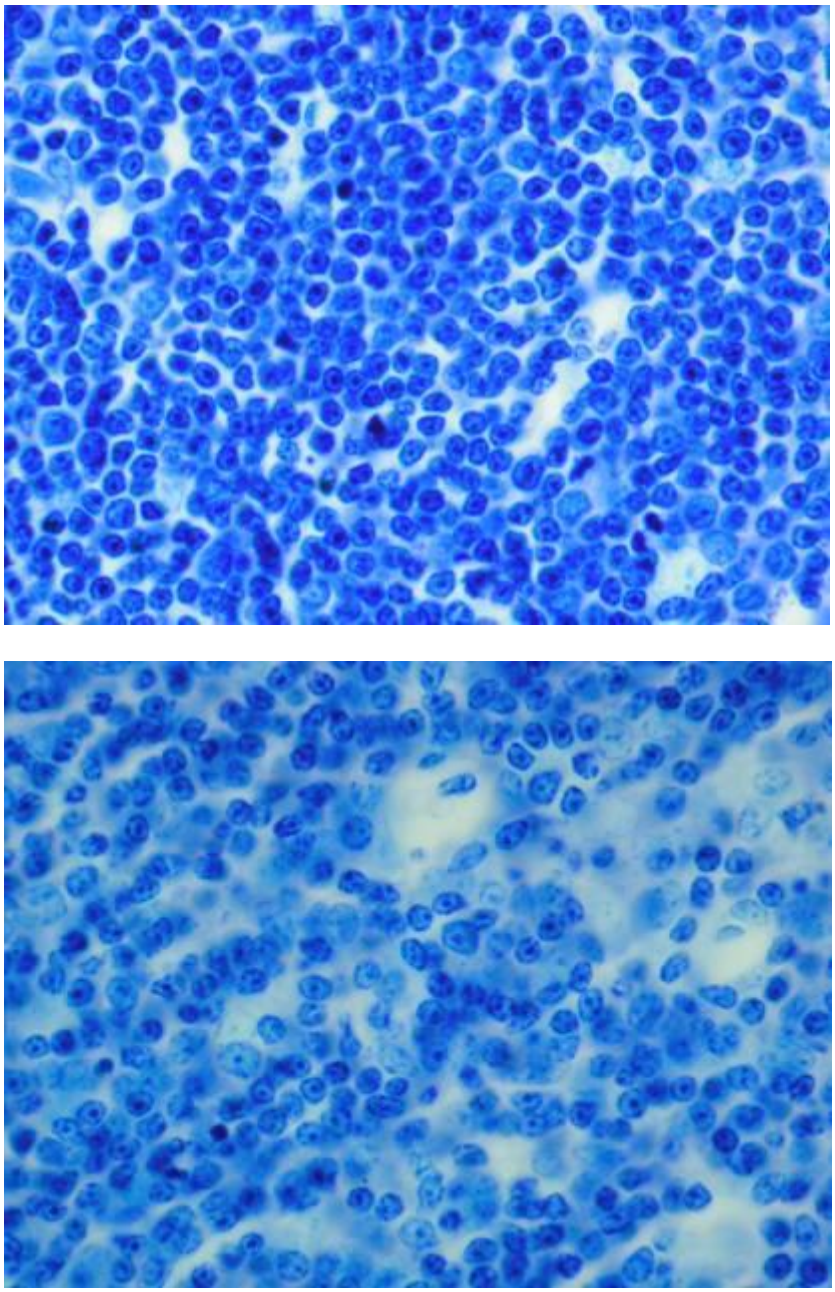

Figure 1. Digital micrographs (magnification 1000x) of the thymus t cortex (A) and medulla (B) stained with DNA-binding toluidine blue dye

Tissues, Pathology, and Diagnostic Microscopy

LS.2.P081
Macrophages and Leydig cells in testicular biopsies of infertile patients: friends or enemies?

D. Jezek[1], A. Boscanin[1], J. Cvetko[1], V. Kozina[1], A. Vukasovic[1]

[1]University of Zagreb, School of Medicine, Histology and Embryology, Zagreb, Croatia

davorjezek@yahoo.com
Key words: testis, Leydig cells, testicular macrophages

One of the most severe forms of male infertility is a non-obstructive azoospermia (NOA) [1]. NOA is frequently characterized by a heavy damage of seminiferous tubules. Much less is known on the changes of the interstitial testicular tissue, where macrophages and Leydig cells reside [2].
We assumed that, in infertile patients, macrophages exert a negative influence on Leydig cells and their androgen production. Therefore, the aim of the current survey was to investigate the above mentioned cells types within the testicular interstitium of infertile men.

In total, 120 testicular biopsies from infertile patients with azoospermia were analysed. According to their histological appearance, the biopsies could be divided into the control group (n=12, normal morphology of the testicular parenchyma) and NOA group (n=108, damaged seminiferous tubules). From paraffin and Durcopan /plastic/ embedded tissue, standard paraffin and semithin sections have been made. For the identification of macrophages, two immunohistochemical markers have been applied: CD68 (DAKO, Denmark) and KiM1P1 (Univ. of Kiel, Germany). Testosterone-producing cells also were identified by immunohistochemistry (anti-testosterone, Biogenex, USA). Leydig cells morphology (the presence of heavy vacuolated cells) was evaluated in semithin sections. Quantification of both macrophages and Leydig cells has been done using stereological methods.

Quantitative and qualitative (stereological) analysis of testicular biopsies pointed out the following changes in the infertile group: a) a significant increase in the number of macrophages; apart from the interstitial compartment, these cells could be found within seminiferous tubules; b) a significant increase in the number of Leydig cells with irregular morphology (abundant vacuolization of the cytoplasm); c) a significant decrease in the number of testosterone-producing cells; d) a negative correlation between the number of macrophages and the number of testosterone-producing cells (the more macrophages, the less testosterone-producing cells).

Based on the above-mentioned results of the histological analysis, it seems that the increased presence of macrophages has a negative impact on Leydig cells morphology and testosterone production.

1. G.R. Dohle, S. Elzanaty, N.J. van Casteren, Asian J Androl. 14 (2012), pp. 88-93.
2. S.C. Esteves, A. Agarwal, Int Braz J Urol. 37 (2011), pp. 5-15.

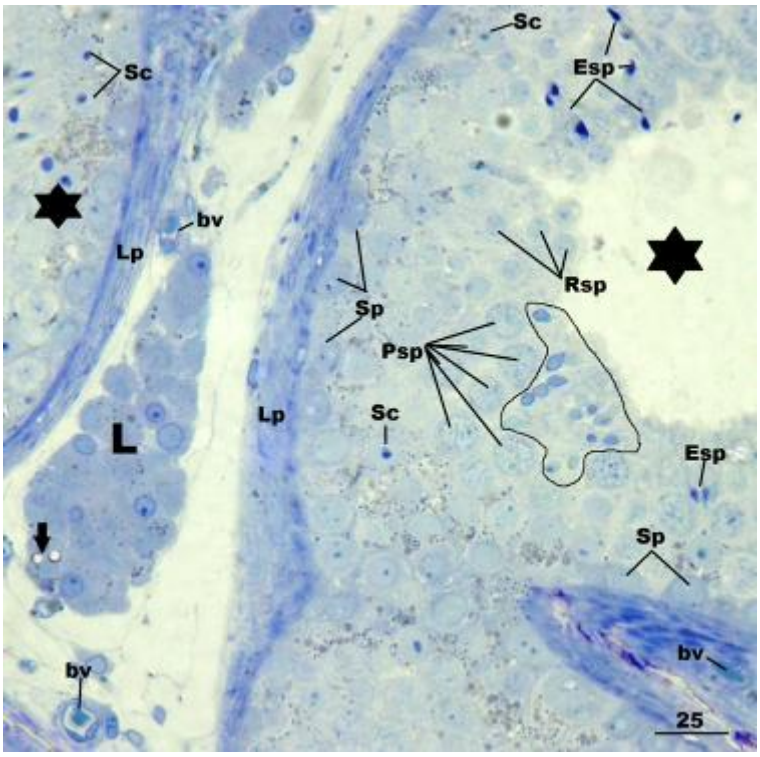

Figure 1. Control testicular biopsy with regular morphology of Leydig cells (L). Some of these cells have occasional lipid droplets (🡻). Within seminiferous tubules (✶) cells of seminiferous epithelium are seen: Sertoli cells (Sc), spermatogonia (Sp), primary spermatocytes (Psp), round (Rsp) and elongated spermatids (Esp, encircled area). (Lp-lamina propria; bv-blood vessels). Toluidine blue, x400, scale bar = 25 µm

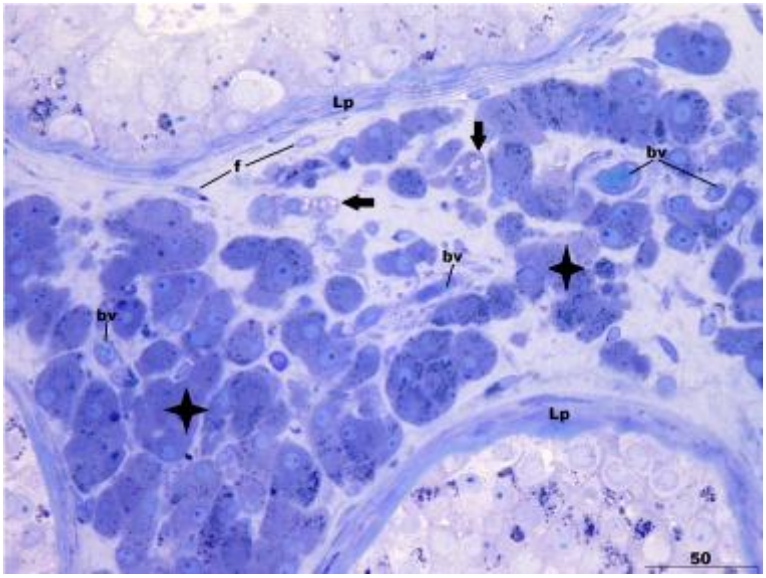

Figure 2. Hypertrophic and hyperplastic Leydig cells (✦) in the biopsy of an infertile patient. In the cytoplasm of some Leydig cells, many vacuoles and lipid droplets (🡻) are visible. (bv-blood vessels; f-fibroblasts; Lp-lamina propria). Toluidine blue, x200, scale bar = 50 µm

Tissues, Pathology, and Diagnostic Microscopy

LS.2.P082
Ultrastructural study of hepatic steatosis associating hepatitis C virus infection

S. Mansy[1], I. Nessim[1], A. AbdelFatah[1], M. Hassanein[1], M. guda[1]

[1]Theodor Bilharz Research Institute, Electron Microscopy Research Department, Giza, Egypt

Hepatic steatosis is an important hallmark of hepatitis C virus (HCV) infection. The underlying mechanisms of HCV-related steatosis however are not yet clarified. This study dealt with the ultrastructural study of mitochondrial changes in hepatic steatosis induced by HCV infection and its relation to serum cytochrome C , apolipoproteins and stage of fibrosis.

54 patients positive for HCV RNA PCR admitted to Theodor Bilharz Research Institute were enrolled in this study. They didn't have other confounding prosteatogenic variables. In addition, 10 apparently age- matched healthy volunteers were selected as a reference group. All patients were subjected to ultrasound-guided liver biopsy and blood sample collection. Meanwhile, only blood was harvested from health volunteers. Liver specimens were processed for light and electron microscopic examination. Measurement of apolipoproteins A, B,and CII and specific estimation of serum cytochrome –C was performed.

Intracytoplasmic fat depositions took the picture of large saturated fat droplets, unsaturated fat droplets or diffuse fat deposition with fluffy appearance. Interpretation of the results revealed significantly lowered serum cytochrome C in patients as compared to the reference mean value. There was significant correlation between serum cytochrome C, apolipoprotein B, and serum triglycerides. Concomitantly,the ultrastructural detected changes in the rough endoplasmic reticulum and mitochondrial ultrastructural alterations may be a contributing factor to this abnormal fat metabolism in HCV.

In conclusion, ultrastructural mitochondrial and RER changes seem to confirm their relation to the associated intracytoplamic fatty acids accumulation, the decreased serum cytochrome C and apolipoproteins A1 and B. Moreover it confirms the cytopathic effect of HCH.

Tissues, Pathology, and Diagnostic Microscopy

LS.2.P083
Hepatic Fibrogenic Cells in HCV Infected Patients: An Ultrastructural and Immunological Study

S. Mansy[1], M. Guda[1], M. Hassanein[1], H. Yehia[1], M. Nosseir[1], B. Bedeir[1], A. Zeedan[1], M. Othman[1]

[1]Theodor Bilharz Research Institute, Electron Microscopy Research Department, Giza, Egypt

Deeper and further study of the three main cells involved in hepatic fibrogenesis: hepatic stellate cell, myofibroplast and fibroblast cells may be a step forward to identify the cell which has the main impact on the process of hepatic fibrogenesis and this can be step toward hampering its action. The present work deals with the morphological and quantitative assessment and distribution of these three cells at an ultrastructural and immunological determination levels in relation to the stages of hepatic fibrosis in a group of infected patients with HCV.

54 cases positive for serum HCV RNA and not suffering from any additional cause of chronic liver diseases were enrolled in this study. Liver biopsies were collected from those patients according to Helsinki rules. Tiny liver pieces were fixed for electron microscopic (EM) examination. Paraffin embedded liver tissues were processed for morphometric image analysis and staging of liver fibrosis. Also, multiple color immunofluorescent labeling of the three studied cells was done and examined using confocal laser scanning microscopy (CLSM).

Significant correlation was detected between the values of the morphometric image analysis of liver fibrosis and the METAVIR scoring of the stage of hepatic fibrosis of the examined cases ($P<0.05$). This equally correlated with the mean value of the recorded number of myofibroblast and stellate cells ($P<0.05$; $P<0.05$). circulating bone marrow fibrocyts were depicted in the portal vein of some sections of stage 3 fibrosis. The three fibrogenic cells work in a synergistic manner in which myofibroblasts constitute the main cellular component involved in fibrogenesis.

Tissues, Pathology, and Diagnostic Microscopy

LS.2.P084
Dark Neuron Formation in uncontrolled Diabetes Mellitus; A study by TEM and Gallyas' Method

S. Ahmadpour[1], K. Foghl[1]

[1]North Khorasan University of Medical Sciences, Bojnurd, Iran, Islamic Republic of

shahahmadpour@gmail.com
Keywords: dark neuron, diabete mellitus, hyperglycemia

Dark neuron formation in uncontrolled diabetes mellitus: study by TEM and Gallyas'methods **Background:** although neuronal death has been known as the main leading cause of diabetic neuropathies the entity of neuronal death has remained as a matter of controversy.The aim of this study was to determine the type of neuronal death in uncontrolled diabetic paradigm. **Method and Material:** diabetes mellitus type 1was induced by single intraperitoneally injection of stereptozotocin in male wistsr rats at a dose of 60mg/kg.Control group recieved only saline.After 8weeks the animsls were sacrified and the hippocampi were removed and studied by Gallyas 'method and TEM.Our results showed that uncontrolled hyperglycemia induced dark neuron formation with dark brown appearance .Ultrastructurally dark neurons showd a wide varity of chromatin changes namely chromatin clumping, margination and condensation.Dark neurons also showed detached border from sorrounding. The integrity of dark neurons was preserved . **Conclusion:** Our study showed uncontrolled hyperglycemia induce dark neuron formation in hippocampus . Although these type of neurons show some criteria of apiptosis but the exact nature of dark neuron seems to be different.

Tissues, Pathology, and Diagnostic Microscopy

LS.2.P085
Distinguishing of fucose linkages in *N*-linked complex glycans at the ultrastructural level

M. Vancová[1,2], J. Štěrba[1,2], J. Langhans[1], L. Grubhoffer[1,2], J. Nebesářová[1,3]

[1]Biology Centre of the ASCR, Institute of Parasitology, Ceske Budejovice, Czech Republic
[2]University of South Bohemia, Faculty of Science, České Budějovice, Czech Republic
[3]Charles University, Faculty of Science, Prague, Czech Republic

vancova@paru.cas.cz
Keywords: labeling efficiency, cryosections, fucose

Fucosylation is an oligosaccharide modification on proteins found in invertebrates, plants, bacteria as well as in vertebrates. This study is aimed to distinguish the different linkages of fucose in *N*-linked glycoproteins in situ. We focused on terminal fucosylation and both possible linkages of core-fucosylation. Core-fucose is linked to the proximal *N*-acetylglucosamine of the pentasaccharide core by either the α1,3-linkage, which is typical for plant, trematode, and arthropod *N*-glycans; or by the α1,6-linkage widespread in mammalian/vertebrate *N*-glycans [1]. Changes in fucosylation pattern are specific hallmarks in several types of cancer cells. For example, α1,6-core-fucose linkage of on the α-1-antitrypsin protein is a cancer specific marker in patient with hepatocellular carcinoma [2].

We used soluble glycoproteins containing fucose in the known type of linkage to oligosaccharide and dissolved them separately in gelatin. We used glycoproteins containing either core-fucose only in α1,6-linkage (porcine thyroglobulin); or core fucose only in α1,3-linkage (horseradish peroxidase type II); or terminal fucose (human α1-acid glycoprotein); or lactoferrin from human milk containing both α1,6- linked core fucose and terminal fucose. After initial formaldehyde fixation, material was prepared using two methods: preparation of cryosections and embedding of the material into LR White resin that was UV polymerized at -20°. Sections of glycoproteins were labeled using fucose-specific lectins and specific antibody directed to α1,3-linked core-fucose (anti-Fuc). Deglycosylation enzymes were used as pretreatment of both cryo- and resin sections prior the specific glycan labeling. Results of gold labeling were quantified and statistically evaluated.

Our results proved the possibility to localize and to distinguish glycoproteins containing both α1,3-core-fucose and/or α1,6-core-fucose from terminal fucosylation in the case of bi- and tri-antennary N-linked complex glycans. α1,6-core-fucosylated glycans were positively labeled with lectins from *Aleuria aurantia* (AAL) and *Lens culinaris* (LCA). Glycopeptidase F (cleaving off the whole N-glycan except of α1,3-core-fucosylated ones) treatment of either cryosections or resin sections lead to negative lectin binding, whereas pretreatment of sections using endoglycosidases F2/F3 (leaving the proximal GlcNAc of N-glycans and the fucoses linked to it) cause negative LCA and positive AAL binding reactions. Generally, the labeling efficiency of fucosylated oligosaccharides was higher in cryosections than in resin sections (Figure 1A); however treatment of resin sections with endoglycosidase increased the AAL labeling of α1,6 core-fucose to values close to the labeling efficiency values of labeled cryosections (Figure 1B). This fact proved that accessibility to the core of the glycosylated glycans is a critical factor in resin embedded material. Efficiency of labeling obtained with antibody against the α1,3-core-fucosylation was 66% in cryosections and was considerable lower in resin sections (16%).

1. B. Ma, J.L. Simala-Grant, D.E. Taylor, Glycobiology 16 (2006), p.158R.
2. M.A. Communale, L. Rodemich-Betesh, J. Hafner, M. Wang, P. Norton, A.M. Di Bisceglie, T. Block, A. Mehta, Plos One 5 (2010), p. e12419.
3. This work was supported by the Grant Agency of the ASCR (Z60220518) and Technology Agency of the Czech Republic (TE 01020118).

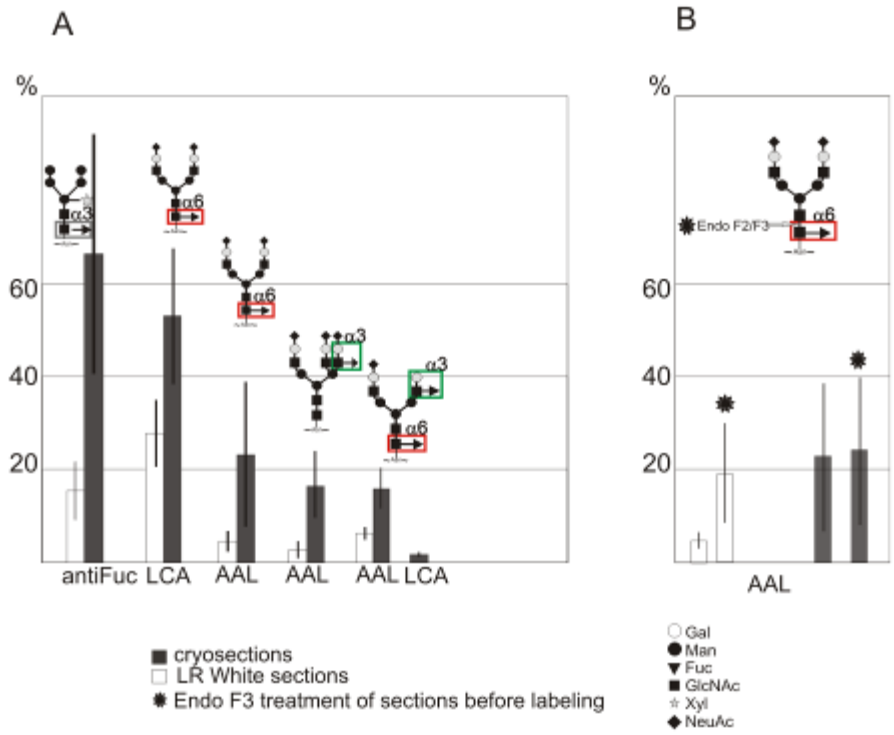

Figure 1. Labeling efficiency of different fucose linkages present in the sections of randomly dispersed soluble glycoproteins (A). Accessibility of α1,6-core fucose is crucial for successful AAL labelling of resin embedded material in contrast to cryosections (B).

Tissues, Pathology, and Diagnostic Microscopy

LS.2.P086
The fine structure of the *Anopheles aquasalis* spermatheca

T. Pascini[1], M. Ortigão[2], G. Martins[1]

[1]Universidade Federal de Viçosa, Biologia Geral, Viçosa, Brazil
[2]Kansas State University, Entomology, Manhattan, United States

gmartins@ufv.br
Keywords: spermatheca*, Anopheles aquasalis*, mosquito reproduction

The mosquito spermatheca is the female organ responsible for storing and maintaining the viability of the male sperm after copulation. Taken that mosquitoes only mate once, understanding how the sperm in maintained throughout the female lifespan may provide clues on to how to control fertilization in mosquitoes [1,2]. Here, we investigated the fine structure of the spermatheca in the saltwater-tolerant mosquito *Anopheles aquasalis*, a vector of malaria in Brazilian coastal marshes.

Virgin and inseminated female spermathecae were dissected and fixed in paraformaldehyde 4% in PBS 0.1M and/or glutaraldehyde 2.5% 0,1M cacodylate buffer pH 7.2. After dehydration in ethanol series samples were embedded in Leica historesin, sectioned and stained with hematoxylin and eosin. For electron microscopy (SEM and TEM) analyzes, samples were post-fixed in 1% osmium tetroxide and dehydrated in ethanol (crescent series). Samples were critical-point dried using CO_2 and gold-coated by sputtering for SEM (LEO 1430VP) or embedded in LR White resin. Ultra-thin sections were stained with uranyl acetate and Reynold's lead citrate and analyzed under TEM (Zeiss EM109).

The spermatheca of *An. aquasalis* consists of a sac-like reservoir connected to the genital chamber by means the spermathecal duct (Figs. 1, 2). Externally to the duct, muscle fibers are found between the duct individual glandular cells (Fig. 3). Glandular cells are also seen in the reservoir epithelial wall. These cells have well-developed structures where glandular secretion is stored before being released into the reservoir lumen (Fig. 5). These cells also have microvilli packed tightly together, particularly where they converge with the cell ductule (Fig. 6). The ductules transport cell secretory products to the spermathecal lumen. The ductule openings form pores surrounded by a very thin epicuticle that is continuous with the spermathecal cuticle and project towards the reservoir lumen together with the laterally-associated epithelial cells (Figs. 4, 5).

The spermatheca in *An. aquasalis* share many features with the three spermathecae found in *Aedes aegypti* [3, 4]. However, significant differences such as the cell types that make up the spermatheca, as well as their numbers and distribution were observed. One of the most remarkable differences observed between these two mosquitoes is the absence of an individualized secretory glandular unit in *An. aquasalis*, which is present in *Ae. aegypti* [3,4]. In *An. aquasalis*, such secretory function is performed by glandular cells distributed along the spermatheca reservoir wall [5].

The spermathecae of anophelines and culicines display significant morphological differences that may be suggestive of species-specific variations. Such differences include the sperm storage capacity measured as the total volume of the organ, as well as the cell types, number and distribution, and the length of the spermathecal duct. In *An. aquasalis* females, the spermatozoa viability is likely maintained by isolating the spermatozoa inside the spermathecal reservoir, and by the spermathecal glandular secretions that provide nourishment to the spermatozoa in the spermathecal lumen. Understanding the spermatheca organization and function will contribute to unknown details of mosquito reproductive biology, and help answer questions related to the reproductive success of these major disease vectors [6,7]. Acknowledgments: Fapemig, CAPES and CNPq for financial support.

1. F. Avila, L.K. Sirot, B.A. LaFlamme, C.D. Rubinstein and M.F. Wolfner, Ann Rev Entomol 56 (2010), p. 21-40. W.A. Foster and E.D. Walker in "Medical and Veterinary Entomology", ed. G.R. Mullen and L.A. Durden,(Elsevier, Amsterdam) (2009), p. 207-59.
2. A.N. Clements and S.A. Potter, J Insect Physiol, 13 (1967), p. 1825-36.
3. T.V. Pascini, M. Ramalho-Ortigão and G.F. Martins, Mem Inst Oswaldo Cruz, 107 (2012), p. 705-12.
4. M.E.C. Giglioli, Riv Malariol, 42 (1963), p. 149-76.
5. D.W. Rogers, M.M.A. Whitten, J. Thailayila, J. Soichotb, E.A. Levashinab and F. Catteruccia, Proc Natl Acad Sci, 105 (2008), p. 19390-395.
6. L.K. Sirot, M.C. Hardstone, M.E.H. Helinski, J.M.C. Ribeiro, M. Kimura, P. Deewatthanawong, M.F. Wolfner, L.C. Harrington, PLoS Negl Tropl Dis, 5 (2011), e989.

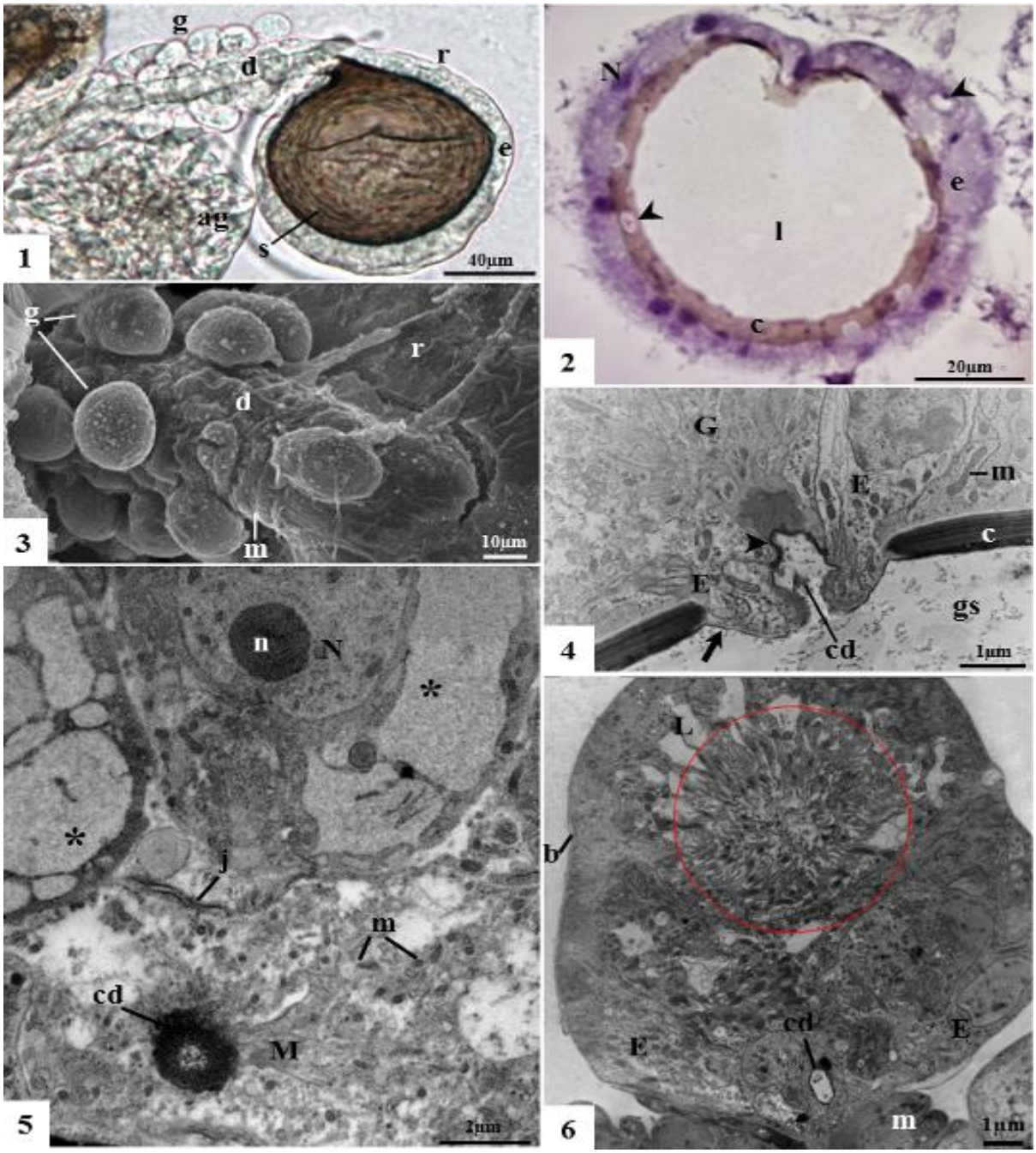

Figure 1. The round sac-like structure of the spermathecal reservoir (r) of the *An. aquasalis* female with a dark-brown cuticular capsule surrounded by the reservoir epithelium (e). The circular orientation of spermatozoa (s) in seen in inseminated female. Duct glandular cells (g) are seen attached to the spermathecal duct (d) surface; ag- accessory gland.

Figure 2. The reservoir lumen (l) is lined by the thick cuticle (c) and the epithelium with prominent glandular cells and their ductules (arrowheads), which co-localize with the cuticle pores; N- reservoir gland cell nucleus. The cell ductule (cd) is lined by the cuticle and is associated to microvilli (M) and mitochondria (m).

Figure 3. The spermathecal duct (d) with attached glandular cells (g) and muscle fibers (m).

Figure 4. The apex of a reservoir glandular cell (G). The cell ductule opens into the cuticle pores of the lamellate cuticle. The arrow points the very thin epicuticle that continues with the cuticle and lines the finger-like projection of the epithelial cells (E). This epicuticle (arrowhead) becomes thicker in the cell ductile bottom. gs- gland secretion.

Figure 5. TEM of the reservoir gland cells tightened by means of septate junctions (j). Note the presence of secretions/nutrients accumulated within cells (*). The cell nucleus and nucleolus (n) are prominent.

Figure 6. TEM of the duct glandular cell with densely package microvilli (red circle) and lacunae (L). Epithelial cells are associated the gland cell lateral sides and ductule; b- basal lamina; p- muscular pump.

Tissues, Pathology, and Diagnostic Microscopy

LS.2.P087
Histopathological and ultrastructural studies on cases of enzootic bovine leukosis in Upper Egypt

S. Elballal[1]

[1]Sadat City University, Pathology, Sadat City, Egypt

salah.elballal@yahoo.com

Enzootic bovine leukosis is a naturally occurring lymphoid cancer of cattle caused by bovine leukaemia virus. A limited outbreak EBL was reported for the first time in Assiut ,Egypt in an imported Holstein Friesian(Zaghawa et al.1998) .The proviral DNA was detected by reverse transcryptase polymerase chain reaction (Zaghawa et al.1998) .Viral particles were demonstrated by transmission electron microscopy in the peripheral blood leukocytes of affected cows(Abd Elrahim and Elballal1999).This report aimed to describe the histopathological and ultrastructural features of lymphoma in the lymph nodes and other organs of the affected cattle. Tissue samples were collected from supramammary, prescapular, mesenteric and retropharngeal lymph nodes as well as spleen and Peyers patches.Tissues were fixed in 10% neutral buffered formalin and 5% cacodylate buffered glutaraldehydefor light and transmission electron microscope respectively. The histologic determinations included lymphoma with diffuse or follicular architecture, presence of sclerosis, and cell type according to the National Cancer Institute Working Formulation(NCIWF) for classification of human non Hodgkins lymphoma (Vernau et al.,1992).Light microscopy of the involved lymph nodes revealed that the majority of the tumors had a diffuse pattern .The predominating cell types were diffuse large cell and diffuse large cleaved cell. Transmission electron microscope further demonstrated the ultrastructural features of the different cell types seen by light microscopy. Fibrillogranular bodies were observed in the nuclei of many neoplastic cells. Apoptotic cells were frequently observed in these tumours lesions. The significance of these results will be discussed.

Tissues, Pathology, and Diagnostic Microscopy

LS.2.P088
Scanning electron microscopy of plasma-filter components and erythrocytes in plasmapheresis and laser irradiation

A. Butaev[1,2], B. Saidkhanov[3], O. Irisov[1], I. Baybekov[2]

[1]Republican Specialized Center of surgery named after V.Vakhidov, Thoracic surgery, Tashkent, Uzbekistan
[2]Republican Specialized Center of surgery named after V.Vakhidov, pathology, Tashkent, Uzbekistan
[3]Republican Specialized Center of surgery named after V.Vakhidov, Experimental Surgery, Tashkent, Uzbekistan

azazello78uz@gmail.com
Keywords: plasmapheresis, laser irradiation, erythrocytes, scanning electron microscopy

The interaction of blood cells and especially erythrocytes (E) with the components of apparatus used for hemosorption and plasmapheresis (PPh) causes changes in their shapes. This can be a leading cause of various complications. It can be assumed, even a priori, that the main part of pathologic E would be retain in the meshes and membranes of plasma- filters. Laser influences contribute to reduction of pathologic forms of E. Scanning electron microscopy is the most objective method in studying forms of E and other structures. However, studies of membranes and meshes of plasma-filters in plasmapheresis and laser irradiation (LI) of these circuits with SEM were not performed. This has determined the objectives of performing such work.

Plasma-filters were studied with SEM after Pph, which was performed with laser irradiation of plasma-filters and without it. Laser irradiation was performed on the initial stages of perfusion with “Matrix-VLOK”, attached to it irradiating nozzle, which emits waves with length of 0.63 microns (red), output power – 1.5 mW. For SEM purposes, the fragments of meshes and membranes were fixed in glutaraldehyde with their after fixation in osmium tetraoxide. SEM samples were dried by processing through critical point in nitrous oxide in “HCP-2” (Hitachi) and ion sputtered in IB-3” (Eiko, Japan), studied with “Hitachi S-405A” SEM and micrographs obtained with attached to SEM Canon camera.

It was revealed that the surface of plasma-filters is even with numerous micropores. Significant accumulations of E with dominating among them pathologic forms are notable after Pph. (Figure.1). The fragments of meshes reveal single discrete complexes, representing mainly pathologically changed E (Figure.2-4). Application of LI leads to restoration of normal discoid shape of erythrocytes and therefore prevents complications.

1. Baybekov I., Mavlyan-Khodjaev R., Erstekis A. Moskvin S. Erythrocytes in norm, pathology and laser irradiation. Tver – “Triad”. 2008. P. 255
2. Baybekov A., Butaev A. Influences of extracorporeal detoxication and laser irradiation of blood on the shape of erythrocytes and microcirculation. Digest of VII International Conference “Urgent issues of extracorporeal detoxication of blood in intensive therapy”. Moscow 2012. P. 60.

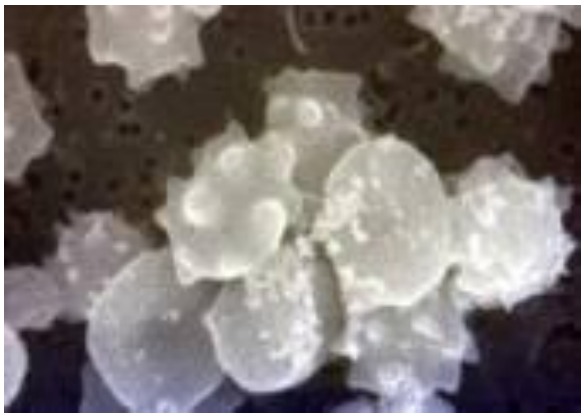

Figure 1. Pathologic forms of erythrocytes on the surface of filter membranes. SEM x2000

Figure 2. Catcher-mesh with single discrete particles SEM x1000

Figure 3. Mesh of plasma-filter SEM x60

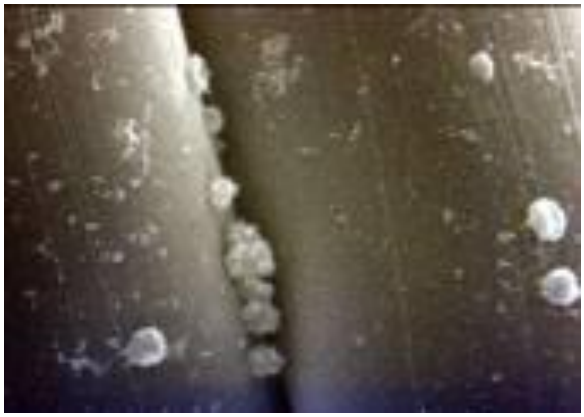

Figure 4. Mesh of plasma-filter SEM x1000

Tissues, Pathology, and Diagnostic Microscopy

LS.2.P089
Correlation of the forms of erythrocytes, microcirculation and ultrastructure of cell in pathology and laser influence.

I. Baybekov[1], A. Butaev[1], B. Ibadov[1], F. Khashimov[2], A. Baybekov[1]

[1]Republican Specialized Center of surgery named after V.Vakhidov, pathology, Tashkent, Uzbekistan
[2]Tashkent state medical academy, dermathology, Tashkent, Uzbekistan

baibekov@mail.ru
Keywords: discocytes, pathologic forms of erythrocytes, microcirculation, ultrastructure, laser irradiation

A number of pathologic conditions: peptic ulcers, liver cirrhosis, dermatoses, myasthenia etc. are accompanied with increase of pathologic forms of erythrocytes - PFE in peripheral blood. Increase of the share of PFE determines disturbances of microcirculation, and is associated with characteristic cellular changes in corresponding organs, which all represent the structural base of pathologic processes [1,2].

Laser irradiation on pathologic areas (local laser irradiation - LLI) as well as intravascularly irradiation of peripheral blood - ILIB) is the effective method for reducing the mentioned changes. [1,2]. Analysis of correlations between the ratios of erythrocyte forms, parameters of microcirculation, structure of pathologically changed organs and actions of laser had not been performed before. This determined the objectives of present work: to find interdependence between the ratios of erythrocyte forms, level of microcirculation and reduction of ultrastructural alterations of cells under influence of laser therapy-LT.

Structural changes of organs in pathology and shifts in the ratios of forms of erythrocytes (mainly ratio of dyscocytes (D) to PFE) in peripheral blood as well as those sampled from areas of lesions were studied by means of light, transmission, scanning electron microscopies, and morphometry. The range of pathologies included hemorrhages, hepatic encephalopathy, myasthenia, some dermatoses, acne and post-acne scars. ILIB was administered every other day (10-12 sessions in total) with “Matrix-VLOK”, with attached to it irradiating nozzle, which emits waves with length of 0.63 microns, output power – 1.5-2 mW, and supplied with special Teflon coated needles. The parameters of LLA on pathologic foci were following: exposition time 5 min, frequency 1000 Hz, every day, number of session 5-10. Microcirculation was assessed with LAKK-01 and Vostok-DVA-01

In all, studied types of pathologies there were some variants of changes in the ratio of D and PFE. Depending on type of pathology there can be 1.5 – 2-fold decrease of the normal share of D, while share of some PFE may increase 1.5 to 10-fold. This is accompanied by corresponding specific changes of microcirculation and of ultrastructure in the areas of lesions in organs. It is characteristic that the share of PFE in the blood sample taken from foci of lesions 1.5 – 2 times higher than in the samples of peripheral blood taken from same patients. Separate LLI and separate use of ILIB cause marked reduction of the changes in organs and normalization of erythrocytes in blood. However, the most obvious normalization could be achieved by complex application of both LLI and ILIB. Among the variety of methods of irradiation of blood the most effective one is that, which has length of waves equal to 0.63 micron. LLI of foci of pathologic changes not only causes reduction of structural alterations but also normalizes the ration of discocytes and PFE. Complex LT, on the other hand, allows achieving even greater normalization of erythrocytes, reduction of intravascular microthrombi, which lead to normalization of microcirculation and to restoration of altered ultrastructures.

Application of LT in various pathologies leads to enhanced correction of specific changes due to restoration of normal discal shape of erythrocytes and therefore improvement of microcirculation, compromise of which is one of the essential pathogenetic mechanisms in many conditions. The most optimal method of LT, in our opinion, is combination of local irradiation of lesions with intravascular irradiation of peripheral blood.

1. Baybekov I., Mavlyan-Khodjaev R., Erstekis A. Moskvin S. Erythrocytes in norm, pathology and laser irradiation. Tver – “Triad”. 2008. P. 255
2. Baybekov I.M., A. I. Ibragimov, S.M. Rizaeva, A.I. Baybekov. Application of laser therapy for reduction of changes in erythrocytes and cells of body in their pathology. Abstracts of Laser Helsinki 2010 Congress. 20-23 August. 25, p. 13.

Tissues, Pathology, and Diagnostic Microscopy

LS.2.P090
Ultrastructure of fat tissue, used for lipofilling with laser irradiation.

A. Baybekov[1], I. Baybekov[1]

[1]Republican Specialized Center of surgery named after V.Vakhidov, pathology, Tashkent, Uzbekistan

baibekov@mail.ru
Key words: lipofilling, grafts, plastic surgery, neovasculogenesis, laser irradiation, Electron microscopy

Usage of own fat tissue to correct shapes and sizes of body parts and organs – lipofilling is ever more widely used in plastic surgery. The method is characterized as having good cosmetic effect and by the fact that it does not leave any pathologic reactions or scars.
We have carried out a morphologic assessment of aspirates, including that with scanning electron microscopy (SEM). The studies proved that good vascularization of transplant plays key role in achieving the highest effect from lipofilling. [1,2].

One of the means of stimulating vasculogenesis is low intensive laser irradiation-LILI. [2]. There were no studies concerning the changes of ultrastructure of fat tissue, exposed to LILI and used for lipofilling. This have determined the aim of present study: to evaluate with electron microscopy the influences of LILI on fat tissue used for lipofilling.

The structural features of fat used for lipofilling were studied with TEM, SEM and light microscopies. Samples were fixed in 2.5% glutaraldehyde solution on phosphate buffer (pH 7.4). After dehydrating in alcohols of ascending concentration, TEM samples were embedded into epon-araldite mixture and ultrathin section, after double contrasting, were studied in “Hitachi H-600” TEM. SEM samples, dried by processing through critical point in nitrous oxide in “HCP-2” (Hitachi) and being ion sputtered in IB-3” (Eiko, Japan), were studied with “Hitachi S-405A” SEM.

Local irradiation was performed with “Mustang 017-MCS-PC” with attached to it magnetic nozzle or “Erga”, having magnetic field strength of 50 and 90 mlT; the time of exposition to irradiation -5 min, frequency 1000 Hz. All types of laser exposures were performed daily, with 5-10 session in total.
The influences of laser on the area of fat accumulation of proposed grafts cause intensification of neovasculogenesis in them. (Figure.1,2.). Although there were ethical and aesthetical peculiarities, restricting possibility to perform full scope morphologic monitoring, the carried out studies showed that LILI improves vascularization of transplanted fat and therefore provides its better survivability rate. This was also accompanied by “rejuvenation” of fat tissue, appearance of various sized adipocytes (Figure.3), and led to increase of relative volume of microvessels.

It was noted that implantation of well vascularized adipose tissue, even into poorly vascularized environment, enhances survivability of grafts. This circumstance requires directional laser influencing on transplants.

The use of local LILI in esthetic surgery facilitates neovasculogenesis, accelerates traceless healing of wounds, restores normal ratio among various forms of RBC, all of which, consequently, lead to marked clinical benefit.

1. Baybekov A., Baybekov I. Scanning electron microscopy of aspirates, used for lipofilling in esthetic surgery. Digest of XVII Russian symposium on scanning electron microscopy and analytical methods of examination of solid bodies M. 2011.- p. 226
2. Baybekov A.I. Possibilities of usage of laser technology for diagnostic and treatment of lipofilling and face-lifting/ Photo diagnostic and Photodynamic therapy. Vol, 9. Supl. 1.-2012. s18.

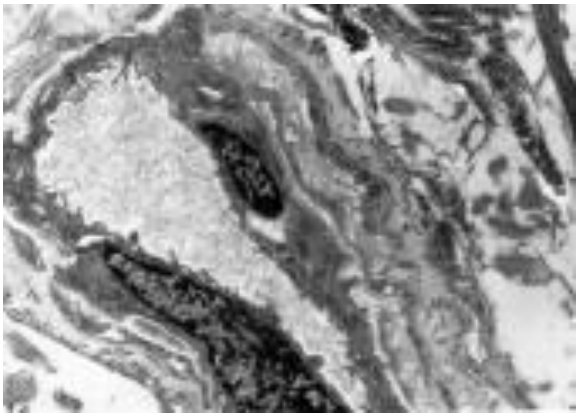

Figure 1. Microvessel of graft derma with signs of its functional activation after LILI. TEM x 7500

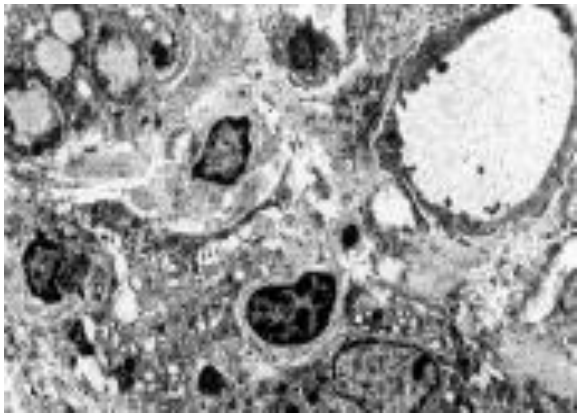

Figure 2. Same. TEM x 3000

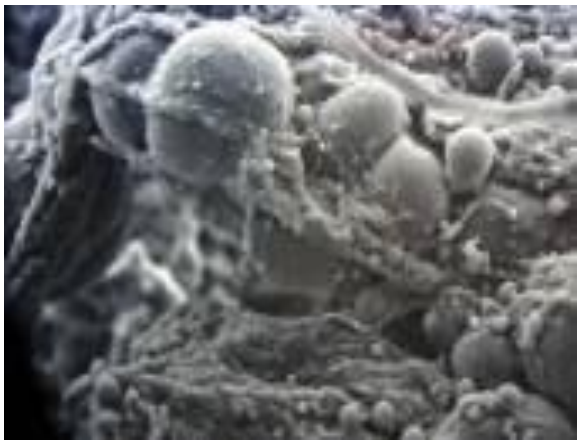

Figure 3. Adipose tissue after LILI. SEM x 1000

Tissues, Pathology, and Diagnostic Microscopy

LS.2.P091
Electron microscopy of skin in post-acne keloid cicatrices and their complex treatment with application of laser technologies

F. Khashimov[1], I. Baybekov[2]

[1]Tashkent state medical academy, dermathology, Tashkent, Uzbekistan
[2]Republican Specialized Center of surgery named after V.Vakhidov, pathology, Tashkent, Uzbekistan

baibekov@mail.ru
Key words: acne, keloids, ultrastructure.

Acne is the most common skin lesions, especially at young ages. It is typical that even after successful treatment, there are quite deep scars on the visible skin surface, at times with formation of keloid proliferates. The ultrastructure of these keloids, and their pathomorphosis in complex treatment with application of laser influences, had not been studied. This has determined the objectives of our study: to assess the ultrastructure of skin in complex treatment of post-acne scars with application of laser therapy.

Local laser irradioation – LLI were performed with “Mustang 017-MCS-PC” with attached to it magnetic nozzle, having magnetic field strength of 50 mlT, the time of exposition to irradiation -5 min, frequency 1000 Hz; and also with defocalized beam of KD-65 (China) – CO_2 laser, which had 5 W output power. All types of laser exposures were performed daily, with 5-10 session in total. Intravascular irradiation of blood-ILIB was administered every other day (10-12 sessions in total) with “Matrix-VLOK”, with attached to it irradiating nozzle, which emits waves with length of 0.63 microns, output power – 1.5-2 mW, and supplied with special Teflon coated needles. All types of laser action were carried out on the background of conventional medicamentous treatment.

Tissue samples were studied by means of light, transmission, scanning electron microscopies, and morphometry.

TEM studies showed thickening of the bundles of collagen fibers, with thickening of fibers themselves. The bundles are noted to be arranged in a rather random manner. Fibroblasts and fibrocytes are notable among the bundles. Pyramidal outgrowths of epidermis, with marked loosening of the surface layers are other features that could be identified (Figure. 1-3). There is also impairment of integrity of desmosomes of spinous layer of epidermis, which determine acantholysis. There are fragments of fungi located between cells of epidermsis and derma. Pathologic forms of erythrocytes (PFE) dominate in the lumen of blood vessels. Prevalence of PFE has also been revealed in peripheral blood. The latter explains the fact of disturbance of main microcirculatory parameters.

Complex treatment of keloids with use of ILIB and LLI leads to significant reduction of existing volumes of cicatrical tissue. This is associated with normalization of the ration of discocytes to PFE in the zone of keloids and in peripheral blood as well. Most beneficial effects are achieved through combination of ILIB, LLI and conventional medicamentous treatment.

LLI contributes to reducing pathologically changed cells and tissues, including forms of erythrocytes in the keloid area. ILIB on the other hand, acting on the peripheral blood and working in similar manner, normalizes normal ratio between various forms of erythrocytes, thus improving microcirculation. Activation of microcirculation potentiates action of medicaments.

Combined application of ILIB, LLI and medicamentous means is an effective complex treatment of post-acne keloids.

1. Baybekov I, Khashimov F., Butaev A., Musaev E., Baybekov A. Possibilities of use of laser technologies in correction of the forms of erythrocytes and microcirculation in pathologic processes. Materials of XXXVIII International scientific-practical conference “Application of lasers in medicine and biology. Yalta, 2012. p. 129-130.
2. Khashimov F., Baybekov I. Scanning electron microscopy of post-acne scars. Digest of XVII Russian symposium on raster electron microscopy and analytical methods of examination of solid bodies. M. 2011.- p. 267
3. Baybekov I.M., A. I. Ibragimov, S.M. Rizaeva, A.I. Baybekov. Application of laser therapy for reduction of changes in erythrocytes and cells of body in their pathology. Abstracts of Laser Helsinki 2010 Congress. 20-23 august. o25, s 13
4. Butaev A.Kh, Saidkhanov B.A., Baybekov I.M. Intravascular laser irradiation of blood in treatment of myasthenia. Abstracts of Laser Helsinki 2010 Congress. 20-23 august. o24, s 13.

Figure 1. SEM x1000

Figure 2. SEM x200

Figure 3.SEM x100

Tissues, Pathology, and Diagnostic Microscopy

LS.2.P092
Inhibition of *Salmonella typhi* Growth by Using Extremely Low Frequency Electromagnetic (ELF-EM) Waves at Resonance Frequency

S.A. Mohamed[1], F.M. Ali[2], A.M. Abdelbacki[3], A.H. El- Sharkawy[4]

[1]Al Jouf University, Physics Department, Faculty of Science, Al Jouf, Saudi Arabia
[2]Cairo University, Biophysics Department, Faculty of Science, Cairo, Egypt
[3]Cairo University, Plant Pathology Department, Faculty of Agriculture, Cairo, Egypt
[4]Ain- Shams University, Physics Department, University College of Women, Cairo, Egypt

shaimaa_abdelraof@yahoo.com
Keywords**:** Bacterial infection, Growth inhibition, Electromagnetic effect, Resonance frequency

Typhoid is a serious disease difficult to be treated with conventional drugs. The aim of the present work was to demonstrate a new method for the control of *S.typhi* growth, through the interference with the bioelectric signals generated from the microbe during cell division by extremely low frequency electromagnetic waves (ELF-EMW) at resonance frequency. Isolated *S.typhi* was subjected to square amplitude modulated waves (QAMW) with different modulation frequencies from two generators with constant carrier frequency of 10 MHz, amplitude of 10 Vpp, modulating depth $\pm$ 2Vpp and constant field strength of 200 V/m at 37 °C. Both the control and exposed samples were incubated at the same conditions during the experiment. The results showed that there was highly significant inhibition effect for *S.typhi* exposed to 0.8 Hz QAMW for a single exposure for 75 min. Furthermore, *S.typhi* became more resistant to the used antibiotics; amikacin, tetracycline, ciprofloxacin and trimethoprim–sulfamethoxazole after exposure to 0.8 Hz QAMW for 75 min. Dielectric relaxation, TEM and DNA results indicated highly significant changes in the molecular structure of the DNA and cellular membrane resulting from the exposure to the inhibiting EM waves. It was concluded that this new non-invasive technique for treatment of bacterial infections is of considerable interest for the use in medical and biotechnological applications.

Tissues, Pathology, and Diagnostic Microscopy

LS.2.P093
Blood-brain barrier changes in pancreatitis: an electon microscopic study

A. Kittel[1], F. Walter[2], S. Veszelka[2], L. Otrokocsi[1], P. Hegyi[3], T. Takács[3], Z. Rakonczay[3], M. Deli[2]

[1]IEM HAS, Budapest, Hungary
[2]Biological Research Centre, Hungarian Academy of Sciences , Szeged, Hungary
[3]University of Szeged, Szeged, Hungary

agneskittel@koki.mta.hu
Keywords: BBB culture model, L-ornithine treatment, alcian blue

The blood-brain barrier (BBB) composed by capillary endothelial cells, pericytes and astrocytes is crucial for the proper working of the central nervous system. The BBB regulates the brain microenvironment, supplies brain cells with nutrients and protects them from toxic materials in the blood. Several diseases, including bacterial and virus infections neurodegenerative diseases and inflammations of different origin can result in lesion of BBB and relatively small changes in its functions may lead to serious neuronal dysfunctions. Acute necrotising pancreatitis may lead to pancreatic encephalopathy. Previous work from our teams demonstrated an elevated BBB permeability in parallel with increased blood cytokine levels in taurocholate induced pancreatitis in rats [1]. A new non-invasive rat pancreatitis model was recently developed and characterised by intraperitoneal injection of the cationic amino acid L-ornithine at the dose of 3 g/kg body weight [2]. Using this in vivo model and our triple co-culture model of the BBB [3] functional and morphological changes were examined. Electron microscopy was used to monitor ultrastructural changes in the cells forming the BBB following L-ornithine treatment.

In the permeability experiments an elevated extravasation of the marker molecules to the brain was determined in rats with pancreatitis. Fragmented glycocalyx, plasma and basal membrane, serious oedema of endothelial cells and glial endfeet, mitochondrial damage and increased number of vesicular elements were observed. Interendothelial tight junctions (TJ) were loosened. Alcian blue used for indication of intact EC function and staining of glycocalyx were found in transcellular vesicles and on /in TJs after 24 h in ornithine-induced pancreatitis (Figure 1), and the dye was also observed in the brain parenchyma.

In case of BBB culture model, the effect of L-ornithine also manifested in increased permeability and decreased resistance and in similar morphological changes as observed in vivo. Deformities of ECs were more profound, including the fragmentation of glycocalyx, spectacularly increased number of caveolae and caveolae-like structures, irregular and open interendothelial junctions and high number of apoptotic bodies (Figure 2).

In conclusion, increased BBB permeability could be observed by both functional and morphological methods in L-ornithine induced pancreatitis in rats, which was at least partially mediated by a direct effect of L-ornithine on brain endothelial cells, as demonstrated by the results obtained on the culture model.

1. G. Farkas, J. Marton, Z. Nagy, Y. Mandi, T. Takacs, M.A. Deli and C.S. Abraham, Neurosci Lett 242 (1998) 147
2. Z. Rakonczay, Jr., P. Hegyi, S. Dosa, B. Ivanyi, K. Jarmay, G. Biczo, Z. Hracsko, I.S. Varga, E. Karg, J. Kaszaki, et al., Crit Care Med 36 (2008) 2117
3. S. Nakagawa, M.A. Deli, H. Kawaguchi, T. Shimizudani, T. Shimono, A. Kittel, K. Tanaka and M. Niwa, Neurochem Int 54 (2009) 253
4. We kindly acknowledge the excellent technical assistence of Győző Goda.

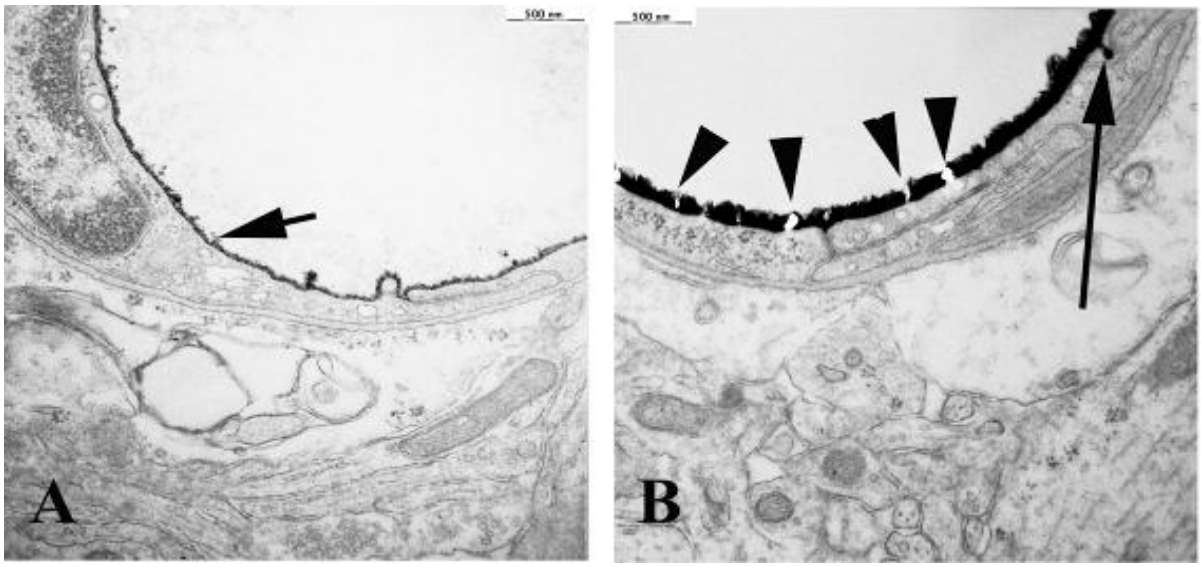

Figure 1. Continuous alcian blue deposit (arrow) covers the luminal plasma membrane of brain capillary endothelial cell in control rat (A). Fragmented glycocalyx (arrowheads) of plasma membrane, caveolae filled with the deposit (arrow) show morphological changes in the endothelial cell of L-ornithine treated (B) rat.

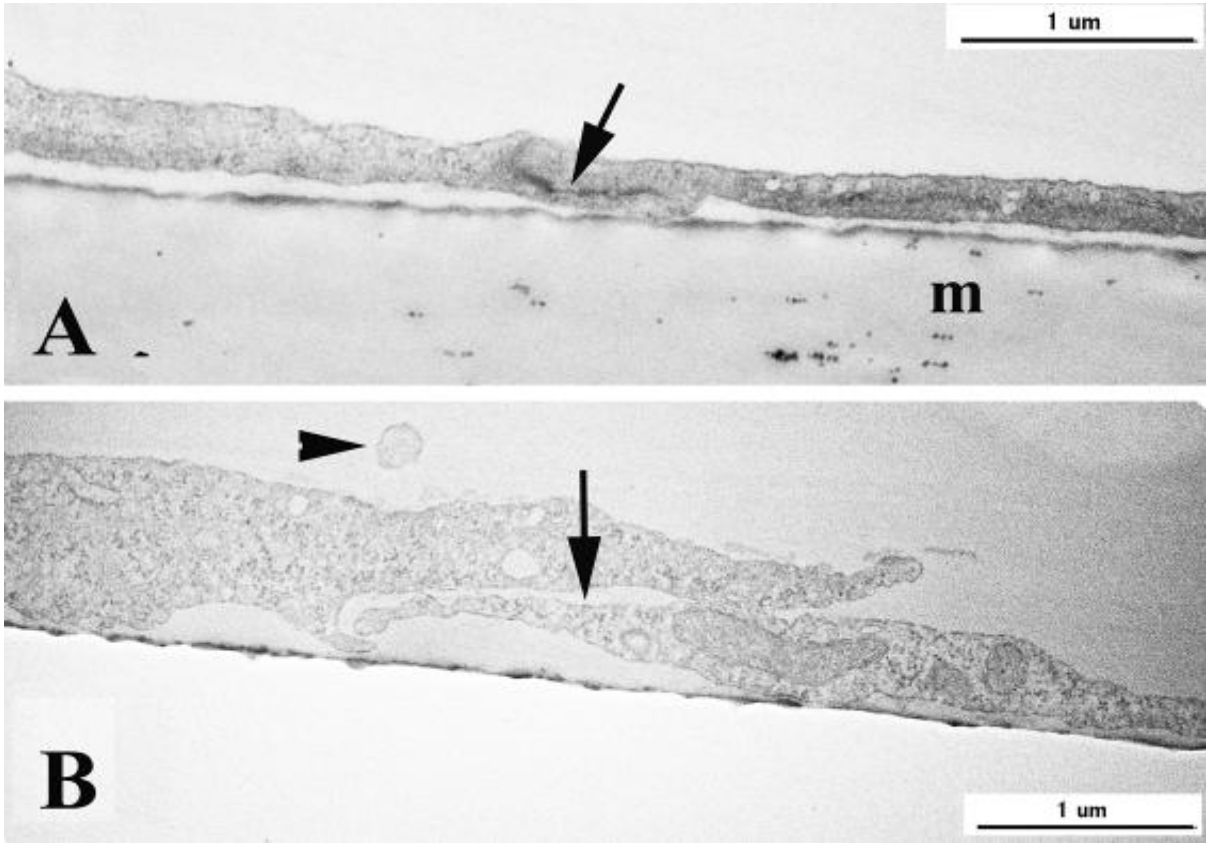

Figure 2. Cultured endothelial cells on plastic membrane (m) show typical tight junction (arrow) in control case, and loosened, almost open interendothelial junction, released vesicle and damaged morphology due to L-ornithine treatment.

Tissues, Pathology, and Diagnostic Microscopy

LS.2.P094
Effects of genistein on gonadotropic cells in middle-aged female rats

I. Medigović[1]

[1]Institute for Biological Research "Siniša Stanković", Department of Citology, Belgrade, Serbia

ivana84@ibiss.bg.ac.rs
Keywords: genistein, estradiol, confocal microscopy, gonadotropic cells, middle-aged female rats

Genistein (G) is a major isoflavone aglycone found in soy based products [1]. It is structurally similar to estradiol and binds to both types of estrogen receptors, with higher affinity for ERβ [2]. Besides mild estrogenic/antiestrogenic activity, genistein also has antiproliferative, antiangiogenic and the antioxidative activities [3]. The present study was conducted to examine the effects of genistein exposure on morphology and immunofluorescent properties of pituitary follicle stimulating (FSH) and luteinizing (LH) cells in middle-aged female rats. Treatment with estradioldipropionate (E) was used as a positive control.

Middle-aged, 12 months old, female rats subcutaneously received 0.625 mg/kg of E, dissolved in olive oil, or 35 mg/kg of G dissolved in a mixture of olive oil and ethanol (9:1), daily, for 4 weeks. Each of the treated groups had a corresponding control group. Thus, females of the control G group (CG) received sterile olive oil and ethanol, while those of the E control group (CE) were given sterile olive oil. Intact control group (C) was also established. All animals were sacrificed 24 h after the last injection. The pituitary glands were excised, fixed in 4% paraformaldehyde for 24h and processed for embedding in paraffin. Tissue sections were deparaffinized in xylene and rehydrated through a decreasing series of ethanol. FSH and LH cells were localized by the immufluorescence using polyclonal anti-rat βFSH (1:300 v/v) and polyclonal anti-rat βLH antibodies (1:500 v/v) as primary antibodies. Donkey anti-goat Alexa Fluor 488 (Invitrogen, 1:200) served as secondary antibody. Images were obtained using a confocal laser scanning microscope Leica TCS SP5 II Basic (Leica Microsystems CMS GmbH; Germany). An Ar-ion 488 nm laser was used for excitation of green fluorescence. Imaging was done with a 40x or 63x objective. Analysis of confocal microscopy images was performed using the Quantify option in LAS AF Lite software (Leica Microsystems CMS GmbH; Germany). Relative intensity of fluorescence (RIF) was calculated according to Waters and Swedlow [4]. Intensity of fluorescence was measured on 100-150 FSH or LH cells per animal, in which the nucleus was apparent.

In this study, we demonstrated a method to quantitate the antigens visualized with indirect immunofluoresence and viewed with confocal microscopy. Since use of confocal microscopy restricted the thickness of optical section from which measurements of emitted fluorescence were obtained, direct comparisons of fluorescence intensity between gonadotropic cells of control and treated females was enabled. The FSH and LH cells of middle-aged females were polygonal, oval or polyhedral in shape with prominent, often eccentrically located nuclei with strong immunofluorescence located in the cytoplasm (Fig. 1 A, D). After estradiol treatment both types of gonadotropes were smaller and the intensity of FSH and LH fluoroscence was significantly decreased by 43.24% and 27.69%, respectively compared to the controls ($P < 0.05$; Fig. 1B, E; Fig. 2). After genistein treatment FSH and LH immunoreactive cells were larger in size, irregularly shaped, and with unhomogenously stained cytoplasm. RIF was unchanged (Fig. 2A). In conclusion, genistein changed morphology of gonadotrophic cells without changing the intracellular content of gonadotropic hormones in the pituitaries of middle-aged female rats.

1. M. de Lima Toccafondo Vieira et al., Phytomedicine. 15 (2008) p31.
2. S. Ramos. J Nutr Biochem. 18 (2007) p427.
3. G. Kuiper et al., Endocrinology. 138 (1997) p863.
4. J.Waters and J. Swedlow. Cell Press. (2008) p37.
5. This work was supported by the Ministry of Education, Science and Technological Development of the Republic of Serbia, grant number 173009.

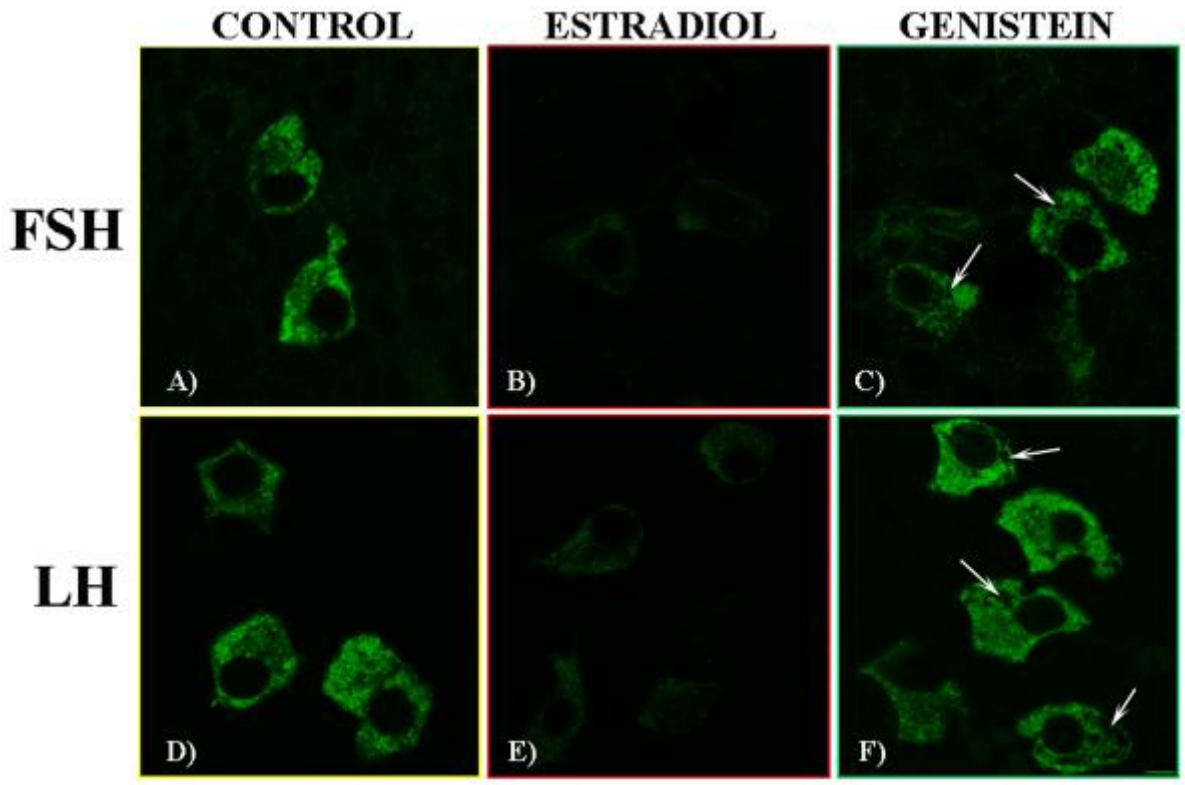

Figure 1. Representative micrographs of immunofluorescently labeled FSH (A-C) and LH (D-F) cells in the pituitary *pars distalis* of control (A, D), estradiol- (B,E) and genistein-treated (C,D) middle-aged female rats. After estradiol (B, E) treatment, FSH and LH cells were smaller in size and irregularly shaped. After genistein (C, D) treatment, FSH and LH cells were larger and with unstained parts of cytoplasm (arrows). Scale bar 50μm.

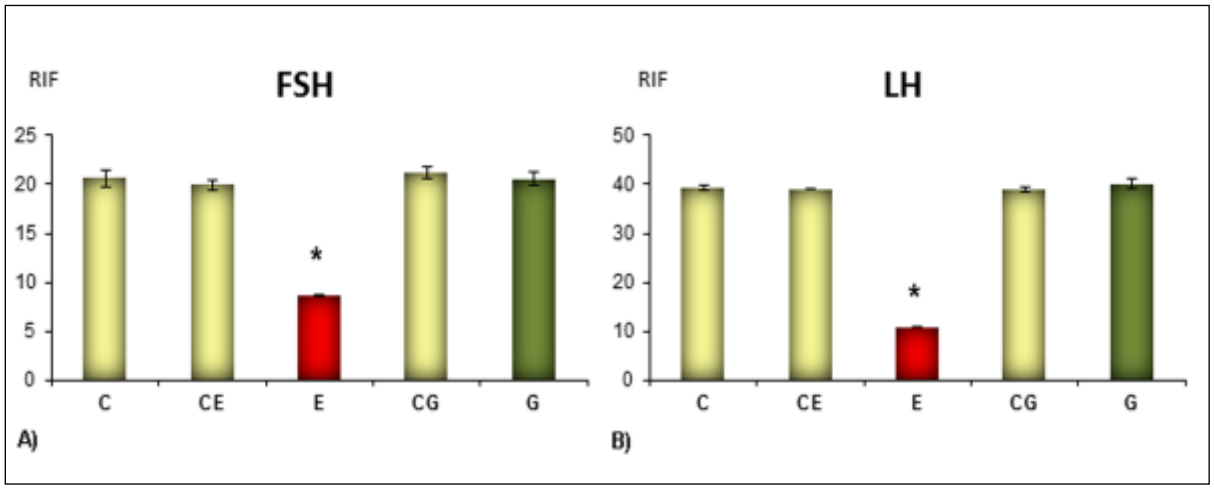

Figure 2. Relative intensity of fluorescence (RIF) of FSH (A) and LH (B) cells in the pituitary *pars distalis* of control, estradiol- and genistein-treated middle-aged female rats. All values are given as means ± SD; *Significantly different from corresponding control (C, CE and CG) (P< 0.05).

Tissues, Pathology, and Diagnostic Microscopy

LS.2.P095
Preservation and Electron Microscopic Presentation of Crystals in Iatrogenic Foscarent - Induced Crystalline Nephropathy

J. Mraz[1], N. Kojc[1], A. Vizjak[1], D. Ferluga[1]

[1]Institute of Pathology, Faculty of Medicine, Ljubljana, Slovenia

jerica.mraz@mf.uni-lj.si
Keywords: foscarnet, crystalline nephropathy, electron microscopy

Drugs can induce kidney injury by various mechanisms. A number of poorly soluble drugs, including foscarnet, can crystallize within renal tubules and cause tubular injury and inflammation [1,2]. Because of its very common adverse effect on kidney function, foscarnet (trisodium phosphonoformate hexahydrate) is a second-line agent for treatment of ganciclovir resistant viral infections. Very few histopathologic data have so far been reported about the unique foscarnet-associated not only tubular but also glomerular crystalline nephropathy [3].

We present a 73-year-old male patient with a past history of autosomal dominant polycystic kidney disease and cadaveric kidney transplantation. After two intravenous foscarnet applications of 21 and 33 days, one week apart, because of ganciclovir – resistant Cytomegalovirus infection, needle allograft biopsy showed a severe glomerular and tubular crystalline nephropathy. An autopsy was performed when he died 17 months after transplantation and 6 weeks after the second foscarnet application.

Irregular empty clefts of various sizes remained after total or subtotal washing out and/or mechanical removal of water-soluble foscarnet crystals in standard paraffin sections (Figure 1), as well thick and ultrathin Epon-embedded sections after routine formalin fixation of kidney biopsy and autopsy specimens. Presentation of birefringent crystals in fairly thick fresh-frozen air-dried sections, visualized best in a polarization microscope, lacked detail. Light microscopy revealed pale yellow rectangular crystals, preserved after 100% alcohol fixation of autopsy tissue but to some extent damaged and removed during cutting of the paraffin sections. Massive crystalline precipitates were observed in 80% of transplanted kidney glomeruli, associated with capillary destruction, fibrin release, extracapillary crescents and focal segmental glomerulosclerosis, as well as in 20 % of proximal tubuli, causing macrophage tubulitis, tubular ruptures and foreign body granulomatous inflammation (Figure 1). Crystals were found in smaller amounts scattered in the bone marrow, heart and skeletal muscles.

We succeeded in preserving the foscarnet crystals for electron microscopy studies after 100% alcohol fixation and O_SO_4 postfixation. However, the crystals were mostly mechanically removed by cutting ultrathin sections but remained in significantly thicker sections of around 1000nm. The numerous rectangular flat plate-like foscarnet crystals measured from 100nm x 80nm to 970nm x 830nm in stacks. To the best of our knowledge, this was the first time that they had been visualized by electron microscopy (Figure 2).

1. G. Zanetta, L. Maurice-Estepa, C. Mousson, Transplantation 67 (1999), 1376-8
2. E. Justrabo, G. Zanetta, L. Martin, Histopatology 34 (1999), 365-9
3. H. Beaufils, G. Deray, C. Katlama, Lancet 336 (1990), 755

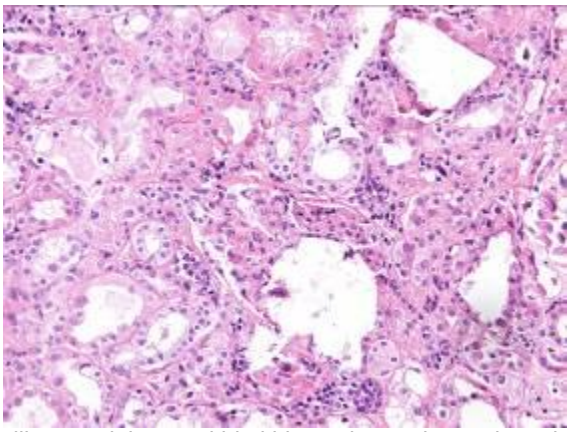

Figure 1. Destructive crystalline precipitates within kidney glomerulus and proximal tubuli. 100% alcohol fixation, paraffin embedding, HE, X20.

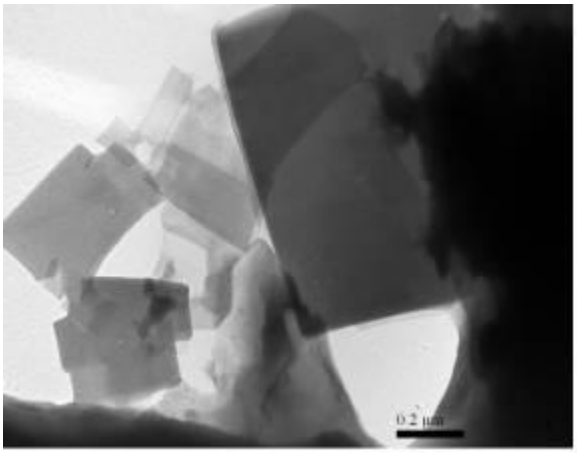

Figure 2. Electron micrograph showing numerous rectangular crystals in the kidney glomerulus. 100% alcohol fixation, O_SO_4 postfixation, Epon embedding, 1000nm section, X80.000.

Tissues, Pathology, and Diagnostic Microscopy

LS.2.P096
Hepatic changes in Schistosoma mansoni-infected mice livers after bone marrow cells transplantion

E. Nagwa[1,2], V. Bruno[3], H. Olfat[4], M. Soheir[2,5], Y. Hoda[5], M. Soheir[6]

[1]Theodor Bilharz Research Institute, Electron Microscopy, Warrak El Hadar, Imbaba, Egypt
[2]Theodor Bilharz Research Institute, Warrak El Hadar, Giza, Egypt
[3]Professional's Association Research Institute for Occupational Medicine, Cell Biology, Bochum, Germany
[4]Theodor Bilharz Research Institute, Pathology, Warrak El Hadar, Giza, Egypt
[5]Theodor Bilharz Research Institute, Electron Microscopy, Warrak El Hadar, Giza, Egypt
[6]Theodor Bilharz Research Institute, Parasitology, Warrak El Hadar, Giza, Egypt

nagwa_elkhafif@hotmail.com
Key words: Bone marrow cells; murine schistosomiasis; liver; Y chromosome; CDYL protein.

The efficiency of differentiation of bone marrow cells (BMCs) into hepatocytes in vivo and its importance in physiopathological processes is still debated. Murine schistosomiasis was used as a liver injury model and unfractionated male mice BMCs were transplanted through intrahepatic injection into nonirradiated

Schistosoma mansoni-infected female mice on their 16th week post-infection. Two weeks after bone marrow transplantation, mice were sacrificed on a weekly basis until 10 weeks. Tracing of male donor-derived cells in female recipient mice livers was carried out by the detection of Y chromosome expression by fluorescent in situ hybridization (FISH) and also of chromodomain Y-linked (CDYL) protein by indirect immunofluorescence (IF). Their transformation into hepatocytes was studied by double labelling indirect IF using antibodies directed against CDYL and mouse albumin. Histopathological and electron microscopic examinations revealed the presence of small hepatocyte-like cells

In the periportal tracts and in between the hepatocytes facing the sinusoids (Fig1,2 and Fig 3,4). Donor-derived cells showing Y chromosome by FISH and expressing CDYL protein by IF were recovered in the infected transplanted livers (Fig 5 and Fig 6, 7). The initial number of these cells increased with increased post-transplantation time. Cells were mainly localized in the periphery of schistosoma granuloma. Only very few donor-derived cells appeared within the hepatic parenchymal tissue and showed positivity for albumin secretion by doublelabelling with IF. We suggest that transplanted bone marrow stem cells can repopulate the Schistosoma-infected liver of immunocompetent mice but their differentiation to hepatic cells is negligible. This differentiation is a complex event controlled by many factors and needs to be further characterized extensively. The extent and type of liver injury and the number of transplanted cells are important variables in the process of stem cell engraftment and differentiation into functioning hepatic cells that still need to be defined.

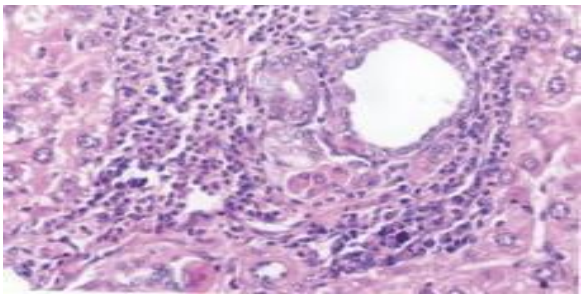

Figure 1. Liver tissue sections from recipient female mice showing newly formed hepatocytic cells scattered within the hepatic lobules exhibiting rounded or elongated dark nuclei (H&E, original magnification 400 X).

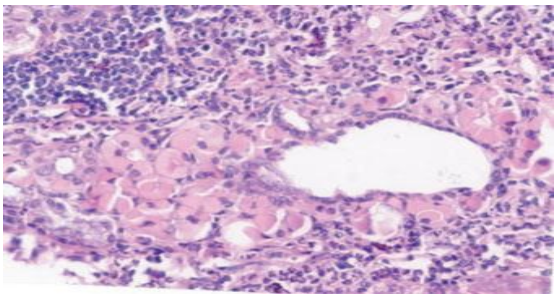

Figure 2. Liver tissue showing newly formed bile ductules in portal areas in the recipient Schistosoma infected female mice close to the schistosomal granulomas (H&E, original magnification x400)

.

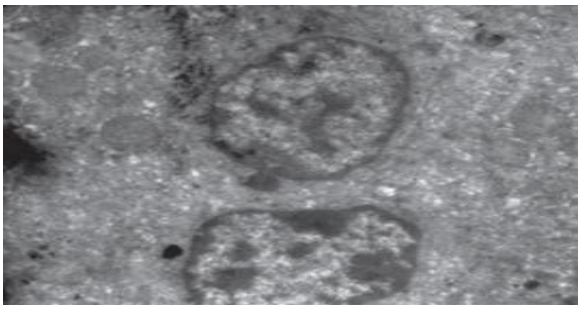

Figure 3. Electron micrograph of liver tissue of the recipient Schistosoma-infected female mice showing small oval juvenile hepatic cells (EM, original magnification x3200).

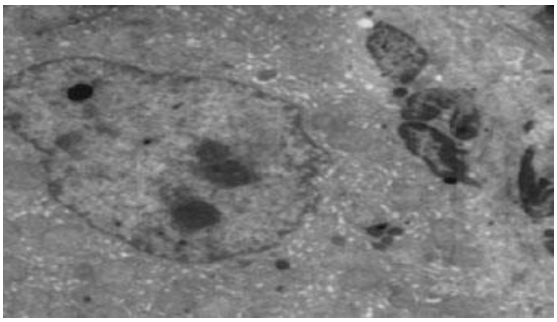

Figure 4. Electron micrograph of the liver of the recipient Schistosoma-infected female mice showing mature hepatocyte with irregular nuclear membrane, prominent nucleoli, proliferated mitochondria and cytoplasm enriched with rough endoplasmic reticulum (EM, original magnification x4000).

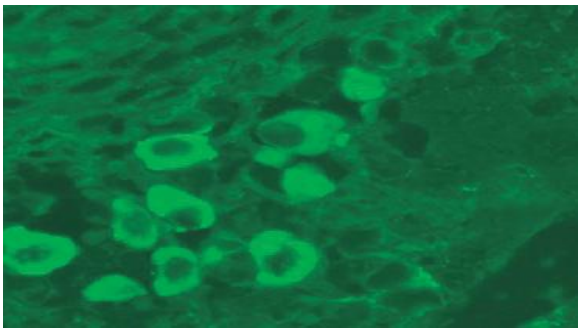

Figure 5. Immunofluorescence of CDYL protein, in liver sections of female mice 7 weeks post-transplantation
with male mice BMCs, and CDYL expression
in the cytoplasm of cells in the perigranulomar area (IF, original magnification x625).

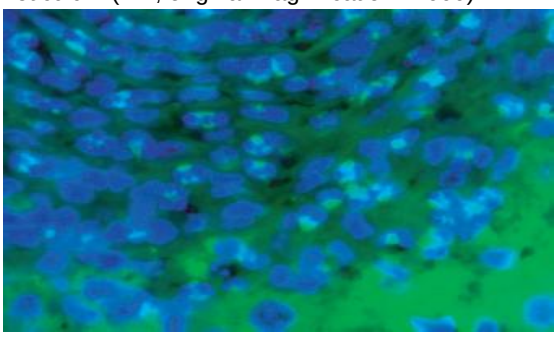

Figure 6. Recipient Schistosoma-infected female mice
liver 10 weeks post-transplantation with male mice BMCs; FISH-positive Y chromosome signals appear as green dots in the nuclei denoting repopulation by male bone marrow-derived cells mainly in the perigranulomar
area (FISH, original magnification x400)

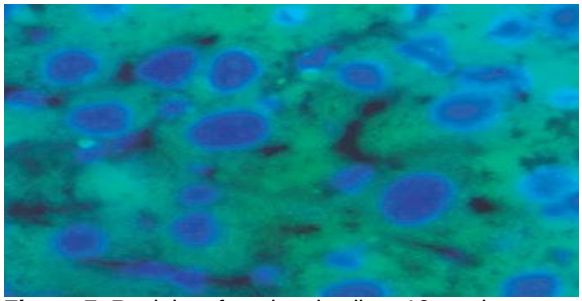

Figure 7. Recipient female mice liver 10 weeks post Transplantation with male mice BMCs showing very few cells in the parenchymal tissue with green signals in the nuclei stained with DAPI (FISH, original magnification x1000).

Tissues, Pathology, and Diagnostic Microscopy

LS.2.P097
Histochemistry for investigating skeletal muscle under sarcopenic and dystrophic conditions

M. Malatesta[1], C. Pellicciari[2], G. Meola[3,4]

[1]University of Verona, Department of Neurological, Neuropsychological, Morphological and Movement Sciences, Anatomy and Histology Section, Verona, Italy
[2]University of Pavia, Department of Biology and Biotechnology "Lazzaro Spallanzani", Laboratory of Cell Biology, Pavia, Italy
[3]IRCCS Policlinico San Donato, Laboratory of Muscle Histopathology and Molecular Biology, Milano, Italy
[4]University of Milano, Department of Neurology, Milano, Italy

manuela.malatesta@univr.it
Keywords: cell nucleus, histochemistry, skeletal muscle, sarcopenia, myotonic dystrophy

Sarcopenia is an age-related condition characterized by the progressive loss of mass, strength and function of skeletal muscle, which affects also healthy subjects [1]. The mechanisms involved in the sarcopenic process are probably manifold, such as denervation and reinnervation of the motor units, alteration in the hormonal levels, elevated concentration of inflammatory mediators, decrease in microvascular function, and reduced regeneration capability of muscle tissue.

From a histological point of view, the aging skeletal muscle is characterized by reduction in fibre size and centrally located nuclei. Muscles rich in fast fibres (such as the *quadriceps femoris*, *gastrocnemius* and *biceps brachii*) are more compromised than muscles mainly containing slow fibres since the age-related atrophy specifically affects fast fibres. The number of satellite cells (SCs) was also observed to decrease with increasing age. SCs are undifferentiated mononuclear myogenic cells present in all skeletal muscles: they occur close to the muscle fibres, juxtaposed between the sarcolemma and the basal lamina, and are quiescent in the adult muscle, but can be activated by appropriate stimuli (such as an injury). After activation, SCs proliferate and fuse together to form new myofibres or fuse to existing muscle fibres: this is the basic mechanism responsible for the physiological renewing of muscle fibres and the maintenance of muscle mass and integrity in the adult.

In our studies we initially analyzed the differences from old to adult skeletal muscle focusing on myonuclei and SC nuclei [2,3]. We used animals of a Balb/c mice strain established 40 years ago, which has been widely used for studies on physiological aging because of their long life (mean life span 25 months) and the relatively low incidence of pathologies, in particular tumours. Two animal groups were considered: adult mice of 12 months and old mice of 28 months having only spontaneous free-moving activity in the cage. *Quadriceps femoris* and *biceps brachii* were isolated and used for fluorescence and transmission electron microscopy investigations: we analyzed the muscle fibre composition and measured fibre cross-section area by morphometry, demonstrating size variability and atrophy of fast fibres in old animals; moreover, we analysed some nuclear morphological and morphometrical features as well as the distribution and amount of transcriptional and post-transcriptional factors, showing quantitative modifications of some nuclear and nucleolar parameters and alterations in the amount of nucleoplasmic splicing and cleavage factors in old muscles.

We then investigated the effects of physical exercise in sarcopenic old mice [4,5]. In fact, several studies have stressed the importance of physical exercise as an effective - though still debated - approach to prevent/limit the sarcopenic process. Twenty-eight month-old mice were trained by treadmill running (30min at 9.5 m/min belt speed, 5 days a week) for one month. The same light and electron microscopy analyses described above were performed on *quadriceps femoris*, demonstrating that fast fibre atrophy may be counteracted by physical exercise even at advanced age, since the fibre size and the nuclear parameters of old trained mice approached the adult values. In addition, immunolabelling at light microscopy for Pax7 (a reliable marker of both quiescent and activated SCs) and MyoD (a suitable marker of activated SCs) allowed to demonstrate that the number of both quiescent and activated SCs decreases in the muscles of old mice in comparison to the adults, and that old trained mice revert to the adult values. We also studied the activation and differentiation in vitro of SCs isolated from skeletal muscles: SC-derived myoblasts were allowed to proliferate and differentiate into myotubes, and analysed at transmission electron microscopy. We found that myoblasts and myotubes from old trained mice show morphological features quite similar to adult subjects, whereas cells from sedentary old mice exhibit marked structural alterations.

On the basis of our results we may conclude that: i) in myonuclei and SC nuclei of old muscles alterations of transcriptional and post-transcriptional factors occur, but ii) physical exercise stimulates

pre-mRNA transcription, processing and export, thus increasing protein synthesis and SC activation in old muscles; moreover, iii) physical exercise improves SC capability to differentiate into structurally and functionally correct myotubes, increasing the regenerative potential of old muscles.

Interestingly, in human myotonic dystrophy (DM) the skeletal muscle shows structural and functional features reminiscent of sarcopenia, such as fibre atrophy, centrally located myonuclei and defective SCs. DMs are autosomal dominant disorders and two forms are presently known [6,7]: the more severe DM1-Steinert's disease (OMIM 160900) is caused by an expanded (CTG)n nucleotide sequence in the 3' untranslated region of the Dystrophia Myotonic Protein Kinase (DMPK) gene (OMIM 605377) on chromosome 19q13; the second form, DM2 (OMIM 602688) displays a milder clinical phenotype and is caused by the expansion of the tetranucleotidic repeat (CCTG)n in the first intron of the Zinc Finger Protein (ZNF)-9 gene (OMIM 116955) on chromosome 3q21. The basic mechanisms of both DMs reside in the nuclear sequestration of the expanded RNAs: CUG- and CCUG-containing transcripts accumulate in intranuclear foci in DM1 and DM2 cells respectively, and sequester the RNA-binding proteins CUGBP1 and MBLN [7]; in addition, we showed that snRNPs and hnRNPs splicing factors (which are essential for the physiological processing of pre-mRNA) are also sequestered into the foci [8]. This general impairment of mRNA pathways could explain the multisystemic pathological features typical of both DMs.

Our studies on DM muscles demonstrated that myonuclei from bioptic samples of *biceps brachii* undergo morphological alterations similar to those found in aged muscles and that an altered distribution of nuclear RNP-containing structures and molecular factors responsible for pre-mRNA transcription and maturation occurs [9,10]. Moreover, we investigated *in vitro* the structural and functional features of SC-derived myoblasts and we observed that DM myoblasts show cell-senescence alterations such as cytoplasmic vacuolisation, reduction of the proteosynthetic apparatus, accumulation of heterochromatin and impairment of the pre-mRNA maturation pathways earlier than myoblasts from healthy patients [11]. In addition, DM myoblasts generate myotubes characterised by structural defects similar to senescent healthy myotubes. The early occurrence of senescence-related features in SC-derived myoblasts would therefore reduce the regeneration capability of DM SCs, thus contributing to the muscular dystrophy in DM patients.

In conclusion, morphological and histochemical evidence shows that skeletal muscles undergo similar alterations under sarcopenic and dystrophic conditions, especially for the nuclear pre-mRNA pathways, suggesting a common involvement of the RNP nuclear components in the onset of muscle cell dysfunctions [12,13]. In this view, the positive effects of physical exercise observed on skeletal muscles of subjects affected by severe sarcopenic atrophy open interesting perspectives for studies aimed at its application to subjects affected by DM.

1. L. D. Thompson, Exp Gerontol. 44 (2009), p. 106.
2. M. Malatesta, F. Perdoni, S. Muller, C. Zancanaro and C. Pellicciari, Eur. J. Histochem. 53 (2009), p. 97.
3. M. Malatesta, F. Perdoni, S. Muller, C. Pellicciari and C. Zancanaro, J. Biomed. Biotechnol. 2010 (2010), p. 410405.
4. C. Zancanaro, R. Mariotti, F. Perdoni, E. Nicolato and M. Malatesta, Eur. J. Histochem. 51 (2007), p. 305.
5. M. Malatesta, P. Fattoretti, M. Giagnacovo, C. Pellicciari and C. Zancanaro, Rejuvenation Res. 14 (2011), p. 543.
6. M. Mahadevan, C. Tsilfidis, L. Sabourin, G. Shutler, C. Amemiya, G. Jansen, C. Neville, M. Narang, J. Barceló, K. O'Hoy, S. Leblond, J. Earle-MacDonald, P.J. de Jong, B. Wieringa, and R.G. Korneluk, Science 255 (1992), p. 1253.
7. C.L. Liquori, K. Ricker, M.L. Moseley, J.F. Jacobsen, W. Kress, S.L. Naylor, J.W. Day and L.P. Ranum, Science 293 (2001), p. 864.
8. F. Perdoni, M. Malatesta, R. Cardani, M. Giagnacovo, E. Mancinelli, G. Meola and C. Pellicciari, Eur. J. Histochem. 53 (2009), p. 151.
9. M. Malatesta, M. Giagnacovo, R. Cardani, G. Meola and C. Pellicciari, Histochem. Cell Biol. 135 (2011), p. 419.
10. M. Malatesta, M. Giagnacovo, M. Costanzo, B. Cisterna, R. Cardani and G.Meola, Eur. J. Histochem. 57 (2013), in press.
11. M. Malatesta, M. Giagnacovo, L.V. Renna, R. Cardani, G. Meola and C. Pellicciari, Eur. J. Histochem. 55 (2011), p. e26.
12. M. Malatesta and G. Meola, Eur. J. Histochem. 54 (2010), p. e44.
13. M. Malatesta, Eur. J. Histochem. 56 (2012), p. e36.

Tissues, Pathology, and Diagnostic Microscopy

LS.2.P098
Angiogenesis in the reparatory mucosa of the mandibular edentulous ridge is driven by tip cells and influenced by circulating fibrocytes

A. Didilescu[1], F. Pop[2], M. Rusu[3]

[1]Carol Davila University of Medicine and Pharmacy, Embryology, Bucharest, Romania
[2]Carol Davila University of Medicine and Pharmacy, Bucharest, Romania
[3]Carol Davila University of Medicine and Pharmacy, Anatomy, Bucharest, Romania

andreea.didilescu@gmail.com
Keywords: oral mucosa; endothelial tip cells; sprouting angiogenesis

Angiogenesis is the process that generates new blood vessels and capillaries from pre-existing blood vessels. This process initially involves proliferation, sprouting, and migration of endothelial cells [1; 2]. The newly generated blood vessel sprout is guided by migrating tip cells [3-7].

It was aimed to perform a qualitative study in order to assess the guidance by tip cells of the endothelial sprouts in the repairing mucosa of the edentulous mandibular crest. In addition, the suitable stromal immune phenotypes for oral mucosa healing were evaluated.

Reparatory mucosa of the edentulous alveolar crest of the mandible was collected prior to healing abutment placement, as well as additional samples of mandibular ridge mucosa collected from patients prior to third molar extractions. The samples were prepared for immunohistochemistry (IHC) and transmission electron microscopy (TEM) examinations. Anti-CD34, anti-CD117(c-kit), anti-PDGFR-α, anti-Mast Cell Tryptase Ab-2, anti-vimentin, anti-CD44, anti-CD45, anti-CD105, anti-α-SMA, anti-FGF2, and anti-Ki67 primary antibodies were used.

In IHC, different stages of sprouts initiation, extension, bridging and lumenization of the newly formed tubes were evidenced in the reparatory samples (Figure 1). By CD34 labeling there were identified extensive processes of sprouting angiogenesis within the lamina propria of non-reparatory samples of oral mucosa. The endothelial stalk cells of resident microvessels were positively stained, as also were the endothelial tip cells (ETCs) involved in active and extensive processes of angiogenesis, in the papillary and the reticular layers. α-SMA positive vascular smooth muscle cells and pericytes were found in both reparatory and control samples. FGF2 was expressed in non-reparatory, but not in reparatory stromal samples. Stromal cells presenting a specific immune phenotype (α-SMA/CD34/CD45 positive) were embedding the microvascular beds, and were identified as being circulating fibrocytes (CFCs). These cells had particular ultrastructural features, different from fibroblasts and immune cells. Morover, ETCs were accurately identified in TEM, penetrating the stromal compartment. Thus, the ETCs were suited for direct interactions with stromal cells. Two patterns of ETCs prolongations were encountered: (a) filopodia, located beneath the endothelial basal lamina, embedded within it, or projected within the stromal compartment; (b) long prolongations emerging from the basal lamina of the endothelial tubes and freely penetrating the stroma. These later processes were moniliform; hook-like collaterals were arising from the dilated segments, suggestive for a staged migration [6].

FGF acts as a key factor in sprouting angiogenesis [8; 9]. The fact that FGF2 was expressed only in non-reparatory samples, suggests that FGF2 acts in physiological reparatory processes, but it may not intervene in wound healing. The pattern proposed is that CFCs contact ETCs, and consequently, when a new endothelial tube is established, the CFCs could be recruited as pericytes [6].

It can be concluded that maintenance and healing of oral mucosa are supported by extensive processes of angiogenesis, guided by ETCs that, in turn, are influenced by the CFCs that populate the stromal compartment both in normal and reparatory states. Therefore, CFCs could be targeted by specific therapies, with pro- or anti-angiogenic purposes.

1. M. J. Siemerink, I. Klaassen, I. M. Vogels, A. W. Griffioen, C. J. Van Noorden, R. O. Schlingemann, *CD34 marks angiogenic tip cells in human vascular endothelial cell cultures*, Angiogenesis, 2012, 15(1): 151-163.
2. R. Blanco, H. Gerhardt, *VEGF and Notch in tip and stalk cell selection*, Cold Spring Harb Perspect Med, 2013, 3(1): a006569.
3. A. Mettouchi, The role of extracellular matrix in vascular branching morphogenesis, Cell Adh Migr, 2012, 6(6): 528-534.
4. D. Ribatti, E. Crivellato, *"Sprouting angiogenesis", a reappraisal*, Dev Biol, 2012, 372(2): 157-165.
5. R. Stanescu, A. C. Didilescu, A. M. Jianu, M. C. Rusu, Angiogenesis in the reparatory mucosa of the mandibular edentulous ridge is driven by endothelial tip cells, Rom J Morphol Embryol, 2012, 53(2): 375-378.
6. M. C. Rusu, A. C. Didilescu, R. Stanescu, F. Pop, V. M. Manoiu, A. M. Jianu, M. Valcu, The mandibular ridge oral mucosa model of stromal influences on the endothelial tip cells: an immunohistochemical and TEM study, Anat Rec (Hoboken), 2013, 296(2): 350-363.
7. M. C. Rusu, A. G. Motoc, F. Pop, R. Folescu, Sprouting angiogenesis in human midterm uterus and fallopian tube is guided by endothelial tip cells, Anat Sci Int, 2013, 88(1): 25-30.
8. O. M. Tepper, J. M. Capla, R. D. Galiano, D. J. Ceradini, M. J. Callaghan, M. E. Kleinman, G. C. Gurtner, Adult vasculogenesis occurs through in situ recruitment, proliferation, and tubulization of circulating bone marrow-derived cells, Blood, 2005, 105(3): 1068-1077.
9. K. J. Woad, M. G. Hunter, G. E. Mann, M. Laird, A. J. Hammond, R. S. Robinson, *Fibroblast growth factor 2 is a key determinant of vascular sprouting during bovine luteal angiogenesis*, Reproduction, 2012, 143(1): 35-43.

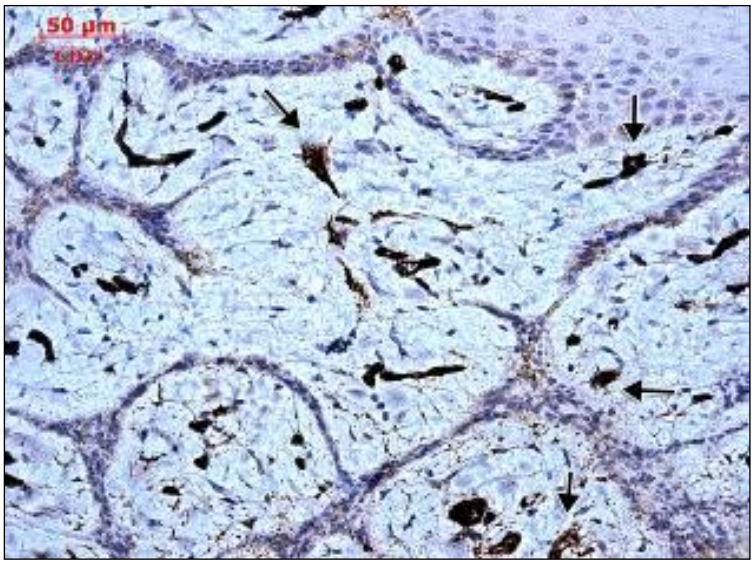

Figure 1. CD34 immune labeling of reparatory oral mucosa. Processes of sprouting angiogenesis are identified (arrows).

Tissues, Pathology, and Diagnostic Microscopy

LS.2.P099
The suburothelial interstitial cells of urinary bladder - an IHC and TEM study

M.C. Rusu[1], F. Pop[1], V.S. Manoiu[1], A.C. Didilescu[1]

[1]Carol Davila" University of Medicine and Pharmacy, Bucharest, Romania

anatomon@gmail.com
Keywords: myofibroblasts; interstitial Cajal cells; telocytes; smooth muscle cells

A number of studies describe the presence of suburothelial myofibroblasts (SUMFs) in the urinary bladder [1-7]. It has been discussed that the normal bladder does not contain myofibroblasts as identified by light and electron microscopy standards [8]. There are also studies available identifying either suburothelial interstitial cells (ICs) [9; 10], or suburothelial interstitial Cajal cells (ICCs) [11-13]. Recently there have been also described telocytes in the upper lamina propria of the urinary tract [14] and uretheral suburothelial telocytes and smooth muscle cells [15].

The telocytes (TCs) were recently defined; these cells project long, slender and moniliform processes termed telopodes [16; 17]; prior to their identification based on TEM criteria, telocytes were regarded as interstitial Cajal-like cells (ICLCs) [18-20]. However, the TEM diagnosis of TCs should be approached with caution, as stromal hybrid morphologies such as telopode-like prolongations, can be encountered [21]. It was claimed that networks of TCs are able to ensure stromal signaling [22; 23].

The possible presence of different cell types in the suburothelial band seems overlooked. It was raised this hypothesis and it was decided to use immunohistochemistry (IHC) and transmission electron microscopy (TEM) in order to elucidate the structure of the suburothelial band in the urinary bladder.

Postautopsic human bladder samples from ten donor cadavers were labeled with antibodies against CD34, CD117/c-kit, vimentin and alpha smooth muscle actin (α-SMA). Stromal cells in the immediate suburothelial band were CD34/vimentin/α-SMA positive, but CD117/c-kit negative (fig.1). However, it is not mandatory for ICCs or ICLCs to label with c-kit antibodies, and electron microscopy (EM) is best suited for identifying this cell type [24].

Bladder samples from six Wistar rats were used for immunohistochemistry (IHC) and transmission electron microscopy (TEM). In IHC, desmin antibodies labeled only the detrusor muscle, while α-SMA positive labeling was found in the suburothelial band, the submucosa, and the inner layer of the detrusor muscle. Also perivascular cells and myoepithelial cells were α-SMA positive. In TEM, the suburothelial band had a layered structure, consisting of inner, middle and outer suburothelial layers (ISUL, MSUL and, respectively, OSUL). THE ISUL contained electrono dense fibroblast-like cells (FLCs), the MSUL consisted of two subtypes of myoid cells (MyCs I and II) which were finally diagnosed as smooth muscle cells (MyCs I = SMCs) and myoid ICCs (MyCs II), while the OSUL contained collagen-embedded interstitial cells (ICs). At this time the diagnosis of suburothelial TCs should be regarded with caution.

1. Sui GP, Wu C, Fry CH. Characterization of the purinergic receptor subtype on guinea-pig suburothelial myofibroblasts. *BJU Int*. 2006; 97: 1327-1331.
2. Fry CH, Sui GP, Kanai AJ, Wu C. The function of suburothelial myofibroblasts in the bladder. *Neurourol Urodyn*. 2007; 26: 914-919.
3. Neuhaus J, Heinrich M, Schlichting N, Oberbach A, Fitzl G, Schwalenberg T, Horn LC, Stolzenburg JU. [Structure and function of suburothelial myofibroblasts in the human urinary bladder under normal and pathological conditions]. *Urologe A*. 2007; 46: 1197-1202.
4. Sui GP, Wu C, Roosen A, Ikeda Y, Kanai AJ, Fry CH. Modulation of bladder myofibroblast activity: i mplications for bladder function. *Am J Physiol Renal Physiol*. 2008; 295: F688-697.
5. Roosen A, Datta SN, Chowdhury RA, Patel PM, Kalsi V, Elneil S, Dasgupta P, Kessler TM, Khan S, Panicker J, Fry CH, Brandner S, Fowler CJ, Apostolidis A. Suburothelial myofibroblasts in the human overactive bladder and the effect of botulinum neurotoxin type A treatment. *Eur Urol*. 2009; 55: 1440-1448.
6. Cheng S, Scigalla FP, Speroni di Fenizio P, Zhang ZG, Stolzenburg JU, Neuhaus J. ATP enhances spontaneous calcium activity in cultured suburothelial myofibroblasts of the human bladder. *PLoS One*. 2011; 6: e25769.

7. Heinrich M, Oberbach A, Schlichting N, Stolzenburg JU, Neuhaus J. Cytokine effects on gap junction communication and connexin expression in human bladder smooth muscle cells and suburothelial myofibroblasts. *PLoS One*. 2011; 6: e20792.
8. Eyden B. Are there myofibroblasts in normal bladder? *Eur Urol*. 2009; 56: 427-429.
9. Kubota Y, Hashitani H, Shirasawa N, Kojima Y, Sasaki S, Mabuchi Y, Soji T, Suzuki H, Kohri K. Altered distribution of interstitial cells in the guinea pig bladder following bladder outlet obstruction. *Neurourol Urodyn*. 2008; 27: 330-340.
10. Grol S, Essers PB, van Koeveringe GA, Martinez-Martinez P, de Vente J, Gillespie JI. M(3) muscarinic receptor expression on suburothelial interstitial cells. *BJU Int*. 2009; 104: 398-405.
11. McHale NG, Hollywood MA, Sergeant GP, Shafei M, Thornbury KT, Ward SM. Organization and function of ICC in the urinary tract. *J Physiol*. 2006; 576: 689-694.
12. Cunningham RM, Larkin P, McCloskey KD. Ultrastructural properties of interstitial cells of Cajal in the Guinea pig bladder. *J Urol*. 2011; 185: 1123-1131.
13. Kim SO, Oh BS, Chang IY, Song SH, Ahn K, Hwang EC, Oh KJ, Kwon D, Park K. Distribution of interstitial cells of Cajal and expression of nitric oxide synthase after experimental bladder outlet obstruction in a rat model of bladder overactivity. *Neurourol Urodyn*. 2011; 30: 1639-1645.
14. Gevaert T, De Vos R, Van Der Aa F, Joniau S, van den Oord J, Roskams T, De Ridder D. Identification of telocytes in the upper lamina propria of the human urinary tract. *Journal of Cellular and Molecular Medicine*. 2012; 16: 2085-2093.
15. Zheng Y, Zhu T, Lin M, Wu D, Wang X. Telocytes in the urinary system. *J Transl Med*. 2012; 10: 188.
16. Popescu LM, Faussone-Pellegrini MS. TELOCYTES - a case of serendipity: the winding way from Interstitial Cells of Cajal (ICC), via Interstitial Cajal-Like Cells (ICLC) to TELOCYTES. *Journal of Cellular and Molecular Medicine*. 2010; 14: 729-740.
17. Nicolescu MI, Bucur A, Dinca O, Rusu MC, Popescu LM. Telocytes in parotid glands. *Anat Rec (Hoboken)*. 2012; 295: 378-385.
18. Hinescu ME, Gherghiceanu M, Mandache E, Ciontea SM, Popescu LM. Interstitial Cajal-like cells (ICLC) in atrial myocardium: ultrastructural and immunohistochemical characterization. *Journal of Cellular and Molecular Medicine*. 2006; 10: 243-257.
19. Popescu LM, Gherghiceanu M, Hinescu ME, Cretoiu D, Ceafalan L, Regalia T, Popescu AC, Ardeleanu C, Mandache E. Insights into the interstitium of ventricular myocardium: interstitial Cajal-like cells (ICLC). *Journal of Cellular and Molecular Medicine*. 2006; 10: 429-458.
20. Popescu LM, Ciontea SM, Cretoiu D. Interstitial Cajal-like cells in human uterus and fallopian tube. *Ann N Y Acad Sci*. 2007; 1101: 139-165.
21. Rusu MC, Nicolescu MI, Jianu AM, Lighezan R, Manoiu VS, Paduraru D. Esophageal telocytes and hybrid morphologies. *Cell Biol Int*. 2012; 36: 1079-1088.
22. Popescu LM, Manole CG, Gherghiceanu M, Ardelean A, Nicolescu MI, Hinescu ME, Kostin S. Telocytes in human epicardium. *Journal of Cellular and Molecular Medicine*. 2010; 14: 2085-2093.
23. Popescu LM, Gherghiceanu M, Suciu LC, Manole CG, Hinescu ME. Telocytes and putative stem cells in the lungs: electron microscopy, electron tomography and laser scanning microscopy. *Cell Tissue Res*. 2011; 345: 391-403.
24. Huizinga JD, Faussone-Pellegrini MS. About the presence of interstitial cells of Cajal outside the musculature of the gastrointestinal tract. *J Cell Mol Med*. 2005; 9: 468-473.

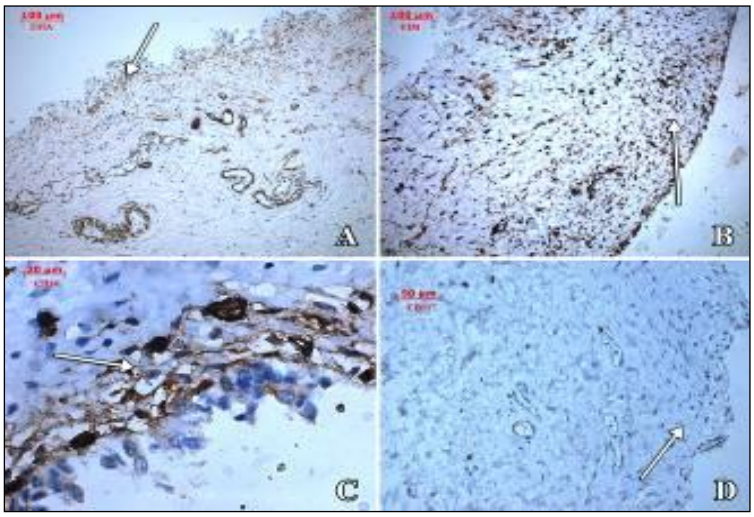

Figure 1. The suburothelial layer (arrow) in human bladder is α-SMA/vimentin/CD34 positive (A, B and, respectively C) and CD117 negative (D).

Tissues, Pathology, and Diagnostic Microscopy

LS.2.P100
Vildagliptin as a DPP4 inhibitor induces beta cell regeneration in neonatal streptozotocin diabetic rats

G. Argun[1], F. Kaya Dagistanli[1], M. Ozturk[1]

[1]Istanbul University, Cerrahpasa Faculty of Medicine, Medical Biology, Istanbul, Turkey

gamzeargun@gmail.com

Vildagliptin (VG), a new inhibitor of DPP-4 which has been developed for type 2 diabetics, increases glucose depended insulin secretion by increasing GLP1 and regulate plasma glucose levels on human researches (1,2). In this study we aimed to observe the effects of VG on possible beta cell regeneration and islet morphology in neonatal streptozotocin-diabetic rat model.

Three groups were performed. The first group was the control group. The second and third groups were injected i.p with 100 mg/kg streptozotocin on the second day after birth. Second group was not given any treatment. The third group received, 60mg/kg/day VG for 8 days by starting from third day. The pancreatic tissue sections were immunostained with insulin, glucagon and PCNA antibodies. Body weight and blood glucose levels of the animals in all groups were measured. All values were analyzed with statistical methods.

In n2-STZ and n2-STZ+VG groups, blood glucose levels were significantly increased ($p<0,001$) when compared with the control group. Insulin positive cells were localized in the central of islets. The islets were detected to be smaller in size in the n2-STZ group compared with the control and the n2-STZ+VG groups. The insulin positive cells area and islets size increased in the n2-STZ+VG group compared with that in the n2-STZ group ($p<0,001$)(Fig. 1). We observed immunopositive insulin cells and cell clusters scattered in exocrine tissue in n2-STZ+VG group. In the n2-STZ and n2-STZ+VG groups the glucagon immunpositive cell area significantly increased ($p<0.001$) in islets compared with control group. The glucagon cells were localized centrally in the islets, whereas in the n2-STZ+VG group they were found to be similar to the control group. The number of PCNA immunopositive cells within the islet was detected to be higher in the n2-STZ+ VG group than the n2-STZ group and control group ($p<0,001$) (Fig. 2).

Our results show that vildagliptin promotes pancreatic beta cell regeneration by increasing of beta cell replication, and also induces morphological reorganization of islet cells in STZ diabetic neonatal rats.

1. Duttaroy A, Voelker F, Merriam K, Zhang X, Ren X, Subramanian K, Hughes TE,Burkey BF. Eur J Pharmacol. 2011 Jan 15;650(2-3):703-7.
2. Kalra S. J Assoc Physicians India. 2011Apr;59:237-45.

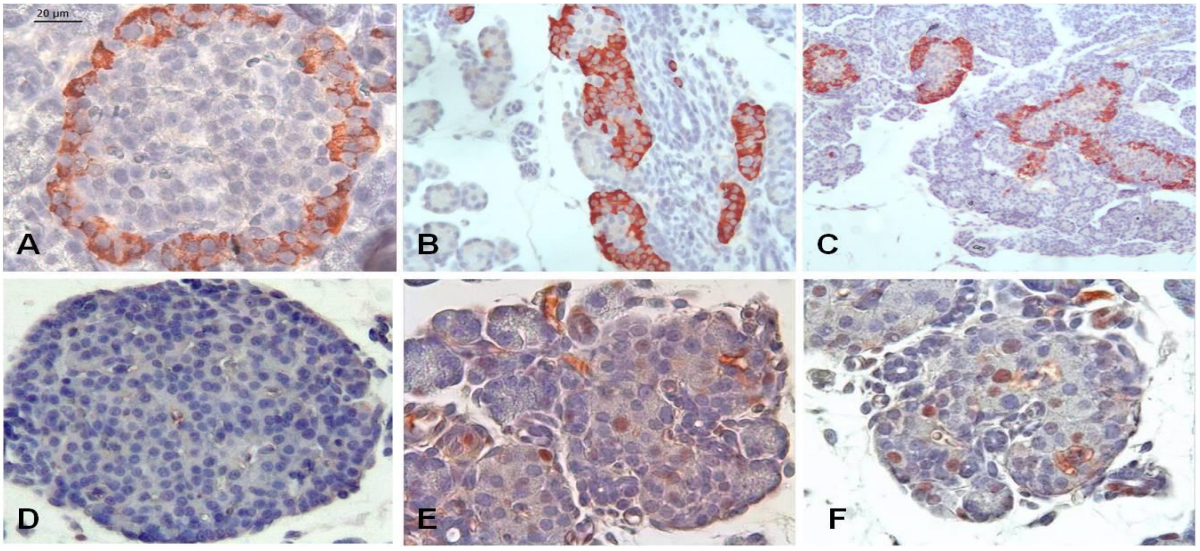

Figure 1. Immunolocalization of insulin in the pancreas of all groups. The increased insulin immunopositive cells are seen in the n2-STZ+VG group compared to the n2-STZ group. (A) Control, (B) n2-STZ and (C-D) n2-STZ+VG groups. Scale bar = 20 µm.

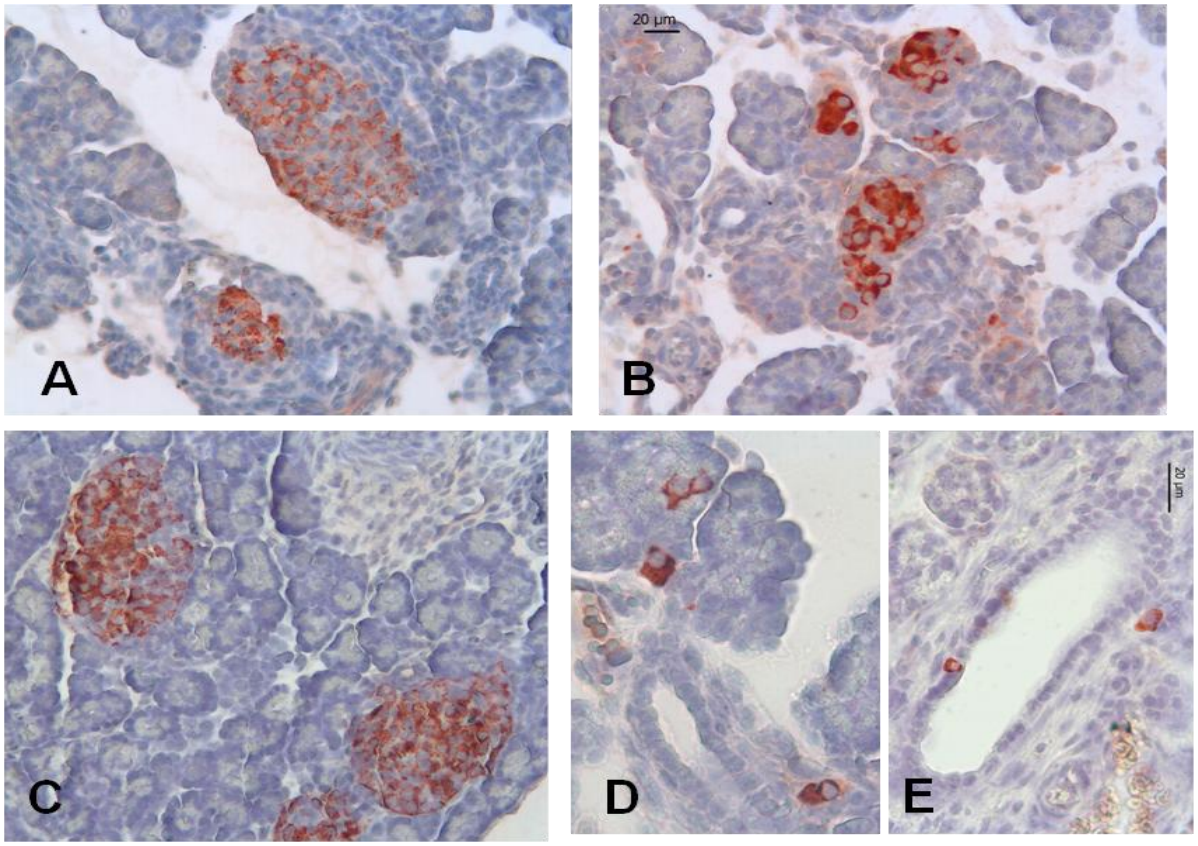

Figure 2. Immunolocalization of (A-C) glucagon and (D-F) PCNA in the pancreas of all groups. (A, D) Control, (B, E) n2-STZ and (C-F) n2-STZ+VG groups. Scale bar = 20 µm.

Tissues, Pathology, and Diagnostic Microscopy

LS.2.P101
Visualization of early Hepatitis B Virus (HBV) infection in *ex vivo* perfused human liver tissue using fluorescence labelled viral particles

K. Esser[1], X. Cheng[1], D. Hartmann[2], A. Walch[3], P. Knolle[4], U. Protzer[1]

[1]Technical University of Munich, Institute of Virology, Munich, Germany
[2]Technical University of Munich, University Hospital Rechts der Isar, Department of Surgery, Munich, Germany
[3]Technical University of Munich/Helmhotz Zentrum München, Department of Surgery, Munich, Germany
[4]University of Bonn, Institute of Molecular Medicine and Experimental Immunology, Bonn, Germany

knud.esser@virologie.med.tum.de

HBV is a hepatotropic pathogen leading to a chronic inflammation of human liver in about 10% of infections. It is a main cause for the development of liver cirrhosis and hepatocellular carcinoma and represents a serious health problem worldwide. Despite many efforts, the early steps in HBV infection are still poorly understood. In humans, HBV is efficiently and selectively separated from the circulation by the liver. However, hepatocytes, the HBV host cells, are shielded from the blood by a fenestrated layer of sinusoidal non-parenchymal cells and bind HBV only inefficiently *in vitro*, especially in the presence of human serum. Thus, non-parenchymal liver cells might take up HBV *in vivo* and mediate host-cell targeting by transcytosis.

To test this hypothesis, we developed a model in which human liver tissue is *ex vivo* perfused via branches of the portal vein under cell culture conditions in the presence of human serum. The intact human liver microarchitecture allowed us to investigate HBV liver cell interactions occurring *in vivo*. When a fraction of fluorescence labelled viral particles (VP) was used for 45 minutes perfusion, accumulation of VP was only observed in sinusoidal CD68 positive liver macrophages -named Kupffer cells- but not in hepatocytes. To exclude artefacts due to the labelling or purification process, supernatant of HBV producing HepG2.215 cells was used for liver perfusion and immunofluorescence analysis confirmed former results. Ultrastructural analysis by electron microscopy showed uptake of virions into endosomes where they exclusively located membrane associated, a geometric constraint essential for component recycling. In line with a recycling within Kupffer cells, VP concentrated in FITC-transferrin positive recycling endosomes in cultured liver macrophages. To reach its host cell, however, the virus needs to be released from Kupffer cells again. When human liver tissue was perfused for further 15 hours with human serum containing but VP negative medium, hepatocytes became positive only when Kupffer cells became negative. Taken together, our data suggest that HBV is removed from the circulation by Kupffer cells *in vivo*. Within these cells, HBV connects to a recycling pathway along that HBV targets and finally trans-infects its host cell.

Tissues, Pathology, and Diagnostic Microscopy

LS.2.P102
Study of proliferating blood cells in *Ciona intestinalis* (Tunicata) immune response

M.A. Di Bella[1], G. De Leo[1]

[1]University of Palermo -I, Palermo, Italy

Ascidians are cosmopolitan marine invertebrates considered to be a sister group of vertebrates being classified in the phylum Chordata, subphylum Tunicata [1]. *Ciona intestinalis,* a reference species of the solitary ascidians, is a valuable model organism for the study of a variety of biological processes.

Following an inflammatory stimulus such as the injection of erythrocytes or foreign material into the body wall, *C. intestinalis* displays acute inflammatory responses consisting in humoral and cellular reactions performed by hemocytes. Hemocytes are essential for recognition of self and non-self, for phagocytosis, encapsulation and lysis of foreign agents, and repair of damaged tissue [2-5]. During inflammatory-like reactions hemocytes migrate by diapedesis from the hemolymphatic lacunae trough the mantle epithelium into the inflamed tissue leading to a subsequent increase of the cell population [6]. In this sense, circulating hemocytes, coming from the hemolymph, pharinx, and hematogenic sites, assume particular interest.

In *C. intestinalis* several hemocyte types have been described [7], and as in other ascidian species hemocytes that have been reported to function in stem cells or regeneration related activities include hemoblasts considered able to proliferate and/or differentiate diverse hemocyte types [8,9,].

Hemopoietic tissue in ascidians is organized into clusters called lymph nodules scattered in the pharyngeal wall, in transverse vessels of the brachial sac, and also in the endostyle region The atrial epithelium, the specialized tissue that underlies the epidermis and encircles the pharinx, is also able to undergo transformation as it becomes multilayered. The cells assume a squamous shape, the nuclei are in general ellipsoidal [10-15]. On response to mitogens or allogeneic cells, *in vitro* proliferation of circulating blood cells have been evidenced by autoradiography and *in vitro* culture medium [16, 17].

The proliferative response of circulating hemocytes and pharynx assume particular interest as it is significantly enhanced during the defence reactions when the hemoblasts in blood lacunae and hematogenic nodules may undergo an increased proliferative activity. We observed the circulating dividing cells and the high presence of precursor cells in hemopoietic tissue. The rapid rate of proliferation is suggested by the presence of undifferentiated cells increased conspicuously in number near the vessel epithelium and the presence of intercellular bridges between hemoblasts circulating in blood lacunae.

1. F. Delsuc, H. Brinkmann, D. Chorrot, P. Hervé, *Nat. Lett.* 439, (2006), pp. 965-968.
2. N. Parrinello, E. Patricolo, C. Canicattì, Biol. Bull. 167, (1984), pp. 229-237.
3. N. Parrinello, E. Patricolo, C. Canicattì, Biol. Bull. 167, (1984), pp. 238-250.
4. G. De Leo, N. Parrinello, D. Parrinello, G. Cassarà, M.A. Di Bella, J. Invert. Pathol., 67, (1996), pp. 205-212.
5. G. De Leo, N. Parrinello, D. Parrinello, G. Cassarà, D. Russo, M.A. Di Bella, J. Invert. Pathol., 69, (1997),1 pp. 4-23.
6. M.A. Di Bella, G. De Leo, J. Invert. Pathol., 76, (2000), pp 105-111.
7. G. De Leo, Boll. Zool. 59, (1992), pp. 195-213.
8. D.A. Raftos, E.L. Cooper, J. Exp. Zool. 260, (1991), pp. 391-400
9. R.K Wright. in: “Invertebrate blood cells” eds. N.A. Ratcliffe, A.F. Rowley, Vol. 2. New York, N Y: Academic Press, (1981), pp. 565-626.
10. W.C. George, Quart. J. Micr. *Sc*. 81, (1939), pp 391-428
11. T.H. Ermak, Experientia. 31, (1975), pp 837-838
12. T.H. Ermak,in “Phylogeny of Thymus and Bone Marrow-Bursa Cells”, eds. R.K. Wright, E.L. Cooper, Elsevier, Amsterdam, North Holland (1976), pp. 45–56
13. T.H. Ermak, Am. Zool., 22 (1982), pp. 795–805
14. R.H. Millar, in: "Memoirs ed. J.S. Colman,. *L.M.B.C.* Liverpool: The University Press; (1953), pp. 1-123.
15. A. Voskoboynik, Y. Soen, Y. Rinkevic, A. Rosner, et al., Cell Stem Cell, 3, (2008), pp. 456-464.
16. D.A. Raftos, D.L. Stillman, E.L. Cooper, Immunol. Cell Biol., 69 (1991), pp. 225–234
17. C.M. Peddie, A.C. Richesr, V.J. Smith, *Dev. Comp. Immunol*, 5, (1995), pp. 377-387.
18. This work has been supported by grants from the Italian Ministero della Università e della Ricerca and the University of Palermo research grant to M.A.D. and G.DL.

Tissues, Pathology, and Diagnostic Microscopy

LS.2.P103
Urban malaria and associated risk factors in Jimma town, south-west Ethiopia

A. Alemu[1]

[1]University of Gondar , Medical parasitology , Gondar, Ethiopia

yanbule@gmail.com

Malaria kills millions around the globe and until recently it was believed to be a disease of rural areas, since the *Anopheles* mosquito, which transmits *Plasmodium* species between people, breeds in stagnant waters. Urban malaria is emerging as a potential, but "avertable" crisis, in Africa. Malaria is also a leading public health problem in Ethiopia where an estimated 68% of the population lives in malarious areas. In Ethiopia, particularly in Jimma, there is scarcity of studies which could provide recent information on the prevalence of malaria. Therefore, the aim of this study was to estimate malaria prevalence and associated risk factors in Jimma town.

A cross-sectional study was carried out in Jimma town from April 1 to May 28, 2010. A total of 804 individuals from 291 households were included in this study. Blood samples were collected by finger prick; both thick and thin blood film was prepared, stained by Giemsa and examined by 100X objective of compound light microscope. All the data were entered and analyzed by using SPSS-15 database programme.

From a total of 804 study participants in current survey only 42 (5.22%) were positive for malaria parasites in which *Plasmodium vivax, Plasmodium falciparum* and mixed infection accounted 71.42% , 26.19% and 2.38%, respectively. Most of the respondents (71.8%) replied that *Plasmodium* is the causative agent of malaria and (67.4%) of respondents replied that malaria is transmittable disease. Large proportion of respondents (78.4 %) had awareness about breeding site of *Anopheles* mosquitoes, that is stagnant water, but 45.7 % respondents did not know the biting time of *Anopheles* mosquitoes. Variation of household socio-demographic variables did not show statistically significant association with malaria prevalence in the study area. Of different risk factors assessed, only presence of stagnant water and ITNs usage were statistically significantly associated with malaria prevalence in the study area.

Malaria is still a major health problem with *P. vivax* becoming a predominant species. Human activity plays a major role in urban malaria ranging from creating breeding sites, ‘importing’ cases, or through treatment-seeking choices. Solutions therefore, must also focus on human behavior.

Tissues, Pathology, and Diagnostic Microscopy

LS.2.P104
Distribution of meiosis controlling proteins during ovarian oocyte development

H.S. Vatansever[1], H. Yesil[1]

[1]Celal Bayar University, Histology and Embryology, Manisa, Turkey

nisalisayy@hotmail.com
Keywords: oocyte, meiosis, emi, MOS, cyclin B, development

Maturation of oocyte is start at embryonic stage, it is hesitate during prohase I of meiosis, start to develop in puberty with developing follicules. During the development stages of oocyte at meiosis I and meiosis II, there is many molecular mechanisms for controlling to oocyte maturation. These mechanisms also provided to transition from one phase to another phase of oocyte and is complemented by the development of mature oocytes for fertilization. Oocyte maturation problems and/or pauses of development of oocyte during meiotic stage (remain in arrest) can not be seen fertilization.For this purpose, to analyze secreted cyclin B, Emi and MOS distributions during ovarian cycle in mouse ovarian tissue will be collect.

To analyze distribution of anti-Cyclin B, anti-Emi and anti-MOS during ovarian cycle, ovarian tissue will also collected (form 5 mouse) and after routine paraffin embedding protocols, the sections will be stained to with anti-cyclin B, anti-MPF and anti-MOS using immunoperoxidase technique

Immunoreactvitiy of Emi is while positive in oocyte cells, weak intensity was detected in primordial follicles. While immunoreactivitiy of Emi was negative in both oocyte and follicular cells in primary follicles, the weak immunoreactivity was only observed in corona radiata and follicle cells of secondary and graafian follicles.

Cyclin B immunoreactivity was detected in all stage of developing ovarian follicles. Cyclin-B staining was weakly or negative in follicular cells and ooctye, respectively,in primordial follicles. In addition, this immunoreactiviy was observed rest of the follicules, however, it was more detectable in follicular cells of secondary follicules. MOS immunoreactiy was negative in both oocyte and follicular cells of primordial follicules, moderate staining in primary follicle oocyte and graafian follicular cells was observed.

Our results suggested that, secretion of Emi was only detected in very early stage of ovarian follicles. Otherwise, the secretion of both MOS and Cyclin-B were triggered in primary follicles and continue during further development of ovarian follicles. In conclusion, activation of MOS and Cyclin B were important in follicular development in mouse ovarian tissue.

1. Lefebvre C, Terret ME, Djiane A, Rassinier P, Maro B, Verlhac MH. Meiotic spindle stability depends on MAPK-interacting and spindle-stabilizing protein (MISS), a new MAPK substrate. J Cell Biol. 2002 May 13;157(4):603-13, 2002.
2. Levi M, Shalgi R. The role of Fyn kinase in the release from metaphase in mammalian oocytes. Mol Cell Endocrinol. 27;314(2):228-33, 2010.
3. Liu W, Yin J, Zhao G, Yun Y, Wu S, Jones KT, Lei A.Differential regulation of cyclin B1 degradation between the first and second meiotic divisions of bovine oocytes. Theriogenology. Oct 1;78(6):1171-81, 2012.

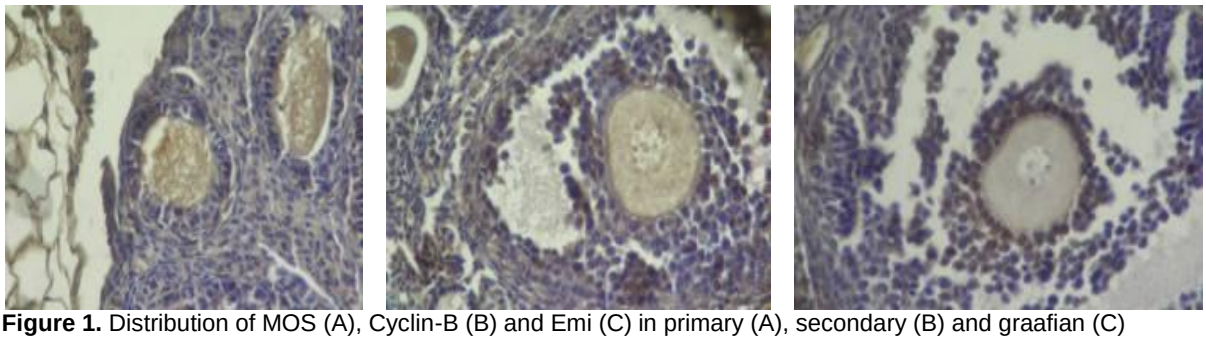

Figure 1. Distribution of MOS (A), Cyclin-B (B) and Emi (C) in primary (A), secondary (B) and graafian (C) follicules in adult mouse ovarian tissue. Scale Bar: 25µm

Tissues, Pathology, and Diagnostic Microscopy

LS.2.P105
Stereochemistry of the gemini surfactant influences the final fate of cationic liposomes in human tumor cells

G. Bozzuto[1,2], C. Bombelli[2], B. Altieri[2], L. Giansanti[2], A. Stringaro[1], M. Colone[1], L. Toccacieli[1], G. Formisano[1], A. Molinari[1], G. Mancini[2]

[1]Istituto Superiore di Sanità, Technology and Health, Rome, Italy
[2]National Research Council , Institute of Chemical Methodologies, Rome, Italy

giuseppina.bozzuto@iss.it
Keywords: nanomedicine, liposomes, endocytosis

Our previous studies demonstrated that the presence of cationic gemini surfactant (S,S)-2,3-dimethoxy-1,4-bis(N-hexadecyl- N,N-dimethylammonio)butane bromide **1a** in the liposomes formulated with dimyristoyl-*sn*-glycero-phosphatidylcholine, DMPC, increases the cell uptake of the photosensitizer *m*-tetrahydroxyphenylchlorin, *m*-THPC [1, 2], in human colon adenocarcinoma cells [1], murine and human glioblastoma cells [2]. In order to explore the influence of the stereochemistry of the gemini surfactants 1 on the delivery efficiency of *m*-THPC to malignant glioma (GBM) cell lines, liposomes were formulated with DMPC, and either cationic gemini surfactant **1a**, or (S,R)-2,3-dimethoxy-1,4-bis(N-hexadecyl-N,N-dimethylammonio) butane bromide (**1b**).

The stereochemistry of the spacer of the gemini was found to strongly influence the delivery efficiency of *m*-THPC to cells and its intracellular distribution. Unexpectedly, the formulation featuring a higher surface potential and a greater stability toward fusion (DMPC/**1a**), was found to be less efficient in the delivery of the photosensitizer.

Since the liposome internalization pathway depends both on the size and nature of the carrier, we investigated the influence of the stereochemistry of the surfactant on the interaction with cell membranes and the intracellular route of liposomes. In a first approach, a combination of different inhibitors was used to selectively block different pathways (Figure 1a). These effects were evaluated by flow cytometry on human (LN229) and murine (C6) glioblastoma cells. The analysis performed revealed that both DMPC/**1a** and DMPC/**1b** followed the endocytic pathway but that the two formulations were influenced by different endocytic inhibitors (Figure 1b). The results strongly suggest that DMPC/**1a** enter into the cells preferentially through the interaction with rafts and caveolae as demostrated by the filipin-indiced inhibition. On the other hand, DMPC/**1b** seems to enter into the cells preferentially upon interaction with clathrin, as showed by the inhibition exerted by chlorpromazine.

In the second approach, several antibodies specific for organelles involved in endocytic routes were employed. The observations performed by laser scanning confocal microscopy (LSCM) on cells treated with DMPC/**1a** or DMPC/**1b** confirmed data obtained by flow cytometry. In addition, it demonstrated that DMPC/**1a** colocalized preferentially with early endosomes (Rab5+), whereas DMPC/**1b** were found in early and late endosomes (Rab7+) and in lysomomes (Lamp1+).

Finally, in order to study at higher resolution the interaction with plasma membrane a comparative study on either ultrathin sectioned or freeze-fractured samples was carried out by TEM. The observations on both freeze fractured and resin embedded sample (Figure 2), confirmed the intracellular transport of liposomes mediated by cytoplasmic organells, as revealed by LSCM.

These results demonstrated that the different mode of interaction results in a different subcellular fate of the two liposome formulations. After binding to the plasma membrane, DMPC/G**1a** liposomes are internalized trough caveolae-coated vesicles. Then, they are preferentially transferred to early endosomes . On the other hand, clathrin-mediated endocytosis of DMPC/G**1b** leads to the formation of an early endosome, which is acidified and fuses with prelysosomal vesicles containing enzymes to give rise to a late endosome and, finally, a lysosome, an acidic and enzyme-rich environment.

1. C. Bombelli et al., J Med Chem 48 (2005), p. 4882.
2. A. Molinari et al., Int J Cancer 121 (2007), p. 1149.

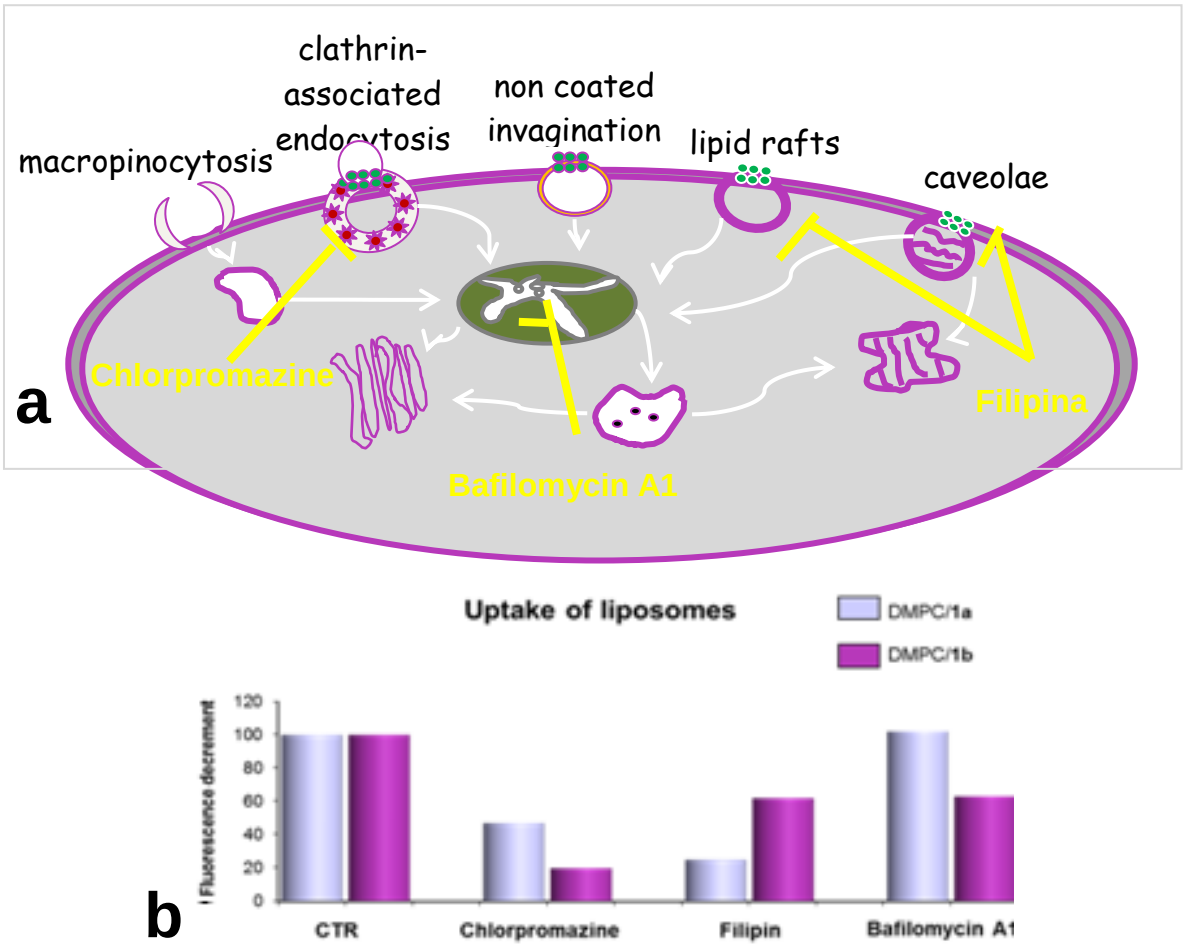

Figure 1. Uptake of DMPC/1a and DMPC/1b liposomes evaluated by flow cytometry in LN229 cells, before and after the treatment with endocytic inhibitors

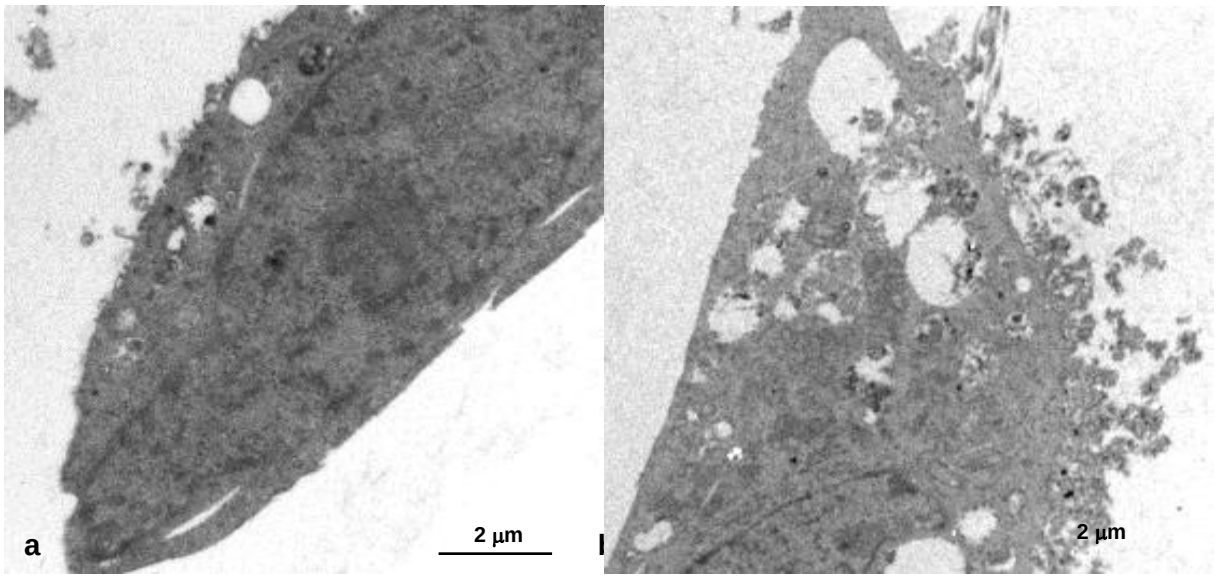

Figure 2. Human glioblastoma LN229 cells interacting with DMPC/a (a) and DMPC/b (b). After 18 h of incubation, DMPC/b liposomes (b) showed to be significantly more numerous on the apical side of LN229 cell, when compared to DMPC/a. In addition, after the interaction with DMPC/b the cytoplasm of glioblastoma cells displayed a number of cytoplasmic organelles (endosomes and lysosomes) (b) higher than cytoplasm of cells treated with DMPC/a formulation.

Tissues, Pathology, and Diagnostic Microscopy

LS.2.P106
Expression of GABA receptors in the mouse cervical epithelium during estrous cycle

M. Curlin[1], M. Skelin[1]

[1]School of medicine University of Zagreb, Department of histology and embryology, Zagreb, Croatia

marija.curlin@mef.hr
Keywords: cervical epithelium, estrous cycle, GABA receptor

Cervical mucus has a significant role in female fertility and protection of the reproductive health [1]. The aim of this study was to determine if mouse cervical epithelium with its specific cyclic changes could serve as an experimental model for investigation of the mechanisms and regulation of secretion of the cervical mucus.

A complete study of the structure and cyclic changes of the mouse cervical mucosa was performed. Additionally, several procedures of collecting samples of vaginal secretions to determine the phases of the ovulatory cycle were tested and the most appropriate method chosen [2].

Cytological and histological analyses showed the correlation between the vaginal secretion and the structural changes in the cervical epithelium and mucus (Figure 1). During the estrous phase of the ovulatory cycle, a simple columnar epithelium appears at the top of the squamous stratified epithelium covering the wall of the cervix [3]. We have shown that this columnar epithelium produces cervical mucus (Figure 1G and 1H). This feature enables the mouse cervical epithelium to serve as a model for investigation of the cervical mucus secretion. Immunohistochemistry and RT-PCR analyses demonstrated the presence of the receptor A of neurotransmitter GABA in the glandular epithelium of the mouse cervix during pro-estrous and estrous phase (Figure 2B and 2C), assuming that GABA plays a role in the cyclic regulation of cervical mucus secretion.

1. M. Ćurlin and D. Bursać, Frontiers in Bioscience S5 (2013) – ready for fall release
2. K.R. Pritchett and R. Taft in “The mouse in Biomedical research”, ed. J.G. Fox, (Academic Press, USA) (2007) p. 100-101.
3. B. Peckham and W. Kiekhofer, Am J Obstet Gynecol 83 (1962), p. 1021-7.
4. This research was supported by Ministry of Science and Technology, Republic of Croatia.

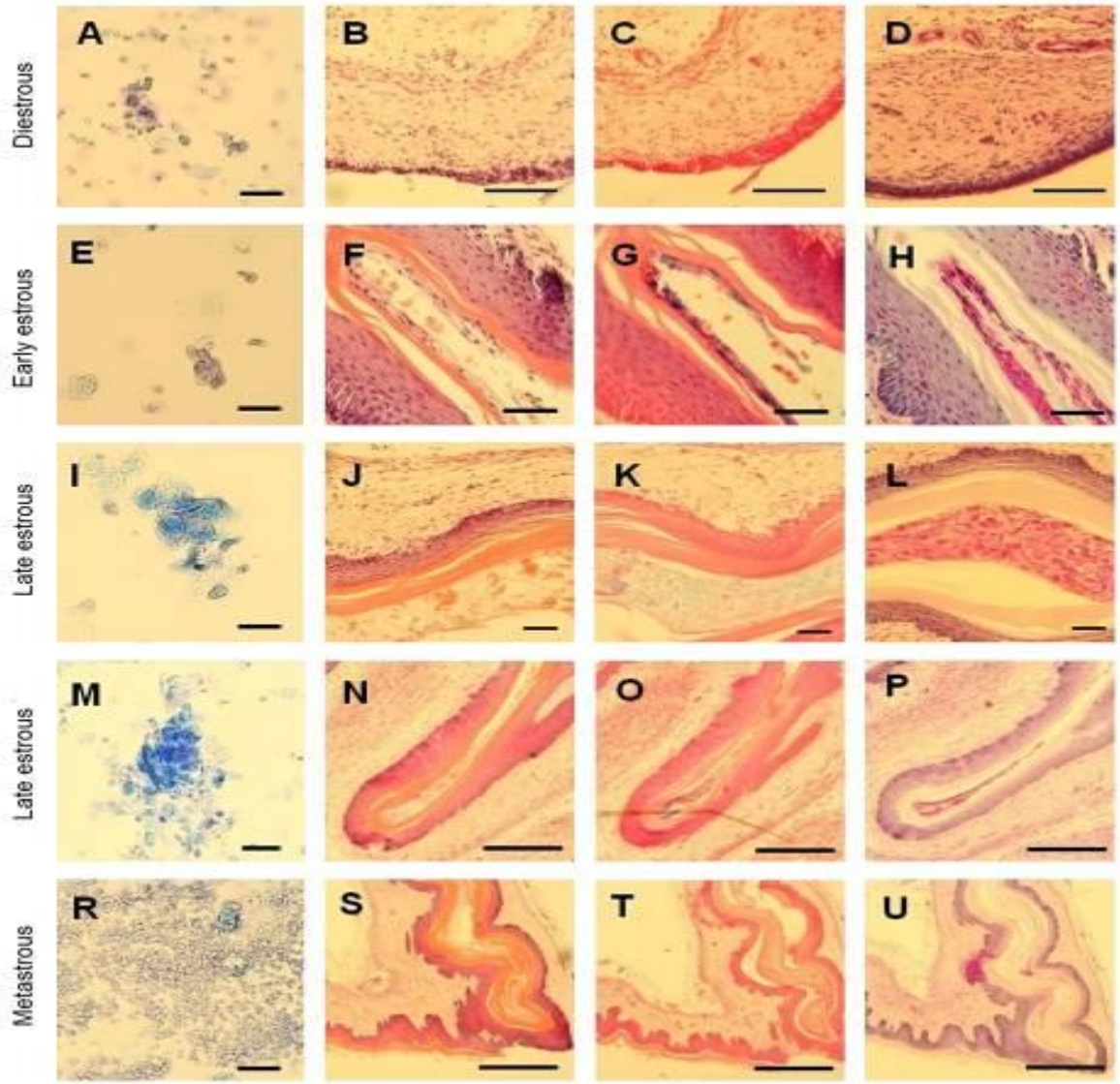

Figure 1. Correlation of the cells from the vaginal secretions and mouse cervix tissue during ovulatory cycle. The cells are stained by methylene blue and eosin (first column), and the tissues by hemalaun and eosin (second column), Astra blue histochemical staining (third column) and PAS histochemical staining (fourth column). Bar A, E, I, M, R - 50 µm. Bar B - D – 0,2 mm. Bar F – H, J - L – 0,1 mm. Bar N - P – 0,5 mm. Bar S - U – 1 mm.

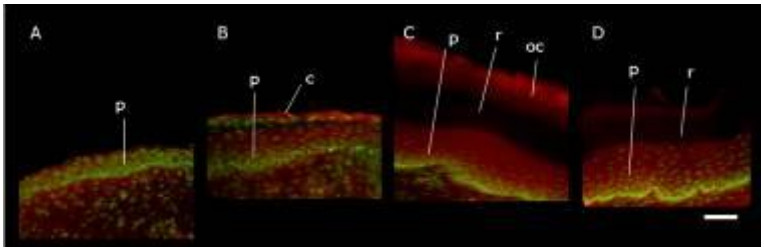

Figure 2. Expression of the GABA A receptor ß2 in the epithelium of mouse cervix (red immunohistochemical fluorescent signal) during proestrus and estrous phase of the ovulatory cycle. A – diestrous, B - proestrous. C - estrous. D - metaestrous. The green signal shows nuclei stained by DAPI flourescent staining. p – stratified squamous epithelium, c – simple columnar epithelium, r – cornified layer, oc – epithelial cell remnants. Bar – 0,1 mm.

Tissues, Pathology, and Diagnostic Microscopy

LS.2.P107
Ultrastructural evaluation to understand *Mycobacterium brumae* and BCG interaction with bladder tumor cells

G. Orpella-Aceret[1], A. Sánchez-Chardi[2], S. Secanella-Fandos[1], M. Luquin[1], E. Julián[1]

[1]Universitat Autònoma de Barcelona, Genètica i Microbiologia, Cerdanyola del Vallès, Spain
[2]Universitat Autònoma de Barcelona, Microscopy Facility, Cerdanyola del Vallès, Spain

Esther.Julian@uab.cat: Alejandro.Sanchez.Chardi@uab.cat
Keywords: immunotherapy agents, human bladder cancer cells (T24), *M. brumae*.

Intravesical bacillus Calmette-Guérin (BCG) is routinely used as immunotherapy agent in non-invasive human bladder tumors. Despite of well known BCG beneficial effects in retarding tumor progression and recurrence, there are adverse side-effects due to the use of a live strain from the *M. tuberculosis* complex, e.g. infections due to BCG. Therefore, there is a growing interest in the use of less deleterious agents. In this line, the efficacy of the non pathogenic *Mycobacterium brumae* as antitumor agent has been recently demonstrated in our laboratory. Although *M. brumae* inhibits tumor growth similarly to BCG in vitro, nothing is known about their interaction with bladder tumor epithelial cells.

A qualitative and quantitative evaluation of *M. brumae* and BCG-infected human bladder tumor cells (T24 cell line) was carried out. T24 cell line was infected with mycobacteria (MOI 10:1) during 48 hours and ultrastructural changes, with respect to non-infected cells, were analyzed using SEM and TEM. In parallel, colony-forming units (cfu) from mycobacteria-T24 infected cells were counted.

Although preliminary, we obtained two main results. Firstly, BCG appears to be more invasive than *M. brumae*. While 17% of T24 cells contain BCG bacilli, only 8% were infected with *M. brumae*. Secondly, a high number of well structured BCG in medium and phagocyted by T24, often in megasomes, was observed. In marked contrast, *M. brumae* cells were mainly found inside little phagosomes with one or two degraded bacilli. This last result is in agreement with cfu counts. Whereas BCG remains viable in T24 cells after 48 hours of infection, *M. brumae* does no persist inside T24 cells. Our results suggest that *M. brumae* is both less invasive and less persistent than BCG on tumor bladder cells.

Plants and their Pathogens

LS.3.108
Pathogen-induced ultrastructural alterations in plants

B. Zechmann[1]

[1]University of Graz, Institute of Plant Sciences, Graz, Austria

bernd.zechmann@uni-graz.at
Keywords: Arabidopsis, Botrytis, Cucurbita, microwave irradiation, Nicotiana, TEM, TMV, Ustilago, ZYMV

Plants are constantly attacked by pathogens (e.g. fungi, viruses, bacteria). In order to cope with them several lines of defense have evolved in plants which protect them against negative effects induced by these invaders [1]. A successful defense of plants against pathogens results in an incompatible interaction where the pathogens are controlled, contained or defeated without the development of systemic symptoms. During compatible interactions plants are unable to control or defeat the pathogens which results in unlimited multiplication and systemic spread of the invaders which lead to physiological changes and to the development of symptoms throughout the infected organ or the whole organism. Many pathogens are able to undermine plant defense which can either result in a biotrophic interaction where the pathogen feeds on living plant cells or in a necrotrophic interaction where the pathogen tries to rapidly kill the host in order to feed from dead cells. Additionally, mutualistic interactions exist where both sides (microbes and plants) co-exist and profit from each other [1-3].

All of these interactions result in ultrastructural adaptations of the host cells either induced directly by the pathogens or indirectly by physiological changes of the plants. Electron and light microscopy allows the study of structural adaptations during plant pathogen interactions which can help to understand defense related processes on the cellular level. They also allow the identification and the diagnosis of the invader. This presentation will give an overview about ultrastructural adaptations of plants to different pathogens. It will demonstrate differences in ultrastructural changes between leaves of *Zea mays* infected with the biotrophic fungi *Ustilago maydis* (Figure 1a) and leaves of *Arabidopsis thaliana* infected with the necrotrophic fungal pathogen *Botrytis cinerea* (Figure 1b). The response of plant cells to the mutualistic fungi *Piriformospora indica* will be demonstrated in roots of *Arabidopsis thaliana* (Figure 1c). Furthermore this presentation will demonstrate differences in the ultrastructural adaptation of leaf cells to virus infections such as *Tobacco Mosaic Virus* (TMV) in *Nicotiana tabacum* (Figure 1d) and *Zucchini Yellow Mosaic Virus* (ZYMV) in *Cucurbita pepo* (Figure 1e). Finally, ultrastructual modifications in leaves of *Arabidopsis thaliana* plants infected with the hemi-biotrophic bacteria *Pseudomonas syringae* will be demonstrated (Figure 1f).

Light and electron microscopy can be used to visualize ultrastructural and physiological changes induced by these pathogens and to clearly identify and diagnose diseases [4]. Throughout this presentation different tools of plant sample preparation for light and electron microscopy will be presented which allow the visualization of reactive oxygen species (a commonly response of plants against pathogens), the quantification of differences in the relative amount of viral particles in plant organs, and the rapid identification and diagnosis of the plant disease. The rapid diagnosis of plant virus diseases can be of great significance in order to identify the viral agent and to limit the spread of the disease. In this presentation a method will be demonstrated that is based on microwave assisted plant sample preparation, negative staining methods, and cytohistochemical localization of viral coat protein and allows the rapid diagnosis of plant virus diseases in altogether about half a day by transmission electron microscopy.

1. C.M.J. Pieterse, A. Leon-Reyes, S. van der Ent, and van Wees S.C.M., Nature Chem. Biol. 5 (2009), p. 308.
2. T. Mengiste, Ann. Rev. Phytopathol. 50 (2012), p. 267.
3. R.P. Oliver and P.S. Solomon, Curr. Opin. Plant Biol. 13 (2010), p. 415.
4. B. Zechmann and G. Zellnig, J. Virol. Methods 162 (2009), p. 163.
5. The author gratefully acknowledges funding from the Austrian Science Fund (P20619, P22988).

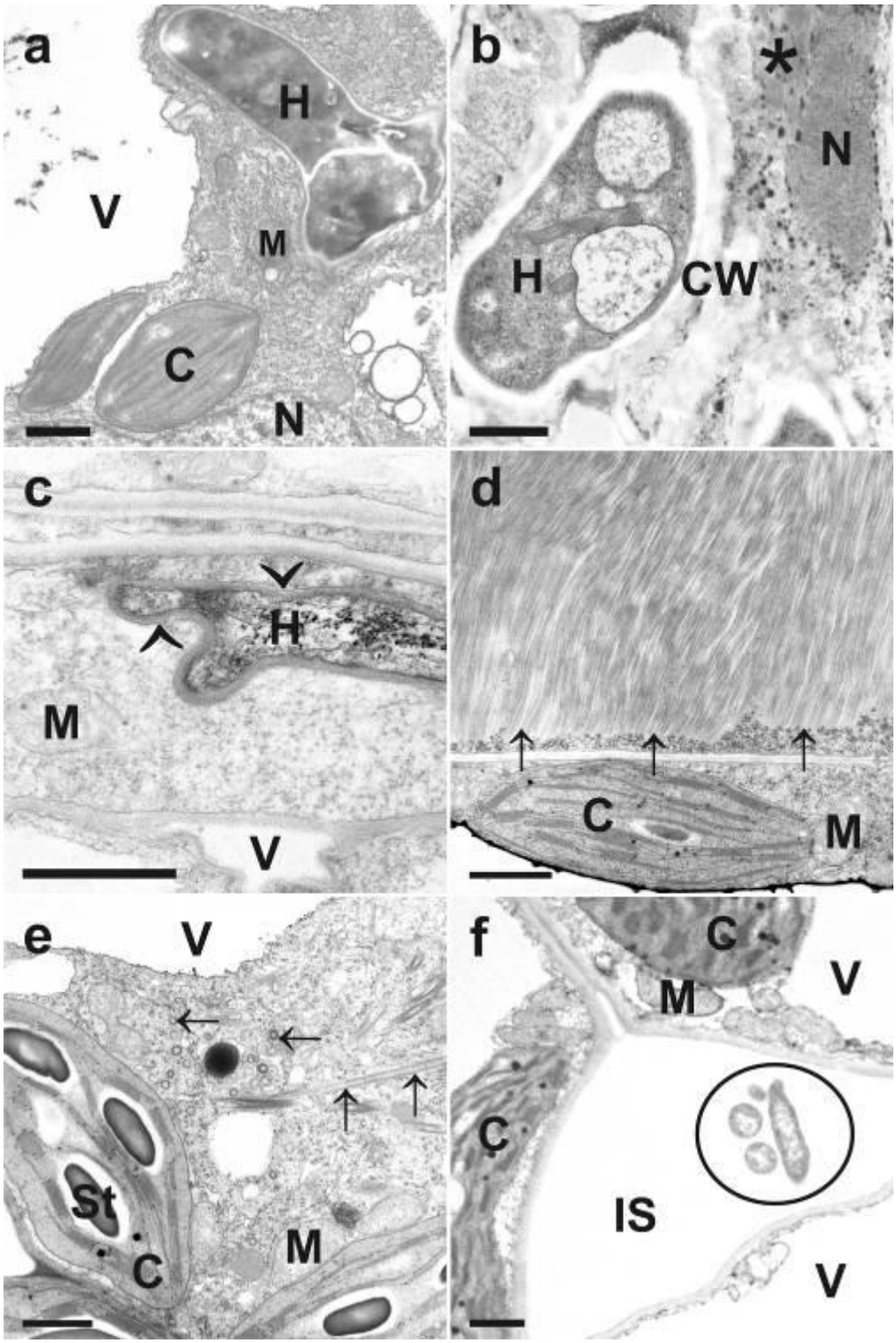

Figure 1. TEM-micrographs of selected ultrastructural modifications during plant pathogen interactions. Fungal hyphae (H) of the biotrophic basidiomycete *Ustilago maydis* are growing intracellulary in leaf cells of *Zea mays* without major alterations of the host cell (a). In opposite strong ultrastructural alterations can be observed at the final stages of *Botrytis cinerea* infection in leaves of *Arabidopsis thaliana* where only remnants of chloroplasts (star) can be found in the condensed cytosol (b). The mutualistic basidiomycete *Piriformospora indica* grows intracellulary within roots of *Arabidopsis thaliana* without damaging the host cell (c). Note the plasmamembrane around the hyphae (arrowheads in c). TMV- and ZYMV-infections are characterized by large areas of virions that accumulate in parallel form (arrows in d) and cylindrical inclusions in the cytosol, respectively (arrows in e). The hemibiotrophic bacteria *Pseudomonas syringae* grows and accumulates intercellulary (black circle) in *Arabidopsis thaliana* leaves without entering the host cells (f). C=chloroplasts with or without starch (St), CW=cell walls, IS=intercellular space, M= mitochondria, N=nucleus, V=vacuoles. Bars=1µm.

Plants and their Pathogens

LS.3.109
Some biochemical and ultrastructural characteristics of pathogenic and non-pathogenic strains of fungus *Verticillium dahliae* Kleb.

T. Vlasova[1], I. Ageeva[1]

[1]Moscow State Univercity, Fac. of Biology, Moscow, Russian Federation

tat_vla@list.ru
Keywords: plant pathology, *Verticillium dahliae*, pathogenicity, fatty acids, ultrastructure

The problem of susceptibility and resistance of phytopathogens to the antifungal compounds is very important for control of pathogens in agriculture. The adaptation of phytopathogenic fungi to the different unfavorable conditions and to the toxics is directly combined with the reorganization of pathogen cell membranes, first of all with the changes of their lipid composition: polar lipids, sterols, fatty acids and their ethers [1].

The aim of our work was to compare some characteristics of pathogenic and nonpathogenic strains of the fungus *Verticillium dahliae* Kleb in regard to their resistance to the toxics. *V. dahliae* causing Verticillium wilt in many plants is one of the major phytopathogens in any countries.

In our experiments, it has been shown that the pathogenic strain of *V.dahliae* in comparison with nonpathogenic strain possessed the higher resistance to the toxics accompanied by considerable changes in lipid metabolism causing changes of the permeability of cell membranes which promoted the membrane complex stabilization..

The depression of the growth of *V.dahliae* in the culture was connected with as the interaction with cell surface as with fungal cytoplasmic structures [2].

The electron microscopic (TEM) study showed principal similarity of ultrastructural features of both strains. However, any differences between the strains were also detected. In the hyphae of nonpathogenic strain the mitochondria were more numerous and had condensed form while in the hyphae of pathogenic one they had appearance of orthodox form. The quantity and the sizes of lipid bodies were in the cells of pathogenic fungus more than in the cells of nonpathogenic one. It is in agreement with data on the higher content of total lipids in the mycelium of the pathogenic strain of *V. dahliae* [3]. The cells of the pathogenic strain of *V.dahliae* contained also more vacuoles in comparison with the nonpathogenic strain. It is possible that the presence of the higher content of lipids and of the more developed vacuolar system that could possibly neutralize some toxics should be factors of fungal resistance to the fungicides and other antifungal substances.

1. V.B. Burlakova, in “The role of lipids in the cell information process”, Nauka, Moscow, 1981, p.23.
2. I. V. Ageeva, in: “Modern fungicides and antifungal compounds”, Agroconcept, Bonn, p.103-107.
3. V.F. Kornilova, I.V. Ageeva and L.V. Kuznetzov, Prikladnaya Biokhimiya i Mikrobiologiya, 22, 1986, p. 828-833.

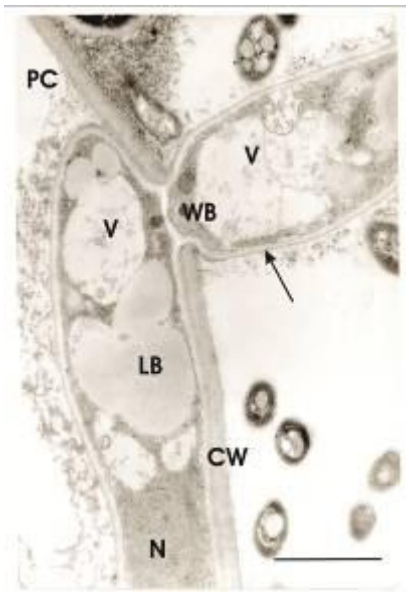

Figure 1. Mycelium of pathogenic strain of *V. dahliae.* PC – plant cell, CW – plant cell wall, arrow – fungal hypha, N – nucleus, V – vacuole, WB –Woronin's body, LB – lipid body. Bar = 1µm

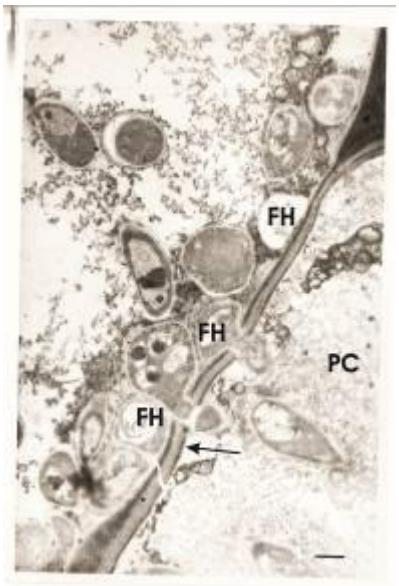

Figure 2. Penetration of cotton root cell by hyphae of pathogenic strain of *V. dahliae.* PC – plant cell, arrow - plant cell wall, FH –fungal hypha. Bar = 1µm.

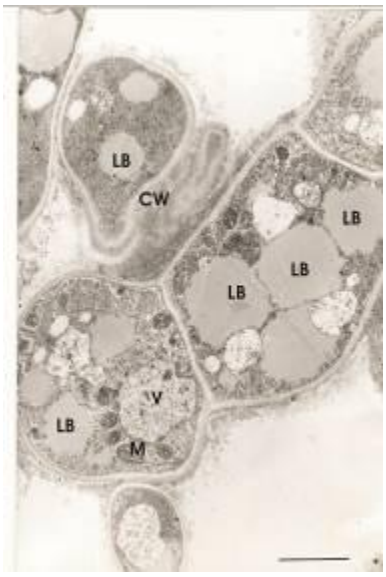

Figure 3. Mycelium of non-pathogenic strain of *V. dahliae.* CW – hyphal cell wall, V – vacuole, LB – lipid body, M - mitochondrium. Bar = 1µm.

Plants and their Pathogens

LS.3.110
Formation of the type III secretion pilus of *Xanthomonas campestris* pv. *vesicatoria* depends on the action of a pilus assembly protein

G. Hause[1], N. Hartmann[2], C. Lorenz[2], S. Fraas[1], S. Schulz[2], D. Büttner[2]

[1]Martin-Luther-University Halle, Biocenter, Microscopy Unit, Halle/Saale, Germany
[2]Martin-Luther-University Halle, Institute of Biology, Genetics Department, Halle/Saale, Germany

gerd.hause@biozentrum.uni-halle.de
Keywords: plant pathogen, type III secretion system, pilus formation

The Gram-negative plant pathogenic bacterium *Xanthomonas campestris* pv. *vesicatoria* utilizes a type III secretion (T3S) system to translocate bacterial effector proteins into eukaryotic host cells and thus to trigger processes in the host necessary for bacterial infection. (Fig. 1). The T3S system consists of a basal apparatus localized in the inner and outer bacterial membrane which is connected to a pilus (outer diameter 6 nm) that penetrates the plant cell wall during infection. Translocation of effector proteins is mediated by a special translocon which inserts into the plasma membrane of the host cell.

Effector protein transport depends on the early T3S substrate HrpB2 which is essential for the assembly of the extracellular pilus of the T3S system. To characterize the role of HrpB2 during T3S and pilus formation we performed a transposon mutagenesis approach which led to the insertion of pentapeptide-encoding sequences into *hrpB2.* Complementation studies revealed that the N-terminal region of HrpB2 tolerates insertions whereas pentapeptide insertions in the central (amino acids 60-74) and the C-terminal region (amino acids 93-130) resulted in a loss of protein function. The C-terminal region of HrpB2 contains a conserved amino acid motif that is present in HrpB2 homologs and predicted inner rod proteins from animal pathogenic bacteria. Mutant studies showed that this motif is required for the contribution of HrpB2 to T3S, pathogenicity and pilus formation and is also essential for T3S of HrpB2 itself, suggesting that HrpB2 promotes its own transport.

Immunogoldlabeling and fractionation studies revealed that HrpB2 is presumably not associated with the T3S pilus but localizes to the bacterial periplasm and the bacterial outer membrane (Fig. 2). For immunoldlabelling bacteria were grown for 6 hours on formvar-coated gold grids, shortly fixed with paraformaldehyde and thereafter treated with antibodies.

To characterize functional areas of HrpB2, derivatives of this protein with amino acid exchanges or lacking certain regions were created. Pilus formation of bacteria expressing the mutated HrpB2 was compared with pilus formation by the wildtype. The pilus formation was determined by negative staining. We could show that HrpB2 is essential for pilus formation and that the amino acids in position 123 to 128 are important for protein function.

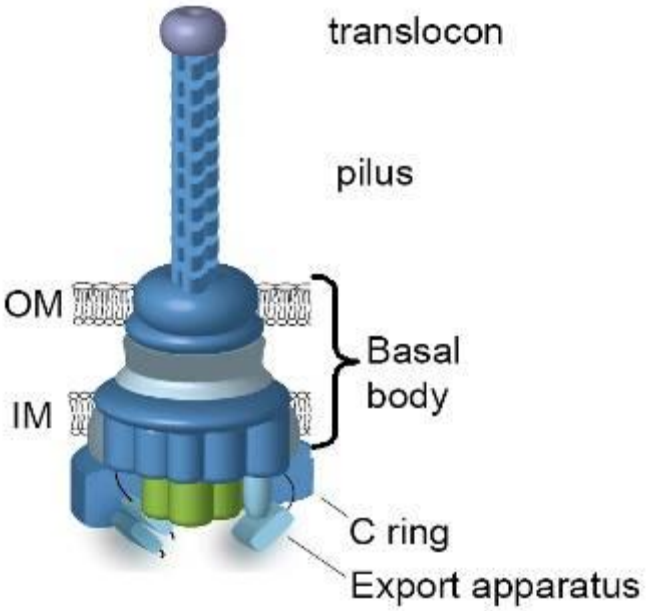

Figure 1. Schematic drawing of the T3S apparatus of *Xanthomonas campestris* pv. *vesicatoria* consisting of cytoplasmic C ring and export apparatus, a basal body located in the membranes and the periplasm, a pilus and a trranslocon. Adapted from Büttner Microbiol. Mol. Biol. Rev. (2012) 76(2) 262-310.

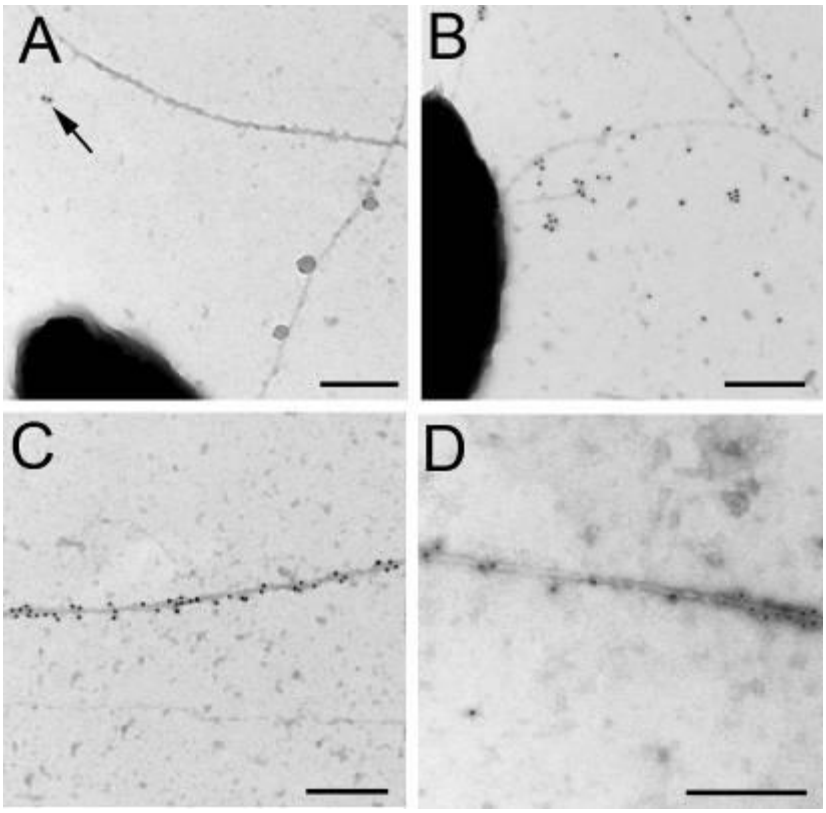

Figure 2. Immunogoldlabelling of HrpB2 (A and B) and the pilus structure protein HrpE (C and D) in the wildtype (A and C) bacteria and bacteria mutated in the secretion control protein hpaC (ΔhpaC; B and D). HrpE could be detected in pili of both strains whereas large amounts of HrpB2 were only found in the environment of pili of the ΔhpaC-strain.

Plants and their Pathogens

LS.3.111
Structural and immunoelectron microscopic studies on the effect of an electrostatic field in Triticum and Arabidopsis leaves

G. Zellnig[1], S. Möstl[1], B. Zechmann[1]

[1]University of Graz, Institute of Plant Sciences, Graz, Austria

guenther.zellnig@uni-graz.at
Keywords: *Arabidopsis*, *Triticum*, electric field, glutathione, microscopy

The influence of electric fields (e-fields) including low-frequency pulsed e-fields and high-voltage electrostatic fields has been described for different organisms. Pulsed e-field treatment is frequently applied for the preservation of food, extraction of biological materials and reduction of bacterial contamination in wastewater [1]. Due to the broad range of applications (static, pulsed, high-, low intensities of e-fields) a wide spectrum of biological effects, e.g. inhibited/enhanced seedling growth, enhanced stress resistance, increased enzyme activities, increase in anthocyanin content, stimulation of the mitotic index, is documented for plants [2,3,4,5]. These differences in the applied kind of e-fields make comparisons of effects induced by e-fields difficult or even impossible. Moreover, data on influences of e-fields on the cell structural level are still rare or missing. In this study germinating seeds of *Arabidopsis thaliana* Col-0 and *Triticum sativum* Lam. were exposed to an electrostatic field with 2kV/cm intensity for five days. The effects of the applied e-field were evaluated immediately (intracellular localization of glutathione) and three weeks after the exposure (leaf area, cell size, cell ultrastructure) of plants to these conditions in climate controlled chambers.

The e-field exposure of seeds for five days during germination showed significant effects on the investigated plants. In *Triticum* the leaf area was significantly decreased (nearly 40%), whereas in *Arabidopsis* the leaf area did not change after e-field treatment when compared to untreated plants. Interestingly, the cell size was significantly decreased (up to 50%) in both *Triticum* and *Arabidopsis* leaves after e-field exposure. In addition light- and electron microscopical investigations of fixed and resin embedded leaves showed granular deposits in vacuoles of epidermal and mesophyll cells of e-field exposed *Triticum* plants (Figure 1). Besides these changes in vacuoles ultrastructural examination of both plants did not reveal further differences in subcellular structures and organelles between e-field treated and control samples (Figure 1c,d). Immunoelectron microscopic localization and quantification of glutathione in *Triticum* leaves five days after e-field exposure revealed significant differences in the gold labelling density of certain cell organelles. Plastids and nuclei were the most affected organelles showing significant reductions of the glutathione content in e-field treated samples (Figure 1e). The decrease of glutathione could be an indicator of oxidative stress on cellular level under these conditions.

This study clearly documents a statistically significant influence of a five day exposure of germinating seeds to a 2kV/cm electrostatic field on both cell physiology and cell structure. The effect is partly different in the investigated plants thereby indicating varying adaptations or responses to e-field conditions and stress, respectively.

1. C. Gusbeth, W. Frey, H. Volkmann, T. Schwartz, and H. Bluhm, Chemosphere 75 (2009), p.228.
2. E. Costanzo, Bioelectromagnetics 32 (2011), p.589.
3. G. Wang, J. Huang, W. Gao, J. Lu, J. Li, R. Liao, and C.A. Jaleel, J. Electrostatics 67 (2009), p. 759.
4. N.M.M.T. Saw, H. Riedel, Z. Cai, O. Kütük, and I. Smetanska, Plant Cell Tiss. Organ Cult. 108 (2012), p.47.
5. D. Ichim, D. Creanga, and A. Rapa, J. Electrostatics 65 (2007), p. 408.

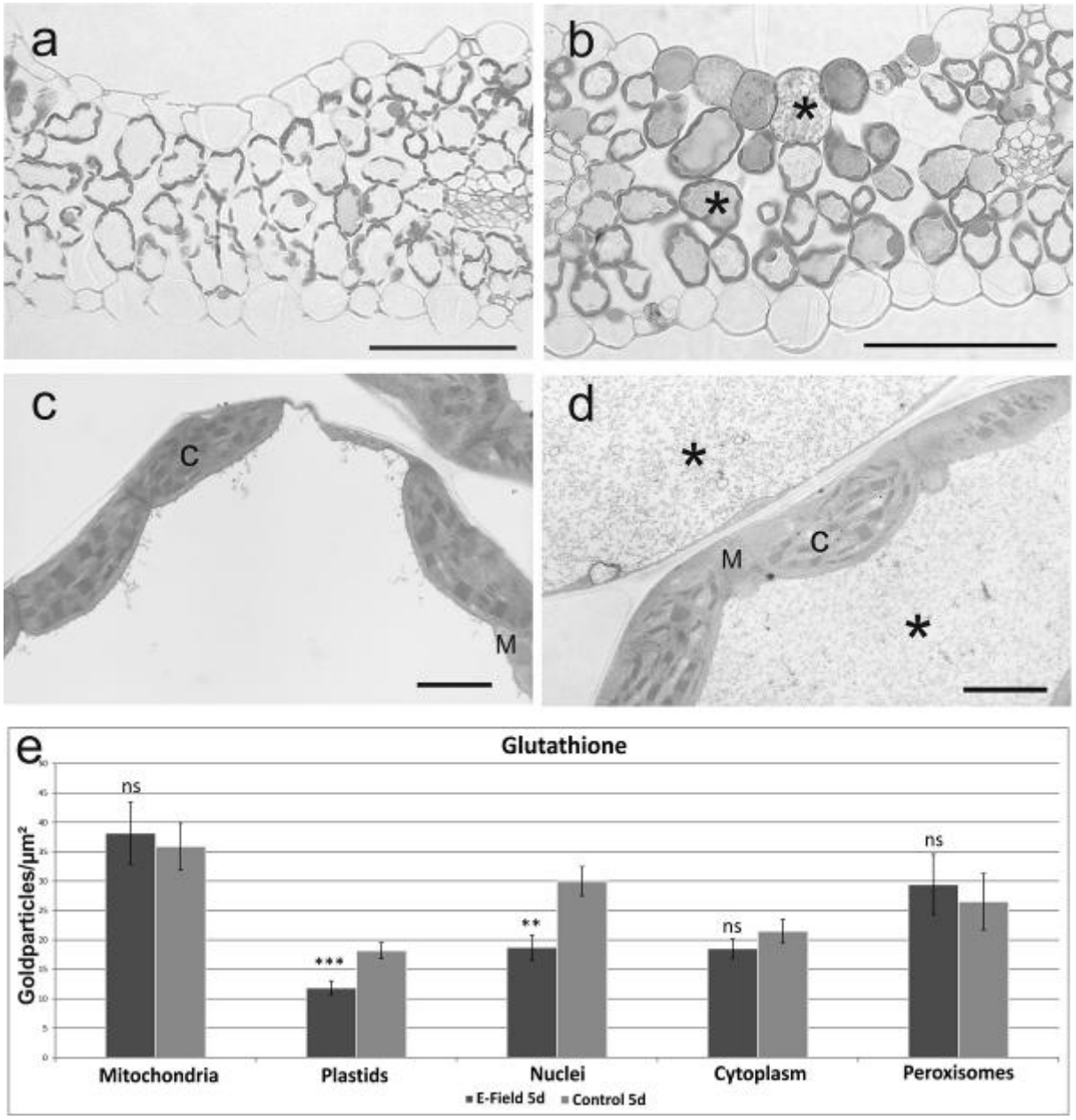

Figure 1. a,b: Semi-thin transverse sections of parts of three weeks old *Triticum sativum* leaves showing control samples (a) and granular deposits (∗) in the vacuoles of epidermal and mesophyll cells of e-field exposed samples (b). Bars=100µm. **c,d**: Transmission electron micrographs of parts of mesophyll cells of three weeks old *Triticum* leaves showing inconspicuous chloroplasts (C) and mitochondria (M) in control (c) and e-field treated (d) samples. Dense granular deposits (∗) are visible only in the vacuole of e-field exposed cells (d). Bars=2µm. **e**: Data represent mean values with standard errors of glutathione gold particle density per μm^2 in different cell compartments of mesophyll cells of five days old *Triticum* leaves. Significant differences were calculated with the Mann-Whitney U-test between control and e-field exposed samples. ns=not significant, (**) if $p<0.01$, and (***) if $p<0.001$. n >15 for peroxisomes and nuclei, n >50 for other cell structures.

Plants and their Pathogens

LS.3.112
The development of silica phytoliths in plants can be artificially modified to produce the particles of requested features

M. Martinka[1,2], M. Soukup[1], M. Švancárová[1], F. Ravaszová[1], A. Lux[1,3]

[1]Faculty of Natural Sciences, Comenius University in Bratislava, Department of Plant Physiology, Bratislava, Slovakia
[2]Slovak Academy of Sciences, Institute of Botany, Bratislava, Slovakia
[3]Slovak Academy of Sciences, Institute of Chemistry, Bratislava, Slovakia

martinkambio@yahoo.com
Keywords: cadmium, development, endodermis, plant, root, silica phytolith, silicon, sorghum

Silicon is the second most abundant element in Earth´s crust [1]. Many plant species are able to take up, transport, and after the distribution to accumulate high amounts of silicon in their bodies [2]. Among those species an agronomic important *Sorghum bicolor* L. is able to accumulate silicon in the amount of several % of dry weight. Silicon is either spread in the form of compounds in the cell walls or accumulated in the relatively large deposits in the intercellular spaces and inside the cells [3]. These deposits are called silica phytoliths and according to the International code for phytolith nomenclature 1.0 [4] *Sorghum* root endodermal cells develop the specific silica phytoliths of semi-globular shape. The silica phytoliths start to develop on the inner tangential (centripetal) parts of endodermal cells in the space between plasma membrane and the cell walls (many times protruding to the cell wall matrix). Their shape, size and distribution are uniform [3]. There is a potential to use the silica phytoliths, because of their physical and chemical features, stable and repeatable morphology, in electro-technical and building industry [5]. The goals of this study were to characterise the endodermal cell wall modifications of *Sorghum* root related to the silica phytoliths development and to test the possibility to change the size and morphology of silica phytoliths with the aim to produce particles of requested features for industry.

It is known that cadmium affects genetic and metabolic processes in living organisms. We have used this metal element in the form of cadmium nitrate tetrahydrate to test its effect on silica phytoliths development. Tested plants of *S. bicolor* were cultivated in hydroponics containing wide concentration ranges of Na_2SiO_3, as silicon source, and of cadmium. After three-day treatment the seminal roots of plants were investigated by light (with a combination of negative phase contrast and differential interference contrast), fluorescent (with a use of fluorescent indicators for silicon – Rhodamine B and for suberin lamellae – Fluorol yellow 088), transmission and scanning electron microscopy (equipped with EDXA) to characterise the development, exact localisation, shape and morphology of silica phytoliths related to the composition of cultivation media and to the endodermal cell wall modifications. For better observation of endodermal silica phytoliths the tissues lying centrifugally to endodermis (rhizodermis, exodermis, mesodermis) were removed by peeling off [3].

At the concentrations of silicon above 0.8 µmol/L the silica phytoliths form uniformly in almost all endodermal cells of *S. bicolor* seminal roots with a positional effect – they development starts firstly opposite to the phloem poles and later opposite to the xylem poles – consistent with a gradual development of a secondary stage (with a formation of suberin lamellae). The low silicon concentrations in the hydroponic media affect negatively the size of silica phytoliths and the continuous size-dependent gradient shifts towards the base of the root. The cadmium affects not only the size, but also the exact localisation of phytoliths. With increasing cadmium concentration they become smaller, not uniform in size, and tend to be formed ectopically outside the central axis of endodermal tangential cell walls (typical for physiological conditions without the presence of this toxic metal). At still relatively low concentrations of cadmium the phytoliths stop to form and the silicon is spread ectopically in the tissues of root.

Based on the results although the silica phytoliths are formed uniformly under natural conditions, their development, size and morphology can be changed by use of compounds affecting the silicon metabolism and/or mechanisms of phytoliths formation in plants. *Sorghum* root is an excellent model for investigation of silica phytoliths development in plants. The further investigation, understanding, and modification of processes involved in the phytoliths development can help to produce particles of requested features for industry.

1. T.I. Balakhnina et al., Plant Growth Regulation 67 (2012), p. 35-43.
2. M.J. Hodson et al., Annals of Botany 96 (2005), p.1027-1046.
3. A. Lux et al., New Phytologist 158 (2003), p. 437-441.
2. M. Madella et al., Annals of Botany 96 (2005), p. 253-260.
5. S. Neethirajan et al., Trends in Biotechnology 27 (2009), p. 461-467.
6. This work was supported by the Slovak Grant Agency [VEGA 1/0817/12]; and by the Slovak Research and Development Agency, under the contract No. APVV-0140-10.

Plants and their Pathogens

LS.3.P113
How different irrigation treatments affect cell size in tomato fruit?

I. Pecinar[1], S. Pekic Quarrie[1], D. Rancic[1], R. Radosevic[1], M. Terzic[1], N. Bertin[2], R. Stikic[3]

[1]Faculty of Agriculture, Agrobotany, Belgrade, Serbia
[2]INRA, Unité PSH (UR 1115), Avignon, France
[3]Faculty of Agriculture, Plant Physiology, Belgrade, Serbia

ilinka@agrif.bg.ac.rs
Keywords: pericarp, wild type, flacca

In comparison with all other types of abiotic stress factors, water reduction has the biggest negative impact on plant productivity and final weight of tomato fruit [1]. The objective of the present study was to determine the effect of different irrigation practices on tomato plants during fruit development, on tomato pericarp cell size. Tomato plants, wild type and flacca mutant, were grown in a growth chamber under controlled conditions. Plants of both genotypes were subjected to following irrigation treatments: full irrigation (FI), partial root-zone drying (PRD) and deficit irrigation (DI). Fruit pericarp was sampled at different developmental days after anthesis (daa) and macerated with pectinase solution [2]. Pericarp cells were observed with a Leica DMLS stereomicroscope and images were acquired with a Leica DC300 digital camera. For each genotype and treatments a minimum of 1000 cells were measured by Image J software package. In flacca mutant under optimal water suply conditions, fruits are smaller compared to wild type, due to a reduction in cell size. In flacca pericarp, cell perimeter, maximal and minimal diameter were 20 do 24% smaller than in wild type (Fig. 1) and mean cell area in pericarp in flacca mutant was 42% smaller in comaparison to wild type. Under water deficit, fruit growth of both flacca and wild type was reduced. Cell perimeter, maximum and minimum diameter decreased during the earlier cell expansion phase, in DI 63% 10daa and in PRD 37% 12daa. In later growth phases, 20daa, impact of PRD and DI on reducing pericarp cell area in wild type was 47 and 59%, respectively. Similarly, in flacca reduction in cell size was observed in later phases of fruit development, after 20daa. Future investigations could compare results from different isolation methods for describing cell size parameters.

1. M.R. Foolad, in “Advances in molecular breeding toward drought and salt tolerant crops”, eds. M.A. Jenks et al., Springer, New Jork, 2007, 669–700
2. N. Bertin, H. Gautier and C. Roche, Plant Growth Regulation 88 (2001), p. 1–8

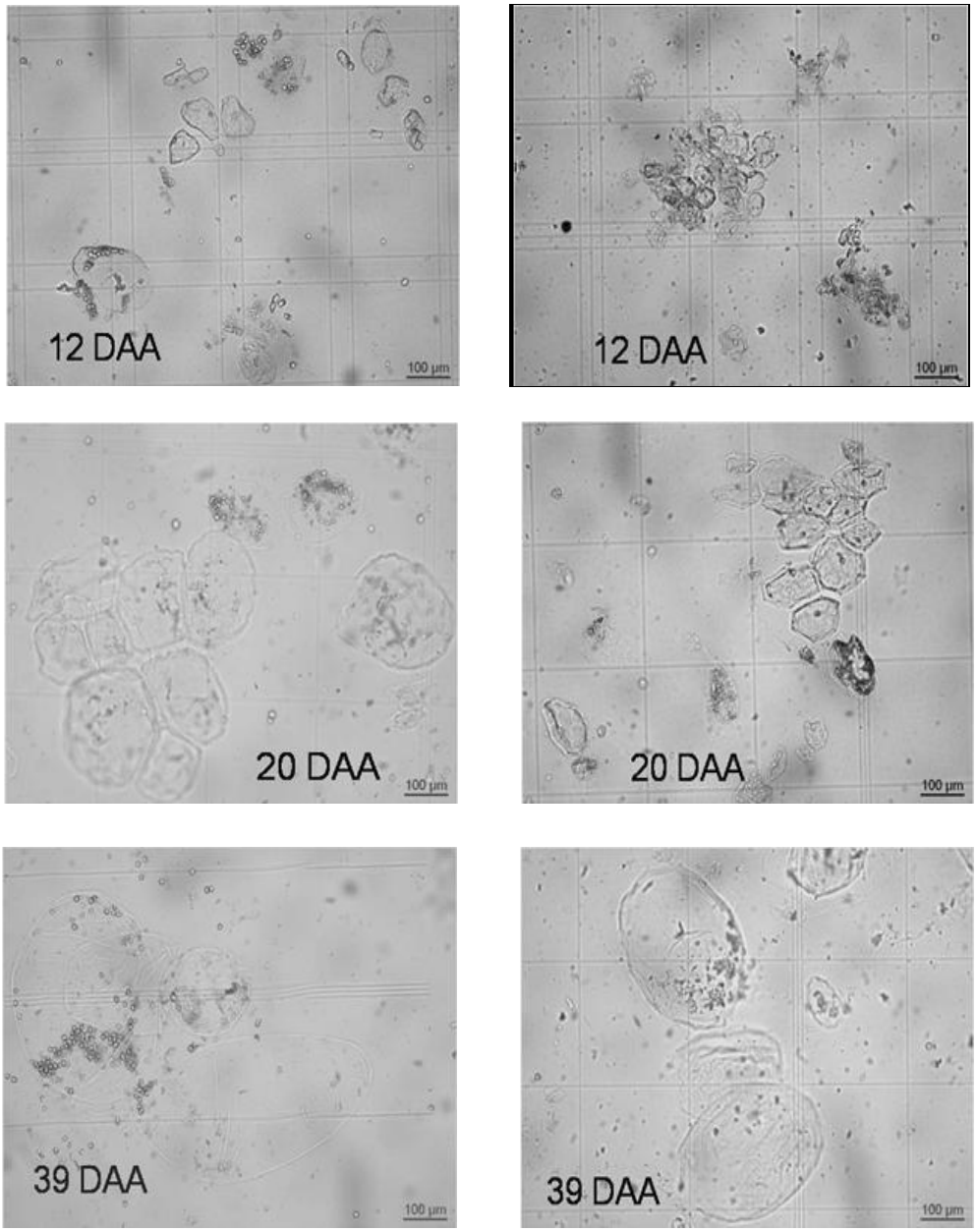

Figure 1. Pericarp cells during the process of fruit development wild type (left column) and flacca (right column) full irrigated tomato plants, photographed using 10 x magnifications. Bars represent 100 µm.

Plants and their Pathogens

LS.3.P114
Pollen morphology of Ligustrum vulgare L. (Oleaceae)

M. Macukanovic-Jocic[1], D. Rancic[1]

[1]Faculty of Agriculture University of Belgrade, Agrobotany, Belgrade, Serbia

marmajo@agrif.bg.ac.rs
Keywords: pollen, LM, SEM

Ligustrum vulgare L. (Common privet or European privet**)** is a semi-evergreen or deciduous shrub, growing to 3 m (rarely up to 5 m) tall, with panicles of small, often unpleasantly scented white flowers in spring or summer. It is a quite common shrub widespread in Serbia in oak and ash forests, and also cultivated in parks, gardens and hedgerows. Since flowers, producing a lot of pollen and nectar, are attractive for insect pollinators, including honeybees, privet is considered a good melliferous plant. In this study, the pollen of *L. vulgare* was examined by both light microscopy (LM) and scanning electron microscopy (SEM), in order to contribute to palynomorphological studies of Serbian apiflora.

For light microscopy, fully matured anthers were removed from the flowers and pollen were prepared according to the Erdtman's acetolysis method [1]. Pollen was analyzed and photographed using a microscope LEICA 2000 equipped with a digital camera (Leica DC 300) and Leica IM1000 software. For SEM studies, the pollen grains were covered with gold (in BAL-TEC SCD 005 Sputter Coater, 100 seconds in 30 mA) and observed using JEOL JSM- 6390 LV electron microscope at an acceleration voltage of 20 kV. Pollen grains were photographed in polar and equatorial views, and observations and measurements were done on a sample of 50 or more grains for each morphological character. The following features describing pollen grains were examined: size, shape, ornamentation, aperture condition, polarity, symmetry, length of polar axis (P), length of equatorial diameter (E), length of colpi, lumina size and exine thickness.

The pollen grains of *L. vulgare* are isopolar and radially symmetrical. Grains are tricolporate with narrow ectocolpi arranged meridionally, regularly, mean length 23.7 ± 2.2 µm and 3 endopores that are poorly visible. According to Erdtman's classification [2] they are medium sized. Polar axis (P) is 35.4 ± 0.9 µm, and equatorial diameter (E) is 23.6 ± 0.9 µm. Ratio of polar axis/equatorial diameter (P/E) was 1.50 ± 0.07 indicating prolate shape. In polar view grains are circular or triangular with obtuse apices and in equatorial view are elliptic (Fig 1). Exine ornamentation is reticulate (Fig 2). The lumina may be irregular to rounded, polygonal or elangated and muri are high and prominently defined. Average value of lumina size was 3.2 ± 0.9 µm and the muri width averaged 0.75 ± 0.09 µm. ***Infratectal*** granular elements are plainly visible in some lumina. The exine thickness averaged 1.2 ± 0.2 µm.

1. G. Erdtman, An Introduction to Pollen Analysis. Waltham, Mass.: Chronica Botany Company. p. 239 (1943).
2. G. Erdtman, Pollen Morphology and Plant Taxonomy. Hafner Publishing, New York (1971).
3. This research was financially supported by the Ministry for Science and Tehnological Development , Project 46009

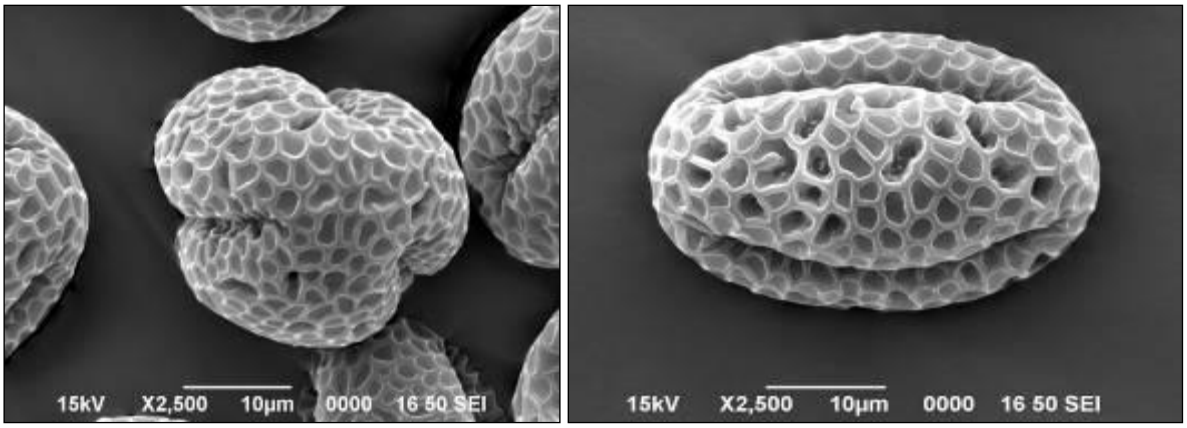

Figure 1. SEM micrographs of pollen grain of *L. vulgare*, in polar (left) and equatorial view (right).

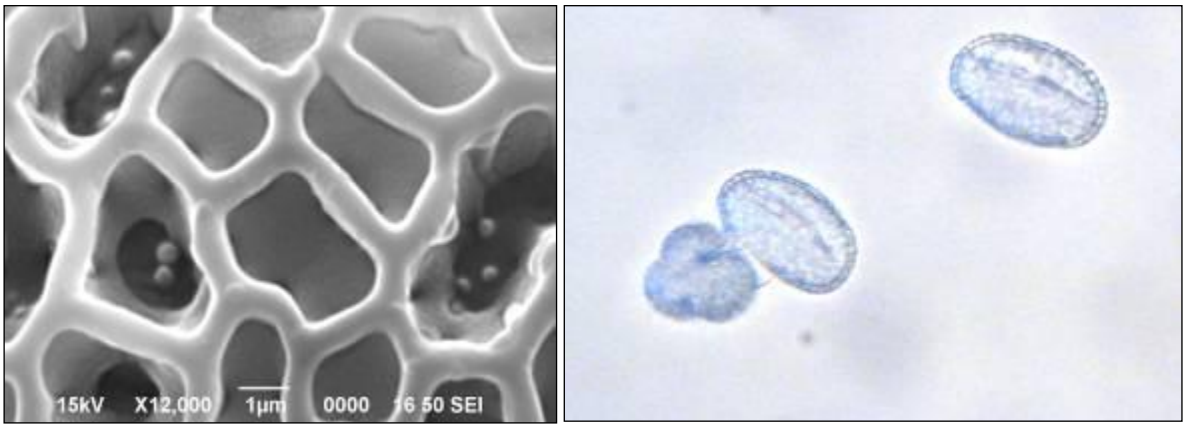

Figure 2. Detail of reticulate exine sculpturing of pollen grain of *L. vulgare* in SEM (left) and LM micrograph of pollen grains (x400) (right).

Plants and their Pathogens

LS.3.P115
Ultrastructural analysis of meristematic cells of fasciated mutant *Pisum sativum* L.

E. Bykova[1], V. Choob[1], E. Labunskaya[1], A. Sinjushin[1]

[1]Moscow State University, Faculty of Biology, Moscow, Russian Federation

katebykova.90@mail.ru

Fasciation is a phenomenon in which the meristem increases in volume (in some cases – 1000 fold and more). Often this process occurs by increasing of the pool of stem cells in the central zone of meristem. The rate of cell division in the central zone depends on signaling cross talk between the rib-zone and upper layers of the tunica. The detailed ultrastractural analysis allows us to estimate the physiological state of central and rib-zone cells.

There are a lot of studies of fasciation referring to *Arabidopsis thaliana* mutants *clavata 1,2,3* [1]. However by the moment fasciated mutants of pea (*Pisum sativum* L.) are investigated insufficiently [2].

In our work we used seedlings of two isogenic lines of pea (*Pisum sativum* L.): fasciated mutant ("Shtambovyj") and wild type (cultivar "Nemchinovskyj."). Meristems were sampled at early stages of development (1st, 4th and 9th day after germination).

In previous investigation it was revealed that fasciated mutants develop their traits when the 5th leaf emerges [3]. The scanning electron microscopy (SEM) allowed us to find out that at the 1st day of germination seedlings of fasciated mutant “Shtambovyj” the meristem flattens and elongates in comparison with wild-type plants of cv. “Nemchinovskyj” (Figure 1).

Then we used transmission electron microscopy (TEM) for investigating of cell ultrastructure in meristems.

In our experiments, it was found that meristematic cells of fasciated plants are extremely vacuolated. This was observed in the rib-zone and in tunica cell layers. Frequently in the central and peripheral zones of tunica cells plasma membranes loose the connection with the cell wall (Figure 3 and 4). In this case, the cell wall in some regions was considerably thinned or undergoes the substantial lysis. In other sites it was strongly thickened. Predominantly cells had a round shape and were arranged as regular rows.

Wild-type plants also had vacuolated cells in the rib-zone (Figure 4). This is probably due to the development of a cavity inside the stem. Cavity formation is typical for *Pisum* stems. But in wild type meristems vacuolization in tunica have not been found, unlike the mutant plants.

All these results allow us to draw a preliminary conclusion that the fasciation in pea may cause defects in the thickening of the cell wall and some mechanical strain and deformation.

The work was supported by Russian Fund of Basic Research, grant № 12-04-01579.

1. S.E. Clark, M.P. Runnig and E.M. Meyerowitz, Development, volume 119, (1993), p. 397-418
2. A.A. Sinjushin and S.A. Gostimsky, Russian Journal of Developmental Biology, volume 37, (2006), p. 375-381
3. V.V. Choob and A.A. Sinjushin, Russian Journal of Plant Physiology, volume 59, (2012), p. 530 - 545

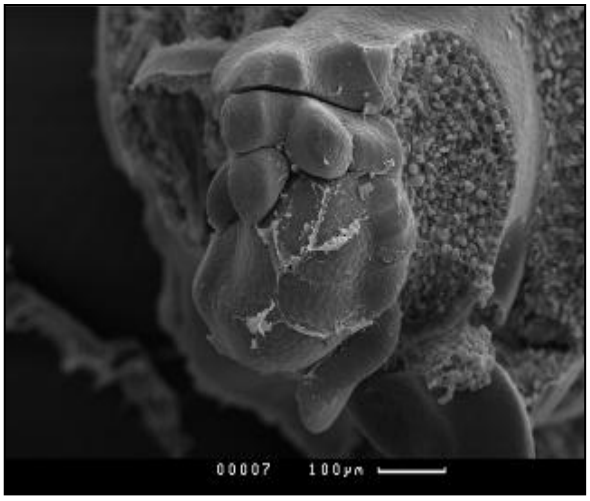

Figure 2. SAM of "Shtambovyj" (1st day after germination)

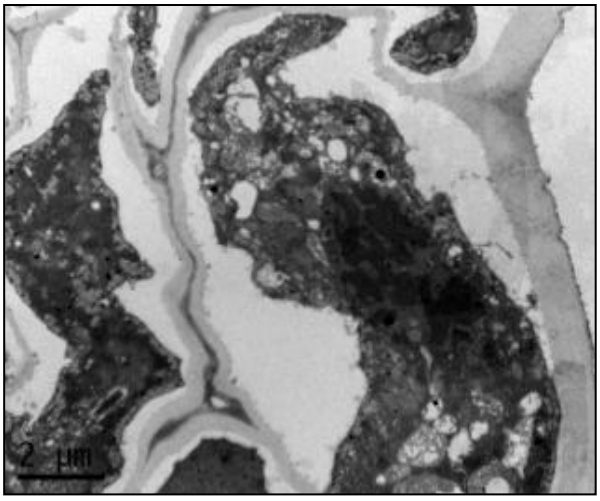

Figure 1. Cells of L1 tunica layer ("Shyambovyj")

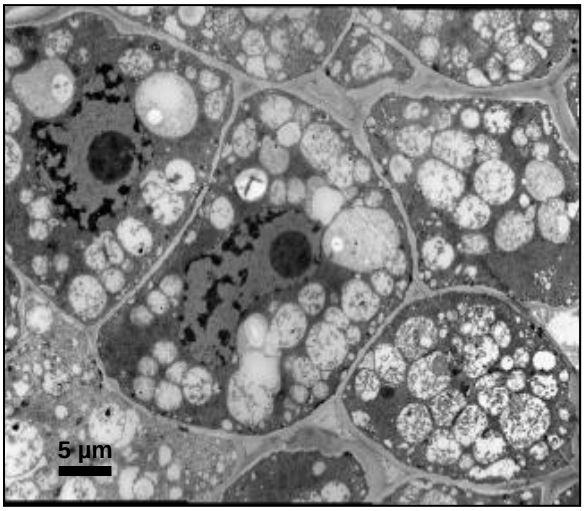

Figure 4. Vacuolated cells of "Shtambovyj"

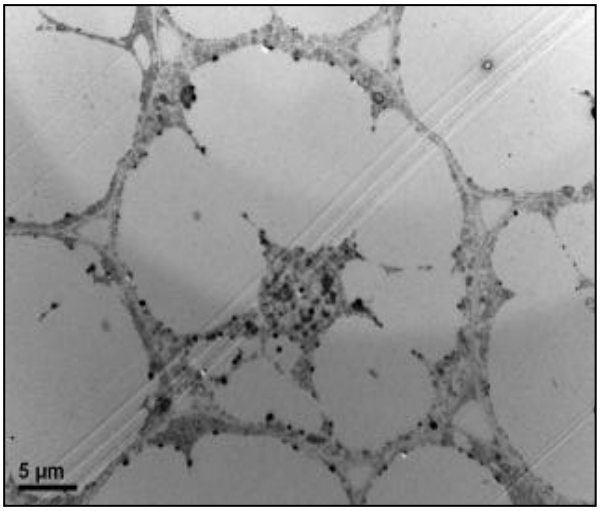

Figure 3. Rib-zone of "Nemchinovskyj"

Plants and their Pathogens

LS.3.P116
Histochemical methods for localization carbohydrate storage tissue in wheat stem

D. Rancic[1], I. Pecinar[1], R. Radosevic[1], S. Pekic Quarrie[1], S. Quarrie[2]

[1]Faculty of Agriculture University of Belgrade, Agrobotany, Belgrade, Serbia
[2]Faculty of Biology, University of Belgrade, Belgrade, Serbia

rancicd@agrif.bg.ac.rs
Keywords: chlorenchyma, parenchyma, saccharides

Wheat and other grasses are capable of storing excess carbohydrates within the stems. These carbohydrates are essential to maintain yields when photosynthetic capacity is reduced, i.e. during periods of environmental and biotic stresses [1]. Wheat stems store carbohydrates in the form of glucose, fructose, sucrose, starch, and fructans [2], though the localization of these carbohydrates within tissues and cells of the stem had not previously been studied. Here we present our initial findings on the histological location of carbohydrates in wheat stem tissues.

In this study we applied histochemical methods to show the distribution and localization of different types of carbohydrates in wheat stems. Wheat stems of breeding line ZP-D 14/I were sampled from the field in the phases of early grain-filling (9-10 d after anthesis) and late dough (35 d after anthesis). Samples were sectioned manually using razor blades, stained and observed under a LEICA 2000 light microscope, equipped with a LEICA DC 300 camera and IM1000 software. The following histochemical tests were performed: Fehling test for monosaccharides [3], Molisch's test (thymol sulphuric acid) for saccharose and fructans [4], Lugol's test for starch [5], and Periodic acid-Schiff test (PAS) for water insoluble polysaccharides [5, 6].

During the early grain-filling phase, the main tissue responsible for non-structural carbohydrates was the chlorenchyma located at the periphery of the wheat. Histochemical staining detected reducing sugars (glucose and/or fructose) (Figure 1), oligosacharides and starch in this tissue. By the phase of maturing grains of wheat (35 d after anthesis), there were no detectable amounts of mmonosaccharides, oligosaccharides or starch in the non photosynthetically-active parenchyma cells in the wheat stem. This evidence provides a new opportunity for targeting future crop improvement, as breeding new genotypes with large amounts of chlorenchyma in the stem are likely to offer a greater possibility for plants to increase productivity, especially in stress conditions.

1. N.G. Halford, T.Y. Curtis, N. Muttucumaru, J. Postles, D.S. Mottram, Annals of Applied Biology 158 (2011)1.
2. V. Wardlaw and J. Willenbrink, Australian Journal of Plant Physiology, 21 (1994) 255.
3. M.J. Purvis, DC Collier, D Walls, Laboratory techniques in botany (London, Butterworths) (1964).
4. D.A. Johansen, Plant microtechnique. (McGraw-Hill, New York) (1940).
5. W.A. Jensen, Botanical Histochemistry. (San Francisco, USA. W. Freeman & Co) (1962).
5. T.P. O'Brien, and M.E. McCully, The Study of Plant Structure: Principles and Selected Methods. (Termarcarphi Pty. Ltd., Melbourne Australia) (1981).
6. We thank the Serbian Ministry of Education, Science and Technological Development for funding this research under project TR31005

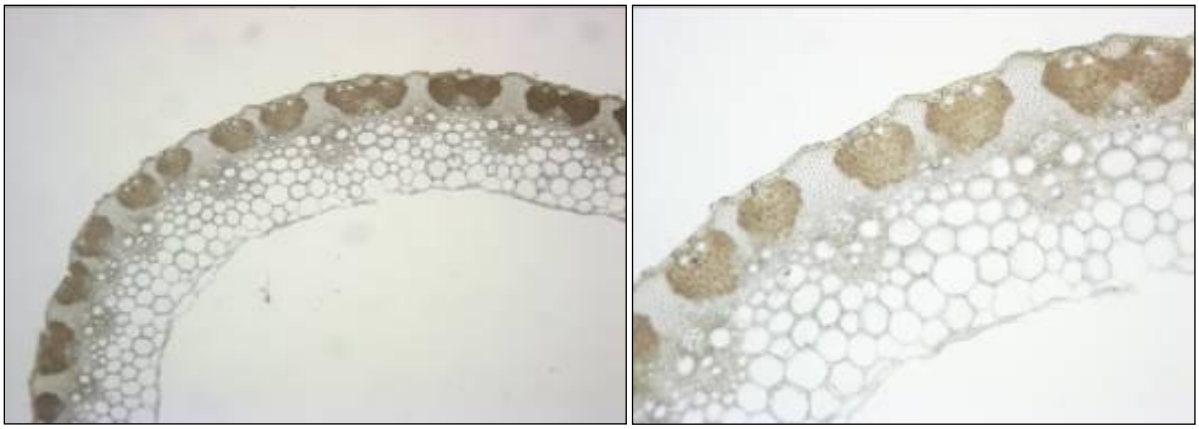

Figure 1. Unstained freehand section of wheat stem in early reproductive growth phase.

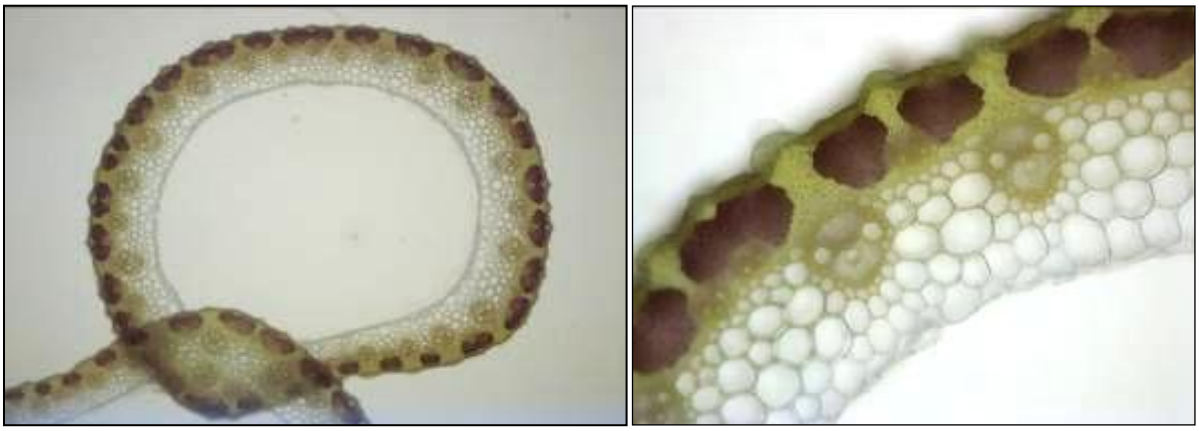

Figure 2. Fehling test applied on section of wheat stem in early reproductive growth phase. The appearance of reddish brown stain in the samples indicating presence of reducing sugars (monosacharides) in the chlorenchyma tissue

Plants and their Pathogens

LS.3.P117
The "native" structure of aggregated plants' thylakoids.

K. Gieczewska[1], R. Mazur[2], J. Grzyb[3], M. Garstka[2], A. Mostowska[1]

[1]Faculty of Biology, University of Warsaw, Department of Plant Anatomy and Cytology, Warsaw, Poland
[2]Faculty of Biology, University of Warsaw, Department of Metabolic Regulation, Warsaw, Poland
[3]Polish Academy of Science, Institute of Physics, Warsaw, Poland

kat.gieczewska@biol.uw.edu.pl
Keywords: thylakoids, membrane aggregation, AFM, freeze fracture

Plants' chloroplasts, the site of the photosynthetic reactions, contain continuous system of thylakoids' membranes. Within these membranes the stromal (unstacked) and granal (stacked) regions can be singled out. Varying light, temperature and abiotic stress conditions can change the stromal to granal regions ratio. In our previous study we showed that the chilling sensitive plant – bean has a smaller content of appressed regions (grana) than the chilling tolerant one, pea [1]. Recently we created a 3D model of whole pea and bean chloroplasts, based on focal sections (CLSM) of isolated, intact chloroplasts [2]. We showed that during magnesium ions induced aggregation pea chloroplasts contain large, distinctly separated, appressed domains, while the appressed regions present in bean thylakoids are less distinguished. So even during forced aggregation we saw distinct differences between species. Visualization of aggregated isolated thylakoids has never been done before.

The aim of this study is to visualize isolated, non-fixed aggregated thylakoids using freeze fracture method and topography of thylakoids by AFM liquid cell microscopy. Aggregated pea thylakoids also contain appressed regions (possibly granal) and some long, singular membranes (stromal) (Fig.1.). Since the aggregated regions are very similar to the ones contained in intact chloroplasts described previously [2], a chloroplast as a whole is probably not necessary for the membrane rearrangement process to occur. We think that such a singular membrane can be transformed into a number of appressed regions. Isolated pea and bean thylakoids retain intact chloroplasts' property of aggregating into stacked regions of different sizes.

1. M. Garstka, J.H. Venema, I. Rumak, K. Gieczewska, M. Rosiak, J. Koziol-Lipinska, B. Kierdaszuk, W.J. Vredenberg, A. Mostowska, Planta, 226 (2007), p. 1165-1181
2. I. Rumak, R. Mazur, K. Gieczewska, J. Koziol-Lipinska, B. Kierdaszuk, W.P. Michalski, B.J. Shiell, J.H. Venema, W.J. Vredenberg, A. Mostowska, M. Garstka, BMC Plant Biol. 12(1), p.72

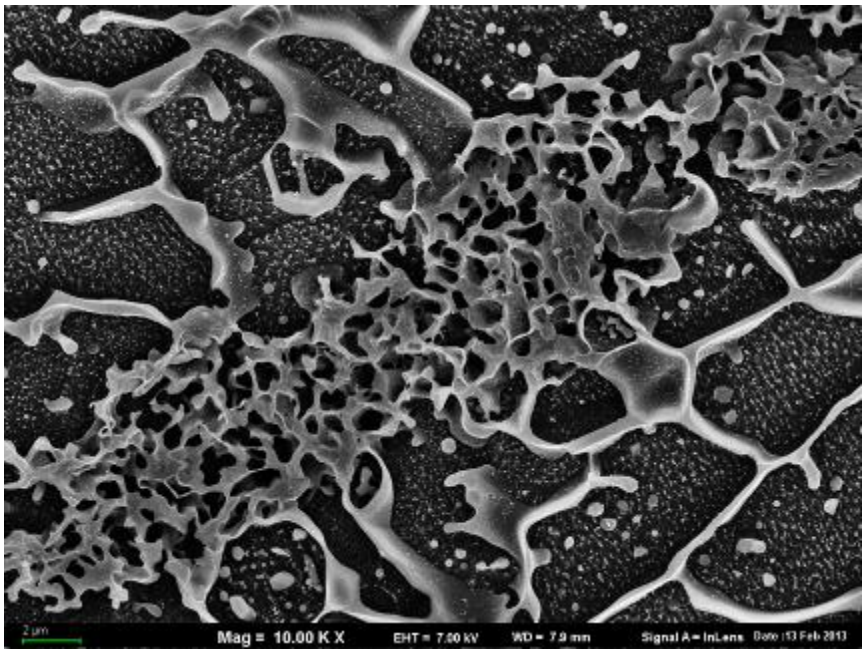

Figure 1. Aggregated pea thylakoids; the green bar is 2 µm long.

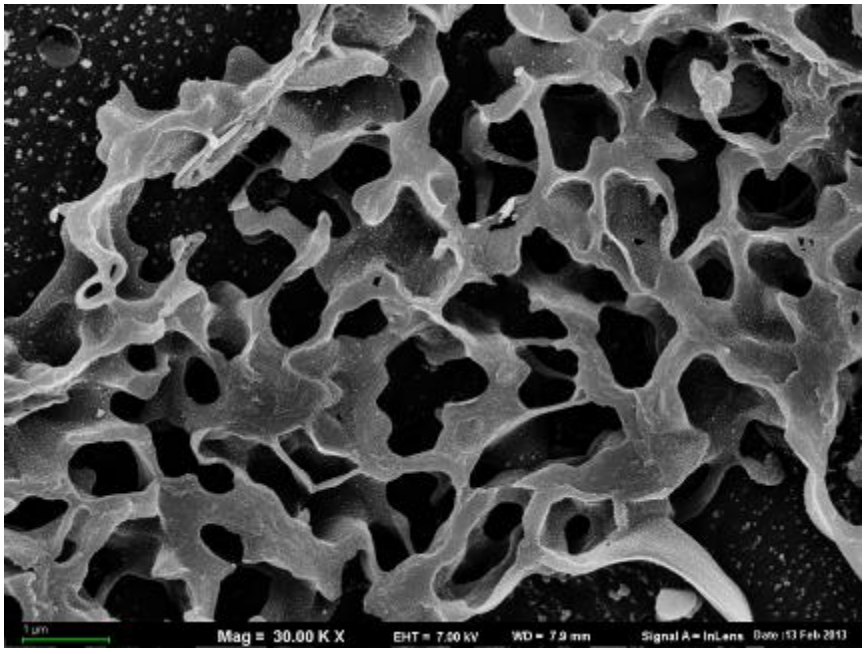

Figure 2. Aggregated pea thylakoids; the green bar is 1 µm long.

Plants and their Pathogens

LS.3.P118
The effect of environmental pollution on morphology and ultrastructure of some lichens

T. Vlasova[1]

[1]Moscow State Univercity, Fac. of Biology, Moscow, Russian Federation

tat_vla@list.ru
Keywords: lichens,*Cladonia*, *Hypogymnia*, environmental pollution, ultrastructure

In the most lichens, mycobiont is responsible for the formation of the lichen thallus. However, the functions of mycobiont depend significantly on the influence of phycobiont. It is shown that isolated mycobiont is not capable to create the form similar to that of symbiotic thallus [1].

The aim of the examination was to detect the effects of any factors on morphology and ultrastructure of the lichens. The thalli of fruticose lichen species of genus *Cladonia* were collected in unpolluted and polluted with SO_2 and heavy metals areas of Cola peninsula. The studied species were *C.stellaris, C. deformis*, *C. cianipes, C. ecmocyna*, *C. cryptochlorophaea* and *C. crispata*. The evident visible morphological alterations in the lichens from the polluted areas were observed. The forms of the thalli of all the lichens were dramatically distorted, and some of them were significantly smaller in comparison with the lichens from the unpolluted areas. The scanning electron microscopy revealed that morphological alterations of the thalli were caused by noticeable ultrastructural alterations: the growth directions of the fungal hyphae in the lichens from the unpolluted areas were more regulate that in the lichens from the polluted ones. Any possible reasons of the growth disorganization in the lichen-forming fungi may be supposed: the fungal cellular damages, deterioration of the fungus-alga interaction or changes of the hormonal status in lichen.

The thalli of foliose lichen *Hypogymnia physodes* were also collected in unpolluted and polluted areas of Cola peninsula and studied by mean of scanning electron microscopy. No principal morphological alterations were observed, however, the thalli of lichen from the polluted area were smaller. The surface of those thalli had also no significant changes. However, the transmission electron microscopy showed many degenerative alterations in the cells of both mycobiont and phycobiont. It was in agree with data of other authors [2]. It is possible that the structure of the surface of the thallus in this case shows no significant alteration because of the thick layer of lichen substances.

.

1. V.Ahmadjian, In:The lichens / Eds. Ahmadjian V., Hale M.E. New York, London, 1973.
2. T.Holopainen, L.Kärenlampi, New Phytol., 98, 1984, p.285-294.

Figure 1. Electron micrography of thallus of *C. stellaris* from the unpolluted area.

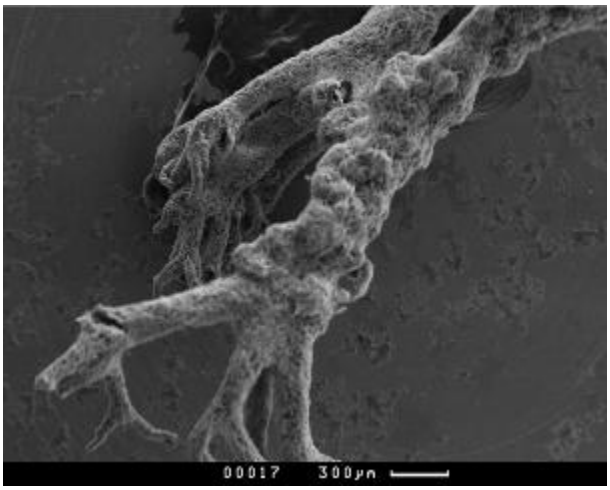

Figure 2. Electron micrography of deformed thallus of *C. stellaris* from the polluted area.

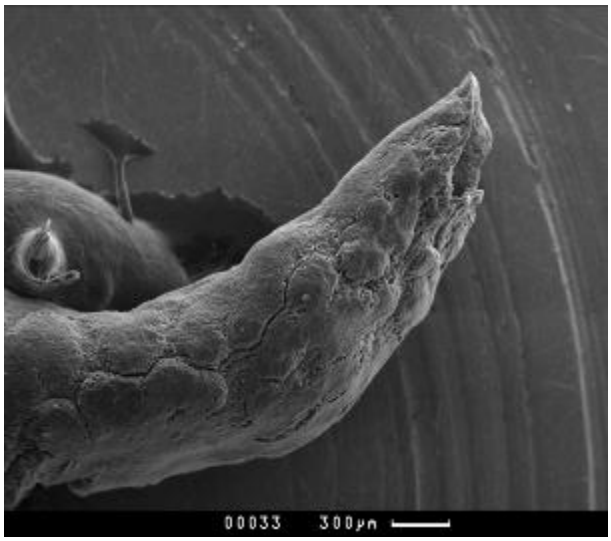

Figure 3. Electron micrography of thallus of *C. ecmocyna* from the unpolluted area

Figure 4. Electron micrography of deformed thallus of *C. ecmocyna* from the polluted area. .

Plants and their Pathogens

LS.3.P119
Comparative morphological and biochemical studies for two Romanian indigenous subspecies of *Achillea distans* Waldst. et Kit.

D. Benedec[1], M. Popovici[1], L. Vlase[1], C. Bele[1], B. Tiperciuc[1], M. Tamas[1], D. Hanganu[1]

[1]Iuliu Hatieganu University of Medicine and Pharmacy, Cluj-Napoca, Pharmacognosy, Cluj-Napoca, Romania

dbenedec@umfcluj.ro
Keywords: *Achillea*, SEM, silver nanoparticles

Genus *Achillea* is represented by 33 species and subspecies in the flora of Romania. *A. millefolium* represents a cytogenetic and chemically polymorph aggregate of 12 species, characterized by a well defined morphological, anatomical and caryological features. In the present paper two samples of *Millefolii herba*, obtained from *Achillea distans* Waldst. et Kit. ex Willd. and *Achillea distans* Waldst. et Kit. subsp. *alpina* (Rochel) Soó were described morphologically by scanning electron microscopy (SEM) and it were also biochemically characterized**.** *Achillea distans* Waldst. et Kit. ex Willd. is an alpino-carpatho-balkan type species that vegetates on the upper limit of mountain forests and in subalpine shrubs. According to the length of ligulate florets and to their color, 2 subspecies are recognized: *A. distans* subsp. *distans* with white flowers and 2 mm length of ligulae and *A. distans* subsp. *alpina*, with pink flowers and 3 mm length of ligulae [1,2]. The secretory and protective tissues were detected in the flower head of *Achillea distans* subsp. *alpina* by SEM. The *glandular* trichomes are *biseriate.* The filamentous hairs were found only on the bracts, with a protective role. The bract has a serrated edge. The tubular corolla contains the echinate pollen grains, with form feature *Asteraceae* family, "Figure 1". *Achillea distans* subsp. *distans* contains the biseriate *glandular* trichomes, the filamentous tector hairs and the pollen grains. The pollen grains were found on the bracts. The edge of bract is serrated and it contains numerous filamentous tector hairs. The *glandular* trichomes were found inside the tubular flower, alongside many grains of pollen, "Figure 2". The identification and quantification of major phenolic compounds was performed by a HPLC-MS method. The total phenolic and flavonoidic content was determined spectrophotometrically. The antioxidant capacity (AC) was determined using the DPPH bleaching method [3]. The growth of silver nanoparticle (SNP)-based method for evaluating the antioxidant capacity of polyphenolic compounds from vegetal extracts was also used [4]. The reduction of Ag^{+} to spherical silver nanoparticles (SNPs) by polyphenols in the presence of trisodium citrate and siver seed was produced an intense absorbtion band of SNPs at 423 nm. The absorbance of SNPs allowed the quantitative spectrophotometric detection of polyphenols.The results of this method were correlated with those of other antioxidant methods (DPPH assay, Folin-Ciocalteu method). In *A. distans* subsp*. distans* flowers tincture, the phenolic profile showed the presence of the phenolic acids and the aglycones of flavonoids in large amounts, while in *A. distans* subsp*. alpina* flowers extract, the flavonoids predominated and they are represented especially by the glycosides and the aglycones. The total polyphenolic (TPC) and flavonoids content values were summarized for *Achillea* extracts in "Table 1". The highest amount of the total polyphenols was determined in the tincture of *A. distans* subsp. *alpina* (80.13±0.72) followed by *A. distans* subsp*. distans* tincture (60.64±0.31). Concerning the content of flavonoids, contrary, the extract of *A. distans* subsp*. distans* (29.32±0.24) was richer in flavonoids, than the extract of *A. distans* subsp. *alpina* (22.75±0.23). The antioxidant effect of *A. alpina* subsp. *alpina* was higher than the activity of *A. distans* subsp. *distans* "Table 1". The comparative study showed significant differences, both qualitative and especially quantitative, between the two taxa of Achillea distans, and it could be used as a potential taxonomic marker in order to distinguish the species.

1. V. Ciocârlan in "Illustrated Flora of Romania. Pteridophyta et Spermatophyta", Ceres Publishing House: Bucharest, Romania (2009), p. 794-799.
2. M. Tamas, M. Popovici, I. Oniga, I. Oprean and G. Coldea, Planta Med 9 (2009), p. 932.
3. D. Benedec, L. Vlase, D. Hanganu and I. Oniga, Dig J Nanomater Bios 3 (2012), p. 1263-1270.
4. M. Ozyürek, N. Güngör, S. Baki, K. Güçlü and R. Apak, Anal Chem. 18 (2012), p. 8052-9.
5. Acknowledgements: "Iuliu Hatieganu" University of Medicine and Pharmacy Cluj-Napoca, Romania (research grant: 27020/43/15.11.2011)

Samples	TPC (mg gallic acid/g plant material)	Flavonoid (mg rutin/g plant material)	DPPH (%)	SNP (µg gallic acid/g plant material)
A. distans subsp. *distans*	60.64±0.31	29.32±0.24	73.43±1.07	0.15±0.001
A. distans subsp. *alpina*	80.13±0.72	22.75±0.23	89.92±0.92	0.17±0.018
Trolox			90.60%±0.65	

Table 1. Total phenolic (TPC) and flavonoids content in *A. distans* and antioxidant activity
Each value was obtained by calculating average of three experiments with ą standard deviation.

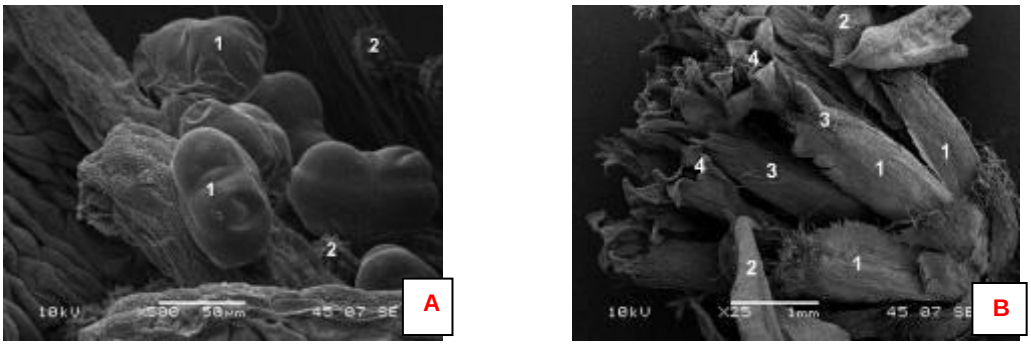

Figure 1. A. *Achillea distans* subsp. *alpina* (tubular flower): 1-biseriate *glandular* trichomes, 2-pollen grains. B. *Achillea distans* subsp. *alpina:* 1= bract, 2- ligulate flower, 3- filamentous tector hairs, 4- tubular flowers

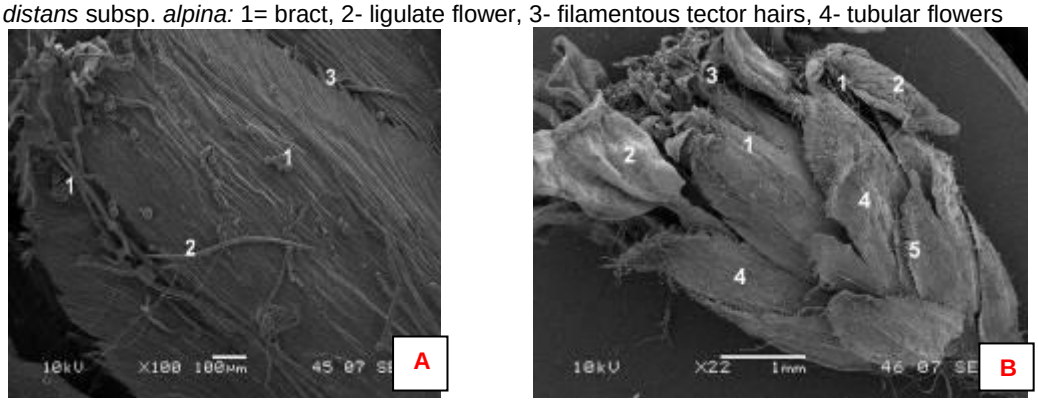

Figure 2. A. *Achillea distans* subsp. *distans* (bract): 1-pollen grains, 2-filamentous hairs, 3-serrated edge. B. *Achillea distans* subsp. *distans* (calatidiu): 1- tector hairs, 2- ligulate flower, 3-tubular flower, 4-bract, 5-serrated edge of bract

Plants and their Pathogens

LS.3.P120
Evaluation of polyphenol and isoflavon profile correlated with antioxidant capacity of *Genistella sagitallis* and *Genista tinctoria* extracts

D. Hanganu[1], L. Vlase[1], N.-K. Olah[2], A. Pintea[3], D. Rugina[3], C. Bele[3], D. Benedec[3], L. Filip[1]

[1]University of Medecine and Pharmacy Iuliu Hatieganu, Pharmacognosy, Cluj, Romania
[2]West University, Arad, Romania
[3]University of Agriculture Sciences and Veterinary Medicine, Cluj-Napoca, Romania

handa_1964@yahoo.com
Keywords:polyphenols,isoflavons, antioxidant

Reactive oxygen and nitrogen species have been involved in many physiological and pathological processes which cause tissue damage. Non–enzymatic antioxidants such as polyphenols prevent the negative effect of oxidative stress to different cellular biomolecules such as proteins and DNA.

Genistella sagittalis and *Genista tinctoria* are species widespread in the Romanian spontaneous flora, traditionally used for their tinctorial, nutritional and medicinal properties (antihepatotoxic, hormonals, diuretic etc.), due to polyphenols (including isoflavons) among others. To evaluate the polyphenolic profile of these species were analyzed the aerial parts.The total polyphenolic content (TPC) was obtained by modified Folin-Ciocalteu method.The identification and quantification of isoflavons was made by LC/MS. In addition, the evaluation of relative antioxidant activity was made by DPPH, ABTS, ORAC, SNP (growth of silver nanoparticles by the extracts of polyphenols) methods [1,2,3,4]. By LC/MS we have determinated the presence of free isoflavons (daidzein, genistein, formononetin) and their 7-O-glycosides (daidzin, genistin, ononin) “Table1”. *Genista tinctoria* had an increased level of genistin, genistein and daidzein along with formononetin and ononin [5]. *Genistella sagittalis* was remarked due to a higher content of genistin. TPC values expressed in Gallic Acid Equivalents (mg GAE/g) were 35,5±021 for *Genista tinctoria* and 5,7±0,35 for *Genistella sagittalis*. ORAC assay (mM TE/g) showed 65,84±2,04 for *Genistella sagittalis* and 68,12±1,77 for Genista tinctoria. The results of DPPH assay (mM TE/g) consisted in 24,72±0,94 for *Genistella sagittalis* and in 236,83±7,84 for *Genista tinctoria*. ABTS assay (mg TE/g) showed a value of 94,44±5,09 for *Genista tinctoria* and one of 40,49±4,88 for *Genistella sagittalis*. The growth of silver nanoparticles (SNP)-based method for evaluating the antioxidant capacity of polyphenolic compounds was also used [5].The reduction of Ag^+ to spherical silver nanoparticles (SNPs) by polyphenols in the presence of trisodium citrate and siver seed produced a very intense absorbtion band of SNPs at 423 nm. The absorbance of SNPs allows the quantitative spectrophotometric detection of polyphenols. Using this method there were found 0,38 ±0,74 µg GAE/g for *Genistella sagittalis* extract and 0,51±0,63 *Genista tinctoria extract* [2].

The results of this method was correlated with those of another electron transfer (ET)-based TAC assay (Folin-Ciocalteu), hydrogen atom transfer (HAT)-based (ORAC), and mixed ET/HAT-based (ABTS, DPPH) assays.

Statistical Analysis was performed using Excel software. Results were expressed as the mean ± standard deviation (SD), Pearson coefficient.

All antioxidant activity values obtained were highly correlated with the total polyphenol and isoflavon content. *Genista tinctoria* had a higher total polyphenol and isoflavon content and also a higher antioxidant activity then *Genistella sagittalis.* Due to their isoflavon content both species can be used as an alternative to phytoestrogens.

1. D. Huang, et al, J Agric Food Chem (2005), 53(6):1841-1856.
2. M. Ozyurek , N.Gungor, S. Baki, K. Guclu and R. Apak, Anal Chem (2012), 84 pp. 8052-8059.
3. M.B. Arnao, et al. Phytochem Anal (2001),12(2):138-143.
4. W. Brand-Williams et al, Lebensmittel Wissenschaft und Technologie (1995), 28:25-30.
5. C.S.Fodorea et al, *Chemistry of Natural Compounds* (2005), 41(4):400-403.

Sample µg/ml	daidzin	genistin	ononin	daidzein	genistein	formononetin
Genistella sagittalis	2,89	51,60	0,89	0,55	9,02	0,84
Genista tinctoria	22,32	130,17	0,24	8,81	73,77	0,68

Table 1. Content of isoflavon compounds from the native extracts

Plants and their Pathogens

LS.3.P121
Evaluation of antioxidant capacity and total polyphenolic content in the tincture of *Hyssopus offinalis* L.

B. Tiperciuc[1], L. Vlase[1], C. Bele[1], D. Hanganu[1], D. Benedec[1]

[1]University of Medicine and Pharmacy Cluj-Napoca, Medicinal Chemistry, Cluj-Napoca, Romania

brandu32@yahoo.com
Keywords: *Hyssopus,* antioxidant, silver nanoparticles

Hyssopus officinalis L. (*Lamiaceae*) is one of the most popular herbal preparations, mainly distributed in the East Mediterranean to central Asia**.** Hyssop is an important perennial culinary and medicinal plant. It has a very strong spicy taste and intensive flavor and it is commonly used in folk medicine. Hyssop is considered to have antiviral, anti-inflammatory, antiseptic, diuretic, expectorant and stimulant properties. As a medicinal herb, it is used in viral infections such as colds, coughs, sore throats, bronchitis and asthma. It can also be used in treatment of chronic indigestion, excessive gas, abdominal bloating and colic. The flowering tops of hyssop produce a pleasant essential oil responsible for most of biological activities of this plant. In addition to the particular aroma, the essential oil exhibit muscle relaxant, antibacterial and antifungal activities [1,2].

The aim of this work was to study the chemical composition and the antioxidant activity of *Hyssopus officinalis L.* from Romania [3,4] The identification and quantification of major phenolic compounds was performed by a HPLC-MS method. The total phenolic compounds (TPC) were determined using the modified Folin-Ciocalteu method and for flavonoids determination was used a colorimetric aluminum chloride method. The antioxidant activity was determined using the 2,2-diphenyl-1-picrylhydrazyl (DPPH) bleaching method and SNP-based method. The growth of silver nanoparticle (SNP)-based method for evaluating the antioxidant capacity of polyphenolic compounds (i.e., hydroxycinnamic acids, flavonoids, simple phenolic) from vegetal extracts was also used [4]. The reduction of Ag^+ to spherical silver nanoparticles (SNPs) by polyphenols in the presence of trisodium citrate and silver seed was produced an intense absorbtion band of SNPs at 423 nm. The absorbance of SNPs allowed the quantitative spectrophotometric detection of polyphenols. The results of this method were correlated with those of other antioxidant methods (DPPH assay). In the aerial parts extract of hyssop four hydrocynnamic acid derivates (caftaric, caffeic, chlorogenic, ferulic acids) and two aglycones of flavone (luteolin, apigenin) were detected. The flavonoid content values were expressed as rutin equivalent (g RE/100 g dry plant) was 0.52%. TPC values were expressed as gallic acid equivalent (g GAE/100 g dry plant) was 9.25%. The total polyphenolic (TPC) and flavonoids content values were summarized for *Hyssopus* tincture in “Table 1”. The tincture was exhibit antioxidant activity 29.58% with an IC_{50} value of 189µg/ml in DPPH radical scavenging method, “Table 1”. Using SNP-based method there was found 0.09±0.74 µg GAE/g. It was found that the radical-scavenging activities of the tincture of hyssop were moderate. The results of the study suggest that hyssop contain a large amount of total polyphenolic compounds, but nevertheless, the antioxidant activity was moderate. The presence of polyphenols in *Hyssopus officinalis* can be related to diuretic or anti-inflammatory properties. Thus hyssop flowers may be considered a source of important polyphenols to be explored for the pharmaceutical applications.

1. J. Bruneton in “Pharmacognosie. Phytochimie. Plantes medicinales” 2emeedition, Londres Technique et Documentation, Lavorsier New York (1993), p.428.
2. V. Ciocârlan in “Illustrated Flora of Romania. Pteridophyta et Spermatophyta”, Ceres Publishing House: Bucharest, Romania (2009), p. 662.
3. D. Benedec, L. Vlase, D. Hanganu and I. Oniga, Dig J Nanomater Bios 3 (2012), p. 1263-1270.
4. M. Ozyürek, N. Güngör, S. Baki, K. Güçlü and R. Apak, Anal Chem. 18 (2012), p. 8052-9.

Samples	TPC (g gallic acid/100 g plant material)	Flavonoid (g rutin/100 g plant material)	DPPH radical scavenging, IC50 (µg/ml)	SNP (µg gallic acid/g plant material)
Tincture of *H. officinalis*	9.25±0.75	0.52±0.06	189±1.25	0.09±0.005
Trolox			12±0.65	

Table 1. Total phenolic (TPC) and flavonoids content in *Hyssopus officinalis* and antioxidant activity

Molecular Structures and High Resolution TEM

LS.4.122
High resolution cryo-EM of protein polymers: new insights into evolutionary divergence

E. Egelman[1]

[1]University of Virginia, Charlottesville, United States

egelman@virginia.edu

Helical polymers are ubiquitous in biology for the reason that helical symmetry arises from the simplest bonding rule between any two asymmetric units. If two identical copies of the same protein have a favorable interaction, in general this interaction can be repeated many times forming a polymer in which every subunit is in an identical environment. Most protein polymers can never be crystallized, since only a helix with exactly 2, 3, 4 or 6 subunits per turn is compatible with a crystal space group symmetry. Electron microscopy is therefore the method of choice for looking at protein and protein-nucleic acid polymers. In principle, low-resolution EM reconstructions can be combined with high resolution crystal or NMR structures to generate pseudo-atomic models of polymers of interest. However, when the resolution is limited to 20 Å or worse, interpretation of such density maps can be both ambiguous and problematic [1]. Recent advances in cryo-EM have now made it possible to routinely achieve sub-nanometer resolutions for a large variety of helical polymers. But there are a number of obstacles to imaging such polymers at the highest resolutions. One is that in the absence of something like a space group (present in a crystal) to maintain long-range order, all helical polymers will show cumulative disorder [2;3]. The only question is what is the scale of this disorder, or what is the persistence length for helical order. A number of years ago we introduced a method for surmounting the lack of long range order, called the Iterative Helical Real Space Reconstruction approach [4], that is now the main technique used for three-dimensional reconstruction of helical polymers by EM. Examples will be given from a number of systems to show how near-atomic resolution, even from fairly disordered and variable polymers, can now be achieved by cryo-EM and image processing. Most of the results have been obtained very recently and are not yet published. The polymers include actin [5], MDA5-RNA filaments [6], filaments formed by the pyrin domain (PYD) of ASC [7], and the adhesion filaments from *I. hospitalis* [8] (Figure 1). In the case of the PYD filaments we have achieved a resolution of 3.8 Å, allowing us to position quite a few of the larger amino acid sidechains. This is a great advance, as all EM structures currently deposited in the EMDB at better than 4.0 Å resolution have been viruses. We can now show that a resolution where the polypeptide chain can be reliably traced can be achieved with very thin protein polymers (~ 85 Å) that have a variable twist.

1. Egelman EH. Problems in Fitting High Resolution Structures into Electron Microscopic Reconstructions. HFSP Journal 2008;2:324-31.
2. Egelman EH, Francis N, DeRosier DJ. F-actin is a helix with a random variable twist. Nature 1982;298:131-5.
3. Egelman EH, DeRosier DJ. The Fourier transform of actin and other helical systems with cumulative random angular disorder. Acta Cryst. 1982;A38:796-9.
4. Egelman EH. A robust algorithm for the reconstruction of helical filaments using single-particle methods. Ultramicroscopy 2000;85:225-34.
5. Galkin VE, Orlova A, Schröder GF, Egelman EH. Structural polymorphism in F-actin. Nat.Struct.Mol.Biol. 2010 Oct 10;17:1318-23.
6. Berke IC, Yu X, Modis Y, Egelman EH. MDA5 assembles into a polar helical filament on dsRNA. Proc.Natl.Acad.Sci.U.S.A 2012 Nov 6;109(45):18437-41.
7. Vajjhala PR, Mirams RE, Hill JM. Multiple binding sites on the pyrin domain of ASC protein allow self association and interaction with NLRP3 protein. J.Biol.Chem. 2012 Dec 7;287(50):41732-43.
8. Yu X, Goforth C, Meyer C, Rachel R, Wirth R, Schroder GF, Egelman EH. Filaments from Ignicoccus hospitalis Show Diversity of Packing in Proteins Containing N-Terminal Type IV Pilin Helices. J.Mol.Biol. 2012 May 30.

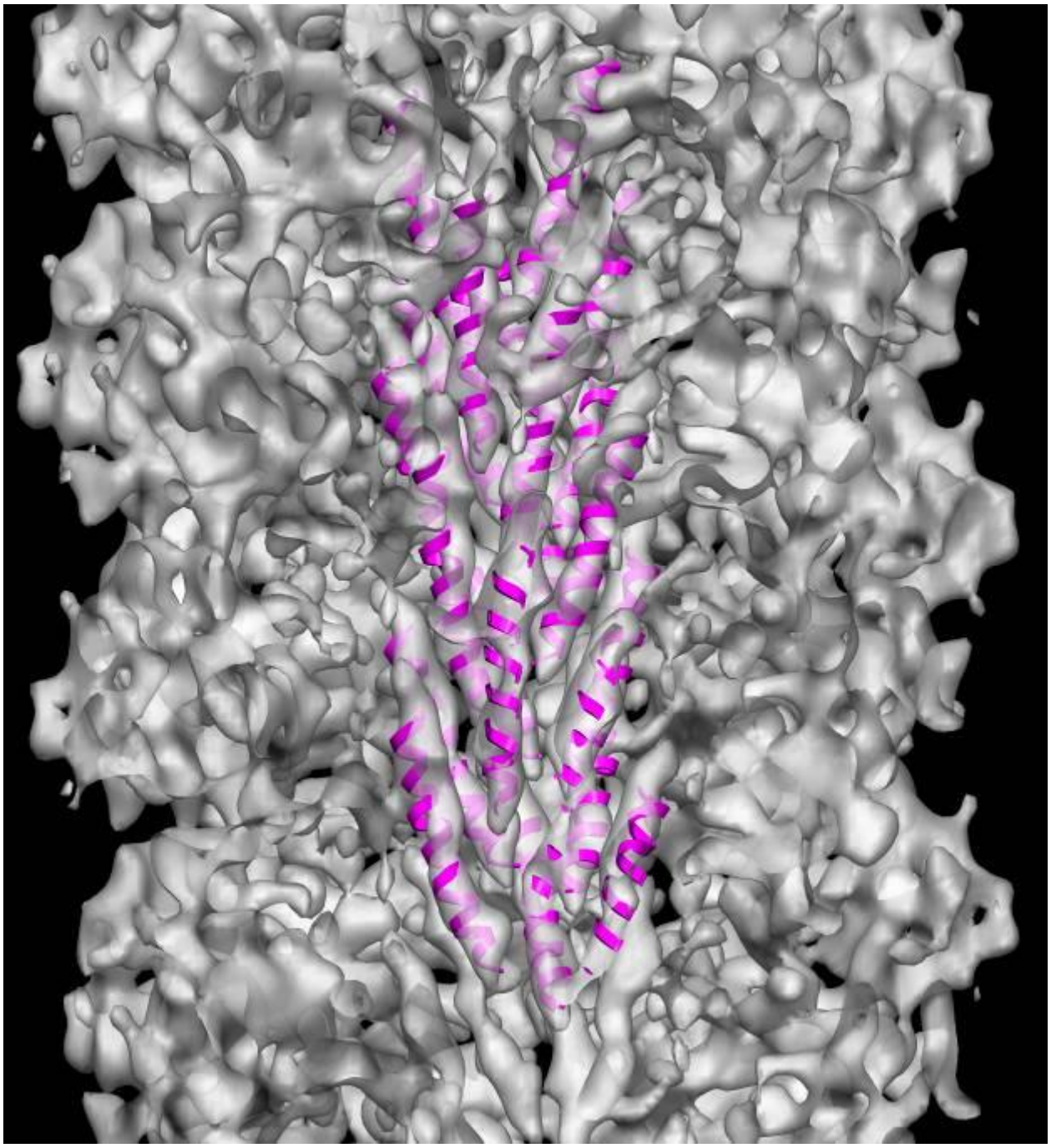

Figure 1. The N-terminal α-helices in the adhesion filaments of *I. hospitalis* can be positioned quite nicely into a three-dimensional cryo-EM reconstruction. As the resolution of such EM reconstructions improves one might expect to be able to fully trace the protein's polypeptide chain.

Molecular Structures and High Resolution TEM

LS.4.123
How to kill a mocking bug

S. Raunser

Photorhabdus luminescens is an insect pathogenic bacterium that is symbiotic with entomopathogenic nematodes. Upon invasion of insect larvae, *P. luminescens* is released from the nematodes and kills the insect through the action of large tripartite ABC-type toxin complexes (Tcs). Tcs are typically composed of TcA-, TcB- and TcC proteins. Functioning as ADP-ribosyltransferases, TcC proteins were identified as the actual functional components that induce actin-clustering and cell death. However, little is known about the translocation of TcC into the cell by the TcA and TcB components. Here, we show that TcA (TcdA1) forms a transmembrane pore and report its structure in the prepore and pore state determined by cryo-electron microscopy and x-ray crystallography. We found that the TcdA1 prepore assembles as a pentamer forming a α-helical vuvuzela-shaped channel less than 1.5 nm in diameter surrounded by a large outer shell. The protomers are composed of eight domains. Comparisons with structures of the TcdA1 pore inserted into a membrane and in complex with TcdB2 and TccC3 reveal large conformational changes during membrane insertion suggesting a novel syringe-like mechanism of protein translocation. Our results demonstrate how ABC-type toxin complexes bridge a membrane to insert their deadly components into the cytoplasm of the host cell. Our proposed mechanism is paradigmatic for the whole ABC-type toxin family. It is an important step towards the understanding of the host-pathogen interaction and the complex life cycle of *Photorhabdus luminescens* and other pathogens, including human pathogenic bacteria.

Molecular Structures and High Resolution TEM

LS.4.124
High Resolution Structure of the Mycobacterial Fatty Acid Synthase - Automated Image Acquisition on a Direct Electron Detector

D. Boehringer[1], N. Ban[1], M. Leibundgut[1]

[1]ETH Zurich, Institute of Molecular Biology and Biophysics, Zurich, Switzerland

Daniel.boehringer@mol.biol.ethz.ch
Keywords: mycobacterium, type I fatty acid synthase, single particle cryo-EM, mycolic acid biosynthesis

The mycobacterial fatty acid synthase (FAS) complex is a large, 2.0 megadalton, multifunctional enzyme that catalyzes the synthesis of fatty acid precursors to mycolic acids, which are major components of the cell wall in Mycobacteria and play an important role in pathogenicity.

Here we present the three dimensional reconstruction of the M. smegmatis FAS complex, highly homologous to the M. tuberculosis multienzyme, by cryo-electron microscopy [1]. Using a direct electron detector we obtained images with a high signal to noise ratio which allowed us to select images representing the main conformation of this heterogeneous macromolecular complex. The mycobacterial FAS structure resembles the cage like architecture of fungal FAS but exhibits larger openings and fewer stabilising linking elements. Based on the secondary structural elements present in the reconstruction, and sequence homology with the fungal FAS, we generated an accurate molecular model of the complex. Our reconstruction reveals structural features that may be important for the interaction with the mycolic acid processing and condensing enzymes that further modify the precursors produced by FAS.

1. D. Boehringer, N. Ban, M. Leibundgut, J Mol Biol. 425 (2013) p. 841

Molecular Structures and High Resolution TEM

LS.4.125
A control freak's approach to CTF corrected tomography

L. Voortman[1], E. Franken[2], A. Voigt[2], L. van Vliet[1], B. Rieger[1]

[1]Delft University of Technology, Delft, Netherlands
[2]FEI Company, Eindhoven, Netherlands

L.M.Voortman@TUDelft.NL
Keywords: TEM, cryo-electron tomography, CTF correction, defocus gradient

Cryo-electron tomography (CryoET) is an essential tool to study the three-dimensional (3D) structure of biological specimens at molecular resolution. The primary contrast mechanism for biological specimens is weak phase contrast. In this weak phase contrast regime, image formation is for an important part described by the contrast transfer function (CTF). The CTF is an oscillating function of the spatial frequency and depends, among other parameters of the imaging system, on the applied defocus.

In CryoET many two-dimensional (2D) projections of the 3D structure of a specimen are recorded at different tilt-angles. Tilting of the specimen induces a defocus gradient which depends on the specimen orientation and the orienation of the tilt-axis. We recently introduced a new global CTF correction method (to process the entire field-of-view at once) which can use different inverse filters, e.g. phase-flipping or Wiener filter, and do so within a reasonable time for large image sizes (4k x 4k) [1].

Contrast Transfer Function (CTF) correction increases the interpretability of the images up to higher resolutions. However, to use CTF correction on tomography data, one needs to know at each tilt-angle the exact defocus distribution over the specimen with an accuracy of ~ 50 nm [2]. A simple solution would be to trust the information from the microscope interface, since the selected defocus and tilt-angles are in principle sufficient. This approach, however, ignores that the actual defocus is not only (substantially) different from the requested defocus but it also varies during acquisition. These defocus variations can be due to the non-perfect mechanics of the stage, the accuracy with which the eucentric height can be adjusted, the auto-focus area being offset from the exposure area or unpredictable fluctuations. In order to account for these variations, the defocus needs to be measured throughout a tilt-series.

Furthermore, we do not know the orientation of the specimen when the stage is at zero tilt. It is not uncommon, however, to observe that the specimen is tilted/warped even up to 10 degrees in an arbitrary direction. This orientation influences the direction and magnitude of the defocus gradient throughout the tilt-series.

We decided to measure the defocus and specimen orientation throughout the tilt-series acquisition. This is achieved by taking four additional high-dose exposures at each tilt-angle on which we measure the defocus. These high-dose exposures are positioned on the carbon grid, away from the area-of-interest, two on the tilt axis and two off-axis (see Figure 1). The defocus at these high-dose areas is measured using the method described in [3].

The defocus measurements on the high-dose exposures are used to estimate the defocus on the exposure area. For this purpose we developed a robust algorithm that automatically detects faulty measurements. Assuming that the specimen is locally flat, we use the redundancy introduced by the four defocus estimation areas to detect outliers. Figure 2 shows the measured defocus, the estimated specimen orientation and the estimated defocus on the exposure area. With this procedure we can robustly estimate the defocus and specimen orientation (which defines the defocus gradient) at each tilt-angle. We are currently processing CTF corrected tomograms to show that this approach can increase the attainable resolution.

1. L.M. Voortman, E.M. Franken, L.J. van Vliet and B. Rieger, Ultramicroscopy 118 (2012), p. 26 – 34.
2. L.M. Voortman, S. Stallinga, R.H.M. Schoenmakers, L.J. van Vliet and B. Rieger, Ultramicroscopy 111 (2011), p. 1029 – 1036.
3. M. Vulović, E.M. Franken, R.B.G. Ravelli, L.J. van Vliet and B. Rieger, Ultramicroscopy 116 (2012), p. 115 – 134.
4. We acknowledge support from the FOM Industrial Partnership program No. 07.0559.

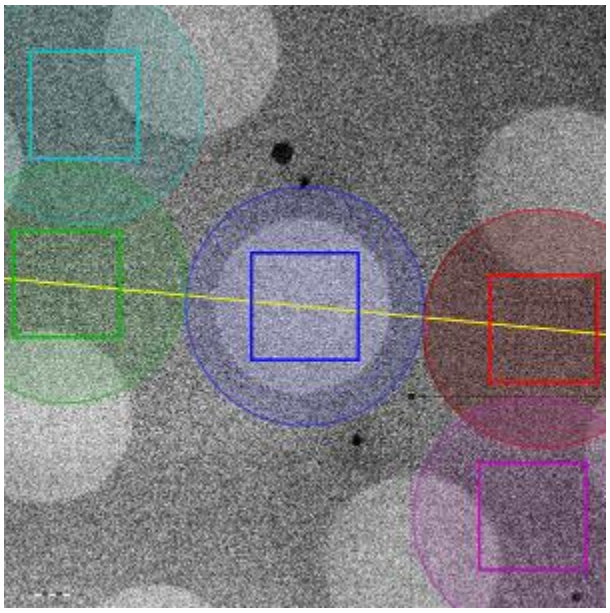

Figure 1. The area-of-interest (in blue) is located on the ice. Two high-dose areas are positioned on the tilt-axis (green and red) and two are positioned away from the tilt-axis (cyan and magenta). The locations are chosen such that also at high tilt-angles the high-dose beam does not overlap with the exposure area.

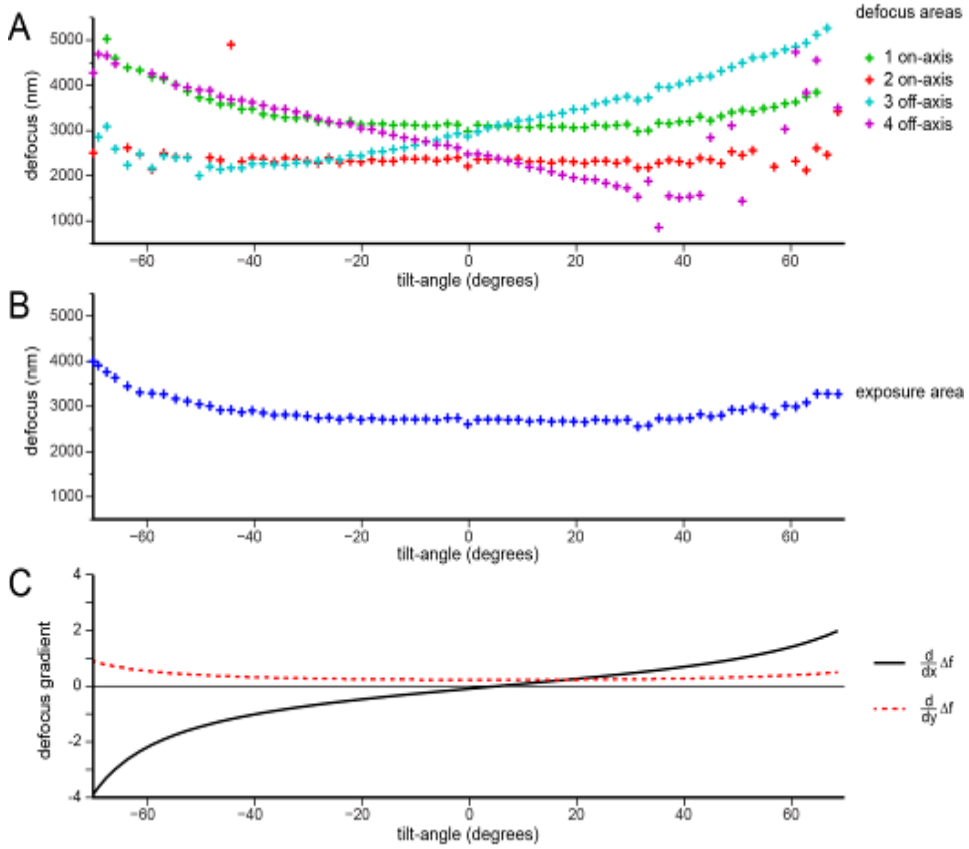

Figure 2. a) Measured defocus on the four high-dose exposure areas for each tilt-angle. b) The defocus at the tilt-axis in the area-of-interest, estimated using the location of the high-dose areas (Figure 1) and the measured defocus values (A). c) The estimated specimen orientation together with the tilt-angle defines the defocus gradient perpendicular to and along the tilt-axis. At high tilt-angles the defocus gradient is dominated by the applied tilt-angle, whereas at low tilt-angles the defocus gradient is a by-product of the non-zero specimen orientation.

Molecular Structures and High Resolution TEM

LS.4.126
Experimental evaluation of a forward model in cryo-electron microscopy

M. Vulovic[1,2], R. Ravelli[2], L. van Vliet[1], A. Koster[2], B. Rieger[1]

[1]TU Delft, Imaging Science and Technology, Delft, Netherlands
[2]Leiden University Medical Center, Molecular Cell Biology, Leiden, Netherlands

m.vulovic@tudelft.nl
Keywords: image simulation, cryo-EM, forward model

Accurate modeling of image formation in cryo electron microscopy (cryo-EM) is an important requirement for optimizing data acquisition and ultimately, interpreting the data at the highest possible resolution. Such a forward model (InSilicoTEM) that accounts for the specimen's scattering properties, microscope optics, and detector response is presented in [1].

The model was validated by comparing simulated and experimental images of 20S proteasome, earthworm hemoglobin, and GroEL acquired under various microscope settings and experimental conditions. The effects and parameters that have been analyzed include: solvent constituents, defocus, integrated electron flux, inelastic scattering, detective quantum efficiency (DQE), acceleration voltage, and amorphousness ("structural noise") of the solvent. All simulation parameters are based on physical principles and, when necessary, experimentally determined. The detector characteristics and CTF parameters (defocus and astigmatism) were determined using toolboxes provided in [2] and [3], respectively.

The dominant part of the interaction potential is calculated via isolated atom superposition approximation (IASA) [4, 5]. The influence of the effective charge redistribution due to the solvent's dielectric and ionic properties and molecular electrostatic distribution is modeled via a Poisson-Boltzmann (PB) approach [6]. Various buffer compositions (50mM up to 3M ammonium acetate) have been used to evaluate our modeling of the influence of charge redistributions for the hemoglobin sample. The contribution of the PB-based potential to the interaction potential appears to be less than 10 % for all these cases. The influence of the PB-based potential inclusion is mostly recognized by slightly less contrast at protein-solvent interfaces compared to the images calculated using only the IASA-based potential.

Various defocus series were acquired for which the simulations correctly predicted changes in the experimental images. After each defocus series another region was imaged with a different integrated electron flux. At acceleration voltage of 80 kV, simulated images at higher integrated fluxes often gave stronger contrast compared to the experiments. This observation is consistent with the effect of random beam-induced movements which depend on the integrated flux and can significantly damp the contrast in cryo-EM [7]. The inclusion of a motion factor blurs the simulated images to become more similar to experimental. The required motion factor to match simulations with experiments is in the range between 0 and 10 Å. It appears to be stronger for higher integrated electron fluxes, thinner ice layers or lower acceleration voltages, which is in agreement with values experimentally measured [7].

Inelastic scattering of electrons is modeled as the imaginary part of the interaction potential. Figure 1. allows a comparison between (B) simulated images where the model of inelastics is incorporated and (C) experimental energy-filtered images of earthworm hemoglobin and proteasome. In addition, simulated images in which only pure phase contrast is considered (A) and unfiltered experimental images (D) are included.

We analyzed images both at 80kV and 300kV. The latter show less contrast compared to the lower voltage images. For both voltages, experimental data were in agreement with simulations.

For typical electron fluxes in cryo-EM we show that the influence of the solvent/specimen amorphousness (structural noise) can be neglected. Apparently Poisson noise is the dominant noise source in the image and the solvent can be modeled as a continuum medium.

InSilicoTEM could be used to predict the optimal experimental parameters and its modularity allows efficient and inexpensive investigation of the influence of new hardware components.

1. M. Vulović, R.B.G. Ravelli, L.J. van Vliet, A.J. Koster, I. Lazić, U. Lücken, H. Rullgård, O. Öktem, B. Rieger, Journal of Structural Biology, 2013, under review
2. M. Vulović, B. Rieger, L.J. van Vliet, A.J. Koster, R.B.G. Ravelli, Acta Crystallographica D66 (2010), p. 97.
3. M. Vulović, E. Franken, R.B.G. Ravelli, L.J. van Vliet, B. Rieger, Ultramicroscopy 116 (2012), p. 115.
4. H. Rullgård, L.G. Öfverstedt, S. Mashic, B. Daneholt, O. Öktem, Journal of Microscopy 243 (2011), p. 234.
5. L.-M. Peng, G. Ren, S.L. Dudarev, M.J. Whelan, Acta Crystallographica A 52 (1996), p. 257.
6. N.A. Baker, D. Sept, S. Joseph, M.J. Holst, J.A. McCammon, Proc. Natl. Acad. Sci. 98 (2001), p. 10037.
7. A.F. Brilot, J.Z. Chen, A. Cheng, J. Pan, S.C. Harrison, C. Potter, B. Caragher, R. Henderson, N. Grigorieff, Journal of Structural Biology 177(2012), p.630.
8. The authors would like to thank O. Öktem, I. Lazic and H. Rullgård, to acknowledge the use of cryo-EM facility at the Netherlands Center for Electron Nanoscopy (NeCEN), and help of Paul Mooney related to the GIF camera. This research is supported by FOM Industrial Partnership Program No07.0599.

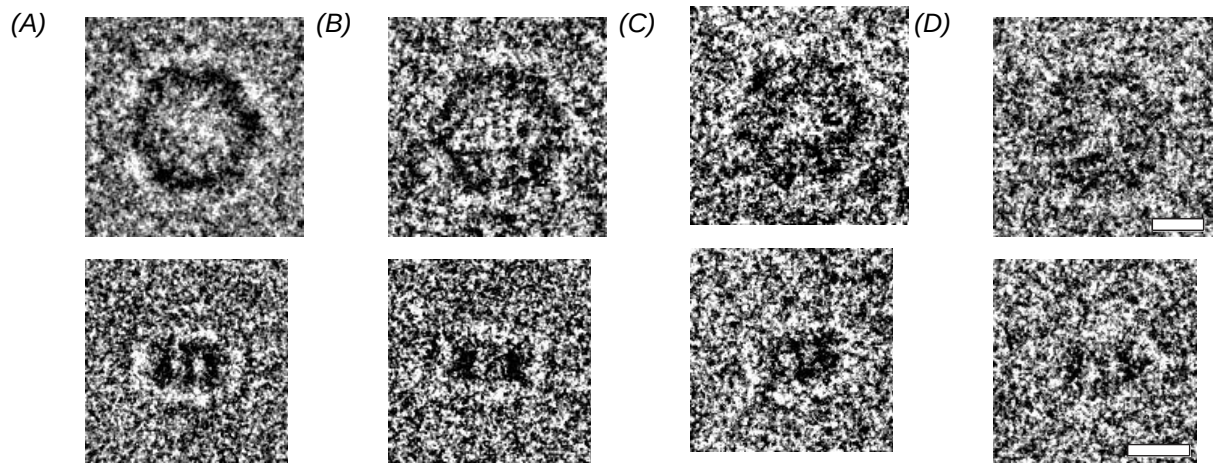

Figure 1. Influence of inelastic scattering. (A) simulations of pure phase contrast, (B) simulations with inelastic scattering, (C) experimental zero-loss filtered images, and (D) experimental unfiltered images. From top to bottom are presented earth worm hemoglobin (t_{exp}=1 s, Δf = 4918 nm, thickness d = 142 nm), and side view of 20S proteasome (t_{exp}=1 s, Δf = 6713 nm, d = 80 nm). Some acquisition and simulation parameters: Krios@80 kV, pixel size 0.135 nm, flux 2.5 $e^-/Å^2/s$, C_s 2 mm, C_c 2 mm, ΔE 0.7eV, illumination aperture 0.03 rad, energy slit 10 eV, conv. factor 20 ADU/pe^-, MTF@0.5Nq 0.223, DQE@0.5Nq 0.315, readout 3 ADU, dark current 0.11 ADU/s. The scale bars correspond to 10 nm.

Molecular Structures and High Resolution TEM

LS.4.127
Retrofittable phase plate system for cryo-TEM

J. Wamser[1]

[1]KonTEM GmbH, Bonn, Germany

joerg.wamser@kontem.de
Keywords: Phase plate, phase contrast, cryo-TEM

With recent advances in sample preparation and instrumentation, cryo-transmission electron microscopy (cryo-TEM) has become an important and powerful technique in structural biology to analyze specimen in their native state [1]. These frozen, hydrated specimen however show only weak image contrast. Nearly all image information is contained in a phase change of the scattered electron beam. This phase information can be made visible in the image by changing focus. Unfortunately, such defocusing introduces additional zeros to the contrast transfer function (CTF) of the microscope. These zeros are visible in the image as “phase flips”, reducing resolution. To compensate this loss in resolution, images at different foci are recorded and the CTF of the microscope is first calculated and then corrected. Unfortunately, cryo-samples are often too beam-sensitive to withstand the recording of multiple images of the same spot which is needed for this compensation. Therefore, particular details or structures might not be visible in these images.

Using a phase plate instead of defocusing can be a viable alternative to gain contrast and preserve resolution. The phase plate is placed at the back focal plane of the objective lens inside the TEM. While passing the phase plate, an additional phase shift is applied to a part of the electron beam. Interference of the two beam parts generates enhanced contrast. Thus, phase plates can show structures that are not visible in the original data gained by defocusing. This holds particular advantage for objects, which cannot easily be averaged [2].

To push TEM phase plates from being used in single experiments towards a routine procedure, three main objectives have to be fulfilled: I) Design of a stable phase plate with high resolution capability that is suitable for commercial production II) Design of a modular, fully encoded, heated and affordable high precision positioning device fitting the most common cryo-microscopes III) Provision of an automated phase plate positioning software and perform its subsequent integration into the TEM and camera software. Here, we present a phase contrast solution whose design was based on the above-mentioned objectives.

I) We developed a new type of Zernike phase plate. It consists of a 5 nm film of amorphous Silicon coated with an additional Chromium layer. The phase shift of pi/2 is controlled by the thickness of the Chromium layer with respect to the desired accelerating voltage. To let pass the unscattered electron beam, a central hole is milled into the film using a focused ion beam system (FIB). Hole diameters vary between 200 and 1000 nm.

Figure 1A shows the currently used array of 65 phase plates to be inserted into the microscope in combination with an objective aperture. Figure 1B shows one of the 65 milled phase plate holes. Figure 2 shows two images of a frozen hydrated mouse retina. Image 2A was acquired without phase plate at 2 µm underfocus. Image 2B was made near focus with the phase plate inserted. The contrast enhancement is clearly visible.

II) We built a piezo-based, encoded positioning device, to exactly align the central hole of the phase plate to the electron beam. A heating element was integrated to reduce contamination of the phase plate. To ensure safe installation and operation, a pole-hit detection device was implemented. The modular design of the positioning device requires that only two parts have to be adapted to the different TEM models. The heart of the drive mechanism consists of three fully encoded piezo-leg motors [3]. In contrast to standard stick-and-slip piezo drives, the leg design allows higher forces along the motor axis. To maximize compatibility, the piezos are located outside the TEM column. The motors allow positioning steps of <1 nm. The encoders ensure a position repeat accuracy of 61 nm. The capabilities of the device were tested on various TEM models. Figure 3 shows the system installed at a Zeiss LEO 922. Other tested models are FEI Titan Krios, JEOL 2200 FS, Zeiss L120 & L200.

III) We developed a software to control all functions of the positioning device (e.g. drive in XYZ direction, changes in motor speed, store and recall phase plate positions, etc.). This allows a user-friendly application in a TEM and is a first step towards a fully automated phase contrast system.

1. Dubochet J. et al., Journal of Microscopy, Vol. 245 (2012), pp. 221-224.
2. Murata K. et al., Structure, (2010), pp. 903–912.
3. Merry R. et al., Sensors and Actuators A 162, 51 (2010).
4. This research was supported by the German Federal Ministry of Economics and Technology (EXIST Forschungstransfer grant 03EFT4NW32).

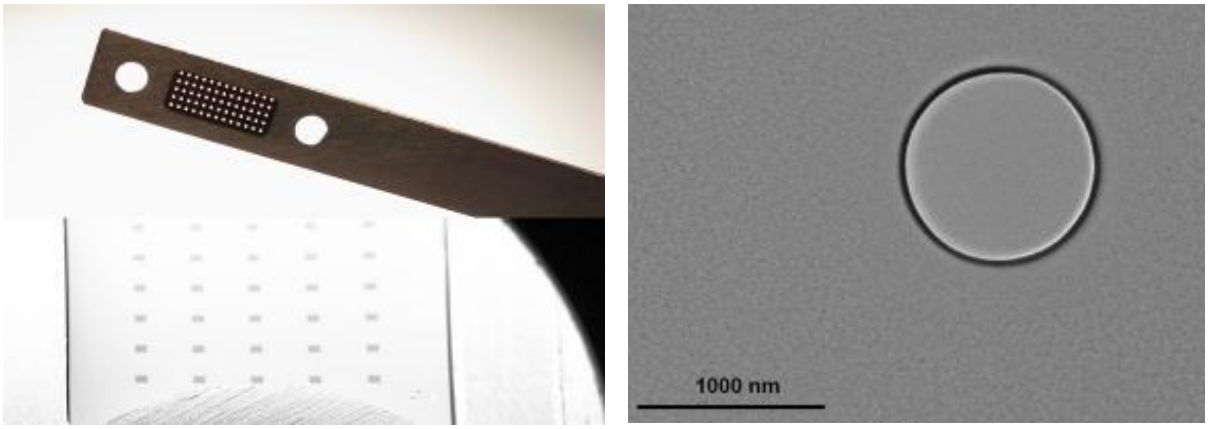

a.) **b.)**

Figure 1. Phase plate array with 65 phase plates (A) and milled phase plate hole (B)

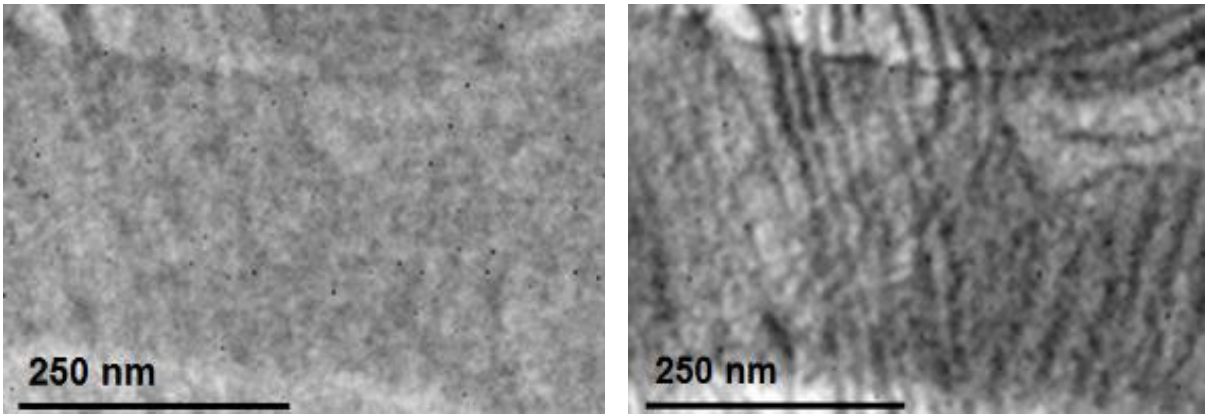

a.) **b.)**

Figure 2. TEM micrographs without (A) and with phase plate (B). The images were taken at 2 µm defocus (A) and near focus (B).

Figure 3. The high precision phase plate positioning device installed in a Zeiss LEO 922

Molecular Structures and High Resolution TEM

LS.4.P128
When to use the projection assumption and the weak-phase object approximation in phase contrast cryo-EM

L. Voortman[1], M. Vulovic[1,2], L. van Vliet[1], B. Rieger[1]

[1]Delft University of Technology, Delft, Netherlands
[2]Leiden University Medical Center, Leiden, Netherlands

L.M.Voortman@TUDelft.NL
Keywords: Cryo Electron Microscopy, multislice, projection assumption, weak-phase object, image simulation, interaction potential

An accurate description of the interaction between incident electrons and the specimen is an essential step in both forward modeling, contrast transfer function (CTF) correction and 3D reconstruction in cryo electron microscopy (cryo-EM). In cryo-EM, incident electrons with typical energies of 80-300 keV interact with the electrostatic interaction potential (IP) of the specimen, e.g. macromolecules that are similar in density to the surrounding vitreous ice. In order to describe the electron-specimen interaction (analytically) two approximations are often made: the weak-phase object approximation (WPOA) and the projection assumption (PA). The WPOA holds for weakly scattering objects and the PA assumes that the exit wave from the specimen can be computed via the projected IP of the whole specimen. These approximations have, of course, limitations as they cannot account for e.g. the curvature of the Ewald sphere or multiple scattering events; effects which become more critical for high resolution imaging. We show that to make the next step in resolution improvement in cryo-EM, it is important to revisit these two approximations as well as their limitations.

We present quantitative criteria for the applicability of the PA (via the Fresnel number) and WPOA (via the probability of multiple interactions) in phase contrast cryo-EM. Using these approximations, we derive four models that describe the electron wave propagation through the specimen (WPOA, PA, PA+WPOA and SWPOA). By combining the two approximations in a new way, we introduce an analytic image formation model that we call semi weak-phase object approximation (SWPOA). This model imposes less strict conditions on the interaction potential than PA or WPOA and gives comparable exit waves as a multislice calculation which is commonly used as a reference.

Figure 1A shows the computed exit waves for a tubulin tetramer (TT) (constructed from PDBid-1SA0) using the four models discussed above, i.e. PA, PA+WPOA, WPOA and SWPOA. In order to better visualize the effect of the approximations, we show in Figure 1B the differences of the four exit waves with a reference. This reference is computed by a multislice approach inspired by [1]. In the difference images we observe that the SWPOA is nearly identical to the multislice reference, whereas the WPOA shows deviations mostly in the stronger phase parts. For the PA we see deviations over the whole extent of TT and, of course, for the combined PA+WPOA the deviations are the largest.

In Figure 2 we present a practical reference to facilitate the model choice for electron wave propagation through an actual macromolecule such as hemoglobin, ribosome, or tubulin. To test the applicability of the four image formation models we compare the simulated exit waves again against a multislice reference. To quantify the difference we use the normalized mean squared error (MSE). Figure 2A shows the result of thresholding the MSE at 10%. We find a horizontal boundary for the WPOA and a vertical boundary for the PA. The boundaries of the combined models asymptotically approach the individual (WPOA and PA) approximations. In Figure 2B a sketched version qualitatively depicts the regions where the different approximations hold.

As practical conclusions we find that, when simulating images at resolutions of 5 Å, the applicability of the PA and WPOA need to be re-considered. Here, the SWPOA offers an excellent solution, as a fast but equally accurate alternative to the multislice approach. For tomograms with typical resolutions >30 Å, the PA and WPOA are generally applicable. In single particle analysis, structures can be obtained up to approximately 3.3 Å resolution [2] at which the PA and WPOA may be violated depending on the size of the macromolecule, while the SWPOA again offers a solid solution.

1. E.J. Kirkland in “Advanced Computing in Electron Microscopy”, (Springer, London) (2010).
2. X. Zhang, L. Jin, W. H. Fang, Q. Hui, Z. H. Zhou, Cell 141 (2010) p. 472 – 482.
3. We acknowledge support from the FOM Industrial Partnership program No. 07.0559.

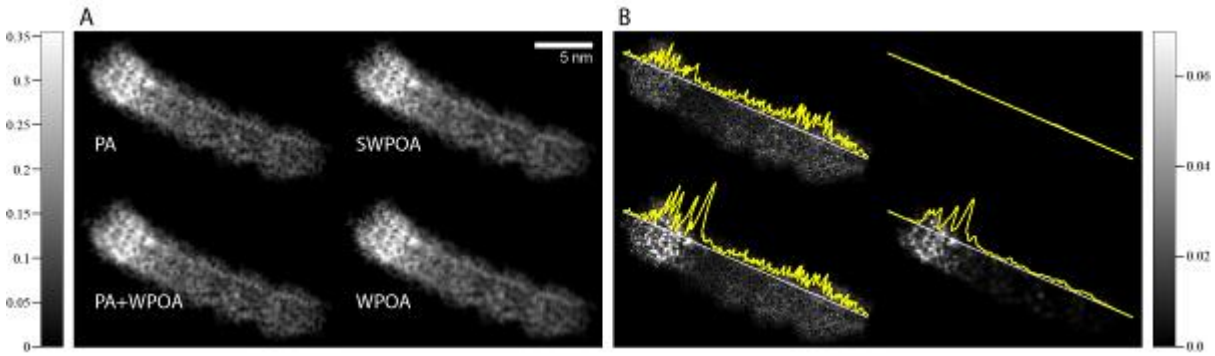

Figure 1. a.) Simulated exit waves of a tubulin tetramer (HT = 80 kV) using the PA, WPOA, PA+WPOA and SWPOA. b.) Difference image of the exit waves in A) and the exit wave computed with a multislice approach. The intensity scale bar indicates the phase of the exit wave subtracted by the mean.

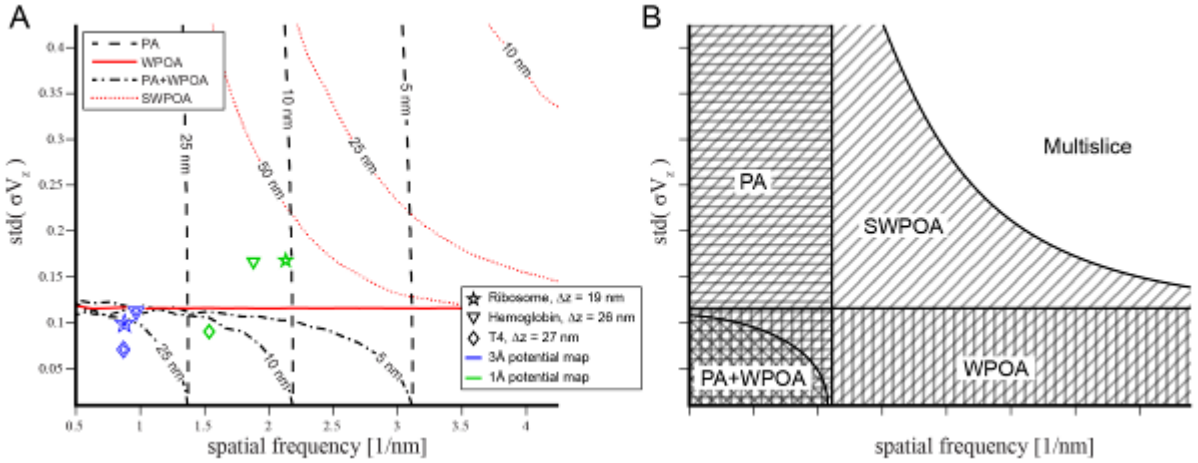

Figure 2. The applicability (at HT = 80 kV) of the PA, WPOA, PA+WPOA and SWPOA. A) Boundaries for each approximation where different lines represent different specimen thickness. Lines indicate 10% normalized MSE error of the respective approximation with a multislice reference. Left/below the boundary the approximation holds for a particular thickness. For three protein-complexes (Ribosome, Hemoglobin, TT) sampled at 1 Å and 3 Å, the potentials map properties are shown. B) A sketched diagram showing the qualitative results of A). The various striped regions depict region where each approximation holds.

Molecular Structures and High Resolution TEM

LS.4.P129
Structural analysis of the processive motor domain of myosin IX bound to actin filaments

S. Oeding[1], U. Honnert[1], A. Freitag[1], P. Nikolaus[1], K. Elfrink[1], A. Henkel[1], U. Pieper[1], M. Bähler[1]

[1]University of Münster, Institute of Molecular Cell Biology, Münster, Germany

s.oeding@uni-muenster.de
Keywords: myosin IX, processive movement, negative staining

Myosins are molecular motors with the ability to convert chemical energy into mechanical force. The hydrolysis of ATP enables myosins to move along actin filament tracks. Myosins have diverse cellular functions and are important for cell morphology and migration. Class IX myosins belong to the unconventional myosins and show several unique motor properties compared to other myosin classes. Remarkably, they are able to take multiple successive steps along actin filaments without dissociating although they are single-headed motors. The successive hand-over-hand mechanism of double-headed myosins where always one of the two heads stays attached to the actin filament cannot be operating in myosin IX. The mechanism of the single-headed processive movement of myosin IX still remains to be determined. It is supposed that a long basic insertion of approximately 120 amino acid residues within loop 2 in the head domain acts as actin tether [1,2]. This would ensure a persistent binding to F-actin during the whole ATPase cycle and allow for a single-headed processive movement. In previous studies we have shown that deletion of the basic insertion in the head domain of myosin IXb from rat (Myo9b) is accompanied with a decreased actin affinity [3]. Furthermore, a calmodulin-binding site (CaM-BS) could be identified within the basic insertion [4]. CaM is sensitive to changes in the Ca^{2+} concentration and reacts with a conformational change. Therefor Ca^{2+}/CaM may regulate the Myo9 motor properties. The contribution of CaM to the processive behavior of myosin IX is still unknown. To elucidate the mechanism of single-headed processive movement, the binding behavior of the *C. elegans* Myo9 motor domain (Figure 1) to actin filaments and the structure of decorated actin filaments were analyzed by electron microscopy using negative staining. Phalloidin stabilized actin filaments were decorated with Myo 9 motor domain on grids with a 10-15 nm thin carbon film. For negative staining 1% uranyl acetate solution was used. Filaments were imaged using a Zeiss Libra 120 transmission electron microscope at an acceleration voltage of 120 kV. First experiments have shown that actin binding of Myo 9 motor domain seems to be regulated by a still unknown mechanism that differs from other myosin classes (Figure 2). Recombinant Myo9 protein fragments were created that contain solely the insertion of the motor domain with and without the CaM-binding site (Figure 1). These constructs will aid in the analysis of the binding behavior of the insertion and the putative regulatory function of the additional CaM-BS and contribute to a better understanding of how processive movement with a single motor domain is achieved.

1. A. Inoue, J. Saito, R. Ikebe and M. Ikebe. Nat. Cell Biol. 4 (2002), p. 302-306.
2. P. L. Post, M. J. Tyska, C. B. O'Connell, K. Johung, A. Hayward and M. S. Mooseker, J. Biol. Chem. 277 (2002), p. 11679-11683F.
3. S. Struchholz, K. Elfrink, U. Pieper, G. Kalhammer, U. Honnert, A. Grützner, W. A. Linke, W. Liao and M. Bähler, J. Biol. Chem. 284 (2009), p. 3663-3671.
4. W. Liao, K. Elfrink and M. Bähler, J. Biol. Chem. 285 (2010), p. 24933-24942.

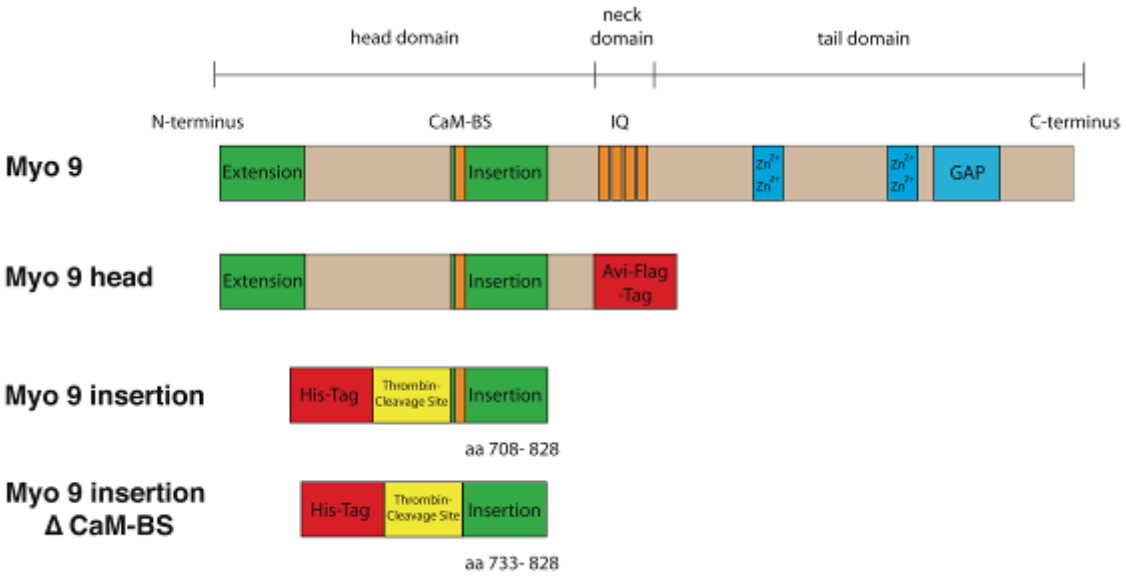

Figure 1. Schematic drawing of myosin 9 and used constructs. Myo 9 head contains a large basic insertion with a CaM-BS. Myo 9 insertion consists of solely the insertion with the CaM-BS. Myo 9 insertion Δ CaM-BS consists of a truncated insertion without the CaM-BS.

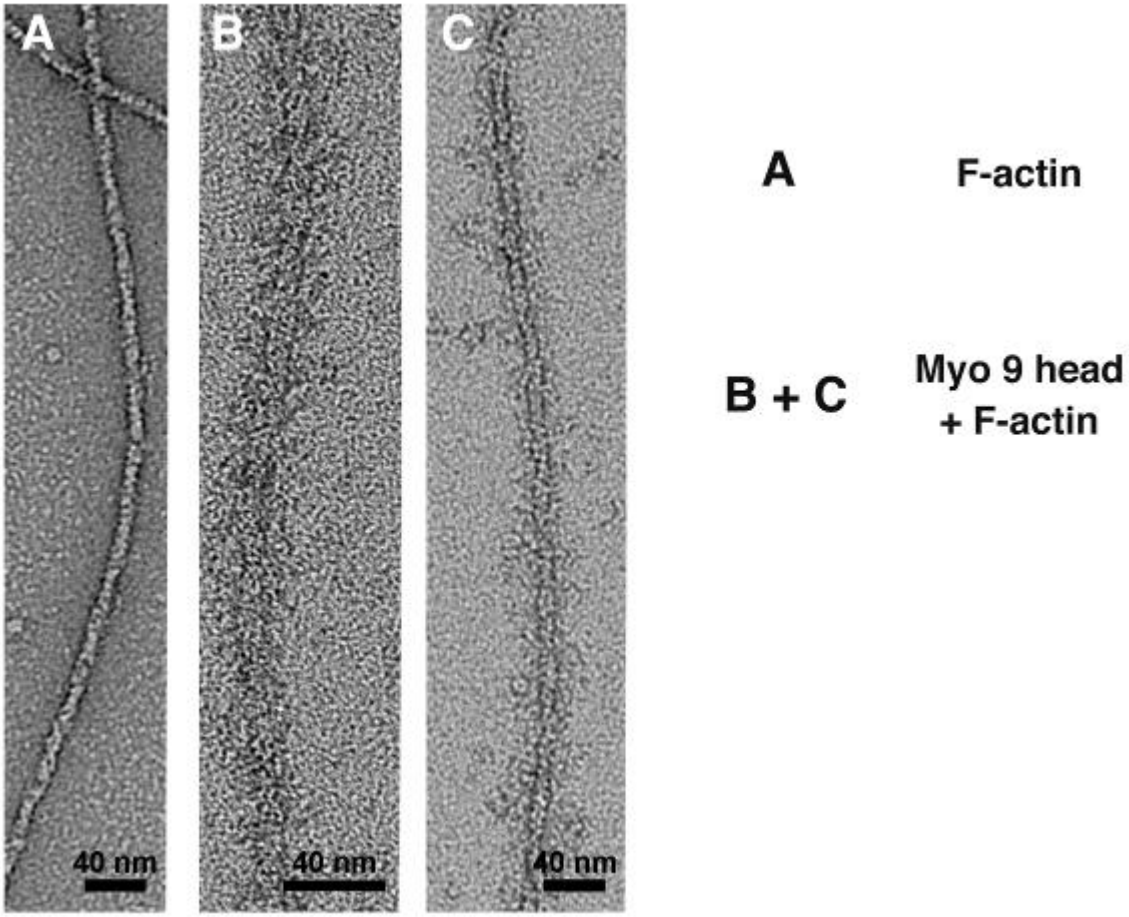

Figure 2. Actin filaments partially decorated with Myo 9 head. A) Phalloidin stabilized actin filament without Myo 9 head. B+C Phalloidin stabilized actin filaments partially decorated with Myo 9 head. Staining with 1% uranyl acetate. Scale bar 40 nm.

Molecular Structures and High Resolution TEM

LS.4.P130
Structural analysis of the bio-silica spicule of the sponge *Monorhaphis Chuni*

P. Werner[1], H. Blumtritt[1], A. Graff[2], Y. Dauphin[3], I. Zlotnikov[4], P. Fratzl[4]

[1]MPI Mikrostrukturphysik, Halle (Saale), Germany
[2]FhI of Mechanics of Materials, Halle, Germany
[3]University P. & M. Curie, Micropaleontologie, Paris, France
[4]MPI of Colloides and Interfaces, Golm, Germany

werner@mpi-halle.de

Biomineralization is a complex process where organic molecules play an essential role for the formation of a mineral, such as calcite or bio-silica. Such biominerals may have a complex structure of organic/anorganic interfaces and of organic inclusions in a mineral matrix, which can be amorphous as well as crystalline. It was found already more then 100 years ago that biominerals contain structural levels of hierarchy from mm-range to nm-range. We have applied TEM/STEM techniques including high-resolution x-ray microanalysis (EDX) to investigate the structure of the deep-sea glass sponge *"Monorhaphis chuni"*, the largest and oldest bio-silica structure on earth. The cylindrical basal spicule, which acts as an anchor of the sponge tissue, reaches a size of 3 m and a diameter up to 8 mm and consists mainly of silica. Figure 1 shows a SEM picture of the front tip of a basal spicule, which has a tree-trunk structure. It consists of circular lamellas of silica with thin organic interlayers between them. In the center of the spicule an axial filament exists, which has a diameter of about 2 µm. It contains organic molecules, especially the enzyme *silicatein*. The essential role of such molecules for the synthesis of silica has been intensively investigated during the last 5 years (see, e.g., [1-2]). However, questions on structure correlations remained. We concentrated our study on the fine structure of the organic interlayers and the axial filaments. Well-defined samples of the lamella region and of the region of the axial filament in different orientations (longitudinal, plan-view and cross-sections) were prepared by focused ion beam technique (FIB). We combined high-resolution TEM imaging (HR-TEM) with the STEM HAADF technique. The latter one has some advantages for imaging of bio-matter/biominerals. Additionally, specific electron diffraction experiments were carried out.

Figure 2 presents a STEM HAADF longitudinal section of the lamella region. The silica layers are separated by organic interlayers, which are marked by arrows. At higher magnification one could detect a structural transition region between the organic layer and the silica (see Figure 3), which influences the mechanical properties of the spicule [3]. Figure 4 shows a longitudinal cross-section STEM HAADF image of the central axial filament. The organic axial filament (dark) is surrounded by silica (gray). Mineral precipitates (lighter gray) were found in the filament as well as at the interfaces. High-resolution HAADF images as well as high-resolution EDX 2D-mapping yielded that the organic matrix consists of a 3-dimensional lattice of organic and silica structure units. This regular arrangement of these structure units has a periodicity in the range of 5 to 7 nm. This strong periodicity was also confirmed by small-angle X-ray scattering. It might be the result of a self-organization process where the organic molecules, e.g., *silicatein*, play an important role [4]. All information provides a better insight of the complex bio-silica matrix in the nm-range.

1. J.N. Cha, et al., Proc. Nat. Acad. Sci. USA 96, 361 (1999)
2. X. Wang, et al., J. Experimental Biology 214, 2047 (2011)
3. I. Zlotnikov, et al., Adv. Mat. 25, (2013), in press
4. W.E.G. Müller, et al., Gene 395, 62 (2007)

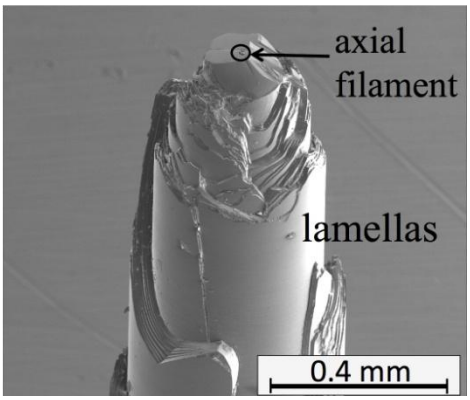

Figure 1. SEM image of the tip of a basal spicule. It consists of a lamellar structure of cylindrical silica shells. In the center an axial filament exits, which has a diameter of about 2 µm. It contains organic material.

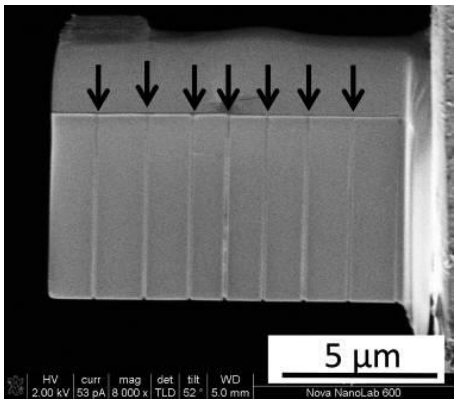

Figure 2. SEM image of a FIB specimen of the lamellar region. This longitudinal section contains 8 silica layers, which are separated by organic interlayers (each 30 nm thick, marked by arrows).

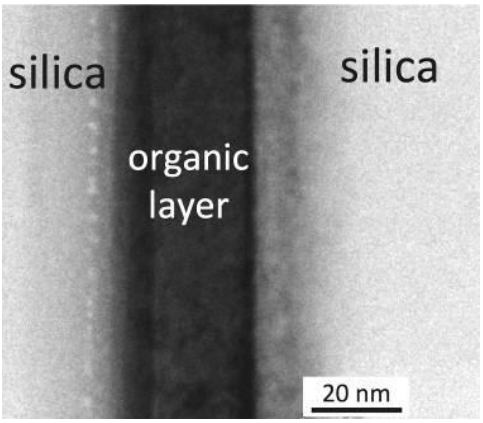

Figure 3. STEM HAADF micrograph of an organic layer at higher magnification (compare Fig.2) showing granular contrast features. Furthermore, the image demonstrates that there is no sharp boundary between the organic layer and the surrounding silica layers, which has an influence on the mechanic properties of the spicule.

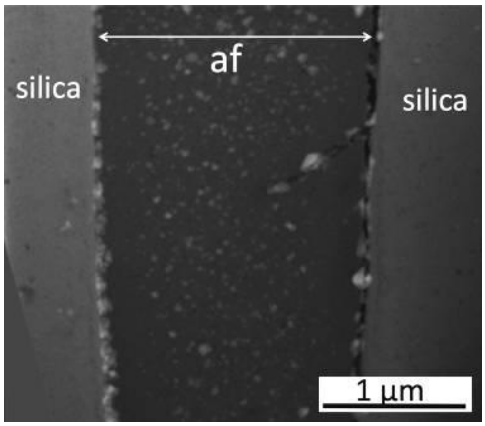

Figure 4. STEM HAADF micrograph of a longitudinal section of the organic axial filament (af), which is embedded in the silica matrix. Mineral precipitates (bright features, mainly NaCl) are embedded in the filament as well as at the interfaces ‘af’/silica.

Molecular Structures and High Resolution TEM

LS.4.P131
Electron microscopic visualization of dipeptidyl peptidase IV influence on the formation of nano-fibrils of amyloid beta peptide

N. Hovnanyan[1], S. Sharoyan[2], A. Antonyan[2], S. Mardanyan[2], K. Hovnanyan[1]

[1]Molecular biology of NAS RA, Electron Microscopy, Yerevan, Armenia
[2]Biochemistry, Yerevan, Armenia

hovnanyan.narek@mail.ru , hovkarl@mail.ru
Keyowords: electron microscopy, amyloid peptide aggregation-disaggregation, dipeptidyl peptidase IV, amyloid beta peptide

The aggregates of amyloid beta peptides (Aβs) are considered as one of the main pathological hallmarks of Alzheimer's disease (AD). Formation of Aβs depends on processing of Amyloid Precursor Protein (APP) by β- and γ-secretases[1-3]. Misprocessing of APP leads to a rise of Aβs including 39-42 amino acids whose amyloid fibril forms constitute a primary component of amyloid plaques found in the brains of AD patients. In the present work, we demonstrated for the first time the principal ability of dipeptidyl peptidase IV (DPPIV) to cleave the commercial Aβ40 and Aβ42 *in vitro*, to influence on their fibril formation property and to participate in the disaggregation of preformed fibrils. In the visualization processes, transmission electron microscope (TEM) was employed, using grid staining (negative staining with UAc, PTA, STA). Measurements of the fibril dimensions were taken on enlarged prints of electron micrographs. In the experiments, Aβ40 and Aβ42 from Sigma, Abbiotec and Bachem were used. We monitored the fibrillation of the peptides both in the absence and in the presence of DPPIV. In Figure 1, A, the transmission electron microscope visualization of fibrils, formed during incubation of 135 μM Aβ40 during 3 days in the phosphate buffer, pH 7.4, is presented. The electron-microscopic measurements were fulfilled on the transmission electronic microscopes of Tesla and Tescan firms, provided with the microanalysis devices. The negative contrast staining of the sample with 2% phosphate-tungsten solution, pH 7.0 was used. To study the influence of DPPIV on the fibrillation process, the same experiment was performed with the addition of 1.3 μM DPPIV. The result of visualization of this sample is presented in Figure 1, B. It demonstrates that the presence of the enzyme in the incubation mixture essentially hindered the fibrillation of the peptide. The possible influence of DPPIV on the preformed fibrils of Aβ40, a sample identical to that, shown in Figure 1, A, was incubated during the next 3 days in the presence of 1.6 μM DPPIV. The result of this incubation (Figure 1, C) manifests that the preformed fibrils are markedly broken down to shorter fibrils with an apparent diameter 8-25 nm as a result of DPPIV including into the assay mixture. The similar results were received with the amyloid peptide Aβ42. In conclusion: the electron microscopic pictures in Figure 1 A, B and C, prove the suggestion regarding the ability of DPPIV to hinder the aggregation of amyloid peptides and to disaggregate the preformed fibrils.

1. Antonyan, A.A., Sharoyan, S.G., Mardanyan, S.S., Galoyan, A.A., Neurochem Res 36, 2011, p.34.
2. Mukherjee, A., Hersh, L.B., J. of Alzheimer's disease 4, 2002, p.341.
3. Sharoyan, S., Antonyan, A., Mardanyan, S., Lupidi, G., Cuccioloni, M., Angeletti, M.,Cristalli G., 2008. Biochemistry (Moscow) 73, 2008,p.1168.
4. Acknowledgments. This work was supported by a research grant awarded in 2012 to S. Sharoyan from he Armenian National Science and Education Fund (ANSEF, # biochem-2811), and by CAEN grant of the International Society for Neurochemistry, awarded to H. Harutyunyan in 2010.

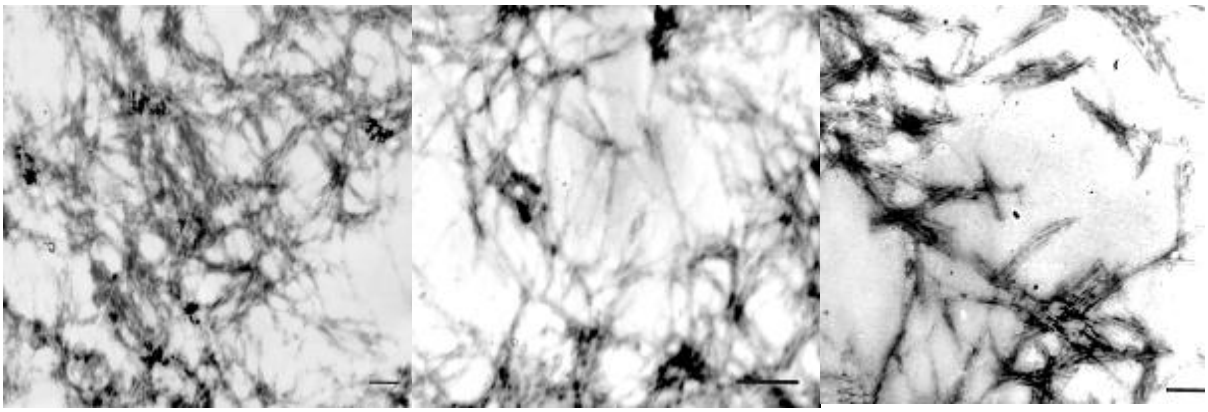

a.) b.) c.)

Figure 1. The transmission electron microscopy visualization of 135 μM Aβ40 (Bachem) fibrils (negative staining) formed during incubation during 3 days of the peptide alone (A); in the presence of 1.3 μM DPPIV (B); the same as in (A), after additional 3 days' incubation with 1.6 μM DPPIV (C). Scale bar: 100 nm

Neurobiology

LS.5.132
Structure-function analysis of inner hair cell ribbon synapses

C. Wichmann[1,2], R. Chakrabarti[1,2], S. Michanski[1], A.B. Wong[1], M.A. Rutherford[1], E.S. Auge[1,2]
E. Reisinger[1,2], F. Göttfert[3], S.W. Hell[3], T. Moser[1,2,4]

[1]University Medical Center Göttingen, Dept. of Otolaryngology/ Inner Ear Lab, Göttingen, Germany
[2]CRC889, Göttingen, Germany
[3]Max-Planck-Institute for Biophysical Chemistry, Department of NanoBiophotonics , Göttingen, Germany
[4]and, CNMPB, Germany

cwichma@gwdg.de

The ribbon-type synapses between presynaptic inner hair cells (IHCs) and postsynaptic spiral ganglion neurons mediate the encoding of auditory signals into a neuronal code, in vertebrates. Acoustic information is transmitted with high temporal precision over long periods of time, requiring high rates of transient and sustained release.

Disruption of the synapse structure can result in deficits in neurotransmitter release that affect hearing function. Presently, we lack an integrated understanding of the molecular machinery regulating vesicle release at the presynaptic active zone (AZ) and transmission through the postsynaptic density (PSD). To approach this question, we study mutations disrupting synaptic proteins such as Otoferlin or RIM, taking advantage of recent advances in electron microscopy technology such as high-pressure freezing and electron tomography (Fig. 1).

We relate structures to functions to address the dynamics of synaptic vesicle pools and their proximity to active zone structures. With high-pressure freezing we compared inhibited versus stimulated, wild type versus mutant IHC ribbon synapses to determine parameters such as the number of membrane-proximal and ribbon-proximal synaptic vesicles and the synaptic vesicle diameter, depending on the activity state.

Moreover, we studied developmental changes upon synapse maturation (Fig. 2), showing that ribbon synapses undergo fundamental changes in structure and function when switching from presensory activity to graded sensory coding. In mature IHCs, one single large AZ apposes one large PSD. In contrast, before hearing onset, each IHC to spiral ganglion neuron synapse showed several pairs of smaller AZ/PSD complexes. Using a combination of electron, confocal, and stimulated emission depletion (STED) microscopy during development of hearing in the mouse, we demonstrate maturation of ribbon shape and anchorage. This was accompanied by a reduction of the number of extrasynaptic Ca^{2+}-channels and an increase in Ca^{2+}-channel colocalization with bassoon protein at AZs with tightly anchored ribbons.

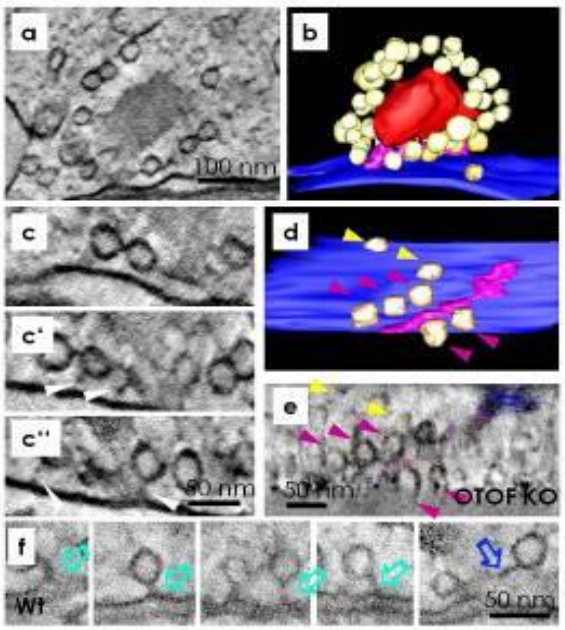

Figure 1: Ultrastructural details of ribbon synapses
(**a**) Electron tomogram (HPF, 250 nm section) of a typical OTOF KO ribbon synapse with the corresponding rendered model (**b**). (**c-c''**) Pool of membrane associated synaptic vesicles, connected via tethers to the membrane (white arrowheads), which are also observed at wild type synapses (**f**, arrows). (**d**) Model of membrane tethered SVs (arrowheads). Five SVs (red arrowheads) are arranged in rows next to the presynaptic density. (**e**) Tomogram according to (**d**), view generated using the slicer tool of the IMOD software package. Blue: active zone membrane; red: ribbon; magenta: presynaptic density; yellow: ribbon associated SVs; orange: membrane associated SVs.

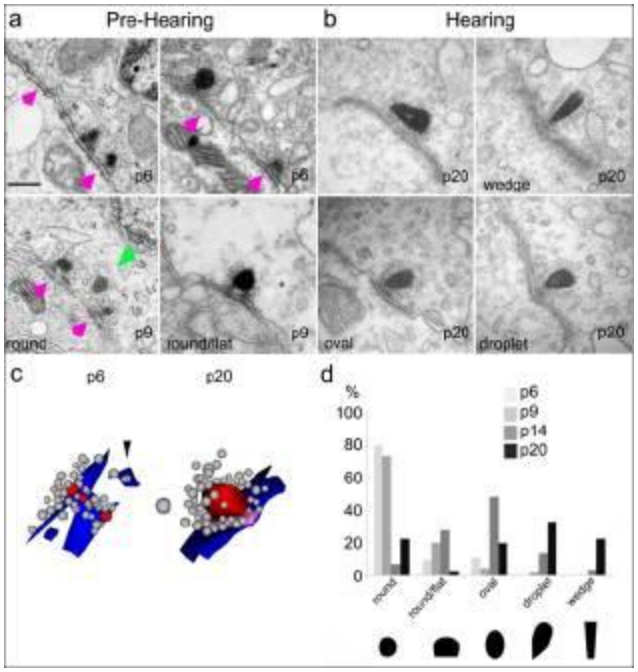

Figure 2: Maturation of inner hair cell ribbon synapses
(**a-b**) Representative electron micrographs of IHC ribbon synapses in pre-hearing (**a**) and hearing (**b**) mice. (**a**) Before the onset of hearing (p6 and p9) multiple appositions of small discontinuous pre- and postsynaptic membrane densities were found (magenta arrowheads), accompanied by one or more round-shaped ribbon(s). In some cases ribbons were "floating" (green arrowhead). (**b**) After the onset of hearing (p20) typically one ribbon occupied the presynaptic cytoplasm at the AZ and the mature pre- and postsynaptic densities were relatively extended and continuous. (**c**) 3D reconstructions from serial sections before (left, p6) and after (right, p20) the onset of hearing. Presynaptic rootlet: density connecting the ribbon the plasma membrane. (**d**) Development of the ribbon-shape. Scale bar in a: 150 nm.

Neurobiology

LS.5.133
Activity of large neuronal populations imaged with high speed 3D random access two photon microscopy

I. Vanzetta

Due to progress in fluorescent marking techniques, to-date, two photon microscopy allows the functional exploration of neuronal activity at multiple scales, from the sub-processes of a single cell (dendrites, single spines…), through single cells or small networks of a few neurons, up to large neuronal populations in the order of a cortical column, in vitro as well as in-vivo. Moreover, recent advances in laser scanning technology using acousto-optical devices has not only increased scanning speed (up to 30 kHz or more), but also warranted to access points randomly distributed within a relatively large volume (order of one cubic millimeter). It becomes therefore possible to investigate in real time the activity of local neuronal networks in three dimensions, at the resolution of the individual neuron. We will report on such measurements, on the challenges encountered when the spike trains have to be reconstructed from fluorescent traces recorded from large neuronal populations and on some approaches to deal with them.

Neurobiology

LS.5.134
Derangement of nerve cell membranes in traumatic human brain edema.

O. Castejón[1]

[1]Biological Research Institute , Electron Microscopy, Maracaibo, Venezuela

ocastejo@cantv.net
Key words:nerve cell membranes, brain edema, electron microscopy

In severe traumatic human brain injuries complicated with subdural hematoma the non-pyramidal neurons, reactive and hypertrophic astrocytes and hydropic oligodendrocytes showed plasma membrane fragmentation, enlargement of rough and smooth endoplasmic reticulum cisterns, extensive areas with detachment of membrane-bound associated ribosomes, and a marked reduction in the number of polysomes The plasma membrane forms endocytic and clathrin coated vesicles internalizing toward the cytoplasm. The nuclear envelope appears irregularly dilated. Areas of focal necrosis of plasma membrane, cytomembranes, outer nuclear membrane, smooth membranes of Golgi endoplasmic sacs, and limiting membrane of lysosomes are observed. At the level of neuropil large extracellular spaces are found with presence of proteinaceous edema fluid (Figures 1 and 2).The degenerated myelinated axons show invaginations of axolemmal membrane and formation of endocytic vesicles. The myelin membranes appear separated forming large intraperiod vacuoles. (Figure.3). [1]

Synaptic vesicle exocytosis at the synaptic active zones, and endocytosis at the non specialized regions of presynaptic ending limiting membrane are frequently observed at sensitized and degenerative synapses. Synaptic disassembly occurs featured by wide separation of pre- and post synaptic membranes and detachment of perisynaptic astrocytic glial ensheathment (Figure 4). [2]

Astrocytic gap junction displayed wide separation, disruption and disassembly. The endothelial cell luminal membrane of brain capillaries exhibits profound activity changes that characterize the increased cerebrovascular permeability, such as increased formation of micro- and macropinocytotic vesicles and clathrin-coated vesicles, deep invaginations and formation of incomplete transendothelial channels, and emission of pseudopods to form endothelial vacuoles.

The role of free radical and lipid peroxidation, disturbed energy metabolism, altered metabolic cascades, glutamate excitotoxicity, hemoglobin toxicity, protein aggregation, and presence of proteinaceous and non-proteinaceous extracellular edema fluid are discussed in relation with the derangement of nerve cells membranes.

1. OJ Castejón. Electron Microscopy of Human Brain Edema. Academic Vicerectory. Astrodata.(2012). Maracaibo. Venezuela, p.13-66.
2. OJ Castejón, C Valero, and M Díaz. Brain Injury 39: 47-65 (1995).
3. OJ Castejón Ultrastruct. Pathol. (USA). 33: 102-111 (2009).
4. Acknowledgments:This paper has been carried out by a subvention obtained from CONDES-LUZ and logistic support from Fundadesarrollo-LUZ.

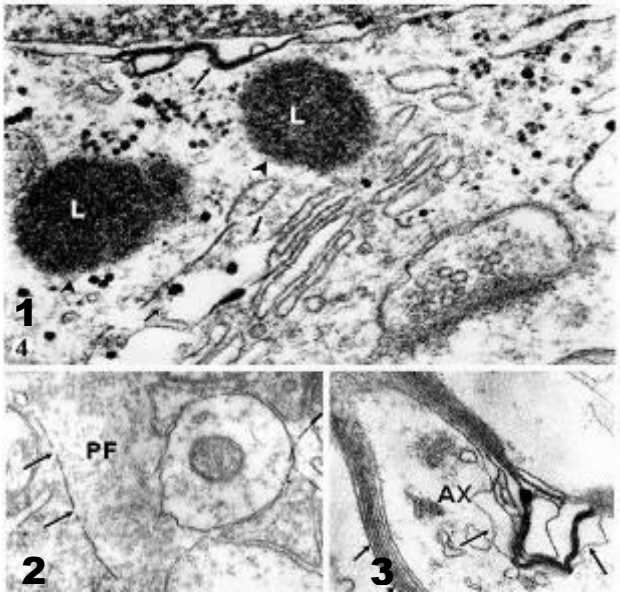

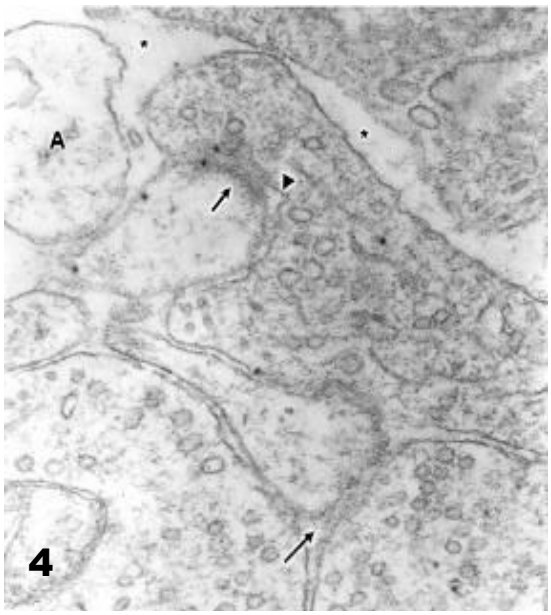

Figure 1. Brain trauma. Subdural hematoma. Right parietal cortex. Non-pyramidal neuron showing focal necrosis of nuclear envelope (long arrow) and of smooth Golgi complex membranes (short arrows). The lysosomes (L) show a discontinuous globular limiting membrane (arrowheads). X 75.000.

Figure 2. Severe frontal contusion. Left frontal cortex. Non-pyramidal neuron showing a high electron dense and fragmented plasma membrane (arrows) in contact with the proteinaceous edema fluid (PF) occupying the enlarged extracellular space. X 60.000.

Figure 3. Brain trauma. Right parieto-tempotal hematoma. Right parietal cortex. Severely edematous neuropil showing a degenerated myelinated axon (AX). The myelin sheath lamellar arrangement appears disrupted and forming intramyelinic vacuoles (long arrows). Note the formation of neighboring axolemmal endocytic vesicles, and the apparently normal and compact arrangement of a segment of myelin sheath at the opposite side (short arrows). X 60.000

Figure 4. Brain trauma. Subdural hematoma. Left parietal cortex. Severely edematous neuropil showing synaptic disassembly and disappearance of pre- and postsynaptic densities (long arrow) of an axospinodendritic contact. The short arrow labels another spine synapse exhibiting partial vestiges of the postsynaptic density, and irregular profile of presynaptic membrane (arrowhead). Note the expansion of extracellular space (asterisks), and the detachment of perisynaptic astrocytic cytoplasm (A). X. 60.000.

Neurobiology

LS.5.135
The effect of kainic acid on hippocampal dendritic spine morphology and motility at the early and late stages of brain development (Electron and multiphoton laser-scanning microscope study)

T. Bikashvili[1], T. Lordkipanidze[1,2]

[1]I.Beritashvili Center of Experimental Biomedicine, Neuroanatomy, Tbilisi, Georgia
[2]Ilia State University, Institute of Chemical Biology, Tbilisi, Georgia

tamarabikashvili@rambler.ru

Dendrites and spines undergo dynamic changes in physiological conditions, such as learning and memory, and in pathological conditions, such as epilepsy [1, 2]. Abnormalities in dendritic spines have commonly been observed in brain specimens from epilepsy patients and animal models of epilepsy [3, 4]. However, the functional implications and clinical consequences of this dendritic pathology for epilepsy are uncertain. Motility of dendritic spines and axonal filopodia has been recently discovered by the advanced imaging techniques, and remains to a large degree an exciting phenomenology in search of function [5]. We demonstrate the effect of kainic acid (KA), which is a structural analog of glutamate, on dendritic spine morphology and motility in hippocampal CA1 area at the different stages of brain development. We used Electron Microscopy and Two-photon Microscopy in our experiments.

In order to reveal the changes that take place in spine and filopodial motility in the epileptic model of brain, time-lapse imaging of acute hippocampal slices treated with various concentrations of KA after different incubation time points was performed. The effects of KA exposure were tested on the slices from young (postnatal day (P7–P10) and adolescent (P28–P30) Thy1-YFPH transgenic mice in which pyramidal hippocampal neurons express green fluorescence (Figure 1). Slices were treated with either 50 µM or 100 µM of KA, for either 30 or 100 min. Three-dimensional reconstruction of spines showed the variability in their morphology: stubby, thin, mushroom and ramified. The results obtained in our experiments show diverse effects of KA in 2 different age groups. According to our results, 100 µM/100 min KA treatment increases spine motility at early stage of brain development (P10) by 41.5%, while in P30 mice spine motility is increased only by 3%. Our findings also indicate that effect of KA on hippocampal dendritic spine motility is predominantly time- rather than concentration-dependent.

Imaging was conducted using multiphoton laser-scanning microscope (Movable Objective Microscope, Sutter) with a Ti-Saphire laser (Chameon Vision II, Coherent) at 920 nm. High-resolution imaging was performed with a long working distance, dipping objective 60X, N.A.1. Images were collected every 30s for a period of 15 min at a digital zoom of 4 (yielding a pixel size of 0.08 × 0.08 µm). At each time point, seven to ten focal planes 0.5 µm apart were collected. Slices were perfused with oxygenated artificial cerebral spinal fluid (ACSF) at 35-37^{0}C, the imaging chamber was kept at 35-370C (Warner Instruments), and the slices were held in place using a platinum and nylon harp (Figure 2, Figure 3).

Spine motility was quantified using “Motility Index” [5]. The motility index measures the overall displacement of a process. We first measure the area of a process at seven time points that differ the most from each other in a single time-lapse movie, then subtract the smallest area from the total projected or accumulated area and divide by the average area.

Data were analyzed using one-way ANOVA test. In the case of significant effect planned comparisons were carried out using student t-test. The level of significance was set as $p<0.05$. All data are presented as a mean +/- standard error of the mean (SEM).

1. Wong, M. Epilepsy Behavior. 2005, 7(4), p.569-577.
2. Bonhoeffer, T., Yuste, R. Neuron. 2002, 35, p.1019–1027.
3. Mizrahi, A., Crowley, J.C., Shtoyerman, E., Katz, L.C. J Neuroscience. 2004, 24(13), p.3147-3151.
4. Trachtenberg, J.T., Chen, B.E., Knott, G.W., Feng, G., Sanes, J.R., Welker, E., Svoboda, K. Nature. 2002, 420, p.788–794.
5. Lippman, J., Dunaevsky, A. J. Neurobiology. 2005, 64(1), p.47-50.

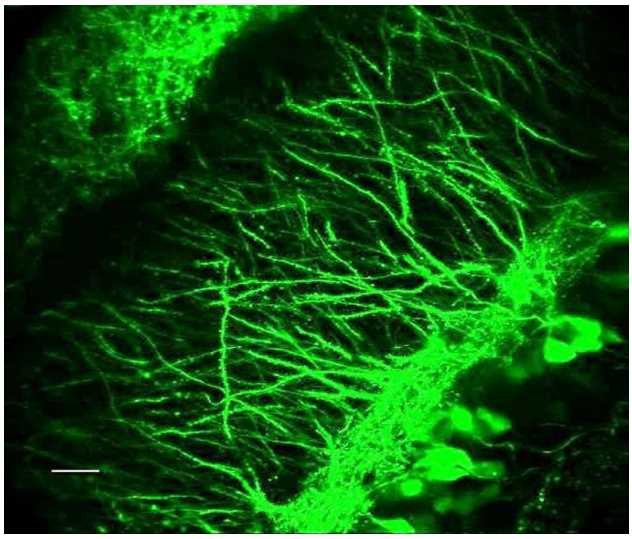

Figure 1. Low magnification (40x objective; zoom 2) image of the dendrites in the hippocampal CA1 area from Thy1-YFPH mouse where all pyramidal neurons express YFP. Scale bar = 22μm.

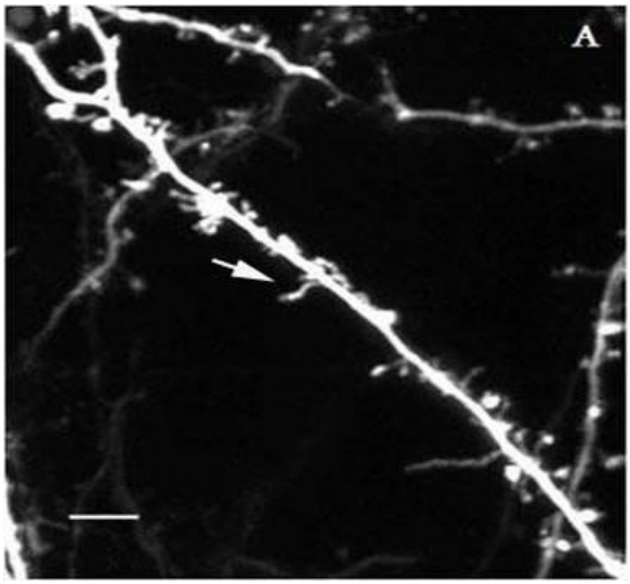

Figure 2. Dendrite with spines from P10 mice. High magnification (60x objective; zoom 4). Time-lapse imaging. Arrow indicates the spine with motility index 2.0. Scale bar = 4 μm.

Figure 3. The most different 7 z- stacks of motile spine.

Neurobiology

LS.5.136
Synaptic architecture and function in *C. elegans*

C. Stigloher[1,2], K. Schuch[1], M. Lang[1], H. Zhan[2], M. Zhen[3], J. Richmond[4], J.-L. Bessereau[2]

[1]University of Würzburg, Electron Microscopy, Würzburg, Germany
[2]Ecole Normale Superieure, IBENS, Paris, France
[3]University of Toronto, Samuel Lunenfeld Research Institute, Toronto, Canada
[4]University of Illinois, Department of Biological Sciences, Chicago, United States

christian.stigloher@uni-wuerzburg.de

Chemical synapses are highly specialized cell-cell contacts containing molecular machineries allowing remarkable signaling precision exemplified by the precise timing and reliability of synaptic transmission. Synaptic fine-architecture is an important organizational basis enabling these properties. Despite the importance of synaptic organization our knowledge of synaptic fine-architecture is still largely enigmatic, due to various technical limitations such as preparation techniques and the necessity of high 3D resolution to resolve structural components.

The combination of high pressure freezing, freeze substitution and electron tomography opens a window to systematically study synaptic fine-architecture in a close-to-native state with high spatial precision. We take advantage of *C. elegans* neuromuscular junctions as highly tractable model synapses to study synaptic architecture and protein function in 3D. Excellent preservation of the tissues is a necessity for high 3D resolution studies. High pressure freezing allows vitrification of intact *C. elegans* adults and therefore provides a snapshot of a living nervous system. By applying these techniques we could resolve and quantify a dense network of filaments interconnecting synaptic vesicles reminiscent of the filament network originally described at mammalian synapses. We are using the advantages of *C. elegans* as model where mutants of many candidate genes are available or can be readily generated. Importantly, many of the synaptic mutants are viable in *C. elegans* and can therefore be easily maintained and manipulated. We are using these advantages to dissect the components and regulators of the filamentous network interconnecting synaptic vesicles and to shed light on the functional role of these architectural

Neurobiology

LS.5.P137
Choroid plexuses of the domestic ruminant brain: vascular corrosion cast, structural and immunocytochemical study

G. Scala[1]

[1]University of Naples FEDERICO II, Veterinary Medicine and Animal Productions, Naples, Italy

gaescala@unina.it

The structural and functional features of choroid plexuses (CPs) in domestic ruminants (buffalo, cattle and sheep) were studied by light microscopy (LM), transmission electron microscopy (TEM) and scanning electron microscopy (SEM). A. LM - CPs (lateral, III and IV ventricles), were immediately removed and cut in small pieces, washed in 0.1 M PBS, immersed in Tissue tech OCT compound, frozen in liquid nitrogen, sectioned by cryostat, and processed for NADPHd histochemistry. To tests NADPHd activity showed that choroid epithelial cells, and blood vessels contain an intense staining.

B. TEM - Heads were perfused through the maxillary artery with 0.1 M cacodilate buffer, pH 7.2, and then fixed with a mixture of this buffer and 2% glutaraldehyde. After 1hr, brains were removed, CPs collected were cut into minute fragments, post-fixed with 2% O_sO_4 for 2hr, dehydrated, and embedded in an EM bed of 812 resin. All embedded specimens were sliced into thin sections, stained with uranyl acetate and lead citrate, and examined under TEM at 40 kV. Transmission electron micrographs of the choroid epithelium show tight junction as well as intercellular spaces of variable extension on the surface of contact between two adjacent epithelial cells. Multiple cellular processes can be seen in cellular spaces. C. SEM – SEM analysis was performed on CP samples obtained by tree distinct procedures: (1) vascular corrosion cast technique, (2) intact tissue technique, and (3) immunogold-labeling SEM analysis. 1 - For the vascular corrosion cast technique, heads were perfused through the maxillary artery with a 0.9% physiological saline solution for cleaning of the vascular system. Next a methylmetacrylate mixture at low viscosity was injected, and after polymerization CPs were soaked by 30% KOH solution for 1-2 weeks. Upon complete corrosion, casts were rinsed with distilled water, dried in a desiccator, mounted on stabs, coated with gold, and examined under SEM LEO 435 VP at 10 kV. CPs microvasculature of domestic ruminants, in general, showed morphological and structural features similar to these reported in other mammalian species.

2 - For the intact tissue technique, heads were perfused trough the maxillary artery with 0.1 M phosphate buffered saline (PBS), pH 7.3, and fixed with Karnovsky's solution. After 12hr, CPs were removed, cut into small fragments, dehydrated in ethyl alcohol, and dried to the critical point. Some fragments, after the treatment with the fixative, were subjected to an ultrasonic treatment in a bath at 35kHz to avoid damage to tissue structures. This treatment latest 5 min for cleaning the apical surface of the choroid epithelium, and 15 min for detach the choroid epithelium from the basal membrane. The same treatment for 30 min allowed for the rupture of the epithelium basal membrane from deeper vessels. The specimens were mounted on stubs, and examined under a LEO 435 VP at 20 kV. The CPs samples subjected to sonication steps show the presence of cells with morphology distinct from their neighboring epithelial cells: extended cellular elements (Fig. 1a), and cells with many protrusions (Fig. 1b).

3 - For the immunogold-labeling SEM analysis CPs were immediately removed from the brain, incubated for 2 hr with a solution containing normal goat serum, diluted 1:10 in PBS and next with primary polyclonal antibodies (NOS I, Ang-2, VEGFR-3 and CD1133) overnight at 4°C. After washing in PBS, all samples were incubated with gold-conjugated goat ant-rabbit IgG, diluted 1:200 in PBS for 1 h at room temperature. After washings in PBS, samples were fixed by 2.5% glutaraldehyde in 0.1 M cacodylate buffer containing $CaCl_2$, pH 7.2, for 30 min. After fixation step and washings with distilled water, samples were subjected to silver enhancement process. Next, samples were dehydrated through an ethanol series, dried to the critical point, mounted in stubs, and examined at variable pressure in the backscattered electron mode. The localization of NOS I, presences of the Ang-2-positivity, VEGFR-3-positivity, and CD133-positivity, confirm that CPs in mammalian brain show a fundamental role for maintenance of the CNS microenvironment.

1. G. Scala, N. Mirabella, G. Paino, G.V. Pelagalli. Anat. Histol. Embryol 23: 93-101 (1994).
2. G. Scala, M. Corona, L.M. Pavone, A. Pelagalli, P. de Girolamo, N. Staiano. Anat. Rec. 290:1399-1412 (2007).
3. L.M. Pavone, S. Tafuri, V. Mastellone, R.D. Della Morte, P. Lombardi, L. Avallone, V. Mahasrajan, N. Staiano, G. Scala. Anat. Rec. 290:1492-1499 (2007).
4. S. Tafuri, L.M. Pavone, V. Mastellone, A. Spina, L. Avallone, A. Vittoria, N. Staiano, G. Scala. Neuropeptides 43:78-80 (2009).
5. G. Scala, M. Corona, E. Langella, L. Maruccio. Microsc. Res. Tech. 74:67-75 (2011).
6. G. Scala, L. Maruccio. Microsc. Res. Tech. 75:1104-1112 (2012).

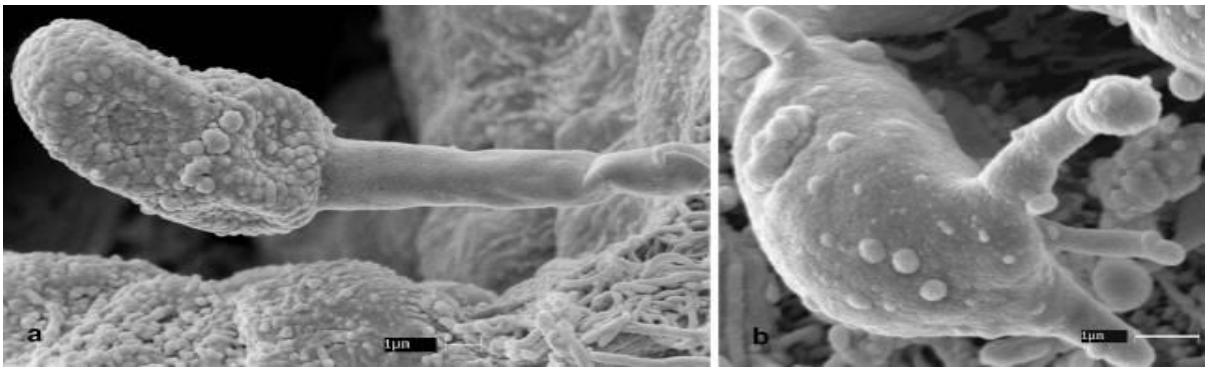

Figure 1. CPs of domestic ruminants. A: View of an extended cellular element of blood capillary. B: A cell with many protrusions.

Neurobiology

LS.5.P138
Microvasculature of the domestic ruminant brain: vascular corrosion casts and immunocytochemical study

G. Scala[1]
[1]University of Naples Federico II, Veterinary Medicine and Animal Productions, Naples, Italy

gaescala@unina.it
Keyword: SEM, microvasculature, immunogold

Blood vessels of the brain in domestic ruminants (buffalo, cattle and sheep) were studied by vascular corrosion cast and immunocytochemical techniques at scanning electron microscopy (SEM).

Microvascular corrosion cast SEM

Nine heads (three of buffalo, three of cattle and three of sheep) were each perfused the maxillary artery with a physiological solution to wash the blood vessels.

Every cerebral hemisphere was supplied by terminal portion of the internal carotis (A. carotis interna), originated in a rete mirabile epidurale rostrale. From internal carotis originate:

A. cerebri rostralis, directs rostro-medially, reached the cerebral longitudinal fissure, and supplies the hemisphere's medial face. By the rostral communicant artery communicates with the contralateral artery in correspondence with optic chiasma.

A. cerebri media, supplies the hemisphere's lateral face by temporal, parietal and frontal branches.

A. communicans caudalis, goes caudally, anastomoses with contralateral artery and A. basilaris, and gave off the A. cerebri caudalis.

From final branches of the cerebral arteries (A. cerebri rostralis, A. cerebri media, and A. cerebri cauallis) originate arterioles that penetrate in perpendicular sense into the cerebral cortex. These arterioles are two types: shorts (capillaries of the gray matter) that supply the cerebral cortex, and longs, that supply the white matter. Capillaries of the gray matter form a thick network with some morpho-structural details (annular and ovoid formations).

Immunogold-Labeling SEM Analysis

For the immunogold-labeling SEM analysis, the brains were cut into small fragments (rostral pole, caudal pole, and dorsal pars). Samples were immersed in PBS for 1hr, incubated for 1hr with a solution containing normal goat serum diluted 1:10 in PBS, and next with a primary polyclonal antibody directed toward CD133, p53 family, and MDM2, diluted 1:1,500 in PBS, overnight at 4°C. After washing in PBS, the samples were incubated with gold-conjugated goat anti-rabbit IgG, diluted 1:200 in PBS for 1hr at room temperature. After washing on PBS, samples were fixed by 2.5% glutaraldehyde, and subjected to silver enhancement. Next samples were dehydrated, mounted on stubs, and examined under a LEO 435 VP at variable pressure in backscattered mode. Samples had not been coated by gold-palladium, so that the only conjugated gold deriving from the immunocytochemical reaction.

Samples show the intense immunoreactivity on the external surface of the blood capillaries, located in the cerebral cortex. No immunoreactivity was observed in the cerebral cortex treated with PBS substituting the primary antibodies (negative control). These results display the presence the angiogenesis phenomena in the cerebral cortex of the domestic ruminant brain.

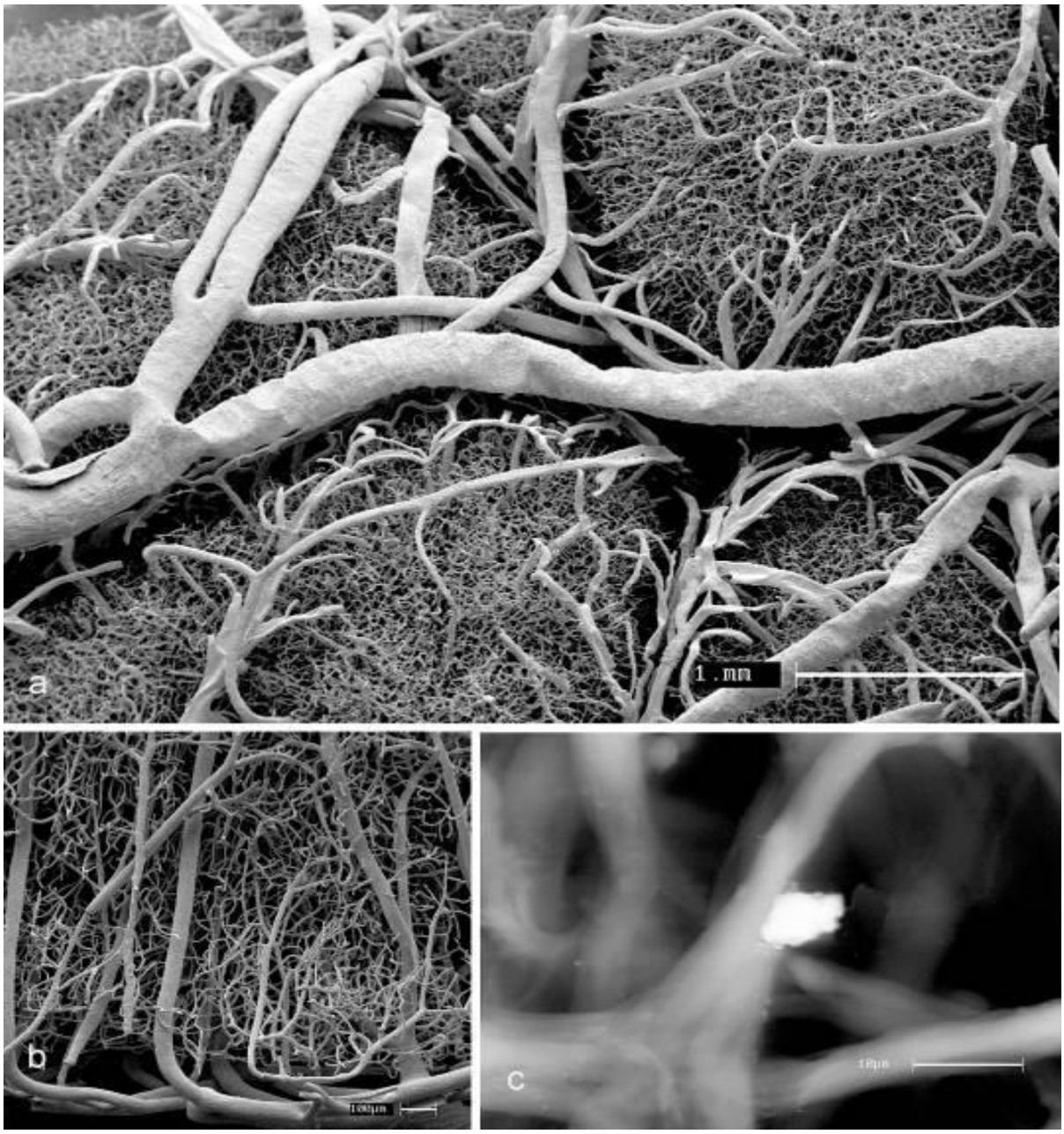

Figure 1

Neurobiology

LS.5.P139
Studying the Wiring and Connectivity of Visual Interneurons in a Locust

G. Leitinger[1], S. Wernitznig[1], A. Zankel[2], F.C. Rind[3], E. Bock[1], E. Pritz[1], P. Pölt[2]

[1]Medical University of Graz, Institute of Cell Biology, Histology and Embryology, Graz, Austria
[2]University of Technology, Institute of Electron Microscopy and Nanoanalysis, Graz, Austria
[3]Newcastle University, Institute of Neuroscience, Newcastle upon Tyne, United Kingdom

Gerd.leitinger@medunigraz.at
Keywords: Serial Block Face SEM, insect, lobula

Knowledge about the wiring and connectivity of neurons is a prerequisite if we aim to understand how these neurons interact with each other. We are studying already identified neurons underneath the eye of locusts that function as a collision sensor [1]. If an object approaches the eye on a collision course, the animals automatically avoid the collision with either steering manoeuvres during flight, or with jumps, or by taking cover. This sensor is robust and simple: only two neurons, the lobula giant movement detectors (LGMD) 1 and 2, are responsible for triggering this response. Whereas the anatomy of the LGMDs, and their response to images of approaching objects have been well described (reviewed in reference [2]), little is known about the wiring and connectivity of so-called afferent neurons, which convey information about changes in light intensity to the LGMDs.

To study the wiring and connectivity of identified neurons, it is necessary to reconstruct their shape and to localise their synaptic connections. Serial block face scanning electron microscopy, a novel technique developed for automated serial sectioning and imaging of soft materials, is being used for this purpose [2,3]. For this aim, tissue samples are embedded in resin, series of micrographs are automatically recorded, and thereafter, the neuronal processes and their synapses are 3D-reconstructed. The micrographs stretch across several hundreds of sections with a section thickness of 70nm.

Results presented in this poster will show how hundreds of afferent neurons are connected with a sample taken from the dendritic arbour of the lobula giant movement detectors (Figure 1). The locations of their synaptic connections will be displayed in 3D, and it will be shown which part of the dendritic arbour appear to be the main input regions.

1. F.C. Rind, D.I. Bramwell, J Neurophysiol. 75 (1996), p. 967.
2. F.C. Rind, P.J. Simmons Trends Neurosci.;22 (1999), p. 215.
3. W. Denk, H. Horstmann, PLoS Biol. 2 (2004). P. e329.
4. A. Zankel et al., J Microsc. 233 (2009). P.140.
5. Grant Sponsor: Das Land Steiermark, HTI:SMApp Programme 2012.
6. We thank Bernhard Robinig and Peter Schönbacher for reconstructing the neurons.

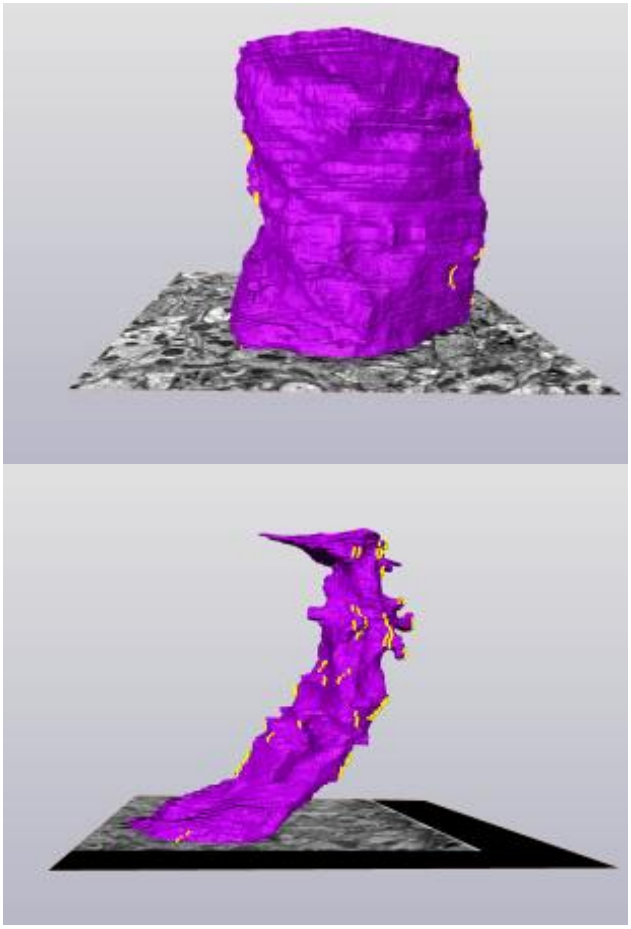

Figure 1. Reconstructions of two 8.4µm long samples of the dendritic tree of the LGMD2 (purple) carried out with Amira® software. Yellow: Locations of synaptic connections of afferent neurons onto the LGMD2.

Neurobiology

LS.5.P140
Optical microscopy of artificially isolated axons on microelectronic measurement platform

J. Mika[1], H. Wanzenboeck[1], P. Scholze[2], E. Bertagnolli[1]

[1]Vienna University of Technology, Institute for Solid State Electronics, Vienna, Austria
[2]Medical University of Vienna, Center of Brain Research, Vienna, Austria

johann.mika@tuwien.ac.at
Keywords: optical microscopy, confocal microscopy, neuronal culture, antibody staining, axon isolation, microfluidic, multi electrode array

To study the cell communication in different animal tissues extracellular recordings are formidable to monitor the dynamics of formation and wiring of populations of neurons. The extensive and complex wiring in cell cultures makes it very difficult to simultaneously observe and analyse neuronal electrical behaviour of multiple cells at the same time. For a comprehensive analysis multi-electrode recordings have proven to be a powerful tool. Yet, optical microscopy plays a crucial role in verifying the position and morphology of nerve cells. Especially the neuronal processes (dendrites, axons) play an essential role for subcellular processes. With a microfluidic setup these neuronal processes could be confined to predefined microchannels which allow for isolated optical investigation of these cell compartments. In this work we present an approach to optically verify the neuronal electrical activity measurements of isolated axons on a self-constructed biochip.

The presented biochip is a versatile platform that allows (i) direct electrical measurement of extracellular potentials originating from isolated axons and (ii) optical inspection of the neuronal network using confocal laser microscopy (Figure 1). The measurement platform consists of a microstructured axon isolating device (AID), which is precisely mounted on top of a microelectrode array (MEA, Figure 2). For this reason specific electrical recordings of neuronal activity of axons can be performed. The AI-device is a transparent PDMS microfluidic device and was fabricated by a soft lithographic process using a SU-8 structured master template with 35 microchannels for axon isolation [1]. The MEA was fabricated by microstructuring techniques and equipped with 60 electrodes [2]. Electrical recordings and analysis were performed using the MEA1060-Inv-BC (Multi Channel Systems).

The proof of isolated axon growth was performed with sympathetic neurons from the superior cervical ganglion of P5 WT mice [3] grown on the AI-MEA platform. 3-days post seeding, neuronal activity (Figure 3) was recorded and analysed with the fabricated platform as shown in Figure 1.

The transparent microelectronic platform enabled optical monitoring of the cells and even of the isolated neurites in the microchannel using confocal laser microscopy. Optical investigations were accomplished by immunocytochemistry. In a first step the cells in the device were fixed using paraformaldehyde. A staining recipe for neurites in microchannels was optimized for simultaneously staining using MAP2 and SMI31 as primary antibodies as well as Alexa 488 and Alexa 568 as secondary antibodies. Optical recordings were performed using a Leica TCS SP5 X (Leica Microsystems GmbH, Wetzlar, Germany) of the cultured cells (Figure 4).

The presented platform will facilitate studies where axons and somata can be treated independently of each other. Optical microscopy is enabled by design and will remain essential to verify the neuronal electrical activity measurements.

1. Anne M. Taylor, Seog Woo Rhee, Christina H. Tu, David H. Cribbs, Carl W. Cotman, and Noo Li Jeon. Microfluidic Multicompartment Device for Neuroscience Research, *Langmuir*, 19, 5 (2003) 1551-1556.
2. C.A. Thomas Jr., P.A. Springer, G.E. Loeb, Y. Berwald-Netter, L.M. Okun. A miniature microelectrode array to monitor the bioelectric activity of cultured cells. *Experimental Cell Research*, 74, 1 (1972) 61-66.F. Author in “Introduction to abstract writing”, ed. D. Writers, (Print-all-books, Regensburg) (year), p. 1.
3. Boehm, S. and Huck, S., α_2-Adrenoreceptor-mediated inhibition of acetylcholine-induced noradrenaline release from rat sympathetic neurons: an action at voltage gated Ca^{2+} channels, *Neuroscience*, 69, 1 (1995) 221-231

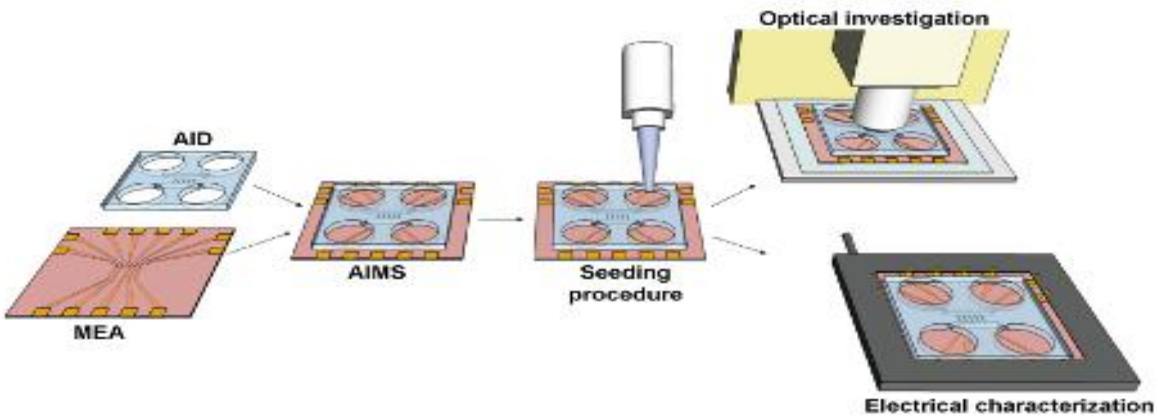

Figure 1. Schematic image of the developed platform with the possible applications.

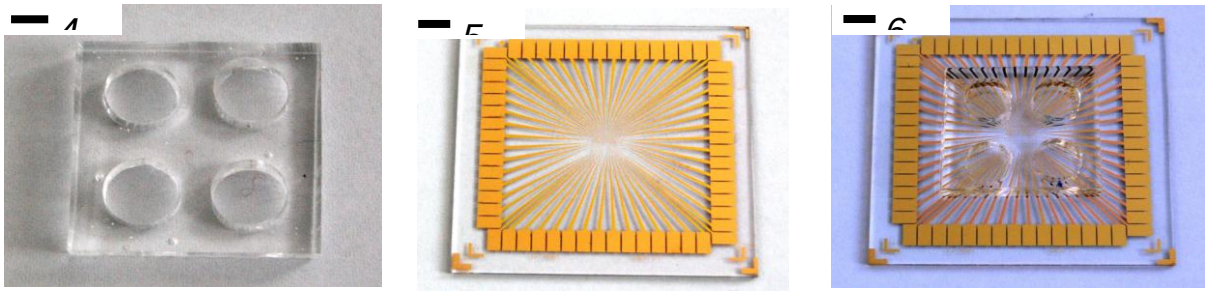

Figure 2. Images of AID, MEA, and AI-MEA.

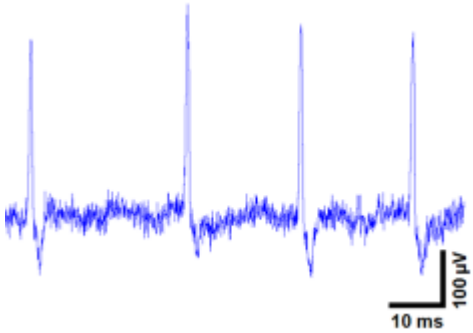

Figure 3. Action potential of a SCG neurite, recorded by an electrode placed in a microchannel

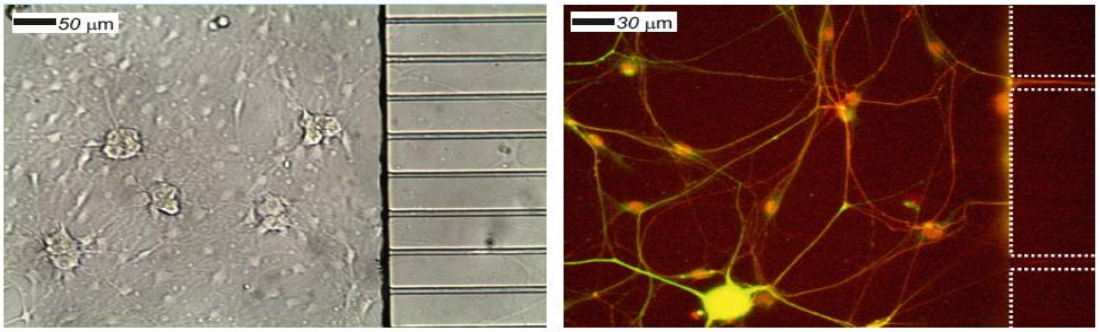

Figure 4. Left: Bright field microscopy of cultured neurons. The cell bodies adhere in the macrochannel of the fabricated platform. Right: Fluorescence microscopy of cultured neurons (SMI31 and MAP2). Only neurites can enter the microchannel.

Neurobiology

LS.5.P141
The effects of 1,25-MARRS silencing on cabindin D28k expression in primary cortical neurons

S. Yilmazer[1], D. Gezen-Ak[1], E. Dursun[1]

[1]Istanbul University Cerrahpasa Faculty of Medicine, Department of Medical Biology, Istanbul, Turkey

drselmayilmazer@gmail.com
Keywords: Vitamin D, 1,25-MARRS, siRNA, neurodegeneration, calbindin D28k

The limited studies have indicated that beta amyloid cytotoxicity can lead depletion of calcium binding proteins such as calbindin in neuronal cells [1, 2]. Vitamin D regulates the expression of calbindin D28k in several cell types [3]. Our previous study has showed that amyloid β (Aβ) treatment eliminated VDR protein in cortical neurons [4]. These results might indicate the potential role of vitamin D and vitamin D mediated mechanisms in neurodegeneration [5]. However there was no data about the regulation of calbindin D28k under the condition of 1,25-MARRS repression. The aim of this study was to investigate the expression levels of calbindin D28k in 1,25-MARRS silenced primary cortical neurons.

Cortical neuron cultures were prepared from Sprague-Dawley rat embryos (Figure 1). 1.25-MARRS was silenced with siRNAs. qRT-PCR was performed for determining the expressions of calbindin D28k. Immunofluorescent labelling was performed for determining the localization of calbindin D28k protein.

Our findings showed that the mRNA levels of calbindin D28k did not change in cortical neurons in response to 1,25-MARRS down-regulation ($p>0.05$). Immunoreactivity for Calbindin D28k was peripherally localized in cytoplasm of cortical neurons (Figure 2).

Our results indicated that the disruption of vitamin D-1,25-MARRS pathway in our model do not exert any effect on calbindin D28k expression.

1. Palop JJ, Mucke L, Roberson ED. Methods Mol Biol. (2011) 670:245-62.
2. Odero GL, Oikawa K, Glazner KA, Schapansky J, Grossman D, Thiessen JD, Motnenko A, Ge N, Martin M, Glazner GW, Albensi BC. Neuroscience. (2010) 11;169(1):532-43.
3. Bouillon R, Carmeliet G, Daci E, Segaert S, Verstuyf A (1998) Vitamin D metabolism and action. *Osteoporos Int* **8**, 13-19.
4. Dursun E, Gezen-Ak D, Yilmazer S. J Alz Dis (2011) 23: 207-219.
5. Gezen-Ak D, Dursun E, Yilmazer S. PLoS ONE (2011) 6(3): e17553.
6. This study supported by TUBITAK (107S041, 111S200) and Istanbul University BAP (548).

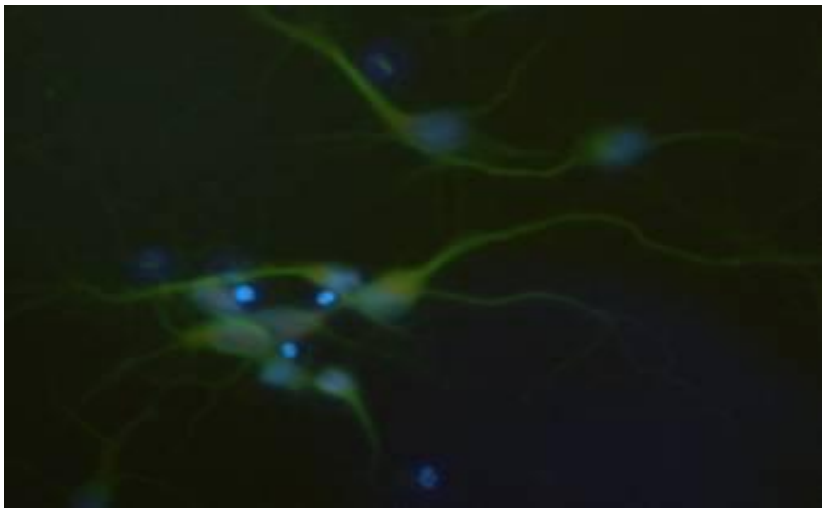

Figure 1. 7 days old primary cortical neuron culture. Neurons (green; FITC tagged Pan Neuronal Marker antibody), nuclei (blue; DAPI), x40.

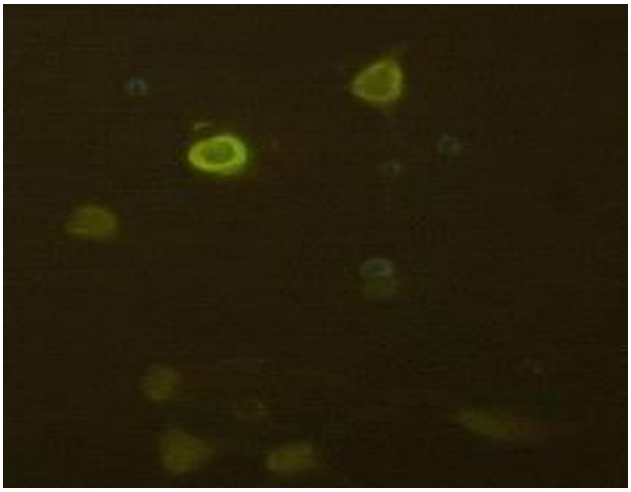

Figure 2. 8 day old primary cortical neurons. Immunoreactivity for Calbindin D28k is peripherally localized. FITC tagged anti-Calbindin D28k antibody. X40

Neurobiology

LS.5.P142
Nucleolar protein Nop2 is expressed in neurons and astrocytes of the mouse central nervous system

N. Vrsaljko[1], M. Kolacevic[1], N. Kosi[1], S. Gajovic[1], D. Mitrecic[1]

[1]Croatian Institute for Brain Research, Zagreb, Croatia
Laboratory for Stem Cells, Croatian Institute for Brain Research, School of Medicine, University of Zagreb, Šalata 12, HR-10000 Zagreb, Croatia

dinko.mitrecic@mef.hr
Keywords: Nucleolar protein Nop2, nucleolus, stem cells, brain

Nucleolar protein Nop2 (Nop2, Nol1, p120) is a gene coding nucleolar- specific protein with RNA-binding function. Until now, its expression has been described in highly proliferative tissues with a rapid cell cycle, including malignant neoplasms [1]. Expression of Nop2 can be used as a marker of tumor malignancy. Following our preliminary observations that Nop2 could be expressed in the brain tissue [2], the main goal of this work was to investigate whether adult mouse brain expresses Nop2, which could suggest existence of a specific cell population with proliferative capacity.

Transgenic mouse expressing Nop2 coupled with beta- galactosidase and control C57Bl6 mouse were used. After isolation, fixation and freezing, 20µm thick frontal and sagittal sections of mouse brain were obtained using criotome. Expression of Nop2 was visualized in Nop2 heterozygous animals by X-gal staining and in wild type animals by immunohistochemistry using antibodies against beta-galactosidase and Nop2. The results were analysed by light and confocal microscopy.

Positive activity of β-galactosidase in X-gal treated sections and a positive signal using antibody against beta- galactosidase confirmed our hypothesis that Nop2 is present in adult mouse brain. Double immunohistochemistry with Nop2 and Map2 (Figure 1) and Nop2 and NeuN antibodies revealed a highly surprising finding that majority of Nop2 positive cells were neurons. Double immunohistochemistry with Nop2 and Gfap revealed that some Nop2 positive cells were astrocytes.

Our finding that adult brain neurons which are terminally differentiated cells express Nop2 is significantly changing a current view of this gene function. Following this finding and a possible role of Nop2 in assembly of ribosomes, we propose an interpretation that apart from highly proliferative cells, Nop2 gene is as well needed in cells with a high synthesis of proteins.

1. A. Bantis, A. Giannopoulos, M. Gonidi, Cytopathology, 15 (2004), p.25.
2. D. Mitrečić, T. Malnar, S. Gajović, Coll Antropol, 32 (2008), p.123.

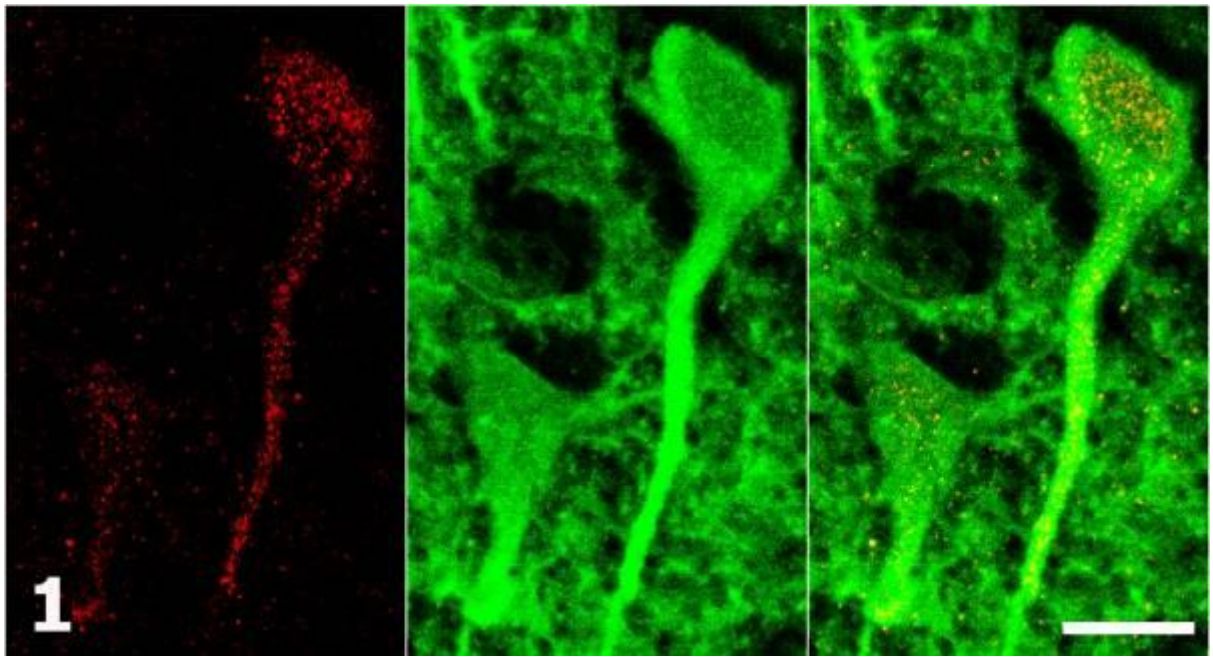

Figure 1. Immunohistochemistry against Nop2 (red) colocalizes with the signal marking neurons (green, Map2).

Neurobiology

LS.5.P143
Array tomography vs. confocal microscopy for studying the nervous system of the smallest insect

A. Polilov[1], E. Vortsepneva[2]

[1]Lomonosov Moscow State University, Department of Entomology, Biologycal faculty, Moscow, Russian Federation
[2]Lomonosov Moscow State University, The White Sea Biological Station, Moscow, Russian Federation

polilov@mail.bio.msu.ru
Keywords: neuron, CNS, *Megaphragma*, array tomography

Confocal microscopy produced a revolution in the study of the structure, physiological processes, development, and many other aspects of research on a wide range of biological objects. Currently it remains one of the most widely used methods of microscopy. But the application of this approach to the study of insects has not resulted in a breakthrough similar to that it produced in studies of many other objects, because the majority of insects have non-transparent chitinous exoskeletons impermeable to large molecules. Of course, studies of particular organs and body parts of insects yield excellent results, but a number of challenges require working with intact specimens, or making preparations that cannot be made (for instance, because of the extremely small size of the object). It is usually impossible to produce sections of insects by freezing or in embedding media, because the insect exoskeleton is too hard for these methods. The array tomography method, developed a few years ago [1, 2] allows applying to insects the whole spectrum of immunofluorescence methods used in Confocal microscopy. Hard embedding medium (LR White) allows readily producing complete series of sections of any thickness. Working with sections solves the problem of the non-transparency of the exoskeleton and permeation of antibodies. This method can be excellently combined with the correlative light and electron microscopy. The algorithm of section digitalization and subsequent computer processing proposed by the authors allows obtaining a complete 3D picture of the object. Array tomography can be successfully used for studying insects, but no studies by this method have been performed to date on this group of objects. To compare confocal microscopy and array tomography, we selected one of the objects most difficult to study: the smallest insects, which have a body length of at most 250 μm. In one of such insects, a member of the genus *Megaphragma* (Hymenoptera: Trichogrammatidae), a unique phenomenon was recently described: almost all cells of the central nervous system in adult insects are anucleate [3], but all basic functions of the central nervous system are retained. This phenomenon, previously unknown in any animals, requires further studies, which would have been impossible without immunolabeling. To estimate the usefulness of confocal microscopy for studying this object, we tried to solve the antibody permeability problem by dividing the body of the insect into separate tagmata and treating them with Triton X-100; to solve the problem with exoskeleton transparency, we used various methods of clearing (including Murray's Clear); and to confront the autofluorescence of the cuticle, we worked in various parts of the light spectrum. Nevertheless, results of the needed quality have not been obtained. On the other hand, array tomography does solve all above mentioned problems, but the principal difficulty of this method is that antibodies label only those antigens that are located on the surface of the section, and in most cases the resulting fluorescence is extremely weak. This problem can largely be solved by pretreatment of sections with Triton X-100 [4] and by heat-introduced antigen retrieval [5], two techniques that strongly enhance the immunolabeling of sections. An important advantage of array tomography is the fact that it allows obtaining complete 3D models of entire organisms with either permeable or impermeable exoskeletons. Another advantage is the resolution, which is considerably higher than in confocal microscopy. The possibility to use sections employed in array tomography in studies using scanning electron microscopes allows simultaneously performing also ultrastructural studies, including immunnogold labeling. As a result, particular cells can be studied even in the smallest known animals.

1. K.D. Micheva and S.J. Smith, Neuron 55 (2007), p. 25-36.
2. K.D. Micheva, N. O'Rourke, B. Busse and S.J Smith, Cold Spring Harb. Protoc. (2010), p. 697-719.
3. A.A. Polilov, Arthropod str. And devel. 41 (2012), p. 29-34.
4. S.S. Ghrbi, G.Rh. Owen and D.M. Brunette, Microscope res. And tech. 70 (2007). P. 555-562.
5. S.-H. Brorson, Micron 30 (1999), p. 319-324.
6. This study was supported by the Russian Foundation for Basic Research (11-04-00496, 13-04-00357), the President of Russia Foundation (МК-375.2012.4) and Alexander von Humboldt Foundation (1128047).

Neurobiology

LS.5.P144
Investigation of Apoptotic Effects of Melatonin in H_2O_2 Induced Glioma Cell Lines

S. Ozdas[1], H. Yapislar[2], D. Akin[2], M. Ersoz[2]

[1]Istanbul Bilim University, Medical Biology and Genetic, Istanbul, Turkey
[2]Istanbul Bilim University, Istanbul, Turkey

sule.ozdas@istanbulbilim.edu.tr
Keywords: Melatonin, apoptosis, immunocytochemistry

Aging, cancer and neurodegenerative diseases are relationship between of free oxygen radicals, which is still one of the research topics. In terms of the etiology of neurodegenerative diseases, genetic and environmental factors as well as the biochemical processes in the body related to aging and the mechanisms put forward to be effective, but could not reach a definitive conclusion. Most emphasis on reasons are oxidative stress and cellular apoptosis. Also, due to the increase of oxygen free radicals are also known as increased apoptosis. Especially, brain tissue is susceptible to oxidative stress [1].

Melatonin (N-acetyl-5-methoxytryptamine) is an endogenous neurohormone derived from tryptophan, that is, mainly released from the pineal gland which is participates in a number of physiological processes like the reproduction regulation and circadian rhythms, at the same time is a well-known potent antioxidant and well tolerant upon its administration [2,3].Moreover melatonin has both neurogenic and neuroprotective effects in mammalian cell lines such as neuroblastoma cells. The mechanisms of action include receptor-coupled processes, direct binding and modulation of calmodulin and protein kinase C, and direct scavenging of free radicals. [4].

We designed this study to investigate the effects of melatonin treatment on oxidative stress induced by H_2O_2 C6 Glioma Cell line using immunocytochemistry methods related to apoptosis and oxidative stress.

This study was performed on C6 glioma cell line at Istanbul Science University's Multidisciplinary Research Laboratory. The cell line was cultured in a medium which contained Dulbecco's Modification of Eagle's Medium (DMEM) and Ham's F12 Medium (3:1). DMEM/Ham's F12 medium was supplemented with 10% fetal bovine serum (FBS), penicillin/streptomycin + L-glutamine (100 U/mL / 100 µg/mL). Cells were incubated in a humidified 5% CO2 atmosphere at 37 °C. After cells were incubated with H_2O_2 for 1 hour, they were treatment with melatonin for 72 hours. Melatonin (Sigma) was taken, and dissolved in ethanol (%95) to form 1 ml of stock solution (10^{-1}M). Thereafter, final concentration ($5x10^{-4}$ M) were obtained by dilution of stock solution with growth medium. At the end of incubation, For immunocytochemical staining, the cells were fixed with methanol. Then cells were incubated for 1 h at room temperature with primary antibodies: a monoclonal Apaf-1, Caspase-3 and CAMK. After the serial washing and secondary antibody labelling procedure, cells were incubated DAB (Dako) for 5min to stain immunolabelling. Detection of the apoptotic cell death in situ using as TUNEL method was used for programme cell death mechanism. It can be detected in cells using a terminal deoxynucleotidyltransferase-biotin nick end-labeling method (TUNEL) performed with a commercial kit (ApopTag® Peroxidase In Situ Apoptosis Detection Kit, Millipore) according to the manufacturer's instructions.

According to our results, there was a significant increase in TUNEL positive cells in H_2O_2-induced group compared with the control and melatonin treated groups (Table-1). Also Apaf-1, caspase-3 and CAMK positive cells in H2O2-induced group compared with the control and melatonin treated groups as expected (Fig-1-2). In Melatonin/H_2O_2 group, we found apoptotic markers decreased compared with H_2O_2-induced group (Fig-3-4). With our findings, melatonin has been shown to prevent apoptosis.

1. Xu C, Wu A, Zhu H, Fang H, Xu L, Ye J, Shen J. Melatonin is involved in the apoptosis and necrosis of pancreatic cancer cell line SW-1990 via modulating on Bcl-2/Bax balance. Biomed Pharmacother. 2013 Mar;67(2):133-9.
2. Rosen RB, Hu DN, Chen M, McCormick SA, Walsh J, Roberts JE. Effects of melatonin and its receptor antagonist on retinal pigment epithelial cells against hydrogen peroxide damage. Mol Vis. 2012;18:1640- Gürpınar T, Ekerbiçer N, Uysal N, Barut T, Tarakçı F, Tuglu MI. The effects of the melatonin treatment on the oxidative stress and apoptosis in diabetic eye and brain. ScientificWorldJournal. 2012;2012:498489.
3. Cary GA, Cuttler AS, Duda KA, Kusema ET, Myers JA, Tilden AR. Melatonin: neuritogenesis and neuroprotective effects in crustacean x-organ cells. Comp Biochem Physiol A Mol Integr Physiol. 2012 Apr;161(4):355-60.F. Author, S. Author and T.H. Author, Journal volume (year), p. 1
4. We kindly acknowledge the help of the organizers of MC 2013 with the online submission procedure.

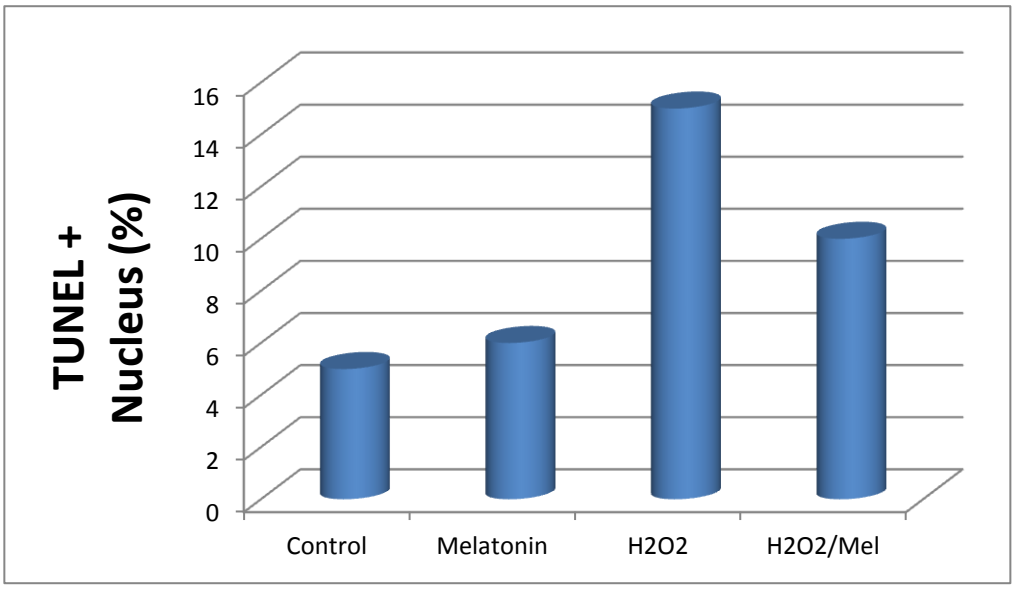

Figure 1. results of the TUNEL + nucleus numbers on all groups. H_2O_2-induced group was shown to be a significant increase in apoptosis compared to control and H_2O_2/Mel group.

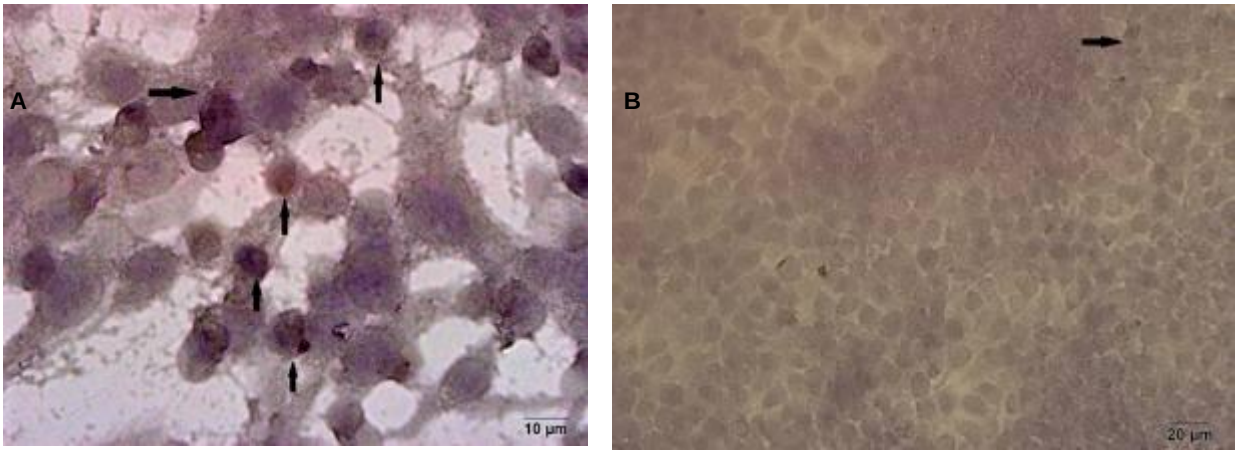

Figure 2. A-H_2O_2 (x100), and B-H_2O_2/Melatonin (x40). TUNEL + cells indicated by an arrow. 500 mM H2O2 H2O2 treated group than the control group in the number of TUNEL + cells led to a significant increase.

Neurobiology

LS.5.P145
Ultrastructural changes of skeletal muscle fibers in Mitochondrial Encephalomyopathies

J. Kostic[1], M. Bajcetic[1], M. Lackovic[1], I. Zaletel[1], V. Lackovic[1]

[1]School of Medicine, Unversity of Belgrade, Serbia, Department of Histology and Embryology, Belgrade, Serbia

koskabg@gmail.com

Mitochondrial encephalomyopathies (ME) comprise heterogeneous group of clinical disorders that occur as a result of structural, biochemical or genetic defects of mitochondria in all tissues, but especially affecting skeletal muscle and nerve tissue, due to the high-energy demands of these tissues, Besides adequate clinical information, diagnosis of ME relies on histology, histochemistry, electron microscopy, biochemistry and molecular genetic analysis. From histological point of view, finding of ragged red fibers (RRF) is considered a pathological hallmark of mitochondrial diseases. RRFs represent abnormal accumulation of altered mitochondria in the subsarcolemmal area of the skeletal muscle fibers.

The aim of our study was to assess the role of electron microscopy examination in the diagnosis of hereditary mitochondrial encephalomyopathies with special reference to the MELAS (Mitochondrial Encephalopathy Lactic Acidosis and Stroke-like episodes). The study included 12 patients with suspected case of MELAS or some other form of ME, based on the clinical signs, endocranial MRI changes and family history. Ultrastructural analysis confirmed the presence of characteristic subsarcolemmal accumulations in 9 patients. Morphological changes also included the variability in size, number and shape of altered mitochondria and the presence of paracrystalline inclusions in the mitochondrial matrix. In addition to changes of muscle fibers we found altered and enlarged mitochondria in endothelial and smooth muscle cells in the wall of endomysial blood vessels.

The ultrastructural examination of skeletal muscle biopsy in patients with ME has an significant role in the diagnosis of cases in which the changes on a light microscopy level are too subtle to safely establish a definite diagnosis.

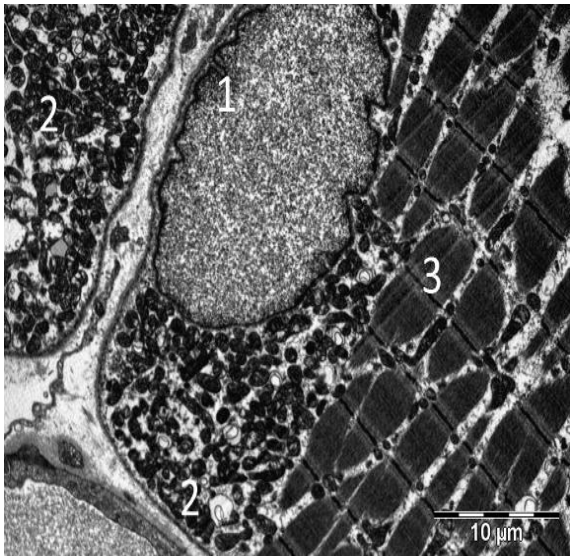

Figure 8. Subsarcolemmal accumulation of mitochondria (TEM). 1. nucleus, 2. numerous mitochondria, 3. Myofibrils

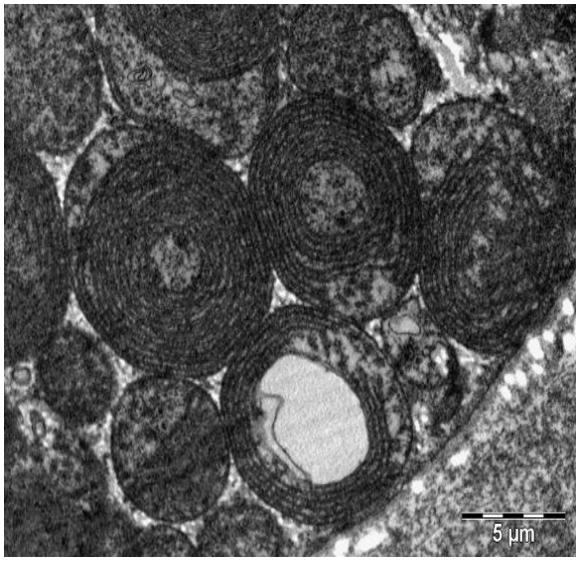

Figure 10. Enlarged mitochondria with concentric cristae.

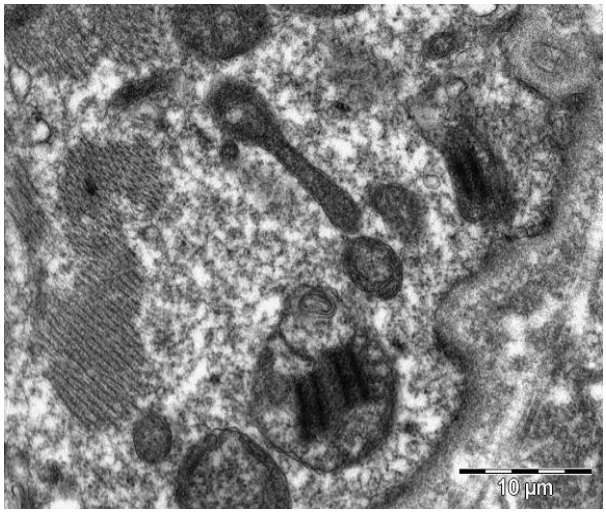

Figure 9. Paracrystalline inclusions in mitochondria

Ultrastructural & Analytical Methods in Life Sciences

LS.6.146
Energy-filtered transmission electron microscopy (EFTEM) and electron energy loss spectroscopy (EELS) in biomedicine

R.D. Leapman[1], M.A. Aronova[1]

[1]Laboratory of Cellular Imaging & Macromolecular Biophysics, NIBIB, National Institutes of Health, Bethesda, MD 20892, USA

leapmanr@mail.nih.gov
Keywords: EFTEM, EELS, biological nanoanalysis, hyperspectral imaging

Electron energy loss spectroscopy (EELS) offers a high sensitivity for detecting biologically important elements at the nanoscale in the transmission electron microscope. In particular, EELS provides quantitative information about elemental distributions within subcellular compartments, as well as the binding of specific atoms to macromolecular assemblies [1]. Spectral data can be acquired either in the fixed beam energy-filtering transmission electron microscope (EFTEM) or in the scanning transmission electron microscope (STEM), and recent progress in the development of both approaches has greatly expanded the range of applications for EELS analysis. Near single atom sensitivity is now achievable for certain elements [2,3], and it has become possible to obtain three-dimensional compositional distributions from sectioned cells using EFTEM tomography [4].

For certain applications, it is necessary to focus nanoampere currents into probe diameters of a few nanometers, and to utilize the high efficiency of STEM-EELS hyperspectral imaging [5,6]. For example, such an approach is needed to detect trace calcium concentrations (millimoles/kg) in freeze-dried cryosections of rapidly frozen cells [7-9]. Typically, the pixel dwell times for such spectrum-images are >100 ms, which limits the total number of pixels to $<10^4$.

When it is required to study compositional variations over cellular regions that are several micrometers across, the EFTEM spectrum-imaging approach can offer advantages relative to STEM-EELS because it is possible to acquire elemental maps that contain ~10^6 pixels in a reasonably short time if concentrations are high enough. For example, this approach can be used to map distributions of nucleic acids based on the phosphorus signal (P $L_{2,3}$ edge at 132 eV) [10,11], and distributions of proteins that are rich in the amino acids cysteine and methionine, based on the sulfur signal (S $L_{2,3}$ edge at 160 eV) [12,13]. However, quantitative analysis of these elements is complicated by the strong overlap of their $L_{2,3}$ edges, so that the background under the sulfur signal cannot be extracted by fitting the pre-edge background according to the standard inverse power law model. We have therefore performed multiple least squares (MLS) fitting of reference spectra to EFTEM spectrum-image data, in order to separate the distributions of phosphorus and sulfur in unstained sections of embedded tissues and cells.

To illustrate the MLS fitting technique, an EFTEM spectrum-image data recorded from a beta cell in a thin section of epon-embedded mouse pancreatic islet [14] is represented in Fig. 1, and the corresponding EELS extracted from regions of dense chromatin and from a secretory granule are shown in Fig. 2. After fitting P $L_{2,3}$, S $L_{2,3}$ and N K edge reference spectra from pure compounds to the spectral data at each pixel in the spectrum-image, the elemental maps in Fig. 3 are obtained. High levels of sulfur are found in the storage granules containing insulin, whose amino acid sequence has 12% cysteine residues. As expected, no phosphorus is observed in the storage granules, but the element is concentrated in the chromatin of the nucleus as well as in ribosomes in the cytoplasm, and nitrogen is seen throughout the cell in both the nucleus and the storage granules. We are also applying this EFTEM spectrum-imaging approach to map distributions of proteins and nucleic acids in cell nuclei to elucidate the role of supramolecular complexes involved in gene regulation.

Finally, we have demonstrated the feasibility of obtaining three-dimensional elemental maps of subcellular phosphorus distributions using quantitative electron spectroscopic tomography, in which tilt series are acquired at energy losses above and below the core edge [4].

In summary, the latest generation of intermediate voltage electron microscopes with beam energies of 200-300 keV, coupled with post-column or in-column imaging filters, enables the complementary approaches of EFTEM and STEM-EELS to be applied to biological systems, thereby enhancing structural information with quantitative compositional information about specific cellular components [15].

1. M.A. Aronova, and R.D. Leapman, *MRS Bulletin* 37 (2012) 53.
2. R.D. Leapman and N.W. Rizzo, *Ultramicroscopy* 78 (1999) 251.
3. R.D. Leapman, *J. Microsc.* 210 (2003) 5.
4. Aronova et al., *J. Struct. Biol.* 160 (2007) 35.
5. C. Jeanguillaume, and C. Colliex, *Ultramicroscopy* 28 (1989) 252.
6. J.A. Hunt, and D.B. Williams, *Ultramicroscopy* 38 (1991) 47.
7. H. Shuman, A.P. Somlyo, *Ultramicroscopy* 21 (1987) 23.
8. R. D. Leapman et al., *Ultramicroscopy* 49 (1987) 225.
9. M.A. Aronova et al., *Ultramicroscopy* 109 (2009) 201.
10. F.P. Ottensmeyer, *J. Ultrastruct. Res.* 88 (1984) 121.
11. Y. Ren, M.J. Kruhlak, and D.P. Bazett-Jones, *J. Hitochem. Cytochem.* 51 (2003) 605.
12. R.D. Leapman, M. Jarnik, A.C. Steven, *J. Struct. Biol.* 120 (1997) 168.
13. G. Goping et al., *Microsc. Res. Tech.* 61 (2003) 448.
14. T. Cai et al., *Diabetologia* 54 (2011) 2347.
15. This research was supported by the intramural program of the National Institute of Biomedical Imaging and Bioengineering, NIH.

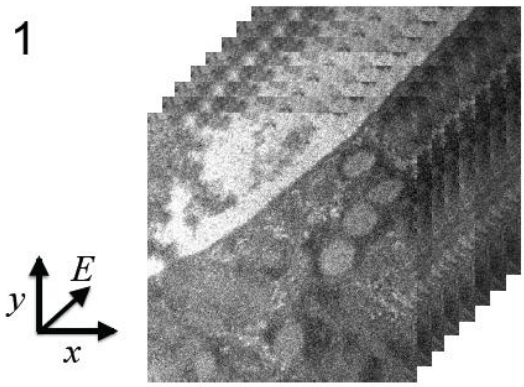

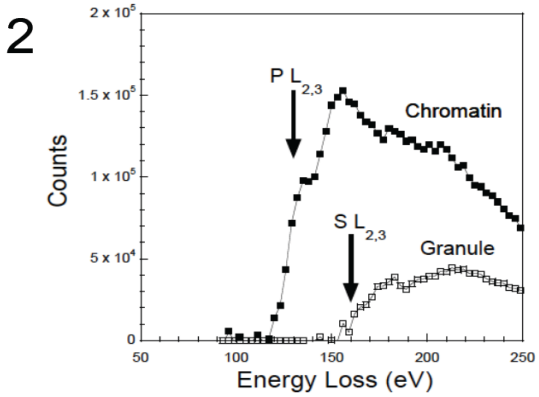

Figure 1. EFTEM spectrum-image containing stack of 83 images, each with 512x512 pixels and 3-eV energy increment, recorded from beta cell in thin unstained section of plastic-embedded mouse pancreatic Islet of Langerhans. Data were acquired with a Gatan Tridiem Imaging Filter coupled to an FEI Tecnai TF30 transmission electron microscope operating at 300 kV accelerating voltage; filter slit was adjusted to 10-eV. Total acquisition time for the spectrum-image was approximately 5 minutes.

Figure 2. Spectra from regions of dense chromatin and a secretory granule: phosphorus $L_{2,3}$ edge signal is mainly localized in the nucleic acid of the chromatin, whereas sulfur $L_{2,3}$ edge signal is mainly localized in the secretory granules. Entire spectrum-image was fitted pixel by pixel to P and S core-edge reference spectra obtained from pure organic compounds, phosvitin and cystine, respectivel

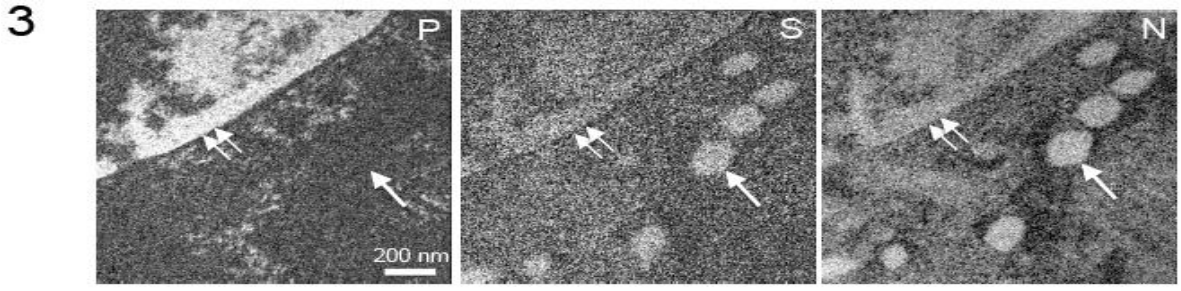

Figure 3. Phosphorus, sulfur, and nitrogen maps derived from spectrum-image by multiple least squares fitting to reference spectra. Phosphorus is evident in the dense chromatin regions (double arrows) and as well as in ribosomes, but not in the secretory granules (single arrows). Sulfur is concentrated in secretory granules that are filled with insulin, a protein rich in cysteine; sulfur is also present at lower levels in the protein component of chromatin.

Ultrastructural & Analytical Methods in Life Sciences

LS.6.147
Ultrastructural cytochemistry is a valuable tool for tracking nanoparticles and monitoring drug delivery in single cells

M. Malatesta[1], M. Costanzo[1,2], B. Cisterna[1], V. Galimberti[3], M. Biggiogera[3], C. Zancanaro[1]

[1]University of Verona, Department of Neurological, Neuropsychological, Morphological and Movement Sciences, Anatomy and Histology Section, Verona, Italy
[2]National Interuniversity Consortium of Materials Science and Technology, Firenze, Italy
[3]University of Pavia, Department of Biology and Biotechnology "Lazzaro Spallanzani", Laboratory of Cell Biology, Pavia, Italy

manuela.malatesta@univr.it
Keywords: cell nucleus, histochemistry, skeletal muscle, sarcopenia, myotonic dystrophy

Sarcopenia is an age-related condition characterized by the progressive loss of mass, strength and function of skeletal muscle, which affects also healthy subjects [1]. The mechanisms involved in the sarcopenic process are probably manifold, such as denervation and reinnervation of the motor units, alteration in the hormonal levels, elevated concentration of inflammatory mediators, decrease in microvascular function, and reduced regeneration capability of muscle tissue.
From a histological point of view, the aging skeletal muscle is characterized by reduction in fibre size and centrally located nuclei. Muscles rich in fast fibres (such as the *quadriceps femoris*, *gastrocnemius* and *biceps brachii*) are more compromised than muscles mainly containing slow fibres since the age-related atrophy specifically affects fast fibres. The number of satellite cells (SCs) was also observed to decrease with increasing age. SCs are undifferentiated mononuclear myogenic cells present in all skeletal muscles: they occur close to the muscle fibres, juxtaposed between the sarcolemma and the basal lamina, and are quiescent in the adult muscle, but can be activated by appropriate stimuli (such as an injury). After activation, SCs proliferate and fuse together to form new myofibres or fuse to existing muscle fibres: this is the basic mechanism responsible for the physiological renewing of muscle fibres and the maintenance of muscle mass and integrity in the adult.
In our studies we initially analyzed the differences from old to adult skeletal muscle focusing on myonuclei and SC nuclei [2,3]. We used animals of a Balb/c mice strain established 40 years ago, which has been widely used for studies on physiological aging because of their long life (mean life span 25 months) and the relatively low incidence of pathologies, in particular tumours. Two animal groups were considered: adult mice of 12 months and old mice of 28 months having only spontaneous free-moving activity in the cage. *Quadriceps femoris* and *biceps brachii* were isolated and used for fluorescence and transmission electron microscopy investigations: we analyzed the muscle fibre composition and measured fibre cross-section area by morphometry, demonstrating size variability and atrophy of fast fibres in old animals; moreover, we analysed some nuclear morphological and morphometrical features as well as the distribution and amount of transcriptional and post-transcriptional factors, showing quantitative modifications of some nuclear and nucleolar parameters and alterations in the amount of nucleoplasmic splicing and cleavage factors in old muscles.
We then investigated the effects of physical exercise in sarcopenic old mice [4,5]. In fact, several studies have stressed the importance of physical exercise as an effective - though still debated - approach to prevent/limit the sarcopenic process. Twenty-eight month-old mice were trained by treadmill running (30min at 9.5 m/min belt speed, 5 days a week) for one month. The same light and electron microscopy analyses described above were performed on *quadriceps femoris*, demonstrating that fast fibre atrophy may be counteracted by physical exercise even at advanced age, since the fibre size and the nuclear parameters of old trained mice approached the adult values. In addition, immunolabelling at light microscopy for Pax7 (a reliable marker of both quiescent and activated SCs) and MyoD (a suitable marker of activated SCs) allowed to demonstrate that the number of both quiescent and activated SCs decreases in the muscles of old mice in comparison to the adults, and that old trained mice revert to the adult values. We also studied the activation and differentiation in vitro of SCs isolated from skeletal muscles: SC-derived myoblasts were allowed to proliferate and differentiate into myotubes, and analysed at transmission electron microscopy. We found that myoblasts and myotubes from old trained mice show morphological features quite similar to adult subjects, whereas cells from sedentary old mice exhibit marked structural alterations.
On the basis of our results we may conclude that: i) in myonuclei and SC nuclei of old muscles alterations of transcriptional and post-transcriptional factors occur, but ii) physical exercise stimulates pre-mRNA transcription, processing and export, thus increasing protein synthesis and SC activation in

old muscles; moreover, iii) physical exercise improves SC capability to differentiate into structurally and functionally correct myotubes, increasing the regenerative potential of old muscles.
Interestingly, in human myotonic dystrophy (DM) the skeletal muscle shows structural and functional features reminiscent of sarcopenia, such as fibre atrophy, centrally located myonuclei and defective SCs. DMs are autosomal dominant disorders and two forms are presently known [6,7]: the more severe DM1-Steinert's disease (OMIM 160900) is caused by an expanded (CTG)n nucleotide sequence in the 3' untranslated region of the Dystrophia Myotonic Protein Kinase (DMPK) gene (OMIM 605377) on chromosome 19q13; the second form, DM2 (OMIM 602688) displays a milder clinical phenotype and is caused by the expansion of the tetranucleotidic repeat (CCTG)n in the first intron of the Zinc Finger Protein (ZNF)-9 gene (OMIM 116955) on chromosome 3q21. The basic mechanisms of both DMs reside in the nuclear sequestration of the expanded RNAs: CUG- and CCUG-containing transcripts accumulate in intranuclear foci in DM1 and DM2 cells respectively, and sequester the RNA-binding proteins CUGBP1 and MBLN [7]; in addition, we showed that snRNPs and hnRNPs splicing factors (which are essential for the physiological processing of pre-mRNA) are also sequestered into the foci [8]. This general impairment of mRNA pathways could explain the multisystemic pathological features typical of both DMs.
Our studies on DM muscles demonstrated that myonuclei from bioptic samples of *biceps brachii* undergo morphological alterations similar to those found in aged muscles and that an altered distribution of nuclear RNP-containing structures and molecular factors responsible for pre-mRNA transcription and maturation occurs [9,10]. Moreover, we investigated *in vitro* the structural and functional features of SC-derived myoblasts and we observed that DM myoblasts show cell-senescence alterations such as cytoplasmic vacuolisation, reduction of the proteosynthetic apparatus, accumulation of heterochromatin and impairment of the pre-mRNA maturation pathways earlier than myoblasts from healthy patients [11]. In addition, DM myoblasts generate myotubes characterised by structural defects similar to senescent healthy myotubes. The early occurrence of senescence-related features in SC-derived myoblasts would therefore reduce the regeneration capability of DM SCs, thus contributing to the muscular dystrophy in DM patients.
In conclusion, morphological and histochemical evidence shows that skeletal muscles undergo similar alterations under sarcopenic and dystrophic conditions, especially for the nuclear pre-mRNA pathways, suggesting a common involvement of the RNP nuclear components in the onset of muscle cell dysfunctions [12,13]. In this view, the positive effects of physical exercise observed on skeletal muscles of subjects affected by severe sarcopenic atrophy open interesting perspectives for studies aimed at its application to subjects affected by DM.

1. L. D. Thompson, Exp Gerontol. 44 (2009), p. 106.
2. M. Malatesta, F. Perdoni, S. Muller, C. Zancanaro and C. Pellicciari, Eur. J. Histochem. 53 (2009), p. 97.
3. M. Malatesta, F. Perdoni, S. Muller, C. Pellicciari and C. Zancanaro, J. Biomed. Biotechnol. 2010 (2010), p. 410405.
4. C. Zancanaro, R. Mariotti, F. Perdoni, E. Nicolato and M. Malatesta, Eur. J. Histochem. 51 (2007), p. 305.
5. M. Malatesta, P. Fattoretti, M. Giagnacovo, C. Pellicciari and C. Zancanaro, Rejuvenation Res. 14 (2011), p. 543.
6. M. Mahadevan, C. Tsilfidis, L. Sabourin, G. Shutler, C. Amemiya, G. Jansen, C. Neville, M. Narang, J. Barceló, K. O'Hoy, S. Leblond, J. Earle-MacDonald, P.J. de Jong, B. Wieringa, and R.G. Korneluk, Science 255 (1992), p. 1253.
7. C.L. Liquori, K. Ricker, M.L. Moseley, J.F. Jacobsen, W. Kress, S.L. Naylor, J.W. Day and L.P. Ranum, Science 293 (2001), p. 864.
8. F. Perdoni, M. Malatesta, R. Cardani, M. Giagnacovo, E. Mancinelli, G. Meola and C. Pellicciari, Eur. J. Histochem. 53 (2009), p. 151.
9. M. Malatesta, M. Giagnacovo, R. Cardani, G. Meola and C. Pellicciari, Histochem. Cell Biol. 135 (2011), p. 419.
10. M. Malatesta, M. Giagnacovo, M. Costanzo, B. Cisterna, R. Cardani and G.Meola, Eur. J. Histochem. 57 (2013), in press.
11. M. Malatesta, M. Giagnacovo, L.V. Renna, R. Cardani, G. Meola and C. Pellicciari, Eur. J. Histochem. 55 (2011), p. e26.
12. M. Malatesta and G. Meola, Eur. J. Histochem. 54 (2010), p. e44.
13. M. Malatesta, Eur. J. Histochem. 56 (2012), p. e36.

Ultrastructural & Analytical Methods in Life Sciences

LS.6.148
"Kinetic Studies" in Streptococcal Pathogenesis Applying Field Emission Scanning Electron Microscopy (FESEM)

M. Rohde[1], K. Branitzki-Heinemann[1], S. Talay[1]

[1]HZI, Medical Microbiology, Braunschweig, Germany

mro@helmholtz-hzi.de

Electron microscopy has long been thought of as providing only a static picture. With time this kind of slight misconception has been changing gradually towards an approach which includes also some kinetic, dynamic data of processes following a triggered process. High resolution field emission electron microscopy (FESEM) is an important tool to study adherence and invasion mechanisms of pathogenic bacteria. As one deals with fixed samples a live-imaging is impossible. Nevertheless, with a consecutive FESEM imaging of a series of experiments one can gain insights into "kinetic mechanisms" of pathogenic bacteria. Here, "kinetic events" of adherence and invasion of GAS via integrin-clustering, intracellular trafficking and the exocytosis of certain serotypes of GAS will be discussed.

Group A Streptococci utilize the surface protein SfbI as a major fibronectin binding protein. Binding of fibronectin to the bacteria results in binding to $\alpha_5ß_1$-integrins. It is known that integrins must cluster to trigger a signaling event. Binding of SfbI to gold-nanoparticles by van der Waals forces, which do not impair the biological function, allowed for the first time to visualize the kinetic of integrin-clustering on a cell surface of endothelial cells (HUVEC). Clustering of integrins subsequentely leads to a caveolae dependent invasion resulting in prevention of lysosomal fusion which was demonstrated by feeding host cells with BSA-coated gold-nanoparticle 12 h before infection. Streptococci have to pass the blood endothelial cell layer to gain access to deeper tissue. With BSA-coated gold-nanoparticle it was demonstrated that certain GAS hijack the exocytosis mechanism of host endothelial cells to pass over the blood endothelium to gain access to the underlying basal membrane and collagen.

Conclusion: High resolution field emission scanning electron microscopy together with gold-nanoparticle coated pathogenicity factors have been proven to be a potent tool to study even "kinetic mechanisms" of pathogenic bacteria.

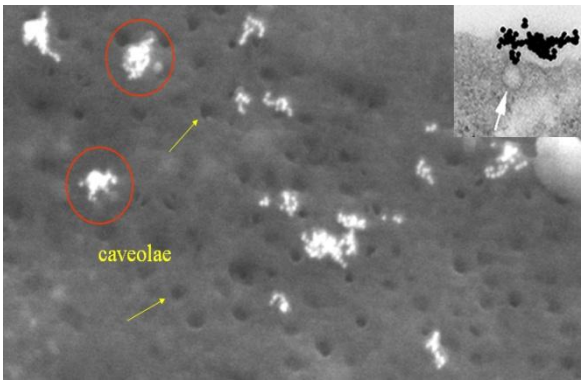

Figure 1.

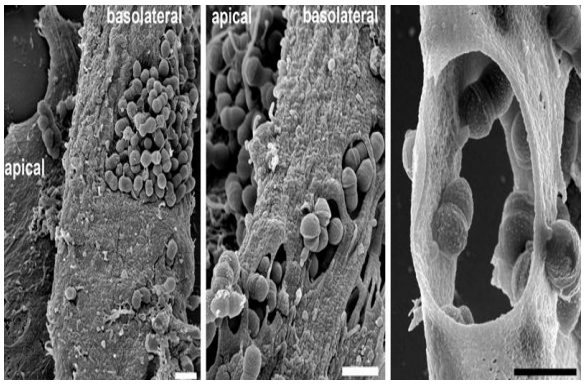

Figure 2.

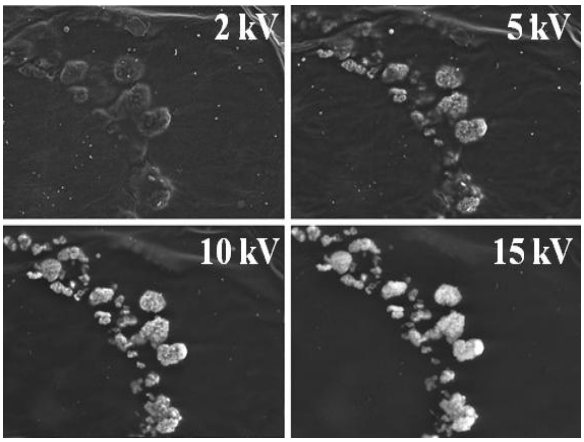

Figure 3.

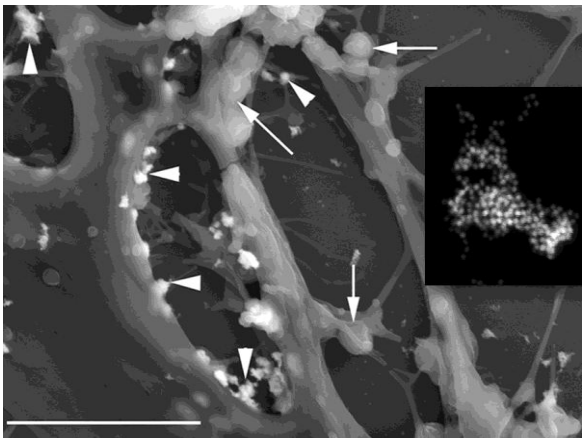

Figure 4.

Ultrastructural & Analytical Methods in Life Sciences

LS.6.149
3D structural analysis of renin-producing kidney cells

D. Steppan[1], A. Zuegner[1], R. Rachel[2], G. Wanner[3], A. Kurtz[1]

[1]University of Regensburg, Inst Physiology, Regensburg, Germany
[2]Universität Regensburg, Centre for EM, Regensburg, Germany
[3]Universität München, Biocentre, Planegg, Germany

reinhard.rachel@biologie.uni-regensburg.de
Keywords: renin-producing cells, renin-angiotensin system, afferent arteriole

The protease renin is the key enzyme regulating the activity of the renin–angiotensin–aldosterone system [1]. It is mainly produced and secreted in the kidney by specialized juxtaglomerular cells, which are located in the terminal parts of afferent arterioles. After synthesis and glycosylation, prorenin is transferred and stored into storage vesicles [2], and then further proteolytically processed to renin. The release of renin is controlled by two oppositely acting signaling pathways. The cyclic adenosine monophosphate (cAMP) signaling pathway stimulates renin release, whereas a Ca^{2+}-related signaling pathway inhibits the release of renin. The mode of renin release from the cells into the circulating blood is still unsolved in several aspects: morphological signs of exocytosis, such as omega-shaped figures, have very rarely been reported in renin-producing cells [3].

For a better understanding of the renin release process, we studied the morphology of renin-storage vesicles inside the renin-producing cells, and the changes during controlled modulation of renin release [4]. For this goal, we combined the model of the isolated perfused mouse kidney, which allows us to modulate renin release under nearly physiological conditions, with an analysis of the 3D ultrastructure of those cells, using serial section electron microscopy.

The mouse kidney was chemically fixed by perfusion with PBS buffer containing 2% glutardialdehyde (GA) at constant pressure (90 mm Hg). Kidneys were cut in half, stored at 4°C overnight in PBS/2% GA, trimmed to 1 mm^3 cubes and further processed in a microwave processor (Leica AMW), including fixation and staining with 1% OsO_4, dehydration, and embedding in resin. The dehydration / embedding protocol lasted about 3 hrs 30 min, and the resin hardening about 2 hrs 10 min. For some kidney samples, OsO_4 was omitted completely; for other samples, perfusion fixation was followed by high-pressure freezing, freeze-substitution fixation in acetone / 2% GA / 0.5% UAc / 5% water and embedding in Epon. Micrographs of up to 110 sections were recorded digitally in form of montages, using a 1k CCD camera (TVIPS, Gauting, Germany) on a CM12 TEM (FEI Co., Eindhoven, NL). Image stacks, generated using ImageJ, were segmented and visualized using AMIRA. Surfaces were computed from the material data, resulting in a 3D model of the juxtaglomerular cell. In most experiments, two cells were reconstructed per kidney.

Ultrathin sections of selected samples were tested for intracellular distribution of renin by post-embedding on-section immuno-labeling using an antibody specifically raised in chicken against mouse renin, and a secondary goat anti-chicken antibody coupled with ultrasmall Gold (Aurion). The quality of the kidney sample was good enough to specifically detect the renin in the storage vesicles [Fig 1], even after post-fixation with OsO_4, although with weaker detection efficiency.

Our 3D structural analysis revealed that renin is not stored in simple round vesicles; the vesicles containing renin have variable shapes, and they form a network of single granules and huge interconnected cavern-like structures (Fig 2). The vesicles cover about 36% of the extranuclear space in the renin-producing cells. Acute stimulation of renin release led to increased exocytosis in combination with intracellular fusion of vesicles to larger caverns and their subsequent emptying [4]. The results obtained so far suggest that renin is released by mechanisms similar to compound exocytosis. We intend to continue our studies by improving the 3D resolution using FIB-SEM analysis [5], and in addition to analyse selected semithin sections by TEM tomography, aiming eventually for a detailed visualization of rare exocytosis events.

1. E Hackenthal, M Paul, D Ganten et al, Physiol Rev 70 (1990) 1067-1116.
2. BJ Morris, J Hypertens 10 (1992) 209-214.
3. R Taugner, CP Buhrle, R Nobiling, Cell Tissue Res 237 (1984) 149-472.
4. D. Steppan, A. Zügner, R. Rachel, and A. Kurtz, Kidney Interntl 83 (2013), p. 233-241.
5. C. Villinger et al., Histochem Cell Biol 138 (2012) 549-556.
6. This study was supported by the DFG, SFB 699.

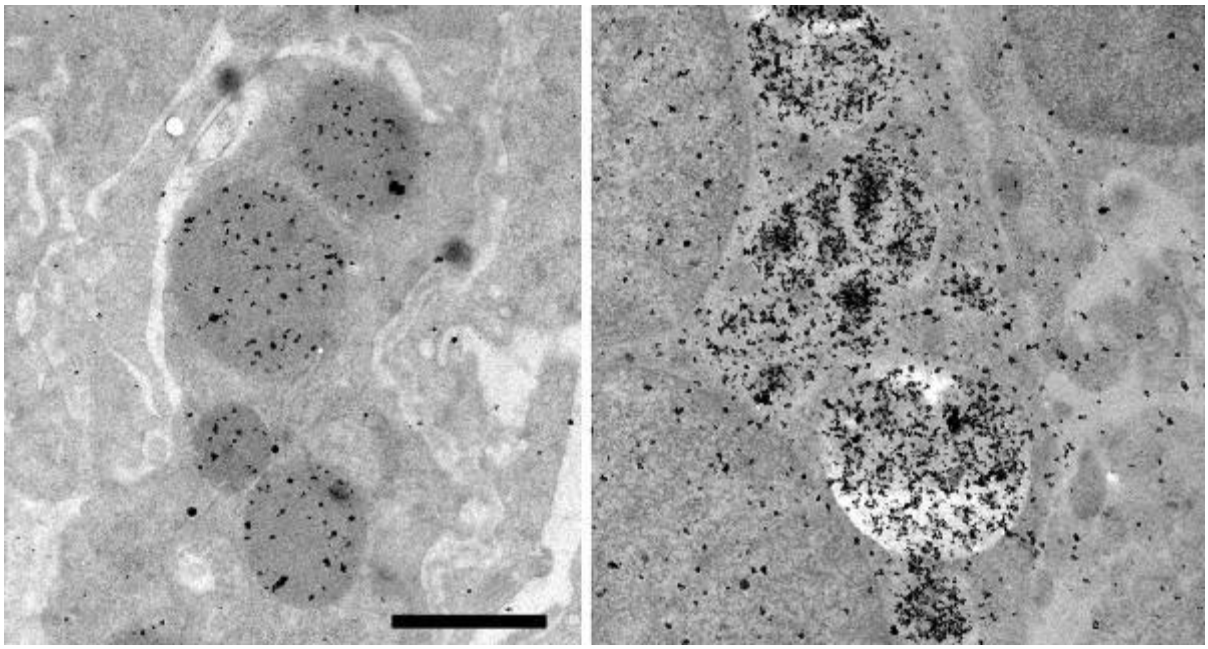

Figure 1. Subcellular distribution of renin in juxtaglomerular renin-producing cells, studied by postembedding immuno-labeling. Kidneys were fixed by perfusion with PBS / 2% GA. Left, postfixation with 1% OsO_4 and AMW embedding in Epon; right, HPF, FSF with GA and UAc, but without OsO_4, and embedding in Epon. Postembedding immuno-labeling with primary and secondary antibodies using standard protocols. Bar, 1 µm for both images.

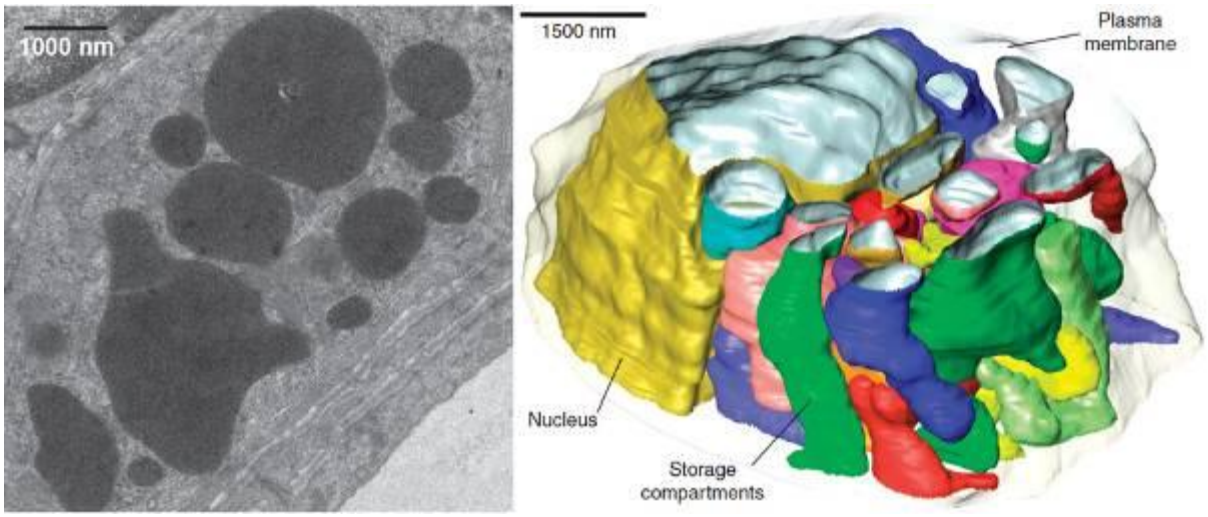

Figure 2. Analysis of juxtaglomerular renin-producing cells by serial-section TEM. Left, single TEM section, original TEM micrograph. Right, 3D reconstruction of the cell with individual renin storage compartments (or vesicles) in different colors.

Ultrastructural & Analytical Methods in Life Sciences

LS.6.150
Branching of cytoplasmic intermediate filaments can be demonstrated using STEM tomography of high-pressure frozen keratinocytes

S. Nafeey[1], E. Felder[2], C. Schmid[1], M. Sailer[1], P. Walther[1]

[1]University Ulm, Central Facility for Electron Microscopy, Ulm, Germany
[2]University, Institute for General Physiology, Ulm, Germany

soufi.nafeey@uni-ulm.de
Keywords: STEM tomography, intermediate filament networks, 3D, high pressure freezing

Intermediate filaments (IFs) constitute together with microtubules (MTs) and microfilaments (MFs) the three main structural elements of the cytoskeleton in metazoans. The large protein family of the IFs is encoded by approximately 65 genes in the human genome [1]. The fibrous proteins are located in the cytoplasm and the nucleus. In contrast to MTs and MFs which break easily by shear stress, IFs are very flexible rodlike structures buffering the mechanical stress in the cells.

It is still not clear how the single intermediate filaments are assembled to one another. The aim of the project is to investigate, whether the filaments are branched.

In previous projects we were able to show branches using SEM tomography of triton extracted cells [2, 3] (Figure 1 and 2). It is, however, not clear, whether the natural state of the filament network is changed due to the harsh extraction procedure. For this reason we investigated the filament network using high pressure freezing, freeze substitution and STEM tomography, a protocol generally accepted to induce fewer artifacts [4]. STEM tomography was further optimized by using a parallel beam alignment [5] and the bright field signal that provides sharper images in the depth of the sample [6].

Here, keratinocytes were seeded on carbon coated and glow discharged sapphire discs (3 mm in diameter, 160 µm thick) for 48 hours (37°C, 5% CO2). The cells were then high pressure frozen (Wohlwend Compact 01) and freeze substituted [4]. Afterwards, 475 nm thick sections were cut by an ultramicrotome (Leica Ultracut) and images were acquired using a Titan (FEI, 300 kV) using the STEM mode. The specimens were tilted from -72° to +72° with 2° increment. The reconstruction of the single images into a 3D construct was performed using the IMOD software.

Figure 3 represents a virtual (computed) 10 nm thick section of a STEM tomogram of a 475 nm thick microtome section (measured in the electron microscope). The green arrows depict the leaflets of the membrane bilayer, the yellow arrow points to a microtubule. The red arrows point to branches of intermediate filaments. We assume that these are real branches, since the thickness of the virtual section is in the range of the thickness of an intermediate filament and there is not enough space in the virtual section for two intermediate filaments to cross without touching each other.

This data demonstrate that branches in intermediate filaments can not only be observed in triton extracted samples (Figures 1 and 2), but also in high pressure frozen and freeze substituted cells, as shown in Figure 3. Since this method is considered to be the gold standard for preventing artifacts, we conclude that the branches are real structures and not preparation artifacts.

1. H. Herrmann and U. Aebi , Annu. Rev. Biochem. 73 (2004), 749–89
2. M. Sailer, K. Höhn, S. Lück, V. Schmidt, M. Beil and P. Walther, Microsc. Microanal. 16 (2010), 462-471
3. Ch. Schmid, M. Beil and P. Walther, Proceedings of the Microscopy Conference (2011), Kiel, Volume 2, Life Sciences, ISBN 978-3-00-033910-3, p426
4. K. Höhn, M. Sailer, L. Wang, L. Lorenz, EM. Schneider and P. Walther, Histochem Cell Biol. 135 (2011), 1-9
5. J. Biskupek, J. Leschner, P. Walther and U. Kaiser, Micron 110 (2010), 1231-1237
6. M. Hohmann-Marriott, A. Sousa, A. Azari, S. Glushakova, G. Zhang, J. Zimmerberg and R. Leapman, Nature Methods 6 (2009), 729-732

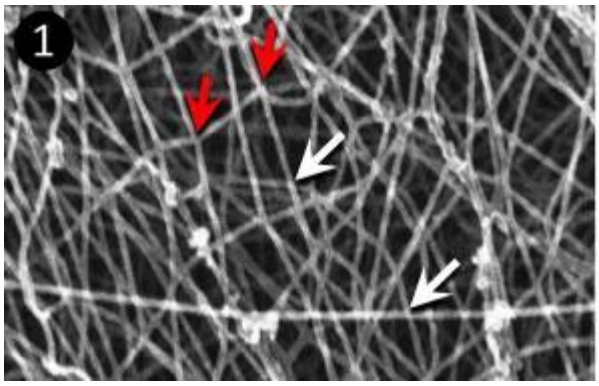

Figure 1. shows one image out of an SEM tilt series of intermediate filaments in a cell prepared by triton extraction. From one image it cannot be decided whether the filaments are branching or just crossing each other.

.

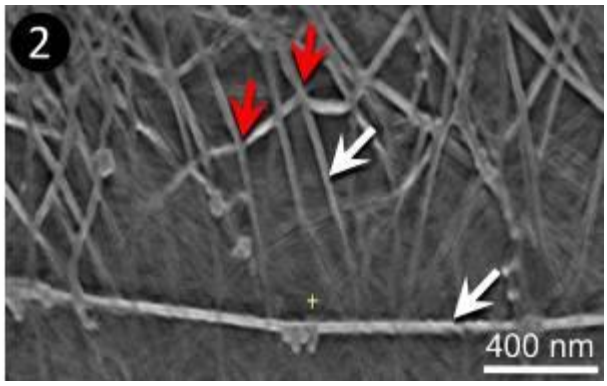

Figure 2. however, is a computed section of the reconstructed tomogram of the SEM tilt series. The red arrows depict real branches, whereas the white arrows depict filaments crossing without touching each other

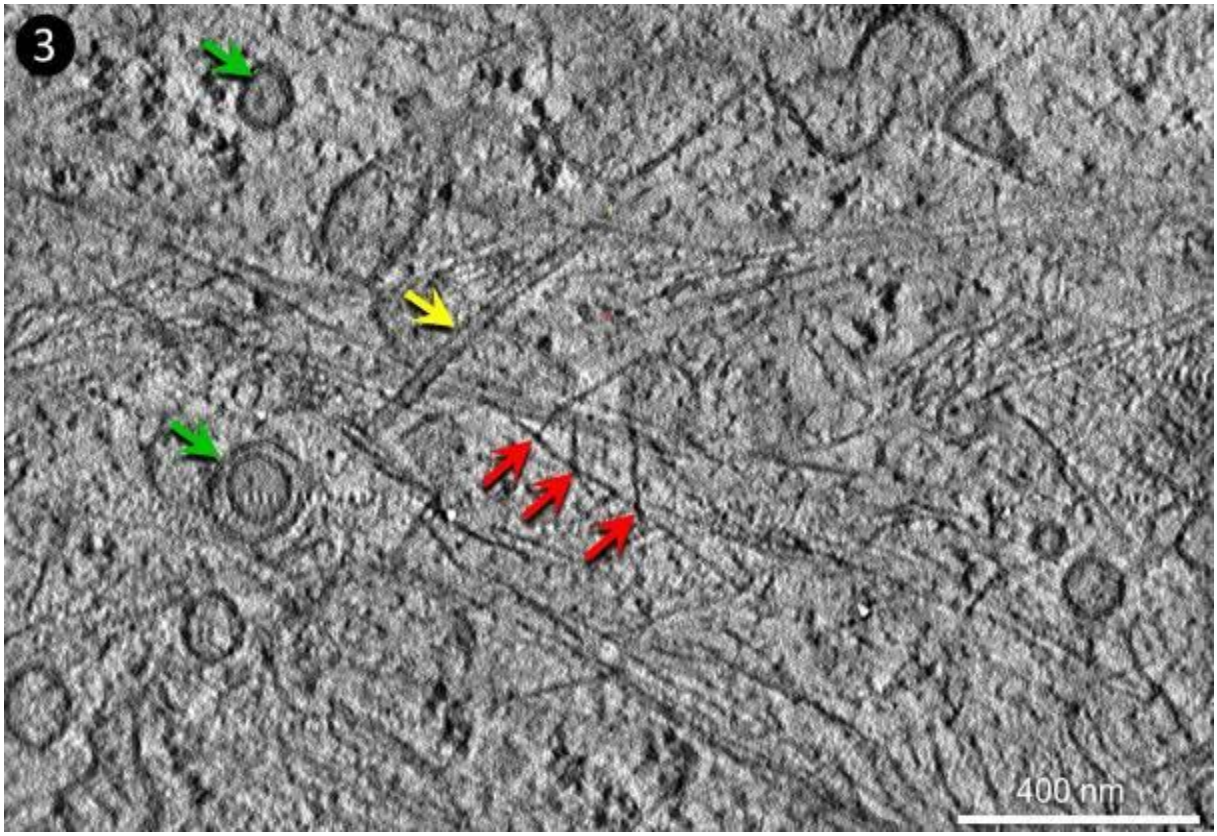

Figure 3. shows a 10 nm thick virtual section of a bright field STEM tomogram of a 475 nm thick epon section of a keratinocyte prepared by high pressure freezing and freeze substitution. Beside membranous structures (green arrows), where the two leaflets of the bilayer are well resolved, microtubules (yellow arrow) and intermediate filaments are visible. We conclude that the red arrows point to real branches of intermediate filaments, since the thickness of the virtual section is in the range of the thickness of an intermediate filamen

Ultrastructural & Analytical Methods in Life Sciences

LS.6.151
Volume imaging of cellular ultrastructure in native frozen specimens using focused ion beam scanning electron microscopy at cryo conditions

A. Schertel[1], N. Snaidero[2], H.-M. Han[3], T. Ruhwedel[4], M. Laue[5], M. Grabenbauer[3], W. Möbius[4]

[1]Carl Zeiss Microscopy GmbH, Training, Application and Support Center (TASC), Oberkochen, Germany
[2]Max Planck Institute of Experimental Medicine, Cellular Neuroscience, Göttingen, Germany
[3]Max-Planck-Institute of Molecular Physiology, Department of Systemic Cell Biology, Dortmund, Germany
[4]Max-Planck-Institute of Experimental Medicine, Neurogenetics, Göttingen, Germany
[5]Robert Koch-Institute, Advanced Light and Electron Microscopy, Centre for Biological Threats and Special Pathogens, Berlin, Germany

moebius@em.mpg.de
Keywords: Cryo FIB-SEM, high-pressure freezing, serial block face imaging, 3D reconstruction, mouse optic nerve, *Bacillus subtilis* spores

To understand cellular functions in the context of three-dimensional assemblies volume microscopy at high resolution is required. Focused ion beam (FIB) milling combined with serial block face imaging in the scanning electron microscope (SEM) is an efficient and fast method to generate such volume data for 3D analysis. In this study, we apply this technique in a cryo FIB-SEM to image fully hydrated frozen specimen of mouse optic nerves and *Bacillus subtilis* spores prepared by high-pressure freezing (HPF). We were able to establish imaging conditions for the direct visualization of the ultrastructure in the block face at −150°C by using an in-lens secondary electron (SE) detector. By serial sectioning with a focused ion beam and block face imaging in the optic nerve we obtained a volume of X=7.72 µm, Y=5.79 µm and Z=3.81 µm with a lateral resolution of 7.5 nm and a Z-resolution of 30 nm. The intrinsic contrast of membranes was sufficient enough to distinguish subcellular structures like Golgi cisternae, vesicles, endoplasmic reticulum and cristae within mitochondria. Serial images could be used for a three-dimensional reconstruction of different types of mitochondria within an oligodendrocyte and an astrocytic process. Applying this technique to dormant *Bacillus subtilis* spores we obtained volumes containing several spores and discovered a novel core structure, which was not visualized before by any other imaging technique. In summary, we describe here the use of cryo FIB-SEM as a tool for direct and fast 3D cryo-imaging of large native frozen samples.

Ultrastructural & Analytical Methods in Life Sciences

LS.6.P152
Does dexamethasone treatment change the expressions of proliferating cell nuclear antigen (PCNA), cyclin D3, p27, p57 in normal and dexamethasone-induced intrauterine growth restricted rat placentas?

H. Er[1], N. Acar[1], A. Ozmen[1], C. Celik-Ozenci[1], I. Ustunel[1], E.T. Korgun[1]

[1]Akdeniz University, Antalya, Turkey

hakaner@akdeniz.edu.tr
Key words: placenta, intra-uterine growth restriction (IUGR), rat, cell cycle, apoptosis

Intrauterine growth restriction (IUGR) described as only to those infants with birth weight and/or birth length below the 10th percentile for GA with a pathologic restriction of fetal growth [1]. It is a major clinical problem which causes perinatal morbidity and mortality and major etiological factor is abnormal placentation [2]. Despite the fact that placental development requires the coordinated action of trophoblast proliferation and differentiation, there are few studies on cell cycle regulators, which play the main roles in the coordination of these events and it is still not determined how mechanisms of coordination of proliferation and differentiation are influenced by dexamethasone-induced IUGR in the placenta.

Female rats were mated with male rats, presence of sperm in vaginal smear accepted day 0 of pregnancy. Rats were injected 100 µg/kg dexamethasone on day 13, 200 µg/kg dexamethasone on days 14-19 of pregnancy. Control animals were injected saline solution. Six rats each group were sacrified for each method. After Rattus norvegicus rats were sacrified on day 20 of pregnancy, blood samples were taken, placentas were formaline fixed-parafin embedded or snap-frozen. We applied Reverse Transcriptase Polymerase Chain Reaction (RT-PCR), immunohistochemistry, Western blotting, terminal deoxynucleotidyl transferase-mediated deoxyuridine triphosphate nick end-labeling (TUNEL), glucocorticoid assay and did transmission electron microscopic observations.

Although there was a statistically significant ($p<0.001$) increase of glucocorticoid levels 60 minutes after dexamethasone injection, it was normal 180 minutes after the injection in IUGR group. Mean embryo and placenta weights of control rats were higher than IUGR group with statistically significant difference ($p<0.005$) (Figure 1) but dexamethasone didn't affect the number of embryos. According to RT-PCR, immunohistochemistry and Western blotting results, expression of PCNA was higher in control group than in IUGR group and it was statistically significant ($p=0,041$), expressions of cyclin D3, p27 and p57 were higher in IUGR group. TUNEL positive cell numbers in IUGR group placentas were higher than control group placentas ($p<0.001$). Electron microscopic observations were compatible with TUNEL results. Spongiotrophoblasts and labyrinth trophoblasts of IUGR placentas showed apoptotic cell characteristics (Figure 2).

Our data suggests that glucocorticoid-induced restriction of fetal-placental growth is mediated, in part, via inhibition of cell cycle proteins and increase in apoptosis. Previous studies showed that dexamethasone caused a decrease in growth-promoting genes [3]. Glucocorticoid metabolism during pregnancy is still debated. How dexamethasone acts in placental growth inhibition hasn't been determined. This study described decrease of proliferation, increase of apoptosis in dexamethasone injected IUGR rat placentas. Since dexamethasone is widely used to women having premature labor risk, reduces fetal growth and predisposes to increased risk of disease in later life, detailed studies should be done.

1. Wollmann HA. Intrauterine growth restriction: definition and etiology. Horm Res. 1998;49 Suppl 2:1-6.
2. Deborah K. Steward, Debra K. Moser. Intrauterine Growth Retardation in Full-Term Newborn Infants with Birth Weights Greater Than 2,500 g. Research in Nursing & Health, 2004, 27, 403–412
3. B. Baisden, S.Sonne, R.M. Joshi, V. Ganapathy, P.S. Shekhawat. Antenatal Dexamethasone Treatment Leads to Changes in Gene Expression in a Murine Late Placenta. Placenta 28 (2007) 1082- 1090
4. This study was supported by a grant from the Akdeniz University Research Fund (2005.02.0122.003), Antalya, Turkey. The authors declared they have *no competing interests.*

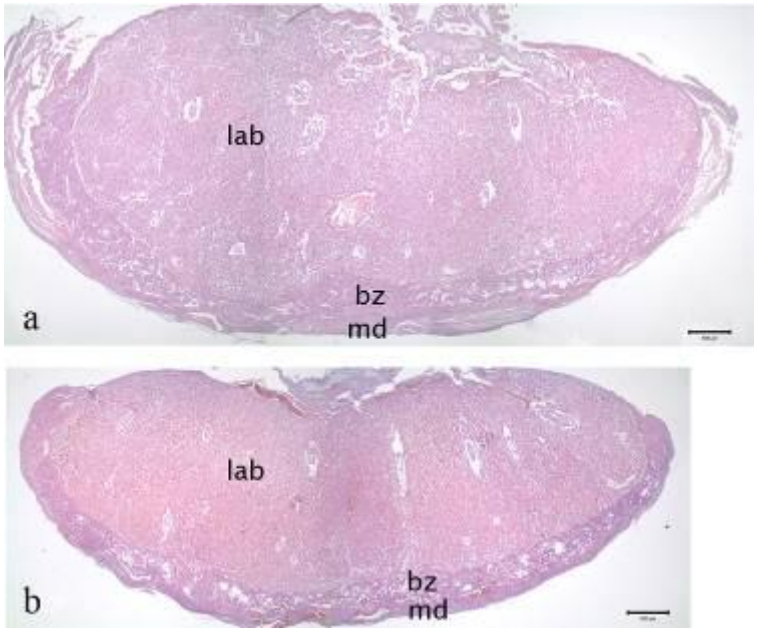

Figure 1. Light microscopy of control (a) and IUGR (b) placentas. The labyrinthine (lab) and junctional zones (bz) of control placenta are greater than the same zones of IUGR placenta. md: maternal decidua. Hematoxylin and Eosin. Bar: 500µm.

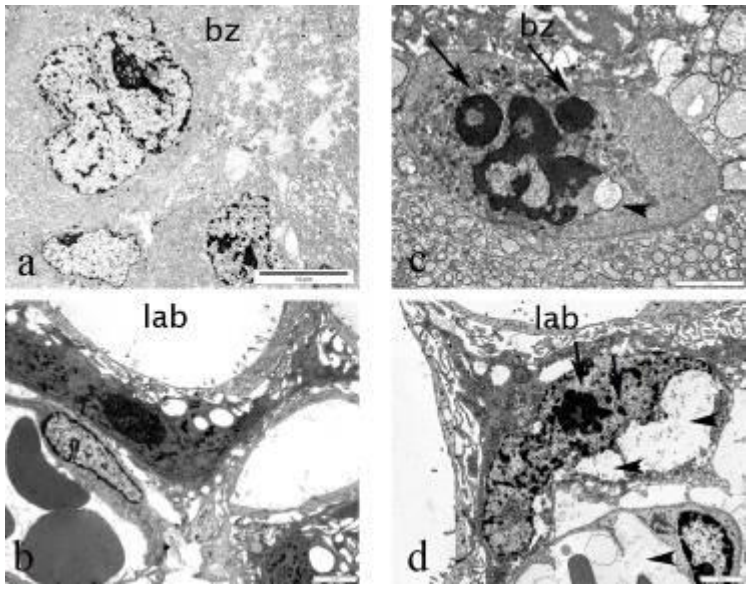

Figure 2. Electron micrographs of control (a, b) and IUGR (c, d) placentas. Normal spongiotrophoblast (a) and trophoblast (b) cells in control labyrinthine (lab) and junctional zones (bz) but a spongiotrophoblast with dense chromatin, fragmentation (arrow) (c) and degradation (arrow head) (c) was seen in junctional zone of IUGR placenta. A trophoblast with fragmentation (arrow) (d) and vacuoles (arrow head) (d) was seen in labyrinthine zone of IUGR placenta. Bars: a: 10µm, b, c, d: 2µm.

Ultrastructural & Analytical Methods in Life Sciences

LS.6.P153
Application of Rhodamine B as a potential marker for silicon in cell walls of higher plants

M. Soukup[1], M. Martinka[1], A. Lux[1]

[1]Faculty of Natural Sciences, Comenius University in Bratislava , Department of Plant Physiology, Bratislava, Slovakia

soukup.em@gmail.com
Keywords: phytoliths, Rhodamine B, root, silica bodies, silicon, *Sorghum bicolor* L.

Silicon is the second most abundant element in earth's crust. Even though it is not considered as an essential element in plant nutrition it is actively taken up by many plant species [1]. Within the plant organism, silicon is mainly deposited into endodermal and epidermal cell walls, and cuticle layer [2, 3]. Besides adjusting cell wall mechanical properties silicon provides also many other benefits and increases plant stress resistance [4].

Grasses are often capable to precipitate silicon into amorphous hydrated silica bodies, also called phytoliths. These microscopic structures are morphologically specific among the species [3, 5]. Their localisation and identification within intact plant tissues and cells is quite difficult because of their transparency and small sizes. In our work we tested application of Rhodamine B, a fluorescent dye used also for diatom silica thecae staining [6], as a possibility for visualisation of silica bodies and silicon cell wall deposits in plant organism by fluorescence microscopy.

Experiments were focused on endodermal silica bodies in *Sorghum bicolor* L. roots because of their known localisation and rapid development [7]. Plants in control variant were cultivated for three days in hydroponics containing distilled water with addition of Na_2SiO_3 as a source of silicon. The RhB variant consisted of control medium enriched with Rhodamine B. Transversal sections of primary seminal roots were prepared from the zone 2 – 3 cm from the root base. Prepared sections were additionally stained with toluidine blue in ethanol (TB) to suppress the fluorescence of lignin. Observations were performed with a fluorescent microscope Axioskop 2 plus (Carl Zeiss) with excitation filter TBP 400 + 495 + 570, dichroic beamsplitter TFT 410 + 505 + 585 and emission filter TBP 460 + 530 + 610 (wavelengths are listed in nm).

Unstained control variant root sections did not show any specific signal and emitted blue-green fluorescence of cell walls, presumably caused by a presence of ferulic acid [8]. Centrifugal parts of xylem cell walls and inner tangential endodermal cell walls displayed enhanced blue fluorescent signal, probably as a consequence of lignin deposition [8, 9]. Endodermal silica bodies also possessed weak blue signal but it might represent a reflection of the endodermal cell wall fluorescence. After additional TB staining the blue-green fluorescence of cell walls was suppressed and no relevant signal was received. In RhB variant without additional TB staining the cell walls emitted strong red fluorescence lacking any specificity within the root anatomical structures. Additional staining with TB suppressed the non-specific red fluorescence after Rhodamine B treatment. The inner tangential endodermal cell walls remained the only structures displaying red fluorescent signal. Anyhow, the endodermal silica bodies did not show any positive signal. According to X-ray analysis of *Sorghum* root transversal sections, the only silicon accumulation occurred in endodermal cells [10]. The deposition of silicon into the inner tangential walls of endodermis is reported also in many other species [2, 3, 4, 11]. On the other hand, the presence of silicon within the silica body is obvious and thus proposing a question whether the mechanism of silicon cell wall deposition and silica body formation is the same.

Application of Rhodamine B with additional toluidine blue staining is a potential method for fluorescence visualisation of silicon deposits within the plant cell walls. Anyhow, the adjustment of this method needs further investigations and testing. On the other hand, staining of silica bodies in *Sorghum* root endodermis by Rhodamine B did not give any satisfying result and thus requires the development and application of another technique.

1. T.I. Balakhnina et al., Plant Growth Regul. 67 (2012), p. 35
2. M.J. Hodson et al., Ann. Bot. 96 (2005), p.1027
3. J.F. Ma, Soil Sci. Nutr. 50 (2004), p. 11
4. M. Rizwan et al., J. Hazard. Mater. 209-210 (2012), p. 326
5. T.B. Ball, R. Ehlers and M.D. Standing, Breeding Sci. 59 (2009), p. 505
6. M. Kucki in “Biological Photonic Crystals: Diatoms Dye functionalization of biological silica nanostructures” (Dissertation Thesis) (Department of Natural Sciences, University of Kassel, Kassel, Germany) (2009), p. 166.
7. A. Lux et al., New Phytol. 158 (2003), p. 437
8. F.W.D. Rost in “Fluorescence microscopy (Volume II)” (Press Syndicate of the University of Cambridge, Cambridge, Great Britain) (1995), p. 473
9. B. Albinsson et al., J. Mol. Struct. 508 (1999), p. 19
10. A.G. Sangster and D.W. Parry, Ann. Bot. 40 (1976), p. 373
11. H.J. Gong, D.P. Randall and T.J. Flowers, Plant Cell Environ. 29 (2006), p. 1970
12. This study was supported by grants 1/0817/12 by Slovak grant agency VEGA and by Slovak Research and Development Agency under the contract No. APVV-0140-10.

Ultrastructural & Analytical Methods in Life Sciences

LS.6.P154
FRAP analysis of dystroglycan, a membrane receptor involved in congenital muscular dystrophies.

V. Palmieri[1], G. Maulucci[1], M. De Spirito[1], A. Maiorana[1], M. Papi[1], A. Brancaccio[2], M. Bozzi[3]
F. Sciandra[2]

[1]Università Cattolica del Sacro Cuore, Istituto di Fisica, Roma, Italy
[2]Istituto di Chimica del Riconoscimento Molecolare, Roma, Italy
[3] Università Cattolica del Sacro Cuore, Istituto di Biochimica e Biochimica Clinica, Roma, Italy

vplabcemi@gmail.com
Keywords: Dystroglycan, congenital muscular dystrophies, FRAP, confocal microscopy

Dystroglycan (DG) is a ubiquitous membrane-spanning protein that plays a crucial role in the assembly of several basement membranes, promoting the recruitment of laminins and other extracellular matrix molecules during morphogenesis, tissue remodelling, cell polarization and wound healing [1]. DG is formed by two subunits, the highly glycosylated and extracellular protein □-DG and the transmembrane protein □-DG. A non-covalent interaction between the two DG subunits anchors □-DG to the plasma membrane.

In skeletal muscle, DG is the central component of the dystrophin-glycoprotein complex (DGC), a multisubunit complex comprised of peripheral and integral membrane proteins, which links the cytoskeleton to the extracellular matrix. DGC ensures structural stability to the sarcolemma during the contraction–relaxation cycle. Primary and secondary mutations in the DGC components lead to distinct forms of muscular dystrophies, a diverse group of inherited disorders characterized by progressive muscle weakness and wasting [Cohn and Campbell, 2000]. In particular, genetic defects in the O-mannosylation pathways underline some congenital muscular dystrophies (CMD) characterized by a hypoglycosylated form of □-DG that displays a reduced affinity for the extracellular matrix proteins destabilizing the muscle fibers [3]. In CMD, the chronic damage of the muscle fibers leads to a continuous sealing of the sarcolemma and to a remodelling of DGC. The hypoglycosylation of □-DG, reducing the binding of □-DG to the surrounding extracellular matrix, may also influence the migration of DG through the plasmalemma influencing the membrane repair process. We analyzed, using confocal microscopy, GFP labelled wild-type DG and DG mutants with an altered glycosylation pattern in 293-EBNA cell line. In particular, cell tracking analysis was used to analyze the influence of the DG binding to extracellular matrix protein laminin on cells velocity and directionality. Moreover, using fluorescence recovery after photobleaching (FRAP) we have analyzed for the first time the DG mobility in plasma-membranes. FRAP allowed to measure diffusion and the mobile and immobile fraction of DG. Our study may give new insights in the cell trafficking of DG and its targeting and dynamics within the plasma membrane.

1. M. Bozzi, S. Morlacchi, M.G. Bigotti, F. Sciandra and A. Brancaccio, Matrix Biol. 28 (2009), 179-187.
2. R.D, Cohn and K.P. Campbell, Muscle Nerve 23 (2000), 1456-1471.
3. F. Sciandra, K.E. Gawlik, A. Brancaccio and M. Durbeej, Trends Biotech. 25 (2007), 262-268.

Ultrastructural & Analytical Methods in Life Sciences

LS.6.P155
3D reconstruction of tick-borne encephalitis virus replication complexes

T. Bílý[1,2], M. Vancova[1], D. Ruzek[1,3], M. Palus[1,2], J. Nebesarova[1,4], L. Grubhoffer[1,2]

[1]Biology Centre of ASCR, Institute of Parasitology, Ceske Budejovice, Czech Republic
[2]University of South Bohemia, Faculty of Science, Ceske Budejovice, Czech Republic
[3]Veterinary Research Institute, Department of Virology, Brno, Czech Republic
[4]Charles University, Faculty of Science, Prague, Czech Republic

thomass@paru.cas.cz
Keywords: Electron tomography, Tick-borne encephalitis virus, Flavivirus

Ixodes ricinus is the main vector of Tick-borne encephalitis virus (TBEV) in Europe. Ticks can be infected during feeding upon infected vertebrates like small rodents [1]. Humans are mostly infected via injected tick saliva. The first phase of the infection has nonspecific influenza-like symptoms. Meningitis, meningoencephalitis or meningoencephalomyelitis occur in the second phase which can be followed by post-encephalitic syndrome.

TBEV is a member of the Flavivirus genus in the family *Flaviviridae*. Flaviviruses are enveloped particles with a 40–60 nm outer diameter and an electron-dense core-nucleocapsid composed of the capsid protein and the positive-sense RNA genome [2]. The RNA genome is translated in a host cell into a polyprotein that is cleaved into structural proteins C (Capsid), M (membrane), E (envelope) and non-structural proteins NS1, NS2A, NS2B, NS3, NS4A, NS4B and NS5 [3].

This study is focused on 3D reconstructions of structural changes of the rough endoplasmic reticulum (ER) induced by TBEV and the organisation of the replication complexes. We describe the presence of induced vesicles (smooth membrane structures) and convoluted membranes (Figure 1) [4]. This TBEV ER derived induced network is the presumed site of replication [5]. Our results prove the presence of a single pore in the wall of TBEV induced vesicles (Figure 2). Similarly, 3D reconstruction of the replication and assembly sites of another flavivirus, the Dengue virus, has proven presence of one such pore in the virus induced vesicle. The presumed function is in an import of factors required for RNA replication and export of newly synthesized genomes [5].

In TBEV infected human primary astrocytes (prepared by high pressure freezing and freeze substitution method), we observed unique microtubule-like structures within of ER cisterns. The average diameter of structures was 17.9 nm (± 0.15 nm, n = 101). The 3D reconstruction revealed its the detailed organisation. The structures were already described in glutaraldehyde fixed neuroblastoma cells infected with TBEV [4]. Their function is not clear. Tubular elongated structures of a 60-100 nm diameter were observed within the ER of Langat virus (Flavivirus genus) infected mammalian cells [6].

Tilt series electron micrographs were collected from sections thinner than 90 nm which provide clearly distinguishable structures in transmission projection images (without overlapping structures arising from object arrangement in the 3D volume). Sections were examined at 200 kV (JEOL 2100F equipped with high tilt stage and Gatan camera Orius SC 1000) using the Serial EM acquisition software [7]. Tomograms were aligned, reconstructed and 3D models were generated by manually masking the area of interest using the IMOD software package [8].

1. M. Labuda, V. Danielova, L.D. Jones, P.A. Nuttall, Medical and Veterinary Entomology 7 (1993), 339-342
2. G.R. Claves, T.D. Dubin, Virology 96 (1979), 159-165
3. R. Bartenschlager, S. Miller, Future Microbiol. 3 (2008),155-165
4. D. Růžek, M. Vancová, M. Tesařová, A. Ahntarig, J. Kopecký, L. Grubhoffer, J. Gen. Virol. 90 (2009), 1649-1658
5. S. Welch et. Al, Cell Host & Microbe 5 (2009), 365-375
6. D.K. Offerdahl, D.W. Dorward, B.T. Hansen, M.E. Bloom, PLoS ONE 7 (2012), Issue 10, 1-14
7. D.N. Mastronarde, J. Struct. Biol. (2005), 152:36-51
8. J.R. Kremer, D.N. Mastronarde, J.R. McIntosh, J. Struct. Biol. (1996), 116:71-6
9. This work was supported by the Grant Agency of the ASCR (Z60220518,P302/12/2490), Czech Science Foundation project No. P502/11/2116, and Technology Agency of the Czech Republic (TE 01020118).

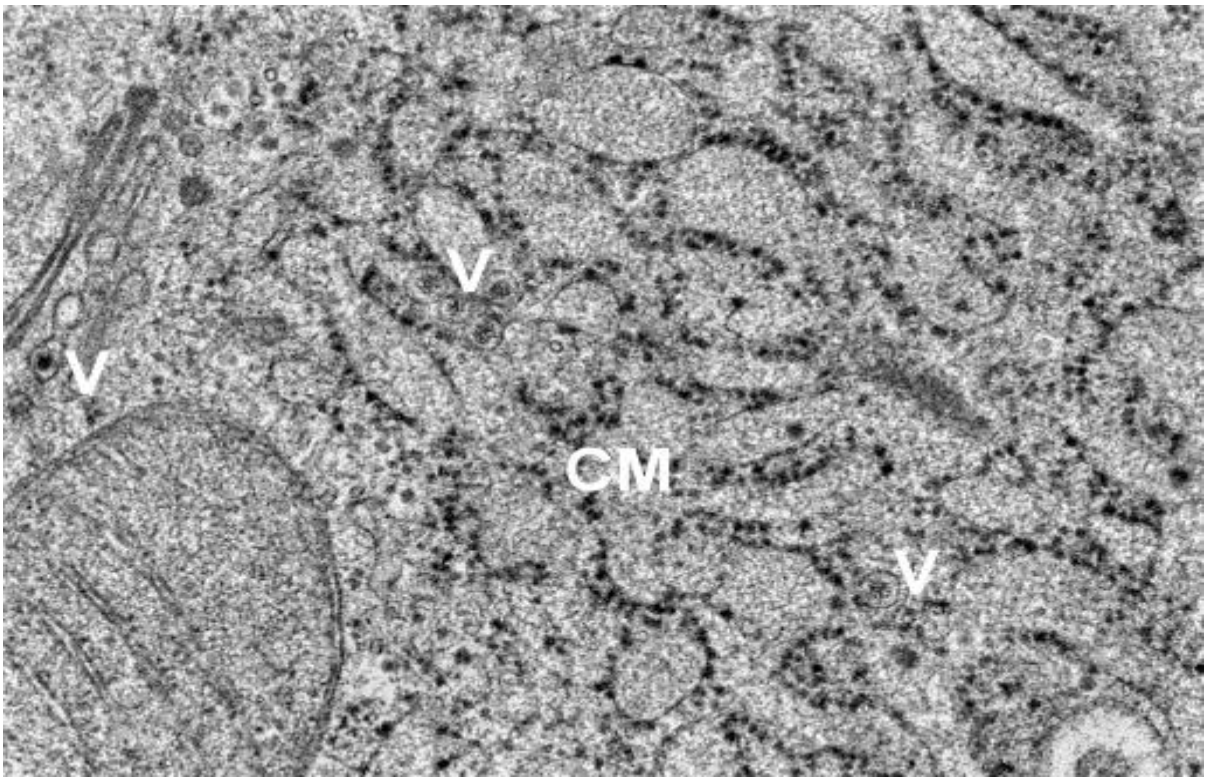

Figure 1: Neuroblast TBEV (V) infected cells, rearranged ER (CM).

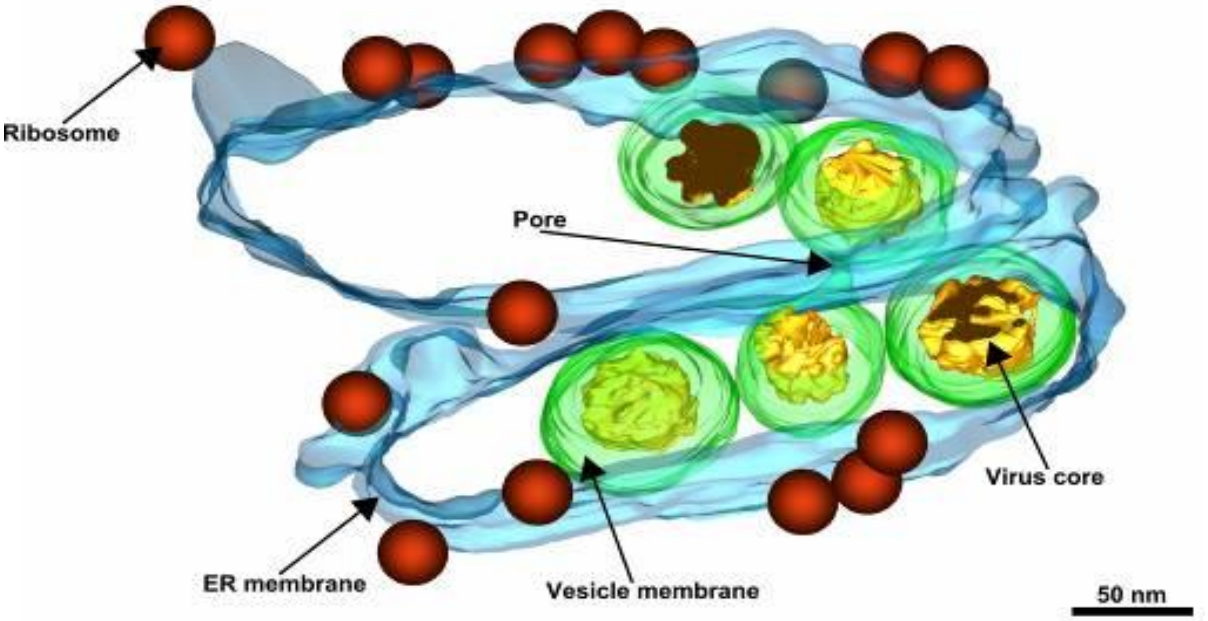

Figure 2: Pore inside induced vesicle.

Ultrastructural & Analytical Methods in Life Sciences

LS.6.P156
Evaluation of the effects of HMG-Co Reductase Inhibitors on the cell proliferation and cell death mechanisms of the breast adenocarsinoma cell line MCF-7

T. Demirci[1], D. Zeybek[1], S. Muftuoglu[1]

[1]Hacettepe University Faculty of Medicine, Histology & Embryology, Ankara, Turkey

smuftuog@hacettepe.edu.tr

Keyword: Statin, Autophagy, Apoptosis, MCF-7

Breast cancer is the most common cancer worldwide among women and is the second leading cause of cancer deaths. In recent years many studies about the new treatment modalities of breast cancer have been conducted. Statins, mostly used for the prevention of cardiovascular and cerebrovasculer diseases, block cholesterol synthesis by specific inhibition of HMG-CoA reductase [1]. In the last few years, use of statins gained interest for cancer preventation and treatment [2]. Although there are many articles that indicate cytotoxic effects of statins on cancer cells, the exact mechanism of antiproliferative and antiapoptotic effects of them on breast cancer cells is not clearly understood. Autophagy is a new insight about death pathways and it is defined as the process by which cells recycle their own unessential organelles and components under stress conditions. Autophagy can be the target for understanding the survival mechanisms and therapeutic strategies for killing preinvasive neoplasms [3]. Autophagic effects of statins on different kinds of cancer cell lines are well known but the effects of statins on breast cancer cells have not been investigated in aspect of autophagy.

In this study, we aimed to determine if statins induce autophagy in breast cancer cells and to investigate the relationship between apoptosis and autophagy specifically induced by statins in MCF-7 human breast adenocarcinoma cells.

MCF-7 breast cancer cells were treated with different concentrations of atorvastatin. At 24 and 48 hours WST, TUNEL, immunohistochemistry (caspase 3, becklin1, LC3) and electron microscopic analysis were performed.

Atorvastatin decreased cell viability of MCF-7 cells in 24 and 48 hours (Figure 1). Increased apoptosis was detected in a concentration-dependent manner by TUNEL labelling in MCF-7 cells treated with 10, 20 and 80 µM concentrations for 24 and 48 hours (Figure 2). Caspase 3 labelling confirmed our TUNEL labelling results. Autophagy observed by beclin-1 and LC3 immunofluoresance staining (Figure 3) was confirmed with electron microscopic examination (Figure 4). Prominent morphologic changes showing necrosis were observed in MCF-7 cells treated with 80 µM atorvastatin for 48 hours by transmission electron microscopy.

Finally, our results present the first demonstration of autophagy of MCF-7 cells induced by statins. Thus our study will help to establish a novel mechanism for apoptotic and antiproliferative effects of statins on breast cancer cells. Additionally in this study, showing the autophagic effects of statins on breast cancer cells, will provide the scientific foundation for subsequent research of new treatment modalities of breast cancer. In order to determine the exact relationship between apoptosis and autophagy induced by statins, further studies should be conducted by using autophagy inhibitors.

1. Camnitz W et al.Clin Transl Med. 1(2012), 23.
2. Qi XF, et al. Cell Death Dis. 4(2013), e518.
3. Espina V et al. Womens Health (Lond Engl). 2 (2013), 157-70.

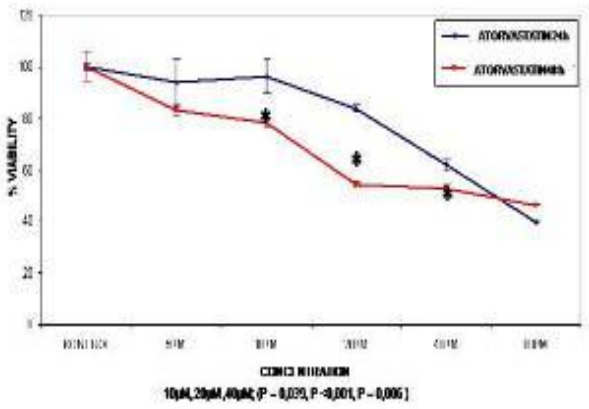

Figure 1. Cell viability of MCF-7 cells treated with diffrerent concentrations of atorvastatin for 24 and 48 hours analysed by WST.

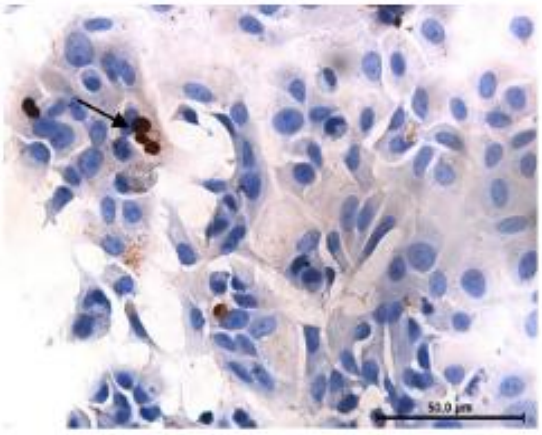

Figure 2. Apoptotic MCF-7 cells treated with 10µM Atorvastatin 48h.TUNEL staining

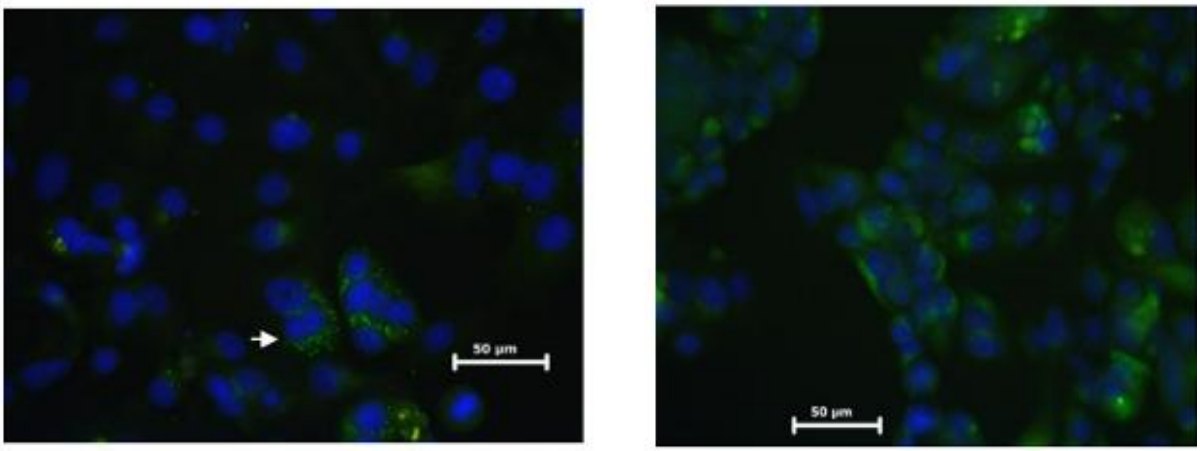

Figure 3. Beclin-1 immunoreactivity in 80µM atorvastatin 24h treated (a), LC3 immunoreactivity in 20µMatorvastatin 48h treated MCF-7 cells (b) (FITC, nucleus: DAPI)

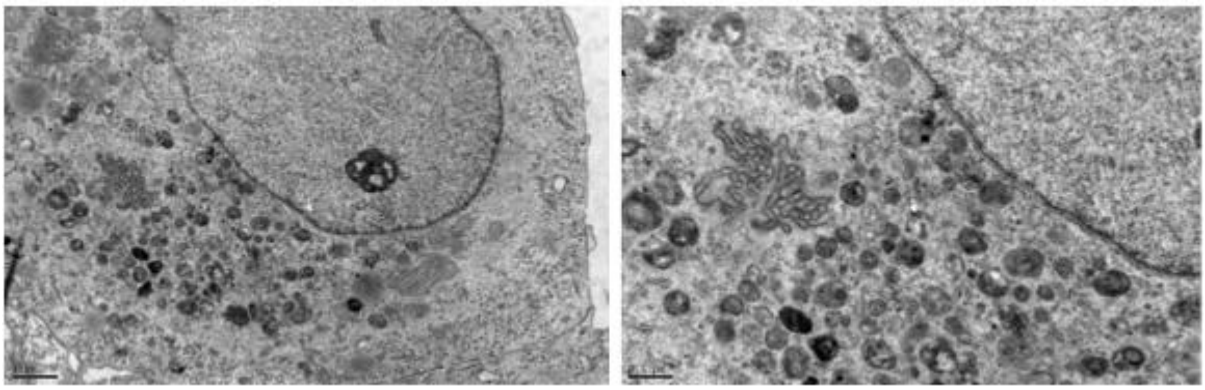

Figure 4. Electron micrograph of MCF-7 cells treated with 80µM Atorvastatin for 24h.

Ultrastructural & Analytical Methods in Life Sciences

LS.6.P157
Light-induced transformation of prolamellar body (PLB) during early stages of bean chloroplast biogenesis visualized by electron tomography.

L. Rudowska[1], S. Suski[2], R. Mazur[1], M. Garstka[1], A. Mostowska[1]

[1]University of Warsaw, Faculty of Biology, Warsaw, Poland
[2]Nencki Institute of Experimental Biology, Laboratory of Electron Microscopy, Warsaw, Poland

lucja.rudo@biol.uw.edu.pl
Keywords: prolamellar body, chloroplast biogenesis, electron tomography

Chloroplast biogenesis is a multistage process leading to fully differentiated and functionally mature plastid. At ultrastructure level this process consists of the transformation of prothylakoids (flat porous membranes, PT) and prolamellar bodies (paracrystalic tubular membrane structures, PLB) into grana and stroma thylakoids This model of differentiation of etioplast to mature chloroplast is based on natural scotomorphogenesis (etiolated growth), which represents the initial seedling growth occurring beneath the soil's surface.

Three-dimensional structure of thylakoid membrane arrangement has been a subject of many studies during last fifty years [1 and literature therein]. In last few years electron tomoghraphy and 3D modelling techniques in particular have contributed to creation detailed model of grana stacks arrangements [1,2].

In our study we focused on visualization of spatial model of thylakoid differentiation during the chloroplast biogenesis. We followed this process step by step from paracrystaline structure of PLB to first stacked membranes observed in ultrastructure of bean chloroplasts. Therefore we selected five main stages of plastid internal membranes arrangements during early stages of photomorphogenesis. Changes in membranes arrangement during subsequent hours of illumination. are schematically shown in Figure 1. Initially the paracrystaline structure of PLB observed in 1.0 plants (8 days of etiolation) transforms into irregular one already after one hour of light exposition (1.1 plants). During subsequent hours degradation of PLB proceeds and more prothylakoids are detected in plastid stroma (1.2 plants) until no PLB structures are found. In this stage only thylakoids and prothylakoids parallely arranged to each other exists(1.4 – plants after four hours of light). In last examinated stage, after eight hours of light exposition (1.8) first stacked membranes are observed in developing chloroplasts.

Electron tomography technique was performed with JEM 1400 (Jeol) microscopy from +60 to -60 at 1 intervals in one axis. Tomograms collected from samples from five selected stages (1.0, 1.1, 1.2, 1.4, 1.8) were reconstructed using tomoJ (ImageJ) software and then isosurfaces of membrane arrangements were prepared using Imaris software. Additionally models of selected details of structures were made with 3dmod software. In Figure 2 the isosurface of paracrystaline PLB (1.0) is presented.

1. J.R. Austin and A. Staehelin Plant Physiol. 155 (2011) p1601.
2. B. Daum and W. Kuhlbrandt J. Exp. Bot. 22(4) (2011) p1299
3. This work is supported by Polish Ministry of Science and Higher Education Grant N N303 530438.
4. TEM images were performed in the Laboratory of Electron Microscopy, Nencki Institute of Experimental Biology on JEM 1400 (JEOL Co. Japan) electron microscope. This equipment was installed within the project sponsored by the EU Structural Funds: Centre of Advanced Technology BIM – Equipment purchase for the Laboratory of Biological and Medical Imaging.

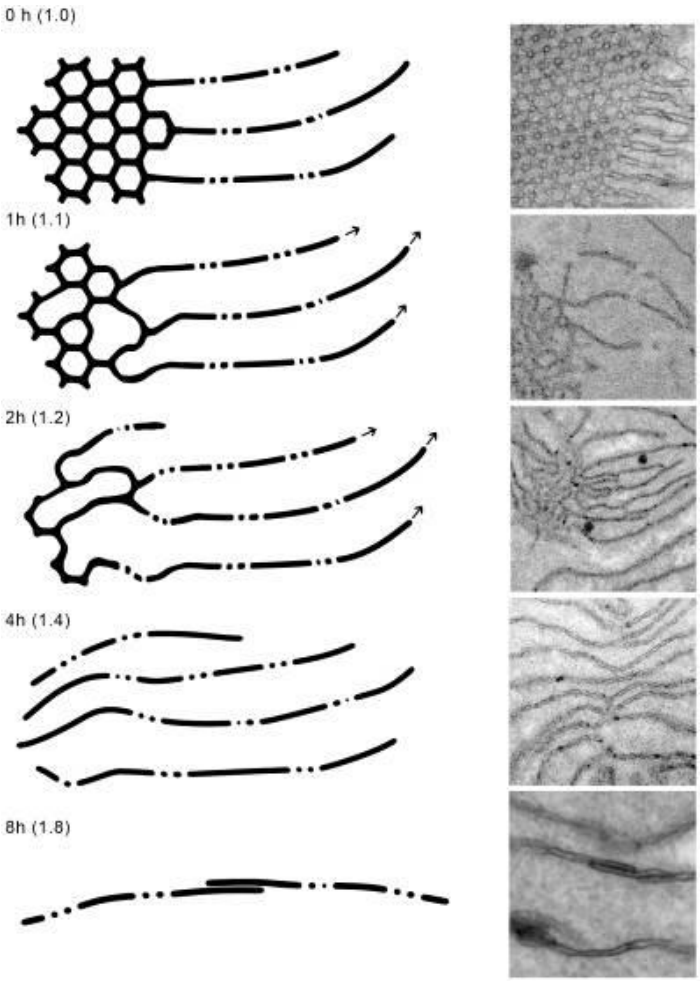

Figure 1. Theoretical model (with corresponding electron micrographs) showing arrangement of inner plastid membranes during prolamellar body transformation in subsequent hours of illumination.

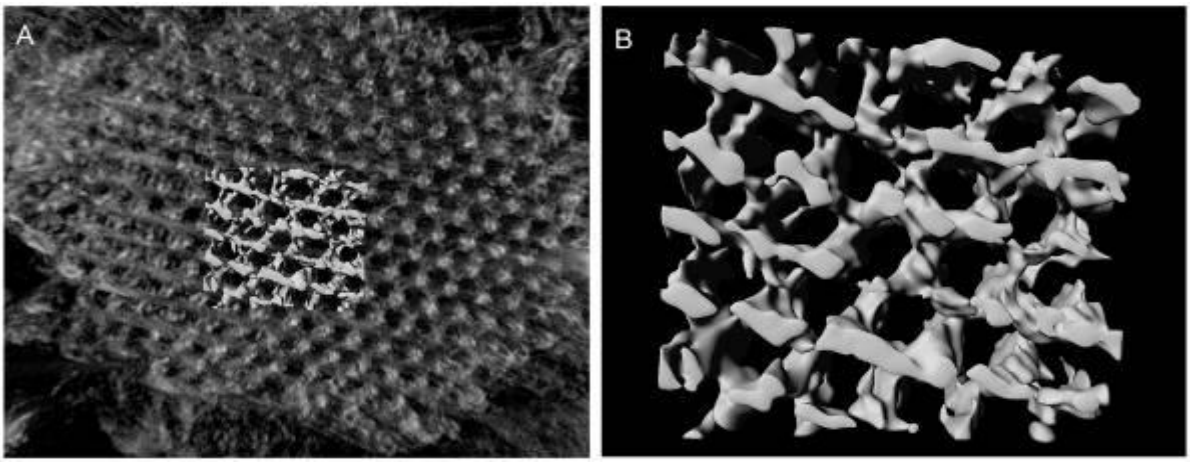

Figure 2. Isosurface visualisation of 3D reconstruction of paracrystaline prolamellar body structure (A volume with isosurface, B – enlargement) prepared with electron tomography technique.

Ultrastructural & Analytical Methods in Life Sciences

LS.6.P158
Effects of Robertsonian fusions on male reproduction: structural and ultrastructural analysis of the testis and epididymis

J. Repullés[1], M.A. Sans Fuentes[2,3], N. Medarde[4], J. Martínez[4], M. Ponsà[5], M.J. López Fuster[2], J. Ventura[4], A. Sanchez Chardi[1]

[1]Universitat Autònoma de Barcelona, Microscopy Facility, Cerdanyola del Vallès, Spain
[2]Universitat de Barcelona, Biologia animal, Barcelona, Spain
[3]University of Arizona, School of Geography and Development, Tucson, Spain
[4]Universitat Autònoma de Barcelona, Biologia animal, Cerdanyola del Vallès, Spain
[5]Universitat Autònoma de Barcelona, Biologia cel·lular, fisiologia i immunologia, Cerdanyola del Vallès, Spain

Alejandro.Sanchez.Chardi@uab.cat
Keywords: Robertsonian fusions, speciation, structure, ultrastructure, male germ cells

Robertsonian translocations (centric fusions between two telocentric chromosomes to form a metacentric one) can act as a mechanism of speciation reducing fertility, and have been described in some mammalian species, such as the house mouse, *Mus musculus domesticus*. To study the effect of these translocations on male reproduction, Robertsonian (Rb, 2n=28-31) and standard mice (St, 2n=40) from the Robertsonian polymorphism area of Barcelona (NE Spain) were analysed. Testis (tubular diameter, epithelium thickness, cell cycle arrest during spermatogenesis) and caput epididymis (percentage of abnormal spermatozoa) were evaluated using both light and electron microscopy.

The preliminary results comparing Rb and St mice can be summarized as follows: 1) the two groups did not show important differences in the structural morphology of the seminiferous tubules; 2) Rb mice showed an increase of cell cycle arrest (mainly ending in apoptosis; Figure 1) during spermatogenesis in comparison with St mice; 3) Rb mice had more mature spermatozoa with ultrastructural abnormalities in the head and the tail (Figure 2).

These results may be explained by the increase of defects during meiosis (e.g. impairment in homologous chromosome pairing) in Rb mice, producing an increase of unviable germ cells, and a subsequent decrease of fertility. These results point out the relationship between Rb reorganizations and both germ cell death and gamete anomalies. Our results using microscopy are concordant with previous studies on the Robertsonian zone of Barcelona, which indicate that in Rb mice the percentage of viable gametes is lower and the spermatogenesis less efficient than in St mice. All these findings suggest that in the study area Rb translocations reduce gene flow among populations as a result of a decrease in fertility in Rb mice with a relatively high number of metacentric chromosomes.

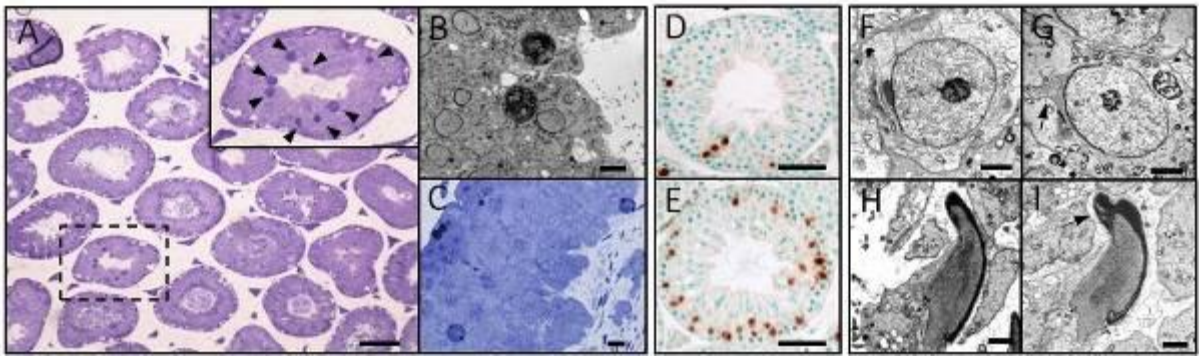

Figure 1. Representative images of testicles of Rb mice showing cell degeneration of tubules (A, B, C) mainly due to apoptosis (arrowheads). Apoptosis was confirmed by TUNEL assay (D: St, E: Rb). F-I micrographs showed normal round (F) and elongated (H) spermatid and abnormal round (G) and elongated (I) spermatids with acrosomal alterations (arrow). Bars: A=100µm; B=5µm; C=10µm; D, E=50µm; F-I = 2µm.

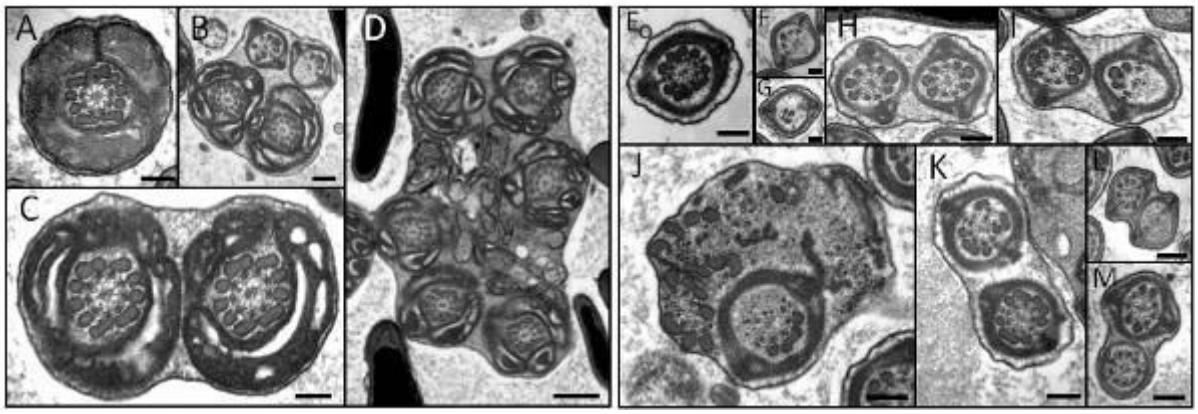

Figure 2. Representative micrographs showing the normal structure (A, E) and the most common ultrastructural alterations in tails of mice sperm. These abnormalities were significantly more frequent in Rb mice and were mainly based in two or more tail sections embedded in the same plasma membrane (C, D, H, M), abnormal microtubule number (F) or organization (G) and multiple alterations (B, I, J, K, L). Bars: A-C, E, H-M = 200nm; D=500nm; F, G = 100nm

Ultrastructural & Analytical Methods in Life Sciences

LS.6.P159
Immunofluorescence distribution of cytoskeletal and extracellular matrix antigens in dogfish Scyliorhinus canicula L. notochord

I. Dujmovic[1], I. Bocina[2], K. Vukojevic[2,3], M. Saraga-Babic[2,3]

[1]Faculty of Philosophy, Education department, Split, Croatia
[2]Faculty of Science, University of Split, Split, Croatia
[3]School of Medicine, University of Split, of histology and anatomy, Split, Croatia

idujmovic@ffst.hr
Keywords: dogfish, *Scyliorhinus canicula*, notochord, cytoskelet, extracellular matrix

Notochord is a structure that defines all members of the phylum Chordata, and plays an important role in the vertebrate development. It occurs during early embryogenesis; it is main skeletal element of embryo and serves as a source for the formation of the surrounding tissue [1]. Dogfish *Scyliorhinus canicula* L., is a cartilaginous fish, evolutionary positioned among cephalochordates (*Cephalochordata)* and teleost fish (*Osteychtyes*), and thus very interesting as an object of research [2].

In most species, notochord cells are vacuolated and becoming bigger in time, producing a thick three-layer sheath composed of collagen fibers and glycosaminoglycans [3-5]. Vacuolated cells permits elongation of growing embryo, as well as amortization and accommodations on biomechanical forces to the spine in the mature stage. Notochord is the first embryonic cellular structure that actively produces fibrillar extracellular matrix [6].

In this study we examined the immunohistochemical composition of notochord in ten young, both sexes specimens of dogfish *Scyliorhinus canicula* L., caught in the Adriatic Sea. The tissues were sectioned at cervical, truncal and caudal parts. Immunofluorescence techniques were applied on paraffin sections and observed under fluorescence microscope (Olympus BX61, Tokyo, Japan). We applied the antibodies against hyaluronic acid, citokeratin 8 and vimentin.

Applied immunofluorescence techniques have shown presence of cytoskeletal and extracellurar components in dogfish notochord and surrounding tissue. Hyaluronic acid positive cells of different intensity were seen in several parts of dogfish vertebra, including neural and hemal arch, as shown in “Figure 1a.”. Positive cells on hyaluronic acid were observed in the centrum of vertebra and in some notochordal cells ("Figure 1b.“). Since, in adult vertebrates the notochord retains only in nucleus pulposus of the intervertebral disc, whose main characteristic is proteoglycan-rich extracellular matrix, the presence of glycosaminoglycan hyaluronic acid in dogfish indicates the notochordal origin of nucleus pulposus cells. Double immunofluorescent staining to citokeratin 8 and vimentin confirmed the presence of these intermediate filaments in notochordal cells and vertebral centrum ("Figure 1c.“), indicating dogfish cartilaginous vertebra. Applied antibodies on sections through the cervical vertebra have shown that some notochordal cells coexpressed citokeratin 8 and vimentin, while some of them were labeled only by vimentin antibody ("Figure 1d.“).

The presence of similar cytoskeletal and extracellular matrix components confirmed in dogfish as well as in other vertebrates indicates the preservation of genes and proteins during evolution.

1. Stemple, D.L., Development 132(11), (2005). p. 2503-12.
2. Coolen, M., et al., CSH protocols (2008) p. pdb.emo111.
3. Adams, D.S., R. Keller, and M.A.R. Koehl, Development 110(1), (1990). p. 115-130.
4. Bocina, I. and M. Saraga-Babic, International journal of biological sciences 2(2), (2006), p. 73-8.
5. Risbud, M.V., T. Schaer, and I.M. Shapiro Developmental Dynamics 239(8), (2010). p. 2141-2148.
6. Risbud, M.V. and I.M. Shapiro, Critical Reviews in Eukaryotic Gene Expression 21(1), (2011). p. 29-41.

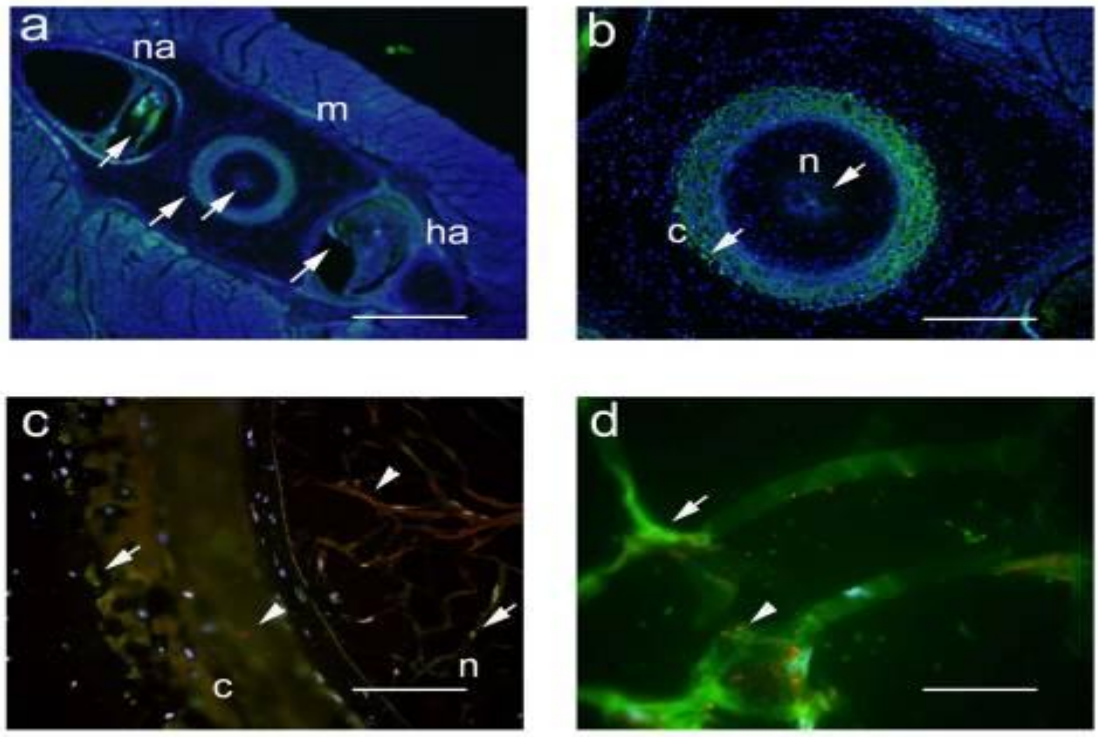

Figure 1. Transverse sections throughout dogfish *Scyliorhinus canicula* L. vertebra. a - Hyaluronic acid positive cells (*arrow*) of different intensity are seen in neural arch (na), hemal arch (ha), centrum (c) and notochord (n) of vertebra, x4. *Scale bar* 250 µm. b - Positive cells on hyaluronic acid observed in the centrum (c) and in several notochordal cells (n), x10. *Scale bar* 100 µm. c – Immunostaining to vimentin (arrow) and citokeratin 8 (arrowhead) confirming presence of these intermediate filaments in vertebral centrum (c) and notochordal cells (n), x40. *Scale bar* 25 µm. d - Section through the cervical vertebra showing some notochordal cells coexpressing citokeratin 8 and vimentin (arrowhead), while some of them are labeled only by vimentin antibody (arrow), x100. *Scale bar* 10 µm.

Ultrastructural & Analytical Methods in Life Sciences

LS.6.P160
Interaction between mammalian cells and bacterial inclusion bodies through light and electron microscopy techniques

J. Seras-Franzoso[1,2], A. Sánchez-Chardi[3], E. García-Fruitós[4,1,2], M. Roldán[3], E. Vázquez[4,1,2]
A. Villaverde[4,1,2]

[1]Universitat Autònoma de Barcelona, Genetics and Microbiology, Cerdanyola del Vallès, Spain
[2]Ciber de Bioingeniería, Biomateriales y Nanomedicina (CIBER-BBN), Cerdanyola del Vallès, Spain
[3]Universitat Autònoma de Barcelona, Microscopy Facility, Cerdanyola del Vallès, Spain
[4]Universitat Autònoma de Barcelona, Institut de Biotecnologia i de Biomedicina, Cerdanyola del Vallès, Spain

Alejandro.Sanchez.Chardi@uab.cat
Keywords: Bacterial inclusion bodies, tumoral cells, microscopy techniques

Bacterial Inclusion Bodies (IBs) are protein aggregates commonly observed during recombinant protein production processes in microbial hosts. These sub-micron particles, firstly regarded as by-products, have been shown to be highly pure, mechanically stable and biocompatible protein deposits able to retain biological activity [1, 2]. In this scenario, several potential applications for bacterial IBs have recently emerged, being particularly appealing the use of this particulate material in biomedicine [3]. In recent years, it has been also demonstrated that these protein deposits, when formed by protein with a therapeutic interest can actually rescue challenged cells in culture [4]. Nevertheless, despite the clear recovery of the IB treated cells, the mechanism by which the targeted cells obtain functional protein from IBs remains unsolved.

To clarify this fact, a complete structural and ultrastructural evaluation of eukaryotic cell-IBs interaction at 0, 0.5, 1, 3, 8 and 24h, after the addition of the IBs, was performed using light (CLSM) and electron microscopy (SEM and TEM) techniques. The evaluation evidenced the fine architecture of IBs (Figure 1) and its interaction with mammalian cells: when placed on cell surface, filopodia of HeLa cells rapidly contact with IBs at early times of the study (Figure 1) being subsequently uptaken via endocytosis at latter times (Figure 2).

In summary, this study reports for the first time the ultrastructure of IBs and the interaction with eukaryotic cells characterized with conventional and non-conventional microscopy techniques.

1. de Marco,A. & Schroedel,A. Characterization of the aggregates formed during recombinant protein expression in bacteria. BMC. Biochem 6, 10 (2005).
2. Garcia-Fruitos,E. et al. Aggregation as bacterial inclusion bodies does not imply inactivation of enzymes and fluorescent proteins. Microb. Cell Fact. 4, 27 (2005).
3. Garcia-Fruitos,E. et al. Bacterial inclusion bodies: making gold from waste. Trends Biotechnol. 30, 65-70 (2012).
4. Vazquez,E. et al. Functional inclusion bodies produced in bacteria as naturally occurring nanopills for advanced cell therapies. Adv. Mater. 24, 1742-1747 (2012).

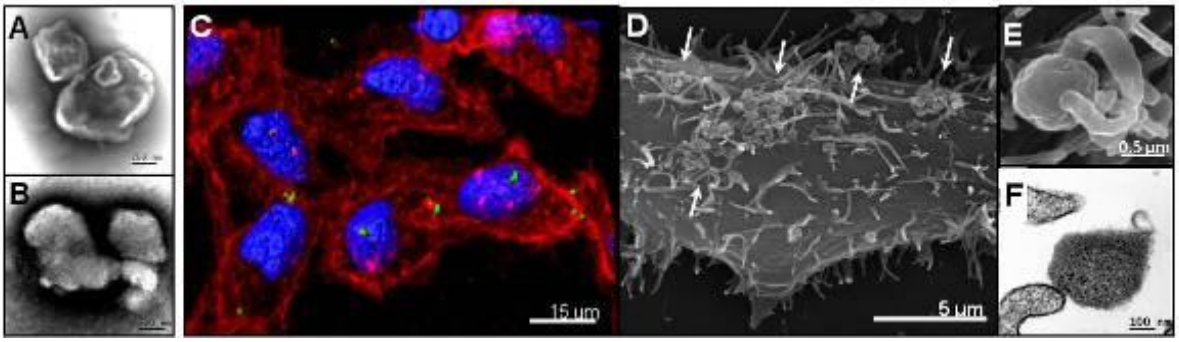

Figure 1. Representative micrographs of IBs and Hela interacting cells. A-B) Negative staining of ultrastructure and immunolocalization of IBs; C-D) General views of IBs on HeLa cells and E-F) Contact of IBs-filopodia at early times of the study (0-3h).

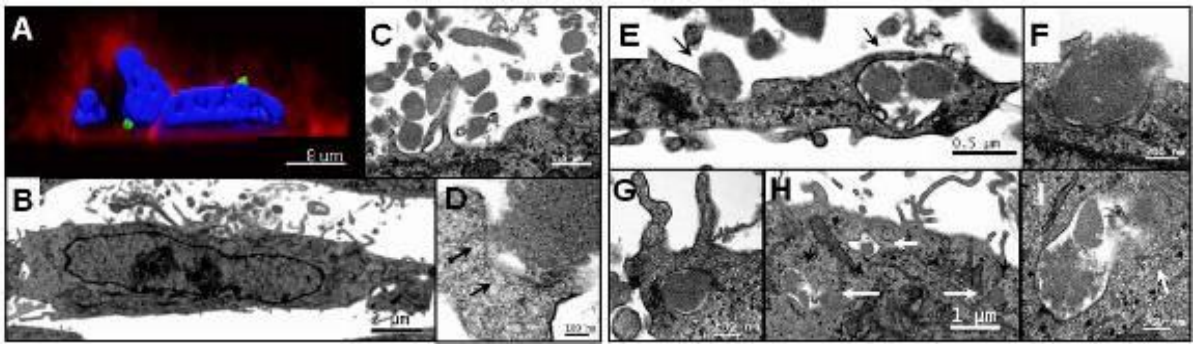

Figure 2. Representative micrographs of IBs and Hela interacting cells. A-C) Structural and ultrastructural details of IBs on HeLa cell surface; D) Detail of filopodia cell membrane disorganization after IB contact at latter times (8h-24h). At these times, several IBs were internalized via endocytosis (E-I) producing membrane disorganization also in endosomes (I).

Ultrastructural & Analytical Methods in Life Sciences

LS.6.P161
Three-dimensional arrangement of the *vasa vasorum* of the human great saphenous vein: a scanning electron microscopy and 3D-morphometry study.

M. Herbst[1], T. Hölzenbein[2], B. Minnich[1]

[1]University of Salzburg, Department of Cell Biology & Physiology, Salzburg, Austria
[2]PMU Salzburg, University clinics for vascular and endovascular surgery, Salzburg, Austria

markus.herbst@stud.sbg.ac.at
Keywords: vasa vasorum, corrosion casting, scanning electron microscopy

"*Vasa vasorum*" derives from Latin and literally means "vessels of the vessels", which describes their function of providing blood and oxygen to the arteries' and veins' wall. They, in turn, supply blood and oxygen to the rest of the body [1].

Hence the *Vasa vasorum* are a system of small blood vessels which supply large blood vessels. In detail a network of small arterioles, venules and capillaries which supply the outer two layers of large blood vessels [2,3].

The largest blood vessels in the body (e.g. the human great saphenous vein, the aorta, etc.) depend on this supporting network to maintain their health and function. Thus, the *Vasa vasorum* are an important part of the blood circulatory system [3,4].

The structure of the *Vasa vasorum* varies first of all with the size as well as with the function and location of the vessel. In the largest vessels it penetrates the tunica adventitia and the outer two third of the tunica media [4]. In smaller vessels the *Vasa vasorum* infiltrates only the adventitia. There are no *Vasa vasorum* in small vessels, because diffusion is sufficient for nourishment.

The aim of this study is the examination of the *Vasa vasorum* of the human great saphenous vein (*Vena saphena magna*, HGSV) in normal and pathological (varicose) conditions. We try to explore the optimality principles (minimal lumen volume, minimal pumping power, minimal lumen surface, minimal endothelial shear force) which may underlie the design of this *Vasa vasorum*. Using vascular corrosion casting (VCC), scanning electron microscopy (SEM) and 3D-morphometry (M^3) we are able to calculate optimum vessel diameter and branching indices of arterial, capillary and venous bifurcations and thus vascular optimality.

Another purpose of the study is the increase of knowledge of venous diseases, respectively to get an insight into the mechanism inducing varicogenesis.

For these purposes we examined explanted segments of the HGSV which were taken during harvesting for coronary bypass grafts or varicose vein segments, from the University clinics for vascular and endovascular surgery, PMU Salzburg. The process of vascular corrosion casting starts with the dissection of the feeding artery from the surrounding tissue under a dissecting microscope, which is then cannulated with a glass cannula (gauge ~80µm).

Prior to the injection of the methacrylic resin "Mercox-CI-2B", the *Vasa vasorum* have to be rinsed with saline using an automatic infusion pump (flow rate is about 7ml/hr). After polymerisation the specimens are macerated with 7.5% potassium hydroxide in order to remove all organic material. Thereafter, the casts are rinsed with distilled water for several times and frozen in distilled water. The ice-embedded casts are freeze-dried and mounted on a stub using the "conductive bridge method" [5]. After sputtering with gold and examination under the scanning electron microscope (FEI/Philips XL-30 ESEM), 3D-morphometry (M^3) is performed.

The *Vasa vasorum* are running predominately with the longitudinal axis of the vein (Figure 1). Arterial feeders (Figure 2) were found to approach the HGSV from nearby arteries every 15 mm forming a rich capillary network within the adventitia and the outer two thirds of the media in normal HGSV. In HGSV with intimal hyperplasia capillary meshes were found, which extended into the inner layers of the media. Within the media capillary meshes of the *Vasa vasorum* ran circularly (Figure 2).

The diameters of (i) arterial VV range from 11.6 to 36.6 µm, (ii) capillary VV from 4.7 to 11.6 µm and (iii) venous VV from 11.6 to 200.3 µm [6].

The three-dimensional network of the *Vasa vasorum* suggests that these layers are metabolically highly active and therefore require a continuous blood supply [6].

1. Ritman Erik L., Lerman A, Cardiovascurlar Research 75 (2007), p. 649-658.
2. Minnich B. *et al*, Microscopy and Microanalysis 13 (2007), p. 488-489.
3. Lametschwandtner A. *et al*, The Anatomical Record. Part A 281 (2004), p. 1372-1382.
4. Kachlík D. *et al*, Vasa - Journal of Vascular Diseases 37 (2008), p. 127-136.
5. Lametschwandtner A. *et al*, Mikroskopie 36 (1980), p. 270-273.
6. Kachlík D. *et al*, Journal of Vascular Research 44 (2007), p. 157-166.

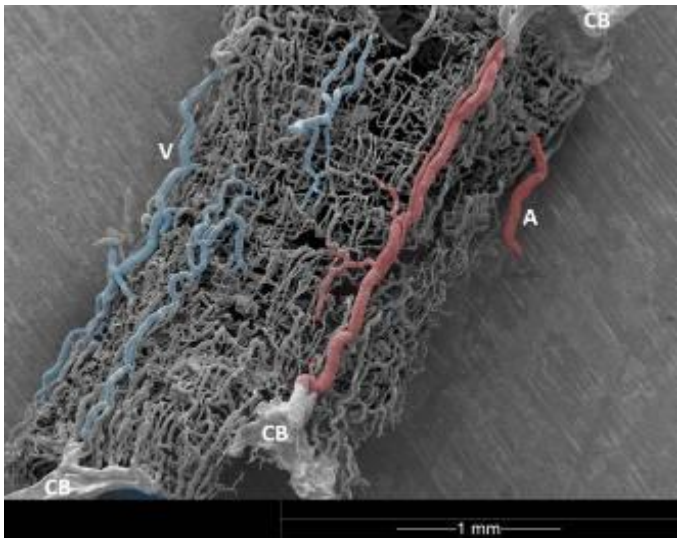

Figure 1. Abluminal view of the *Vasa vasorum*, which run predominately with the longitudinal axis of the vein. A part of the venous vessels is coloured in blue (V) and some arterial vessels in red (A). Conductive bridges (CB) with colloidal silver.

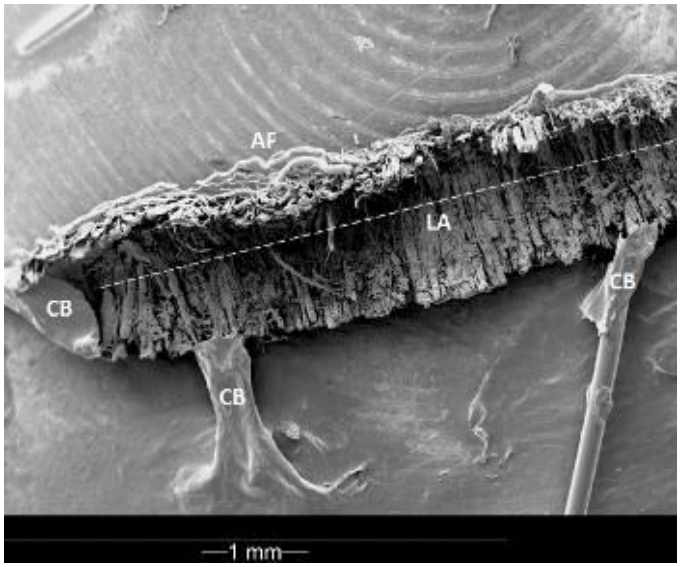

Figure 2. Luminal and abluminal view of the *Vasa vasorum*. The *Vasa vasorum* mainly run along the longitudinal axis (LA) of the vessel and radially to the muscle cells. Note the arterial feeder (AF) infiltrating this part of the HGSV. Conductive bridges (CB) with colloidal silver.

Ultrastructural & Analytical Methods in Life Sciences

LS.6.P162
Iron-rich hard dental tissues from the feral coypu investigated by STEM-EELS and -EDX

V. Srot[1], U. Salzberger[1], B. Bussmann[1], B. Pokorny[2], I. Jelenko[2], P.A. van Aken[1]

[1]Max Planck Institute for Intelligent Systems , Stuttgart Center for Electron Microscopy , Stuttgart, Germany
[2]Ecological Research and Industrial Cooperation, Velenje, Slovenia

srot@is.mpg.de
Keywords: analytical TEM (EDX and EELS), biomaterials, dental tissues, hydroxyapatite, iron

Many living organisms have the ability to form a diversity of biominerals. A large number among these biominerals are composite materials, where an organic matrix is closely linked with crystalline or amorphous minerals [1]. These unique combinations formed under controlled conditions possess masterpiece architectures which often lead to extraordinary physical and mechanical properties compared to their inorganically formed mineralogical counterparts [2, 3].

Rodents have enlarged front upper and lower pairs of incisors that continuously grow through their lives; rodents maintain these at constant length through dental wear from gnawing hard surfaces. The front surface of the incisors is enamel, which is the hardest tissue of the body consisting of 96 wt.% of inorganic material; the inner surface represents softer dentine that forms the bulk of the teeth [4]. The characteristic orange-brown color of the surface of incisors of different rodent species is identified with the presence of iron [5]. A report on the characterization of the surface layer of enamel from rat incisors by using electron microprobe analysis [6] demonstrated that the amount of iron (Fe) is 10-30 wt.%.

For our study, incisors of the adult male of feral coypu (*Myocastor coypus* Molina), free-ranging in the swamp habitat near Ljubljana, Slovenia, were investigated. The microstructure and the chemical composition at the enamel surface were studied in detail by using energy-dispersive X-ray spectroscopy (EDX) and electron energy-loss spectroscopy (EELS) combined with scanning transmission electron microscopy (STEM). P-$L_{2,3}$, C-K, Ca-$L_{2,3}$, O-K and Fe-$L_{2,3}$ energy-loss near-edge structures (ELNES) were acquired at high energy and high spatial resolution using a VG HB501UX microscope.

Our preliminary experiments unveiled the layer with a thickness of approximately 0.4 □m (Fe-SL in Figure 1) present on top of the Fe-rich enamel (Fe-E in Figure 1) that has not been reported in the present literature. Annular dark-field (ADF)-STEM images of the cross-sectional view showing the interface between the Fe-rich surface layer (Fe-SL) and the Fe-rich enamel (Fe-E) are presented in Figure 1. According to our EDX measurements (not shown here) the amount of Fe present in this layer (Fe-SL) is much higher compared to the concentration levels for hard dental tissues in rodents reported by now. In addition, we observed lines of different thicknesses (10-20 nm) within the Fe-rich layer (Fe-SL in Figure 1), where minor variations in the elemental composition were detected by EDX. In Figure 2, O-K and Fe-$L_{2,3}$ ELNES acquired from the Fe-rich enamel (Fe-E) and from the Fe-rich surface layer (Fe-SL) are compared. The O-K ELNES (Figure 2a) is distinctly different when comparing the spectra of both compounds. The Fe-$L_{2,3}$ edges (Figure 2b) of Fe-rich surface layer (Fe-SL) and of Fe-rich enamel (Fe-E) appear similar. They show two main spin-orbit split L_3 and L_2 peaks exhibiting characteristics of the Fe valence state [7,8]. Based on ELNES fingerprinting we can conclude that Fe in the Fe-rich layer (Fe-SL) and in the Fe-rich enamel (Fe-E) is predominantly in Fe^{3+} state. In the course of our work a detailed chemical composition of enamel at different positions with respect to the Fe-rich layer were studied and the corresponding Ca/P ratios were determined and will be discussed. In addition, EDX and EELS measurements were performed at the dentine-enamel junction and at the dentinal tubules.

There is wide occurrence of iron minerals in many living organisms where they fulfil several different functions. The present discovery of this highly Fe-enriched compound will give us new insight in the linkage between the functional properties and the microstructure and chemical composition of hard dental tissues.

1. P.U.P. Gilbert *et al*., Rev Mineral Geochem 59 (2005), 157.
2. U.G.K. Wegst and M.F. Ashby, Philos Mag 84 (2004), 2167.
3. A.P. Jackson and J.F.V. Vincent, J Mater Sci 25 (1990), 3173.
4. B.A. Niemec in “Small animal dental, oral & maxillofacial disease”, (Manson Publishing Ltd, London) (2010).
5. E.V. Pindborg, J.J. Pindborg and C.M. Plum, Acta Pharmacol 2 (1946), 294.
6. A. Halse, Archs Oral Biol 19 (1974), 7.
7. L.A.J. Garvie, A.J. Craven and R. Brydson, Amer Mineral 79 (1994), 411.
8. P.A. van Aken, B. Liebscher and V.J. Styrsa, Phys Chem Minerals 25 (1998), 323.
9. The research leading to these results has received funding from the European Union Seventh Framework Programme [FP7/2007-2013] under grant agreement n°312483 (ESTEEM2).

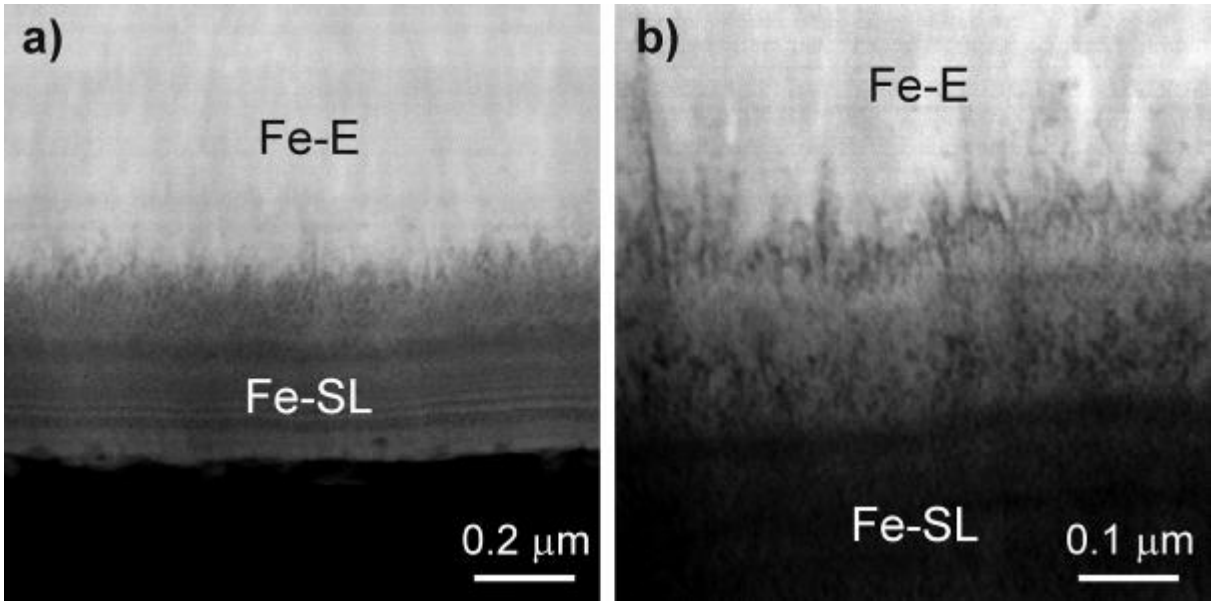

Figure 1. ADF-STEM images (a, b) of the interface between the Fe-rich surface layer (Fe-SL) and the Fe-rich enamel (Fe-E).

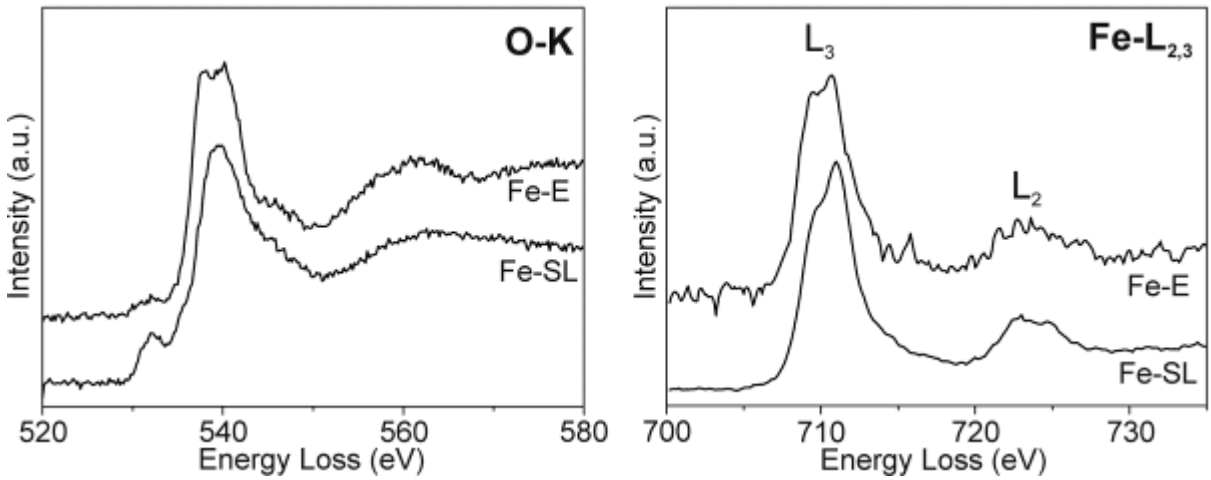

Figure 2. O-K and Fe-$L_{2,3}$ ionization edges acquired from the Fe-rich enamel (Fe-E) and from the Fe-rich surface layer (Fe-SL).

Ultrastructural & Analytical Methods in Life Sciences

LS.6.P163
Correlation of structure and mass via scanning transmission electron microscopy

S. Tacke[1], V. Krzyzanek[1,2], R. Reichelt[1], J. Klingauf[1]

[1]University of Muenster, Institute for Medical Physics and Biophysics, Muenster, Germany
[2]Institute of Scientific Instruments of the ASCR, v.v.i., Brno, Czech Republic

s.tacke@uni-muenste.de
Keywords: quantitative scanning transmission electron microscopy, mass measurement

Scanning transmission electron microscopy (STEM) is known for its strength of offering high-resolution images [1] and tomographs of thick samples [2]. Beyond imaging, STEM enables the access to quantitative data, e.g. by electron energy loss spectroscopy [3]. Additionally, STEM also allows the mass determination of nano-scaled structures like organelles [4], or protein complexes [5]. Despite this technique was already introduced in 1962 by Zeitler and Bahr [6], only a few institutions worldwide established this method (for review see e.g. [7,8]). This might be owed to the excellent alternatives like quantitative mass spectrometry [9] or mass measurements utilizing nanochannel resonators [10]. Nevertheless, quantitative scanning transmission electron microscopy (q-STEM) offers still an advantage towards these techniques: the strong correlation between structure and quantitative data. For quantitative studies, like local thickness or mass measurements, commercial electron microscopes require modifications of the hardware as well as specific software packages for image processing and simulation of electron scattering.

Here, we present progress in the development of this analytical tool in terms of hard- and software extension as well as samples preparation. In our case, an “in-lens” high-resolution scanning electron microscope (S-5000, Hitachi Ltd., Japan) was equipped with a sensitive annular dark-field (ADF) detector. Consisting of a plastic scintillator with a time constant of 2.2 ns, a light pipe with high transparency, a ultra fast photomultiplier and a high-speed discriminator and counter (Figure 1 a)) [11,12] the ADF detector enables single electron counting. In combination with the dedicated software packages for image processing [13] and the electron scattering simulation [14], our system is capable to measure thicknesses up to approximate 7-fold mean free electron path λ within the specimen (e.g., 7λ at 30 keV carbon is approximate 180 nm) and molecular masses in the range of 100 kDa to a few GDa. Since the analysis requires a high level of purity of the specimen [15], we additionally investigated in a novel cryo high-vacuum transfer system for the contamination free transfer of freeze-dried samples (Figure 1 b)).

Therefore, our set-up seems to be well suited for the measurement of mass related parameters, such as mass of globular particles, mass per unit length, and mass per unit area of structures. With this progression we aim for interdisciplinary applications like simultaneous structure and mass thickness investigations of, for example, nanoparticles, hollow spheres, nanotubes, organic films and DNA-protein complexes [16].

1. D. A. Muller, Nature Materials 8 (2009), p. 263.
2. K. Aoyama et al, Ultramicroscopy 109 (2008), p. 70.
3. J. C. H. Spence, Reports on Progress in Physics 69 (2006), p. 725
4. S. Takamori et al, Cell 127 (2006), p. 831.
5. R. Reichelt et al, The Journal of Cell Biology 110 (1990), p. 883.
6. E. Zeitler and G. F. Bahr, Journal of Applied Physics 33 (1962), p. 847.
7. A. A. Sousa and R. D. Leapman, Ultramicroscopy 123 (2012), p. 38.
8. A. Engel in “Advances in Imaging and Electron Physics”, ed. P. W. Hakes, (Elsevier) (2009), p. 357.
9. M. Bantscheff et al, Analytical and Bioanalytical Chemistry 389 (2007), p. 1017.
10. J. Lee et al, Nano Letters 10 (2010), p. 2537.
11. V. Krzyzanek and R. Reichelt, Microscopy & Microanalysis 13 (Suppl. 3) (2007), p. 80.
12. H. Nusse et al, in: Proc. Microscopy Conference MC2011, Kiel (2011).
13. V. Krzyzanek and R. Reichelt, Microscopy and Microanalysis 9 (Suppl. 3) (2003), p. 110.
14. V. Krzyzanek et al, Journal of Structural Biology 165 (2009), p. 78.
15. S. Müller et al, Ultramicroscopy 46 (1992), p. 317.
16. This research is supported by the DFG Grants RE 782/11-1,-2. Vladislav Krzyzanek acknowledges the support by the grant CZ.1.07/2.3.00/20.0103 (EC and MEYS CR). We kindly acknowledge the help of Harald Nüsse and of the precision mechanical workshop, especially Martin Wensing. R. Reichelt initiated the project but unfortunately he passed away to early to see the results.

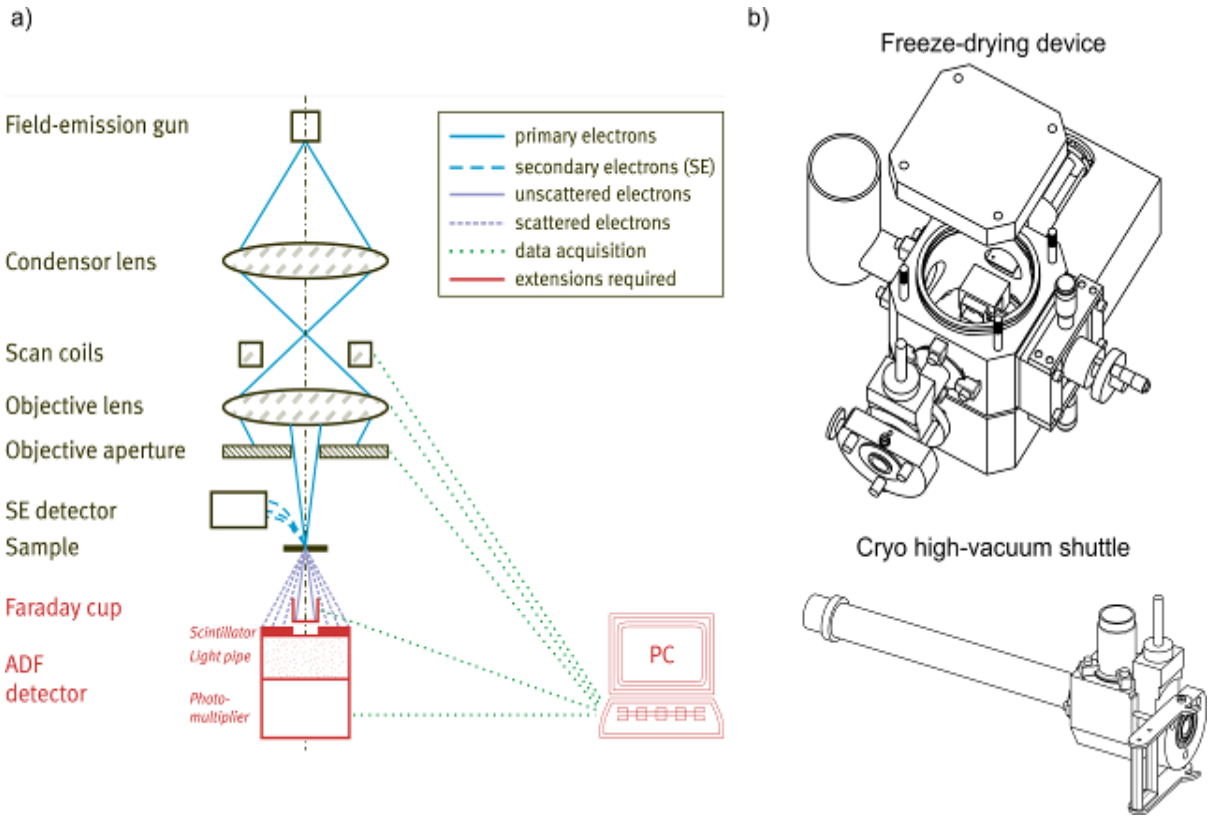

Figure 1. a) Schematic overview of the extended microscope and its main components. b) Schematic overview of the freeze-drying device and the cryo high-vacuum shuttle as well as the main components.

Ultrastructural & Analytical Methods in Life Sciences

LS.6.P164
Visualization of chlorophyll-protein complexes in thylakoid and artificial membranes

R. Mazur[1], L. Rudowska[2], E. Janik[3], J. Bednarska[3], A. Mostowska[2], W.I. Gruszecki[3], M. Garstka[1]

[1] University of Warsaw, Faculty of Biology, Department of Metabolic Regulation, Warsaw, Poland
[2]University of Warsaw, Faculty of Biology, Department of Plant Anatomy and Cytology, Warsaw, Poland
[3]Maria Curie-Skłodowska University, Institute of Physics, Department of Biophysics, Lublin, Poland

rmazur@biol.uw.edu.pl

Thylakoid membranes in chloroplasts of higher plants are sophisticated assemblies of chlorophyll-protein complexes (CP), lipids and free carotenoids, organized into two distinct domains: grana arranged in stacks of appressed membranes and non-appressed membranes consisting of stroma thylakoids and margins of granal stacks. CP complexes are organized hierarchically and spatially segregated in supercomplexes and megacomplexes. The LHCII-PSII supercomplexes are present in grana regions while LHCI-PSI supercomplexes are localized in unstacked thylakoids [1]. The lipids phase of thylakoids is formed mainly by monogalactosyldiacylglycerol (50% of the total lipid content), digalactosyldiacylglycerol (~30%) and sulfoquinovosyldiacylglycerol (~5-12%) as well as phosphatidylglycerol (~5-12%). These lipids not only form the bilayer structure of membranes but also stabilize the CP complexes and play an important role in forming uniquely curved thylakoids structure [2].

Spatial network of thylakoid membranes is investigated by electron microscopy (EM) and electron tomography (ET) [3]. Previously, based on confocal laser scanning microscopy (CLSM) images of chlorophyll (Chl) fluorescence, attributed mainly to LHCII-PSII [4,5], we constructed three-dimensional (3D) computer models of the whole chloroplasts in nearly intact state (*in situ*) [1]. We also presented 3D models of chloroplasts with different thylakoid stacking [6].

Now we present the improved 3D models of Mg^{2+}-dependent thylakoid stacking based on high numbers of CLSM images. As shown in Figure 1A at low magnesium ions concentration the Chl fluorescence exhibits wide dispersion within chloroplasts. Furthermore the 3D models revealed that grana stacks are unfolded and LHCII-PSII migrated to stroma thylakoids (Figure 1B-D). At stacked conditions Chl fluorescence is condensed (Figure 1E) and grana regions are clearly separated and merge only at the edge of stacks (Figure 1F-H). Furthermore, the distribution of PSI and PSII in thylakoids is analyzed by specific excitation of chlorophyll *a* and *b* species as well as by selective detection of fluorescence emission from both photosystems.

The arrangements of CP complexes in relations to lipid phase is present in LHCII-containing model membranes. Red fluorescence is attributed to LHCII (Figure 2A), while the green fluorescence is related to lipid phase (Figure 2B). As shown in Figure 2C (co-localization of fluorescence emissions) the LHCII complexes are incorporated in lipid multilayer similarly to native thylakoid membranes.

1. I. Rumak, R. Mazur, K. Gieczewska, J. Kozioł-Lipińska, B. Kierdaszuk, W.P. Michalski, B.J. Sheill, J.H. Venema, W.J. Vredenberg, A. Mostowska, M. Garstka. BMC Plant Biology 12 (2012) p.72.
2. T. Pália, G. Garab, L. I. Horváth and Z. Kóta. Cell. Mol. Life Sci. 60 (2003) p. 1591.
3. Ł. Rudowska, K.B. Gieczewska, R. Mazur, M. Garstka and A. Mostowska. Biochim. Biophys. Acta 1817 (2012) p. 1380.
4. M. Garstka, A. Drożak, M. Rosiak, J.H. Venema, B. Kierdaszuk, E. Simeonova, P.R. van Hasselt, J. Dobrucki and A. Mostowska. Biochim. Biophys. Acta 1710 (2005) p. 13.
5. M. Garstka, J.H. Venema, I. Rumak, K. Gieczewska, M. Rosiak, J. Kozioł-Lipińska, B. Kierdaszuk, W.J. Vredenberg and A. Mostowska. Planta. 226 (2007) p. 1165.
6. I. Rumak, K. Gieczewska, B. Kierdaszuk, W.I. Gruszecki, A. Mostowska, R. Mazur and M. Garstka. Biochim. Biophys. Acta. 1797 (2010) p. 1736.
7. This research was partially supported by Polish Ministry of Science and Higher Education founds (N303 4185 33).

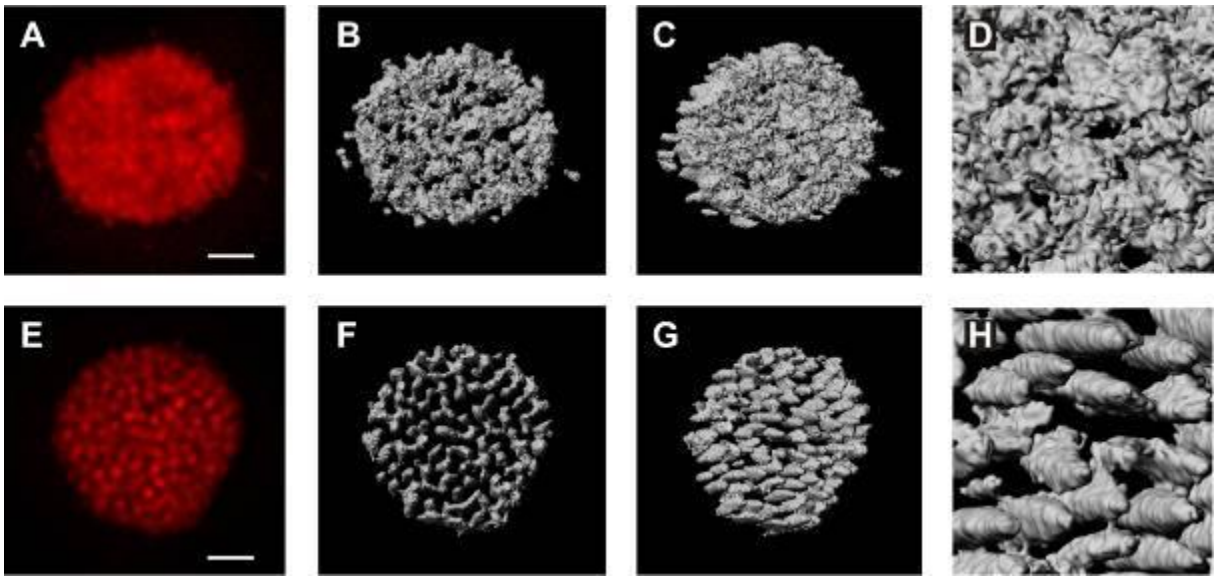

Figure 1. CLSM images (A, E) and computer models (B- D, E-G) of pea intact chloroplast incubated without (A-D) and in presence of 6 mM $MgCl_2$ (E-H). Scale bar = 2 µm

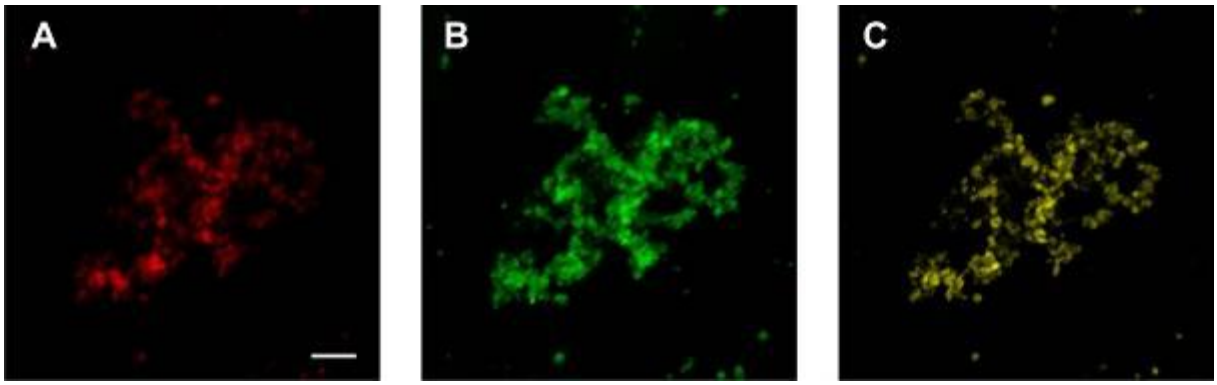

Figure 2. CLSM image of LHCII-containing model membranes stained with 3,3′-dioctadecyloxacarbocyanine perchlorate ($DiOC_{18}(3)$) membrane lipid dye. Red fluorescence of LHCII-bound chlorophylls (A), green fluorescence of $DiOC_{18}(3)$ in membranes (B) and co-localization analysis (C). Bar = 5 µm.

Ultrastructural & Analytical Methods in Life Sciences

LS.6.P165
Beta-glucan, from mushroom *Pleurotus ostreatus*, induces apoptosis and increases B16F10 cell adhesion and spreading

S. Biscaia[1], B.S. Borges[1], D.D.L. Bellan[1], L.F.D. Andrade[1], E. Carbonero[2], M. Iacomini[3]
S.M.D. Oliveira[1], C.C.D. Oliveira[1], D.D.F. Buchi[1], E.D.S. Trindade[1], C. Franco[1]

[1]Universidade Federal do Paraná, Cell Biology, Curitiba, Brazil
[2]Universidade Federal de Goiás, Biochemistry, Catalão, Brazil
[3]Universidade Federal do Paraná, Biochemistry, Curitiba, Brazil

stellee.biscaia@gmail.com
Keywords: polysaccharides, □□-glucan, *Pleurotus*, B16F10, murine melanoma.

The most aggressive form of skin cancer among several cancer types is the malignant melanoma [1]. Its occurrence is one of the most common in the world population [2]. Natural bioactive products discovery is of particular interest to cancer treatment, specially polysaccharides and compounds obtained from plants [3, 4, 5, 6]. *In vitro* assays showed yeast polysaccharides action on B16F10. Cell adhesion was over 75 to 80%, of cell invasion 89-99%, and there was an 80%reduction in metastases, in a dose-dependent manner [5]. Others have demonstrated that treatment with polysaccharides induced cytotoxicity [7], reduced solid tumor in murine models when treated *in vivo* [8]. The treatment with polysaccharide of *Pleurotus ostreatus* mushroom in Sarcoma 180 reduced tumor cells in 90% [9]. Literature suggests that these compounds antitumor mechanism of action involves cellular apoptosis [8].

The aim of this study was to assess the biological potential of □-glucan (P2) polysaccharide isolated [10] from *Pleurotus ostreatus var. Florida* mushroom. “In vitro” assays with B16F10 cell line (BCRJ) (murine melanoma) were treated with different concentrations (1, 10, 50, 100, 250 □g/mL) and times (24, 48 and 72 h).

MTT method (Fig. 1A), which evaluates cellular cytotoxicity, showed that 1 and 10 □g/mL of P2 after 72 hours was able to induce cell cytotoxicity. Neutral red method (NR) (Fig. 1B), which evaluates cell viability, demonstrated that this polysaccharide decreased cell viability, only with 250 □g/mL after 24 h of exposure. . After 48 h of exposure, a significant increase in viability was noted, with 1, 50 and 100 □g/mL of P2. Also, we have demonstrated that P2 induced cell death mechanisms, using Anexin V/ 7AAD. There was an increase in apoptosis, after 48 hours of treatment with the polysaccharide and an even more significant increase after 72 h (Fig. 1C). Significant difference in necrosis was seen after 48 hours of treatment (Fig. 1D) with decreased cell viability (Fig.1E). Adhesion assay showed that B16F10 cell line tends to adhere more to Fibronectin (FN) when compared to other examined substrates (Fig. 2A, B, C, D). We have also observed that this polysaccharide induced adhesion to Laminin (LN) compared to its control, after 48h of exposure. However, adhesion to Fibronectin, was reduced only after 72 h of treatment, compared to its control (Fig. 2E, F, G, H, I, J). Cells were more sprawled over Vitronectin (VIT), showing increased cell body after 24, 48 and 72 h (Fig. 1F), significantly. No ultra-structural changes were observed in cells treated with polysaccharide (P2) by Transmission Electron Microscopy (TEM) (Fig 2K, L, M, N) and Scanning Electron Microscopy (SEM) (Fig. 2O, P, Q, R). The cells remained without contact inhibition, stacking on one another, which is a typical characteristic of tumorigenic cells, and with similar morphology.

In summary, □-glucan treatment on B16F10 cells: was not cytotoxic and did not induce loss of viability, only in a few specific concentrations and times; induced cell death mechanisms, both apoptosis and necrosis; increased cell adhesion and spreading over specific substrates; did not induce ultrastructural cell changes in the concentrations and times analyzed. Interestingly, the increased cell adhesion and spreading, with a possible negative modulation of cell migration and invasion dynamics, may suggest that these cells may become more stationary. Thus, "in vitro" and "in vivo" assays showing efficacy in tumorigenic models, especially lung colonization model and solid tumor growth, employing B16F10 lineage in C57BL/6 Black mice should be performed next.

1. Long, J.S.; Ryan, K. M . Nature, 31 (2012) p.5045-5060.
2. WHO (World Health Organization). http://www.who.int/cancer/en/index.html. Acessed in 01/02/2013.
3. Ho, M.; Hsieh, Y.; Chen, J.; Chen, K.; Chen, J.; Kuo, W.; Lin, S.; Chen, P. Evidence-Based Complementary and Alternative Medicine. 2011 (2011): article ID 507920, 13 pages.
4. Zhang M, S.W.; Cui, P.C.K.; Cheung, Q.; Wang. Trends in Food Science & Technology. 18 (2007), p.4-19.
5. Han, S.; Lee, C.W.; Kang, J.S.; Yoon, Y.D.; Lee, K.H.; Lee, K.; Park, S.; Kim, H. M. International Immunopharmacology. 6 (2006), p.697– 702.
6. GUIMARÃES, FSF; ANDRADE, LF; MARTINS, S.T.; ABUD, APR; SENE, RV; Wanderer, C; TiscorniaI, I.; Bollati-Fogolin, M.; Buchi, DF.; Trinade, ES. *BMC Cancer*. **10** (2010), 113, 14 pages.
7. Tong, H.; Xia, F.; Feng,L.; Sun, G.; Gao, X.; Sun, L.; Jiang, R.; Tian, D.; Sun, X. Bioresource Technology. 100 (2009), p.1682–1686.
8 Bae, J.; Jang, K.; Yim, H.; Jin, H. Cancer Letters. 218 (2005), p.43-52.
9. Sarangi, I.; Ghosh, D.; Bhutia, S.K.; Mallick, S.K.; Maiti, T.K. International Immunopharmacology. 6 (2006), p.1287-1297.
10. Santos-Neves, J.C.; Pereiera, M.I.; Carbonero, E.R.; Gracher, A.H.; Gorin, P.A.; Sassaki, G.L.; Iacomini, M. Carbohydr Res. 343(2008), p.1456-62.
11. We thank CME (Centro de Microscopia Eletrônica) from UFPR, for acquiring images.
12. This research was supported by CNPq (Brazil).

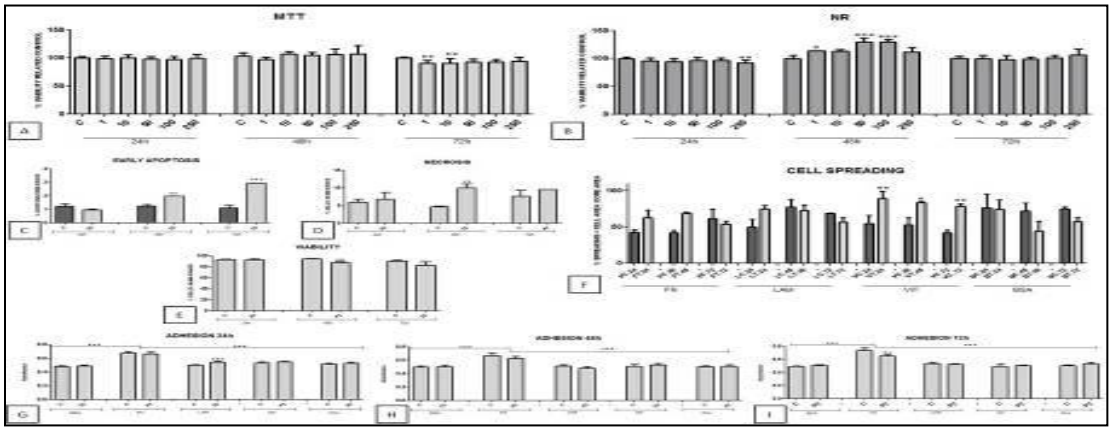

Figure 1. Statistical Results. [A] Cytotoxicity (MTT) and [B] viability (NR) assays B16F10 cells were exposed to P2 polysaccharide, in different concentrations (1, 10, 50, 100, 250 □g/mL), for a period of 24, 48 and 72h. These assays were performed in sextuplicata, in three independent experiments. [C] Early apoptosis; [D] Necrosis; [E] Viability; B16F10 cells were exposed to 100 □g/mL of polysaccharide P2, , for a period of 24, 48 and 72 h. Ten thousand events were analyzed by flow cytometry. These assays were performed in triplicate, in three independent experiments. [F] Spreading Assay. Evaluation of cell spreading degree by analyzing light microscopy images. B16F10 cells were subjected to adhesion assay, and images were acquired by the end (10 images for each replicate). ImageJ software was used to calculate cell area relative to nucleus area. [G] Adhesion Assay 24h; [H] Adhesion Assay 48h; [I] Adhesion Assay 72h. B16F10 cells were exposed to 100 □g/mL of P2, for a period of 24, 48 and 72 h. Subsequently, cells were subjected to adhesion on the following substrates: bovine albumin (BSA), Fibronectin (FN), Laminin (LAM), Vitronectin (VIT) and the plastic plate (PLA); for 2 hours. These assays were performed in triplicate, three times independents. Statistical analysis was assessed by one-way ANOVA and TUKEY post-test (* p<0,05, ** p<0,01 e *** p<0,001). C=control; T=treated.

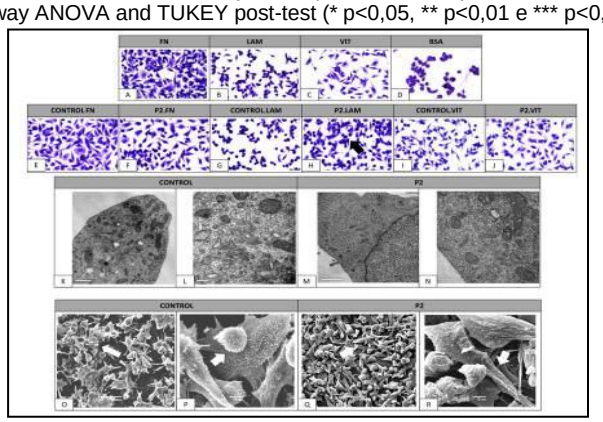

Figure 2. Images of Results. [A, B, C, D] Adhesion Assay Images between groups. The images in the first row represent the difference between groups (the same for all treatment times and concentrations). [E, F, G, H, I, J] Adhesion Assay Images between control and treatment. The second row shows the control with their respective treatment corroborating with statistic data viewed in adhesion assay above. ( ) Cells prefer the FN substrate; ( ) Increase adhesion on LN substrate. [K, L, M, N] Transmission Electron Microscopy (TEM). B16F10 cells were exposed to 1, 10 and 100 □g/mL of polysaccharide (P2), for a period of 24, 48 and 72 h. *The results are the same for all. The images A and C, show 1 □m, magnification 20.000X, and B, D show 0,5 □m, magnification 80.000X. [O, P, Q, R]* Scanning Electron Microscopy (SEM). B16F10 cells is the same morphology ( ) were exposed to 1, 10 and 100 □g/mL of polysaccharide (P2), for a period of 24, 48 and 72 h. *The results are the same for all. The images A and C, show magnification 500X, and B, D magnification 3.000X.*

Ultrastructural & Analytical Methods in Life Sciences

LS.6.P166
Quantitative 3D Analysis of Bioartificial Neovascular Assemblies with Focus on Angiogenesis by means of SEM

E. Polykandriotis[1,2], A. Lametschwandtner[3], A. Dragu[2], A. Arkudas[2], J.P. Beier[2], U. Kneser[4]
R.E. Horch[2]

[1]Sana Klinikum Hof, Division Plastic and Hand Surgery, Hof, Germany
[2]University of Erlangen, Dept. Plastic and Hand Surgery, Erlangen, Germany
[3]University of Salzburg, Dept. Cell Biology and Physiology, Salzburg, Austria
[4]University of Heidelberg, Dept. Hand, Plastic and Reconstructive Surgery, Burn Unit, Ludwigshafen, Germany

elias.polykandriotis@gmail.com

The cardinal role of vascularization and angiogenesis in regenerative medicine has become evident during the last years. The notion that cells, matrices and bioactive molecules would be sufficient to generate tissues and organs has long been overturned. Animal models of vascularization concentrate on two distinct patterns: The extrinsic mode and the intrinsic mode of vascularization (Fig. 1).
In the first one, a nascent capillary network is formed in the matrix by expansion of the surrounding vascular environment. Classic models of subcutaneous implantation belong to this class of experiments. In the latter one the matrix is vascularized by vascular outgrowth from its core outwards. These models of intrinsic vascularization, and the AV Loop Model in particular, possesses a plethora of advantages. The resulting bioartificial construct has a dedicated axial vascularity that permits secondary interventions, like cell loading, is readily transferable by standard microsurgical techniques in the sense of a free tissue transfer and it can be isolated from the surrounding environment by means of an isolation chamber (Fig 2).

Only morphological approaches are able to elucidate the three dimensional dynamics behind generation of an axially vascularized constructs. During the early stages of angiogenesis the onset of vascular induction was postponed until day 10-13 after implantation of a fibrin matrix in combination with an AV Loop in an isolation chamber. The neovascularization, contrary to earlier belief, propagated directly from the lumen of the axis by formation of angiogenic sprouts both from the venous and the interpositional venous graft, but not from the arterial segment of the arteriovenous loop (Fig 2). Results concerning the endothelial lining of the vein and the graft were unequivocal. Addition of proangiogenic growth factors had an effect both on the quantitative as well as on the morphological level.
During later stages, after 4 weeks, all features of orderly and vivid angiogenesis could be visualized by means of scanning electron microscopy of corrosion casts. Both intussusceptive as well as sprouting angiogenesis could be detected. All intussusceptive branching remodelling, intussusceptive arborisation and intussusceptive microvascular growth were documented (Fig 3).
Sprouting angiogenesis was concentrated at “hot spots”, indicating a temporospatial interplay of hypoxia, growth factors and alterations in microperfusion.

The AV Loop model is very suitable platform for morphological studies on angiogenesis. The resulting bioartificial construct is essentially an organoid with an arteriovenous vascular axis and a surrounding vascularized parenchyma. Perfusion techniques work perfectly with this pattern of perfusion and can deliver valuable information not only with corrosion casting methods but also with micro CT and MRI modalities.

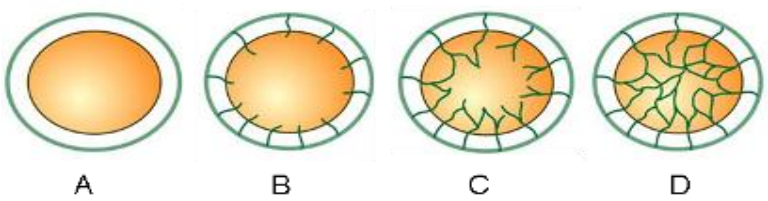
A
B
C
D

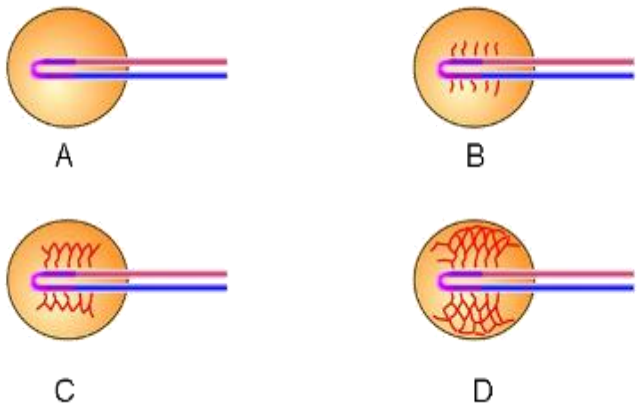
A
B
C
D

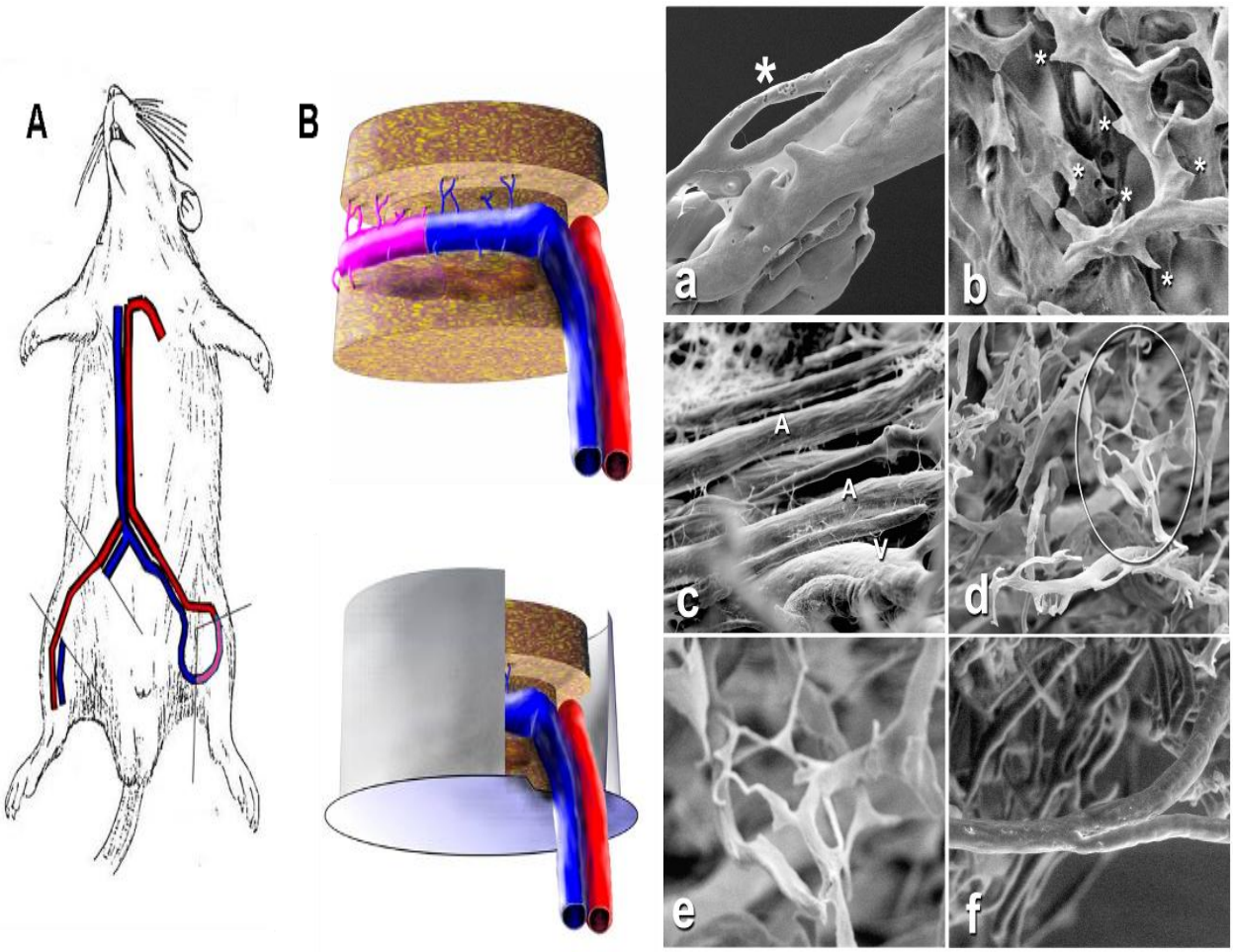
A
B
a
b
c
d
e
f

Ultrastructural & Analytical Methods in Life Sciences

LS.6.P167
Ultrastructural characterization, pathogenicity and host parasite relationship of microsporidian parasites infecting some marine fishes of the Red Sea, Egypt

F. Abdel-Ghaffar[1]

[1]Faculty of Science-Cairo University, Zoology, Cairo, Egypt

Fish represent one of the most important sources of high-quality protein essential for human feeding. They provide about 16% of the animal protein consumed by the world's population, according to the Food and Agriculture Organisation (FAO) of the United Nations. Parasitic infection is one of the most important problems facing fish production especially in the development of aquaculture. Among them, phylum Microsporidia constitutes the obligate intracellular protozoan parasites that contribute to mortality in fishes. In the infected cells, these parasites may either cause serious degradation of the cytoplasm and admise of the cell or they may elicit host cell hypertrophy. These produce a parasite hypertrophic host cell complex, the xenoma. It is quite clear that the electron microscopy is the gold standard for identifying specific species and diagnosing microsporidiosis and allows the understanding of their life cycle stages and their pathogenicity. In the present study 600 marine fish from the Red Sea in Egypt belonging to three different species were collected and examined for microsporidian parasites infection. Seventy eight fish specimens with a percentage of 14.5 were found to be infected. Regarding host parasite relationship, both parasite and host seem to benefit from the xenoma formation, the first offered an optimal growth conditions protecting it against host attack. The host benefits by confining the parasite to several or many infected cells to limit the free spread of the parasite. Xenomas were recovered, ruptured and the liberated spores were examined by photo research Zeiss light microscope. Each spore was elongated to ellipsoidal in shape and possessed a posterior vacuole which is characteristic to phylum Microspora. At the same time, materials were prepared in the usual way for transmission electron microscopic study. Ultrastructural microscopic study showed the presence of smooth membranes of the sarcoplasmic reticulum forming a thick, amorphous coat surrounding various developmental stages of the parasite. These were uninuclear, binucleated, and multinucleated meronts followed by detachment of the plasmalemma of the sporont from the sporophorous vesicle producing sporoblasts. Mature spores consist of a spore coat and spore contents. Ultrastructure characteristic organelles of the examined spores including uninucleated sporoplasm and a posterior vacuole located at the posterior end revealed that these different species are belonging to the genus *Pleistophora*. The polar tube consists of a straight shaft and a coiled region which was 20-26 coils for the type isolated from *Saurida tumbil*, 8-10 for *Pagrus pagrus* and 28-32 coils for *Epinephelus chlorostigma* arranged in many rows along the inside periphery of the spore. The polaroplast consisted of an anterior region of closely and loosely packed membranes. This study indicated that the parasites examined are belonging to three different species of the genus *Pleistophora*.

1. Abdel-Ghaffar F, Bashtar AR, Mehlhorn H, Al-Rasheid K, Al-Olayan E, Koura E, Morsy K (2009)Ultrastructure, development, and host-parasite relationship of a new species of the genus *Pleistophora* a microsporidian parasite of the marine fish *Epinephelus chlorostigma* Parasitol Res 106(1):39–46
2. Abdel-Ghaffar F, Bashtar AR, Mehlhorn H, Al-Rasheid K, Morsy K (2011) Microsporidian parasites :a danger facing marine fishes of the Red Sea. Parasitol Res 108(1):219–225
3. Morsy K, Abdel-Ghaffar F, Mehlhorn H, Bashtar AR, Abdel-Gaber R (2012)Ultrastructure and molecular phylogenetics of a new isolate of *Pleistophora pagri* sp. nov. (Microsporidia, Pleistophoridae(fromPagrus pagrusin Egypt.Parasitol Res 111(1):1587–1597
4. Abdel-Ghaffar F, Bashtar AR, Morsy K, Mehlhorn H, Al Quraishy S, Al-Rasheid K, Abdel-Gaber R (2012) Morphological and molecular biological characterization of *Pleistophora aegyptiaca* sp. nov .infecting the Red Sea fish Saurida tumbil. Parasitol Res 111(1):1587–1597

Ultrastructural & Analytical Methods in Life Sciences

LS.6.P168
Immunolabelling on sections in 2D and 3D, with speed and ecstasy

J. Flechsler[1], T. Heimerl[1], V. Heinz[1], R. Rachel[1]

[1]Universität Regensburg, Zentrum für Elektronenmikroskopie, Regensburg, Germany

Jennifer.Flechsler@ur.de
Keywords: Immuno gold labelling, 3D-reconstruction, CO_2-fixation

Antibody incubation steps in commonly used protocols for immunolabeling on ultrathin sections usually last for one hour or two hours. Here we show that shorter incubation times (down to 5 min) are absolutely sufficient and moreover, help to better preserve structural details. For this, we labeled ultrathin sections of cells of the autotrophic, anaerobic, hyperthermophilic Crenarchaeon *Ignicoccus* [1], embedded in Epon after high-pressure freezing (HPF) and freeze-substitution fixation (FSF) (Figure 1). Beside our methodical interest in speeding up the labeling protocol, our biological interest was in the localization of enzymes of the unique CO_2-fixation pathway - the dicarboxylate/4-hydroxybutyrate cycle. This also includes an enzyme converting 4-hydroxybutyrate, which is also known as "liquid ecstasy" (GHB), into 4-hydroxybutyryl CoA [2].

Among Archaea, *Ignicoccus* cells exhibit an extraordinary ultrastructure. In addition to a cytoplasmic membrane, there is an outer cellular membrane (OCM), which encases an intermembrane compartment (IMC). The IMC contains huge amounts of vesicles or tubes [3]. Another curiosity is that the archaeal ATP synthase is located in the OCM [4]. From this structural and functional compartmentalization of the cells, the question arose about the subcellular distribution of enzymes involved in different steps of the CO_2 fixation pathway.

Using our accelerated immunolabeling protocol, we could detect the acetyl-CoA-synthetase in association with the OCM and the 4-hydroxybutyryl-CoA-synthetase (the key enzyme) in the cytoplasm. For investigating spatial distribution we generated 3D-models on the basis of immunolabeled serial sections (Figure 2). From our results, it becomes evident that the CO_2 fixation takes place in different cell compartments. Thus, we are currently about to target further proteins of this CO_2-fixation pathway, to track down its route and get a deeper understanding in the physiology of these highly unusual cells.

1. H. Huber et al., PNAS 105 (2008), p. 7851
2. U. Jahn et al., J. Bacteriol. 189 (2007), p. 4108
3. R. Rachel et al., Archaea 1 (2002), p. 9
4. U. Küper et al., PNAS 107 (2010), p. 3152
5. This research was supported by a grant of the DFG (Germany)

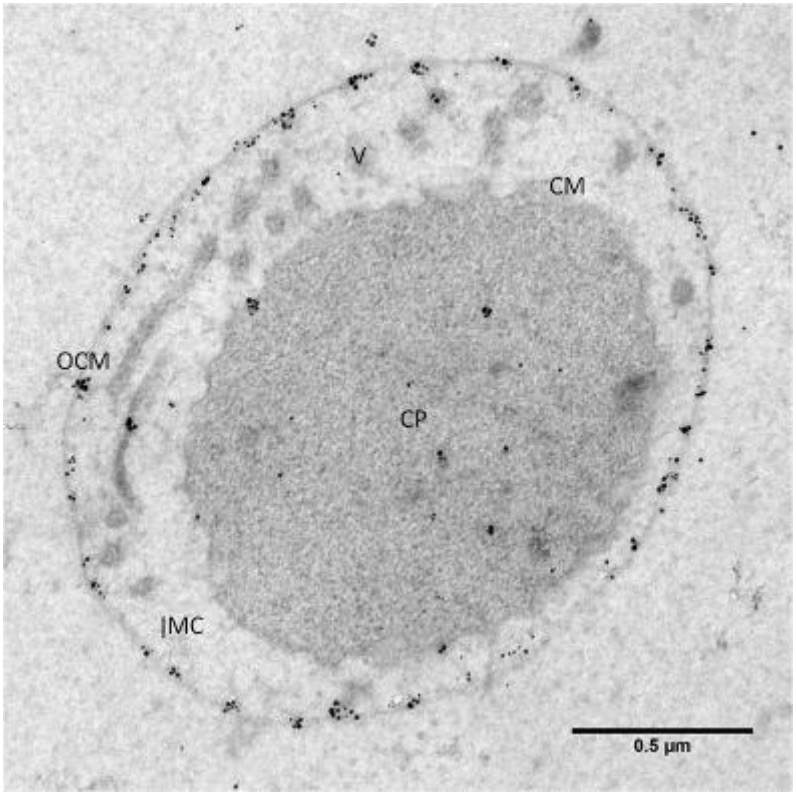

Figure 1. Ultrathin section of *Ignicoccus*. Cell was cryo-fixed, freeze-substituted, and embedded in Epon. Section was labelled with antibodies directed against the ATP synthetase; incubation time of antibodies 25 min; detection with goat anti-rabbit immunoglobulin “ultrasmall-gold”; bar, 0.5 µm.

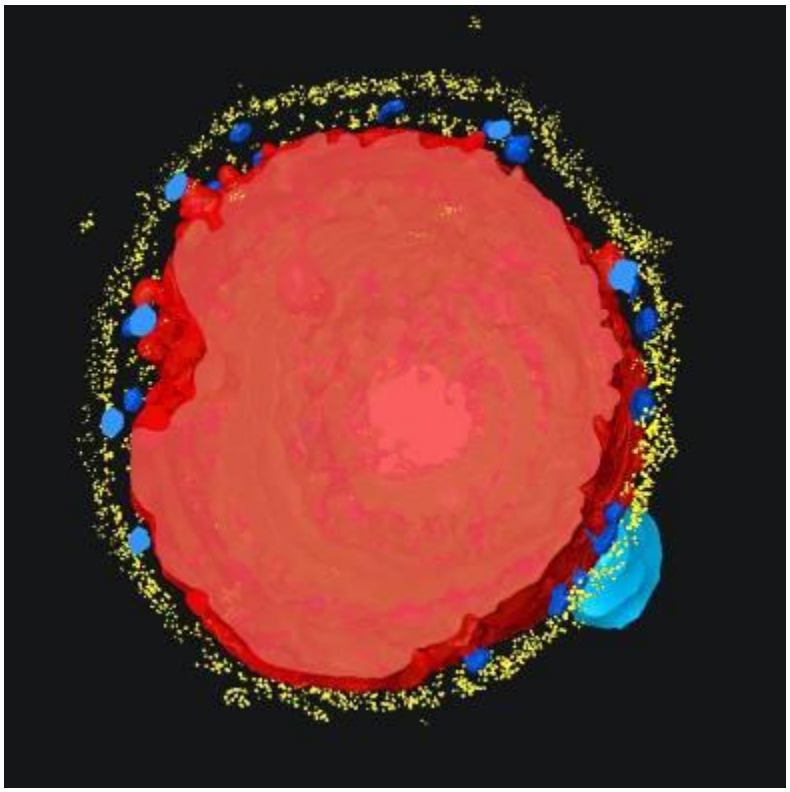

Figure 2. 3D-reconstruction and visualization of a data set of serial sections from an *Ignicoccus* cells, prepared as described, and labeled with antibodies directed the Acetyl-CoA synthetase. Alignment, segmentation, and visualization were done using AMIRA. Red: cytoplasm; blue: vesicles in the IMC; yellowish/white: gold; light blue: *Nanoarchaeum*.

Ultrastructural & Analytical Methods in Life Sciences

LS.6.P169
Freeze-Fracture Replica Immunolabeling revealed insights into the dynamics of urothelial plaques during blood-urine barrier formation *in vitro*

M.E. Kreft[1], T. Višnjar[1], H. Robenek[2]

[1]University of Ljubljana, Faculty of Medicine, Institute of Cell Biology, Ljubljana, Slovenia
[2]University of Münster, Leibniz Institute for Arteriosclerosis Research, Münster, Germany

robenek@uni-muenster.de
Keywords: FRIL, urothelium, urothelial plaque

The high-resolution imaging technique of freeze-fracture electron microscopy combined with immunogold labelling, i.e. freeze-fracture replica immunolabeling technique (FRIL) targets membrane proteins (or less commonly, the lipids) on an outer surface and deep within the cells or tissues. In the FRIL technique, conventional freeze-fracture replicas are first prepared; the biological material is then dissociated using sodium dodecylsulphate. The remaining layer of cellular components is so thin that it is transparent to the electron beam of electron microscope. The proteins or lipids are then localized by immunogold labelling, which reveals their spatial distribution superimposed upon a standard planar freeze-fracture view of the membrane interior. Moreover, because samples are freeze fractured prior to immunogold labelling step, both membrane leaflets of the plasma membrane (PM) and those of intracellular membranes are accessible for labelling [1].

As an illustration how FRIL has recently contributed to advances in cellular and molecular medicine, we will present the spatial organization of plasma membrane (PM) proteins uroplakins into urothelial plaques in urothelial cells (UCs) *in vitro*. Mouse and porcine UC cultures were prepared as described previously [3, 4]. After 2 months in culture, we performed FRIL experiments. The formation of urothelial plaques was additionally evaluated by molecular and ultrastructural analysis and by measuring TER.

By revisiting the localization of uroplakins in cultured UCs with the FRIL technique, the first unequivocal evidence for uroplakin-positive urothelial plaques in primary mouse and secondary porcine UC cultures has been achieved "Figure 1.". Apart from highly specific immunolabeling of molecular epitops, FRIL provides also new insights into dynamics of molecular aggregates, such as urothelial plaques, which contribute to the blood-urine barrier, the tightest and most impermeable barrier in the body.

To sum up, our findings illustrate that the information provided by FRIL is unique; without its wider application, substantial gaps in our knowledge of how membranes, organelles, cells, tissues and organs function in health and disease will remain.

1. NJ. Severs and H. Robenek, Methods Cell Biol 88 (2008), 181-204.
2. M.E. Kreft and H. Robenek, PloS ONE 7 (2012), e38509.
3. T. Višnjar et al., Histochem Cell Biol 137 (2012), 177-186.
4. We kindly acknowledge the technical assistance of Karin Schlattman and Sanja Čabraja.

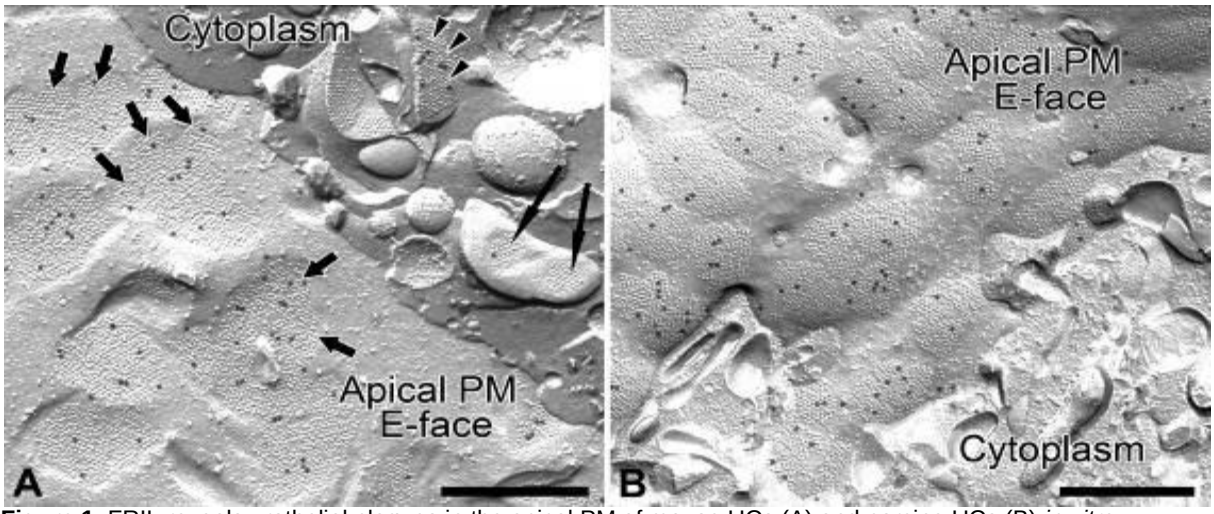

Figure 1. FRIL reveals urothelial plaques in the apical PM of mouse UCs (A) and porcine UCs (B) *in vitro*. Immunogold labelling for uroplakins is seen in urothelial plaques on the E faces of the apical PM, and also on E faces of discoidal-fusiform vesicles (DFV) membranes (arrowheads and long arrows in A). The number and ordering of uroplakin particles in urothelial plaques varies between DFVs. The DFVs marked with arrowheads, bear more uroplakin particles than those marked with long arrows. This could be interpreted as the sequential assembly of uroplakin particles into DFV membranes. Variations in the number of uroplakin particles in the urothelial plaques are also seen in the apical PM (A, B), suggesting that the gradual aggregation of small urothelial plaques into larger ones is not only limited to DFVs but still takes place in the apical PM (thick arrows). The edges of urothelial plaques appear rounded or straight. Bars, 500 nm.

Ultrastructural & Analytical Methods in Life Sciences

LS.6.P170
Differentiation of Epidermal and Hair Follicle Stem Cells in Rat Newborn Skin from Maternal Diabetes After Treated with Propolis or Olive Leaf Extract

H.S. Vatansever[1], M. Kivanc[1], E. Boz[2], S. Cakir[2], H. Cankorur[2], N.H. Mansoub[3], S. Samancioglu[4] G. Ercan[3]

[1]Celal Bayar University, Histology and Embryology, Manisa, Turkey
[2]Rahmi Kula High Scholl, , Balikesir, Turkey, Turkey
[3]Ege University, Biochemistry, Izmir, Turkey
[4]Ege University, Department of Internal Medicine Nursing, Izmir, Turkey

sedavatansever@yahoo.com
Keywords: stem cell, diabetes mellitus, hair follicle, propolis, olive leaf extract

The homeostasis of all self-renewing tissues is dependent on adult stem cells. The epidermis is maintained through self-renewal of stem cells and differentiation of their progeny to form the lineages of the interfollicular epidermis and adnexal structures, including the hair follicles and sebaceous glands. One location of epidermal stem cells is the permanent portion of the hair follicle, known as the bulge. It is likely that the adult stem cell repertoire responsible for maintaining the different components of the mammalian skin is established during late prenatal/early postnatal development.
Diabetes mellitus is a chronic metabolic disease which is one of the major contributors to chronic wound healing problems. Diabetic dermopathy is the most common cutaneous findings in diabetes patients and progressive thickness lost in the skin epithelium was also seen in early diabetes. Maternal diabetes could increase deformation of hair follicles, vacuolation, and degeneration of epidermal cell layers and disrupt epidermal cell differentiation in newborns.

The aim of this study was to evaluate epidermis and hair follicle stem cells function in newborn skin from maternal diabetes using immunohistochemical staining.

Adult female Wistar Albino rats were intraperitoneally injected with streptozotocin (45 mg/kg) dissolved in 0.1 ml sterile citrate buffer (0.01 M sodium citrate, pH 4.5) for 5 consecutive days. A week later after the 1st injection, tail vein blood glucose levels of mice with at least 12 hours starvation was measured by using glucose strips when blood glucose levels were 280 mg/dl, they were accepted as “diabetic” and they were mated with non-diabetic males to obtain newborns and randomly divided into 3 groups. First group pregnant rats were used a control group and were fed a standard diet, and water. Second and third group pregnant rats were fed standard diet but in their water was added olive leaf extract (50 mg/kg/day) or propolis (50 mg/kg/day), respectively. The blood glucose was measured every week. The first day of postnatal period, skin biopsies were taken from newborn from all groups. They were fixed with 10% formalin solution and embedded in paraffin using routine paraffin embedding protocols. The sections were stained with hematoxylen-eosine for histochemical analyses, or anti-cytokeratin-8, anti-cytokeratin-14, anti-CD133 and anti-CD117 antibodies for analyses immunohistochemical distribution of them.

The blood glucose levels were lower in mother with feeded with propolis. After histochemical analyses, all epidermal layers were detected in skin biopsies from all groups, but, vacuoles in epidermal cells were observed in all group, but, they were less in propolis feeding group. After immunohistochemical analyses, the cytokeratin-8 immunoreactivity was negative in all groups, cytoceratine-14 immunoreactivity was more abundant in newborn skin feeded with olive leaf extract or propolis. While CD133 immunoreactivity was detected in both basal layer of epidermis and hair follicle cells in newborn skin feeded with propolis, it was only detected in basal layer of epidermis in newborn skin feeded with olive leaf extract. In addition, CD117 immunoreactivity was only observed hair follicle cells in newborn skin treated with propolis.

Our results suggested that, the mitotically active basal layer of the newborn skin from maternal diabetes was more expressed cytokeratin-14 after feeding with olive leaf extract or propolis. However, epidermal and hair follicle stem cells were more active in newborn skin feed with propolis. When the propolis feeding may regulate blood glucose levels and its may provide to differentiation and function of stem cells in skin.

1. El-Sayyad HI, Khalifa SA, Fouda YA, Yonis AS. Basic nutritional investigation: Effects of diabetes and/or hypercholesterolemia on skin development of rat fetuses, Nutrition 28; 698–706, 2012.
2. Barker, N, Bartfeld, S, Clevers, H. Tissue-Resident Adult Stem Cell Populationsof Rapidly Self-Renewing Organs, Cell Stem Cell, 7; 656-670, 2010.
3. Forni, MF, Trombetta-Lima,M, Sogayar, MC. Stem cells in embryonic skin development. Biol Res 45: 215-222, 2012.

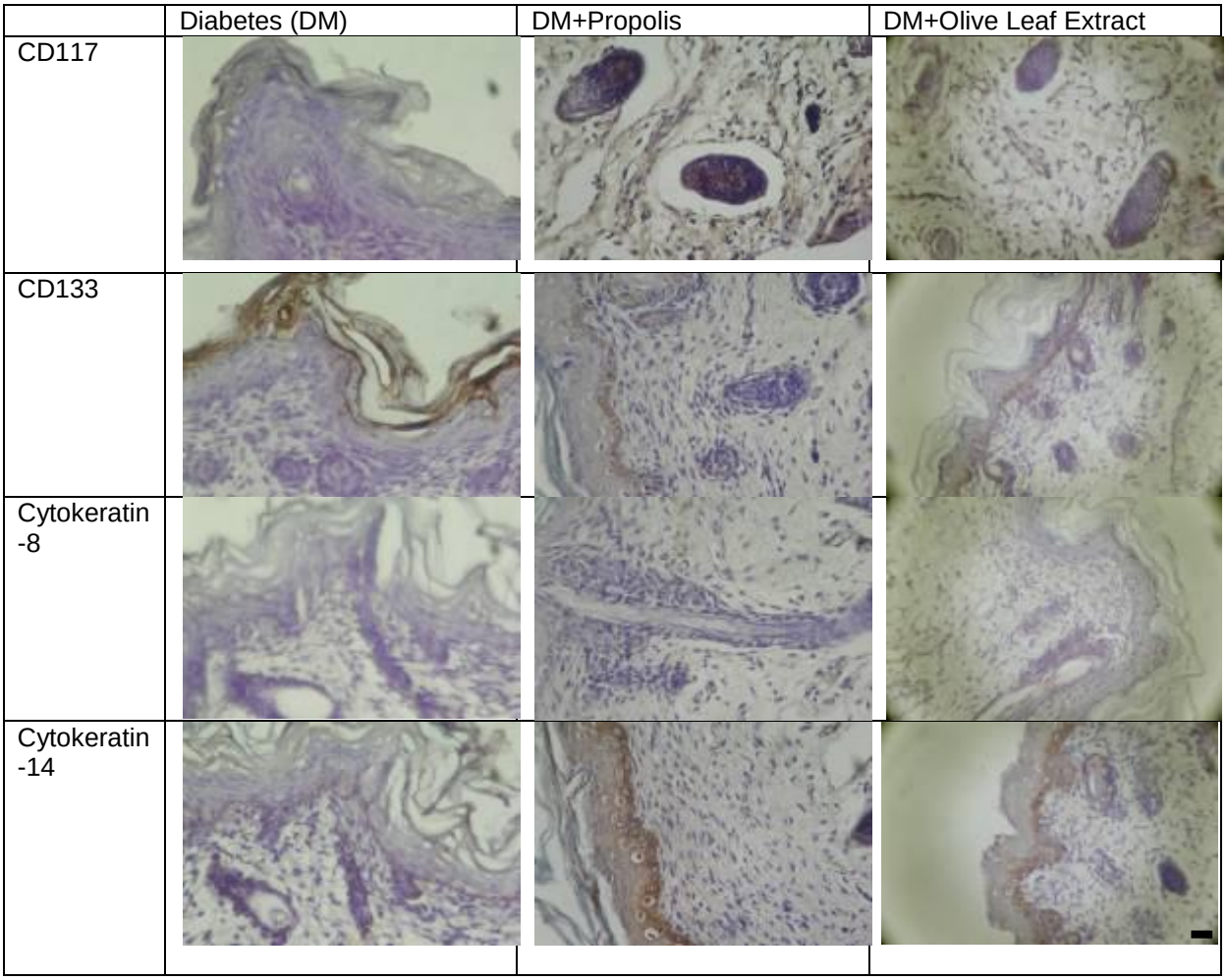

Figure 1. Expression of CD117, CD133, Cytokeratin 8 and 14 in skin from diabetes, DM+propolis or DM+olive leaf extract feed newborn (scale bar = 25 μm).

Ultrastructural & Analytical Methods in Life Sciences

LS.6.P171
3-D analysis of dictyosomes and multivesicular bodies in the unicellular model alga *Micrasterias* by FIB-FESEM series

G. Wanner[1], T. Schaefer[1], U. Luetz-Meindl[2]

[1]Ludwig-Maximilians-University, Ultrastructure, Munich, Germany
[2]University of Salzburg, Cell Biology Department, Salzburg, Austria

ursula.meindl@sbg.ac.at
Keywords: dictyosomes, ER, FIB-FESEM

The plant Golgi apparatus positioned at the cross-road between the secretory-biosynthetic and the endocytotic-vacuolar pathway fulfills a great number of different functions ranging from polysaccharide synthesis, protein glycosylations and transfer, sorting of products, regulation of vesicle trafficking up to vacuole formation and participation in degradation processes. As synthesis site for most constituents of the cell wall, it is central in plant development and plays an important role in response to environmental impact. The diverse functions of the Golgi apparatus are reflected in the unique morphology and structural integrity of the numerous motile dictyosomes of a plant cell [1]. Whereas secretory processes are structurally well investigated in different species, role and structural transformation of dictyosomes during endocytosis and degeneration are not yet well understood. Particularly, formation of multivesicular bodies (MVBs) essential for membrane recycling and as important constituents of the degeneration pathway, is still obscure. New 3-D analysis methods such as electron tomography [2] and focused-ion-beam-milling [3] combined with field emission scanning electron microscopy (FIB-FESEM) are able to throw new light on these structure dependent Golgi functions.

In the present study we employ FIB-FESEM for analyzing the 3-D architecture of dictyosomes and MVB formation in high pressure frozen and cryo-substituted interphase cells of the green algal model system *Micrasterias* [4] and take advantage of the ability of this technique to section very thin slices (5-10 nm) parallel to the block face and to capture cytoplasmic volumes of several hundred μm^3.

Our FIB-FESEM series and 3-D reconstructions show that interphase dictyosomes of *Micrasterias* are not only closely associated to an ER system at their cis-side which is common in different plant cells, but are surrounded by a huge “trans-ER” sheath (Figure 1) leading to an almost completely enwrapping of dictyosomes by the ER. This is particularly interesting as the presence of a trans-dictyosomal ER system is well known from mammalian secretory cells [5] but not from cell of higher plants to which the alga *Micrasterias* is closely related. In contrast to findings in plant storage tissue [6] indicating that MVBs originate from the trans-Golgi network or its derivatives our investigations show that MVBs in *Micrasterias* are in direct spatial contact with both trans-Golgi cisternae and the trans-ER sheath which provides evidence that both endomembrane compartments are involved in their formation.

1. C.Hawes,New Phytol 165 (2005), 466
2. B.H. Kang, E. Nielsen, M.L. Preuss, D. Mastronarde and L.A. Staehelin, Traffic 12 (2011), 313
3. C. Villinger, H. Gregorius, C..Kranz, K. Hohn, C. Munzberg, G. von Wichert, B.Mizaikoff, G. Wanner, and P. Walther, Histochem Cell Biol 138 (2012), 549
4. U. Meindl, Microbiol. Reviews 57 (1993), 415
5. S. Mogelsvang, B.J. Marsh, M.S. Ladinsky, and K.E. Howell, Traffic 5 (2004), 338
6. M.S.Otegui, R. Herder, J. Schulze, R. Jung and L.A. Staehelin, Plant Cell 18 (2006), 2567
7. We acknowledge the financial support by the Austrian Science Fund (project21035-B16 to U.L.-M)

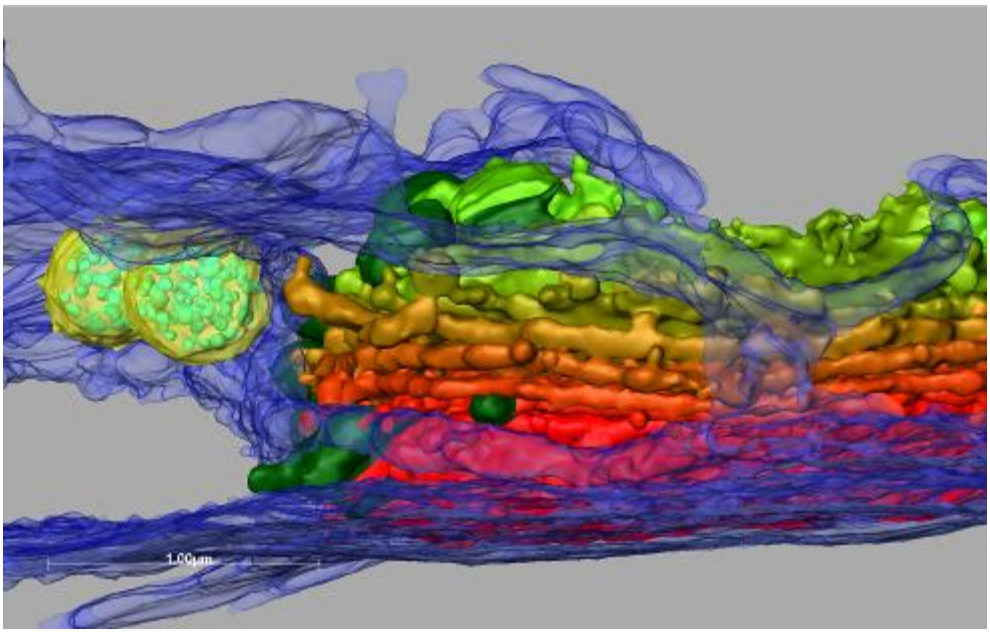

Figure 1. 3-D reconstruction of dictyosome (trans-side in green), ER (blue) and mulitvesicular bodies (yellow) of the alga *Micrasterias* from FIB-FESEM series. The ER envelopes cis- and trans-side of the dictyosome. Two MVBs are in contact with the ER.

Ultrastructural & Analytical Methods in Life Sciences

LS.6.P172
Accumulation of fluoride in plants and crops after hydrogen fluoride explosion in Gumi industrial area - Korea

H. Kim[1,2], W.K. Lee[1], S.N. Yoo[2], T.W. Kim[2,3]

[1]Koera University, School of life science and biotech, SEOUL, Korea, Republic of
[2]Hankyong National University, Institute of Ecological Phytochemistry, Ansung, Korea, Republic of
[3]Hankyong National University, of Plant Life and Environmental Science, Ansung, Korea, Republic of

502hyun@hanmail.net

Fluoride content was determined in plants near explosion accident region (Gumi, South Korea). A lot of plants have been found to contain high levels of fluorides, which were suddenly death within 24 hours.

Accumulation of fluoride in the leaf tissue of rice, melon, red pepper, corn and some fruit trees occurred after fatal hydrogen fluoride explosion. Severe injury of epidermal tissues of exposed plants was observed following cytosolic leakage and finally cell death. Using SEM-EDAX, fluoride was semi-quantitatively detected in some fruits and cereal crops.

Most of the samples were collected during October, 2012 according to the following procedure: plant samples were first taken from paddy field and upland near accident area, i.e. areas most remote from the sources of accident site and then from areas closer to fluoride explosion site.

For analyses of plant materials, samples were oven-dried in paper sacks at 80°C for at least 48 hours, finely ground in a Wiley mill, and stored in a dry place until used. A potentiometric method outlined by the Association of Official Analytical Chemists was followed in preparing the various samples for fluoride determinations and in making fluoride standard curves [1]. Small fragments of the leaves examined as above were treated for light and electron microscopy as follows: they were kept in 0.1 M phosphate buffered 3% glutaraldehyde pH 7 for 3 h at 4 °C, post fixed in aqueous 1% osmium tetroxide, dehydrated in acetone series and embedded in araldite. The cytosolic leakage on epidermal surface tissues was observed (Figure 1). A lot of plants were severely injured and fluoride distribution on epidermal surface tissues was analysed by SEM-EDAX (Figure 2). Typical symptoms, attributable to fluoride pollutants, consist in tip and margin necrosis by sudden membrane oxidation following cytosolic leakage (Figure 3). Particularly chlorophylls were severely damaged by Mg complex so called ‘metal-fluorine’ compounds [2, 3]. Fluoride distribution was able to be detected by SEM-EDAX compared to other mineral ions as calcium and phosphorus. Anthocyanin accumulating plants were relatively tolerant than crops only with green leaves as early observation [4].

1. Association of Official Analytical Chemists. *Official Methods of Analysis*. 13th ed. Horwitz W. editor. Washington DC, 1980
2. R. B. Fornasiero, Plant Science (2001),161, p. 979.
3. R. L. Heath, in: Biological Markers of Air-Pollution Stress and Damage in Forests”, ed National Academic Press (Washington, DC) (1989), p. 347.
4. L. Chalker-Scott, Photochem. Photobiol. (1999) 70, 1–9.
5. We kindly acknowledge the financial support by Agenda Project (No. PJ009220005 to T. W. Kim) from Rural Development Administration.

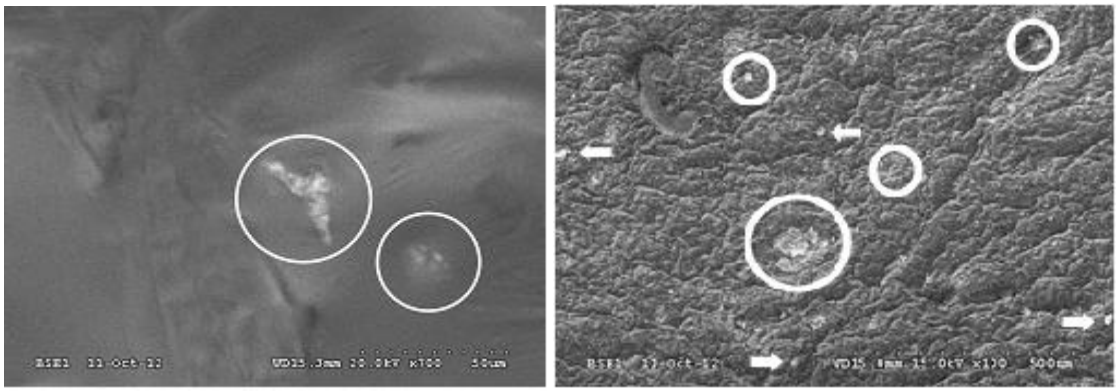

Figure 1. Cytosolic leakage (circle and arrow) on epidermal surfaces of red pepper leaf (left) and persimmon fruit (right) after HF explosion.

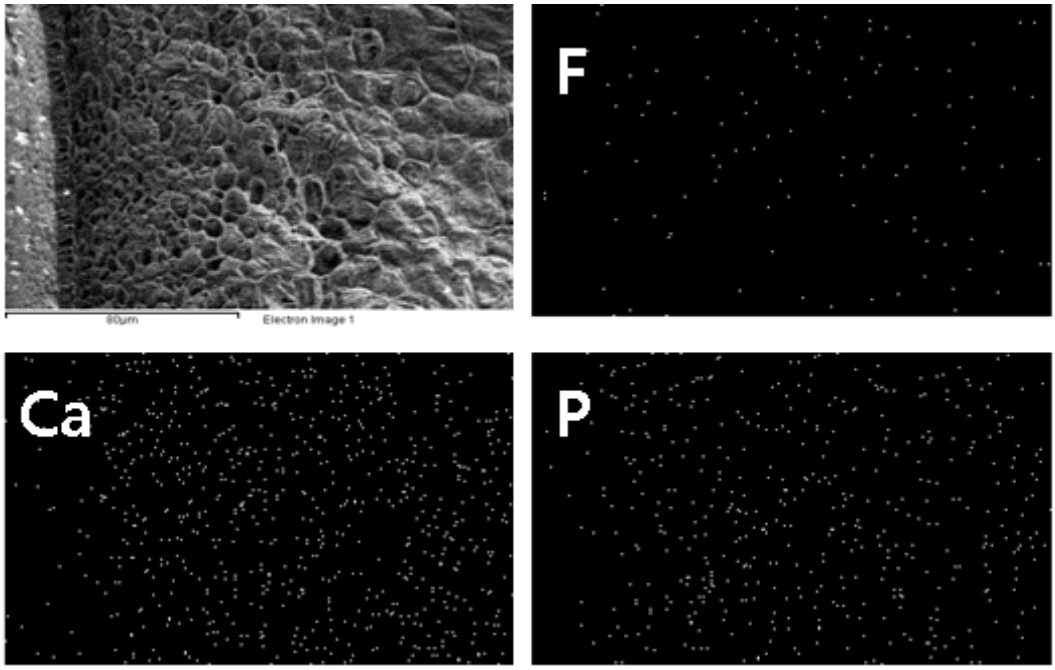

Figure 2. .Distribution of fluoride, phosphorus and calcium on epidermal surface of melon fruit (upper left) after HF explosion. Field emission SEM-EDAX analysis was conducted after cryo-SEM preparation.

Figure 3. Severe damaged crops (A: red pepper, B: pumpkin, C: peach, D: jujube)

LS.6.P174
A novel channel-like structure in the smooth endoplasmic reticulum of chicken retinal pigment epithelial cells visualized by rapid-freeze deep-etch technique

K. Miyaguchi[1]

[1]Shinsapporokeiaikai Hospital, Sapporo, Japan

kmiyaguchi@mbr.nifty.com
Keywords: rapid-freeze deep-etch technique, smooth endoplasmic reticulum, channel

The endoplasmic reticulum (ER) is a network of interconnected membranous tubules and flattened cisternae that extends throughout the cytoplasm. The smooth ER (sER) lacks ribosomes and is the predominant site of phospholipid and fatty acid synthesis and metabolism, and is also involved in Ca^{2+} storage and release. Although the sER plays crucial biological roles, its ultrastructure at the macromolecular level has not been fully elucidated. In this study, tubular sER in chicken retinal pigment epithelial (RPE) cells was visualized by rapid-freeze deep-etch method for the first time. Well-developed tubular sER membranes were densely packed to form distinct domains in the cytoplasm (Fig. 1A). Characteristic large, sphere-like protrusions extending from the ER membrane into the cytoplasm were found exclusively in the sER (Fig. 1B). These spherical protrusions had a hexagon or semicircle shape in a longitudinal cross-fracture, and a circle or rhombus shape in a tangential cross-fracture (Fig. 2). The dimensions of each protrusion were approximately 52×52×45 nm. High magnification images revealed that the protrusions contained many substructures and a large internal cavity. Filamentous structures sometimes attached a side protrusion of the spherical structure to the adjacent ER membrane. The protrusion is similar in appearance to the cytoplasmic domain of the ryanodine receptor, the major Ca^{2+} channel and the largest known ion channel. However, the protrusion is much larger than the cytoplasmic domain of the ryanodine receptor. This structure may be the cytoplasmic domain of a novel ion channel that is larger than any known ion channel.

1. K. Miyaguchi and T. S. Reese (1996) J. Struct. Biol. 116, 413-417.

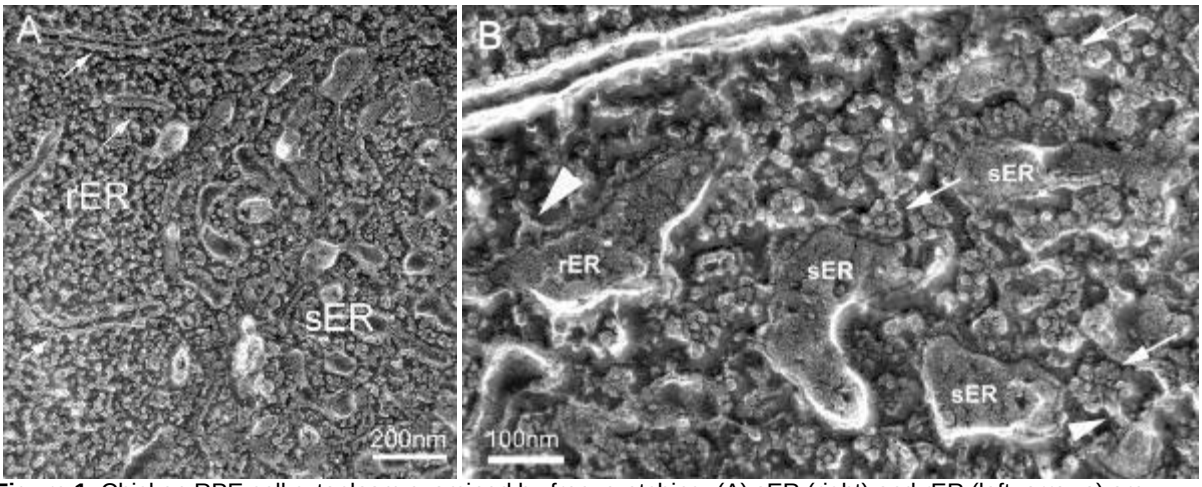

Figure 1. Chicken RPE cell cytoplasm examined by freeze-etching. (A) sER (right) and rER (left, arrows) are visible. Well-developed sER membranes form an abundant network of interconnected tubules. (B) Characteristic spherical structures (arrows) are frequently observed in the sER. These structures are not detected in the rER. Large arrowhead indicates a ribosome on the rER membrane. Small arrowhead points a filament between the spherical structure and ER membrane.

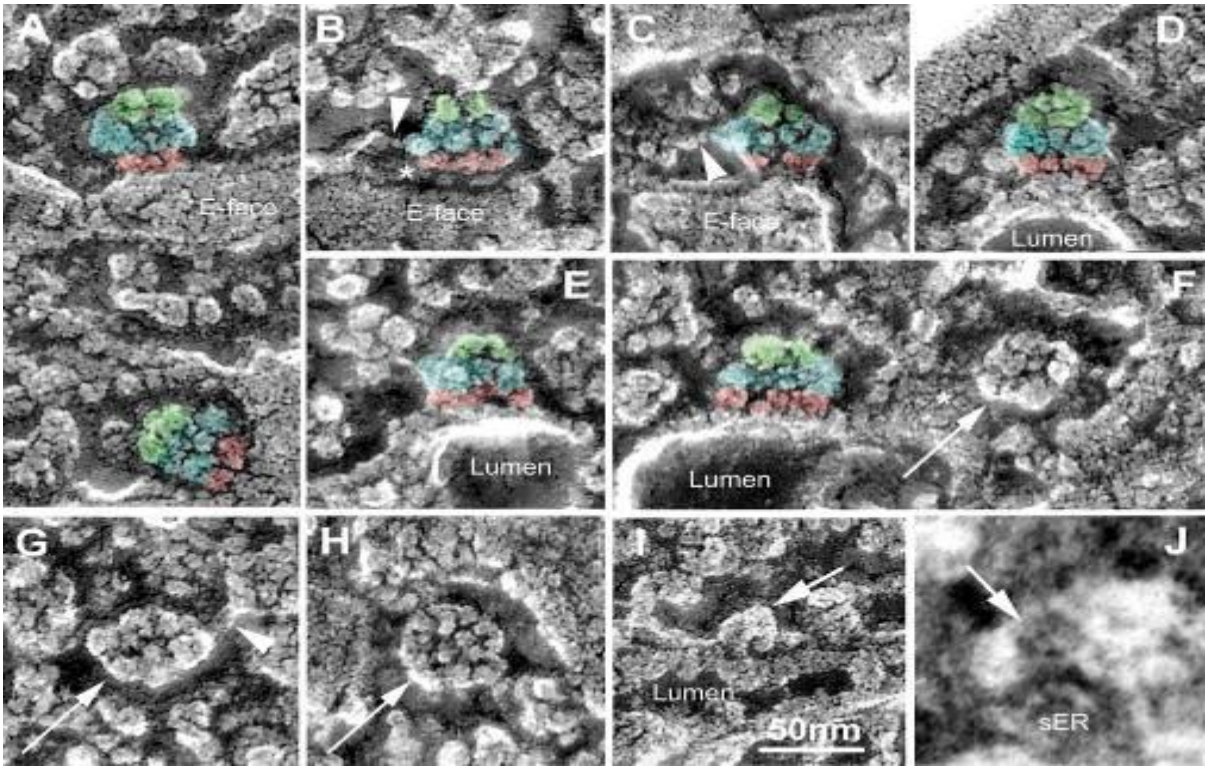

Figure 2. High magnification images of sER membranes examined by freeze-etching (A-I) and thin-section. (J). (A-F) Longitudinally cross-fractured spherical structures. The fractured protrusion has a hexagon or semicircle shape, several substructures, and an internal cavity. These substructures are located in the apical layer (green), the middle layer (blue), or the basal layer (red). The protrusions do not extend into the sER lumen (D-F). (F-H) Tangentially cross-fractured protrusions (arrows). The fractured protrusion has a circle or rhombus shape. By comparing B, C and H, it appears that the protrusion in H has been tangentially cross-fractured through the middle layer. (I) Ribosome on the rER membrane at the same magnification. The ribosome (arrow) appears to be bound to a pair of transmembrane particles (1). (J) An electron-dense structure (arrow) in a thin-section, reflecting a side view of the spherical structure. Filamentous structure (arrowheads) links a side protrusion of the spherical protrusion with the adjacent ER membrane. Asterisks indicate the true cytoplasmic surface of the sER membrane.

Ultrastructural & Analytical Methods in Life Sciences

LS.6.P175
Ultrastructure of plasma membrane and membrane-microtubule linker of the connecting cilia in rat retinal rod cell examined by rapid-freeze deep-etch technique

K. Miyaguchi[1]

[1]Shinsapporokeiaikai Hospital, Sapporo, Japan

kmiyaguchi@mbr.nifty.com
Keywords: rapid-freeze deep-etch technique, microtubule-membrane linker, connecting cilia,

Mutations in human CEP290 cause cilia-related disorders. It has been recently shown that CEP290 is a component of radial Y-shaped structures observed between nine microtubular doublets of the axoneme and plasma membrane in transverse section of the connecting cilia and transitional zone of motile cilia (1). In spite of special attention to the Y-shaped cross-linker, its detailed structure and its manner of association to the plasma membrane have not been clarified yet.

In the present study, the plasma membrane and internal architecture of the connecting cilia in fresh rat retinal rod cell were examined with rapid-freeze deep-etch technique. The extracellular surface (ES) of the ciliary plasma membrane was decorated with large protrusions (11-15nm in diameter) in the form of periodic transverse strands. (Figs. 1A, B). Center to center distance of the adjacent arrays was about 25nm. The arrays were at an angle of 5-10° with respect to the transverse axis of the cilium. The spacing of ES protrusions in line (about 25nm) was similar to that of the necklace particles seen on the E-face, suggesting that both of them represent aspects of single transmembrane protein (necklace protein). About thirty-six necklace proteins were located along a perimeter of the cilium.

The cross-fractured and deep-etched cilia revealed cross-linkers between microtubules and plasma membrane (Figs. 1C, D). Each cross-linker consists of a proximal stem and a peripheral branching part, which seems to be composed of four feet, perpendicular to each other. The distance between adjacent feet-membrane contact sites was about 25nm. Stereo view showed that the cross-linkers were spirally lined up along the longitudinal axis of the cilium. Based on these observations, three-dimensional model about ciliary membrane-microtubule linkage is proposed (Fig. 1E). In this model, each foot in the cross-linker is shown to be connected to each necklace protein. Two feet of a cross-linker are connected to two necklace proteins in an array and the other two feet of the same cross-linker are attached to two necklace proteins in the neighboring array. Then, thirty-six necklace proteins along a perimeter of an array are linked by feet from eighteen cross-linkers. The parallel necklace arrays are supposed to be portions of continuous spiral array. These results may suggest that the necklace proteins, lined along spiral arrays and connected to microtubules by four-legged cross-linkers, may play an important role in conveying opsin molecules from the cell body toward the rod outer segment.

1. B. Craige, C. Tsao, D. Diener et al. (2010) J. Cell Biol. 190, 927-940.
2. K. Miyaguchi and P. H. Hashimoto (1992) J. Neurocytol. 21, 449-457.

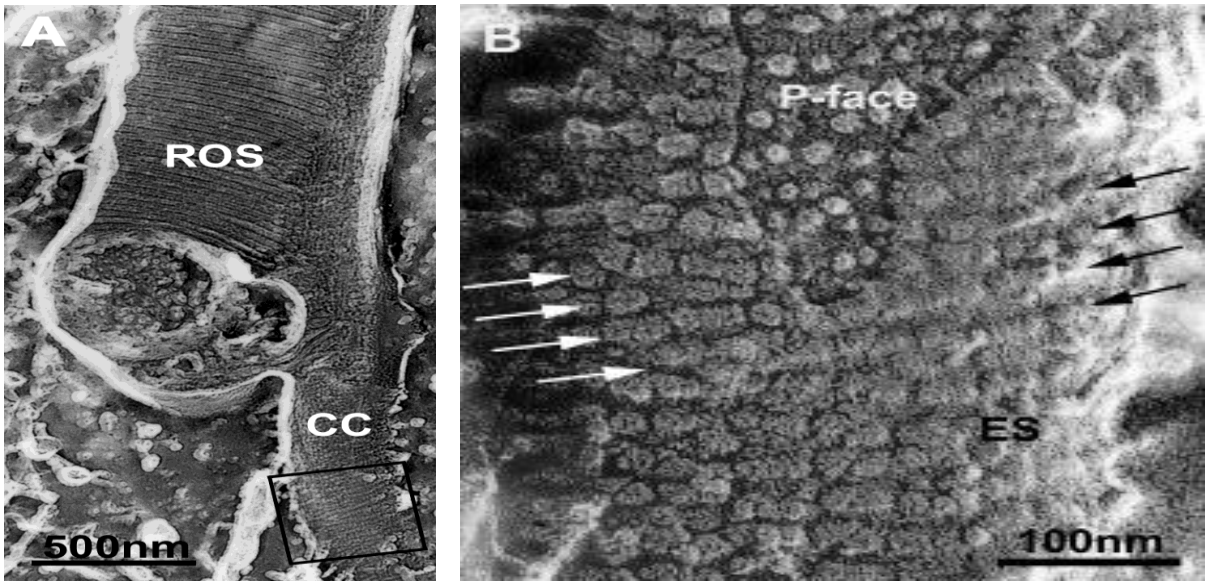

Figure 1. (A) Rod outer segment (ROS) and connecting cilium (CC) of rat retinal rod cell visualized by rapid-freeze deep-etch technique. (B) Higher magnification of the connecting cilium. On the extracellular surface (ES) of the plasma membrane, protrusions are arranged in a form of parallel arrays (between arrows). (C) Cross-fractured and deep-etched view of connecting cilium. Nine doublet microtubules are connected to the plasma membrane by nine cross-linkers (arrows). (D) Higher magnification of a cross-linker. Each cross-linker is composed of a proximal stem (arrowhead) and peripheral feet (short arrows) perpendicular to each other. Long arrow indicates doublet microtubules. (E) Schematic diagram of internal architecture of the connecting cilium. The spiral array of necklace proteins is shown in the left, and linkage between the four-legged cross-linker and necklace proteins is in the right. Each necklace protein is linked to each foot of the cross-linker in this model.

Ultrastructural & Analytical Methods in Life Sciences

LS.6.P176
Novel cross-linking structure between mitochondrial outer membranes in chicken retinal pigment epithelial cells revealed by rapid-freeze deep-etch technique

K. Miyaguchi[1]

[1]Shinsapporokeiaikai Hospital, Sapporo, Japan

kmiyaguchi@mbr.nifty.com
Keywords: rapid-freeze deep-etch technique, mitochondrial outer membrane, cross-linking structure

Mitochondria are highly dynamic. They frequently change their morphology by fusion and fission. These dynamic processes are important for mitochondrial function, and defect lead to neurodegenerative diseases. Several large GTPase such as Drp1, Fis1, Mfn1,2, OPA1 have been recently identified as key molecules in mitochondrial fission or fusion. However, structural data concerning association between adjacent mitochondria are quite limited.

In the present study, mitochondria in chicken retinal pigment epithelial (RPE) cells were examined with rapid-freeze deep-etch technique. In the basal region of RPE cells, various sized mitochondria were highly packed to form a distinct domain, where larger mitochondria were located at the center and smaller ones were at periphery (Fig. 1A). Distance between adjacent mitochondria was quite stable. High magnification showed that mitochondria outer membranes were cross-linked by a novel structure resembling a “pear”. This characteristic cross-linker was composed of basal globular structure shaped like a slightly leaned snowman (21-25nm wide, 20-27nm high) and apical thin filamentous structure (3-6nm wide, 11-19nm long) (Fig. 1B). Some mitochondria were cross-linked to other organella such as ER membranes by filamentous structure (5-9nm wide, 19-25nm long), which differed in shape from the intermitochondrial structure. Some mitochondria had focal contacts to adjacent mitochondria, where parallel curved arrays were occasionally found on the cytoplasmic true surface of the outer membrane (Fig. 1C). Center to center distance of the arrays is 9-10 nm. Theses arrays are similar to those observed in dynamin and Dnm1 helices (1), suggesting that this focal contact with parallel arrays is the site of mitochondrial fission.

These observations may indicate that the pear–shaped intermitochondrial cross-linker plays an important role in keeping and controlling mitochondrial morphology and might be also involved in mitochondrial fission/fusion events.

1. J. A. Mears, L. L. Lackner, S. Fang et al. (2011) Nature Struct Mol Biol 18, 20-27.

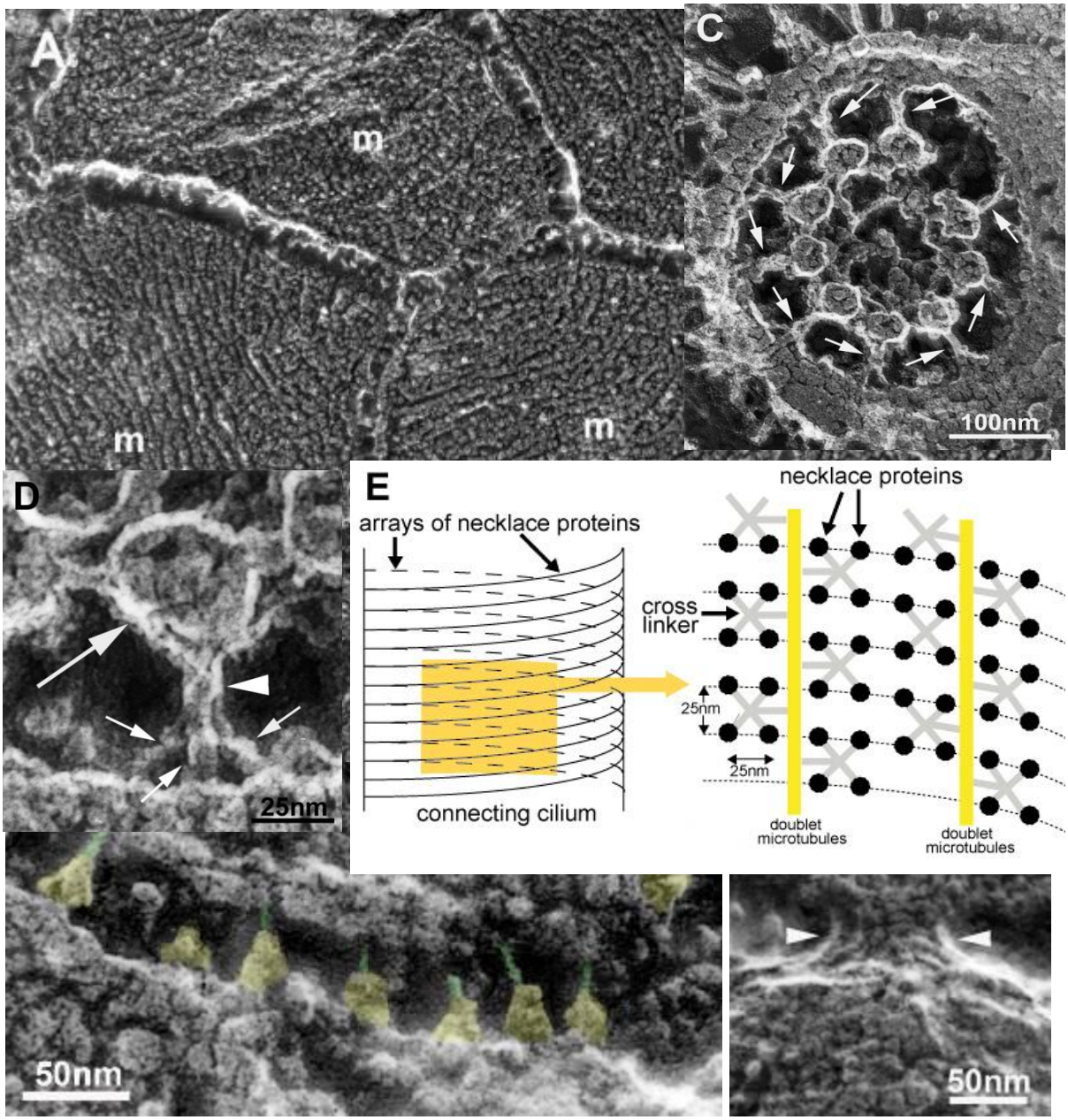

Figure 1. Rapid-freeze deep-etch view of mitochondria in chicken RPE cells. (A) Mitochondria (m) are tightly packed and distance between adjacent mitochondria is quite constant. Globular and filamentous structures are found between mitochondria. (B) Higher magnification of intermitochondrial structure. Mitochondrial outer membranes are cross-linked by pear-like structures which is composed of basal globular part shaped like a slightly leaned snowman (colored in yellow) and apical thin filamentous part (colored in green).(C) At the focal contact between adjacent mitochondria, parallel curved arrays (between arrowheads) are seen on the cytoplasmic surface of mitochondrial outer membrane.

Ultrastructural & Analytical Methods in Life Sciences

LS.6.P177
The effect of electrocauterization for internal thoracic artery harvesting during coronary artery bypasses grafting: an ultrastructural study

S. Gonca[1], B. Onan[2], I.S. Onan[2], S. Solakoğlu[3], I. Bakır[2], M. Yeniterzi[2]

[1]Kocaeli University, Histology and Embriology, Kocaeli, Turkey
[2]Istanbul Mehmet Akif Ersoy Thoracic and Cardiovascular Surgery Training Hospital, Department of Cardiovascular Surgery, Istanbul, Turkey
[3]Istanbul University Medical Faculty, Department of Histology and Embriology, Istanbul, Turkey

suhgonca@gmail.com
Key words: Internal thoracicartery, harvesting methods, TEM, CABG

Preparation methods of internal thoracic artery(ITA) as a coronary graft can be performed by different dissection techniques [1,2]. We aimed to morphological investigate the effects of electrocautery during ITA harvesting on vessel wall morphology at the cellular or ultrastructural level.

Ethics committee approval was received for this study. Proximal sections of ITA grafts from total 10 patients who underwent coronary artery bypass surgery(CABG) were studied in two groups. The ITA grafts were harvested in the control group with mechanical dissection (n=5) using scalpel and clips. Conventional electrocautery was used in the study group (n=5).Transmission electron microscope(TEM): The fixation process was performed for 24h within 2.5% phosphate buffered glutaraldehyde solution at +4 ºC. Then, post fixation was performed within 1% phosphate buffered osmium tetroxide (OsO_4) for an hour, dehydrated by ethyl alcohol series and then embedded in Epon 812. Thin sections (400-600 Aº) were cut with ultramicrotome (LKB) and were stained using uranyl acetate and lead citrate. Finally, sections were evaluated with Jeol JEM 1011 TEM.

In control group, luminal surfaces were lined by normal limits of the original squamous epithelium. The endothelial cell had a very distinct attachment to the basal membrane and cytoplasmic organelles were evident (Figures1a and 1b). However, morphologic integrity of endothelial cells was distorted in the electrocautery group. Endothelial cells showed numerous large cytoplasmic vacuoles and nonvisible cytoplasmic organelles.In subendothelial layer was showed disintegration(Figures 2a, 2b).

We analyzed the incidence of damage to the vascular layers after harvesting of ITA using electrocautery.There were ultrastructurally significant differences in both groups. The integrity of endothelial cells and the vessel layers of the ITA were better preserved when the ITA was removed from its native vascular bed using the scissor method rather than using electrocautery method.

1. Lehtola A, Verkkala K, Järvinen A. Is electrocautery safe for internal mammary artery (IMA) mobilization? A study using scanning electron microscopy (SEM). ThoracCardiovasc Surg. 37(1989), p. 55-7.
2. Yoshida H, Wu MH, Kouchi Y, Onuki Y, Shi Q, Sauvage LR. Comparison of the effect of monopolar and and bipolar cauterization on skeletonized, dissected internal thoracic arteries. J ThoracCardiovascSurg 110(1995), p. 504–10.

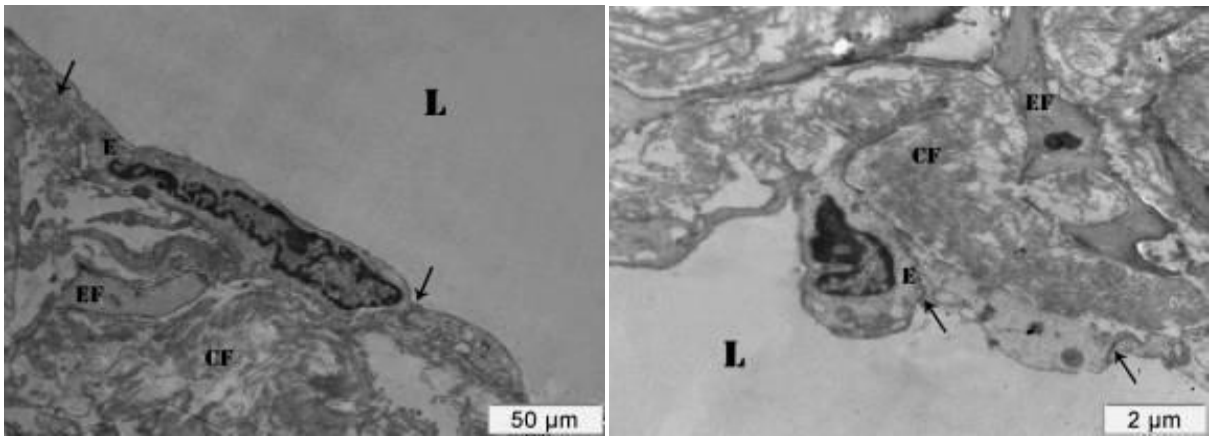

Figures 1a.) 1b.) In control group, luminal surface lined by normal limits of the original squamous epithelium(1a)x6000. The endothelial cell had a very distinct attachment to the basal membrane and cytoplasmic organelles were evident(1b)x10.000. Also, intercellular junctional complex were indicated(arrows). EF: Elastic fibril, CF: Collagen fibril

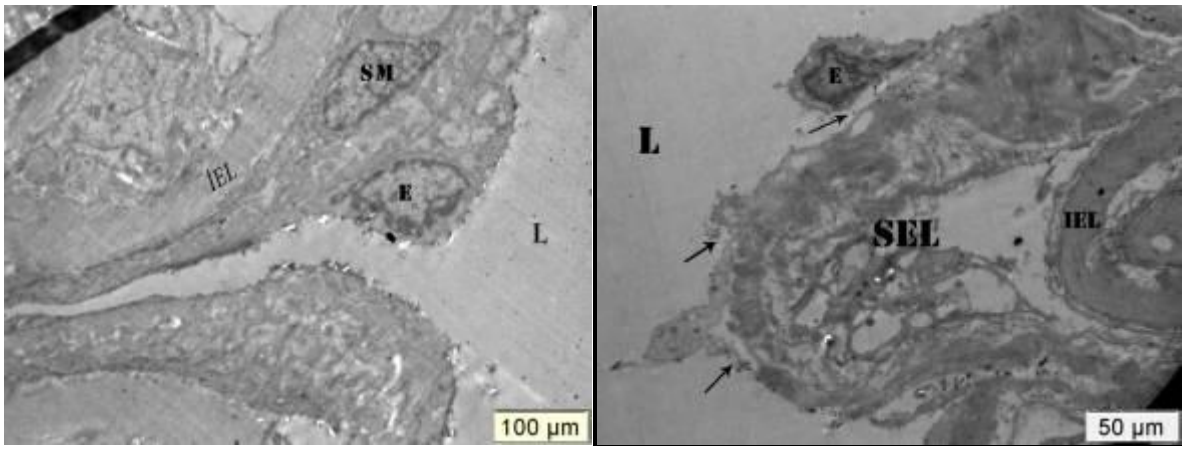

Figures 2a, 2b.Endothelial cells showed numerous cytoplasmatic vacuoles, also indicated nonvisible cytoplasmic organelles(2a)x2500.In luminal surface, contracted endothelial cells and splits were evident(arrows), also subendothelial layer showed disintegration(2b)x6000. E:Endothelial cell, L: Lumen, IEL: Internal elastic membrane, SM: smooth muscle cell, SEL: Subendothelial layer

Subcellular Processes in Plants and Animal Cells

LS.7.178
Stem cells and progenitor cells in decapod crustaceans: diversity, cytological peculiarities and dynamics

G. Vogt[1]

[1]University of Heidelberg, Faculty of Biosciences, Heidelberg, Germany

gunter.vogt@web.de
Keywords: stem cells, Decapoda, microscopy

The philosophy in a scientific discipline is much dependent on the features of the research models used. In stem cell research, the best investigated systems come from vertebrates, mainly man, mouse and medaka. Exploitation of their specific features laid the foundation of modern stem cell biology. However, there are some interesting stem cell systems in sponges, cnidarians, flatworms, *Drosophila melanogaster* and *Caenorhabditis elegans* that have come into the focus of stem cell researchers in the last decade (references in [1]). Sponges and cnidarians have the advantage of simple body plans, flatworms are the masters of regeneration and the fly and nematode are genetically particularly well characterized. Indeterminately growing free-lancing invertebrates that can reach large body sizes and ages of decades have been neglected so far. The decapod crustaceans could fill this gap because they possess a remarkable diversity of embryonic and adult stem cells. The latter operate with high fidelity until old age resulting in the scarcity of age-related diseases and cancer in these animals [2, 3].

The Decapoda are conspicuous and abundant marine and freshwater invertebrates comprising some 14,760 species and dating back to the late Devonian (~360 million years ago). They include the commercially valuable shrimps, lobsters, crayfish and crabs and are keystone species in numerous aquatic habitats. Reliably determined life spans reach from 40 days to 72 years [2]. Due to their ecological and economical importance and traditional use as experimental animals they are amongst the best investigated invertebrates. Nevertheless, research on their stem cells is still at its infancy.

There are several well identified embryonic stem cells, among them the ectoteloblasts and mesoteloblasts that give rise to the ectoderm and mesoderm of the successively emerging thoracic and pleonal segments [4]. These stem cells form a highly ordered structure in the caudal papilla of the developing embryo that is composed of a superficial ring of 19 ectoteloblasts and a subjacent ring of 8 mesoteloblasts. The ecto- and mesoteloblasts remain active until completion of all body segments at the end of embryonic or larval development. Particularly interesting adult stem cells are the E-cells of the hepatopancreas, the satellite cells of the heart and skeletal musculature, the neurogenic stem cells of the brain, the stem and progenitor cells of the haematopoietic tissue and the germline stem cells.

The hepatopancreas is the most voluminous organ of the digestive tract and includes intestinal, hepatic and pancreatic functions. It is composed of hundreds of blindly ending tubules, which fuse together to form collecting ducts that finally terminate in the stomach. The hepatopancreatic stem cells, the so-called E-cells, are confined to stem cell niches located at the blind ends of the tubules (Figure 1A). These stem cells give rise to three mature cell types, the nutrient absorbing R-cells, the digestive enzyme synthesizing F-cells and the functionally obscure B-cells. Propagation of their descendants in one direction only produces a distinct age gradient along the tubules. E-cells divide in a late phase of the digestive cycle to replace discharged epithelial cells and are apparently regulated by a feeding-related signal. Consequently, they are virtually inactive during starvation.

In contrast to mammals, there are plenty of stem cells in the heart of decapods, the so-called satellite cells. These cells are small and spindle-shaped and scattered throughout the muscularis layer of the heart. Usually, they are adjoined individually to the muscle fibres (Figure 1B). Satellite cells are quiescent during intermoult and become active after ecdysis for a short period of time. Their descendants are integrated into the existing muscle fibre network in order to enlarge the heart after moulting. The activity of the satellite cells is regulated by the moulting hormone 20-hydroxyecdysone.

Decapods show a continuous production of new neurons in several parts of the brain, particularly in the olfactory deutocerebrum [5]. Each hemi-deutocerebrum includes a neurogenic system consisting of one neurogenic niche, two migratory streams and lateral and medial proliferation areas (Figure 1C). Progenitor cells are produced in the neurogenic niche from stem cells and migrate then to the proliferation areas where they divide and differentiate into various types of neurons, resembling closely the situation in higher vertebrates. In crayfish, the persistence of such new neurons depends very much on the social status of the animal, being higher in dominants than in subordinates [5].

The haematopoietic tissue contains stem and progenitor cells (Figure 1D), which give rise to three mature types of haemocytes, the hyaline cells, granular cells and semigranular cells. These blood cells have different functions in wound healing and immune defence. Decapods can autotomize and regenerate their limbs in response to injury or mechanical forces exerted by a predator's grip. Regenerated are the chelipeds, walking legs and antennae but not the eyestalks. Autotomy is a reflex and occurs at a pre-formed fracture plane. Regeneration of a lost limb is initiated by formation of a blastema that is produced by mitotically active cells in the epidermis and undifferentiated cells immigrating in large quantities along the pedal nerve. The latter are probably dedifferentiated cells from various sources [8]. The regenerative blastema produces different types of tissue such as musculature, connective tissue, epidermis, nervous tissue and sense organs.

The various types of stem cells in the Decapoda show quite different activity patterns. Some of them are continuously active for weeks such as the ectoteloblasts and progenitor cells of the regenerative blastema or for a lifetime such as the neurogenic stem cells. Others are cyclically activated and silenced in periods of a day such as the hepatopancreatic E-cells, weeks and months such as the satellite cells of the heart and skeletal musculature or months and years such as the germ cells. Proliferation is triggered by signals related to feeding, moulting or reproduction, respectively.

The biggest treasure that could be raised by stem cell research in the Decapoda concerns the regulatory mechanisms that guarantee error-free division of stem cells until high age, largely preventing age-related diseases and tumours in this taxon [2, 3]. Of course, it is presently not foreseeable whether uncovering of such mechanisms is exploitable for medicine but there is hope that research in this direction might evoke new ideas for the development of anti-ageing and anti-cancer interventions in humans.

1. G. Vogt, Stem Cell Rev. Rep. 8 (2012), p. 305.
2. G. Vogt, Zool. Anz. 251 (2012), p. 1.
3. G. Vogt, Int. J. Cancer 123 (2008), p. 2727.
4. F. Alwes and G. Scholtz, Dev. Genes Evol. 216 (2006), p. 169.
5. C.-K. Song, L.M. Johnstone, M. Schmidt, C.D. Derby and D.H. Edwards, J. Exp. Biol. 210 (2007), p. 1311.
6. G. Vogt, Biogerontol. 11 (2010), p. 643.
7. G.G. Martin, J.E. Hose, M. Choi, R. Provost, G. Omori, N. McKrell and G. Lam, J. Morphol. 216 (1993), p. 65.
8. P.M. Hopkins, AC.-K. Chung and D.S. Durica, Am. Zool. 39 (1999), p. 513.

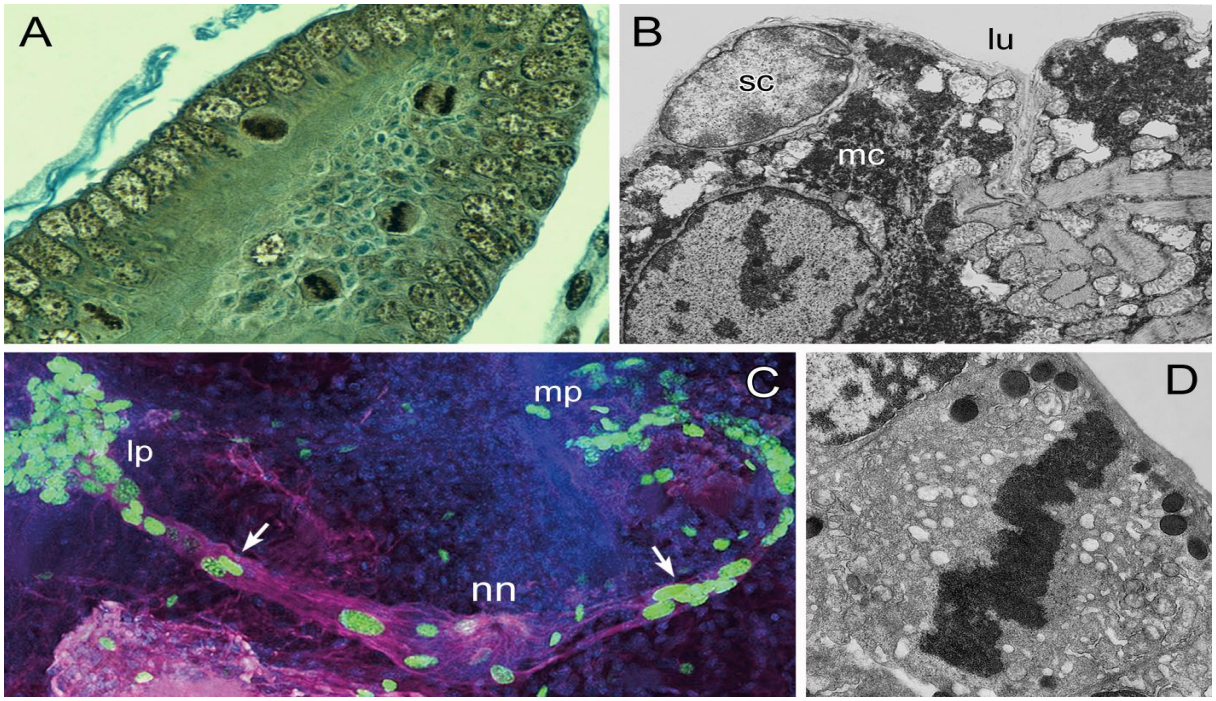

Figure 1 Adult stem and progenitor cells in decapod crustaceans. a) E-cell zone at blind end of hepatopancreas tubule of marbled crayfish with mitotic stages [3]. b) Satellite cell (sc) located between large myocardium cell (mc) and heart lumen (lu) in marbled crayfish [6]. c) Neurogenic system in hemi-deutocerebrum of red swamp crayfish showing migration of newborn cells (arrows) from neurogenic niche (nn) to lateral (lp) and medial (mp) proliferation areas [5]. d) Mitotic stage of progenitor cell of semigranulocyte in haematopoietic tissue of lobster [7].

Subcellular Processes in Plants and Animal Cells

LS.7.179
Discovery and functional analysis of the novel regulators of autophagosome formation and maturation

D. Gozuacik[1]

[1]Sabanci University, Biological Sciences and Bioengineering Program, Istanbul, Turkey.

dgozuacik@sabanciuniv.edu
Keywords: autophagy, lysosomes, signaling, mechanism, miRNA, disease

Autophagy is a biological process allowing the cell to recycle long-lived proteins and damaged organelles. Following sequestration in double or multimembrane autophagic vesicles, the cargo is delivered to lysosomes for degradation. This phenomenon ensures cell survival under stress conditions and plays an important role in the elimination of abnormal or misfolded proteins and damaged organelles [1]. Autophagic vesicle formation and maturation relies on around 30 ATG proteins. Yet, recent studies indicate the presence of an complex network integrating the basic autophagy pathway into fundemental cellular events allowing a coordinated response in times of stress [1, 2].

In our lab in Sabanci University, we focus on signaling events regulating mammalian autophagy and connecting it to cellular pathways. We discovered a role for the Death-Associated Protein Kinase in apoptosis and autophagy crosstalk during drug-induced endoplasmic reticulum stress (Figure 1) [3]. To discover new autophagy regulators and coordinators, we performed several unbiased functional screens. Our search for caspase cleavage sites in autophagy proteins revealed a caspase-8-mediated autophagy regulation mechanisms during death receptor activated cell death [4]. Our microRNA screens led to the discovery of several miRNAs targeting autophagy at various steps of the pathway (Figure 2) [5, 6]. miRNAs are able to affect the expression of a number of proteins at once. Therefore, miRNA networks seem to integrate cellular stress response pathways including autophagy and coordinate them to shape cell faith. We also discovered novel proteins involved in autophagy regulation. In fact, some of these proteins were directly interacting with core autophagy machinery components [7]. Unexpected direct links between autophagy and other cellular pathways were found, allowing us to reveal new entry points for autophagy regulation and coordination in cells. Results from these studies including those obtained using fluorescent confocal microscopy and transmission electron microscopy will be presented.

1. Gozuacik D and Kimchi A. Oncogene, 2004 Apr 12;23(16):2891-906.
2. Gozuacik D and Kimchi A. Current Topics in Developmental Biology, 2007 78:217-45.
3. Gozuacik D, Bialik S, RavehT, Mitou G, Shohat G, Sabanay H, Mizushima N, Yoshimori T, Kimchi A. Cell Death and Differentiation, 2008 15: 1875-86.
4. Oral O, Oz-Arslan D, Itah Z, Naghavi A, Deveci R, Karacali S, Gozuacik D. Apoptosis, 2012 Aug; 17(8):810-20.
5. Korkmaz G, le Sage C, Tekirdag AK, Agami R, Gozuacik D. Autophagy, 2012 February; 8 (2): 165-176.
6. Tekirdag AK, Korkmaz G, Ozturk DG, Agami R, Gozuacik D. Autophagy, 2013 March; 9(3): 1-12.
7. Oral O, Mitou G, Gokce G, Demiroglu D, Gulacti F, Ercan F, Gozuacik D. Submitted.
8. This work was supported by The Scientific and Technological Research Council of Turkey (TUBITAK) 1001 grant, EMBO Strategical Development and Installations Grant (EMBO-SDIG) and Sabanci University.
9. D.G. is a recipient of Turkish Academy of Sciences (TUBA) GEBIP Award.

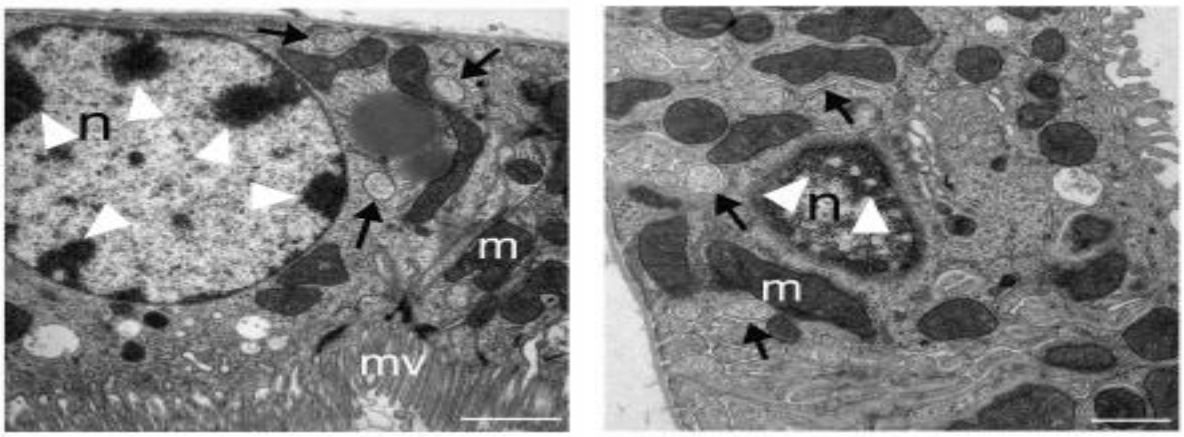

Figure 1. ER stress induces hallmarks of apoptosis and autophagy in vivo in the intact kidney. Ultrastructural analysis of ER stress-induced autophagy and apoptosis features in the kidney by TEM. Shown are images of kidneys from tunicamycin injected mice. Scale bar, left panel, 2µm; right panel, 1µm. n, nucleus, mv, microvilli. Arrows, double membrane bounded autophagic vesicles. Note extensive chromatin condensation in the nuclei (arrowheads) and mitochondrial condensation (m) indicative of apoptotic pathway activation in cells with autophagic vesicles.

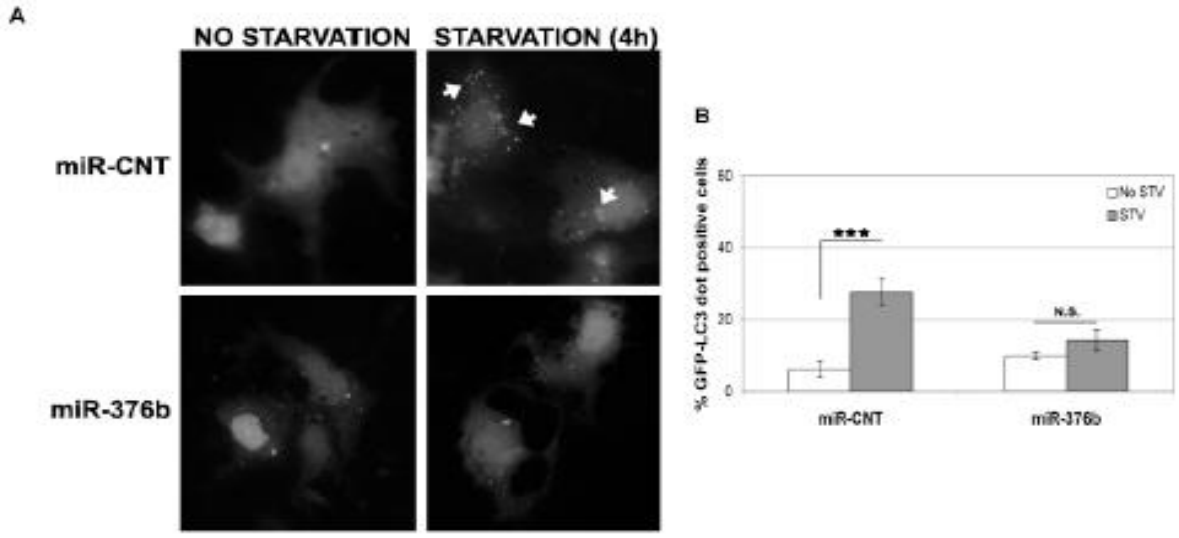

Figure 2. Blockage of starvation-induced autophagy in Huh-7 cells shown using fluorescent confocal microscopy. (A) miR-376b blocked starvation-induced autophagy (GFP-LC3 dot formation). White arrows indicate clusters of the GFP-LC3 dots in cells. (B) Quantitative analysis of GFP-LC3 dot positivity (mean ± S.D. of independent experiments, n=3, ***p<0,01. N.S., not significant.).

Subcellular Processes in Plants and Animal Cells

LS.7.180
First observations of the nucleoplasmic lipid islets: “black holes” in the cell nucleus?

M. Sobol[1], S. Yildirim[1], V. Filimonenko[1], A. Filimonenko[1], P. Hozak[1]

[1]Institute of Molecular Genetics of the ASCR, v. v. i., Biology of the Cell Nucleus, Prague, Czech Republic

sobol@img.cas.cz
Keywords: cell nucleus, chromatin, PIP2, 3D electron tomography, super-resolution microscopy

The nucleus is a highly organized cell compartment, where controlled gene expression, DNA replication, and RNA processing occur. These processes are spatially ordered via the nucleoskeleton, which is involved in nuclear compartmentalization and critical for nuclear functioning [1]. In spite of the growing interest and extensive research concerned to the nuclear organization, so far mostly protein complexes have been found as important for spatial nuclear ordering. We describe novel structures containing phosphatidylinositol 4,5-bisphosphate (PIP2) which seem to contribute as well. Based on scarce literature data relating to PIP2 presence in interchromatin granule clusters and in the nucleolus, we carried out ultrastructural mapping of PIP2-containing structures using pre-embedding immunolabeling and 3D electron tomography. We showed that these structures propagate through the nucleolus where they connect individual fibrillar centers (containing enzymes and transcription factors for ribosomal DNA transcription) and the dense fibrillar component (where the transcription and maturation of rRNA takes place). Besides PIP2 detected in interchromatin granule clusters, the PIP2-positive structures stretch into the nucleoplasm where they appear as previously undescribed 70-100 nm roundish “lipid islets” (Figure 1). We mapped the elemental content of these islets using electron energy-loss microscopy. They appear surrounded by chromatin, and carbon mapping showed high density of organic compounds inside the islets indicating that lipids might be the main inner constituents of these structures (Figure 2). To reveal the plausible functions of these PIP2-containing islets, we mapped mutual localization of PIP2 with nuclear proteins involved in transcription, splicing, and higher order chromatin organization using advanced immunogold electron microscopy and super-resolution light microscopy. We show that at the periphery of the islets, PIP2 co-localizes or is located in immediate vicinity with nascent transcripts, pre-lamin A, LAP2α, H3K4me2, and H3K9me2 (Figures 3-5). Direct binding and mobility assays also showed nucleoplasmic interactions between PIP2 and nuclear myosin 1 (NM1), which is a part of chromatin remodelling complex B-WICH [2] and promotes Pol I and Pol II transcription [3, 4]. Furthermore, the recruitment of lamin A into NM1-bound lipo-protein complex via interactions with PIP2 was demonstrated. We also revealed the association of PIP2 with core histones in pull-down experiments, and showed that the mobility of histone H2B depends on PIP2. Since lamin A is involved in chromatin remodelling via binding to DNA directly or to BAF and core histones, we propose that PIP2 might modulate the state of chromatin by interactions with NM1, core histones and lamin A. Taken together, this data allow us to suggest that PIP2 plays an important role in the organization of chromatin architecture and thus in regulation of gene transcription.

1. D.N. Simon and K.L. Wilson, Nat Rev Mol Cell Biol. 12 (2011), p. 695-708.
2. P. Percipalle et al., EMBO Rep 7 (2006), p. 525–530.
3. V.V. Philimonenko et al., Nat Cell Biol 6 (2004), p. 1165-1172.
4. W.A. Hofmann et al., J Cell Biochem 99 (2006), p. 1001-1009.
5. We acknowledge GACR (GAP305/11/2232), TACR (TE01020118), MEYS CR (LD12063 LD-COST CZ; LH12143 LH-KONTAKT II) for financial support and Iva Jelínková, Ivana Nováková, Karel Janoušek for excellent technical help

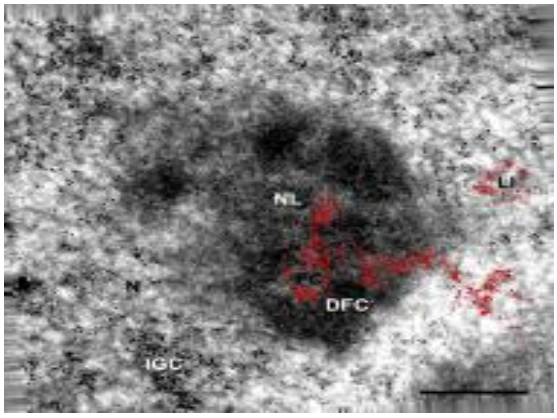

Figure 1. 2D-projection image acquired during single-axis electron tomography of PIP2-containing structures. PIP2 is localized using pre-embedding procedure with 0.8 nm immunogold particles (marked in red). N, nucleus; IGC, interchromatin granule cluster; LI, lipid islet; NL, nucleolus; FC, fibrillar center; DFC, dense fibrillar component. Bar, 100 nm.

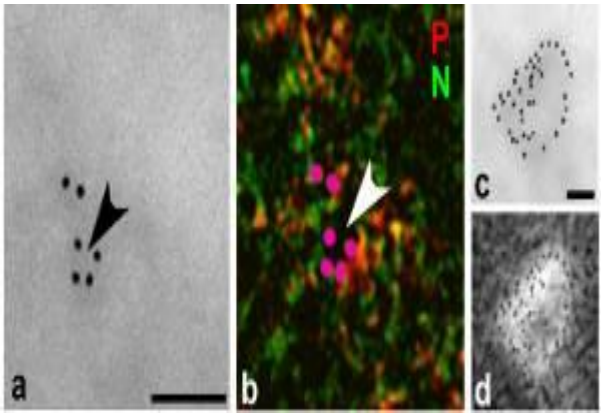

Figure 2. Elemental mapping of phosphorus (P), nitrogen (N), and carbon (C) in lipid islets. a, bright-field TEM image of a lipid islet in the nucleoplasm, visualized by PIP2 immunogold labeling. b, color-coded overlay of elemental maps of P (red) and N (green); the gold particles are marked with magenta. Arrowhead shows to the inner part of the lipid islet. A bright-field TEM image (c) and a carbon map (d) of a different lipid islet. Bars, 100 nm.

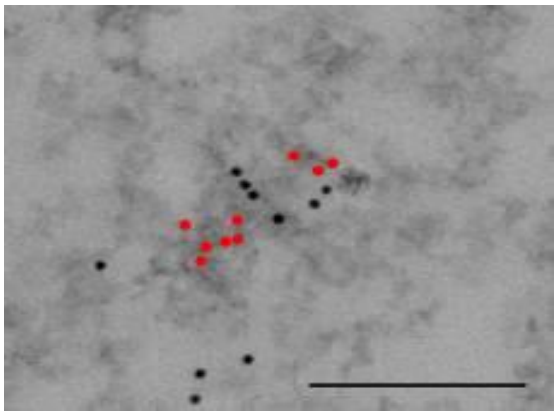

Figure 3. Electron microscopy co-localization of PIP2 with rRNA transcripts (marked in red) after BrUTP incorporation. Bar, 200 nm.

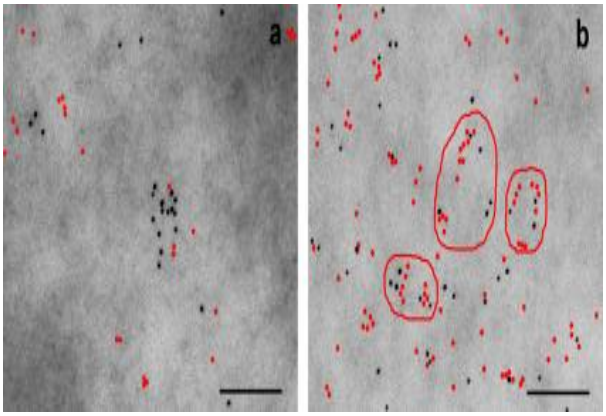

Figure 4. Co-localization of PIP2 with either pre-lamin A (a, marked in red) or LAP2α (b, marked in red). PIP2 is detected with two-dimensional on-section labeling; pre-lamin A and LAP2α are detected with three-dimensional pre-embedding labeling. Lipid islets are outlined in red (b). Bar, 200 nm.

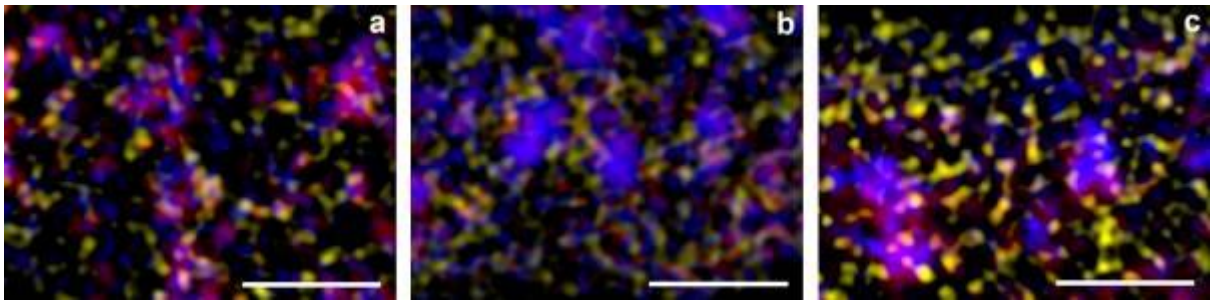

Figure 5. Triple immuno-localization of PIP2 (blue) with Sm (red) and either pre-lamin A (a, yellow), H3K4me2 (b, yellow), or H3K9me2 (c, yellow) detected using super-resolution structured illumination microscopy. Bar, 2 µm.

Subcellular Processes in Plants and Animal Cells

LS.7.181
Syndapin II interacts with caveolin 1 and participates in shape control of caveolae

M. Westermann[1], D. Koch[2], B. Qualmann[2], M. Kessels[2]

[1]Jena University Hospital, Electron Microscopy Center, Jena, Germany
[2]Jena University Hospital, Institute for Biochemistry I, Jena, Germany

martin.westermann@uni-jena.de
Keywords: caveolin 1, syndapin II, freeze-fracture replica immunolabeling (FRIL)

F-BAR domain proteins like syndapins are dimeric, lipid-binding, peripheral membrane proteins. They induce membrane curvature by partial membrane insertion and by imposing their curved shape onto the lipid bilayer [1]. Syndapin I is a predominantly neuronal protein, syndapin II is expressed ubiquitously [2]. Syndapin I and II were shown to play a promoting role in endocytosis and in vesicle formation processes [3, 4]. The direct observation of such membrane shaping processes by peripheral membrane proteins was hitherto hindered by the difficulty to combine cytochemistry with a high-resolution view of the membrane topology.

Using the new freeze-fracture replica immunolabeling technique (FRIL) we solved this limitation by achieving large and detailed ultrastructural views of cellular membranes in the transmission electron microscope combined with the immuno-localization of membrane components. In particular we established conditions for the efficient labeling of the peripheral membrane protein syndapin II at electron microscopic resolution.

When applying the FRIL technique chemically unfixed cellular samples are rapidly cryofixed in their natural environment. In a second step the samples are fractured, replicated and immobilized by a platinum/carbon evaporation followed by a careful SDS treatment. After the “SDS-digestion” [5] molecules like membrane proteins or lipids that are in direct contact with the platinum-carbon replica keep bound to the replica film and are accessible to immunolabeling [6].

In this work we show the localization of endogenous syndapin II at the plasma membrane of NIH-3T3 cells using the FRIL technique (Figure 1, 2).

Syndapin II was detected at flat and curved membrane domains at the protoplasmic fracture face of the plasma membrane (Figure 1). Co-localization studies at both the cellular and the ultrastructural level identified these sites as caveolin 1-positive areas and thus elucidated syndapin II as new component of caveolae (Figure 2). Biochemical analyses revealed that syndapin II binds caveolin 1 via its F-BAR domain and that over-expressed syndapin II F-BAR domain affects caveolin 1 distribution in NIH3T3 cells. Ultrastructural analyses showed that syndapin II loss-of-function by RNAi lead to a shift of the proportion of invaginated caveolae towards flat caveolin 1 positive areas suggesting that syndapin II is required for the invagination of caveolae at the plasma membrane. Mechanistic insights into syndapin II mediated caveolar shaping was revealed by tilt series analysis of immunolabeled freeze-fracture replicas showing syndapin II asymmetrically localized at the neck of caveolae.

In summary, the freeze-fracture replica immunolabeling technique showed that plasma membrane-localized syndapin II binds to both flat and curved membrane domains *in vivo* and that it plays an important role in caveolar shaping. Our data are an excellent example for studying peripheral membrane proteins in terms of localization and function at the ultrastructural level using FRIL.

1 . Qualmann B, Koch D, Kessels MM, EMBO J. 30 (2011), 3501-3515
2. Qualmann B, Roos J, DiGregorio PJ, Kelly RB, Molecular Biology of the Cell 10 (1999), 501–513
3. Kessels MM, Qualmann B, EMBO Journal 21 (2002), 6083–6094
4. Koch D, Spiwoks-Becker I, Sabanov V, Sinning A, Dugladze T, Stellmacher A, Ahuja R, Grimm J, Schüler S, Müller A, Angenstein F, Ahmed T, Diesler A, Moser M, Tom Dieck S, Spessert R, Boeckers TM, Fässler R, Hübner CA, Balschun D, Gloveli T, Kessels MM, Qualmann B, EMBO Journal 30 (2011), 4955–4969
5. Fujimoto K, Journal of Cell Science 108 (1995), 3443–3449
6. Westermann M, Steiniger F, Richter W, Histochemistry and Cell Biology 123 (2005), 613-620

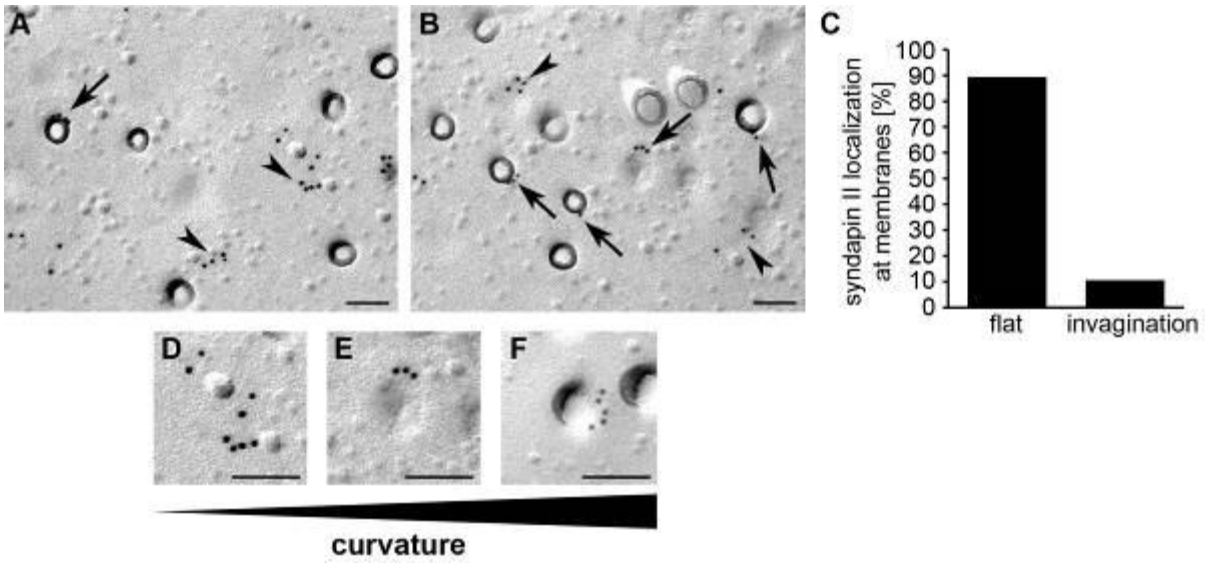

Figure 1 Syndapin II is localized to both flat and deeply invaginated plasma membrane of NIH 3T3 cells. NIH 3T3 cells were grown to confluence and subsequently processed for freeze-fracturing and immunolabeling. **A**, **B** Besides the presence of syndapin II at flat membranes (arrowheads), a substantial fraction of syndapin II signal was detected at circular deep membrane depressions with diameters of about 60 nm (arrows). **C** Quantification of immunolabeling revealed that a profound fraction of syndapin II was present at invaginated membranes. **D–F** Detail views of syndapin II at membranes with different curvatures (increasing from left to right). Scale bars 100 nm

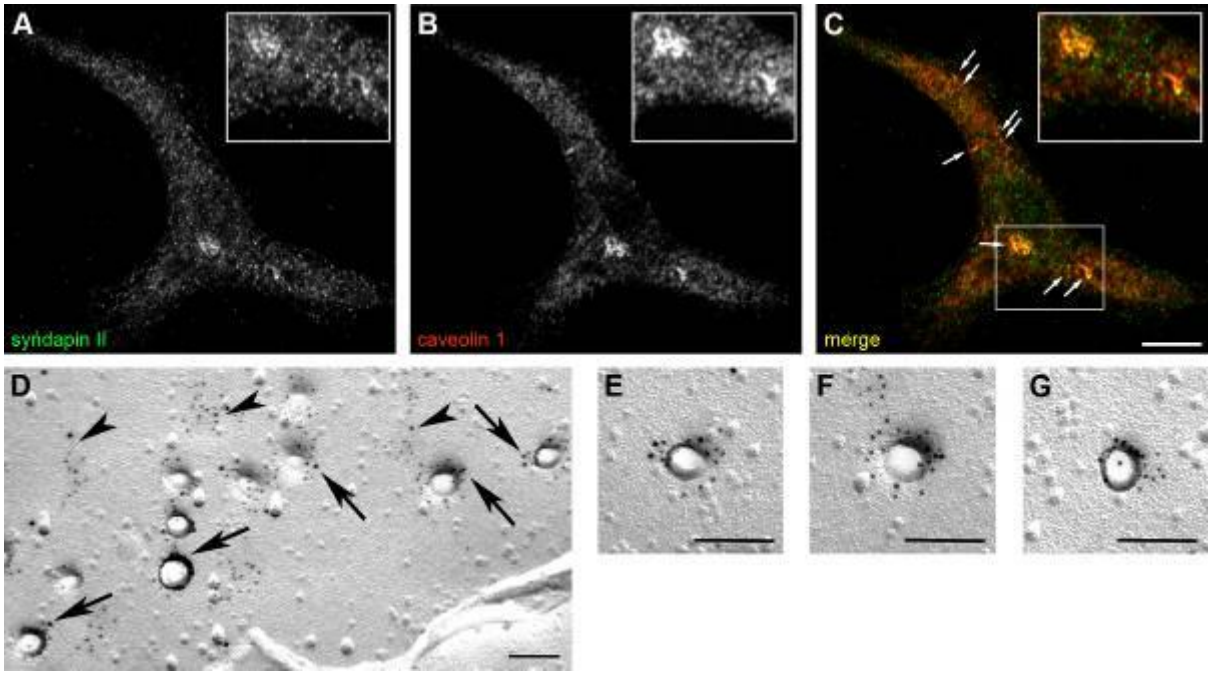

Figure 2 Syndapin II localizes to caveolin 1-positive structures in NIH 3T3 cells. Apotome image of methanol-fixed NIH 3T3 cells stained for endogenous syndapin II a) and caveolin 1 b) showed high degree of colocalization (c, merge). d–g Freeze-fracture electron micrographs of the plasma membrane of NIH 3T3 cells. Caveolin 1 (indicated by 5 nm gold particles) and syndapin II (indicated by 10 nm gold particles) colocalize at invaginated caveolae (arrows), but also at flat caveolin 1-positive spots (arrowheads) (d). Exemplary detail views of syndapin II (arrows) and caveolin 1 colocalizing at caveolae are shown in (e–g). Scale bars 10 µm (c) and 100 nm (d–g)

Subcellular Processes in Plants and Animal Cells

LS.7.182
Cuticle formation during marsupial development of the crustacean Porcellio scaber: Imaging and analysis

P. Mrak[1], N. Žnidaršič[1], K. Žagar[2], M. Čeh[2], J. Štrus[1]

[1]University of Ljubljana, Biotechnical faculty, Department of Biology, Ljubljana, Slovenia
[2]Jožef Stefan Institute, Department for Nanostructured Materials, Ljubljana, Slovenia

polona.mrak@bf.uni-lj.si
Keywords: embryo, marsupial manca, terrestrial isopods, exoskeleton, ultrastructure, mineralization, chitin

Introduction: Crustacean exoskeleton is a chitin-protein matrix, formed apically by a single-layered epidermis. Organic cuticle constituents are hierarchially ordered in horizontal layers and incorporate minerals, mostly calcium carbonate and phosphate. The data on *de novo* formation of crustacean cuticle during embryogenesis provide knowledge of cell biology of chitin-based mineralized matrices, biomineralization processes and the role of hard biological materials. In this study several intramarsupial developmental stages of terrestrial isopod *Porcellio scaber* are examined, including analysis of cuticle ultrastructure, localization of N-acetylglucosamine (chitin monomer) and presence of mineral component. The embryonic development of terrestrial isopods takes place in the fluidic environment of the female marsupium. Embryos hatch into mancae and continue their development in marsupium for another week. Our results are compared with two model arthropod species, insect *Drosophila melanogaster* with non-mineralized exoskeleton and different reproductive strategy [1, 2] and aquatic amphipod crustacean *Parhyale hawaiensis* [3].

Methods: A detailed staging system through twenty progressive stages [4] was used to characterize the stages of *P. scaber* embryos and mancas, isolated from the marsupium. Conventional ultrastructural study and labelling of N-acetylglucosamine with WGA lectin were performed on ultrathin sections. The elemental composition of the cuticle was examined in methanol-fixed specimens by energy-dispersive x-ray spectroscopy (EDXS) in scanning electron microscope.

Results and discussion: Ultrastructural and compositional study of *Porcellio* epidermal extracellular matrices was performed in two sequential stages of late embryos and in two sequential stages of marsupial mancae. A substantial layer of apical matrix, synthesized by embryonic epidermis, is observed in late embryo in stage 16. It is elaborated underneath the vitelline membrane and consists of fibrous material without any prominent pattern, lined distally by a thin dense layer (Figure 1). Morphologically it resembles the *Drosophila* and *Parhyale* embryonic cuticle [1, 3]. Our results indicate that this matrix differs from adult chitinous cuticle also in composition as WGA labelling is not conspicuous. The matrix persists during stages of embryo bending, indicating its flexibility. In the further development of late embryo (stage 18) the formation of the electron dense epicuticle and homogenous procuticle begins underneath the matrix (Figure 2). Prominent positive WGA labelling with similar pattern as in adults is shown in cuticles of advanced stages 19 and 20 that already display characteristic sublayers in procuticle, indicating their similarity in chitin-protein arrangement. EDXS analysis reveals that cuticle in early mancae just after hatching is not strongly calcified in comparison to adult. Cuticle calcification appears much more prominent in advanced marsupial mancae where cuticle becomes ultrastructurally more similar to adult cuticle (Figures 3, 4). These results suggest the importance of exoskeleton formation and calcification and its involvement in animal mobility which was observed already within marsupium. It is noteworthy to expose the role of the exoskeleton during the release of mancae from the marsupium followed by absence of maternal care in the external environment.

1. B. Moussian, C. Seifarth, U. Müller, J. Berger and H. Schwarz, Arth. Struct. & Dev. 35 (2006), p. 137-152.
2. B. Moussian, Insect Biochemistry and Molecular Biology 40 (2010), p. 363-375.
3. J. Havemann, U. Müller, J. Berger, H. Schwarz, M. Gerberding and B. Moussian, Cell Tissue Res. 332(2) (2008), p. 359-370.
4. M. Milatovič, R. Kostanjšek and J. Štrus, Journal of Crustacean Biology 30(2) (2010), p. 225-235.

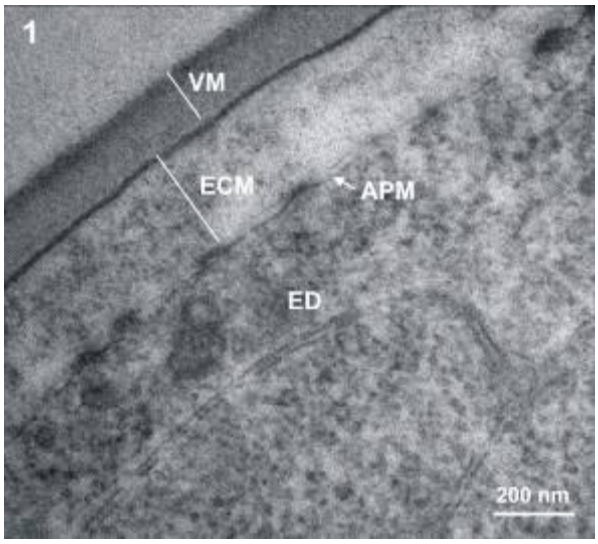

Figure 1. Late embryo of *P. scaber*, stage 16: Ultrastructure of apical extracellular matrix (ECM), lying between the vitelline membrane (VM) and apical plasma membrane (APM) of epidermal cell (ED).

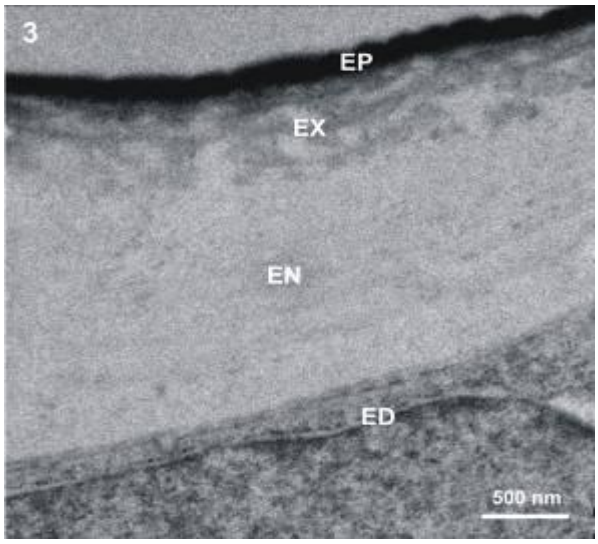

Figure 3. Marsupial manca of *P. scaber*: Ultrastructure of exoskeletal cuticle, overlying the epidermis (ED) and differentiated in three main layers: epicuticle (EP), exocuticle (EX) and endocuticle (EN).

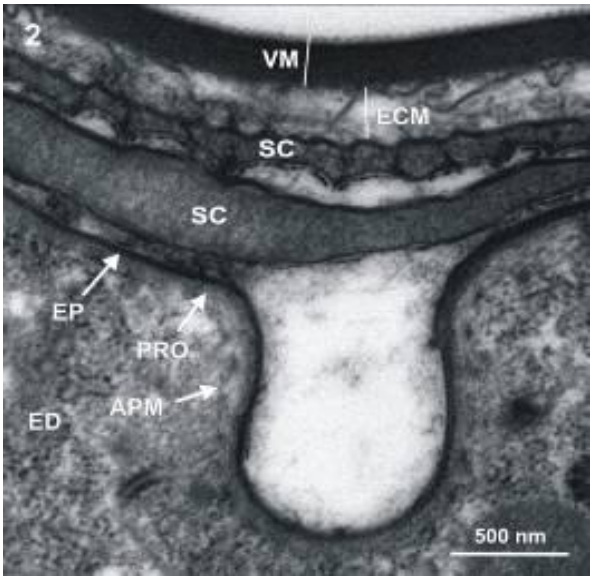

Figure 2. Late embryo of *P. scaber*, stage 18: Ultrastructure of epicuticle (EP) and procuticle (PRO), lying above apical plasma membrane (APM) of epidermal cell (ED) and underneath the matrix (ECM) and the vitelline membrane (VM). Epicuticular scales (SC), one covering the other, are fully developed.

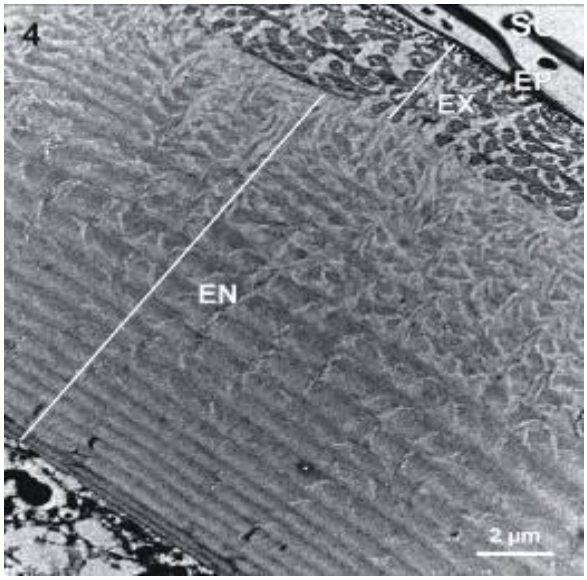

Figure 4. Ultrastructure of *P. scaber* adult exoskeletal cuticle, consisting of distinct horizontal layers: endocuticle (EN) with lamellar chitin-protein sublayers, exocuticle (EX) with chitin–protein fibers arranged in characteristic pattern and thin electron dense epicuticle (EP). Scales (SC) are epicuticular structures.

Subcellular Processes in Plants and Animal Cells

LS.7.183
Controlled disassembly and new formation of Golgi apparatus stacks in cultured hepatoma cells

C. Ranftler[1], D. Rouhani[1], A. Ellinger[1], J. Neumüller[1], C. Meisslitzer-Ruppitsch[1], M. Pavelka[1]

[1]Center for Anatomy and Cell Biology, Department of Cell Biology and Ultrastructural Research, Vienna, Austria

carmen.ranftler@meduniwien.ac.at
Keywords: 2-deoxy-D-glucose, ATP-depletion/-replenishment, Golgi apparatus

The non-metabolizable glucose-analogue 2-deoxy-D-glucose (2DG) has become an important target of interest during the last decade due to its medical and basic-biological effects. 2DG is under clinical evaluation for cancer therapy [1] and other diseases like epilepsy, Morbus Alzheimer and malignant astrocytoma; on the other hand, it is a highly interesting tool for studying the dynamic organization of the Golgi apparatus [2, 3].

Previous research in our laboratory on the effect of 2DG on human hepatoma cells (HepG2) revealed that replacement of D-glucose by 2DG (50mM) leads to transformations of the well-structured Golgi cisternae in tubulo-glomerular bodies and networks [3]. Moreover, the intracellular ATP-content decreases within 10min to 15-30% of the control (Fig.1A and 1B). Experiments mimicking a simple starvation process by abolishing D-glucose from the growth medium do not gain the same results (Fig.1C). HepG2 cells grown in glucose- and pyruvate-free (GPF) medium showed moderately reduced ATP-levels (90% ATP after 3 hours) and no alterations of the Golgi apparatus structure (Fig. 2C).

The cultured HepG2 cells rapidly recover from ATP-depletion and rebuild their well organized Golgi apparatus stacks after removal of 2DG and replenishment of D-glucose (50mM) in the growth medium (GLUC). The ATP-levels arise continuously (Fig.1D) and stacks of cisternae reappear. Detailed correlative biochemical and ultrastructural analyses revealed that both the disassembly of the Golgi apparatus and new formation of the well structured stacks of cisternae correlate well with the changes of the ATP-levels (Fig.2A-E) and 2DG-treatment can be used for exploration of Golgi apparatus dynamics under controlled conditions.

Experiments employing an ATP-replenishment protocol without glucose proved to be particularly helpful. When cells are grown in GPF medium after removal of 2DG, the ATP-level of the cells increases only slowly (Fig.1E). By comparison of the 2 protocols (Fig.1D and 1E), it becomes apparent that a total recovery of the cells' ATP-content in D-glucose can be observed within 2-3 hours, while after even 4 hours incubation in GPF medium the ATP-level remains clearly under 100%. More precisely, cells grown in medium containing D-glucose reach 80% ATP-amount of untreated controls within 60min (Fig.1D), whereas it takes cells in GPF medium four times longer. Morphologically, a similar delay is evident concerning the new formation of the Golgi apparatus stacks. Regularly organized stacks are detectable at 120min after 2DG elimination, while these can already be observed within 30-45min during D-glucose replenishment. The delayed reassembly of the Golgi apparatus allows studying the subsequent steps of reformation much more precisely and helps to define intermediate stages during Golgi apparatus new formation (Fig.2E).

1. H. Xi, M. Kurtoglu, H. Liu, M. Wangpaichitr, M. You, X. Liu, N. Savaraj, T.J. Lampidis. Cancer Chemother. Pharmacol. 67 (2011), p. 899.
2. M. del Valle, Y. Robledo, I.V. Sandoval. J. Cell Sci. 112 (1999), p. 4017.
3. C. Meisslitzer-Ruppitsch, C. Röhrl, C. Ranftler, J. Neumüller, M. Vetterlein, A. Ellinger, M. Pavelka. Histochem. Cell Biol. 135 (2011), p.159.
4. The authors thankfully acknowledge the technical help of Mrs. Regina Wegscheider, Mag. Beatrix Mallinger, Mr. Peter Auinger, Mr. Ulrich Kaindl and Mr. Thomas Nardelli.

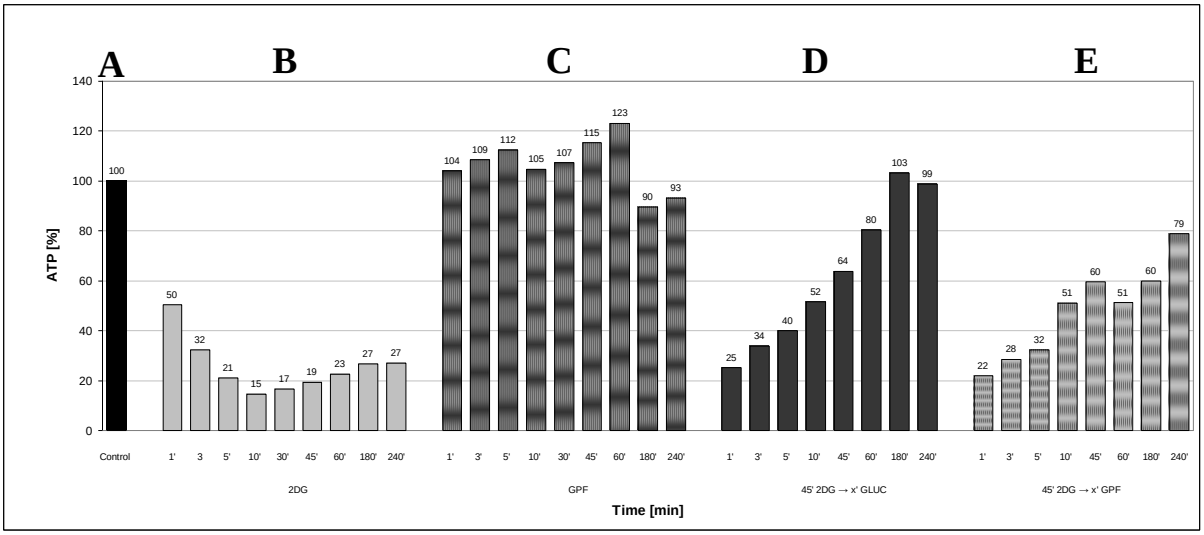

Figure 1. Cellular ATP-levels in response to the various treatments.

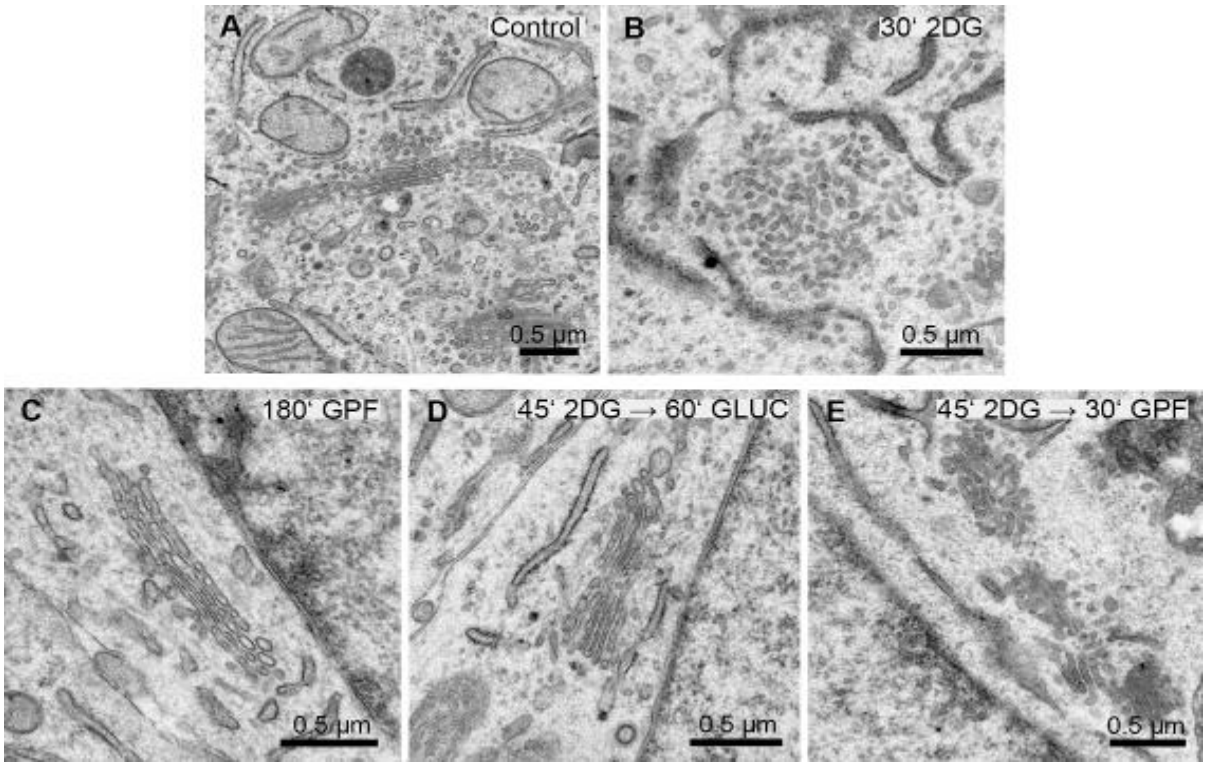

Figure 2. Golgi apparatus morphologies correlating with the ATP-contents shown in Fig.1

Subcellular Processes in Plants and Animal Cells

LS.7.P184
Thermal treatments induce ultrastructural changes in oil cavities of *Copaifera langsdorffii* Desf. (Leguminosae)

T. Rodrigues[1], A. Coneglian[1], P. Buarque[1], S. Machado[1]

[1]UNESP, Botany, Botucatu, Brazil

tatiane@ibb.unesp.br
Keywords: cell ultrastructure, secretory epithelium, temperature

Copaifera langsdorffii Desf. is a legume tree widespread in different ecosystems in Brazil [1] where the annual average temperature is around 25ºC. This species presents cavities and canals secreting oil which is exhaustively exploited by cosmetic and pharmaceutical industries and protects the plant against microbial infection and predator attacks [2]. Oil cavities, constituted by a uniseriate secretory epithelium and a wide lumen, occur in the cortex of the stem and in the mesophyll of the leaves of seedlings and adult plants [3]. Studies suggest that exogenous factors can influence the production of the oil in the cavities of this species [4, 5]; however, nothing is known about the subcellular responses of the secretory cells to such factors.

In order to evaluate the influence of the temperature on the ultrastructure of the epithelial cells of oil cavities in *C. langsdorffii* eophylls, seedlings were maintained in climatic chamber under 1250lux, 35% of relative humidity, and submitted to different thermal treatments: 15ºC, 25ºC and 35ºC. After the full expansion of the eophylls, samples were collected from the median region of the proximal leaflets and were prepared following conventional techniques of transmission electron microscopy [3].

Our results showed that the temperature can modify the ultrastructure of the epithelial cells of oil cavities in the eophylls of *C. langsdorffii*. In seedlings maintained under 25ºC (Figures 1-3), the epithelial cells showed thin walls, small vacuoles, large nucleus and abundant and dense cytoplasm containing ribosomes, voluminous mitochondria, extensive smooth endoplasmic reticulum forming elongated cisterns and polymorphic plastids. The plastids are surrounded by periplastidial reticulum, present homogenous strome and are devoid of tylakoids. Such features are similar to those described to young leaves of adult plants growing in natural conditions in the Brazilian savanna [3] and are typical of cells actively secreting lipophilic substances [3, 6]. In seedlings under 15ºC e 35ºC, the epithelial cells presented smooth endoplasmic reticulum forming whorls indicating some reduction of their metabolic activity [7]. Under 15ºC (Figure 4), osmiophilic granules are observed in the plastidial strome and mitochondrial matrix. The presence of a dense cytoplasm rich in organelles, small vacuoles and voluminous nucleus in seedlings under this condition suggest the maintenance of the secretory activity of the epithelial cells suggesting their acclimation to low temperature. Epithelial cells of seedlings under 35ºC (Figure 5) show higher electron-density of organelles, dilatation of membranes of plastids and mitochondria, accumulation of electron-lucent globules in plastids, increment of vacuome and lyses of the cytoplasmic matrix suggesting damage to their secretory activity. This fact deserves attention if we consider that increases of 1.5 to 5ºC in the global temperature are expected to next the years [8]. These data collaborated in understanding the response of secretory systems, a complex and dynamic system in plants, to environmental factors

1. M.A.S. Salgado, A.V. Rezende, J.M. Felfili, A.C. Franco, J.C. Sousa-Silva, Brasil Florestal 70 (2001), p.13-21.
2. J.H. Langenheim, Plant resins: chemistry, evolution, ecology, ethnobotany, (Timber Press, Cambridge) (2003), 586p.
3. T.M. Rodrigues, S.P. Teixeira, S.R., Flora 206 (2011), p. 585-594.
4. E.B. Feibert, J.H. Langenheim, J.H., Phytochemistry 7 (1988), p. 2527-2532.
5. J.H. Langenheim, C.L. Clovis, C.A. Macedo, W.H. Stubblebine, Biochemical Systematics and Ecology 14 (1986), p. 41-49.
6. T.M. Rodrigues, D.C. Santos, S.R. Machado, Comptes Rendus Biologies 334 (2011), p. 535–543.
7. H.A. Ishikawa, American Journal of Botany 83 (1996), p.825-835.

8. J.T. Houghton, Y. Ding, D.J. Griggs, M. Noguer, P.J. van der Linden, X. Dai, K. Maskell, C.A. Johnson, in "Third Assessment Report of the Intergovermental Panel on Climate Change", ed. J.T. Houghton, Y. Ding, D.J. Griggs, M. Noguer, P.J. van der Linden, X. Dai, K. Maskell, C.A. Johnson, (Cambridge University Press, Cambridge) (2001), p. 1-881.
9. We kindly acknowledge FAPESP (2008/55434-7) and UNESP for the financial support. A.G.Coneglian receives scholarship from FAPESP (2010/15153-9) and P.F.M.S.Buarque from CAPES.

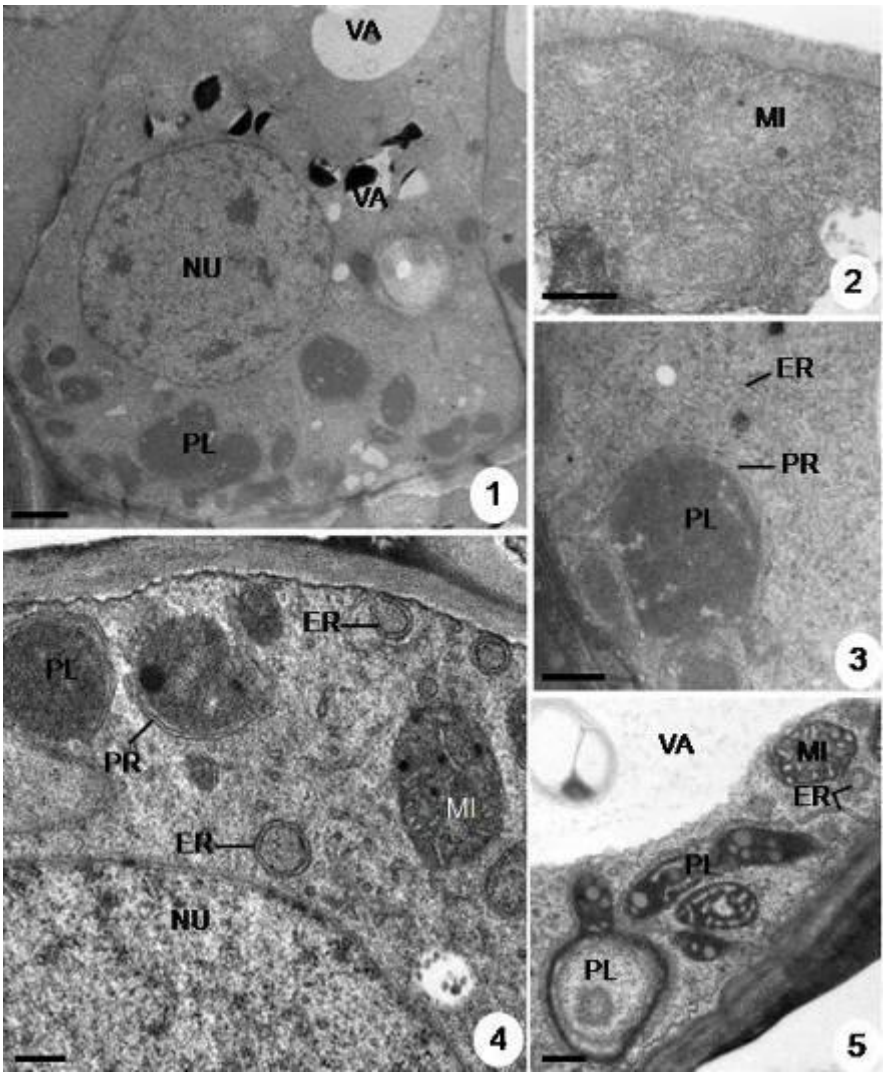

Figures 1-5. Electronmicrographies of secretory cells of oil cavities in eophylls of *C. langsdorffii*. 1-3. Cells from seedlings maintained under 25ºC. 1. General view showing thin wall, dense cytoplasm, small vacuoles (VA), voluminous nucleus (NU) and plastids (PL). 2, 3.Details showing mitochondria (MI), smooth endoplasmic reticulum (ER), ribosomes, plastids (PL) and periplastidial reticulum (PR). 4. Cell from seedling maintained under 15ºC showing dense cytoplasm, nucleus (NU), mitochondria (MI) and plastids (PL) with electron-dense inclusions, periplastidial reticulum (PR) and whorls of smooth endoplasmic reticulum (ER). 5. Cell from seedling maintained under 35ºC showing developed vacuole (VA), mitochondria (MI) with dilated cristae, plastids (PL) with osmiophilc strome containing electron-lucent globules and endoplasmic reticulum (ER). Observe the dilatation of membranes of plastids and mitochondria. Scale bars: 1= 3.0µm; 2, 3 =0.2µm; 4= 0.4µm; 5= 0,6µm.

Subcellular Processes in Plants and Animal Cells

LS.7.P185
Histochemistry and ultrastructure of leaf glands colonized by bacteria in *Styrax camporum* Pohl. (Styracaceae)

S. Machado[1], T. Rodrigues[1]

[1]UNESP, Botany, Botucatu, Brazil

smachado@ibb.unesp.br
Keywords: bacteria, gland, infection, morphology, *Styrax camporum*, ultrastructure

Styracaceae is a wood family best known as the source of benzoin (gum benjamin) and storax resin used as an antiseptic, inhalant and expectorant, as well as in the manufacture of perfumes and vanilla cream candies; it is also noted for several beautiful ornamentals shrubs and trees [1]. Symbiosis between a bacterium and *Styrax camporum*, a shrubby member of Styracaceae from the Brazilian savanna [2], is described here for the first time. We characterized the ultrastructure of the leaf glands and the cellular changes associated with the bacterial colonization. Samples of shoot apices and leaves in different stages of development were collected and fixed for studies under light and scanning and transmission electron microscopy according to conventional techniques [3]. Glands in *S. camporum* leaves are emergences constituted by a short stalk and a multicellular body (Figure 1) producing lipids and protein/carbohydrate-based mucilage. These glands show anatomical, histochemical and ultrastructural similarities to colleters [4] but they cannot be considered functionally analogous. Glands are persistent on the margins of the mature leaves and under normal circumstances all of them are colonized with bacteria. The bacteria are Gram-negative and variously rod or ovoid in shape and are confined to the gland body (Figure 2). Each bacterium usually contains a conspicuous chromatic region and a capsule surrounding the cell wall. The bacterial colony resides in the mucilage which fills the intercellular channels resulting from the dissolution of middle lamellae along the anticlinal cell walls of both epidermal and parenchyma cells of the glands (Figure 2). The host cell wall forms a tube-like projection that grows inside the protoplast of the epidermal cell (Figure 3). The infection thread advances through the host cells and the bacteria are released into the cytoplasm. Colonized cells show electron-dense bodies in the cell wall, evidences of nucleus degeneration, mitochondrial alterations, proliferation of vesicles and signals of cytoplasm lyses. These features are indications of stress-associated ultrastructural alterations caused by the invasion by bacteria, possibly as a defense mechanism [5]. Mature glands show a large central space filled with mucilage and numerous bacteria which are becoming tightly appressed to one another. This central space is surrounded by a sheath constituted by thick-walled and juxtaposed parenchyma cells containing vacuoles filled with electron dense material identified as phenolic substances (Figure 2). This sheath is very similar to reported for bacterial leaf nodules of *Psychotria bacteriophila* [6] may serve as a barrier which limits the spreading of bacteria throughout the foliar organs. As described for many species which maintain leaf association with bacteria [7], the mucilage produced by *S. camporum* glands seems to play a key function in the symbiosis with bacteria, as their secretion probably constitutes the carbon substrate for the endophyte in the buds.

1. V.H. Heywood, R.K. Brummitt, A. Culham and O. Seberg in “Flowering plant families of the world”, ed. V.H. Heywood (Royal Botanic Gardens, Kew) (2007), p. 313.
2. J.N. Nakajima and R. Monteiro, Eugeniana 12 (1986), p. 3-10.
3. S.R. Machado, D.P. Barreiro, J.F.Rocha and T.M. Rodrigues, Flora 207 (2012), p. 868-877.
4. E.A.S. Paiva and S.R. Machado, Brazilian Journal of Biology 66 (2006), p.301-308.
5. P.J. Dart and F.V. Mercer, Archiv für Mikrobiologie 49 (1964), p. 209-235.
6. R.E. Whitmoyer and H.T. Horner, Botanical Gazette 131 (1970), p.193-200.
7. C. Van Hove and K. Kagoyre, Annals of Botany 38 (1974), p. 989–991.
8. We kindly acknowledge the financial support from FAPESP (2008/55434-7) and UNESP.

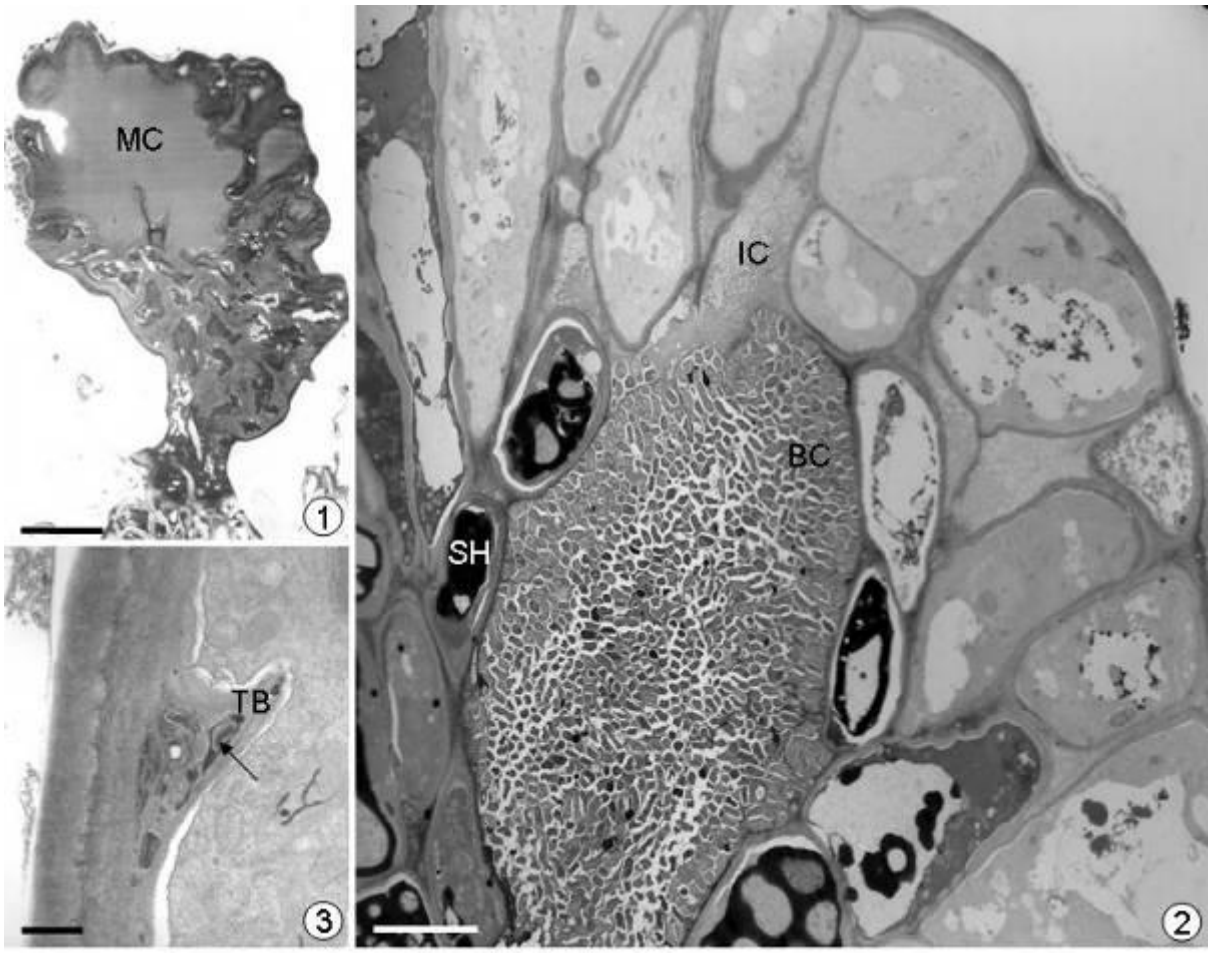

Figures 1-3. Electronmicrographies of leaf glands in *S.camporum*. 1. General view showing short stalk and multicellular body of the gland containing large space filled with mucilage (MC). 2. Part of the gland body showing cells in different physiological stages, intercellular canal (IC) filled with mucilage and a sheath (SH) surround the central space with bacteria (BC) immersed in the mucilage. 3. Detail showing tube-like projection (TB) of the cell wall growing toward the protoplast of the epidermal cell. The arrow indicates bacteria (Scale bars: 1= 100µm; 2= 1.0µm; 3= 0.5µm).

Subcellular Processes in Plants and Animal Cells

LS.7.P186
Ultrastructural analysis of sink-source relations between green and white areas of variegated plant chimera *Ficus benjamina* var. Starlight

E. Labunskaya[1], V. Choob[1]

[1]Moscow State University, biology, Moscow, Russian Federation

styxelenalab@gmail.com
Keywords: variegated plants, plant chimera, sink-source relations, mesophyll ultrastructure

Ficus benjamina var. Starlight is the green-white periclinal chimera with green edge and white center of leaves. Arrangement of areas in the leaf is constant whereas proportion of green and white zones may vary from leaf to leaf. It has been investigated that proportion of white area depends on the order of branching but not on the distribution of future white and green cells in meristem [1]. In mosaic chimeras the sink-source status appears to be dependent on leaf position in the axial system, and products of photosynthesis may act as metabolic signal for leaf primordium [1]. Mesophyll cells in white area of young leaves have few photosynthetically active chloroplasts: the quantum yield of photosystem II averages 0,5 (quantum yield of PSII for green mesophyll averages 0, 54). Mature leaves have no chloroplasts in white cells. Some leaves have 95% of white area per leaf but (однако) they grow and develop. Therefore white zone appears to be the sink, and green areas act as source region. In an effort to estimate ultrastructural changes in white and green areas of young and mature leaves owing to sink-source relations we investigated the ultrastructure of green and white areas of chimera's leaves. We have found that young leaves possess few agranal chloroplasts with huge starch grains. Presumably starch accumulation is connected with sink status of the entire leaf. When leaf becomes mature and switch its sink status to source [2] the condition of white mesophyll declines, and cells degrade. Supposedly the reason of degradation is the carbohydrate starvation.

Ultrastructural traits of white mesophyll resemble to the auphagy [3] that can be summoned by the carbohydrate starvation [4]. Nevertheless there are two different types of white mesophyll cells. The first type includes cells that are far from vascular strands (Figure 1). They obtain numerous extensive lythic vacuoles with degrading organelle, electron-dense droplets and myelinic bodies [5] (Figure 2). The second type incorporates cells that are situated near vascular strands (Figure 3). The cytoplasm in these cells is near cell walls only, there are no organelle and rare electron-dense bodies are exposed. The condition of white mesophyll in mature leaves suggests that the direct transfer of photosynthetic products from the source (green zone) to the sink (white zone) lacks. However the difference between cells that are located near and are situated far from a vascular bundle leads to the conclusion that some carbohydrates from green areas enter to the white zone and slow down the degradation in it.

1. Labunskaya E.A., Zhigalova T.V., Choob V.V.Russian Journal of Developmental Biology. V. 38 (2007), p. 397-405
2. Walter A., Rascher U., Osmond B. Plant Biol. V. 6 (2004),. p. 184 – 191
3. Aubert S., Gout E., Bligny R., Marty-Mazars D., Barrieu F., Alabouvette J., Marty F., Douce R. JCB. V. 133 (1996), p. 1251 – 1263
4. Toyooka, K., Okamoto T., Minamikawa T. JCB. V. 154 (2001), p. 973 – 982
5. Douce R., Joyard J. Annu. Rev. Cell Biol. (1980).V 6, p. 173 – 216
5. The work is performed at User Facilities Center of M.V. Lomonosov Moscow State University under financial support of Ministry of Education and Science of Russian Federation

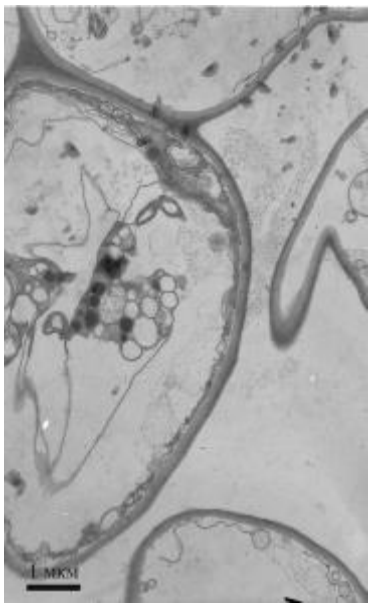

Figure 1. White mesophyll cell that is far from any vascular bundle. Electron-dense bodies and thin cytoplasmic layer are presented.

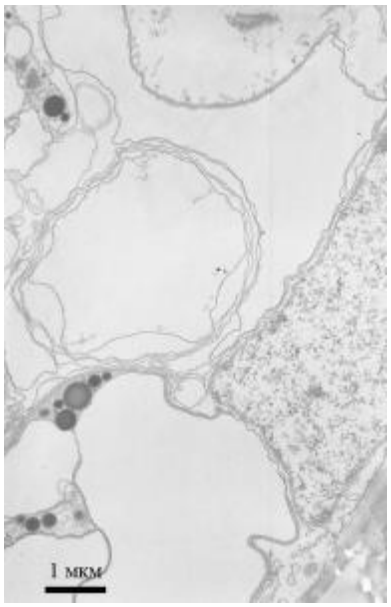

Figure 2. Myelinic bodies in a degrading cell of white mesophyll.

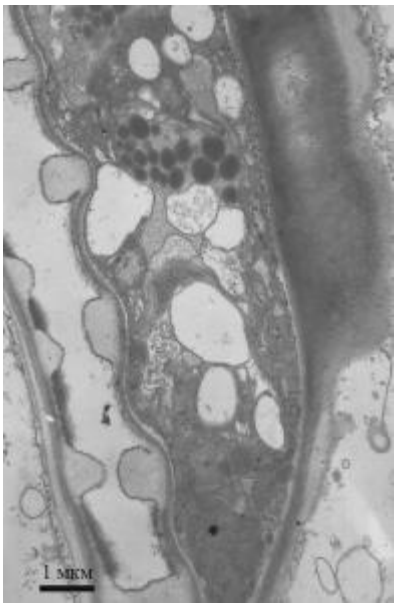

Figure 3. White mesophyll cell near the vascular bundle. There are numerous lipid oils, electron-dense bodies and lythic vacuoles. The cytoplasm is not degraded.

Subcellular Processes in Plants and Animal Cells

LS.7.P187
3D reconstruction of *in situ* Short Intraflagellar Transport trains in flagella of *Chlamydomonas reinhardtii*.

F. Cantele[1], E. Paccagnini[2], E. Vannuccini[2], S. Lanzavecchia[1], P. Lupetti[2]

[1]Università degli Studi di Milano, Dipartimento di Chimica, Milano, Italy
[2]University of Siena, Department of Life Sciences, Siena, Italy

francesca.cantele@unimi.it
Keywords: electron tomography, intraflagellar transport, 3D averaging

Cilia and flagella are filiform organelles with multiple and fundamental physiological functions protruding form the surface of most non dividing eukariotic cells. Such organelles are highly dynamic structures whose integrity and function depend on a selective mechanism of active transport knows as Intraflagellar Transport (IFT). We have previously demonstrated that two distinct classes of IFT trains are present in full length flagella of the biflagellate model organism *Chlamydomonas reinhardtii*: the long anterograde IFT and the short retrograde IFT [1]. In the past years we reconstructed the long IFT trains by double tilt electron tomography and averaging of its repeating particle extracted from the tomogram. The attempts performed by other labs to image and reconstruct IFT trains in situ by cryo electron tomography encountered, so far, major technical problems. We report here new data on the 3D structure of *in situ* short IFT trains we obtained by electron tomography on fixed and flat embedded full length flagella. Such strategy gave us good detection opportunities for IFT trains providing high contrast and sufficiently resolved imaging of them (“Figure 1.”) Working with embedded specimen and double-tilt tomography, however, has its own technical constraints coming from section shrinkage, different orientation of the samples and stain in-homogeneities.To overcome such limits we developed a method to reconstruct portions of tomograms arbitrarily rotated, starting from submaps of the original tomograms, that allowed us to use a “single particle” strategy for the average process and to take into account for distortion, missing wedge and in-homogeneities [2,3,4].

We reconstructed by this method more than sixty short IFT trains and we aligned them with global and local methods. After that, we classified the aligned IFTs. We selected for further processing, the class containing the IFTs clearly showing some repeating units between "head" and "tail" regions, as shown in “Figure 2a.”. The periodicity of these units is about 16 nm.

We then made the average of the repeating units and obtained the structure shown in “Figure 2b.” Each IFT unit shows, a four-major densities structure we labelled as A,B,C and D.
The A, B and C blocks display higher densities, while the D looks more faint: a fact which can be explained with a more flexible or not always present feature along IFT trains which thus appears weaker after averaging of multiple units.

The periodicity is evident in C and D blocks, while A and B don't seem to have it and appear like continuous rods in longitudinal views of averaged IFT trains.
Links are clearly present both with flagellar membrane and microtubule. The membrane seems to be linked with all the blocks, with the B block displaying the thicker connection with flagellar membrane. The IFT short trains are linked to microtubules by two rod domains, with different thickness in reconstructed subtomograms. The one with B block is clearly visible. The second one, with the C block, is only hinted, probably due to his very variable orientation, but it becomes visible using low thresholds or inspecting single unaveraged IFT short trains. Both links connected the IFT with the B tubule of its neighbouring axonemal doublet.

1. G. Pigino, S. Geimer, S. Lanzavecchia, E. Paccagnini, F. Cantele, D. R. Diener, J. L. Rosenbaum and P. Lupetti, The Journal of Cell Biology 187 (2009), p. 136.
2. F. Cantele, L. Zampighi, M. Radermacher, G. A. Zampighi and S. Lanzavecchia, Journal of Structural Biology 158 (2007), p. 59.
3. F. Cantele, E. Paccagnini, G. Pigino, P. Lupetti and S. Lanzavecchia, Journal of Structural Biology 169 (2010), p. 192.
3. G. Pigino, F. Cantele, E. Vannuccini, S. Lanzavecchia, E. Paccagnini and P. Lupetti, Methods in Enzymology 524 (2013) p. 325.

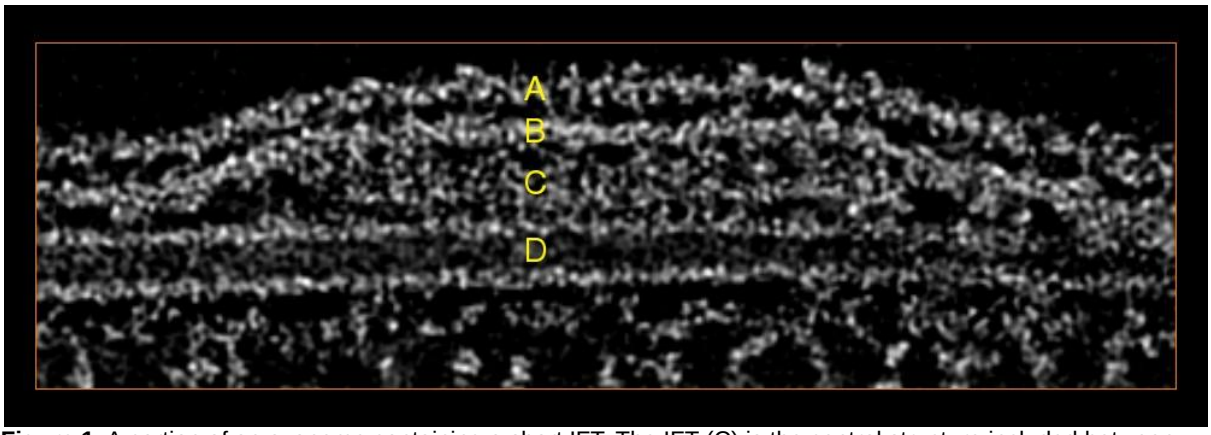

Figure 1. A portion of an axoneme containing a short IFT. The IFT (C) is the central structure included between the membrane (B) glycocalyx (A) pair and the microtubule (D). IFT links are clearly visible, with both membrane and microtubule.

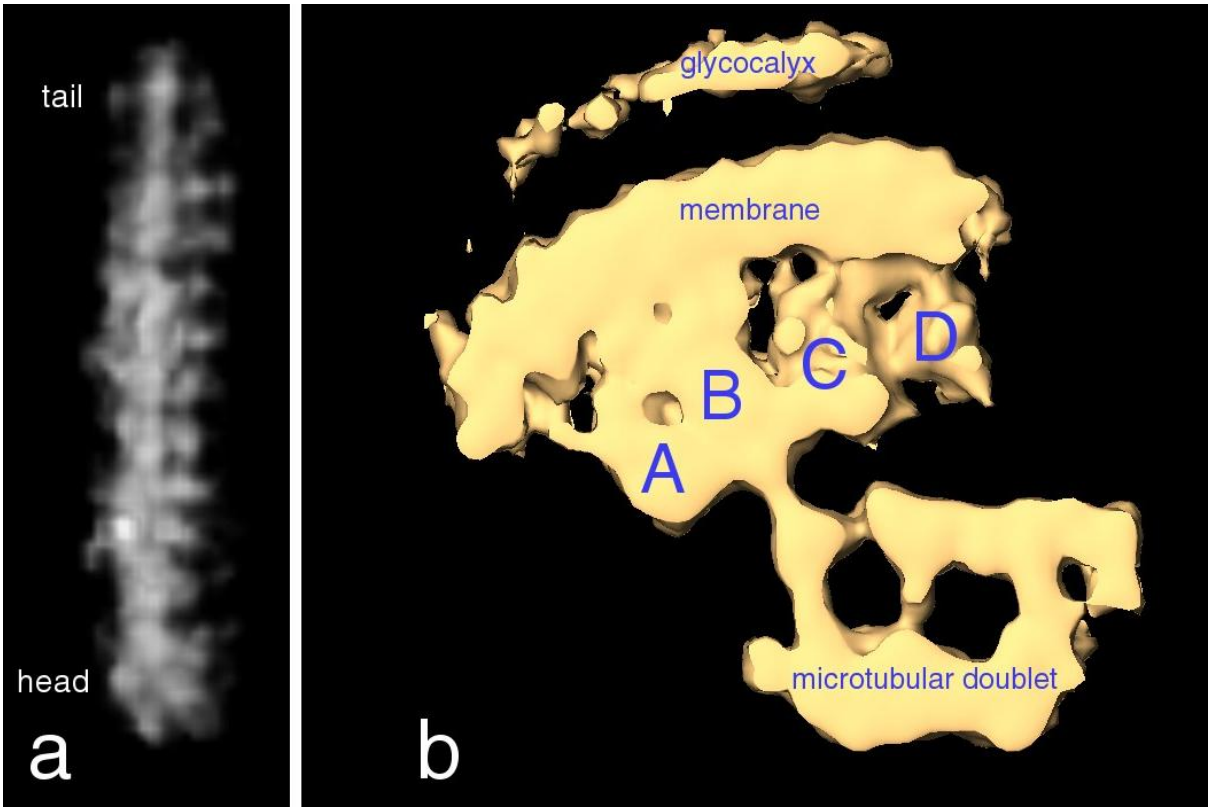

Figure 2. The average reconstruction of short IFT. a) The entire IFT, with head, tail and repeating units in the centre. b) A single repeating unit, together with microtubular doublet and membrane, over the membrane a small portion of glycocalyx is visible. The IFT is made by four blocks (A, B, C and D), that are linked to membrane and microtubule.

Subcellular Processes in Plants and Animal Cells

LS.7.P188
KillerRed expressing Tol2 transposon enhancer trap transgenics for in vivo studies of protein transport during zebrafish development.

M. Sin[1], C. Teh[2], V. Korzh[2]

[1]Institute of Molecular and Cell Biology, Central Imaging Facility, Singapore, Singapore
[2]Institute of Molecular and Cell Biology, Fish Developmental Biology, Singapore, Singapore

wlsin@imcb.a-star.edu.sg
Keywords: KillerRed protein, enveloping layer, intracellular distribution

KillerRed (KR) protein is a genetically-encoded photosensitizer that fluoresces red upon illumination with green light. Membrane-tagged KillerRed (mem-KR) contains the membrane localization signal of neuromodulin. The Tol2-based transgenic approach was used to generate several stable transgenic lines expressing mem-KR in tissue-specific manner. For example, SqKR1 embryos mem-KR is found at the membrane and/or Golgi apparatus domains of cells in the most superficial cell layer of embryonic and larval zebrafish - enveloping layer (EVL). Interestingly, intracellular distribution of mem-KR in the dorsal and ventral EVL cells differs. In the ventral EVL mem-KR was found primarily in large aggregates representing Golgi, whereas in the dorsal EVL mem-KR localisation varies between Golgi and plasma membrane. Currently, we use various inhibitors of signalling pathways to identify a pathway responsible for developmental regulation of membrane protein transport.

.

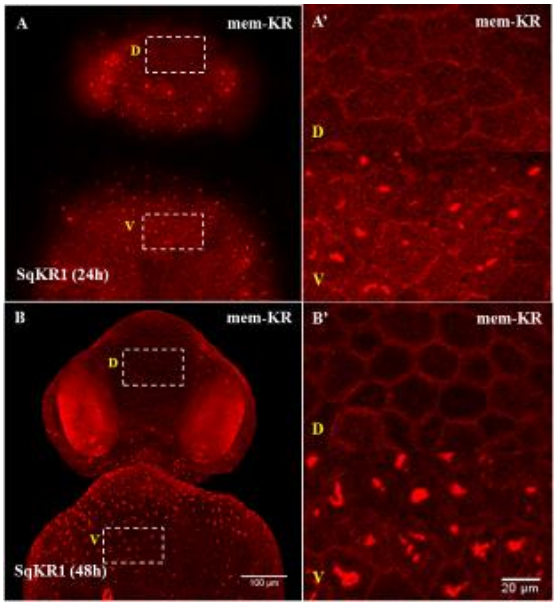

Figure 1. Protein distribution pattern of mem-KR is different in dorsally situated and ventrally situated EVL cells of SqKR1 embryos. (A, B and C) Confocal stack image of SqKR1 embryos at 24, 48 and 72 hpf show differential protein distribution pattern of mem-KR in dorsal versus ventral EVL cells. (A', B' and C') Magnified view of dorsal versus ventral EVL cells at 24, 48, and 72 hpf show that mem-KR in dorsally situated EVL cells are mainly localized to the plasma membrane while mem-KR in ventrally situated EVL cells are localized to the plasma membrane but also found in large aggregates.

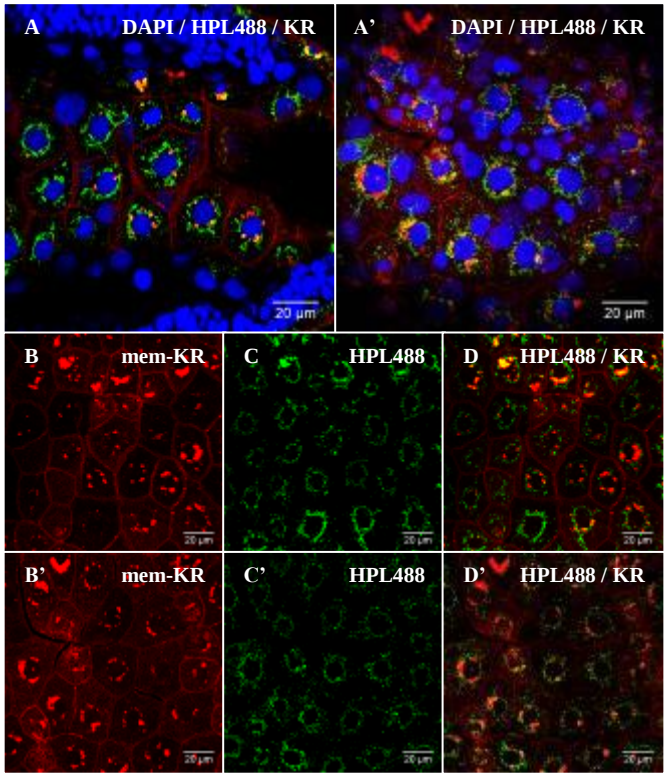

Figure 2. Aggregates of mem-KR proteins co-localize with a Golgi apparatus marker. SqKR1 embryos were fixed at 30hpf and stained for nucleus with DAPI, stained for Golgi apparatus with HPL488 and stained for mem-KR with Alexa Fluor 555 conjugated antibody against anti-KillerRed antibody. (A – D) Confocal stack image of dorsally situated EVL cells of stained 30hpf SqKR1 embryos show that mem-KR is found mainly at the plasma membrane while small aggregates co-localize with the Golgi apparatus, which is peri-nuclear. (A' – D') Confocal stack image of ventrally situated EVL cells of stained 30hpf SqKR1 embryos show that a vast amount of mem-KR are present as large aggregates that co-localize with the Golgi apparatus.

Subcellular Processes in Plants and Animal Cells

LS.7.P189
Microscopy investigation of glandular trichomes of Satureja horvatii Šilić (Lamiaceae)

M. Marin[1], L. Ascensao[2], N. Jasnic[3], S. Brankovic[4]

[1]Faculty of Biology, University of Belgrade, Institute of zoology, Belgrade, Serbia
[2]Faculdade de Ciencias da Universidade de Lisboa, . Centro de Biotecnologia Vegetal, Portugal, Portugal
[3]Faculty of Biology, University of Belgrade, . Institute of Physiology and Biochemistry, Belgrade, Serbia
[4]Faculty of Science, University of Kragujevac , Department of Biology and Ecology, Kragujevac, Serbia

majamarin@bio.bg.ac.rs
Keywords: *S.horvatii*, trichome, micromorphology

The essential oils isolated from various *Satureja* species, which belong to the family Lamiaceae, have been shown to posses biological and pharmacological activities, such as antibacterial, antifungal, antiviral, antioxidant [1,2]. *Satureja horvatii* Šilić is an endemic species [3] of the Orjen-Lovćen mountain massif in Montenegro with a high content of the essential oil.
Considering the importance of *Satureja horvatii* Šilić as an endemic plant, and due to the essential oils produced in its glandular trichomes, we carried out micromorphological and ultrastructural analyses of plant's glandular trichomes as a primary secretory organs and have also analysed autofluorescense of their secreted products.

The investigation was carried out using scanning electron (JEOL JSM T 220 15 kV), transmission electron (Philips TEM 208 S.), confocal laser scanning (CLSM 510 Carl Zeiss with Axioskop FS2 mot), and light fluorescence (Leica DM LS with a 13 BLU 450-490 nm filter) microscopy.
A leaf cross-section of *Satureja horvatii* indicated the presence of several different morphological types of glandular and non-glandular trichomes Figure 1. The adaxial and abaxial leaf sides of *Satureja horvatii* were covered by an indumentum containing peltate, capitate and digitiform trichomes, as well as unicellular and multicellular unbranched non-glandular trichomes with wart-like cuticular structures Figure 2. Peltate trichomes distributed on the adaxial and abaxial leaf sides consisted of one basal epidermal cell, a wide stalk cell and a multicellular head consisting of twelve cells. Capitate trichomes, uniformly distributed on both leaf surfaces, were divided into two types according to the shape of the unicellular secretory head. Type I was composed of one basal cell, one stalk cell and spherical unicellular head, while type II was composed of one basal cell, one stalk cell and an ellipsoid unicellular head. Capitate trichomes were more numerous than peltate and digitiform trichomes on the both leaf sides. Digitiform trichomes, which do not show a clear distinction between the apical glandular cell and the subsidiary cells, occurred between the peltate and capitate trichomes with a smaller distribution. Non-glandular trichomes were densely distributed on the adaxial and abaxial leaf sides and on the margins of the leaves. Ultrastructural analyses showed the presence of numerous lipid globules and proliferations of the granular endoplasmatic reticulum in secretory phases of the heads of glandular trichomes. The outer cell wall was covered with a thick cuticle Figure 3.
Strong red autofluorescence of the lipophilic and hydrophylic secreted material was observed with CLSM Figure 4. While intensive light yellow autofluorescence was noticed in peltate trichomes using fluorescence microscope Figure 5.

With the increasing tendency to use volatile oils, our investigation, together with the results of chemical investigations, indicate that *S. horvatii* essential oil could be applied in the pharmaceutical industries.

1. Ciani, M., Menghini, L., Mariani, F., Pagiotti, R., Menghini, A.,and F. Fatichenti (2000). Antimicrobial properties of
essential oil of *Satureja montana* L. on pathogenic and spoilage yeasts. Biotechnol. Lett. 22, 1007-1010.
2. Ćavar, S., Maksimović, M., Šolić, M. E., Jerković-Mujkić, A., and R. Bešta (2008). Chemical composition and antioxidant and antimicrobial activity of two Satureja essential oils. Food Chem. 111, 648-653.
3. Šilić, Č. (1979). Monografija rodova Satureja L., Calamintha Miller, Micromeria Bentham, Acinos Miller i Clinopodium L. u flori Jugoslavije, Zemaljski Muzej BiH, Sarajevo.
4. Acknowledgments: We thank prof. Dmitar Lakušić for providing the plant material.

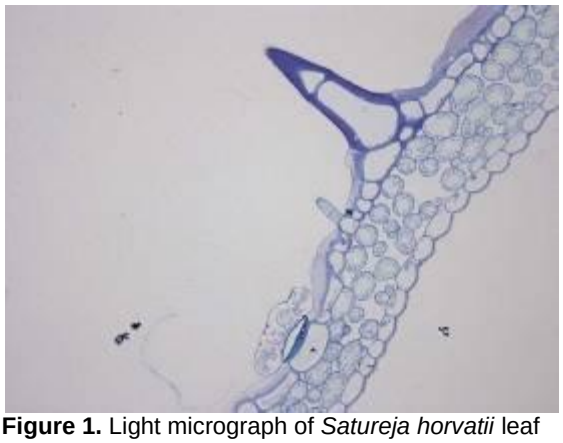

Figure 1. Light micrograph of *Satureja horvatii* leaf 40x.

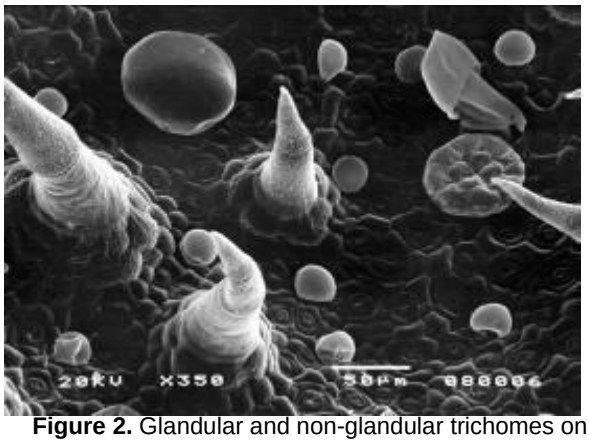

Figure 2. Glandular and non-glandular trichomes on abaxial leaf surface of *Satureja horvatii*. Bar = 50µm.

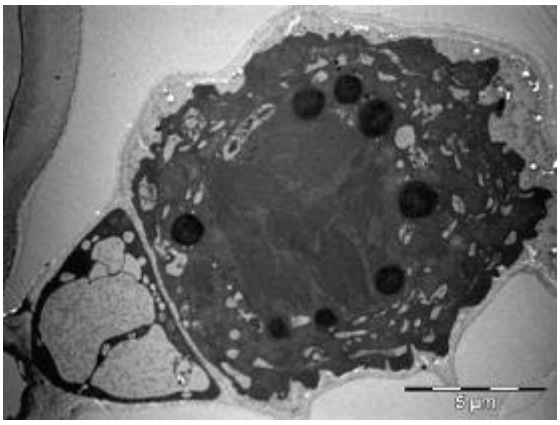

Figure 3. Transmission electron micrographs of glandular trichome of *Satureja horvatii*. Bar = 2 µm.

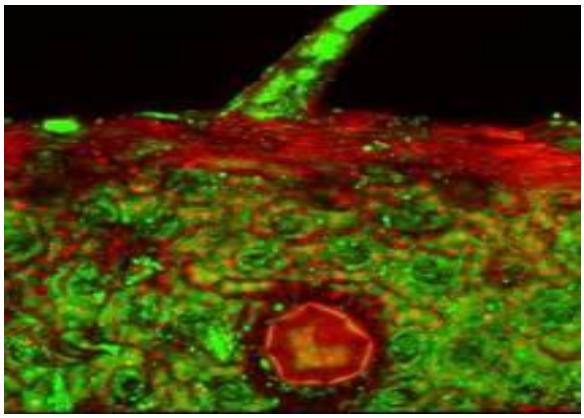

Figure 4. CLSM micrographs of leaf of *Satureja horvatii* 100x.

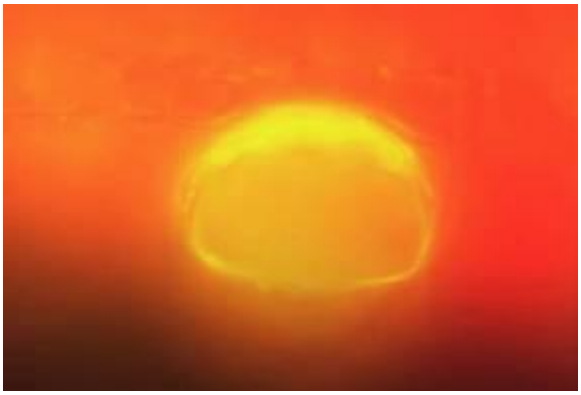

Figure 5. Bright yellow autofluorescence of secreted material in the peltate trichome of *Satureja horvatii* 100x.

Subcellular Processes in Plants and Animal Cells

LS.7.P190
Stomach and hindgut cuticular lining differentiation during embryogenesis of the crustacean *Porcellio scaber*

P. Mrak[1], N. Žnidaršič[1], U. Bogataj[1], M. Tušek-Žnidarič[2,1], J. Štrus[1]

[1]University of Ljubljana, Biotechnical faculty, Department of Biology, Ljubljana, Slovenia
[2]National Institute of Biology (NIB), Ljubljana, Slovenia

polona.mrak@bf.uni-lj.si
Keywords: cuticle, digestive tract, ultrastructure, embryo, marsupial manca, terrestrial isopods

Crustaceans possess a cuticle that covers body surface and ectodermal parts of the digestive system. Exoskeletal cuticle in adult terrestrial isopod crustaceans is a thick apical extracellular matrix secreted by epidermis, characterized by organization into several layers and displaying helicoidal arrangement of fibers [1]. Cuticle lining the lumen of the hindgut is thinner, consisting of a proximal lucent homogenous matrix and electron dense distal layer [2] (Figure 1). Cuticular structures inside the stomach are very diverse and complex, forming grinding and filtering devices. Both, exoskeletal cuticle and cuticle of the digestive tract are based on the chitin-protein network, but differ in architecture and functions. So, general as well as specific features are expected in the *de novo* formation of these matrices during embryogenesis. Here we present a microscopic characterization of the cuticle formation in the stomach and hindgut during embryonic and larval development of *Porcellio scaber*. The results are discussed with respect to data obtained on exoskeletal cuticle formation during embryogenesis [3].

Embryos and mancae of the isopod crustacean *Porcellio scaber* were isolated from the marsupium. Staging was performed as reported in developmental staging system of *Porcellio scaber* distinguishing twenty different morphological stages, from fertilized egg, through early-, mid- and late-stage embryos to hatched larva manca [4]. Specimens were fixed in 2.5% glutaraldehyde in 0.1 M cacodylate buffer (pH 7.2), postfixed in 1% OsO_4 and embedded in Agar 100 resin. Semithin and ultrathin sections were made with Ultracut S (Leica), stained with Azure II – Methylene Blue or contrasted with 4% uranyl acetate and 10% lead citrate, respectively.

In late embryo stomach differentiation into a grinding and filtering device is observed and the typhlosole formation is noticeable in the anterior hindgut [5]. Cuticular lining is discerned in the stomach and hindgut, consisting of homogenous lucent matrix and a thin intensely ruffled dense layer facing the lumen (Figure 2). It morphologically resembles the embryonic epidermal matrix, that is formed before formation of typical exoskeletal cuticle [3]. In early marsupial manca formation of the typhlosole throughout the anterior hindgut region is evident, appearing as a ridge of cells in dorsal wall, protruding in the lumen (Figure 3a). In late marsupial manca the ridges and folds of the hindgut epithelium forming typhlosole channels are fully developed and similar to adults. The cuticle lining the lumen of the hindgut is not ruffled as it is in embryos and ultrastructurally resembles the adult hindgut cuticle. It is composed of the thick homogenous lucent layer overlaid with a thin trilaminar sheet (Figure 3b). The thickness of manca hindgut cuticle is only about one third of the adult one. The exoskeletal cuticle in the same specimen is divided in principal layers and displays characteristic pattern of chitin-protein fibers arrangement [3]. Our results show that formation of the gut and exoskeletal cuticles occurs already in late embryos and in this stage both are composed of structurally similar matrices. In marsupial mancae specialization of both cuticles is evident, hindgut cuticle acquires smooth outline and more prominent surface dense layer and exoskeletal cuticle differentiates in several layers displaying chitin-protein fibers patterns.

1. B.H.M. Seidl, A. Ziegler, Zookeys 176 (2012), p. 73-85.
2. J. Štrus, D. Drobne, P. Ličar in "Terrestrial isopod biology, Crustacean issues 9", ed. M. A. Alikhan, (A. A. Balkema, Rotterdam) (1995), p. 15-23.
3. P. Mrak, N. Žnidaršič, M. Tušek-Žnidarič, W. Klepal, D. Gruber, J. Štrus, Zookeys 176 (2012), p. 55-72.
4. M. Milatovič, R. Kostanjšek and J. Štrus, Journal of Crustacean Biology 30(2) (2010), p. 225-235.
5. J. Štrus, W. Klepal, J. Repina, M. Tušek-Žnidarič, M. Milatovič, Ž. Pipan, Arthropod Structure and Development 37 (2008), p. 287-298.

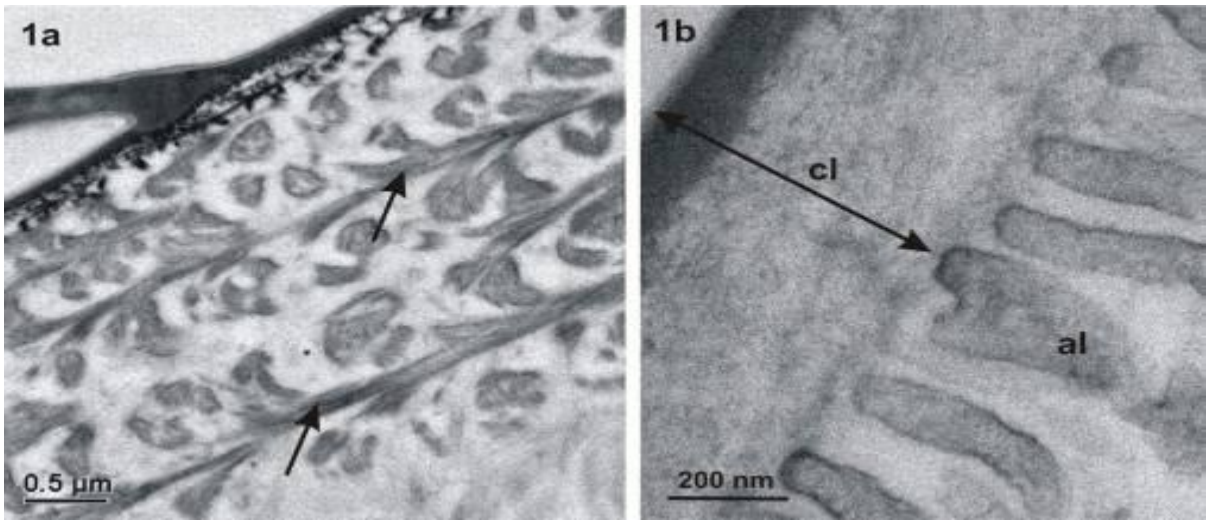

Figure 1: Adult *Porcellio scaber* (a) Distal part of exoskeletal cuticle. Bundles of chitin-protein fibers (arrows) are clearly resolved and are arranged in helicoidal layers. (b) Cuticular lining (cl) of the hindgut consists of a non-patterned proximal layer and a dense layer facing the lumen. Epithelial cells have a distinctive apical labyrinth (al).

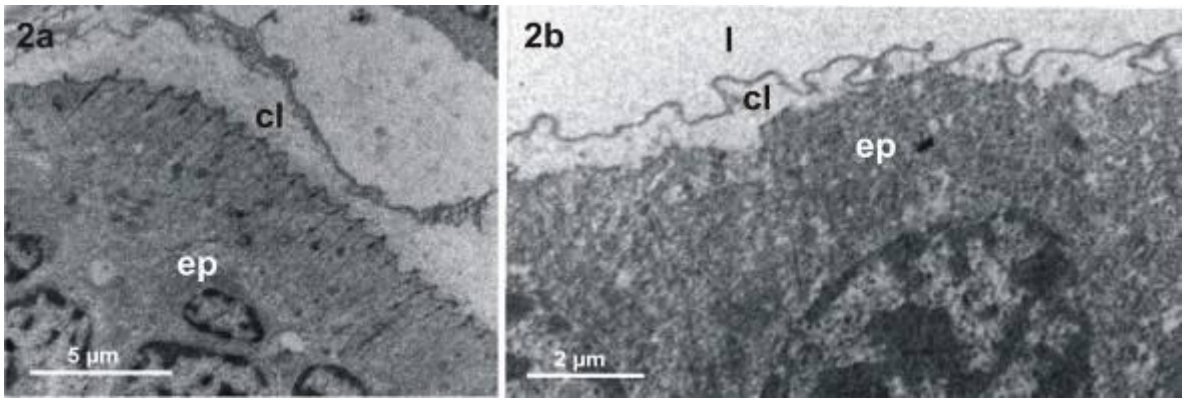

Figure 2: Late embryo of *Porcellio scaber*. Cuticular lining (cl) is distinctive in the filtering region of stomach (a) and the hindgut region (b). The matrix is intensely ruffled and consists of homogenous lucent material, lined distally by a thin dense layer. l – lumen of hindgut; ep – epithelium.

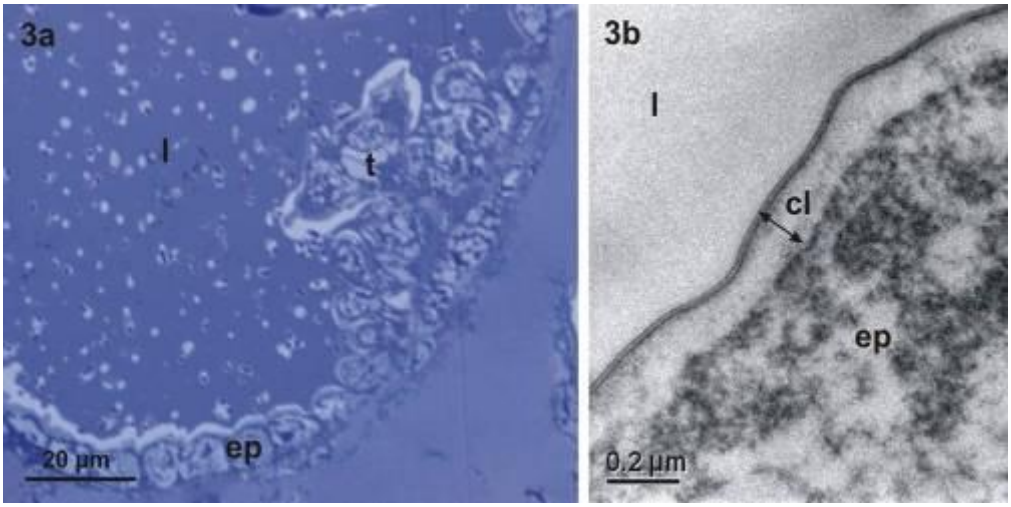

Figure 3: Early marsupial manca of *Porcellio scaber.* (a) Typhlosole formation (t) is evident in the anterior region of the hindgut. (b) Cuticular lining (cl) of the posterior hindgut region is an apical matrix, consisting of a homogenous lucent layer, lined by a trilaminar surface layer. l – lumen of hindgut; ep – hindgut epithelium.

Subcellular Processes in Plants and Animal Cells

LS.7.P191
Fluorescent methods in recent studies of pollen physiology

M. Breygina[1], N. Matveyeva[1], I. Yermakov[1]

[1]Lomonosov Moscow State University, Plant Physiology, Moscow, Russian Federation

pollen-ions@yandex.ru

Pollen grain is a 2- or 3-cellular organism specified for fertilization in plants. Two sperms or their progenitor cell are located within the large vegetative cell. Mature pollen that is released from stamen is dehydrated and dormant. After landing on a pistil of a flower, it hydrates, activates metabolism and vegetative cell forms a pollen tube, which grows with an amazing speed and brings sperms to the ovule. The first microscopic observations of pollen were described in the middle of XVII century. Early studies were focused on pollen morphology and the role of pollen grain in fertilization. In recent works spotlight is shifted towards fundamental mechanisms of cell polarization and polar growth. The least studied is the process of pollen release from the dormant state and its activation, due to the massive pollen wall, which causes significant methodological limitations. Our investigations have been focused on the role of inorganic ions in germination. Earlier it has been demonstrated that calcium and protons form an intracellular gradient with the peak concentration of calcium close to the pollen tube tip [1] and an alkaline band in subapical region [2]. The role of anions remained a mystery. We studied the role of anion channels in pollen activation and the regulation of pollen tube growth with qualitative and quantitative fluorescence microscopy. One of the most important parameters of physiological activity is plasmalemma membrane potential. We used two fluorescent dyes for detection of membrane potential shifts - slow potential-dependent dye $DiBAC_4(3)$ and fast voltage-sensitive indicator Di-4-ANEPPS. Both dyes hadn`t been previously used for plant cell studies. Along with that, to assess the distribution and movement of organelles in the cytoplasm, we used widely applied dies for mitochondria (NAO) and membrane traffic (FM 4-64). We found that during pollen activation membrane hyperpolarization of the vegetative cell plasmalemma occurs (Figure 1). Anion channel blocker NPPB caused membrane depolarization in pollen (Figure 1) and totally blocked germination, reflecting the key role of anion channels in the induction of this process [3]. A novel technique of membrane voltage mapping was applied to pollen tubes, revealing a longitudinal gradient along the pollen tube, which is maintained predominantly by NPPB-sensitive anion channels and, to a lesser extent, by H^+-ATPase. In normal (growing) tubes subapical region was relatively depolarized and the shank of the tube was hyperpolarized (Figure 2); NPPB completely dissipated the gradient in both regions and arrested the tube growth [4]. An important feature of tip-growing cells is polar organelle distribution. It can be clearly seen in double-stained pollen tubes: the tip is tightly packed with membrane vesicles travelling towards apical membrane and forming a cone (Figure 3a). Subapical region contains mitochondria, moving along a reversed fountain trajectory. We found that NPPB severely disrupted this pattern, with tip-adjacent cone dissipating and mitochondria entering the apical zone (Figure 3b).

Obtained results demonstrate the role of anion channels in pollen germination and a tight connection between ionic regulation of polar growth and morphological mechanisms underlying the process.

1. Rathore, K.S., Cork, R.J., Robinson, K.R. Dev. Biol. 148 (1991), p. 612–619.
2. Feijo, J.A., Sainhas, J., Hackett, G.R., Kunkel, J.G., Hepler, P.K. J. Cell Biol. 144 (1999), p. 483–496.
3. Breygina, M.A., Matveyeva, N.P., Yermakov, I.P. Rus. J. Devel. Biol. 39 (2009), p. 157–164.
4. Breygina, M.A., Smirnova, A.V., Matveyeva, N.P., Yermakov, I.P. Cell Tiss. Biol. 3 (2009), p. 573-582

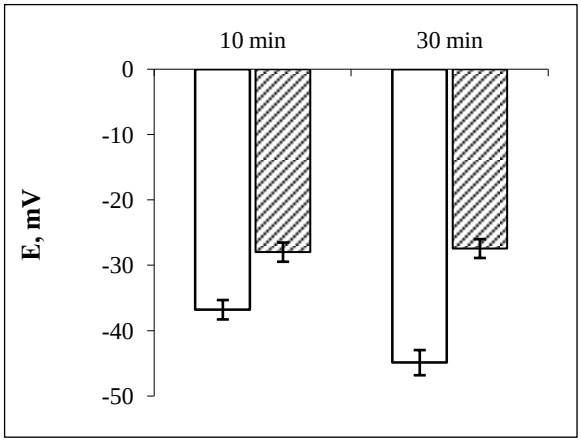

Figure 1. Changes in membrane potential of vegetative cell plasmalemma measured at the initial (10-min incubation) and final (30-min incubation) stage of pollen activation; white bars – control pollen, hatched bars – pollen incubated in the presence of 40 µM NPPB. Measurement was performed with $DiBAC_4(3)$.

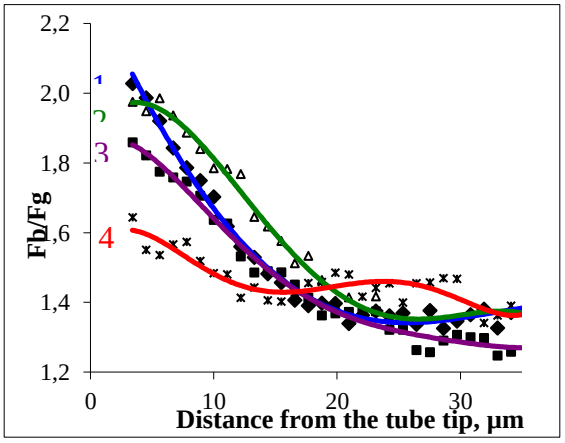

Figure 2. Longitudinal membrane potential gradient in tobacco pollen tube, revealed by a change of the Fb/Fg ratio in control (1) and under effect of 1 mM sodium orthovanadate (2), 1 µM fusicoccin (3) or 40 µM NPPB (4). Measurement was performed with Di-4-ANEPPS. Fb – intensity of fluorescence measured in the red spectral range at excitation in the blue range, Fg – the same at excitation in the green range.

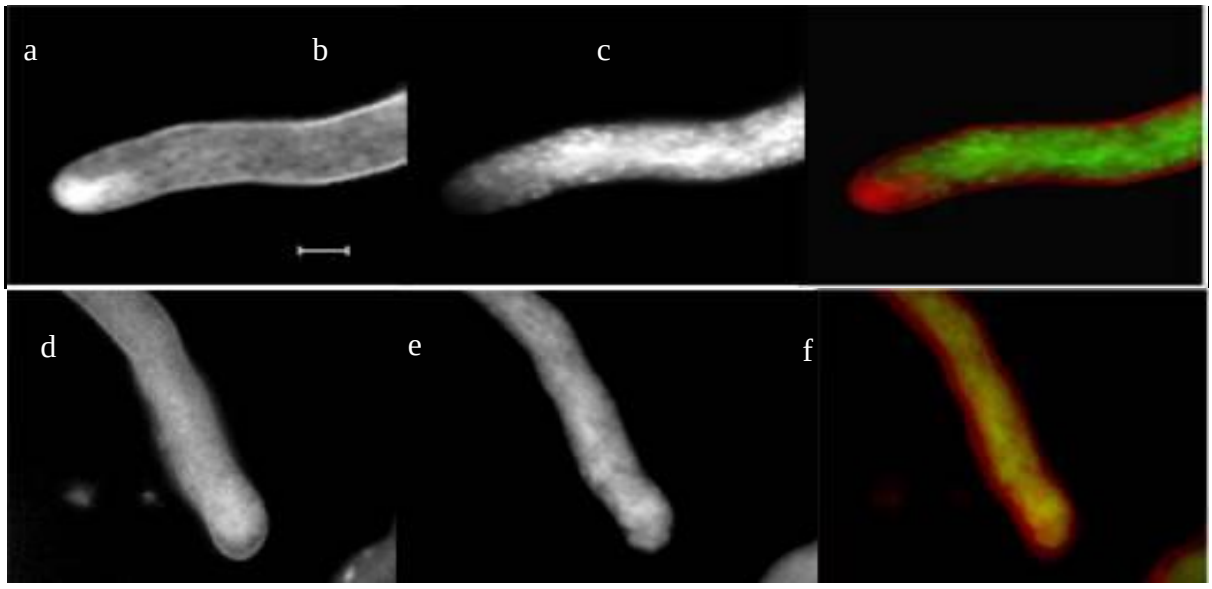

Figure 3. Effect of anion channel blocker on the distribution of transport vesicles and mitochondria in pollen tubes identified by double staining (c, f). Pollen germination and tube growth took place in medium with two dyes, FM4-64 (a, d) and NAO (b, e). Later samples were transferred into a dye-free medium with (d, e, f) or without (a, b, c) 40 µM NPPB.

Subcellular Processes in Plants and Animal Cells

LS.7.P192
The cell makers in tolerant plant to air pollutants in Rain Forest, Brazil

A. Nunes Vaz Pedroso[1], M. Domingos[1]

[1]Institute of Botany, Center of Research Ecology, São Paulo, Brazil

andreanvpedroso@gmail.com
Keywords: cell wall, organelles, phenolic compounds

Tibouchina pulchra (Cham.) Cogn., a pioneer tree species commonly found in coastal mountains, in the Cubatão city – southeast Brazil, has been used as a biomonitor due to its high tolerance to air pollutants. This region which the plants were exposed is contaminated by air pollutants, mainly sulphur dioxide, oxides of nitrogen, ozone and particulate matter, from a petrochemical industry. Biochemical and physiological responses on this species has been found in the literature, indicating the ability to environmental change [1, 2]. However, ultrastructural analyses are of major importance to understanding of cellular mechanisms which this plant is subject. In the literature are cited ultrastructural markers that identify changes caused by oxidative stress used in active (young plants) and passive (adult plants) biomonitoring [3]. Therefore, this study aimed to verify that these markers are found in plants of *T. pulchra* and which distinguish among the different types of biomonitoring.

Samples of the material were fixed in Karnovsky's solution [4] for 24h, washed in phosphate buffer and post-fixed in 1% osmium tetroxide for 2h, and kept on uranyl acetate overnight. The fixed material was washed and then dehydrated using a graded ethanol series, infiltrated and embedded in Spurr or LR White resin. TEM sections was being cut at about 90nm using a glass knife and a Leica EMUC6 ultramicrotome. Sections were stained with uranyl acetate and lead citrate. The permanent slide was also taken for interpretation. Preliminary results showed: thickening, collapse and strand protrusion of cell walls and degradation of lamella media. The chloroplasts presented starch grains, numerous plastoglobuli with different intensities of the electron density, but thylacoids membranes were healthy and organized. Mitochondria showed slight swelling in their cristae. Additionally, it was observed the condensation of chromatin and nucleus degeneration. There was the production and accumulation of phenolic compounds on vacuole in adult when compared to young plants (Figure 1). Thus, *T. pulchra* showed the cell markers and these indicate that adult plants tend to have higher production of antioxidants and consequently a higher level of tolerance to oxidative stress.

1. Klumpp, G., Furlan, C. M., Domingos, M., Klumpp, A. 2000. Response of stress indicators and growth parameters of *Tibouchina pulchra* Cogn. exposed to air and soil pollution near the industrial complex of Cubatão, Brazil. Science of Total Environment 246, 79 – 91.
2. Moraes, R.M., Furlan, C.M. , Bulbovas, P., Domingos, M., Meirelles, S.T., Salatino, A., Delitti, W.B.C. & Sanz, M.J. 2004. Photosynthetic responses of tropical trees to short-term exposure to ozone. Photosynthetica 42 (2): 291-293.
3. Vollenweider, P., Ottiger, M. & Günthardt-Goerg. 2003. Validation of leaf ozone symptoms in natural vegetation using microscopical methods. Environmental Pollution 124: 101-118.
4. Karnovsky, M.J. 1965. A formaldehyde-glutaraldeyde fixative of high osmolality for use in electron microscopy. Journal of Cell Biology 27: 137-138.

5. Acknolwedge: We gratefully acknowledge FAPESP (Fundação de Amparo à Pesquisa ao Estado de São Paulo; proc. 2011/11102-3) for financial support,

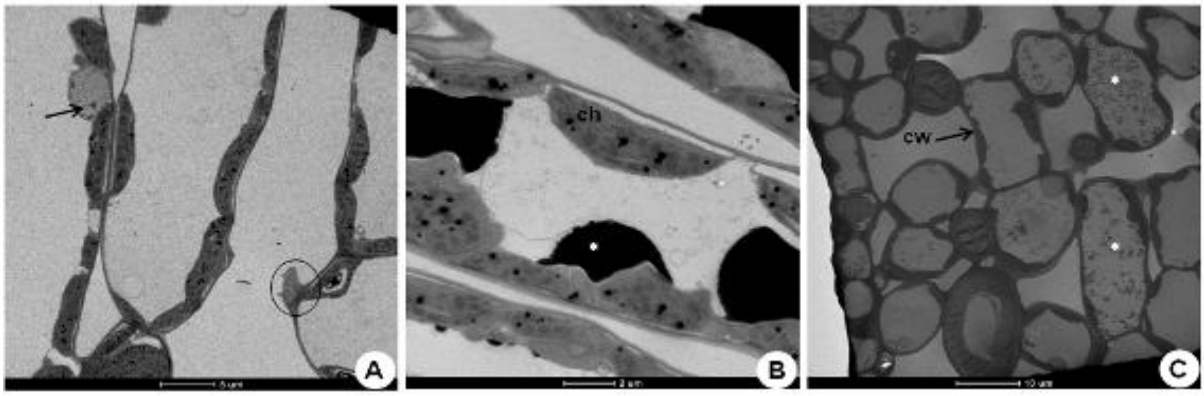

Figure 1. Ultrastructural features of *Tibouchina pulchra*. (A) Mesophyll cells, arrows indicate nucleus degeneration and ellipse indicate strand protrusion; (B) palisade mesophyll with chloroplast (ch) and asterisks indicate phenolic compounds; (C) thickening cell wall (cw) in spongy mesophyll and asterisks indicate phenolic compounds.

Subcellular Processes in Plants and Animal Cells

LS.7.P193
Ultrastructural studies of mucilage secretion in stipular colleters of Ixora heterodoxa (Rubiaceae)

F. Tresmondi[1], S.R. Machado[1]

[1]São Paulo State University, UNESP/Institute of Biosciences of Botucatu, Department of Botany, Botucatu, Brazil

ftresmondi@ibb.unesp.br
Keywords: colleter, mucilage, ultrastructure

Colleters are multicellular secretory structures found on the adaxial surface of young reproductive and/or vegetative organs in many angiosperm families [1]. These structures produce a mucilaginous or resinous substance, and function to protect the shoot meristem and leaf primordia against desiccation and pathogens [2,3].

In Rubiaceae, colleters are grouped into standard, dendroid and brush-like types on the basis of their morphology and structure [1]. Although colleters are reasonably common in this family, studies of their subcellular structure and function are lacking. We examined the cell features and secretion mechanism of the stipular colleters of *Ixora heterodoxa*, an evergreen species of Rubiaceae.

Vegetative apices from five specimens were collected during the plant regrowth period in a semideciduous forest located in Botucatu city (S 22º 47' 30" to 22º 50' and W 48º 26' 15"), São Paulo state, Brazil. The samples were processed by the usual methods for histology, histochemistry and ultrastructure.

In *Ixora heterodoxa* the shoot apex is protected by persistent stipules. The pale-yellow colleters are located on the adaxial surface of the stipules, and produce a mucilaginous secretion in the sprouting period. The colleters are of the standard type, consisting of a multicellular stalk and a head composed of a central core of axially elongated parenchyma cells surrounded by a layer of palisade epithelial cells. All the epithelial cells react positively to pectin, acid polysaccharides and protein.

The cuticle has two distinct regions: the cuticle proper, and the cuticular layer, which has an electron-dense network in the amorphous matrix. The epithelial cells of colleters in the secretory phase have large nuclei, abundant cytoplasm with free ribosomes, numerous mitochondria with well-developed cristae (Figure 1A), rough and smooth endoplasmic reticulum, plastids, and many Golgi bodies with numerous cisterns and associated vesicles (Figure 1B). The large plastids are polymorphic and contain electron-dense bodies with variable shapes (Figure 1A). The vesicles are filled with fibrillar material and osmiophilic granules.

The vesicles fuse together to form vacuoles, or fuse with the plasma membrane to form the periplasmic spaces (Figure 1C). The secretion (seen as dense fibrillar material mixed with osmiophilic granules) can be observed in the prominent periplasmic space in the distal portion of the epithelial cell, in the large intercellular spaces formed by the dissolution of the middle lamella along the anticlinal cell walls, and inside pockets in the outer periclinal walls (Figure 1C).

The ultrastructure of colleters in *I. heterodoxa* is similar to colleters of other species of Rubiaceae that produce mucilage [3, 4, 5]. The large number of Golgi stacks close to the large vesicles indicates that these organelles are intensely active in mucilage secretion and transport [6]. The degradation of the epithelial cell walls, combined with pressure from the accumulated material in the periplasmic space, can facilitate the passage of the secretion through the cell wall [7]. Pockets in the outer periclinal cell wall may also facilitate the passage of the secretion, which reaches the subcuticular space and finally the external environment [8]. The presence of microchannels in the cuticular layer allows the exudates to be externalized through the intact cuticle.

Acknolwedge: We gratefully acknowledge FAPESP (Fundação de Amparo à Pesquisa ao Estado de São Paulo; proc. 2011/02488-5) for financial support.

1. Thomas V. 1991. Structural, functional and phylogenetic aspects of the colleter. Annals of Botany 68: 287–305.
2. Fahn, A. 1979. Secretory tissues in plants. Academic Press, New York.
3. Machado, S. R., Barreiro, D.P., Rocha, J.F., Rodrigues, T.M. 2012. Dendroid colleters on vegetative and reproductive apices in Alibertia sessilis (Rubiaceae) differ in ultrastructure and secretion. Flora 207: 868-877.
4. Klein, D.E., Gomes, V.M., Silva-Neto, S.J. & Da Cunha, M. 2004. The structure of colleters in several species of *Simira* (Rubiaceae). Annals of Botany 94: 733-740.

5. Miguel, E.C., Klein, D.E., Oliveira, M.A., Da Cunha, M., 2010. Ultrastructure of secretory and senescence phase in colleters of Bathysa gymnocarpa and B. stipulata (Rubiaceae). Rev. Bras. Bot. 33, 425–436.
6. Fahn, A. 1988. Secretory tissues in vascular plants. New Phytologist 108: 229–257.
7. Paiva, E.A.S., 2009. Occurrence, structure and functional aspects of the colleters of Copaifera langsdorffi Desf. (Fabaceae, Caesalpinioideae). Compt. Rend. Biol. 332, 1078–1084.
8. Evert, R.F., 2006. Esau's Plant Anatomy, Meristems, Cells, and Tissues of the Plant Body: Their Structure, Function, and Development. John Wiley & Sons, Inc., New Jersey.

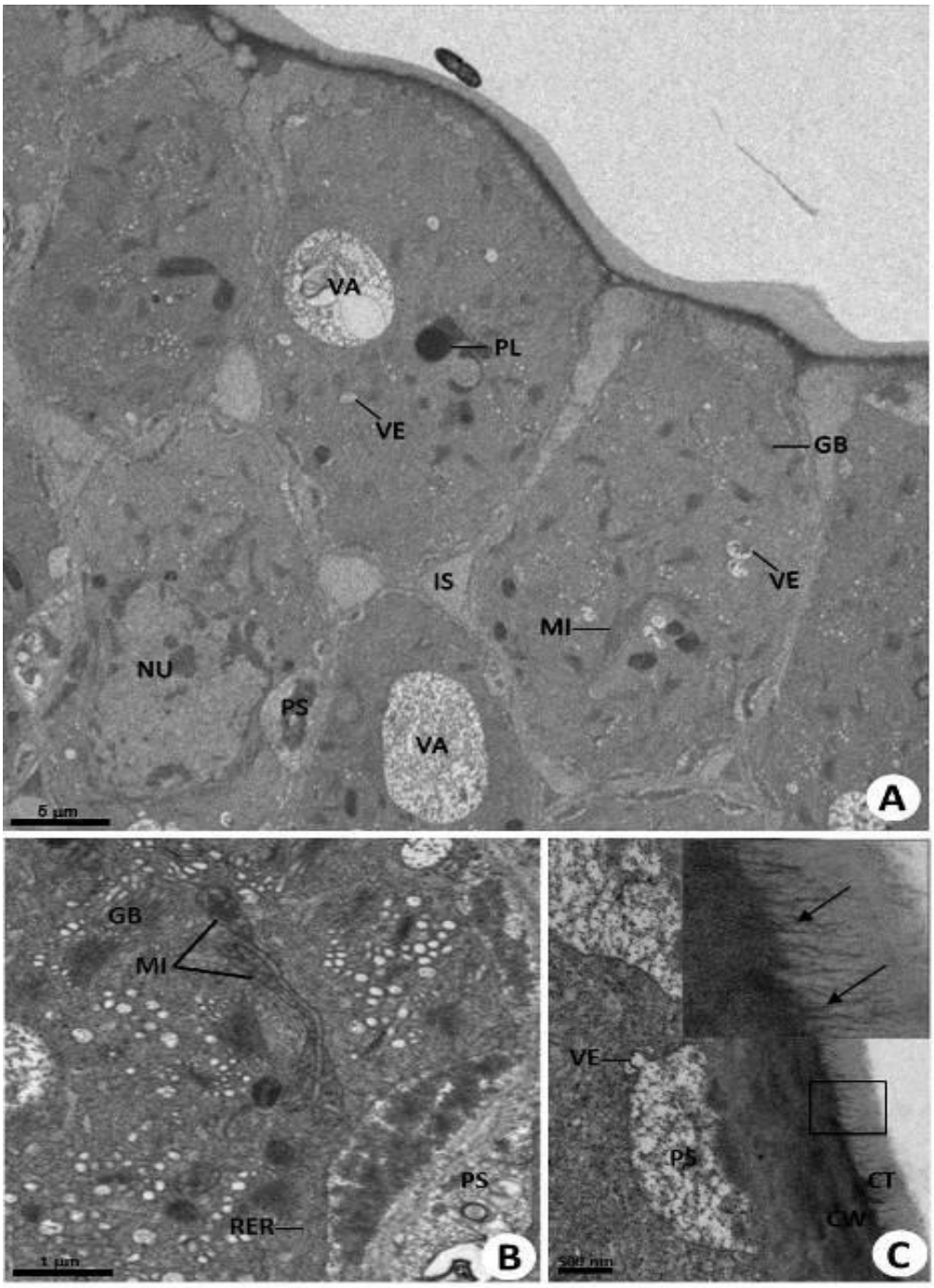

Figure 1. (A–C) Transmission electron micrographs (TEM) of epidermal cells of standard colleters in stipules of *Ixora heterodoxa*. (A) General view of epidermal cell showing abundant cytoplasm containing ribosomes, a voluminous nucleus, Golgi bodies, plastids, mitochondrias and vesicles. Notice the intercellular and periplasmic spaces. (B) Epidermal cell with rough endoplasmic reticulum, numerous Golgi bodies associated with vesicles, mitochondria with well-developed cristae. (C) Fusion of vesicles to the plasmalemma release content to the periplasmic space.(C) Periplasmic space containing fibrillar material. The insert shows fibrillar material mixed with osmiophilic granules in the cuticle (arrows). CT: cuticle; CW: cell wall; GB: Golgi bodies; IS: intercellular space; MI: mitochondria; NU: nucleus; PL: plastid; PS: periplasmic space; RER: rough endoplasmic reticulum; VA: vacuoles; VE: vesicles.

Subcellular Processes in Plants and Animal Cells

LS.7.P194
Interaction of heavy ions with nuclear chromatin: Spatiotemporal investigations of biological responses in a cellular environment

B. Jakob[1], M. Beuke[1], I. Alber[2], J. Engelhardt[3], S. Hell[3], M. Durante[1,4], G. Taucher-Scholz[1,5]

[1]GSI Helmholtzzentrum für Schwerionenforschung, Biophysik, Darmstadt, Germany
[2]GSI Helmholtzzentrum für Schwerionenforschung, Materialforschung, Darmstadt, Germany
[3]DKFZ, High Resolution Optical Microscopy, Heidelberg, Germany
[4]Technische Universität Darmstadt, Festkörperphysik, Darmstadt, Germany
[5]Technische Universität Darmstadt, Biologie, Darmstadt, Germany

b.jakob@gsi.de

Ion beams offer the possibility to generate strictly localized DNA lesions within subregions of a cell nucleus. The distribution of the ion induced damage can be indirectly visualized by immunocytochemical detection or, in living cells, by GFP-protein constructs of repair related proteins in the form of ionizing radiation induced foci (IRIF). The observed inhomogeneous spatial pattern of lesions depends mainly on the radial dose profile of the traversing particle, but biological properties of the target like chromatin distribution and/or chromatin movement can also affect the obtained images. Introducing an irradiation geometry characterized by a small angle between the plane of the cellular monolayer and the incoming ion-beam allows the spatial analysis of protein accumulations along linear ion trajectories, revealing an unexpected clustering. To study the chromatin and protein dynamics during and after irradiation, a remote controlled microscope device was used at the accelerator facility of GSI. The system enables the acquisition of high-resolution fluorescence images of stained living cells during ion irradiation. This allows us to study early radiation effects without the time lag of minutes presently conditional on limitations of access to the irradiation device.

Time-lapse images of GFP-coupled proteins during irradiation proved accumulations within seconds at sites of ion hits indicating a very fast recognition of DNA damage in combination with a quite stable location of damage processing. The number of observed radiation-induced foci along the ion tracks did not match the expected amounts of DSBs. To gain further insight in the distribution of lesions along the ion path, we applied high resolution 4Pi and STED microscopy revealing a central focus of repair proteins Mre11 or RPA representing multiple DSBs embedded in a speckled cloud of γ-H2AX or 53BP1 visualizing the response on megabase-pair domains. In addition, first attempts to image the DNA damage and IRIF along the ion tracks using scanning electron microscopy (SEM) in combination with immunogold-labeling under conditions preserving the 3D topology of the chromatin are shown.

Subcellular Processes in Plants and Animal Cells

LS.7.P195
Comparison of different fixation methods for the acoel worm Symsagittifera roscoffensis

A. Pfannkuchen[1], X. Bailly[2], R. Entzeroth[3], T. Kurth[1]

[1]TU Dresden, CRTD, EM-Facility, Dresden, Germany
[2]Universite´ Pierre et Marie Curie- CNRS, Station Biologique de Roscoff, Roscoff, France
[3]TU Dresden, Biologie, Dresden, Germany

anja.pfannkuchen@web.de

Symsagittifera roscoffensis GRAFF (1882) belongs to the class of the acoela, which are marine worm-like animals without gut or anus. Recently several studies on genomic sequences of acoela showed that this group may be the sister taxon to all remaining bilateria [1]. Some species (e.g. *S. roscoffensis*) can form symbioses with green algae, which allows them to live like photoautotroph organisms. The larvae of *S. roscoffensis* acquire their algae (*Tetraselmis convolutae*) shortly after their hatching, and there is no vertical transfer of the symbionts via the egg cytoplasma [2]. Without this symbiosis the larvae cannot reach the adult stage. After infection the symbionts arrange dircectly under the epidermis, where they are exposed to the light.

Recently *S. roscoffensis* was established as a model for basic CNS-organisation [3], regeneration [4], or the relationship between an invertebrate and symbiotic algae [5].

For such studies a good ultrastructural analysis is necessary. In the present study we tested different fixation methods on *S. roscoffensis*. At first we compared conventional chemical fixation (3,5 % glutaraldehyde in 50 mM HEPES- buffer with 3 % NaCl and 8 % sucrose [6], figure 1A) and sample processing with high pressure freezing (HPF, figure 1 C,D) followed by freeze substitution. After high pressure freezing the tissue is dense and packed with organelles and vesicles in contrast to the samples after conventional sample processing, where vesicles are extracted.

For samples that cannot be cultured and must be collected in the field, high pressure freezing is not practicable. For such samples a combination of chemical fixation followed by a freeze-substitution (see figure 1 B) is advisable. The results of this procedure are comparable to those of the HPF-samples. Chemical fixation and freeze substitution may also be a good alternative for samples that cannot be frozen properly.

1. A. Mwinyi, X. Bailly, S. Bourlat, U. Jondelius, D. Littlewood and L. Podsiadlowski, BMC Evol Biol 10 (2010), p. 309.
2. R. Hinde, International Journal for Parasitology 17 (2006), p. 383-390.
3. A. Bery, A. Cardona, P. Martinez and V. Hartenstein, Develop. Growth Differ 52 (2010), p. 701-713.
4. A. Bery and P. Martinez, Acta Zoologica 92 (2010), p. 383-392.
5. S. Dupont, A. Moya and X. Bailly, PLoS ONE 7 (2012), p. 1-8.
6. W. Salvenmoser, B. Egger, J. Achatz, P. Ladurner and M. Hess, Methods Cell Biol 96 (2010), p. 307-330.

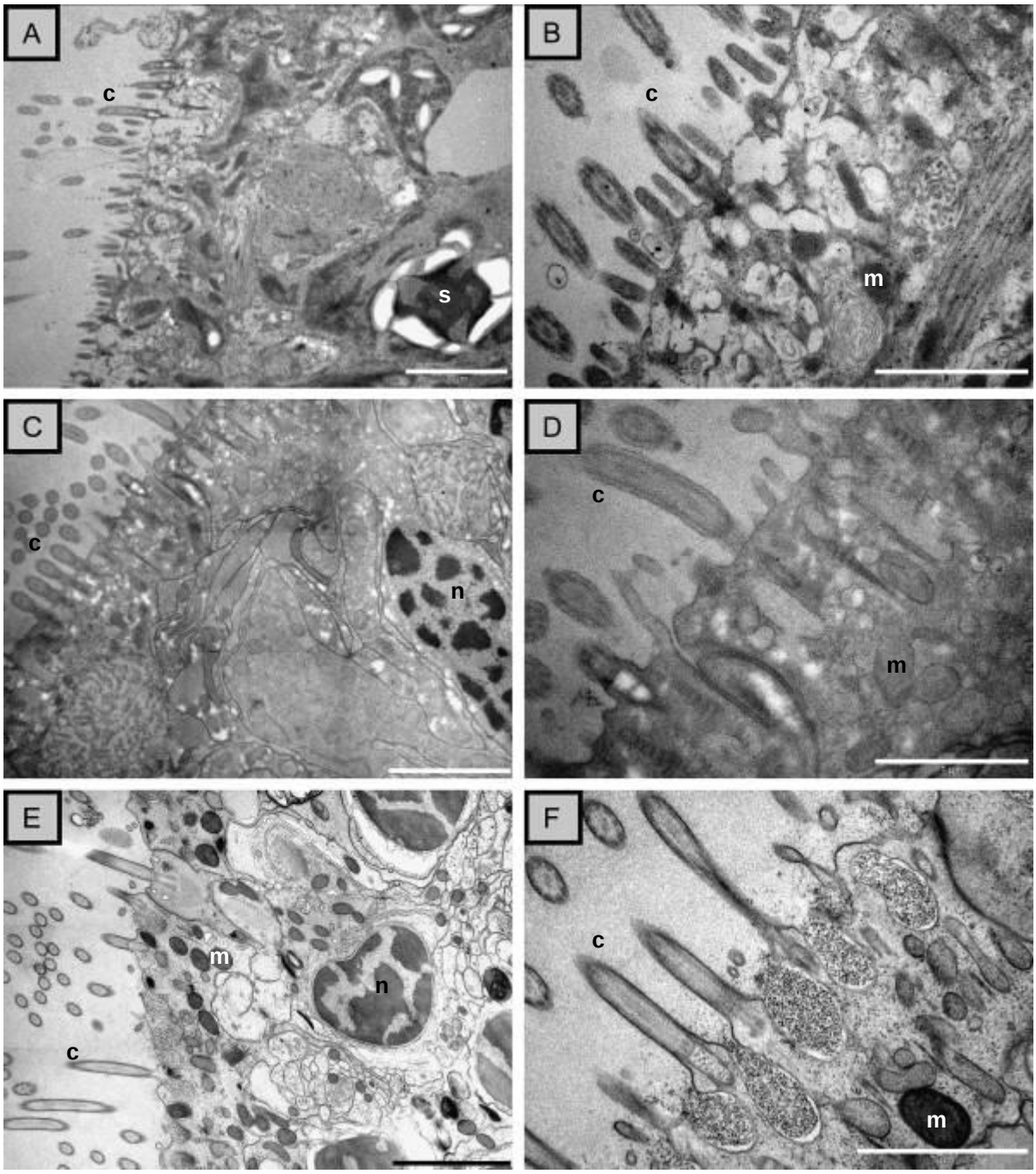

Figure 1: Comparison of different fixation methods for *Symsagittifera roscoffensis*, all pictures show the epidermis of adult worms; a) chemical fixation with 3,5 % glutaraldehyde in 50 mM HEPES- buffer containing 3 % NaCl and 8 % sucrose, scale bar 2 µm; b) chemical fixation as in A, details, scale bar 1 µm; c) chemical fixation as in A followed by freeze-substitution, scale bar 2 µm; d) chemical fixation as in A followed by freeze-substitution, details, scale bar 1 µm; e) high pressure freezing (HPF) followed by freeze substitution, scale bar 2 µm; f) HPF, details, scale bar 1 µm; c, cilia; m, mitochondrium; n, nucleus; s, symbiont.

Subcellular Processes in Plants and Animal Cells

LS.7.P196
Visualization of Benzo[a]pyrene (B[a]P) and its metabolites in live Hepa1c1c7 cells

R. Ali[1,2], T. Hanke[2], S. Trump[2]

[1]NUI Galway, Galway, Ireland
[2]Max-Bergmann Zentrum TUDresden , Bio-materials, Dresden, Germany

rizwanali79@gmail.com

The uptake and intracellular distribution of carcinogenic polycyclic aromatic hydrocarbon (PAH), benzo[a]pyrene (B[a]P) was studied in Hepa1c1c7 cells using time-lapse two-photon microscopy and transmitted light microscopy. Rapid internalization of B[a]P was observed with aggregate formation near nucleus. Time-lapse imaging showed B[a]P aggregation in lipid vesicles. These lipid vesicles were characterized as lipid droplets (LDs). Time-lapse two-photon microscopy also revealed fusion events of B[a]P. In this study, distribution of several metabolites of B[a]P was also visualized using two-photon (2-P) microscopy in Hepa1c1c7 cells. Whole wavelength time-lapse imaging showed localization of B[a]P and its metabolites in lipid droplets (LDs) predominantly. In addition, one of the metabolite (1-OH-B[a]P) was found localized in the plasma and nuclear membranes of Hepa1c1c7 cells. We have also showed possible metabolism of B[a]P into its metabolites during time-lapse fluorescence imaging. 3-D image stacks of B[a]P exposed cells after 24 hours also revealed parent B[a]P stored alongside its metabolites in LDs (arrow in *Fig. 1*).

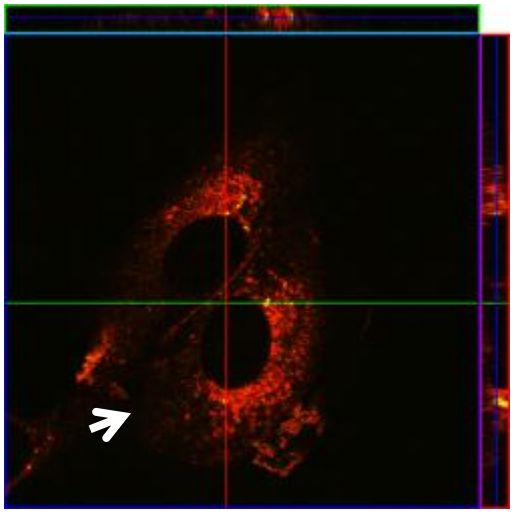

Figure 11. Orthogonal view. Ortho-view reveals B[a]P aggregates within cell cytoplasm. *Scale bar, 20 µm.*

Subcellular Processes in Plants and Animal Cells

LS.7.P197
Characterization of HBV transport pathways in macrophages

X. Cheng[1,2], J. Wettengel[1], K. Esser[1,2], U. Protzer[1,2]

[1]Institute of Virology, Technische Universität München , Munich, Germany
[2]Institute of Virology, Helmholtz Zentrum München, Munich, Germany

xiaoming.cheng@virologie.med.tum.de

The human hepatitis B virus (HBV) is a DNA virus with high species specificity and liver tropism. Our preliminary studies suggest that in human liver HBV is initially sequestered by Kupffer cells, which represent the residential macrophages, and subsequently transcytosed towards its host cell, the hepatocyte. This study aims at identifying the transportation route of HBV within Kupffer cells.

To trace the intracellular transportation of HBV, fluorescence labelled viral particles (VP) were produced. VP were harvested from HBV producing HepG2.215 cells, purified by different density gradient centrifugation and chemically labelled with an Alexa Fluor® dye. Successful labelling of viral surface proteins was confirmed by immunoassays and fluorescence analysis of protein gels. Detection of labelled VP in monocyte derived macrophage (MDM) using confocal microscopy found that after binding to MDM, VP first enter into early endosomes but were not targeted to lysosome in the later time point. Filipin was used to label free cholesterol in the cell, which was shown to localize within identical organelles as VP, suggesting a linked transport of both components. To further characterize VP transportation, intracellular cholesterol transport was blocked by a specific inhibitor U18666a and it was found that VP recycling to the plasma membrane was inhibited at the same time. To further analyse compartmentalization of HBV in macrophages, cholesterol transporting protein NPC1 was labelled by indirect immunofluorescent staining and was shown to be colocalized with VP. Finally, associated transportation of HBV with lipoprotein derived free cholesterol could be confirmed in Kupffer cells by colocalization of HBV with NBD-cholesterol originated from NBD-cholesterol labelled triglyceride rich lipoproteins.

Taken together, we propose that HBV highjacks the free cholesterol transport machinery in monocyte derived macrophages and Kupffer cells to escape lysosomal degradation and to become cellularly transcytosed which lead to trans-infection of the host cell.

Subcellular Processes in Plants and Animal Cells

LS.7.P198
Ultrastructural analysis of *Drosophila* nephrocytes by transmission electron microscopy

F. Hochapfel[1], M. Krahn[1]

[1]University of Regensburg, Molecular and Cellular Anatomy, Regensburg, Germany

florian.hochapfel@vkl.uni-regensburg.de
Keywords: nephrocytes, patj, minisog

Drosophila nephrocytes are podocyte-like epithelial cells which exhibit a complex network of labyrinthine channels in the cell periphery, which are covered by filtration slit diaphragms. They are located inside the fly body cavity anterior to the protoventriculus and alongside the dorsal heart, respectively. Their main function is the filtration of the haemolymph, thereby taking up toxins and wastes into the channel system in a size- and charge-selective manner, followed by endocytosis and storage [1].

In our study we describe the ultrastructure of the *Drosophila* nephrocytes in more detail using transmission electron microscopy. In order to investigate the subcellular localization of certain polarity regulators, we apply photoconversion using proteins tagged with MiniSog.

Furthermore, we aim to elucidate the role of several known polarity regulators in the formation and function of this cell type. Here, we have already found that a null-mutation (Δ1) of the cell polarity protein *PATJ* (Pals1-associated tight junction protein) severely impairs the development of both filtration slits and channel networks. In L3 larvae, the overall number of diaphragms is reduced and the distinct transition between the channel layer and the intracellular area is lost.

From these experiments, we hope to obtain insights into the mechanisms that regulate the formation and function of *Drosophila* nephrocytes, which might also be conserved in mammals, thereby qualifying nephrocytes as a model for mammalian podocytes and kidney function.

1. Weavers, H., Prieto-Sanchez, S., Grawe, F., Garcia-Lopez, A., Artero, R., Wilsch-Brauninger, M., Ruiz-Gomez, M., Skaer, H. and Denholm, B. (2009). The insect nephrocyte is a podocyte-like cell with a filtration slit diaphragm. Nature 457, 322-326.
2. We kindly acknowledge the help of the organizers of MC 2013 with the online submission procedure.

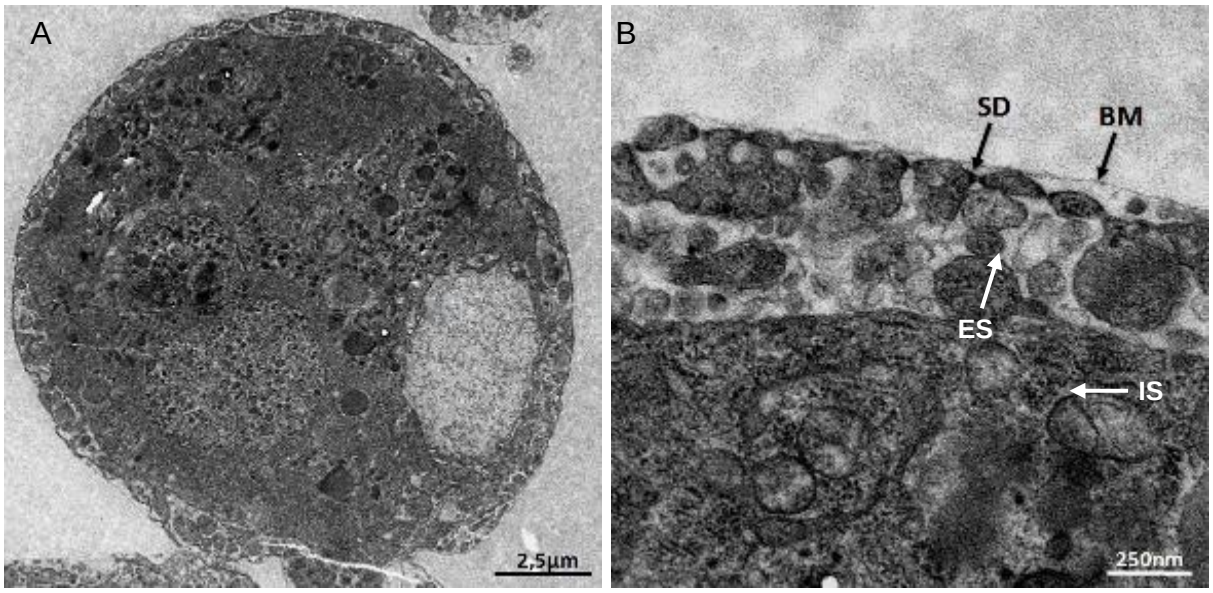

Figure 1. Wild-type organisation of nephrocyte ultrastucture. (A-B) TEM of the cortical region of nephrocytes from *sns-stinger* third-instar larva. (A) Cortical channel system made up of foot processes and extra-cellular space is apparent and distinct from the intracellular areas. (B) Slit diaphragms present throughout outer surface. Clear distinction between extra- and intracellular space. BM, basement membrane. ES, extracellular space. IS, intracellular space. SD, slit diaphragm.

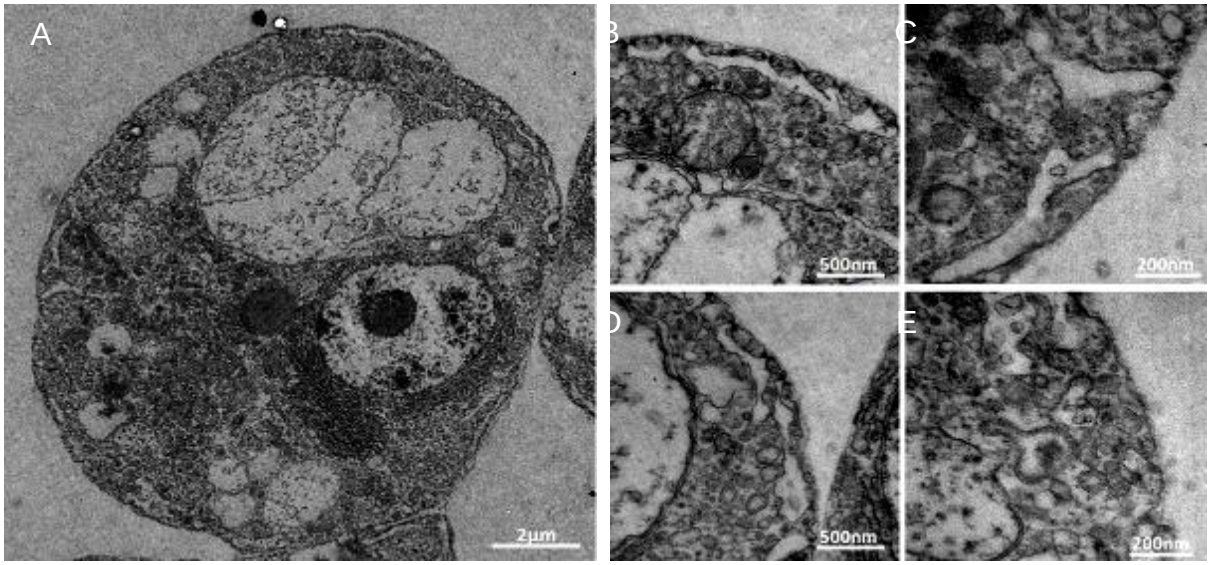

Figure 2. *PATJ* null-mutation leads to strong reduction of cortical channel layer and reduced number of slit diaphragms. (A-E) TEM of the cortical region of nephrocytes from *PATJ*$^{\Delta 1}$ third-instar larvae. (A) Cortical channel system shows reduced complexity. (B-E) Reduction or loss of slit diaphragms correlates with reduction of cortex complexity and loss of foot processes. (E) Slit diaphragms are almost completely lost.

Molecular Structures and High Resolution TEM

LBP.LS.P01
The examination with microscopic labelling methods of pancreatic β cells surface glycoconjugates' profiles in *diabetes mellitus*

Y. Mater[1], T. Uygur[1]

[1]Gebze Institute of Technology, Faculty of Science, Molecular Biology and Genetics, Gebze-Kocaeli, Turkey

ymater@gyte.edu.tr
Keywords: Diabetes mellitus, glycoconjugates profile, immunofloresans microscopy

In *Diabetes mellitus*, alterations of pancreatic β cell surface glycoconjugate profiles are influent in emerging of this disease. In several studies are showed that high levels of Sialic acid that seen in blood serum decreased of pH, binding of insulin to receptors and increased blood glucose levels in Diabetes mellitus .Reported that the increase of glucose levels are caused of more production of Sialic acid. (1)

Thus, a vicious cycle is occured. This situation showed that the sialic acid is very efficient in function of insulin, signal production and signal transduction.Also,this situation is accepted one of the causes insulin resistance that is seen in Diabetic patients.This view is supported with shown the elevation of sialic acid via neuraminidase from adipocyte and dependently inhibited the action of insulin in same study.In this study again is showed that the presence of cell surface glycoproteins are important in detection of insulin from cells in blood.It was showed using of cell surface labelling and specific exoglycosidases, structure of Insulin receptor is asparagine bound glycoprotein and it have mannose, galactose, N-acetylglucosamine and sialic acid.In following step of same study, glycosylation was inhibited with inhibitors like that tunicamysin showed that insulin receptor couldn't bind insulin and glycosylation is very important for synthesis of insulin receptor (1).Similar consequences are seen also Kavaler et al 2011 paper. Accordingly,it is determinded that loss of pancreatic β cell function, worsening glucose tolerance and sialylation with *N*-glycolylneuraminic acid (Neu5Gc) are played important roles in β cell function (2). Therefore, it is determined that monosaccharides take charge in Diabetes mellitus and occurance of insulin resistance. For this reason, characterization of glycoprotein profiles, research and visualization is very important which is found insulin receptors.For this purpose, in one study,immunohistochemical localization of O-Glc-NAc and O-Glc_NAc transferase is observed in diabetic and nondiabetic pancreas in normal and diabetic mice, is preformed using different methods like that immunoelectron microscopy and colloidal gold labelled antibodies and is tried support this data (3). Proffered our project is planned examination of pancreatic β cell surface glycoconjugate profiles in diabetic and normal mice pancreas biopsies that provided from Bilim University Medical Biology, using with fluorescent labelled antibodies and/or collodial gold labelled lectins. Thinking that,Determined and specifically labelled glycan profiles will be played a role in recognition and adherence mechanism studies, sialic acid resistance that is occurred in patients' blood directed medicine studies with changing of glycan profiles in future.

1. G.R. Hayes and D.H. Lockwood, The Role of Cell Surface Sialic Acid in InsulinR eceptor Function and Insulin Action J.of Biol.Chem., Vol261, 25(6), p:2791-2798,1986.
2. S. Kavaler, H. Morinaga, A. Jih, W.Q. Fan, M. Hedlund, A. Varki and J. J. Kim, Pancreatic -cell failure in obese mice with human-like CMP-Neu5Ac hydroxylase deficiency The FASEB Journal, Vol. 25, p:1887-1893, 2011.
3. Y. Akimoto, G. W. Hart, L. Wells, K. Vosseller, K. Yamamoto, E. Munetomo, M. Ohara-Imaizumi, C. Nishiwaki, S. Nagamatsu, H. Hirano and H. Kawakami, Elevation of the post-translational modification of proteins by O-linked N-acetylglucosamine leads to deterioration of the glucose-stimulated insulin secretion in the pancreas of diabetic Goto–Kakizaki rats Glycobiology, Vol. 17 no. 2 p: 127–140, 2007

Tissues, Pathology, and Diagnostic Microscopy

LBP.LS.P02
Ultra-large high-resolution Electron Microscopy mapping of Islets of Langerhans of Rats developing Type 1 Diabetes

R. Ravelli[1], R. Kalicharan[2], C. Avramut[1], K. Sjollema[2], J. Pronk[1], F. Dijk[2], B. Koster[1], J. Visser[2]
F. Faas[1], B. Giepmans[2]

[1]LUMC, Leiden, Netherlands
[2]UMCG, Groningen, Netherlands

raimond.nl@gmail.com
Keywords: Large scale electron microscopy, correlated microscopy, nano-anatomy, large-scale imaging, Islets of Langerhans, diabetes

Electron microscopy (EM) is the method to visualize tissue composition, cellular interactions and physiological conditions. However, conventional EM only covers a small area and usually lacks the context of the tissue. We present large-area EM imaging [1] that allows to characterize entire cross-sections of Islets of Langerhans during Type 1 diabetes onset [2]. In Type 1 diabetes, insulin producing beta cells are destroyed by the auto-immune system. Upon diagnosis, life-long exogenous insulin therapy is immediately initiated. However, this does not allow the fine-tuning as done by Islets, making it impossible to maintain proper glucose control, and patients cannot be cured. The causes and triggers of the disease are still unknown, yet several potential triggers have been named, including enteroviruses.

Our data [2], totaling over 25.000 electron micrographs stitched together in 6 datasets, shows the progressive destruction of the Islets of Langerhans, especially of the insulin-producing cells (Figure 1). The ultrastructural morphology allows the identification of individual cell types (Figure 2). Our datasets show leukocyte infiltration as well as damage to the organelles of the beta cells under attack, including mitochondrial damage and endoplasmic reticulum stress. Moreover, molecular abnormalities can be identified at higher zoom, including the debated rare filamentous nuclear actin [3]. Putative viral particles appearing in the beta cells are shown to be glycogen. Our technology will help to get a better insight into Islet changes at the cell, organelle, and molecular level during diabetes, but will also be applicable to numerous other tissues and diseases. The data will be made publicly accessible on electronmicroscopy.lumc.nl and www.nanotomy.nl .

1. Faas, F.G.A., M.C. Avramut, B.M. van den Berg, A.M. Mommaas, A.J. Koster, and R.B.G. Ravelli. Virtual nanoscopy: generation of ultra-large high resolution electron microscopy maps. *J Cell Biol* 198(3): p. 457-69 (2012).
2. Ravelli, R.B.G., R.D. Kalicharan, M.C. Avramut, K.A. Sjollema, J.W. Pronk, F. Dijk, A.J. Koster, J.T.J. Visser, F.G.A. Faas, and B.N.G. Giepmans. Destruction of Tissue, Cells and Organelles in Rats Developing Type 1 Diabetes Presented at Macromolecular Resolution. *Scientific Reports* 3: 1804-181 (2013).
3. de Lanerolle, P. and L. Serebryannyy, *Nuclear actin and myosins: Life without filaments.* Nat Cell Biol, 2011. 13(11): p. 1282-1288.

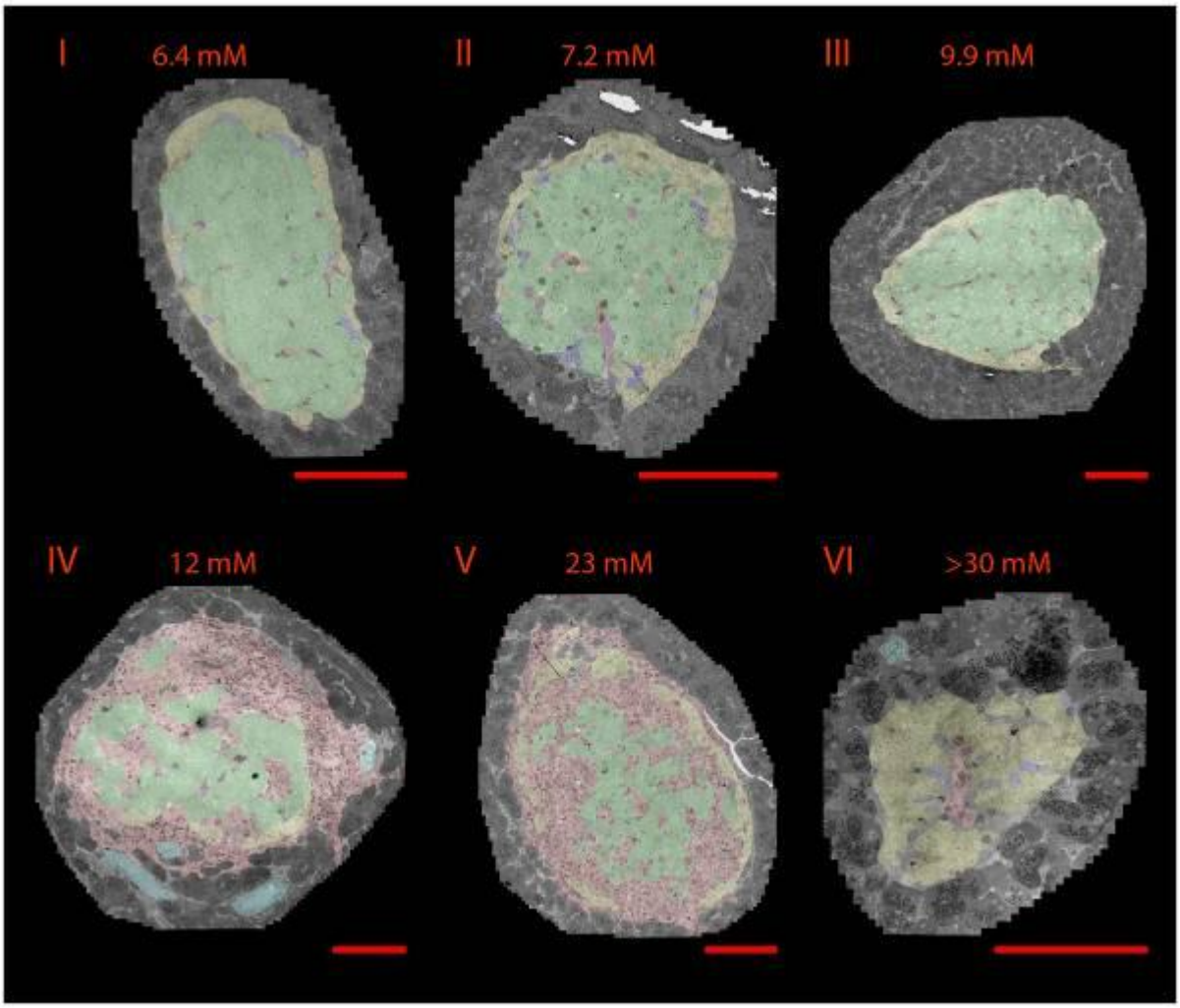

Figure 1. Islets of Langerhans during autoimmune diabetes progression. Cross-sections of entire Islets of Langerhans were acquired with a pixelsize of 3.2nm, resulting in images varying between 5 and 25 gigapixels in size. Individual cells were morphologically characterized and false-coloured according to cell-type: beta cells (green), alpha cells (yellow), leukocytes (red), ducts (purple), vasculature (cyan). (I) Diabetes resistant rat; (II)-(VI) diabetes prone rats at different stages of (pre)diabetes, as indicated by the blood sugar (BG) level. Note the massive infiltration of leukocytes (red) and the destruction of beta cells (green). Bars: 0.1mm.

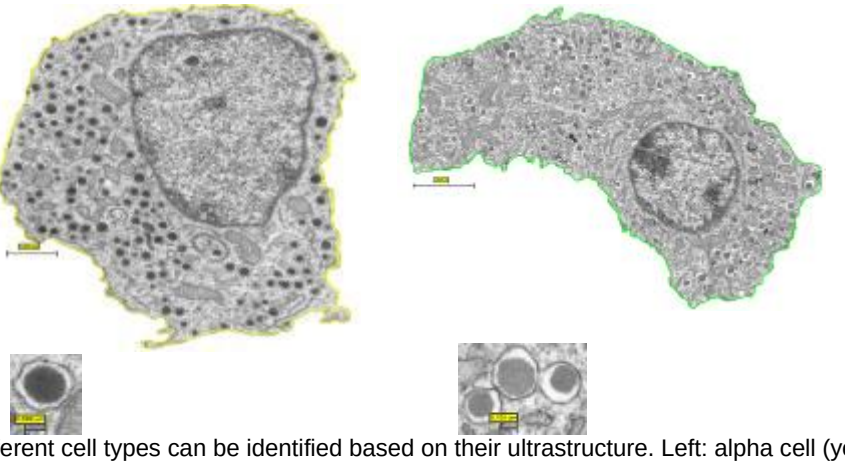

Figure 2. Different cell types can be identified based on their ultrastructure. Left: alpha cell (yellow) with granules containing darker stained glucagon; right: beta cell (green) with granules containing slightly lighter stained crystalline.

Ultrastructural & Analytical Methods in Life Sciences

LBP.LS.P03
Ultra-large high-resolution Electron Microscopy mapping of a Zebrafish Embryo

R. Ravelli[1], C. Avramut[1], M. Wiweger[1], B. Koster[1], F. Faas[1]

[1]LUMC, Leiden, Netherlands

raimond.nl@gmail.com
Keywords: ultra-large scale electron microscopy, zebrafish, cilia

Zebrafish has become a favorite model organism for biologists to study development, physiology, medicine and human diseases. The embryos are transparent which allows researchers to monitor the fate of each dividing cell during the first days of their lives [1]. Consequently, these vertebrates are studied over vastly different time and length scales. Mapping molecular events into a supracellular context remained, however, cumbersome. Here, we employed large-scale automated transmission electron microscopy [2] to visualize entire transverse sections of a 5 days old zebrafish embryo at nanometer resolution. The atlas, composed of more than 100,000 micrographs, reveals the structure of large macromolecular complexes as well as the architecture of organelles, cells, and organs within the context of the entire animal. As an example of what can be learned from such data, we scrutinized our atlas for the presence of basal bodies, centrioles and primary cilia. Primary cilia are tiny hair-like organelles emerging from most vertebrate cells during interphase. They act like an antenna that sense a wide range of signals including smell, sight, movement and intercellular signals such as Wnt and Hedgehog [3]. Primary cilia have remained elusive when viewed by electron microscopy, as the probability of observing a cross-section of a primary cilium on a given thin section is only 1% or less [4]. Within our atlas, we could identify approximately 1000 centrioles, basal bodies and primary cilia, classify their structures, and analyse their positional characteristics within their ultrastructural context.

Upon publication, the atlas will be made available via electronmicroscopy.lumc.nl as a reference for morpholino studies (Figure 1). The project was inspired by an ultrastructural study of the skeleton from five zebrafish lines with known mutations in genes involved in proteoglycan synthesis [5]. The atlas will complement anatomical atlases that are based on optical microscopy (such as http://zfatlas.psu.edu/). Our technology will also be applicable to numerous other organisms, tissues, and disease [6].

1. Keller, P.J., A.D. Schmidt, J. Wittbrodt, and E.H.K. Stelzer. Reconstruction of zebrafish early embryonic development by scanned light sheet microscopy. *Science* 322(5904): p. 1065-1069 (2008).
2. Faas, F.G., M.C. Avramut, B.M. van den Berg, A.M. Mommaas, A.J. Koster, and R.B.G. Ravelli. Virtual nanoscopy: generation of ultra-large high resolution electron microscopy maps. *J Cell Biol* 198(3): p. 457-69 (2012).
3. Wilson, C. and D. Stainier. Vertebrate Hedgehog signaling: cilia rule. *BMC Biology* 8(1): p. 102 (2010).
4. Farnum, C.E. and N.J. Wilsman. Axonemal positioning and orientation in three-dimensional space for primary cilia: what is known, what is assumed, and what needs clarification. *Dev Dyn* 240(11): p. 2405 31 (2011).
5. Wiweger, M.I., Avramut, M.C., de Andrea, C.E., Prins, F.A., Koster, A.J., Ravelli, R.B.G., and P.C. Hogendoorn. Cartilage ultrastructure in proteoglycan-deficient zebrafish mutants brings to light new candidate genes for human skeletal disorders. *J. Pathol* 223(4): 531-542 (2011).
6. Ravelli, R.B.G., R.D. Kalicharan, M.C. Avramut, K.A. Sjollema, J.W. Pronk, F. Dijk, A.J. Koster, J.T.J. Visser, F.G.A. Faas, and B.N.G. Giepmans. Destruction of Tissue, Cells and Organelles in Rats Developing Type 1 Diabetes Presented at Macromolecular Resolution. *Scientific Reports* 3: 1804-181 (2013).

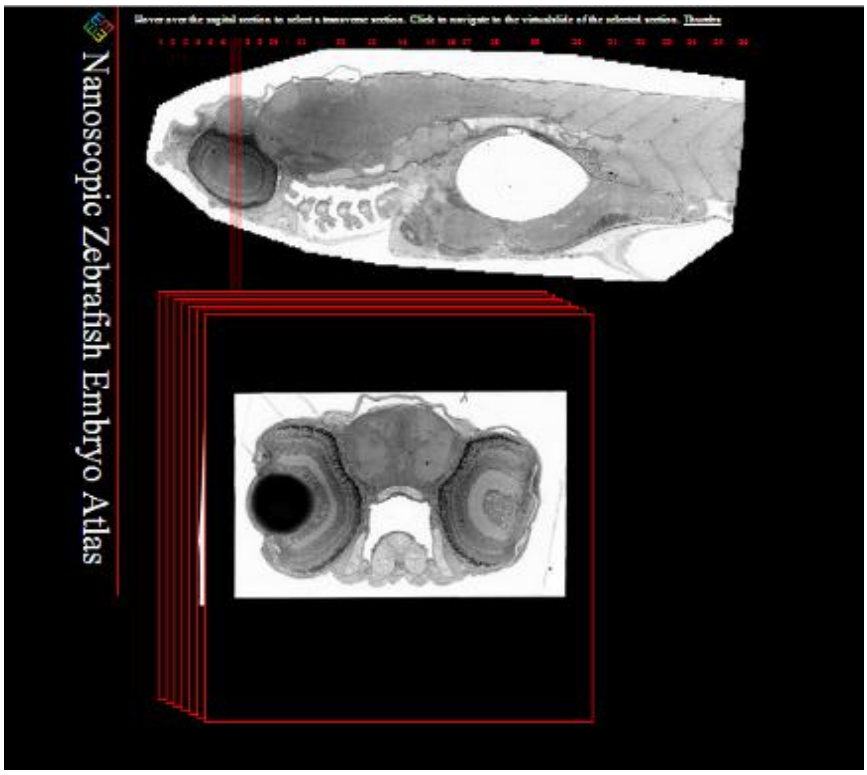

Figure 1. Overview of an ultrastructural 5dpf zebrafish atlas. The atlas consists of 26 transverse sections varying between 1 and 27 gigapixels in size per section. Each section was recorded with a pixelsize of 3.2 nm square.

Molecular Structures and High Resolution TEM

LBP.LS.P04
High-resolution cryo-EM Single Particle Structures of Macromolecular Complexes in Action

R. Ravelli[1], C. Linnemayr-Seer[2], S. de Carlo[3,4], B. Allewijnse[1,3], M. Schatz[5], R. Portugal[6]
R. Matadeen[3], M. van Heel[1]

[1]Leiden University, Leiden, Netherlands
[2]University Hospital Zürich, Zürich, Switzerland
[3]NeCEN, Leiden, Netherlands
[4]FEI, Eindhoven, Netherlands
[5]Imagic Science, Berlin, Germany
[6]Brazilian Nanotechnology National Laboratory, Campinas, Brazil

raimond.nl@gmail.com

Cryo-electron microscopy has the potential to provide insight into structural dynamics by statistically analysing the conformational state of cryo-trapped individual molecules. Traditionally, sample heterogeneity would lead to a compromised resolution when the data is merged into a single 3D structure. There has been tremendous progress in improving the electron beam illumination characteristics, the data acquisition, the detector quality, the account of radiation damage (1) and beam-induced movements (2, 3). These improvements will lead to higher resolution structures if the system is allowed to refine towards multiple 3D structures simultaneously. We present parallel four-dimensional processing of large single particle cryo-EM data sets (4) acquired at the NeCEN (www.necen.nl) and illustrate its promise to provide new mechanistic insight of action of large biological machineries.

1. Karuppasamy M, Karimi Nejadasl F, Vulovic M, Koster AJ, & Ravelli RBG (2011) Radiation damage in single-particle cryo-electron microscopy: effects of dose and dose rate. *J Synchrotron Radiation* 18(Pt 3):398-412.
2. Bai X-c, Fernandez IS, McMullan G, & Scheres SH (2013) Ribosome structures to near-atomic resolution from thirty thousand cryo-EM particles. *eLife Sciences* 2.
3. Karimi Nejadasl F, Karuppasamy M, Newman ER, McGeehan JE, & Ravelli RBG (2013) Non-rigid image registration to reduce beam-induced blurring of cryo-electron microscopy images. *J Synchrotron Radiation* 20(1):58-66.
4. Van Heel M*, et al.* (2012) Four-Dimensional Cryo Electron Microscopy at Quasi Atomic Resolution: IMAGIC 4D. *International Tables for Crystallography Volume F, 2nd edition, Crystallography of Biological Macromolecules*, eds Arnold E, Himmel DM, & Rossmann MG (Wiley), pp 624-628.

Ultrastructural & Analytical Methods in Life Sciences

LBP.LS.P05
Effects of Rapamycine and Progesterone on endometrial cancer cells

S. Muftuoglu[1], D. Zeybek[1], T. Demirci[1]

[1]Hacettepe University Faculty of Medicine, Histology & Embryology, Ankara, Turkey

smuftuog@hacettepe.edu.tr
Keywords: Endometrial Cancer, Rapamycine, Progesterone

PTEN is the tumor supressor protein, necessary for the appropriate regulation of the phosphatidylinositol 3-kinase/Akt. Mutations of the PTEN gene causes hyperactivation of the PI3K/Akt/mTOR pathway in endometrium cancer. Rapamycin, the main mTOR inhibitor drug, potentiates the effects of treatments on endometrium cancer cells in the aspect of inhibition on cell proliferation and induction of apoptosis [1]. It has been shown in endometrial cancer cells that exposure to mTOR inhibitor increased progesterone mRNA expression. Additionally treatment with rapamycine alone does not affect apoptosis in the endometrial cancer cell lines [2]. Autophagy has been shown to be important in pathogenesis of cancer, infection and neurodegenerative diseases. PI3Ks play important roles in the supression of autophagy by the induction of the target of rapamycine (mTOR) signaling [3]. It has been known that mTOR inhibitor rapamycin exerts its antitumor effect on some tissues by inducing autophagy, not apoptosis. The purpose of this study is to determine the effect of rapamycin and progesterone combination treatment on the cell proliferation and cell death via autophagy induced by rapamycin.

The endometrial carsinoma (ECC) cell line was treated with different concentrations of rapamisin, progesterone alone and together at different durations. After treatments WST-1, immunolabeling of Caspase-3, beclin-1 and LC3B, ELISA, TUNEL analysis and electronmicroscopy were performed. This study is granted by Hacettepe University Research Fund 010 D03 101 002.

Decreased cell viability was detected in endometrial carcinoma cell line with both rapamisin and progesterone treatments. Apoptosis was not detected in all groups. We observed positive immunoreactivity of beclin-1 as an early autophagy marker on ECCs treated with rapamycine alone and together with progesterone. The immunoreactivity of LC3B as a later autophagy marker was decreased in rapamisin and progesterone treated ECCs. Ultrastructure of autophagy on endometrium cells have been examined with electron microscope.

Rapamycin exerts its cytotoxic effect on endometrial carcinoma cells by inducing autophagy. The autophagy inducing effect of rapamisin can be overcome by progesterone treatment. The effects of rapamycine and progesteron combination on cell proliferation and cell death suggested that combination therapy of hormonal treatment and mTOR inhibitors might let high success rates in prognosis of endometrium cancer. This study will provide the scientific foundation for subsequent clinical trials concerning the limited success with traditional therapies of significant cytotoxic agents and hormones in advanced or recurrent endometrium cancer. The effects of rapamycin and progesteron combination on cell proliferation and cell death suggested that combination therapy of hormonal treatment and mTOR inhibitors might let high success rates in prognosis of endometrium cancer. The improved understanding of the molecular and genetic basis of endometrial cancer will supply opportunities for development of targeted therapies that inhibit the molecules of cellular signaling pathways involved in cell proliferation.

1. A. Shafer et al.Int J Cancer 126 (2010) 1144-1154
2. Y.Xie et al. J steroid Biochem & Mol Biol 126(2011)113-120
3. B.Li et al. Int J Gynecol Cancer (2013) Mar23

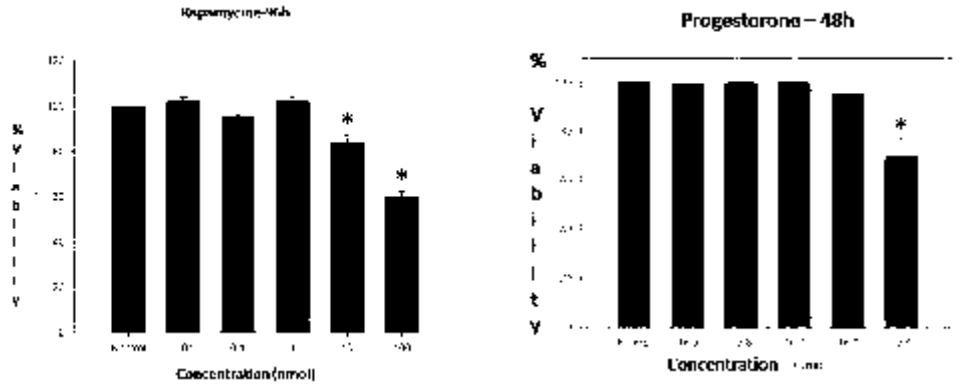

Figure 1. Cell viability of ECC treated with different concentrations of Rapamycin and progesteron for 96 hours. Data are expressed as percentage of cell viability with respect to control. Each column represents the mean ± SEM of 3 replicates of 3 experiments. (*p<0,01).

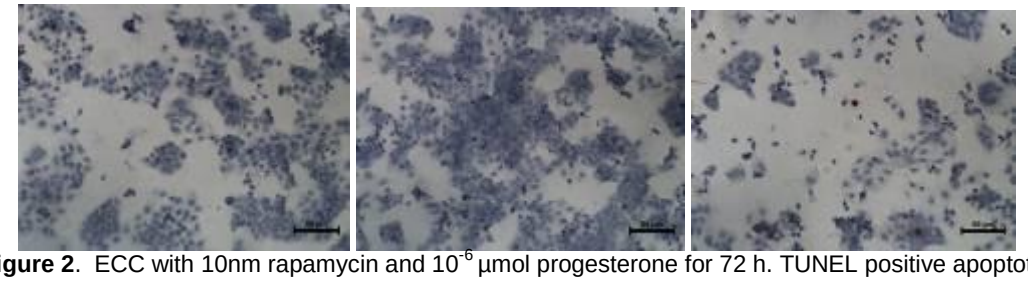

Figure 2. ECC with 10nm rapamycin and 10^{-6} µmol progesterone for 72 h. TUNEL positive apoptotic cells

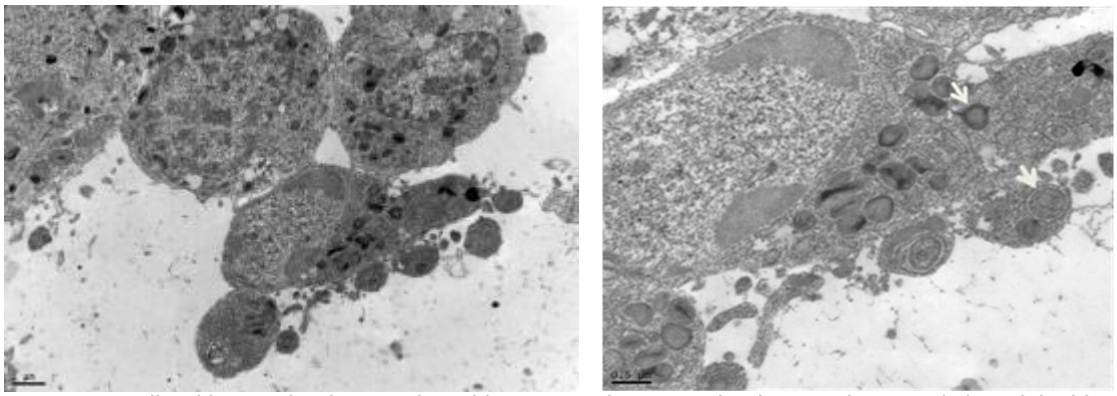

Figure 3 ECC cells with autophagic vacuole. White arrows show autophagic vacuoles, consisting of double-layered membranes. Uranyle acetat-Lead citrate X 12000.

Tissues, Pathology, and Diagnostic Microscopy

LBP.LS.P06
Histopathological alterations in body wall and alimentary canal of the earthworm as biomarker of copper oxychloride exposure

G. Aydogan Kilic[1], V. Kilic[1], M. Kececi[1], S. Cin[1]

[1]Anadolu University, Faculty of Science, Eskişehir, Turkey

gozdea@anadolu.edu.tr
Kewords: copper oxychloride, earthworm, biomarker, histopathology

Copper oxychloride is a broad-spectrum fungucide applied to the foliage of a wide variety of fruits and vegetables. [1]. It is sprayed directly on crops and may contaminate soils. Since its general toxicity is considered to be low, there are only a few studies about the toxicity of this substance on soil fauna [2]. However it has been shown to reduce populations of some earthworm species in field trials [3].

Earthworms are continuously exposured to soil chemicals through their alimentary surfaces and skins. Because of the capacity to accumulate and concentrate large quantities of inorganic and organic pollutants, they are widely recognized as suitable organisms for biomonitoring the effects of heavy metals and other chemicals in contaminated soils. Histopathological alterations in earthworms have been reported as valuable markers of heavy metal toxicity in previous studies which may signal a prior or ongoing damaging effect on these organisms [4,5,6].

Hence, the present study focused on the histopathological responses in body wall and alimentary canal of earthworm (*Aporrectodea caliginosa*) resulted from copper oxychloride exposure. Samples consisted of control and experimental group animals which were exposed to different doses of copper oxychloride (35, 100, 350 mg/kg artificial soil) during 2,7 and 14 days of periods. Healthy worms weighing between 300-400 mg each were left on filter paper in petri dishes for 24 h in order to reduce the soil content in their gut. Worms were cut into 0.5 cm pieces and were fixed in paraformaldehyde(4%) in phosphate buffer pH 7.2. They were dehydrated in a graded series of ethanol and treated with a mixture of LR White and ethanol (2:1) (v:v) for 1 h at RT. Samples were then embedded in LR White Resin, sectioned at 700 nm thickness, stained with toluidin blue and observed under a Leica DM 750 bright field microscope. Significant changes were observed at the doses of 100 and 350 mg/kg and after the periods of 7 and 14 days with the increasing intensity of lesions depending on exposure time. These lesions were generally characterized by enlargement and torsion of epithelial cell lining, hyperplasia of glandular cells, increased mucus production and deformation of musclar structure. Intestinal epithelium and chloragogenous cells lost their intact nature. Necrosis was also observed at the dose of 350 mg/kg after 14 days in epidermal and intestinal tissues of animals. The study showed that copper oxychloride exposure may result in a crucial toxicity in bioindicator organism *Aporrectodea calliginosa* depending on the dose and duration of exposure leading to significant deformation of tissuses in vital parts of their body.

1. Synman, R.G., Reinecke, S.A., Reinecke, A.J. Ecotoxicology and Environmental Safety. 60:47-52
2. Helling, B., Reinecke, S.A., Reinecke, A.J. Ecotoxicology and Environmental Safety 46 (2000) 108-116.
3. Maebota, M.S., Reinecke, S.A., Reinecke, A.J. Ecotoxicology and Environmental Safety 56 (2003) 411-418.
4. Ware, G.W., Environmental Contamination and Toxicology 165 (2000) 141.
5. Reddy, N.C., Rao, J.V. Ecotoxicology and Environmental Safety (2008) 71, 574-582
6. Kılıç, G.A. Chemosphere (2011) 83, 1175-1180

Tissues, Pathology, and Diagnostic Microscopy

LBP.LS.P07
Effects of copper oxychloride on the histology of earthworm coelomocytes

V. Kilic[1], G. Aydogan Kilic[1], N.N. Şimsek[1], D. Koca[1]

[1]Anadolu University, Faculty of Science, Eskişehir, Turkey

vkilic1@anadolu.edu.tr
Keywords: copper oxychloride, histology, earthworm, coelomocyte

Environmental contamination of soils by copper containing agrochemicals is a current problem. Copper oxychloride-based fungicides are the most widely used agents as foliar sprays against fungal diseases in a number of crops. Earthworms are keystone species within ecosystems since they play a major role in physical, chemical and biological processes in the soil [1]. The coelomic fluid of earthworms has functions in pollutant disposition and tissue distribution while coelomocytes are responsible for the immune defense of the animal. Any impairment of coelomocyte functioning can compromise the health of the entire organism. However there are very limited studies on the use of histological features of earthworm coelomocytes as biomarker of exposure to the environmental contaminants [2].

Therefore we investigated histopathological changes as a result of copper oxychloride exposure in earthworm (*Aporrectodea caliginosa*) coelomocytes. Samples consisted of control and experimental group animals which were exposed to 35 and 100 mg/kg (artificial soil) doses of copper oxychloride during 7 days. Healthy worms weighing between 300-400 mg each were left on filter paper in petri dishes for 24 h in order to reduce the soil content in their gut. Non-invasive extursion technique of Eyambe et al., (1991) was used for collecting earthworm coelomocytes with slight modifications [3]. Freshly isolated *cell suspension* was then *dropped onto* specimen *slides***.** Samples were stained with toluidin blue after ethanol (95 %) fixation.

Granulocytes and ameobocytes did not show any significant alterations while the most significant changes were observed in eleocytes such as swelling and deformation of cells at the dose of 100 mg/kg. This response of eleocytes was thought to be a result of their natural function making them the primary target for copper oxychloride toxicity, since they are the cells capable of synthesizing extracellular respiratory pigments responsible of storing exogenous pigments such as heavy metals [4]. These results manifested that observation of isolated earthworm coelomocytes with simple histological staining can be a primary and effective way for the evaluation of structural changes as a result of environmental exposure.

1. Helling, B., Reinecke, S.A., Reinecke, A.J. Ecotoxicology and Environmental Safety 46 (2000), p.108-116.

2. Calisi, A.,Lionetto, M.G., Schettino, T., Ecotoxicology and Environmental Safety 72 (2009), p.1369-1377.

3. Eyambe, G.S., Goven , A.J., Fitzpatrick, L.C., Venables, B. J., Cooper, E.L. Laboratory Animals 25 (1991), p.61-67.

4. Adamowicz, A. Tissue and Cell, 37 (2005), p.125-133.

Microorganisms and Biofilms

LBP.LS.P08
Analysis of Microbial Populations by Flouoescein in-SITU Hybridization (FISH) in water samples of Lake Van

M.B. MUTLU[1], A. Penezoğlu[1]

[1]Anadolu University, Biology, Eskisehir, Turkey

mbmutlu@anadolu.edu.tr

Alkaliphilic microorganisms are important group of extremophilic microorganisms. Van Lake is one of the largest soda lake in the world and harboring extreme conditions. However its microbial diversity has never yet been studied in detailed. In this study, water samples from different locations of Van Lake were analysed by Fluorescein in-situ hybridization (FISH) technique. Two different water samples were collected from the lake (Tatvan and Edremit). *Archaea* and *Bacteria* spesific probes were used in FISH technique. Total cell number was found by DAPI staining. DAPI staining results showed that the density of bacteria is much more in Edremit water samples. The prokaryotic community of Van Lake samples were found to be dominated by *Bacteria.*

Ultrastructural & Analytical Methods in Life Sciences

LBP.LS.P09
Confocal Electron Microscopy of C6 Glioma Cells

E. Çakır[1], M. Kutlu[1], D. Vejselova[1]

[1]Anadolu University, Biology, Eskisehir, Turkey

ecakir@anadolu.edu.tr

Cell culture is the complex process by which cells are grown under controlled conditions, generally outside of their natural environment. In practice, the term "cell culture" now refers to the culturing of cells derived from multi-cellular eukaryotes, especially animal cells. However, there are also cultures of plants, fungi and microbes, including viruses, bacteria and protists. Brain tumors include all tumors inside the cranium or in the central spinal canal. They are created by an abnormal and uncontrolled cell division, usually in the brain itself, but also in lymphatic tissue, in blood vessels, in the cranial nerves, in the brain envelopes (meninges), skull, pituitary gland, or pineal gland. Within the brain itself, the involved cells may be neurons or glial cells (which include astrocytes, oligodendrocytes, and ependymal cells). Brain tumors may also spread from cancers primarily located in other organs (metastatic tumors).

In this study we aimed to reveal C6 glioma cell's nuclus and cell skeleton structure by confocal microscopy using dual staining technique. Alexa Fluor 488 Phalloidin and Acridine Orange dyes have been used and cell stucture were shown.

Tissues, Pathology, and Diagnostic Microscopy

LBP.LS.P10
Microvascular changes of periodontal tissue after inflammation using vascular injection method.

M. Matsuo[1,2], S. Takahashi[3], S. Takahashi[3], A. Iimura[1,2], S. Matsuo[1]

[1]Kanagawa Dental University, Dept. of Oral Science, Dental Anatomy , Yokosuka, Japan
[2]Kanagawa Dental University, Institute for Research of Disaster Dental Medicine in Yokosuka and Shonan, Yokosuka, Japan
[3]Kanagawa Dental University, Dept. of Oral Science, Dentistry of circulation control , Yokosuka, Japan

m.matsuo@kdu.ac.jp

Introduction : In this study, microcirculation changes in the periodontal tissues after experimental induction of the inflammation are examined. A vascular resin cast model was used to observe the morphological changes of vasculature under scanning electron microscope (SEM). Also laser Doppler flowmetry (LDF) was used to estimate physiolosical changes in gingival blood flow (GBF) in.

Materials and Methods : The microvascular resin cast method is a way to make three-dimensional observations of the vasculartur e [1]. This method is to inject the synthetic resin and dissolve the peripheral hard and soft tissues by hydrochloric acid (HCl) and potassium hydroxide(KOH). By using these decalcifying and maceration solutions, it is impossible to observe the relationship between the bone and vascular network . In this regard, the proteinase digestion method is usefull for periodontal research. Unlike acid and alkaline digestion methods, this method does not decalcify newly formed immature bone at all, and makes the observation of new bone apposition possible [2]. All gingival blood flow was estimated by a LDF with a probe . These parameters were determined control and inflammation group. The output signals of gingival blood flow were analyzed using data analysis software .

Surgical procedures : Beagle dogs were divided into two groups for the performance of all experimental procedures, which adhered to the Animal Care Committee guidelines of our institution. To induct inflammation, dental floss was placed around the cervical area of teeth for ninety days (periodontitis group). Healthy periodontal tissue was used as Control group. After this period, resin cast models were created.

Results and Discussion : In SEM observation of the control group, gingival vasculature formed regular vascular loops with diameter of 10-30□m (Figure.1). These vessels were anastomosed by periodontal ligament. The vascular network of periodontal ligament forms a polygonal ring shape. Vessels in the periodontal ligament are anastomosed to gingival and alveolar bone vessels through Volkman's canal.

In the periodontitis group, gingival blood vessels changed into extended vascular loops (Figure.2). These infected glomerulus vascular loops grew towards the root apex. Glomerulus blood vessels are anastomosed with the vascular networks in the alveolar bone marrow at the back of the absorped thin bone wall.

In the analysis of LDF, periodontitis (22.27 ± 2.17 mL/min/100g) group significantly decreased in GBF as compared to the Control (34.56 ± 2.92 mL/min/100g) group.

Conclusion : The findings of this study indicated that gingival vasculature changed easily by experimetal inflammation and that it is difficult to maintain the vascular structure of periodontal tissue. Meticulous plaque control and adequate protection of microcirculation from inflammation in perodontal tissues would assure that infection would be amenable to treatment.

1. M. Matsuo, K. Takahashi , Microscopy research and technique 56 (2002), p.3-14.
2. M. Matsuo, Tamaki K. Microvascular Reviews and Communications 3 (2010), p.25-31.
3. MEXT-Supported Program for the Strategic Research Foundation at Private Universities, 2012-2014, P1-5.

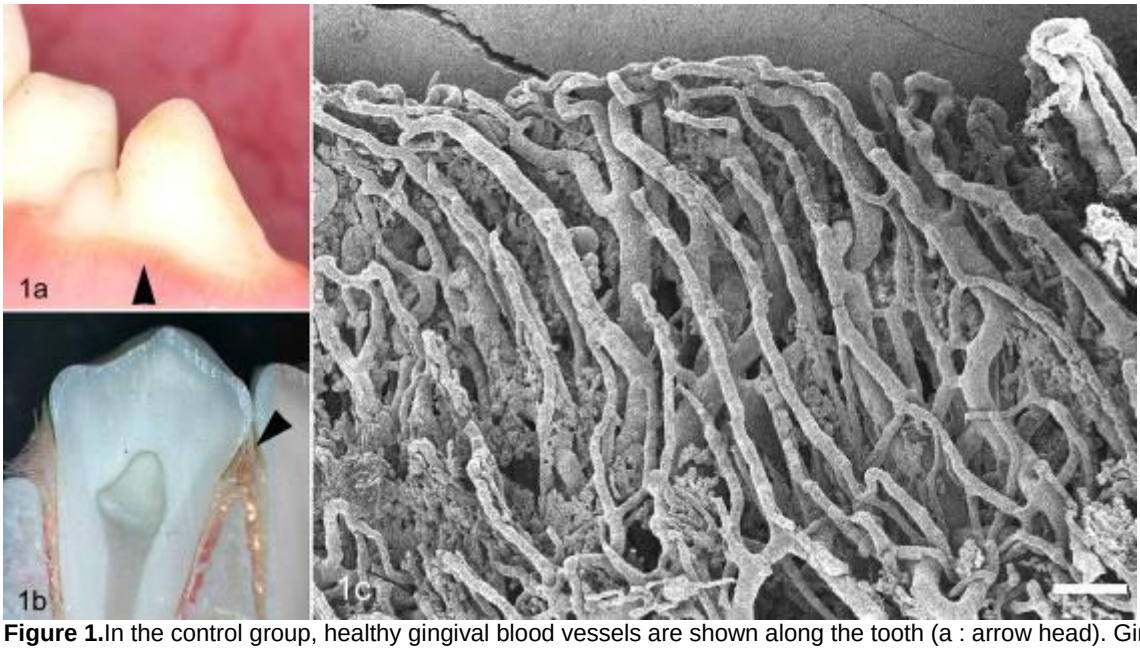

Figure 1. In the control group, healthy gingival blood vessels are shown along the tooth (a : arrow head). Gingival blood vessels of vascular resin cast model of healthy periodontal tissue indicated as arrowhead (b). SEM observation of resin cast model, gingival vasculature formed regular arrangement of U-turn vascular loops (c).

Figure 2. In the periodontitis group, inflamed gingival blood vessels are shown along the tooth which attached dental plaque and pus gathers along the gingival margin (a : arrow head). Gingival blood vessels of vascular resincast model of inflamed periodontal tissue indicated as arrowhead (b). In the SEM observation, gingival blood vessels changed into extended glomerurus vascular loops (c).

Ultrastructural & Analytical Methods in Life Sciences

LBP.LS.P11
Development of Microwelll arrays: Studying the metabolic responses of single Mitochondrial

V.S. Vajrala[1], E. Suraniti[1], A. Devin[2], M. Rigoulet[2], N. Sojic[1], A. Devin[2], S. Arbault[1]

[1]University of bordeaux, Institute of Molecular Sciences, Pessac, France
[2]University of Bordeaux Segalen, IBGC - CNRS, Bordeaux, France

vv.sureshreddy@yahoo.com
Keywords: PDMS; Optical fiber, milli-to-microwell arrays; mitochondria; fluorescence; metabolism

Mitochondria play a central role in cellular respiration, ageing process and also in the onset of degenerative diseases. These duties are performed by the collections of mitochondria (within a cell) that are heterogeneous, dynamic, and subject to fusion and fission to form a network [1]. Since the valuable information regarding mitochondrial physiology is missing during averaged analysis of a large population of these organelles, development of methods to probe the properties of individual mitochondria simultaneously at single organelle level is, therefore, a challenge for analyticians. In this context, we developed microwell array platforms based on fiber optic [2] and PDMS micro-structuration [3] that allow the screening of a large number of individual mitochondria simultaneously using fluorescence microscopy.We used either a chemical etching procedure to create a high-density array of femtoliter (fL) containers from optical fiber bundles, or puncturing method to create milli to micrometric wells in PDMS- polymer thin layers. Mitochondria organelles were entrapped in these wells and independently imaged via reflecting optical signals. We developed experimental techniques which are required for the immobilization of mitochondria and also the screening of whole population and individual responses within those populations using optical fiber based microwell arrays and PDMS wells.We studied the endogenous NADH (auto-fluorescence) variation of populations of individual mitochondria under activation with EtOH (substrate) and inhibition with Antimycin A (respiratory inhibitor). Statistical studies of mitochondrial NADH value distributions evidenced three different kinds of responses within the mitochondrial population, the metabolic performance being not related to the size of the mitochondrion. This individual mitochondrion analysis approach is now extended to the monitoring of different mitochondrial metabolic parameters, including mitochondrial membrane potential [4] (oxidative phosphorylation activity) and oxidative stress markers for the detection of superoxide radical ($0_2^{\cdot-}$) [5].

1. M.Liesa *et al. Physiol Rev*, 2009, *89(3)*, 799-845.
2. V.S.Vajrala *et al. Anal Bioanal Chem, In Press (accepted as paper in forefront).*
3. E.Suraniti *et al. Anal. Chem*., 2013, *85* (10), pp 5146–5152.
4. Perry SW *et al*. *Biotechniques,* 2011, *50*, 98-115.
5. B kalyanaraman *et al. Free Radical Biology & Medicine*, 2009, *52*, 1-6.
6. The author acknowledges ANR MULTIDIM-LAB (ANR-09-BLANC-0418) for his PhD fellowship.

Tissues, Pathology, and Diagnostic Microscopy

LBP.LS.P12
Ultrastructural study on vitrification and slow freezing of the ovarian tissue

E. Erdemli[1], F.T. Çelikkan[1], S. Özkavukçu[2], D. Balcı[3], S.S. Kılıçoğlu[4]

[1]Ankara University, Histology & Embryology, ankara, Turkey
[2]Ankara University, Center for Assisted Reproduction and Fertility Preservation, ankara, Turkey
[3]Ankara University, Biotechnology Institute, ankara, Turkey
[4]Ufuk university, Histology & Embryology, ankara, Turkey

esraerdemli64@gmail.com

Infertility can occur as a result of cancer therapy (kemotherapy and radiotherapy) and the other reasons [1]. Oocyte, embryo and ovarian tissue freezing which is still experimental are developed options for fertility preservation [2]. There are two main ways of cryopreserving biologic tissue: slow freezing or vitrification [3] [4]. Copper grids were used as carrier when we studied method of vitrification. We examined slow freezed and vitrified tissues with electron microscopy.

Eighteen pairs of ovaries were collected from eight-week-old female BALB-C type mice. There were three groups in our groups; vitrification, slow freezing, and control. SF was performed in dimethyl sulfoxide (DMSO) and sucrose with the help of a controlled freezer (SY-LAB, ICECUBE 14S, Austria). Tissues were equilibrated in solution of DMSO, ethylene glycol and sucrose before loading on copper electron microscope grid in vitrification group. After ultimate thawing, tissues transferred through the series of gradually decreasing CPAs for 5 minutes each (20% - 10% - 5% - 0% DMSO and EG with 0.4 M sucrose) for the removal of CPAs osmotically. Eventually, all thawed tissues and six fresh ovarium tissues as the control group were washed in L-15 and fixed in glutaraldehyde for electron microscopy.

In control group, oocyte nuclei, distribution of cytoplasm and the junctions between oocyte-granulosa were intact in non-degenerating primordial and primary follicles in the thin sections (figure 1-A, 1-B, 1-C, 2-A, 2-B). In slow freezing group the linkage of follicle cells between both each other and oocytes were preserved. ZP and the basal lamina between granulosa and theca cells were regular. Spaces and vacuolizations inside the cytoplasm of granulosa cells were noticed (figure 1-D, 1-E, 1-F, 2-C, 2-D). In vitrification group, shrinkage in granulosa cells and an increase in condensation were noticed. Junctions of oocyte and degenerated granulosa cells were disappeared and plazmalemma was not noticed (figure 1-G, 1-H, 1-I, 2-E, 2-F).

The distinction of experimental groups was that the number of degenerate follicles was more than that of normal follicles. Both vitrification on EM grids and slow freezing seem to preserve primordial follicles effectively. This study is supported by Ankara University BAP 10B 3330003

1. S.S. Kim, Fertility Preservation in female cancer patient: Current developments and future directions, Fertil Steril (2006) 85:1-11.
2. A. Revel, In vitro maturation and fertilization oocyte from an intact ovary of surgically treated patient with endometrial carcinoma: A case report. Hum Reprod (2004) 19: p. 1608-1611.
3. S.S. Kim, D.E. Battaglia, and M.R. Soules, The future of human ovarian cryopreservation and transplantation: Fertility and beyond. Fertil Steril (2001) 75: p. 1049-1056.
4. V. Isachenko, Human ovarian tissue vitrification versus conventional freezing: morphological, endocrinological, and molecular biological evaluation, Reproduction (2009) 138(2), p. 319-27.

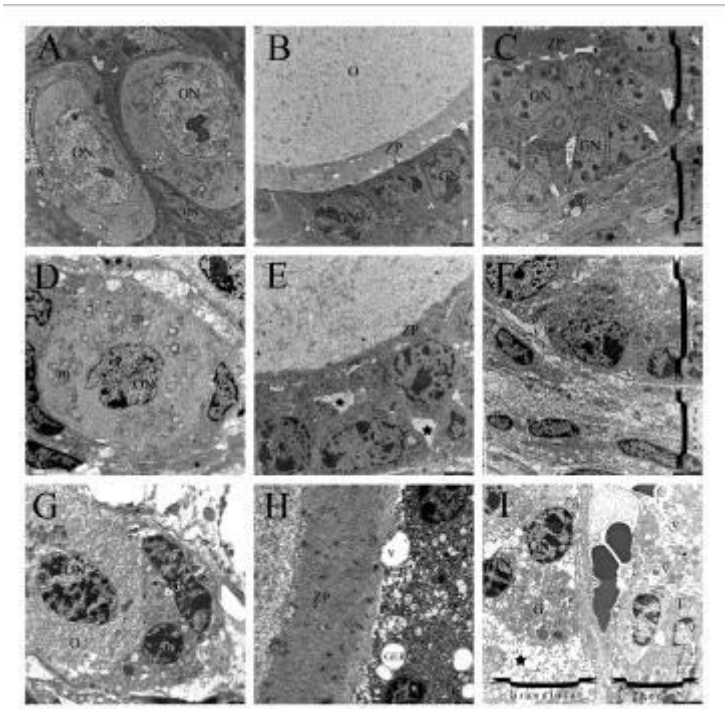

Figure 1. A, B, C: control group, D, E, F: slow freezing group, G, H, I: vitrification group. ON: oocyte nucleus, GN: granulosa nucleus, O: oocyte, ZP: zona pellucida, T: theca, m: mitochondrion, v. vacuole, GER: rough endoplasmic reticulum, star: intercellular spaces.

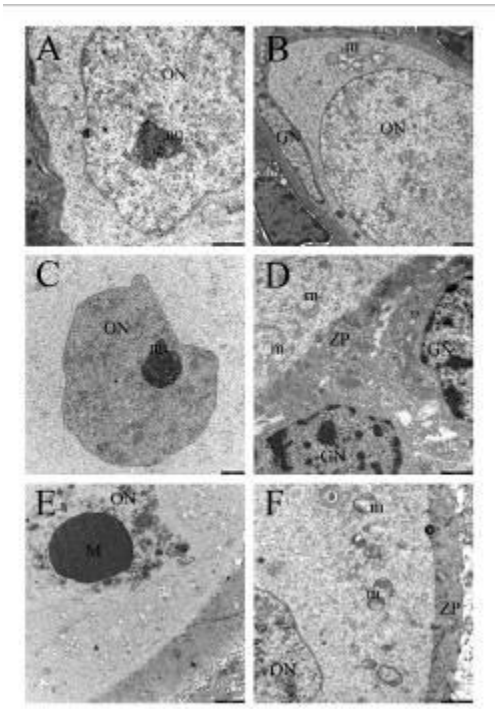

Figure 2. A, B: control group, C, D: slow freezing group, E, F: vitrification group. ON: oocyte nucleus, GN: granulosa nucleus, nu: nucleolus, GN: granulosa nucleus, O, m: mithocondrion, ZP: zona pellucida, M: dark mass of nuclear remnant.

Neurobiology

LBP.LS.P13
Microvasculature of the domestic ruminant brain: a vascular corrosion cast and immunocytochemical study

G. Scala[1]

[1]University of Naples FEDERICO II, Veterinary Medicine and Animal Productions, Naples, Italy

gaescala@unina.it

Blood vessels of the brain in domestic ruminants (buffalo, cattle and sheep) were studied by vascular corrosion cast and immunocytochemical techniques at scanning electron microscopy (SEM).

Microvascular corrosion cast SEM

Nine heads (buffalo, cattle and sheep) were each perfused the maxillary artery with a physiological solution to wash the blood vessels. Next a methylmetacrylate mixture at low viscosity was injected, and after polymerization brains were soaked by 30% KOH solution for 1-2 weeks. Upon complete corrosion, casts were rinsed with distilled water, dried in a desiccator, mounted on stabs, coated with gold, and examined under SEM LEO 435 VP at 10 kV. The brain microvasculature of domestic ruminants, in general, showed morphological and structural features similar to these reported in other mammalian species.

Every cerebral hemisphere was supplied by terminal portion of the internal carotis (A. carotis interna), originated in a rete mirabile epidurale rostrale. From internal carotis originated:

- A. cerebri rostralis, directed rostro-medially, reached the cerebral longitudinal fissure, and supplies the hemisphere's medial face. By the rostral communicant artery communicates with the contralateral artery in correspondence with optic chiasma.
- A. cerebri media, supplied the hemisphere's lateral face by temporal, parietal and frontal branches.
- A. communicans caudalis, went caudally, anastomoses with contralateral artery and A. basilaris, and gave off the A. cerebri caudalis.

From final branches of the cerebral arteries (A. cerebri rostralis, A. cerebri media, and A. cerebri caudalis) originated arterioles that penetrated in perpendicular sense into cerebral cortex. These arterioles were the two types: shorts that supplied the cerebral cortex (Fig. 1a), and longs that supplied the white matter (Fig. 1b). Capillaries of the gray matter formed a thick network with some morpho-structural details (annular and ovoid formations). The capillary casts showed on the external surface ovoid formations single or double that represented the beginning of the neo-capillary. The neo-capillary proceeded in the direction of other neo-capillary that formed a normal capillary.

Immunogold-Labeling SEM Analysis

For the immunogold-labeling SEM analysis, the brains were cut into small fragments (rostral pole, caudal pole, and dorsal pars). Samples were immersed in PBS for 1hr, incubated for 1hr with a solution containing normal goat serum diluted 1:10 in PBS, and next with a primary polyclonal antibody directed toward CD133, diluted 1:1,500 in PBS, overnight at 4°C. After washing in PBS, the samples were incubated with gold-conjugated goat anti-rabbit IgG, diluted 1:200 in PBS for 1hr at room temperature. After washing in PBS, samples were fixed by 2.5% glutaraldehyde, and subjected to silver enhancement. Next samples were dehydrated, mounted on stubs, and examined under a LEO 435 VP at variable pressure in backscattered mode. Samples had not been coated by gold-palladium, so that the only conjugated gold deriving from the immunocytochemical reaction.

Samples showed the intense immunoreactivity on the external surface of the blood capillaries, located in the cerebral cortex (Fig. 1c). No immunoreactivity was observed in the cerebral cortex treated with PBS substituting the primary antibodies (negative control). These results display the presence the angiogenesis phenomena in the cerebral cortex of the domestic ruminant brain.

Figure 1.

Molecular Structures and High Resolution TEM

LBP.LS.P14
Structure of C1-immune complexes revealed by cryo-electron tomography

C. Diebolder[1,2], R. Koning[1], A. Koster[1], P. Gros[2]

[1]Leiden University Medical Center, MCB-EM, Leiden, Netherlands
[2]Bijvoet Center, Crystal & Structural Chemistry, Utrecht, Netherlands

Keywords: complement, classical pathway, cryo-electron microscopy, cryo-electron tomography, dual axis cryo-electron tomography, sub tomogram averaging

The complement system enables the mammalian host to recognize and clear bacteria, viruses, fungi and parasites from blood and interstitial fluids. The so-called classical pathway of complement activation may be initiated by antibodies [1]. Whereas the structural insights are advanced for antibodies recognizing antigens and binding Fc receptors, it is currently unclear how antibodies activate the complement system. By using dual axis cryo-EM tomography [2] and sub tomogram averaging [3] we reveal the three-dimensional arrangement of antibodies that binds and activates the first component, i.e. the C1 complex (790 kDa), of the classical pathway and thereby initiates the complement cascade that leads to clearance of the invading microbes.

For cryo-EM tomography we used functionally active antigen-antibody-C1 complexes formed on liposomes (Figure 1). Dual axis cryo electron tomography (FEI Titan Krios), followed by sub tomogram averaging and classification, resulted in a 4.5 nm resolution structure of the complex (Figure 2). This averaged EM map reveals the quaternary structure of the active C1-Ab complex on a biological membrane in a close to native state. Guided by biochemical experiments and atomic structures we were able to generate a pseudo-atomic model of the C1-antibody arrangement (Figure 3).

The model shows that six Ab bind to the antigen surface with Fab, while the remaining Fab and Fc form a platform through Fc:Fc interactions for C1 binding. Mutagenesis data and functional assays confirm that this interaction is mandatory for complement activation by all IgG Ab sub classes.

Requirement of hexameric Ab arrangement for classical complement activation on a haptenated surface forms a novel activation model which improves our understanding of (auto) immune diseases and might enable design of improved antibodies as vaccines or cancer therapeutics.

1. Ricklin, D., Hajishengallis, G., Yang, K. & Lambris, J. D. Complement: a key system for immune surveillance and homeostasis. *Nat Immunol* 11, 785-797 (2010).
2. Mastronarde, D. N. Dual-axis tomography: an approach with alignment methods that preserve resolution. *J Struct Biol* 120, 343-352 (1997).
3. Nicastro, D. et al. The molecular architecture of axonemes revealed by cryoelectron tomography. *Science* 313, 944-948 (2006)

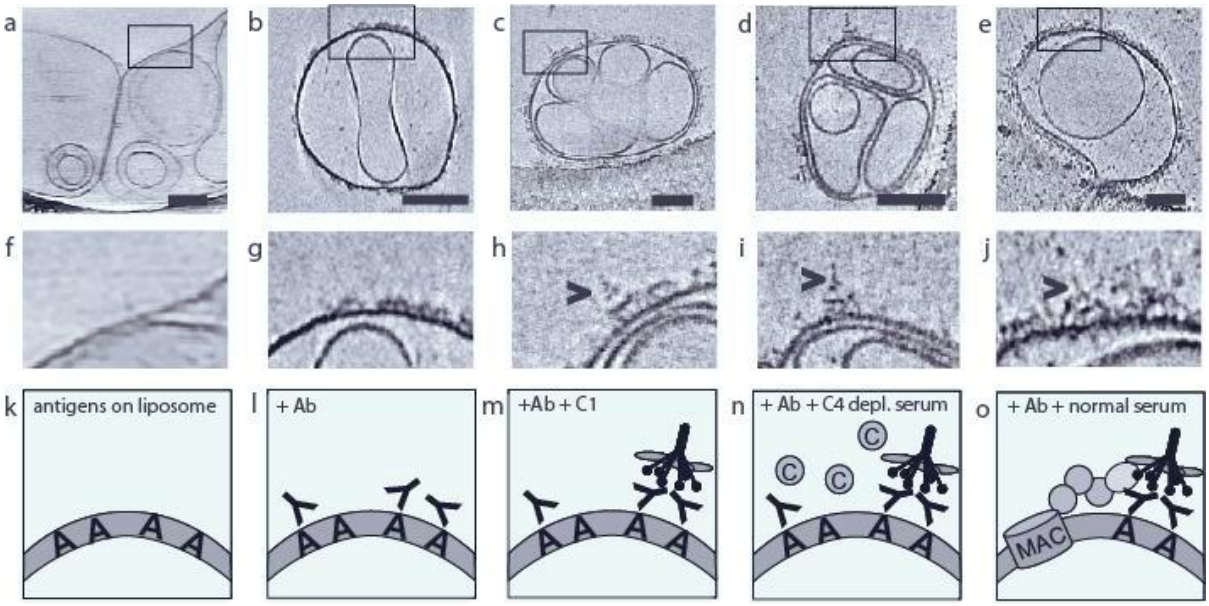

Figure 1. Cryo-ET imaging of complement-activation steps. a, Series of sections through tomograms of haptenated liposomes **b**, antibody opsonized liposomes **c,** followed by addition of C1 or **d**, addition of C4-depleted serum or **e,** normal serum leading to full complement activation. Black scale bars represent 100 nm. **f-j** enlargements from the areas indicated by a rectangle. Arrowheads point at C1-immune complexes. **k-o**: schematics.

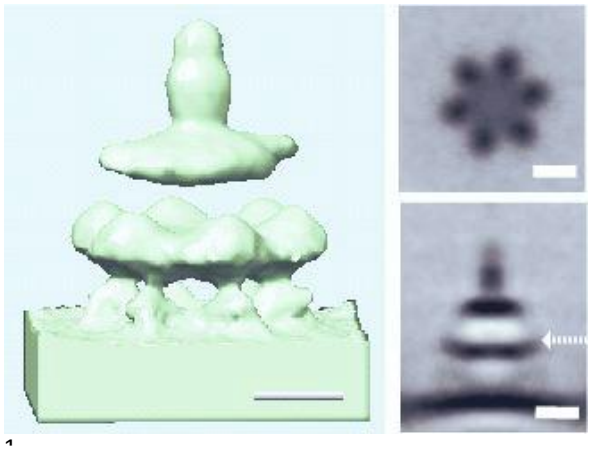

Figure 2. Sub tomogram average of C1-immune complexes. Isosurface (left) as well as horizontal and vertical sections (right). Scale bars represent 10 nm.

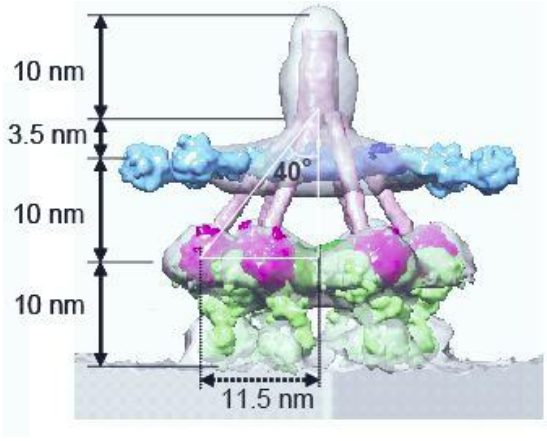

Figure 3. Atomic model if the C1-immune complex docked into cryo-ET map. Side view of the model with indication of overall dimensions.

Tissues, Pathology, and Diagnostic Microscopy

LBP.LS.P15
Towards automated Virus Detection and Identification using TEM

I.-M. Sintorn[1], G. Kylberg[2], R. Nordström[3], L. Haag[3], E. Coufalova[4], M. Drsticka[4]

[1]Swedish University of Agricultural Sciences, Centre for Image Analysis, Uppsala, Sweden
[2]Uppsala University, Centre for Image Analysis, Uppsala, Sweden
[3]Vironova AB, Solna, Sweden
[4]Delong Instruments, Brno, Czech Republic

ida.sintorn@it.uu.se
Keywords: image analysis, segmentation, texture analysis, classification

Transmission electron microscopy (TEM) is an important virus diagnostic tool. The main drawbacks are that an expert in virus appearance in electron microscopy needs to perform the analysis at the microscope, and the cost and bulkiness of the microscope. Relatively few experts exist around the world that have the capability to perform such image based diagnoses. In addition, in emergency situations due to suspected viral pathogens or infectious viral disease outbreaks, important time might be lost due to transporting the sample to the expert's microscope. A cheaper and smaller microscope and software that could automatically detect virus particles and determine the species in high resolution TEM images would hence be desirable virus diagnostic decision support tools. The sample could be imaged and analyzed at the closest TEM to save transporting time. Only images of the detected and identified virus particles could then be sent/shown to the expert for verification. The software would also be useful as an educational tool for new virologists and electron microscopists.

Here we present our work towards building such a system. Our final goal is to combine automated microscopy with image analysis into a system that efficiently and automatically searches for virus particles in a sample and identifies the viral pathogen. A new table-top 25keV TEM suitable for biological specimen is currently under construction as is software for automated content driven image acquisition and analysis to detect and identify viruses in TEM images.

Figure 1 illustrates the tasks/steps that need to be performed for automated virus identification. Samples are prepared using standard techniques that require only ordinary lab equipment. The sample is inserted into the microscope and low and medium magnification images at multiple scales (low and medium resolution) are acquired to automatically determine likely virus containing areas for high resolution image acquisition. This is an important step towards automating the virus identification process and thereby creating a rapid, objective, and user independent virus detection and identification system. By introducing the multi-scale acquisition approach the grid area where high magnification images need to be acquired is estimated to be reduced with more than 99.99% [1]. Once high resolution images eventual virus particles need to be identified. The identification task consists of segmenting virus particles with different shapes and sizes [2] and extracting descriptive features of both shape and texture to enable the classification into virus species by comparing the descriptive features with those extracted from images of known and manually annotated samples. Using only texture (surface morphology) measures we currently achieve a mean classification accuracy of 86% on 16 classes (15 virus classes plus one debris/false class) on automatically segmented particles.

This work was carried out jointly by the Centre for Image Analysis at Uppsala University and Swedish University of Agricultural Sciences, Vironova AB, and Delong Instruments, as part of the Eurostars miniTEM project, in which a low-voltage TEM with built in automated acquisition and analysis functionally is being developed.

1. G. Kylberg, I. Sintorn, G. Borgefors, Towards Automated TEM for Virus Diagnostics: Segmentation of Grid Squares and Detection of Regions of Interest, *in Proc. Scand. Conf. on Image Analysis, Oslo, Norway, LNCS 5575, pp. 169-178, 2009.*
2. G. Kylberg, M. Uppström, K. Hedlund, G. Borgefors, I. Sintorn, Segmentation of Virus Particle Candidates in Transmission Electron Microscopy Images, *Journal of Microscopy, Vol. 245, pp. 140-147, 2012.*

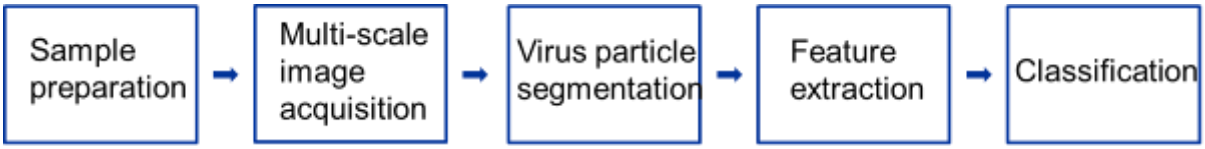

Figure 1. The steps in our virus identification system under development. All steps but the sample preparation are fully automatic.

Ultrastructural & Analytical Methods in Life Sciences

LBP.LS.P15
The use of a color palette for TEM images to recognize cuticular channels in the epidermis of *Litchi chinensis* (Sapindaceae)

A. Papini[1], M. Belli[1], C. Tani[1], P. Di Falco[1], U. Santosuosso[1]

[1]University of Florence, Biology, Firenze, Italy

alpapini@unifi.it
Keywords: color palette, cuticular channels, *Litchi chinensis*, Transmission Electron Microscope

The human eye can see more colors than grey tones due to the features of the photoreceptors (cones and rodes) of the retina [1] and should allow to improve the observation of fine details of the image. The Transmission Electron Microscope (TEM) images are formed as grey scale in relation to the different electron density of the material encontered by the electrons beam. For this reason we implemented a method to transform TEM images in false colors images. The software TEMPALETTE was written in Python 2.7.3 and is available under GPL licence at www.unifi.it/caryologia/PapiniPrograms.html.

The images were equalized with GIMP software (www.gimp.org) and then the grey tones were transformed to RGB colors with the software TEMPALETTE. This program works by maximizing the distance between 256 RGB colors (each corresponding to a grey scale tone) in the RGB cube, formed by the three axes R, G, B. *Litchi chinensis* is a plant belonging to family Sapindaceae of high interest for its commercial value. One of the main problems related to the commercialization of *Litchi* fruit is the relatively easy deteriorability of its epidermis. For this reason we began an in-depth study of the epidermis of the *Litchi* fruit, with particular reference to the structure of its cuticle.

One hypothesis about the water permeability of plant cuticle (mostly composed of hydrophobic substances, such as cutin and waxes), was that that the diffusion of water occurs along polysaccharide strands across the cuticle [2]. We investigate the ultrastructure of the cuticle of *Litchi chinensis* fruit, a cuticle of relatively notable thickness and whose resistence to water loss/entrance, is related to the fruit deteriorability. *Litchi chinensis* fruit were fixed overnight in 1.25 % glutaraldehyde at 4° C in 0.1 M phosphate buffer at pH 6.8. The samples were then post-fixed in 1% OsO_4 in the same buffer for 1 hr. After dehydration in an ethanol series and a last step in propylene oxide, the samples were embedded in Spurr's epoxy resin. Transverse sections approximately 80 nm thick were cut with a diamond knife and a Reichert-Jung ULTRACUT E ultramicrotome, stained with uranyl acetate and lead citrate. The images were recorded with a PHILIPS EM 300 Transmission Electron Microscope (TEM) at 80Kv. The main observed result is the observation of what appear to be channels crossing the cuticle of the external epidermis of *Litchi chinensis* (Fig. 3, arrow). The application of a Laplace contouring filter [2] apparently provided complimentary results (Fig. 4, arrow). One hypothesis is that such channels observed in the cuticle of *Litchi chinensis* fruit pericarp epidermis may be related to the polysaccharide strands across the cuticle observed by Riederer [3]. Reticulated structures in the thin cuticle of *Halodule* was also observed by Papini et al. [4]. Conclusion: the application of a color TEM palette appear to be of interest to improve the observation of fine structures in TEM images. Further investigation will be needed to understand the correspondence of the observed ultrastructure with the proposed function.

1. *Castleman*, K. R. 1998. Concepts in Imaging and *Microscopy*: *Color* Image. Processing for *Microscopy*.. The *Biological Bulletin*. 194 (2): 100-107.

2. Haralick R. and L. Shapiro (1992**)** Computer and Robot Vision, Vol. 1. Addison-Wesley Publishing Company, pp 346 - 351.

3. Riederer M. (2006): *"Thermodynamics of the water permeability of plant cuticles: characterization of the polar pathway*". Journal of Experimental Botany, Vol. 57, No. 12: 2937–2942.

4. Papini A, Sordo L, Mosti S (2011) Surface interactions of the epiphytic macroalga *Hincksia mitchelliae* (Phaeophyceae) with the shoalgrass, *Halodule wrightii* (Cymodoceaceae). Journal of Phycology, 47(1): (118-122.

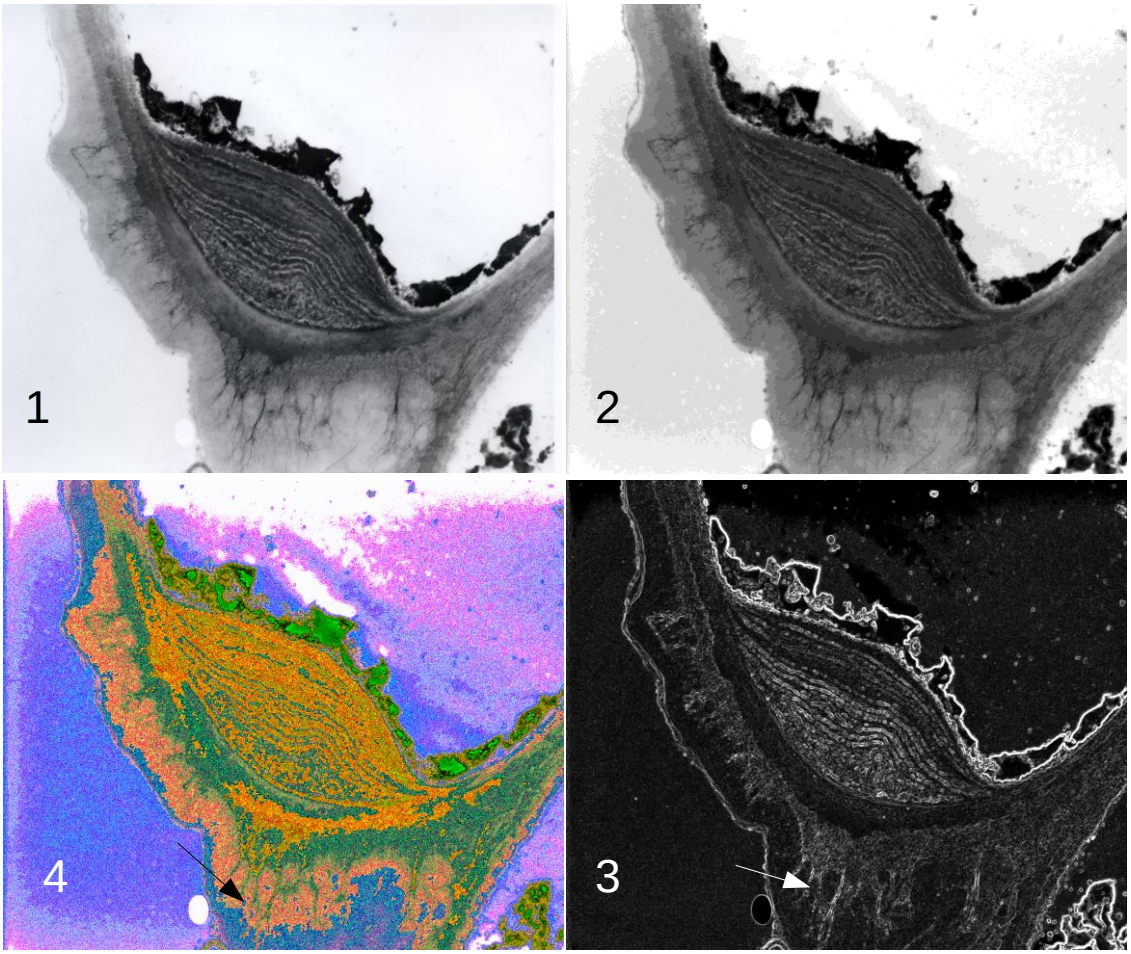

Figure 1. TEM image (magnification x14850) as it is scanned from a negative film.
Figure 2. same image as Fig. 1 but equalized with GIMP.
Figure 3. shows the result of the application of TEMPALETTE on Fig. 2.
Figure 4. shows the effect of the application of a Laplace contouring filter implemented in the GIMP package.

3D in SEM, (S)TEM, Ion Imaging, incl. FIB-SEM and SBF-SEM

MIM.1.001
Microtome and Focus Ion Beam for serial block face scanning electron microscopy: tools to explore the three dimensional ultrastructure

C. Genoud[1]

[1]Friedrich Miescher Institute for Biomedical research and C-CINA, Biozentrum, University of Basel

The study of biological systems together with the understanding of their fine molecular mechanisms requires new microscopy and image processing approaches. In particular, it is often necessary to image the same biological sample at different scales, ranging from a few millimeters down to a few nanometers. To achieve this goal, different techniques of light microscopy associated with electron microscopy need to be combined. Recently, both serial block face techniques, microtome as well as FIB serial block face SEM, have opened the field of 3D EM to new dimensions, extending the field of view in the 3 dimensions. Neuroanatomy is typically a field where this approach is crucial to better understand how physical interactions between cells contribute to inputs processing.

Correlation of light and electron microscopy require the acquisition of threedimensional datasets at the light and electron microscopy level. To obtain a 3D volume at the ultrastructural level that is covering a field of view compatible with the field of view obtained by light microscopy, samples are processed using an SEM containing a microtome inside the vaccum chamber (Denk and Horstmann 2004; GATAN 3View; FEI Quanta 200F). This technique allows the visualization of large volume at the ultrastructure level. At the same time, by matching coordinates systems between microscopes and by using landmarks, it is possible to link the fluorescence information obtained by light microscopy in vivo or after fixation with the three dimensional ultrastructure. In order to extract the components to be analyzed, different image processing tools have been developed. The microtome SBFSEM allows the reconstruction of entire neurites arborescence. In complement, the FIB technique allows extracting more high resolution information from a smaller volume, highlighting the cytoplasmic structures. These two methods are highly complementary techniques for studying neural ultrastructure.

3D in SEM, (S)TEM, Ion Imaging, incl. FIB-SEM and SBF-SEM

MIM.1.002
Finding the needle in the haystack: Hierarchical imaging workflow combining array tomography with FIB-SEM

I. Wacker[1,2], C. Bartels[1], C. Grabher[2,3], A. Schertel[4], R. Schroeder[2,5]

[1]KIT, Institute for Biological Interfaces, Eggenstein-Leopoldshafen, Ghana
[2]HEiKA, Correlative Imaging Platform, Heidelberg-Karlsruhe, Germany
[3]KIT, Institute of Toxicology and Genetics, Eggenstein-Leopoldshafen, Germany
[4]Carl Zeiss Microscopy GmBH, Oberkochen, Germany
[5]Universitätsklinikum Heidelberg, Cryo-EM, CellNetworks, BioQuant, Heidelberg, Germany

irene.wacker@kit.edu
Keywords: array tomography, FIB-SEM, 3D imaging

Problems in cell or developmental biology often ask for ultrastructural characterisation of a small volume such as a rare event or a specialized substructure inside a large bulk specimen. We propose an intelligent workflow consisting of hierarchical imaging cascades, potentially also relying on different imaging modalities for different resolution ranges. Based on array tomography (AT) [1] this allows a stepwise zooming in to a structure of interest from light microscopy via conventional SEM to FIB-SEM.

First we used this approach to characterize rare immune cell populations of unknown function from different hematopoietic organs of Zebrafish isolated by fluorescence activated cell (FAC) sorting on the basis of an XFP-reporter gene. Since only e.g. about 30 000 of these cells can be recovered from the spleens of five adult fish we concentrated them by pelleting in agarose followed by conventional aldehyde fixation and embedding in epoxide (Figure 1a). Long ribbons of serial sections were deposited on silicon wafers (Figure 1b), inspected in a reflected light microscope (rLM) for interesting cells (Figure 1c), which were then imaged in a FEG-SEM (Figure 1d). Images were aligned in Fiji and segmented in Amira. Using these 3D reconstructions we could define an inventory of organelles.

For functional characterization, isolated cell populations were co-cultured with human tumor cells. Analysis of such co-cultures by the described multimodal hierarchical AT (hAT) revealed immunological synapses between fish immune cells and human target cells (Figure 2a). To further characterize the contact region between the cell pair with its typical arrangement of organelles we did FIB-milling (Figure 2b) on selected sections to analyze at higher z-resolution only those regions of interest that enclosed centrosomes, Golgi complex, and other membrane-bound organelles (Figure 2c).

Next we used hAT to identify a rare structure – the neuromuscular junction (NMJ) – within a large tissue block. Tibialis muscle from mouse was chemically fixed, embedded, and serially sectioned as described above. In a single cross-section containing hundreds of muscle cells usually only a few cells exhibit part of an NMJ (circle in Figure 3a). Once an NMJ was found it was imaged in xy on the surface of the section which in this case was nominally 1µm thick (Figure 3b). Then FIB-stacks were recorded from a 10µm x 10µm x 1µm volume of interest with 10nm slice thickness and 5nm lateral pixel size. Figure 3c shows several images of such a stack with one postsynaptic fold on the left and actomyosin filaments on the right. Currently we are recording more stacks from the same region of interest in consecutive sections. Fusion of individual stacks into a larger 3D volume will allow to observe the convoluted network of the postsynaptic folds at a resolution that allows unambiguous tracking of the membranes.

A combination of hAT with FIBSEM is a good approach whenever it is not necessary for a given problem to create a quasi-native molecular atlas of a cell or a total wiring diagram of a brain as needed in many connectomics approaches. In many cases a mere inventory of organelles or the architecture of just one, however rather large, synapse such as the NMJ might be sufficient. Generally, hAT can help to extend AT – with its non-isotropic voxels resulting from discrete z-sampling – to classical electron tomography with its more isotropic and continuous sampling.

1. K.D. Micheva and S.J. Smith, Neuron 55 (2007), p. 25.
2. We acknowledge the German Federal Ministry for Education and Research, project NanoCombine, grantnos. FKZ: 13N11401 and FKZ: 13N11403 for financial support.

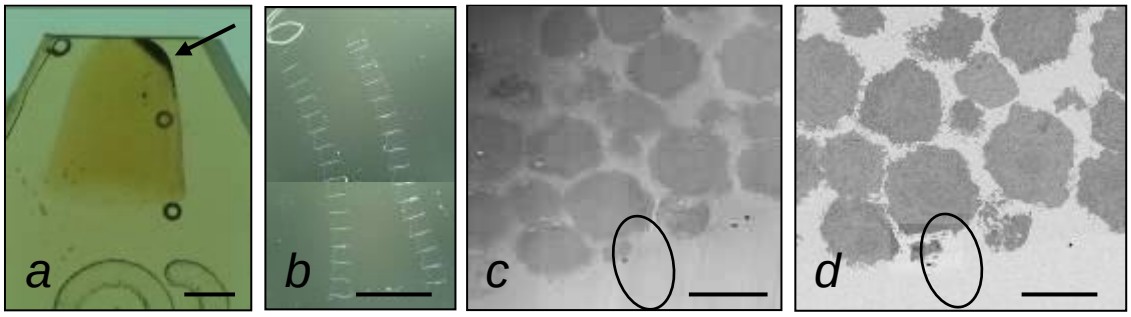

Figure 1. Preparation of FAC-sorted immune cells from Zebrafish for array tomography: a) agarose enrobed cell pellet (arrow) embedded in epon block, b) serial sections on silicon wafer, c) pre-selection of cells in reflected light microscope, d) imaging sections in SEM; scale bars: 1mm (a), (b), 10µm (c), (d)

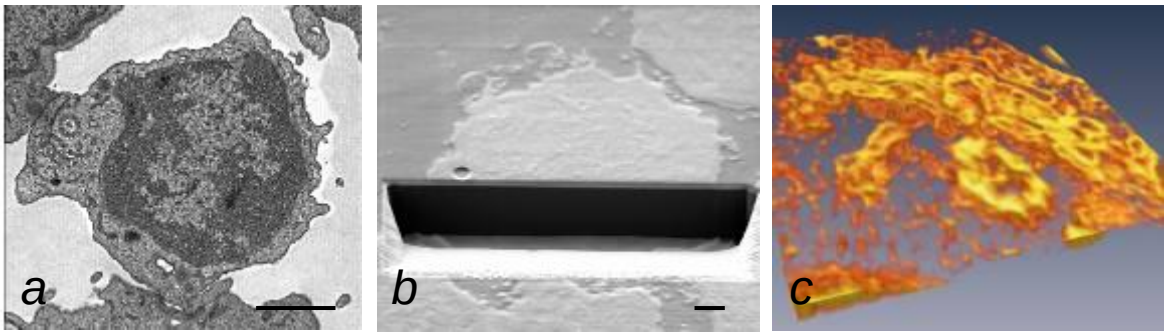

Figure 2. (a) Immunological synapse between Zebrafish immune cell and human cancer cell imaged in SEM (Carl Zeiss Ultra), (b) trench milled into a 200nm thick section by FIB (Carl Zeiss Auriga Crossbeam®), (c) volume rendering of Golgi complex and centrosome in Amira, scale bars: 1µm

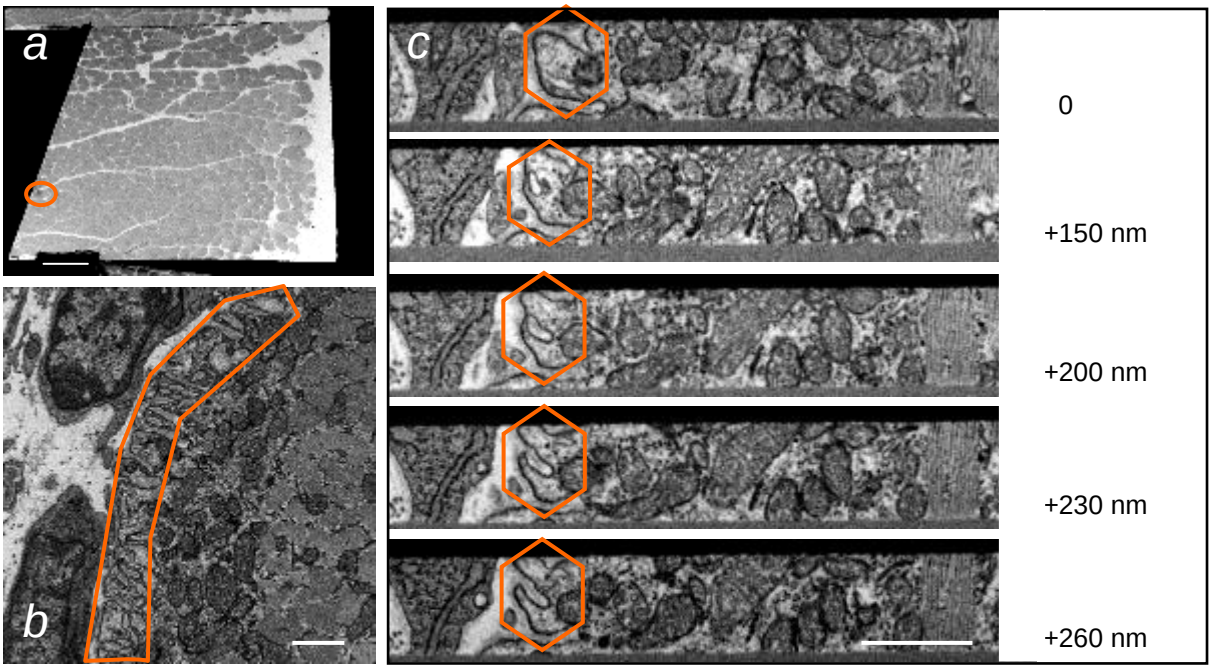

Figure 3. Imaging of NMJ (Carl Zeiss Auriga Crossbeam®): (a) overview of a cross section from mouse leg muscle, circle shows muscle cell containing part of an identified NMJ; (b) postsynaptic folds (orange overlay) imaged on surface of 1µm thick section; (c) postsynaptic folds (orange) in FIB-stack; scale bars: 100 µm in (a), 1µm in (b), (c)

3D in SEM, (S)TEM, Ion Imaging, incl. FIB-SEM and SBF-SEM

MIM.1.003
High resolution structural analysis of a centromere-specific histone H3 in mitotic plant chromosomes with FIB/FESEM tomography

E. Schroeder-Reiter[1], G. Wanner[1]

[1]LMU München, Ultrasctructural Research, Planegg-Martinsried, Germany

e.schroeder-reiter@bio.lmu.de

Chromosome architecture and the ultrastructure of centromeres have been a central research topic in our group over last two decades. Centromeres have varying morphological characterics, but are generally composed of parallel fibrils and bunched fibrils, or chromomeres, of both chromatin and proteinaceous nature [1]. With high resolution analytical FESEM techniques the distribution of different histones in the centromere were investigated.

Of particular interest is the distribution of the centromere-specific histone H3, CenH3. Combined LM and FESEM techniques including DNA-specific platinum staining and FluoroNanogold labeling allowed quantification and high resolution analysis of 3D distribution of CenH3. The majority of CenH3 localizes to two distinct areas, presumably on each sister chromatid, of the primary constriction [2]. In addition, cummulative results from several studies on histone variants in barley shows that the lateral outermost fibrils of the centromere i) do not stain for DNA, ii) do not label for phosphorylated histone H3 (serine 10), iii) do not label for canonical H3P, iv) do not label for CENH3 [2]. With low voltage SEM analysis, it could be determined that only very few CENH3 markers are located on the centromere surface [3].

In order to determine the 3D distribution of CenH3, barley centromeres were investigated using FIB tomography. Marker quantification, 3D reconstruction and animations of the CENH3 domain were calculated using FIB/FESEM tomographic data. It could be shown that, contrary to consensus models for centromere organization and kinetochore assembly, CENH3 is located in the chromosome interior of both the centromere proper and the pericentric region. 3D tomography confirmed the interior localization of CENH3, also showing distribution of individual markers in their spatial context with the highest resolution achieved to date [3]. In parallel investigations, the same interior localization of CenH3 could be found in pea centromeres [4].

This partially challenges the current trilaminar model of centromere structure, that is, however, based on human chromosomes [5]. This raises classical questions about how resolution limitations may influence interpretation of data, as well as how much influence preparation methods may have on the fidelity of immunolocalization for SEM. There is a possibility that CENH3 distribution may differ between plant and animals, as there exists an early uncontested postulation of a "ball-and-cup" structure for plant kinetochores based on TEM data [6, 7]. For convergence of seemingly contradictory findings it will be necessary to continue combining biochemical, cytological and high resolution structural approaches. Further SEM studies localizing tubulin and other centromere-related proteins such as CENPC will be necessary to determine whether and where residues are detectable on both isolated chromosomes and *in situ* chromosomes, allowing for successful preparation and labeling methods. Since immunolocalization of more than one epitope for SEM investigations is currently only a remote possibility, it is important to maintain a correlative LM-SEM approach, aiming toward super-resolution labeling of multiple antigens in order to achieve the goal of atttaining a high resolution structural kinetochore model.

1. Wanner G, Formanek H (2000) A New Chromosome Model. *J Struct Biol* 132:147-161
2. Houben A, Schroeder-Reiter E, Nagaki E, Nasuda S, Wanner G, Murata M, Endo TR (2007) CENH3 interacts with the centromeric retrotransposon *cereba* and GC-rich satellites and locates to centromeric substructures in barley. *Chromosoma* 116(3):275-283
3. Schroeder-Reiter E, Sanei M, Houben A, Wanner G (2012) Current SEM techniques for de- and re construction of centromeres to determine 3D CENH3 distribution in barley mitotic chromosomes. *J Microscopy* 246 (1) 96-106

4. Neumann P, Navrátilová A, Koblízková A, Chocholová E, Novaák P, Schroeder-Reiter E, Wanner G, Macas J. Stretching the rules: monocentric chromosomes with multiple centromere domains. *PloS Genetics* (in press)
5. Blower MD, Sullivan BA, Karpen GH (2002) Conserved organization of centromeric chromatin in flies and humans. *Dev Cell* 2: 319-330
6. Braselton JP (1971) The ultrastructure of the non-localized kinetochores of *Luzula* and *Cyperus*. *Chromosoma* 36: 89-99
7. Yu HG, Hiatt EN, Dawe RK (2000) The plant kinetochore. *Trends Plant Sci* 5(12): 543-547
8. We gratefully acknowledge excellent technical assistance over the years by Sabine Steiner, and financial support from LMU Mentoring and the Deutsche Forschungsgemeinschaft (SCHR 1157/2-1,-2).

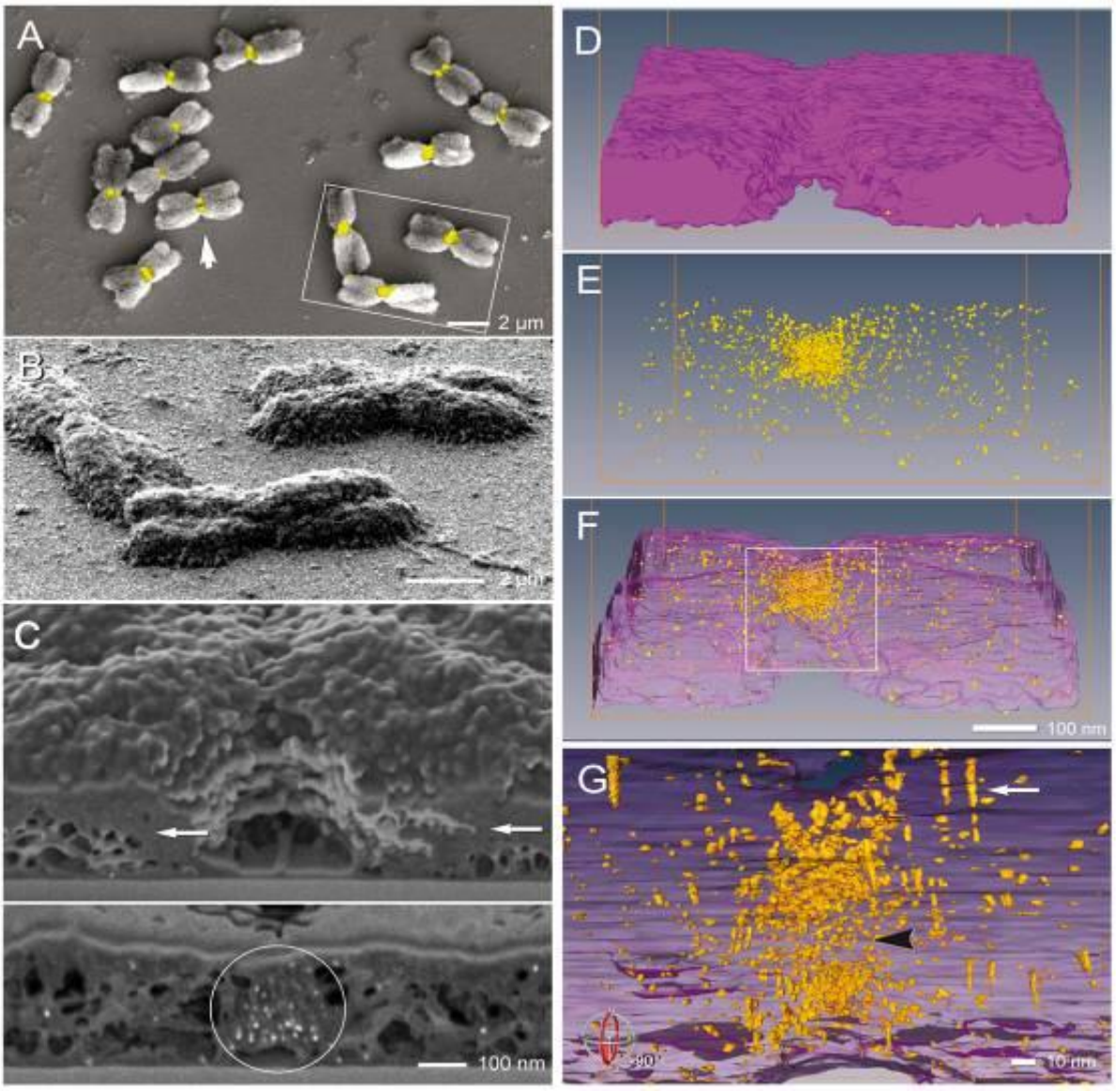

Figure 1. SEM micrographs and 3D reconstructions from FIB/FESEM tomographic series of barley chromosomes that are immunolabeled for the centromere-specific histon H3 variant CenH3. A Orthographic view of one chromosome complement in metaphase (2n=14) with superimposed backscattered electron signal (yellow) showing CenH3 labels. B Chromosomes (frame in A) after tilting for FIB tomography. C Image of milled surface of centromere at onset (arrows indicate cut surface), and after several "sections". CenH3 markers (white signals in circle) are concentrated in the centromere. D-G 3D reconstruction of CenH3 distribution in the centromere and in the pericentric region (CenH3=yellow, chromosome surface=magenta). When the chromosome surface is transparent, it is obvious that the CenH3 signal is not localized on the centromere surface. High resolution animation confirms a CenH3 gap between the chromatids (black arrowhead), and also shows occasional distortion of signals due to FIB "stalling" during series (white arrow) (see Schroeder-Reiter et al. 2012).

3D in SEM, (S)TEM, Ion Imaging, incl. FIB-SEM and SBF-SEM

MIM.1.004
Focussed ion beam/scanning electron microscopy (FIB/SEM) has the potential of a powerful tool in virus research

C. Villinger[1,2], G. Neusser[3], C. Kranz[3], B. Mizaikoff[3], J. von Einem[1], T. Mertens[1], P. Walther[2]

[1]University Hospital Ulm, Institute of Virology, Ulm, Germany
[2]Ulm University, Central Facility of Electron Microscopy, Ulm, Germany
[3]Ulm University, Institute of Analytical and Bioanalytical Chemistry, Ulm, Germany

clarissa.villinger@uni-ulm.de
Keywords: FIB/SEM, virus research, correlative microscopy, high pressure freezing

Introduction: Microscopic examinations of virus infected cells including localization of viral and cellular proteins are crucial tools in virus research. Viral tegument protein accumulations can be found at the cell base in cells infected with the human cytomegalovirus (HCMV) in fluorescent microscopy. However, light microscopy is not powerful enough for characterization of these accumulations in more detail and especially to answer the two questions (I) are these proteins part of infectious (DNA containing) virus particles and (II) are these accumulations intra- or extracellular. We have recently shown that the resolution of FIB/SEM is comparable to transmission electron microscopy (TEM) [1]. Hence, we applied FIB/SEM tomography to HCMV infected cells to investigate these accumulations of viral protein at the electron microscopic level and to access them from a different direction than usually given by ultrathin sectioning and TEM.

Experimental procedure: Fibroblasts were seeded on sapphire discs with (*protocol A*) or without (*protocol B*) coordinate system (Wohlwend GmbH, Switzerland), respectively, and infected the next day with either GFP-labeled (*protocol A,* Figure 1) HCMV or non-labeled HCMV (*protocol B*, Figure 2). The z-stack in Figure 1A was acquired with the fluorescence microscope Axio-Observer.Z1 (Zeiss, Germany) from HCMV infected fibroblasts stained for a viral protein as described in [2]. The cells infected with GFP-labeled HCMV were imaged immediately before high pressure freezing (Figure 1B). For the FIB/SEM samples, high pressure freezing, freeze substitution and embedding in epoxy resin was conducted as described in [3]. The height of the resin block was reduced to 1 mm with a jigsaw after removal of the sapphire disc and the resulting resin disc was mounted on an SEM specimen stub and coated with 5 nm of platinum by electron beam evaporation [1]. In the FIB/SEM Helios Nanolab 600 (FEI, Eindhoven, The Netherlands) we located the area of interest at a relatively high acceleration voltage of 10 kV (Figure 1C and 1D). For FIB milling of the samples shown in Figure 2C and 2D an additional layer of platinum was deposited using ion-beam induced deposition (IBID) [4], starting with a deposition of a thin layer at 48 pA, followed by a thicker layer at 0.28 nA. For all images in Figure 2 a regular cross-section was milled, followed by a cleaning cross-section at 53°. The sample was then tilted back to 52° and the block-face was imaged with the through the lens mode with an extraction voltage of 70 V at an acceleration voltage of 5 kV.

Conclusion: We could show that the FIB/SEM approach can be successfully applied for virological research since we were able to visualize virus particles, their membranes and the different states of HCMV capsid formation inside the nucleus in high resolution. Hence, we were able to clarify that the accumulations of viral protein detected in the fluorescence microscope obviously originate from infectious virus particles underneath the cell monolayer. This result supplements the model of HCMV egress and has not been shown so far. In order to facilitate the localization of virus infected cells in the FIB/SEM we used GFP-labeled virus particles together with sapphire discs with a coordinate system. By performing FIB/SEM in combination with this correlative approach, we established a tool for further experiments aiming at visualization of virus infected cells in three dimensions in order to answer urgent questions concerning the mechanisms of virus entry and morphogenesis.

1. C. Villinger, H. Gregorius, Ch. Kranz, et al., Histochem Cell Biol 138 (2012), pp. 549-556.
2. M. Schauflinger, D. Fischer, A. Schreiber, et al., J Virol 85 (2011), pp. 3821–3832.
3. K. Höhn, M. Sailer, L. Wang, et al. Histochem Cell Biol 135 (2011), pp. 1–9.
4. A.J. Bushby, K.M. P'ng, R.D. Young, et al., Nat Protoc 6:6 (2011), pp. 845-858.
6. We kindly acknowledge E. Schmid for expert technical assistance.

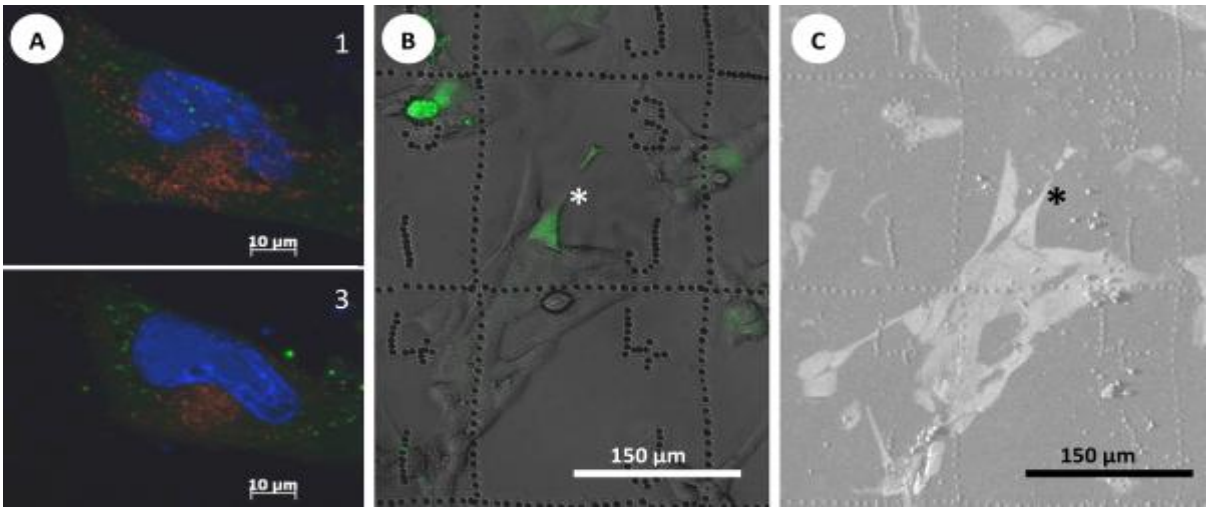

Figure 1. Fibroblasts infected with GFP-labeled HCMV. (A) Two images from a z-stack (1 µm between images, numbers indicate the number of the optical section counted from the cell base to the top). In the first section patches of red fluorescence signal (viral tegument protein) are distributed throughout the entire plane, in the third section the accumulation is only located in the assembly complex (=circular structure enclosed by a kidney shaped nucleus in blue). (B) Combination of the transmitted light image with the fluorescence image of fibroblasts on the sapphire disc prior to high pressure freezing. Infected cells are indicated by green fluorescence. The cell of interest is marked with an asterisk. (C) It can then be easily found in the FIB/SEM after embedding.

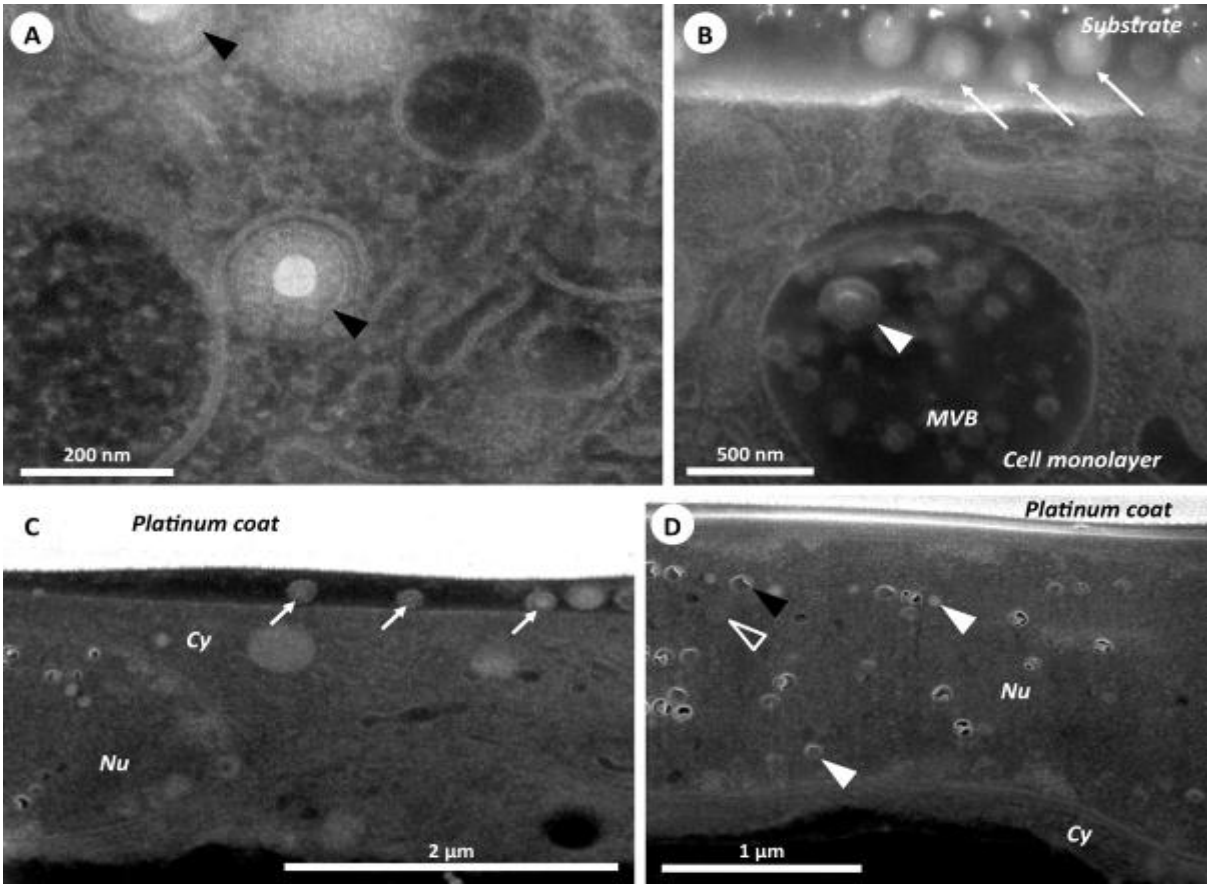

Figure 2. FIB/SEM images of other HCMV infected cells. (A) Virus particles (arrowheads) within a cell. Note the TEM like resolution of the membrane bilayers. (B) The interface between cell monolayer and the substrate is easily accessible with the FIB/SEM approach. Virus particles can be identified (white arrows). (C) and (D) Cross section after additional platinum coating to avoid beam damage (*Cy* cytoplasm, *Nu* nucleus). (C) Virus particles at the interface cell/substrate (white arrows). (D) Different states of virus capsid formation inside the nucleus. Virus capsids containing DNA (white arrowhead) can be distinguished from virus capsids with a scaffold ring (empty arrowhead) or empty capsids (black arrowhead).

3D in SEM, (S)TEM, Ion Imaging, incl. FIB-SEM and SBF-SEM

MIM.1.005
Helium Ion Microscopy: Extending the frontiers of nanotechnology

P. Gnauck[1], L.-O. Kautschor[1]

[1]Carl Zeiss Microscopy, Oberkochen, Germany

peter.gnauck@zeiss.com
Keywords: Helium, Ion, Microscopy

The Helium Ion Microscope has been described as an impact technology offering new insights into the structure and function of nanomaterials [1]. Combining a high brightness Gas Field Ion Source (GFIS) with unique sample interaction dynamics, the helium ion microscope provides images offering unique contrast and complementary information to existing charged particle imaging instruments such as the SEM and TEM [2]. Formed by a single atom at the emitter tip, the helium probe can be focused to below 0.25nm offering the highest recorded resolution for secondary electron images. The small interaction volume between the helium beam and the sample also results in images with stunning surface detail .

Besides imaging, the helium ion beam can be used for fabricating nanostructures at the sub-10nm length scale. Researchers have used the helium ion beam for exposing resist and features as small as 4nm have been reported [3]. The main advantage of helium ion lithography over electron beam lithography is the minimal proximity effect [Fig 2,3]. The helium ion beam has also been used for deposition and etching in conjunction with appropriate chemistries [4]. Helium induced deposition results in higher quality deposits than with Ga-FIB or EBID (Electron Beam Induced Deposition). Finally, the helium ion beam can be used for direct sputtering of different materials. Patterning of graphene has resulted in 5nm wide nanoribbons [Fig.1] and 3.5nm holes in silicon nitride membranes have been demonstrated. However, due to its lower mass, the helium sputter rate is significantly lower than with gallium. Further, helium tends to implant rather than sputter silicon which is an issue for FIB applications in semiconductors. To overcome these issues, we have developed the GFIS to operate with Ne.

The Gas Field Ion Source has been modified and the gun redesigned to allow the use of both He and Ne source gases. Although Best Imaging Voltage (BIV), defined as the optimal voltage to get the highest source brightness, is lower for Ne, the system is optimized to operate under the same column conditions for both gases. The neon probe size is greater than helium and is measured between 1-2nm although additional improvements are expected. However this is not a limitation from a nanofabrication standpoint. The sputter yield of Ne is about 30X higher than He, and the Ne beam has a shallower penetration depth resulting in lower sub-surface damage. The sputtering of materials with Ne is significantly better than He and generally within a factor 2X of Ga. Neon ion beam has been used for Lithography and is shown to be 1000X more efficient than 30keV electron beam with the ability to print 7nm lines [5]. This work has culminated in the development of an ion microscope with a gas field ion source that can operate with both He and Ne.

1. Smentkowski, V.S., Denault, L., Wark, D., Scipioni, L., and Ferranti, D, Microscopy and Microanalysis 16(Suppl.2), (2010) p.434
2. Bell, D. C., Microscopy and Microanalysis 15, (2009), p.147
3. Li, W., Wu, W., and Williams, R.S., SPIE Lithography Conference (2012)
4. Sanford, C.A., Stern, L., Barriss, L., Farkas, L., DiManna, M., Mello, R., Maas, D.J., Alkemade, P.F.A., J. Vac. Sci. Technol. B 27(6), (Nov/Dec 2009), p.2660
5. Winston, D., Manfrinato, V.R., Nicaise S.M., Cheong, L.L., Duan, H., Ferranti, D., Marshman, J., McVey, S., Stern, L., Notte, J., Berggren, K.K., Nano Letters 11(10), (2011), p.4343

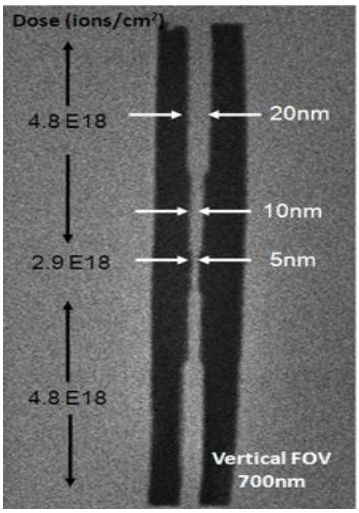

Figure 1. Nanoribbons milled into Graphene sheets by using the Helium beam
(Results courtesy of Dan Pickard NUS)

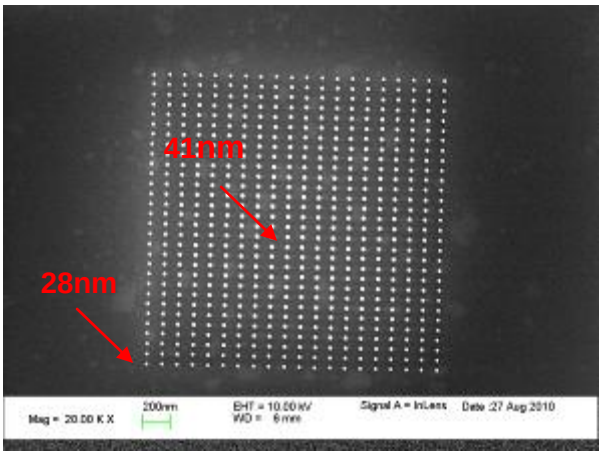

Figure 2. SEM suffers from proximity effects: Exposed dots near the center are much bigger than the same exposed dots at the corners.
(Results courtesy of Karl Bergren of MIT)

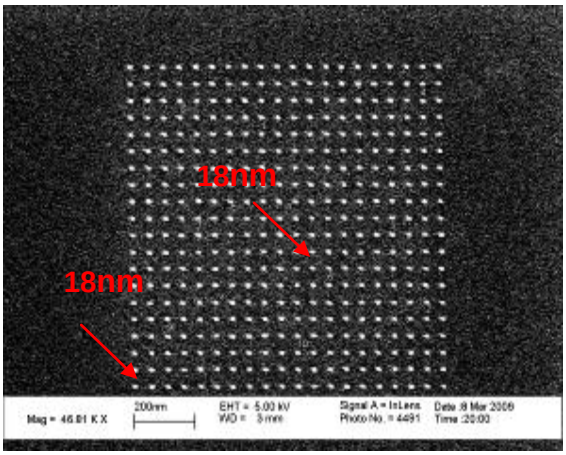

Figure 3. When exposed with a helium beam, the exposed region is smaller, AND more consistent independent of nearby exposures.
(Results courtesy of Karl Bergren of MIT)

3D in SEM, (S)TEM, Ion Imaging, incl. FIB-SEM and SBF-SEM

MIM.1.006
SEM tomography of nanostructures by scanning-transmission imaging

M. Ferroni[1], A. Migliori[2], V. Morandi[2], L. Ortolani[2], A. Pezza[2], G. Sberveglieri[1]

[1]University of Brescia and CNR, Information Engineering, BRESCIA, Italy
[2]CNR, Institute for Microelectronics and Microsystems, BOLOGNA, Italy

matteo.ferroni@ing.unibs.it
Keywords: SEM, STEM, tomography

This paper highlights the implementation of electron tomography in the SEM and discusses the potential of this 3-D imaging technique. Electron tomography is one of the most promising and rapidly developing techniques for 3-D reconstruction at the nanoscale as it combines a reliable reconstruction algorithm with the signal corresponding to incoherently scattered electrons in the Scanning-Transmission (STEM) imaging mode 00. The STEM-in-SEM imaging has been successfully implemented in the SEM, where it takes advantage from some peculiar characteristics of the experimental set-up 0. The STEM approach attains nanometric resolution and is free from aberrations caused by post-specimen imaging lenses; in addition it is possible to collect transmitted electrons over a wide angular range 00. The optimization of detector design and performance, together with the formulation of a tailored detection strategy, make the contrast comply with local variations of composition or projected thickness. The bright-field component of the transmitted electrons can be effectively separated from the dark-field one, by varying the specimen-detector distance and the collection conditions of the detector [4]. The capability of the STEM-in-SEM imaging mode to preserve the monotonic variation of the signal with specimen thickness meets the basic projection requirement for reconstruction, and thus opens up the perspective for the 3-D analysis of volumes in approximately the 100 μm^3 range, such as nanowires, carbon based nanostructures or biological specimens. In addition, the large value for the maximum detection angle ensures a complete detection of the scattered electrons, even in case of relatively large specimen thickness. In the case of tomography, these features are essential to maintain the proper image contrast when the specimen is rotated through the tilt series. To demonstrate the technique, different systems were investigated: Fig. 1 shows the perspective view of the reconstructed volume of a ZnO crystalline nanostructure This comb-like structure exhibits a number of parallel nanowires with uniform section (average width 176 ± 15 nm) and tapered termination. The tilt series of STEM images was obtained by rotating the sample over a 110° range, with 1° step. ImageJ [0] with the TomoJ plug-in allowed obtaining the tomographic reconstruction 0. The main features of the samples are properly retrieved such as the disposition of the wires, their uniform section and the tapered termination. Similarly, carbon based tubes, filled with cobalt nanoclusters, were reconstructed and imaged in Fig. 2. The tomogram from the tilt series of STEM images, that feature compositional contrast, clearly shows the heavier cobalt clusters inside the tube. These results demonstrate the potential of the method and optimization of the experimental set-up is under development to consolidate this technique in the set of 3-D methods of electron microscopy.

1. P.A. Midgley et al. Journal of Ultramicroscopy 223 (2006) 185.
2. S. Bals et al. Adv. Mat. 18 (2006) 292.
3. P.G. Merli et al. Ultramicroscopy 88 (2001) 139.
4. V. Morandi and P.G. Merli, Journal Applied Physics 101 (2007) 114917.
5. V. Morandi et al. Applied Physics Letters 90 (2007) 163113.
6. ImageJ: Image Processing and Analysis in Java - http://rsbweb.nih.gov/ij/
7. Messaoudii C. et al, BMC Bioinformatics 8 (2007) 288.

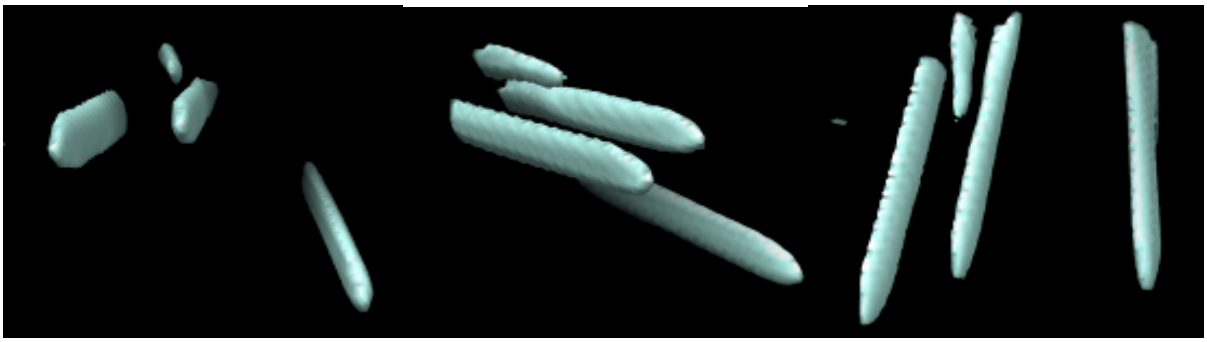

Figure 1. Volume renderings of ZnO nanowires. The disposition of the wires, their uniform section and the tapered termination are properly retrieved by the tomographic reconstruction based on a STEM-in-SEM tilt series of 110 images at 1° tilt. The reconstructed area of interest measures 4.5×4.5 □m, corresponding to a primary magnification of 50.000×.

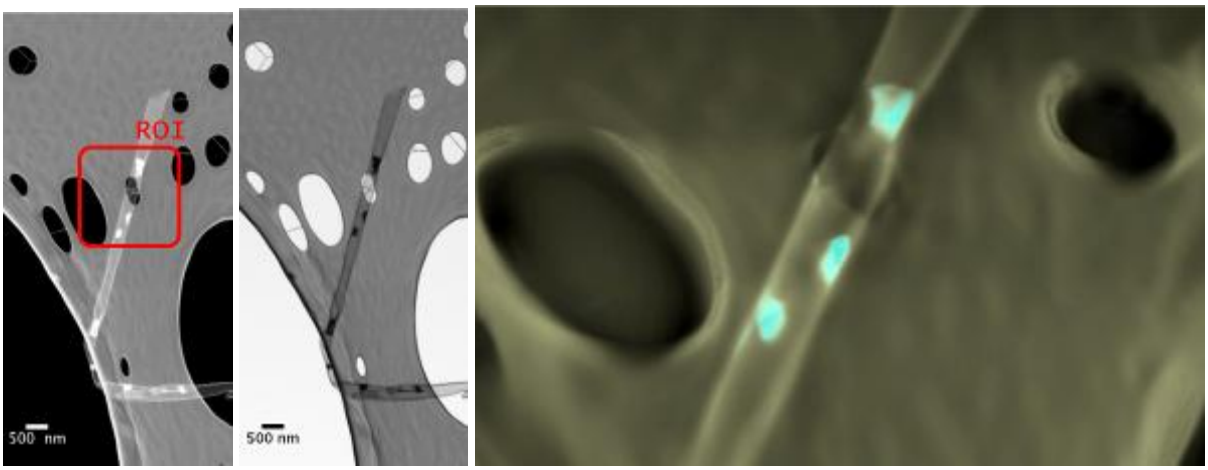

Figure 2. (Left and Center) STEM Bright- and Dark- field compositional images of carbon tubes filled with Co nanoclusters - Beam 30 keV – (Right) Tomogram from the Bright-Field tilt-series showing the cobalt clusters inside the carbon tubes.

3D in SEM, (S)TEM, Ion Imaging, incl. FIB-SEM and SBF-SEM

MIM.1.007
STEM tomography and CBED polarity analysis of crystallographic pores in InP

A.M. Beltran[1], B. Winter[1], E. Spiecker[1]

[1]CENEM-University of Erlangen-Nürnberg, Department of Materials Science and Engineering, Erlangen, Germany

ana.m.c.beltran@ww.uni-erlangen.de
Keywords: electron tomography, porous InP

The sophisticated 3D architecture of crystallographic pores produced by electrochemical etching in III-V compound semiconductors, like GaAs, GaP and InP, has attracted considerable research interest [1,2]. During formation of such pores the crystal polarity plays a key role in selecting the pore growth directions and pore branching which together determine the 3D architecture. In a previous work the morphology of crystallographic pores in n-type InP(001) was analysed by conventional transmission electron microscopy (TEM) [3]. By a detailed study of thin TEM lamella prepared in different crystal orientations combined with convergent-beam electron diffraction (CBED) for polarity analysis a qualitative model of the pore branching and 3D pore morphology could be derived. A few results of this earlier study are summarized in Figure 1. More details can be found in reference [3].

Here we present results of an electron tomographic study of these crystallographic pores. Electron tomography (ET) is an advanced microscopy technique which allows obtaining 3D information from the reconstruction of a tilt series consisting of two-dimensional images [4]. For the investigation a (101) TEM lamella inclined from the (001) surface by 45° has been chosen since it contains two <111> pore growth directions enabling the study of extended pores and of pore branching.

A STEM image acquired with a FEI Titan^3 80-300 at 200 keV using a camera length of 46 mm (Figure 2a) reveals the distribution of pores parallel and inclined to the surface. However, the real 3D morphology (faces and branches of the pores) cannot be clearly distinguished. Therefore, ADF-STEM electron tomography has been performed at the same microscope working at 300 keV, using a microprobe mode with a convergence semi-angle of 3 mrad to obtain enough depth of focus [5]. A camera length of 29.5 mm was used during the acquisition of the tilt series which was recorded from -64° to +59°, with 1° tilt increments. For 3D-reconstruction the Simultaneous Iterative Reconstruction Technique (SIRT) has been applied with 50 iterations. From these reconstructions the 3D-morphology of the pores and of pore branches can be studied (Figure 2b). The pores possess a triangular cross-section with oscillating pore diameter. For some pores, like the one shown in Figure 2b), the oscillation is small resulting in a more or less uniform pore channel. Other pores show much stronger oscillation and appear to consist of interconnected tetrahedrons. From the CBED analysis (Figure 1) it can be concluded that the inner surfaces of such pores are dominated by polar In-terminated {111}A facets.

A detailed 3D analysis of crystallographic pores in InP will be presented. In particular, by combining electron tomography and CBED polarity determination the relation between the crystal polarity and the three-dimensional pore distribution and pore shape will be clarified.

1. V.P. Ulin, S.G. Konnikov, Semiconductors 41 (2007) 832.
2. M. Leisner, D. Dorow-Gerspach, J. Carstensen, H. Föll, Physica Status Solidi (A) 208 (2011) 1378.
3. E. Spiecker, M. Rudel, W. Jäager, M. Leisner and H. Föll, Physica Status Solidi (A) 202 (2005) 2950.
4. P.A. Midgley and M. Weyland, Ultramicroscopy 96 (2003) 413.
5. J. Biskupek, J. Leschner, P. Walther and U. Kaiser, Ultramicroscopy 110 (2010) 1231.
6. The authors thank Prof. Föll from the University of Kiel for providing the sample used in this study. They gratefully acknowledge the financial support by the German Research Foundation (DFG) through the Priority Program 1570 “Porous media with defined porous structure in Chemical Engineering” and the Cluster of Excellence EXC 315 “Engineering of Advanced Materials”.

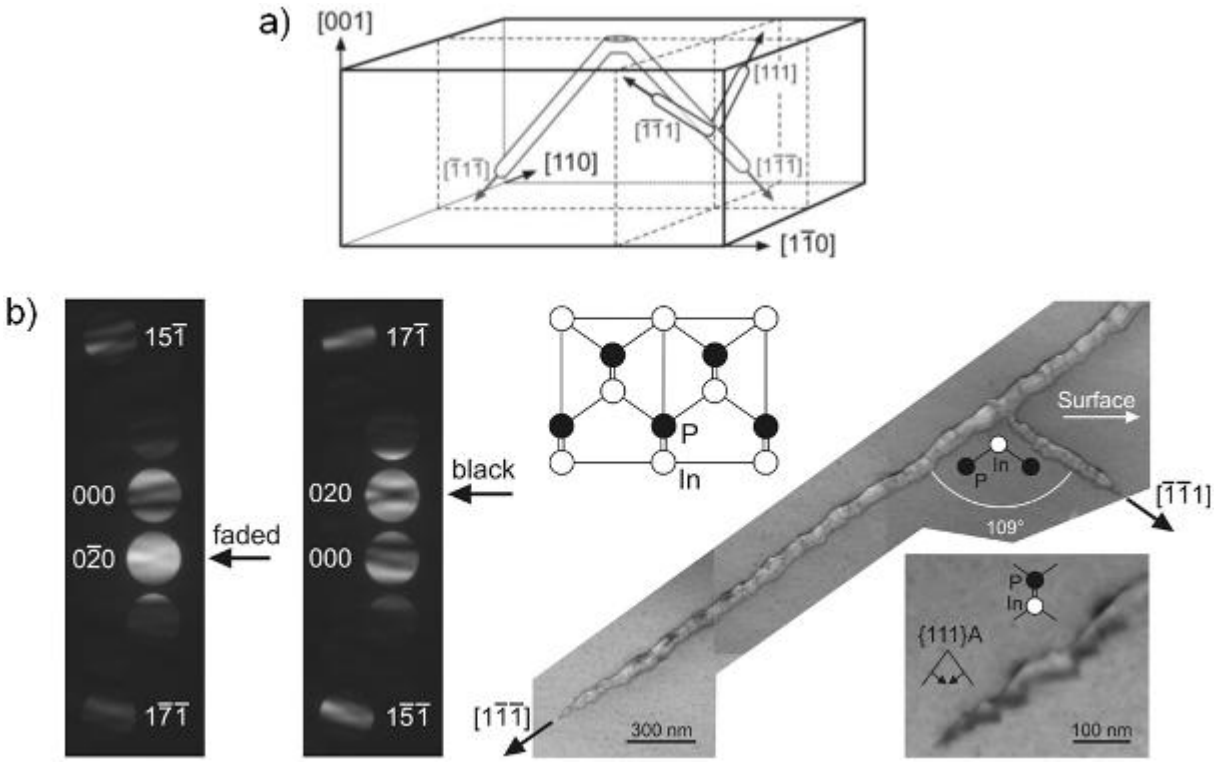

Figure 1. Crystallographic pores in InP obtained by electrochemical etching [3]: a) Schematic of pore branching along four <111> directions of equal polarity. b) Determination of crystal polarity by CBED and TEM bright-field imaging of a branching pore and a very pore tip showing oscillating contrast.

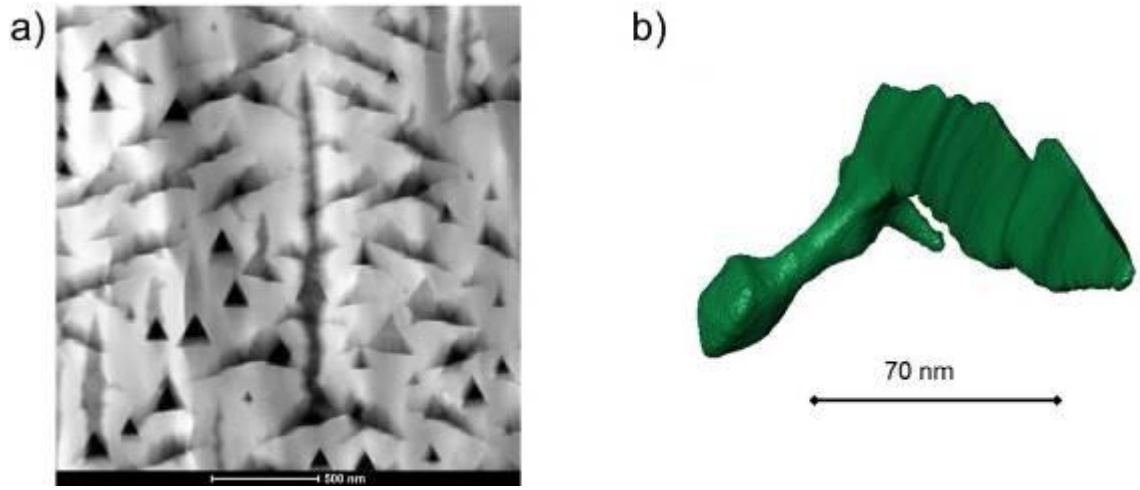

Figure 2. a) HAADF-STEM contrast used for acquisition of tomographic tilt series, b) Tomographic reconstruction of a larger pore showing triangular cross-section with oscillating pore size and sideward branching of a smaller pore.

3D in SEM, (S)TEM, Ion Imaging, incl. FIB-SEM and SBF-SEM

MIM.1.P008
Evaluation of Effect Pigment Orientation using combined SEM, TEM and X-ray CT analysis and conclusion for interpreting gonio-spectrophotometric data of effect coatings

M. Roesler[1], L. Berthold[2], J. Schischka[2], M.J. Heneka[3]

[1]Merck KGaA, Darmstadt, Germany
[2]Fraunhofer Institute for Mechanics of Materials IWM, Halle, Germany
[3]RJL Micro & Analytic GmbH, Karlsdorf-Neuthard, Germany

michael.roesler@merckgroup.com

Plate-like effect pigments (with diameters between 5-40µm and less than 1µm thick) are widely used to create decorative appearance in coatings, prints, plastics and cosmetics. Thereby the color and texture do not only depend strongly on type and concentration of the effect pigment, but also on their orientation distribution in the corresponding medium. In order to predict the appearance of a given effect pigment, its orientation distribution obtained using a specific method of application (spray application, roller blade application, offset printing, brushing, etc.) should be measured. This is usually done by preparing mechanical cross sections and obtaining the 2D particle inclination distribution N(□) by semiautomatic image processing of microscope images.

The present poster describes the method of X-ray tomography (SkyScan model 2011 nano-CT) as a noncontact, nondestructive and fast method to examine the 2D and 3D particle orientation in effect coatings. In comparison to X-ray CT a step-by-step ion beam slicing using a FIB V600 CE+ (FEI) was utilised for the same coatings volume. These cross-sections were inspected to find the identical particles already seen in the tomogram and to evaluate them with respect to inclination, thickness and inter-particle distances by SEM (SU70 / Hitachi) and TEM imaging (Tecnai G2 F20 S TWIN / FEI). Although the lateral resolution of all methods is quite different a good correlation could be found for individual particles as well as for big ensembles. In case of adding disorienter particles to the effect pigments this data were used successfully to interpret high resolution macroscopic gonio-spectrophotometric measurements (Murakami GCMS-4 Gonio-Photospectrometer).

In order to follow the logical way of this research figures on the next page are shown consecutively: Fig. 1 gives the accustomed view of an ensemble of effect pigments as generated by (BF) light microscopy. The effect pigments are seen as platelets from the top to estimate particle areas and equivalent diameters. Fig. 2 represents a mechanical cross-section through the effect coating imaged by SEM. Here we get the side view of the particles in order to estimate the thicknesses and more importantly the two-dimensional angular particle inclination □ with respect to the surface normal. N(□) is close to a Gaussian with a standard deviation of less than 10°. Fig. 3a depicts the SEM view of the marked coatings area (volume enclosed between both crosses under the metal protection bar) to be analyzed by X-ray CT. The crosses are identified then in the X-ray CT images as shown in fig. 3b (for X-ray CT principles see the scheme in fig. 4). The measured and reconstructed ensemble of the effect particles in the volume is given in fig. 5. Along the line between both crosses a TEM lamella was prepared using FIB technique. One of the cross-sections is shown in fig. 6a as an X-ray CT section, in fig. 6b as a SEM – and in fig. 6c as a TEM – cross-section image. There is not a full correspondence between the pictures due to the different depth of analyzing, which is much bigger in X-ray CT than in TEM.

Identical volumes are marked by squares and the particles are evaluated with respect to inclination □ and thickness. Due to the fact that TEM analysis need thin electron transparent sections of the volume (prepared from both sides of the lamella) a continuous transversal shift of the interface was followed by SEM imaging and correlated with X-ray CT images for a large volume. The TEM-SEM-X-ray CT correlation in fig. 6a, b, c was carried out only at the final stage, having a thin lamellar residue suitable for TEM. The usage of X-ray CT evaluation of particle inclinations in correspondence to measured goniometric lightness distributions (here light incidence is 45° and the detection angle varies from +75° to -75°, corresponding to an aspecular angle φ from 30° to -120°) is demonstrated in fig. 7a – for a series of different effect pigment concentrations, where the lightness curves are shifted to higher values and fig. 7b – for a series of effect coatings with rising disorienter concentration, with a "rotation" of the lightness curves: less lightness in direction close to the specular and more lightness in strong aspecular directions. The behavior of log(L*)=f(φ) in both cases fits well with the X-ray CT data of particle inclinations as given in the captures. Therefore the gonio-spectrophotometric approach and the X-ray CT data are best suited to study the effect particle orientation distribution in a sufficient large coatings volume and SEM /TEM analysis can be used to investigate detectability of the pigments, resolution and local peculiarities of the methods.

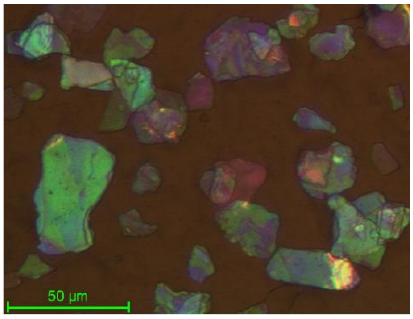

Fig. 1: Light microscope bright field image of the paint film

ir, (2)clear coat, (3)base coat (15 µm thick), (4)filler layers and (5)substrate

Fig. 2: Mechanical cross-section of the paint film imaged by SEM

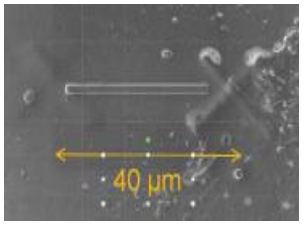

Fig. 3a: Paint surface area marked by crosses in the FIB and imaged by SEM

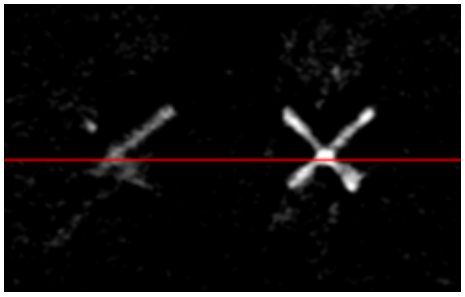

Fig. 3b: X-ray CT identification of the sample by finding the cross-markers

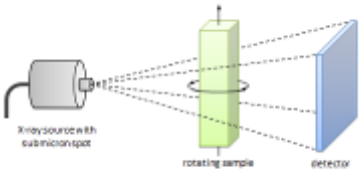

Fig. 4: Scheme of the X-ray CT imaging method

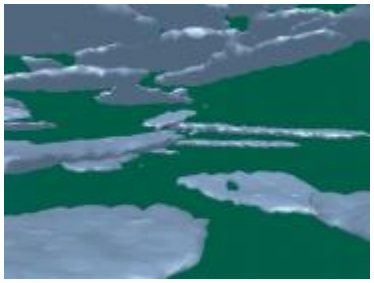

Fig. 5: Still picture of a movie showing the 3D particle ensemble

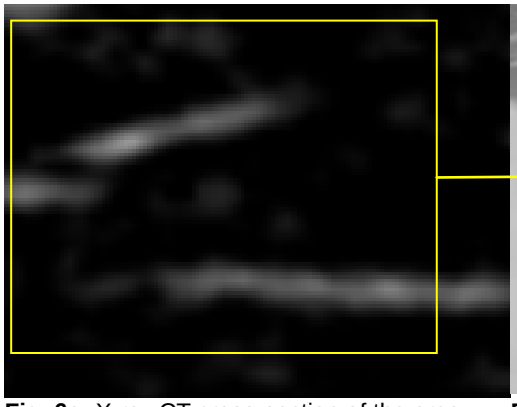

Fig. 6a: X-ray CT cross-section of the area imaged in 6b and c.

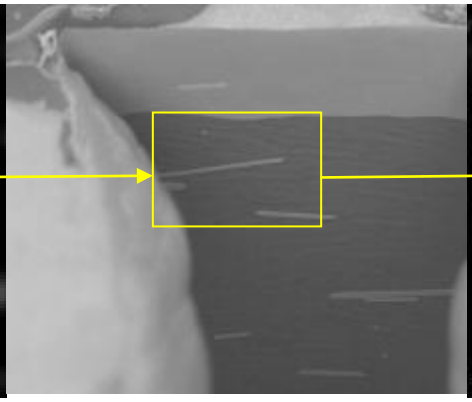

Fig. 6b: SEM image of the FIB lamella

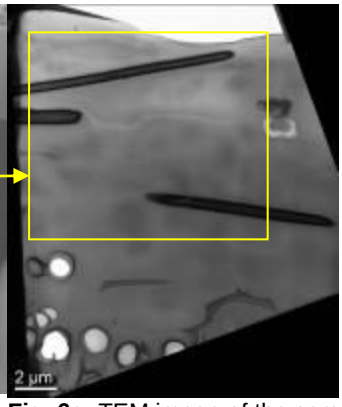

Fig. 6c: TEM image of the same location

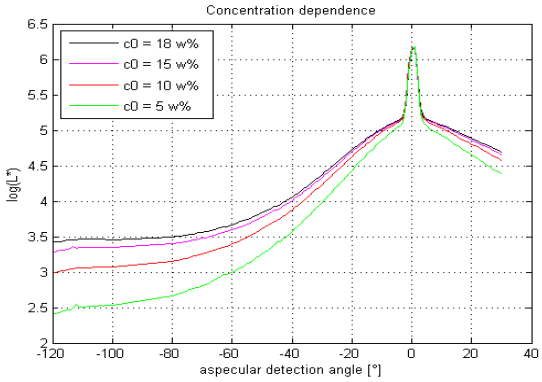

Fig. 7a: Log(L*) =f(φ) for different effect pigment concentration c0: the disorientation measured by X-ray CT is always δ=9.2° ± 0.5°.

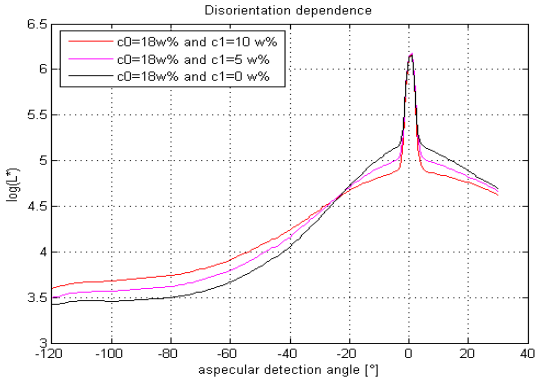

Fig. 7b: Log(L*) =f(φ) for 18w% effect pigment and different concentration of a disorienter c1: the disorientation measured by X-ray CT rises from 9.2°, via 10.5° to 13.1°.

3D in SEM, (S)TEM, Ion Imaging, incl. FIB-SEM and SBF-SEM

MIM.1.P009
Automated geometric SEM calibration

M. Hemmleb[1], M. Ritter[1], D. Berger[2]

[1]m2c, Potsdam, Germany
[2]Technische Universität Berlin, Zentraleinrichtung Elektronenmikroskopie ZELMI, Berlin, Germany

Matthias.Hemmleb@m2c-calibration.com
Keywords: SEM calibration, metrology, nanomarker

Several SEM applications (e.g. layer thickness in solar cells or dielectric optical layers, pore and grain sizes) require well calibrated measurements of distances. For some applications (e.g. wave guides) the precise determination of angles is needed in addition. Usually, reference samples with line features are used to calibrate the scale of SEM images in x- and y-direction. Due to the more or less manual measurements and the reduction of the geometrical calibration parameters to a single distance, this procedure is not very accurate and a time consuming process. Moreover, it might not provide information of the shear factors between x and y and cannot be used to calibrate angles.

Although SEM is mostly applied for 2D imaging and analysis, it is more and more used for 3D applications. Hence, 3D calibration standards are required. A sophisticated solution for 3D calibration are samples with pyramidal structures and circular reference marks, already applied for SPM and SEM detector calibration [1,2]. In this paper, the application of such calibration structures for automated geometrical SEM calibration with high accuracy is presented.

The calibration structures (Figure1) consist of three pyramidal structures. The spherical element necessary for the calibration of BSE detectors [2] is not used here. Following the principle of marker-based calibration, the pyramidal structures contain circular nanomarkers at specific three-dimensional coordinates, which serve as reference for the scale and shear calibration in all three spatial directions. The necessary reference measurement of the calibration structure is performed at the PTB with the Met.LR-SPM, (Metrological Large-Range SPM) based on a NanoMeasuringMachine (SIOS GmbH). The position of all three translation axes of the Met.LR-SPM are monitored by laser interferometers and thereby direct traceability to the SI unit meter is guaranteed [3].

For a successful calibration, the operator has to select appropriate SEM parameters (detector type, magnification, beam voltage, working distance). After acquisition of the calibration sample image, the calibration is performed by the calibration software in an easy way. The software automatically detects and measures all markers on the base plane with sub-pixel accuracy by image processing methods. This includes the detection of the sample orientation and the allocation of special reference marks by using coded targets. The calibration results in the calculation of all linear geometrical parameters: scale in x- and y-direction, shearing between x and y, as well as the sample orientation (rotation and translation). The approach applied here is based on LSM (least-squares methods) and allows the statistical analysis of the results, including data snooping for outlier detection and analysis of non-linearities. All results can be saved as reports and the calibration data are stored in external files. These calibration files enable an automated SEM image correction (rectification) when using the image correction software included in the calibration software package. Alternatively, the calibration parameters can be transferred manually to your SEM software in order to obtain calibrated images.

Figure 1 shows the 2D calibration of the SEM Hitachi S520 with the calibration structure MMC-40. The size of MMC-40 is about 40 x 40 x 1.5 µm³, the base edge length of every pyramid is 10 µm, allowing fields of view (FOV) of 15 to 50 µm for the SEM calibration. Table 1 shows calibration results using various geometric parameters. Compared to non-calibrated image data, the maximum remaining deviations between the coordinates of the reference and the calibrated image are reduced from 268 to 27 nm in x-direction and from 534 to 56 nm in y-direction when applying shear corrections (2D affine). This result shows, that the application of a single scale (2D similar) or even the application of two scales (2D nonisotrop) is not sufficient to get the highest accuracy.

1. M. Ritter, T. Dziomba, A. Kranzmann, L. Koenders: A landmark based 3D calibration strategy for SPM. Meas. Sci. Tech. 18 (2007), pp. 404 – 414.
2. D. Berger, M. Ritter, M. Hemmleb, G. Dai, T. Dziomba: A new quantitative height standard for the routine calibration of a 4-quadrant-large-angles-BSE-detector. EMC 2008, Vol.1 (2008), pp.533-534.
3. G. Dai, F. Pohlenz, H. Danzebrink, M. Xu, K. Hasche, G. Wilkening: Metrological large range scanning probe microscope. Rev. Sci. Instr., Vol.75, Issue 4 (2004), pp. 962-969.

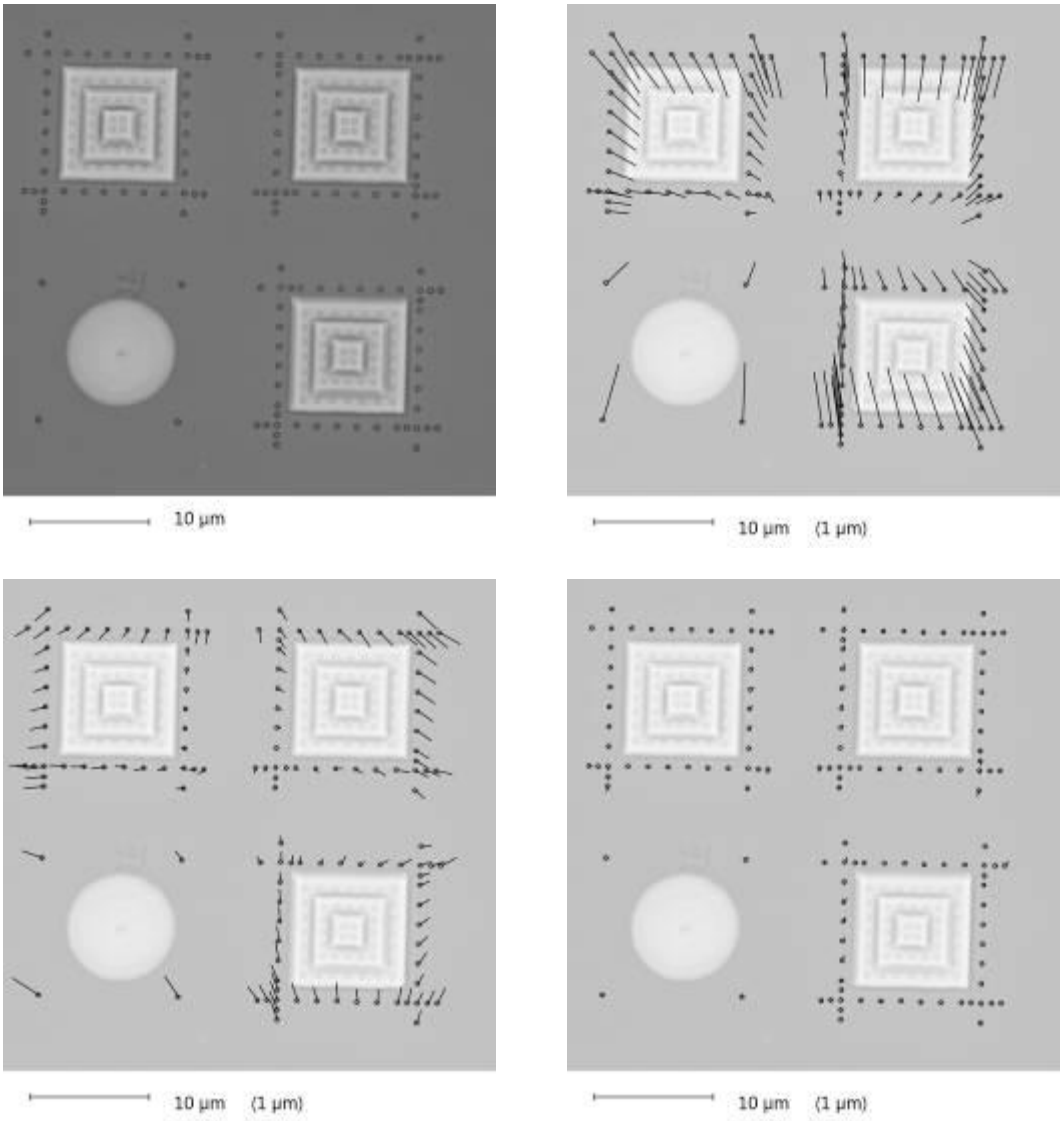

Figure 1. Original SEM image of MMC-40 (upper left), with deviations against reference data (upper right, deviation vectors 10x enlarged), with remaining deviations after scale calibration (2D similar, lower left) and with full 2D calibration (2D affine, lower right).

calibration approach	maximal deviation in x (nm)	maximal deviation in y (nm)	scale correction in x	scale correction in y	shear correction
2D rigid	268	534	-	-	-
2D similar	229	177	1,019	1,019	-
2D nonisotrop	36	66	1,011	1,027	-
2D affine	27	56	1,010	1,026	-0,002

Table 1. Results of different 2D calibration approaches with the marker-based calibration method (first line: comparison with reference data, second and third line: scale calibration, fourth line: complete calibration with scales in x- and y-direction and shearing).

3D in SEM, (S)TEM, Ion Imaging, incl. FIB-SEM and SBF-SEM

MIM.1.P010
Serial block-face scanning electron microscopy (SBEM) of soft materials for 3D reconstruction - How to get contrast

A. Zankel[1], C. Mayrhofer[2], H. Reingruber[1], S. Wernitznig[3], G. Leitinger[3], P. Poelt[1]

[1]Graz University of Technology, Institute for Electron Microscopy and Nanoanalysis , Graz, Austria
[2]Center for Electron Microscopy Graz, Graz, Austria
[3]Medical University of Graz, Institute of Cell Biology, Histology and Embryology, Graz, Austria

armin.zankel@felmi-zfe.at
Keywords: SBEM, ESEM, 3D reconstruction

Serial block-face scanning electron microscopy (SBEM) is a method that uses an ultramicrotome mounted in the chamber of a variable pressure scanning electron microscope (VPSEM) or an environmental scanning electron microscope (ESEM). For the investigation of electrically nonconductive materials the compensation of specimen charging is fundamental, which can be realized in the low vacuum mode with a pressure of the imaging gas in the range of 10 to 200 Pa. The combination enables the automated serial sectioning and imaging of the respective block-faces of the specimen. This new technique was originally developed for the investigation of neuronal tissues [1] and up to now most of the publications originate from the field of life sciences. However, this method can also be applied in the field of materials science if the respective specimens are sliceable with diamond knives [2,3]. It gives three dimensional information about the inner structure of materials and thus from 3D representations of selected volumes from the data sets, software programs like amira® or Avizo® deliver additional data which are fundamental for the development of new materials.

Work was carried out using an ESEM Quanta 600 FEG (FEI, Eindhoven, the Netherlands) and the serial block-face sectioning and imaging tool, 3View™ of Gatan, Inc. (Pleasanton, CA, USA, see Figure 1.). For imaging with secondary electrons a special version of a gaseous secondary electron detector (GSED), the so called large field SE detector (LFD) from FEI and for imaging with backscattered electrons (BSE) a specially designed detector from Gatan was used. This BSE-detector (BSED) provides enhanced performance at low electron energies. The 3View™ system is controlled by the software Digital Micrograph™.

Because ultramicrotomy creates smooth surfaces typically compositional contrast is used for imaging [1]. Concerning biological samples generally a preparation analogue to TEM-protocols is carried out. Typical preparation steps include block contrast enhancement using ruthenium tetroxide, osmium tetroxide or uranyl acetate. The block-face of a neuronal tissue, which is prepared in such a way can be seen in Figure 2.a. Because the block contrast protocols are applied before the tissue blocks are incubated in resin, biological specimens are usually stained throughout the whole block, but in polymers the penetration depth of the stain is often limited and also a concentration gradient can be observed, giving rise to contrast changes in the images recorded at various depths [1,2].

Aside from chemical contrast enhancement by staining, specimens may also show intrinsic compositional contrast because they consist of several different chemical phases. In Figure 2.b the block-face of a talcum filled polypropylene specimen can be seen, where the talcum particles are much brighter than the matrix. Using a threshold technique without any preceding image enhancement may suffice to get a 3D reconstruction of the distribution of the particles [4]. Moreover, a difference in the chemical composition between a sample and a resin can facilitate a 3D reconstruction of the investigated volume. In Figure 2.c the block-face of a porous polyethersulfone filtration membrane (sulfur containing) embedded in resin can be seen.

However in the case of specimens which deliver no compositional contrast, it may help to image small topographic surface variations resulting from cutting different phases. In Figure 2.d the SE-image of a hyper-cross-linked poly(styrene−divinylbenzene) monolith embedded in resin can be seen. In [5] this was used for the 3D reconstruction of the sample volume yielding significant information about the sample's micromorphology.

1. W. Denk & H. Horstmann PLoS Biol 2 (2004): e329.
2. A. Zankel, B. Kraus, P. Poelt, M. Schaffer, E. Ingolic, J. Microsc. 233 (2009) p. 140.
3. H. Reingruber, A. Zankel, C. Mayrhofer, P. Poelt, J. Membr. Sci. 372 (2011) p. 66.
4. T. Koch, D. Salaberger, A. Zankel, H. Reingruber, A. Steiger-Thirsfeld, Y. Voronko, S. Seidler, Macromol. Symp. 315 (2012) p. 115.
5. T. Muellner, A. Zankel, C. Mayrhofer, H. Reingruber, A. Hoeltzel, Y. Lv, F. Svec, U. Tallarek, Langmuir 28 (2012) p. 16733.

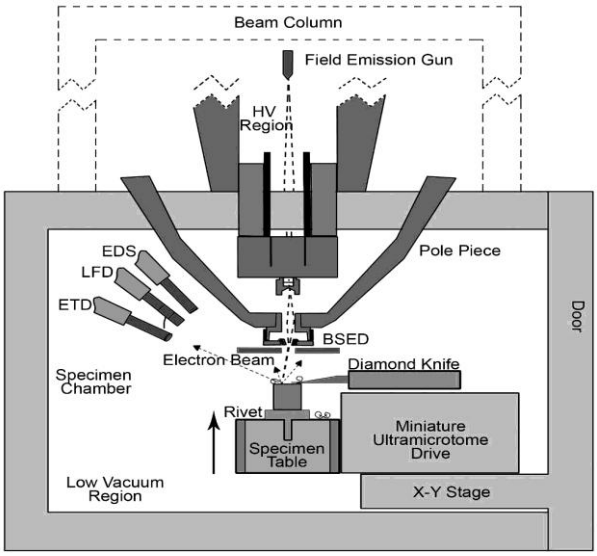

Figure 1. Schematic of the serial block-face scanning electron microscope (SBEM). Here an ultramicrotome is built into a scanning electron microscope. Several signals can be used for imaging. BSED: backscattered electron detector; ETD: Everhart Thornley detector, SE-detector of the high vacuum mode; LFD: large field detector, SE-detector of the low vacuum mode; EDS: detector for energy dispersive x-ray spectroscopy (reproduced from [2]).

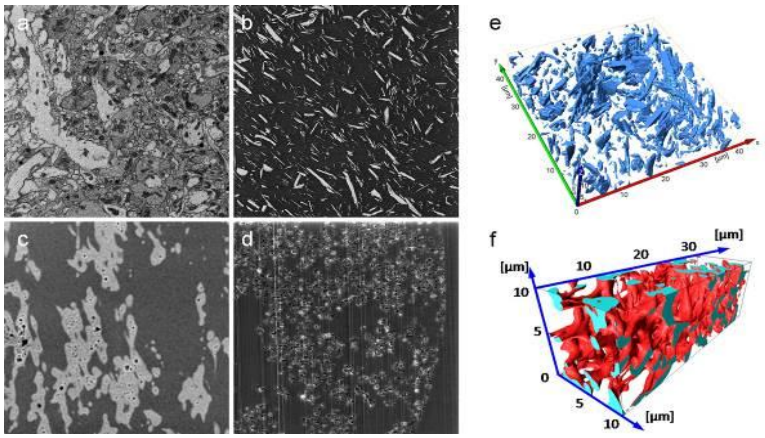

Figure 2. a: Block-face of a neuronal tissue prepared with typical TEM protocol (BSE image); b: Block-face of a talcum filled polypropylene specimen (BSE image); c: Block-face of a polyethersulfone membrane embedded in resin (BSE image); d: Block-face of a hyper-cross-linked poly(styrene−divinylbenzene) monolith embedded in resin (SE image; image widths a: 19 µm b: 76 µm c: 40 µm d: 30 µm); e: 3D reconstruction of a polypropylene sample filled with 20 percent talcum; f: 3D reconstruction of a polyethersulfone membrane.

3D in SEM, (S)TEM, Ion Imaging, incl. FIB-SEM and SBF-SEM

MIM.1.P011
Examples of application an electron-ion scanning microscopy for research biological, quantum and solid-state materials in different areas of science and technology

Y. Anufriev[1,2], V. Galkov[1], A. Dudin[2], E. Eganova[2]

[1]JSC Nanopromimport, Moscow, Russian Federation
[2]Moscow State University, Faculty of Physics, Moscow, Russian Federation

hf_hf@newmail.ru

Recently, research techniques development in various fields of science leads to use the scanning electron microscopy. Although that this type of research provides detailed information about the surface morphology and material composition, single-beam systems loose to the functional capabilities of Dual-beam microscopes. The main problem of modern scanning electron microscopy is the incompatibility of some techniques and research facilities.

This article discusses the adaptation of scanning electron-ion microscopy for different objects of study. Provided results of work performed at the Physics Department of Moscow State University using a Quanta 3D FEG FEI workstation.

Originally, electron microscopy allowed to study only highly conducting metal or semiconductor materials at high energies of the primary beam. Modern electron microscopes allow us to investigate the dielectric and biological materials, as in a high vacuum, and in the natural environment mode (Figure 1,2). Choosing the right mode and method, you can minimize the damage to the sample surface to give the maximum information. For these purposes, the cryosystem or dew point mode are used.

Well-known application of ion microscopy is researching and editing electronic semiconductor circuits. However, the capacity of the gas chemistry with the FIB allows prototyping and creating the semiconductor quantum structures (Figure 3,4). One of the advantages of such systems is the possibility of gradually removing material from a localized area, thus obtaining 3D reconstruction of the object of study as shown in Figure 5. Equipping microscope with electrical testing system (Figure 6) allows you to record real-time processes of change in the surface morphology as a function of the applied voltage and current, monitor emission processes in nanostructures. Separate mechanical manipulators mounted directly on the microscope table and manipulators installed in the free port of the camera allows high-precision movement of micro-objects across the surface or to transfer them to the grid for analysis. In addition, the sharing of a scanning electron microscope and microprobe enhances diagnostic modern integrated devices. The opportunity to research nanostructures audit methodology current induced by the electron beam. Also, this technique allows you to search defects in the tracks of live circuits without thermal heating. The proposed research technique using nano-analytical equipment based on the precision of electron-ion scanning microscopy allow the study of almost any object of interest of modern nanotechnology.

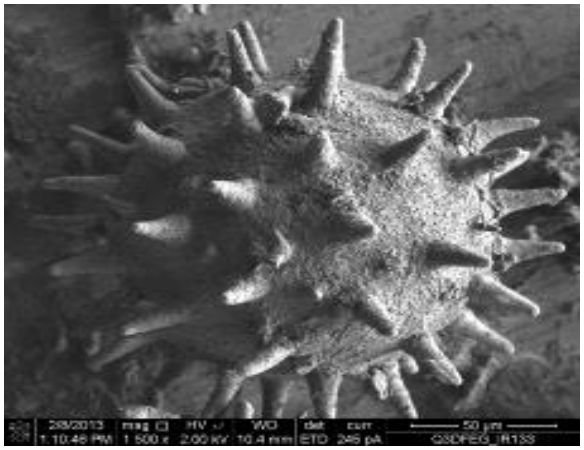

Figure 1. Tea rose pollen.

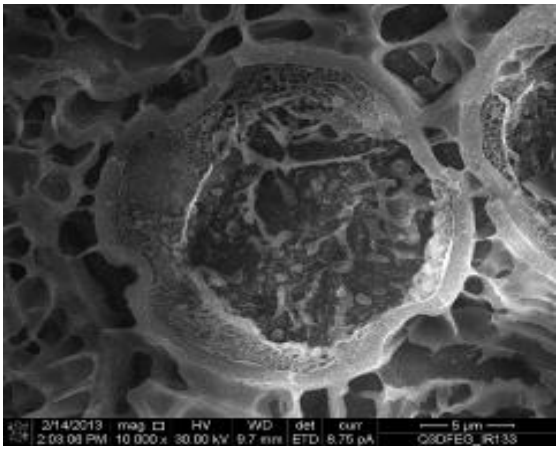

Figure 2. Fractured tobacco pollen cell.

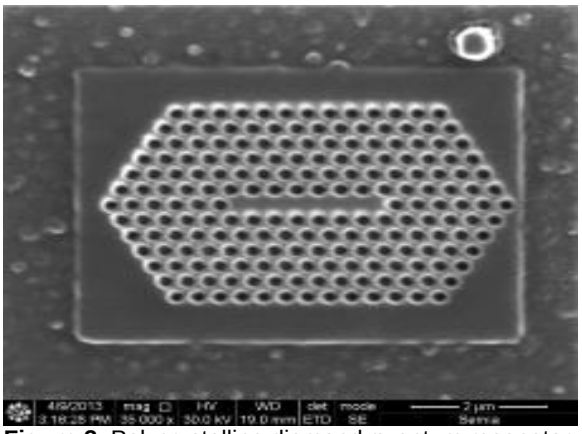

Figure 3. Polycrystalline diamond quantum resonator.

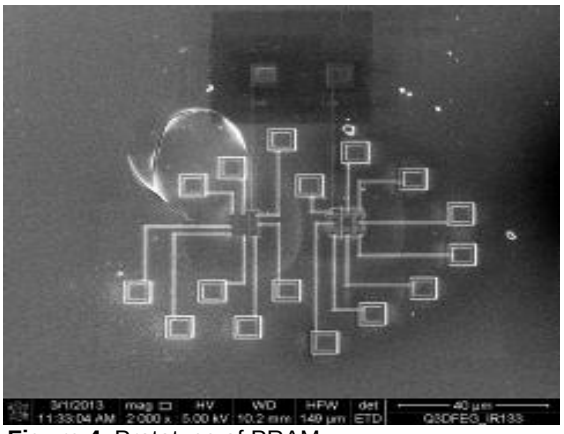

Figure 4. Prototype of PRAM.

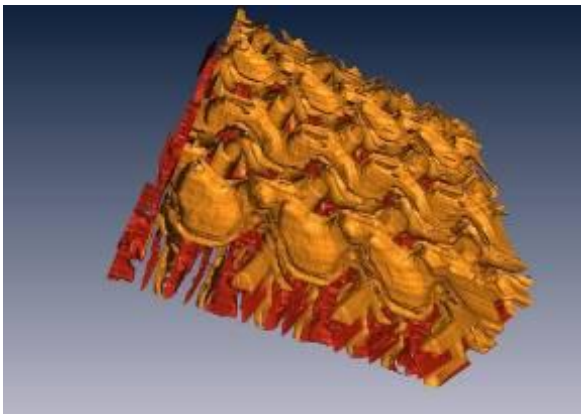

Figure 5. 3D reconstruction of microchip sample.

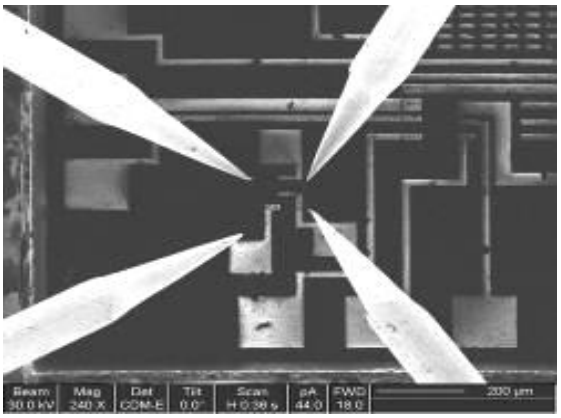

Figure 6. The process observation of contacting probes installed in the chamber.

3D in SEM, (S)TEM, Ion Imaging, incl. FIB-SEM and SBF-SEM

MIM.1.P012
3-dimenstional Processing and Imaging of Gold and Platinum Nanostructures with a SEM

M.M. Shawrav[1], H. Wanzenböck[1], D. Belic[1], M. Gavagnin[1], E. Bertagnolli[1]
[1]Vienna University of Technology, Institute of Solid State Electronics, Vienna, Austria

mostafa.shawrav@tuwien.ac.at

Nanofabrication techniques play an important role for numerous advanced applications. Controlling the atmosphere in a Scanning Electron Microscope (SEM) allows to perform dynamic experiments on the micro- and nanoscale including chemical reactions such as the focused electron beam induced deposition (FEBID). Direct write lithography technique produced by FEBID offers important benefits over classical resist based process. It is possible to deposit metals and dielectrics in situ with a single process step. This mask-free and resist-free technique has gained popularity due to its nanometer precision of material deposition [1,2].

FEBID is also a potential candidate for 2D and 3D Noble Metal nanostructures. 3D imaging with a SEM allows also investigation of physico-chemical properties as well as morphology of the fabricated micro- and nanostructures and facilitates to correlate between the microstructure of a material, its composition and its mechanical and electrical behaviour.

This work represents nano deposition of different noble metals with lateral feature size under 50nm. Different shapes of gold and platinum structures including nanopillars, nanospirals and nanosquares have been grown with different acceleration voltage ranging from 1KV to 20 KV.

The fundamental growth process of direct-write deposition has been imaged during different growth phases. The impact of process parameters (such as dwell time, refresh time, beam current, substrate temperature, precursor temperature) on the geometry and the chemical composition have been investigated. Approaches towards high purity depositions are discussed. Composition of Nanostuctures have been probed by the Energy Dispersive X-ray Spectroscopy (EDX).

Novel applications of patterned structures for electronic devices, photonic components and MEMS can be quickly realized by this technique. Potential applications of this rapid pattern fabrication process for nanoscale electronic devices and for photonic, magnetic or biofunctional structures are discussed in this work. Structural and morphological properties of the deposited structures have been investigated by High Resolution Transmission Electron Microscopy (HR-TEM).

With this work we have successfully demonstrated that SEM is a versatile tool for fabricating 3D structures on the nanoscale and is as well inevitable helpers for 3D analysis of these structures. The presented method is capable of mix-and-match fabrication of nanodevices which makes it attractive for a multitude of applications.

1. I. Utke, P. Hoffmann, and John Melngilis, J. Vac. Sci. Technol. B 26 (2008), 1197.
2. G. Hochleitner, M. Steinmair, A. Lugstein, P. Roediger, H. Wanzenboeck and E. Bertagnolli, Nanotechnology 22 (2011).
3. We kindly acknowledge European Community's Seventh Framework Programme (FP7/2007-2013) under grant agreement number ENHANCE-238409.
We kindly acknowledge the support of Center for Micro- and Nanostructures at Vienna University of Technology.

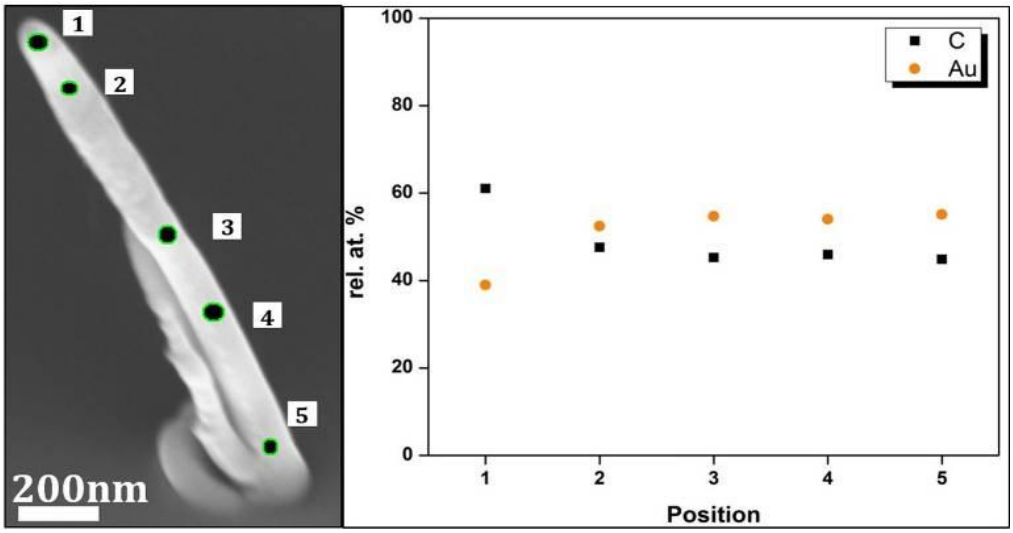

Figure 1. Gold nanopillars fabricated by FEBID and EDX analysis which shows the purity of the gold content.

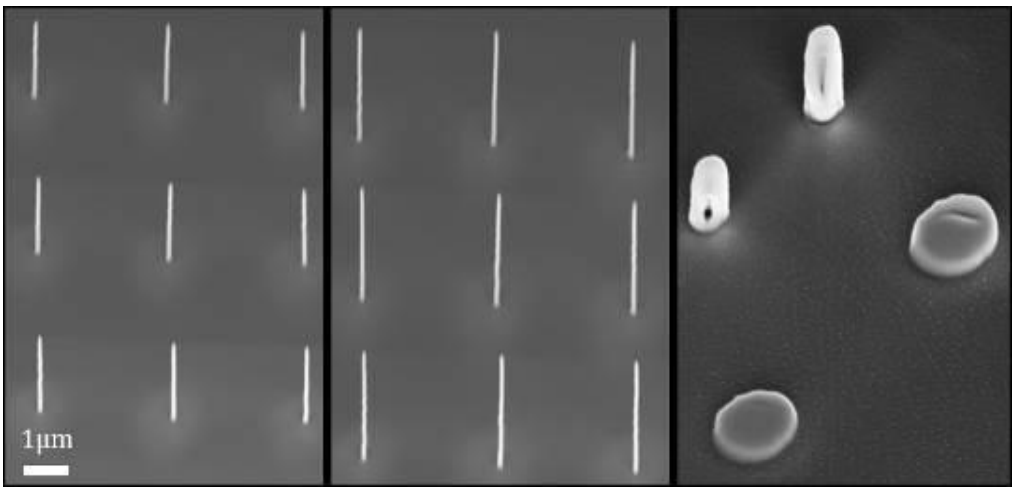

Figure 2. Platinum nanopillars deposited by FEBID for 30 sec, 60 sec and defocusing.

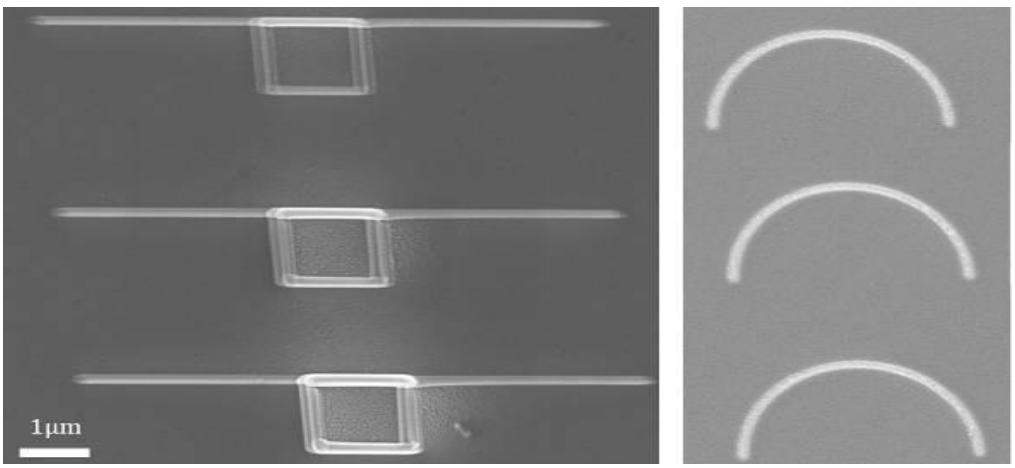

Figure 3. Different shapes of gold nanostructures deposited by FEBID.

3D in SEM, (S)TEM, Ion Imaging, incl. FIB-SEM and SBF-SEM

MIM.1.P013
Comparison of biofilm formation of mixed yeast/bacterial cultures by FIB-SEM tomography

K. Dobranska[1], J. Nebesarova[2], F. Ruzicka[3], J. Dluhos[4], O. Samek[1], V. Krzyzanek[1]

[1]ISI ASCR, Brno, Czech Republic
[2]Biology center of the ASCR, Ceske Budejovice, Czech Republic
[3]St. Anne´s hospital, Brno, Czech Republic
[4]Tescan, Brno, Czech Republic

dobranska@isibrno.cz
Keywords: biofilm, mixed yeast/bacteria cultures, FIB-SEM

Yeasts and bacteria are considered as microscopic organisms. We focus our research on microbial strains, namely on yeast *Candida albicans* and bacteria *Staphylococcus epidermidis*, which are widely studied organisms in many medical and microbiological laboratories. These studies are of high interest because microbes can cause serious complications associated with infections after surgery attacks, although they are a part of normal microflora of human body in physiological conditions.

The complications start with the uncontrolled growth of biofilm. Because besides the planktonic way of living, microbes are able to adhere to surfaces or interfaces and to form organized communities. These communities are covered by extracellular polymer matrix composed mostly of polysaccharides, that structure creates so-called biofilm. In medicine the biofilm formation allows microorganisms to colonize the surface of implants and it also protects the microbial cells from attacks by the immunity system as well as from the effect of antibiotics. Therefore, the biofilm is considered to be important virulence factor. The characteristic features of the biofilm infections, especially high resistance to antifungal agents could complicate therapy [1]. The structure of the biofilm layer and proportion and composition of extracellular matrix differs by type of organism and environmental conditions - where bacterial/yeast cultures are evolving and growing. Knowledge of the biofilm structure can contribute to understanding the biofilm formation and basic biochemical mechanisms underlying this process. It may help to develop more efficient treatment strategy for biofilm infection.

Yeast like *Candida albicans* and bacteria *Staphylococcus epidermidis* have been recently recognized as an important cause of serious biofilm infections associated with implanted medical devices. In our experiments the multi-layered biofilms formed by these microorganisms were investigated by Focused Ion Beam Scanning Electron Microscope (FIB-SEM) tomography that allows the 3D reconstruction of large volumes with high resolution.

Here we present comparison of two mixed yeast-bacterial cultures grown on sapphire disks. The first sample contains one-day cultivation of *C. albicans* followed by additional one-day cultivation of bacteria *S. epidermidis* on the same disk (two-steps cultivation) [Fig 1]. The second sample represents a two-day cultivation of mixture of the two above mentioned microbes [Fig 2]. After the cultivation sample preparation for FIB-SEM investigations was performed to preserve the biofilm with its extracellular polymer substance which is very soft and sensitive. Both samples were fixed by high pressure freezing (HPF Leica EM Pact II), followed by freeze-substitution procedure (Leica EM AFS). To increase the contrast in BSE imaging samples were stained with an osmium-thiocarbohydrazide-osmium (OTO) method. The preparation procedure was finished by embedding into Epon resin.

A focused ion beam technique was used for both precise cross section preparations as well as for FIB-SEM tomographical acquisition of 3D dataset using the signal of backscattered electrons (BSE) [3]. The microscope LYRA 3 FIB-SEM (Tescan, Czech Republic) was used in our experiments. The resulting 3D reconstruction was processed with the software ORS visual.

Our results show that the FIB-SEM tomography is suitable method for structural investigation of microbial biofilms. We present that final 3D reconstructions well demonstrate the disparity between above mentioned mixed microbial cultures. In the first sample with the two-step cultivation, separated colonies of yeast-bacteria are clearly visible. On the other hand, the second sample which contains the mixture shows quite uniform structure without visible separation. We believe that the described methodology of biofilm preparation combined with FIB-SEM tomography will be helpful in clinical research of microbial infection.

1. R. M. Donlan and J. W. Costerton, Clin. Microbiol. Rev. 15 (2002), p. 167.
2. K. Dobranska in “Characterisation of bacterial/yeast biofilms by scanning electron microscopy”, et al., (EMC 2012 Proceedings, Manchester) (2012), p. 671.
3. M. Zadražil in “The Step Towards an Ultimate Multifunctional Tool for Nanotechnology” et al., (3M Nano 2012 Proceedings, X'ien) (2012), p. 175
4. The authors acknowledge the support for VK and KD by the grant CZ.1.07/2.3.00/20.0103 (EC and MEYS CR). FR was supported by GACR (project P205/11/1687).

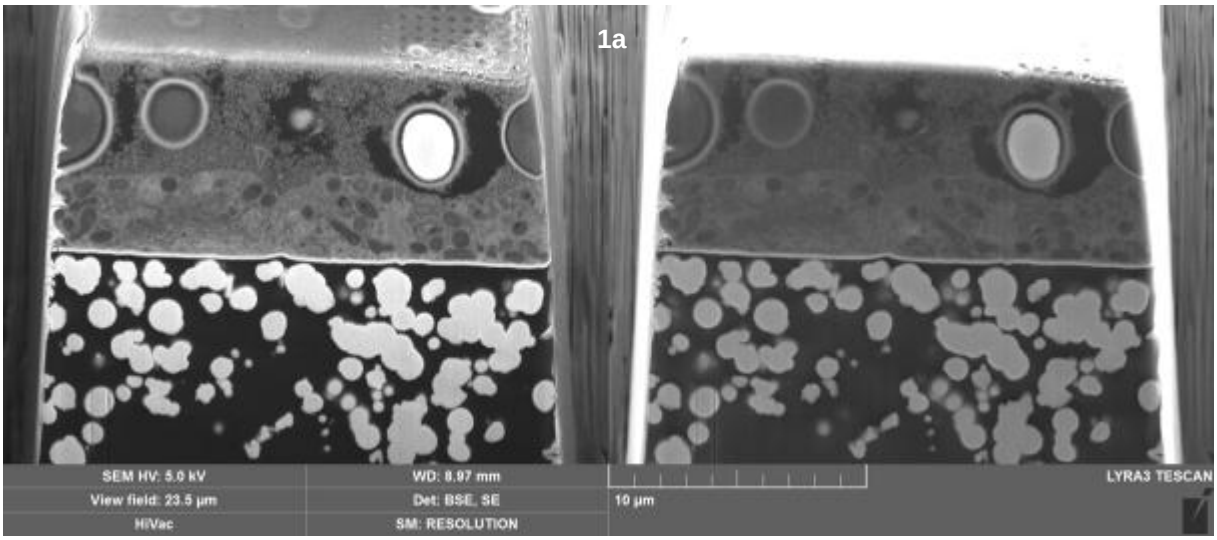

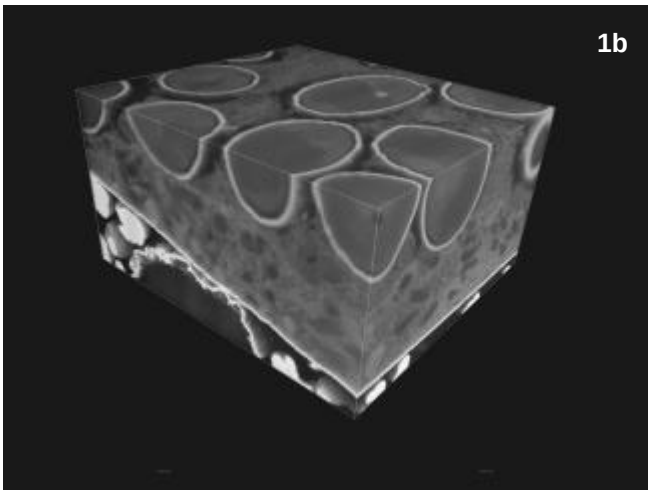

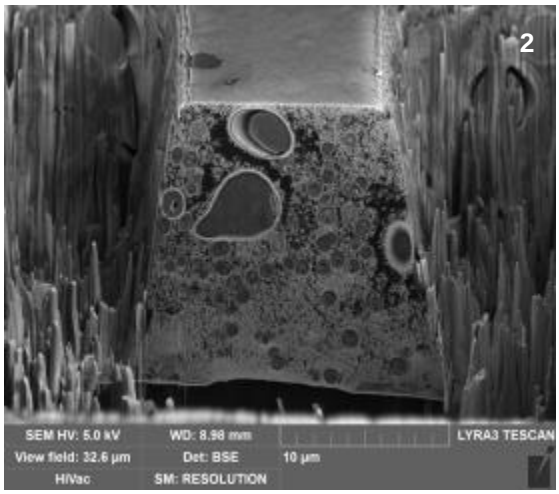

Figure 1a. Back-scattered electron (BSE) and secondary electron (SE) image of the two-steps cultivation of the two microbes culture.

Figure 1b. 3D reconstruction (FIB-SEM tomography) of the two-steps cultivation.

Figure 2. BSE image of two-day cultivation of the mixture *C. albicans* and *S. epidermidis.*

3D in SEM, (S)TEM, Ion Imaging, incl. FIB-SEM and SBF-SEM

MIM.1.P014
A 3D TEM study supported by EELS chemical analysis of the catalytic cutting process of few-layer graphene

G. Melinte[1], I. Florea[1], O. Ersen[1], R. Arenal[2], I. Janowska[3], S. Begin-Colin[1], W. Baaziz[3], C. Pham-Huu[3]

[1]IPCMS, UMR 7504 CNRS-Université de Strasbourg (UdS), Strasbourg, France
[2]LMA, Instituto de Nanociencia de Aragon (INA), Universidad de Zaragoza,, Zaragoza, Spain
[3]LMSPC, UMR 7515 CNRS-Université de Strasbourg (UdS), Strasbourg, France

georgian.melinte@ipcms.u-strasbg.fr
Keywords: 3D TEM, EELS mapping, few-layer graphene

During the last decade, considerable attention has been devoted to the development of new methods for the preparation of graphene and few-layer graphene (FLG) nanostructures, as well as to their subsequent use in applications [1, 2]. They are characterized by several exceptional physical and chemical properties, such as high electrical and thermal conductivity or mechanical strength. In addition, they possess high specific surface area and a controlled surface chemistry, parameters essential for their potential use as support in catalysis [3]. We have recently developed a synthesis method for the production of large amounts of FLGs from expanded graphite aggregates immersed in a solution containing a surfactant, the whole being then placed in an ultrasonic bath. The as-synthesized FLGs could be then decorated with various nanometric structures such as metal or iron oxide nanoparticles. It has been shown that FLG surface has strong interactions with nanoparticles, inducing thus a relatively high stability even after annealing at high temperatures.

In the case of iron-based nanoparticles deposited on FLGs, a treatment in hydrogen can be used to activate the catalytic effect of iron with respect to carbon. The result is a nanostructuring process of the FLG layers by the creation of geometrical trenches, with well-defined depths, widths and crystallographic orientations. To characterize the catalytic cutting process and determine the characteristics of the as-obtained nanostructure, we used an analysis approach combining high resolution electron microscopy with electron tomography and EELS spectroscopy. The current cutting conditions (temperature, H2 pressure) seems to favor the metallic iron nanoparticles relative to iron oxide ones. The influence of the size, morphology, chemical composition and initial positions of the nanoparticles on the cutting process was investigated.

1. M. Choucair, P. Thordarson, J.A. Stride, Nat Nanotechnol 4 (2009) p.30–3.
2. I. Janowska, M. S. Moldovan, O. Ersen, H. Bulou, K. Chizari, M. J. Ledoux, C. Pham-Huu, Nano Res. 4(5) (2011), p. 511–21.
3. S. Park, R. S. Ruoff, Nat Nanotechnology 5 (2009), p. 217-24.

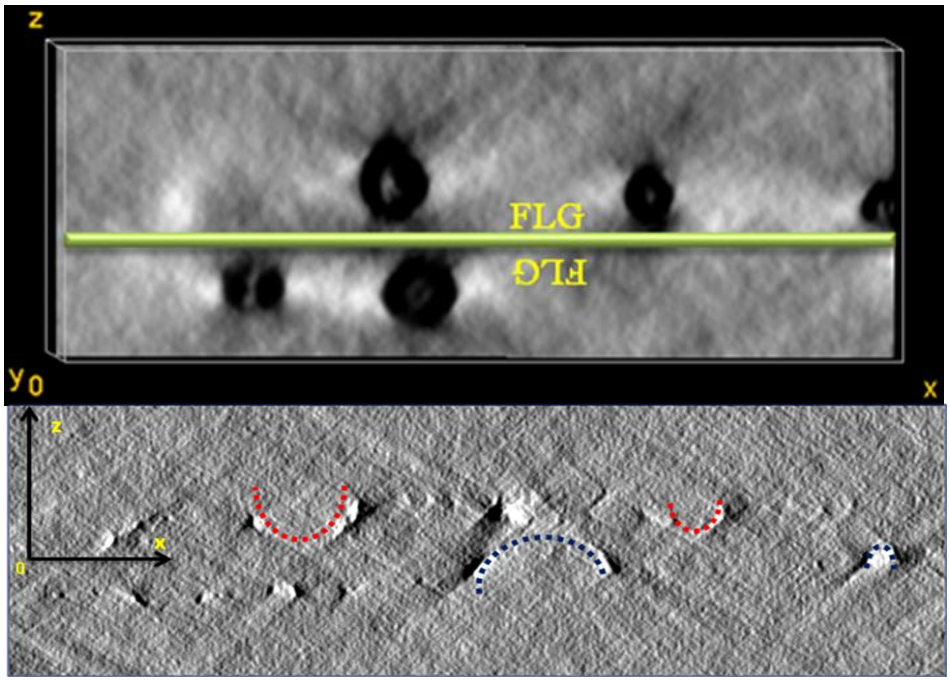

Figure 1. Longitudinal slices through the reconstructed volume showing NPs (a) and tranches (b) located on both sides of the FLG sheets.
XZ slices through a reconstructed volume; Georgian Melinte

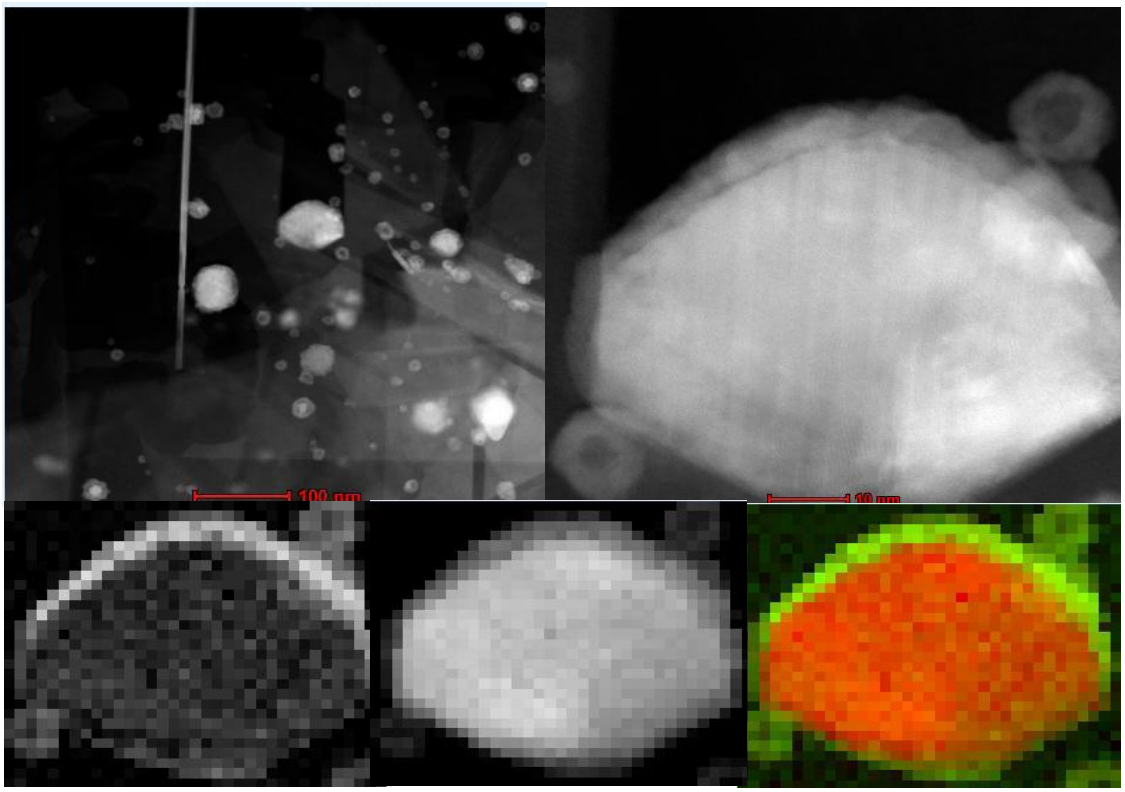

Figure 2. EELS chemical mapping of a catalytically active iron-based NP showing that the metal part is always the leading part in the cutting process.
STEM EELS mapping; Raul Arenal

3D in SEM, (S)TEM, Ion Imaging, incl. FIB-SEM and SBF-SEM

MIM.1.P015
Practical Aspects of 3D Crystalline Defect Analysis for Engineering Materials using Scanning Transmission Electron Microscopy

L. Agudo Jácome[1,2]

[1]Bundesanstalt für Materialforschung und -prüfung, Abteilung für Werkstofftechnik, Berlin, Germany
[2] Ruhr-Universität Bochum, Institut für Werkstoffe, Bochum, Germany

leonardo.agudo@bam.de
Keywords: dislocations, scanning transmission electron microscopy (STEM), high angle annular darkfield detector (HAADF), stereography

Structural and functional engineering materials under thermal, mechanical or thermomechanical service conditions suffer from microstructural degradation which is due to crystalline defects such as dislocations. Since the introduction of the transmission electron microscope (TEM), diffraction contrast has been implemented in conventional (C)TEM to image and analyze crystalline defects, based on the effect of the displacement vector R, characteristic for crystalline defects. Nevertheless, when applying diffraction contrast in conventional (C)TEM by setting proper two-beam conditions, the presence of strong phase contrast artefacts such as bending, thickness and extinction contours often hinders proper observation of highly defected material volumes. Although already in the 1970s it was proven that diffraction contrast using scanning (S)TEM helps eliminating these artefacts [1-3], only in the past few years STEM has started to gain intensive application in this field, thanks to the accessibility of field emission gun (FEG) TEMs and the development of more efficient STEM detectors. These allow for an increased signal-to-noise ratio (comparable to CTEM imaging) and larger and more flexible divergence angle tolerances. Thus, interest in STEM diffraction contrast imaging has been increasing in recent years in the field of defect analysis [4-6]. At the EC2009, a first approach on using multibeam contrast and stereomicrocopy in STEM mode to facilitate quantitative evaluation of three-dimensional (3D) dislocation structures was introduced [7]. In the present contribution practical aspects to be considered when applying the aforementioned TEM techniques, e.g., the effect of camera length, of the depth of focus and of surface effects on STEM stereomicroscopy are discussed. Finally differences arising from using different microscopes with similar equipment are highlighted.

The applicability of STEM stereo-imaging is mostly shown here on TEM-foils of a single crystalline Ni-based superalloy subjected to creep deformation. Under creep conditions, dislocations in different regions of the microstructure, i. e., in the matrix phase (γ), in the ordered precipitate (γ') and between γ/γ' interfaces. The effect of surface damage on 3D appearance in stereograms is shown by preparing the electron transparent TEM foils by different conventional techniques. TEM was performed on two analytical FEG-TEMs with similar characteristics operating at 200kV: a TECNAI F20 S-Twin and a Jeol 2200FS. STEM images were acquired with the high angle annular dark field (HAADF) detector in both TEMs with optimized illumination conditions.

By acquiring a diffraction contrast stereo-pair in STEM, the absence of bending contours, thickness contours and extinction contours enables a clear 3D impression of regions of up to 40 μm^2. In Figure 1, three material examples are provided, which demonstrate this possibility. Another particular feature of STEM imaging has to do with the depth of field, which is considerably reduced compared to CTEM at a similar magnification. To illustrate the consequence of a reduced depth o field, Figure 2a shows a stereogram that appears focused only in its central region. The depth of field in this case is of ~250 nm and the TEM foil has a similar thickness at the imaged region. Nevertheless, in order to obtain the two-beam condition for both micrographs of the stereogram, the sample had to be tilted strongly by using both the eucentric tilt axis and its orthogonal tilt axis. Consequently, if one focuses the center of the image for both tilt positions of the stereogram, the inclination of the specimen will cause an increasing defocus towards the sides of each of the micrographs of the stereogram, leading to the blurred appearance outside the central area of Figure 2a. Nevertheless, this effect may be corrected by simultaneously varying the focus height while each of the images of the stereogram is acquired, resulting in a stereogram such as that in Figure 2b.

1. D.M. Maher and D.C. Joy, Ultramicoscopy 1 (1976) p. 239.
2. C.J. Humphreys, Ultramicroscopy 7 (1981) p. 7
3. T. Yamamoto and H. Nishizawa, Physica Status Solidi A 28 (1975) p. 237.
4. J. Pešička, A. Aghajani, Ch. Somsen, A. Hartmaier and G. Eggeler, Scr. Mater. 62 (2010) p. 353.
5. P.J. Phillips, M.C.Brandes, M.J. Mills and M. DeGraef, Ultramicroscopy 111 (2011) p. 1483.
6. L. Agudo Jácome, G. Eggeler, A. Dlouhý, Ultramicroscopy 122 (2012) p. 48.
7. L. Agudo Jácome, Ch. Somsen, and G. Eggeler, in MC2009, eds. W. Grogger, F. Hofer and P. Pölt, (Verlag der TU Graz, Graz) (2009), p. 201.

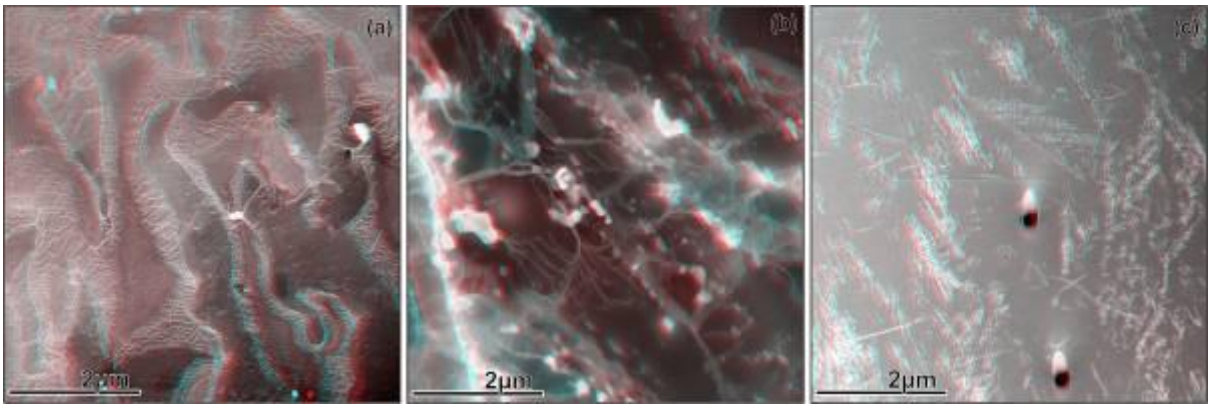

Figure 1. 3D stereograms of the microstructures of (a) a single crystal Ni-base super alloy after creep. **g** = (111), (b) a tempered martensite ferritic steel after creep. **g** = (200), (c) the B2 phase (austenite) of a NiTi shape memory alloy after 5 transformation cycles; **g** = (200)..

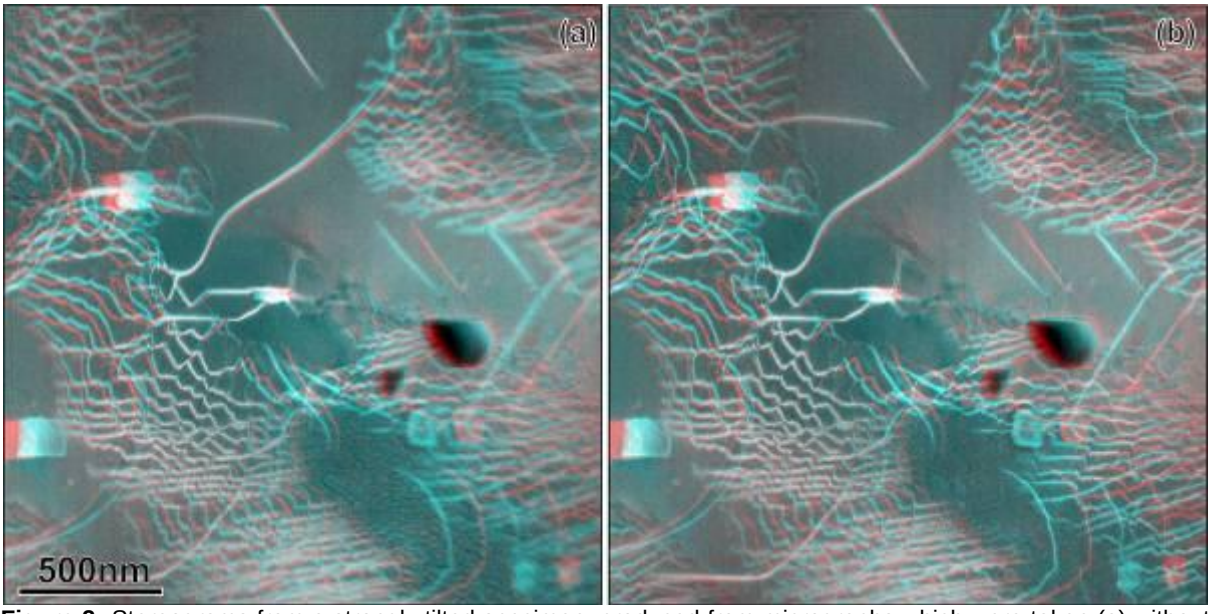

Figure 2. Stereograms from a strongly tilted specimen, produced from micrographs which were taken (a) without focus correction and (b) with dynamic focus correction. **g** = (111)..

3D in SEM, (S)TEM, Ion Imaging, incl. FIB-SEM and SBF-SEM

MIM.1.P016
Focused Ion Beam Tomography as a versatile tool in basic biomedical research

C. Wigge[1], D. Akemeier[2], A. Hütten[2], A. Frangakis[1]

[1]Buchmann Institute for Molecular Life Science, Frankfut, Germany
[2]Thin Films and Nanostructres, Physics, Bielefeld, Germany

wigge@biophysik.org

In mammals urine is filtered from the blood circulation in the kidney. The primary filtrate is formed in the glomerulus that is surrounded by Bowmans space and enclosed by Bowmans capsule. In the glomerulus the primary filtrate is formed by ultrafiltration across the glomerular filtration barrier, which consists of a fenestrated endothelium, the basement membrane and the slit diaphragm between the podocyte feet processes [1]. Alterations in the structure and morphology of this delicate structures as well as changes in their number and size have been associated with renal and systemic diseases [2].

Up to now different imaging approaches were used to analzye and reconstruct renal tissue like magnetic resonance imaging (MRI) or light and electron microscopy (EM). The combination of different imaging techniques is necessary to cover the range of scales from whole organ to macromolecular ultrastructure. However, each technique suffers from limitations e.g. MRI from the low resolution and e.g. electron microscopy from the susceptibility to artifacts and from the low volume imaging capability.

The method of sequentially milling a resin embedded biological structure with a focused ion beam (FIB) and imaging the emerging surface with a scanning electron microscope (SEM) has several advantages in biomedical research compared to the methods mentioned before. Larger volumes (> 10 μm^3) of interesting structures than in serial sectioning EM can be visualized with large fields of view (100 x 100 µm) obtaining SEM resolution.

In this study we applied focused ion beam (FIB) tomography to visualize the 3D cellular architecture of stained and resin embedded wild type mouse glomerulus. We reconstructed a large volume (40% of a complete glomerulus) from renal tissue with 100 nm resolution and a smaller part of the filtration barrier with a 6.4 fold higher magnification and 20 nm resolution. We visualized the structure and the interface between podocytes and capillaries inside the wild type mouse glomerulus. Podocytes that were in direct contact with capillaries formed a cavity between the cell body and the vessel as well as cellular extensions between distant podocytes. Furthermore, we performed direct measurements of surface area, volume and number of podocytes inside the glomerulus.

The unique volume and resolution range of FIB/SEM tomography offers the possibility to visualize and further analyze multicellular systems of high medical relevance (kidney), which are inacessible by other imaging techniques like micro comuputer tomography (CT) due to lower resolution and transmission electron microscopy (TEM) due to volume constraints.

1. Neal, C.R. et al. Journal of the American Society of Nephrology:JASN, 16(5) (2005)
2. Beeman, S.C. et al. American Journal of Physiology. Renal Physiology, 300(6) (2011)

3D in SEM, (S)TEM, Ion Imaging, incl. FIB-SEM and SBF-SEM

MIM.1.P017
Focused ion beam ablation tomography

C. Parmenter[1], T. Wang[2], K. Webb[3]

[1]University of Nottingham, Nottingham Nanotechnology and Nanoscience Centre, Nottingham, United Kingdom
[2]University College London, Dept Medical Physics, London, United Kingdom
[3]University of Nottingham, Institute of Biophysics, Imaging and Optical Science, Nottingham, United Kingdom

Christopher.parmenter@nottingham.ac.uk
Keywords: Cryogenic, Focussed Ion Beam, ImageJ, Tomography

Addition of a second beam (Focused Ion Beam or FIB), of accelerated gallium ions to a scanning electron microscope (SEM), it is possible to remove layers of material and see beneath the surface. If performed at cryogenic temperatures (-150°C) the technique is known as cryogenic-FIB-SEM (Cryo-FIB-SEM).

During Cryo-FIB-milling, it was noted that some areas of cells were removed more rapidly by the beam than others (Fig 1), which resulted in columns of material forming on the cut-face, an artefact know as curtaining [1]. It was postulated that the difference in resistance to the path of the ions was responsible for the curtaining, the minimization of which has previously been addressed [2,3].

Our idea was to use this difference in susceptibility, often perceived as a weakness of Cryo-FIB-SEM, to obtain information about 3D structures inside biological samples. By imaging the cut face of the sample between sweeps of the ion beam, features created by the differential ablation rate within the sample were plotted and the material removed per sweep calculated as an ablation vector. By pooling these values for a 3D data set it was hoped that internal structures of differing susceptibility to the ion beam would be revealed. To aid with image processing, a software analysis plug-in was developed for ImageJ, an open-source image analysis package, to extract and reconstruct ablation susceptibility values as 3D datasets. Several cell types (cardiac, fibroblast, retinal epithelial cells) were prepared for Cryo-FIB, which provided a stack of images of the tissues. Protocols were adapted to include metal deposition (Pt and W) to enhance grounding and minimise artefacts. Cultured cells reacted heterogeneously, with delicate features appearing obvious to the human eye during milling, but which proved difficult to extract using automated image analysis. A semi-automated approach was chosen where the milled features were delineated manually before an automatic algorithm extracted susceptibility vectors and reconstructed the data set in 3D. Segmentation between “hard” and “soft” areas was thus obtained by differential susceptibility between these regions, effectively calculating an erosion rate along each column of the sample which represents susceptibility to erosion by the beam. Gradually stripping away layers of the sample away allowed us to build a picture in terms of its resistance to the ion beam (Fig 3). The method was applied to other samples including “woody” onion cells and “hard-soft” Diatoms from the University of Nottingham lake (Fig 2.). These creatures proved to be excellent imaging subjects as they are composed of biological material which incorporates a silicate structure which is hard with a soft cell inside. We were able to see a difference in the ion beam susceptibility and to reconstruct details of the Diatom bodies including internal anatomy. This investigation explored the potential of a novel tomographic imaging method to reveal 3D nanoscale information from biological samples. The potential of Focussed Ion Beam Ablation Microscopy (FIBAT) has been demonstrated in a range of samples and it is believed that the FIBAT method, used in combination with Confocal Microscopy or other 3D imaging modality, can be used to realise the 3D tomography of cells and supply a novel contrast mechanism which may provide information on internal nano-structure within a range of sample types. A number of technical considerations have been identified and work is ongoing to improve the technique. Further development of the methodology should allow this novel contrast mechanism to be exploited in imaging of a variety of samples.

1. D Drobne *et al.,* Microscopy Research and Technique, **70,** (2007), p. 895.
2. D. Stokes, M. Hayles, SPIE Conference Proceedings (2009) p 7378G1
3. Hayles *et al.*, Journal of Microscopy, **226** (2007), 263 – 269
4. The authors gratefully acknowledge funding from the Bridging the Gaps scheme at the University of Nottingham and their home institutions.

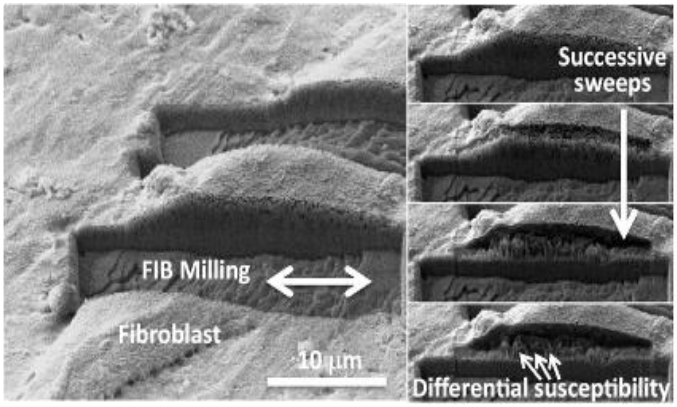

Figure 1. Human Osteoblast cells showing differential susceptibility with successive sweeps of the Ion Beam

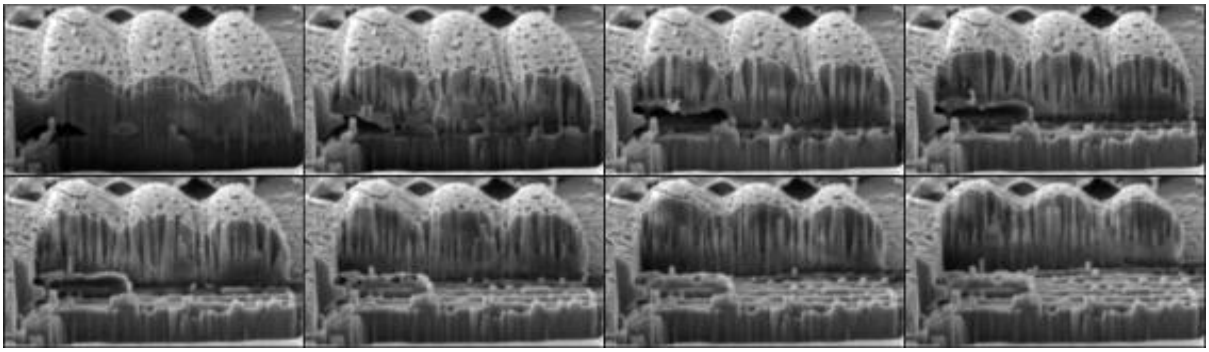

Figure 2. A selection of images through an entire cyanobacteria sourced from the University of Nottingham lake. The columns can be clearly seen; each is tracked and analyzed using the ImageJ plugin.

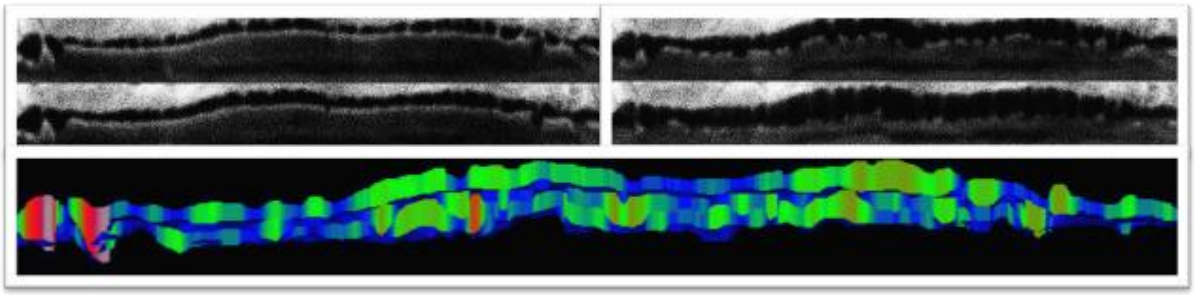

Figure 3. A series of images of T3T cells with the corresponding FIB Susceptibility plot. Red shows high susceptibility, blue shows more resistive material

3D in SEM, (S)TEM, Ion Imaging, incl. FIB-SEM and SBF-SEM

MIM.1.P018
New FIB design combines extremely high beam currents with nanometer precision possibilities

K. Fladischer[1], K. Schultheiss[1], C. Kübler[1], H. Doemer[1], R. Hill[2]

[1]Carl Zeiss Microscopy GmbH, Oberkochen, Germany
[2]Carl Zeiss Microscopy, LLC, Ion Microscopy Innovation Center, Peabody, United States

katrin.fladischer@zeiss.com
Keywords: focused ion beam, high current ablation, high resolution FIB

For more than thirty years FIB technology has revolutionized nanotechnological applications [1]. With the unique ability to combine both high-resolution imaging and flexible micromachining in one single platform, FIB opened completely new fields in science research as well as technological applications.

Due to the upcoming demand of larger material removal rates, new technologies have been developed which allow massive ablation, like a FIB based on plasma sources [2]. With the microscale virtual size of these sources, the application is however limited to rather coarse milling tasks and with that high resolution imaging or patterning processes are not possible. By using a Ga FIB machine combined with a microfocused pulsed laser it is possible to overcome this application gap and use the whole range from massive ablation until highest resolution [3], [4]. Nevertheless, the overall speed of the workflow using a combined laser and Ga FIB tool may be limited due to the maximum available ion current.

Up to now, commercially available Ga FIBs offer currents up to 50 nA at the most. For reaching higher current values without losing the resolution in the low current region beyond 1 pA it is indispensable to overcome several challenges in the electron-optical design. Working with low currents especially at low energies requires a minimal chromatic aberration of the lenses, yet the spherical aberration has to be minimized in order to achieve good beam profiles in the high-current region. Besides the aberrations of the lenses, also the ion interactions of the beam itself has to be considered [5] while optimizing the column design. To minimize these Coulomb effects it is necessary to optimize the aperture placements inside the column as well as the operating conditions.

In this work we present a new Ga FIB column with optimized design concerning all mentioned issues, which allows the full range of currents up to 100 nA and beam densities in excess of 70 nA/cm². Fig. 1 shows the calculated beam performance of the new column. The high-resolution performance is excellent and the smallest probe size could be experimentally measured to be 2.2 nm at 1 pA using a statistically averaged edge measurement [6].

The new column design provides six orders of magnitude of possible Ga currents and with this the full range of applications is covered (see Fig. 2). With the 100 nA option the process time of large material removals will be reduced by a factor of two compared to conventional Ga FIBs. The ultimate precision at the nanometer scale of the low currents is also available.

1. R.L. Seliger *et al*, Appl. Phys. Lett., 34 (1979), p. 310.
2. P. Tesch *et al*, EIPBN conference, Portland (2008).
3. R. Salzer *et al*, Microsc. Microanal. 18 (Suppl. 2) (2012), p. 636.
4. R. Rosenkranz *et al*, Imaging & Microscopy 1 (2012), p. 34.
5. P. Kruit and X.R: Jiang, J. Vac. Sci. Technol. B 14 (1996), p.3.

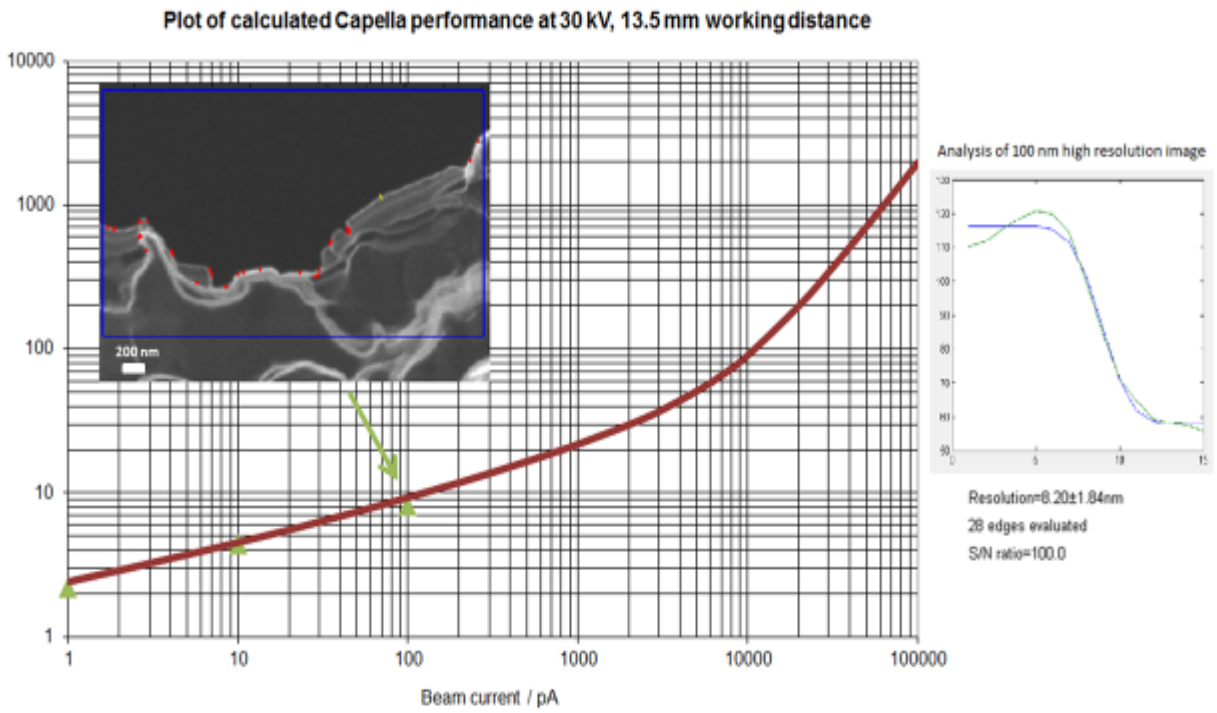

6. J. Orloff and L.Y. Roussel, Microsc. Microanal. 16 (Suppl. 2) (2010), p. 192.

Figure 1. The calculated probe size (r50) at a working distance of 13.5 mm and an ion energy of 30 kV is shown as the red curve. Measured resolution values are shown as green data points. The insert displays the measurement at 100 pA: The statistically averaged edge method [6] results in an r50 value of less than 8.2 nm.

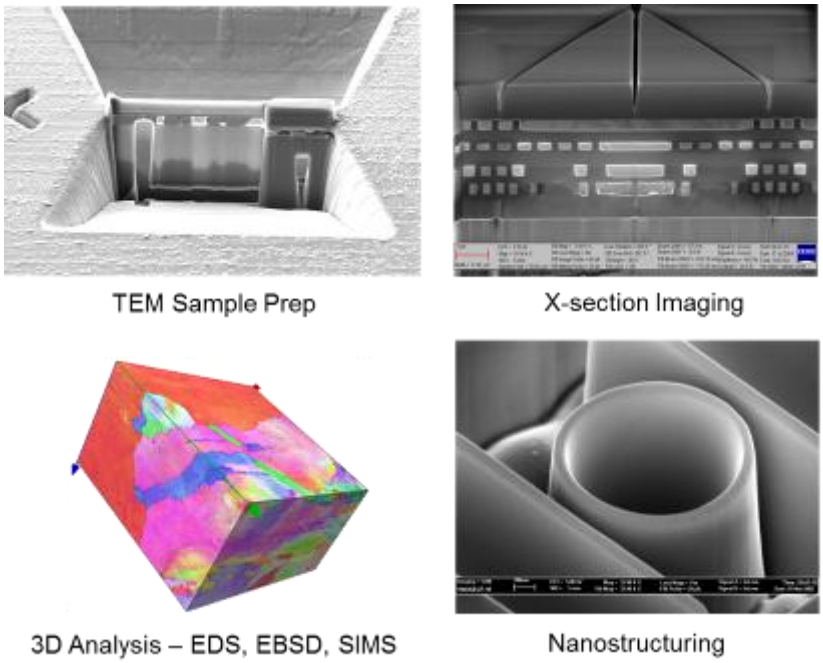

Figure 2. Applications such as (a) TEM sample preparation (b) preparation of cross-sections and (c) 3D analysis will greatly benefit from the increased current that is maximally available. At the same time no precision is lost and even delicate nanopatterning tasks may be performed (d).

Emerging Techniques in Modern Microscopies

MIM.2.020
STED nanoscopy of the living mouse brain

KI Willig, H Steffens, SW Hell – Max Planck Institute for Biophysical Chemistry, Goettingen, Germany

Confocal or two-photon microscopy are powerful techniques for imaging of structures inside living cells, tissue or living animals. However, they cannot show fine details or substructures of the cell because of their diffraction limited resolution of about half of the wavelength of light (~200-350nm). Recently, however, this limit has been overcome by a whole family of superresolution microscopy or nanoscopy concepts, including STED, RESOLFT, PALM, STORM and others[1]. These concepts are based on modulating the fluorescence emission such that adjacent labeled features fluoresce sequentially in time. The first technique to attain such diffraction-unlimited resolution was STED microscopy, which stands out for its recording speed and the ability to record 3D images from deep inside transparent specimens. Further, STED microscopy is live-cell compatible, especially when using fluorescent proteins.
It was shown that STED microscopy is capable to image dendritic spines up to 120 µm deep inside living organotypic brain slices and to resolve distinct distributions of actin inside dendrites and spines[2]. The basic function of spines is to interconnect with the neighboring cells by forming a synapse. It is therefore important to study them in a natural environment, which is ideally the living animal. We therefore developed an upright STED microscope to image the cerebral cortex of a living mouse through a glass window, so that we could observe the dynamics of dendritic spines in the molecular layer of the visual cortex[3]. The results show that STED nanoscopy is a highly suitable tool for neuroscience which can play a substantial role in the study of the living brain.

1. Hell, S.W., *Microscopy and its focal switch.* Nature Methods, 2009. 6(1): p. 24-32.
2. Urban, N.T., et al., *STED Nanoscopy of Actin Dynamics in Synapses Deep Inside Living Brain Slices.* Biophysical Journal, 2011. 101(5): p. 1277-84.
3. Berning, S., et al., *Nanoscopy in a living mouse brain.* Science 2012. 335(6068): p. 551.

Emerging Techniques in Modern Microscopies

MIM.2.021
Direct, spatial imaging of randomly large supermolecules by using parameter unlimited TIS imaging cycler microscopy

W. Schubert[1,2,3], A. Gieseler[1], R. Hillert[1], A. Krusche[1]

[1]Otto-von-Guericke University, Medical Faculty, Molecular Pattern Recognition Research Group, Magdeburg, Germany
[2]Chinese Academy of Science and Max Planck Society (CAS-MPG), Partner Institute for Computational Biology (PICB), Shanghai, Germany
[3]ToposNomos Ltd., Human TOPONOME project (HUTO), Munich, Germany

walter.schubert@med.ovgu.de
Keywords: TIS imaging cycler, supermolecules, functional superresolution, fluorescence microscopy, correlative microscopy

The recent development of parameter-unlimited functional super-resolution microscopy TIS™ (Toponome Imaging System) is based on the Imaging Cycler™ principle [1,2]. It provides direct access to protein networks of randomly large supermolecules at high 2D and 3D resolution in a single tissue section or inside cells, with many thousand distinct protein-complexes in one cell [1,2], as featured in Fig. 1 (cover stories). TIS™ is a device that can overcome both the spectral and the resolving power of conventional light microscopy without having to change hardware. It is the first ready-to-use Imaging Cycler™ technology for dimension- and parameter-unlimited histological diagnostics and systematic decoding of the toponome at functional super-resolution (toponome: defined as the spatial protein network code in morphologically intact cells and tissues providing direct access to the supramolecular order of biological systems). TIS™ is a highly flexible machine that can adapt to the needs of the researcher: a 4-in-one microscope including (1) routine transmitted light functions, (2) conventional epifluorescence functionalities, (3) paramater-unlimited protein network visualization in realtime and at relational stoichiometric resolution for at least 100 distinct molecules (approx. 40 nm resolution) (Fig. 2), and (4) functional super-resolution of subcellular structures and protein complexes in tissue sections, cultured or isolated cells at 3D (Fig. 3). It is a novel platform providing the robustness needed for the human toponome project, combining industry partners and research institutions. The technology has shown to solve key problems in cell-, tissue-, and clinical toponomics by directly decoding cellular (disease) mechanisms *in situ/in vivo*, in particular at the target sites of cancer in human tissue ([3-9] reviewed in [10]). Several next-generation toponome biomarkers and toponome drugs are on the way to clinic. The human toponome project has at its goal to unravel the complete toponome in all cell types and tissues in health and disease. The technology is scalable as large cooperative parallel screening devices extracting the most relevant disease targets from protein network hierarchies in situ: a novel efficient way to find selective drugs, by escaping the low content trap in current drug target and diagnostic marker discovery strategies, which, as yet, have disregarded the spatial topology of the protein network code.

1. Schubert W, Bonnekoh B, Pommer AJ, Philipsen L, Boeckelmann R, Malykh Y, Gollnick H, Friedenberger M, Bode M., Dress AW. Analyzing proteome topology and function by automated multidimensional fluorescence microscopy. Nature Biotechnology. 2006; 24(10): 1270 – 1278 (front cover story; Res highlight “Mapping togetherness” in Nature. 443, 609, 2006).
2. Friedenberger M, Bode M, Krusche A, Schubert W. Fluorescence detection of protein clusters in individual cells and tissue sections by using toponome imaging system (TIS): sample preparation and measuring procedures. Nature Protocols 2007;2(9):2285-94 (front cover story).
3. Schubert W. A three symbol code for organized proteomes based on cyclical imaging of protein locations. Cytometry A. 2007 Jun;71(6):352-60.
4. Schubert W, Friedenberger M, Bode M, Krusche A, Hillert R. Functional architecture of the cell nucleus: towards comprehensive toponome reference maps of apoptosis. Biochim Biophys Acta. 2008 Nov;1783(11):2080-8.
5. Bode M, Irmler M, Friedenberger M, May C, Jung K, Stephan C, Meyer HE, Lach C, Hillert R, Krusche A, Beckers J, Marcus K, Schubert W. Interlocking transcriptomics, proteomics and toponomics technologies for brain tissue analysis in murine hippocamapus. Proteomics. 2008 Mar;8(6):1170-8.
6. Schubert W, Gieseler A, Krusche A, Hillert R. Toponome mapping in prostate cancer: detection of 2000 protein clusters in a single tissue section and cell type specific annotation by using a three symbol code. J Proteome Res. 2009 Jun;8(6):2696-707.
7. Schubert W. On the origin of cell function encoded in the toponome J Biotechnol. 2010 Sep 15;149(4):252-9.
8. Bhattacharya S, Mathew G, Ruban E, Epstein DB, Krusche A, Hillert R, Schubert W, Khan M. Toponome imaging system: in situ protein network mapping in normal and cancerous colon from the same patient reveals more than five-thousand cancer specific protein clusters and their subcellular annotation by using a three symbol code. J Proteome Res. 2010 Dec 3;9(12):6112-25.

9. Schubert W, Gieseler A, Krusche A, Serocka P, Hillert R. Next-generation biomarkers based on 100-parameter functional super-resolution microscopy TIS. N Biotechnol. 2012 Jun 15;29(5):599-610.
10. Schubert W. Toponomics. In: Encyclopedia of Systems Biology. Dubitzky, W.; Wolkenhauer, O.; Yokota, H.; Cho, K.-H. (Eds.) Springer 2013, in press.

Editorials:

1. Murphy F. Putting proteins on a map. ***Nat Biotechnol.*** 2006 Oct;24(10):1223-4 (comment on ref 1, above)
2. Sage, L The molecular face of prostate cancer. ***J Proteome Res.***2009; 8, No 6, 2116 (editorial to ref 6, above)
3. Cottingham, K. Human Toponome Project. ***J Proteome Res.*** 2008; 7, No. 5, 1806. (editorial to invited lecture. HUPO world congress 2008)

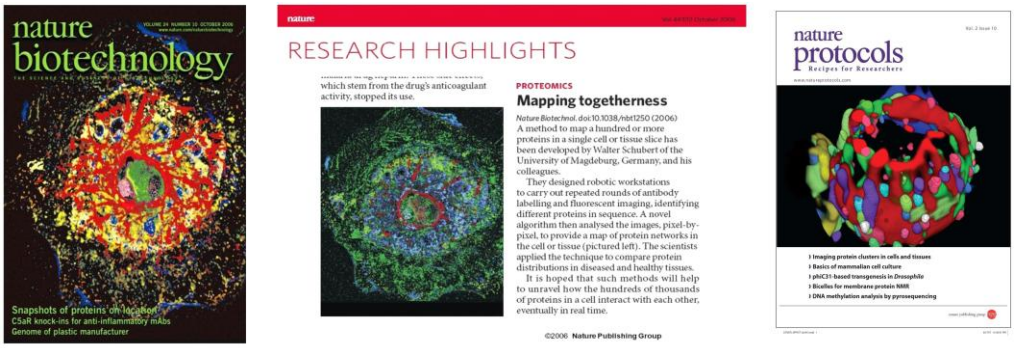

Figure 1. Featured Toponome maps: (a) Cover image from [1, above]: over 7,000 Protein clusters in a single human liver cell; (b) Corresponding Research Highlight referring to (a) (text of this highlight is found in Abbot A. Nature, 443, 609, 2006); (c) Cover image from [2, above] showing a cell surface protein cluster network of a single human peripheral blood T lymphocyte. Applications in real time at 20 – 40 nm resolution are shown on the web page of the human toponome (HUTO) project www.huto.toposnomos.com): the highest ever shown resolution of giant supermolecules at stoichiometric measures in real time in a tissue section using traditional fluorescence microscopy.

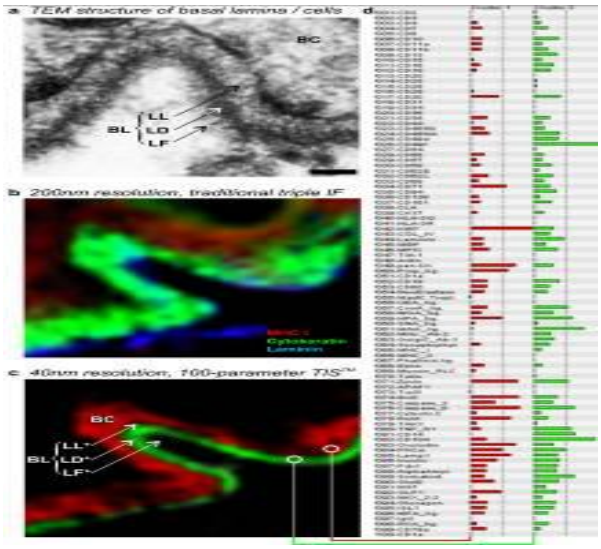

Figure 2. Detection of skin lamina densa as a giant supermolecule
(a) TEM micrograph of the dermoepithelial junction (b) traditional epifluorescence image of this area (c) TIS functional super-resolution image of this area in a human skin tissue section showing the relational stoichiometric molecular profiles of 100 distinct proteins and glyostructures captured by cyclical imaging at approx. 40 nm resolution (from Schubert et al, N Biotechnol. [9]) lamina lucida (LL), Lamina densa (LD, green profile) and lamina fibroreticularis (LF). Bar: 50nm (a)

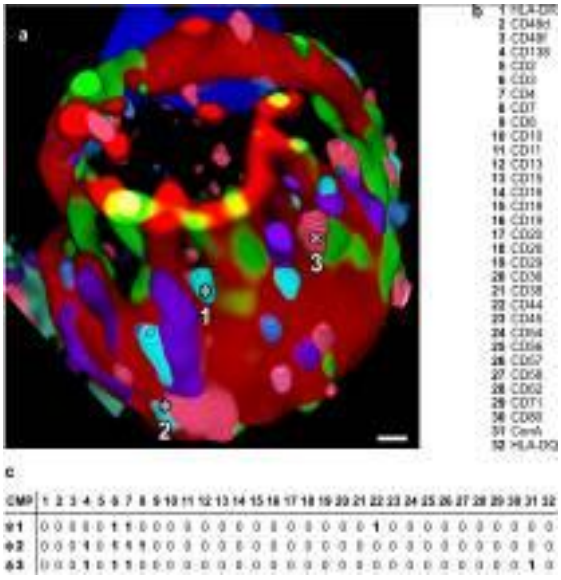

Figure 3. Cell Surface protein complexes (a) different spherical bodies formed by differential clustering of 27 distinct simultaneously mapped proteins (b) in a human blood T lymphocyte, from [2, 9]. (c) Note: CMP = protein com-plexes with colocation and anticolocation code (1/0). Bar: 1µm

Emerging Techniques in Modern Microscopies

MIM.2.022
Correction of the "Deterministic" Part of Space-Charge Interaction in Momentum Microscopy of Charged Particles

G. Schönhense[1], K. Medjanik[1], M. de Loos[2], B. van der Geer[2]

[1]Johannes Gutenberg-Universität Mainz, Institut für Physik, Mainz, Germany
[2]Pulsar Physics, BC Eindhoven, Netherlands

schoenhense@uni-mainz.de
Keywords: PEEM, momentum microscopy, space charge

Ultrahigh-brightness sources like (X-ray) free electron lasers (XFELs), but also table-top higher harmonics sources with their inherent time structure in the range of few femtoseconds offer fascinating experimental possibilities for spectromicroscopy. Unfortunately, electron imaging methods like *Photoemission Electron Microscopy* (PEEM) or *Photoelectron Momentum Microscopy* [1] at such sources are facing a dramatic loss in performance due to the space-charge problem. Coulomb interaction in the beam can induce prohibitively large energy broadenings ΔE of hundreds to thousands of eV. In this contribution we present a theoretical study of the space charge effect in a special type of electron microscopy and propose a way to eliminate part of the effect by exploiting its "deterministic" nature. The Coulomb interaction in the beam can be separated into two parts. The first, integral part reflects the charge distribution and its temporal evolution; this part leads to a rotation of the distribution in six-dimensional phase-space. This is referred to as *deterministic* part of the space charge interaction. The second part describes the individual electron-electron scattering processes that are *stochastic* and lead to irreversible heating of the electron beam. We have considered the space-charge effect for the case of a momentum microscope in the hard X-ray range, based on simulations with the General Particle Tracer (GPT) code [2]. We find that momentum microscopy offers a pathway for a correction of the deterministic part of the Coulomb interaction, since the instrument detects the k||- distribution in an imaging microscope column. For XFEL applications in the hard X-ray range (i.e. photon energies in the range of 5-10 keV) a strong immersion field of 5 MV/m accelerates and widens the electron beam very rapidly, in order to reduce Coulomb repulsion. The correction makes use of the fact that the best-fit line of the electron distribution in an energy-vs-radius plot for the electron beam is strongly tilted. This line can thus be used for a re-normalization of the measured kinetic energies. A calculation for a model distribution assuming a 5 keV core-level signal in the presence of a 10 times more intense low-energy signal from the secondary electron cascade predicts a gain in energy-resolution by almost an order of magnitude. In practice, energy discrimination can exploit concepts of time-of-flight electron microscopy [3] using a delayline image detector. Furthermore, the method allows implementing an imaging spin filter into the microscope column [4, 5]. The results are important for other spectroscopic methods dealing with charged particles at high-brightness femtosecond-sources
Funded by BMBF (05K12UM2) and COMATT, Mainz.

1. B. Krömker, M.Escher, D.Funnemann, D.Hartung, H. Engelhard, and J.Kirschner, *Rev. Sci. Instrum.* 79, (2008) 053702.
2. S.B. van der Geer, O.J. Luiten, M.J. de Loos, G. Pöplau, U. van Rienen, *Institute of Physics Conference Series,* No. 175, (2005), p. 101
3. G. Schönhense, A. Oelsner, O. Schmidt, G. H. Fecher, V. Mergel, O. Jagutzki, H. Schmidt-Böcking, *Surf. Sci.* 480 (2001) 180.
4. D. Kutnyakhov, P. Lushchyk, A. Fognini, D. Perriard, M. Kolbe, K. Medjanik, E. Fedchenko, S.A. Nepijko, H.J. Elmers, G. Salvatella, C. Stieger, R. Gort, T. Bähler, T. Michlmayer, Y. Acremann, A. Vaterlaus, F. Giebels, H. Gollisch, R. Feder, C. Tusche, A. Krasyuk, J. Kirschner and G. Schönhense, *Ultramicroscopy* in print.
5. K. Medjanik, this conference

Emerging Techniques in Modern Microscopies

MIM.2.023
A New Method of Online Specimen Drift Compensation in TEM

A. Tejada[1], A.J. den Dekker[2]

[1]Delft University of Technology, Precision and Microsystems Engineering , Delft, Netherlands
[2]Delft University of Technology , Delft Center for Systems and Control, Delft, Netherlands

a.tejadaruiz@tudelft.nl
Keywords: Specimen drift compensation, ARMA processes, systems and control theory

Transmission electron microscopes (TEMs), the tools of choice in materials science, semiconductor, and biological research, will be increasingly used to perform high-volume, repetitive measurements in industrial settings. Hence, there is need for a new generation of TEMs capable of autonomously performing and reporting high-throughput nano-scale measurements [1].

An important TEM process in need of automation is the compensation of specimen drift, which affects all types of electron microscopes due to factors such as specimen charging, electromagnetic interference, holder relaxation, thermal changes, etc. [2]. At low magnification, it slowly shifts the content of the microscope's image stream. At high magnification the shift is much more pronounced and can potentially lead to image blurring, especially for long-exposure TEM images [2], or to image distortions [3]. Specimen drift can be ameliorated by carefully setting up the experimental conditions under which the images are acquired [2]. For instance, one could allow the microscope to reach thermal and mechanical equilibrium by waiting several minutes (sometimes hours) before acquiring the images. Such passive procedures, however, are not compatible with high-throughput TEM operation. Similarly, offline image restoration techniques could be used to remove the drift effects (see, e.g., [4]). However, they do so at the expense of processing times that may not always be compatible with high-throughput TEM operation, especially if the latter involves image analysis.

On the other hand, online drift compensation techniques akin to optical image stabilization used in high-end digital cameras [5] can attain the same level of results, provided the optical system under consideration is equipped with fast enough sensors and actuators. Unfortunately, most TEMs are equipped with fast actuators only, so online drift compensation schemes based solely on feedback information cannot prevent the blurring of long-exposure images.

To address this problem, we have recently developed a methodology based on minimum variance control (MVC) [6]. This methodology treats the drift a stochastic process and, hence, aims to reduce its variance over time. To do so, an autoregressive moving-average (ARMA) model is first fit to drift data extracted directly from a short sequence of images using cross-correlation techniques [6]. The ARMA model is then used to predict future drift values, which are then used to pre-emptively shift the electron beam using the image shift coils. This procedure is illustrated in Figure 1, which shows an experimental drift sequence recorded with a Tecnai F20 and the one-step-ahead predictive drift values. As Figure 1 shows, our technique can also handle drifts with deterministic trends.

Although our technique cannot eliminate the drift completely, the residual drift after compensation has a smaller variance than the original one, even for large prediction horizons. Thus, this technique can be used to compensate drift during long-exposure image acquisition. Also, note that the ARMA drift model is updated with each new image acquisition. Thus, our technique can both adapt to changing drift properties and reduce the residual drift variance over time. The latter is illustrated in Figure 2, which also compares our results to those of standard MVC (which requires prior knowledge of the drift model). Figure 2 also shows that our technique can significantly reduce the drift variance even under large drift measurement errors. Finally, note that the proposed methodology is an illustration of the benefits that systems and control theory can bring to electron microscopy.

1. A. Tejada, A. J. den Dekker, and W. Van Den Broek, "Introducing Measure-by-Wire, the Systematic Use of Systems and Control Theory in Transmission Electron Microscopy", Ultramicroscopy, Vol. 111(11), pp. 1581-1591, 2011.
2. J. C. H. Spence, High-Resolution Electron Microscopy, 3rd. Ed., New York: Oxord University Press, 2003.
3. M. T. Snella, “Drift correction for scanning-electron microscopy,” MSc. thesis, Massachusetts Institute of Technology, 2010.
4. J. M. Plitzko and J. Mayer, “Quantitative thin film analysis by energy filtering transmission electron microscopy,” Ultramicroscopy, Vol. 78(1-4), pp. 207 – 219, 1999.
5. Sachs D, Nasiri S, Goehl D, “Image stabilization technology overview”. Online: http://goo.gl/YVHiN, accessed on April 12, 2013.
6. A. Tejada, A. and A. J. den Dekker, "A Comparison between Minimum Variance Control and Other Online Compensation Methods for Specimen Drift in Transmission Electron Microscopy", Multidimensional Systems and Signal Processing (to appear) 2013.

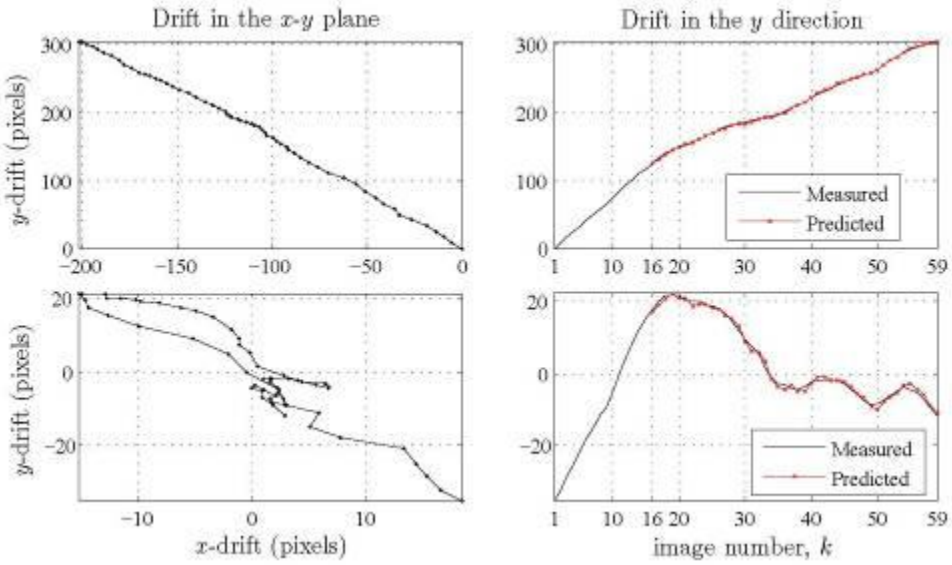

Figure 1. Top left: *x-y* plane specimen drift present in a TEM bright-field image sequence recorded with a TEM Tecnai F202. The drift has a clear linear trend from the bottom right to the upper left (the dots mark the recorded data points). Bottom left: De-trended *x-y* drift data. Top right: *y* -direction drift and the one-step ahead forecast sequence (doted line). Bottom right: De-trended *y* -direction drift and its one-step ahead forecast sequence.

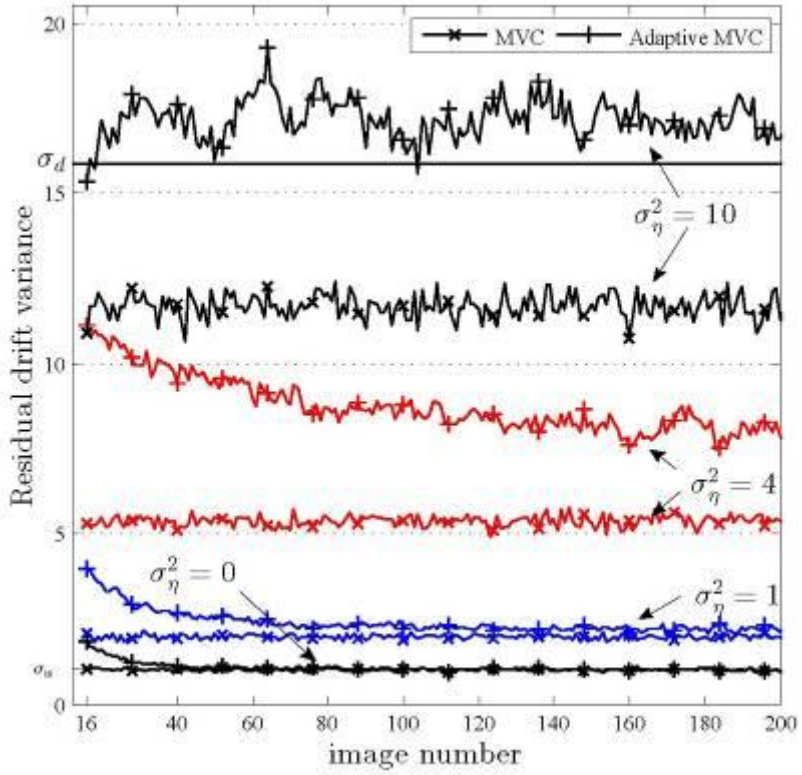

Figure 2. Residual drift variance when MVC is applied to 500 simulated specimen drift sequences. The plots marked with a (×) correspond to the results of the proposed technique that does not use any prior knowledge regarding about the drift process. The plots marked with a (+) correspond to the results based on standard MVC, which requires a-priori drift information. Note that the uncompensated drift variance is $\sigma_d = 16$ and that the residual drift variance reaches the theoretical limit of $\sigma_w = 1$ when there is no drift measurement noise (i.e., $\sigma_\eta = 0$). However, the proposed drift compensation technique can still yield good results even for large drift measurement noise (e.g., $\sigma_\eta = 2$) , which is important when the drift is measured from short-exposure images

Emerging Techniques in Modern Microscopies

MIM.2.024
K2: A Super-Resolution Electron Counting Direct Detection Camera for Cryo-EM

A. Kastenmüller[1], C. Booth[2], P. Mooney[2], B. Lee[2], S. Gubbens[2]

[1]Gatan GmbH, München, Germany
[2]Gatan, Inc., Pleasanton, CA 94588, United States

cbooth@gatan.com

Direct detectors have great promise for improving resolution and sensitivity over indirectly coupled, scintillator-based cameras. However, direct detection alone does not raise the DQE at low spatial frequency significantly and falls short of its potential at high spatial frequency due to residual noise in the electron energy deposition process. An electron counting detector eliminates any signal variation between incident electrons and information about the electron path through the detector can be used to extract more precise positional information than the physical pixel size otherwise allows, similar to super-resolution methods common to light microscopy. Both electron counting and electron super-resolution require that events be physically separated and can be accomplished by providing a very fast camera readout. By counting electrons rather than integrating charge, as is done in traditional cameras, the noise of the detector can be reduced thereby increasing DQE to levels closer to unity than ever before achieved in a TEM imaging detector. Gatan, Inc., in collaboration with Lawrence Berkeley National Lab and members of the Howard Hughes Medical Institute, has developed a detector capable of acquiring electron-counted images under typical cryo-EM microscope conditions. A 3838 x 3710 sensor is read out at 400 full frames per second and images are processed in real time to identify individual electron events. The sensor is thinned to allow the electron beam to pass through the sensor without backscatter. Small-feature CMOS technology is combined with proprietary radiation hardening measures to provide a sensor lifetime of greater than 5 billion electrons per pixel.

Testing has shown a significant boost in DQE from counting and extension of the DQE to above the physical Nyquist frequency from electron super-resolution. Results will be presented that show improvements in camera performance using test samples and biological samples.

Emerging Techniques in Modern Microscopies

MIM.2.P025
Momentum Microscopy based on Time-of-Flight Filter and Imaging Spin Detector

K. Medjanik[1], S. Chernov[1], R. Janzen[1], H.-J. Elmers[1], C. Tusche[2], A. Krasyuk[2], J. Kirschner[2]
G. Schönhense[1]

[1]Johannes Gutenberg-Universität Mainz, Institut für Physik, Mainz, Germany
[2]Max Planck-Institut für Mikrostrukturphysik, Halle, Germany

medyanyk@uni-mainz.de
Keywords: PEEM, momentum microscopy

Imaging of momentum space is exploited for structure analysis in the diffraction mode of a TEM or, more generally, in all diffraction experiments. Momentum space is also of high relevance for the electronic bandstructure of solid materials. In common experiments aiming at the electronic structure, the energy spectra are acquired under various angles in real space and later "back-transformed" into momentum coordinates. It would be more adequate to acquire the spectroscopic information directly in momentum space. This contribution presents an innovative novel approach, termed momentum microscopy.

Momentum microscopy [1] studies the electronic structure of surfaces using the cathode-lens technique, well-known from PEEM. Whereas a PEEM is optimized for best resolution in real space, momentum microscopy aims at an ultimate resolution in k-space (reciprocal space). Up to now, dispersive spectrometers have been used as energy filter and an imaging spin filter of W(001) type was employed [2]. In this contribution we present first results using time-of-flight (ToF) energy dispersion using a delayline detector, adopting concepts of ToF-PEEM [3]. By setting a ToF condition in the 3D (x,y,t) data sets, we define sections in k-space. In extended simulations we optimized the electron optical design such that for start energies up to 80eV the full half space above the sample surface (more than the first Brillouin zone) can be imaged with high k-resolution.

Starting from the imaging Ir(001)-type reflection spin filter [4], we were able to extend the lifetime of the surface by orders of magnitude via coating with a thin, pseudomorphic Au(001) overlayer that also stabilizes the surface in the non-reconstructed 1x1 phase. The instrument allows simultaneous spin filtering of many energy sections through momentum space. TOF filtering bears the potential of very high energy resolution in the few meV range. It can be selected via the drift energy and length of drift space. Aberrations are very small because a linear electron-optical column is retained. The instrument is operated in the lab using pulsed laser sources and will be installed at BESSY II (beamline RGBL-PGM).

Funded by BMBF (05K12UM2 and 05K12EF1) and COMATT.

1. B. Krömker, M.Escher, D.Funnemann, D.Hartung, H. Engelhard, and J.Kirschner, Rev. Sci. Instrum. 79, (2008) 053702.
2. C. Tusche, M. Ellguth, A. Ünal, C.-T. Chiang, A. Winkelmann, A. Krasyuk, M. Hahn, G. Schönhense and J. Kirschner, Applied Physics Letters 99, (2011) 032505.
3. G. Schönhense, A. Oelsner, O. Schmidt, G. H. Fecher, V. Mergel, O. Jagutzki, H. Schmidt-Böcking, Surf. Sci. 480 (2001) 180.
4. D. Kutnyakhov, P. Lushchyk, A. Fognini, D. Perriard, M. Kolbe, K. Medjanik, E. Fedchenko, S.A. Nepijko, H.J. Elmers, G. Salvatella, C. Stieger, R. Gort, T. Bähler, T. Michlmayer, Y. Acremann, A. Vaterlaus, F. Giebels, H. Gollisch, R. Feder, C. Tusche, A. Krasyuk, J. Kirschner and G. Schönhense, Ultramicroscopy in print.

Emerging Techniques in Modern Microscopies

MIM.2.P026
Energy Filtered Imaging with the energy selecting in-lens Duo detector

M. Boese[1]
[1]Carl Zeiss Microscopy, Oberkochen, Germany

markus.boese@zeiss.com
Keywords: SEM, spectroscopy, contamination

In SEM imaging, secondary electrons (SE) and backscattered electrons (BSE) of different energies are carrying different information, for example on the escape depth in the material and on the material itself [1]. Energy selective detection of SE and BSE in conventional SEM columns requires complex, separate detector systems. The Carl Zeiss In lens Duo detector is a compact in lens detector for the GEMINI SEM column that uses a tunable retarding grid to select, for instance, low loss BSE or high energy SE for image formation. In this study it is shown how the Carl Zeiss In lens duo detector can be used to select electrons depending on their energy for the image formation. Filtering Secondary electrons: High energy SE Energy filtering is achieved by setting the grid voltage of the in lens duo detector to different values and obtaining energy filtered SEM images (Fig.1 to 3). Contamination is a common and unwanted imaging artifact (Fig. 1) in the SEM. The use of a filtering detector can minimize this effect by selecting a mixed signal from high energy secondary electrons and back scattered electrons. In Fig 2 the energy selecting grid is set up to allow only high energy SEs and additionally all BSEs to form the energy filtered image. Using the in lens Duo detector this way enables a variation of the BSE and SE signal component with only one detector. The high energy component of the SEs is less effected by the sample surface[4]. Other examples can be found in recent publications. In a quantitative approach a variation of the detected electron is achieved by a systematic variation of the grid voltage and subsequent image acquisition. By simply subtracting those images from each other, topographic and material contrast can be separated in the resulting energy pass band filtered images [2] The Gemini lens has a unique property of spectroscopy due to the imaging of the secondary electrons onto the in lens detector. The dispersion caused by the chromatic aberration can be used for imaging p,n junctions [3] with secondary electrons. Filtering Backscattered electrons: Low loss BSE The underlying spectroscopic information of the low loss BSE imaging results in a strong material contrast (Fig3). Especially the energy filtering properties under low loss BSE imaging conditions were explored by H. Jaksch [1] and contrasts were shown which can not be explained with the common BSE contrast mechanism. In conclusion the In lens duo detector can be used as an energy filtering detector like the EsB detektor. It is capable of low loss BSE imaging and it can be used to select high energy SE for suppressing contamination effects in the SEM image.

1. H. Jaksch, Microsc. Microanal. 17,Suppl. 2(2011), 902
2. M. Nagoshi, T. Aoyama and K. Sato, Ultramicroscopy 124 (2013)
3. J. Jatzkowski, M. Simon-Najasek and F. Altmann, Microelectron. Reliab. 52 (2012) 2098
4. D. Tsurumi, K. Hamada and Y. Kawasaki, Jpn. J. Appl. Phys. 51 (2012), 106503
5. The author would like to thank H. Jaksch for his support

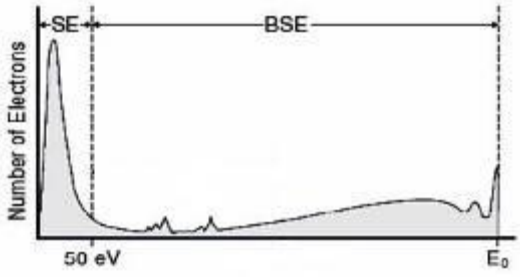

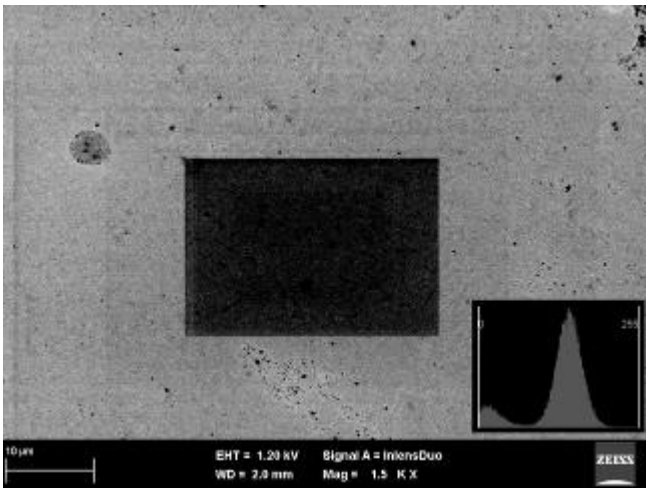

Figure 1. Schematic Spectrum of emitted electrons.(left) Unfiltered image of a Tungsten carbide sample using all the electrons from the spectrum. This imaging conditions are clearly showing a contaminated area in the middle of the image (right).

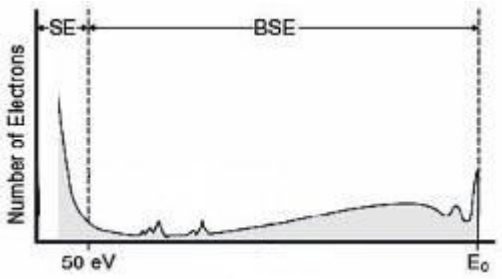

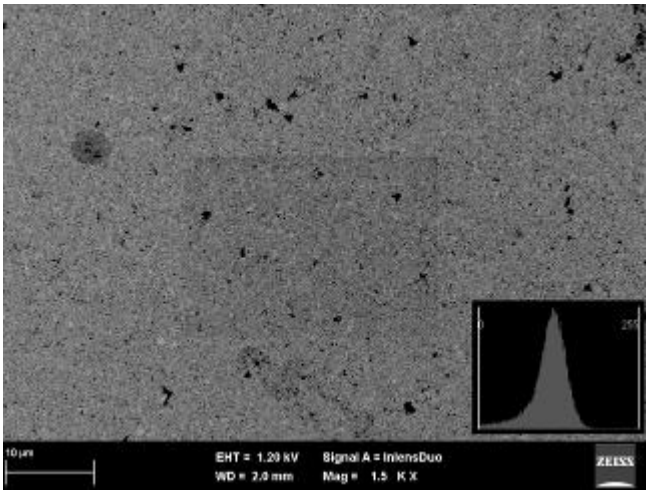

Figure 2. The low energy SEs are cut off by the in lens Duo detector (left).By simply applying a grid voltage only high energy SEs and all BSEs are used for imaging. The filtered image is less effected by the contamination (right).

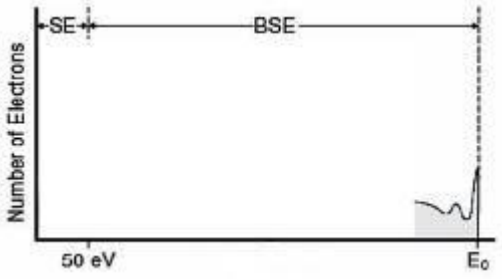

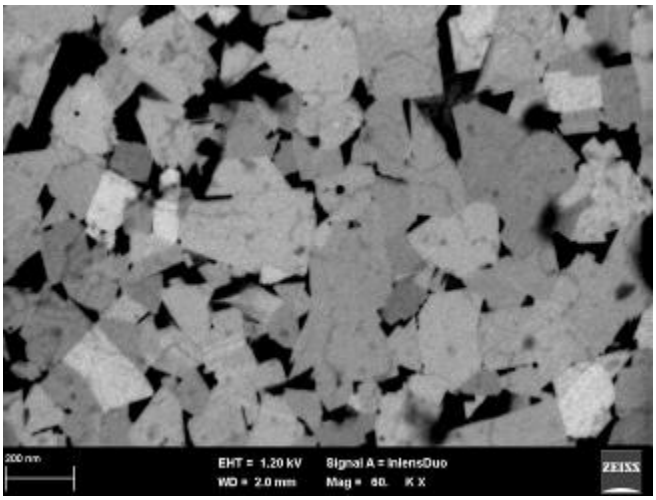

Figure 3. In this Experiment only low loss BSEs are used for imaging the Tungsten carbide sample (same as in Fig 1 and 2), providing a good material contrast (right).

Emerging Techniques in Modern Microscopies

MIM.2.P027
Spectral “bleed-through” correction makes possible FRET microscopy of intracellular organelles

Y. Kalaidzidis[1], I. Kalaidzidis[1], R. Villaseñor[1]

[1]MPI-CBG, Dresden, Germany

kalaidzi@mpi-cbg.de
Keywords: FRET, spectral, bleed-through

Quantitative Forster resonance energy transfer (FRET) microscopy provides a mean for studying protein interactions in cells. FRET microscopy has unavoidable spectral “bleed-through”. Spectral cross-talk or bleed-through (SBT) is an acronym for appearance of unwanted signal in a microscopy image as result of excitation/emission spectra overlaps between different fluorescence markers. Common wisdom recommends carefully choose fluorescent markers combination, emission filters and use sequential excitation to avoid SBT effect. Unfortunately in FRET microscopy spectral cross-talk is inevitable, since the FRET signal and fluorescence of directly excited acceptor have the same spectrum (for review FRET principle and technology see, for example, Jares-Erijman & Jovin, 2003; Berney & Danuser, 2003; Jares-Erijman & Jovin, 2006; Ishikawa-Ankerhold et al, 2012; Preus & Wilhelmsson, 2012, Knox, 2012). In the last 15 years multiple methods were developed to handle FRET for spectral cross-talk. They include indirect methods, like acceptor photo-bleaching [Wouters et al, 1998; Gu et al., 2004] as well as direct corrections of SBT [Cordon et al., 1998; van Rheenen et, al, 2004; Wallrabe et al., 2006]. It was shown that correction provides reliable result in relatively large fluorescent areas with relatively high ratio of FRET signal to SBT. When either area of interest becomes small or ratio of donor/acceptor is far from unity, the correction becomes unstable and results even in negative FRET signal. This effect makes impossible direct FRET microscopy of single intracellular organelles, like endosomes or secretory granules. Moreover, it was shown that intensity of donors influence the measured FRET efficiency even after correction [Wallrabe, 2006].

The most commonly used FRET correction of SBT [Cordon et al, 1998] includes 9 images, which comes from 3 combinations of excitation/emission (Table I) and 3 combination of sample staining (Table II).

In these tables only second lines correspond to FRET measurement *per se*. Other combinations are used for calculation the SBT correction coefficients. In other word for proper direct FRET measurement researcher has to make eight calibration images and one FRET image. Since all staining combination impossible to have on the same sample, in addition to FRET sample (line # 2, Table II), other two samples are used for SBT coefficient calibration. In sake of simplicity we consider the major SBT contribution, which corresponds to direct excitation of acceptor by donor-exciting wavelength. This contribution could not be suppressed by emission filter selection and, unfortunately, is not much suppressible by excitation laser selection for most commonly used FRET donor/acceptor couples and commercially available microscopes. Another SBT of red wing of donor through FRET emission filter could be minimized in expense of some decrease of method sensitivity.

First, we revisit correction of SBT in the control conditions where we can directly separate real signal of interest from SBT. For this we took images of endosomes labeled with EEA1 antibodies conjugated to Alexa555 and follow pulse of Alexa488 labeled LDL. The two channel imaging was done with exciting lasers 488 and 561 sequentially. Set of emission filters was chosen to allow significant bleed-through from Alexa-555 excited by 488nm laser line to the 488 channel (Fig.1). As control we have repeated the same experiment without EEA1-Alexa555 staining. Endosomes were found on both channels independently as described before (Rink et al, 2005). Classical SBT correction procedure [Cordon et al., 1998] despite gave correct estimation of mean intensity of endosomes, but for many individual endosomes predicted negative signal in intensity-of-interest channel.

In this work we revisited the mechanism of spectral bleed-through image formation and demonstrate that source of correction failure for individual endosomes is intrinsic Poisson noise of fluorescence microscopy. We develop new spectral bleed-through correction formulas, which a) properly corrects bleed-through that was confirmed by control experiment without EEA1-Alexa555 staining, b) produces only positive estimation of intensities-of-interest (Fig.2C).

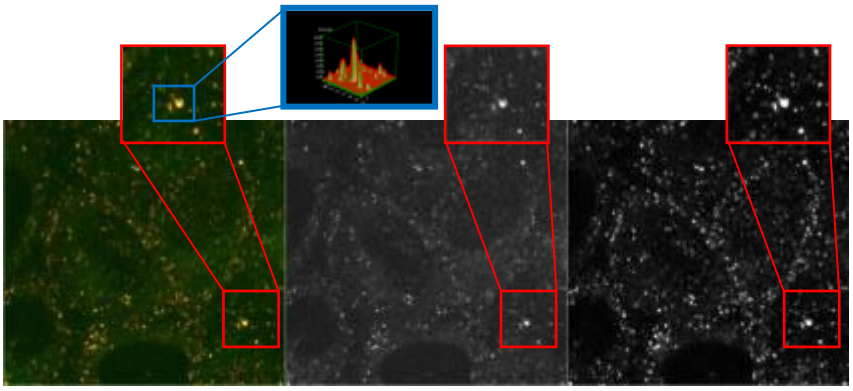

Merged | **Excitation by 488nm laser** | **Excitation by 561nm laser**

Figure 1. Control images: HeLa cells stained only by APPL1-Alexa555 antibodies. Images were obtained by Zeiss 510 confocal microscope with individual gain selection and separate excitation by 561 and 488 lasers. Individual endosomes were recognized and quantified by image intensity fitting as described before (Rink et al, 2005).

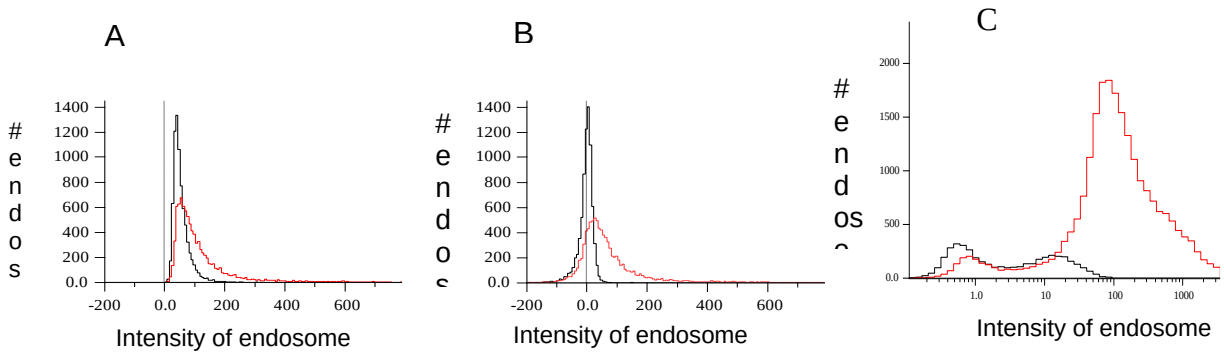

Figure 2. Control in absence of A-488 labeled marker (SBT only) – black. LDL-A-488 uptake for 5 min (real signal + SBT) - red. A. Non-corrected endosome intensity (integral intensity of endosome divided by endosome area) distribution. B. Corrected endosome intensity distribution with constant SBT coefficient.
C. Corrected endosome intensity distribution with probabilistic SBT estimation

Table I

Excitation	Emission
Donor	Donor
Donor	*Acceptor*
Acceptor	Acceptor

Table II

Donor Staining	Acceptor Staining
+	-
+	+
-	+

Emerging Techniques in Modern Microscopies

MIM.2.P028
Dissolution dynamics of lignin of poplar fiber cell wall during hydrothermal pretreatment by analytical microscopy approaches

J. Ma[1], J.-F. Ma[1], F. Xu[1]

[1]Beijing Forestry Univ, Beijing, China

majing678@hotmail.com
Keywords: Hydrothermal pretreatment, Topochemical changes, Confocal Raman microscopy, Scanning electron microscopy

Increasing attention has been paid to the converting lignocellulosic materials (LCMs) into bio-energy, bio-chemicals and bio-based materials in the biorefinery. However, the efficiency of the conversion has been limited due to the native recalcitrance of plant cell walls, which can be partially eliminated through various pretreatments [1]. Therefore, a detailed investigation on the chemical and structural changes in different morphological regions of the cell walls during the pretreatment process is critical to the development of optimal pretreatment conditions**.** In this study, poplar that is a potential feedstock for bioethanol production was subjected to liquid hot-water pretreatment at the desired reaction time. Confocal Raman microscopy (CRM) and scanning electron microscopy (SEM) were utilized to analyse the influence of the hydrothermal pretreatment time on the chemical composition of the cell wall at the sub-cellular level. The Raman images demonstrated that the removal of lignin was mainly from the middle layer of secondary wall (S2) and compound middle lamella (CML) and remarkably increased with increasing reaction time (Figure 1a-1e). Meanwhile, the removing rate in S2 was found to be faster than in CML and CCML after 20 min, whereas there was an opposite trend for 10 min (Figure 1f, 1g). SEM images revealed that a small amount of droplets appeared in the CCML after 5 min (Figure 2b). A high density of droplets accumulated in the CML and S2 over time (Figure 2c-2e). As the pretreatment time extended to 40 min (Figure 2f), droplets principally existed in the CML. These results suggest that the migration of the lignin from the cell wall matrix could be oriented on the whole both from the S2 adjacent to CML to CC and from the S2 close to S3 to cell lumen although it actually occurs from every direction. Furthermore, the distribution of the residual lignin and redeposited lignin in the different morphological regions of the cell walls varies with the hydrothermal pretreatment time. This study provides valuable new insights towards the dissolution dynamics of lignin during hydrothermal pretreatment and can potentially contribute to the development of efficient cell wall deconstruction using liquid hot-water.

1. Y. Q. Pu, F. Hu and A.J. Ragauskas, 6 (2013), p. 1.
2. We kindly acknowledge the National Science and Technology Program of the Twelfth Five-Year Plan Period (2012BAD32B06).

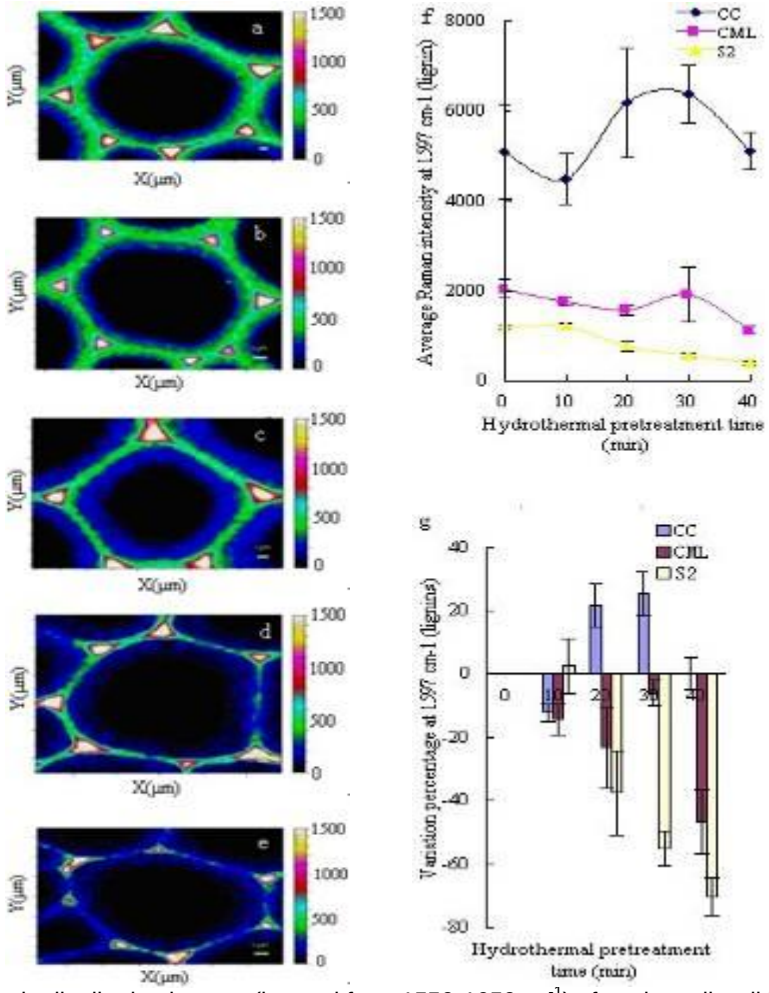

Figure 1. Lignin distribution images (integral from 1550-1650cm^{-1}) of poplar cell wall in cross section before (a) and after hydrothermal pretreatment (b-e) at 170°C for 10, 20, 30, 40 min respectively. Changes in average Raman intensity at 1597cm^{-1} (f) located in different morphological cell wall regions with the increasing pretreatment time. Variation percentage in average Raman intensity at 1597cm^{-1} (g) located in different morphological cell wall regions with the increasing pretreatment time.

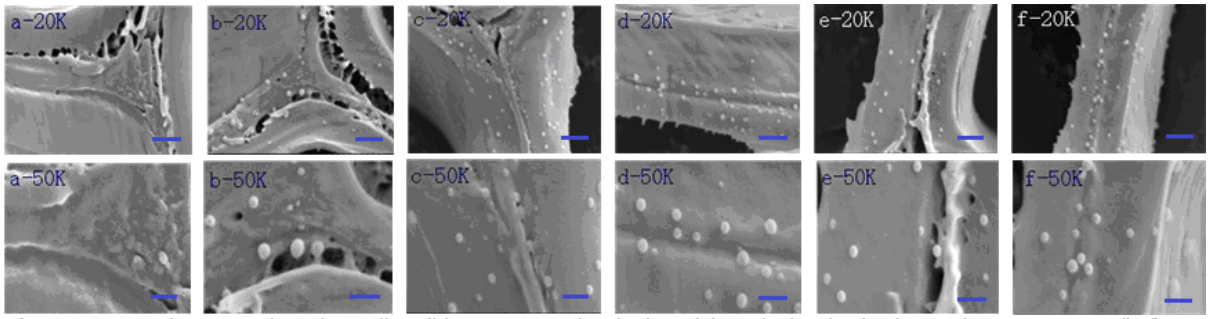

Figure 2. SEM images of poplar cell wall in cross section before (a) and after hydrothermal pretreatment (b-f) at 170°C for 5, 10, 20, 30, 40 min respectively. Scale bar: 1 μm (a-f, 20K), 0.5 μm (a-f, 50K)

Emerging Techniques in Modern Microscopies

MIM.2.P029
DNA microspectroscopic infrared (IR) signatures using Fourier Transform-IR microscope ARO objective

B. de Campos Vidal[1], M.L.S. Mello[1]

[1]University of Campinas, Dept of Structural and Functional Biology, Campinas, Brazil

camposvi@unicamp.br
Keywords: FT-IR, DNA, ARO objective

The infrared absorption profile and marker bands of dry samples of DNA and DNA-protein complexes obtained with an IR microspectroscope using a diamond attenuated total reflection (ATR) objective has recently been reported as a contribution to support forthcoming interpretation of FT-IR signatures of chromatin [1]. However, the examination of samples on gold-covered slides with the "all reflecting objective" (ARO) has also been recommended for FT-IR analysis to avoid direct contact with the preparations [2]. In the present study we investigated the adequacy of using an ARO objective for analysis of DNA dry samples.

Calf thymus and salmon testis double-stranded DNA samples (Sigma, St. Louis, USA) differing in base composition [3,4] were examined with the Illuminat IR II™ microspectrometer (Smith Detection, Danbury, USA) equipped with a liquid-cooled mercury-cadmium-telluride detector and Grams/AI 8.0 spectroscopy software (Thermo Electron Co., Waltham, USA), Olympus microscope and ARO objective (magnification, 15 x). The performance validation of the equipment used a low signal-to-noise ratio (7929:1). The spectral absorption signatures were obtained at wavenumbers between 4000 cm^{-1} and 650 cm^{-1}, with a spectral resolution of 4 cm^{-1}. Ten spectral profiles were obtained for each sample. Each spectral profile was subjected to baseline correction and normalization; an average profile was then calculated by the Grams software. Peak fitting and "estimate" procedures were applied to absorption band peaks especially assigned to DNA PO_2^- symmetric (v_s) and antisymmetric (v_{as}) stretchings.

Similar to findings obtained with the ATR objective, those obtained with the ARO objective permitted to clearly identify the DNA PO_2^- (v_s) and (v_{as}) stretchings and that the intensity of the PO_2^- v_s was greater than that corresponding to PO_2^- v_{as} for both DNA types. As regards the ratio PO_2^- v_{as}/ PO_2^- v_s, it was practically the same for the salmon DNA analyzed with both ARO (after peak fitting) and ATR objectives, but differed for the calf DNA because the intensity of the PO_2^- v_{as} of this DNA was not much different from that of the PO_2^- v_s when estimated with the ARO objective (Table 1). In contrast with the results obtained with the ATR objective, the most prominent band peak obtained after using the ARO objective was found at the ~3420-3410 cm^{-1} range for both DNA types (hydrogen bonds?). The peak assigned to adenine (1660 cm^{-1}) was more prominent for the salmon DNA in comparison with the calf DNA when the ARO objective was used. In contrast, the peak at 1400 cm^{-1}, assigned to nitrogen bases [1], that was the highest one in the salmon DNA profile when using the ATR objective became less evident when using the ARO objective.

Despite the differences on the FT-IR profiles of the DNA samples when comparing results obtained with the ARO and ATR objectives, the discrimination of important vibrational characteristics of the DNA could be made with the ARO objective. Selection of the microscope objective to be used in FT-IR DNA comparative studies will thus depend on specific vibrational groups of interest.

1. M.L.S. Mello and B.C. Vidal BC, PLoS ONE 7 (2012), e43169.
2. A. Whitley et al, http://license.icopyright.net/uswer/viewFreeUse.act?fuid=MTcwNzA5NTY%3D (2009)
3. L. Pivec et al, BBA 272 (1972), 179-190.
4. E. Chargaff et al, J. Biol. Chem. 192 (1951), 223-230.
5. We kindly acknowledge the support of FAPESP (2010/50015-6) and CNPq (301943/2009-5, 475261/2012-2).

DNA samples	ARO objective (after peak fitting)		ATR [1] objective	
	v_{as}/ v_s ratio	Wn (cm^{-1})	v_{as}/ v_s ratio	Wn (cm^{-1})
Calf thymus[a]	0.92	1215/1085	0.67	1220/1079
Salmon testis[b]	0.58	1262/1085	0.54	1220/1079

[a]Plurirmodal base composition [3]; [b]AT-biased DNA [4]; Wn, wavenumbers at which absorbances were obtained for the calculation of the ratio

Table 1. The PO_2^- v_{as}/ v_s ratio for calf thymus and salmon testis double-stranded DNA

Emerging Techniques in Modern Microscopies

MIM.2.P030
Calibration of multispectral and multimodal light emitting diode microscope for staining free malaria automate *parasitemia* determination

Z. Jeremie[1,2]

[1]Institut National Polytechnique, Yamoussoukro, Cte D'ivoire
[2]Institut National Polytechnique, Laboratoire Instrumentation Image et Spectroscopie, Yamoussoukro, Cte D'ivoire

jeremie.zoueu@inphb.edu.ci

We report the strategies we employed to adjust a modified commercial optical microscope to a multispectral and multimodal light emitting diode microscope for staining free malaria automated diagnosis and analysis. Automated counting and differentiation of healthy and parasitized red blood cells is achieved by the use of spectral fingerprint of the individual cell in transmission, reflection and scattering modes. The optimal contrast of the erythrocytes states images is reached by performing the angular dependence of both transmission and scattering measurements. The wavelength dependence and microscope objective achromaticity effects on the measurements and spectral images correlation are estimated. We also discuss how multivariate techniques like principal components analysis, k-mean and histogram analysis have been suitable for the image contrast function construction. The *Matlab* based automated counting and differentiation algorithm performance is presented and discussed.

Nanomaterials, Environment, Nanotoxicology & Health

MIM.3.031
Delivery of nanocarriers for pulmonary vaccination: recent advances and challenges

F Blank[1], P Stumbles[2,3,4], D Strickland[2], B Rothen-Rutishauser[5], P Holt[2], E Seydoux[1], Ch von Garnier[1]

[1]Respiratory Medicine, Bern University Hospital, Bern, Switzerland
[2]Telethon institute for Child Health Research, Perth, Australia,
[3]School of Veterinary and Biomedical Sciences, Faculty of Health Sciences, Murdoch University, Perth, Australia,
[4]Centre for Child Health Research University of Western Australia, Perth Australia
[5]Adolphe Merkle Institute, University of Fribourg, Fribourg, Switzerland

fabian.blank@dkf.unibe.ch
Keywords: nanocarriers, immunomodulation, antigen presenting cells cells

The respiratory tract is an attractive target for the delivery of vaccine antigens. Nano-sized carriers have been proposed as promising novel diagnostic, therapeutic, and vaccination approaches for a variety of human diseases. In particular, delivery of nano-sized carriers to the lung has been receiving increasing interest due to the large surface area provided by the gas exchange region, limited local proteolytic activity, non-invasiveness, and fine anatomical barriers for systemic access[1]. Pulmonary antigen presenting cells (APC) are considered as sentinels of the immune system due to their strategic localization, their phagocytic activity, and their ability to present antigen[2]. To improve efficiency of vaccination and develop new strategies, a well-founded knowledge about composition and characterization of APC populations throughout the respiratory tract is essential. In particular, respiratory tract dendritic cells, as key APC in the lung, constitute an ideal target for vaccine delivery[1]. Furthermore, carrier size is a key factor when designing new inhalable vaccines, as size determines not only deposition in different respiratory tract compartments, but also how an antigen and its carrier will interact with lung tissue components and immune cells[3]. Clarifying which APC / dendritic cell populations primarily interact with nano-sized carriers and traffic these from different respiratory tract compartments to lung draining lymph nodes is paramount to understanding related downstream inflammatory and immune responses. A very efficient approach to analyse particle-cell interactions in respiratory tissue is to combine flow cytometry and laser scanning microscopy in order to obtain profound quantitative (frequency of particle uptake, expression of APC surface markers) and qualitative data (in situ localisation of nanoparticles), respectively (Figure 1). Such data will be fundamental to rationally develop future novel particulate systems in the nano-size range for therapeutic or diagnostic applications in the respiratory tract.

Acknowledgements: Grant funding by the Swiss National Science Foundation and the Swiss Society for Pneumology

1. Blank F, Stumbles P, von Garnier C: Opportunities and challenges of the pulmonary route for vaccination, Expert Opin Drug Del 2011, 8:547-563
2. Blank F, von Garnier C, Obregon C, Rothen-Rutishauser B, Gehr P, Nicod L: Role of dendritic cells in the lung: in vitro models, animal models and human studies, Expert Rev Respir Med 2008, 2:215-233

3. Blank F, Stumbles PA, Seydoux E, Holt PG, Fink A, Rothen-Rutishauser B, Strickland DH, von Garnier C: Size-dependent uptake of particles by pulmonary antigen-presenting cell populations and trafficking to regional lymph nodes, Am J Respir Cell Mol Biol 2013, 49:67-77

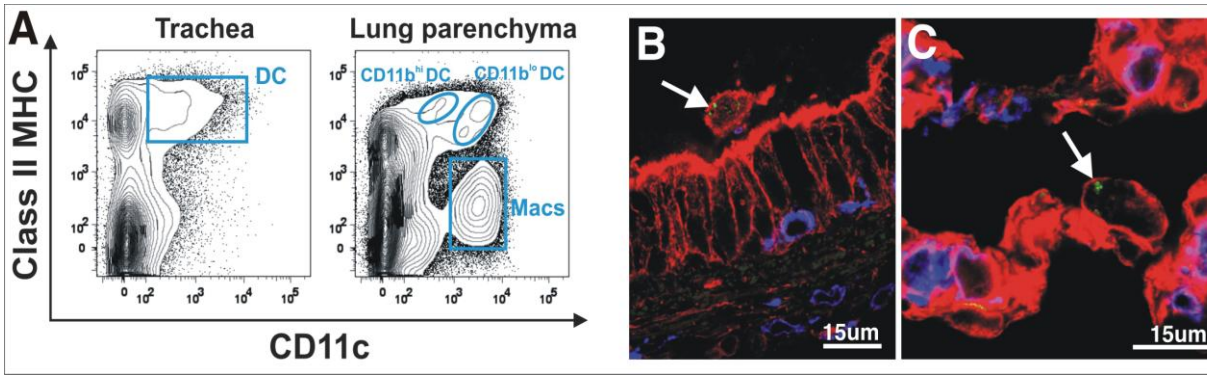

Figure 1. Analysis of nanoparticle trafficking in the respiratory tract using flow cytometry and laser scanning microscopy. Tissue from main conducting airways and lung parenchyma of mice was collected and processed for flow cytometry analysis (A) and confocal microscopy (B, C). A: Macrophages and different subsets of dendritic cells can be identified and analysed in airways and lung parenchyma. B, C: Localisation of nanoparticles (white arrows) in airways (B) and lung parenchyma (C). Particles: green; actin cytoskeleton: red; MHC class II: blue.

Nanomaterials, Environment, Nanotoxicology & Health

MIM.3.032
Silver nanoparticles decrease nuclear fractal dimension in buccal epithelial cells

I. Pantic[1], M. Basailovic[2], M. Perovic[3], S. Pantic[4], D. Djuricic[5], J. Paunovic[2]

[1]University of Belgrade, Faculty of Medicine, Institute of Medical Physiology, Belgrade, Yugoslavia
[2]University of Belgrade, Faculty of Medicine, Belgrade, Serbia
[3]Hospital Center "Narodni Front", Belgrade, Serbia
[4]University of Belgrade, Faculty of Medicine, Institute of Histology, Belgrade, Serbia
[5]Health Center Savski Venac, Belgrade, Serbia

milos.basailovic@live.mfub.rs
Keywords: Nanomaterials, DNA, Complexity

Recently, it was suggested that silver nanoparticles (AgNPs) may have substantial cytotoxic and genotoxic potential in cell cultures. In this study, we present the evidence that AgNP treatment significantly affects fractal dimension of buccal cell nuclei.

Epithelial buccal cells were kept in RPMI 1640 cell culture medium supplemented with L-glutamine at 37 ^{0}C and treated with 10 mg/L colloidal silver NPs (size 7-20 nm). Before the treatment, as well as immediately after the treatment, digital micrographs of the cell nuclei in a sample of 40 cells were created using Pro-MicroScan DEM 200 camera (Oplenic Optronics, Hangzhou, CN), mounted on the American Optical Spencer 1036A light microscope (Buffalo, NY, USA) (Figure 1). The micrographs were analyzed using fractal analysis (FA) and grey level co-occurrence matrix (GLCM) methods [1, 2]. For each nucleus, values of fractal dimension, lacunarity, entropy, angular second moment and inverse difference moment were determined.

Fractal dimension of the cell nuclei significantly decreased after the AgNP treatment, while the lacunarity increased ($p<0.01$). Nuclear entropy, angular second moment and inverse difference moment remained unchanged. These results indicate that treatment with AgNPs may affect fractal properties of buccal cell nuclei similarly as during the cellular senescence and apoptosis, previously reported [1, 2]. These findings further suggest that AgNPs might have significant genomodulatory and cytotoxic effects in human epithelial cells in *in vitro* conditions.

1. I. Pantic, G. Basta-Jovanovic, V. Starcevic, J. Paunovic , S. Suzic, Z. Kojic and S. Pantic. Nephrology. 18 (2013), p. 117-124.
2. I. Pantic, L. Harhaji-Trajkovic, A. Pantovic, N. T. Milosevic, V. Trajkovic. J Theor Biol 303 (2012), p. 87-92.

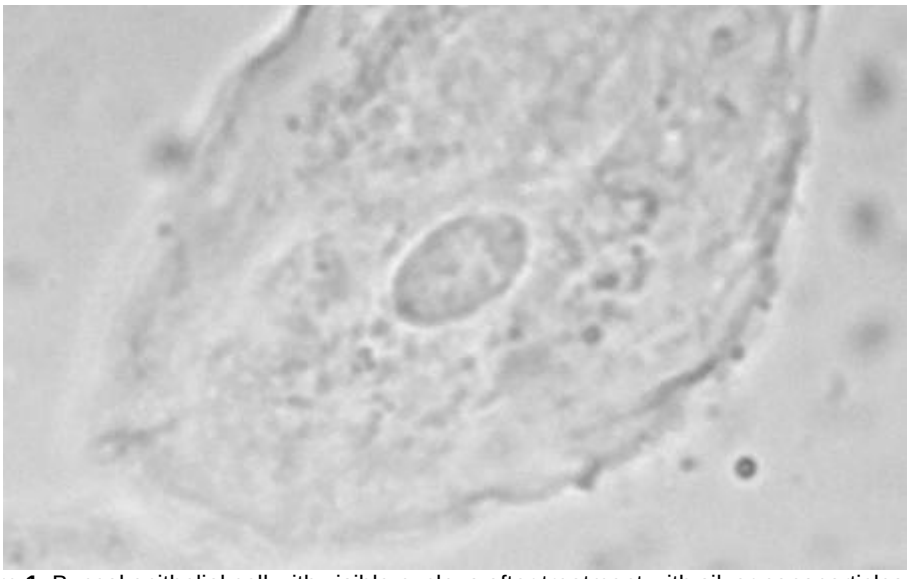

Figure 1. Buccal epithelial cell with visible nucleus after treatment with silver nanoparticles

Nanomaterials, Environment, Nanotoxicology & Health

MIM.3.033
High-resolution imaging and spectroscopy of CoO octahedral nanoparticles

Z.-A. Li[1], N. Fontaíña-Troitiño[2], S. Liébana-Viñas[1], M. Spasova[1], V. Salgueiriño[2], M. Farle[1]

[1]Uni Duisburg-Essen, Faculty of Physics, Duisburg, Germany
[2]Universidade de Vigo, Departamento de Física Aplicada, Vigo, Spain

zi-an.li@uni-due.de
Keyword: CoO; nanoparticles; ferromagnetism; antiferromagnetism

As the size of a magnetic system decreases, the significance of the surface magnetic moments increases. The finite-size effect is highly relevant for nanoparticles consisting of an antiferromagnetic (AFM) material. Since an antiferromagnet usually has two mutually compensating sublattices, the surface can break the pairing of the sublattices and thus leads to ‘‘uncompensated’’ surface magnetic moments. Néel first discussed this effect in AFM nanoparticles with a net magnetic moment [1]. Later many experimental studies have suggested various scenarios for the unusual magnetic properties, e.g., spin-glass or cluster-glass-like behavior of the surface spins [2–3], core-shell interactions [3-4], or weak ferromagnetism [5]. However, the nature of the surface magnetic contribution has not been fully understood. We have encountered unexpected magnetic phenomena in octahedral-shaped CoO-Co_3O_4 core-shell nanoparticles—exhibiting room temperature ferromagnetic behavior as evidenced by their magnetization hysteresis loop. Hard X-ray magnetic circular dichroism measurements confirmed the absence of metallic Co clusters inside the samples. To investigate possible structural and compositional reasons for the observed magnetic behavior, we conducted structural and spectroscopy characterizations using transmission electron microscopy. Figure 1(a) shows a typical TEM image of CoO-Co_3O_4 core-shell nanocrystals (NCs). In most of these NCs, contrast of voids is present as indicated in the inset. The different 2D projections (FIG.1(b)) are from an octahedral shape, as confirmed by 3D electron tomography (not shown here). Fig.1(c) shows a HRTEM image revealing different structures of theCo_3O_4-shell and the CoO-core. We also performed spot-EELS in STEM mode with a beam diameter of around 1 nm (FIG.1(d)). The spectra further confirm the CoO core and Co_3O_4-like shell structure.

To quantitatively analyse the interfacial as well as the spectroscopic structure concerning the Co-O bond length and electronic states, the atomically-resolved HAADF in combination with EELS analysis was performed. Additional high-resolution imaging and spectroscopic studies of these Co oxides nanoparticles are still in progress and will be reported and discussed in context to temperature and magnetic field dependent magnetic measurements.

1. L. Neel, Comptes Rendus 252, 4075 (1961).
2. E. L. Salabas¸, A. Rumplecker, F. Kleitz, F. Radu, and F. Schueth, Nano Lett. 6, 2977 (2006).
3. E. Winkler, R.D. Zysler, M. Vasquez Mansilla, and D. Fiorani, Phys. Rev. B 72, 132409 (2005).
4. J. Nogues, J. Sort, V. Langlais, V. Skumryev, S. Surinach,J. S. Munoz, and M. D. Baro, Phys. Rep. 422, 65 (2005).
5. A. Punnoose and M. S. Seehra, J. Appl. Phys. 91, 7766 (2002).

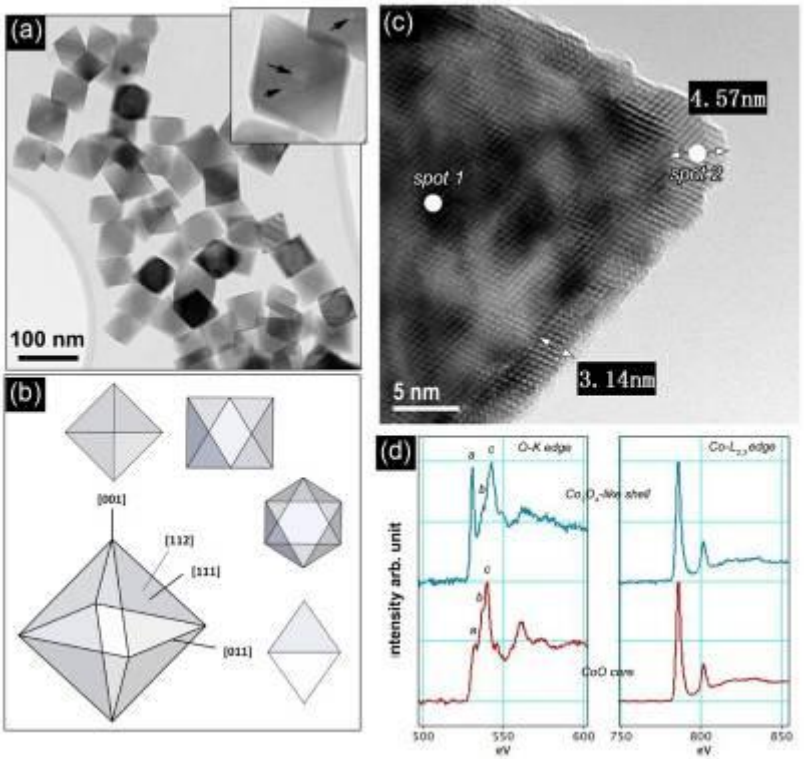

Figure 1. (a) Typical TEM image of octahedral CoO-Co_3O_4 core-shell nanocrystals. In most of these NCs, voids contrasts are present as indicated in the inset. (b) The different 2D projections are from an octahedral shape, as confirmed by 3D electron tomography (not shown here). (c) HRTEM image of the Co_3O_4-shell and CoO-core. (d) Spot-EEL spectra were taken at two positions in STEM mode with a beam diameter of about 1 nm. These spectra confirm the CoO core and Co_3O_4-like shell structure.

Nanomaterials, Environment, Nanotoxicology & Health

MIM.3.034
HRTEM contrast of nanoparticles embedded in a metallic matrix

M. Peterlechner[1], M. Mohamed[1], G. Wilde[1]

[1]WWU Münster, Institute of Materials Physics, Münster, Germany

martin.peterlechner@uni-muenster.de

Melting, crystallization and e.g. mechanical properties of small particles are in focus of current research due to size effects. However, nanoparticles embedded in a matrix may show additional contributions to their properties caused by the character of the interfaces. In the present study, the contrast in high-resolution transmission electron microscopy (HRTEM) arising from metallic nanoparticles embedded in a metallic matrix are studied. It is the aim of the present work to explain moiré effects observed in experiments by image simulations using a multislice algorithm and a simple atomistic model.

Samples for the experimental observation of embedded nanoparticles were made using the melt-spinning technique. Aluminium bands with embedded indium nanoparticles were ion-milled using a Gatan PIPS with acceleration voltages between 3.5 and 1 kV. HRTEM images were made using an aberration-corrected Titan 80-300.

For the image simulations atom positions of a freestanding nanoparticle with a flat Al-matrix above were generated using the Mathematica™ software platform. An example of a generated ensemble of atomic coordinates is shown in Figure 1. For simplicity, the crystallographic orientation was always [100] parallel to the incident electron beam. The thickness of the matrix as well as the size of the nanoparticles were systematically varied. HRTEM images of the as-generated structures were simulated using the multislice algorithm by Kirkland [1]. To fit experimental conditions, the partial coherence of the propagating electron wave was included. Therefore, the acceleration voltage was set to 300 kV, with 1 mrad spread in illumination and a slightly negative Cs-value (thermal vibrations were not taken into account). Results of the simulation are shown in Figure 2. A matrix thickness of 1, 10 and 20 unit cells is simulated in (a), (b) and (c), respectively. A matrix of 10 unit cells with a larger spherical nanoparticle is shown in (d). The propagation of the electron wave through the matrix and the nanoparticle leads to a moiré pattern. The moiré intensity variation consequently leads to local regions where the lattice information of the matrix is dominant, and local regions were the lattice plane spacing of the nanoparticle can be seen almost entirely. At a similar thickness of the matrix and the particle this local contrast variation gets strong, leading to situations where parts of the nanoparticle apparently disappear (cf. arrow in Figure 2 (c)). For a larger particle the moiré pattern stays fairly homogenous across the particle, whereas the interface becomes artificially rough. Measured atomic distances show strong variations with the moiré pattern, making it difficult to obtain real atomic positions.

An experimental HRTEM image of an In nanoparticle in an Al-matrix is shown in Figure 3. The power spectrum is shown as an inset, where many moiré spots are visible. The moiré pattern in this HRTEM image is fairly uniform across the faceted particle, however, small variations of the orientation of the moiré fringes can be observed. Moreover, two missing wedges can be observed on two opposite sites of the particle. Intensity modulations due to the moiré effect possibly exterminate a weak contrast arising by atoms at corners of the nanoparticle.

As a conclusion it should be pointed out, that the spacing of the moiré pattern can be used to determine the difference of the involved lattice planes with a high accuracy, however, measurements of absolute atomic positions are not possible and even atoms and atomic columns can become “invisible” at local regions of the moiré pattern. Moreover, apparent interface roughening can occur by moiré effects. Therefore, image simulation is inevitable to interpret atomic positions at interfaces, in particular when a nanoparticle is embedded and not of constant thickness.

1. Kirkland, E. J. “Advanced Computing in Electron Microscopy” Springer (2010).
2. We kindly acknowledge the help of Di Wang and Christian Kübel at the Karlsruhe-Nano-Micro-Facility (KNMF) at KIT for help with the experiments.

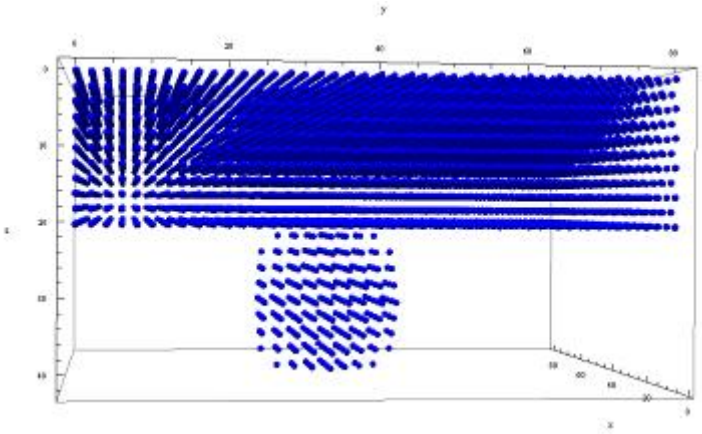

Figure 1. Simulation box of a matrix structure (on top) and an underlying nanoparticle (bottom). For the multislice simulation including partial coherence the size of the matrix as well as the size of the particle were varied. The nanoparticle is slightly facetted.

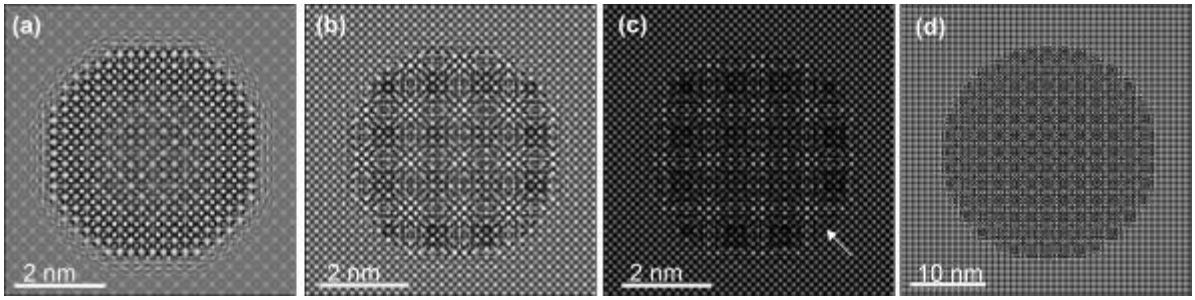

Figure 2. Multislice simulated HRTEM images of a nanoparticle and an Al-matrix. The thickness of the matrix was varied: 1 unit cell in (a), 10 unit cells in (b), and 20 unit cells in (c). The arising moiré pattern overlays the contrast of the atom columns. At a similar thickness of the matrix and the particle the local contrast of the nanoparticle gets weak, as marked by the arrow in (c). For a larger particle the moiré pattern stays fairly homogenous across the particle, whereas the interface becomes artificially rough.

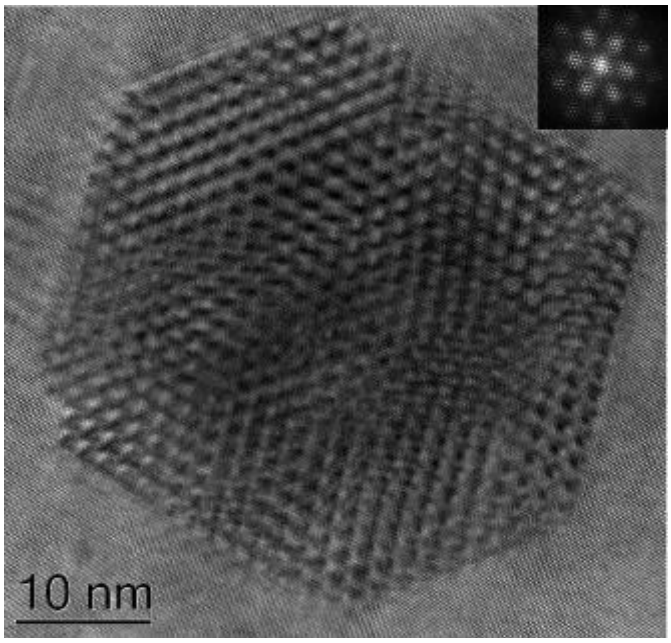

Figure 3. Experimental HRTEM image of an In nanoparticle in an Al-matrix, the insert shows the power spectrum. The moiré pattern is fairly uniform across the faceted particle. Two missing wedges can be observed on opposite sites of the particle. However, intensity modulations due to the moiré effect possibly exterminate a weaker contrast of atoms/atomic columns at corners of the nanoparticle.

Nanomaterials, Environment, Nanotoxicology & Health

MIM.3.035
Size determines the ultrastructural uptake mode of silica nanoparticles into cultured cells

C. Messerschmidt[1], I. Lieberwirth[1], A. Kröger-Brinkmann[1], D. Hofmann[1], V. Mailänder[1,2], K. Landfester[1]

[1]Max Planck Institute for Polymer Research, Mainz, Germany
[2]University Medical Center of the Johannes Gutenberg University, Mainz, Germany

dietze@mpip-mainz.mpg.de
Keywords: silica nanoparticles, endocytosis, cytotoxicity

Silica nanoparticles are widely used in commercial products. As additives in food, drinks, cosmetics and pharmaceuticals they directly get into contact with different human tissues. Therefore, a thorough examination of nanoparticle – cell interactions is of paramount importance.

In our study we applied electron microscopic methods (TEM, SEM, FIB-SEM) to investigate the interaction of differently sized, small silica nanoparticles with cultured cells on the ultrastructural level. For high resolution of the cellular details high pressure freezing was utilized as the fixation method for TEM. Additionally, we used some standard biochemical assays to test for the type of cell death occurring after the exposure to high concentrations of the respective particles.

Our observations clearly indicate that the mode of uptake into cells strongly depends on particle size. For each size of silica particle used we could identify characteristic membrane morphologies during the uptake process (Figure 1, Figure 2). These morphologies have proven reproducible in five completely different cell types and could give a hint at the mechanism of silica nanoparticle toxicity. Interestingly, though it forms large agglomerates in cell culture media, one of the particle sizes we tested enters cells as single particles (Figure 3).

From the electron microscopic evaluation of cell morphology and the findings yielded by analytical TEM and biochemical assays we conclude that high concentrations of small silica nanoparticles induce necrotic cell death. We could not find evidence for apoptosis.

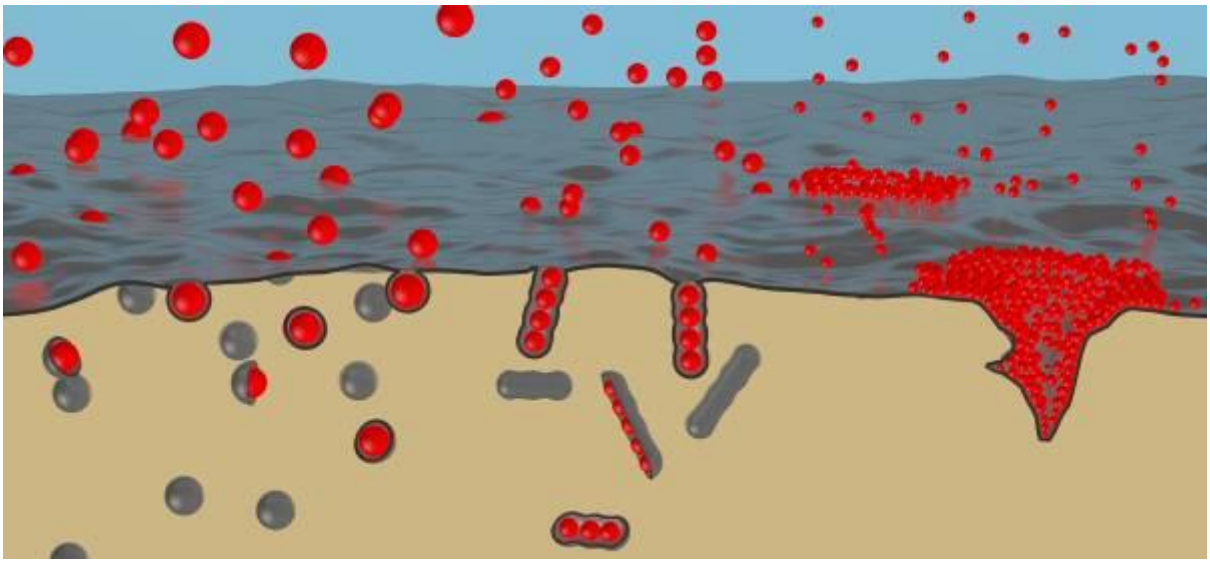

Figure 1. Scheme of the uptake modes observed for three differently sized, small silica nanoparticles (represented by red spheres).

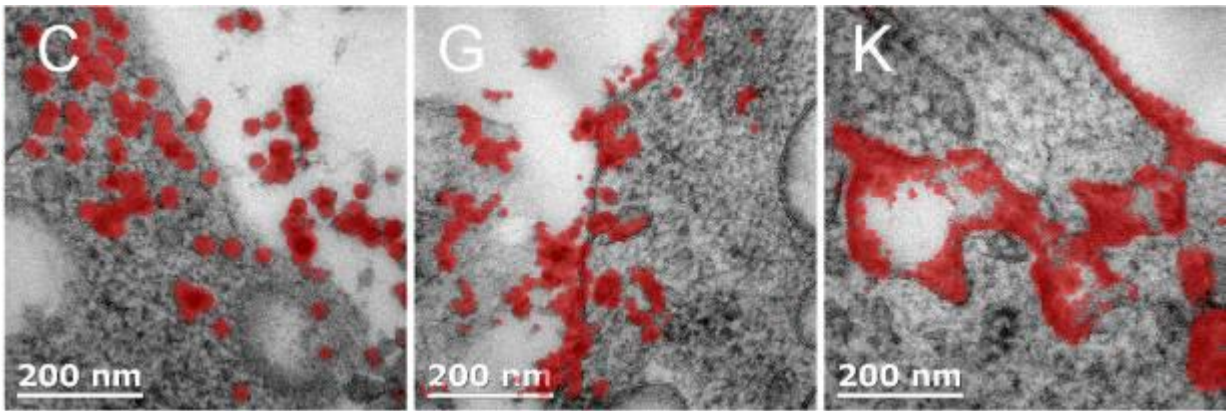

Figure 2. TEM micrographs showing the three different uptake modes observed. Silica nanoparticles are coloured red for better visibility.

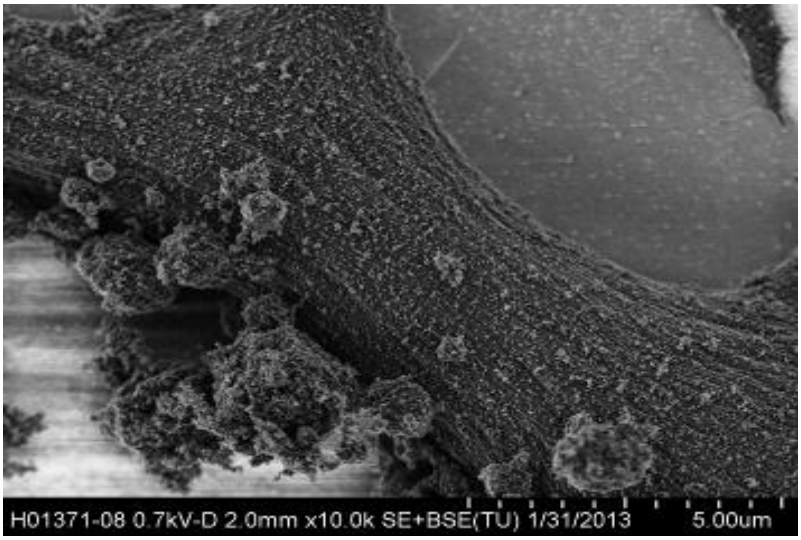

Figure 3. SEM micrograph showing the coverage of a cell membrane with single and aggregated silica nanoparticles.

Nanomaterials, Environment, Nanotoxicology & Health

MIM.3.036
Investigating the formation mechanism of three-dimensional mesocrystalline rutile nanospheres synthesized by the resin-gel method.

A. Narrandes[1], P. Franklyn[1]

[1]University of the Witwatersrand, Chemistry, Johannesburg, South Africa

ashvir.narrandes@students.wits.ac.za
Keywords: Resin-gel, rutile, mesocrystalline nanospheres

Three dimensional hierarchical mesocrystalline rutile nanospheres, synthesized using various methods, are not a new find in study of titanium dioxide nanoparticles [1,2]. Resin-gel is a modification of the Pechini method for the fabrication of mixed metal oxide nanoparticles [3]. The underlying principle is the addition of a long chain coordinating polymer to a stable solution of metal ions thus forming a gel [3]. It is believed that the after complete solvent evaporation, the metal-polymer complexes are held in positions apart from each other as a consequence of binding to the long chain polymer [3]. Flame induced ignition of the resin causes scission of the polymer chains and results in the aggregation of the metal complexes to form nanoparticles. Resin-gel is a beneficial technique as it has the potential to form single phase, nonstoichiometric, multi-metal oxides within a single reaction step. Previous work based on investigating the effect of polymer chain length, stoichiometry, heating rate and the effect of citric acid gave rise to the concept of the formation of a polymer reaction chamber within which metal ion complexes aggregate to form anatase. Anatase then transforms into rutile single crystals that grow anisotropically forming 3D rutile superstructures.

The aim of this study was to investigate the formation of rutile superstructures using an interrupted resin-gel synthesis technique and rationalise the cause of their formation using the new hypothesis of resin-gel.

Polyethylene glycol (PEG) of different average molecular weights was incorporated in a 1:1 stoichiometric ratio with $TiCl_4$ in excess distilled water. Concentrated nitric acid was added to allow for complete dissolution of the metal ion precursor in water. Following complete solvent evaporation under incandescent lamps, each resin was heated gradually in glazed alumina crucibles in a sand bath. Periodically during the heating step, a thin, aluminium rod was rapidly inserted into selected crucibles and rapidly removed. The captured drop of hot wax was transferred directly onto a holey carbon copper TEM grid. Upon reaching the auto-ignition point, each sample was ignited using a Bunsen burner and selected waxes were collected using the described aluminium dipping technique. The residual sample after the burn was collected and calcined at 773 K for one hour to remove the formed carbon material that had coated the particles. XRD analysis was performed to determine phase purity using the Spurr and Myers equation [4] and particle size analysis was performed using the instrumentally corrected Scherrer equation with K = 0.91. A Tecnai Spirit 120 kV and JEOL 3011 300 kV were used to image selected samples.

XRD analysis showed that low PEG molecular weights favoured the formation of small amounts of rutile and high PEG molecular weights allowed for the formation of greater amounts of rutile (figure 1). A curious observation was that no polymer resulted in the formation of phase pure material. As was expected, calcination caused an increase in the amount of rutile formed. The exception to this trend occurred for the 400 and 1500 g/mol PEG molecular weights that exhibited a decrease and no increase in the amount of rutile formed post-calcination respectively. This is an unexpected result as anatase irreversibly converts to the more stable rutile phase at elevated temperatures [5]. The error bars associated with the 400 g/mol PEG is however significantly large and hence accounts for the unusual data. Figure 2 illustrates the increase in particle size post-calcination. This is due to effects such as sintering during the calcination process. The large error bars are consistent with resin-gel being a thermodynamically favoured synthetic technique that lacks kinetic control and hence particle size is difficult to tailor. HRTEM revealed that the nanospheres were composed of nanowires originating from an apparently common point (figure 3a). It was also noted that the tips of each wire (figure 3b) were significantly more ordered than the points at which they make contact with the sphere (figure 3c). This suggests that the nanowires grow from a common point. The rutile phase was confirmed by comparing calculated and experimentally determined power spectra. This comparison also confirmed growth of the nanowire along the (001) direction as was documented by Hu et al [2]. TEM analysis of the partially synthesized titania revealed the presence of numerous cone-type structures in most samples (figure 4a). It is believed that these structures were formed as a result of the polymer chains unwinding to form sheets during the synthesis and these sheets then folded around themselves during the heating step. Figure 4b shows an expanse of polymer that appears to have formed an enclosure containing metal particles. This is consistent with the new polymer reaction chamber hypothesis. These chambers formed a common nucleation site for the conversion of anatase to rutile crystals and due to their high energy (001) surface, the rutile continued to grow along this direction. Figure 4c was generated from a sample during ignition and shows the presence of crystalline material arranged in a circular manner consistent with the shape of the polymer in figure 4b; adding further evidence to the proposed hypothesis.

1. Zhang. D, Li. G, Wanga. F, Yu. C, CrystEngComm 12 (2010), 1759.
2. Hu. W, Li. L, Tong. W, Li. G, Yan. T, J. Mater. Chem 20 (2010), 8659.
3. Lin. J, Yu. M, Lin. C, Liu. X, J. Phys. Chem. C 111 (2007), 5835.
4. Spurr. R, Myers. H, Anal. Chem 29 (1957), 760.
5. Chen. X, Mao. S, Chem. Rev. 107 (2007), 2891.

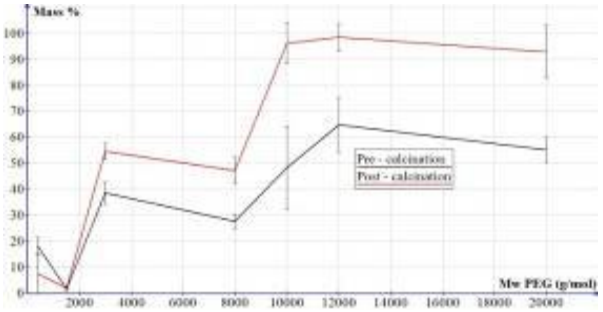

Figure 1. Mass percentage of rutile formed as a function of increasing PEG molecular weight

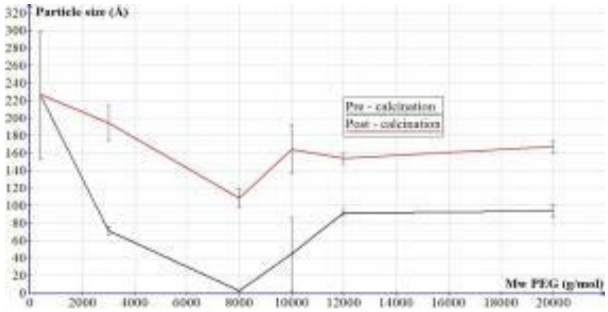

Figure 2. Rutile particle size as a function of increasing PEG molecular weight

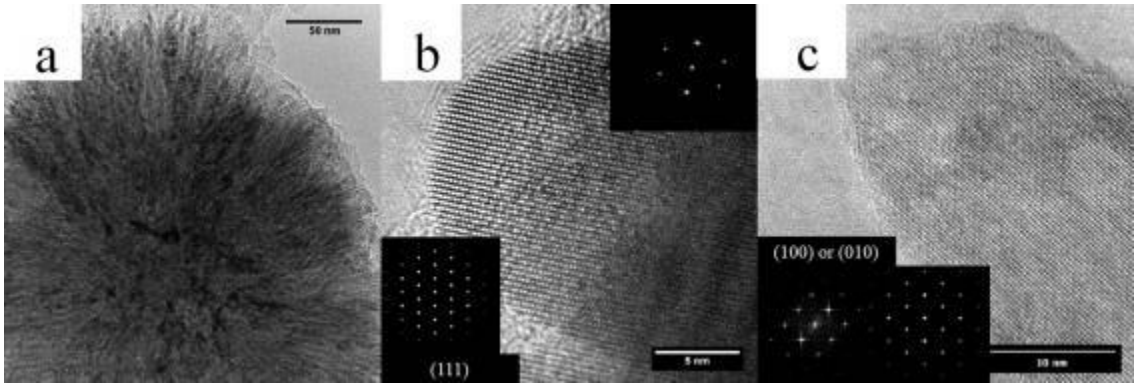

Figure 3. (a) rutile nanosphere composed of nanowires; (b) tip of a nanowire and (c) base of a nanowire including calculated and experimentally determined power spectra

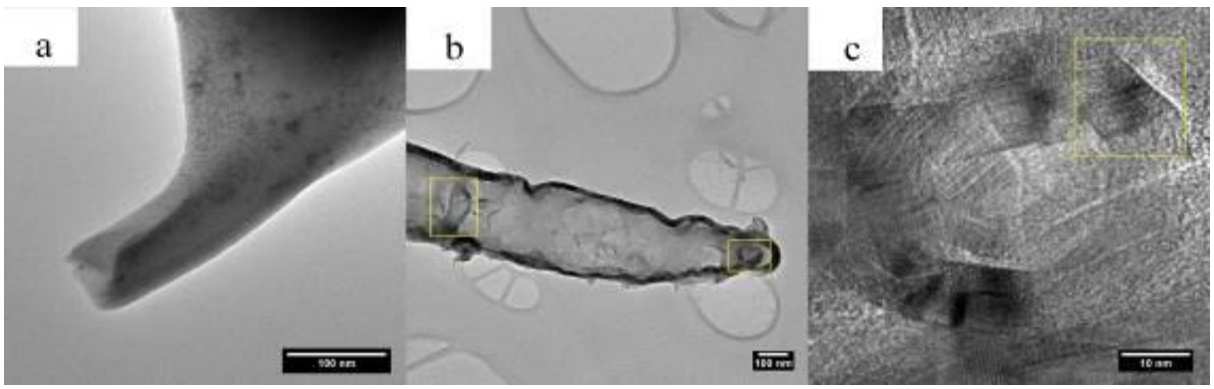

Figure 4. (a) PEG 'cone' structure; (b) formation of polymer reaction chambers; (c) formation of crystalline material in a circular pattern

Nanomaterials, Environment, Nanotoxicology & Health

MIM.3.037

Visualisation of the attachment, possible uptake and distribution of ferric based technical nanoparticles on small test organisms with electron microscopy methods

A. Springer[1], S. Scholz[2], D. Kühnel[2], W. Busch[2], K. Mackenzie[3], S. Bleyl[3], K. Duis[4], M. Weil[4]
M. Gelinsky[1]
[1]Medical Faculty of the Technical University Dresden, Centre for Translational Bone, Joint and Soft Tissue Research, Dresden, Germany
[2]Helmholz Centre for Environmental Research, Department of Bioanalytical Ecotoxokology, Leipzig, Germany
[3]Helmholz Centre for Environmental Research, Department of Environmental Engineering, Leipzig, Germany
[4]ECT Oecotoxikology GmbH, Flörsheim/Main, Germany

armin.springer@tu-dresden.de
Keywords: technical nanoparticles, Fe-NANOSIT, toxicity, EDX

Ferric based technical nanoparticles are beginning to be used in a wide variety of products. They have great potential in cleaning of halogen-organic contaminated ground and waste water (project Fe-NANOSIT; funded by the German Federal Ministry of Education and Research [BMBF]). But there is little known yet about the possible impacts of released nanoparticles on the environment and their organisms. On water born organisms like zebra fish, potential toxic effects should be investigated. This research also should help to understand how the particles interact with organism, organs, tissues, cells and cell organelles and whether they have negative effects on general vital functions. In order to identify these particles a simple morphological analysis with conventional electron microscopic methods is not always sufficient [1] due to the possible risks of misinterpretation. Therefore, an additional reliable identification method is necessary. One technique which allows a secure identification of nanoparticles is elemental analysis with energy dispersive X-ray spectroscopy (EDX) performed in the scanning electron microscope (SEM) [2]. In this work we demonstrate a proper identification of ferric nanoparticles both attached at zebra fish egg shells (not shown here) and larvae (Figure 1, A-F) after *in vitro* exposure of test organisms with ferric nanoparticle containing products. Further SEM, TEM and STEM investigations should also contribute to identify possible uptake (i. e. oral uptake) and distribution (i. e. gastrointestinal tract) of ferric nanoparticles within the organisms.

1. Gatti, A.M., Montanari, S., Monari, E., Gambarelli, A., Capitani, F. and Parisini, B., Journal of Materials Science: Materials in Medicine, 15(4), (2004).
2. A. Springer, W. Pompe, S. Bastian, M. Iwe, H. Ikonomidou, W. Busch, D. Kühnel, A. Potthoff, V. Richter, M. Gelinsky: *Visualisation of the attachment, possible uptake and distribution of technical nanoparticles in cells with electron microscopy methods.* 14th European Microscopy Congress, Aachen, 1.-5. 9. 2008. ECM 2008, *Vol. 3 - Life Science*, S. 389-390. Springer-Verlag, Berlin und Heidelberg 2008.

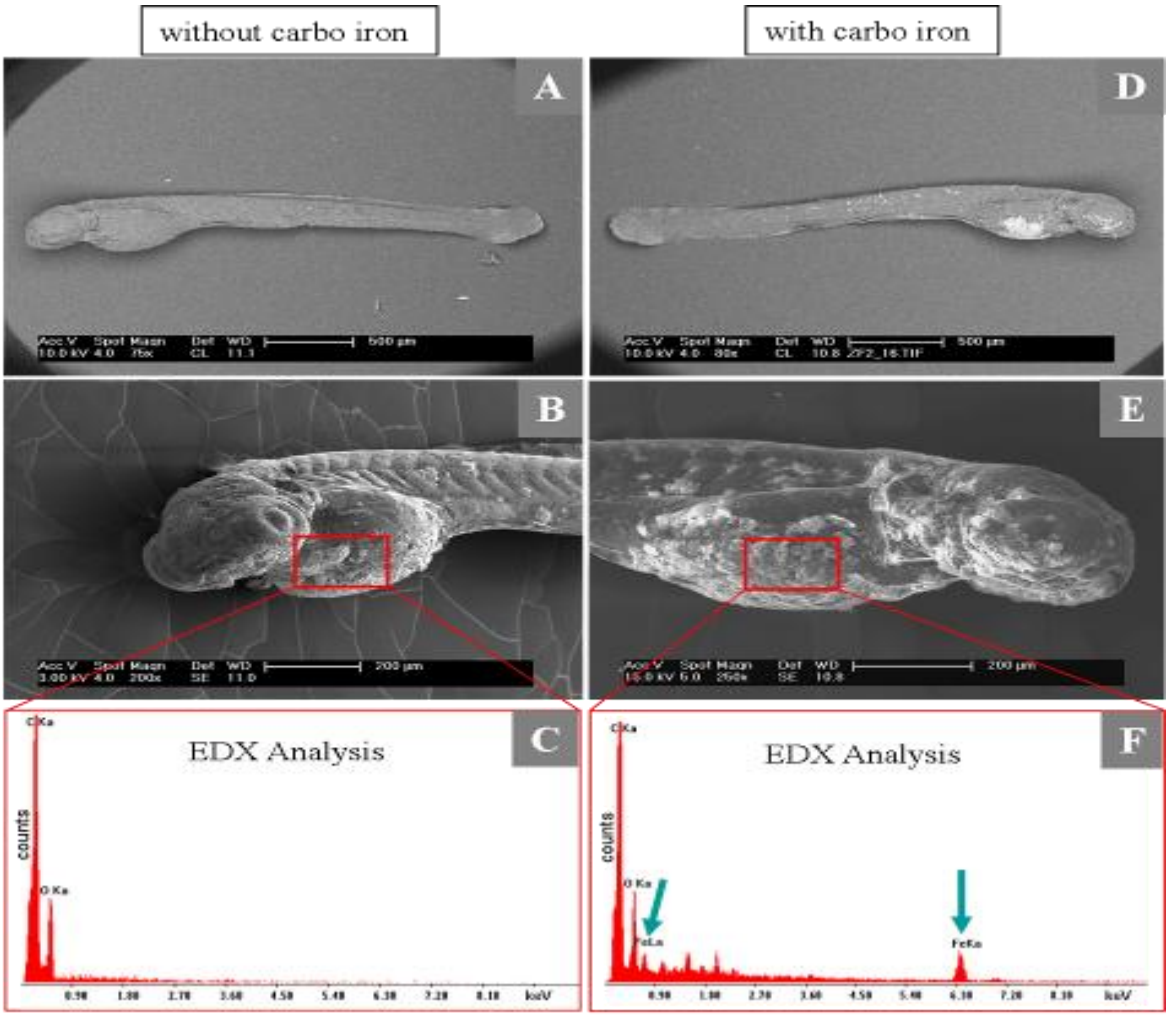

Figure 1: Zebra fish embryos (96 hours old) incubated without (Figure A – C) and with (Figure D – F) carbo iron.
a.) Back scatter electron (BSE) image of zebra fish embryo incubated without carbo iron.
d.) BSE image of zebra fish embryo incubated with carbo iron; Different BSE signal intensity on discontinuous distributed surface areas (different “material contrast”).
b.) Secondary electron (SE) image of zebra fish embryo incubated without carbo iron; plaque like depositions on the surface area (breast and head region) visible.
e.)SE image of zebra fish embryo incubated with carbo iron; also plaque like depositions on the surface area (breast and head region) visible.
c.)EDX analysis (red rectangle in B): shows only peaks for C and O.
f.)EDX analysis (red rectangle in E): besides the peaks for C and O there are also peaks for Fe (arrows) with is the active component of the carbo iron.

Nanomaterials, Environment, Nanotoxicology & Health

MIM.3.P038

Interactions of ingested tungsten (WO_X) nanofibers with a model digestive gland tissue studied by SEM/EDS and FTIR

S. Novak[1], D. Drobne [1,2,3], L. Vaccari[4], M. Kiskinova[4], P. Ferraris[4], G. Birarda[5], M. Remškar[6] M. Hočevar[7], A. Millaku[8]

[1]Biotehnical faculty, Department of Biology, Ljubljana, Slovenia
[2]Centre of Excellence, Advanced Materials and Technologies for the Future, Ljubljana, Slovenia
[3]Centre of Excellence, Nanoscience and Nanotechnology (Nanocentre), Ljubljana, Slovenia
[4]Sichrotrone Trieste, Trieste, Italy
[5]Lawrence Berkeley National Laboratory, California, United States
[6]Jožef Stefan Institute, Condensed Matter Physics Department, Ljubljana, Slovenia
[7]Institute of Metals and Technology, Ljubljana, Slovenia
[8]Limnos-Company for Applied Ecology, Ljubljana, Slovenia

sara.novak@bf.uni-lj.si
Keywords**:** tungsten nanofibers, digestive gland cells, Fourier transform infrared spectroscopy, Scanning electron microscopy, Energy dispersive x-ray spectroscopy

Tungsten nanofibers, whiskers or needles are recognised as biologically reactive [1]. We study deviations in molecular composition between normal digestive gland tissue and digestive gland tissue of WO_x nanofibers (nano-WO_x) fed test organism *Porcellio scaber* with synchrotron based Fourier transform infrared (FTIR) spectroscopy. The FTIR analyses were supplemented by toxicity and cytotoxicity analyses. We also study interaction of ingested tungsten nanofibers with epithelial cells of digestive tube of test animals by scanning electron microscopy (SEM) and by energy dispersive x-ray spectroscopy (EDS).

The differences in the FTIR spectra of the WO_x-treated and control cells showed up in the central region of the digestive cells and are related to a changed protein to lipid ratio, lipid peroxidation and structural changes of nucleic acids. The conventional toxicity parameters failed to show toxic effects of nano-WO_x. Cytotoxicity biomarkers indicate sporadic effects of WO_x nanofibers. Scanning electron microscopy reviled that when the nanofibers entered the digestive system in some areas they react physically with epithelial cells of digestive tube leading to trusting of nanofibres into the cells (Figure 1). Energy dispersive x-ray spectroscopy confirmed presence of tungsten in cells trusted fiber-like structures (Figure 2).

The FTIR results obtained in our study are in agreement with toxicological and cytological measurements, which indicate that ingestion of nano-WO_x does not affect severely the cell membrane stability and feeding behaviour. However, nanofibers can cause injuries on the epithelial cells of digestive gland tube. Scanning electron microscopy results suggest that physical forces of peristaltic may have important role in nanofiber digestive/intestinal cell interactions what could not be predicted *in vitro*.

1. P. Leanderson and W. Sahle. Formation of Hydroxyl Radicals and Toxicity of Tungsten-Oxide Fibers. *Toxicol in Vitro* 1995, 9(2):175-183.

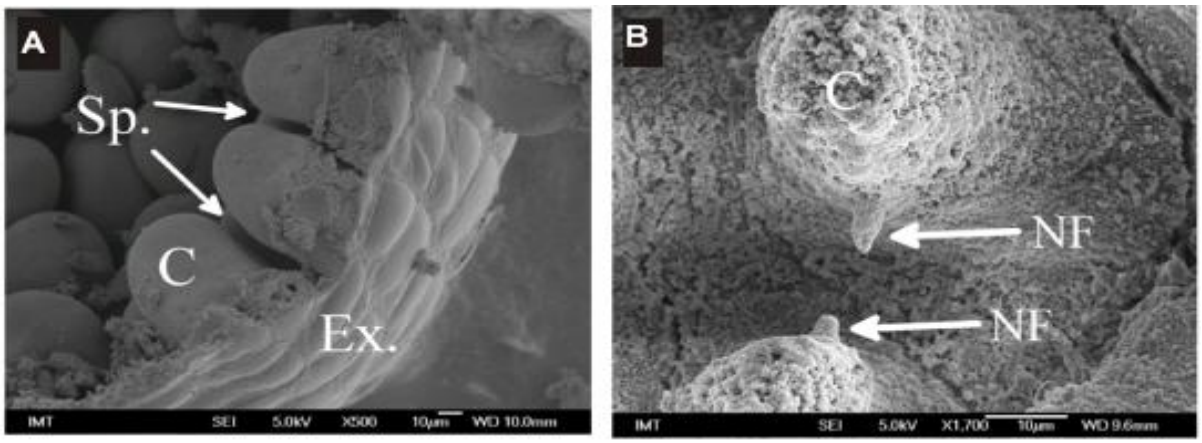

Figure 1. a) Part of digestive gland of control animal where spaces (Sp.)between cells are shown. (Ex.-external part of gland). b) Digestive gland cells (c) with trusted tungsten nanofibers (NF).

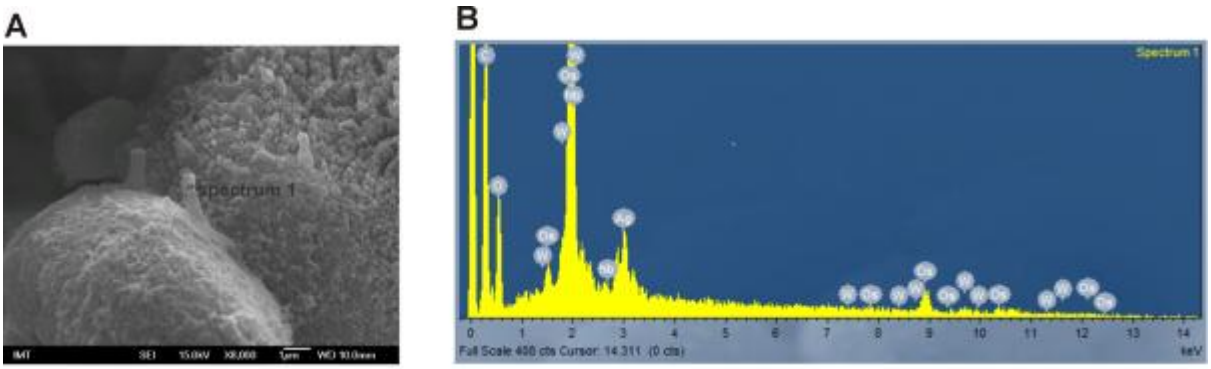

Figure 2. a) digestive gland cell with trusted nonofibers where EDS spectra was taken. b) EDS spectra confirming presence of tungsten in nanofiber trusted in the cell (spectrum 1 in figure A).

Nanomaterials, Environment, Nanotoxicology & Health

MIM.3.P039
TEM investigations of the sintering behavior of noble metal nanoparticles

M. Faulhaber[1], P. Müller[1], R. Schneider[1], K. Gao[2], M. Seipenbusch[2], D. Gerthsen[1]

[1]Karlsruhe Institute of Technology, Laboratory for Electron Microscopy, Karlsruhe, Germany
[2]Karlsruhe Institute of Technology, Institute for Mechanical Process Engineering and Mechanics, Karlsruhe, Germany

matthias.faulhaber@partner.kit.edu

Supported catalysts such as Pt or Pd deposited on an oxide carrier like, e.g., silica are widely used in chemical industry today. However, sintering of the noble metal nanoparticles (NPs) results in severe deactivation of the active metal phase. To enhance the stability of the catalyst particles, a comprehensive understanding of the kinetics of NP growth is crucial. For Pd NPs Binder and Seipenbusch [1] proposed three different mechanisms of ripening, based on the theoretical description by Wynblatt and Gjostein [2, 3]. According to literature [4] the dominant factors for particle growth at low temperatures or short times are surface migration, collision, and coalescence of particles of nearly equal size. This process as illustrated in Fig. 1a is also known as Smoluchowski ripening. Smoluchowski ripening is competing with the process of Ostwald ripening, where an atomic transport from small particles to larger ones takes place resulting in a reduction of the total surface energy of the system. This interparticle transport was described by Wynblatt and Gjostein [3] and is sketched in Fig. 1b. Goal of the present research was to investigate the influence of annealing temperature on the contact angle between NP and surface of the carrier material, surface-migration velocity, and surface-collision frequency of the NPs. This would gain insight into the deactivation process of the active phase of supported noble metal catalysts.

Pt NPs supported on Al_2O_3, TiO_2, and SiO_2 carrier particles were chosen as model system to study the sintering behavior at temperatures from 100°C to 800°C. The Pt/carrier particle systems were fabricated in the gas phase by chemical vapor synthesis (CVS) and metal-organic chemical vapor deposition (MOCVD) at atmospheric pressure. The size distribution and number density of Pt NPs were controlled by the concentration of Pt precursor and the partial pressure of O_2 in the gas phase during the CVS process. Pt/Al_2O_3 and Pt/SiO_2 nanostructures were deposited on Si_3N_4 grids with a foil thickness of 20 nm for transmission electron microscopy (TEM). The NPs were characterized *ex-situ* after annealing in nitrogen atmosphere and *in-situ* in the microscope. For the *in-situ* TEM measurements, Pt/Al_2O_3 and Pt/SiO_2 samples were heated from room temperature to the desired annealing temperature (100 °C to 800 °C) under high vacuum in a Philips CM200 FEG/ST transmission electron microscope. TEM bright-field (BF) images were taken at a frequency of $1min^{-1}$ to determine the surface-migration velocity and contact angle between the noble metal NPs and the support.

Smoluchowski ripening was observed both for *ex-situ* and *in-situ* heat treatment. The change of Pt-NP size distribution at different temperatures and the average surface-migration velocity were measured. Fig. 2 shows exemplarily the results of the Pt/SiO_2 system examined *ex-situ* after intervals of two hours of annealing at 600 °C in an N_2 atmosphere. Annealing of Pt catalyst NPs on SiO_2 carrier particles results in a measurable increase of NP sizes, which can be observed in the TEM images given in Fig. 2. Histograms of the relative frequency distribution q_0 of NP sizes after the corresponding annealing times are also illustrated in Fig. 2. The relative frequency is given by $q_0=n_i/(N\cdot\Delta x_i)$ where n_i denotes the number of NPs within a distinct size interval with a width Δx_i (here 0.5 nm) and N the total number of NPs. A significant shift of the maxima from about 2.5 nm (0 h) towards larger particle sizes of about 4.5 nm (8 h) can be observed, which demonstrates the ripening process of the catalyst NPs. The analysis of the contact angle between Pt and silica from high-resolution TEM images is subject of current investigations.

1. A. Binder and M. Seipenbusch, Applied Catalysis A: General 396 (2011) 1-7.
2. P. Wynblatt, N.A.Gjostein, Acta Metallurgica, 24 (1976) 1165-1174.
3. P. Wynblatt, N.A. Gjostein, Acta Metallurgica, 24 (1976) 1175-1182.
4. J.P.F. Harris, International Materials Reviews, 40 (1995) 97-115.
5. This work was supported by the Land of Baden-Württemberg, Germany and Joint-Lab IP³, BASF, SE.

Figure 1. Schemes describing the processes of a) Smoluchowski ripening and b) Ostwald ripening.

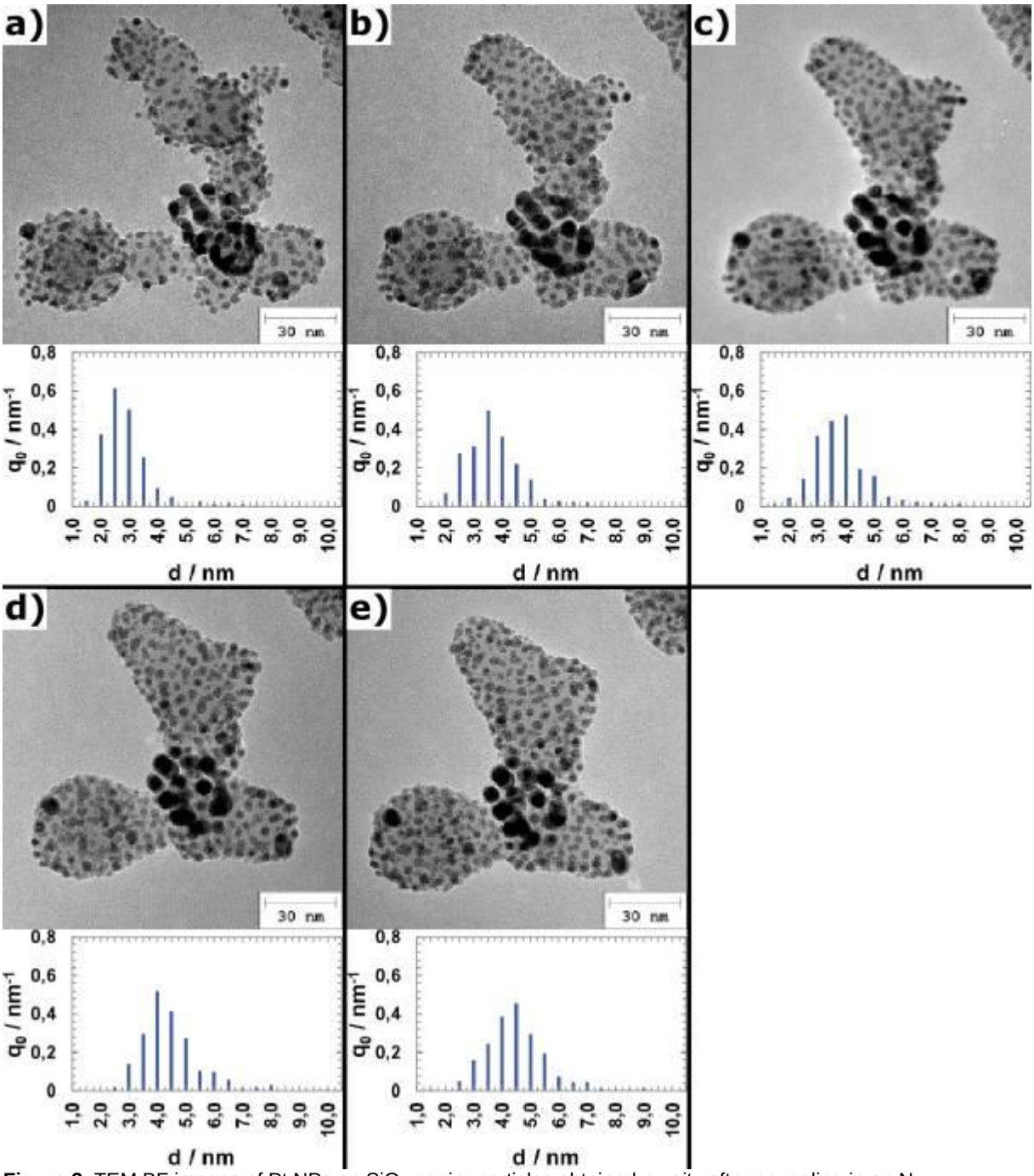

Figure 2. TEM BF images of Pt NPs on SiO_2 carrier particles obtained *ex-situ* after annealing in an N_2 environment at 600°C and corresponding frequency distribution of NP sizes after (a) 0 h, (b) 2 h, (c) 4 h, (d) 6 h, and (e) 8h.

Nanomaterials, Environment, Nanotoxicology & Health

MIM.3.P040
Low voltage TEM - new tool for nanoparticle characterization

M. Drsticka[1], J. Nebesarova[2,3], M. Vancova[2], T. Bily[2,4], E. Coufalova[1], P. Stepan[1]

[1]DELONG INSTRUMENTS a.s., R&D, Brno, Czech Republic
[2]Biology Centre ASCR, v.v.i., Lab. electron microscopy, Ceske Budejovice, Czech Republic
[3]Charles University in Prague, Faculty of Science, Praha, Czech Republic
[4]Univ. South Bohemia, Faculty of Science, Ceske Budejovice, Czech Republic

nebe@paru.cas.cz
Keywords: nanoparticles, nanotubes, low voltage TEM,

The characterization of the morphology of nanoparticles and nanotubes is becoming a growing task in last few years. The two well established techniques of electron microscopy (EM), scanning electron microscopy (SEM) and transmission electron microscopy (TEM) are suitable for imaging and measuring the morphology of materials including nanoparticles [1]. All the main problems involving imaging nanoparticles are well addressed. Some of the issues concerning the applicability of EM are particle-vacuum compatibility, core-shell nanoparticles, and/or low Z-contrast materials.

An electron microscopy technique using low energy electron beam in TEM and STEM modes to improve low Z materials contrast is available. Decreased working energy leads to higher scattering of electrons in the sample and thus to increased contrast [2, 3, 4, 5].

As light elements scatter imaging electrons very little, weak contrast at low Z materials is one of the EM applicability issues for biological and polymer samples as well as nanomaterials. Stronger scattering to increase contrast can only be achieved in two ways:

- Staining techniques that result in an increased contrast, thus improving the image, however also create artefacts, structures that do not belong to the object of interest.
- Decreasing the electron energy.

DELONG has designed a TEM (LVEM5) with markedly reduced electron beam energy (5 keV) [6, 7, 8]. Recently, this microscope can be equipped with a double projector lens system that fully exploits the resolution power of the objective lens. The parameters of the basic model (magnification of 202,000×, resolution of 2 nm) have thus been improved to magnification of 700,000× and resolution of 1.2 nm.

The sample thickness for this technology shall be as low as 10 – 50 nm, which makes it suitable for nanoparticles or nanotubes characterisation. On the other hand the sample thickness might be an important consideration limit due to the reduced transparency of slow electrons through the object.

We used LVTEM for characterisation of nanoparticles and nanotubes (shape, size and size distribution). The critical step proved to be specimen preparation due to the tendency of nanoparticle suspensions to create aggregates. We used the method of the indirect carbon evaporation for preparing of supporting films with the thickness about 3 nm. As proved Figure 1., thus prepared carbon film shows smooth, no granular structure in LVTEM with clearly visible nanoparticles or nanotubes. The great advantage is the possibility to visualize the interaction of nanoparticles with e.g. organic ligands, macromolecular complexes, antibodies, without adding of staining agents (Figure 1b.).

In this study it was demonstrated that LVTEM is capable to provide a quick and reliable characterization of the nanoparticles and nanotubes morphology. Due to the high image contrast, nanoparticles and nanotubes made of light elements can be examined. The small size of LVTEM, which is able to operate without any cooling, allows its exploitation as a screening tool for a quick check of prepared nanoparticles close to the site of their production and as a metrological tool for the evaluation of shape and size distribution.

1. http://publications.jrc.ec.europa.eu/repository/bitstream/111111111/26399/2/irmm_nanomaterials%20%28online%29.pdf
2. L. F. Drummy, H. Koerner,K. Farmer, A. Tan, B. L. Farmer, and R. A. Vaia, J. Phys. Chem. B (2005), 109, p. 17868-17878
3. M. Bendayan, D. Gingras, E. Ziv,Y. S., MICROSCOPY RESEARCH AND TECHNIQUE (2008)
4. M. N. Tchoul, S. P. Fillery, H. Koerner, L. F. Drummy, F. T. Oyerokun, P. A. Mirau, M. F. Durstock, R. A. Vaia, Chem. Mater., 22 (5) (2010)
5. A. Tesfai, B. El-Zahab, A. T. Kelley, M. Li, J. C. Garno, G. A. Baker, I. M. Warner, ACS Nano VOL. 3, No. 10, (2009).
6. Delong et al. Proc. EUREM 12, I197 (2000)
7. Coufalova and Delong. Proc. EUREM 12, I183 (2000)
8. Štěpán and A. Delong. Proc. EUREM 12, I195 (2000)

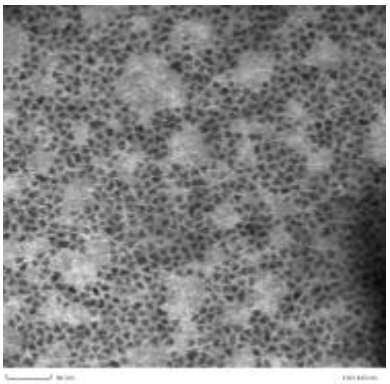

a.) 6nm CdSE NPs on a thin C film.

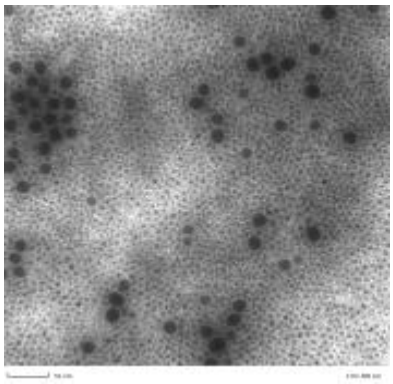

b.) Fe NP with Oleylamine ligands on a thin C film

c.) Multiwall CNTs

d.) Pd nanocubes on a thin C film

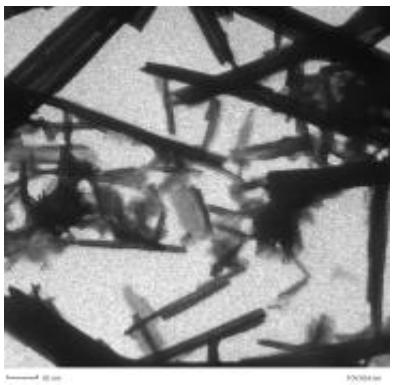

e.) Modified TiO_2 nanotubes

Nanomaterials, Environment, Nanotoxicology & Health

MIM.3.P041

Free vibration analysis of armchair double-walled carbon nanotubes embedded in an elastic medium using nonlocal Euler-Bernoulli beam theory.

Z. Mohamed[1,2], B. Mokhtar [3], D. Tahar Hassaine[1,2], H. Lazreg [1,2], T. Abdelouahed [2]

[1]Ibn Khaldoune , genie civil , Tiaret, Algeria
[2]djillali liabesse, genie civil, Sidi Bel Abbés, Algeria
[3]Béchar , genie civil, Béchar, Algeria

Zidour.mohamed@yahoo.fr
Keywords: nanotube; vibration; armchair

In the present work, nonlocal Euler-Bernoulli beam theory is used to investigate the free vibration response of armchair double-walled carbon nanotube (DWCNT) embedded in an elastic medium. It is noticed in the present study that the equivalent Young's modulus for armchair DWCNT is derived using an energy-equivalent model. The results indicate the dependence of nonlocal effects, the mode number and Winkler modulus parameter on the frequency of DWCNT.

Carbon nanotubes are tubular structures with nanometre diameter and micrometer length. Since the single-walled carbon nanotube (SWCNT) and multi-walled carbon nanotube (MWCNT) are found by Iijima [1]. Recently, considerable attention has been turned to the mechanical behavior of single and multi-walled carbon nanotubes embedded in polymer or metal matrix [2,3]. Vibration and buckling analyses [4-5] of CNTs have shown the employment of Winkler-type elastic foundation for modelling continuous surrounding elastic medium.

Although several studies on the vibration behavior of CNTs have been carried out based on nonlocal Euler-Bernoulli beam theory, no studies can be found for the vibration behavior of armchair CNTs embedded in an elastic medium. In this paper, nonlocal Euler-Bernoulli beam theory has been implemented to investigate the vibration response of armchair double-walled carbon nanotubes (DWCNTs) embedded in an elastic medium.

The general equation for transverse vibrations of an (DWCNTs) elastic beam under distributed transverse pressure with the surrounding elastic medium on the basis of nonlocal elasticity. [6,7]

$$\boldsymbol{p}_{12} = \boldsymbol{EI}_1 \frac{\partial^4 \boldsymbol{w}_1}{\partial \boldsymbol{x}^4} + \boldsymbol{\rho A}_1 \frac{\partial^2 \boldsymbol{w}_1}{\partial \boldsymbol{t}^2} - (\boldsymbol{e}_0 \boldsymbol{a})^2 \left(\boldsymbol{\rho A}_1 \frac{\partial^4 \boldsymbol{w}_1}{\partial \boldsymbol{x}^2 \partial \boldsymbol{t}^2} - \frac{\partial^2 \boldsymbol{p}_{12}}{\partial \boldsymbol{x}^2} \right) \tag{1}$$

$$\boldsymbol{f} - \boldsymbol{p}_{12} = \boldsymbol{EI}_2 \frac{\partial^4 \boldsymbol{w}_2}{\partial \boldsymbol{x}^4} + \boldsymbol{\rho A}_2 \frac{\partial^2 \boldsymbol{w}_2}{\partial \boldsymbol{t}^2} - (\boldsymbol{e}_0 \boldsymbol{a})^2 \left(\boldsymbol{\rho A}_2 \frac{\partial^4 \boldsymbol{w}_2}{\partial \boldsymbol{x}^2 \partial \boldsymbol{t}^2} - \frac{\partial^2 \boldsymbol{f}}{\partial \boldsymbol{x}^2} + \frac{\partial^2 \boldsymbol{p}_{12}}{\partial \boldsymbol{x}^2} \right) \tag{2}$$

The parameters used in calculations for the armchair (DWCNTs) are given as follows: the effective thickness of (CNTs) taken to be 0.258 nm [8], the mass density ρ = 2.3 g cm-3 [9] and layer distance h=0.34 nm [10].

Figure 1 show the effect of small scale parameter on the higher vibration response of embedded armchair (DWCNT) with elastic medium modeled as Winkler-type foundation. The aspect ratio L/d is taken as 40. The Winkler modulus ratio parameter (k_W/c) values were taken in the range of 0 – 60. From the figure, it is observed that with increase in $e_0 a$ values, the frequencies obtained by nonlocal Euler-Bernoulli theory become smaller compared to local model. Furthermore, it is seen that as the Winkler modulus ratio parameter increases the frequency ratio increases. This increasing trend is attributed to the stiffness of the elastic medium. Figure 2 it is observed that the nonlocal effects on vibration response are more significant for higher modes of vibration. This is interpreted from the fact that frequency ratio values for higher modes ($k = 3, 4$) are quite less than $k = 1$. This significance of nonlocal effects in higher modes is attributed to the influence of small wavelength for higher modes. For smaller wavelengths, the interactions between atoms are increasing and this leads to an increase in the nonlocal effects. Furthermore, as the Winkler modulus parameter increases, the frequency ratios increase for higher modes except for first mode of vibration. This implies that there is comparatively less effect of elastic medium on higher mode frequency of armchair (DWCNT).

This paper studies the vibration of armchair (DWCNTs) embedded in elastic medium based on the

Euler-Bernoulli beam theory. According to the study, the results showed the dependence of the vibration characteristics on the nonlocal parameter, mode number and surrounding elastic medium. this dependence is attributed to the influence of small wavelength for higher modes. For smaller wavelengths, interactions between atoms are increasing and this leads to an increase in the nonlocal effects. Furthermore, as the Winkler modulus parameter increases, the frequency ratios increase for higher modes.

1. S. Iijima, Nature 354 (1991) 56.
2. C.Q. Ru, J Mech Phys Solids, 49 (2001) 1265.
3. Qian, D., Dickey, E.C., Andrews, R., Rantell, T., Appl.Phys.Lett 76 (2000) 2868.
4. Ranjbartoreh A.R, Ghorbanpour A and Soltani B, Physica E, 39 (2007) 230.
5. Yoon J, Ru C.Q., Mioduchowski A. Int. J. Solids Struct. 43 (2006) 3337
6. B. Reulet, A. Yu. Kasumov, M. Kociak, R. Deblock, I. I. Khodos, Yu. B. Gorbatov, V. T. Volkov, C. Journet, H. Bouchiat, Phys. Rev. Lett. 85, 2829 (2000).
7. H. Heireche, A. Tounsi, A. Benzair, Nanotechnology 19 (2008) 185703.
8. Y. Wu, X. Zhang, A.Y.T. Leung, W. Zhong, Thin-Walled Structures 44 (2006) 667 – 676.
9. H. Heireche, A. Tounsi, A. Benzair, M. Maachou, E.A. Adda Bedia, Physica E 40 (2008). 27911-2799.
10. Z.C Tu, Z.C Ou-Yang, Phys. Rev. B 65, 233407 (2002).

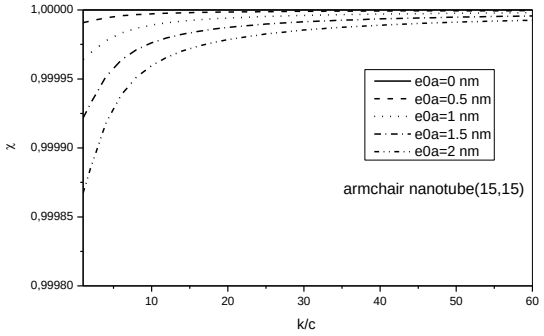

Figure 1: Effect of Winkler modulus ratio parameter on the higher frequency ratio of armchair DWCNT for various small-scale coefficients with ($\boldsymbol{L/d} = 40$ and $\boldsymbol{k} = 6$).

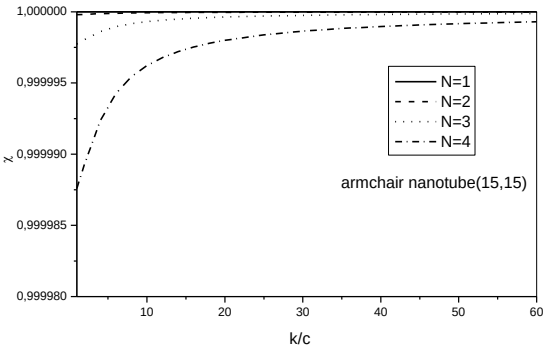

Figure 2: Effect of Winkler modulus ratio parameter on the higher frequency ratio of armchair DWCNT for various mode numbers with ($\boldsymbol{e_0 a} = 2\,\mathrm{nm}$ and $\boldsymbol{L/d} = 40$).

Nanomaterials, Environment, Nanotoxicology & Health

MIM.3.P042
Does ZnO nanoparticle size induce ultrastructural alterations in midgut of *Daphnia magna*?

N. Santo[1], F. Torres[2], N. Guazzoni[2], R. Bacchetta[2], P. Mantecca[3], M. Ascagni[1], P. Tremolada[2]

[1]Università degli Studi di Milano, CIMA, MIlano, Italy
[2]Università degli Studi di Milano, Biosciences, Milano, Italy
[3]Università degli Studi di Milano Bicocca, Environmental Sciences, Milano, Italy

nadia.santo@unimi.it
Keywords: Zinc oxide toxicity, *Daphnia magna*, ultrastructure

The growing use of nanoparticles (NPs) in a wide range of applications is inducing the scientific Community to investigate their possible effects on human health and ecosystems. During their life cycle, NPs will enter the environment, and experimental evidences have already shown that exposure to them is associated with an increased number of diseases, not only for aquatic organisms [1], but also for humans [2,3].

NPs have particular properties related to their nanosize. For instance, NPs of Zinc oxide (nZnOs) can protect human skin against UV radiation. For this reason they have a wide use in UV sunscreen products, but not only [4]. The application of this kind of cosmetics may lead to a release of these NPs into the aquatic compartments. Previous studies have reported the cytotoxic and teratogenic potential of nZnOs on aquatic organisms [4,5].

We used the water flea *Daphnia magna* to study ZnO effects *in vivo*, looking at the morphological alterations, the internalization patterns and the cellular localization of two differently sized ZnO particles.Five different nanoZnO suspensions (0.1, 0.33, 1, 3.3 and 10 mg/L) were tested. The results of the 48-h acute toxicity tests performed with ZnO < 100 nm (bZnO) and ZnO < 50 nm (sZnO), expressed as Immobilization Concentration (IC), showed slight effects with IC_{50} values of 3.1 and 1.9 mg/L for bZnO and sZnO, respectively. Specimens exposed to 1 and 3.3 mg/L have been analysed by transmission electron microscopy and nZnOs from both concentrations have been found into midgut cells: *i*) in the microvilli, bound to the cellular membrane; *ii*) in endocytic vesicles near the upper cell surface; *iii*) in some endosomes, as well as in mitochondria, in multivesicular and multilamellar bodies; *iv*) into the nucleus; *v*) free in the cytoplasm; *vi*) in the paracellular space between adjacent cells; *vii*) into the folded basal plasma membrane, and *viii*) in the gut muscolaris (Figure 1), suggesting that not only both nZnOs are able to interact with the plasmatic membranes of *D. magna* enterocytes, but also that they are capable to cross epithelial barriers. The ultrastructural changes increased with increasing concentrations and the worst morphological fields came from samples exposed to 3.3 mg/L of both nZnOs. No significant differences between the two nanomaterials have been detected. Particle size distribution inside cell compartments was very similar, only the intensity of the effect changed between the two nanoparticles (IC_{50} values were significantly different: χ^2=4.63, n=240, P<0.031). Data from ICP-OES analyses demonstrated that the maximum Zn^{++} concentration in our tested suspensions was 0.137 mg/L, which is below the reported NOEC for nZnO, suggesting that nZnO toxicity is not directly driven by the solubilized ions in the test solution. The large presence of NPs inside the midgut cells after only 48-h exposure to nZnOs and their effects on the intestinal barrier highlighted the toxic potential of these nanomaterials also suggesting that studies of chronic effects are needed.

1. H. Ma, P.L. Williams and S.A. Diamond, Environmental Pollution 172 (2013), p. 76.
2. C.A. Pope, R.T. Burnett, M.J. Thun, E.E. Calle, D. Krewski, K. Ito and G.D. Thurston, JAMA 287 (2002), p. 1132.
3. G. Oberdörster, E. Oberdörster and J. Oberdörster, Environmental Health Perspectives 113 (2005), p. 832.
4. K. Wiench, W. Wohlleben, V. Hisgen, K. Radke, E. Salinas, S. Zok and R. Landsiedel, Chemosphere 76 (2009), p. 1356.
5. X. Zhu, J. Wang, X. Zhang, Y. Cahng and Y. Chen, Nanotechnology 20 (2009), p. 195.

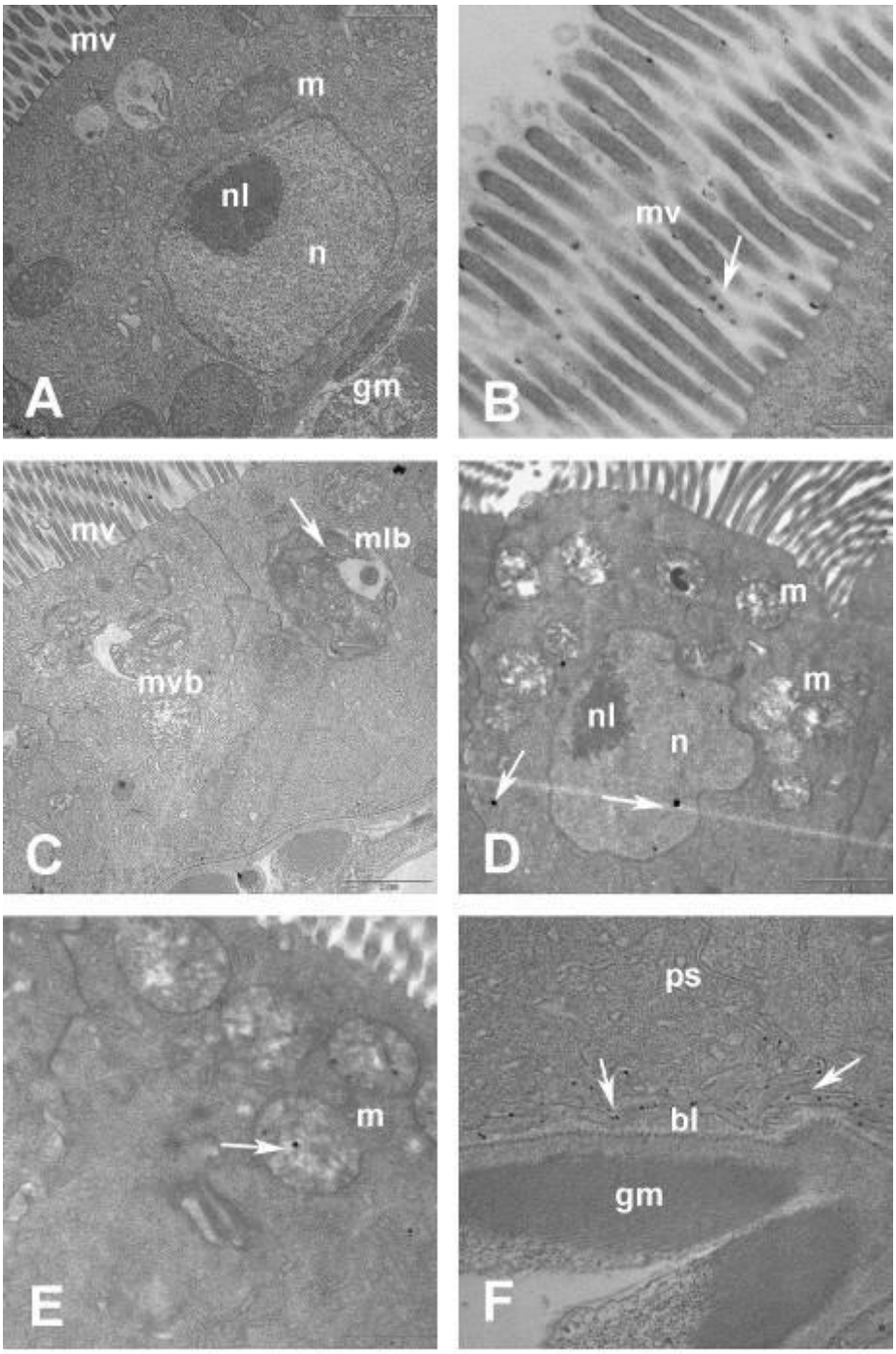

Figure 1. Ultrastructural analysis of enterocytes of 48-h D. magna. Control (A) and 1 and 3.3 mg/L exposed individuals (B-F) have been analysed by transmission electron microscopy and nZnOs from both concentrations have been found in different parts of the enterocyte: e.g into the microvilli (B), bound to the cellular membrane; in multivesicular and multilamellar bodies (C); into the nucleus and free in the cytoplasm (D); into the mitochondria (E); in the paracellular space between adjacent cells and into the folded basal plasma membrane (F). bl basal laminae, gm gut muscolaris m mitochondria, mlb multilamellar bodies, mv microvilli, mvb multivescicular bodies, n nucleus, nl nucleolus, ps paracellular space. The arrows indicate nanoparticles

Nanomaterials, Environment, Nanotoxicology & Health

MIM.3.P043
Size effects on the Mossbauer and Magnetic properties of Cobalt ferrite nanoparticles

K. Batoo[1]

[1]King Saud University, King Abdullah Institute for Nanotechnology, Riyadh, Saudi Arabia

Khalid.mujasam@gmail.com

Ferrimagnetic oxides may contain single or multi domain particles and they convert into superparamagnetic state near a critical size. To explore the existence of these particles $CoFe_{2-x}Cu_xO_4$mixed ferrite nanoparticles of different sizes were prepared through citrate-gel method. The structural aspects of the samples were explored by a wide variety of experimental techniques namely, X-ray diffraction, field emission transmission electron microscopy, vibrational sample magnetometery and Mössbauer spectroscopy. XRd analysis confirmed that grown ferrite samples are in single phase without any additional undesirable phase corresponding to any structure. The high crytslline order of the samples was further confirmed by SAED patter. The avergare crystallite size of the sampels has been found in the range 23 to 42 nm. The magnetic and Mössbauer properties were found strongly dependent on size. The saturation magnetization (Ms) increased with the growth of the grain size while the coercitivity decreased. The Mossbauer spectrum is fitted with two broad sextets confirming that Fe is in 3+ valence state in the grown nanoparticles.
.

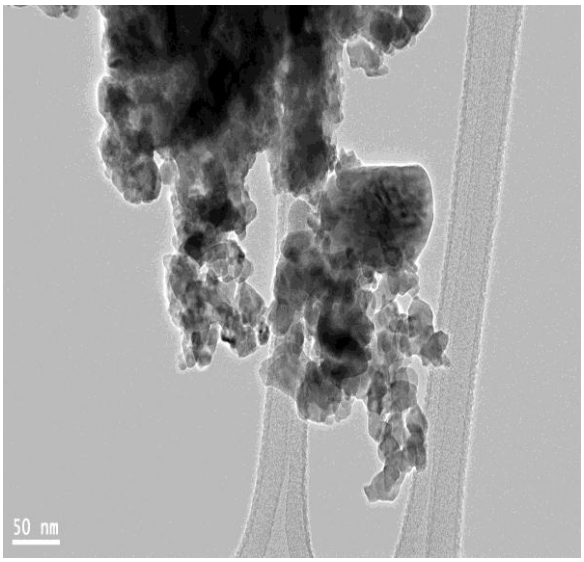

Figure 1.

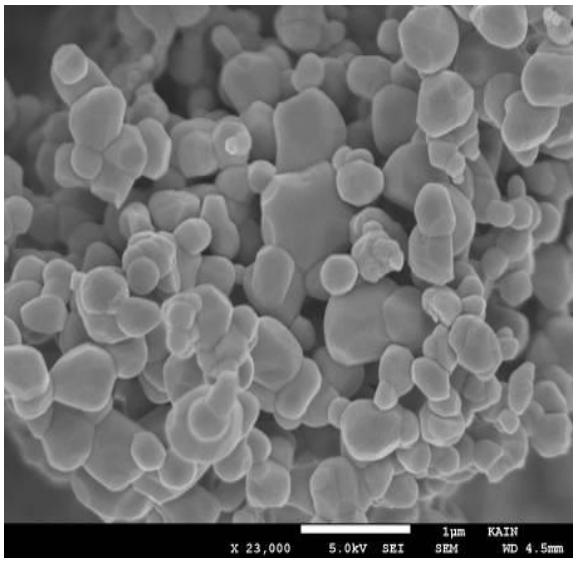

Figure 2.

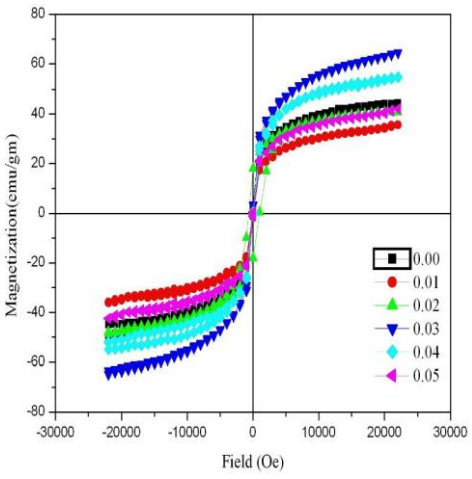

Figure 3.

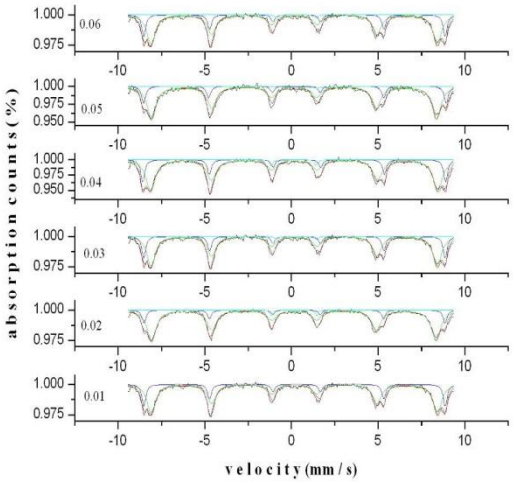

Figure 4.

Nanomaterials, Environment, Nanotoxicology & Health

MIM.3.P044
Unbiased estimation of surface area of single gold nanostars

D. Vanhecke[1], L. Rodriguez-Lorenzo[1], C. Kinnear[1], B. Rothen-Rutishauser[1], A. Petri-Fink[1]

[1]Adolphe Merkle Institute, Bionanomaterials Group, Marly, Switzerland

Dimitri.Vanhecke@unifr.ch
Keywords: gold nanostars, electron tomography, design-based stereology, local geometry

Chemical and physical properties of anisotropic metal nanoparticle (NP) are strongly dependent on geometrical factors such as shape and volume [1,2]. Knowledge of such factors is required to adjust the desired properties, e.g. in catalytic and biological applications. Especially the surface area is important: since reactions take place on the surface, the surface area is a major parameter for the assessment of the activity of particles. The 3D complex morphology of anisotropic NP adds to the difficulty to evaluate these parameters as well as the resolution limit of typical characterization techniques.

Transmission electron microscopy delivers a direct and open view of any object, as long as it is small enough (usually < 100nm). The output of its add-on technique, electron tomography, is a digital three-dimensional (3D) dataset that can be sliced at random angles *in silico*. Such slices are known as independent uniform random (IUR) slices, which can be directly used by a set of geometrical tests for the estimation of morphometric parameters of 3D objects based on measurements made on 2D sections (stereology) [3]. Such stereological analysis of Au nanostars [4,5] yielded local characteristics for each randomly chosen particle. Besides volume and surface area [6], other local factors such as curvature [7] could are easily estimated. The basic geometrical estimates related well to data obtained by thresholding and rendering. However, thresholding methods took longer, required smoothing algorithms and where biased due missing edge noise effects. The determination of the surface area by means of electron tomography followed by stereological estimation provides a basis to establish a relationship between surface factors (surface area, curvature, pointyness, ...) and their optical and chemical properties of gold nanostars.

1. P. R. Sajanlal, T. S. Sreeprasad, A. K. Samal, T. Pradeep, Nano Reviews 2 (2011), p. 5883.
2. T. K. Sau, A. L. Rogach, F. Jäckel, T. A. Klar, J. Feldmann, Advanced Materials 22 (2010), p. 1805.
3. Vanheck D, Studer D, Ochs M, Journal of Structural Biology Volume 159 (2007), p. 443.
4. L. Rodriguez-Lorenzo, R. A. Álvarez-Puebla, I. Pastoriza-Santos, S. Mazzucco, O. Stéphan, M. Kociak, L. M.
Liz-Marzán, F. J. García de Abajo , Journal of the American Chemical Society 131 (2009), p. 4616.
5. P. S. Kumar, I. Pastoriza-Santos, B. Rodríguez-González, F. J. García de Abajo, L. M. Liz-Marzán, Nanotechnology 19 (2008), p. 015606(1-5).
6. L. Kubínová, J. Janácek, Journal of Microscopy 191 (1998). p. 201.
7. V. Beneš, M. Hlawiczková, K. Voleník, Journal of Microscopy, 200 (2000). p. 26.

Nanomaterials, Environment, Nanotoxicology & Health

MIM.3.P045
Environmental scanning electron microscopy applied to visualize and quantify gold nanoparticle storage in whole, hydrated lung cancer cells

D. Peckys[1], N. de Jonge[1,2]

[1]INM Leibniz Institute for New Materials, Innovative Elektron Microscopy, Saarbrücken, Germany
[2]Vanderbilt University School of Medicine, Nashville, TN, USA, Germany

diana.peckys@inm-gmbh.de
Keywords: whole cell imaging, gold nanoparticles, environmental scanning electron microscopy, scanning transmission electron microscope detector

The interaction of cells with nanoparticles (NPs) is a research field with strongly growing interest. Despite an increasing body of publications on NP uptake, transport, and storage, many fundamental aspects remain poorly understood. One of the main limitations is the difficulty to unite three important requirements for the imaging of NP-cell interactions: a) a resolution sufficient to image NPs, b) intact samples of whole cells, and c) a preparation and imaging protocol with a speed allowing to gain data of multiple regions on multiple cells as needed for quantitative and statistical analysis. The resolution requirement of several nanometers for these types of samples can only be achieved with electron microscopy (EM). Unfortunately, for conventional EM, samples have to be cut into thin sections, which cannot provide suitable data for NP quantifications, because the usual storage compartments of NPs, i.e. intracellular vesicles, are cut at random levels and not at their equatorial plane. In addition, the sample preparation is elaborate and carries the risk for artifacts. Gaining data from a high number of cells would therefore require an impractically long amount of time. Our approach for meeting the three above-mentioned requirements is to reduce the sample preparation to a minimum, similar to methods used in light microscopy, and to image NPs in whole, hydrated cells with a scanning transmission electron microscope (STEM) detector [1]. Imaging is done at 30 kV electron beam energy with an environmental scanning electron microscope (ESEM) equipped with a STEM detector [2]. The unique design of ESEM overcomes the usual EM associated need for a high vacuum and allows to directly image samples in hydrated state in a water vapor atmosphere. Alternatively, the cells can be imaged at 200 kV using a microfluidic chamber in a dedicated STEM [1].

We investigated the storage of uptaken gold nanoparticles (AuNPs) in a total of 176 intact and hydrated lung cancer cells (A549). The focus of the study was to examine if specific features of the AuNPs, such as their size and the presence of bound serum proteins, could affect the intracellular AuNP storage vesicles. Both parameters, AuNP size and presence or absence of serum proteins, have been shown to affect the early phases of AuNPs uptake, but for later periods in time, i.e. >24h after the AuNP uptake, their influence remained unclear [3]. Especially in view of the high potential of AuNPs to serve medical applications, quantifiable data are needed for assessing long-term intracellular storage and/or possible ways of elimination and removal from the cells.

The cells were grown on microchips with thin electron transparent SiN windows. For the AuNP uptake, the cells were incubated with citrate stabilized AuNPs of 10 or 30 nm diameter in cell medium without serum. For experiments with serum proteins, 10, 15 or 30 nm large, citrate stabilized AuNPs were first incubated for 2 h with cell medium supplemented with 10% serum in order to yield serum proteins coated AuNPs. These AuNPs were then diluted in serum containing medium and incubated with the cells. For both groups of AuNPs, with or without serum proteins, the AuNP incubation time was set to 2 h, followed by a 22 or 43 h incubation period under normal cell growth conditions, thus without AuNPs. Subsequently, the cells were fixed, cooled to 3 °C, rinsed with ultrapure water and placed in the ESEM (FEI Quanta 400 FEG). Two detectors were used synchronously: a STEM detector underneath the sample, for the recording of high-resolution images from the AuNPs, and a gaseous secondary electron (GSE) detector above the sample, serving the control of a thin water layer over the cells (see scheme in Figure 1A). The specimen chamber was kept at 3 °C, and was successively filled with saturated water vapor, whereby the chosen pressure settings avoided evaporation. During imaging the pressure was set to 740 Pa.

The image in Fig. 1B shows a group of confluently grown cells, fixed 24 h after they had been incubated with AuNPs of 30 nm diameter without serum proteins. The image was recorded with a low magnification of 2,000 × in order to provide an orienting overview. The randomly scattered distribution of round, electron dense structures in the cells can be seen. The dispersed character of the distribution was in contrast to findings from earlier, similar AuNP uptake studies in live COS7 cells (a monkey kidney fibroblast cell line), were the majority of AuNP storage compartments had gathered in a dense accumulation close to the nucleus [4]. Fig. 1C was taken with a magnification of 50,000 × at the indicated location in Fig. 1B. The image gives insight into the individual vesicles, revealing a mostly uniform density of AuNPs. This uniform intravesicluar distribution points to the adherence of AuNPs at the vesicle membrane, instead of a filling of the whole vesicle volume, and was in agreement with earlier results from COS7 cells [4]. Fig 1D is an exemplary image recorded with a magnification of 50,000 × from a cell that had been incubated under similar conditions but with serum coated AuNPs of 30 nm. The vesicles look very similar to those found with AuNPs without serum proteins. We found similar distributions of AuNPs in the

vesicles and similiar distributions of the vesicles throughout the cells for all images, also those with incubation times of 45 h. For further analysis, the sizes of 1,106 AuNP containing vesicles were determined. A statistical analysis of the size distribution found in each experimental group revealed a significant effect of the AuNP size on the size of the vesicles. The vesicles containing 30 nm AuNPs were on average 80 nm larger than those containing 10 or 15 nm AuNPs. Remarkably, this difference was not found for AuNPs without serum proteins.

These results show that the cellular storage vesicles for AuNPs found after >24 h of incubation can be influenced by the AuNPs themselves, i.e. their size, and this effect is triggered by the presence of serum proteins. Future studies aiming to examine cellular effects of different NP features should therefore also take account of a possible interplay of distinct NP features.

This study exemplifies how STEM detection in an ESEM opens new ways to study intracellular routing mechanisms for nanoparticles with nanometer precision in statistically relevant amounts of intact and minimally processed cells.

1. N. de Jonge, et al., Proc Natl Acad Sci U S A 106 (2009), p. 2159.
2. A. Bogner, et al., Ultramicroscopy 104 (2005), p. 290.
3. T.-G. Iversen, T. Skotland and K. Sandvig, Nano Today 6 (2011), p. 176.
4. D.B. Peckys and N. de Jonge, Nano Lett 11 (2011), p. 1733.

5. We thank M. Koch for help with the experiments, A. Kraegeloh for discussion and support of the experiments, and Protochips Inc, NC, USA for providing the microchips with silicon nitride support windows. We thank E. Arzt for his support through INM.

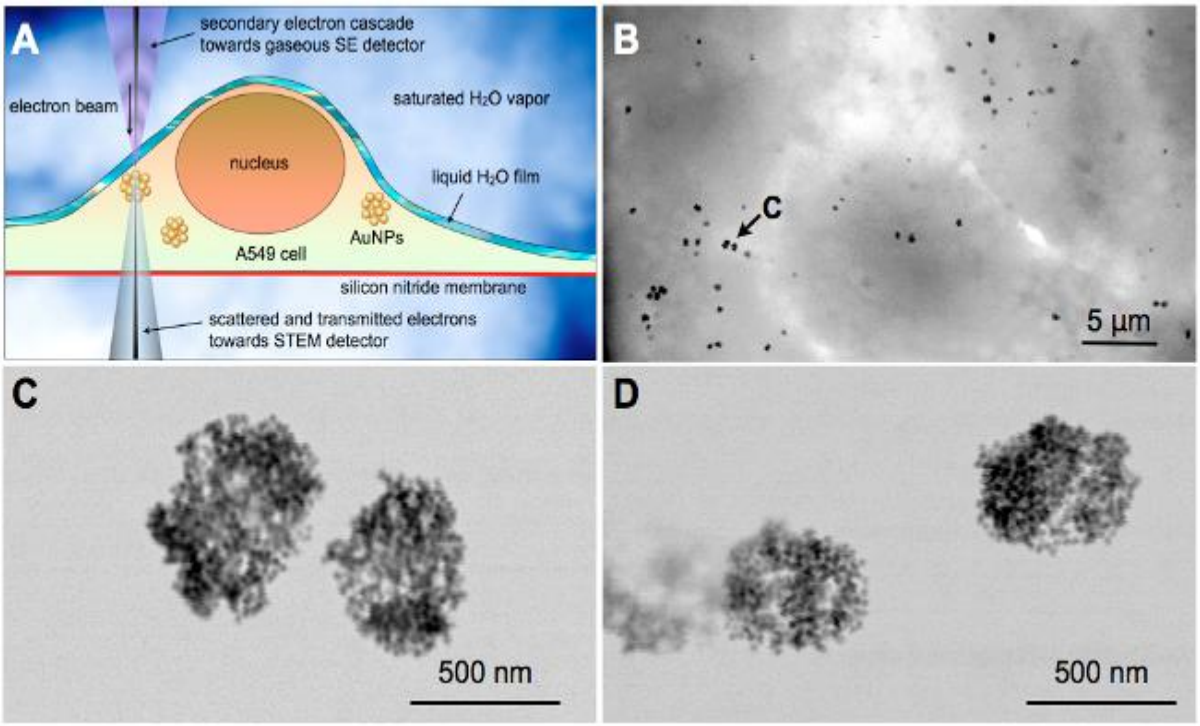

Figure 1. Whole A549 cells were imaged in hydrated state, 24 or 48 h after the uptake of differently sized AuNPs (10, 15 or 30 nm), with or without bound serum proteins A) Schematic representation of environmental scanning electron microscopy (ESEM) of whole cells in wet state. A focused electron beam (30 kV) was scanned over the cell, whereby a gaseous secondary electron detector (GSED), located above the sample, and a scanning transmission electron microscopy (STEM) detector, located beneath the sample, simultaneously collected the signals. B) STEM image showing several cells fixed 22 h after the 2 h during uptake period of 30 nm large AuNPs without serum proteins. The AuNPs concentrated in dark spots, diffusely scattered throughout the cell. C) Detail from a new image recorded with 50,000 × from the 2 vesicles indicated with an arrow in B. AuNPs were dispersed with an almost uniform density within the vesicles, pointing to the adherence of AuNPs at the vesicle membrane. D) Image recorded with a magnification of 50,000 × from a cell incubated under similar conditions as those shown in B and C, except for in the presence of serum proteins on the 30 nm AuNPs. The vesicles show a similar pattern of AuNP distribution.

Nanomaterials, Environment, Nanotoxicology & Health

MIM.3.P046
TEM studies of W/C_{60} mixture prepared in a ball-mill.

I. Perezhogin[1], B. Kulnitskiy[1], A. Grishtaeva[1], S. Perfilov[1], R. Lomakin[1], V. Blank[1]

[1]Technological Institute for Superhard and Novel Carbon Materials, Troitsk, Moscow, Russian Federation

i.a.perezz@gmail.com
Keywords: TEM, tungsten nanoparticles, fullerene

Many of tungsten-based materials are known for their prominent mechanical, thermal end electronic properties. At the present time new tungsten materials are intensely developed and fundamental mechanisms determining most interesting properties of tungsten compounds are actively studied.

In our work the mixture of tungsten nanoparticles powder and fullerene was treated in a ball-mill. The obtained mixture is supposed to be used for the preparation of mechanically tough material by subsequent baking. Tungsten nanoparticles in the precursor powder had size about tens of nm and mostly were faceted. The sample after the treatment was investigated in TEM (JEM2010 with 200kV acceleration voltage) using also EDS, EELS and EFTEM techniques.

Our studies have shown that the sample contains mainly nanoparticles of tungsten, tungsten carbide and minor amount of tungsten oxides nanoparticles (this was established by the crystal lattice analysis in high resolution images and by the EFTEM analysis of nanoparticles) (fig. 1, fig. 2). The size of the particles was approximately the same as in the precursor powder (sometimes smaller particles having size of some nanometers were observed) but almost all of the particles had irregular (non-faceted) shape. Apart of this we observed nanosized fragments of fullerene fcc-lattice (fig. 1). The EEL spectra taken from the carbon surrounding the tungsten nanoparticles also indicated the presence of fullerene. Some of the observed tungsten oxide particles were heterogeneous, and consisted of two different phases of tungsten oxide having different crystal lattices (fig. 2b).

Therefore, the treatment of the tungsten and fullerene in a ball-mill resulted in deformation of the initial nanoparticles and formation of tungsten carbide nanoparticles. The obtained sample represents itself a mixture of tungsten, tungsten carbide nanoparticles and nanosized fullerene lattice fragments with minor amount of tungsten oxides.

Observation of tungsten oxide nanoparticles with complex composition and the examination of their crystallographic features are of a big interest for both the fundamental studies and applications because of the important role of the tungsten oxides in gas sensor devices. It is well known from the scientific literature (see, for example, [1]), that there is a number of tungsten oxide phases with different crystal lattices and different physical properties, and their crystal structure is mostly determined by the content of the oxygen. The presence of two different phases of tungsten oxide in the same nanoparticle testifies complex kinetics of the tungsten nanoparticles oxidation, and can be studied further in order to find more details on this process.

1. M.R. Field, D.G. McCulloch, S.N.H. Lim, A. Anders, V.J. Keast and R.W. Burgess, J. Phys.: Condens. Matter 20 (2008), p. 175216.

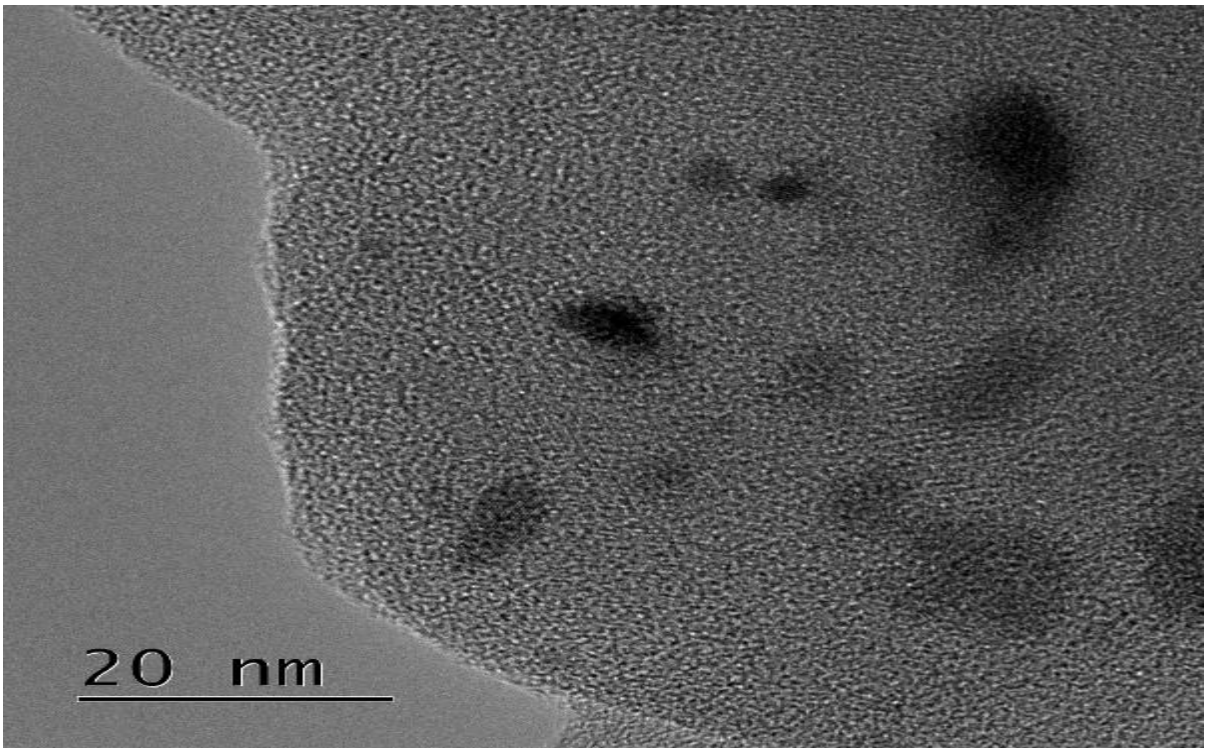

Figure 1. Nanoparticles of tungsten, tungsten oxide and carbide surrounded by nanofragments of fullerene fcc-lattice.

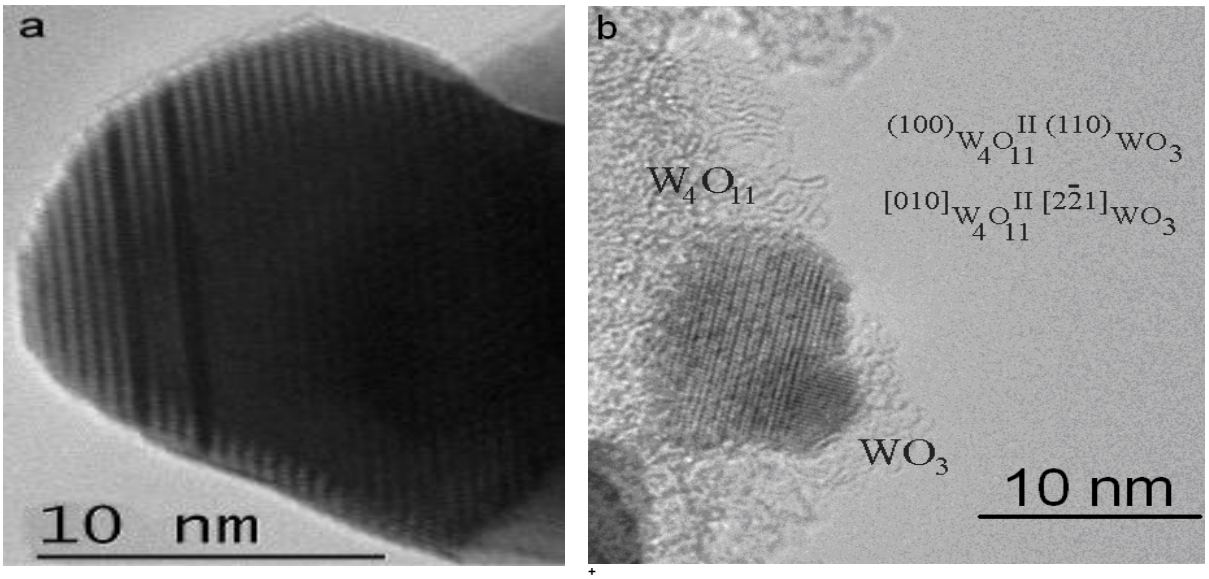

Figure 2. Nanoparticle of □-W_2C (a) and the nanoparticle containing WO_3 and W_4O_{11} (b).

Nanomaterials, Environment, Nanotoxicology & Health

MIM.3.P047
Action of Zinc(II)phthalocyanine free or encapsulated into nanoparticles of poly-e-caprolactone internalized by peritoneal macrophages

A. Santos Franco da Silva Abe[1], E. Ricci-Júnior[2], M. Teixeira Lima Castelo Branco[3], L. de Brito-Gitirana[1]

[1]Federal University of Brazil, Biomedical Sciences Institute - Laboratory of Integrative Histology, Rio de Janeiro, Brazil
[2]Federal University of Brazil, Universitary Pharmacy - Laboratory of galenic development, Rio de Janeiro, Brazil
[3]Federal University of Brazil, Biomedical Sciences Institute - Laboratory of Cell Imunology, Rio de Janeiro, Brazil

amandasantosfranco@gmail.com
Keywords: Zinc(II)phthalocyanine, nanoparticles, macrophages

Nanoparticles (NPs) are promising delivery systems applied in various fields, such as medicine and pharmacy, which exhibit particular properties like elevated reactivity and high penetration ability in living organisms. Zinc (II) pthalocyanine (ZnPc), an antitumor photosensitizer used in the photodynamic therapy (PDT), is known to have phototoxic activity by inducing the production of singlet oxygen, which promotes tumor cell death.

In a previous study, our group has investigated the effect of free and encapsulated ZnPc in nanoparticles (NP) of poly-ε-caprolactone (PCL) on A549 cell line, obtained from lung carcinoma. Since drugs do not interact only with tumor cells in live organism, the present study aimed to analyze the activity of Np, with and without ZnPc, and ZnPc in solution, using peritoneal macrophages from Swiss mice as a model of non-neoplastic cells. Thus, Np were produced using the emulsion and solvent emulsification-evaporation method (SEEM) and characterized by dynamic light scattering (DLS) and transmission electron microscopy (TEM). After cell-drug interaction, assays as MTT, Trypan blue, light microscopy, laser scanning confocal microscopy were performed in order to evaluate the action of free ZnPc and of Np containing or not this active, in the presence or absence of the laser light applied in PDT.

The results indicate that NPs show dimensions that varied between 290 and 350nm, exhibiting rounded shape and smooth or roughening surface (figure 1). The empty NPs of PCL did not affect cell viability, indicating that these nanocarriers are convenient drug delivery systems. Free ZnPc was distributed randomly in the cells, while the nanoencapusulated ZnPc was preferably located near nucleus (figure 2). The concentration of 5 □g/mL of free drug caused greater loss of cell viability in the laser absence compared to the treatment with the nanoencapusulated form of this drug, in the presence or absence of irradiation. However, at concentration of 0.5 □g/mL, free or nanoencapsulated drug promoted cell death to the same extent in cells treated or not treated with laser light. This result demonstrates that ZnPc performance is dose dependent when in solution, but not when it is nanoencapsulated. The laser dose of 50J/cm^2 can promote activation of mitochondrial functioning, but the cells irradiated with this dose and treated with free nanoencapsulated ZnPc displayed morphological changes such as cytoplasmic vacuolization and thinning of cellular extensions (figure 3). These observations indicate that, at high concentrations, ZnPc does not only cause damage in tumor cell lines but also in normal cells, such as peritoneal macrophages.

1. J.W. Pollard. Nature Reviews Cancer v. 4 (2004), p. 71.
2. D. K. Chatterjee, L.S. Fong, Y. Zhang, Advanced Drug Delivery Reviews v. 60 (2008), p. 1627.
3. M.V. Soares, M.R. Oliveira, E.P. dos Santos, L.B. Gitirana, G.M. Barbosa, C.H. Quaresma, E. Ricci Júnior, International Journal of Nanomedicine v. 6 (2011), p. 227.
4. We acknowledge the financial support of FAPERJ and CNPq

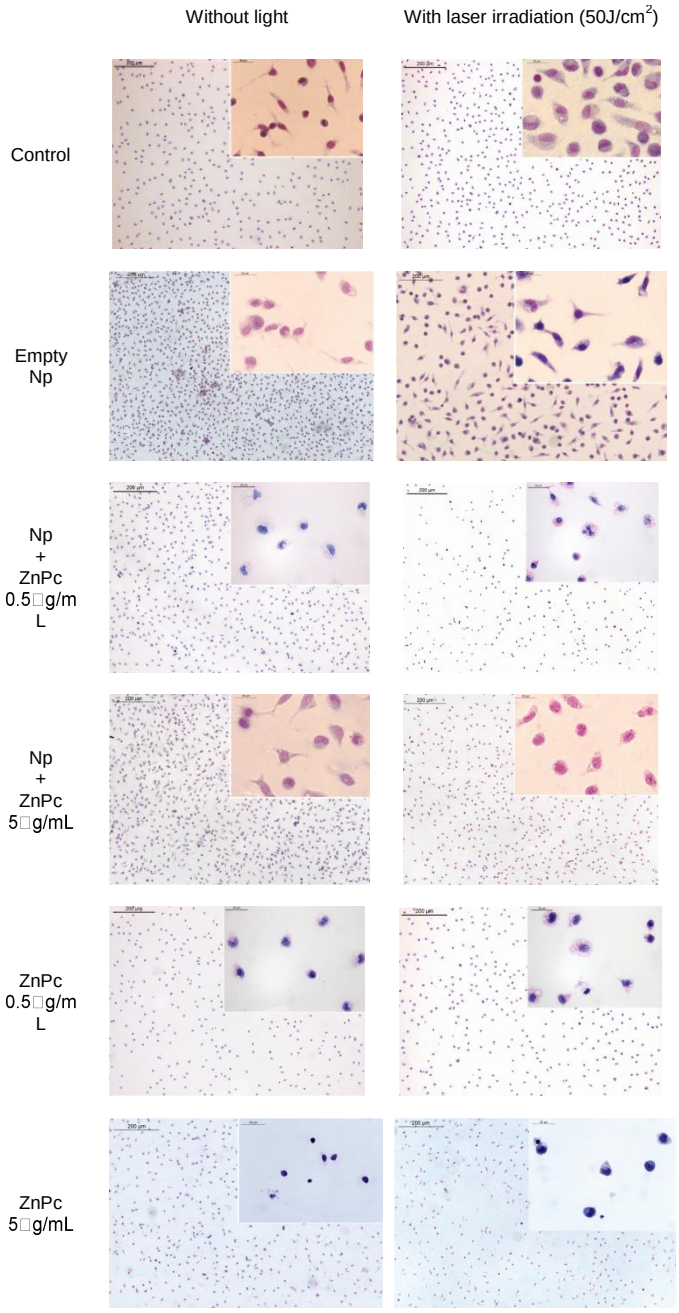

Figure 3. Micrographs of peritoneal macrophages treated with free or nanoencapsulated ZnPc (0.5 or 5μg/mL), in the presence or absence of laser light irradiation (50J/cm^2). There are evident morphological changes (cytoplasmic vacuolization, loss of cellular prolongations), when compared the control cells with those treated with ZnPc and submitted to irradiation.

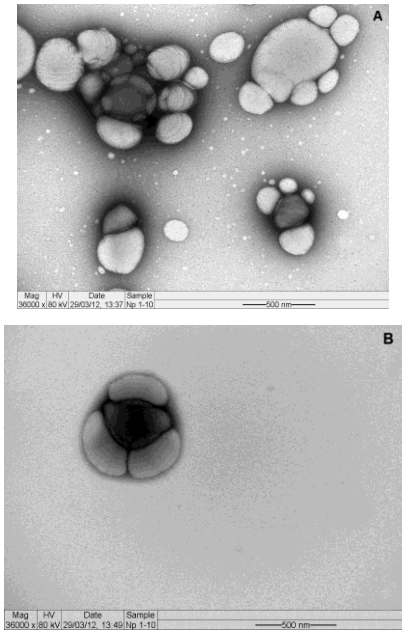

Figure 1. Electron micrographs of poly-ε-caprolactone nanoparticles.
A: empty nanoparticles.
B: Nanoparticles containing ZnPc (5μg/mL).

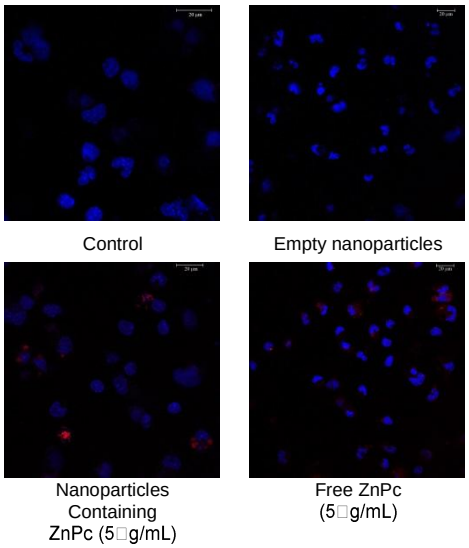

Figure 2. Cellular localization of free and nanoencapsulated ZnPc 5μg/mL (red) compared to the nuclei (blue) of peritoneal macrophages by laser scanning confocal microscopy. NPs containing ZnPc are located preferably near nucleus, while free ZnPc reveals random distribution inside and between cells.

Correlative Microscopy in Life and Materials Science

MIM.4.048
Lights Will Guide You:
Integrated Correlative Microscopy in Life an Material Science

M. Karreman[1,2], A. Agronskaia[2], E. Van Donselaar[2], I. Buurmans[2], T. Verrips[2], B. Weckhuysen[2], H. Gerritsen[2]

[1]EMBL Heidelberg, Cell Biology and Biophysics, Heidelberg, Germany
[2]Utrecht University, Faculty of Science, Utrecht, Netherlands

matthia.karreman@embl.de
Keywords: iLEM, muscle dystrophy, fluid catalytic cracking

Combining the advantages of both fluorescence microscopy (FM) and electron microscopy (EM), correlative microscopy is currently increasingly employed to find answers to a large diversity of scientific questions. Correlative microscopy, however, also poses a number of challenges. A major bottleneck is the keeping track of the regions of interest (ROIs) in both imaging modalities. To overcome this hurdle, the integrated laser and electron microscope (iLEM) was developed [1,2]. Now commercially available as the iCorr™ (FEI Company), this novel imaging tool embodies a custom made FM that is mounted on the side port of a conventional TEM. A single sample is imaged with both microscopes without intermediate transfer or processing steps, allowing for direct and automated correlation between FM and TEM.

The iLEM was employed in the study of Facio Scapulo Humeral Dystrophy (FSHD), the third most common form of muscle dystrophy worldwide. Here, we show how integrated correlative microscopy facilitated to navigate to diseased cells within muscle biopsies of FSHD animal model: mice overexpressing FRG-1 [3], a protein that is candidate to be involved in FSHD pathology. Moreover, the value of iLEM was demonstrated by allowing navigating to FSHD affected cells in patient muscle biopsy samples.

Furthermore, iLEM was employed in the characterization of Fluid Catalytic Cracking (FCC) particles. In industry, the FCC process is employed for the breakdown of large molecules in crude oil fractions to compounds of lower molecular weight that can be used for the production of gasoline. The catalytic bodies employed in this process, FCC particles, are composed of clay, silica, alumina and the main active ingredient: zeolite crystals. Previously, a method was developed to selectively visualize the main catalytically active areas, the Brønsted acid sites in the zeolites. Oligomerization of 4-fluorostyrene at the Brønsted acid sites results in the formation of fluorescent products [4].

The iLEM uniquely allowed to perform a combined structural and functional study of FCC particles: intra- and interparticle differences in activity could be assessed based on fluorescence intensity of the fluorescent probe, and next the ultrastructure of these areas could be studied with TEM [5,6]. We characterized the deactivation processes in FCC particles employed in an industrial FCC Unit. Amongst other features, we revealed a rim of fully inactived zeolite crystals surrounding the FCC particles was revealed. Finally, we propose a model for the structural deactivation of the catalyst particles [5].

1. A.V. Agronskaia, J.A. Valentijn, L.F. Van Driel, C.T.W.M. Schneijdenberg, B.M. Humbel, P.M. Van Bergen En Henegouwen, et al. Journal of Structural Biology 164 (2008),183–189.
2. M.A. Karreman, A.V. Agronskaia, A.J. Verkleij, A.F. Cremers, H.C. Gerritsen, B.M. Humbel. Biology of the Cell 101 (2009), 287–299.
3. D. Gabellini, G. D'Antona, M. Moggio, A. Prelle, C. Zecca, R. Adami, et al. Nature 439 (2006), 973–977.
4 .M.A. Karreman, I.L.C. Buurmans, J.W. Geus, A.V. Agronskaia, J. Ruiz–Martínez, H.C. Gerritsen, B.M. Weckhuysen. Angewandte Chemie International Edition 51 (2012), 1428–1431.
5. M.A. Karreman, I.L.C. Buurmans, A.V. Agronskaia, J.W. Geus, H.C. Gerritsen, B.M. Weckhuysen. Chemistry – A European Journal 19 (2013), 3846-3859

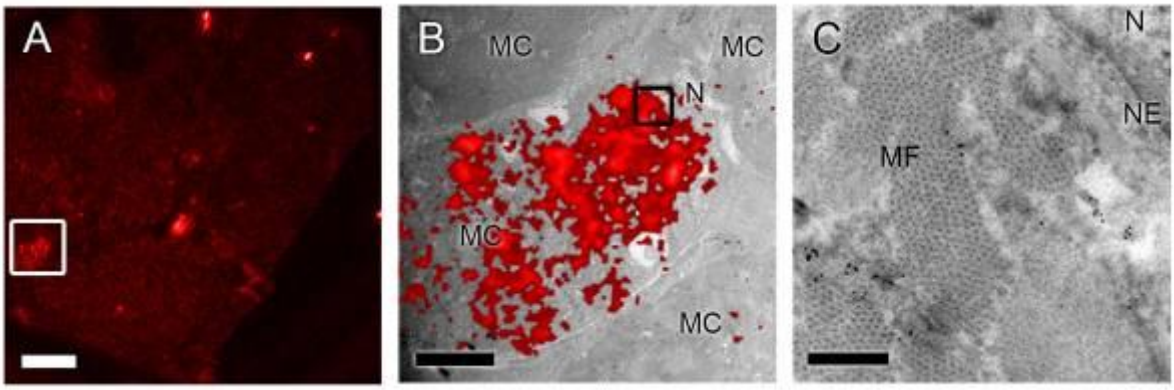

Figure 1. iLEM identifies apoptotic muscle fibers in FRG1 overexpressing mouse muscle biopsies. iLEM imaging of thin 90 nm thawed cryosections of Vastus Lateralis samples, showing high levels of IF and IG labeling for Cleaved Caspase 3. (A) Fluorescence image of an area of 210 x 210 µm on the grid. Note the fluorescence signal from folds in the section and dirt (arrowheads). The fluorescence signals from the areas indicated with the white square are overlaid on TEM images of the same area (B). The images show various muscle cells (MC), and a positively labeled nucleus (N). Panel C shows a high magnification TEM image of the area indicated in panel B. At this magnification the PAG labeling for CC3 becomes apparent. The nuclear envelope (NE) and the muscle fibrils (MF) are indicated. Scalebars represent 30 µm in panel A, 5 µm in panel B and 500 nm in panel C.

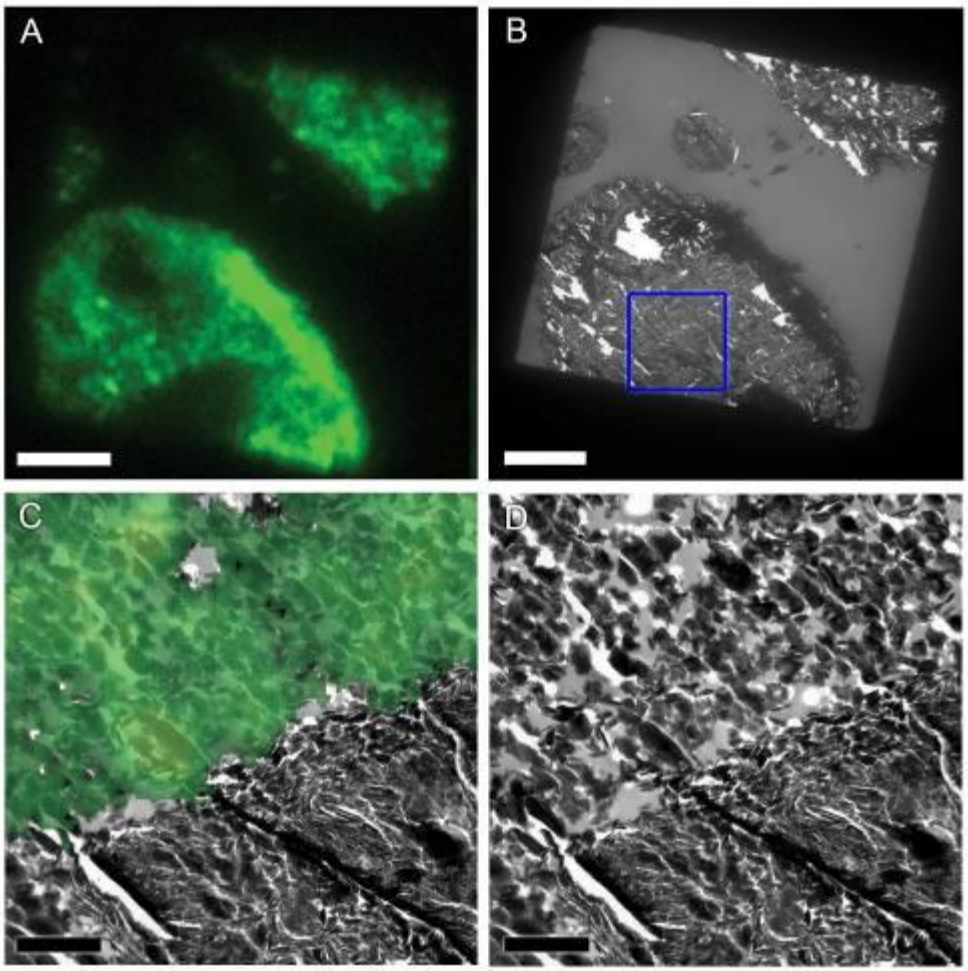

Figure 2. iLEM analysis of a sectioned FCC catalyst particle. A. FM image, B. TEM image, taken from the same region. The area highlighted in panel B with the blue square is shown at higher magnification in panel C, an overlay of a TEM and FM image, and in panel D, the TEM image. Scalebars represent 10 **µ**m in panels A and B and 2 **µ**m in panels C and D [4].

Correlative Microscopy in Life and Materials Science

MIM.4.049

Correlated fluorescence and 3D electron microscopy temporally resolves ultrastructural changes during endocytosis

W.Kukulski[1,2], M. Schorb[1], M. Kaksonen[2,1], J. A. G. Briggs[1,2]

[1]Structural and Computational Biology Unit, [2]Cell Biology and Biophysics Unit, European Molecular Biology Laboratory, Heidelberg, Germany

The application of fluorescence and electron microscopy to the very same specimen has the potential to reveal ultrastructural details of dynamic and rare cellular events. We have developed a correlative approach combining high accuracy of correlation, high sensitivity as well as robustness to permit large dataset collections. Using a fiducial-based correlation, signals of fluorescent proteins can be mapped into 3D electron tomograms. The versatility of the approach was demonstrated by application to various cellular systems. Recently, we used it to describe how the plasma membrane is reshaped during endocytosis in a time-resolved manner. We systematically located 211 endocytic intermediates, assigned each of them to one of nine defined time windows during endocytosis, and reconstructed their ultrastructure in 3D. Combined with a quantitative analysis of the membrane shapes, correlative microscopy allowed us to produce a virtual 4D-movie of how protein-mediated shape changes occur during transition from a plane membrane into a tubular invagination and to scission of a vesicle. This study demonstrates the capability of our simple, robust correlative microscopy approach to answer structure-function related questions in cell biology.

MIM.4.050
Correlative Light and Electron Microscopy (CLEM) for Characterization of Light Converting Inorganic Phosphors

T. Ogbazghi[1], F. Tappe[1], J. Meyer[2], C. Thomas[3]

[1]Hamm-Lippstadt University of Applied Sciences, Department Lippstadt, Lippstadt, Germany
[2]Hamm-Lippstadt University of Applied Sciences, Photonics and Materials Science, Lippstadt, Germany
[3]Hamm-Lippstadt University of Applied Sciences, Micro- and Nanotechnology, Lippstadt, Germany

christian.thomas@hshl.de
Keywords: Solid state lighting, LED, phosphors, correlative microscopic imaging techniques, microstructure, characterization, particle analysis

Light Emitting Diodes (LED) have been introduced in all fields of lighting applications and are increasingly overcoming established technologies. Not only since the prohibition of incandescent lamps within the European Union LEDs are attractive candidates for replacement of classic lighting concepts in the consumer market as they are highly efficient. White LEDs with luminous efficacies of more than 250 lm/W have already been demonstrated [1]. Further advantages of the LED are a long lifetime and their small size, which allows high design flexibility.

Since LEDs are optical semiconductor devices with a well-defined bandgap, they basically emit monochromatic radiation. White LED light can for example be achieved by the combination of two (yellow and blue) or three (red, green and blue) LEDs. But next to other disadvantages the color rendering of this multispectral approach is very low. Higher color rendering indices can be achieved by phosphors which convert the short-wavelength radiation of a blue or UV LED into broad emission bands covering a large spectral range [2].

Next to good color rendering properties, the phosphor materials also have to be very efficient to obtain a high luminous efficacy together with the emitting semiconductor device. To minimize losses, optical absorption should be kept low. This is also important to minimize thermal effects since degradation or other aging artefacts should not occur over the whole lifetime of a LED [3]. Furthermore, sustainable materials should be used for light conversion due to environmental issues. A high uniformity of the phosphor materials over a long time of production is another important demand to ensure a stable LED quality. Therefore, the performance of a LED as shown in Figure 1 strongly depends on the phosphor materials and their microstructure plus its stability during the LED operation.

In this contribution we will present microstructural investigations of light converting inorganic phosphors using light microscopy (LM) and scanning electron microscopy (SEM). Different phosphor materials will be analyzed and changes in the microstructure after light exposure will be shown. Additionally, the advantages of different contrast mechanisms like color, polarization, and dark field imaging in LM combined with backscattered electron imaging or energy dispersive x-ray analysis will be demonstrated. Combining both imaging techniques by the correlative light and scanning electron microscopy (CLEM) enables characterization of identical regions of interest with both microscopes [4,5], whereas this method is very efficient and flexible. As an example Figure 2 shows the same sample area within a distribution of different phosphor particles. In these CLEM images the same particle formation is visible under different contrasts. This technique is very useful to correlate information of the LM (e.g. color, optical activity, particle density) with the visualization and analysis techniques of the SEM (e.g. particle size, surface morphology, cathodoluminescence, element distribution) for a deeper understanding. Furthermore, quantitative data analysis and statistics about the microstructural parameters can be performed effectively now.

1. Cree Inc., http://www.cree.com/news-and-events/cree-news/press-releases/2012/april/120412-254-lumen-per-watt (accessed March 28, 2013)
2. R. Mueller-Mach, G.O. Mueller, M.R. Krames, T. Trottier, IEEE J. Sel. Top. Quantum Electron. 8, no.2 (2002) p.339.
3. R. Mueller-Mach, G.O. Mueller, M.R. Krames, H.A. Höppe, F. Stadler, W. Schnick, T. Jüstel, P.J. Schmidt, Phys. Stat. Sol. A 202, no.9 (2005), p.1727.

4. Ch. Thomas, M. Edelmann, C. Hafner, T. Bernthaler and G. Schneider, Microsc. Microanal. 16, Suppl. 2 (2010), p.784
5. A.F. Elli, Ch. Thomas, Ch. Böker, M. Wiederspahn, Optik & Photonik 7, no.1 (2012), p.32
6. We kindly acknowledge financial support from the “Akademische Gesellschaft Lippstadt” as well as from the “Ministerium für Innovation, Wissenschaft und Forschung des Landes Nordrhein-Westfalen”.

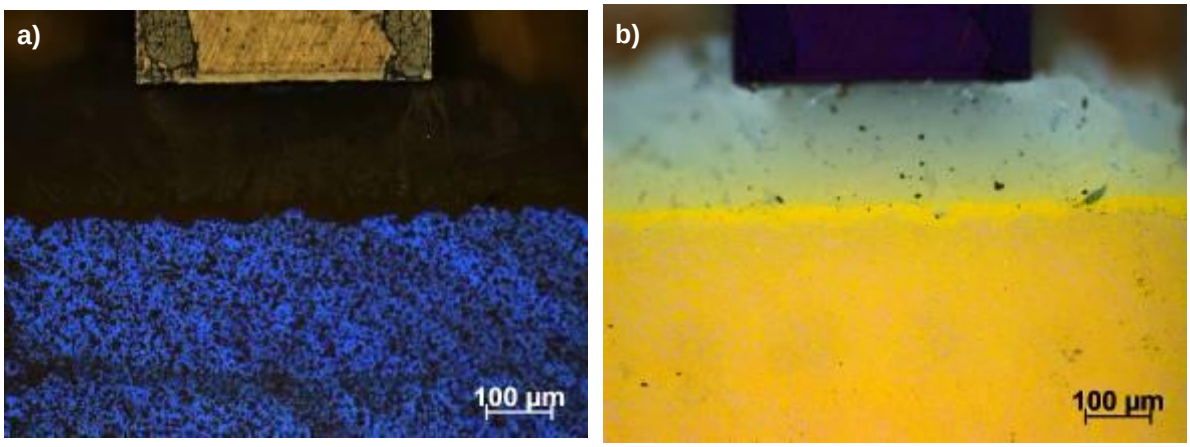

Figure 1. LM images of a LED chip with active area (below) and contact pad (above). a) Brightfield image; b) Polarized light image showing emission from the yellow phosphor.

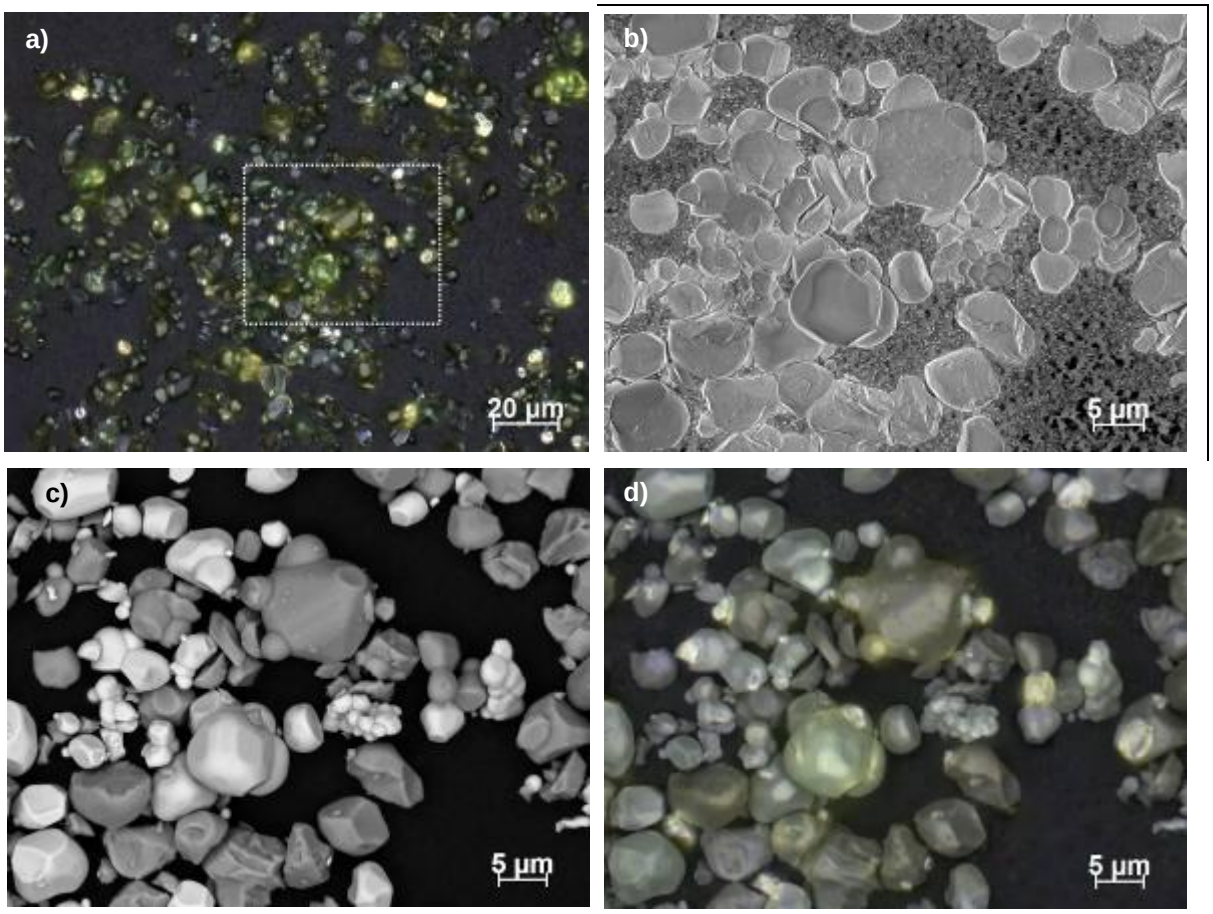

Figure 2. CLEM images of a distribution from inorganic phosphor particles. a) Brightfield LM overview image with color information, dotted rectangle indicates image area of b)-d); b) Inlens SE image showing surface morphology of the particles; c) BSE image with material contrast; d) Overlay of color information and corresponding material contrast.

Correlative Microscopy in Life and Materials Science

MIM.4.051
Correlative Light and Low-Voltage Scanning Electron Microscopy

J. Zeelen[1], C. Schmid[2], M. Grabenbauer[2], R. Schröder[1]

[1]CellNetworks, Bioquant, Universitätsklinikum Heidelberg, CryoEM, Heidelberg, Germany
[2]MPI for Molecular Physiology, Department of Systems Cell Biology, Dortmund, Germany

johan.zeelen@bioquant.uni-heidelberg.de
Keywords: photo-oxidation, fluorescent markers, low-voltage scanning electron microscopy, low loss back-scattered electrons.

Conventional correlative microscopy (CLEM) can be used for a relative localization of fluorescent markers in the combination of light and electron microscopy. The fluorescent signal can therefore be used to identify the regions of interest in the light microscope (LM), while electron microscopy (EM) is then used for a detailed analysis of the ultrastructural context of the labelled epitope of interest [1]. This method requires a sample preparation for the electron microscope, where the fluorescent signal is still maintained. And the accuracy of such multi-modal signal identification strongly depends on the resolution and possible alignment of the images from the light and electron microscope.

To overcome the large alignment error in the above described conventional CLEM workflow several approaches were reported for the quasi-molecular, direct or indirect detection of the fluorescent signal in the electron microscope. Jaksch showed that in low voltage scanning electron microscope (LV-SEM) not only material contrast but also compositional contrast becomes visible by detecting the Low Loss Back-Scattered Electrons (LL-BSE) [2]. In collaboration with Heiner Jaksch we tried to verify his experiments for isolated fluorescent markers. The samples used here are purified green fluorescent protein (GFP) dried on Silica wafers or bound to Q-Sepharose. The fluorescent signal was analysed before and after the LV-SEM experiments in a fluorescence LM. LV-SEM images showed a clear material contrast for the silica wafer and signal from contamination on the sample, but the GFP signal was not detected (Figure 1). Images were recorded in a Zeiss Ultra SEM at 0,4-4,0 keV primary electron energy, examining the multidimensional parameter space (high voltage, working distance, dwell time and detector settings) around the condition described by Jaksch. The fluorescent images after the LV-SEM experiments showed, the GFP fluorophor was destroyed by the electron beam (Figure 2). The remaining fluorescent signal did also not colocalize with the LL-BSE signal. A reason could be that the interaction depth of the low voltage electron beam is significantly smaller that the penetration depth of light. More experiments to find imaging conditions, which maintain fluorescence are under way, however, improved imaging parameters have so far not been found.

In another approach photo-oxidation of diaminobenzidine (DAB) is routinely used for the visualization of fluorophores in correlative microscopy [3]. The DAB polymer formed can be stained with osmium tetroxide or other electron-dense compounds [4] for imaging in an electron microscope (Figure 3). Metal ions such as $NiCl_2$, $CoCl_2$ and $CuSO_4$ have been used to modify the colour of the DAB for light microscopy [5].

We will discuss the possibility of using other metal ions for the localization of the DAB-polymer using LV-SEM, and other applications of LV-SEM.

1. As another example of this multi-modality imaging cf I.V. Röder et al., Poster MC 2013.
2. H. Jaksch, LL-BSE electron contrast from Hybridization & Band Gaps, EMC 2012, Manchester UK (Poster)
3. M. Grabenbauer in “Methods in Cell Biology”, ed. T. Müller-Reichert and P. Verkade (Elsevier Inc.) (2013), p. 117-138
4. G.R. Newman, B. Jasani and E.D. Williams, J Histochem Cytochem 1983 p. 1430-1434
5. S.-M. Hsu and E. Soban, J Histochem Cytochem 1982 p. 1079-1082
6. The authors would like to acknowledge many interesting and stimulating discussions with the late Heiner Jaksch. We dedicate this work to him in the interest to contribute to his original ideas and to make them available in future applications.
7. The work of J.Z., C.S. and M.G. was supported by the German Ministry of Education and Research, project NanoCombine, grant no. FKZ: 13N11401, 13N11404.

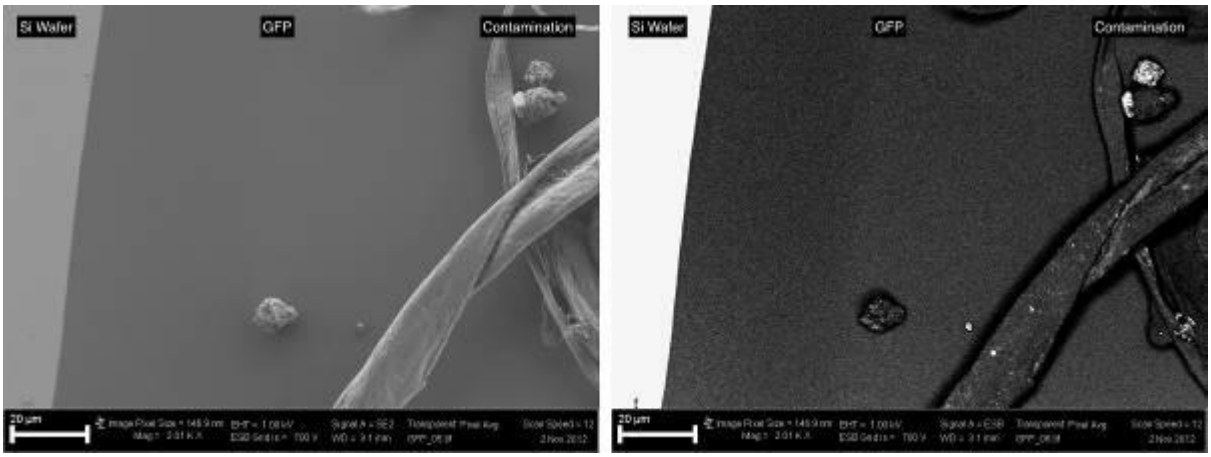

Figure 1. Green fluorescent protein on Silica wafer in LV-SEM, detection of secondary electrons (left) and low loss back-scattered electrons (right). Scale bar 20 µm

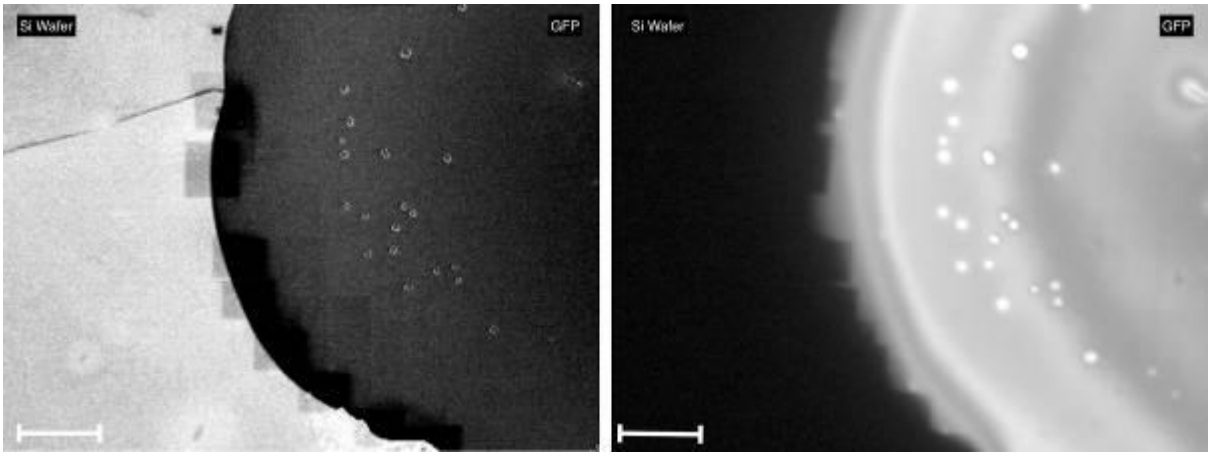

Figure 2. Green fluorescent protein on silica wafer after LV-SEM imaging. LV-SEM image, using the Inlens-SE detector showing the scanned – and therefore bleached – areas (left) and fluorescent LM (right). Scale bar 50 µm

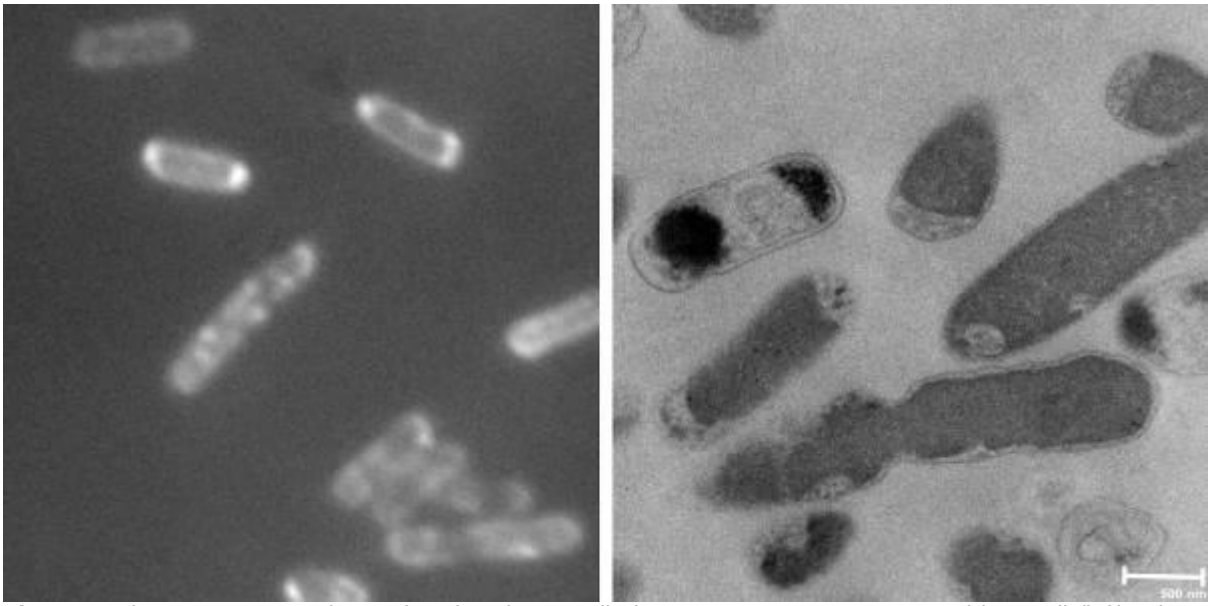

Figure 3. Fluorescence LM of GFP fused to the E. coli glutamate transporter expressed in E.coli (left). Photo-oxidation of DAB through GFP (right). Scale bar 500 nm.

Correlative Microscopy in Life and Materials Science

MIM.4.052
Correlative microscopy using SIMS for high-sensitivity elemental mapping

T. Wirtz[1], D. Dowsett[1], Y. Fleming[1], P. Philipp[1]

[1]CRP - Gabriel Lippmann, Belvaux, Luxembourg

wirtz@lippmann.lu

Important progress and breakthrough developments in materials science and life sciences are more and more often hampered by the absence of adequate analysis techniques. In particular, an analytical tool allowing mapping of samples with both excellent resolution and high-sensitivity chemical information is cruelly missing. Electron Microscopy, Helium Ion Microscopy and Scanning Probe Microscopy are commonly used for high-resolution imaging. However, these techniques have all the same important drawback: they provide no or only very limited chemical information. In electron microscopy, chemical information can be obtained by using techniques like Electron Energy Loss Spectroscopy (EELS) or Energy Dispersive X-ray Spectroscopy (EDS), but the sensitivity is limited. Moreover, these techniques do not permit to distinguish between isotopes, which is a major handicap today due to the increasing use of isotopic labelling, and have limitations in the low mass range. By contrast, Secondary Ion Mass Spectrometry (SIMS) is an extremely powerful technique for analyzing surfaces owing in particular to its excellent sensitivity, high dynamic range, very high mass resolution and ability to differentiate between isotopes.

In order to get chemical information with a highest sensitivity and highest lateral resolution, we have investigated the feasibility of combining SIMS with Transmission Electron Microscopy, Scanning Probe Microscopy and Helium Ion Microscopy and developed three prototype instruments corresponding to the mentioned three combinations of techniques:

- TEM & SIMS: FEI Tecnai F20 equipped with a Ga^+ FIB column and dedicated SIMS extraction optics, mass spectrometer and detectors (figure 1)
- HIM & SIMS: Zeiss ORION Helium Ion Microscope with dedicated SIMS extraction optics, mass spectrometer and detectors [1,2]
- SPM & SIMS: Cameca NanoSIMS 50 with integrated AFM/SPM [3-5]

In order to reach the targeted excellent detection limits with SIMS while using a finely focused analytical probe, high secondary ion yields are crucial. As the intrinsic yields obtained with non-reactive primary ions (as is the case on the TEM & SIMS where a Ga^+ beam is used and on the HIM & SIMS where helium and neon beams are used) are relatively low, we use reactive gas flooding during analysis, namely oxygen flooding for positive secondary ions and cesium flooding for negative secondary ions [1]. With such reactive gas flooding, the yields can be enhanced by up to four orders of magnitude. Based on these yields, we calculated detection limits for various samples under typical analysis conditions for the three combined instruments. An example of the detection limits reached on the HIM & SIMS is shown in figure 2.

By combining the known information channels of TEM, SPM and HIM on the one hand and SIMS on the other hand in one unique and novel analytical and structural tool, new multi-channel nanoanalytical experiments become possible, which open the pathway to qualitatively new types of information about the investigated samples. Different possibilities arise from these in-situ instrument combinations. One can for instance first image in 2D or 3D the sample with TEM/HIM/SPM, then analyze the same zone with SIMS, and finally very precisely overlap the 2 data sets (see example in figure 3 for SPM & SIMS). Another approach consists of first imaging the sample by SIMS to localize hot spots (for instance high concentration of a given element or a given isotope one is interested in), and then to zoom onto this hot spot by TEM/HIM/SPM to identify the feature corresponding to this hot spot. It is important to note that ex-situ multi-technique combinations do not allow the same performances as such an approach is hampered by several limitations, including precise re-localization of analyzed zones after transferring the sample between the standalone instruments and artifacts due to surface oxidation and surface reorganization during sample transfer between the instruments.

The results are very encouraging and the prospects of performing SIMS in combination with TEM, HIM and SPM are very interesting. The combination of high-resolution microscopy and high-sensitivity chemical mapping on a single instrument leads to a new level of correlative microscopy.

1. T. Wirtz et al., Appl. Phys. Lett. 101 (2012) 041601
2. D. Dowsett et al., J. Vac. Sci. Technol. B 30 (2012) 06F602
3. T. Wirtz et al., Surf Interface Anal. 45 (1) (2013) 513-516
4. T. Wirtz et al., Rev. Sci. Instrum. 83 (2012) 063702
5. C. L. Nguyen et al., Appl. Surf. Sci. 265 (2013) 489-494

Figure 1: TEM & SIMS - Prototype of a combined TEM-SIMS instrument: modified Tecnai F20 equipped with a Ga^+ gun and dedicated SIMS column

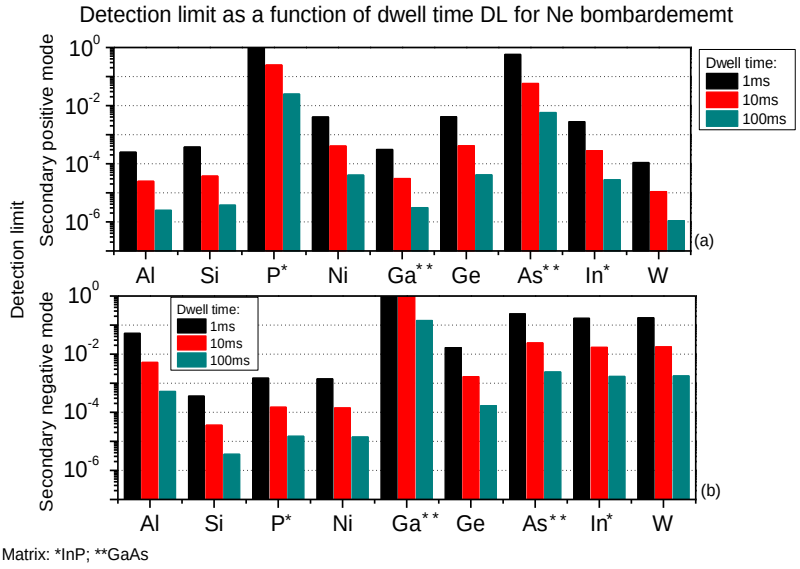

Matrix: *InP; **GaAs

Figure 2: HIM & SIMS - Detection limit for Ne^+ bombardment in secondary positive mode with O_2 flooding (a) and in secondary negative mode with Cs flooding (b). Typical dwell times of 1ms, 10ms and 100ms and a primary ion current of 10 pA are considered.

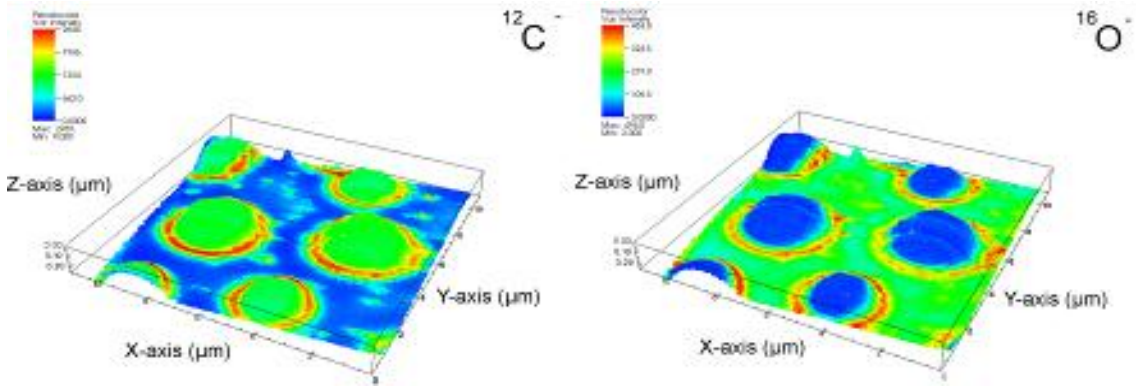

Figure 3: SPM & SIMS - Combined SIMS-SPM 3D reconstruction of a PS/PMMA blend (Field of view: 22.3x17.3 μm^2): (a) $^{12}C^-$ secondary ion signal. (b) $^{16}O^-$ signal, which is characteristic of PMMA [4].

Correlative Microscopy in Life and Materials Science

MIM.4.053
How to implement a virtual correlative light and electron microscope

T. Voigt[1]

[1]University of Bern, Institute of Anatomy, Bern, Switzerland

til-voigt@t-online.de
Keywords: virtual, correlative, microscopy

The widespread use of slide scanners by pathologists requires an adaptation of teaching methods in histology and cytology which also points to these new possibilities of image processing and presentation via the internet. Accordingly we were looking for a tool with the possibility to teach microscopic anatomy, histology and cytology of tissue samples which independently of suppliers of microscopes is capable to combine image data from light and electron microscopes.

A commercially available image-presentation software was adapted to our needs allowing the presentation of huge image files divided as so called pyramid-image-stacks via the internet. Next to these adaptations, we describe here the workflow how to process two consecutive sections, a semi-thins section and the next ultra-thin section, in order to get correlative image data which can be merged in one pyramid-image-stack. With this pyramid-image-stack a virtual correlative microscope was implemented which allows a correlation of structures from the microscopic anatomic to the cytologic level. The technical problems of the image processing as well as the image quality loss due to these image manipulations are discussed. However the quality loss can be neglected.

The workflow was described with the example of a 500*300µm large sections through a whole villus of the jejunum of a mouse. Thus within this section plane every layer, tissue, cell and its organelles building up a villus of the jejunum can be shown. Since this supplier independent tool allows for the presentation of any kind of image data, we implemented an internet platform with the possibility to zoom from the macroscopy to the cytology (Fig. 1)

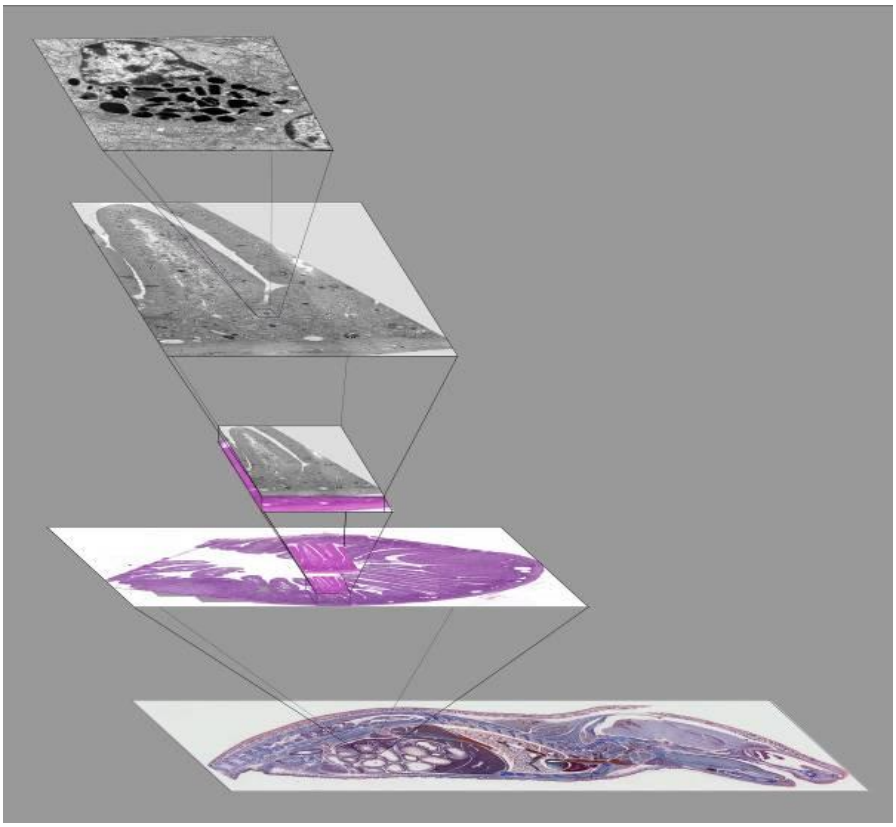

Figure 1. Possible combination of pyramid-image-stacks of different microscopic sources to one virtual microscope allowing for the visualisation of macroscopic, microscopic anatomic, histologic and cytologic structures.

Correlative Microscopy in Life and Materials Science

MIM.4.P054
Detection of specific lanthanum signal in a metal-organic compound as approach for correlative high-resolution microscopy

M. Pfannmöller[1], C. Hedberg[2], M. Grabenbauer[2], R. Schröder[1]

[1]Universitätsklinikum, CellNetworks, Heidelberg, Germany
[2]Max-Planck-Institute for Molecular Physiology, Systems Cell Biology, Dortmund, Germany

martin.pfannmoeller@bioquant.uni-heidelberg.de
Keywords: correlative microscopy, metal-organic compounds, low energy-loss, electron spectroscopic imaging

Correlating information from light and electron microscopes from identical specimen areas helps in understanding function in relation to cellular structures at high resolution [1]. Such an approach requires super-imposing regions of interest from two different imaging modalities. This is still a challenging endeavour since fluorescence emission from light microscopy creates an entirely different visualization of the object than electron microscopy. For the latter bright-field transmission electron microscopy (TEM) is typically applied. In the past, analytical TEM has been shown to be useful to map spectroscopic signals. This is also feasible with bio-organic materials, which can be associated to specific energy-loss spectra [2]. Direct detection of a functional signal at TEM level would allow for direct embedding of targeted molecules into the surrounding ultrastructure. This was shown for fluorescent nanocrystals, which were identified by optical absorption signals from inelastic scattering using low energy-loss electron spectroscopic imaging (LoESI) [3].

Additionally, by spectral visualization of core-losses analytical TEM offers mapping of element specific ionization signals [4]. Thus, introducing non-natural metals near target molecules and spectroscopic imaging at the respective ionization energies should allow for another possibility to directly combine functional and ultrastructural imaging in TEM. This can be done by adding metals to an organic, polymeric precipitation in the vicinity of fluorescent markers. Large precipitates were already found to bind to nickel or cobalt metal ions as visualized by light microscopy [5]. Here, we show that a specific lanthanum signal at organic precipitations can be mapped by analytical TEM. Precipitates are found at membranes of resin embedded HeLa cells (Fig. 1A). As shown in Fig. 1B, high-loss electron energy-loss spectroscopy (EELS) reveals $M_{4,5}$ edges of lanthanum at 832 and 849 eV in such areas. Since LoESI requires much less electron dose for collection of significant signal we also performed a multispectral analysis of a set of ESI images from 4 to 80 eV (in steps of 1 eV). Segmentation of membrane associated metal-organic precipitates is depicted in Fig. 1C. Extracted spectra from segmented and background regions, can be used to compute a difference spectrum (Fig. 1D). It reveals specific features, e.g. around 30 and 60 eV, which can again be attributed to specific lanthanum edges.

The technique illustrated here can be used to identify different metals with distinguishable features in the analytical electron microscope. Targeting multiple metal-organic compounds specifically to various structures or molecules of interest might allow labelling and detection of multiple cellular targets with simultaneous correlation to their local structural environment.

1. M. Grabenbauer, W.J.C. Geerts, J. Fernadez-Rodriguez, A.T. Nilsson, Nature Methods 2 (2005), p. 857.
2. M.A. Aronova and R.D. Leapman, MRS Bulletin 37 (2011), p. 53.
3. M. Pfannmöller, I. Röder, G. Benner, I. Angert, I. Wacker and R.R. Schröder, Microscopy and Microanalysis 17 (2011), p. 818.
4. R.F. Egerton, Springer, New York (2011).
5. S.M. Hsu and E. Soban, Journal of Histochemistry & Cytochemistry 30 (1982), p. 1079.
6. We kindly acknowledge financial support of the German Federal Ministry for Education and Research, project NanoCombine, grant no. FKZ: 13N11401 and 13N11404.

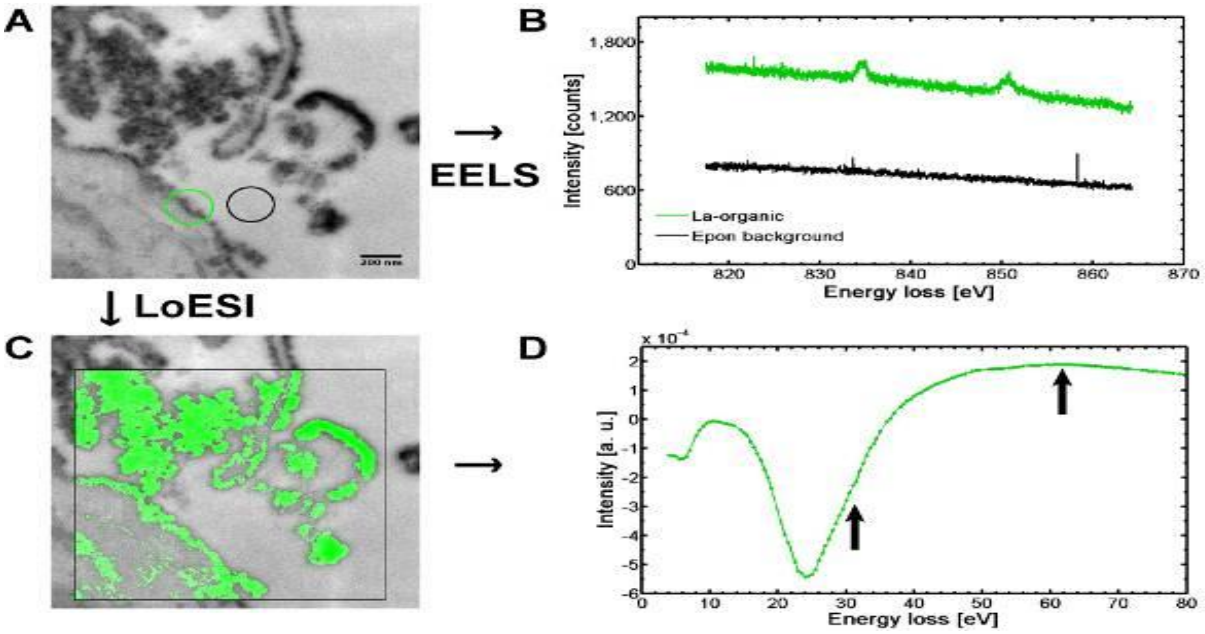

Figure 1. Segmentation of lanthanum-organic precipitates by EELS and ESI. A: Transmission electron micrograph of resin embedded HeLa cells with precipitates at membranes. B: EELS spectra from selected areas (circles in A) with precipitate and with resin background only, showing $M_{4,5}$ edges at 832 and 849 eV energy-loss. C: Multispectral segmentation using a low energy-loss ESI series with inelastic images from 4 to 80 eV using steps of 1 eV. Membrane regions with precipitates are well separated from resin background and intracellular regions. D: Normalized spectrum of segmented pixels in C (difference between averaged ESI spectrum of segmented pixels and background pixels). Features around 30 and 60 eV (arrows) indicate specific lanthanum signals from the $O_{2,3}$ edges.

Correlative Microscopy in Life and Materials Science

MIM.4.P055
Preservation of Alexa Fluor® fluorescence in tissue for correlative light and electron microscopy

I.V. Röder[1], C. Dietrich[2], J. Fuchs[3], I. Wacker[4,5], R.R. Schröder[1,5]

[1]CellNetworks, BioQuant, Universitätsklinikum Heidelberg, Cryo-EM, Heidelberg, Germany
[2]Carl Zeiss AG, Jena, Germany
[3]Carl Zeiss AG, Oberkochen, Germany
[4]Karlsruhe Institute of Technology, Institute for Biological Interfaces, Karlsruhe, Germany
[5]Heidelberg Karlsruhe Research Partnership, HEiKA Correlative Imaging Platform, Heidelberg, Karlsruhe, Germany

ira.roeder@bioquant.uni-heidelberg.de
Keywords: Alexa Fluor®, Lowicryl HM20 resin, tissue, correlative microscopy, neuromuscular junction, fluorescence preservation

It is a demanding task to locate single, rare events or structures in big cellular volumes or, even worse, within tissue samples prepared for electron microscopic investigations. Therefore correlative light and electron microscopy is a useful method to not only find the event or structure of interest again much faster but also to gain valuable information about the ultrastructural context of the labelled feature. We established two protocols to maintain Alexa Fluor® fluorescence during the embedding of mouse muscle tissue in Lowicryl HM20 resin. The structure of our interest is the neuromuscular junction (NMJ), the synapse between the axon of a motoneuron and a skeletal muscle fibre which is responsible for voluntary movement [1]. Both approaches start with the excision of diaphragm muscle. In both cases the acetylcholine receptors (AChR) of the NMJs are labelled using α-bungarotoxin (BGT), a snake venom, conjugated to Alexa Fluor® 555 (AF555, Invitrogen) or 647 (AF647, Invitrogen). The first method is a high pressure freezing approach. After excision of the diaphragm we dissect it into pieces small enough to put them into planchettes suitable for high pressure freezing. During this time the muscle is labelled with BGT-AF555/-AF647. Subsequently the appropriate pieces are high pressure frozen, freeze substituted and embedded in Lowicryl HM20 resin [protocol modified on the basis of 2]. The second method is a chemical fixation approach starting with excision and chemical fixation of muscle tissue. Afterwards the muscle is labelled and dissected into pieces for further processing steps. A progressive lowering of temperature method is applied to embed the tissue at low temperature [protocol modified on the basis of 3]. We obtained preservation of the Alexa Fluor® fluorescence during embedding of the mouse muscle tissue in resin with both methods.

In the first instance the whole block can be investigated using confocal laser scanning microscopy providing the possibility to relocate predefined regions. The fluorescence is further detectable in ultrathin sections by either common fluorescence light microscopic techniques or by more sophisticated methods such as high numerical aperture (NA) fluorescence microscopy (Figure 1), confocal laser scanning or localization microscopy (Figure 2). Following light microscopic investigations the same sections can be imaged with transmission or scanning electron microscopy and images from all modalities can be correlated (Figure 2). An intermediate step of immunogold on section labelling can be performed to specifically label molecules of interest within the tissue section. This allows complementing the fluorescence signal detectable in light microscopy with an electron-dense marker (Figure 3). Using our approaches it is possible to use a commercially available fluorescence dye to label molecules or structures of interest and to monitor the fluorescence in electron microscopic preparations. With this tool rare events can be relocated within bigger volumes and be further investigated in their ultrastructural context enabling the researcher to “see” not only the labelled entities but to explore much more about their actual cellular environment.

1. J.R. Sanes and J.W. Lichtman, Nature Reviews Volume 2 (2001), p. 791.
2. S. Hillmer, C. Viotti and D.G. Robinson, Journal of Microscopy Volume 247 (2012), p. 43.
3. D. Robertson et al., Journal of Microscopy Volume 168 (1992), p. 85.
4. We acknowledge financial support of the German Federal Ministry for Education and Research, project NanoCombine, grant no. FKZ: 13N11401, 13N11402.

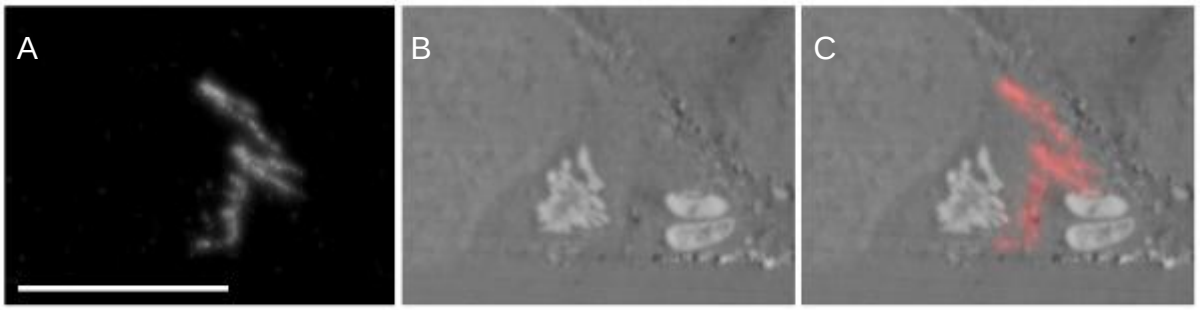

Figure 1: Light micrograph of a 70 nm HM20 section on an indium tin oxide (ITO)-coated cover slip recorded with an oil immersion objective lens (100x/1.4 Plan Apochromat, Carls Zeiss). A: fluorescence image of AChR labelled with BGT-AF555; B: bright field image; C: Overlay of fluorescence and bright field image. Scale bar: 10 µm.

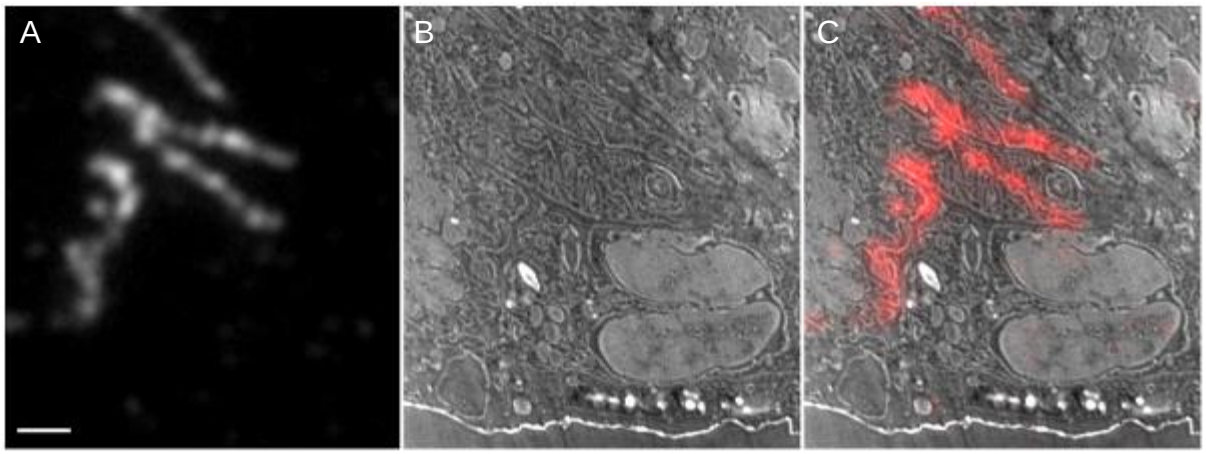

Figure 2: Correlation of high resolution light and scanning electron micrograph of a 70 nm HM20 section on an ITO-coated cover slip. AChR are labelled with BGT-AF555. A: Fluorescence light micrograph recorded with an oil immersion objective lens (100x/1.4 Plan Apochromat, Carl Zeiss); B: scanning electron micrograph recorded with a Supra 40 (Carl Zeiss); C: Overlay of fluorescence light and scanning electron micrograph. Scale bar: 1 µm. Please note also abstract at this conference: „*Comparison of localization algorithms for correlative 3D reconstruction of super-resolution fluorescence images of ultrathin serial sections*" by J. Fuchs et al.

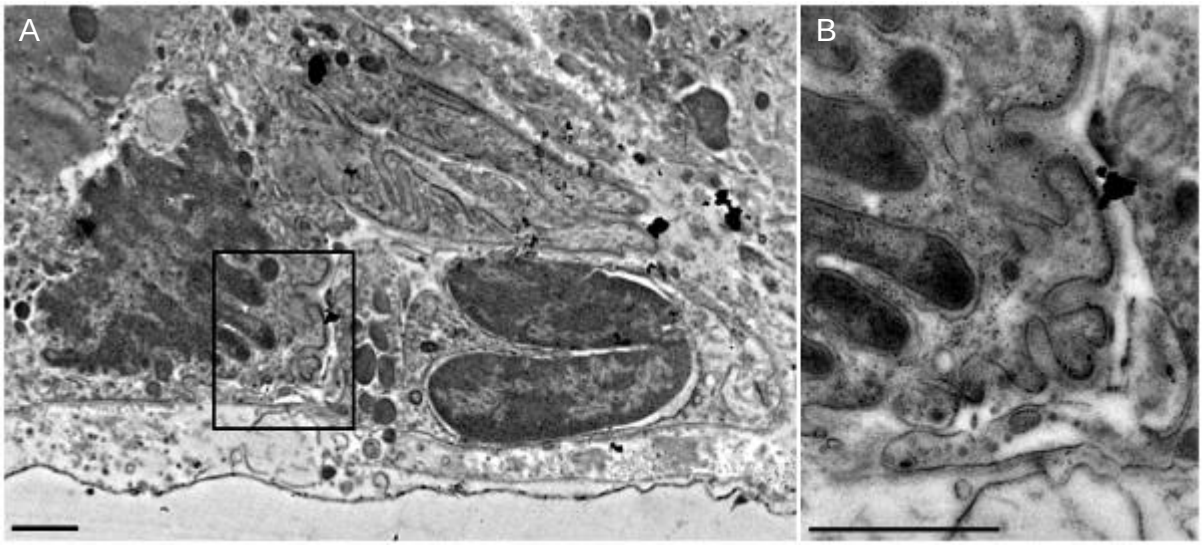

Figure 3: Transmission electron micrograph of a 70 nm HM20 section on a grid. AChR are labelled with anti-AChRα-antibody (BD Biosciences) and Protein A Gold (cmc). A: Overview; B: Magnification of the boxed region in A. Scale bars: 1 µm.

Correlative Microscopy in Life and Materials Science

MIM.4.P056
Integrating 3D surface imaging with FIB/SEM microscopy

A.J. Smith[1], S. Kleindiek[1], G. Renka[1], A. Lieb[2], M. Dadras[3], K. Schock[1]

[1]Kleindiek Nanotechnik, Reutlingen, Germany
[2]Nanosurf AG, R&D, Liestal, Switzerland
[3]CSEM SA, Centre Suisse d'Électronique et de Microtechnique, Neuchâtel, Switzerland

andrew.smith@kleindiek.com
Keywords: AFM, SPM, in-situ AFM, SEM, FIB

With the large amount of current research and development focused on nano wires, carbon nano tubes, and other nano scale materials, imaging these materials has become a large part of the challenges involved.

The two most prominent methods for imaging at the nano scale are Scanning Electron Microscopy (SEM) and Atomic Force Microscopy (AFM). These complimentary methods utilize fundamentally different principles for generating imagery - SEM exploits the interaction of electrons with matter, while AFM is based on physical interaction of a sharp tip with the sample surface.

Both approaches have strengths and weaknesses. The SEM's strength is to quickly generate images with a large range of magnifications, making it easy to locate the area of interest. However, it doesn't yield 3D information, e.g. "invisible" contamination layers. The AFM's main advantage is its ability to obtain 3D information, the downsides are that it is hard to find the target area and image generation is slow.

Combining these two tools into one setup - putting an AFM inside an SEM - gives quick access to a more complete data set. Additionally, FIB-milled or FIB-deposited structures can be characterized using this combination of tools in a FIB/SEM system.

The SFAFM is a small compact solution for in situ AFM experiments. Based on a 4" wafer size platform, with a height of just 10 mm, the system is comprised of an ultra-flat piezo scanner and a next generation three-axis micromanipulator to which a piezo-resistive force measurement cantilever is mounted. These cantilevers can detect deflection without the use of a laser read-out system, making them ideal for in situ applications.

The utility of this combination of tools is demonstrated with several examples where locating the area of interest purely by AFM or light microscopy would have been highly impractical.

Figure 1. SuperFlat-AFM. The load-lockable platform can be mounted into almost any SEM on the market.

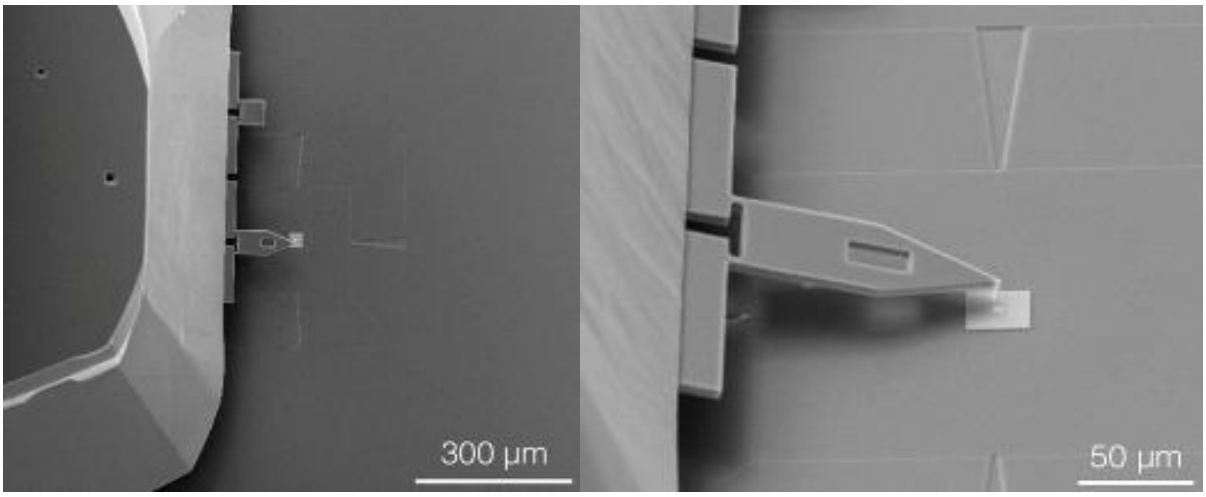

Figure 2. Addressing the target area for AFM inspection is fast and easy using the SEM.

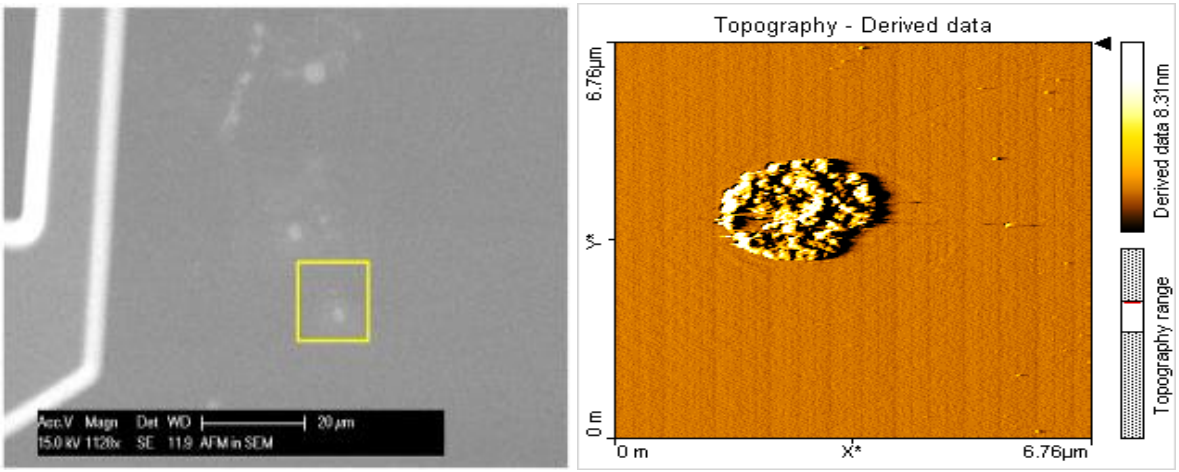

Figure 3. Si surface observation by SEM and AFM characterization of defects. The defects have a height of about 12nm

Correlative Microscopy in Life and Materials Science

MIM.4.P057
High Resolution SEM, 3D-Applications and Correlative Light/Electron Microscopy

R. Neujahr[1]

[1]Carl Zeiss Microscopy, Microscopy Labs, Muenchen, Germany

ralph.neujahr@zeiss.com

Light and electron microscopy are two powerful, yet mainly independently used imaging
Recently, more and more researchers want to combine the strengths of these tools to gain new insights into the functionality and the associated ultra-structure of biological specimen.
A prerequisite is the precise retrieval of one and the same regions of interest within the sample.
Due to the different image contents this can be a very time-consuming to nearly impossible task. With the introduction of “Shuttle & Find” Carl Zeiss made a straight-forward workflow available that allows to easily transferring a sample together with the corresponding coordinates between wide-field light and scanning electron microscopes (SEM). Repositioning to the regions of interest became a matter of only a few mouse clicks. Combined with high resolution SEM and 3D imaging this tool provides extreme flexibility detecting fluorescent signals and corresponding ultrastructural organization.

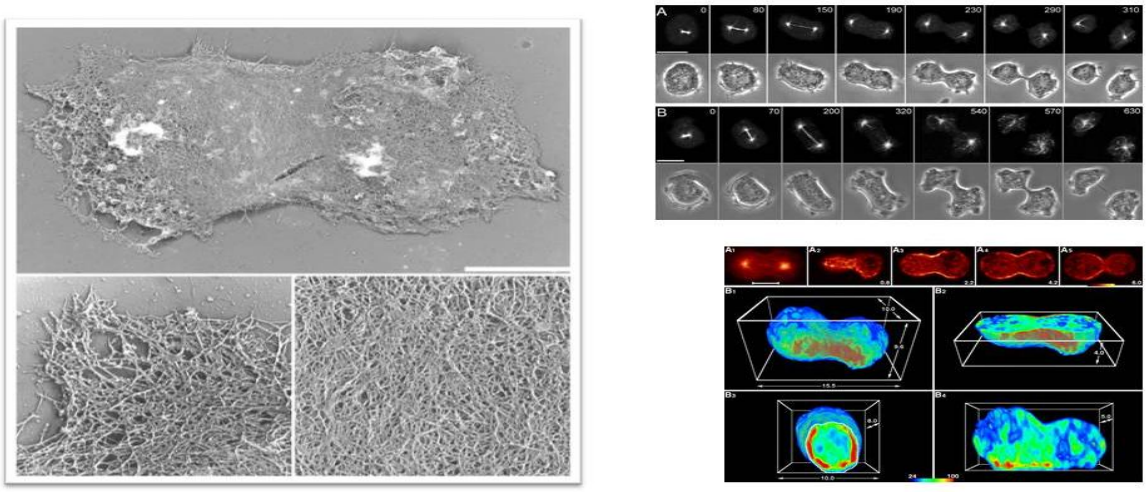

Figure 1.

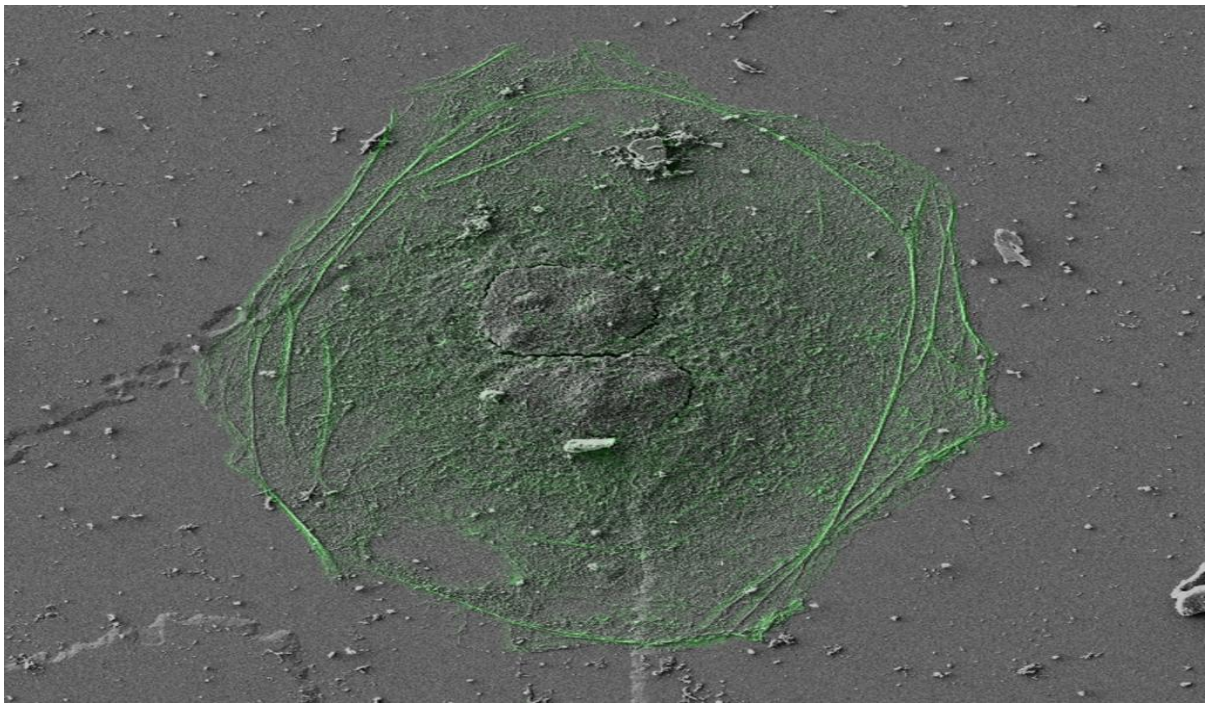

Figure 2.

Correlative Microscopy in Life and Materials Science

MIM.4.P058
Correlative light and electron microscopy of ultrathin sections

S. Kretschmar[1], D. Eberle[2], M. Ader[2], H. Gandhi[3], C. Bökel[2], T. Weidemann[3], T. Kurth[1]

[1]TU Dresden, CRTD, EM-Facility, Dresden, Germany
[2]TU Dresden, CRTD, Dresden, Germany
[3]TU Dresden, BIOTEC, Dresden, Germany

thomas.kurth@crt-dresden.de

Correlative microscopy combines the versatility of the light microscope with the high spatial resolution of the electron microscope. However, many CLEM approaches, in particular those combining *in vivo* fluorescence and TEM-imaging, are used preferentially in cell culture systems [1,2]. For the correlative analysis of tissues an alternative approach is the on-section labeling of resin or cryo-sections using fluorochrome-coupled antibodies and gold probes [3-7].

Here, we describe fast and simple protocols for correlative immunofluorescence and immunogold labeling on the very same section. The protocols are demonstrated on sections of tissue samples embedded in the methacrylate Lowicryl K4M (Figure 1) and on Tokuyasu cryo-sections through transfected cells expressing a GFP-labeled protein. Ultrathin sections are mounted on EM-grids and stained simultaneously with fluorescent and gold markers. The samples are analyzed at the fluorescence microscope (FLM), demounted from the microscope slide, stained with uranyl acetate and then imaged in the transmission electron microscope (TEM). Labeled structures selected at the fluorescence microscope can be identified in the TEM and analyzed at high resolution. This way, fluorescent signals can be directly correlated to the corresponding subcellular structures and a corresponding immunogold signal in the area of interest. Alternatively, the samples are processed completely, and the dried grids are analyzed in the FLM and the TEM. The latter approach is mandatory for the correlative imaging of sections in integrated systems such as the Tecnai™ with iCorr™, and to achieve a reasonable balance between fluorescence and EM contrast in these samples is a challenging task [8].

1. RS Polishchuk, EV Polishchuk, P Marra, S Alberti, R Buccione, A Luini, and A Mironov, J. Cell Biol. 148 (2000), p. 45-58.
2. P Verkade, J. Microsc. 230 (2008), 317-328.
3. H Schwarz and BM Humbel, Methods Mol. Biol. **369** (2007), p. 229-256.
4. T Takizawa and JM Robinson, Methods Mol. Med. 121 (2006), p. 351-369.
5. G Vicidomini, MC Gagliani, M Canfora, K Cortese, F Frosi, C Santangelo, PP Di Fiore, P Boccacci, A Diaspro, and C Tacchetti, Traffic 9 (2008), p. 1828-1838.
6. D Eberle, T Kurth, T Santos-Ferreira, J Wilson, D Corbeil, and M Ader, PLOS One 7, e46305.
7. G Fabig, S Kretschmar, S Weiche, D Eberle, M Ader, and T Kurth, Methods Cell Biol. 111 (2012), p. 75 93.
8. MA Karreman, EG Van Donselaar, AV Agronskaia, CT Verrips, and HC Gerritsen, J Histochem Cytochem 61 (2013), p. 236-247.
9. The authors gratefully acknowledge funding from the European Fund for Regional Development (EFRE).

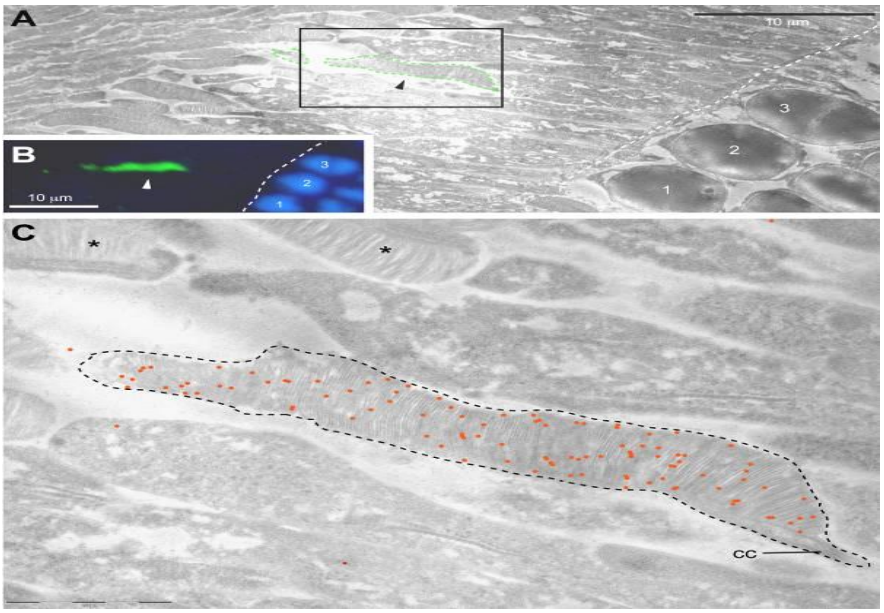

Figure 1: CLEM of a K4M section through mouse retina after transplantation of GFP-labeled photoreceptor precursor cells (PPCs with Rhodopsin-GFP) into a wt-mouse. **A**,**B** An integrated PPC (A, fluorescence: rabbit anti-GFP, goat anti-rabbit Alexa488, B, TEM: rabbit anti-GFP, protein A 10 nm Gold) **C** Higher magnification of the area highlighted in A. Gold-labeling in the outer segment of the PPC is highlighted in red. The unlabeled reference space with inner segments and unlabeled outer segments of the host (*) is visible; cc, connecting cilium of the transplanted cell (A and B from [6]).

Correlative Microscopy in Life and Materials Science

MIM.4.P059
Comparison of localization algorithms for correlative 3D reconstruction of superresolution fluorescence images of ultrathin serial sections

J. Fuchs[1], T. Kalkbrenner[2], I.V. Röder[3], R.R. Schröder[3,4], C. Dietrich[5]

[1]Carl Zeiss AG, Corporate Research and Technology, Oberkochen, Germany
[2]Carl Zeiss Microscopy GmbH, Jena, Germany
[3]University, CellNetworks, BioQuant, Heidelberg, Germany
[4]University, HEIKA Correlative Imaging Platform, Heidelberg Karlsruhe, Germany
[5]Carl Zeiss AG, Jena, Germany

christian.dietrich@zeiss.com
Keywords: 3D correlative light and electron microscopy, correlative array tomography, superresolution light microscopy

Light and electron microscopy are highly successful technologies when used independently. They are increasingly used together by researchers in the field of Correlative Microscopy as combining the strength of different microscope technologies allows to gain new insights into the functionality and the associated ultra-structure of biological specimens. One popular approach to image three-dimensional objects is to slice them into ordered arrays of ultrathin, resin-embedded sections and reconstruct the volume from the recorded images [1].

Here we applied this method to Neuromuscular Junctions (NMJ) in muscle tissue, which was specifically prepared for correlative light and electron microscopy. For detailed description of the preparation, see [2]. Under intense laser illumination the fluorophores show specific blinking behavior (Figure 1), which offers the option to apply the method of localization microscopy [3]. Since the tissue is embedded into a resin to enable sectioning, fluorophores are less accessible for manipulation of their blinking behaviour. For our sample, the density of the active fluorophores per image frame didn't allow analysis of single, well separated fluorophores. Therefore we applied algorithms accounting for several fluorophores within one resolution limited spot (Figure 2).

For evaluation and judgment of the algorithms, we compared the reconstructed fluorescence images with the morphology of the membrane of the NMJ, provided by scanning electron microscopy. Therefore we employed Shuttle & Find [4] to image the ROI with superresolution fluorescence microscopy (Elyra PS.1, Carl Zeiss Microscopy GmbH) and with a scanning electron microscope (Neon 40, Carl Zeiss Microscopy GmbH). This allows direct comparison of morphological and functional information provided by electron and fluorescence imaging, respectively. Furthermore, a 3D reconstruction of the section images yields high resolution volume data of the sample. The fluorescence allocated by the employed algorithm has to correlate between successive sections, which are only 70 nm thick. Artifacts introduced by the data analysis become readily visible.

We could identify a suitable multi-emitter localization algorithm that provides a robust and correct representation of fluorescence distributions, while providing superresolution. For ultrathin sections we estimated a lateral localization accuracy in the range of 50 nm, when recording time series with 1000 frames.

1. K. D. Micheva and S. J. Smith, Neuron 55 (2007), p. 25-36.
2. I. V. Röder, C. Dietrich, J. Fuchs, I. Wacker, and R.R. Schröder, Preservation of Alexa Fluor® fluorescence in tissue for correlative light and electron microscopy. Microscopy Conference 2013, August 15-30, Regensburg, Germany
3. Sengupta, P., S. van Engelenburg, and J. Lippincott-Schwartz, Dev Cell, 2012. 23(6): p. 1092-102.
4. M. Wiederspahn, Shuttle & Find for Life Sciences, Imaging & Microscopy 3 (2010), p. 19.
5. The authors gratefully acknowledge funding provided by the German Ministry for Education and Research, project NanoCombine, grant no. 13N11402 and 13N11401

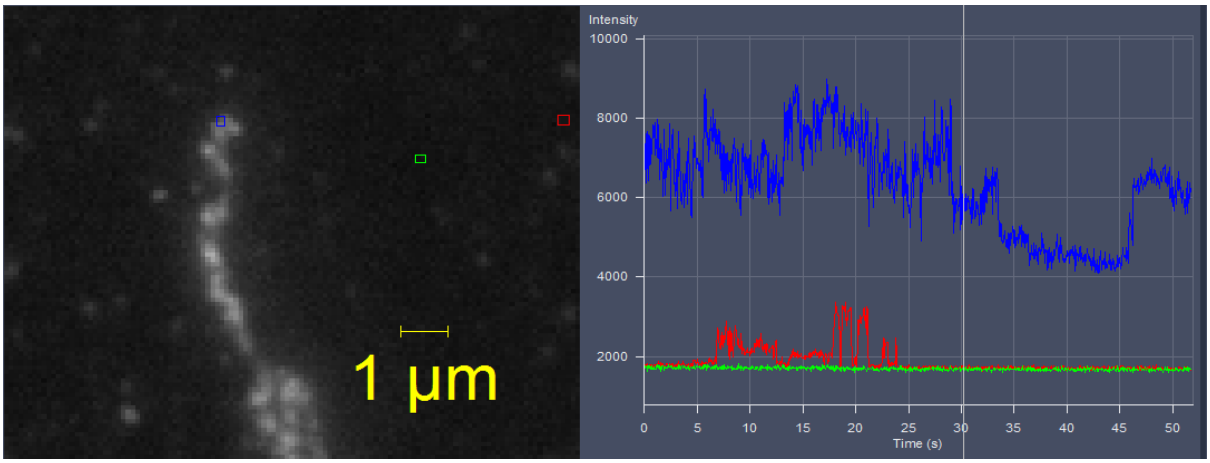

Figure 1: Analysis of fluorescence signal for time series (1000 frames) of a labeled Neuromuscular Junction (NMJ) recorded with a superresolution setup (Elyra PS.1, Carl Zeiss Microscopy GmbH). A 100x/1.46 alpha - Plan Apochromat objective lens (Carl Zeiss Microscopy GmbH) was employed.
Left: Single frame of the time series with colored boxes indicating different regions (0.2 x 0.2 µm^2). NMJ (blue) and reference measurements outside the NMJ (red; green).
Right: Time course of fluorescence signals for the three boxes are given in corresponding colors.

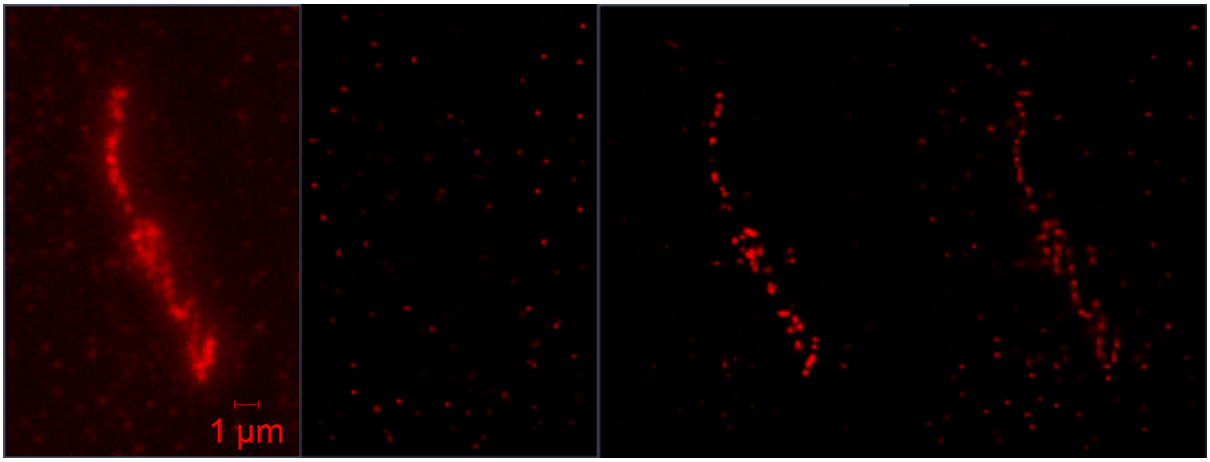

(A) (B) (C) (D)

Figure 2. Comparison of different emitter localization analysis algorithms applied to a series of 1000 time frames (A). Single time frame of the recorded time series. Result of analysis demanding well separated emitters (B), ignoring overlapping emitters within one PSF (C) and accounting for overlapping emitters within one diffraction limited spot (D).

Correlative Microscopy in Life and Materials Science

MIM.4.P060
Structure-property relationships in thin-film solar cells by scanning electron microscopy in combination with focused ion beam

N. Schäfer[1]

[1]Helmholtz-Zentrum Berlin für Materialien und Energie, Institute "Nanoarchitectures for Energy Conversion", Berlin, Germany

norbert.schaefer@helmholtz-berlin.de
Keywords: EBSD, FIB, EBIC, strain measurements

Chalcopyrite-type solar cells based on Cu(In,Ga)Se_2 absorber layers have shown power-conversion efficiencies of more than 20 % on glass and polyimide substrates [1,2]. The analysis of the microstructure of the Cu(In,Ga)Se_2 absorber layer and of the corresponding structure-property relationships is essential for further improvement of the photovoltaic performance.

Scanning electron microscopy (SEM) offers several techniques for investigating the microstructure of the Cu(In,Ga)Se_2 absorber layers. The investigated layers showed average grain sizes of 0.5-1.5 µm, depending on their compositions [3], which allowed us to perform electron backscatter diffraction (EBSD), electron-beam-induced current (EBIC) and energy-dispersive X-ray spectroscopy measurements on identical positions of the specimens, in order to correlate microstructural and electrical properties as well as elemental distributions to the performances of the solar cells. Focused ion beam (FIB) was used to prepare the cross-sectional specimens for SEM imaging and analysis by slicing and polishing of the ZnO/CdS/Cu(In,Ga)Se_2/Mo/glass solar-cell stacks without delamination of the individual layers. Evaluation of microstrain within individual grains from EBSD data was performed for the first time on Cu(In,Ga)Se_2 layers using CrossCourt3 analysis software (see Fig. 1 for an example). Small shifts of features within the measured EBSD patterns can be related to variations in microstrain, which were found to be of the order of 10^{-3}.Advanced EBSD analysis of Cu(In,Ga)Se_2 solar cells by extraction of strain distributions in combination with EBIC measurements at identical specimen positions gives information on structure-property relationships in thin-film solar cells that complements state-of-the-art grain-boundary analysis [4,5]. First insights on the effect of strain on the charge-carrier collection influencing the EBIC signal (see Fig. 2) will be presented.

1. P. Jackson *et al*, Prog. Photovolt.: Res. Appl. 19 (2011), p. 894.
2. See press release at http://www.empa.ch/plugin/template/empa/*/131441
3. D. Abou-Ras, S.Schorr and H.W. Schock, J. Appl. Cryst. 40 (2007), p. 841.
4. D. Abou-Ras et al., Sol. En. Mat. Sol. Cells 95 (2011), p. 1452
5. S. Sadewasser, D. Abou-Ras, et al., Thin Solid Films 519 (2011) p. 7341.
6. Special thanks are due to B. Bunn, C. Kelch, M. Kirsch, T. Münchenberg, and J. Schniebs for solar-cell processing. Financial support by the Helmholtz Virtual Institute Microstructure Control in Thin-Film Solar Cells, VI-520, is gratefully acknowledged.

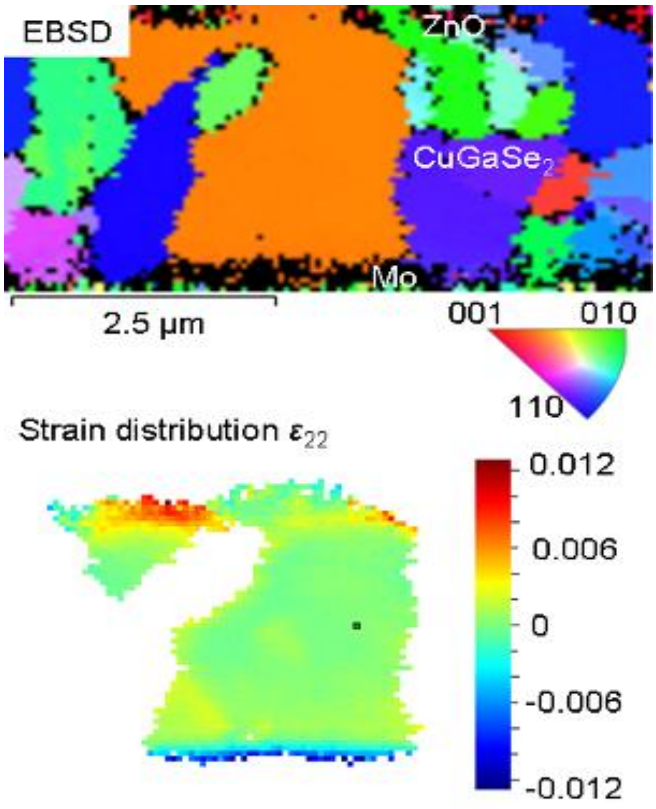

Figure 1. Cross-sectional EBSD orientation distribution map of a ZnO/CdS/$CuGaSe_2$/Mo/glass solar-cell stack (top), and calculated strain distribution within one grain using the software CrossCourt3 (bottom).

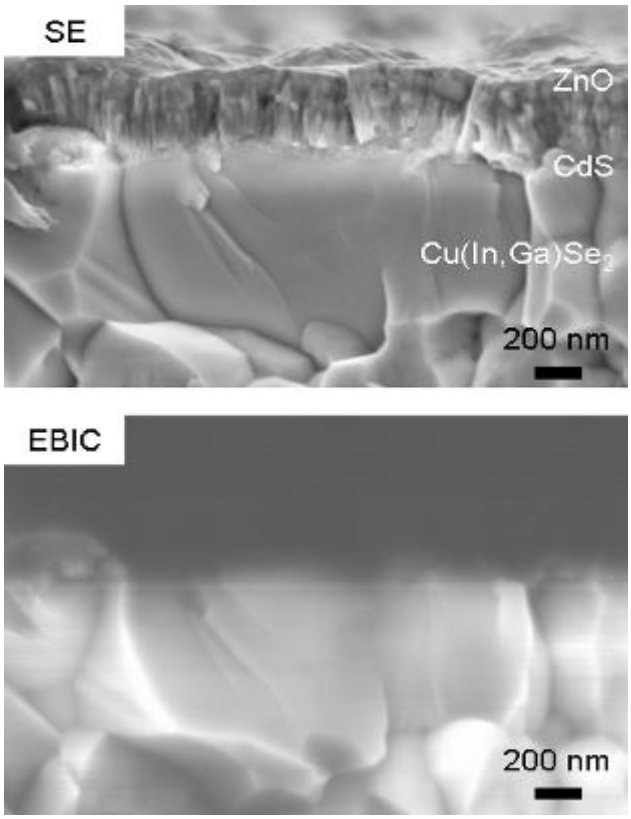

Figure 2. Secondary electron (SE) and EBIC images of the cross-section of a ZnO/CdS/$Cu(In,Ga)Se_2$/Mo/glass solar-cell stack.

Correlative Microscopy in Life and Materials Science

MIM.4.P061
Interactions of bacteria and yeast in biofilms: transmission and scanning electron microscopic analysis

K. Hovnanyan[1], A. Pepoyan[2], M. Hovnanyan[1], L. Navasardyan[3], L. Hovnanyan[1], A. Trchounian[4]

[1]Molecular biology of NAS RA, Electron Microscopy, Yerevan, Armenia
[2]Agrarian University, Microbiology, Yerevan, Armenia
[3]Yerevan State University, Biochemistry, Yerevan, Armenia
[4]Yerevan State University, Biophysics, Yerevan, Armenia

hovkarl@mail.ru
Keword:biofilm, bacteria, yeast, transmission and scanning electron microscopy

The processes of the shaping biofilms of bacteria and yeast as cultures on surfaces of metals, mucous surface of the cavities of the organisms and in external ambience are among actual problems of microbial ecology those having an important medico-biological importance; they are not more valuable for new biotechnology [1-3]. In the present work ultra-structural particularities of biofilms from some bacteria and yeast have been studied in order to install the intercellular contacts between cells *in vitro* and *in vivo.*

The main object of the study were bacteria referred to different taxonomic groups as *Escherichia coli serogroup O124*, *Shigella flexneri 130, Salmonella typhimurium 546, Staphylococcus aureus 906, Salmonella enterica ATCC700931,* Lactobacillus *Oenococcus oenii* as well as yeast *Candida guilliermondii NP-4.* Bacteria and yeast were cultivated on the ceramic plate porous of Zirconia from samples[4] of the mucous gastro-duodenal intestine tract sucked by *Helicobacter pylori* as well as of experimental models animal. For study of the bacterial surface structure bacteria used the electron microscopy with negative staining and ultrathin sections (TEM) and scanning (SEM) were used. The localization of mucopolysaccharides was determined by the method Luft. The computer analysis of the scenes was organized using the programs "Video-test; Struktura-5; Nanotechnology" and “Morphology”.

Ultrastructure analysis of bacterial colonies *in vitro* showed a typical fine construction for gram-negative and gram-positive bacteria. The clarification of the structured particularities of the intercellular contacts zones is realized with more detailed presentation of the surface structures and cellular wall. The study of the surface structures of gram-negative bacteria has revealed the different forms of intercellular contacts: for enteropathogenic *E. coli* with adhesive characteristics, fimbriae formation (Fig.1) might be taken part in delivering of plasmid and in fastening to the other substrate. By means of computer program, reconstruction of stereo-metrical orientation of the saw was managed. The sizes of the saw varied within 100 to 200 μm, but diameter was 8 nm. The other varieties of intercellular contacts for bacteria revealed itself in the manner of thick adhesion to be taken to cellular wall beside of *Shigella* as well as thick contact peptidoglycan of microcapsule.TEM research the mutual relation salmonella with the lactobacillus -probiotics has revealed close intercellular contacts and changes surfaces of a cellular wall of salmonella (fig.2).

TEM and SEM of intact yeast cultures *C. guilliermondii NP-4* have shown typical ultrastructure images for yeast cells and visualizations of intercellular contacts in biofilms (Fig. 3). Measurement of *Candida guilliermondii* by means of the program "Morphology" has shown:diameter =1.15-2,71 μm, length=3,22μm, buds=0,318μm. Adhesion of yeast on the surface of plate porous of Zirconia and multiform division of cells and multitude of buds (Fig. 4).

Thereby, studied by electronic microscope as well as by computer picture analysis ultrastructure peculiarities of cellular interactions of different gram-positive and gram-negative bacteria and yeast in biofilms are being formed as fimbria, close contact, membranes adhesion and cellular plexus [1-3]. This revealed ultrastructure particularities of cellular contacts to consider that the process of the shaping biofilm from bacteria and yeast depends from ultrastructure architectonic of microbial surfaces and morphological properties of substrates.

1. Avakyan A.A., Kats L.N., Pavlova I.B. Atlas to anatomies bacteria pathogenic for person and animal. M.: Medicine, 1972, 182 p.
2. Hovnanyan K.O., Navasardyan L.H., Hakobyan H.A. et al. Biological Journal of Armenia 60 (2008), p.67.
3. Hovnanyan K.O., Trchounian A.. Cell wall and cytoplasmic membrane structures of some bacteria: novel data and role in pathology. In Bacterial membranes, ultrastructure, bioelectrochemistry, bioenergetics and biophysics Ed. A. Trchounian, Kerala: Research Signpost, 2009, p.1-23.
4. Manukyan K., Amirkhanyan N., Aydinyan S.et al. Chemical Engineering Journal, 2010, 162(1), p. 406.

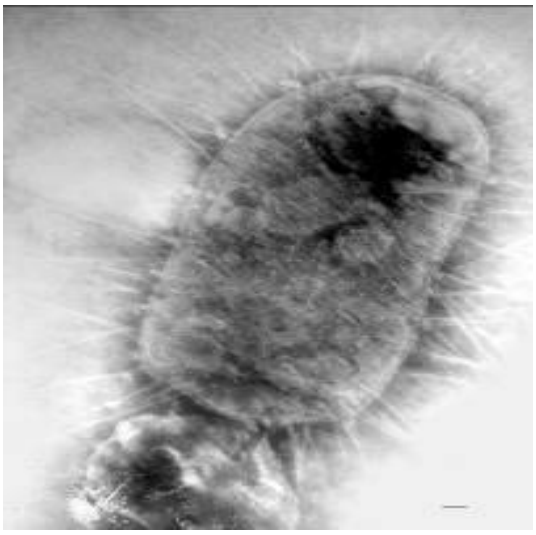

Figure 1. TEM of *E. coli serogroup O124* (negative staining).Bar:0,3 µm

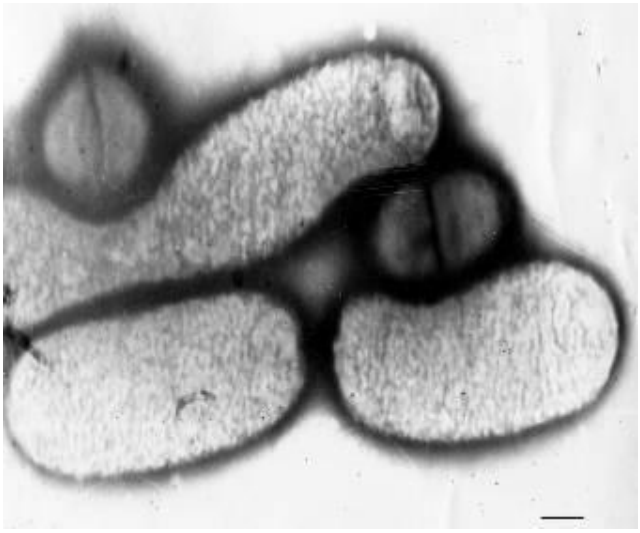

Figure 2. SEM of biofilm of *C. guilliermondii* NP-4. Bar:0,3 µm

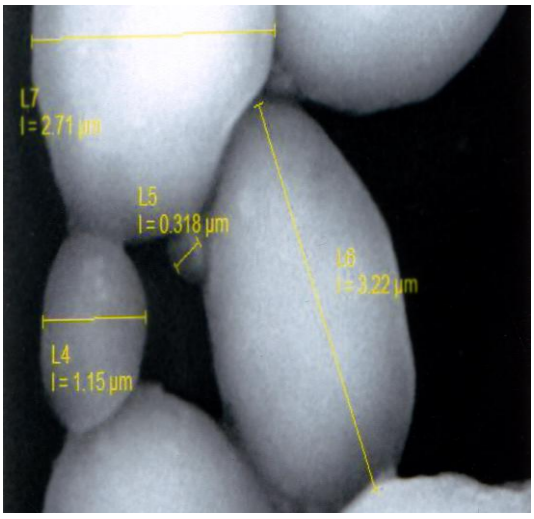

Figure 3. SEM of biofilm of *C. guilliermondii* NP-4.

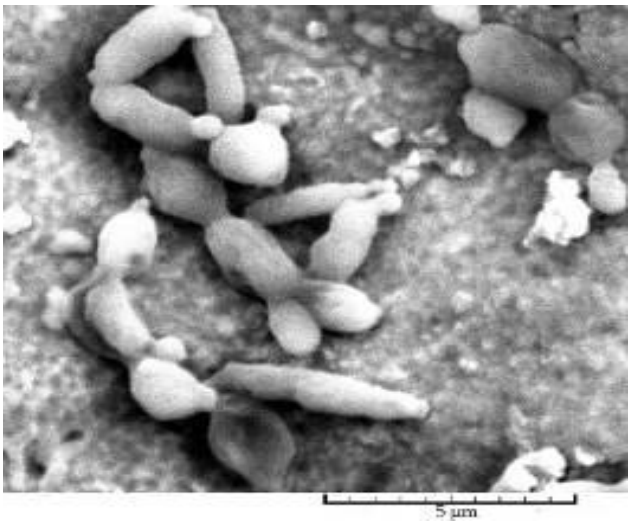

Figure 4. SEM of biofilm of *C. guilliermondii* NP-4. Formation of biofilm on ceramic porous plate of Zirconia.

Correlative Microscopy in Life and Materials Science

MIM.4.P062
Towards SIMS on the helium ion microscope: detection limits and experimental results on the ORION

D. Dowsett[1], L. Pillatsch[1], N. Vanhove[1], P. Philipp[1], T. Wirtz[1], S. Sijbrandij[2], J. Notte[2]

[1]CRP - Gabriel Lippmann, Belvaux, Luxembourg
[2]Carl Zeiss Microscopy LLC, Peabody, MA, United States

philipp@lippmann.lu

The ORION Helium Ion Microscope has become a well-established tool for high resolution microscopy [1] and nanofabrication [2]. The instrument is based on the atomic-sized ALIS gas field ion source, which has a brightness of $4x10^9$ A cm^{-2} sr^{-1} and which leads to a probe size of less than 0.5 nm. The source can operate with both helium and neon [3]. While secondary electrons are used for high resolution imaging, some compositional information can be obtained from backscattered He/Ne ions. In order to get chemical information with much higher sensitivity, we have previously investigated the feasibility of performing Secondary Ion Mass Spectrometry on the Helium Ion Microscope [4]. Our earlier studies concentrated first on potential useful yields, detection limits and achievable resolution and then on the practicality of secondary ion collection [5]. We have determined experimentally secondary ion yields under helium and neon bombardment for a range of semiconductor and metal samples. High secondary ion yields are crucial when using a small low current analytical probe. While basic yields are low due to the use of noble gas primary ions, they may be enhanced by several orders of magnitude for both negative and positive secondary ions by caesium and oxygen flooding respectively. Measurement of yields has allowed us to calculate detection limits for these samples under typical ORION imaging conditions (see figure 1).

More recently an extraction and detection system for secondary ions has been developed for the Helium Ion Microscope by the CRP - Gabriel Lippmann. We have investigated secondary ion emission for both semiconductor (Si, InP and GaAs) and metal (Cu, Ni) samples on the ORION. Secondary to primary ion current ratios have been measured under He bombardment on the ORION and are consistent with those determined previously. Both total secondary ion depth profiles and secondary ion images (see figure 2) have been obtained under helium and neon bombardment.

The obtained results are very encouraging and the prospects of performing SIMS on the ORION are very interesting. By combing high resolution imaging with high sensitivity chemical mapping new nanoanalytical experiments will become possible leading to enhanced information about analyzed samples.

1. L. Scipioni et al, J. Vac. Sci. Technol. B 27, 3250 (2009)
2. D. Winston et al, Nano Letters 11 4343 (2011)
3. F. Rahman et al., Scanning 33 (2011) 1
4. T. Wirtz et al, Appl. Phys. Lett. 101 041601 (2012)
5. D. Dowsett et al, J. Vac. Sci. Technol. B 30 06F602 (2012)

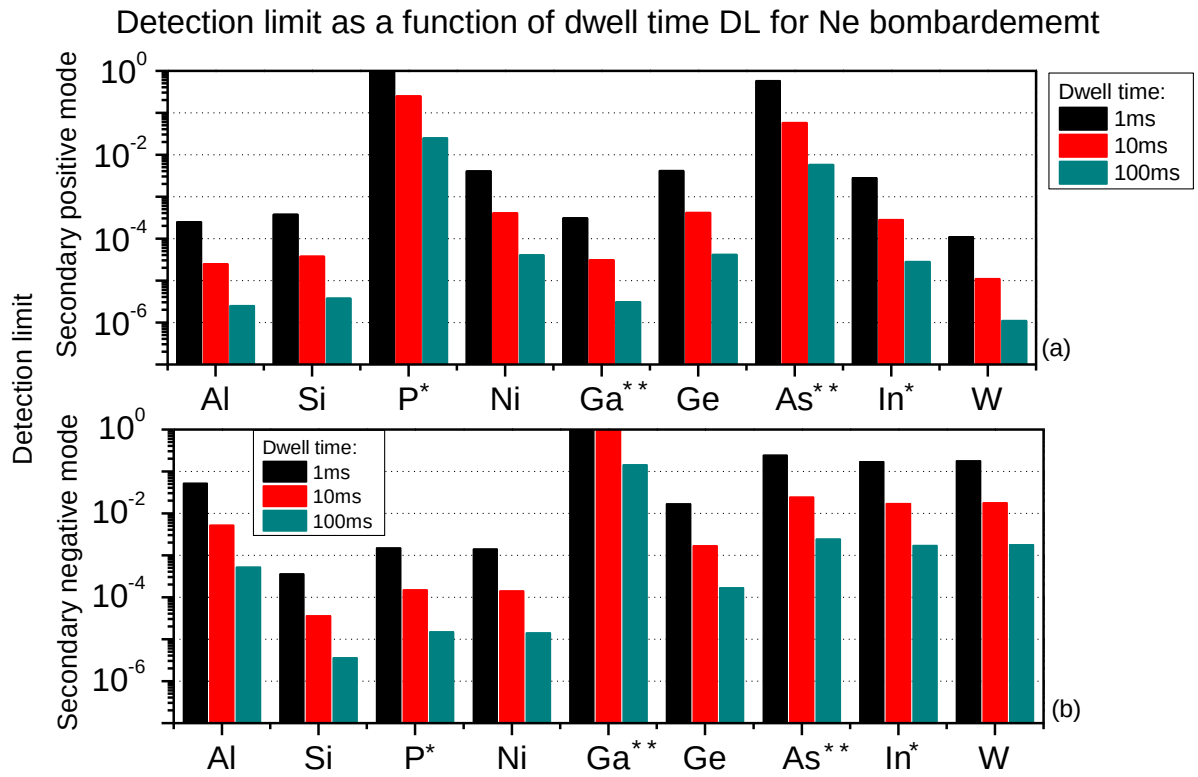

Figure 1: Detection limits for various semiconductor and metal samples under neon bombardment a) secondary positive mode with oxygen flooding b) secondary negative mode with caesium flooding.

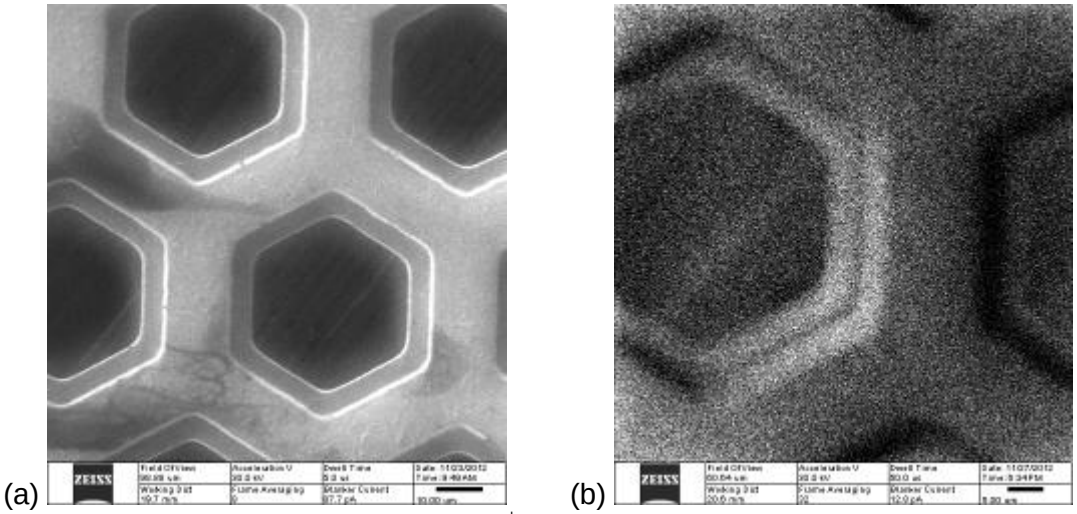

Figure 2: 400 mesh TEM grid imaged with a 13pA Ne^+ beam – (a) secondary electron image, (b) secondary ion image.

Correlative Microscopy in Life and Materials Science

MIM.4.P063
Detecting photosensitizing molecules at transmission electron microscopy by fluorescence photoconversion of diaminobenzidine

C. Pellicciari[1], M. Giagnacovo[1], B. Cisterna [2], M. Costanzo [2], A.C. Croce [3], G. Bottiroli [3], M. Malatesta [2]

[1]University of Pavia, Biology and Biotechnology, Pavia, Italy
[2]University of Verona, Department of Neurological, Neuropsychological, Morphological and Movement Sciences, Anatomy and Histology Section, Verona, Italy
[3]CNR, Institute of Molecular Genetics, Histochemistry and Cytometry Section, Pavia, Italy

pelli@unipv.it
Keywords: DAB photoconversion, transmission electron microscopy, photosensitizers

Photodynamic therapy (PDT) is an effective and moderately invasive therapy based on the action of photosensitizers (PSs). These compounds exert their cytotoxic effect when excited by light at proper wavelengths [1] and this is due to their capability to preferentially dissipate the adsorbed energy through photochemical processes rather than by fluorescence emission. As a consequence of these photochemical processes, oxidizing chemical species are produced (singlet oxygen, free radicals or reactive oxygen species) which can injure cell structures, and induce either necrosis or other regulated forms of cell death [2].

For the cytotoxic effect to be induced, PSs must effectively enter the cell and localize to sensitive subcellular sites: in fact, the oxidizing chemical species which are produced upon irradiation of PS-loaded cells are very unstable and can only affect closely surrounding molecules. Localization of the photoactive molecules at a fine subcellular resolution is therefore crucial for detecting the target organelles and, consequently, for understanding the subcellular bases of damage and death of photosensitized cells.

The aim of the present investigation was to directly visualize PS molecules at transmission electron microscopy (TEM) exploiting the fluorescence properties of the photoactive molecules to obtain the photoconversion of diaminobenzidine (DAB) into an electrondense product.

Human HeLa cells were grown in 25 cm^2 flasks in Dulbecco's minimal essential medium supplemented with 10% fetal bovine serum, in a humidified air atmosphere containing 5% CO_2. The cells were seeded onto glass coverslips 24 hr before being incubated for different times (5 to 60 min) in the dark with either 10^{-5} M Rose Bengal acetate (RB-Ac) or 10^{-6} M Hypocrellin B acetate (HypB-Ac): these molecules have been obtained by addition of two acetate groups to the PSs, RB and HypB, with the aim to increase their capability to enter the plasma membrane [3]. These modified compounds cannot serve, *per se*, as PSs (since the photophysical and photochemical properties of the native PSs are quenched), but they behave as fluorogenic substrates (FSs): after entering the cell, the acetate groups are removed by cell esterases, and the native molecules are restored with their fluorescence and photosensitizing properties.

At the concentrations used, these FSs are non-cytotoxic for cultured HeLa cells under dark conditions, while inducing massive cell death after light irradiation [4,5]. At the end of the incubation times, slides were removed from the medium, either to be immediately observed as fresh preparations by conventional or confocal fluorescence microscopy, or to be processed for TEM (see below). To investigate the phototoxic effects of either PS, some FS-loaded cell samples were submitted to light emission diode (LED) irradiation (FRAEN Company, Milan, Italy), using a 530 ± 15 nm LED for RB, and a 480 ± 15 nm LED for HypB; the total dose was 1.6 J/cm^2, with a uniform light fluency of 20 mW/cm^2 at the surface of the coverslips with the cells. In the attempt to detect early cell photodamage, cells were collected 5 to 30 min post irradiation (P-I).

For TEM, RB-Ac- or HypB-Ac-loaded HeLa cells on coverslips were fixed with 2.5% (v/v) glutaraldehyde and 2% (v/v) paraformaldehyde in 0.1 M phosphate buffer, pH 7.4, at 4° C for 1h, washed and incubated with 3,3' diaminobenzidine (DAB) (20 mg/10 ml in 0.05 M Tris HCl, pH 7.6) under simultaneous irradiation with two 8W Osram Blacklite 350 lamps for 2 h (these lamps have two emission peaks of high intensity at 550 and 580 nm, thus being suitable for RB or HypB excitation); the cells were then post-fixed with 1% OsO_4 and 1.5% potassium ferrocyanide at room temperature for 1 h, dehydrated with acetone and embedded in Epon resin. As controls, some samples were processed as described above but omitting both DAB incubation and exposure to light. For better visualization of the reaction product, ultrathin sections were weakly stained with 2.5% aqueous solution of uranyl acetate for 2 min. The same procedures of fixation and embedding reported above

were used for HeLa cell samples treated with RB-Ac or HypB-Ac and submitted to light irradiation. The thin sections from these samples were stained with 4.7% aqueous solution of uranyl acetate for 5 min and Reynolds lead citrate for 2 min, to visualize the occurrence of organelle photodamage.

After short incubation times (2 to 5 min) with either FSs, brightly fluorescing spots were detected, initially near the plasma membrane and then in clusters close to the nucleus; for longer incubation times (30 min onwards) a weak diffuse fluorescence was also observed in the cytoplasm. Confocal microscopy demonstrated that photoactive molecules were never present in the nucleus even for long incubation times (up 60 min).

As for the distribution pattern of the reaction products and the organelles involved, comparable results were obtained at TEM for HeLa cells loaded with either FSs. At 5 min incubation, a fine granular reaction product was observed at the surface of invaginations of the plasma membrane as well as in vesicles which were often found near the plasmalemma; this proves that the FSs are already converted to the native PS molecules by membrane-bound esterases, and supports endocytosis as the main mechanism for the internalization of these FSs. At 15 to 30 min incubation times, most of the DAB reaction product was observed in multivesicular bodies and residual bodies, and for longer incubation times DAB positivity was also found in the cytosol, consistent with the evidence of diffuse fluorescence at light microscopy. On the contrary, DAB-photoconversion product was never found inside the nucleus.

After 5 to 15 min P-I of FS-laded cells, ruptures of the plasma membrane and of the limiting membranes of residual and multivescicular bodies were found. At 30 min P-I, also the microfilaments and the microtubules were found to undergo clustering and fragmentation, thus demonstrating the presence and action of photoactive molecules in the cytosol.

Since the pioneering paper by Maranto [6], a variety of fluorochromes proved to be DAB photo-convertible into reaction products for light and electron microscopy, and especially in recent years, this procedure has been used in correlative microscopy to investigate at the high spatial resolution of TEM the subcellular localization of specific fluorescently-labelled molecules [7,8]. The present report demonstrates that this procedure may be suitable to convert the fluorescence emission of a PS into an electron dense product.

The ultrastructural localization of photoactive molecules we have observed is fully consistent with the multiorganelle photodamage described after irradiation in culture of RB-Ac- or HypB-Ac-loaded cells [5,6]: both membrane-bounded organelles as well as cytosolic structures such as microtubules and microfilaments undergo massive photodamage eventually leading to necrotic or apoptotic cell death, depending on the FS concentration used.

The efficacy of PDT basically depends on the accumulation of photoactive molecules at specific subcellular sites where photodamage may trigger different forms of either regulated or catastrophic cell death [4,9]. DAB photoconversion promises to be an appropriate tool for directly visualizing the PS molecules at high resolution in single cells: this would allow to elucidate the mode of intracellular penetration and the dynamics of cytoplasmic redistribution and organelle targeting. It is worth noting that DAB deposits do localize in the very close proximity of the sites where photoactive molecules elicited the production of reactive oxygen species upon light irradiation: actually, the half-life of oxidizing chemical species such as singlet oxygen and superoxide or hydroxyl radicals is very short (from 1 ns to 1 □s) and their mobility extends to 1 to 30 nm only [10].

1. P. Agostinis, K. Berg, K.A. Cengel, T.H. Foster, A.W. Girotti, S.O. Gollnick, S.M. Hahn, M.R. Hamblin, A. Juzeniene, D. Kessel, M. Korbelik, J. Moan, P. Mroz, D. Nowis, J. Piette, B.C. Wilson and J. Golab, CA Cancer J. Clin. 61 (2011), p. 250.
2. A.D. Garg, D. Nowis, J. Golab and P. Agostinis, Apoptosis 15 (2010), p. 1050.
3. G. Bottiroli, A.C. Croce, P. Balzarini, D. Locatelli, P. Baglioni, P. Lo Nostro, M. Monici and R. Pratesi, Photochem. Photobiol. 66 (1997), p. 374.
4. C. Soldani, M.G. Bottone, A.C. Croce, A. Fraschini, M. Biggiogera, G. Bottiroli and C. Pellicciari, Histochem. Cell Biol. 128 (2007), p. 485.
5. A.C. Croce, E. Fasani, M.G. Bottone, U. De Simone, G. Santin, C. Pellicciari and G. Bottiroli, Photochem. Photobiol. Sci. 10 (2011), p. 1783.
6. A.R. Maranto, Science 217 (1982), p. 953.
7. C. Röhrl, C. Meisslitzer-Ruppitsch, R. Bittman, Z. Li, G. Pabst, R. Prassl, W. Strobl, J. Neumüller, A. Ellinger, M. Pavelka and H. Stangl, Curr. Pharm. Biotechnol. 13 (2012), p. 331.
8. W. Kukulski, M. Schorb, S. Welsch, A. Picco, M. Kaksonen and J.A.G. Briggs, J. Cell Biol. 192 (2011), p. 111.
9. E. Buytaert, M. Dewaele, P. Agostinis, Biochim. Biophys. Acta 1776 (2007), p. 86.
10. T. Karuppanapandian, J.-C. Moon, C. Kim, K. Manoharan and W. Kim, Aust. J. Crop. Sci. 5 (2011), p. 709

Correlative Microscopy in Life and Materials Science

MIM.4.P064
ProVIS Centre - Correlative Microscopy for imaging microbial-mediated biochemical processes

N. Musat[1], H. Stryhanyuk[1], H.-H. Richnow[1]

[1]UFZ Leipzig, Isotope Biogeochemistry, Leipzig, Germany

niculina.musat@ufz.de

Microbial processes drive the biogeochemical cycles of elements on earth. The assessment of structure, function and metabolic activity of microorganisms as well as their abundance in natural systems is essential to our understanding of ecosystem functioning. The study of microbial metabolic activities of single cells in situ is challenging mainly due to the complexity of physicochemical and structural interactions between members of the microbial communities (i.e. cell to cell interactions) and due to the interactions between microbes and organic and inorganic components of their living environment.

Here we introduce the correlative microscopy facility at Helmholtz Centre for Environmental Research - UFZ in Leipzig. This facility will offer a series of microscopy techniques within the ProVIS Center, enabling visualization of cell structural features and quantitative imaging of microbial mediated biochemical as well as geochemical processes with micron- to nanometer scale resolution. The main instruments and techniques available are Helium Ion Microscope (HIM) for high-resolution imaging of cell surface (Figure 1); Confocal Raman combined with Atomic Force Microscopy (AFM) for chemical imaging along with cell surface topography (Figure 2) and physical properties; Nano-scale Secondary Ion Mass Spectrometry (nanoSIMS) for elemental and isotopic quantitative imaging of cellular and subcellular structures (Figure 3). Expertize in Fluorescence In-situ Hybridisation (FISH, CARD-FISH) and the use of epifluorescence microscopy will be employed for the identification of single cells. Laser Micro-Dissection system (LMD) equipped with laser tweezers will be used for cell marking, separation and isolation. In addition, the facility will be fully equipped for biological sample preparation and surface treatment, e.g. high-pressure freezing, cryo-ultramicrotomy, critical point and sublimation drying. The broad expertise of the scientists and the high-resolution correlative microscopy platform will enable comprehensive single cell studies on microorganisms morphology, identity and activity in biofilms and aquifers, interaction of microbial cells with metals and minerals and further applications in life sciences.

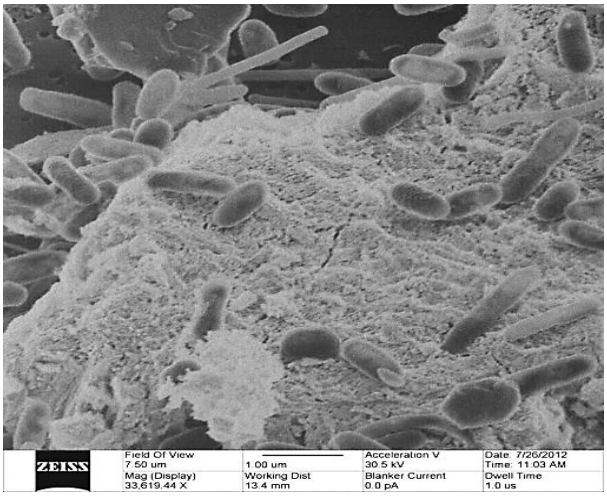

Figure 1. HIM image of bacteria growing on manganese oxides

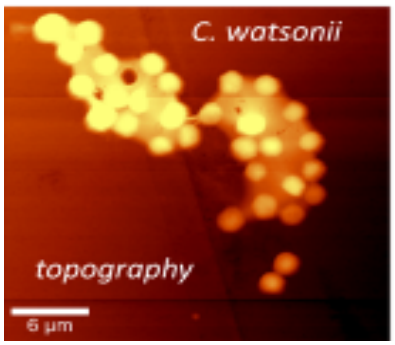

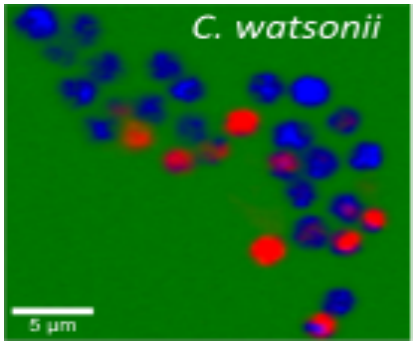

Figure 2. AFM image of *C. watsonii* Fluorescence image of *C. watsonii*

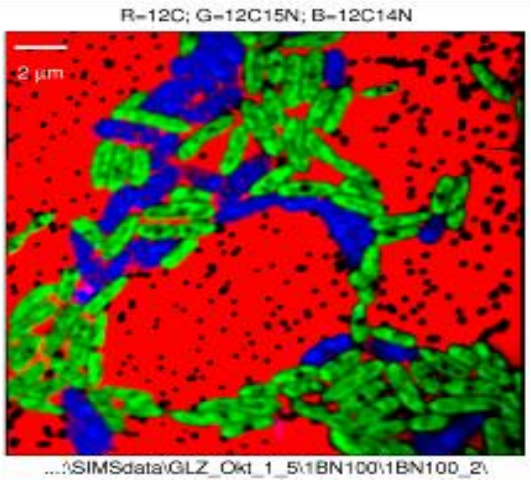

Figure 3. *NanoSIMS* image (RGB) showing ^{15}N ammonium assimilation by *P. putida* (green)

Correlative Microscopy in Life and Materials Science

MIM.4.P065
Prerequisites for correlative light microscopy and scanning electron microscopy of viral infections.

C. Bayer[1], N. Subramanian[1], L. Wang[1], G. Frascaroli[1], T. Mertens[1], P. Walther[1]

[1]Ulm University, Z. E. Elektronenmikroskopie, Ulm, Germany

paul.walther@uni-ulm.de
Keywords: CLEM, HCMV, SEM, backscattered electrons

Correlative light and electron microscopy (CLEM) is a powerful approach to combine the unsurpassed resolution capacities of electron microscopy with the capabilities of fluorescence light microscopy to label and identify distinct proteins [1]. Methodic challenges are to perform the labeling in a manner that does not destroy the surface structures, so that observation of the fine structure with the scanning electron microscope (SEM) is not impaired. This is best realized, when cells express a fluorescent tag, such as xFP, so that no additional labeling procedures are necessary [2]. In this work, however, we did the labeling after fixation with paraformaldehyde without extracting membranes or other sensitive structures by detergents or organic solvents. The second methodic challenge is to identify the same area in the fluorescence light microscope and in the SEM. For this purpose Zeiss developed the “shuttle and find” solution. In this preliminary study, however, we used small (3 mm) sapphire discs with an imprinted coordinate system, as used for our high pressure freezing, freeze substitution and embedding approaches [3]. The coordinate system is visible in the light microscope as well as in the SEM. The biological purpose of this study is to better visualize and, thereafter, better understand the processes at the early stages of viral infection [2]. Since it has been difficult to unambiguously discern viral particles from other structures on the cell surface, we will combine CLEM with the standard SEM immunolabeling method using 10 nm colloidal gold particles, which can be detected in the SEM by using the material dependent backscattered electron signal [4].

For the preliminary experiments of this study (Figures 1 to 3) human monocyte-derived macrophages were seeded on carbon-coated sapphire discs with an imprinted coordinate system (Engineering Office M. Wohlwend, Switzerland). After having attached to the sapphire discs (1 day), the cells were fixed with 4% formaldehyde and incubated with primary mouse antibodies directed against major histocompatibility complex class II (MHC-II) for 1 hour at 37 °C. For immunofluorescence a secondary anti-mouse antibody conjugated with a red-fluorescent dye (AlexaFluor555) was used and the nucleus was counterstained with the blue-fluorescent stain DAPI (4',6-diamidino-2-phenylindol). Afterwards, cells were fixed with 2% glutaraldehyde, dehydrated in a graded series of propanol and critical point dried. A Zeiss Axioskop2 microscope was used for fluorescence microscopy. Then, the sample was coated with 10 nm of carbon by electron beam evaporation to enhance electrical conductivity and imaged with a SEM (Figures 1 to 3). The coordinate system was used to align the light microscopical and the SEM images. For Figures 4 to 6 human cytomegalovirus (HCMV) particles were attached on a silicon chip, fixed with 4% paraformaldehyde and labeled with an antibody against viral surface proteins that is detected with a secondary antibody conjugated to 10 nm colloidal gold. Afterwards samples were processed for SEM as described above. In further projects we plan to use the tools developed in this work to study the early stages of HCMV infections in macrophages. [5]

1. C. Buser in “Electron Microscopy of Model Systems” ed. T. Müller-Reichert (Methods in Cell Biology, Vol. 96, Elsevier Inc.) (2010) 217-234.
2. C. Bayer, S. Varani, L. Wang, P. Walther, S. Zhou, S. Straschewski, M. Bachem, D. Söderberger-Naucler, T. Mertens and G. Frascaroli, J. Virol. 87 (2013) 67-79.
3. K. Höhn, C. Schmid and P. Walther. Proceedings of the Microscopy Conference (2011), Kiel, Volume 2, Life Sciences, ISBN 978-3-00-033910-3, p322.
4. P. Walther, B.H. Ariano, S. R. Kriz and M. Müller, Beitr Elektronenmikroskop Direktabb Oberfl 16 (1983) 539–5456
5. This work is supported by the BMBF grant NanoCombine.

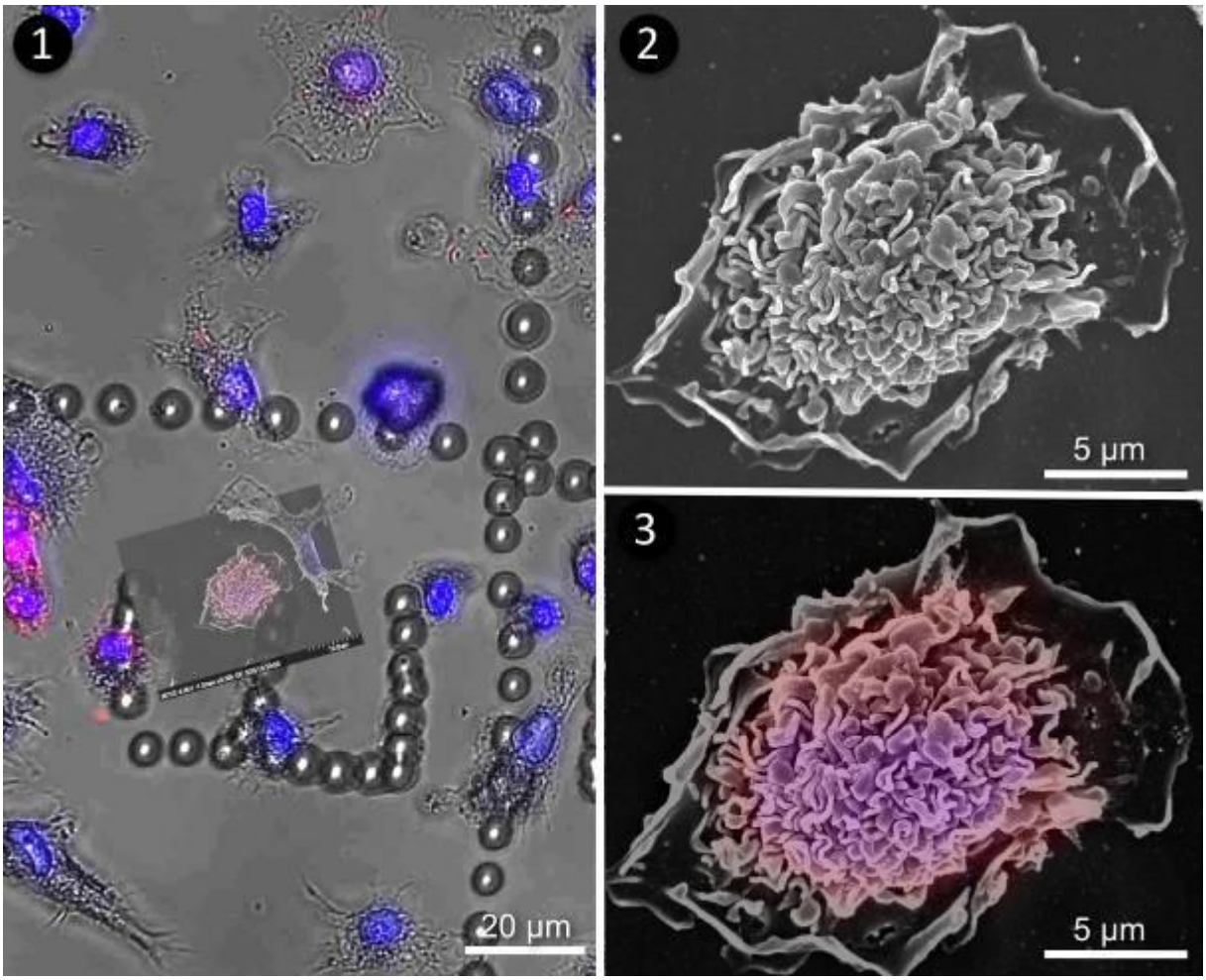

Figure 1 to 3. CLEM of macrophages labeled for major histocompatibility complexes (red) and DNA (blue). Figure 1 immunofluorescence and phase contrast images showing a portion of the imprinted coordinate system for correlation, in the centre a superimposed SEM image. Figure 2. SEM surface image. Figure 3. Correlation of SEM image and fluorescence image. Major histocompatibility complexes are cell surface molecules which are important for presentation of antigens to T cells and therefore for the activation of the immune system.

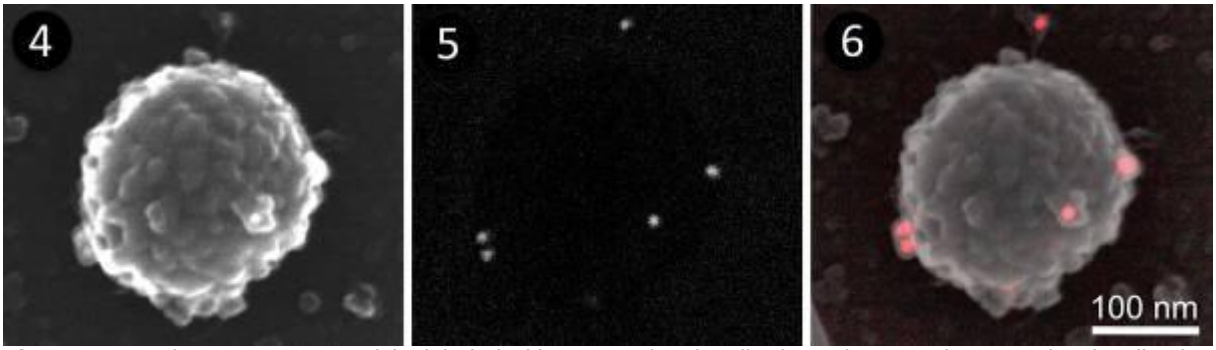

Figure 4 to 6. show an HCMV particle, labeled with a monoclonal antibody against a surface protein, visualized with a secondary antibody coupled to 10 nm gold. The secondary electron image (Figure 4) shows the surface, the material dependent backscattered image (Figure 5) shows the distribution of the colloidal gold. Figure 6 is an overlay of both images, the backscattered image is smoothed and red colored. This approach should help us in the future to unambiguously detect viral particles on the highly structured macrophages.

Correlative Microscopy in Life and Materials Science

MIM.4.P066
Scanning electron microscopy observation of erythrocyte ghosts isolated from slaughterhouse blood by gradual hemolysis

I. Kostic[1], K. Bukara[1], V. Ilić[2], S. Mojsilović [2], V. Đorđević [1], B. Isailović[1], Ļ Veljović[1], B. Bugarski[1]

[1]University of Belgrade, Faculty of Technology and Metallurgy, Belgrade, Serbia
[2]University of Belgrade, Institute for Medical Research, Belgrade, Serbia

ikostic@tmf.bg.ac.rs
Keywords : red blood cells, erythrocyte ghosts, scanning electron microscopy

Slaughterhouse blood, although usually treated as waste and discarded, represents an inexpensive source of red blood cell membranes (ghosts). Detailed chacterization of ghosts and use of advanced biotechnological tools for their modifications, could enormously contribute to its application for delivery of active compounds and for manufacturing of complex delivery systems (e.g. multilayer microcapsules with the core of ghosts).

In this work, isolation of erythrocyte ghosts from bovine slaughterhouse blood is based on gradual hypotonic hemolysis [1]. The obtained bovine ghosts were analysed from the aspect of morphology and structural integrity by means of flow cytometry, phase-contrast and scanning electron microscopy.

Flow cytometric analysis was performed on CyFlow® SL flow cytometer (Partec, Münster, Germany) using FlowMax 2.4 software (Partec, Münster, Germany). The samples for scanning electron microscopy were prepared as follows: Packed erythrocytes and ghosts were fixed in 2.5 % glutaraldehyde solution in PBS for 1h and washed twice in PBS. The preparations were post-fixed in 2 % osmium tetroxide for 1 h, rinsed in PBS, dehydrated through a graded ethanol series (10, 30, 50, 70, 95 and 100 %) for ten minutes each, and then subjected to critical point drying using liquid carbon dioxide (Bal-Tec CPD030 Critical Point Dryer). After gold coating, samples were visualised on a field emission scanning electron microscope (FE-SEM), a TESCAN MIRA 3 XMU, operated at 10 kV.

The morphological changes of erythrocytes and appearance of erythrocyte ghosts after gradual hemolysis and restoration of isotonicity, were assessed by phase contrast microscopy using Olympus CKX 41 inverted microscope (Olympus Europa Holding GmbH, Hamburg, Germany). (Figure 1.) The micrographs showed intact cellular structures of ghosts, having altered cellular content (without the content of hemoglobin), and approximately the same size of ghosts and starting erythrocytes. The assessment of erythrocytes and ghosts size was performed by forward scatter (FSC) analysis on flow cytometer. As presented in Figure 2a, two populations of erythrocytes are visible (populations R1 and R2), while the same analysis of ghosts (Figure 2b) revealed another population of small “events” (population R5). We assumed that fragmentation of ghosts was induced by shear stresses associated to flow cytometric measurements. The presence of small vesicles (R5) was not detected under phase contrast microscope. Detailed insight into ghosts morphology obtained by FE-SEM (Figure 3b), showed slightly distortion from erythrocyte shape (Figure 3a), an altered surface texture with increased bilayer curvature and existence of numerous invaginations. This kind of morphology has been reported for human erythrocytes when hypotonic PBS buffer was used in a production of ghosts [2]. Scanning electron micrographs have indicated that there is no difference in size between red blood cells and ghosts obtained by gradual hemolysis. The morphological alterations of bovine ghosts observed by FE-SEM, may be related to the changes of transbilayer lipid asymmetry or cytoskeleton content (as reported for human ghosts [2]). They probably triggered formation of small vesicles during flow cytometry analysis.

1. R. Stojanović, V. Ilić, V. Manojlović, D. Bugarski, M. Dević, B. Bugarski, Applied Biochemistry and Biotechnology 166 (2012) p. 1491-506.
2. F.M. Harris, S.K. Smith, J.D. Bell, The Journal of Biological Chemistry 276 (2001) p.22722-31.

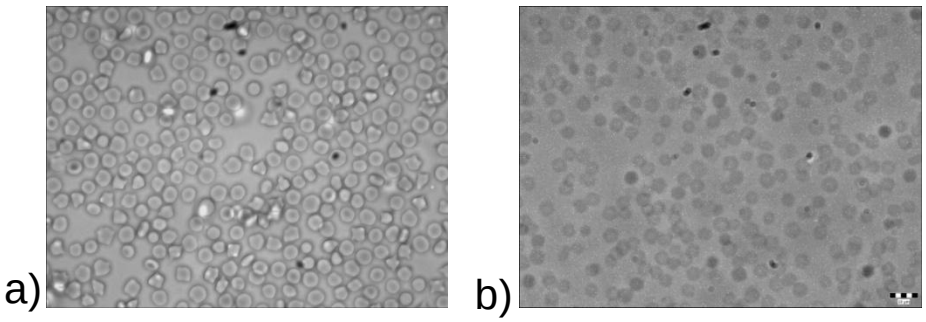

Figure 1. Phase contrast micrographs of erythrocytes from bovine slaughterhouse blood (a) and erythrocyte ghosts obtained by gradual hypotonic hemolysis (b); Magnification ×400.

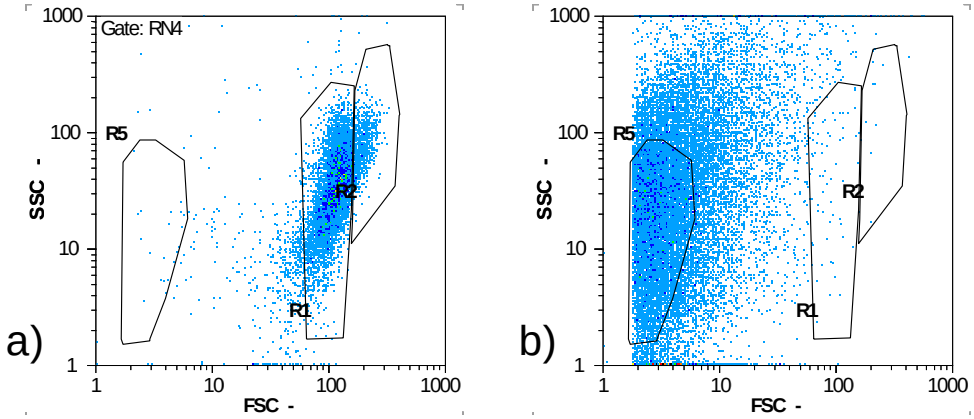

Figure 2. Flow cytometric analysis of bovine erythrocytes (a) and ghosts obtained by gradual hemolysis (b); R1 and R2 - erythrocyte populations, R5 - small vesicles.

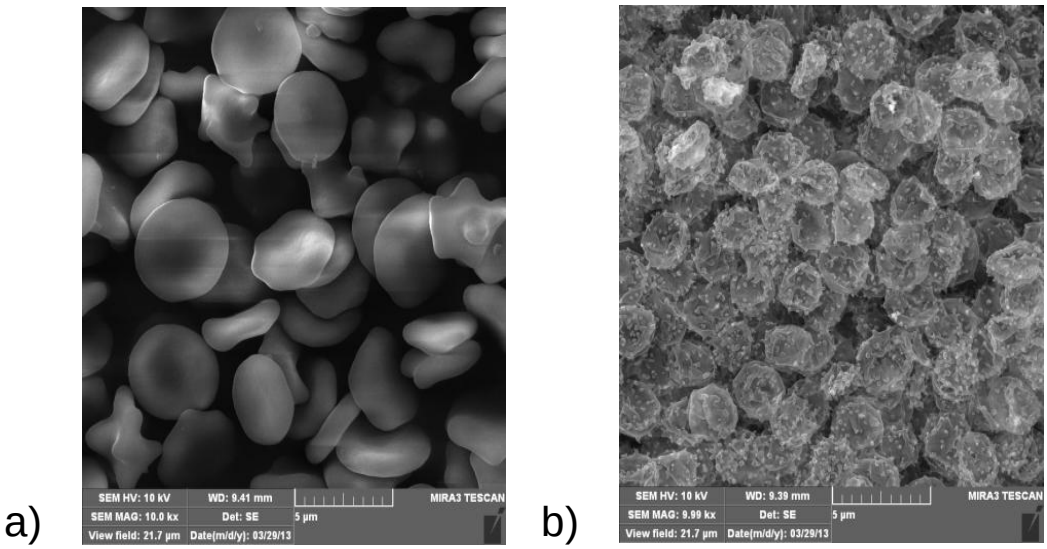

Figure 3. Scanning electron micrographs of bovine erythrocytes (a) and ghosts obtained by gradual hemolysis (b).

Biomaterials

MIM.5.067
Microscopy techniques in muscle tissue engineering

H. Kenar[1,2], C. Muratgul[2], G. Kose[3], C.C. Kesemenli[4], E. Karaoz[1,5], V. Hasirci[6,7]

[1]Kocaeli University, Institute of Health Sciences, Stem Cell Department, Kocaeli, Turkey
[2]Kocaeli University, Graduate School of Natural and Applied Sciences, Polymer Science and Tech. Dept., Kocaeli, Turkey
[3]Yeditepe University, Department of Genetics and Bioengineering, Istanbul, Turkey
[4]Kocaeli University, Faculty of Medicine, Department of Orthopedics and Traumatology, Kocaeli, Turkey
[5]Kocaeli University, Center for Stem Cell and Gene Therapies Research and Practise, Kocaeli, Turkey
[6]METU, BIOMATEN Center of Excellence in Biomaterials and Tissue Engineering, Ankara, Turkey
[7]METU, Department of Biological Sciences, Biotechnology Research Unit, Ankara, Turkey

halime.kenar@kocaeli.edu.tr, halimekenar@gmail.com
Keywords: cell alignment, muscle tissue engineering, microscopy

Tissue engineered muscle constructs have been developed as alternatives to autografts or allografts to be used especially in regeneration of normal anatomy and physiology of the damaged tissue. Components of tissue engineering approach are cells, scaffolds and regulators. Since lots of cells are needed for production of a tissue equivalent, stem cells have drawn attention due to their ability to proliferate easily in *in vitro* and to differentiate into many cell types. The most prominent stem cell candidates that can be safely used in clinical treatments are the mesenchymal stem cells (MSCs).

The tissue engineering approach involves cell propagation *in vitro* and a subsequent cell seeding on 3D biodegradable scaffolds where the cells attach, grow and form the new tissue substitute as they differentiate. It is well known that the cell carriers, with their chemical, biological, architectural and physical properties, have a substantial effect on the behavior of anchorage dependent MSCs. Both skeletal and cardiac muscle fibers are oriented parallel to each other in their native tissue and this structural organization is very important in terms of proper tissue functionality. Fibrous scaffolds that mimic the natural ECM and possess an aligned structure can be used to control cellular orientation.

Both natural and synthetic biodegradable polymers are used to obtain 3D scaffolds for muscle tissue engineering. Besides serving as cell carries, natural polymers can provide biological cues to the cells to control stem cell fate. On the other hand, synthetic polymers can be easily modified to obtain tailor-made scaffolds and may better preserve tissue integrity until the new tissue is fully regenerated. It is very common nowadays to combine the natural and the synthetic polymers to form a hybrid scaffold that possesses the properties of both and thus may have a synergistic effect on the cells. Microscopy is of utmost importance in characterization of both the scaffolds and the final tissue engineered constructs.

The goal in this study was to design polymeric mats with aligned microfibers that can serve as scaffolds in tissue engineering of both skeletal muscle and myocardial tissues. Aligned microfibrous mats were obtained by electrospinning a polyester blend (PHBV (5% HV), P(L-D,L)LA (70:30) and poly(glycerol sebacate) (PGS)) and a blend of hyaluronic acid (HA), collagen (COLL) and PLA/PCL (70:30). Fiber diameter and orientation in the mats were determined via scanning electron microscopy (SEM). The distribution of the biological component in the HA:COLL:PLA/PCL fibers was revealed by bright field microscopy of histochemically stained mats. Human skeletal muscle stem cells (hSkMSCs) were seeded on the PHBV:PLDLLA:PGS mats to align them and promote unidirectional myofiber formation. Simultaneous construct vascularization protocol was developed by coculturing hSkMSCs with human endothelial cells (HUVEC or ECFC). Cell alignment and capillary network formation was assessed with fluorescence microscopy: the endothelial cells formed both unidirectional and transverse capillary networks, and hSkMSCs were able to form aligned myotubes.

The microfibrous PHBV:PLDLLA:PGS mats were seeded with MSCs from human umbilical cord matrix (Wharton's Jelly) to obtain a construct that can serve as a myocardial patch [1]. Cellular alignment and cell penetration within the mats were investigated with confocal microscopy. The 3D myocardial construct design involved two biodegradable macroporous tubes, to allow transport of growth media to the cells within the construct, and cell seeded, aligned fiber mats wrapped around them. SEM was used to visualize the final construct. The 3D construct was cultured in a microbioreactor by perfusing the growth media transiently through the macroporous tubing, sectioned at the end of the culture and examined by fluorescence microscopy: enhanced cell viability, uniform cell distribution and preservation of the cell alignment in the perfused 3D construct were confirmed.

1. Kenar H, Kose GT, Toner M et al. Biomaterials 32 (2011), p.5320.

Biomaterials

MIM.5.068
Evaluation of nanocoated polymeric biomaterials in term of surface properties

S. Gümüş[1], S. Polat[1], J. Lackner[2], W. Waldhauser[2]

[1]Kocaeli University, Metallurgical & Materials Engineering, Kocaeli, Turkey
[2]JOANNEUM RESEARCH Forschungsgesellschaft mbH, Funktionelle Oberflächen, Leoben, Austria

gumus.serap@gmail.com
Keywords: biomaterials, biocompatibility, polymeric materials, nanosized topography, roughness

Biomaterials are natural or artificial based materials that are used to support or replace a part of the function of living tissue of human body. Biocompatibility is the major property of a material to evaluate it as biomaterial and depends on a series of biological responses occurring at the interface of the material's surface and biological system [1]. It is of great importance to know the cell/biomaterial interaction mechanism in designing biomaterial surfaces with improved biocontact properties.

Surface properties of a biomaterial such as composition, roughness, topography, wettability play a major role in the events occurring at material interface. When the biomaterial comes in contact with the biological system containing different types of proteins e.g. blood, cell culture media, interstitial fluid etc., proteins will adsorb on the surface of the material, rapidly [2]. The type and amount of the adsorbed proteins determine the bioactive sites for cell interactions. Therefore, influence of the surface properties such as chemistry, roughness, topography to adsorption of the protein should be understood for controlling the cellular response. Polymeric materials provide most of the requirements for biomedical applications [3]. However, polymeric materials are inadequate in many cases in terms of biocontact. Surface engineering offers a multi-purpose approach for solving this problem by creating nanosized layer to control the chemical composition, topography and roughness, hydrophilic /hydrophobic balance on the surface. Pulsed laser coating (PLC) is a method to produce such surfaces at room temperature which is appropriate for coating polymers. One of the major effects of the surface properties on the protein adsorption is the characteristics of the surface topography including shape and size of features, roughness parameters etc. Also, the surface wettability and energy which will further influence the behavior of biological molecules are significantly affected by roughness. It has recently been revealed that cell adhesion is also influenced by surface features as small as 10 nm [4, 5]. Recently, atomic force microscopy (AFM) is widely used for imaging of nanometer-sized surface structures due to its ability of providing high-resolution images in atomic scale. Three dimensional (3D) images of the surface are obtained by AFM, providing information about the surface morphology, roughness, features formed at the surface, their shape and distribution.

In this study, surface properties like topography, roughness, surface energy, hydrophobicity and hydrophilicity are determined for nanocoated polymers to be evaluated as biomaterials. Polyurethane (PU) and polycarbonate (PC) based polymeric materials are coated with titanium (Ti), titanium nitride (TiN) and diamond like carbon (DLC) nanosized layer by PLC.

The AFM images taken in tapping mode of Ti, TiN and DLC coated PC and PU are given in Figure 1, respectively. As it is seen, the surface morphology of stiff polymer, PC differs from the surface of the soft polymer, PU. Dome-shaped topographic features are dominant at the surface of PC whereas wrinkle structures are seen at the surface of PU. Stiff materials overcome the deformation that occurs near the surface under high stress if the adhesion of the coating on the substrate is very strong, while the soft materials start to wrinkle [6]. Roughness parameters such as average roughness (R_a), root mean square (R_q), skewness (R_{sk}) and kurtosis (R_{ku}) are determined from AFM analysis.

1. W. Song, H. Chen, Chinese Science Bulletin, 52, (2007), pp. 3169-3173.
2. R. A. Latour, Jr., in “Encyclopedia of Biomaterials and Biomedical Engineering”, 2nd. Edition, vol.1, G. E. Wnek, G. L. Bowlin (eds.), pp. 270-284, Informa, NY (2008).
3. Y. X. Wang, J. L. Robertson, W. B. Spillman, Jr., R. O. Claus, Pharmaceutical Research, 21, (2004), pp. 1362-1373.
4. M. S. Lord, M. Foss, F. Besenbacher, Nano Today, 5, (2010), pp.66-78.
5. M. J. Dalby, M. O. Riehle, H. Johnstone, S. Affrossman, A. S. G. Curtis, Cell Biology International, 28, (2004), pp. 229-236.
6. J. M. Lackner, W. Waldhauser, P. Hartmann, O. Miskovics, F. Schmied, C. Teichert, T. Schöberl, Thin Solid Films, 520, (2012), pp. 2833-2840.

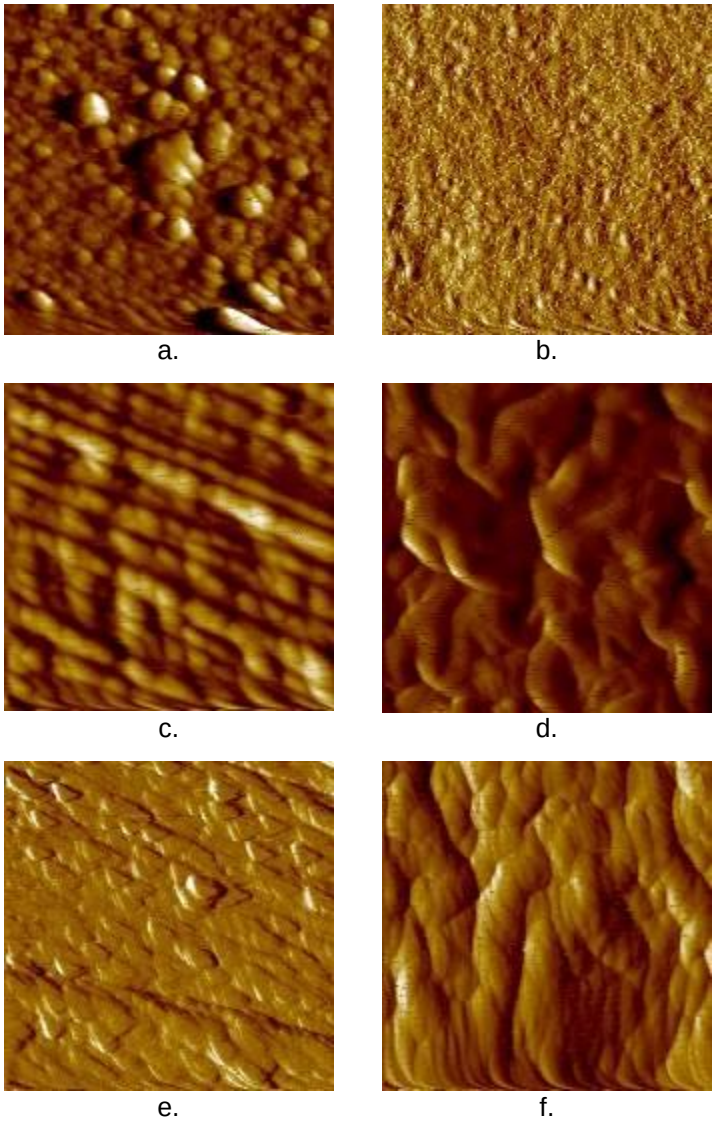

Figure 1. AFM images of PC coated with a) Ti, c) TiN, e) DLC and PU coated with b) Ti, d) TiN, f) DLC.

Biomaterials

MIM.5.069
Synergistic Effects Among Cellulases during Enzymatic Cellulose Degradation, Visualized by In-situ Atomic Force Microscopy

T. Ganner[1], P. Bubner[2], M. Eibinger[2], C. Mayerhofer[1,3], H. Plank[1,3], B. Nidetzky[2]

[1]Graz University of Technology, Institute for Electron Microscopy and Fine Structure Research , Graz, Austria
[2]Graz University of Technology, Institute of Biotechnology and Biochemical Engineering, Graz, Austria
[3]Graz Centre for Electron Microscopy, Graz, Austria

thomas.ganner@felmi-zfe.at
harald.plank@felmi-zfe.at
Keywords: Cellulose, Atomic Force Microscopy, Enzymatic degredation

Cellulose, a biopolymer consisting of linked sugar molecules as polymer-units, is used by plants as a structural compound in their cell walls. It is the most abundant polymer of this kind on earth and by degrading it to sugar and then into ethanol it is a valuable resource of energy referred to as 2nd generation biofuels. These fuels do not only show a zero emission footprint since burned CO_2 is used again by plants to build up there cellulose livestock, it also triggers no food vs. fuel concerns as for 1st generation biofuels. In nature a variety of organisms use cellulose as energy resource via enzymatic degradation into sugar. The specialized enzymes, which can degrade cellulose, are called cellulases and are bio-catalytic protein units. An important and well investigated model organism in this research field is the fungus *Trichoderma reesei* which has also been used for this study.

Enzymatic cellulose decomposition is known for almost 70 years and has been investigated by various methods like electron microscopy and biochemical methods [3]. The process itself is empirical understood by combining results of electron microscopy and biochemical measurements but there are some missing links and unresolved questions related to it. While electron microscopy allows nanometer resolution, it cannot provide an appropriate environment for the enzymes due to vacuum conditions, thus inhibiting in-situ investigations. In contrast, biochemical methods allow time resolved characterization but lack microscopic information. Combing both processes would be a highly desirable way to answer fundamental questions and find solutions to the problems still attendant for the efficient fuel production out of cellulose.

In this study we have used atomic force microscopy in liquid environments, which allow dynamic in-situ characterization with single molecule resolution on a nanoflat cellulose surfaces (see Figure 1A). While most natural cellulose sources do not show sufficiently flat surfaces, we use a special method for the fabrication of nanoflat and reproducible cellulose substrates with tuneable crystalline / amorphous ratios (see Figure 1 B & C). The combination of such substrates with the supernatant of *Trichoderma reesei*, characterized via with liquid AFM, allow dynamic nanoscale observation of cellulose degradation on crystalline and amorphous areas, simultaneously (see Figure 2 A).

The core part of this contribution is the precise understanding of synergistic effects between different types of cellulases which plays a major role in decomposition of crystalline / amorphous mixed cellulose substrates. We first analyse the degradation behaviour of the supernatant followed by investigations of individual enzyme activities. Based on these results we can reconstruct the synergistic effects and gain new mechanistic understanding of the underlying degradation processes.

In particular, it is found that not only the ratio of individual enzymes in the supernatant plays a major role, but also the substrate morphology is of significant influence to the process. In more detail, two different degradation velocities are observed which depend on the structural properties of the substrate (see Figure 2 B) [1]. This is triggered by the individual enzyme activities with respect to the substrate structure and their mutual interaction which will be discussed in detail.

As a result of this in-situ AFM study in combination with biochemical experiments, it can be shown that exclusive tuning of the enzymatic ratio is not enough to achieve highest decomposition efficiencies. The substrates structure has to be taken into account as an essential part of the process.

1. Ganner, T., Bubner, P., Eibinger, M., Mayerhofer, C., Plank., H. & Nidetzky, B. (2012). Dissecting and Reconstructing Synergism: IN SITU VISUALIZATION OF COOPERATIVITY AMONG CELLULASES. *J. Biol. Chem. 2012 287: 43215-43222*
2. Bubner, P., Dohr, J., Plank, H., Mayerhofer, C. & Nidetzky, B. (2012) Cellulases Dig Deep: IN SITU OBSERVATION OF THE MESOSCOPIC STRUCTURAL DYNAMICS OF ENZYMATIC CELLULOSE DEGRADATION. *J. Biol. Chem. 2012 287: 2759-2765*
3. Bubner, P., Plank, H. & Nidetzky, B. (2013). Visualizing cellulase activity. *Biotechnol. Bioeng.* DOI: 10.1002/bit.24884
4. Acknowledgments are given to the Austrian Science Fund FWF for supporting this research (Grant P 24156-B21)

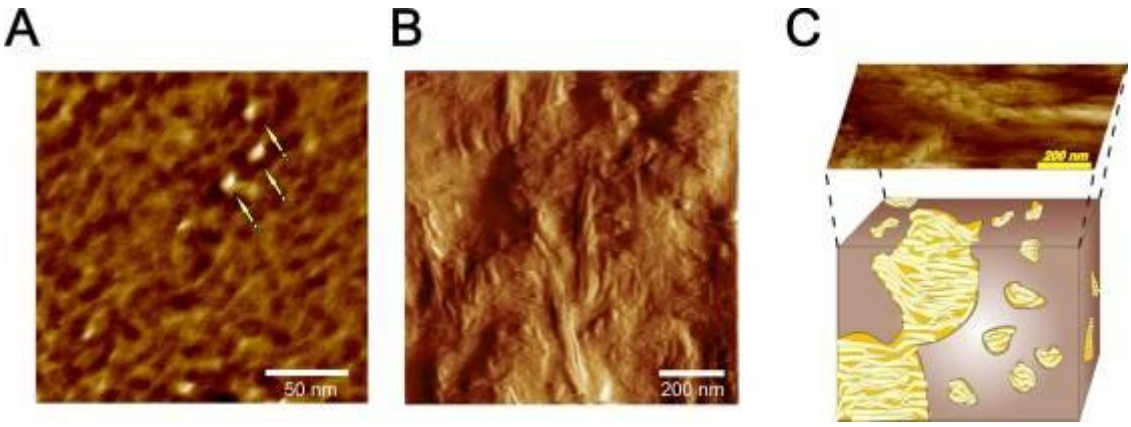

Figure 1 a.) Single enzymes (yellow arrows) on a cellulose surface [2]. b.) Cellulose surface during degradation, showing cellulose fibre-bundles (crystalline) embedded in an amorphous matrix as schematically shown in c.)

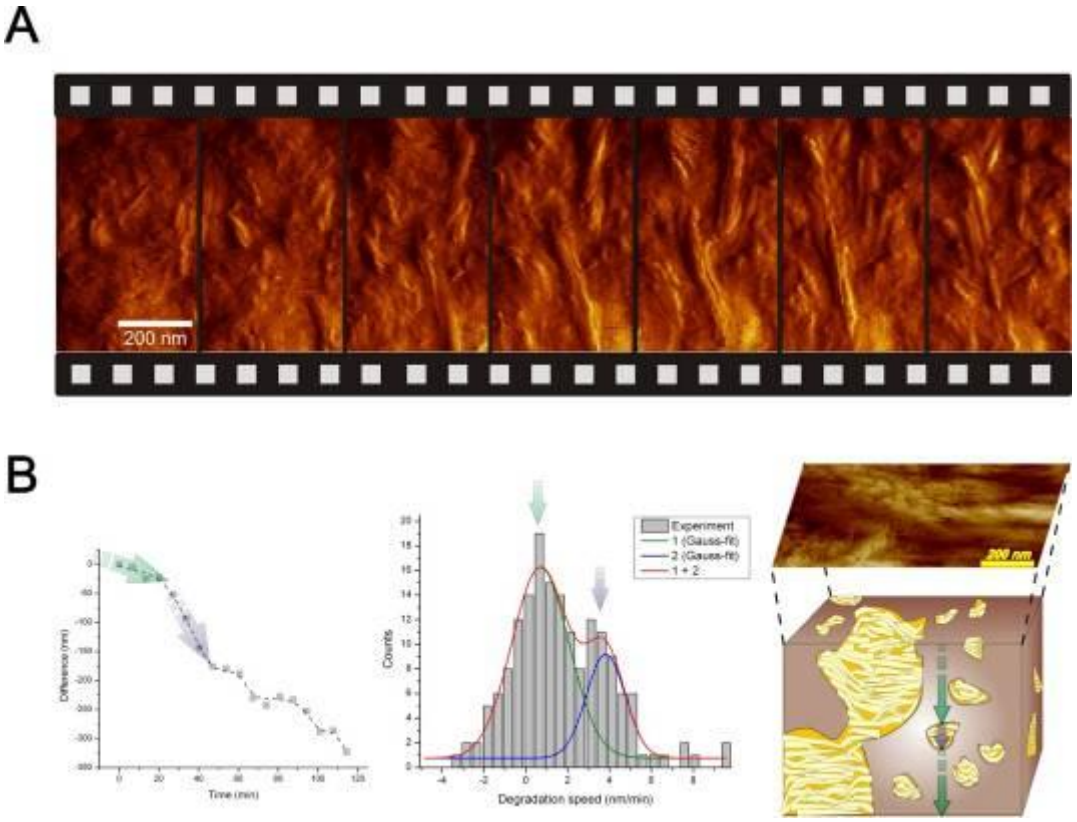

Figure 2 a.) Real time AFM in-situ observation of enzymatic cellulose degradation revealing cyclic appearance and decomposition of cellulose fibre-bundles. b.): representative degradation behaviour of one isolated spot (left), which reveals two different velocities. Statistical analyses (centre) confirm the presence of two distinct degradation rates which can be correlated to crystalline and amorphous areas (right) based on in-situ AFM experiments.

Biomaterials

MIM.5.070
The cement float: morphology, biochemistry and mechanical properties of the cement of the barnacle *Dosima fascicularis* (Crustacea, Cirripedia Thoracica)

V. Zheden[1], A. Kovalev[2], I. Grunwald[3], S. Gorb[2], W. Klepal[1]

[1]University of Vienna, Core Facility Cell Imaging and Ultrastructure Research, Vienna, Austria
[2]University of Kiel, Zoological Institute: Functional Morphology and Biomechanics, Kiel, Germany
[3]Fraunhofer Institute for Manufacturing Technology and Advanced Materials, Department of Adhesive Bonding Technology and Surfaces, Bremen, Germany

vanessa.zheden@univie.ac.at
Key words: adhesive, formation, material properties

These days, natural adhesives are one of the focal points of research [1,2]. Marine animals like barnacles, echinoderms, mussels and tubeworms are of particular interest because they produce adhesives which cure under water. The understanding of these adhesives can be helpful for the production of non-toxic artificial glues for medical and technical applications [3].

The barnacle adhesive is called cement. It is used for the attachment of the animal to the substratum. Our interest focuses on the stalked barnacle *Dosima fascicularis* which is unique in using its foam-like cement not only for attachment, but also as a float allowing the sedentary organism some mobility [4]. The cement is produced in large gland cells “Figure 1” in the upper part of the stalk and transported through a canal system to the base of the stalk where it is extruded through pores “Figure 2”. In the fibrous cement “Figure 3” are gas-filled bubbles enclosed. The cement is deposited in concentric layers around the stalk. The outer layers are narrow forming a kind of rind and enclose small bubbles. Inside the float are large, elongate bubbles radiating outwards “Figure 4”.

EELS and EDX spectra of the cement float show high counts of carbon, oxygen and nitrogen “Figure 5”, corresponding to the organic nature of the cement. Biochemical analyses indicate that the cement is made up of at least 85% of proteins. Gel electrophoresis of the polymerized cement revealed six prominent protein bands which are different in comparison with other barnacles. Infrared spectral analysis indicates the presence of amide I, II and III bands in the *D. fascicularis* cement. DOPA, a posttranslational modification of tyrosine, which plays an important role in the adhesive system of mussels and tubeworms, has not been identified in the cement of *Dosima* nor in that of any other barnacle [5]. Mechanical properties were studied by means of micro-indentation. The results show that the *Dosima* cement is much softer than any other barnacle cement. The elastic modulus of the wet cement lies in the range of 5-20 kPa and the hardness in the range of 1-3 kPa. Dehydration hardens the originally soft barnacle adhesive “Figure 6”. The dry cement has an elastic modulus of about 0.8 MPa and a hardness of about 40 kPa. Further, the barnacle cement has visco-elastic properties, which is common in natural fibrous structures [6]. The cement of *D. fascicularis* differs from that of all the other barnacles in the high amount which is produced, the morphological appearance, the protein composition and its softness.

1. A.M. Smith and J.A. Callow, “Biological adhesives”, (Springer, Berlin Heidelberg New York) (2006).
2. J. von Byern and I. Grunwald, “Biological adhesive Systems: From nature to technical and medical application”, (Springer, Wien New York) (2010).
3. L. Khandeparker and A.C. Anil, International Journal of Adhesion and Adhesives 27 (2007), p. 165.
4. V. Zheden et al., The Biological Bulletin 223 (2012), p. 192.
5. K. Kamino et al., The Biological Bulletin 190 (1996), p. 403.
6. S. Gorb et al., Journal of Comparative Physiology A 186 (2000), p. 821.
7. This work was supported by the FWF project P 21132-B17.

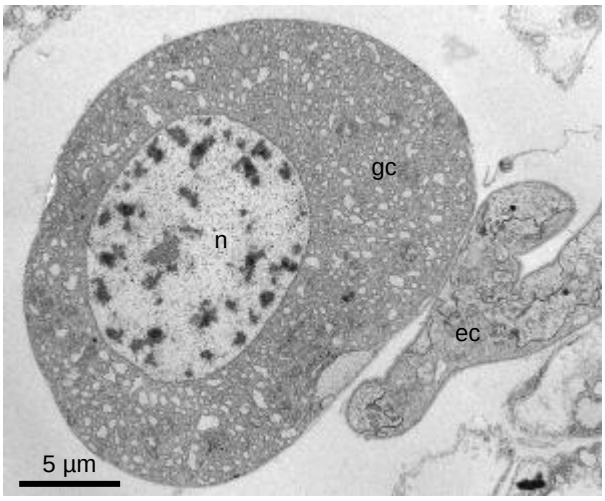

Figure 1. Overview of a cement gland cell (gc) of *Dosima fascicularis*. The extracellular canal (ec) is seen next to the gland cell; nucleus (n)

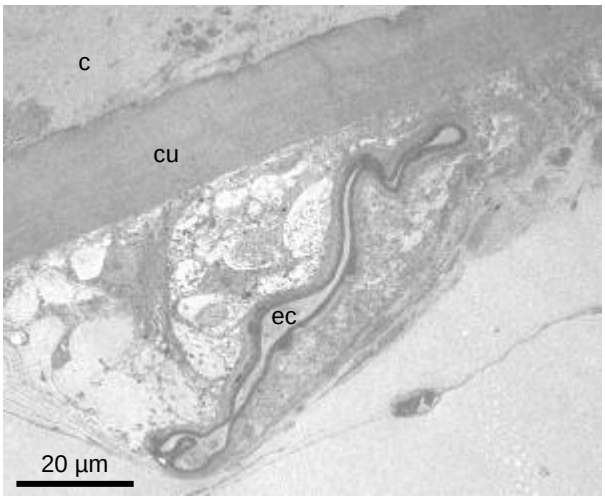

Figure 2. Extracellular canal (ec) next to the base of the stalk before opening through a pore in the cuticle (cu); cement (c)

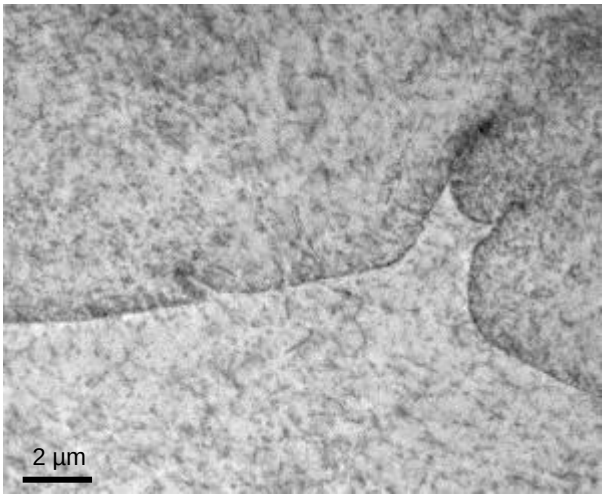

Figure 3. The fibrous structure of the cement.

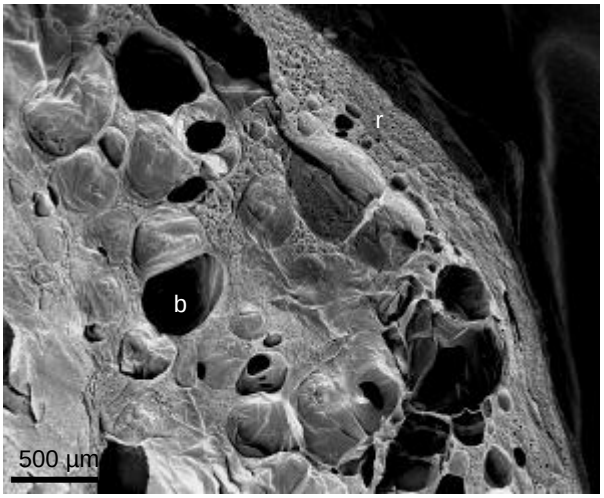

Figure 4. Cross section through the cement float. The outer region forming a rind (r) contains small bubbles, in the inner region are larger bubbles (b).

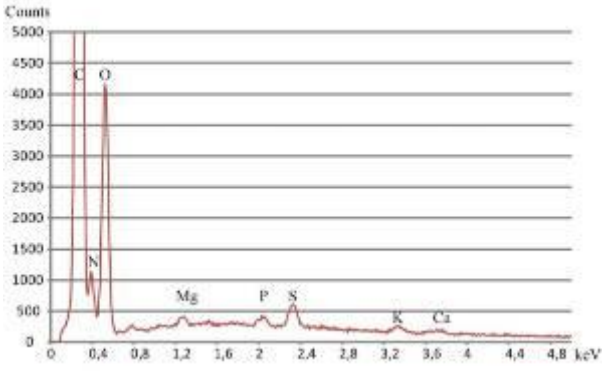

Figure 5. The EDX spectrum of the cement shows high counts of carbon, oxygen and nitrogen. Magnesium, phosphorus and sulphur are only detected in small quantities.

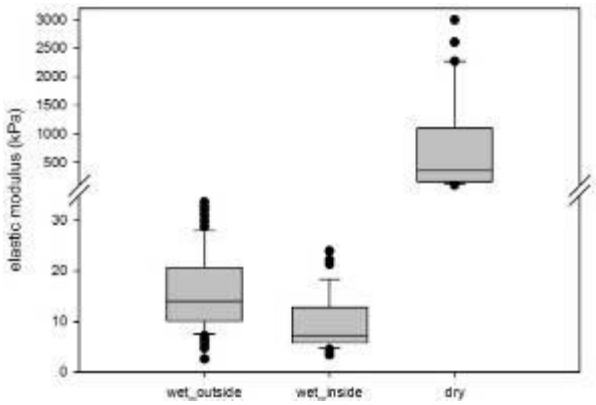

Figure 6. Comparison of the elastic modulus of the wet and the dry cement. The wet cement, measured outside and inside, is much softer than the dry cement.

Biomaterials

MIM.5.P071
Scanning study of single magnetosomes: a crystal structure tailored by preparation procedure

H. Gojzewski[1,2], A. Hashim[3], M. Grzeszkowiak[2,4], M. Makowski [2], M. Molcan[3], M. Batkova[3], I. Batko[3] D. Pawlowska[1], M. Timko[3]

[1]Max Planck Institute of Colloids and Interfaces, Department of Interfaces, Potsdam, Germany
[2]Poznan University of Technology, Institute of Physics, Poznan, Poland
[3]Slovak Academy of Sciences, Institute of Experimental Physics, Kosice, Slovakia
[4]NanoBioMedical Centre, Poznan, Poland

hubert.gojzewski@mpikg.mpg.de
Keywords: biomineralization, magnetosome, magnetite.

Magnetosomes are intracellular organelles of widespread aquatic microorganisms called Magnetotactic bacteria. Magnetosomes consist of magnetite or greigite crystals enclosed in a bio-membrane. Their sizes and morphologies are specific, and related to the species of the bacteria. Magnetosomes have become one of the most intriguing examples of the biological synthesis of iron minerals and biomineral formation by a biomineralization process [1]. Biomineralization within magnetosomes leads to a narrow size distribution of magnetite crystals, with a diameter range of 20-120 nm [2]. It is a demanding task to create structures of this size scale, narrow distribution and crystal quality by any technical means. Moreover, magnetosomes naturally tend to form chains of 7-25 magnetite crystals, stabilized by a bio-membrane. It has been also shown that the magnetite's diameter range corresponds to a single magnetic domain [3, 4]. The unique properties of magnetosomes and the biomineralization process itself have attracted wide interdisciplinary interest because they can be exploited for a variety of applications in diverse disciplines, including nanobiotechnology, geobiology, cell biology, and microbiology [5, 6]. One of the most promising applications seems to be a cancer treatment via hyperthermia, in which magnetosomes are used to heat the malignant tissue [7, 8]. It is known that the heating effect in hypertermia is strictly related to the physical properties of the magnetic nanoparticles (size, crystal structure, etc.) [9]. This fact results in tumor prevention efficacy. Therefore it is of particular importance to study the structure of magnetosomes biomineralized under different conditions as prospective materials for the effective hyperthermia. Recently our group has shown that adding a higher amount of Wolfe's vitamin solution (WVS) or ferric quinate (FQ) during biomineralization process of magnetotactic bacteria *Magnetospirillum sp.AMB-1* results in an increase of the mean diameter of magnetosomes as compared to magnetosomes obtained under normal condition (NP) [10, 11]. Furthermore, the WVS and FQ samples reveal an increase of coercivity, unlike the NP samples, which show no coercivity and behave superparamagnetically. In our ongoing study of the magnetosomes, we performed statistical investigation by means of (HR)TEM, SEM and AFM (Fig. 1). We found that the NP samples consist of noticeably fewer crystal planes in individually examined magnetites than the WVS and the FQ samples. This is probably due to different nucleation and growth scenarios of magnetite crystal during the bacterial cultivation procedure [12]. Thus, the crystal structure of magnetosomes can be tailored by the bacterial cultivation procedure.

1. D. Faivre, D. Schueler, Chem. Rev. 108 (2008) 4875.
2. A. Komeili, Z. Li, D.K. Newman, G.J. Jensen, Science 311 (2006) 242.
3. R.F. Butler, S.K. Banerjee, J. Geophys. Res. 80 (1975) 4049.
4. H. Gojzewski, M. Makowski, A. Hashim, P. Kopcansky, Z. Tomori, M. Timko, Scanning 34 (2012) 159.
5. E. Baeuerlein, Angewandte Chemie - International Edition 42 (2003) 614.
6. D. Schueler, R.B. Frankel, Appl. Microbiol. Biotechnol. 52 (1999) 464.
7. R. Hergt, R. Hiergeist, M. Zeisberger, D. Schueler, U. Heyen, I. Hilger, W.A. Kaiser, J. Magn. Magn. Mater. 293 (2005) 80-86.

8. M. Timko, A. Dzarova, J. Kovac, A. Skumiel, A. Jozefczak, T. Hornowski, H. Gojzewski, V. Zavisova, M. Koneracka, A. Sprincova, O. Strbak, P. Kopcansky, N. Tomasovicova, J. Magn. Magn. Mater. 321 (2009) 1521.
9. R. Hergt, W. Andrae, C.G. d'Ambly, I. Hilger, W.A. Kaiser, U. Richter, H.-G. Schmidt, IEEE Trans. Magn. 34 (1998) 3745.
10. M. Timko, M. Molcan, A. Hashim, A. Skumiel, M. Muller, H. Gojzewski, A. Jozefczak, J. Kovac, M. Rajnak, M. Makowski, P. Kopcansky, IEEE Trans. Magn. 49 (2013) 250.
11. A. Hashim, M. Molcan, J. Kovac, Z. Varchulova, H. Gojzewski, M. Makowski, P. Kopcansky, Z. Tomori, M. Timko, Acta Phys. Pol. A 121 (2012) 1250.
12. J. Baumgartner, A. Dey, P.H.H. Bomans, C. Le Coadou, P. Fratzl, N.A.J.M. Sommerdijk, D. Faivre, Nature Materials (2013), in press.
13. H.G. acknowledges the Polish Ministry of Science and Higher Education for the project "Mobilnosc Plus" No.650/MOB/2011/0. M.M. acknowledges the Polish Ministry of Science and Higher Education for the DS-MK 62-190 funds.

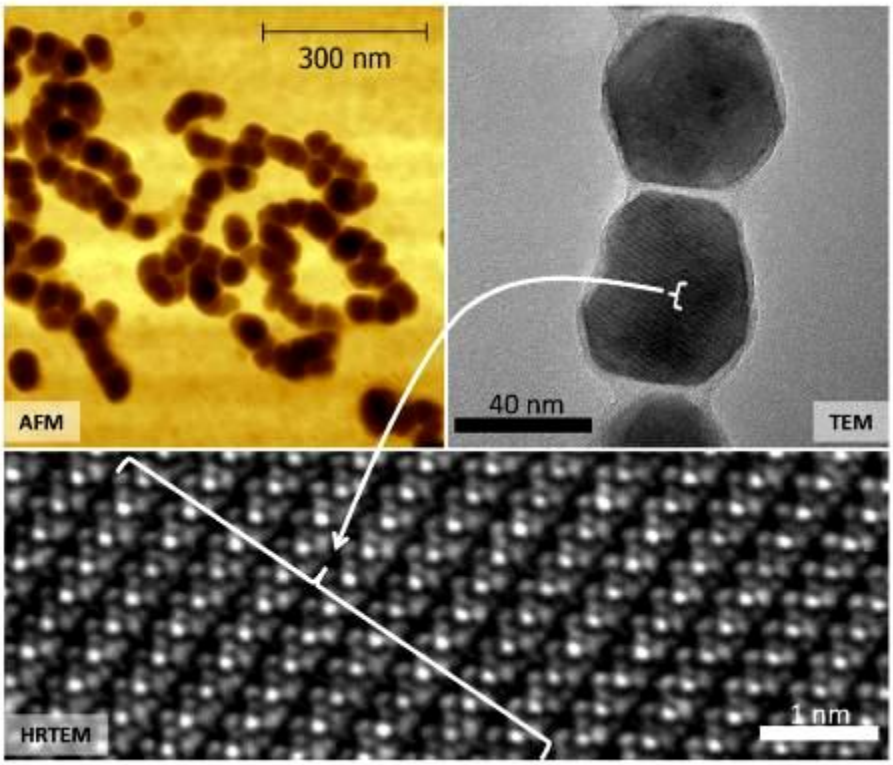

Figure 1. Examples of AFM and (HR)TEM results of magnetosomes. AFM shows chains of magnetosomes and their tendency to form closed loops. TEM shows a part of magnetosome chain. One can see the position of each magnetite crystal is stabilized by the bio-membrane. HRTEM shows magnetite crystal lattice, including the position of Fe and O atoms.

Biomaterials

MIM.5.P072
AFM study of a calcium hydroxyapatite morphology

N. Kurgan[1]

[1]G.V.Kurdumov Institute of Metal Physics NASU, Solid State Surface, Kiev, Ukraine

nataly_kurgan@imp.kiev.ua
Keywords: hydroxyapatite, atomic force microscopy, morphology

During the last 20 years bioactive materials based on calcium hydroxyapatite with chemical composition and structure similar to that of mineral constituent of bone tissue are widely used in surgery. However, the problems of synthesis of nanodispersed calcium apatite with highly developed surface, which are the most similar to the morphology of particles of mineral component of bone, are still relevant.

In this paper, the morphology of nanopowder apatite was investigated by scanning probe microscope JSPM-4500/4610 (JEOL, Japan) using the atomic force microscopy method.

The image parameters were as follows: the image size 90.0 x 90.0 nm, image height - 12.2 nm, the exposure time at single point – 83.33 microseconds. The cantilever with diamond whiskers NSG10-DLC was used as a probe. The high-dispersion powders of HAP were obtained by sol-gel method. The particle size were proved to be of about 40 nm (Fig.1), and the specific surface area of ~ 500 m^2/g.

We observed the characteristic shape and “texturing” of apatite particles. The sizes of apatite particle were very close to those in natural bone. However, the particles in natural bone have needle shape, and the “horseshoe” shape was due to the drying in the synthesis process.

The ends of the particles were not fixed, which was caused by the surface tension. For example, by drying the particles in acetic acid remained needle-shaped. Because in recent cancer treatment, for example bone cancer treatment, gold nanoparticles were used the study of interaction between the particles of calcium apatite nanopowder and gold nanoparticles becomes of great relevance. In particular, it was found that due to deposition (physical adsorption) gold nanoparticles are formed of ~ 3 nm size on apatite surface, and it can be practically used for delivery the drugs to diseased bone.

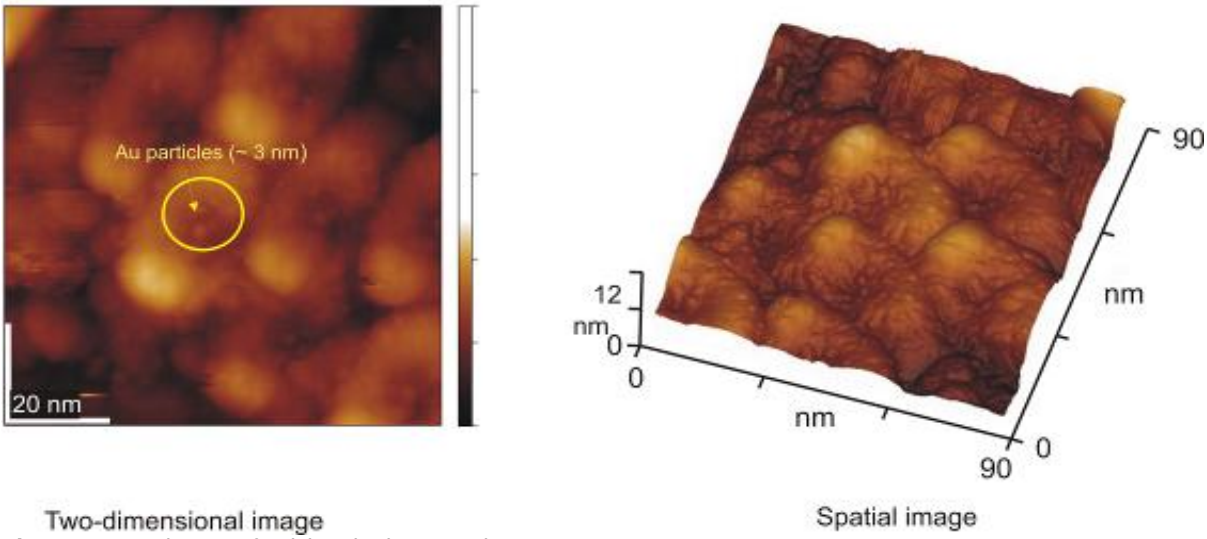

Figure 1. AFM image of calcium hydroxyapatite.

Biomaterials

MIM.5.P073
Analysis of the fretting corrosion deposits on biomaterials

K. Geric[1], S. Lazarevic[1], J. Grujic[1]

[1]Faculty of Technical Sciences, Department for Production Engineering, Novi Sad, Serbia

gerick@uns.ac.rs
Keywords: fretting corrosion, biomaterials

Metal implants in living organisms are constantly exposed to degradation of the metal surface. All processes that occur, such as wear, corrosion and damage, are covered by the concept of tribocorrosion. Tribocorrosion is a general term that covers all mechanical (wear) and chemical (corrosion) interactions that cause degradation of materials in relative motion [1]. Fretting corrosion is a type of tribocorrosion that occurs in area of contact of two materials in presence of repetitive relative movement under load. Fretting occurs when the environment takes part in the destruction of the metal. Repeated (frequent) oscillatory motion occurs in orthopaedic implants when the multicomponent implants are placed in the limbs carrying weight, or when the fixation is achieved by screwing a metal plate to a bone in places where connections can become loose [2]. There are small oscillation amplitudes in corrosive environment of bodily fluids, which in the beginning causes strengthening of the contact surfaces and cyclic flow of subsurface. In this case, we have the metal-to-metal contact. The testing in this study was carried out using the device for testing fretting corrosion that was designed at the Department of Production Engineering and G&G. The testing device enables the movable part with the tip in shape of hemispherical pin to perform rotationally oscillating movement along the groove of a fixed sample in the shape of a hemisphere, in order to simulate the behaviour of plate and screw in fixated bone, in case of a loosened screw. The tests were performed in physiological saline containing 9% NaCl (pH 7.4) heated to 37°C to simulate the conditions that exist in a living organism. Test was performed for 21600 cycles for all materials.

Moving part is made of stainless steel 316L, for all cases, and three materials were tested as a fixed sample, stainless steel 316L, CoCrMo alloy of cobalt and titanium alloys TiAl6V4. The chemical composition of the investigated materials is given in Table 1. The tested surfaces were mechanically polished and initial mean roughness (Ra) of stainless steel and cobalt alloy was 0.03 μm, and of the titanium alloy 0.08 μm Metals used for implants are highly resistant to corrosion, due to the creation of the passive oxide layer on the surface, but due to fretting corrosion and cyclic movement of the surface, passive film gets destroyed. Metallic implants are exposed to bodily fluids that are corrosive environment, and so the behaviour of the metals changes significantly and their corrosion resistance reduces [3]. On the surface of the stationary part, a dark brown corrosion deposite was created in all three materials, which has been tested using a scanning electron microscope Jeol JSM 6460LV, with Oxford EDS analyzer instrument, the INCA X-sight program. The test results of EDS analyzer deposite are presented in tables and by energy dispersive X-ray spectrum with peaks of elements present. The tests were conducted for several locations in a sample. The analyzed surface layer of stainless steel consists of oxygen, chromium (14 to 27%), and nickel (7 to 14%.) In one location sulphur appears, up to 1%, and also aluminium Al (4.8%), Fig 1 On the surface of cobalt alloy, corrosion layer had iron present in large amounts (48.96%), which indicates the presence of mechanical wear in moving part made of stainless steel. It also has a layer of nickel (up to 7%), which probably also comes from stainless steel, Fig.2. The surface layer of titanium alloy had small amounts of Cl (0.9%), probably originating from the saline. Chromium (up to 2%), Ni (1.7%) and iron (7%) also occur, indicating again the existence of mechanical wear of moving part made of stainless steel caused by metal to metal contact, Fig.3 The surface layers of cobalt and titanium alloys show presence of iron and nickel, which indicates the highest surface damage of moving stainless steel part.

1. M. T.Mathew, P. Srinivasa Pai, R. Pourzal,. Fischer, and M. A.Wimmer; Significance of Tribocorrosion in Biomedical Applications: Advances in Tribology, Volume 2009, 12 pages, Hindawi Publishing Corporation
2. S. Kumar, T.S.N. Sankara Narayanan, S. Ganesh Sundara Raman, S.K. Seshadri , Fretting corrosion behaviour of thermally oxidized CP-Ti in Ringer's solution Corrosion Science 52 (2010) 711–721

3. V. Swaminathan, J. Gilbert, Fretting corrosion of CoCrMo and Ti6Al4V interfaces Biomaterials 33 (2012) 5487-5503
4. We kindly acknowledge to the Ministry of Education and Science, Republic of Serbia to support research project TR35025

Sastav	C	Cr	Ni	Si	Mn	Mo	Co	Fe	Al	V	Ti
316L	0,02	17,67	14,3	0,50	1,87	2,72	0,027	Bal.			
CoCrMo	0,43	27,2	1,50	0,92	0,8	5,23	Bal.				
TiAl6V4	0,02							0,14	6,08	4,04	Bal.

Table 1. Chemical composition of tested materials

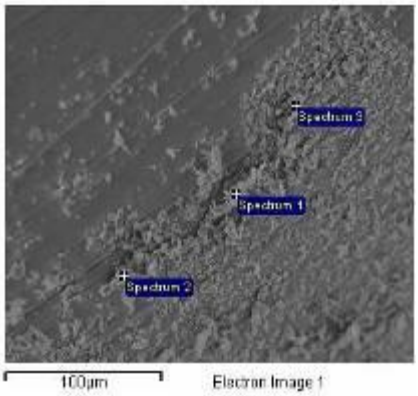

Sp1	C	O	Al	Cr	Fe	Ni
Wt%	19.55	10.20	4.80	26.86	31.66	6.93

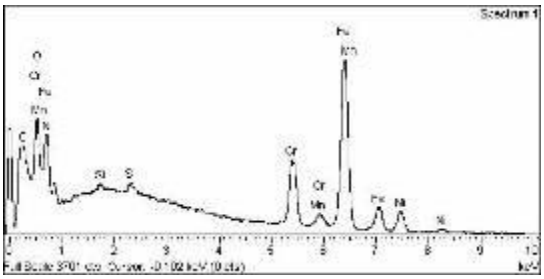

Figure 1. Deposit on stainless steel

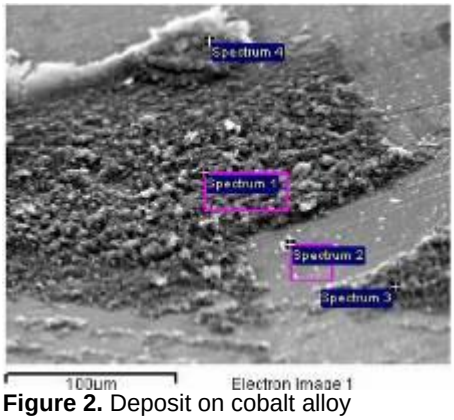

Sp 4	C	O	Cl	Cr	Fe	Co	Ni	Mo
Wt%	12.25	21.0	0.22	20.10	30.3	3.86	7.16	3.99

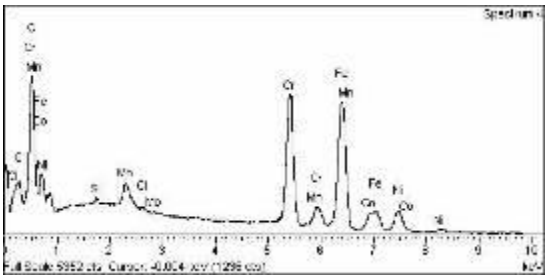

Figure 2. Deposit on cobalt alloy

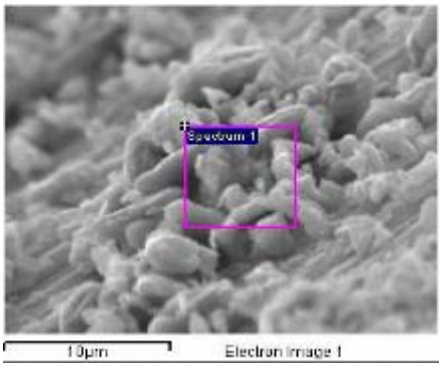

	C	O	Al	Ti	V	Cr	Fe	Ni
Wt%	6.96	13.68	4.29	60.97	2.80	2.11	6.95	1.68

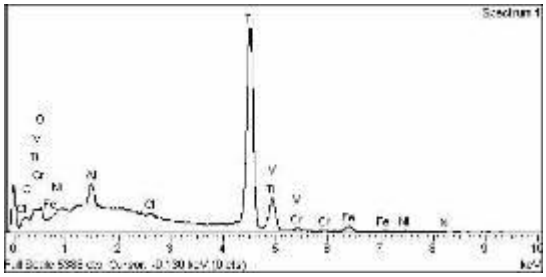

Figure 3. Deposit on titanium alloy

Biomaterials

MIM.5.P074
Microscopic study of Calcium Oxalate Crystallization in presence of *Triticum aestivum* L extract

K. Sekkoum[1]

[1]Bioactives Molecules & Chiral Separation Laboratory, University of Bechar, Bechar, Algeria

khalidos669@yahoo.fr
Keywords: Urolithiasis, Calcium Oxalate, Triticum aestivum L, Microscopic study.

Urolithiasis is a renal pathological condition that occurs due to formation of calculi in the urinary tract. Among the different types of stone constituents, calcium oxalate. The formation of these stones involves several physicochemical events, beginning with crystal nucleation, growth and aggregation, and ending with retention within the urinary tract [1]. The principle causative factor of the formation of stones is attributed to the supersaturation of precipitating salts [2]. As part of our investigation into medicinal plants used by indigenous population in the Algerian Sahara [3], we report here the *in vitro* effect of wheat bran (*Triticum aestivum* L) aqueous extract on calcium oxalate crystallization. The microscopic study of crystallization in absence and in presence of plant extract show the decrease in the size of crystals in the test made in the presence of the wheat bran extract compared with that made in its absence.

1. K. Sekkoum, A. Cheriti, S. Taleb and N. Belboukhari. *Arab. J.Chem*. (2011), doi: 10.1016/j.arabjc .2011.10.010 .
2. K Sekkoum, A Cheriti, S Taleb Y Bourmita and N Belboukhari. *E.J.E.A.F.Ch*. (2011), 10(8): 2616-2622.
3. K. Sekkoum, A. Cheritia and S. Taleb. *Nat. Prod. Comm*. (2011),Vol. 6 (10): 1445 – 1446

Biomaterials

MIM.5.P075
Acoustic microscopy - a powerful tool for teeth characterization and dental materials development

M. Warkentin[1], O. Specht[2], D. Trostmann[1], P. Ottl[3], J. Geis-Gerstorfer[4], M. Rosentritt[5], D. Behrend[1]

[1]University Rostock, Department of Material Science and Medical Engineering, Rostock, Germany
[2]Institute of ImplantTechnology and Biomaterials e.V., Rostock, Germany
[3]University Rostock, Department of Prosthodontics and Materials Science, Rostock, Germany
[4]University Tuebingen, Department of Prosthodontics with Section Medical Materials & Technology, Tuebingen, Germany
[5]University Regensburg, Department of Prosthetic Dentistry, Regensburg, Germany

mareike.warkentin@uni-rostock.de
Keywords: scanning acoustic microscopy, tooth, dental materials

The ultrasonic material testing is a well-established method as a non-destructive diagnostic tool for technical structures. This technique was investigated concerning its suitability for the development of dental restorative materials. The challenge is to develop a material which is equivalent in his viscoelastic properties to the human tooth. Therefore, the different mechanical properties of enamel and dentine have to be considered. The acoustic properties of the dental hard tissues, which can be correlated directly with the mechanical material properties e.g. hardness and density, are of particular interest in this context

Human molars were embedded in epoxy resin and sliced transversally and longitudinally to the tooth axes into 2 mm thick disks. They were investigated with an acoustic scanning microscope (SAM 300, PVA TePla) in reflection mode over a frequency range from 25 to 100 MHz. The acoustic velocity was calculated from the elapsed time between the echoes of surface and lower surface (A-scan) at different positions in enamel and dentine. The acoustic scans were additionally verified with a µCT (SkyScan 1172), which is similar to the conventional X-ray technique. In comparison to the dental hard tissue, dental composites with different filler content were acoustically measured.

The ultrasonic measurement is well suited to differentiate the dental compartments enamel and dentine. The acoustic absorption can be visualized by a gray scale image, i.e. the darker the image the softer the material. The acoustic velocities of enamel and dentine were determined at different positions. Dentine showed on average acoustic velocities < 4500 m s^{-1} whereas velocities up to 7700 m s^{-1} were measured in enamel. In general, dentine reached up to 40 % lower acoustic velocities than enamel and the acoustic velocities differed with the longitudinal and transversal measuring position (Figure 1). Moreover, these results correlated well with the spatial resolved microhardness values. Dentine showed hardness values < 100 MHV whereas enamel reached up to 480 MHV [1]. In comparison, dental composites showed acoustic velocities lower than 4200 m s^{-1} nearly similar to dentine. However, these materials are often used to substitute regions of carious or missing enamel.

Moreover, the ultrasonic measurement allows detecting material defects at an early stage of processing [2]. Most often air bubbles were found which negatively influence the mechanical properties of the composites (Figure 2). They originate from the manual handling and could not outgas before the polymerization reaction has finished.

The ultrasonic measurement is an excellent tool in dental research which allows a non-invasive and real-time characterization of dental materials using their acoustic parameters. The ultrasonic derived imaging reached a higher resolution than conventional X-ray techniques. This is due to the shifts in impedance of different materials, e.g. dentine and enamel, whereas the differences in radiopacity are less pronounced [3]. Due to its compact structure (prism arrangement and collagen matrix) enamel reached higher ultrasonic velocities than dentine which is crossed by liquid filled tubules. The acoustic velocities of most common dental composites were in the range of dentine velocities. Although filler contents > 80 % are common for high filled composites the mechanical and acoustical properties of enamel could not be reached yet.

In summary, the correlation of acoustic and mechanical properties is one of the basics for development of enamel similar composites in prospective dental research. Thus, the structural analysis by acoustic microscopy is a sophisticated, accurate and fast method.

1. M. Warkentin, D. Behrend, M. Rosentritt and P. Ottl, Journal of Dental Research 90A (2011), Abstract 1112
2. M. Warkentin, O. Specht, S. Kopp, P. Ottl, O. Kessler, M. Rosentritt, and D. Behrend, Special Edition Practical Metallography 44 (2012), p. 155
3. M. Warkentin, D. Behrend, K. Thurow, K.H. Sandmann, P. Ottl and N. Stoll, 1st IT supported health Conference (01.-03.12.2011) Washington D.C., USA

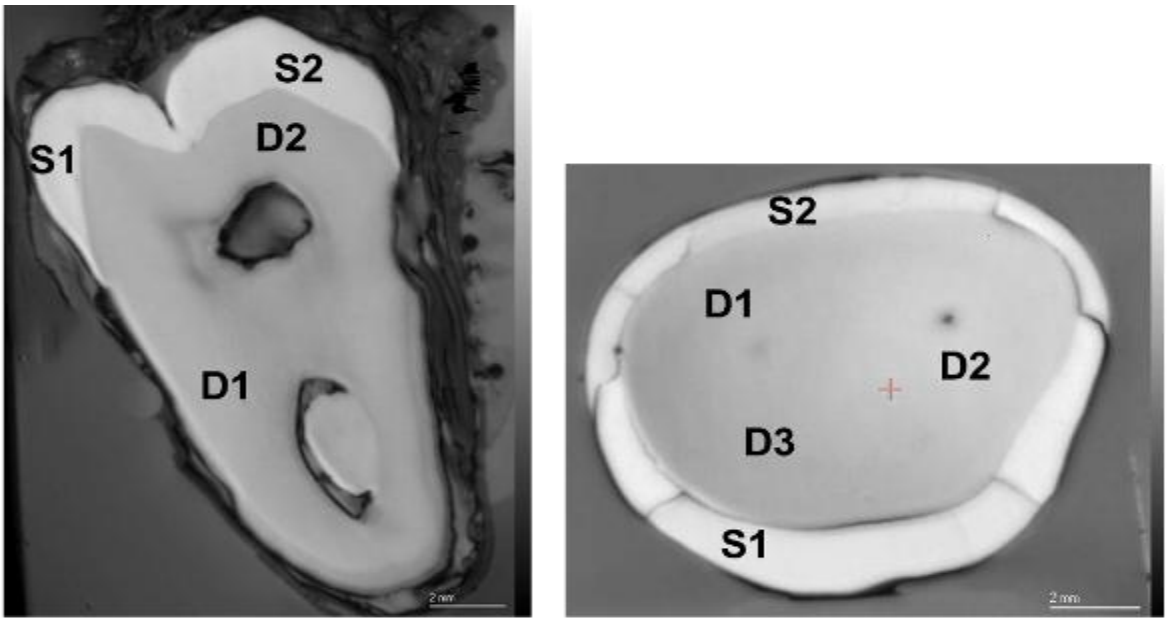

Figure 1. Acoustic image with mapping of acoustic velocities of enamel and dentine depending on location and direction in tooth

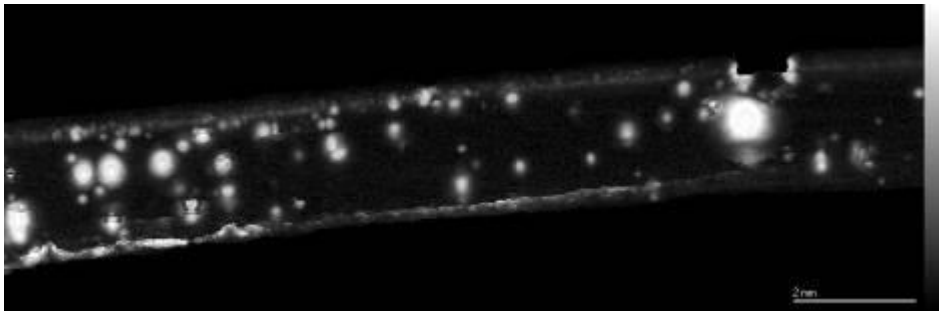

Figure 2. Acoustic image (25 MHz transducer) of a dental composite; white dots represent air bubbles.

Biomaterials

MIM.5.P076
Calcite mineralisation of bacterial surface-layer proteins

P. Simon[1], D. Gruner[2,3], E. Rosseeva[1,4], O. Kai[3], G. Rödel[3]

[1]Max-Planck-Institute, Inorganic Chemistry, Dresden, Germany
[2]Max Planck Institute of Molecular Cell Biology and Genetics, Dresden, Germany
[3]Technical University of Dresden, Institute of Genetics, Dresden, Germany
[4]University of Konstanz, Physical Chemistry, Konstanz, Germany

paul.simon@cpfs.mpg.de

Biomineralization of bacteria plays a decisive role in geological mineral formation, e.g. large parts of Poland are formed by sedimentation of calcium carbonate giving rise to agglutinated colonies of bacteria [1,2]. In this work we investigated the mechanism of calcium carbonate deposition at the nanoscale on the surface-layer of the heat resistant bacterium Geobacillus stearothermophilus. The structure of the surface layer is composed of rhombohedral motifs at the nanoscale of different sizes. The surface of the isolated surface layer and also the complete bacterium was mineralized stepwise by calcium carbonate.

In our biomineralization experiments the S-layer serves as biotemplate and induces crystalline calcite coverage as indicated by the FFT analysis of the high-resolution TEM micrographs (Figures 1 and 2). The nucleation takes place at the corners of the rhombohedral motifs (unit cells) and extends over the interconnecting bars till the whole S-layer sheet is mineralised. Assumably, firstly vaterite nanocrystals are formed which by time are successively transformed to the more stable calcite crystal phase. The vaterite crystals are observed at the thin areas around the corners of the rhombohedral S-layer unit cell. On the corners and on the bars the crystallisation is advanced and thus only calcite is detected. The calcite crystals are 3-5 nm in size and follow the topography of the S-layer showing the (1-10) plane towards the substrate. At the bars the crystals are lying flat on the smooth surface in the same direction (oriented attachment) and at the corners they are standing up 60° or 75° due to the pyramidal form of the corner. These observations are in accordance with results of the synthesis of silicate layers on S-layers but stand in contrast with results of *Schultze-Lam et al.*, where a mineralisation starting in the pores was observed [3,4].

1. J. Kazmierczak,Nature (1976) 264, 49-51.
2. M. Obst, M. Dittrich, H. Kuehn, Geochem. Geophys. Geosyst. (2006). 7, Q06011.
3. S. Schultze-Lam, T. J. Beveridge, Appl. Environ. Microbiol. (1994) 60, 447-453.
4. C. Göbel B. Schuster, D. Baurecht, U. B. Sleytr, D. Pum, Coll. Surf. B (2010).75, 565-572.
5. We kindly acknowledge Prof. H. Lichte for the possibility to measure at the Triebenberg Laboratory at the TU Dresden, Germany.

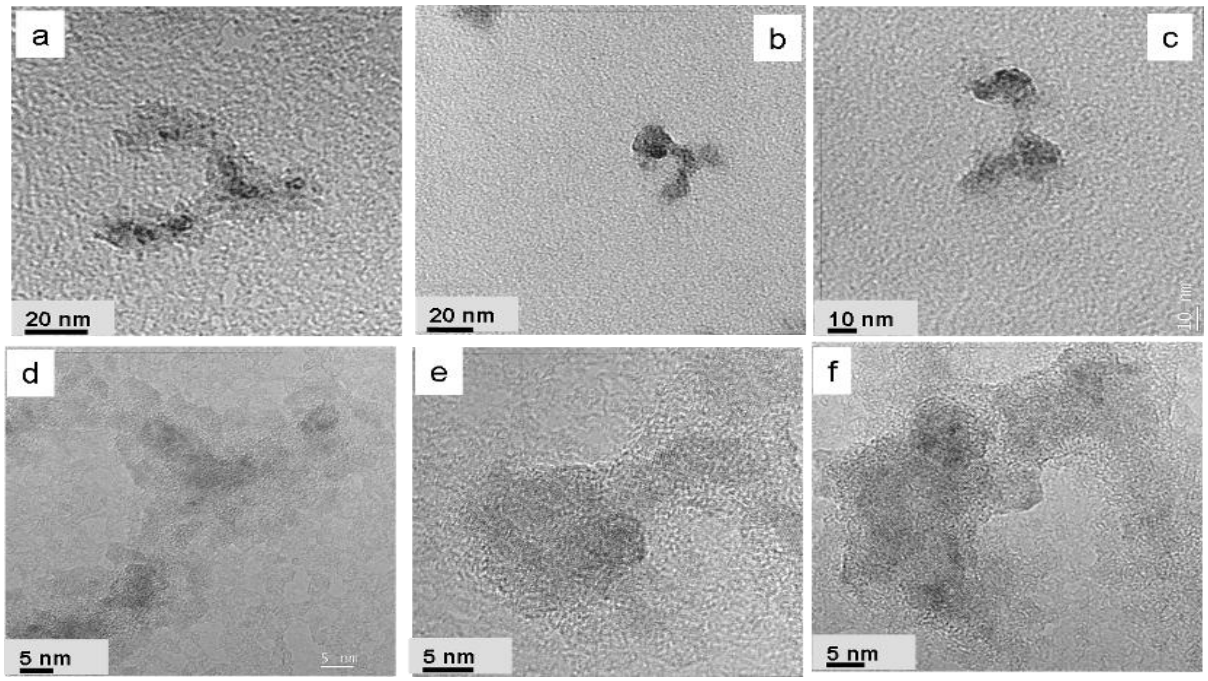

Figure 1.

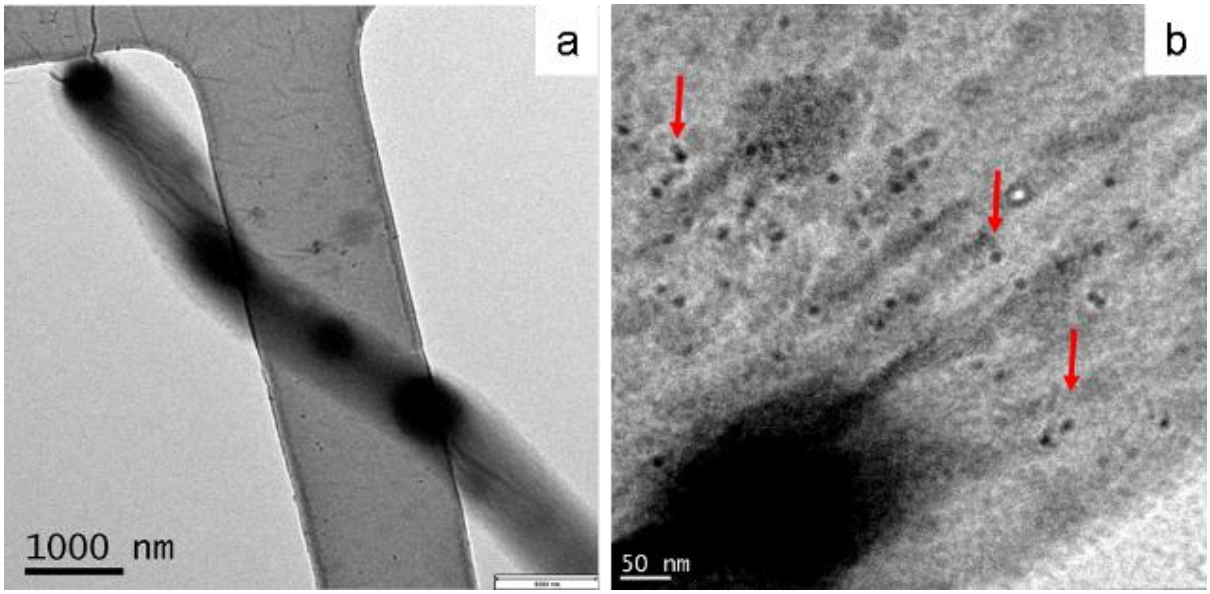

Figure 2.

Biomaterials

MIM.5.P077
Tooth lead signal obtained by SEM-EDS may be useful for detection of environmental contamination with this metal

J. Mardegan Issa[1], F.A. Tocchini de Figueiredo[1], J. Ramos[1], R.F. Gerlach[1], E. Reiko Hashimoto Kawakita[1]

[1]Universidade de São paulo, Morfologia, Fisiologia e Patologia Básica, Ribeirão Preto, Brazil

jpmissa@forp.usp.br
Keywords: SEM, Lead, Tooth, environmental toxin, pollution

Lead is a highly toxic metal to human health that is ubiquitous in certain environments, such as industrial areas [1].
SEM with multielemental detectors may be a good alternative for conventional chemical detection, specially “ambiental” SEMs, which are easy to operate, have a short analysis time and to not require the standard sample preparation usually required for SEM analysis.
The aim of this study was to evaluate whether lead could be detect by SEM on the surface of rat molars that had been exposed lead at 30 mg / L of lead in drinking water for 60 days.
In this work we tested the hypothesis that exposure of animals to lead could be determined by analyzing the surface of rat molars, and detecting higher than normal lead signals there. Wistar males rats were exposed for 60 days to 30 mg / L of lead in drinking water (n=5), while control animals received water with lead <0.1 ug/L (n=5). After this time, teeth were removed and blood was collected for lead analysis

Superficial Enamel of lower molars was analyzed for microelements by Scanning Electron Microscopy (SEM) coupled to Electron Dispersive Spectroscopy (EDS) accessories. Semiquantitative analysis was also obtained using SEM Wavelength Dispersive Spectroscopy.

For this analysis, it was used the Electron Dispersive Spectroscopy accessory that generates a rapid and multielement analysis [2], being possible to check the tooth constituents alterations in animals exposed to lead (n = 5) compared with controls (n = 5). For this study we tested a technique without coating, and without any samples treating for electron microscopy, aiming to evaluate the elements determination at these samples. It was established the following parameters for this: two regions of each first molar were chosen, incisal and cervical, at 10mm of distance between the emitter and the sample, with 15 to 25 kV of emission, possibiliting around 10um of depth penetration in these samples. Considering the fact that lead focuses on the enamel surface, this mineral was detected only at groups exposed to 60 days, in both regions, but more at cervical region (Figure 1) by SEM-EDS, and where the lead was found, there is no calcium, considering that in this study it was obtained full maps of the most abundant elements (Figure 2). Lead oxide was found, by extrinsic deposition, which may be useful for forensic purposes or to determine unknown contamination agents.

1. Aelion, C.M., et al., Soil metal concentrations and toxicity: associations with distances to industrial facilities and implications for human health. Sci Total Environ, 2009. 407(7): p. 2216-23.
2. Vermeij, E.J., et al., Analysis of microtraces in invasive traumas using SEM/EDS. Forensic Sci Int, 2012. 214(1-3): p. 96-104.

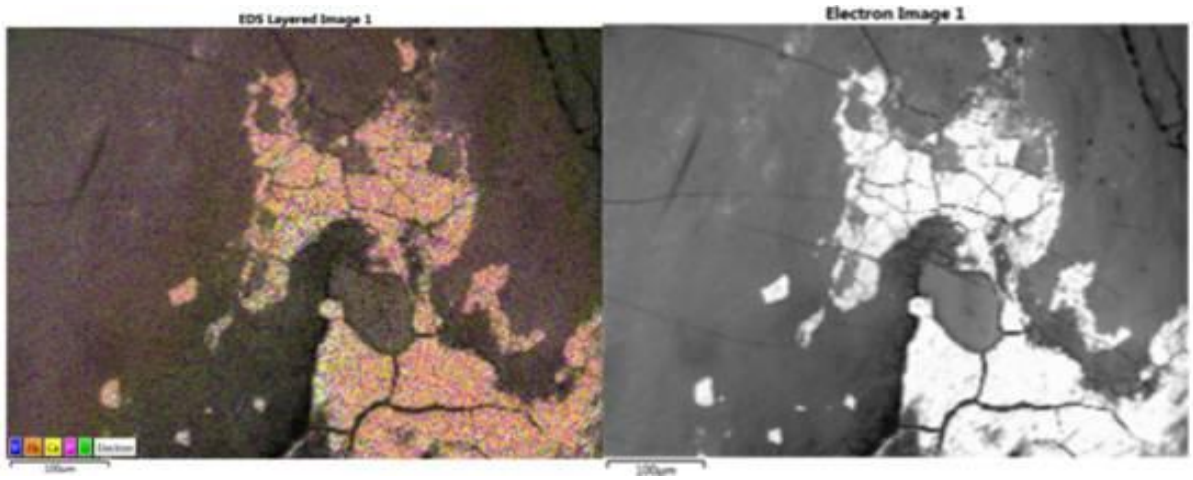

Figure 1. Cervical area of the first molar exposed to 60 days of lead, schema generated by the software Aztec Oxford instruments from SEM-EDS [6]. On left we have the Map Sum of the elements, on the right we have the Image of the sample.

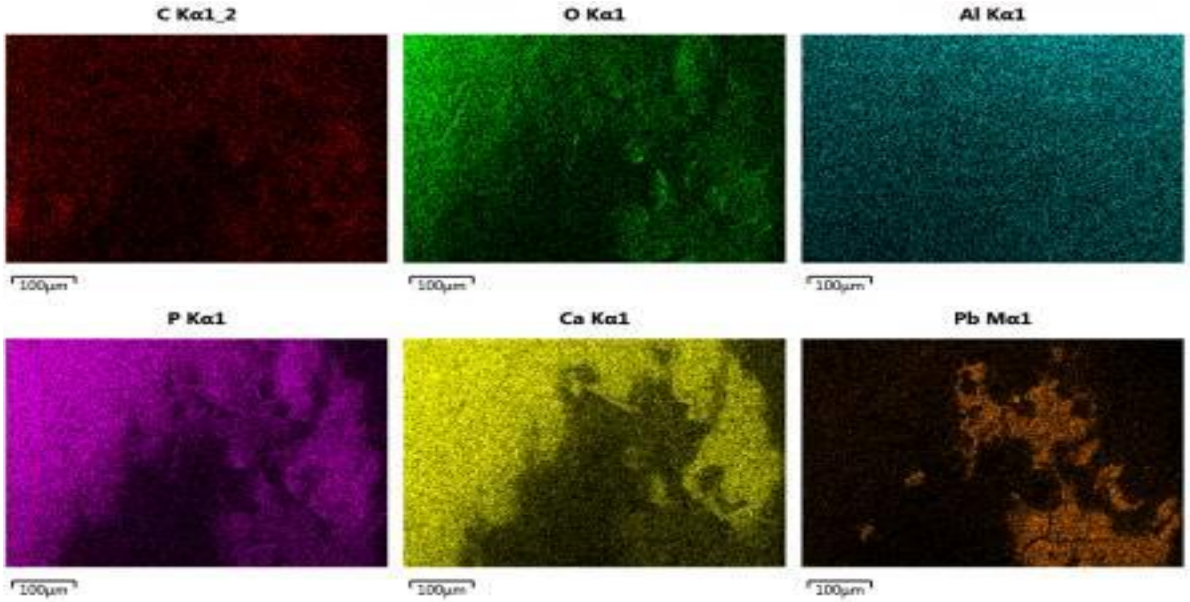

Figure 2. Map of the elements present in the same area relative to Figure 1, generated by Oxford Instruments software Aztec from the SEM-EDS [6], which shown the separate spectrum of the elements with a spatial distribution.

Biomaterials

MIM.5.P078
Microscopical alterations of the anterior tibial muscle after sciatic nerve crushing treated with lasertherapy and natural latex protein

J. Mardegan Issa[1], K. Lemos Muniz[1], F. José Dias[2], L.G. Souza[1], V. Pedrazzi[3] R.A. Junqueira Calzzani[1], B.G. dos Santos Kotake[1], F.A. Tocchini de Figueiredo[1]
I.-S. Watanabe[2], J. Mardegan Issa[1]

[1]Universidade de São paulo, Morfologia, Fisiologia e Patologia Básica, Ribeirão Preto, Brazil
[2]Universidade de São Paulo, Ciências Biomédicas, São Paulo, Brazil
[3]Universidade de São Paulo, Materiais Dentários e Protese, Ribeirão Preto, Brazil

jpmissa@forp.usp.br
Keywords: Damaged Nerve, sciatic pain, oxidative metabolism, low intensity laser

Peripheral nerve injury results in damage not only to nerve tissue, but also to muscle that is affect by various changes [1], [2] because the nerve injury compromises the nerve supply of the muscular tissue, restoration and function preservation of this structure [3]. This study evaluated the tibialis anterior muscle after sciatic nerve crush (15 kgf, 5.2 MPa, 10 min) treated with low level laser therapy (LLLT, 15J/cm^2, 780nm) and the protein purified from natural latex (P1, 0.1%). It was used 60 Wistar rats, male, 200-250g, which were divided into 6 groups (n = 10): G1. control; G2. exposed nerve; G3. injured nerve; G4. injured nerve irradiated with LLLT; G5. injured nerve treated with protein extracted of the latex, and G6 injured nerve treated with protein and irradiated. After 4 or 8 weeks of the injury, morphological (hematoxylin-eosin) and histochemical (NADH – nicotinamide adenine nucleotide, and SDH – succinate dehydrogenase) analyses were performed. Morphological data of the treated groups after nerve injury (G4, G5 and G6) showed improvement of these parameters in comparison with the injured group (G3), in both periods. After 8 weeks, the morphological aspects of the treated groups resembled the control group, G5 presented the best results, at 4 and 8 weeks after nerve injury. The NADH and SDH data of injured animals showed loss of the fibers typing, increasing the intermediary fibers areas, which was more evident at 4 weeks after the injury, and reduced aspects after 8 weeks. For the last period of time, the distribution of fiber types more similar to the control group, according to the NADH reaction, was the G5 groups, and for SDH reaction was the G6 group. In conclusion, the treatments applied on the injured sciatic nerve led to improved morphology and oxidative metabolism of the anterior tibial muscle. The loss typing of the fibers was common at four weeks after the lesion, and in general, the treatment performed with only the protein extracted from the latex was the most efficient, revealing no positive integration between the protein and the LLLT treatment, according to the parameters used in this study.

1 Meek, M.F.; Varejão, A.S.; Geuna, S. Use of skeletal muscle tissue in peripheral nerve repair: review of the literature. Tissue Eng., v.10, n.7-8, p.1027-36, 2004
2 Shen, C.C.; Yang, Y.C.; Liu, B.S. Large-areairradiatedlow-levellasereffect in a biodegradablenerveguideconduit on neuralregeneration of peripheralnerveinjury in rats.Injury.,v.41, n.8, p. 803-13, 2011
3 Lehnert, M.; Steudel, W.I.; Marzi, I.; Mautes, A. Histochemical alterations of re-innervated rat extensor digitorumlongus muscle after end-to-end or graft repair: a comparative histomorphologicalstudy.J Anat., v.203, n.1, p.21-9, 2003

Open Topics

MIM.6.079
Future Trends in Electron Optics and Instrumentation

H. Rose[1]

[1]Ulm University, Center for Electron Microscopy, Albert-Einstein-Allee 11, 89069 Ulm, Germany

Analytical electron microscopy enables (a) the visualization of the atomic structure of thin objects owing to the extremely short wavelength of the electrons at voltages above about 10kV and (b) the determination of the elemental composition and the electronic properties of the object on an atomic scale. Unfortunately, the attainable resolution is limited by the aberrations of the electron lenses, mechanical and electromagnetic instabilities, pure vacuum, and by radiation damage. Solid objects such as metals are primarily damaged by atom displacement resulting from knock-on collisions of the incident electrons with the atomic nuclei, whereas organic objects are mainly damaged by ionization destroying bonds and by etching caused primarily by water molecules and hydrocarbons. In order to further improve the capabilities of the electron microscope, it is necessary to eliminate or to reduce sufficiently the performance-limiting effects of present electron microscopes, to design novel electron optical elements, and to introduce improved techniques which enlarge the attainable information about the static and dynamic properties of the object. At present, several promising developments are proposed which will be discussed in detail. These developments are

1. Dynamic TEM with time resolution in the range between 1µs to 10ps. Such microscopes equipped with a pulsed electron source will enable the observation of reactions, phase transformations, the movement of dislocations and knock-on cascades.
2. High-performance monochromator providing quasi-monochromatic electron beams with an extremely small energy width of about 10meV. If this monochromator is combined with a spectrometer with the same energy resolution, local phonon spectroscopy will be possible with electrons.
3. Improved correctors enabling usable apertures up to 80mrad because these aperture angles are necessary for effective optical sectioning by means of "*holographic*" phase-contrast imaging in STEM. This imaging mode requires a segmented bright-field detector and a Fresnel phase plate which can be formed with a sufficient degree of accuracy by adjusting appropriately the third-order spherical aberration and the defocus of the corrected objective lens, as illustrated schematically in Fig. 1. By subtracting the signals of the annular detector segments covering the region of destructive interference of the scattered wave with the non-scattered wave from that recorded by the annular segments covering the regions of constructive interference (Fig. 2), we obtain a pure phase contrast image which may be conceived as a holographic image because the terms of the intensity which depend quadratic on the scattering amplitude cancel out.
4. Pulsed cathode triggered by laser pulses for DTEM and spin polarized sources for investigating magnetic fields.
5. Cold stable double-tilt stage to reduce radiation damage and for enabling controlled shift and motion-free tilt of the sample in two perpendicular angular directions.
6. Ultra-high vacuum (UHV) to reduce contamination and specimen etching.
7. Incorporation of a superconducting objective lens which eliminates the motion of adsorbed surface atom and provides stable focusing.
8. Fast 8K detectors with high DQE at low voltages.
9. Obstruction-free phase plate for increasing the image contrast of weak phase objects.

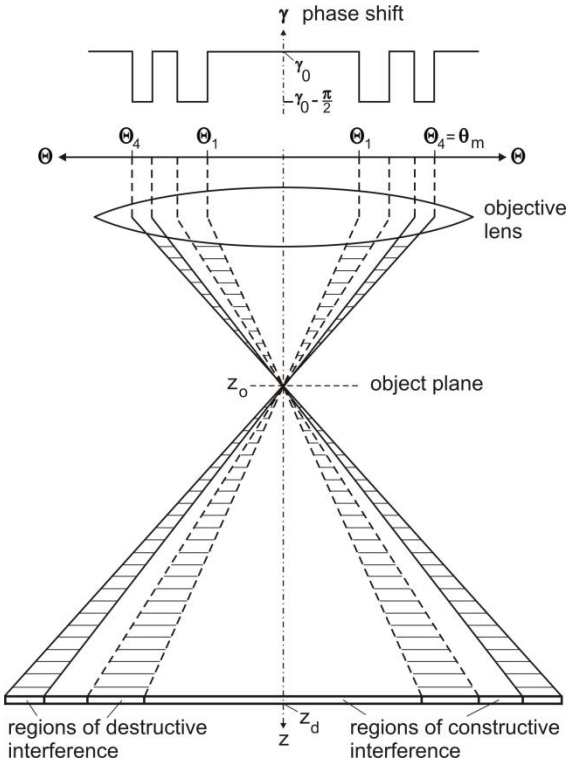

Figure 1. Formation of regions with low and high intensity beneath the object plane in STEM by interference of the scattered wave with the non-scattered wave whose phase is modulated by a Fresnel phase plate located behind the object. In practice, the phase plate is formed approximately in an aberration-corrected STEM by choosing appropriately the defocus and the third-order spherical aberration of the objective lens.

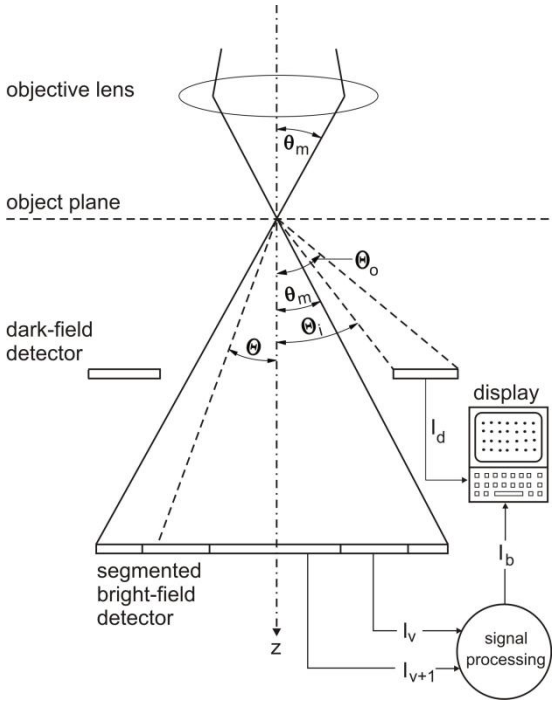

Figure 2. Holographic phase contrast in STEM formed by the difference of the signal recorded by the segmented detectors covering the regions with constructive interference from that of the regions with destructive interference

Open Topics

MIM.6.080
Quo Vadis, Transmission Electron Microscopy?

M. Rühle[1]

MPI for Intelligent Systems, Heisenbergstr. 3, 70569 Stuttgart, Germany

ruehle@is.mpg.de
Keywords: quantitative microscopy, microstructure, properties

Over the last two decades impressive progress has been made in all areas of transmission electron microscopy. A major advancement was the theoretical design and experimental realisation of correctors for the omnipresent aberrations of electron lenses. Instrumentation could profit from technological advancements: magnetic materials with excellent properties are available nowadays, the high voltage of the instruments as well as the currents of the lenses and correctors can be stabilised with extremely high accuracy. However, any technological progress will sooner or later push against the physical limits of the instruments. It seems likely that the physical limits will be reached soon.

Also the understanding of contrast phenomena made progress and is now also close to the limit, as summarized in a recently published book [1]. In that book microscopy at high resolution is called “nanoscopy”. This suggestion follows the present trend to identify many phenomena as “nano”. In principle, this new name is not necessary but may be important for political reasons.

Microscopy as a field of science is, of course, of great importance. The main contributions of microscopy will be expected in areas of materials science, solid state physics, solid state chemistry, Revealing the microstructure of the materials may lead to an understanding of the relationship between the microstructures and properties of the materials or materials systems.

It looks like everything is available from an instrumentation point of view to determine positions, compositions, and bonding of individual atoms in a solid, in 3 dimensions and as a function of time. Major problems have to be solved in achieving the goals.

One important challenge is to determine all data quantitatively (numbers with error bars) not just images. The precision of the data has to be evaluated.

Other challenges for quantitative microscopy are:

- Determination of the 3D structure of the materials. Tomography with high accuracy is needed.
- 4D electron microscopy by ultrafast microscopy by which stroboscopic images can be made at (nano-, femto-) second time intervals [2]. These studies will yield insight on the dynamics of various chemical as well physical processes.
- Reduction of radiation damage by applying lower high voltages of the instrument (as low as possible) with aberration-corrected lenses.
- Specimen preparation techniques have to be improved. This is a long-standing problem. The quality of the (best) specimen influences the data obtained by TEM.
- Non-conventional imaging extracting the phase of the waves will lead to information on the fields inside a specimen.
- It is presently not quite clear what the contributions of TEM will be with regard to revealing the structure of amorphous materials.

Concerning amorphous materials progress has been made by “fluctuation electron microscopy FEM” in combination with phonon scattering [3].

The mechanical properties of metallic glasses (MG) depend strongly on their structural ordering at the nanoscale. Many studies have been completed on the short-range order of metallic glasses, indicating a preference for icosahedral-type short-range order. However, the prevalent nanostructure present at medium-range length scales in most metallic glasses remains open to debate. Cu-Zr binary metallic glasses are good glass formers over a large composition range and serve as a useful model system to study medium-range structural order in metallic glasses. Investigations have been performed so far for different Cu-Zr MGs (Wochner et al [3], Bogle et al [4]).

There are great challenges ahead in the area of microscopy of materials. These can be overcome by improving present day analysis techniques with higher and better accuracy or by developing new techniques. New techniques can be achieved either by deep thinking or/and by serendipity.

1. G.Van Tendeloo, D.Van Dyck, S. J.Pennycook (eds), Handbook of Nanoscopy, (Wiley-VCH Publ.) (2012).
2. A.H Zewail, J.M. Thomas, 4D Electron Imaging in Space and Time, (Imperial College Press) (2010).
3. P. Wochner, et al., PNAS 106, (2009), 11511-11514.
4. S. N. Bogle et al, Proc. M& M Meeting, Phoenix/AZ (2012).

Open Topics

MIM.6.081
High-resolution low-voltage electron microscopy and spectroscopy - current status of the SALVE project.

U. Kaiser[1], J. Biskupek[1], U. Golla-Schindler[1], S. Kurasch[1], Z. Lee[1], P. Wachsmuth[1], O. Lehtinen[1]
M. Haider[2], G. Benner[3], H. Rose[1]

[1]Uni Ulm, Ulm, Germany
[2]CEOS, Heidelberg, Germany
[3]Carl Zeiss Microscopy GmbH, Oberkochen, Germany

ute.kaiser@uni-ulm.de

Recent technical advances in transmission electron microscopy (TEM) [1,2] enabled also trends towards lower accelerating voltages and a microscope with tuneable accelerating voltage from 200kV to 20kV is coming into reach. At low voltages, down to 20kV, this enables atomically-resolved analysis of materials of low-dimensions and low atomic number Z [3]. At higher voltages, the low intrinsic contrast and the high susceptibility of these materials to electron-beam induced knock-on damage prevented the atomically-resolved analysis of pristine materials. However, knock-on damage is only one limitation for the attainable specimen resolution in electron micrographs of radiation-sensitive objects, the other most important limitation is ionisation. We will discuss specimen-electron beam interaction's complexity on the example of different materials: calcite, metal-and molecule-filled carbon nanotubes [4-7], SiO2 [7], MoS2 [8], graphene [9-11] and molecules on graphene using imaging-side Cs-corrected TITAN and SALVE I-prototype microscopes.

In order to achieve atomic resolution and high contrast at low acceleration voltages, the correction of both spherical and chromatic aberration is mandatory. The novel Cs/Cc-corrector of the SALVE (Sub-Angstrom Low-Voltage Electron) microscope compensates for these aberrations. In addition, the corrector is designed to eliminate the off-axial coma providing a large field of view with more than 2000 equally-well-resolved image points per diameter. We demonstrate by means of image calculations that at 20keV the high-resolution image contrast, even for graphene, a one-carbon-atom-thin material, cannot be described by means of the weak phase-object approximation. As at these voltages all atoms are strong scatters, we must incorporate the effect of inelastic scattering into image calculation [12]. We show first results for energy-filtered elastic and inelastic images of graphene and silicon [13]. The Cc/Cs-corrector has recently been installed into the SALVE microscope, and is tested at present. We will report on contrast and resolution, currently achievable with the SALVE II instrument based on experimental results for graphene, molecules-filled and metal-filled carbon nanotubes as well as molecules on top of graphene.

Apart from high-resolution imaging, we take advantage of the exceptionally low background noise of the SALVE microscope at low voltages enabling the investigation of plasmons in single and multi-layer graphene using angle-resolved electron energy loss spectroscopy.

1. M Haider et al., Nature 392, 768 (1998).
2. O L Krivanek et al., Ultramicroscopy 78, 1 (1999).
3. U Kaiser et al. Ultramicroscopy 111, 1239 (2011).
4. A Chuvilin et al., Nature Materials, 10, 687(2011).
5. T W Chamberlain et al., Nature Chemistry, **3,** 732 (2011).
6. T Zoberbier et al. J. Am. Chem. Soc. 134(6), 3073 (2012).
7. P Y Huang, et al., Nano Letters, 12, 2 (2012).
8. H P Komsa et al. PRL 109, 035503 (2012).
9. A Chuvilin, et al., Nature Chemistry, 2, 450 (2010).
10. J C Meyer, *et al.*, Phys. Rev. Lett. 108, 196102 (2012).
11. J C Meyer, *et al.*, Nature Materials 10, 209 (2011).
12. Z. Lee, J.C. Meyer, H. Rose and U. Kaiser, Ultramicroscopy 112, 39 (2012).
13. Z. Lee, H. Rose, R. Hambach, P. Wachsmuth and U.Kaiser, Ultramicroscopy (submitted).
14. The financial support of SALVE (Sub Angstrom Low-Voltage Electron microscopy) project by the DFG (German Research Foundation) and the Ministry of Science, Research and the Arts (MWK) of Baden-Württemberg is gratefully acknowledged.

Open Topics

MIM.6.082
Mode conversion, peculiar rotations, and the Landau-Zeeman-Berry phase in electron vortex beams

P. Schattschneider[1,2,3], T. Schachinger[3], M. Stöger-Pollach[1], S. Löffler[1], A. Steiger-Thirsfeld[1]
K. Bliokh[4]

[1]Vienna University of Technology, Univ. Service Centre for Electron Microscopy, Wien, Austria
[2]Ecole Centrale Paris , CNRS UMR8579, F-92290 Châtenay-Malabry, Austria
[3]Vienna University of Technology, Institute of Solid State Physics, Vienna, Austria
[4]National Academy of Science, Charkov, Ukraine

schattschneider@ifp.tuwien.ac.at
Keywords: electron vortex, Berry phase, mode converter

Vortex beams are characterized by a spiraling wavefront and a phase singularity at the center. They were predicted for optical beams in 1974 [1] and experimentally realized two decades later. Today, there are many applications of optical vortices ranging from tweezers exerting a torque, over optical micromotors, cooling mechanisms, toroidal Bose-Einstein condensates to exoplanet detection [2]. Shorty after the discovery of vortex electrons [3], the holographic mask technique for routinely producing free electrons with quantized angular momentum was established [4]. Owing to their short wavelength, fast vortex electrons can be focused to atomic size. Another interesting aspect is their quantized magnetic moment, even without spin polarization. Both features make them extremely attractive as a novel probe in solid state physics. A technical problem is that the holographic masks drastically reduce the intensity in the outgoing vortex. Here, we describe a novel method for vortex production, based on astigmatic mode conversion [5]. It allows the generation of electron vortices with almost tenfold intensity, and at the same time provides easy detection of vorticity as shown in Figure 1. The theory of propagating electron vortices has been developed in a series of papers [6-8]. For non-diffracting Laguerre-Gaussian electron vortices, a peculiar rotation mechanism in a homo-geneous magnetic field is predicted. The important practical problem of how vortices behave in the lens fields of the TEM has not been tackled yet. Our analysis shows that coherent superpositions of vortices with different orbital angular momentum (OAM) show internal structure. This structure rotates in a homogeneous magnetic field with cyclotron, Larmor, or zero frequency, independent of the topological charge itself, but depending on the sign of the inner product between magnetic field and net angular momentum ⟨L⟩ of the vortex. The rotation can be shown to be caused by the *Landau-Zeeman* phase acquired over a wave packet's trajectory; it is analogous to the image rotation of optical beams caused by a Berry phase. Experimental results, using a blocking edge in the illumination system [9] as sketched in Figure 2, confirm the peculiar rotation of vortices with ⟨L⟩ - dependent frequency as shown in Figure 3. More involved ray-tracing simulations of convergent beams reveal rich details of vortex propagation that are not covered by the simplified description based on non-diffracting Laguerre-Gaussian modes; for details see reference [10]. Finally we discuss possible applications of Landau-Zeeman (or Berry) phases in electron microscopy, as well as the consequences of the peculiar rotation, seemingly challenging the paradigm of the co-moving Larmor coordinate system in electron optics [11].

1. J. Nye and M. Berry, Proceedings of the Royal Society of London, Series A 336 (1974), 165–190.
2. S. Franke-Arnold, L. Allen and M. J. Padgett, Laser Photonics Rev.2 (2008), 299.
3. M. Uchida and A. Tonomura, Nature 464 (2010), 737–739.
4. J. Verbeeck, H. Tian and P. Schattschneider, Nature 467 (2010), 301–304.
5. P. Schattschneider,M. Stöger-Pollach and J. Verbeeck, Phys. Rev. Lett. 109 (2012), 084801.
6. K. Y. Bliokh, Y. P. Bliokh, S. Savel'ev, and F. Nori, Phys. Rev. Lett. 99 (2007), 190404.
7. P. Schattschneider and J. Verbeeck, Ultramicroscopy 111 (2011), 1461.
8. K.H. Bliokh, P. Schattschneider, J. Verbeeck and F. Nori, Physical Review X 2 (2012), 041011.
9. G. Guzzinatti, P. Schattschneider, K. Y. Bliokh, F. Nori and J. Verbeeck, PRL 110 (2013), 093601.
10. T. Schachinger, MC2013.
11. W. Glaser, Grundlagen der Elektronenoptik, Springer-Verlag Wien,1952.
12. P.S., T.S. and S.L. acknowledge the financial support of the Austrian Science Fund (FWF) under grant no. I543-N20.

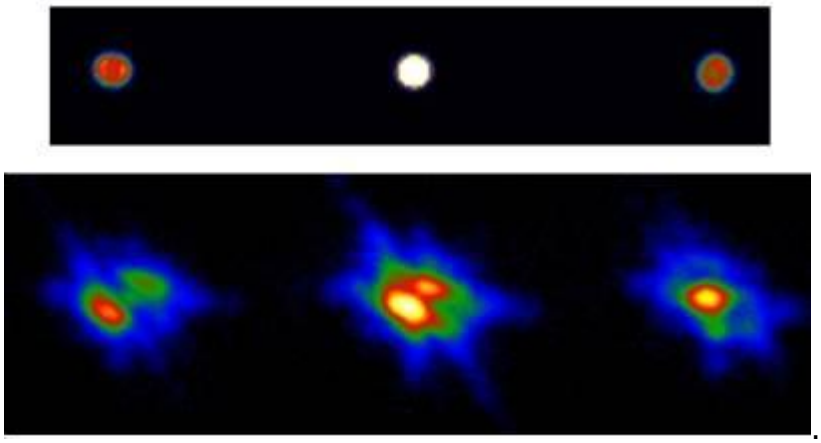

Figure 1: Top: Experimental nm-scaled vortices of topological charge -1, 0, and 1. Bottom: After mode convertsion, they appear as Hermite-Gaussian modes of order -2, -1, and 0, allowing discrimination of vorticity.

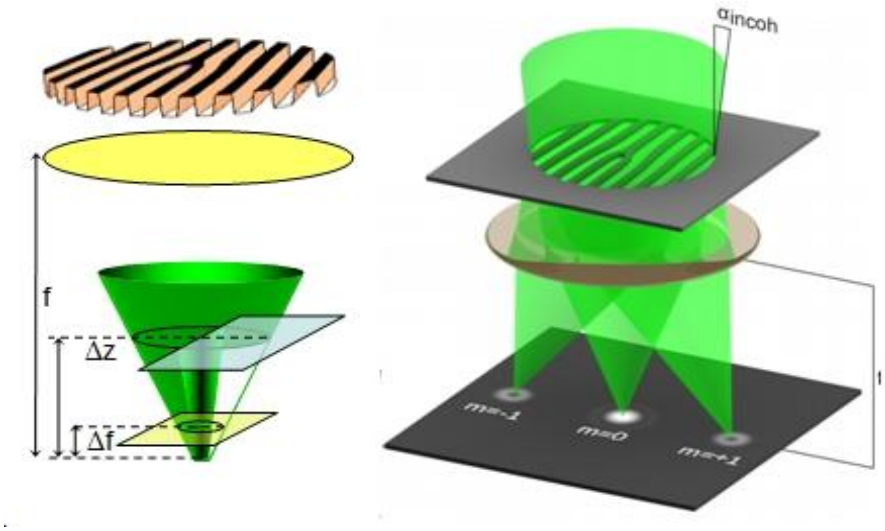

Figure 2. Sketch of the geometry (not to scale). Left: Holographic mask and lens (yellow) create a vortex in the back focal plane. The observation plane (light yellow) is slightly above the vortex for easier measurement and to minimize Gouy rotation from focus variations. A sharp edge far from the focus blocks half of the converging cone. The z-position of the knife is varied in order to see the quantized rotation. Right: Creation of a line of vortices with fundamental modes (the higher topological orders are not shown).

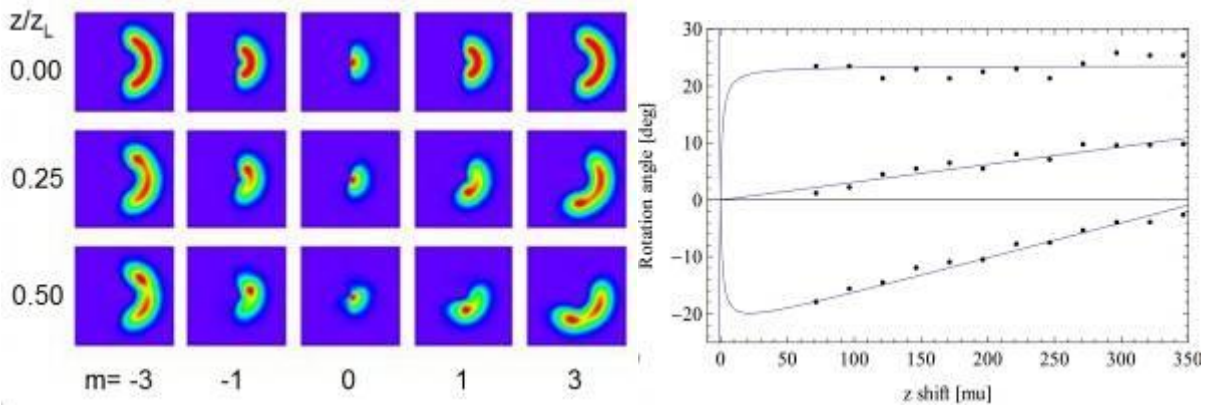

Figure 3. Left: Wave mechanical simulation of a series of cut vortices of angular momentum quantum numbers = -3 to m = 3 after a propagation distance of 0 to 0.5 Larmor lengths from the cutting edge. Rotations with zero, Larmor (for m=0) and cyclotron frequency are seen. Right: Measured rotation angles of vortices m = 3 (lowest data set), m = 0 (middle set) and m = -3 (upper set), as a function of the position z of the blocking edge. The curves are theoretical predictions.

Open Topics

MIM.6.P083
Chemical characterization of painting layers by means of electron and FT-IR microscopy

T. Zubin Ferri[1]

[1]Istrian Developement Agency, Material research centre METRIS, Pula, Croatia

tea.zubin@ida.hr, tea.zubin@gmail.com
keywords: paint layers, preparation, pigments, overpainting

In the reported study paint and preparation layers of a copy of “The rape of Europe” of Paolo Veronese, which is currently being restored at Croatian Conservation Institute, were studied. The suitability of two different analytical techniques, both rapid and requiring a very little amount of sample, was investigated.

Microscopic samples were taken from the painting which original size had been increased by adding a piece of canvas on the right side. Moreover, unlike the original painting, the sine of Europe was covered with a white drapery. The aim of the study was to help dating the artifact, to determine the presence of any remakes as well as to determine when the canvas was enlarged and which materials have been used in the repainting as in the original part.

Samples were embedded in polyester resin and the obtained cross-sections were analyzed with different microscopic techniques. First of all the sections were observed by optical microscope in order to determine the number of layers, their thickness and color. The composition of the pigments was determined by SEM/EDS using a Quanta FEG 250 FEI and IR spectrum of each layer was acquired using a Bruker Tensor 27 FTIR spectrometer coupled with infrared microscope Hyperion 1000 fitted with a MCT detector and a micro ATR objective in Ge crystal. The results obtained with both techniques have been compared in order to confirm the findings.

Micro FT-IR analyzes showed that both the original canvas and the subsequently added part were prepared with a ground preparation made of gypsum and animal glue and that above this layer a white colored imprimature was applied, composed by a mixture of white lead and barium sulfate. Above the layer of imprimature pigments were applied. All collected spectra of the paint layers shown characteristic peaks due to the presence of oil (particularly well visible C-H and C=O stretching bands at 3800-3000 cm^{-1} at 1730-1750 cm^{-1} respectively) which indicate the nature of the binder. The structure of the painting’s layers in the added part of the canvas was practically the same as the one found in the original piece. The ground, the imprimature, the binder and the pigments had the same composition. In both canvas parts pigments have been mixed with white lead before being laid on the canvas. The only difference was observed in the imprimature; optical microscope analysis has shown that the one in the original canvas contained black small particles of carbonized wood that gave it a grayish tone. The imprimature on the added part of canvas has the same composition as the original but did not contain those particles, which indicates that the piece of canvas was added and painted at a later time. It can be assumed that the canvas has been enlarged in order to adapt the size of the painting to the new frame or site of exposure.

The cross-section analyzes have proved the first assumption that the sine of Europe has been overpainted at a later time. The microscope image clearly shown a pinkish layer covered by a thin white layer, which indicates that the painting was primarily identical as the original Veronese’s one. SEM/EDS as the μFT-IR analyzes have shown that this repainting was done using white lead.

The composition investigations have shown that the repainting on the Europe’s sine, as well as the paint layers on the added canvas, were made with the same pigments used in the original part, which indicates how all the remakes were probably made by the same hand or workshop and in a relatively short period of time. By the identification of the pigments and the determination of the composition of the imprimature (prussian blue used for the sky and barium sulfate crystals present in the imprimature) it was possible to narrow the dating frame, at first carried out on the basis of style, to the end of the 18^{th} to the first half of the 19th century.

1. M.P. Mateo, T. Ctvrtnickova, G. Nikolas, Applied surface science, 255 (2009), p. 5172-5176.
2. M. Spring, C. Ricci, D. A. Peggie, S.G. Kazarian, Analytical and Bioanalytical Chemistry, 392 (2008), p. 37-45.
3. M. R. Derrick, D. Stulik, J. M. Landry, Infrared spectroscopy in Conservation Science, Scientific tools for conservation, (1999), The Getty Conservation Institute, Los Angeles.
4. M. Schreiner, M. Melcher, K. Uhlir, Analytical and Bioanalytical Chemistry, 387 (2007), p. 737-747

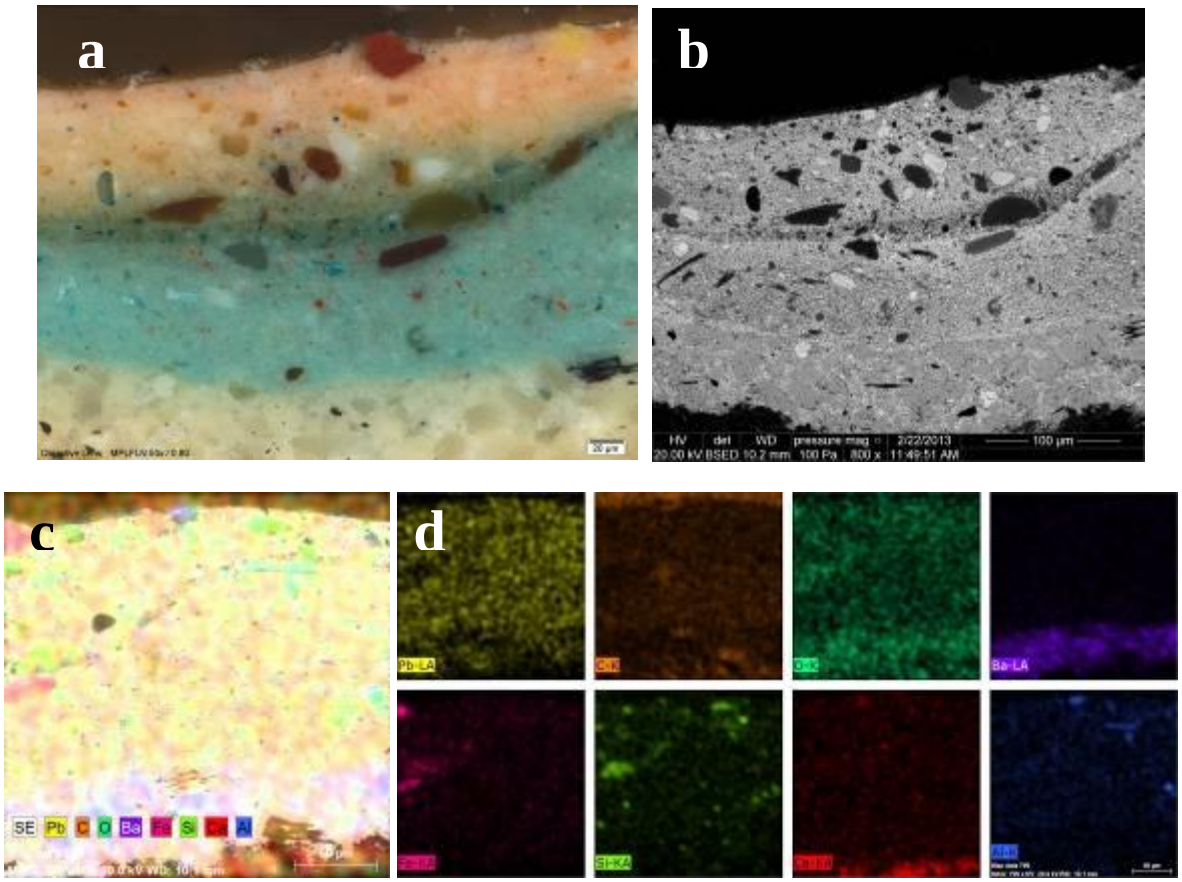

Figure 1. Sample 4; **a.)** optical microscopic image; **b.)** BSE SEM image; **c.)** EDS map; **d.)** EDS maps of singular detected elements.

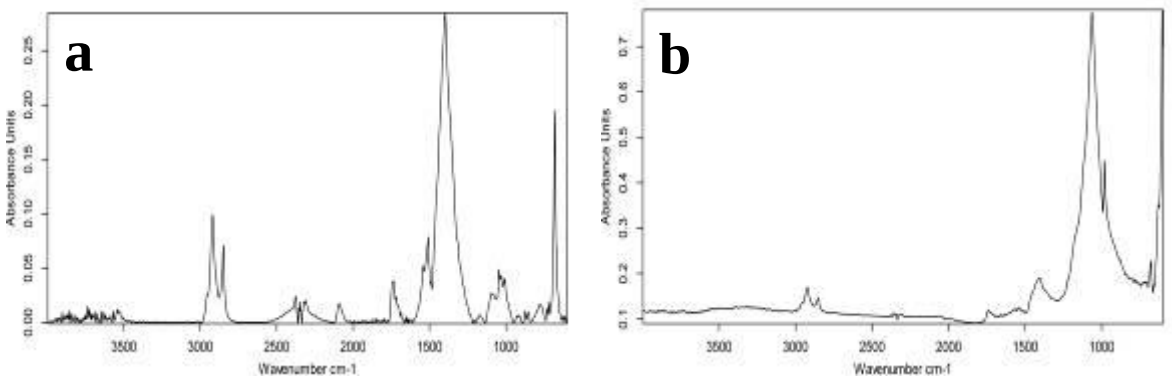

Figure 2. a µFT-IR spectrum of the blue pigment (white lead, prussian blue, ultramarin blue, oleic binder)**; b** µFT-IR spectrum of the imprimatura (barium sulfate, oleic binder).

Open Topics

MIM.6.P084
Iterative filtering algorithm for denoising HR(S)TEM micrographs

H. Du[1,2,3], C.-L. Jia[1,2], J. Mayer[1,2,3]

[1]Forschungszentrum Jülich GmbH, Ernst Ruska-Centrum für Mikroskopie und Spektroskopie mit Elektronen, Jülich, Germany
[2]Forschungszentrum Jülich GmbH, Peter Grünberg Institut, Jülich, Germany
[3]RWTH Aachen, Gemeinschaftslabor für Elektronenmikroskopie (GFE), Aachen, Germany

h.du@fz-juelich.de
Keywords: image denoising, filtering algorithms, HR(S)TEM

HR(S)TEM micrographs are usually superimposed with different kind of noise, such as counting noise and scanning noise etc. Removal of noise from a micrograph therefore is an important task in electron microscopy. It is possible, more often necessary, to quantitatively compare the denoised and recorded images by their difference (residual), which is considered to be the noise. We have compared the performance of low-pass, Wiener, and our developed iterative filters by examining their residuals for noise reduction in HR(S)TEM micrographs.

Low-pass filtering is one of the simplest way to reduce high special frequency noise in atomic-resolution HR(S)TEM micrographs. Figure 1 shows the results of a Gaussian low-pass filtered HAAD-STEM micrograph of a $SrTiO_3$ thin film at [001] zone-axis. The peak attenuation is evidently seen in the residual image and its line profiles (Figure 1c), which hinders faithful quantification of the peak intensity. The Wiener filter and background subtraction filters can effectively reduce peak attenuation.[1] However, these filters tend to have artifacts when variation of background or nonperiodic defects are present in the images (Figure 2). To solve these problems we have developed an iterative filtering algorithm that can efficiently reduce noise in HR(S)TEM micrographs without noticeable artifacts even in the presence of variation of background and defects.

Reduction of peak attenuation has been reported by low-pass filtering to the 1D input signal and its residual.[2] To eliminate peak, background, and defects attenuation we applied the low-pass and wiener (or background subtraction) filters iteratively to the recorded 2D HR(S)TEM images and their residuals respectively. Figure 3 shows the results from the filtered HAAD-STEM image with 15 iterations. The high special frequency noise from iterative filtering has quite similar features to the Wiener filtering in quantitative sense as seen from the line profiles of the residuals (Figure 2b and 3b). The iterative filter performs as efficiently as Wiener filter in removing the high special frequency noise and reduce the so-called scanning noise. However, the advantage of the iterative filter over Wiener filter is without the artifact of low special frequency background ground attenuation. This is because that the signal with special frequency around zero is less touched in the iterative filtering algorithm (Figure 3c). The residual appears to follow a Gaussian distribution with an average value of zero (Figure 3c, inset). The signal-to-noise ratio (SNR) of the recorded image can be estimated from the standard deviation of the denosied image to that of the residual, which turns out to be 1.5 for Figure 1a).

Though the presented example is a HAADF-STEM image with variation of background, the iterative filtering method appears to perform well in denoising other kind of high-resolution electron micrographs, such as HRTEM, EFTEM, BF-STEM micrographs, even when defects are present.

1. R. Kilaas, J. Microscopy 190 (1998), p. 45.
2. J. McNames and B. Goldstein, Acoustics, Speech, and Signal Processing (ICASSP), IEEE International Conference, (2002), p. II-1529-II-1532.
3. We kindly acknowledge the financial support from the Deutsche Forschungsgemeinschaft (SFB 917).

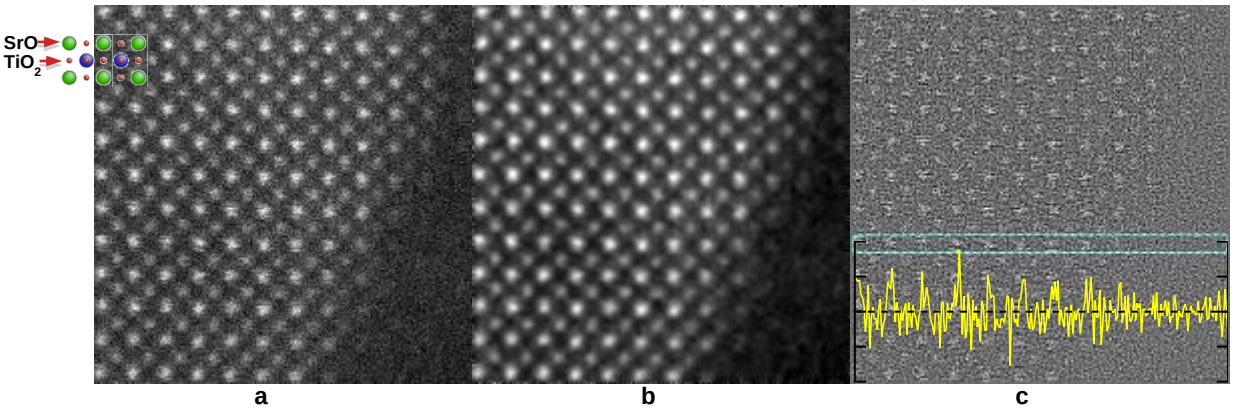

Figure 1. a) HAAD-STEM image of a $SrTiO_3$ film at [001] zone-axis, the dark area at the right side is the amorphous part at the edge of the lamellar, b) low-pass filtered image using a 5×5 Gaussian kernel, c) difference of the recorded and filtered images, inset: line profile of the framed area in horizontal direction.

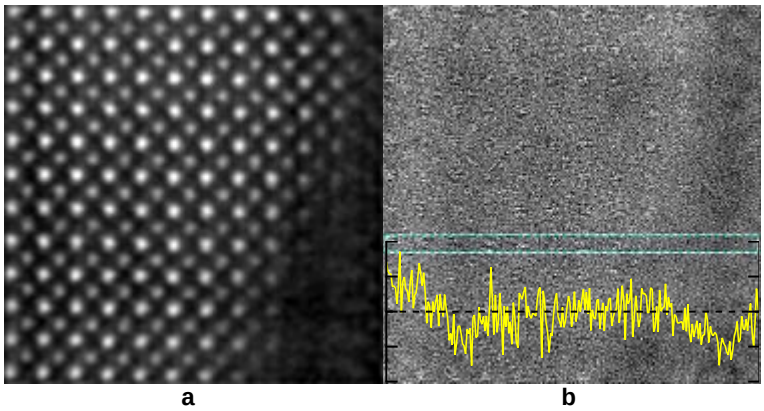

Figure 2. a) Wiener filtered image of Figure 1a), b) difference of the recorded and filtered images, inset: line profile of the framed area in horizontal direction. Background subtraction filter gives quite similar results.

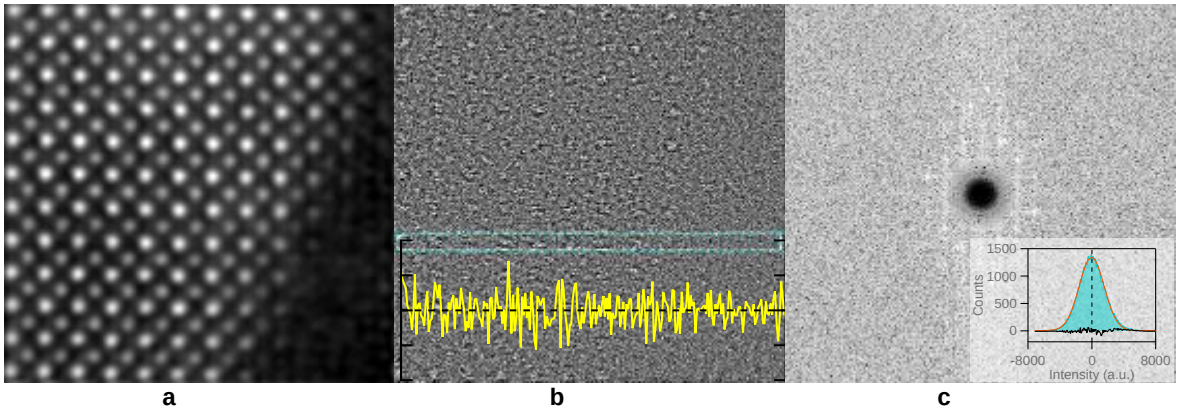

Figure 3. a) Iterative filtered image of Figure 1a), b) difference of the recorded and filtered images, inset: line profile of the framed area in horizontal direction, c) FFT of the difference image, inset: histogram of b).

Open Topics

MIM.6.P085
Nanoflight Movies - Getting a synoptic view on Microstructures

S. Diller[1], H. Mantz[2], M. Holder[3]

[1]Scientific Photography, Wuerzburg, Germany
[2]University of Applied Sciences , Mathematics, Ulm, Germany
[3]IRIS Solutions GmbH, Software, Wuerzburg, Germany

stefan.diller@t-online.de
Keywords: nanoflight, scanning electron microscope, movie, synoptic view, remote microscoping, splines, software

The scientific community and with it every researcher should be committed to share the aesthetics of the microworld with as many people as possible. In scanning electron microscopes (SEMs), data is usually shown using grayscale images. Colours can be added using additional detector signals. This procedure is widely accepted for communicating results on up-to-date research to newspapers, magazines and TV outside the scientific world.

In the past mostly still shots of the specimen had been shown. We thought it would be worth to bring movement, colour and lighting effects into the microworld and developed a modular software called „nanoflight.creator“ [1] to take control of a lot of parameters in the SEM. Sequencing the specimen movements, detector values, focus, colours of each detector channel results in a series of RGB images. Put together as a movie, this yields the impression like flying around the microstructure.

The most demanding difficulty during the development of the control software had been to make it modular, easily extendable for other remotely controllable SEMs. The main program handles only data and UI functions and supplies a framework for all plug-ins used.

We have different levels of software modules: Extensions for proprietary hardware like specimen stages, remote functions on the SEM etc.; livecontrollers to control this hardware; add-ins like timelines to control the execution of programmed sequences within the overall time-schedule; pre-effect plug-ins like autofocus and after-effect plug-ins like color-correction or sharpness.

Within each timeline (and therefore hardware-function on the SEM) the user can read, correct and send microscope values in correlation with sequence time, in that way setting up multidimensional waypoints. Frames between these waypoints will be automatically generated with different possibilities of interpolation and graphic manipualtion „on-the-fly“, where applicable by multidimensional splines to get smooth curves and functions, see „Figure 1“.

When preparing the movie, different target points / function values are selected with the use of the livecontrollers within the software, the 3dconnexion mouse [2] or within the software of the purpose-build scanning system [3], see „Figure 2“. All of them are represented by vectors in a multidimensional space that stand for the settings of all axes used. We use eight axes, three with the motorstage of the SEM and five with a piezo-controlled substage made by Kleindiek nanotechnik [4] and more than thirty hardware-specific parameters.

To get the impression of smooth translations in the final movie, the transitions between the target points have to be interpolated by using splines. For this purpose, we used a special cubic Hermite spline, the so called Catmull / Rom approach. Thus, we generalized the basic principle of creating a smooth curve through all data points (normally in 2D or 3D) to arbitrary dimensions. Tangents at all points are calculated with respect to adjacent points to obtain a continous path.

The software can be used to remote the SEM in all the accessable functions available within the extension modules.

1. „nanoflight®“ is a registered trademark
2. „3dconnexion“ is a trademark of 3Dconnexion, 330 Bear Hill Road - Suite 301, Waltham, MA 02451
3. DISS 5 Scanning System, made by point electronic GmbH, Halle, Germany
4. Piezo Substage made by Kleindiek nanotechnik, Reutlingen, Germany

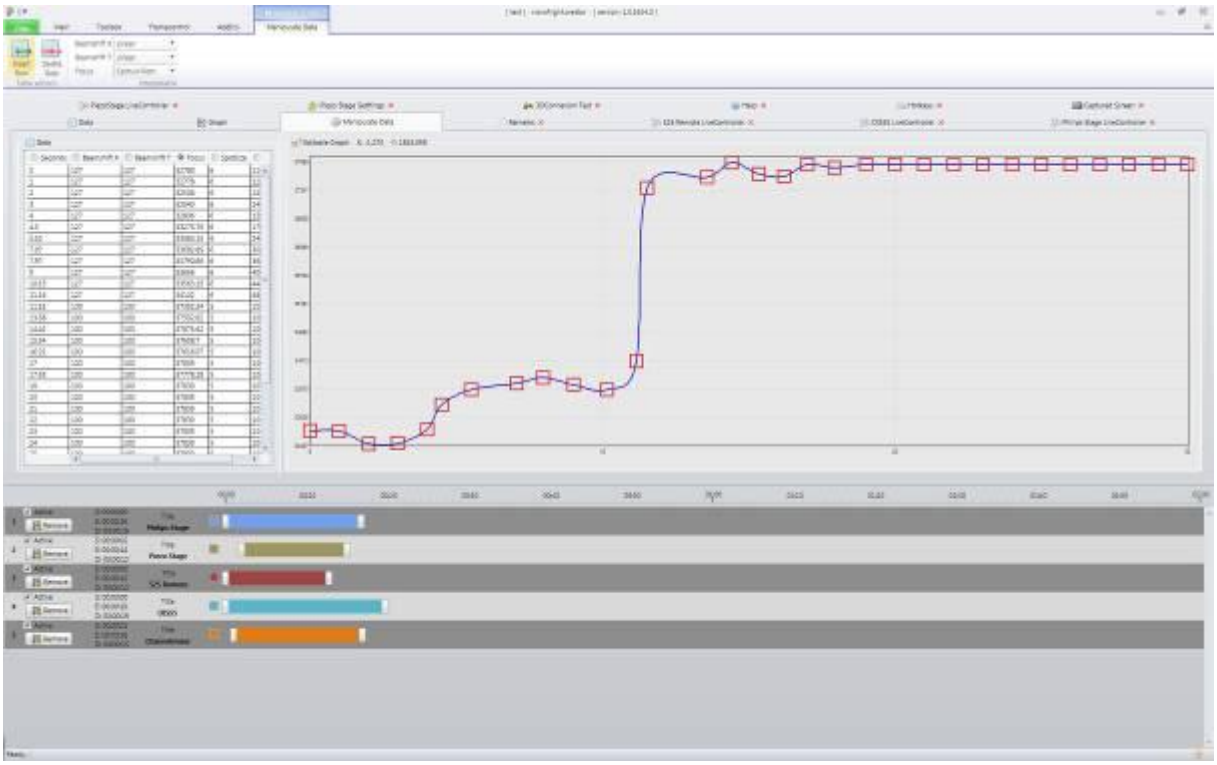

Figure 1. Menu for manipulating parameters in the nanoflight.creator software

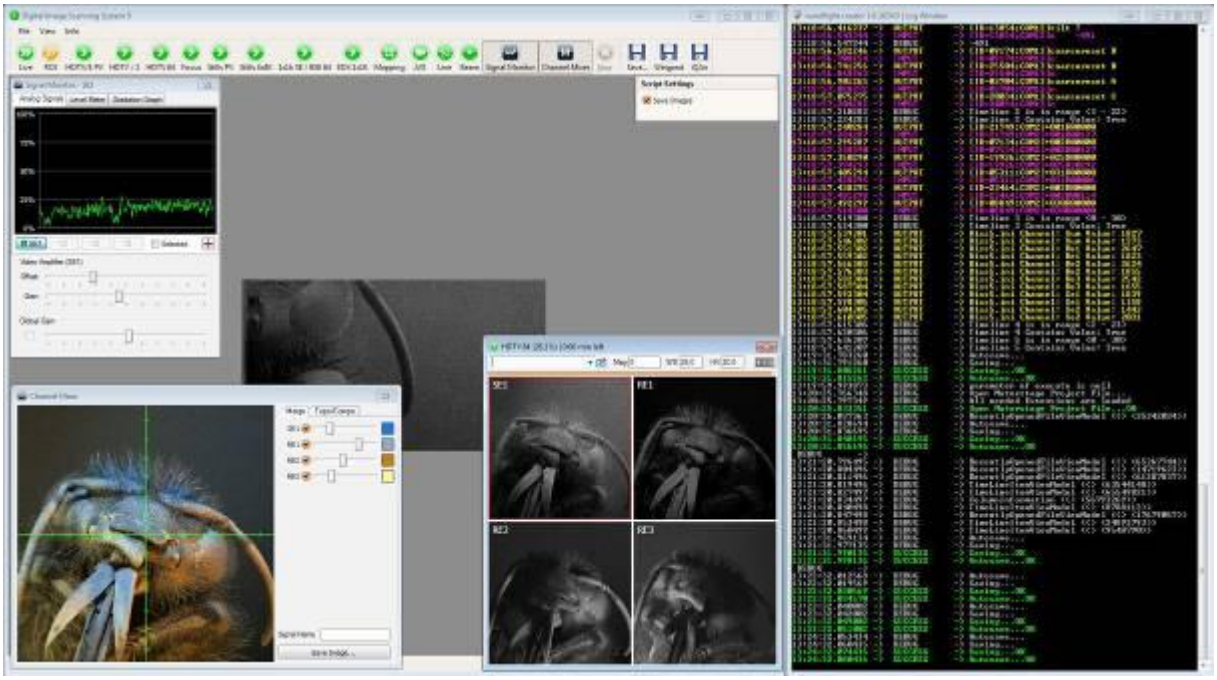

Figure 2. Scanning software window and nanoflight.creator log window

Open Topics

MIM.6.P086
The ultrastructure of the adhesive organs of *Macrostomum lignano* (Macrostomida, Platyhelminthes)

W. Salvenmoser[1], B. Lengerer[1], R. Pjeta[1], L. Schärer[2], R. Arbore[2], J. Wunderer[1], M. Rodrigez[1] P. Ladurner[1]

[1]University of Innsbruck, Institute of Zoology, Innsbruck, Austria
[2]University of Basel, Institute of Zoology, Basel, Switzerland

Willi.salvenmoser@uibk.ac.at
Keywords: flatworm, adhesion, electron microscopy, RNAi

Adhesion is a wide spread phenomenon among the animal kingdom. In most cases adhesion is permanent and serves as an attachment to the substrate. In some animal groups the attachment is not permanent and they can stick and release to the substrate many times quite rapidly. Here we describe the adhesive organs of the free living flatworm *Macrostomum lignano* which lives in a sandy habitat of marine shores in Northern Italy. The adhesive system shows a horse shoe like organization at the end of the tail plate and is formed by up to 120 individual adhesive organs visible as papillae. The adhesive organ itself is composed of only 3 cell types, an anchor-cell, one viscid and a one releasing gland cell [1]. The papilla is formed by a modified epidermal cell called anchor cell which surrounds the gland neck by long modified microvilli containing many actin filaments. The cytoskeleton of the anchor cell shows a dense network of intermediate filaments. Long necks of the two gland cells lead to the cell bodies deep in the tail plate tissue. 15 genes related to the adhesive system have been found so far. Functional knock down by RNA interference of one gene encoding for an intermediate filament variant resulted in a non-adhesive phenotype. TEM analysis revealed the absence of intermediate filaments in the anchor cell. Further knock down experiments are currently performed to find more non-adhesive and or non-releasing phenotypes. In addition regeneration experiments are used to clarify how these organs develop.

1. Tyler, S. (1976). Comparative Ultrastructure of Adhesive Systems in Turbellaria. Zoomorphologie *84*, 1-76.

Open Topics

MIM.6.P087
The Sad and Sorry State of Phage Electron Microscopy

H.-W. Ackermann[1]

[1]Laval University, Microbiology and Immunology , Quebec, QC, Canada

ackermann@mcb.ulaval.ca
Keywords: Bacteriophage, negative staining, quality

About 6,300 bacterial viruses have been examined in the electron microscope until 2012. Each year, 100 novel phages are desribed. A total 261 publications from the years 1966 to 2012 were sorted according to the quality of micrographs. They were classified as good (71), mediocre (22), and poor (168). This is in agreement with a downward trend already noticed 10 years ago. The publications originated from 36 countries and appeared in 76 journals. Two journals featured 56 articles with phage descriptions. Micrographs were obtained by means of an astonishing selection of 80 different electron microscopes or models, all produced by 4 manufacturers (Philips/FEI, 24; Hitachi and JEOl, 23 each; Zeiss, 10).

The classification of micrographs is evidently subjective. The benchmark is the atlas of viral electron microscopy by Dalton and Haguenau (1973). Poor papers typically feature low-magnification, unsharp, contrastless, grey to dark micrographs with pint-size viruses without details such as tail striations and tail fibers. Some do not show micrographs at all and many are silent on virus purification, calibration, dimensions, and even the types of EMs and stains used. Micrographs are often vastly inferior to the very first pictures of negatively stained phages published in 1959 (Brenner et al.). The most common problem is lack of contrast (all is grey in grey). Due to absence of magnification control (calibration), dimensions are often unlikely. Such kind of investigation is useless for virology.

This situation cannot be attributed to a particular country, journal, electron microscope, or camera. Indeed, any countries or electron microscopes may produce good or poor pictures. However, manual EMs (with films and darkrooms) offers the possibility of improving contrast with graded filters and paper, whereas digital EMs (in particular a certain JEM model) seem to have intractable contrast problems. The deterioration of phage electron microscopy (this extends to all viruses) is attributed to generally lowered standards, due to the disappearance of excellent electron microscopists (Bradley, Kellenberger, Tikhonenko), absence of instructions and EM courses, lenient or incompetent reviewers, uncritical journals, bulk-sequencing of virus genomes, and over-emphasis on genomics to the detriment of electron microscopy.

1. A. Dalton, F. Haguenau, eds. Ultrastructure of Animal Viruses and Bacteriophages. An Atlas. (Academic Press, New York-London) (1973), 413 p.
2. S. Brenner, G. Streisinger, R.W. Horne, S.P. Champe, L. Barnett, S. Benzer and M.W. Rees. Strucural components of bacteriophage. J. Mol. Biol. 1 (1959), p. 281.
3. I kindly acknowledge the help f the organizers of MC 2013 with the online submission procedure.

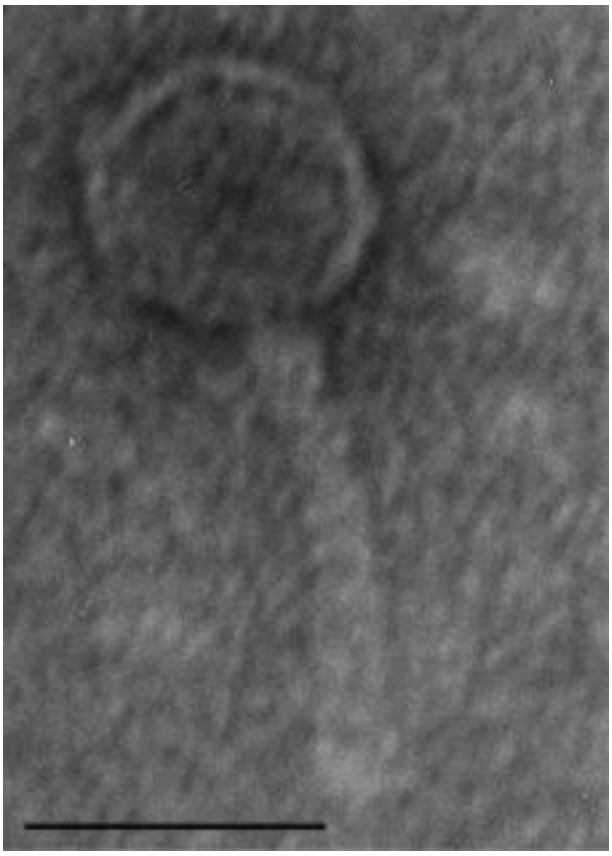

Figure 1. Two examples of *Pseudomonas* myoviruses that almost were published:

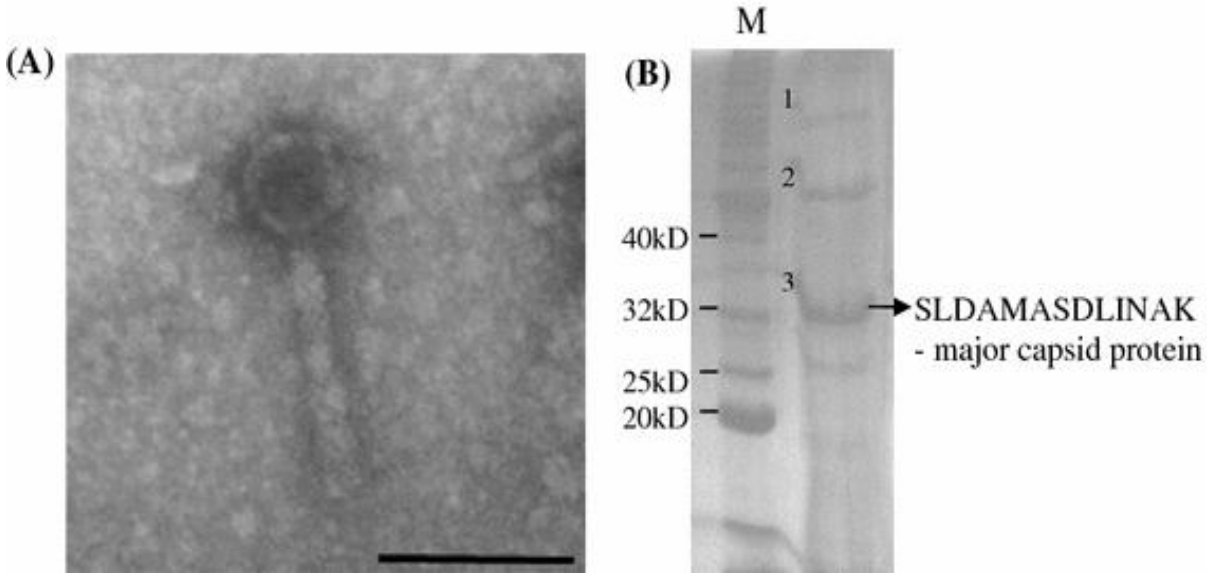

Open Topics

MIM.6.P088
Piezo-based focusing solution for high-speed scanning of microtiter plates with a continuously moving scanning stage

R. Schmitt[1,2], F. Schenk[1]

[1]Fraunhofer Institute for Production Technology IPT, Metrology, Aachen, Germany
[2]RWTH Aachen university, Laboratory for Machine Tools and Production Engineering, Aachen, Germany

friedrich.schenk@ipt.fraunhofer.de
Keywords: Piezo z-focus, fast acquisition, high-throughput microscopy, continuous stage movement, automation

In cell culture based production processes like the automated production of pluripotent stem cells [1] continuous microscopic analysis of cells usually cultured in microtiter plates (MTPs) is vital for process and quality control. Hereby the acquisition time has to be as short as possible to avoid microscopy becoming the bottleneck in large scale production processes where dozens of microtiter plates have to be scanned every day (e.g. for cell colony detection or confluence measurements). The previously developed high-speed scanning solution with a continuously moving scanning stage [2] was extended by a real-time synchronized piezo-based z-focus solution which will be presented here.

Even when scanned with a relatively low magnification of 4x in an inverted microscope with a standard 2/3" CCD camera, a microscopic overview of a whole microtiter plate (footprint ca. 128 mm x 85 mm) consists of more than 3000 single images. Therefore short positioning times between the single acquisitions are necessary for fast scanning of whole microtiter plates. Although acceleration, speed and deceleration of the stage can be tuned, the augmentation of these parameters is limited by the culture medium that starts shaking when moved abruptly. This affects image quality by introducing different lighting conditions for each image. The stitched overview image of a well with shaking liquid appears inhomogeneous which makes automated image processing tasks more difficult. That is why smooth acceleration values and waiting times between the single image captures are indispensable when using standard microscopy for MTP scanning leading to scanning times of half an hour and longer depending on the magnification. Clearly this is a problem for every production scenario.

In order to speed up the microscopic image acquisition, this "stop-and-go" mode was overcome by combining a continuously moving scanning stage with a real time triggered LED flash and a high-speed camera. Core piece of this high-speed microscopy solution is a motorized scanning stage equipped with a high-resolution stepper motor controller (from Märzhäuser Wetzlar) with position dependent triggering functionality. We use a pco.edge camera with a 4/3" sCMOS sensor that can record up to 100 fps with a dual Camera Link interface. All components are integrated into a Nikon Ti-E inverted microscope and controlled by specially developed LabVIEW® software. The stroboscopic illumination of a few micro seconds leads to exposure times short enough to capture sharp images of the moving object without motion blur. Our system can process images at 45 frames per second (fps) which allows scanning speeds of up to 120 mm/s (max. travel speed of stage) using a 4x magnification. The positioning and triggering accuracy provides perfect alignment in x- and y- direction and allows overlap free stitching of the single images.

In microtiter plates adherent cells like iPS cell colonies grow attached to the well plate bottom. The most frequently used material of labware products as microtiter plates is plastic. This is cheap and favors cell growth; however the injection moulding production process introduces deviations especially to the geometry of the microtiter plate bottom. The thickness of the plastic bottom varies up to 200 µm over the whole MTP. The variance of the flatness is in a similar range. The cells that are attached to the plate bottom therefore do not lie in the same z-plane. These deviations easily exceed the depth of focus for higher magnifications objectives (> 10x). To compensate the tolerances of the plate bottom, the focus position has to be adjusted during the scan. For the high-speed acquisition mode with the continuously moving scanning stage the z-focus has to be adjusted in real-time while the stage is moving. In order to provide a magnification independent and sufficiently fast focusing solution, a piezo z-stage (Märzhäuser Wetzlar) was mounted onto the x-y scanning stage. It moves the microtiter plate up and down with a travel range of 300 µm and a settling time of 40 ms (under load). The analog output of the x-y controller is connected to the digital controller of the piezo z-stage thereby synchronizing x-, y- and z-position. The corresponding z-positions are derived from a focus map that is calculated before the scan based on certain z-focus measurements using an autofocus algorithm. This way the scan of the whole microtiter plate can be acquired in less than 3 minutes using a 4x magnification with a focus adjustment of up to 25 fps. Our solution works with bright field and phase contrast microscopy and different magnifications.

1. «Ziel2.NRW» research project "StemCellFactory", www.stemcellfactory.de.
2. R. Schmitt, F. Schenk, High-speed light microscopy with continuously moving scanning stage for fast acquisition of microtiter plates, Focus On Microscopy (FOM), Maastricht, 2013.

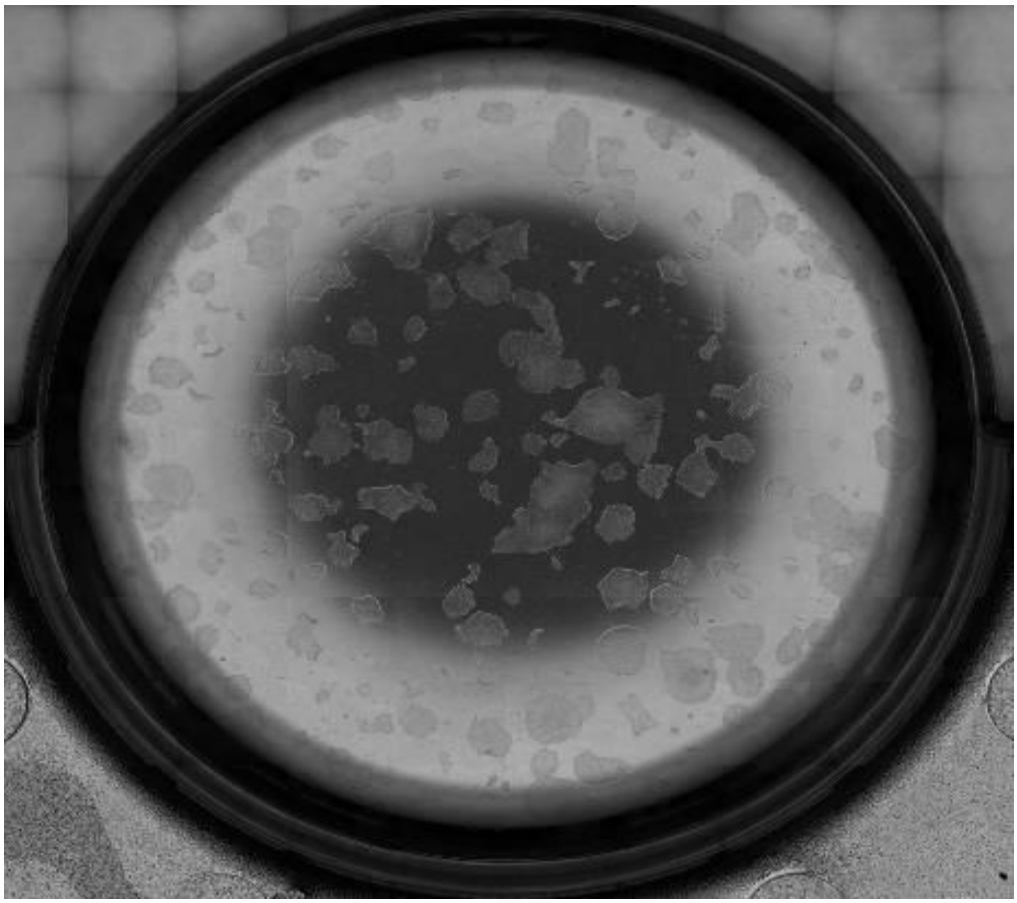

Figure 1. Stitched overview image of one well of a 6-well MTP with human iPS cell colonies on Matrigel acquired with 4x magnification in high-speed mode at 34 mm/s.

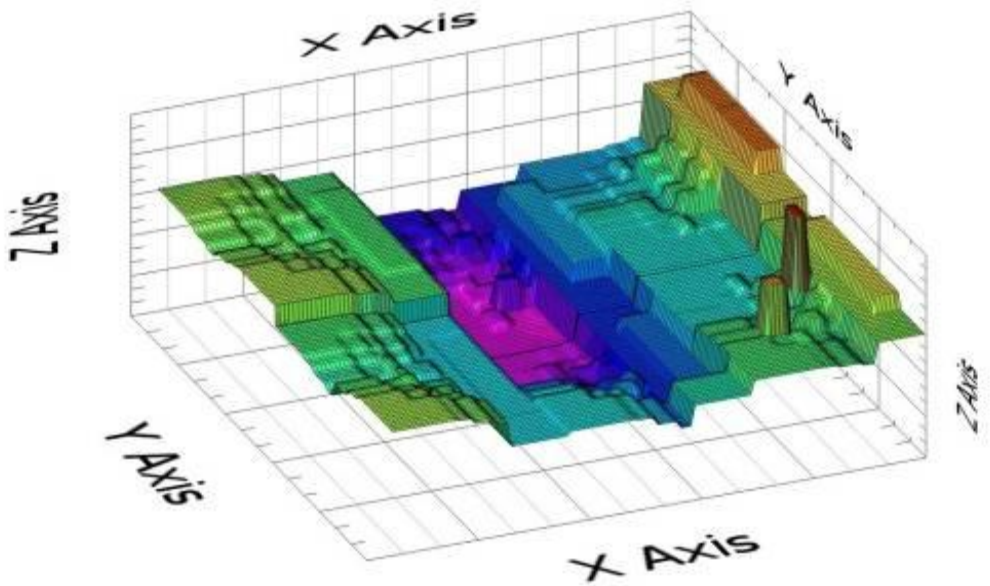

Figure 2. Calculated focus map for one well to compensate the well plate bottom deviations. The difference between the lowest and the highest z-position is around 200 µm.

Open Topics

MIM.6.P089
Ultrastructure and cellulose distribution of *Miscanthus sinensis* internode tissues by TEM and Raman imaging

J. Ma[1], J. Ma[1], Z. Ji[1], X. Zhang[1], X. Zhou[1], F. Xu[1]

[1]Beijing Forestry University, Institute of Biomass Chemistry and Technology, Beijing, China

xfx315@bjfu.edu.cn
Keywords: Layering structure, Cellulose microfibrils orientation, Cellulose localization, TEM, Confocal Raman microscopy

Plant cell walls have a heterogeneous and complex hierarchical structure, which is primarily made up of cellulose, hemicelluloses and lignin [1,2]. Previous researches showed that the plant cell wall ultrastructure and components spatial distribution varies from species to species, between different cell types and even between cell wall layers [3]. Using TEM combined with confocal Raman microscopy, the ultrastructure and cellulose distribution of *Miscanthus sinensis* internode tissues were visualized. TEM observations revealed the layering structure of protoxylem vessel (Pxv), metaxylem vessel (Mxv), sclerenchymatous fiber (Sf) adjacent to vascular bundle, sieve tube (St), companion cell (Com), and parenchyma (Par) (Figure 1a-1g). Noteworthy was the observation that a great degree of inhomogeneity in the layering structure of the Sf adjacent to vascular bundle was visualized (Figure 1c-1e). Moreover, it was noted that the cellulose microfibrils in the secondary wall of Pxv were predominantly oriented lamellar (Figure 1a). The two-dimensional Raman spectroscopic images acquired with linear polarized light revealed changes in the orientation-dependent band (1098 cm^{-1}) intensity of various cells. In the Pxv and Mxv secondary wall, higher relative band intensity in the tangential direction indicated that the cellulose microfibrils orientated more perpendicular to the fiber axis than that of Sf and Par (Figure 2). Raman images by integrating over the cellulose band at 2897 cm^{-1} clearly displayed higher cellulose concentration within the secondary wall of Sf and Par, whereas the secondary wall of Pxv and Mxv showed less intensity (Figure 3a). Within the individual cell wall layers of Sf, the heterogeneous distribution of cellulose was also visualized, with the highest cellulose concentration occurring in the secondary wall (Figure 3b). The investigation of cell wall ultrastructure and cellulose localization at sub-cellular level of *Miscanthus sinensis* will contribute to the further understanding of mechanical and chemical properties of grass species. Meanwhile, these complementary micro-analytical methods can be used to provide more accurate and complete information with regard to ultrastructural and compositional characterization of plant cell walls.

1. N. Chaffey, P. Barlow and B. Sundberg, Tree physiology (22) 2002, 239-49.
2. D. J. Cosgrove, Nature Reviews Molecular Cell Biology (6) 2005, 850-861.
3. L. A. Donaldson, IAWA (29) 2008, 345-386.
4. We kindly acknowledge the National Science and Technology Program of the Twelfth Five-Year Plan Period (2012BAD32B06).

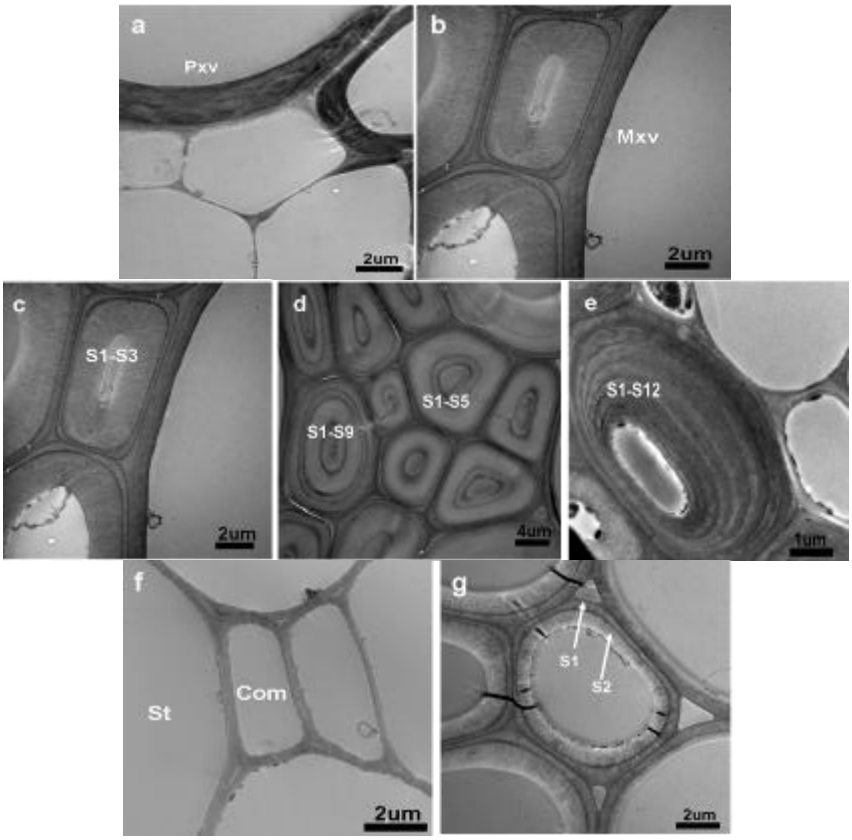

Figure 1. TEM images of cross sections of *M. sinensis* internode tissues showing the layering structure of various cells. (a) protoxylem vessel (Pxv); (b) metaxylem vessel (Mxv); (c-e) sclerenchymatous fiber (Sf) adjacent to vascular bundle; (f) sieve tube (St) and companion cell (Com); (g) parenchyma (Par).

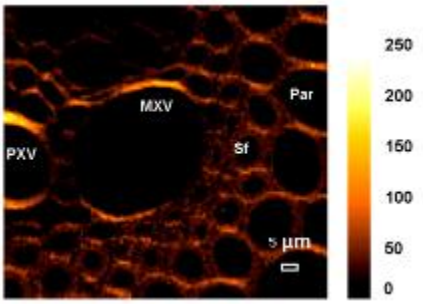

Figure 2. Raman images of cross section of *M. sinensis* internode tissues calculated by integrating over the band at 1098 cm^{-1}. The variation of cellulose orientation in various cells.

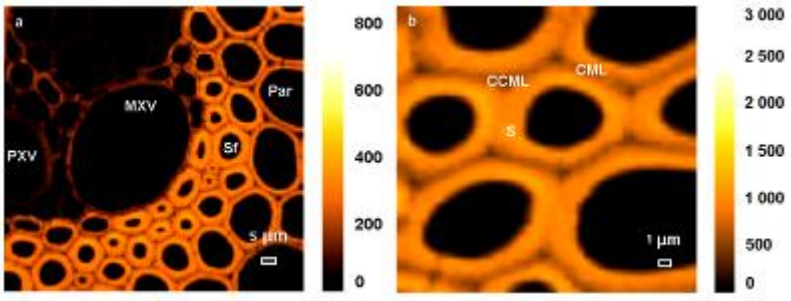

Figure 3. Raman images of cross section of *M. sinensis* internode tissues calculated by integrating over the band at 2897 cm^{-1}. (a) Cellulose distribution within the secondary wall of various cells; (b) Cellulose distribution within morphologically distinct regions of Sf.

Open Topics

MIM.6.P090
SEM and confocal Raman microscopic study of morphological and topochemical changes of poplar cell walls during alkali pretreatment

Z. Ji[1], X. Zhang[1], J.F. Ma[1], F. Xu[1]

[1]Beijing Forestry University, Beijing Key Laboratory of Lignocellulosic Chemistry, Beijing, China

xfx315@bjfu.edu.cn
Keywords: poplar; alkali pretreatment; morphology; topochemistry; SEM; confocal Raman microscopy

Poplar is a fast growing feedstock with potential for biofuel production showing renewable and sustainable advantages. However, physical and chemical barriers caused by the recalcitrance of plant cell walls hinder the hydrolysis of polysaccharide fractions to fermentable sugars. Pretreatment is an essential step to reduce biomass recalcitrance for increasing the enzyme accessibility. Alkali pretreatment is attractive among the most promising pretreatment technologies that can effectively reduce the lignin content to enhance sugar release performance.

In this study, poplar cross-sections of 6 μm thickness were subjected to aqueous sodium hydroxide (2% w/v) pretreatment at 121 °C and analytical microscopy approaches were used to assess the impact of pretreatment upon morphology and topochemistry of plant cell walls.

SEM images revealed a great deal of pore formation on the surface of cell walls and structural disruption of biomass to some extent after pretreatment, especially in the areas adjacent to the cell corner middle lamella (CCML). The phenomenon was reasonably consistent with lignin removal during pretreatment (Figure 1.).

In order to track the topochemical changes of poplar, confocal Raman microscopy was used to acquire chemical images and spectra of main components within plant cell walls during pretreatment. As shown in Figure 2., before alkali pretreatment the highest level of lignification occurred in the CCML and the highest carbohydrate concentration was found in the secondary wall (S).

Comparison of Raman images of lignin distribution at various pretreatment time indicated that lignin concentration decreased significantly during pretreatment, especially within the first 60 min (Figure 2b.). It also indicated that cell wall swelling was mainly in the S and slight effect was observed on the CCML in terms of swelling, which was confirmed by the bright field images (Figure 2a-b.). These results suggested that it was easier for alkaline liquids to penetrate into cell walls from lumen. As a result of preferential swelling, the rate of delignification in the S was much faster than that in the CCML where there was a higher level of lignification.

As illustrated in the Figure 2c., carbohydrate dissolution in the S regions visibly occurred within the first 10 min, which was probably due to partial dissolution of hemicelluloses accompanied by delignification. Subsequently, reduction of carbohydrate concentration became slower for the S regions. It should be noted that significant dissolution of carbohydrate occurred again after about 90 min of pretreatment when a large amount of lignin was removed.

Further Raman spectral analysis allowed a semi-quantitative comparison of the chemical compositions within cell walls and showed a decrease of lignin Raman intensity to about 20% within the 10 min and to 82% under pretreated time of 180 min (data not shown).

Based on these findings, alkali pretreatment appeared to increase lignin solubilization, cell wall swelling and porosity of the biomass. These results were meaningful in bioconversion and utilization of renewable lignocellulosic biomass for providing valuable new insights toward the mechanism of alkali pretreatment. In this work, it also demonstrated that a combination of SEM and confocal Raman microscopy is capable of rapidly determining the morphological and topochemical changes of plant cell walls during alkali pretreatment.

1. We kindly acknowledge financial support from Natural National Science Foundation of China (31225005, 31070526) and National Science and Technology Program of the Twelfth Five-Year Plan Period (2012BAD32B06).

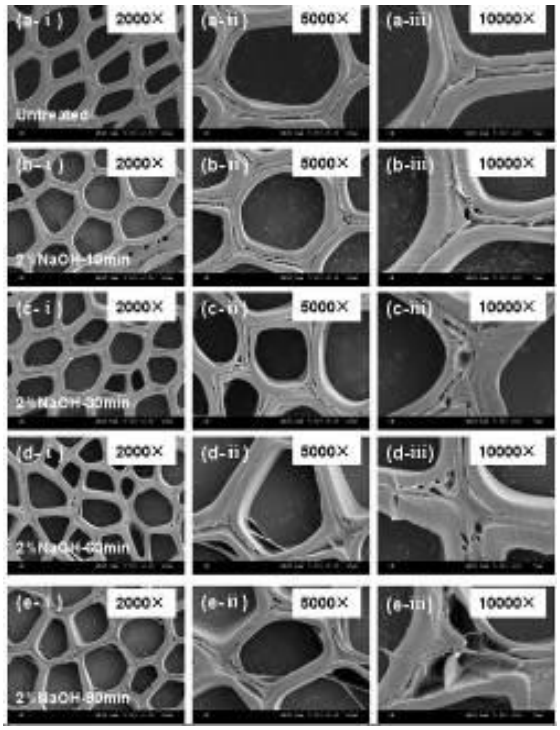

Figure 1. SEM images at various magnifications of poplar cross-sections at various pretreatment time of 0 min (a); 10 min (b); 30 min (c); 60 min (d); 90 min (e).

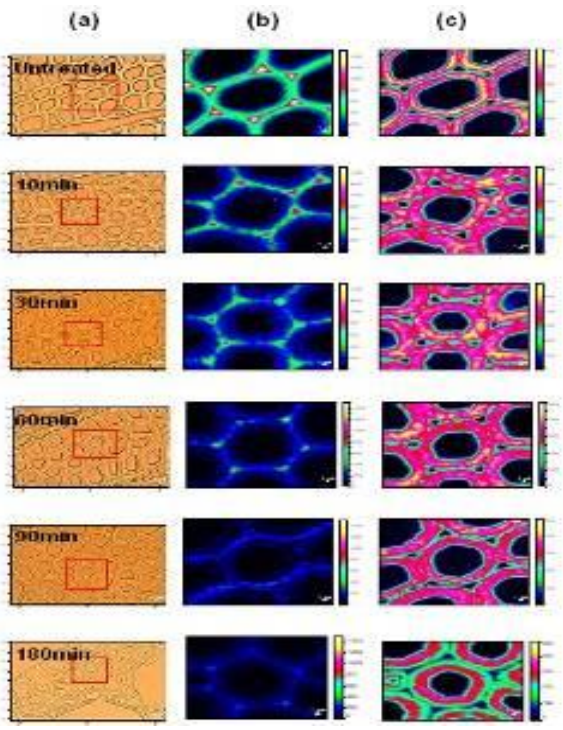

Figure 2. Bright field images of poplar cross-sections showing selected area (*red rectangle*) for Raman imaging (a); Raman images showing the distribution of main components within cell walls at various pretreatment time by integrating from 1570 to 1680 cm^{-1} (b, lignin) and 2850-2920 cm^{-1} (c, carbohydrate).

Open Topics

MIM.6.P091
Room-facelift for new JEOL JEM-ARM 200F instruments

K. Hahn[1]

[1]Max-Planck-Institut für Intelligente Systeme, Stuttgart Center for Electron Microscopy, Stuttgart, Germany

hahn@is.mpg.de

During the last decade there has been an immense progress in the field of transmission electron microscopy (TEM) development. Due to the application of aberration-corrected electron optics it is nowadays possible to perform structural and analytical investigations in the sub-nm range in TEM and STEM-mode.

At the same time, the environmental conditions in the TEM laboratories became more critical. The microscope manufacturer demands to have several requirements and room specifications to be fulfilled. As a consequence significant efforts have to be carried out to achieve all these parameters. The temperature constancy has to be better than 0.2° C/h, fluctuations of 0.05 °C/min or less. The air flow should be below 100 mm/s at the column position and the air humidity 60 % or less. The acoustic noise has to be less than 50 dB. Also the reduction of stray-magnetic fields (to < 20 nano-Tesla (DC and AC) is important. Mechanical vibrations should be kept as low as possible (< 0.2 µm for frequencies higher than 3 Hz).

In our case there are two laboratory rooms, which were built 11 years ago. At that time these rooms were equipped with the best available technology, but for the new generation TEMs the environmental tests failed the specified requirements. Neither the acoustics nor the other parameters were acceptable. Thus, an elaborate room-reconstruction procedure was necessary in order to meet all the requirements in the existing building. In the microscope rooms (Fig. 1), there are the TEMs, the high voltage tanks and water valve units. Everything else has to be outside in the engineering rooms (power supply units for lenses and correctors, camera and energy-filter controllers as well as water chillers, air compressors and further equipment).

For avoiding air-pressure fluctuations, which should be as small as 1 Pa or less during the measurement period, we had to install an airlock, which we use as an anteroom for both TEM laboratories. The microscope rooms are equipped with noise prevention doors. On the ceiling and on the walls of the TEM labs cooling panels are installed with a cooling efficiency of 3 kW for each room; additionally the texture of the surfaces of the walls is designed in a way such as to reduce acoustic noise. In order to keep air-flow speed and the acoustic noise of the air-conditioning system at low level air duct socks are used at the intakes. The microscopes themselves are mounted on concrete blocks of 40 tons each, which are completely isolated from the floor accessible to the user. An active compensation system for stray-magnetic fields using three pairs of Helmholtz coils is installed in each microscope room. Fiber-reinforced concrete (instead of steel reinforcement) is applied for the upper part of the microscopes' foundations in order to avoid interference with the compensating magnetic fields. In addition, one microscope (the TEM/STEM) is equipped with a passive damping system to minimize mechanical vibrations. In order to avoid stray-magnetic fields resulting from possible leakage currents in the power-supply lines for the peripherical electrical equipment these power lines are disconnected while the main laboratory light is switched off.

Figure 1. Room design for the new JEOL JEM-ARM 200F microscopes at the Stuttgart Center for Electron Microscopy

Open Topics

MIM.6.P092
Low-keV electron diffractive imaging based on a single-atom electron source

I.-S. Hwang[1], W.-T. Chang[1], C.-Y. Lin[1], W.-H. Hsu[1], M.-T. Chang[1], T.T. Tsong[1]

[1]Academica Sinica, Institute of Physics, Taiwan

ishwang@phys.sinica.edu.tw
Keywords: electron sources, single-atom tips, electron microscopy, coherent electron diffractive imaging, in-line electron holography

Brightness and spatial coherence of electron sources are two key factors for their application to electron interferometry, electron holography, coherent electron diffraction, and many other electron microscopic techniques. Nanotips or single-atom tips (SATs) are of great interest for emitting coherent and bright electron beams because of their small source sizes. Use of these field emitters may greatly improve the resolution and performance of electron-beam based microscopic techniques. It has been shown that noble-metal covered W(111) SATs can be reliably prepared [1,2]. A process to fabricate tungsten tips with good control of tip profiles has also been demonstrated [3]. The growth of the faceted pyramidal tips is a thermodynamic process. Even if a tip apex is destroyed or contaminated, the single-atom sharpness can be restored through a simple annealing, ensuring a long operation lifetime. These SATs are also chemically stable. When a SAT is exposed to air, a clean SAT can be regenerated after annealing in vacuum. Due to a small source size and a small opening angle, both the brightness and spatial coherence of these single-atom electron sources are orders of magnitude better than those of the state-of-the-art electron sources used in current electron microscopes [4].

We have built a low-energy electron point projection microscope (PPM) to image nano-objects. A schematic is shown in Figure 1. The PPM is a shadow microscope where a specimen is placed between a field emission electron point source and a detector. The detector (Microchannel plate, MCP) is mounted on a retractable support. The magnification of the projected image (bright-field unscattered beam) at the screen is (D+d)/d. A higher magnification bright-field projection image can be obtained as the tip approaches the object (smaller d) or as the detector is retracted (larger D). When the detector is moved close to the sample (small D), the dark-field diffraction patterns of the sample at large angles can also be recorded. The patterns we have obtained at large angles are similar to the convergent-beam electron diffraction patterns obtained in TEM. Combined the low-resolution projection image with the high-angle dark-field diffraction patterns, it will be possible to obtain a high resolution image via some phase retrieval algorithms. Figures 2(a) and 2(b) show a projection image and the corresponding diffraction pattern of a graphene sample, respectively. For the image shown in Figure 2(b), fine structures inside each diffraction disk of graphene can be clearly seen.

Figure 3 illustrates a new design of a low-keV electron microscope based on a single-atom electron source and a focusing lens. The tip is mounted on a holder that can be positioned, tilted, and rotated in nano-meter scale by several piezo-driven positioners. Therefore, the tip-lens alignment can be done in vacuum without any alignment coil. Owing to the small virtual source size and opening angle of the single-atom electron source, it will be possible to focus electron beams into a small spot through a simple electrostatic lens. To equip with appropriate signal collectors, the low-keV electron microscope allows different imaging modes, including secondary electron imaging, coherent electron diffractive imaging, and in-line holographic imaging, etc. This new instrument may allow determination of the atomic structures of individual thin nano-objects, such as graphene, carbon nanotubes, DNA molecules, or protein molecules.

1. H. S. Kuo, I.-S. Hwang, T.-Y. Fu, J.-Y. Wu, C.-C. Chang, and T.T. Tsong, Nano Lett. 4(12) (2004), p. 2379.
2. H. S. Kuo , I.-S. Hwang, T.-Y. Fu, Y.-C. Lin, C.-C. Chang, and T. T. Tsong, Jpn. J. Appl. Phys. 45 (2006), p. 8972.
3. W. T. Chang, I.-S. Hwang, M.-T. Chang, C.-Y. Lin, W.-H. Hsu, and J.-L. Hou, Rev. Sci. Instrum. 83 (2012), p. 083704.
4. C. C. Chang, H.-S. Kuo, I.-S. Hwang, and T. T. Tsong, Nanotechnology 20 (2009), p. 115401
5. We kindly acknowledge the help of the organizers of MC 2013 with the online submission procedure.

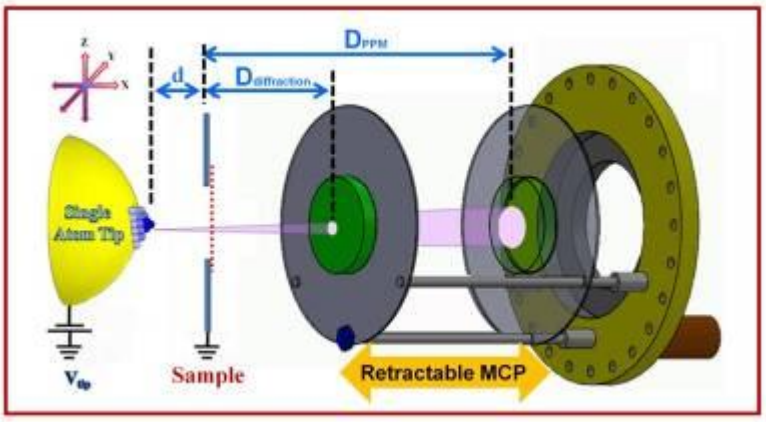

Figure 1. Schematic of an electron point projection microscope with a retractable MCP. The bright-field projection images can be obtained when D = D_{PPM} =13 cm, and the diffraction patterns of the object at large angles can be recorded when D = $D_{diffraction}$ = 3 cm. The magnification of the bright-field image is M = (D+d)/d.

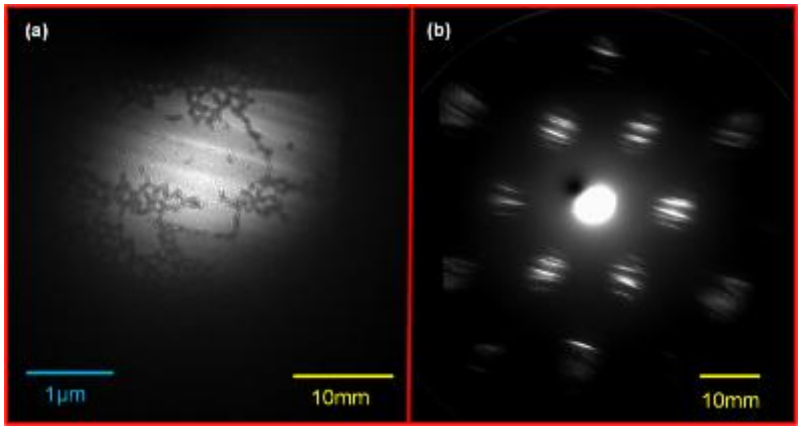

Figure 2. Study of a suspended graphene sheet. (a) Bright-field PPM image taken at D = D_{PPM}. (b) Diffraction pattern taken at D = $D_{diffraction}$. The yellow scale bar at the lower right-hand corner indicates a length on the screen; the blue scale bar at the lower left-hand corner indicates a length on the sample plane.

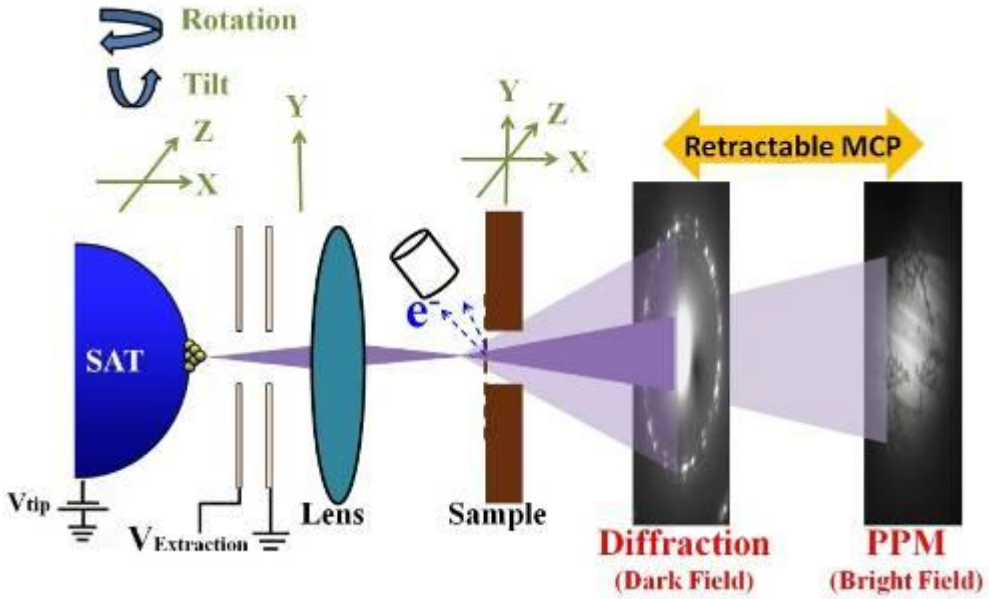

Figure 3. Schematic of a low-keV electron diffraction microscope.

Open Topics

MIM.6.P093
Chitosan disrupts urinary bladder urothelium regardless of the differentiation stage of superficial urothelial cells

T. Visnjar[1], M. Erdani Kreft[1]

[1]University of Ljubljana, Faculty of Medicine, Institute of Cell Biology, Ljubljana, Slovenia

tanja.visnjar@mf.uni-lj.si

Urinary bladder epithelium called urothelium presents one of the most resistant biological barriers composed of superficial, intermediate, and basal urothelial cells (UCs) [1]. This low permeability barrier is the result of high resistance tight junctions (TJ), a specialized apical plasma membrane with uroplakins and surface glycans, and hindered apical endocytosis [1, 2, 3, 4]. To improve drug absorption across the urothelium, paracellular transport pathways modulated by chitosan were studied. So far the effect of chitosan was studied only on normal urinary bladders with highly differentiated superficial UCs [5, 6]. The effect of chitosan on partially or low differentiated UCs that could be found at the surface of urinary bladder in the case of continuous infections or urothelial carcinomas is still unknown. In order to determine whether the effect of chitosan depends on the differentiation stage of superficial UCs, we applied chitosan to partially and highly differentiated urothelial models *in vitro*.

Partially and highly differentiated urothelial models were established by culturing UCs in UroM medium supplemented with fetal bovine serum or physiological concentration of calcium [7]. The effects of 15 minutes treatment with chitosan (0.05% (w/v), pH 4.5) on partially and highly differentiated urothelial models were analysed by monitoring molecular, ultrastructural, and physiological changes.

The transepithelial resistance (TER) measurements revealed complete loss of TER in both urothelial models, which shows that chitosan has the effect on partially and highly differentiated UCs. Furthermore, in order to explore the cause of this quick loss of TER, we performed detailed molecular and ultrastructural analyses. The results showed that reduction of TER in both urothelial models was due to opening of TJs and necrosis of partially and highly differentiated UCs "Figure 1.".

Data presented here show clear evidence that chitosan causes TJs disruption at the molecular level, desquamation of UCs, and consequently complete loss of TER in partially and highly differentiated urothelial models. According to these results, chitosan is a promising tool for ridding the infected UCs and removing urinary bladder superficial transitional cell carcinoma.

1. R.M. Hicks, J Cell Biol 26 (1965), p. 25-48.
2. M.E. Kreft, et al., Differentiation 77 (2009), p. 48-59.
3. J.D. Lilly, et al., Surg Gynecol Obstet 171 (1990), p. 493-496.
4. G. Min, et al., J Cell Sci 116 (2003), p. 4087-4094.
5. M.K. Kos, et al., Biol Pharm Bull 29 (2006), p. 1685-1691.
6. P. Veranič, et al., Histochem Cell Biol 131 (2009), p. 129-139.
7. T. Višnjar, et al., Histochem Cell Biol 137 (2012), p. 177-186.

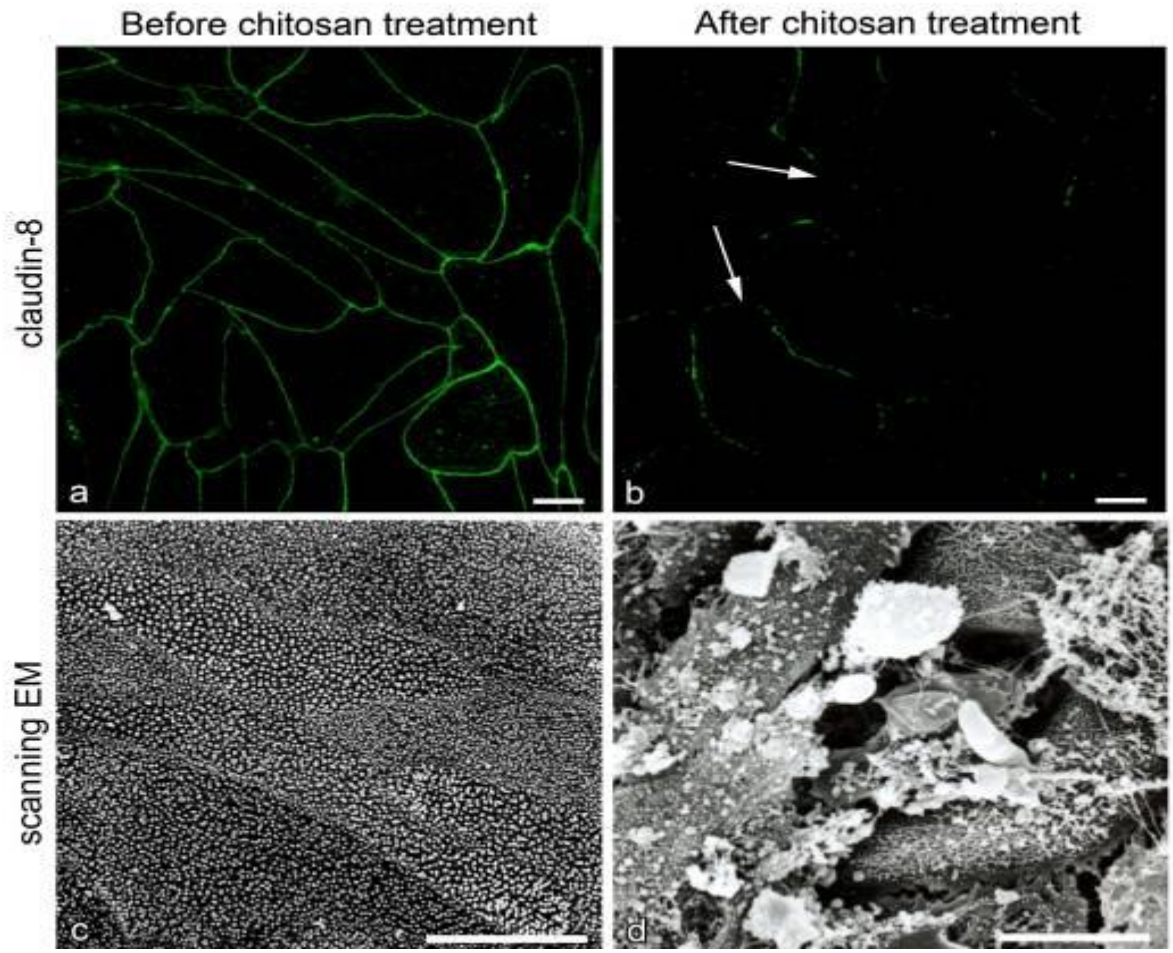

Figure 1. TJs and cell surface of partially differentiated urothelial models before and after chitosan treatment. Immunolabeling and scanning electron microscopy (EM) of chitosan treated urothelial models revealed disrupted TJs, claudin-8 localization in discontinuous lines (arrows b) and desquamation of necrotic UCs. Bars: 10 µm (a-d).

Open Topics

MIM.6.P094
Quantification of Apoptotic Cell Death of Using the Internal Thoracic Artery in Coronary Artery Bypass Grafting (CABG)

U. Uslu[1], S. Gonca[2], I.S. Onan[3], B. Onan[3], L. Kilickan[4]

[1]Yeditepe University Faculty of Medicine, ATASEHIR, Turkey
[2]Kocaeli University Medical Faculty, Histology and Embryology, Kocaeli, Turkey
[3]Mehmet Akif Ersoy Hospital, Cardiovascular Surgery, Istanbul, Turkey
[4]Acibadem Family Hospital, Anaesthesia and Reanimation, Istanbul, Turkey

unaluslu@yeditepe.edu.tr
Keywords: Apoptosis, internal thoracic artery, thoracic epidural anesthesia

Internal thoracic artery is the preferred conduit for coronary artery bypass grafting (CABG). We investigated whether thoracic epidural anesthesia (TEA) as an adjunct to general anesthesia (GA) plays a role on of apoptosis (programmed cell death) of ITA.

Ethics committee approval was received for this study. Thirty patients scheduled for elective CABG were randomized to receive either GA (n=15) or GA+TEA (n=15). In the preoperative period, the patency of the left ITA was confirmed by coronary angiography in all patients. A short segment of ITA was excised from patients who underwent coronary artery bypass grafting surgery with the GA+TEA group and GA group. Tissue samples were fixed in 0.9% NaCl followed by 4% buffered formaldehyde fixative, then preperad for cryomicrotome. Tunel procedure was used for about 10 µm thickness cryosections obtaining from ITA. Each section sample was fractionated optically into approximately 100 frames with the used of image analysis software and the apoptotic index was calculated as apoptotic cells/total cells.

The apoptotic index in tissue samples of GA+TEA group was significantly lower than the GA group (0.110±0.020 vs. 0.529±0.014, respectively; $p<0.001$).

We were analysed comparatively of the incidence in endothelial cells and smooth muscle cells of survival/apoptosis [1] and we have obtained statistically significant differences of both groups [2]. The result of this study indicated that GA group induced apoptosis in the ITA compared to GA+TEA group. Therefore, TEA as an adjunct to GA might be considered as an alternative approach for increasing ITA flow in CABG [3].

1. Mallat Z, Tedgui A. Apoptosis in the vasculature: mechanisms and functional importance. Br J Pharmacol. 130 (2000), p. 947-62.
2. Frischknecht K, Greutert H, Weisshaupt C, Kaspar M, Yang Z, Luscher TF, Carrel TP, Tanner FC. Different vascular smooth muscle cell apoptosis in the human internal mammary artery and the saphenous vein. Implications for bypass graft disease. J Vasc Res. 43(2006), p. 338-46.
3. Kiliçkan L, Gonca S, Dalçik C, Dalçik H, Solak M, Bayindir O, Süzer K, Omay O, Calikan E. General anesthesia with thoracic epidural anesthesia in the cardiopulmonary bypass surgery reduces apoptosis by upregulating antiapoptotic protein Bcl-2.J Cardiovasc Surg (Torino). 47(2006), p. 315-22.

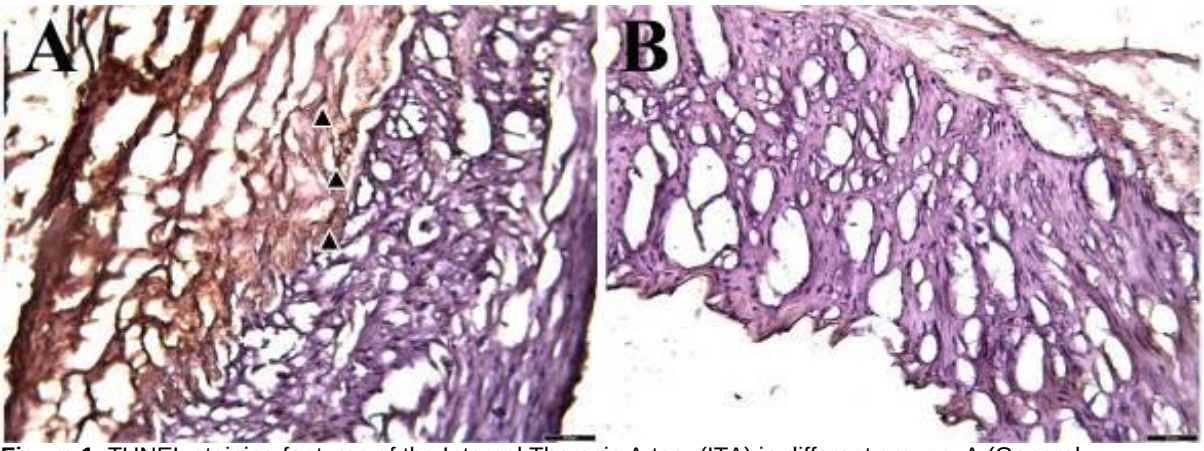

Figure 1. TUNEL staining features of the Internal Thoracic Artery (ITA) in different groups: A (General Anesthesia), and B (General Anesthesia + Thoracic Epidural Anesthesia). Apoptotic cells are demonstrated with arrow head in the ITA. Scale Bar: 50 µm.

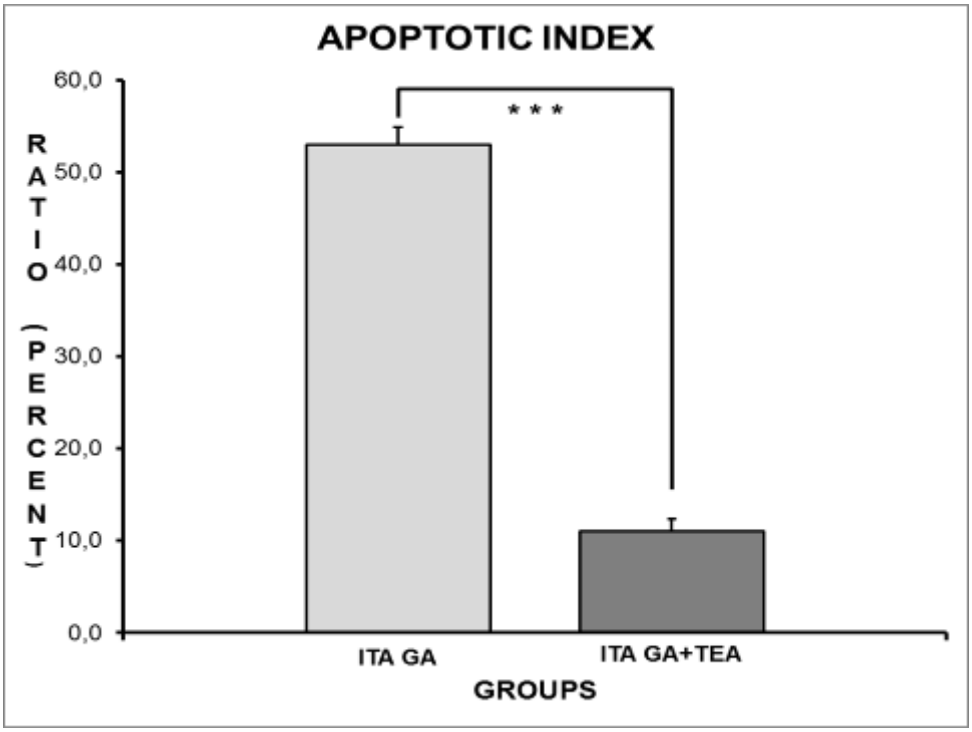

Figure 2. The apoptotic index of Internal Thoracic Artery (ITA) shows Tunel (+) cells ratio. Graphs compare to GA and GA+TEA groups. Ther was significant decreases apoptotic index of ITA in GA+TEA groups (*** p< 0,001).

Open Topics

MIM.6.P095
Apoptotic index of Harvesting the Saphenous Vein for Coronary Artery Bypass Grafting (CABG)

S. Gonca[1], O. SEN[2], U. Uslu[3], A. Zeybek[4]

[1]Kocaeli University, Histology and Embriology, Kocaeli, Turkey
[2]Mehmet Akif Ersoy Hospital, Cardiovascular Surgery, Istanbul, Turkey
[3]Yeditepe University Medical Faculty, Histology and Embriology, Istanbul, Turkey
[4]Kocaeli University Medical Faculty, Anatomy, Kocaeli, Turkey

suhgonca@gmail.com
key words: Apoptosis, saphenous vein, harvest methods

Preparation methods of saphenous vein as a coroner graft may be performed by different dissection techniques. The aim of this study was to investigate the possible role of apoptosis in differences for CABG using conventional and no-touch saphenous vein (SV) harvesting methods. We aimed to compare the potential apoptosis[1] caused by mechanic trauma in vascular layer[2, 3] at the cellular level by analyzing human saphenous vein, prepared with classic method and human saphenous vein prepared with “no touch” technique.

Ethics committee approval was received for this study. Almost 4 cm samples received from proximal section of SV planned to be used as graft from total 20 patients at the age of 40-70 who underwent aorta coronary bypass surgery between January 2010 and May 2010 at Cardiovascular Surgery clinic and ejection fractions of whom were ≥40% were used. The harvested SV tissue samples were divided into two groups (n=10). The No-touch (NT) technique consists in removing the SV with perivascular tissue. The conventional technique consists in harvesting with “in situ” removal of the perivascular tissue. Small pieces of SV tissues were fixed for 24 to 48 hours by 4% paraformaldehyte in 0.1 mol/L of phosphate buffer (ph - 7.4). Up to 5µm thickness cryosections were obtained by cryostat. Then TUNEL procedure was used to evaluate of samples obtaining from saphenous ven. For the apoptotic index, each section was fractionated optically into approximately 100 frames with the used of Stereo Investigator version 7.5 image analysis software and the apoptotic index was calculated as apoptotic cells/total cells.

The apoptotic index in tissue samples of conventional technique group was significantly higher than that of the notouch technique group (0.367±0.012 vs. 0.078±0.027, respectively; $p<0.001$).

The aim of this work was to evaluate the effect of two SV harvesting techniques: conventional and no-touch. We were analysed comparatively of the incidence in vascular endothelial and smooth muscle cell survival/apoptosis and we have obtained statistically significant differences of both groups.The integrity of endothelial cells and the vessel layers of the SV were better preserved when the SV was removed from its native vascular bed using the no-touch method than using traditional method.

1. Mallat Z, Tedgui A. Apoptosis in the vasculature: mechanisms and functional importance. Br J Pharmacol. 130 (2000), p. 947-62.
2. Lee JD, Yang WK, Lai CH. Involved intrinsic apoptotic pathway in the varicocele and varicose veins. Ann Vasc Surg. 24 (2010), p.768-74.
3. Frischknecht K, Greutert H, Weisshaupt C, Kaspar M, Yang Z, Luscher TF, Carrel TP, Tanner FC. Different vascular smooth muscle cell apoptosis in the human internal mammary artery and the saphenous vein. Implications for bypass graft disease. J Vasc Res. 43 (2006), p. 338-46.

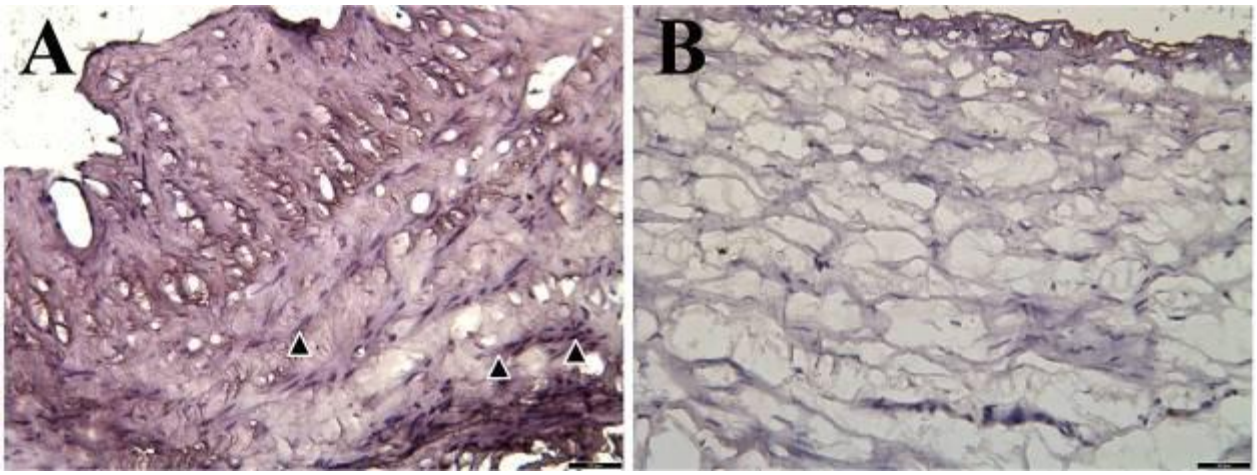

Figure 1. Immunohistochemical evaluation of TUNEL stained saphaneous vein: A (Conventional Technique), and B (No Touch Technique). Apoptotic cells are demonstrated with arrow head in tunica media of saphaneous vein. Scale Bar: 50 µm

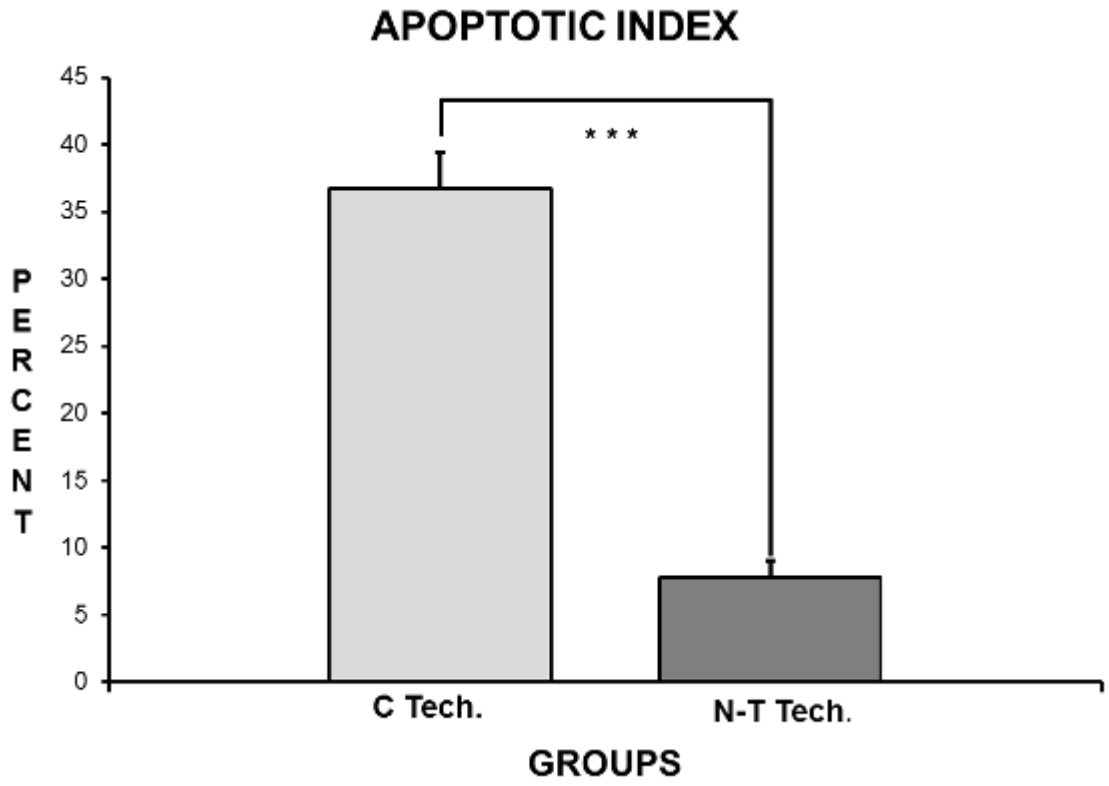

Figure 2. Apooptotic Index of Saphenous Vein (SV). Data expressed as means ± SEM (n=10). No touch technique significantly prevented cell apoptosis in the saphenous vein (*** p< 0,001).

Open Topics

MIM.6.P096
Histomorphometrical and Clinical Evaluation of the Effects of Decortication Procedure Using Er:Yag Laser on Tooth Movement in Rats

A. Cumbul[1], S. Erdem[2], F. Isik[2], U. Uslu[1], O. Oztoprak[2]

[1]Yeditepe University, Histology and Embryology, Istanbul, Turkey
[2]Yeditepe University, Orthodonty, Istanbul, Turkey

alev.cumbul@yeditepe.edu.tr
Keywords: tooth movement, decortications, Er:YAG lasers

The aim of this study was to histomorphometrically and clinically evaluate the effect of decortication procedure, which has been prepared transmucously with the use of Er:YAG laser, on tooth movement.

28 Sprague-Dawley rats were used for this purpose. The upper first molar teeth were mesialized with the use of a Sentalloy closed coil spring that was placed between the upper first molars and the incisor teeth.

Rats were separated into experimental and control groups. Each group consisted of one week and two weeks follow-ups. Total experimental time was 2 weeks. Experimental groups were treated with an Er:YAG laser right after the appliance insertion (1). Three decortication points were prepared on the mesial, palatal and buccal sides of the first upper molar teeth. The power of the laser applied was 1 watt and the duration was 8 seconds (2). Tooth displacements were measured on model casts which were prepared from impressions of the upper jaw taken before placement of the appliance, on day 7 and day 14. At the end of the experiment, upper jaws of the sacrified rats were dissected and prepared for histological examination.

The obtained tissue samples were fixed in 10% neutral formaldehyde in 0.1 M phosphate buffered saline (PBS; pH=7.4) and submitted to histological evaluation. Paraffin-embedded upper jaw tissues were sectioned to 10 µm. Physical fractionators and systematic sampling methods were used and stained with Hematoxyline and Eosin technique. Alveolar bone volume was examined under a stereological station and Cavalieri method (3).

The histological evaluation revealed that alveolar bone volume and total volume between the roots of upper first and second molar teeth of the experimental groups were statistically higher than the control groups on day 7 ($p<0,001$, $p<0,001$) and day 14 ($p<0,001$, $p<0,05$). Histopathologic findings revealed new bone formation areas and increased vascularization between the roots of experimental groups. (Table 1, Figure 1 and 2).

In our study decortication procedure, which is known to accelerate orthodontic tooth movement, was applied with a different and novel method (4). The results suggested that decortication procedure which is applied transmucously with the use of an Er:YAG laser, contributed favorably during bone remodeling and accelerated tooth movement consequently.

1. Peavy GM. Lasers and laser-tissue interaction. The Veterinary Clinics Small Animal Practice, 32: 517-534, 2002.
2. Sun G, Tuner J. Low-level laser therapy in dentistry. Dent Clin N Am, 48: 1061-1076, 2004.
3. Dehoff, R.T., 2000, Probes, populations, samples, measurements and relations in sterelology, Image Analize Stereology, 19, 1-8 p.
4. Mello EDA, Pagnoncelli RM, Munin E, Filho MS, Mello GPS, Arisawa EAL, Oliveira MG. Comparative histological analysis of bone healing of standardized bone defects performed with the Er:YAG laser and steel burs. Lasers Med Sci, 23: 253-260, 2008.

	C7	D7	C14	D14
	n=7	n=7	n=7	n=6
Section Thickness	10	10	10	10
Number of Sampled Sections	16,7	14,7	16,7	15,8
Mean Interdental Point Number	6870	5346	5239	5288
CE InterdentaLRegion	0,006	0,006	0,007	0,006
Mean Interdental Alveolar Bone Point Number	2609	2926	1796	1695
CE Interdental Alveolar Bone	0,008	0,007	0,009	0,007

Table 1: Mean point number , section thickness and number of sample section for the interdental and alveolar bone region volume estimation Coefficient of Error (CE) of stereological analysis in the groups of rats applied to decortation during the period of 1 and 2 weeks after ER-YAG Laser exposed groups (D7, D14) and theirs controls (C7, C14)

.

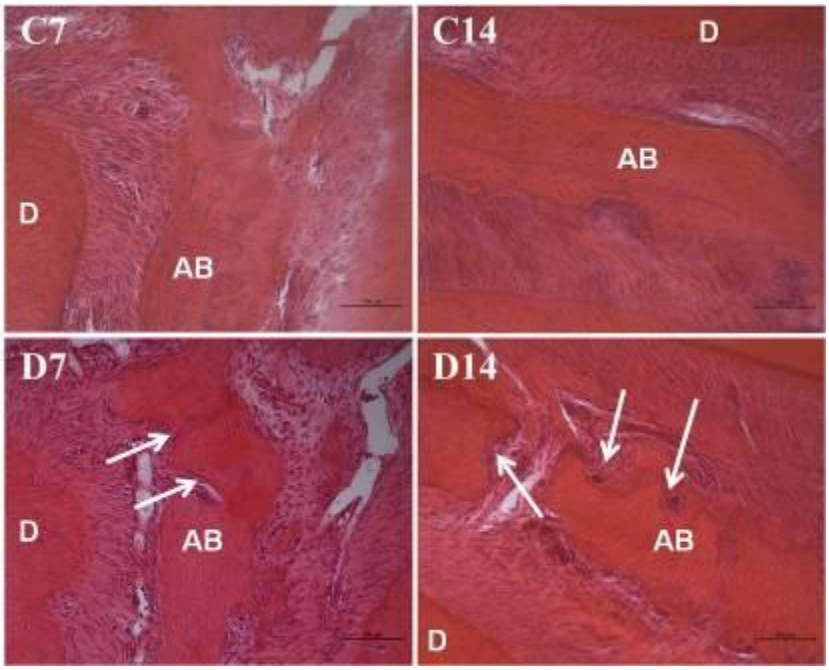

Figure 1. In decortation groups, the new ossification and vascularization areas are increased. Photomicrographs are demonstrated of sections taken from decortation and control groups and stained with Hematoxylin-eosin. Groups: C7; Control 7 day, C14; Control 14 day, D7; Decortation 7 day and D14; Decortation 14 day. Alveolar bone is demonstrated with (AB), dentin (D), new ossification and vascularization areas (arrow). The magnification is x20. Scale bar represents 100 µm.

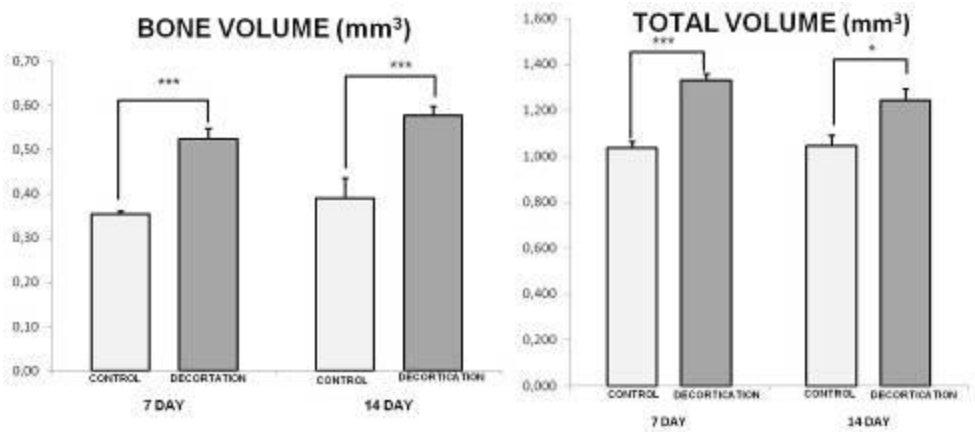

Figure 2. Graphs comparing the control and decortation groups (*p< 0,05 and *** p<0,001). The left panel of the figure is alveolar bone volume, the right panel of the figure is total volume.

Open Topics

MIM.6.P097
Localization of SNAREs in the mouse urothelium

S. Hudoklin[1], R. Romih[1]

[1]University of Ljubljana, Faculty of Medicine, Institute of Cell Biology, Ljubljana, Slovenia

samo.hudoklin@mf.uni-lj.si
Keywords: urinary bladder, SNARE, membrane trafficking

Urothelium, an epithelium of the mammalian urinary bladder, is a perfect model for studying membrane traffic. In the process of differentiation, urothelial cells synthesize uroplakins, characteristic transmembrane proteins that are arranged into urothelial plaques in the post-Golgi compartments. Most prominent of these compartments are mature fusiform vesicles (FVs), which contain two plaques connected by thin hinge region. FVs store and transport urothelial plaques. During bladder filling FVs are fused with the apical plasma membrane of the superficial urothelial cells, where plaques contribute to the barrier function of the urinary bladder [1]. The mechanisms that regulate transport and fusions of the FVs are currently not completely understood, but might involve MAL proteins, Rab proteins (8a, 11a, 27b) and myosin 5b [2-4]. Data about SNARE proteins, which are major players in the final stage of the docking and the subsequent fusion of diverse vesicle-mediated transport events [4], are missing.

Our aim was to localizeze SNARE proteins syntaxin 6, 11, Vti1a and Vti1b in the mouse urothelial cells.

The experiments were performed on urinary bladders of 6-8 weeks old male C57B6 mice. Cryo- thin and ultrathin sections were prepared by modified Tokuyashu method and labelled with anti- syntaxin 6, 11, Vti1a, Vti1b mouse monoclonal antibodies (BD Transduction Lab.), and with anti-uroplakin rabbit polyclonal antibody, generated against mature bovine uroplakins (a kind gift from Prof. T.T. Sun, NYU, USA). Briefly, urothelium was fixed with 4% PA in 0.1M phosphate buffer for 48 hours, washed in PBS, embedded in 12% gelatine and cryoprotected by incubation in 2.3M saharose. Samples were frozen in LN_2 and cut with a Leica FCS cryo-ultramicrotom at -120°C. Semithin and ultrathin sections were cut for light and electron microscopy, respectively. Sections were incubated overnight with primary antibodies, washed in PBS, and incubated with secondary antibodies for 1.5 hours (AlexaFlour 555 goat anti-mouse and AlexaFlour 488 goat anti-rabbit for LM, goat anti-mouse conjugated with 16 nm colloidal gold for EM). Semithin sections were mounted with VectaShield (Vector laboratories) containing DAPI and visualized with a Nikon T300 light microscope. Ultrathin sections were counterstained with MC/UA and examined with a Philips CM100 transmission electron microscope.

Results showed that urothelium consist of basal, intermediate and superficial cells. Superficial cells were labelled with anti- uroplakin, syntaxin 6, 11, Vti1a and Vti1b antibodies (Figure 1). All these proteins were detected on some mature FVs. In the intermediate cell layer, cells were weakly labelled with anti-uroplakin antibody and contained more immature FVs (iFVs) which are characteristics of less differentiated urothelial cells. Nevertheless, more of studied SNARE proteins were found in the intermediate cells than in the superficial cells. SNAREs were associated with the hinge regions of the iFVs located beneath the plasma membrane (Figure 2). Basal cells were uroplakin-negative and contained no FVs.

The presence and location of SNARE proteins on hinge regions of FVs shows that hinge regions contain some key features enabling them to fuse with the apical plasma membrane. Observation that more SNAREs were found on iFVs in the intermediate cells than on terminally differentiated superficial cells, and since it is known that iFVs do not fuse with plasma membrane, it is possible that SNAREs in intermediate, less differentiated cells enable homo- and/or heterotypic fusions between iFVs during maturation of FVs.

1. M.E.Kref, S. Hudoklin S, K. Jezernik and R. Romih, Protoplasma 246:1-4 (2010), p. 3-14.
2. G. Zhou, F.X. Liang, R. Romih, Z. Wang, Y. Liao, J. Ghiso, J.L. Luque-Garcia, T.A. Neubert, G. Kreibich, M.A. Alonso, N. Schaeren-Wiemers and T.T. Sun, Mol Biol Cell. 23:7 (2012), P. 1354-1366.
3. P. Khandelwal, H.S. Prakasam, D. Clayton, W.G.Ruiz, L.I. Gallo, D. van Roekel, S. Lukianov, J. Peränen, J.R. Goldenring and G. Apodaca, Mol Biol Cell. 24:7 (2013), p. 1007-1019.
4. X. Guo, L. Tu, I. Gumper, H. Plesken, E.K. Novak, S. Chintala, R.T. Swank, G. Pastores, P. Torres, T. Izumi, T.T. Sun, D.D. Sabatini and G. Kreibich, Traffic 10:9 (2009), p. 1350-1361.
5. W. Hong, Biochim Biophys Acta 1744:3 (2005), p. 493-517.

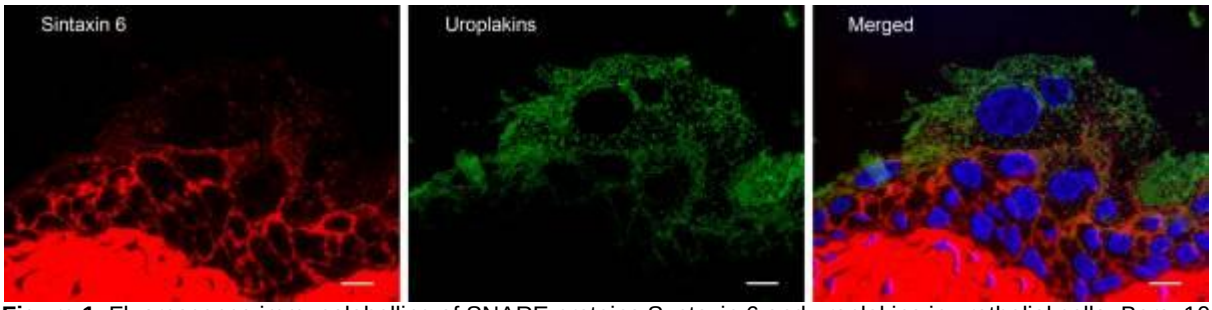

Figure 1. Fluorescence immunolabelling of SNARE proteins Syntaxin 6 and uroplakins in urothelial cells. Bars: 10 µm.

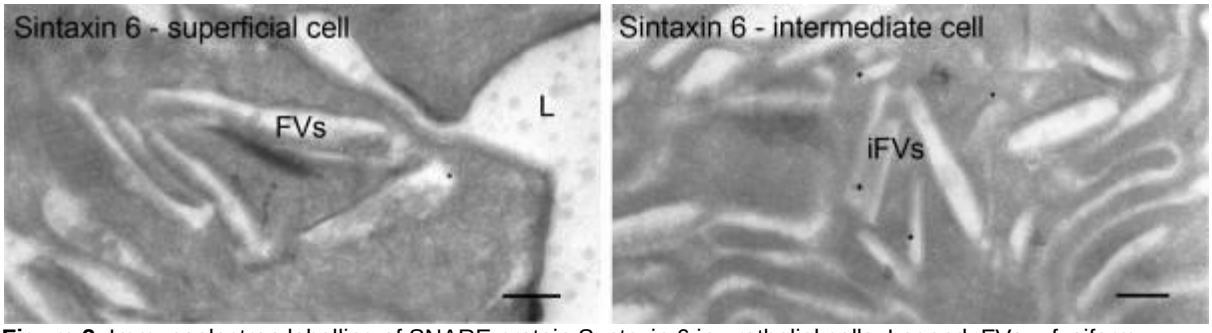

Figure 2. Immunoelectron labelling of SNARE protein Syntaxin 6 in urothelial cells. Legend: FVs – fusiform vesicles, L – lumen, iFVs – immature fusiform vesicles; bars: 200 nm.

Open Topics

MIM.6.P098
Effect of grape fruit juice on concor-induced nephrotoxicity and apoptosis in albino rats

A. Elshabka[1], S. Sakr[1]

[1]Faculty of Science, Zoology Department, Shebin Elkom, Egypt

sabsak@yahoo.com

Objective.To evaluate the effect of grapefruit juice on the renal damage induced by the antiarrythmic drug, concor in albino rats. Methods: Animals were divided into 4 groups. The 1st group was considered as control. The 2nd group was given grapefruit juice at a dose level of 27 mL / kg body weight. The 3rd group was orally administered concor (0.09 mg / kg body weight) daily for 5 weeks. Animals were sacrificed after five weeks of treatment. Kidneys were removed and stained with H&E for histological examination. DNA damage was detected by total genomic damage method using gel electrophoresis. Results: Concor treatment caused many renal histopathological alterations. The renal tubules lost their characteristic appearance and their lining epithelial cells were degenerated.

The glomeruli were atrophied and the renal blood vessels were dilated and congested. The intertubular spaces were infiltrated by inflammatory leucocytic cells. Marked elevation in serum creatinine and urea was recorded. Inhibition of spermatogenesis and morphometric changes.

Moreover, the gel electrophoresis method showed that there was an increase in DNA fragmentation (apoptosis). Treating animals with concor and grapefruit juice caused a reduction in the histopathological alterations recorded in the kidney, DNA damage and decrease of serum creatinine and urea. Conclusions: The results of this study indicated that grapefruit juice ameliorates the nephrotoxicity induced by concor in albino rats and this is may be due to the potent antioxidant effects of its components.

Open Topics

MIM.6.P099
Rocking curves of few layer graphene by evaluation of TEM dark field tilt series

C. Dolle[1], B. Butz[1], F. Niekiel[1], D. Waldmann[2], H. Weber[2], E. Spiecker[1]

[1]University, CENEM, Erlangen, Germany
[2]University, Lehrstuhl für Angewandte Physik, Erlangen, Germany

christian.dolle@ww.uni-erlangen.de

Graphene is one of the most promising materials of the new century; besides its peculiar behavior in electronic applications it is also the mechanically most robust material known so far with a breaking strength of 42 N/m [1]. Not only the mechanical strength but also the potential for developing devices is challenging at the moment. Especially membranes of mono or bilayer graphene can be utilized to engineer chemical sensors, resonators or for a recently developed DNA sequencing procedure employing small holes in a sheet of graphene [2]. To produce such free-standing membranes different approaches can be followed while in most cases a transfer of the layers is part of the preparation. We employ a recently developed method to grow epitaxial graphene on SiC [3] and remove the substrate in an additional processing step [4]. The preparation route allows the production of TEM conform samples by employing 3 mm disks of 6H-SiC, a mechanical thinning, the growth of graphene under reduced inert gas atmosphere, the definition of a metal mask by Lithography and the etching of the substrate via an electrochemical treatment in KOH (see figure 1). The Lithography allows the definition of arbitrary shapes of the resulting membranes with a size up to 500 µm². With the chosen growth parameters we obtain membranes consisting of mostly bi- and tri-layer graphene which can be readily investigated with complementary microscopic techniques to probe the local distribution of the number of layers, study the interaction of substrate and graphene and evaluate the microstructure of the membranes in detail accounting eg. for stacking order and defects. Dark-field TEM (DFTEM) tilt series and the evaluation of intensity variations during tilting allows to reassemble the projected structure amplitude of graphene and makes a precise evaluation of local number of layers possible. A much finer lateral resolution compared to mappings acquired by e.g. Raman Microscopy can be achieved. Complementary to a method suggested by Meyer et *al*. [5] who conducted tilting experiments on diffraction patterns of graphene, not only the number of layers in a given field of view can be investigated but the microstructure of the layers can be observed at the same time (not shown). The rocking curves measured from the tilt series are compared to theoretical curves calculated from kinematic diffraction theory. The theoretical rocking curves not only account for partially constructive/destructive interference due to deviation from Bragg condition but also for damping resulting from the angular dependence of the atomic scattering amplitude. The atomic scattering amplitude has been used in the form parameterized by Kirkland [6] and thermal vibrations (Debye-Waller factor) contribute only in a minor effect to the damping. Thus for comparison of experiment and calculation the Debye-Waller factor is not included and an excellent agreement between calculations and experiment is achieved (Figure 2). By utilizing DFTEM tilting series with a conventional sample holder it is possible to precisely evaluate the local number of layers in bi- tri- and four-layer graphene. No advanced analytical procedure has to be applied while the evaluation gives not only qualitative but quantitative results of the local distribution of layers with a resolution limited only by the magnification of the microscope. In addition the inter-layer spacing, stacking order and the topography of inclined surfaces can be examined with this approach.

1. C. Lee et *al*., Science 321, 385 (2008)
2. S. Garaj et *al*., Nature 467, 190 (2010)
3. K.V. Emtsev et *al*., Nature Mater. 8, 203 (2009)
4. D. Waldmann et *al*, submitted (2012)
5. J. C. Meyer et *al*., Solid State Communications 143, 101 (2007)
6. E. J. Kirkland: "Advanced Computing in Electron Microscopy" (2nd ed.), Springer, New York (2010)

Financial support from the German Research Foundation (DFG) via the SFB 953 “Synthetic Carbon Allotropes” and the Erlangen Cluster of Excellence EXC 315 “Engineering of Advanced Materials” is gratefully acknowledged

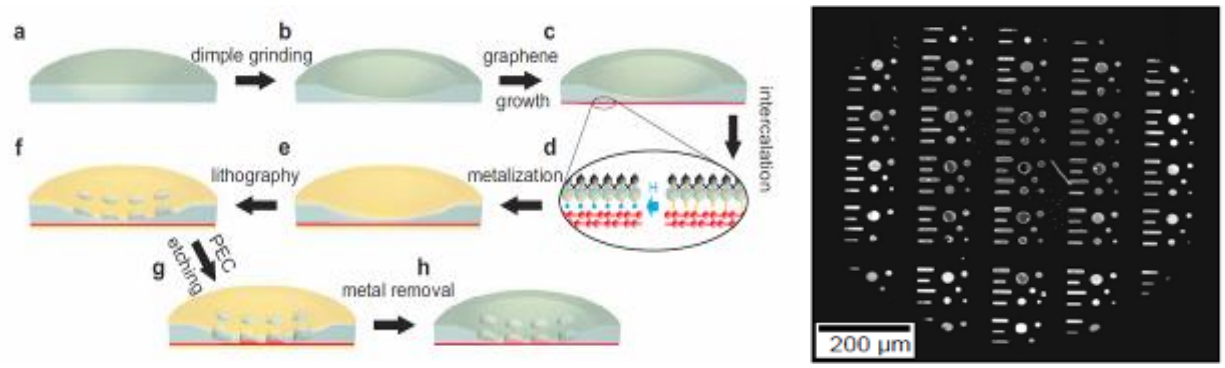

Figure 1. Preparation route for free-standing graphene membranes and low-kV STEM overview of prepared sample.

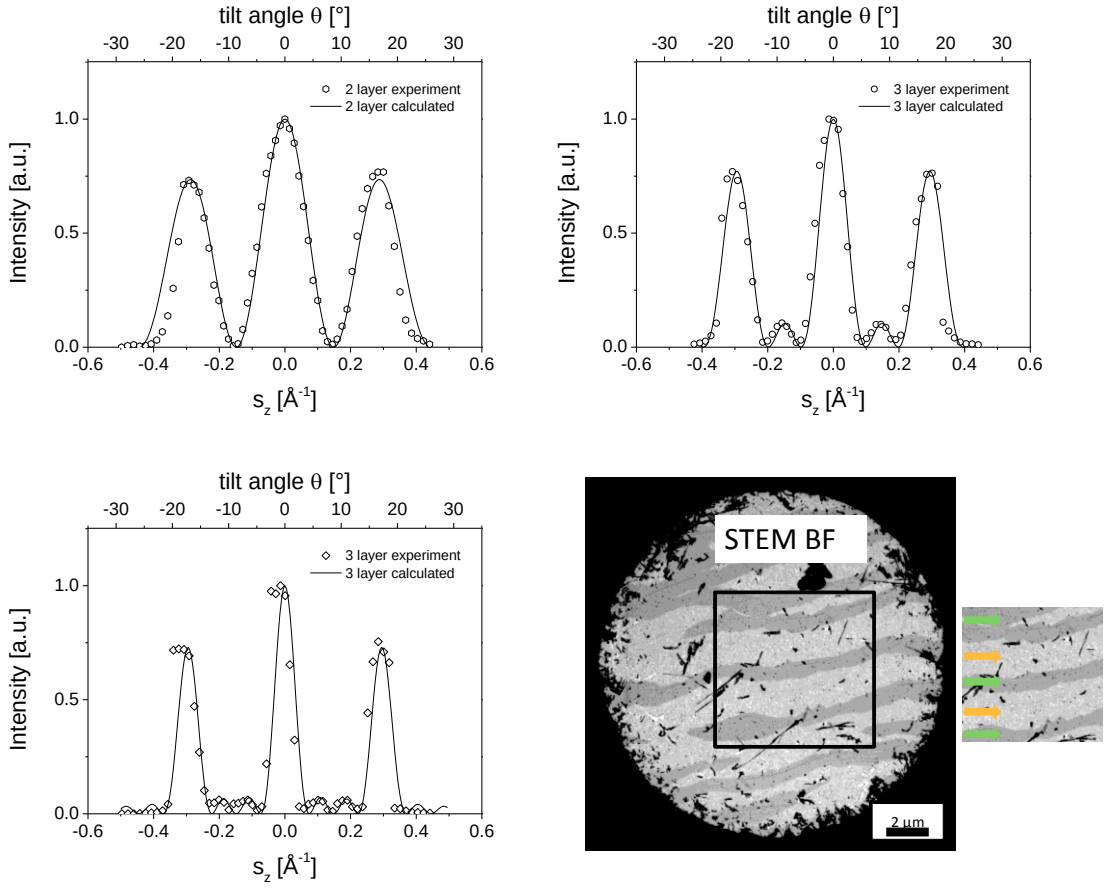

Figure 2. Normalized rocking curves of 2-, 3- and 4-layer graphene (open symbols experiment, solid lines calculated) and STEM BF image of representative round free-standing membrane showing the distribution of 2- (light grey, yellow arrows) and 3- (dark gray, green arrows) layer areas.

Crossdisciplinary Applications of Microscopy Techniques, e.g. Physic-Life Science Interfaces

MIM.7.100
Preparation of Soot-in-oil samples from diesel engines for HRTEM analysis

M. Fay[1,2], A. La Rocca[2]

[1]University of Nottingham, Nottingham Nanotechnology and Nanoscience Centre, Nottingham, United Kingdom
[2]University of Nottingham, Faculty of Engineering, Nottingham, United Kingdom

michael.fay@nottingham.ac.uk

The combustion process in an internal combustion engine produces an amount of particulate matter, most of which is carbon soot. Although much of this is expelled with the exhaust gases, a small proportion is transferred to the lubricating oil. Over time, the amount of carbon soot will accumulate to levels that affect the performance of the lubricating oil, worsening fuel economy, increasing CO_2 emissions, and increasing engine wear [1,2,3].

Soot is widely accepted to be constituted by irregular, branched agglomerates formed by several spherical primary particles. It is important to characterise the structure of these agglomerates as they are found in the lubricating oil. In particular, it is important to know the concentration of soot particles of size thicker than the lubricating film thickness, and to understand their formation.

TEM and HRTEM are commonly used to investigate the characteristics of individual and agglomerated particles from diesel exhaust, to understand the structure and distribution of the carbon sheets in the primary particles and the nanostructure morphology. While the aggregate structures reported in the literature vary in size from tens to hundreds of nanometres, the primary particles are reported as being generally below 50nm, in some reports as small as a few nanometres across. However, high resolution imaging of soot-in-oil is more challenging, as mineral oil is a contaminant for the electron microscope and leads to instability under the electron beam. Cryogenic vitrification and imaging have been used in the past [4], but issues related to viscosity of the typical used engine oil lead to localised thick layers. Alternatively, solvent extraction and ultracentrifugation have been used to prepare specimens for conventional TEM.

In this work we have compared solvent extraction and centrifugation techniques on soot-in-oil samples drawn from the sump of a diesel engine. Solvent extraction, diluting the oil in heptane, followed by dispersion onto the grid and a 30 second 25%O_2/75%Ar plasma clean is suitable for limited TEM imaging, but not for high resolution analysis due to significant carbon contamination. The Centrifugation process, where the soot samples are first cleaned with heptane and then followed by five stages of centrifugation, has been found to produce samples with minimal remnant oil and hydrocarbon contamination, suitable for high resolution TEM analysis, but is found to produce a differing particle size distribution to samples produced using the solvent extraction process.

1. Christine Esangbedo, André L. Boehman, Joseph M. Perez Characteristics of diesel engine soot that lead to excessive oil thickening Tribology International (November 2011)
2. D A Green, R Lewis Proceedings of the Institution of Mechanical Engineers Part D Journal of Automobile Engineering (2008) Volume: 222, Issue: 9, Pages: 1669-1689
3. M. Gautama, K. Chitoora, M. Durbhaa, J. C. Summers, Tribology International 32 (1999) 687–699
4. M. Kawamura, T. Ishiguro, K. Fujita and H. Moromoto, Wear, 123 (1988) 269-280

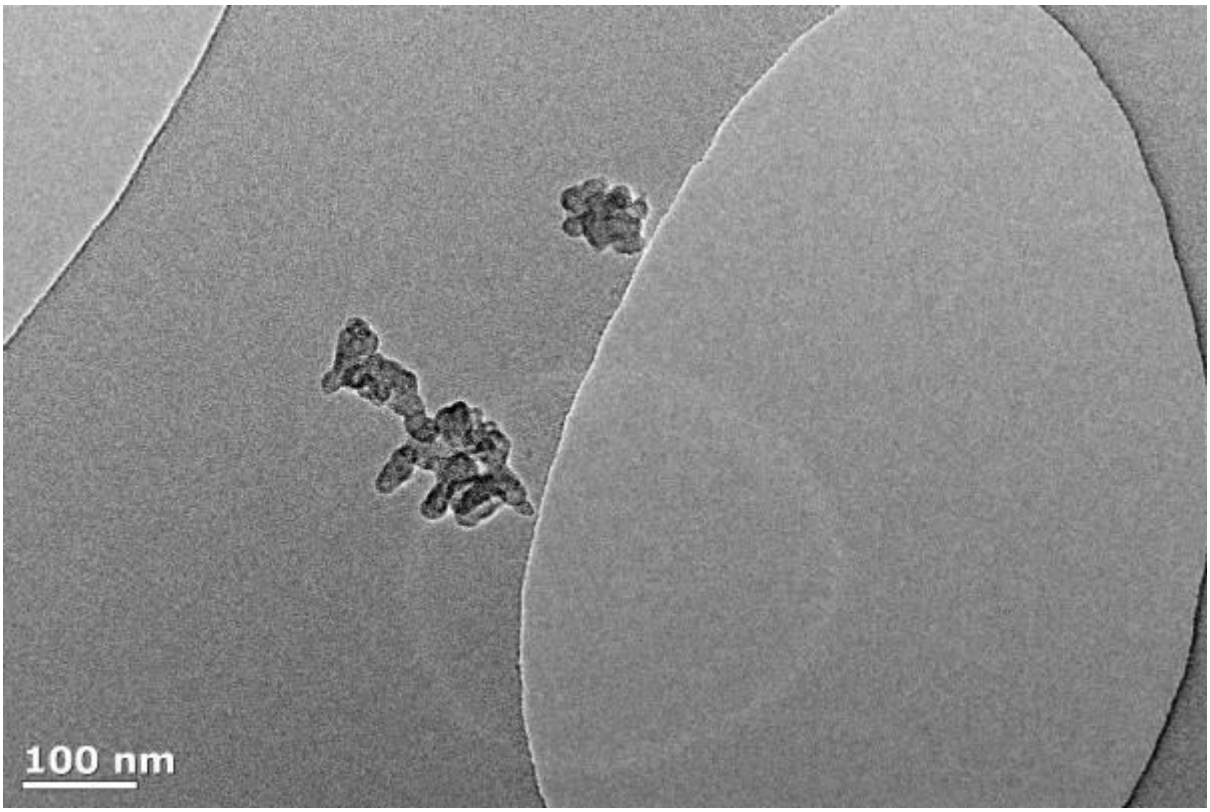

Figure 1. Bright field TEM image of soot-in-oil agglomerates extracted from a diesel engine operating on second generation biodiesel fuel and its blends, after the centrifugation process.

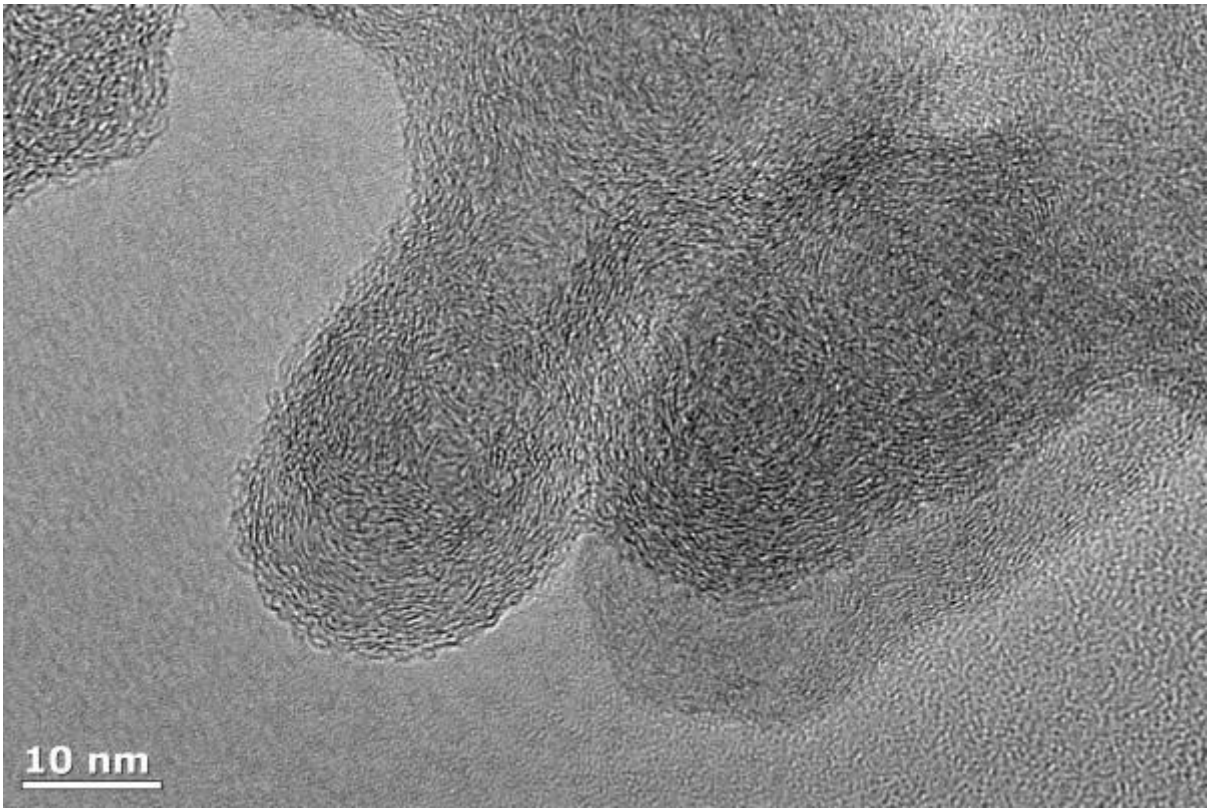

Figure 2. High Resolution TEM image showing primary particles within an agglomerate, extracted from soot-in-oil from a diesel engine operating on second generation biodiesel fuel and its blends, after the centrifugation process. Minimal remnant oil and hydrocarbon contamination after this cleaning process allows HRTEM images to be acquired.

Crossdisciplinary Applications of Microscopy Techniques, e.g. Physic-Life Science Interfaces

MIM.7.101
X-Ray Nano-Imaging of Biomatter and Cells

B. Weinhausen[1], M. Brennich[1], V. Piazza[1], S. Köster[1]

[1]Institute for X-Ray Physics, Georg-August-University Göttingen, Friedrich-Hund-Platz 1, 37077 Göttingen, Germany

sarah.koester@phys.uni-goettingen.de
Keywords: x-ray imaging, microfluidics, cells, proteins

Biological systems such as cells and cellular components are governed by processes, which take place on the nanometer to micrometer length scales. X-ray scattering and diffraction techniques are extremely well suited to study such processes as the spatial resolution extends well into the relevant length scales. At the same time, the investigation of such systems, in particular in the field of biophysical research requires well-defined and controllable sample environments. One way to establish such environments is by employing microfluidic devices tailored for the particular experiment. The combination of both microfluidics and X-ray nano-/micro-diffraction provides an innovative tool for biomatter research.

There are two principal approaches to shedding light on the nanometer-scale assemblies found in biological cells. (i) By studying purified *in vitro* systems such as individual proteins “bottom up” and following the assembly kinetics *in situ*, we can access the biophysical principles underlying assembly. In our experiments, the biomolecular assembly of proteins is studied by diffusively mixing in assembly buffer and following the subsequent assembly steps downstream in the flow channel [1,4] (see Figure 2). (ii) In whole cells, structures as assembled *in vivo* can be observed, corresponding to a “top down” approach. Cells are imaged on the nanometer scale by scanning X-ray diffraction using a nanometer-focused beam [2,3] (see Figure 1).

Thus, X-ray imaging provides a complementary tool to electron microscopy, with the advantage of a high penetration depth and the option of dynamic imaging.

1. M. E. Brennich, J.-F. Nolting, C. Dammann, B. Nöding, S. Bauch, H. Herrmann, T. Pfohl and S. Köster, Lab on a Chip 11 (2011) 708-716
2. B. Weinhausen, J.-F. Nolting, C. Olendrowitz, J. Langfahl-Klabes, M. Reynolds, T. Salditt and S. Köster, New Journal of Physics 14 (2012), 085013
3. B. Weinhausen and S. Köster, Lab on a Chip 13 (2013), 212-215
4. M. Brennich and S. Köster , Microfluidics and Nanofluidics (2013), accepted for publication

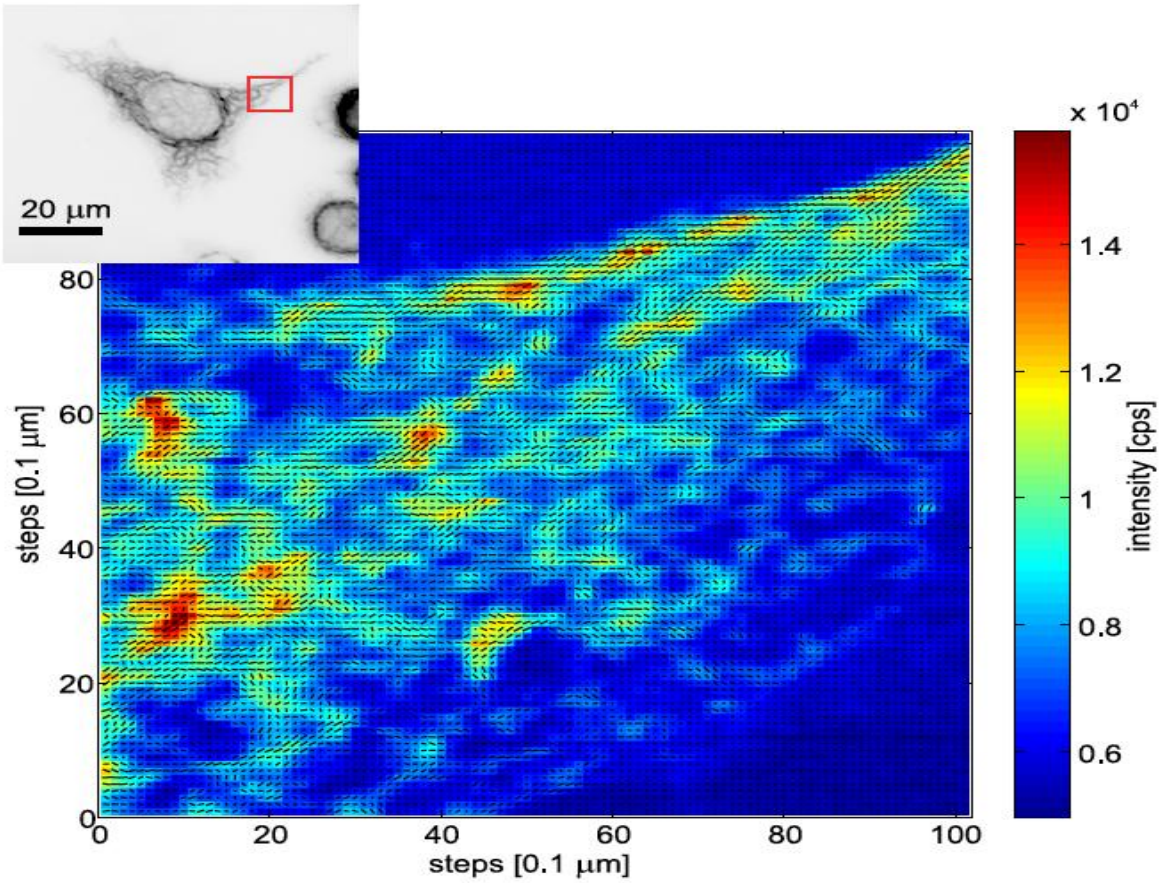

Figure 1. Orientation map and dark-field image of the keratin network in a freeze-dried eukaryotic cell reconstructed from a mesh scan with a step size of 100 nm and 1 s exposure time. The inset shows a fluorescence microscopy image of the keratin network recorded before freeze-drying and the scanned region is marked by a red box (taken from ref. [2]).

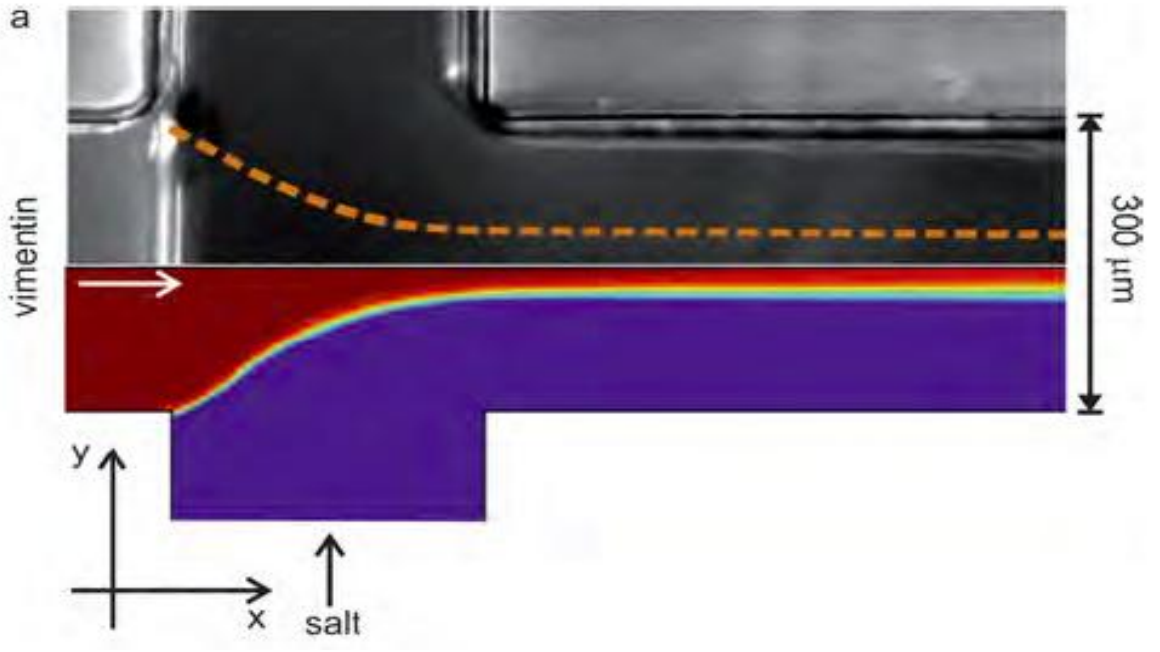

Figure 1. Simulation of protein (vimentin intermediate filaments) and salt concentrations during the assembly process. Shown is the mid-plane of a microfluidic device in the x–y direction. The lower part of the image shows the simulation of the vimentin concentration, the upper part a corresponding DIC image. The dotted line marks the border line in the DIC image (taken from ref. [1]).

Crossdisciplinary Applications of Microscopy Techniques, e.g. Physic-Life Science Interfaces

MIM.7.102
The Nanoworbench: Automated Nanorobotic system inside of Scanning Electron or Focused Ion Beam Microscopes

I. Burkart[1], V. Klocke[1], E. Maynicke[1]

[1]Klocke Nanotechnik GmbH, Aachen, Germany

burkart@nanomotor.de

Many every day developments would not exist today without preparation, handling and assembly of materials under optical microscopes. There would be no wristwatch, no in vitro fertilization, no mini-gearbox, just to mention a few. These products depend on using toolsets like tweezers, knives, hooks, probes and several different measurement tools in combination with optical microscopes. But material properties and functionalities also depend on structure dimensions that are smaller than the wavelength of light.

The operators of SEM, FIB or Dual Beam systems generally work without toolsets. One reason for this is the disconnected closed loop operation between human eyes and hands that enable complex operations under optical microscopes without even thinking about it.

The Nanoworkbench is the first system substituting eye-hand coordination effectively with nano-precision in a SEM/FIB-system. It can be imagined how technology could evolve, when tools within a SEM/FIB can be used as easily as tools used under optical microscopes. The two main aspects of this new system, the development of its Nanorobotics technology and the applications enabled by it, are described in this paper.

Aspect 1, development of the technology: In general the success of in-SEM/FIB Nanorobotics depends on the co-operation of several important modules in one global system. The main developments include:

- Nanomanipulators in automation, for movement of end-effectors and sample handling,
- Different end-effectors for nano- probing, cutting, cleaning, force distance or wear measurements, gripping, sorting or material preparation and processing,
- Automatic in-situ tip cleaning process
- Automatic 3D position detection of all tools and SEM/FIB
- A control of all tool and SEM/FIB sample stage positions in a common global coordinate system,
- SEM picture assisted haptic interface by “Live Image Positioning”,
- Modular design for fast configuration & teaching of nano-analytical or nano-handling processes,

With instantiating these technical demands the Nanoworkbench enables secure and easy usage of toolsets within SEM/FIB systems, for manual operation, for non-professional users and in high level of automation, e.g. for high throughput industrial processes, even as job-shop [1].

Aspect 2, development of a series of new applications in one system: Expanding the SEM/FIB to a material processing system and a nano-analytical workbench opens the door to many applications in all fields of research and development up to industrial production [5]. Several examples of these new interdisciplinary research and development fields will be described during the presentation.

A few examples of Nanoworkbench applications are highlighted in Figure 1. Although these examples may raise the impression of a review about different machines and their usage, this is not the case. Described is the development of the Nanoworkbench.

1. D. Morrant, EIEx Magazine of European Innovation Exchange, 1 (2009)
2. G. Schmid, M. Noyong, Colloid Polym Sci., (2008)
3. C.-H. Ke1, H.D. Espinosa, Journal of the Mechanics and Physics of solids, 53 (2005)
4. Seong Chu Lim, Keun Soo Kim, Kay Hyeok An, Dept. of Phys., Sungkyunkwan University, Korea (2002)
5. Supported by European Commission, IST and Ziel2.NRW

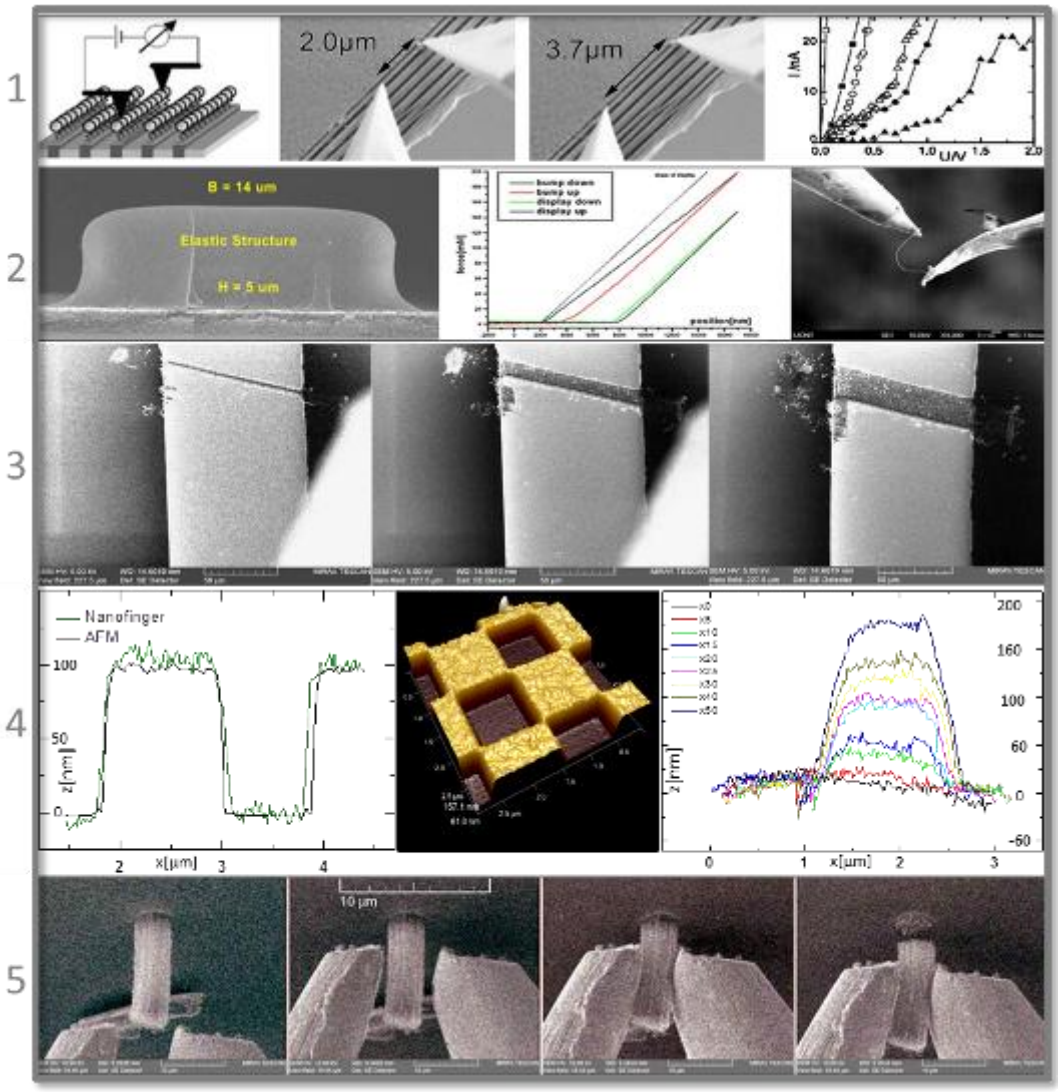

Figure 1. includes the rows:

1.) Nano-Probing: of Gold55-Clusters arranged in chains [2]: The electrical conductivity along these gold chains is measured over different distances and compared with the conductivity of bare gold wires.
2.) Nano-Tribology and similar measurements can be performed in high resolution [4]
3.) Nano-Cutting: fast milling of structures
4.) 3D-Nanofinger: measurement of gold and EBID structures grown and measured in situ
5.) Particle-Sorting: Gripping of a rigid CNT bundle with high force and separation from the ground [3]

Crossdisciplinary Applications of Microscopy Techniques, e.g. Physic-Life Science Interfaces

MIM.7.103
Observing the kinetics of single enzyme molecules enclosed in femtoliter arrays by fluorescence microscopy

H.-H. Gorris[1]

[1]University of Regensburg, Institute of Analytical Chemistry, Chemo- and Biosensors, Regensburg, Germany

hans-heiner.gorris@ur.de

The development of new technologies for the analysis of single enzyme molecules has considerably increased our understanding of biochemical processes, as the observation of single enzyme molecules uncovers subpopulations and kinetic details that remain hidden in traditional ensemble experiments. For example, single enzyme molecules exhibit a broad distribution of individual activities due to different protein conformations, which is known as static heterogeneity. A large number of single enzyme molecules are required to investigate the static heterogeneity within an enzyme population. However, most single molecule techniques only enable the investigation of a single or few molecules at a time. By contrast, so-called femtoliter arrays consist of thousands of reaction chambers each defining a volume of approximately 50 μm^3 (fL). Femtoliter arrays are suitable for isolating and analysing hundreds of individual enzyme molecules simultaneously. A highly diluted enzyme solution together with a large excess of a fluorogenic substrate is enclosed in the femtoliter chambers. In chambers that contain a single enzyme molecule, the activity is determined by the enzymatic turnover of the substrate into a fluorescent product. In the confinement of a femtoliter volume, a single enzyme molecule can generate a sufficiently high concentration of the fluorescent product to be detected by wide-field fluorescence microscopy [1]. In this way, we have shown that individual molecules of β-galactosidase [2] and horseradish peroxidase [3] possess constant turnover rates that are different for each enzyme molecule in the array. The large number or enzyme molecules observed in parallel provides excellent statistics on the activity distribution in an enzyme population. Furthermore, we have shown that enzyme inhibition at the single molecule level is a stochastic process because a single enzyme molecule is either free and catalytically active or an inhibitor has bound to the enzyme and no turnover is observed [4]. More classes of enzymes are currently under investigation to elucidate differences in their activity distribution. Additionally, femtoliter arrays can be used for the detection of single molecules of an analyte and thus reach the ultimate detection limit. For this so-called single molecule ELISA, the surface of femtoliter chambers is derivatized with a capture antibody, which for example is directed against a protein present in blood. After protein binding by the capture antibody, an enzyme-labeled detection antibody binds to the protein. As the enzyme activity can be detected on the single molecule level, also the protein is detectable at the single molecule level. The protein concentration can then be determined by counting the number of active wells that contain a single molecule of the protein [5].

1. H.H. Gorris, and D.R. Walt, Angew. Chem. Int. Ed. 49 (2010), p. 3880.
2. D. M. Rissin, H.H. Gorris and D.R. Walt, J. Am. Chem. Soc. 130 (2008), p. 5349.
3. H.H. Gorris, and D.R. Walt, J. Am. Chem. Soc. 131 (2009), p. 6277.
4. H.H. Gorris, D.M. Rissin and D.R. Walt, Proc. Natl. Acad. Sci. USA 104 (2007), p. 17680.
5. D.M. Rissin et al. Nat. Biotech. 28 (2010), p. 595.

Crossdisciplinary Applications of Microscopy Techniques, e.g. Physic-Life Science Interfaces

MIM.7.104
SHG imaging of mature collagen fibers produced in vitro for tissue engineering applications

Z. Burdikova[1]

[1]Institute of Physiology, Biomathematisc, Prag, Czech Republic

burdikova@biomed.cas.cz
Keywords: collagen, second harmonic generation imaging, scanning electron microscopy

Collagen is important component of extracellular matrix (ECM) of connective tissue. Therefore, analysis of collagen deposition and remodeling is essential in tissue engineering. Second harmonic generation (SHG) imaging technique allows the imaging of non-centrosymetric structures such as collagen. The primary pig valve interstitial cells (VICs), derived from the aortic heart valve, actively produce type I collagen and are therefore suitable for optimizing collagen visualization methods. Human osteoblast cell line Saos-2 are able to grow extensively and they can differentiate and produce ECM under specific conditions as well. They can be used for evaluation of biocompatibility of biomaterials for bone implants coatings, such as nanocrystalline diamond films (NCD) [1].

We analyzed type I collagen production by Saos-2 cells on nanocrystalline diamond films (NCD) and on glass coverslips after 2 weeks cultivation in medium with addition of 50 μg/ml ascorbic acid. The VICs were used as a positive control for the production and visualisation of type I collagen and for SHG signal measurements (Table 1). The native type I collagen fibers were visualized by two-photon excitation microscopy and SHG imaging, together with immunofluorescence staining and fluorescence microscopy. In order to recognize all collagen content and extracellular collagen by immunofluorescence we used permeabilization treatment. Type I collagen was stained either in permeabilized cells, where both the intracellular and extracellular collagen was stained, or in non-permeabilized cells, where only extracellular collagen was stained. Additionally, the amount of collagen in ECM was measured by the Sircol assay in both VICs and Saos-2 cells.

The mature collagen fibers were detected in Saos-2 cells after a two-week culture in a osteogenic medium, on both glass and NCD films. In VICs, both the immunofluorescence staining and SHG imaging depicted collagen structures, although in permeabilized cells, also intracellular and immature collagen was observed. In non-permeabilized samples, only extracellular collagen was stained, which corresponded with the SHG signal of these samples(Fig 2A). We also detected the detailed collagen structure by scanning electron microscope (Fig. 2B). To be concluded, SHG imaging technique is promising tool for analysis of collagen I production associated with testing of material biocompatibility.

1. Grausova L, Kromka A, Burdikova Z, Eckhardt A, Rezek B, et al., PLoS ONE 6(6): e20943. (2011)
2. This work was supported within the project “The Centre of Biomedical Research” (CZ.1.07/2.3.00/30.0025). This project is co-funded by the European Social Fund and the state budget of the Czech Republic. Other supports were provided by the Grant Agency of the Czech Republic (grant No. P108/11/0794) and the Academy of Sciences of the Czech Republic (grant No. IAAX00100902).

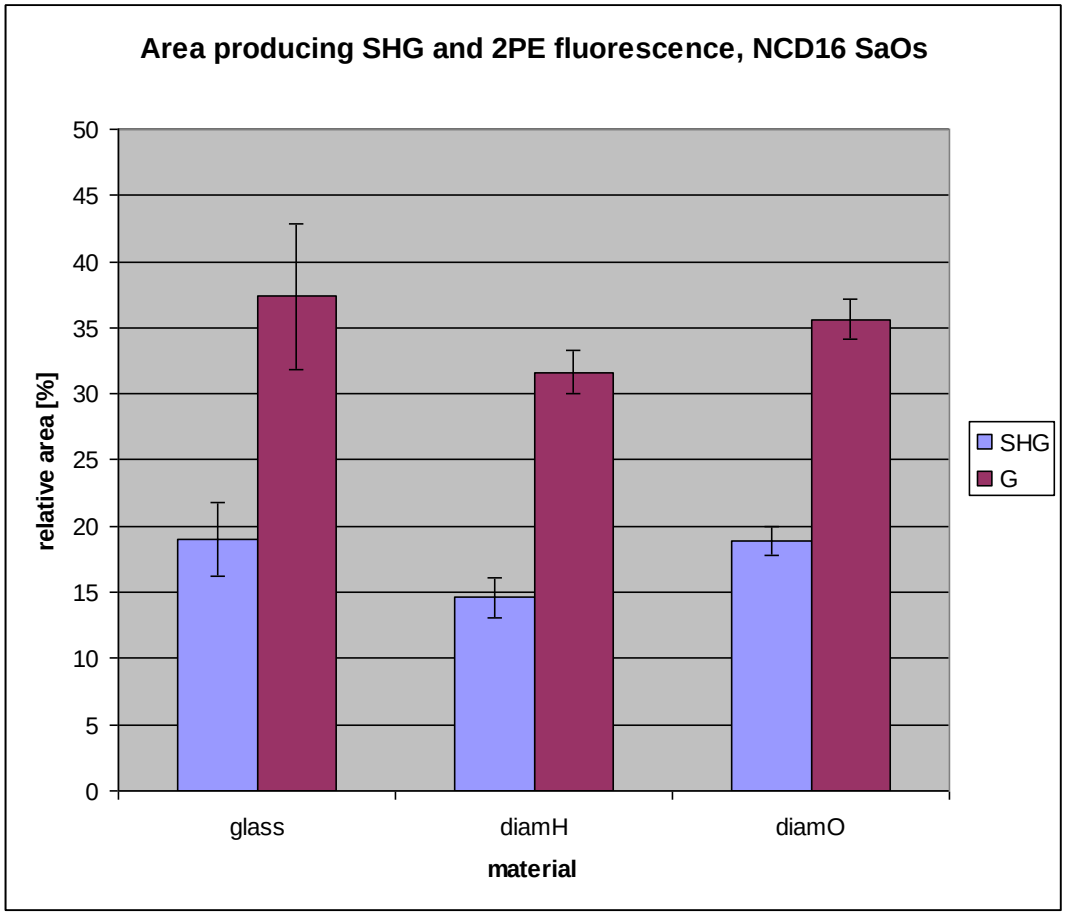

Table 1. Production of collagen by VIC cells, comparison of SHG signal and immunofluorescence labelling on the nanodiamond O and H.

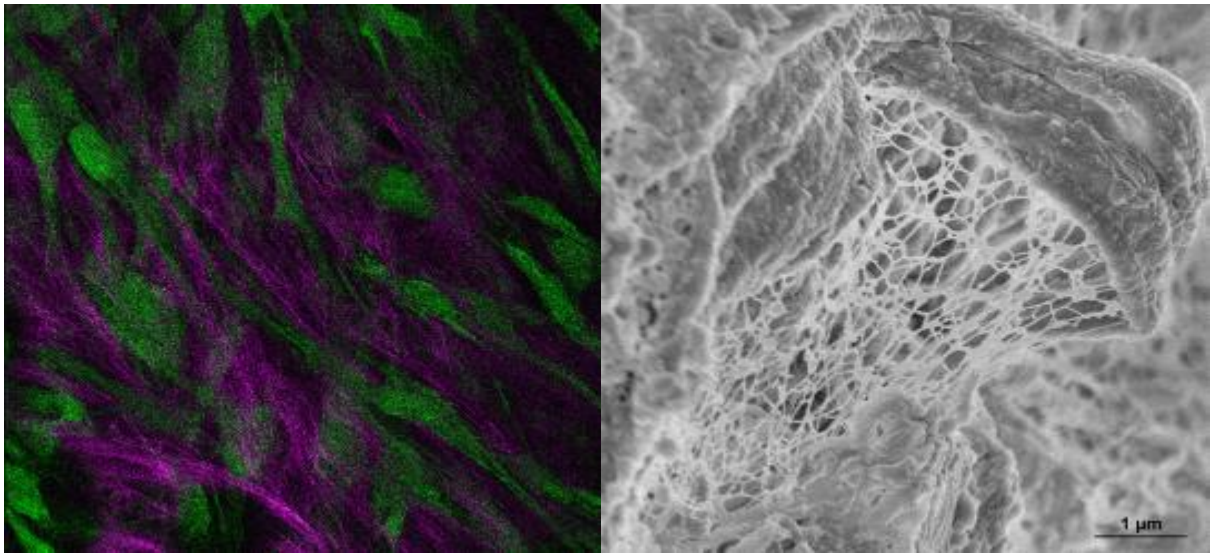

Figure 2a.) VICs stained with Cell Tracker, following optical sections, physical distance 1 μm.
2b.) SEM image of VICs with collagen after fixation by glutaraldehyde, dehydratatrion by ethanol series and critical point drying

Crossdisciplinary Applications of Microscopy Techniques, e.g. Physic-Life Science Interfaces

MIM.7.105
Application of multiphoton microscopy in diagnosis and therapy of cancer

J. Chen[1], S. Zhuo[1], X. Zhu[1], X. Jiang[1], Y. Wu[1]

[1]Fujian Normal University, Institute of Laser and Optoelectronics Technology, Fujian Provincial Key Laboratory for Photonics Technology, Key Laboratory of OptoElectronic Science and Technology for Medicine of Ministry of Education, Fuzhou, China

chenjianxin@fjnu.edu.cn
Keywords: multiphoton microscopy, diagnosis, therapy, cancer

Multiphoton microscopy uses ultrafast, near-infrared laser as excitation sources and bases on nonlinear optical signals of intrinsic fluorophores in tissues such as two or three photon-excited fluorescence (2PEF or 3PEF) and second or third harmonic generation (SHG or THG), providing enhanced imaging penetration depths in scattering samples, reduced overall specimen photodamage, photobleaching and phototoxicity. These advantages make it more suitable for studying intact living tissues at the cellular level without the need of fluorescent dyes. Multiphoton endoscopy has been regarded as a method which may be capable of providing immediate histological images. Using LSM 510 META system (Zeiss, Jena, Germany) coupled to a Ti:sapphire laser (Coherent Mira 900-F), the application of multiphoton microscopy in diagnosis and therapy of cancer were investigated. We focus on esophageal cancer, gastric cancer, colorectal cancer and cervical cancer. We established relevance between optical diagnostic features and physiological and pathological states of tissue which was used to identify tumor tissue [1-8]. The targeted ablation of preinvasive cancer cells with micrometer-sized volume precision was also performed [9]. Our findings provided a “seek-and-treat” medical photonics technology for cancer in epithelial tissues at the molecular level. With the implementation of multiphoton microscopy concept in endoscopy applications, multiphoton endoscopy might realize in vivo histological diagnosis goal of endoscopists.

1. J.X. Chen*, S.M. Zhuo, R. Chen, X.S. Jiang, S.S. Xie and Q.L. Zou, New Journal of Physics, 9(2007), p.212
2. J.X. Chen*, S.M. Zhuo, G. Chen, J. Yan, H.Q. Yang, N.R. Liu, L.Q. Zheng, X.S. Jiang and S.S. Xie, Gastrointestinal Endoscopy, 73 (2011), p.802-807
3. J. Yan, G. Chen, J.X. Chen*, N.R. Liu, S.M. Zhuo, H.Yu, M.G. Ying. Surgical Endoscopy, 25(2011), p.1425-1430
4. N.R. Liu, J.X. Chen*, G. Chen, J. Yan, S.M. Zhuo and X.S. Jiang, Laser Physics Letters, 9(2012), p.155–159
5. S.M. Zhuo, J. Yan, G. Chen, J.X. Chen* and S.S. Xie, PLoS ONE, 7(2012), p.e38655
6. S.M. Zhuo, X.Q. Zhu, G.Z. Wu, J.X. Chen and S.S. Xie, Journal of Biomedical Optics Letters, 16 (2011), p.120501
7. S.M. Zhuo, J.X. Chen*, G.Z. Wu, S.S. Xie, L.Q. Zheng, X.S. Jiang and X.Q. Zhu, Applied Physics Letters, 96(2010), p.213704
8. S.M. Zhuo, L.Q. Zheng, J.X. Chen*, S.S. Xie, X.Q. Zhu and X.S. Jiang, Applied Physics Letters, 97(2010), p.173701
9. S.M. Zhuo, J.X. Chen*, G. Z. Wu, X.Q. Zhu, X.S. Jiang, and S.S. Xie, Applied Physics Letters, 100 (2012), p.023703
10. We kindly acknowledge the support of the Program for Changjiang Scholars and Innovative Research Team in University (Grant No. IRT1115), the National Natural Science Foundation of China (Grant Nos. 81271620, 81101209, 61275006).

Crossdisciplinary Applications of Microscopy Techniques, e.g. Physic-Life Science Interfaces

MIM.7.P106
Textural variations in experimental metallurgical coke: insights from optical microscopy and wavelet-based image analysis

S. Gornostayev[1], J. Heino[1], T. Kokkonen[1], H. Makkonen[1], S. Huttunen[1], T. Fabritius[1]

[1]University of Oulu, Oulu, Finland

ssg@sun3.oulu.fi

Carbonization of coals during coking process leads to the formation of various microscopic textures, which amongst other parameters, govern chemical and physical properties of the resulting coke. The formation of microscopic textures is a function of parental coal mix and coking conditions. The textures of coke are usually characterized on the basis of their optical behaviour in polarized light. There are three dominating textures, which have different orientation degree and, consequently, reactivity in CO/CO_2 atmosphere [1]. These textures are: highly oriented banded, mosaic and isotropic [1,2]. The shortage of a high quality coking coals, as well as environmental and economic considerations, have lead to the attempts of utilization of various additives to a coal mix. Among them - plastic [3]. This study is devoted to the characterization of major textures of experimental cokes, prepared with waste polyethylene (PE).

The samples of experimental metallurgical coke were prepared in a laboratory-scale ovens [4] using one type of coal, obtained from Ruukki Metals, Finland. The coal was mixed with varying amounts of PE, $(C_2H_4)n$. In total, six samples of coke were made with 2.5, 5, 7.5, 10 and 12.5 % of PE, and one from 100% coal (without PE). The PE plastic and the coal were comminuted to a < 5 mm fraction and then sieved. The coking process (20 - 1200^{o}C) was performed in a Nabertherm type HT08/18 chamber furnace during 16 hours and the quenching process (in nitrogen) has lasted 6 hours. The samples of coke were then sliced to 4-5 mm pieces, molded into a resin and polished (Figure 1, A) according to a procedure reported by Kokkonen & Gornostayev [5].

Optical investigations of the samples were done with an Olympus BX51 microscope equipped with a digital camera. Special software [2] was used to perform wavelet-based image analysis. According to Makkonen et al. [6], any given sample of coke can be representatively characterized with wavelet-based image analysis by studying 7-11 areas (points). In every point, 4 images under different positions (20°, -20°, 0° and 90°) of polarizing lenses should be taken. The program then divides (Figure 1, B) the images (2048x1536 pixels) into 12 sub-areas (512x512 pixels) and calculates each sub-area separately. As a result, it gives the amount (%) of isotropic, mosaic and banded textures, as well as pores and a map of textures (Figure 2) for each sub-area. Inert portions [1,6] can not be recognized by the program [6], and they should be excluded from the observations. It was also verified by Makkonen [*pers. comm*.] that the calculations presented in a research report on image analysis of industrial coke samples [6], are in agreement with traditional point counting on the same set of samples. The later method is common for characterization of coke textures [1,7,8]. In this study, each sample was photographed and subsequently analyzed in 10 areas (Figure 1, A), which gave 120 sub-areas for the image analysis, and 120 datasets per sample for subsequent statistical calculations.

The investigations of experimental samples of metallurgical coke prepared with different amounts of PE plastic have shown that the addition of PE leads to the increase of pore size, and their shape is more often has rounded outlines (Figure 2, A,C). The wavelet-based image analysis (Figure 2, B,D) has revealed general increase of isotropic texture in the PE coke, compared to PE-less coke. Also, there is a strong negative correlation (approx. -0.9) between isotropic and mosaic textures in the samples, when the increase of isotropic texture is accompanied by the decrease of mosaic texture. The latter observation can generally suggest that the isotropic texture, at least partly, can be formed for the expense of mosaic, when PE plastic is added to a coal mix. The reason for this phenomenon can be related to the activities of one or several gas phases (ethylene, propylene, isobutylene, 1-hexene and heptane) formed during thermal decomposition of PE [9]. The other related research [Heino, *pers. comm*.] has also found a correlation between porosity and cold strength of a coke with the amount of PE.

1. F. Hideo, H. Mitsumasa and N. Seiji, Fuel 62 (1983), p. 875.
2. O. Mattila and P. Salmi in “Scanmet III – International conference on process development in iron and steelmaking”, eds. J.-O. Wikström et al. (Luleå, Sweden) (2008), p. 237.
3. S. Nomura, K. Kato, T. Nakagawa and I. Komaki, Fuel 82 (2003), p. 1775.
4. J. Heino, S. Gornostayev, T. Kokkonen, S. Huttunen and T. Fabritius, in “Carbon 2012 Conference” (Krakow, Poland) (2012) ISBN 978-83-60958-99-5.
5. T. Kokkonen and S. Gornostayev, in “Department of Process and Environmental Engineering”, Report 339, ISBN 978-951-42-6119-0 (University of Oulu) (2010), p. 1.

6. H. Makkonen, O. Mattila and S. Gornostayev, in “Department of Process and Environmental Engineering”, Report 335, ISBN 978-951-42-9189-0 (University of Oulu) (2009), p. 1.
7. L. Patrick, M. Sims and E. Stacey, Journal of Microscopy 109 (1977), p. 137.
8. C. Coin, Fuel 66 (1987), p. 702.
9. J. Nisar, M. Ali and I.A. Awan, Journal of the Chilean Chemical Society 56 (2011) p. 653.
10 This research was funded by the Academy of Finland.

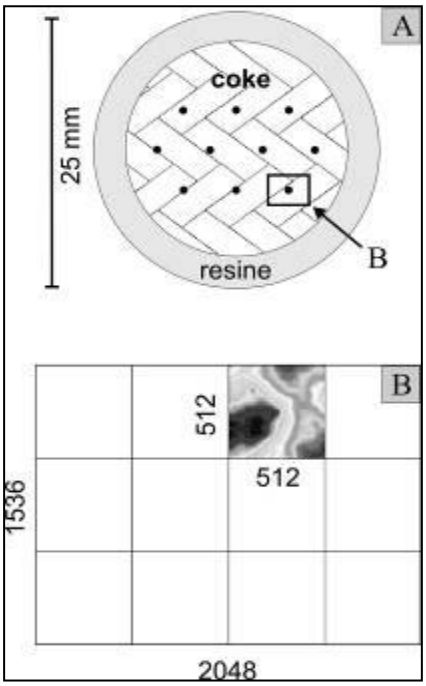

Figure 1. Polished section, locations of the points (A) and map of sub-areas for image analysis (B).

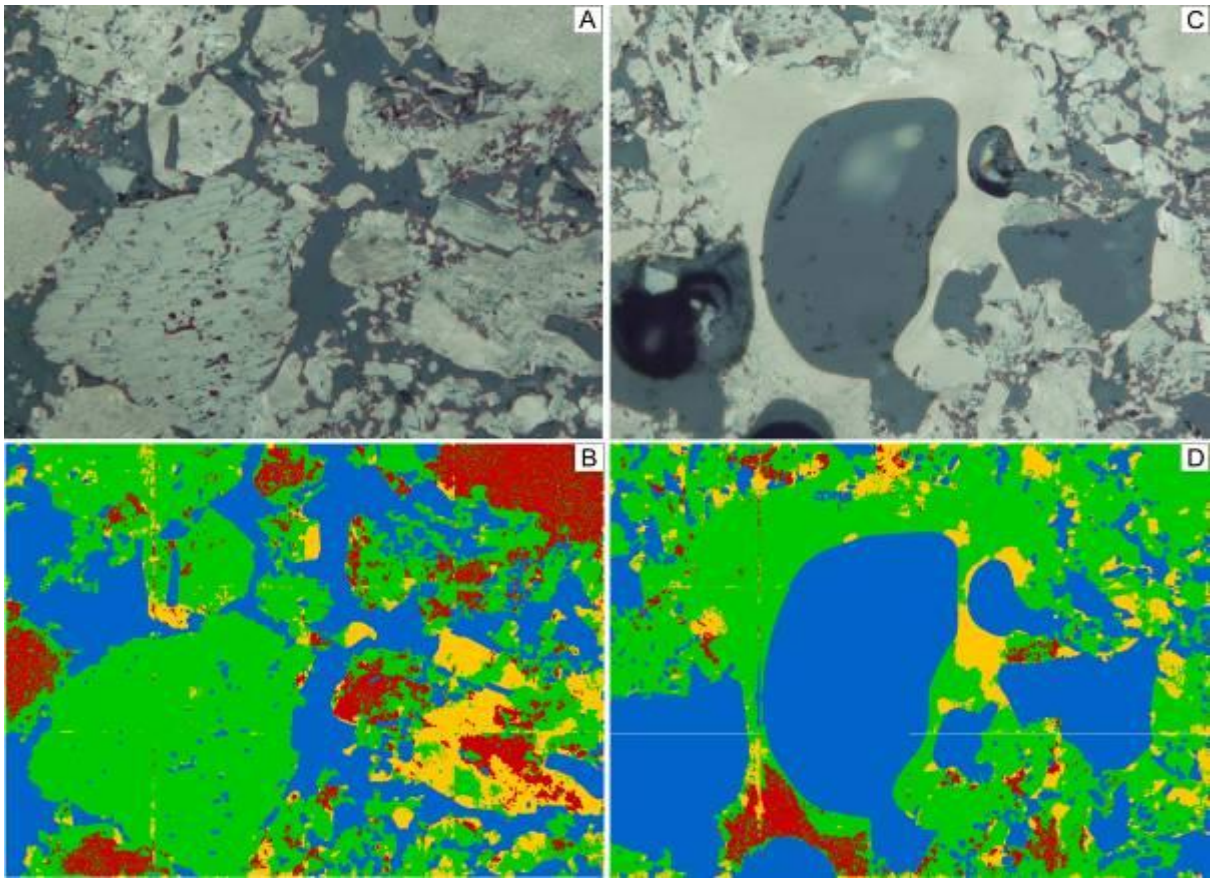

Figure 2. Wavelet-based image analysis of experimental metallurgical coke. A,B - 100% RI coal, C,D – 87.5% RI coal, 12.5% PE. Magnification - x20. Textures: isotropic – green, mosaic – red, banded – yellow, pores - blue.

Crossdisciplinary Applications of Microscopy Techniques, e.g. Physic-Life Science Interfaces

MIM.7.P107
Lensless Chip-Microscope for in situ Cell Microscopy

M. Hubl[1], M. Blechert[1], M. Engelhardt[1], S. Seifert[1], A. Ziolkowska[1], E. Jung[1], L. Georgi[2]

[1]Fraunhofer IZM, Medical Microsystems, Berlin, Germany
[2]Technische Universität Berlin, Berlin, Germany

Moritz.Hubl@izm.fraunhofer.de
Keywords: lensless, Chip-Microscope, cell microscopy, in-situ microscopy, cell growth, cytotoxicity, point-of-care, microfluidic, microreactor

Cell Microscopy in new Dimensions: Lensless in situ Cell Microscopy over a wide Field of View

The Lensless Chip-Microscope is a miniaturized microscope tool which uses a new lensless imaging technology in combination with reasonable standard components and a simple and modular assembly. It was initially developed for the characterization of cells and microparticles in microfluidic systems [1]. The technology is based on in-line holography, which allows to image cells and microparticles without lenses or apertures. Combined with a commercial off-the-shelf 10 MP CMOS sensor and a microfluidic chip it is possible to achieve spatial resolution up to a few micrometers on a large-scaled field of view of 4.6 mm x 6.4 mm, which is only limited by the sensor area. “Figure 1.” shows a virtual model and the first prototype of the Lensless Chip-Microscope.

A red laser diode emits coherent light into the microfluidic channel and on the objects of interest. The wave front scatters at the object and overlays with the unscattered laser light and forms unique holograms on the sensor surface. This pattern of the micro-object is dependent on the shape, size, transmission, intercellular elements and distance to the sensor [1]. The microscope image and the corresponding hologram of a threadworm as well as the lensless imaging technology are illustrated in “Figure 2.” The distance between object and sensor is adjustable to achieve less overlapping of the holograms or high-resolving templates for software operations. Template matching algorithms enable identification and counting of certain cell types in a cell solution. The specially programmed software “Lensless” runs the camera in stand-by mode for minimal thermal influence on the sample. Due to its small dimensions of only 4 cm x 4 cm x 6 cm the microscope can be placed into an incubator for observing cells for example in a microfluidic channel. The hologram of incubated cells reveals their type, shape and adherence, sequential imaging also cell mobility and division status. Cells in solution, due to cell division or cell death, show differences in their hologram pattern to attached cells. This fact can be used for continuous monitoring of the cell growth or cytotoxicity tests. “Figure 3.” illustrates the change of the cell holograms during the cell division (left) and the cell adherence and growth of injected fibroblasts after 23 hours (right). With the large field of view of 29,4 mm^2, which is 15-times the field of view of a conventional 10x microscope objective it is possible to detect up to 10.000 of cells within just one image. One crucial benefits of using the Chip-Microscopy is the small investment. It is only a fraction of the cost of a conventional lens based microscope system. Furthermore the Lensless Chip-Microscope can be used for numerous applications in biotechnological microfluidic systems or point-of-care diagnostic tools. Further steps for realization of a stand-alone “Lensless Cell-Microscope” are the implementation of a Peltier cooling to the camera sensor with temperature regulation. The cooling system enables live imaging or video recording and better temperature handling of the sample. A thermoregulated extern incubation chamber around the Chip-Microscope completes the “Lensless Cell-Microscope” for portable cell incubation and simultaneous in situ cell microscopy.

1. M. Hubl, “Linsenloses Chip-Mikroskop zur digitalen Charakterisierung von Zellen und Mikropartikel”, Diploma Thesis (2011)
2. S. Isikman, I. Sencan, O. Mudanyali, W. Bishara, C. Oztoprak, A. Ozcan, “Color and monochrome lensless on-chip imaging of Caenorhabditis elegans over a wide field-of-view”, Lab on a Chip (2010)
3. W. Bishara, H. Zhu, A. Ozcan, “Holographic opto-fluidic microscopy“, Optics Express, Vol. 18 (2010)

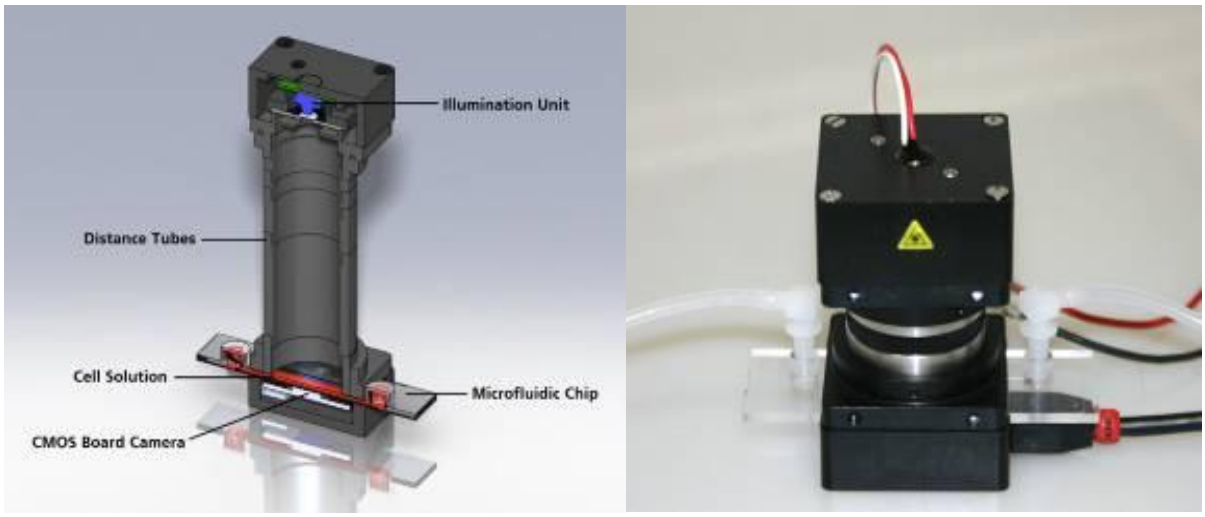

Figure 1. Virtual model (left) and prototype of the Lensless Chip-Microscope (right) with laser illumination and integrated microfluidic chip [1]

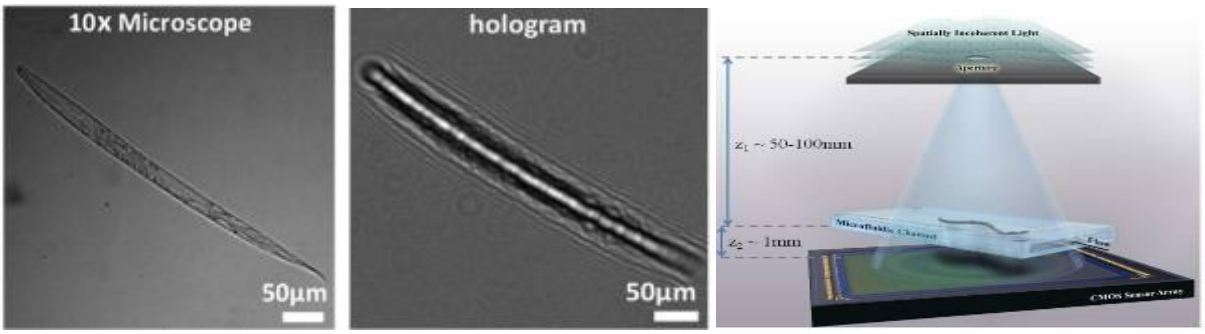

Figure 2. Image of C. elegans under a transmitted light microscope (left) and as hologram under the Chip-Microscope (middle) [2]. On-chip imaging technology of the Lensless Chip-Microscope (right) [3].

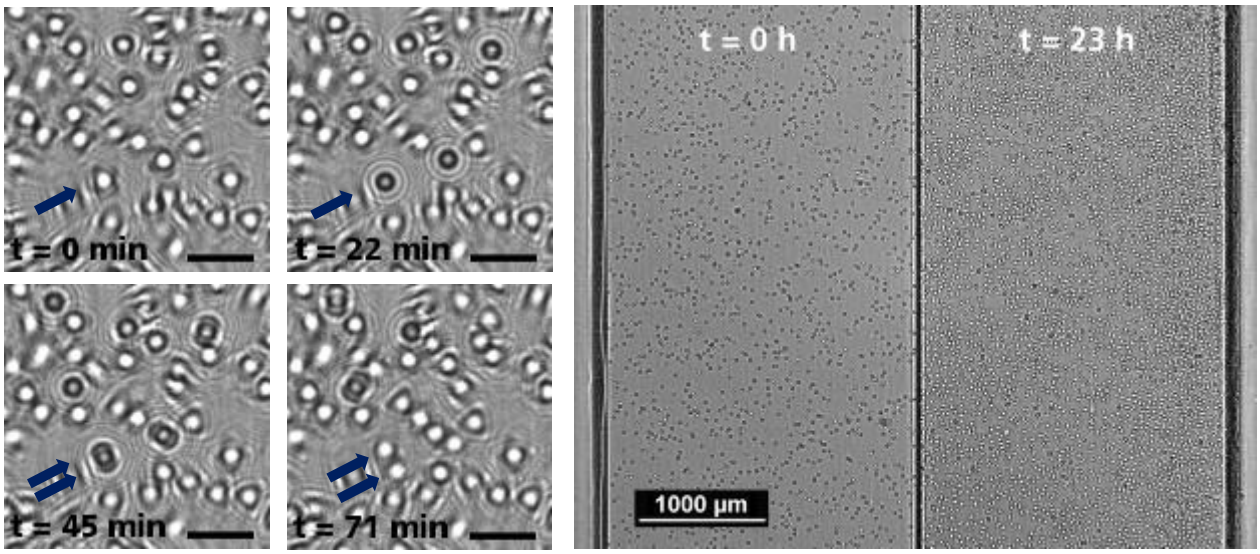

Figure 3. Cell division of incubating fibroblasts cells (left, scale = 100 µm) and fibroblast cell adherence and growth in a microfluidic channel observed over the entire field of view with the Lensless Chip-Microscope (right).

Crossdisciplinary Applications of Microscopy Techniques, e.g. Physic-Life Science Interfaces

MIM.7.P108
Influence of ultraviolet radiation on spider silk - electron microscope studies

N. Ismail[1], K.L. Goh[2], P. Pasbakhsh[3], S.P. Chang[3], L. Wee Loong[3]

[1]MIMOS Berhad, Analytical Service Lab, Kuala Lumpur, Malaysia
[2]Newcastle University, School of Mechanical and System Engineering, Singapore, Malaysia
[3]Monash University Sunway Campus, , School of Engineering, Sunway, Malaysia, Malaysia

norhazlina.ismail@mimos.my

The purpose of this work is to investigate the effects of ultraviolet radiation (UVR) on the physical properties of spider silk. Spider silk comprises protein fibroin [1], which are layers of antiparallel beta sheet assembled from the recurrent amino acid sequence; the high glycine (and, to a lesser extent, alanine) content allows for tight packing of the sheets henceforth contributing to the strength and toughness of the material. The formation of hydrogen bonds within the beta sheets and between neighbouring beta sheets in turns regulates the fine structure of the silk [2]. The final macroscopic structure of the spider silk depends on the viscosity of the protein fluid, which is regulated by the shear rate, during the spinning process [1, 2].

In this study, spider silk harvested from a conservatory was exposed to UVR at wavelength 254 nm over three different exposure times, *t* (= 10, 20 and 30 min) to determine the effects of *t* on the physical properties. Wavelength 254 nm falls within the range of wavelengths known as UVC; UVC is normally filtered out by the ozone layer so that none reaches the earth's surface. A control group (not UVR treated) was used for the purpose of comparison. Scanning electron microscopy (SEM, JEOL JSM-7600F, at 1 kV) was carried out at JEOL Asia Pte Ltd. Analysis of the SEM images from the control group revealed that spider silk featured relatively smooth texture (at low magnification; Figure 1A), with small crevices and humps (at larger magnification; Figure 1B), on the surface of the silk. However, when treated to UVR, silk dissociated into distinct fascicles, and the number of fascicles delaminated from the silk increased with increase in *t*. Figure 2A shows the distinctive (delaminated) fascicles from a UVR treated silk thread (*t* = 30 min; x5000). Further analysis at higher magnification revealed numerous small disorientated fibrils on the surface of the threads (Figure 2B). The small crevices and humps present in the control groups were noticeably absent in the UVR treated silk. Although these dramatic structural changes did not give rise to any new functional groups (as observed from the FTIR spectra; results not shown), the wavenumber of the Amide I peak decreases with increase in *t*. A decreasing wavenumber suggests an increasing number of disrupted hydrogen bond within the fibroin molecule; this lends support to the findings of a decreasing tensile strength and stiffness of the silk thread with increase in *t* ($P < 0.05$). These structure-function findings are important from an environmental perspective. Overall, the findings suggest that increase exposure time of spider thread to UVR, i.e. arising from decreases in the ozone layer, could lead to diminution of the mechanical properties, resulting in weaker and reduced stiffness, of the spider silk and this could in turn affect the foraging capability of spiders and long term adaptability in the face of the climate change. Further studies is underway to relate the molecular changes [3] underlying the structural changes seen here.

1. J. Sirichaisit, R.J. Young and F. Vollrath, Polymer 41 (2000) p. 1223
2. J.E. Trancika, J.T. Czernuszka, D.J.H. Cockayne and C. Viney, Polymer 46 (2005) p. 5225
3. S. Keten and M.J. Buehler, Applied Physics Letters (2010) 153701-1

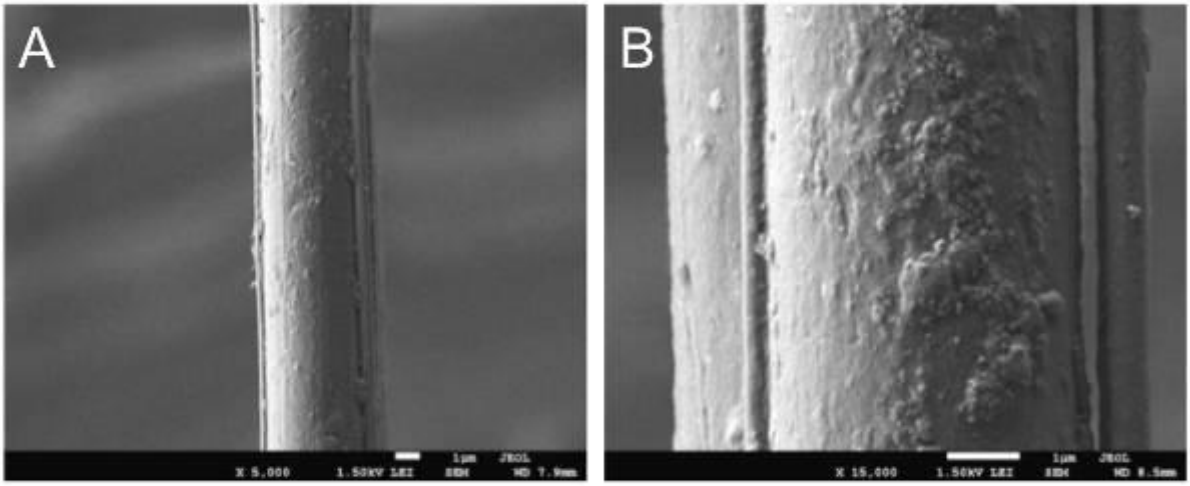

Figure 1. SEM images of spider silk (controls) at magnifications of 5000 (A) and 15000 (B); scale bars,1 □m.

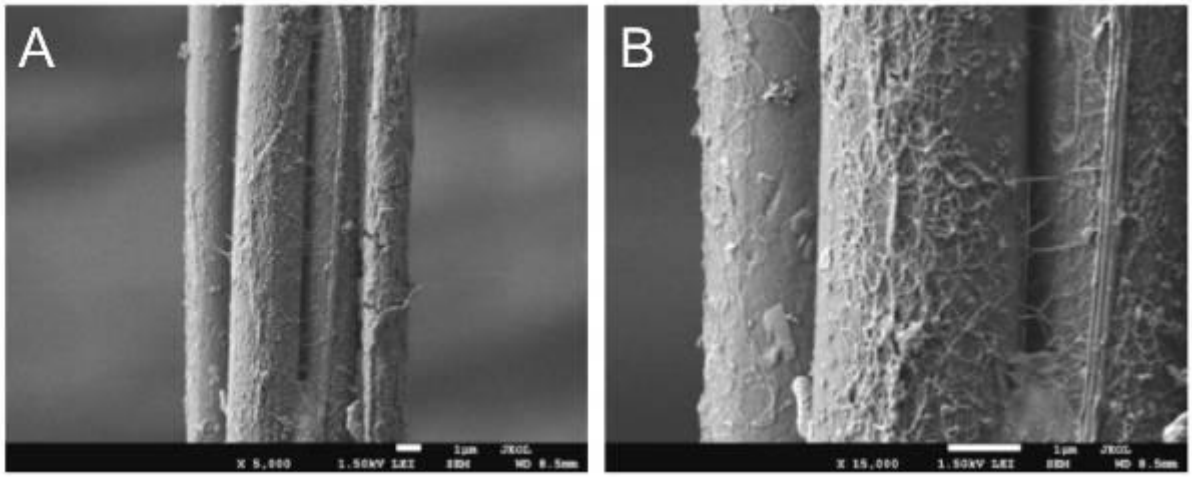

Figure 2. SEM images of spider silk (30 minutes exposure to UVR) at magnifications of 5000 (A) and 15000 (B); scale bars,1 □m.

Crossdisciplinary Applications of Microscopy Techniques, e.g. Physic-Life Science Interfaces

MIM.7.P109
Correlation of the nanoindentation induced pop-in effects with SEM and TEM observation of nanocomposite nc-TiC/a-C:H coatings

V. Bursikova[1], J. Bursik[2], L. Zabransky[1], P. Soucek[1], P. Vasina[1]

[1]Masaryk University, Faculty of Science, Brno, Czech Republic
[2]Institute of Physics of Materials, Brno, Czech Republic

vilmab@physics.muni.cz
Keywords: SEM, TEM, nanoindentation

In the present work a set of nc-TiC/a-C:H coatings was prepared using magnetron sputtering of a titanium target in an acetylene-containing atmosphere [1,2]. The acetylene flow was varied to obtain films with different chemical compositions with carbon content ranging from 30 at.% C to 68 at.% C. The thicknesses of the prepared films were in the range from 5 to 7 μm.

Nanoindentation tests were used to study the mechanical properties of the film/substrate system from near surface up to film-substrate interface. Indentation loads ranging from 20 to 1000 mN were applied to each sample to obtain the hardness and elastic modulus as a function of indentation depth. The highest hardness and Young's modulus of (46±2) GPa and (415±5) GPa respectively was reached for films with the Ti/C ratio of approximately 3/4.

In case of films with complex structures (different phases, micro- or nanocrystallites, columnar structure, differences in grain orientation) measurements at the low depths are giving a large scatter because the indentation response corresponds with the material structure. The resulting load-penetration curves contain a lot of information about the tested material. We can visualize them using the so called differential hardness curves. The differential hardness H_{dif} (H_{dif} = k$\partial L/\partial(h^2)$, where L is the load, k is geometric constant and h is the indentation depth) represents the ratio of the small load increase and the corresponding change in the square of the indentation depth (i.e. change in contact area of the indenter and the tested material). This value is very sensitive to any changes occurring during indentation test. The H_{dif} dependence on the indentation depth may be used to visualize the increase of the substrate influence, moreover it can be used to determine the depth of indentation induced crack creation or film delamination. The extended evaluation of H_{dif} curves can give us image about the grain boundaries, layered structures, pressure induced phase transformations etc. In order to study the indentation induced deformation and cracking indentation tests made with maximum load of 1N. In Figure 1 an example of SEM image of an indent performed using a load of 1N on film with the highest hardness is shown in both secondary electrons and backscattered electrons signals. The corresponding loading-unloading curves and the differential hardness H_{dif} on the indentation depth are shown in Figure 2. The crack lines inside the indentation print correlate with the pop-ins on the loading curves. Using the differential hardness curves it is possible to determine the depths of the crack creations. The first crack appeared at indentation depth around 850 nm. The crack creation started when the titanium interlayer influence became dominating. The single crystal titanium hardness (H_{Ti}=1 GPa) and elastic modulus (Y_{Ti}=129 GPa) are substantially lower than those of both the coating and the stainless steel substrate. The fracture did not spread further, it was observed only inside indentation prints. TEM results obtained from the lamella taken from the surroundings of the indentation print did not show any cracks in the material structure. The diffraction studies revealed that the deformation was proceeded by rearrangement of crystallites within the a-C:H matrix.

Details of microstructure in the vicinity of the indentation print were studied using a Philips CM12 STEM transmission electron microscope on thin lamellas prepared using focused ion beam (FIB) technique in a LYRA 3 XMU FEG/SEM×FIB by Tescan.

1. The work was supported by the Czech Science Foundation (Project No. P205/12/0407) and OP R&DI CZ.1.05/2.1.00/03.0086.
2. P. Souček et al., Evaluation of composition, mechanical properties and structure of nc-TiC/a-C:H coatings prepared by balanced magnetron sputtering, Surf. Coat. Tech. 211, (2012) p. 111.
3. P. Vašina et al. Depth profile analyses of nc-TiC/a-C:H coating prepared by balanced magnetron sputtering, Surf. Coat. Tech. 205, (2011) p. 53.

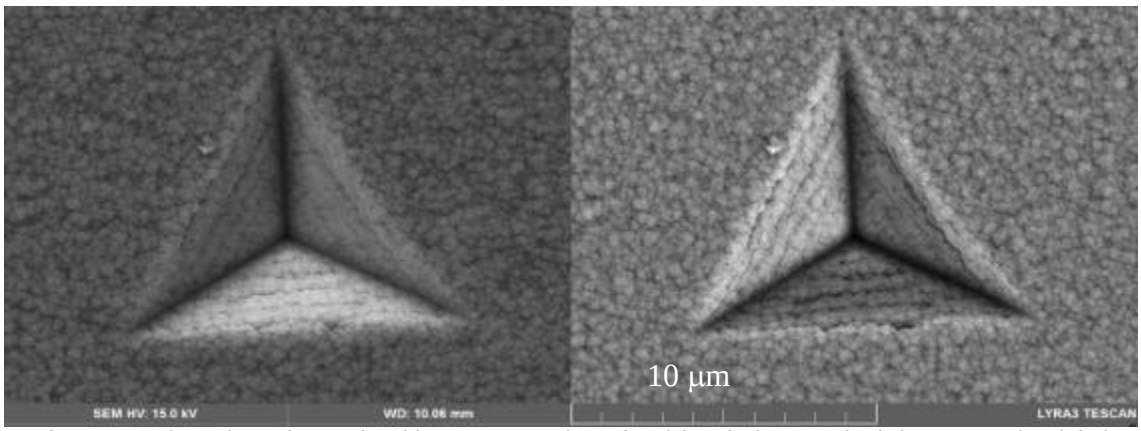

Figure 1. Indentation print made with 1N on tested coating (signal of SE on the left, BSE on the right.)

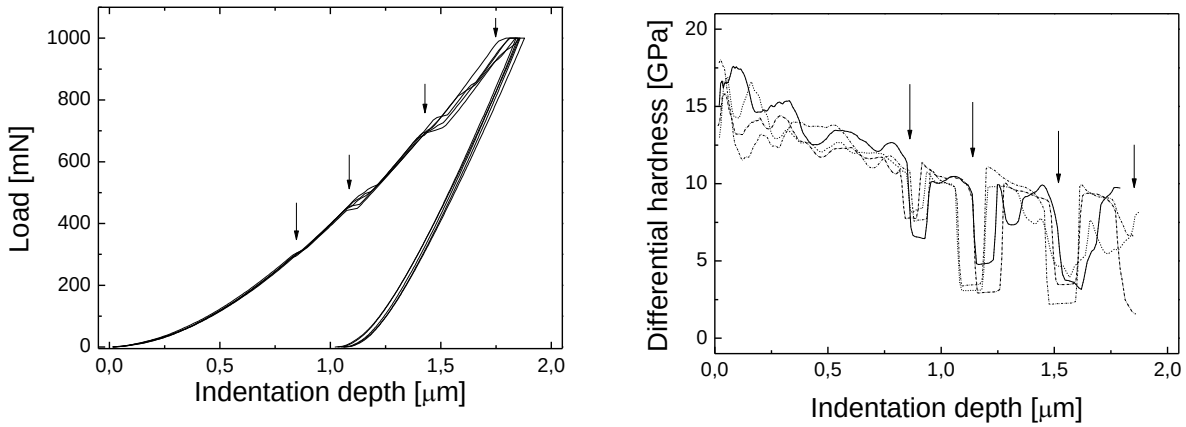

Figure 2. Loading and unloading dependences (on the left) on the indentation depth made with maximum load of 1N and the corresponding differential hardness dependences on the indentation depth (on the right). The arrows indicate the crack creation in the inner part of the indentation print.

Crossdisciplinary Applications of Microscopy Techniques, e.g. Physic-Life Science Interfaces

MIM.7.P110
Enhancing effective depth-of-field using spectra-specific wavelet based multi-focus image fusion for digital pathology applications

S. Conjeti[1], B. Ghosh[1], S.P.K. Kari[1], D. Sheet[1], J. Chatterjee[1]
[1]Indian Institute of Technology Kharagpur, School of Medical Science and Technology, Kharagpur, India

sailcon.131@gmail.com
Keywords: Multi-focus Imaging, Wavelets, Focus Profile Measurement, Image Fusion.

Optical microscopy is inherently characterised by diffraction-limited wavelength-specific depth-of- focus causing objects beyond this limit to appear defocused in the image. We present a wavelet-based multi-focus image fusion algorithm aimed at enhancing the effective depth of field of bright-field optical microscopy. The objective of the proposed algorithm is to generate an "All-in-Focus" image within the microscope's field of view by selectively fusing multiple partially focussed images acquired as a focus-merging z-stack. All-in-Focus image has higher extended depth of focus and can be subsequently used by human and machine vision platforms for image analysis [1].

The proposed method for image fusion utilizes a pixel-by-pixel non-linear image fusion scheme i.e. fusion of the images at the highest resolution level. In the present application, images are acquired using Lieca DM750 Bright-field (white light illumination) Compound Microscope under 40x A-plan objective magnification (NA – 0.65), manually maintaining an inter slice-distance of 2 µm in Z-direction on either side of a user-defined plane (central focus). The effective depth of field at this objective magnification is 1µm at an image depth of 12.8 mm. The number of slices in the z-stack acquisition is selected to have the complete depth of the sample covered. In order to reduce blurring due to accumulated averaging and relax the computational burden on the fusion routines, images corresponding to spectra-specific local maximas of focus measures are incorporated into the fusion pool for further processing. These spectra-specific focus graphs are generated using focus measure calculated as the ratio of Daubechies 'Db6' wavelet coefficients [2]. The focus profiles for a selected sample dataset are presented in Figure 1. Further, the selected images are fused pair-wise using the proposed wavelet-based multi-focus fusion algorithm as described below. The results of fusion using this framework on a sample dataset are presented in Figure 1.

Stage 1: Coefficient Extraction: The source images are decomposed using Discrete Wavelet Transform using the selected wavelet basis with a decomposition level of 2, to obtain the approximate and detail wavelet coefficients.

Stage 2: Approximate Component Blending: A weighted-average based approach is used to blend the approximate components of the source images. The weights are determined proportional to the gradient based focus measures derived using Gaussian Steerable Filters as proposed in [3]. This composite approximate coefficient image is used for reconstruction of the fused image.

Stage 3: Detail Component Blending: The coefficient-specific activity of the detail components is determined by the absolute value of the corresponding coefficients. For the composite coefficient selection, a Choose-Max strategy is implemented, followed by a 5×5 window-based majority filter consistency verification step to remove spurious selections [4].

Stage 4: Fused image reconstruction: The final fused image is generated by applying Inverse Wavelet Transform to the reconstructed composite wavelet coefficients obtained after Step 2 and 3.

The above fusion procedure is applied pair-wise on each of the selected images in the fusion pool. At each stage of fusion, the improvement in the cumulative focus measure is evaluated. For the present application, to choose an optimal wavelet family for optimal fusion, the relative improvement in the focus measure measured as ratio between the focus measure of the fused image and the most focussed source image, is used as an evaluation metric. An exhaustive evaluation on the sample dataset presented here using wavelet families like Daubechies, Biorthogonal, Morlet, Coiflets and Symlets, it was observed that Daubechies 'Db4' wavelet basis gave the most optimal improvement in the focus measure of 4.783. The experiments on the image z-stacks obtained for the current application established the applicability of the proposed method to generate images with better information and higher focus measure than any of the source images. To conclude, the presented strategy is envisaged to solve the inherent problem of short depth of focus of optical microscopes and generate sharp in-focus images of the imaged sample.

1. G. Pajeres and J.M. de la Cruz, Pattern Recognition 37 (2004), p. 1855-1872.
2. S. Pertuz, D. Puig and M.A. Garcia, Pattern Recognition 46 (2013), p. 1415-1432.
3. R. Minhas, A.A.Mohammed, Q.M.J.Wu and M.A. Sid-Ahmed, Image Analysis and Recognition LCNS 5627 (2007), p. 573-583.
4. Z. Zhang and R.S. Blum, Proceeding of IEEE 87(1999), p. 1315-1326.

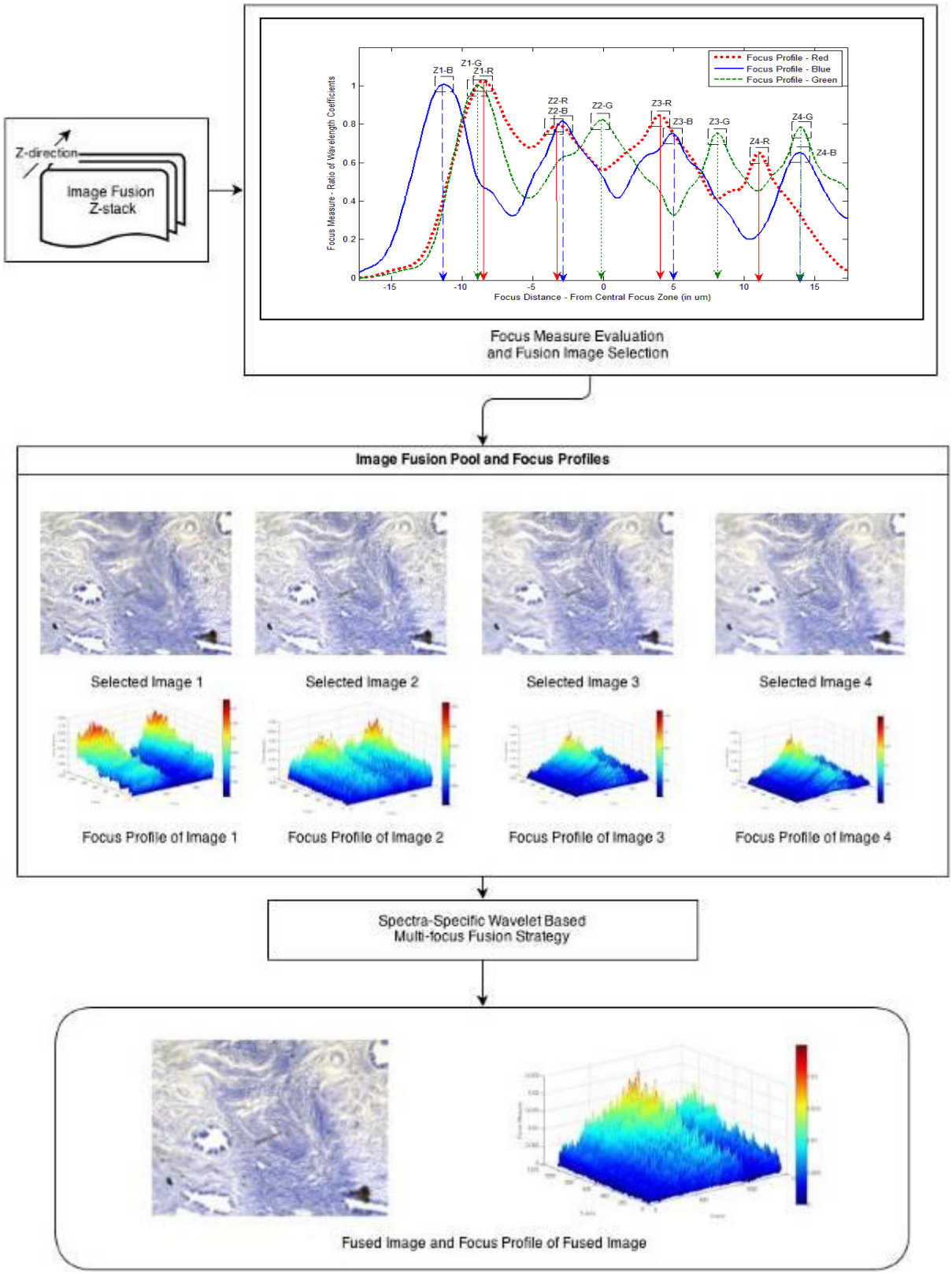

Figure 1. Schematic drawing of the framework for Spectra-Specific Multi-focus Fusion Scheme for extension of Depth of Focus. The images to be fused are selected from the image z-stack based on the Focus measure evaluation and the selected images are fused using the proposed spectra specific wavelet based multi-focus strategy to generate an “All-in-focus” Image.

Crossdisciplinary Applications of Microscopy Techniques, e.g. Physic-Life Science Interfaces

MIM.7.P111
Trajectory analysis of *Navicula pavillardii* cells by using semi-circular microgrooves

K. Umemura[1], T. Haneda[1], M. Tanabe[1], A. Suzuki[1], Y. Kumashiro[2], K. Itoga[2], T. Okano[2], S. Mayama[3]

[1]Biophysics Section, Department of physics, Tokyo University of Science, 1-3 Kagurazaka, Shinjuku, Tokyo 1628601, Japan
[2]Institute of Advanced Biomedical Engineering and Science (TWins), Tokyo Women's Medical University, 8-1 Kawada-cho, Shinjuku-ku, Tokyo 162-8666, Japan
[3]Faculty of Education, Tokyo Gakugei University, 4-1-1 Nukui-kita-machi, Koganei, Tokyo 184-8511, Japan

meicun2006@163.com
Keywords: diatom, micropattern, trajectory, gliding

The use of microchambers has significantly altered the prospects of studying detailed motions of microorganisms. If target cells were to be observed without microchambers, the cells would easily escape from the observation field. However, when the cells are confined to a microchamber, continuous observation is possible by using an optical microscope. Thus, the cell division of *Escherichia coli* was studied in detail. [1]

Diatoms are one of the major photosynthetic planktons in rivers, seas, and lakes. Some diatom types can glide on solid surfaces. Although several studies have assessed diatom cell movements, the trajectory analysis of moving diatom cells specifically have been assessed in only a few studies. Further, only few studies show the use of microchambers, including a few by our research group. [2-4]

In this study, we used semi-circular microgrooves to observe the movements of *Navicula pavillardii* cells. Compared to straight microgrooves, semi-circular microgrooves provide longer contour length. By using the semi-circular microgrooves, we successfully conducted long-term movement trajectory analysis of *N. pavillardii* that were stimulated using *N*,*N*-dimethyl-*p*-toluidine (DMT).

Isolated *N. pavillardii* cells were cultured in Daigo's Artificial Seawater SP for Marine Microalgae Medium (395-01343; Nihon Pharmaceutical Co. Ltd, Tokyo, Japan) by using Guillard's (f/2) Marine Water Enrichment Solution (G9903; Sigma-Aldrich Co. LLC, Munich, Germany) at 18 °C. The samples were irradiated using fluorescent lights (3800 lx) from 1000 to 2200 every day. Eight-day-old cultures after passaging were used for microscopic observations.

A semi-circular microgroove template was fabricated on a silicon wafer by using a previously published method. [4] Disposable replicas of the microgrooves were prepared using polydimethylsiloxane (PDMS; Sylgard 184, Dow Corning Toray Co. Ltd, Tokyo, Japan). The replica was treated using a mixture of acrylamide (1 g), ethanol (4 mg), (+/-)-camphorquinone (50 mg), and DMT (5 µl) to increase hydrophilicity.

The replica was placed in a Petri dish (diameter, 90 mm), and a 7-µl cell suspension was dropped on the pattern. After 3-min incubation, the Petri dish was filled using 40-ml culture medium. The samples were observed using inversed optical microscopy (IX70; Olympus Co., Tokyo, Japan) at room temperature. The cell movements for 30 min were captured as video data. The data were analyzed using 2-dimensional video analysis software (Move-tr/2D7.0; Library Inc., Tokyo, Japan).

Thus, we observed single-cell movements by using the semi-circular microgrooves (Fig. 1). Most of the active cells glided along the outer edge of each pattern. This suggested that the cells typically glide in a forward direction. Although the diameters of the grooves at the center were smaller than those of the outer area, the velocities of a diatom cell were similar in the center and outer area. Thus, frictional force between the cell body and wall of the chamber was negligible in this experiment.

When DMT was added to the sample, the diatom cell velocity significantly increased. Because the same cell in a groove was continuously observed, it was obvious that the increase in velocity was caused by the addition of DMT. Conversely, although the average velocity of 150 cells had increased after adding DMT, the maximum velocity (about 19 µm/s) did not increase (Fig. 2), which indicates the mechanical limit of the diatom cell velocity.

Our data showed that the use of semi-circular microgrooves was effective for single-cell researches. Further, the effects of DMT stimulation on diatom cells were successfully observed.

1. S. Umehara, I. Inoue, Y. Wakamoto, K. Yasuda, Biophys. J. 93(2007), p. 1061.
2. A. Murase, Y. Kubota, S. Hirayama, Y. Kumashiro, T. Okano, S. Mayama, K. Umemura, J. Microbiol. Meth. 87(2011), p. 316.
3. A. Murase, Y. Kubota, S. Hori, S. Hirayama, S. Mayama, Eur. Biophys. J. 41(2012), p. 545.
4. K. Umemura, T. Haneda, M. Tanabe, A. Suzuki, Y. Kumashiro, K. Itoga, T. Okano, S. Mayama, J.

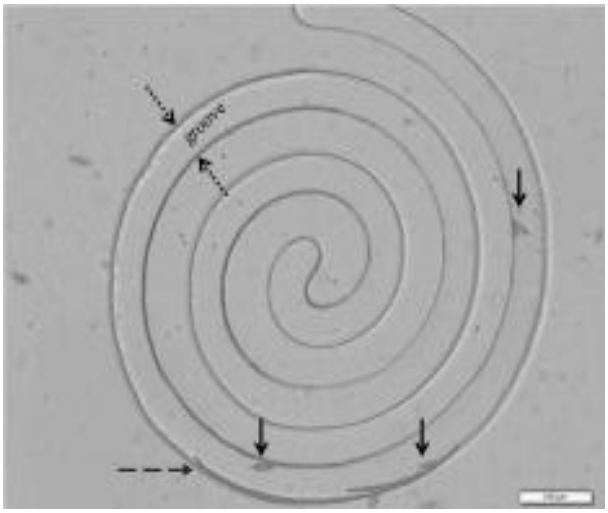

Figure 1. Optical microscopic image of *Navicula pavillardii* cells (solid arrows) in the semi-circular microgroove (dotted arrows). Dashed arrows indicate the trajectory of a cell.

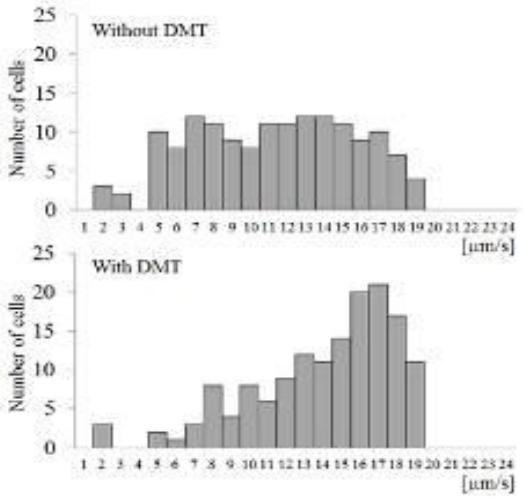

Figure 2. Histograms showing the velocity distribution of 150 cells. Upper: without adding *N*,*N*-dimethyl-*p*-toluidine (DMT). Lower: after adding DMT.

Crossdisciplinary Applications of Microscopy Techniques, e.g. Physic-Life Science Interfaces

MIM.7.P112
A new level-dependent noise reduction method applied to high resolution SEM images

S. Kockentiedt[1], U. Gernert[2]

[1]Otto-von-Guericke-Universität, Institut für Simulation und Graphik, Magdeburg, Germany
[2]Technische Universität Berlin, Zentraleinrichtung Elektronenmikroskopie (ZELMI), Berlin, Germany

stephen@isg.cs.uni-magdeburg.de
Keywords: scanning electron microscopy, SEM, noise reduction, noise estimation, Poisson noise, shot noise

State of the art scanning electron microscopes (SEM) are equipped with in-lens detectors which clearly separate between SE- and BSE-signals and even perform energy filtered electron detection. This gives the ability to investigate a wide spectrum of samples from metals to organics with low atomic number and poor contrast like carbon nanotubes or insulating materials like organic layers in thin film transistors. But there are several acquisition conditions leading to a low number of detected electrons:

- To keep the interaction volume of the detected electrons small, we have to use a low accelerating voltage.
- To prevent the sample from radiation damage and contamination, the probe current must be set very low.
- In order to not modify the sample surface, there is no sputter coating with gold or other metals.
- To avoid charging of non-conductive samples, the scan speed has to be fast.

The low electron count produces a weak signal, which has to be strongly amplified leading to increased image noise.

In [1], a noise estimation method for SEM images is proposed. The basic assumption is that the image intensity I is a linear function of the number of detected electrons C: $I = aC + b$. The parameters of this linear function are changed by the microscope operator using the contrast (a) and brightness (b) settings. The method tries to estimate these parameters so that the strength of the noise can be calculated from the local image brightness. The noise variance $\mathrm{Var}(N)$ is a linear function of the expected image brightness $\mathrm{E}(I)$ depending on the estimated parameters: $\mathrm{Var}(N) = a\mathrm{E}(I) - ab$. This means that the absolute noise level is higher in brighter parts of the image than in darker areas. This kind of noise is called shot noise or Poisson noise. It occurs where independent events such as electrons are counted. Common noise removal methods assume a constant noise strength. This results in filtered images where dark parts are filtered too much whereas bright areas stay noisy. To circumvent this problem, we use a combination of noise estimation from [1], Anscombe transformation [2] and non-local means noise filtering [3] as proposed in [1]. At first, the parameters a and b are estimated. Then, the number of electrons C is recovered: $C = (I - b) / a$. Next, the Anscombe variance stabilizing transformation is applied in order to make the noise level constant. After that, non-local means is applied with h = sqrt(2). As a last step, the Anscombe transformation is reversed and the image intensity is recomputed using $I = aC + b$. Because of the properties of non-local means, the filter does preserve edges as opposed to other common noise removal methods based on smoothing. Even SEM artifacts are preserved which speaks for the filter's ability to remove noise while keeping all other image features. Another side effect of the noise estimation method is that, because it estimates the scaling parameters, it is possible to compute the number of electrons gathered to produce each pixel without any knowledge except the image itself. The employed filter can be applied to any image generated by counting independent events. This means, it can also be applied to X-ray maps or transmission electron microscopy (TEM) images.

The effect of the filter proposed in [1] can be seen in Fig. 1-4. In the filtered image, small features which are concealed in the originally noisy image become visible and thus the effective image resolution is improved. The resolution change for several images is given in Table 1.

The images were recorded with a Hitachi SU8030 SEM with cold field emitter source, equipped with a DISS 5 image acquisition system from point electronic.

1. S. Kockentiedt, K. Tönnies, E. Gierke, N. Dziurowitz, C. Thim and S. Plitzko, "Poisson shot noise parameter estimation from a single scanning electron microscopy image", Proc. SPIE 8655, Image Processing: Algorithms and Systems XI (2013), 86550N.
2. M. Mäkitalo and A. Foi, “A closed-form approximation of the exact unbiased inverse of the Anscombe variance-stabilizing transformation", IEEE transactions on image processing 20 (2011), pp. 2697-2698.
3. A. Buades, B. Coll and J.-M. Morel, “A Non-Local Algorithm for Image Denoising", IEEE Computer Society Conference on Computer Vision and Pattern Recognition 2 (2005), pp. 60-65.

Unfiltered	2.7	2.1	3.2	8.7	4.8	2.9
Filtered	1.9	1.8	2.2	6.0	3.2	2.7

Table 1. Resolution [nm] of several images before and after the noise filter was applied. The images were taken from a gold-on-carbon sample, using variable accelerating voltages, probe currents and detector signals, thus leading to different noise levels.

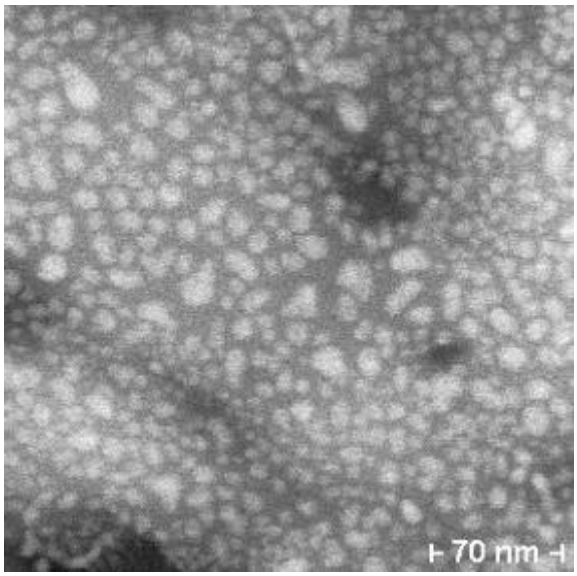

Figure 1. Detail of an original BSE image of gold-sputtered magnetic tape

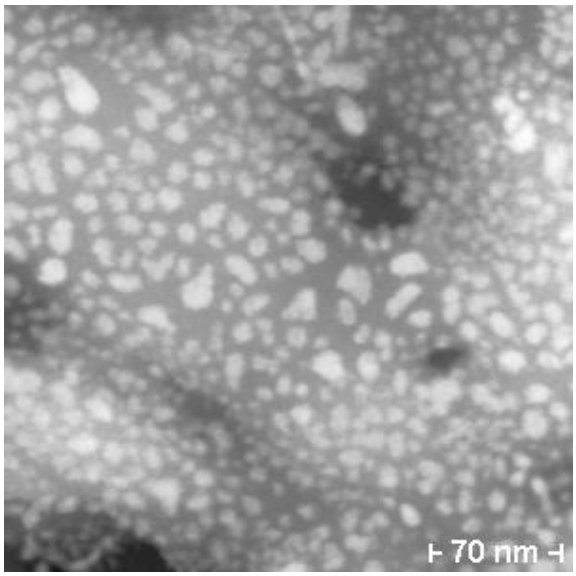

Figure 2. Detail of the filtered BSE image of gold-sputtered magnetic tape

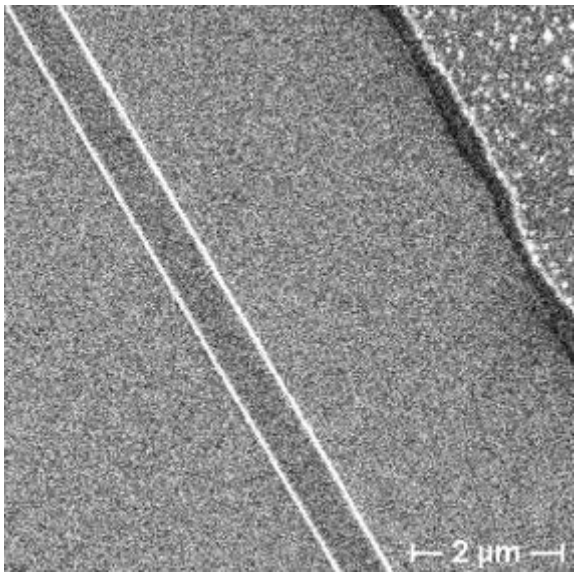

Figure 3. Detail of an original in-lens SE image of silicon etch structures

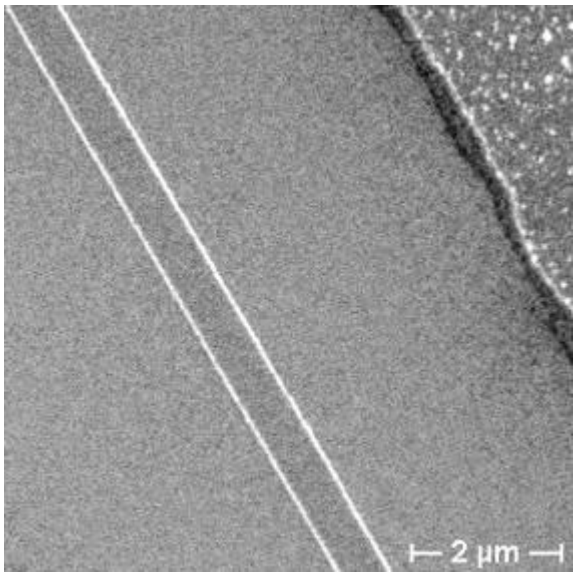

Figure 4. Detail of the filtered in-lens SE image of silicon etch structures

Open Topics

LBP.MIM.P01
Sem of *in Situ* Microbial degradation of Biopol®-based plastic materials

M. Matavulj[1], D. Radnović[1], M. Karaman[1], H.P. Molitoris[2]

[1]University of Novi Sad, Department of Biology and Ecology, Faculty of Sciences, Novi Sad, Serbia
[2]University of Regensburg, Botanical Institute, Faculty of Sciences, Regensburg, Germany

milan.matavulj@dbe.uns.ac.rs
Keywords: SEM, BIOPOL, in situ, biodegradation

Summary. Biodegradability of BIOPOL®-based plastic have been investigated *in situ* by scanning electron microscopy (SEM). It has been shown that the best conditions provided for expression of microbial degradative potential are those in bank mud of the River Danube where the annual weight-loss of the plastic samples of about 63% has been recorded. Judging by quantitative composition of microbial population it may be concluded that the principal role in biodegradation-process occurring in Danube water play bacteria. On the other hand, degradation in terrestrial environments was found to be result of a joint activity of both bacteria and fungi.

Introduction. Studies motivated by replacement of biologically undegradable materials with degradable ones have been intensified recently. Biodegradable plastics based on copolymer of poly-β -hydroxybutyrate (PHB) and poly-β-hydroxyvalerate (PHV), under the trade name BIOPOL® [1] has been designed and commercialized as packaging material. Some of them are designed as completly biodegradable; others are designed by blending and mixing more or less compatible hemosynthetic and biosynthetic materials, becoming partially degradable. These consisting mainly of nondegradable with only small percentage of biodegradable components have been designated as biodestructible ones [2]. Being aware of the potential pollution problems caused by introducing this new materials into our environment, a research has been focused on biodegradability of those plastics under conditions in which, used and discarded, they probably would be degraded by microbial enzymes. Part of this research was published earlier [3,4]. In this paper the focus is on microorganisms potentially responsible for biodegradation of these materials in water and bank mud of the river Danube, as well as in the Danube bank meadow and forest soils.

Material and methods. Preweighted samples of BIOPOL® have been exposed to the microbial enzymes in 30-40 cm depth and investigated at five-weeks intervals. The investigation had started in April, and ended in March next year. The weight loss was followed gravimetrically and qualitative changes of material were determined by scanning electron microscopy. The qualitative and quantitative composition of samples from surrounding microbial population were investigated by counting aerobic saprotrophic bacteria and fungal particles [2]. In order to obtain comparable results on microbial density/activity from four different aquatic, terrestrial and intermediary environments all nonaquatic original natural samples were brought to 100% water saturation and therefore brought to the comparable parameters ($1cm^3$ = 1g). The soil samples were passed through the fine sieve; saturated by sterile tap water (until the first surplus drop of water appeared set apart of soil sample) and then homogenized under the aseptic conditions. 1g of each pretreated sample was then diluted in 9ml of sterile tap water and sonicated 5x1 min with intermittent stirring and cooling for 1 min each. Serial dilution of the resulting suspension were plated onto appropriate media and incubated at 22^oC. The obtained results allowed the comparison of data for different: water, river bank mud, and bank meadow- and forest soils of the complex River Danube ecosystem [3, 4].

Results and discussion. After one-year-period of exposing BIOPOL® to *in situ* microbial action, the most intensive biodegradation was recorded in bank mud of Danube (about 63% of sample weight-loss), than in Danube water (about 30%), while soil samples offered less favourable conditions: meadow soil about 17% and forest soil about 12% (Fig.1) The results of statistical analysis of accompanied bacteria potentially responsible for BIOPOL® degradation are shown in Fig. 2. The highest annual ratio of saprotrophic bacteria was recorded in meadow soil while the lowest values were found to be the characteristics of the Danube water. The number and the seasonal dynamics of mycopopulation is shown in Fig. 3. Differences in quantitative composition of this part of microbial population in different environments were found to be more clear than in the case of bacteria, although in this case the highest number of the fungal particles and active fungi were also recorded in meadow soil, while the lowest annual rates were found to be the characteristics of Danube water.

Conclusion. On the basis of characteristics of microbial population in the investigated environments, it could be concluded that the principal role in degradation of the plastic samples in Danube water play bacteria (Fig 5), and that the most intensive BIOPOL® biodegradation in bank mud of the river is a result of synergistic activity of both bacterial and fungal enzymes. Important role of fungi in biodegradation of this material in investigated natural conditions was confirmed by SEM analysis of the plastic samples (Fig 6). The lack of correlation between the intensity of BIOPOL® degradation and the number of investigated groups of microorganisms shows the importance of other, first of all, abiotic ecological factors (humidity, temperature, pH), providing conditions for the expression of microbial degradable potentials.

1. ICI (Imperial Chemical Industries), Bioproducts and Fine Chemicals, Biopolymers group, Billingham, Cleveland, UK (1990): ICI Information Leaflet.
2. M. Matavulj and H.P. Molitoris (1992): Fungal degradation of polyhydroxyalkanoates and a semiquantitative assay for screening their degradation by terrestrial fungi. - FEMS Microbiol. Rev., 103: 323-332.
3. M. Matavulj, S.T. Moss, and H.P. Molitoris (1993): Degradation of Poly-3-hydroxyalkanoate-based plastics in natural environments. - Proc. Int. Symp. Bact. Polyhydroxyalkanoates (Schlegel, H.-G. and Steinbüchel, A., Eds.), Goltze-Druck, Göttingen, pp. 465-466.
4. Matavulj M., Molitoris H.P. (2000): Biodegradation of polyhydroxy-alkanoate-based plastic (BIOPOL) under different environmental conditions – I. weight loss of substrate. Hoppea, 61, 735-749.

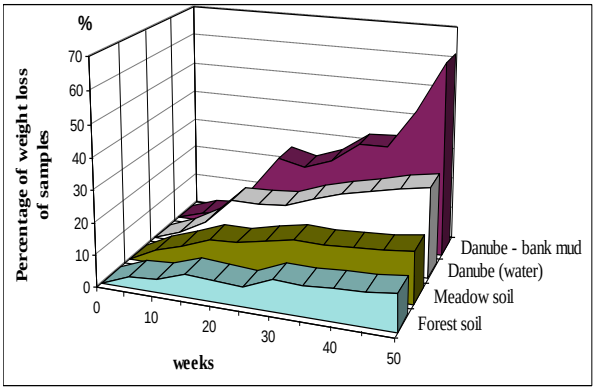

Figure 1. In situ biodegradation of biosynthetic plastic BIOPOL

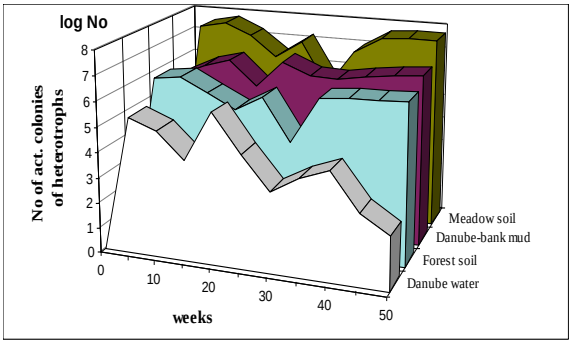

Figure 2. Number of saprotrophic bacteria potentially responsible for degradation of BIOPOL in different environmental conditions

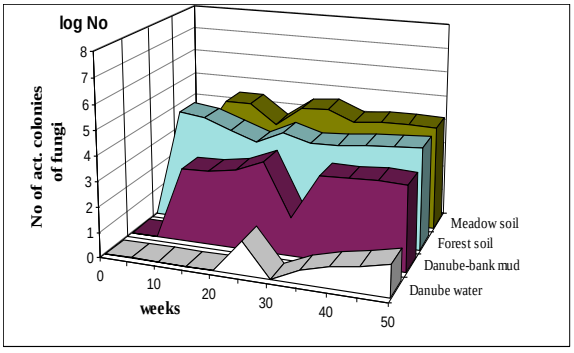

Figure 3. Number of particles of mycelial fungal potentially responsible for degradation of BIOPOL in different environmental conditions

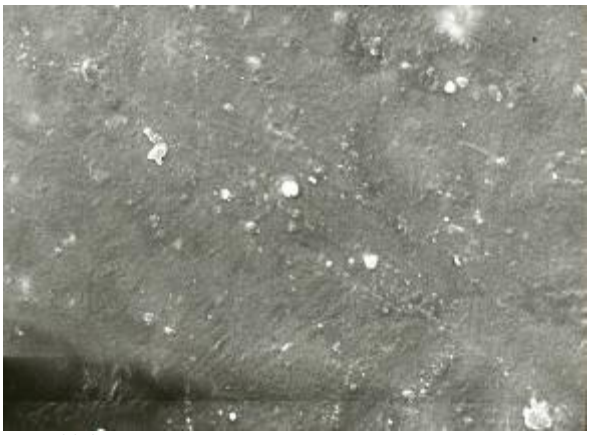

100.0 µm

Figure 4. Surface of BIOPOL plastic not exposed to microbial degradation

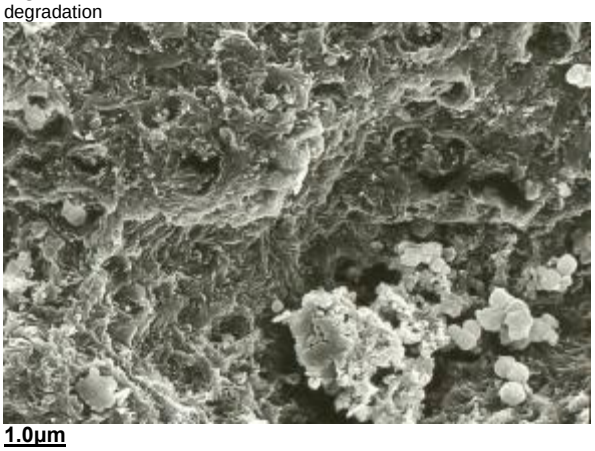

1.0µm

Figure 5. Dominating bacteria in the Danube water, by their enzyme action, caused superficial crater-like erosion of BIOPOL samples

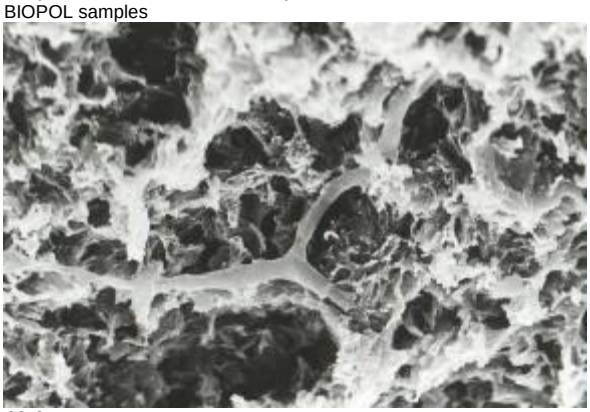

10.0 µm

Figure 6. Dominating mycelial fungi in soil samples, by their enzyme action, caused deeper degradaton of the core of BIOPOL samples

Open Topics

LBP.MIM.P02
Sem Of Microbial Degradation Of Biopol®-Based Plastic Materials In Wastewater Purification Plant

M. Matavulj[1], M. Karaman[1], D. Radnović[1], H.P. Molitoris[2]

[1]University of Novi Sad, Department of Biology and Ecology, Faculty of Sciences, Novi Sad, Serbia
[2]University of Regensburg, Botanical Institute, Faculty of Sciences, Regensburg, Germany

milan.matavulj@dbe.uns.ac.rs
Keywords: SEM, BIOPOL, in situ, biodegradation

Summary. Biodegradability of BIOPOL®-based plastic have been investigated *in situ* in municipal wastewater treatment plant by scanning electron microscopy (SEM). It has been shown that the best conditions provided for expression of microbial degradative potential are those in the pool for aerobic wastewater post-treatment. According to the quantitative composition of microbial population it may be concluded that the principal role in biodegradation process occurring in wastewater treatment plant play bacteria, but, on the other hand, the highest biodegradation rate was found in the basin where microfungi were the most abundant (documented by SEM).

Introduction. Biodegradable plastics based on copolymer of poly-β -hydroxybutyrate (PHB) and poly-β-hydroxyvalerate (PHV), under the trade name BIOPOL® [1] has been designed and commercialized as packaging material. Some of them are designed as completly biodegradable; these consisting mainly of nondegradable with only small percentage of biodegradable components have been designated as biodestructible ones [2]. Increased awareness of potential new type of environmental contamination initiated our research of biodegradation of these new plastic materials under conditions in which, used and discarded, is likely to be subjected to biodegradable processes [3]. In addition, PHA, as a solid or granular organic mater, was proposed for use in potable water treatment [4]. Since in the municipal wastewater purification process are involved microorganisms adapted to high concentrations of difficult to degrade pollutants, we were interested to see the potential of the indigenous microbial population, especially microfungi, in terms of biodegradation of these new potential polluters of the environment.

Material and methods. Municipal wastewater treatment plant in Regensburg (Germany) as a multi-stage modern system was chosen for the research of the rate of biodegradation of "BIOPOL®-based plastic samples": 1 - Flotation-sedimentation basin; 2 - Aeration basin with active sludge; 3 - Pool with aerobic post-treatment and 4 - Plastic container, volume of about 200 liters with activated sludge colected from the anaerobic bioreactor. Preweighted samples have been exposed to the microbial enzymes in 30-40 cm depth and investigated at five-weeks intervals. The investigation had started in April, and ended in March next year. The weight loss was followed gravimetrically and qualitative changes of material were determined by SEM [2].

Results and discussion. With regards to the Danube water, as a recipient of treated wastewater, in which in the frame of one year weight loss of the BIOPOL®-based plastic sample was approximately 30% [5]., in three stages of wastewater purification plant, biodegradation in the same period was nearly completed in flotation-sedimentation basin and in aeration basin of the activated sludge, and completed in the basin for aerobic post treatment. The low level of biodegradation in plastic container with activated sludge originating from anaerobic bioreactor (16%) is probably caused by disturbed, semianaerobic conditions and due to the exposure to significant temperature fluctuations (Tab.1). According to the annual averages, the highest number of heterotrophic mesophilic bacteria was recorded in the pool with the agitated aerated activated sludge (2,197.000.000 cfu/ml), followed by sedimentation-flotation basin (552 million cfu/ml) and finally 152.300.000 cfu/ml in the pool for aerobic posttreatment. A similar correlation was found between the rate of degradation and percentage of active microfungi (Tab 1, Fig. 1), which testifies to the joint action of these two groups of microorganisms in BIOPOL®biodegradation.

The importance of fungi in the degradation of this material was confirmed earlier for molds [3]. In the water of the investigated treatment plant, among active fungi were dominant yeasts, best adapted to the conditions of liquid environment (Fig. 2). A high degree of correlation between the number of active microbes and BIOPOL® degradation rate testifies on the joint action of bacteria and fungi in studied environments. The low level of biodegradation of plastics in semianaerobic conditions of activated sludge (16.3%) can be explained by the complete absence of active microfungi.

Conclusion. On the basis of characteristics of microbial population in the investigated environments, it could be concluded that the principal role in degradation of the plastic samples in municipal wastewater purification plant play bacteria, but the most intensive BIOPOL® biodegradation is a result of synergistic activity of both bacterial and fungal enzymes. Important role of fungi in biodegradation of this material in investigated natural conditions was confirmed by SEM analysis of the plastic samples.

1. ICI (Imperial Chemical Industries), Bioproducts and Fine Chemicals, Biopolymers group, Billingham, Cleveland, UK (1990): ICI Information Leaflet.
2. M. Matavulj and H.P. Molitoris (1992): Fungal degradation of polyhydroxyalkanoates and a semiquantitative assay for screening their degradation by terrestrial fungi. - FEMS Microbiol. Rev., 103: 323-332.
3. M. Matavulj, S.T. Moss, and H.P. Molitoris (1993): Degradation of Poly-3-hydroxyalkanoate-based plastics in natural environments. - Proc. Int. Symp. Bact. Polyhydroxyalkanoates (Schlegel, H.-G. and Steinbüchel, A., Eds.), Goltze-Druck, Göttingen, pp. 465-466.
4 Wurmthaler, J., Müller, W.,R. (1992): Use of PHB/PHV in Water Treatment. Proc. Int. Symp. Bact. PHA. (Schlegel, H.G. and Steinbuchel Ed.) Goltze-Druck, Göttingen, pp: 475-476.
5 Matavulj M., Molitoris H.P. (2000): Biodegradation of polyhydroxy-alkanoate-based plastic (BIOPOL) under different environmental conditions – I. weight loss of substrate. Hoppea, 61, 735-749.

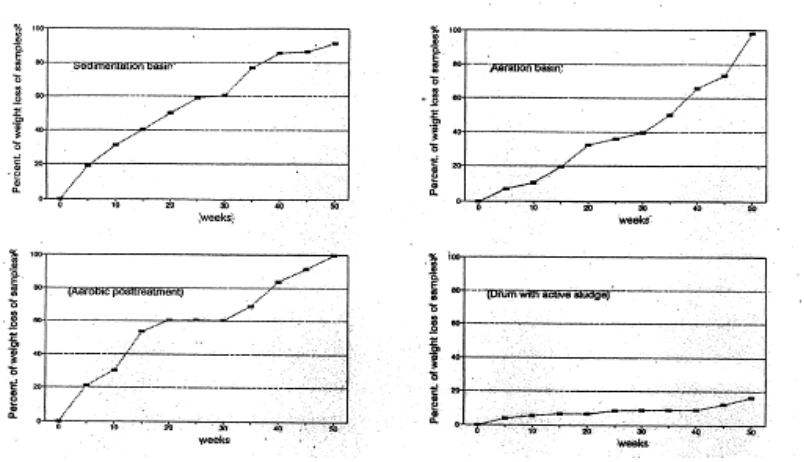

Figure 1. BIOPOL® Biodegradation rate (% of weight loss) in wastewater purification plant

Site	BIOPOL® biodegradation rate (% in 50 weeks)	% of active heterotrophic bacteria	% of active microfungi
Aerobic posttreatment basin	100.00	10.01	13.88
Basin with aerated active sludge	98.30	4.05	9.27
Flotation-sedimentation basin	91.10	2.50	5.00
Container with active sludge	16.31	1.04	0.00

Table 1. Correlation of the percentage of active microorganisms (annual average) and BIOPOL® degradation rate

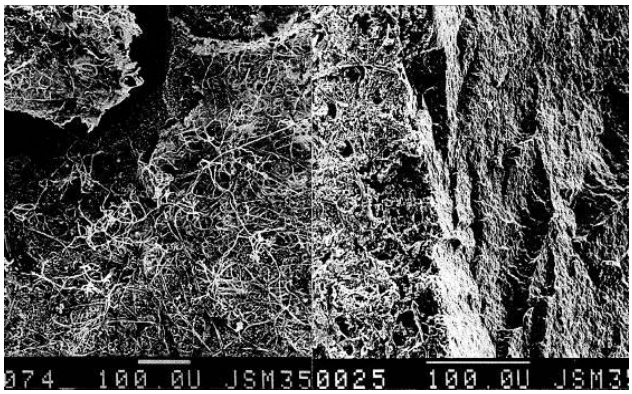

Figure 2. Domination of mycelial microfungi (molds) on the surface of sample from the aerobic posttreatment basin (left) and the domination of yeasts and bacteria on the surface of sample from the flotation-sedimentation basin (right)

Open Topics

LBP.MIM.P03
Molecular architecture and mechanical properties of the kinetochore: a biophysical approach.

J. Gregan[1], I. Tolic-Norrelykke [2], D. Cimini[3]

[1]University of Vienna, Max F. Perutz Laboratories, Vienna, Austria
[2]Max Planck Institute of Molecular Cell Biology and Genetics, Dresden, Germany
[3]Virginia Polytechnic Institute and State University, Biological Sciences, Blacksburg, United States

juraj.gregan@univie.ac.at

Accurate chromosome segregation depends on proper attachment of kinetochores to microtubules. Mounting evidence suggests that mechanical properties of the kinetochore make fundamental contributions to faithful segregation of chromosomes. However, such kinetochore properties have not been experimentally analyzed. Merotelic kinetochore orientation, a major cause of aneuploidy, is an error in which a single kinetochore binds microtubules emanating from opposite spindle poles. During anaphase, merotelically attached kinetochores have a stretched appearance due to pulling forces exerted by microtubules emanating from both spindle poles. We are developing an assay where we use laser ablations to sever one of the microtubule bundles attached to a merotelic kinetochore in anaphase cells. We argue that the change of the kinetochore shape after laser severing should reflect its elasto-plastic properties and our ultimate aim is to establish merotelic kinetochores as a model for studying structural and mechanical properties of the kinetochore in vivo. We will present our progress on developing this assay in both the fission yeast *Schizosaccharomyces pombe* and in mammalian tissue culture cells.

Nanomaterials, Environment, Nanotoxicology & Health

LBP.MIM.P04
New pegylated aliphatic polyesters as biocompatible and thermosensitive nano-carriers and their applications in tumor-targeting drug delivery systems

D. Bikiaris[1], V. Karavelidis[1]

[1]Aristotle University of Thessaloniki, Chemistry, Thessaloniki, Greece

dbic@chem.auth.gr
Keywords: aliphatic polyesters, thermosensitive materials, targeting drug delivery systems

Aliphatic polyesters are biodegradable and biocompatible polymers which are nowadays commercially available in a variety of types and are used in pharmaceutical delivery systems [1]. The physical properties of such polyesters, (e.g, melting point or degree of crystallinity), are directly affecting drug release behaviour [2,3]. This study is taking advantage from the low melting point of the prepared materials which is near to human body (42-43^{o}C) in order to prepare thermosensitive nanoparticulate systems. The aim of the study is to achieve higher release rate of the anticancer drug paclitaxel from the nanoparticles at 42^{o}C, which is used during mild hyperthermia therapies, compared to 37 ^{o}C, which is the normal temperature of human body. This selective release can lead to controlled and targeted anticancer activity of such pharmaceutical systems reducing the side effects of the cytotoxic active ingredient [4].Copolymers were synthesized using methoxy polyethylene glycol (mPEG) and poly(propylene adipate) (PPAd) with different molecular weights. The used mPEG polymers had a molecular weight of 750 and 2000 Da and the PPAd polymers had intrinsic viscosity values [η]=0,20 and [η]=0.38. The morphology of these copolymers was studied with Scanning Electron Microscopy (SEM), Figure 1. The mPEG-PPAd copolymers were used to prepare core-shell paclitaxel loaded nanoparticles. The particles size of the prepared nanoparticles is a critical parameter affecting the dissolution behaviour of such drug delivery systems and was studied by two ways, by Dynamic Light Scattering (DLS) and by SEM. The prepared nanoparticles have a mean diameter of 100-200nm according to SEM and DLS results shown in Figure 2.

In vitro dissolution analysis was performed at both 42 ^{o}C and 37 ^{o}C in order to study the thermosentivity of the prepared nanoparticles. The release rate was found to be higher at 42 ^{o}C compared to 37 ^{o}C showing that the prepared copolymers can be used as thermosensitive drug nanocarriers for targeting release applications (Figure 3). It was also shown that the release rate is not only affected by the melting point of the polymers, it is affected by the used polymers molecular weight and degree of crystallinity as well. In-vitro cytotoxicity studies were performed in HepG2 and HeLa cell cultures in order to determine the effectiveness of these nanoparticulate systems against the selected cancer cells. The control, placebo and Paclitaxel loaded samples were observed by reverse phase microscopy and photos were taken at the time point that the effect on the cancel cells was clear. In the case of HepG2 cell cultures Trypan Blue was added after the incubation in order to obtain the cells that are in the necrosis or apoptosis stage. According to the in vitro cytotoxicity it was shown that cell cultures remained unaffected by placebo nanoparticles but when the paclitaxel loaded nanoparticles were used over 80% of the HeLa cells were found to be in the phase of necrosis (Figure 4).

It can be concluded that the studied copolymers could be used as thermosensitive nanocarriers in tumor-targeting drug delivery systems.

1. Chasin M, Langer R. Biodegradable polymers as drug delivery systems. Marcel Dekker Incorporated, 1990, 347 pages.
2. Karavelidis V, Giliopoulos D, Karavas E, Bikiaris D, Eur J Pharm Sci 41 (2010): 636-643
3. Karavelidis V, Karavas E, Giliopoulos D, Papadimitriou S, Bikiaris D, Int J Nanomedicine 6 (2011): 3021–3032.
4. Karavelidis V, Bikiaris D, J Nanomedic Nanotechnol (2012), 3:134.
5. The authors wish to acknowledge co-funding of this research by European Union- European Regional Development Fund and Greek Ministry of Education/EYDE-ETAK through program ESPA 2007-2013 / EPAN II / Action “SYNERGASIA” (09SYN-41-659).
6. We kindly acknowledge the help of the organizers of MC 2013 with the online submission procedure.

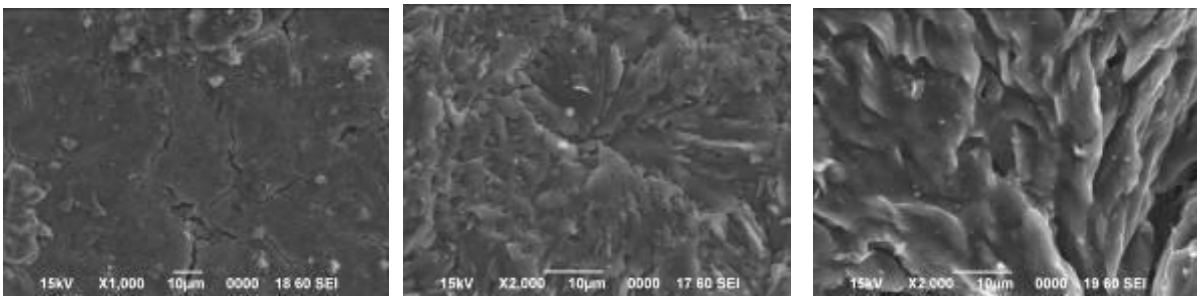

a) b) c)

Figure 1. Morphology according SEM micrographs of a) PPad0.38 pure polymer b) mPEG750-PPAd0.38 copolymer and c) mPEG2000-PPAd0.38 copolymer.

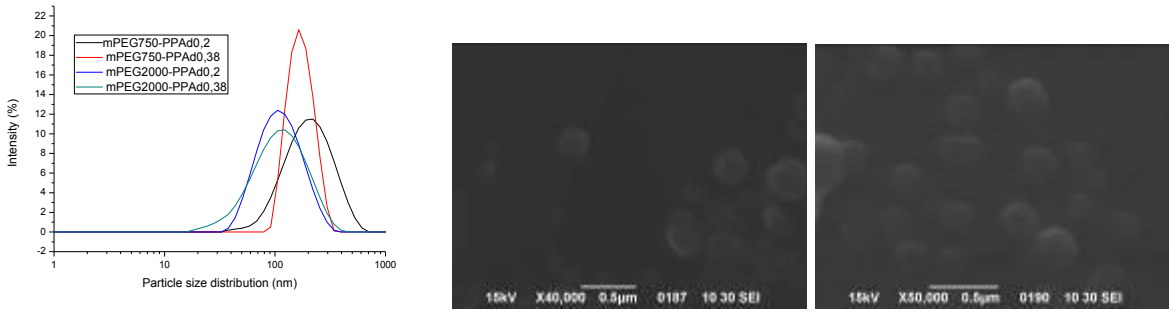

a) b) c)

Figure 2. a) particle size distribution of nanoparticles prepared by the copolymers according to DLS b) SEM micrograph of mPEG2000-PPAd0.38 paclitaxel loaded nanoparticles and c) SEM micrograph of mPEG750-PPAd0.38 paclitaxel loaded nanoparticles

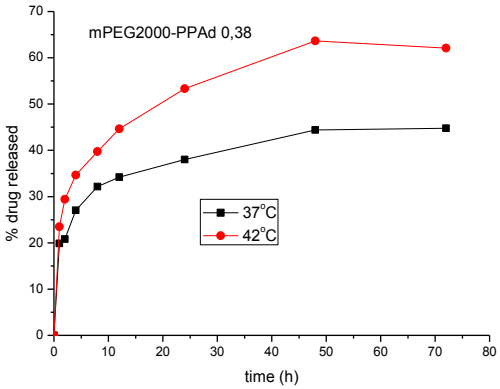

Figure 3. Representative comparative dissolution profile of mPEG2000-PPAd0.38 paclitaxel loaded nanoparticles at 37°C and 42°C. Higher dissolution rates were observed at 42°C

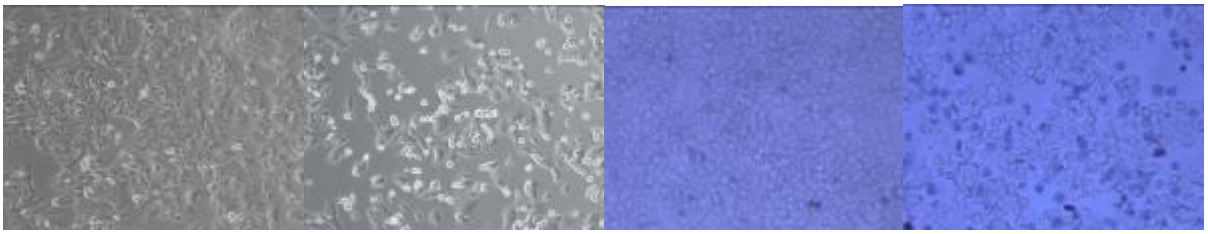

a) b) c) d)

Figure 4. a) HeLa cells treated with mPEG2000-PPAd0.2 placebo nanoparticles, b) HeLa cells treated with mPEG2000-PPAd0.2 paclitaxel loaded nanoparticles, c) Tryptan Blue addition after incubation on cells treated with mPEG2000-PPAd0.2 paclitaxel loaded nanoparticles.

Correlative Microscopy in Life and Materials Science

LBP.MIM.P05
Delamination buckling of thin metallic film studied by digital holographic light microscope interferometry

O. Milat[1], N. Demoli[1], N. Radić[2]

[1]Institute of Physics, Zagreb, Croatia
[2]Rudjer Boškovic Institute, Zagreb, Croatia

milat@ifs.hr
Keywords: holographic interferometry, thin film delamination pattern

Here, we present an application of our Digital Optical Holographic Microscope (DOHM) [1] in the study of morphology and topography of buckling patterns that can be observed on thin film, during or after its delamination from thick substrate [2]. For deposition of tungsten thin films by magnetron sputtering [3], it is well known that argon pressure significantly affects the film internal stress. In the case of tensile residual stress a network of through-thickness cracks forms in the film, while the residually compressed thin films may delaminate from substrate and buckle [4]. As it is shown in Figure 1, buckling of thin tungsten film can result in a number of topographical patterns such as disordered surface wrinkles, regular herringbone, straight-sided or telephone cord buckles and circular blisters [5]. The associated mechanics has been studied [6] and evaluated for a number of cases of all types of buckles (circular, straight-sided, ...), but for the telephone cord (TC) ones, more precise microscopic observation (complemented by topographic measurements) are still needed for testing the corresponding models [6]. Delamination usually start as straight-sided linear blisters, but then deviate to the TC periodic wavy geometry due to the fact that the compressive residual stress in the film is biaxial. In general, buckling profiles can be characterized depending on scale, by mechanical or laser-scanning profilometry, optical interferometer microscopy, or by using an atomic force microscope [7].

Our DOHM is a home-adapted commercial metallurgical instrument. It is an extended set-up that provides simultaneous or alternative white-light or monochromatic illumination. A parallel arm is added for the interference of object and reference beams, plus an extra arm for hologram reconstruction. The later is fitted by a LCOS display operated in real-time via PC; coupled pair of CCD cameras enables acquisition of the corresponding images [1]. Two pairs of independent sources (laser plus LED) are implemented: one for imaging, and one for hologram reconstruction. This set-up provides traditional microscopic imaging in succession with holographic imaging and the real-time optical reconstruction, as well as processing and correlation of digital images. Figure 2. displays traditional microscopic and correlative holographic interferometry data (λ/2-fringes) of the very same object area.

White-light microscopy of top surface of highly compressed tungsten thin film clearly reveals (at lower magnification: <500X), lateral morphology of the buckling patterns Figure 1. At higher magnification (>500X), reduction of focus depth affects imaging contrast, so that the lateral as well as vertical wrinkles` features can hardly be measured down to submicron precision, as is represented in Figure 2. By imaging and optical processing in holographic mode, one can display interferometric fringes patterns that reveal lateral and vertical buckling features with precision: $\Delta l \approx \Delta h \approx 0.3$ μm. Correlation of traditional microscopy and holographic interferometry of the very same imaging area can provide data basis for quantitative 3-D modeling of TC buckling morphology and associated stress-strain mechanics.

1. N. Demoli, and O. Milat, in preparation (not to be published yet).
2. L.B. Freund and S. Suresh in “Thin Film Materials”, Cambridge University Press, 2003, pp 86-153
3. N. Radić, B. Gržeta, O. Milat, J. Ivkov, and M. Stubičar, Thin Solid Films 320 (1998), 192–197
4. A.A. Volinsky, P. Waters, and G. Wright, Mat. Res. Soc. Symp. Proc. Vol. 855E, (2005), W3.16.1
5. J.W. Hutchinson, M.D. Thouless, and E.G. Liniger, Acta Metall. Mater. 40 (1992) 295-308.
6. J-Y Faou, G. Parry, S. Grachev, and E. Barthel, PRL 108 (2012), 116102
7. M.W. Moon, H.M. Jensen, J.W. Hutchinson, K.H. Oh, and A.G. Evans, Journal of the Mechanics and Physics of Solids 50 (2002) 2351-3159

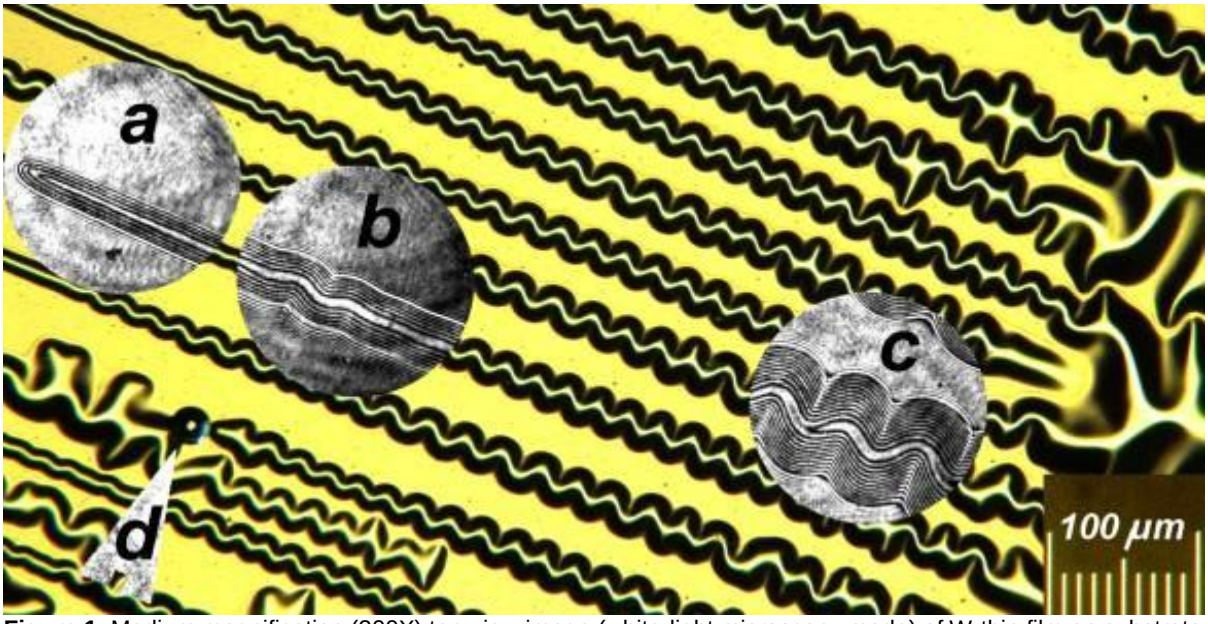

Figure 1. Medium magnification (200X) top-view image (white-light microscopy mode) of W-thin film on substrate revealing straight-sided and TC buckles (insets: a, b, c), as well as disordered surface wrinkles and a circular blister (arrowhead: d). Insets (magnification: 500X) represent interferometric fringes recorded by monochromatic-light holography mode).

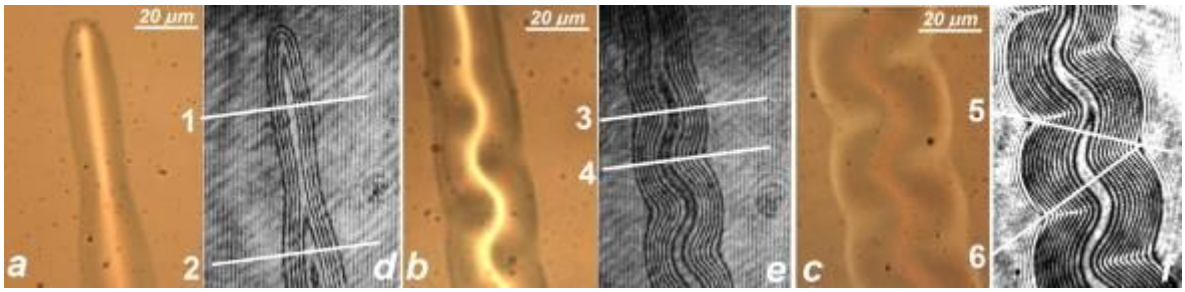

Figure 2. Correlative images of straight and TC delamination buckles in W-thin film (like in Fig.1.), with the corresponding interferometric fringes patterns (d, e, f) as recorded by reconstruction and optical processing of holographic images. White lines (1 to 6) indicate traces for heigth profile characterization. Consecutive dark fringes reveal trajectories of constant heigth in steps of Δh ≈ 0.3 µm. Observation magnification (1000X).

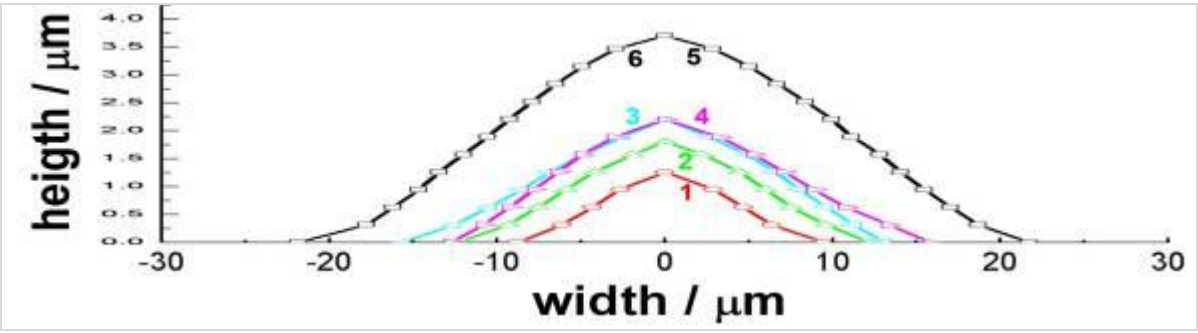

Figure 3. Heigth profiles of straigth-side and telephone-cord buckles from Fig.2. Labels 1 to 6 correspond to traces marked in Fig.2. Profile symmetry along the median line for straight buckle starts to deviate with lateral waviness in the case of TC buckles as revealed for traces 3 & 4.

Nanomaterials, Environment, Nanotoxicology & Health

LBP.MIM.P06
Microscopy study of graphene oxide based multilayer microcapsules and cell uptake.

G. Wang[1], Y. Yang[1]

[1] King Abdullah University of Science and Technology, Imaging and Characterization Core Lab, Thuwal, Saudi Arabia

Keywords: microscopy, graphene oxide, microcapsule, cell uptake

Layer-by-layer (LBL) assembled microcapsules have been well studied and played an important role in drug and other biomacromolecules delivery systems for cancer therapy and cell imaging. Recently, graphene oxide (GO) based microcapsules has attracted great research interest because of its unique permeability properties [1]. Moreover, extraordinary chemical, optical, electrical and mechanical properties of graphene can also be introduced into microcapsules [2]. Therefore, GO based microcapsules can be developed as remote controlled release system with unique release kinetics [3]. Herein, we prepared branced polyethylenimine/graphene oxide (bPEI/GO) hybrid microcapsules using a sacrificial poly(styrene sulfonate)-doped $CaCO_3$ (PSS-doped $CaCO_3$) as template (Scheme 1). Moreover, we investigated Internalization of bPEI/GO microcapsules by Hela cells using confocal laser scanning microscopy (CLSM), transmission electron microscopy (TEM), scanning electron microscopy (SEM) and Raman microscopy.

PSS-doped $CaCO_3$ particles were prepared according to the previous literature [4]. bPEI/GO microcapsules were prepared by layer-by-layer assembly of positively charged bPEI and negatively charged GO. This bilayer assemble was repeated for 3 times and followed by EDTA (pH 7.0) washing to remove $CaCO_3$. Two strong peaks, so-called D and G bands, were observed at around 1350 and 1580 cm^{-1}, respectively (Fig. 1 B), suggesting that multilayer graphene has been assembled in microcapsules while the bright field image showing a hollow sphere structure (Fig. 1 A). The collapsed structure of microcapsules captured with a SEM was formed by air dry during preparation may tell the hollow core of microcapsules (Fig. 1 C). Moreover, the TEM image of a ~80 nm thickness section of epoxy embedded microcapsules showing a closed round circle indicated the removal of $CaCO_3$ core and capability of carrier (Fig. 1 D).

For cellular uptake and subcellular localization tests, Hela cells were seeded in petri dish and cultured at 37 °C. The bPEI/GO microcapsules were added to dish when they reached around 70 % confluence. After 24 hours incubation at 37 °C, cells were fixed and prepared separately for SEM and TEM study. The cytoplasm membrane and nucleus were stained first before adding microcapsules for LSCM study following Du's method [5] with miner modification. The size of cells and microcapsules can be observed contradistinctively from a LSCM image (Fig. 2A). Cellular uptake of microcapsule by cell was captured with a 1 hours live imaging after 1 hour incubation with microcapsules, determining the microcapsule may relocate cytoplasm of cell (Fig. 2 B~F). A ~80 nm thickness section of cells shows that the microcapsule was taken up to a cell causing nucleus deformed (Fig. 1 E). The image of microcapsule inside cell determines that cellular uptake may be done with a different mechanism rather than endocytosis since the internal microcapsule doesn't have a membrane shell (Fig. 1 E). The SEM images show that the microcapsules were stick to the cells (Fig. 1 F).

Generally, the bPEI/GO microcapsules were fabricated LBL assembly and studied with multi microscopy, showing that it may be an efficient carrier for cellular drug, protein or gene delivery applications.

C. Du, J. Zhao, J. Fei, Y. Cui, Junbai Li.

1. R. Kurapatia and A. M. Raichur. ***Chem. Commun.***, 2012, **48**, 6013-6015.
2. Y. Jin, J. Wang, H. Ke, S. Wang, and Z. Dai. ***Biomaterials.*** 2013, 34, 4794-802.
3. R. Kurapatia and A. M. Raichur. ***Chem. Commun.***, 2013, **49**, 734-736.
4. W. Tong, W. Dong, C. Gao, and H. Mohwald. ***J. Phys. Chem. B.***, 2005, 109, 13159-13165.
C. Du, J. Zhao, J. Fei, Y. Cui, J. Li. ***Advanced Healthcare Materials***, 2013, doi: 10.1002/adhm.201200414.

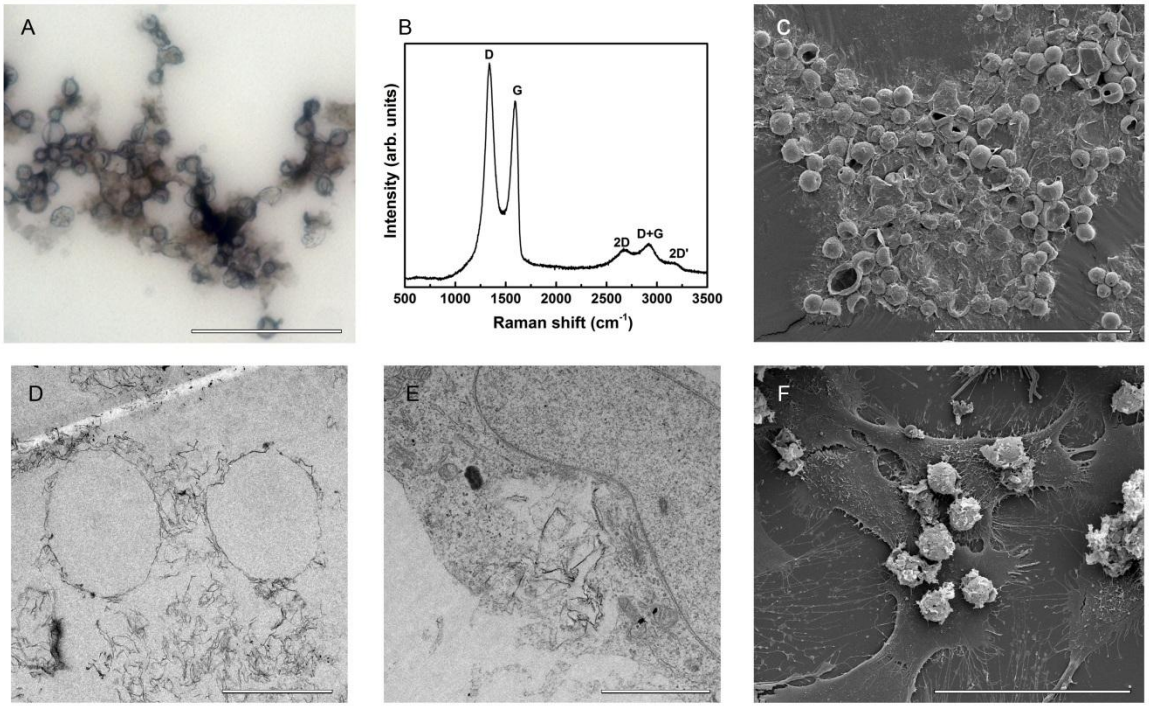

Figure 1. Multi microscopy images of bPEI/GO microcapsules: A, bright field image of air dried microcapsules; B, Raman scatting spectra; C, SEM image of air dried microcapsules; D, TEM image of a around 80 nm thickness section image of microcapsules; E, TEM image of sliced microcapsules inside a Hela cell; F, SEM image of Hela cells after incubated with microcapsules for 24 hours. Scale bar: A, C, F, 50 μm; D, 5 μm; E, 2 μm.

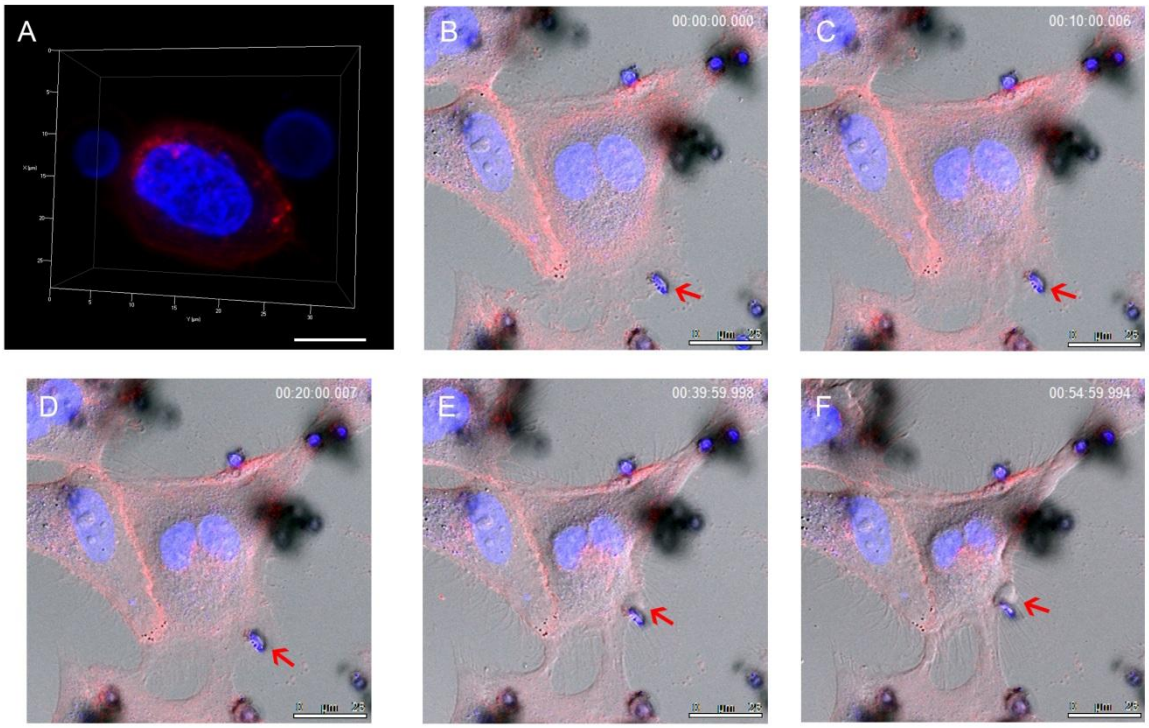

Figure 2. Laser scanning confocal microscopy images of Hela cells incubated with bPEI/GO microcapsules: A, 3D image of stained cell and micro capsules; B-F, live images of cells uptake microcapsules with a vesicle (red arrow) within 60 minutes after 1 hour incubation. Scale bar: A-F, 25 μm.

Emerging Techniques in Modern Microscopies

LBP.MIM.P07
Simultaneous detection of scattering angles for Scanning Transmission Electron Microscopy using a segmented diode-detector with dedicated High-Angle Annular Dark-Field view

M. Aliman[1], R. Arnold[1], W. Berger[1], S. Meyer[1]

[1]Carl Zeiss, Microscopy GmbH, Oberkochen, Germany

michel.aliman@zeiss.com
Keywords: 4 video-output STEM

Scanning Transmission Electron Microscopy (STEM) is a powerful tool to analyze sub-nanometer structures of materials. The sample is usually prepared in very thin lamellas in a Scanning Electron Microscope equipped with a Focused Ion Beam (e.g. in a Crossbeam), then transferred in a TEM-device for highest-resolution material analysis. In many applications though where low landing energy is required and/or where no ultimate resolving power is needed, it is a great advantage to make an in-situ STEM-analysis on the same instrument to reduce cost, analysis-time and risks of material-degradation. For the detection of different scattering angles a large and segmented photo-diode with low threshold energies of a few hundreds of electron-volts is used; the segmented photo-diode is composed of a bright-field segment (for small transmission angles) and several dark-field segments (for high and very high transmission angles) (see Figure 1) [1]. Usually these segment-views are unfortunately sequentially scanned for STEM-analysis. Furthermore, given that the maximum achievable scan-speed (pixel-frequency or inverse of pixel-dwell-time) decreases with the capacity of the diode-segment in use - this capacity strongly increases with the transmission angle - the scan-speed becomes even much lower for very high transmission angles. As a result only very low scan-speeds can be achieved: This significantly increases the exposure-time of the sample (high sample dose), which can damage beam-sensitive and charging samples. A further negative effect is the signal-drift due to the very low sequential reading of the transmission angles.

We present a simultaneous detection of different transmission angles, which enables a fast imaging of all signals, even for the outer High Angle Annular Dark Field HAADF, in order to minimize drift and the exposure-time of the sample; the novel detection method makes use of a low noise, low-drift and wide-band quad-video-output amplifier [2], which has been especially designed for STEM-applications, to ensure a perfect correlation of imaging frames for all transmission angles (sample-position and sample-status are the same for all transmission modes).

The detector acceptance angles are configurable and all diode-segments can be arbitrarily combined for an optimal matching of scattering and acceptance angles. Each video-output can deliver trans-impedance-gains up to 194 dB□□(200pA diode current is amplified to a full scale 1V video-output signal!) while ensuring a high signal-to-noise ratio.

High speed processing (with a pixel dwell-time down to 50 ns!) enables fast sample navigation and quick finding of regions of interest (e.g. Figure 2a).

Figure 2b shows a high-resolution quad-video image of the new STEM detector at low scan-speed and high gain for different transmission angles, whereas figure 2a demonstrates high scan-speed with still good image-quality (100 ns pixel-dwell-time!).

Further investigations on biological- and material-samples will also show the improvement of image-resolution and scan-speed by means of the simultaneous recording of several transmission angles using the new STEM-electronics and the novel segmented photo-diode.

1. R. Salzer, J. Ackermann, R. Arnold, S. Meyer, C. Kübler; M & M 2013
2. M. Aliman, W. Berger, J. Paluszynski, EMC 2012, Simultaneous Compositional- and/or Topographical Material Analysis using Low Drift and High Speed Four Video-Outputs Backscattered Electron Detector (AsB4), Electron Microscopy Congress Manchester 2012

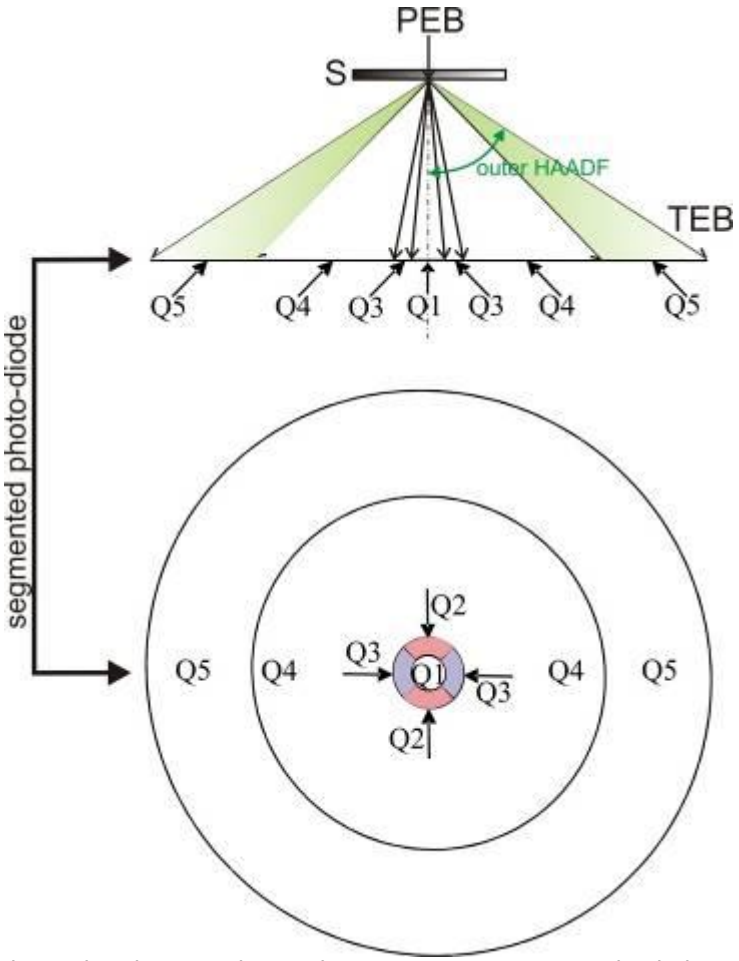

Figure 1. S: sample to be analyzed; PEB: Primary Electron Beam; TEB: Transmitted Electron Beam; segmented photo-diode: Q1: Bright Field BF; Q2 & Q3: Annular Dark Fields ADF; Q4: inner High Angle Annular Dark Field HAADF; Q5: outer High Angle Annular Dark Field HAADF

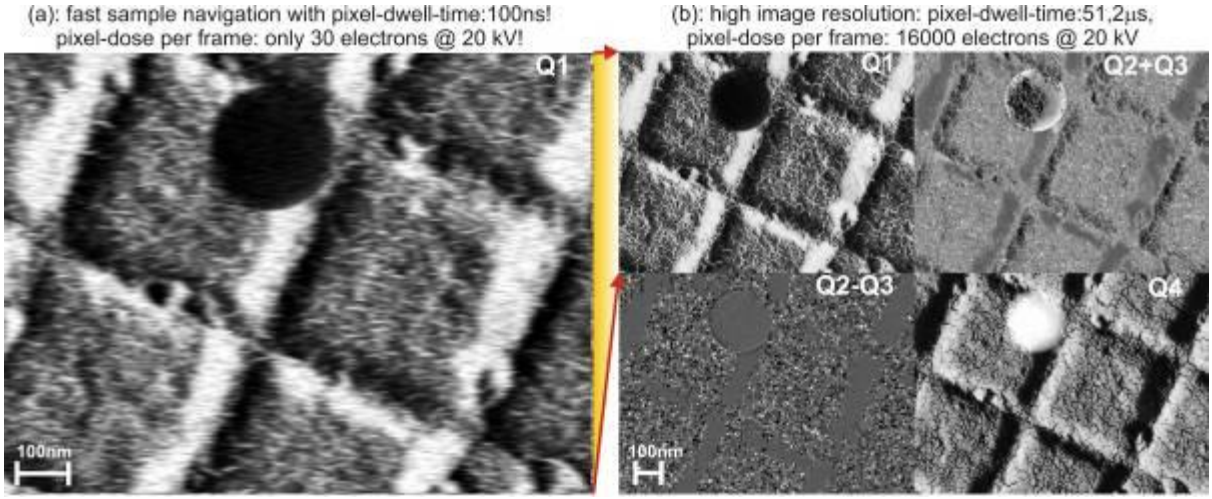

Figure 2. Live quad-view of the STEM-detector (a): at high scan-peed (100 ns dwell-time!) for fast sample navigation using the bright Field Q1 and (b): at low scan-speed (51,2 □s pixel-dwell-time) for high image-resolution. (b): Image of various transmission angles: upper left quad: Bright Field BF (Q1); upper right quad: Annular Dark Field ADF (Q2+Q3); lower quad left: orientation-contrast using the difference-signal of the Annular Dark Field segment (Q2-Q3); lower quad right: inner High Angle Annular Dark Field HAADF (Q4)

Nanomaterials, Environment, Nanotoxicology & Health

LBP.MIM.P08
Visualization of cell-nanoparticle interactions by scanning electron microscopy

K. Loza[1], D. Kozlova[1], M. Epple[1]

[1]University of Duisburg-Essen, Inorganic Chemistry and Center for Nanointegration Duisburg-Essen (CeNIDE), Essen, Germany

kateryna.loza@uni-due.de
Keywords: silver nanoparticles, HeLa cells, scanning electron microscopy

We report on the possibilities of the visualization of inorganic nanoparticles after interaction with cells by means of scanning electron microscopy. Silver nanoparticles were used with the HeLa cell line. PVP-coated silver nanoparticles were synthesized by reduction with glucose in the presence of PVP according to Wang et al [1]. The final silver concentration in all dispersions was determined by atomic absorption spectroscopy. By-products from the synthesis, i.e. nitrate, excess polymer, excess glucose and glucose oxidation products were removed by ultracentrifugation. The particles were analysed by dynamic light scattering, scanning electron microscopy, energy-dispersive X-ray spectroscopy and X-ray powder diffraction. HeLa cells were pre-seeded on the coverslip for 24 hours at 37 °C in a 5% CO_2 atmosphere. The cells were incubated with silver nanoparticles for 1 hour. Cells were fixed with 2.5% glutaraldehyde in phosphate buffer saline (PBS), and then the cells were extensively washed with PBS and dehydrated with a graded ethanol row. After critical-point drying and gold-palladium coating, the samples were observed with FEI Quanta 400 ESEM instrument at a voltage of 15 kV. We observed silver nanoparticles mostly on the cell surface, but in some cases, nanoparticles were detected also in the surface layer. The presence of silver nanoparticles was also confirmed with energy-dispersive X-ray spectroscopy mapping.

5. H. Wang, X. Qiao and S. Ding, 256, (2005) p.111-115.

Nanomaterials, Environment, Nanotoxicology & Health

LBP.MIM.P09
TEM Characterisation of Graphitisation Process of Amorphous Layers in Ion Implanted Diamond

S. Rubanov[1], A. Suvorova[2], V. Popov[3], I. Kupriyanov[4], Y. Pal'yanov[4]

[1]University of Melbourne, Bio21 Institute, Melbourne, Australia
[2]University of Western Australia, Perth, Australia
[3]Rzhanov Institute of Semiconductor Physics, Novosibirsk, Russian Federation
[4]Sobolev Institute of Geology and Mineralogy, Novosibirsk, Russian Federation

sergey@unimelb.edu.au
Keywords: diamond, ion implantation, graphitisation

Ion implantation has been successfully employed for fabrication of ultra-thin diamond films and in combination with Ga focused ion beam (FIB) technique for fabrication of device structures in diamond at submicron level [1, 2]. FIB technique could be also used as ion implantation tool in diamond for fabrication of buried amorphous layers and cap diamond layers with thickness of few nanometers [3]. The graphitisation of these amorphous layers is attracting significant interest due to ability to fabricate device structures containing two stable structural forms of carbon: diamond and graphite. In the present work we have performed 30 keV Ga^+ FIB implantation into (001) and (111) synthetic diamond samples and have examined the structure of the implanted regions after implantation and after HPHT annealing by means of TEM.

For the lowest dose 3×10^{14} ions/cm^2 implanted region in (001) sample is metastable and contains islands of amorphous and crystalline materials between two interfaces of distorted diamond (Figure 1a). The swelling of implanted region was not observed which indicates the same density of implanted layer and bulk diamond. The implanted regions have been found to be amorphous with corresponding density reduction and swelling for the dose 4×10^{14} ions/cm^2 and above in (001) diamond and for all doses in (111) sample. HPHT annealing resulted in re-ordering of amorphous and crystalline components in the region implanted with dose 3×10^{14} ions/cm^2 ((001) sample) and formation of sharp interfaces parallel to (111) planes (Figure 1b). For all other fluences and both sample orientations HPHT annealing resulted in graphitisation of implanted layers with predominant orientation of graphene planes parallel to (111) diamond planes (Figure 2).

1. P. Olivero, S. Rubanov, P. Reichart, B. C. Gibson, S. T. Huntington, J. R. Rabeau, A. D. Greentree, J. Salzman, D. Moore, D. N. Jamieson, S. Prawer, Diamond & Related Materials 15 (2006), p. 1614.
2. B. A. Fairchild P. Olivero, S. Rubanov, A. D. Greentree, F. Waldermann, R. A. Taylor, I. Walmsley, J. M. Smith, S. Huntington, B. C. Gibson, D. N. Jamieson and S. Prawer, Advanced Materials, 20 (2008), p. 4793.
3. S. Rubanov, and A. Suvorova, Diamond and Related Materials, 20 (2011), p. 1160.

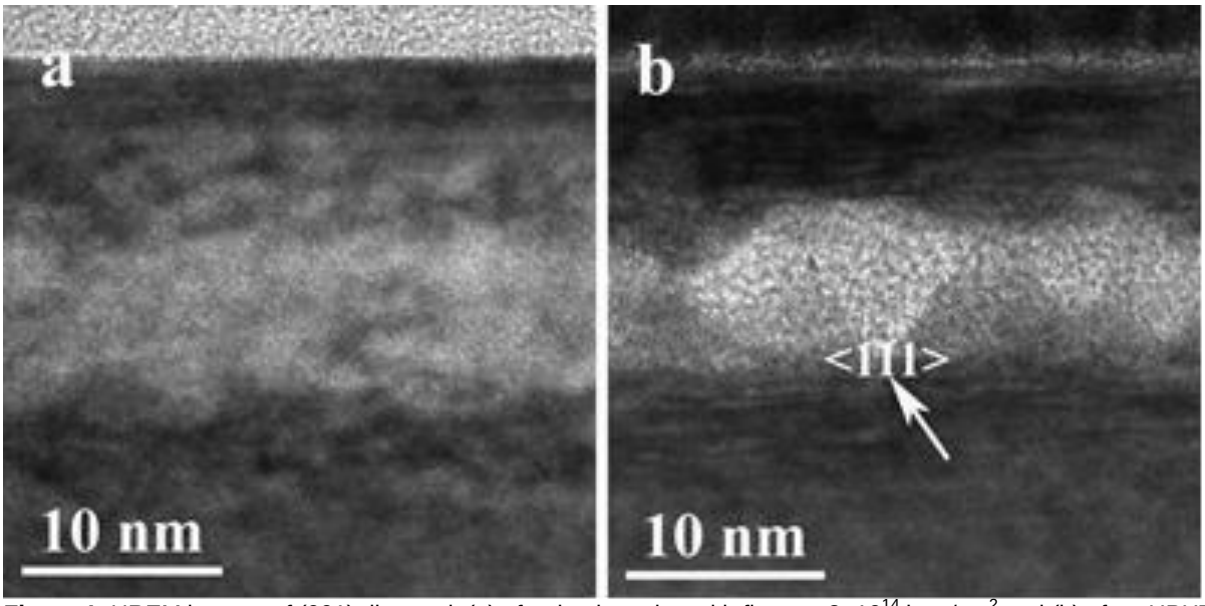

Figure 1. HREM images of (001) diamond (a) after implantation with fluence 3×10^{14} ions/cm^2 and (b) after HPHT annealing.

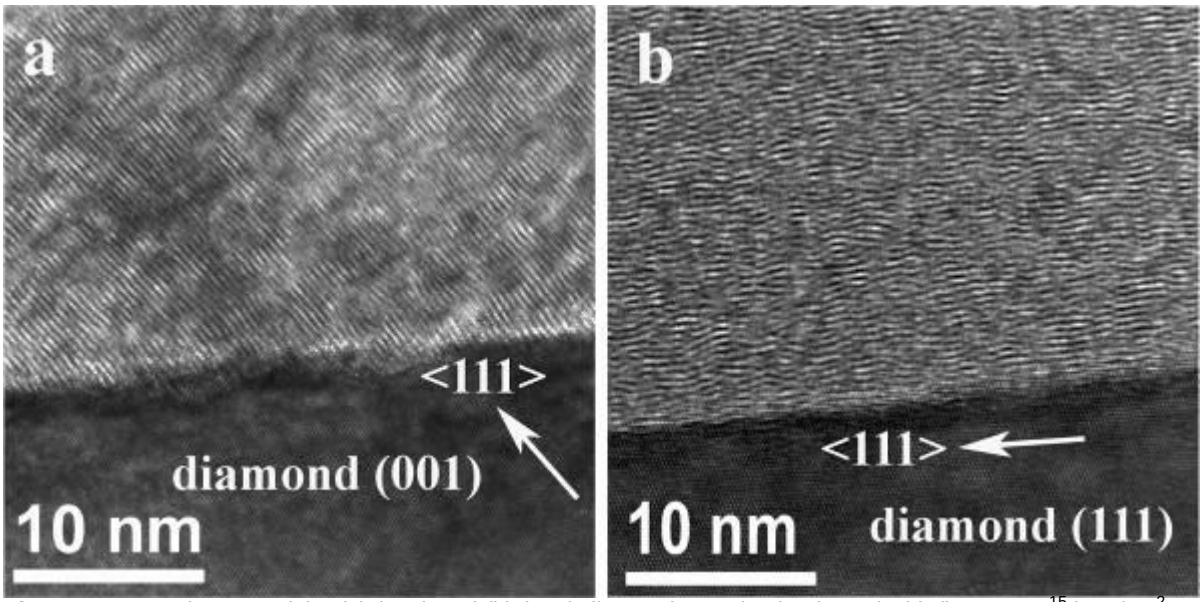

Figure 2. HREM images of the (a) (001) and (b) (111) diamond samples implanted with fluence 10^{15} ions/cm^2 and HPHT annealed at 1200 ^{o}C and 4 GPa.

3D in SEM, (S)TEM, Ion Imaging, incl. FIB-SEM and SBF-SEM

LBP.MIM.P10
3D visualization of HIV-1 in mature dendritic cells.

K. Höhn[1], M. Anders-Össwein[1], C. Kranz[2], B. Müller[1], P. Walther[3], H.-G. Kräusslich[1]

[1]University Hospital Heidelberg, Infectious Diseases, Virology, Heidelberg, Germany
[2]Ulm University, Institute of Analytical and Bioanalytical Chemistry, Ulm, Germany
[3]Ulm University, Central Facility of Electron Microscopy, Ulm, Germany

katharina.hoehn@bioquant.uni-heidelberg.de

Dendritic cells are potent antigen-presenting cells and play a unique role in initiating the primary immune response. HIV-1 has developed strategies to subvert the dendritic cell antiviral activity. HIV-1 virions specifically bind SIGLEC-1 on the mature dendritic cell (mDC) surface and are captured and stored in these cells *via* a non-infectious pathway. Particles stored in mDCs can subsequently be transferred to susceptible T-cells in a process called *trans*-infection. Light microscopy revealed captured HIV-1 Gag virus like particles (VLPs) accumulating in a large, apparently intracellular sac-like compartment [1]. The nature of this compartment is so far unknown. Here we investigated the DC ultrastructure using scanning transmission electron tomography (STEM) and focused ion beam milling combined with scanning electron tomography (FIB/SEM). These methods allow 3D analysis of cellular structures with comparable resolution as transmission electron microscopy (TEM) [2].

Peripheral blood mononuclear cells were isolated from blood of HIV-1-seronegative donors and $CD14^+$ populations were cultivated in the presence of granulocyte-macrophage colony-stimulating factor and interleukin-4 to differentiate DCs. Maturation was induced by stimulation with lipopolysaccharide. mDCs were incubated for 5 h with 50-100 ng HIV-1 VLPs fluorescently labeled by enhanced green fluorescent protein (eGFP) inserted into the structural Gag polyprotein ($VLP_{HIV\text{-}Gag\text{-}eGFP}$). Subsequently, cells were seeded on top of 160 µm thick carbon-coated, glow-discharged and PEI-coated sapphire discs 30 min before high pressure freezing (HPF010, Bal-tec). The frozen samples were freeze substituted (AFS2, Leica, Germany) in acetone, uranyl acetate, osmium tetroxide and 5% of water and embedded in Epon. STEM tomography and FIB/SEM tomography were carried out as described earlier [2, 3]. In addition, mDCs were seeded on glass coverslips and fixed with PFA for confocal imaging.

Confocal microscopy analysis (SP2, Leica, Germany) of mDCs showed that internalized $VLP_{HIV\text{-}Gag\text{-}eGFP}$ accumulated in a large, apparently intracellular compartment (Figure 1A). The captured $VLPs_{HIV\text{-}Gag\text{-}eGFP}$ within this compartment could also be visualized in 80 nm thick sections by TEM (EM10, Zeiss, Germany) (Figure 1B). Although, the ultrastructure of the compartment is perceptible by TEM analysis, the dimensions of the storage compartment as well as its potential connection to the plasma membrane remain unclear. Hence, we applied STEM tomography of 1 µm thick sections using a Titan microscope (FEI, Eindhoven, The Netherlands) to investigate the 3D architecture of the capture compartment. Accumulation of $VLP_{HIV\text{-}Gag\text{-}eGFP}$ within an intracellular compartment could be visualized over the entire tomographic reconstruction (Figure 1 C), but the size of the storage compartment extended the thickness of the respective section. For a more complete reconstruction, FIB/SEM was performed using a Helios Nanolab 600 (FEI, Eindhoven, The Netherlands). Preliminary results obtained on a single cell revealed well-resolved $VLP_{HIV\text{-}Gag\text{-}eGFP}$ in close proximity to the plasma membrane (Figure 1D), but the particular cell chosen for analysis did not display uptake of HIV-1 particles into an intracellular compartment.

We show here that STEM tomography and FIB/SEM approaches can be successfully used to analyze the architecture of the HIV-1 storage compartment within mDCs. In our further experiments we will characterize the ultrastructure of this compartment and investigate its potential connection to the plasma membrane.

1. N. Izquierdo-Useros, M. Lorizate, F.-X. Contreras, et al., PLoS Biol 10 (2012), pp. 1-15.
2. C. Villinger, H. Gregorius, Ch. Kranz, et al., Histochem Cell Biol 138 (2012), pp. 549-556.
3. K. Höhn, M. Sailer, L. Wang, et al., Histochem Cell Biol 135 (2011), pp. 1-9.
4. We kindly acknowledge Jacomine Krijnse-Locker for valuable discussions, Androniki Kolovou and Eberhard Schmid for expert technical assistance and Walter Muranyi for providing confocal images.

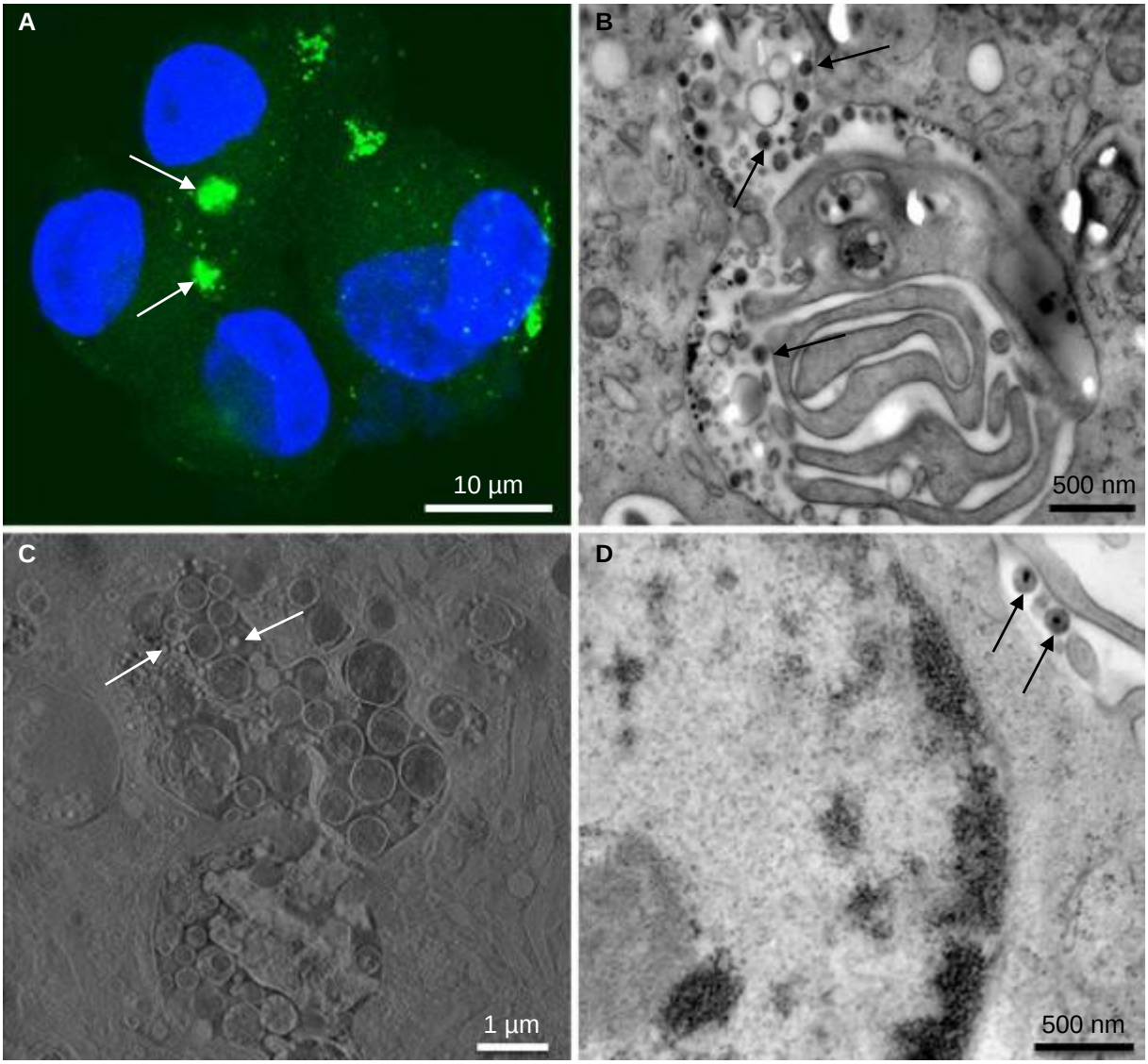

Figure 1. mDCs with internalized $VLP_{HIV\text{-}Gag\text{-}eGFP}$. (A) Confocal image of a z-stack displaying the captured $VLP_{HIV\text{-}Gag\text{-}eGFP}$ aggregated within an intracellular compartment (green fluorescent signal) (white arrows) besides a DAPI-stained nucleus (blue fluorescent signal). (B) TEM image of a 80 nm section of a mDC. A compartment including $VLP_{HIV\text{-}Gag\text{-}eGFP}$ (black arrows) is visible within the cell. (C) Virtual section of a STEM tomogram of a 1 µm thick section. A compartment with stored $VLP_{HIV\text{-}Gag\text{-}eGFP}$ (white arrows) can be visualized in the tomographic reconstruction. (D) FIB/SEM image of a $VLP_{HIV\text{-}Gag\text{-}eGFP}$ incubated mDC. Well-resolved $VLPs_{HIV\text{-}Gag\text{-}eGFP}$ (black arrows) can be found in close proximity to the plasma membrane.

Open Topics

LBP.MIM.P11
Multidimensional image analysis with a flexible sequence of operators and cluster computing

D. Haumann[1], J. van Wezel[2], F. Pampaloni[3], C. Mattheyer[3], E.H.K. Stelzer[1], S. Pfeiffer [1]

[1]da-cons GmbH, Karlsruhe (Eggenstein-Leopoldshafen), Germany
[2]Karlsruhe Institute of Technology (KIT), Steinbuch Centre for Computing (SCC), Karlsruhe (Eggenstein-Leopoldshafen), Germany
[3]Goethe University Frankfurt am Main, Buchmann Institute for Molecular Life Sciences (BMLS), Frankfurt am Main, Germany

david.haumann@da-cons.de
Keywords: image analysis, big data, microscopy, cluster computing

Expanding research possibilities and experiment schemes with High Technology Image Analysis Service

Advance in development of image acquisition methods led to an explosion of image data volume. Due to multidimensional recording of biological samples in life sciences, e.g. different color channels, different excitation wavelength, different angles of detection and illumination, extension to the third dimension by generation of image stacks (z-stacks) cause single time point image data volume up to several gigabytes. Extreme examples in light sheet microscopy even give rise to 100 GB per time point. In material science or quality control of components with safety relevance, in industry, tomography can generate terabyte data volume with high resolution per single component control.

Explosion in data volume caused a bottle neck in image data processing, visualization and analysis for experiments and control steps. Computing power, image analysis and data management expertise easily become an expensive and difficult to get requirement for further progress in research or increase of productivity in industry.

This poster presents a solution to eliminate these bottle necks. Complex image analysis and high data volume through put can be managed with the help of the High Technology Image Analysis Service from da-cons (figure 1). The customer explains the desired information in the image data, transfers the image data to the provider and gets back extracted information, statistics, visualizations or videos. The usage of external partner eliminates the necessity to invest in own expensive hardware. It accelerates the process and the development of methods for resolution of new tasks, because well-educated and highly specialized stuff for image analysis is concentrated in one institution [1, 2].

Customers can benefit from a foreign and proven algorithm pool as well as bring their own algorithms or offer them via da-cons to third parties. The speed of analysis can be massively increased with cluster computing and access to computing centres.

Depending on the image quality, a variety of features in objects can be identified, measured and analysed. Cells or objects with a certain repetitive pattern can be automatically identified (segmented), surface area can be measured, volume determined and movements can be tracked.

In figure 2 one can see the analysis of a ceramic sample. It is a task in the field of material science to figure out correlations between the micro structure and the material properties. With flexible image analysis, identification and quantity of special grain or crystal shape, size as well as their orientation in the sample helps to find relevant characteristics for desired material properties [3, 4].

The second example in figure 3 shows a large spheroid from human cell line. A 2D image slice from a 3D z-stack is showed. Analysis of 3D spheroids can help to identify effects of chemicals, drugs or any kind of molecules on the cell shape, cell quantity, distances between cells and effects in the spatial anatomy of the spheroid. Potential applications are manifold and range from drug screen before cancer therapy in personalized medicine to research about anti-angiogenesis agents for pharmacy. The da-cons system (dcs) allows identification and quantification of the cells, evaluation for shape parameters, measurement of distances and thus to get information about effects of molecules on the cells, e. g. cancer cells [5, 6].

1. A. Garcia et al. "The large scale data facility: data intensive computing for scientific experiments." *Parallel and Distributed Processing Workshops and Phd Forum (IPDPSW), 2011 IEEE International Symposium on*. IEEE.
2. J. van Wezel et al. "Data Life Cycle Labs, A New Concept to Support Data-Intensive Science." *arXiv preprint* (2012).
3. F. Weygand and M. Syha. "Conditions for the Occurrence of Abnormal Grain Growth Studied by a 3 D Vertex Dynamics Model.". *Materials Science Forum*, (2012), p. 563-567.
5. M. Syha et al. "Validation of three-dimensional diffraction contrast tomography reconstructions by means of electron backscatter diffraction characterization." *Journal of Applied Crystallography* 46.4, (2013), p. 1145-1150.
6. F. Pampaloni, *Recent Patents on Biotechnology 3.2*, (2009), p. 103-117.
7. F. Pampaloni, E.G. Reynaud, and E.H.K. Stelzer, "The third dimension bridges the gap between cell culture and live tissue.", *Nat Rev Mol Cell Biol*, (2007), 8(10): p. 839-845.

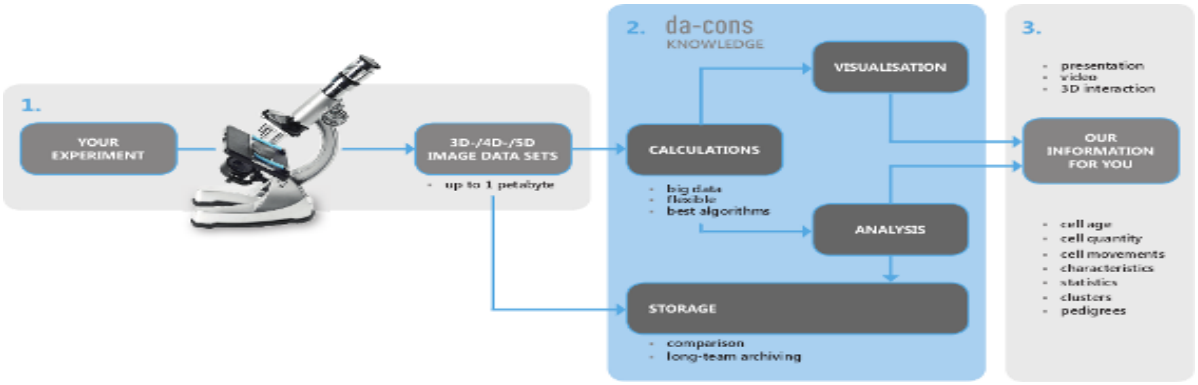

Figure 1. Process flow of High Technology Image Analysis Service, da-cons system (dcs), to eliminate bottle necks image analysis and data management expertise and computing power [1, 2]

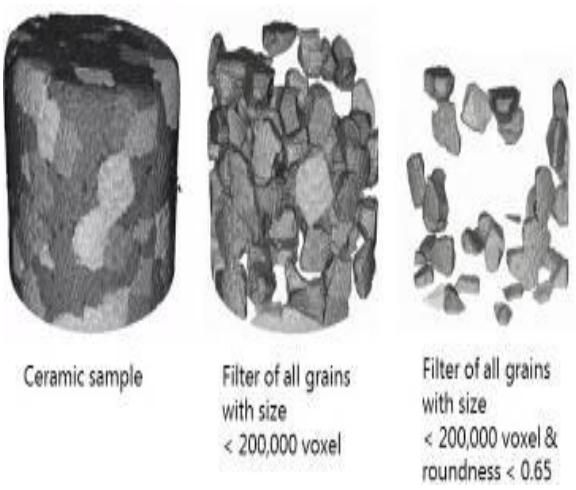

Figure 2. Analysis of crystals in ceramic sample [3]. Image acquisition: CT. Objective is to find correlations of crystal size and shape with material properties**. Left:** ceramic sample. Middle: ceramic sample, crystals with size > 200.000 voxel shown. **Right:** Crystals with size > 200.000 voxel and roundness<0.65 shown [3, 4].

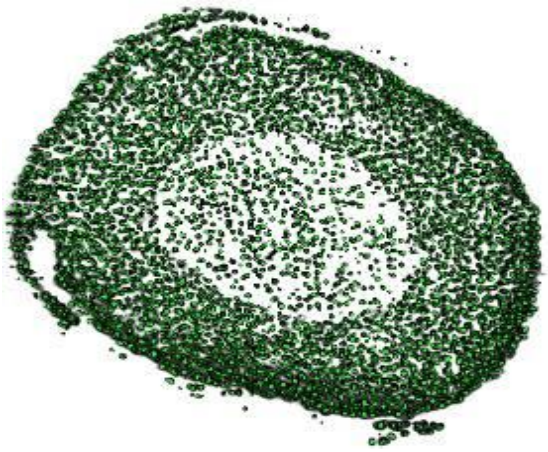

Figure 3. Cellular spheroid of human cells. Image acquisition with mDSLM (monolithic Digital Scanned laser Light-sheet fluorescence Microscope) [5, 6]

Open Topics

LBP.MIM.P12
Big data in microscopy

C. Schmidt[1], J. van Wezel[2], G. Günay[1], S. Pfeiffer [1]

[1]da-cons GmbH, Karlsruhe (Eggenstein-Leopoldshafen), Germany
[2]Karlsruhe Institute of Technology (KIT), Steinbuch Centre for Computing (SCC), Karlsruhe (Eggenstein-Leopoldshafen), Germany

christian.schmidt@da-cons.de
Keywords: image analysis, big data set, microscopy, cluster computing, high content screening

What do scientists and companies do with their large image data sets?

Modern microscopy methods and high content screening methods produce big image data sets and impose challenging image analysis tasks on researchers and companies. On the one hand, new image acquisition methods offer scientists the opportunity to get new scientific findings. Companies can introduce imaging methods for detailed quality control, which is especially important for safety relevant components.

Time lapses acquired with multidimensional imaging methods like light sheet fluorescence microscopes or confocal laser microscopes enable scientists to get insights into dynamic processes of development and change in biological samples. That is a highly interesting tool to understand processes in developmental biology or tissue dynamics much better than before. The other side of the coin is, that experimenters face a tsunami of image data as well as meta data.

Handling of data, transfer to computing units, application of algorithms, visualization of single volume data sets with tens of GB requires means, that life science research groups need to invest in employees with core IT, informatics and image analysis core-competence, far from the original core competence concerning scientific questions the working group is focusing on.

Figure 1 shows the analysis from developmental stages in Zebrafish Danio rerio [1]. Repetitive image acquisition every two minutes gives rise to a large volume time lapse data set. From this time series it is possible to identify the cells, install a cell tracking, analyse the quantity of progenitors for organs like for example parts of the brain. Statistics about cell quantity of organ progenitors in different time stages as well as size of cells can be generated. Via repetition of such experiments standardization of development processes or status in defined time points allow statistical analysis of effects from drugs, toxins or any molecule on the normal development. Change or influence on organs can be detected within very early stages of development. A method that can be further developed to sophisticated screening methods in the future [1, 2].

Figure 2 shows the visualization and analysis of a cellular spheroid of BxPC3 human pancreatic cancer cells with nuclear staining [2]. Image acquisition is done with a Selective Plane Illumination Microscope. In a first step, background noise was removed via algorithms. Second, nuclei were identified by segmentation which allows quantification of the cell number within spheroids. Features like sizes, volumes, surface areas, distances between nuclei and cluster can be identified [3, 4].

1. B. Wetterauer et al. "Toxicity, dioxin-like activities, and endocrine effects of DDT metabolites—DDA, DDMU, DDMS, and DDCN." *Environmental Science and Pollution Research* 19.2, (2012), p. 403-415.
2. Garcia, A. O., et al. "Data-intensive analysis for scientific experiments at the Large Scale Data Facility." *Large Data Analysis and Visualization (LDAV), 2011 IEEE Symposium on*. IEEE, (2011), p. 125-126
3. F. Pampaloni, Recent Patents on Biotechnology 3.2, (2009), p. 103-117
4. F. Pampaloni and E.H.K. Stelzer, "Three-dimensional cell cultures in toxicology." *Biotechnology and Genetic Engineering Reviews* 26.1, (2009), p. 117-138.

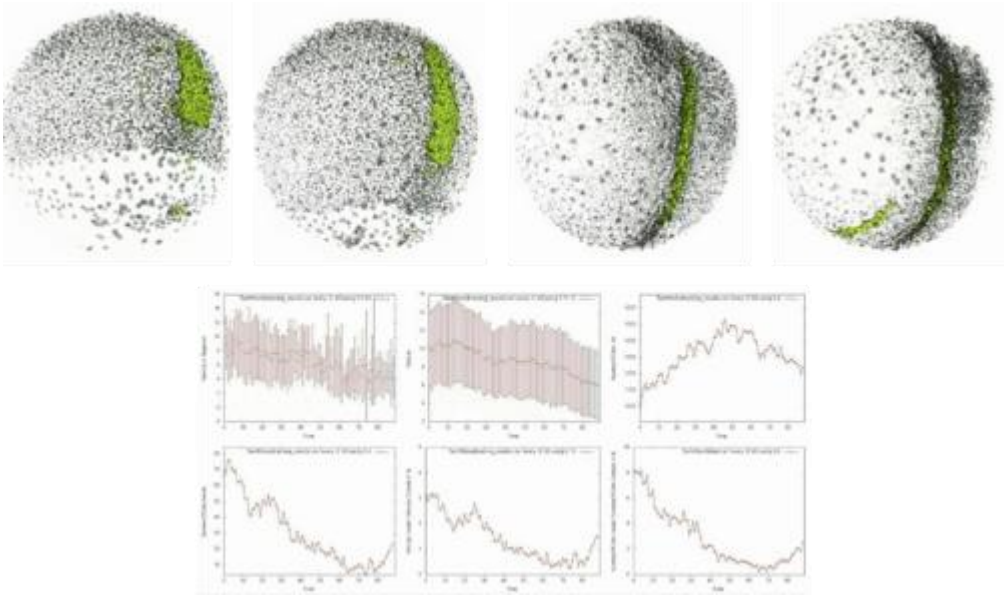

Figure 4. Time series embryonic development of a zebrafish; Green labeled cells later form the midbrain; Statistics on cell size, cell number, ratio of cells in the midbrain compared to the rest; Possible use: measurement of effects of molecules/chemicals on embryonic phase [1, 2]

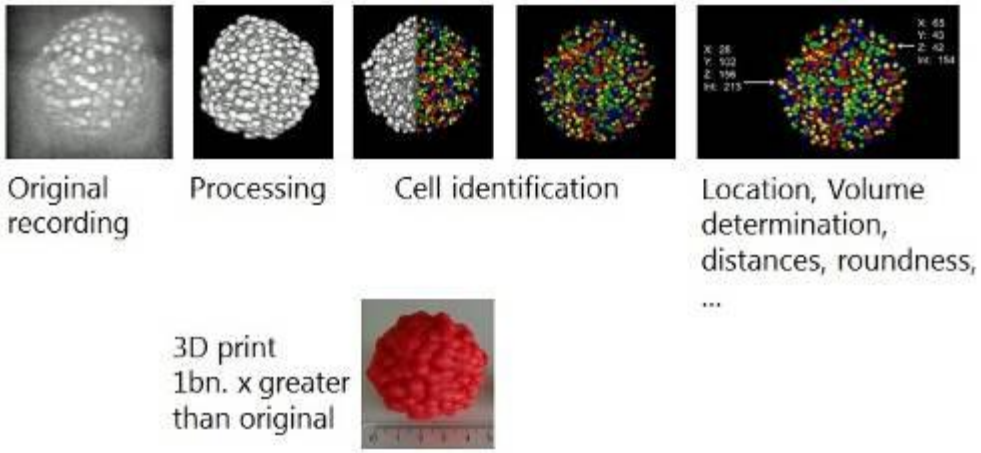

Figure 2. Cellular spheroid of BxPC3 human pancreatic cancer cells [3, 4]. Image acquisition with SPIM (Selective Plane Illumination Microscope). Left: Original image data set, followed by elimination of background noise. Next two images show segmentation, the process that identifies the cell nuclei. Right: Position and statistic about each cell. Picture in second row: red colored 3D print of the spheroid.

Author Index

Author Index

Author Index

Author Index

Author Index

Author Index

L

Author Index

Author Index

Author Index

Author Index

Author Index

Author Index

Author Index